Astrophysics and Space Science Library 407

Alexander Lazarian
Elisabete M. de Gouveia Dal Pino
Claudio Melioli *Editors*

Magnetic Fields in Diffuse Media

ASSL

Springer

Magnetic Fields in Diffuse Media

Astrophysics and Space Science Library

More information about this series at
http://www.springer.com/series/5664

Alexander Lazarian •
Elisabete M. de Gouveia Dal Pino • Claudio Melioli
Editors

Magnetic Fields in Diffuse Media

Springer

Editors
Alexander Lazarian
Department of Astronomy
University of Wisconsin-Madison
Madison, WI, USA

Elisabete M. de Gouveia Dal Pino
Instituto de Astronomia, Geofísica e
Ciências Atmosféricas
Universidade de São Paulo
São Paulo, SP, Brazil

Claudio Melioli
Instituto de Astronomia, Geofísica e
Ciências Atmosféricas
Universidade de São Paulo
São Paulo, SP, Brazil

ISSN 0067-0057 ISSN 2214-7985 (electronic)
ISBN 978-3-662-44624-9 ISBN 978-3-662-44625-6 (eBook)
DOI 10.1007/978-3-662-44625-6
Springer Heidelberg New York Dordrecht London

Library of Congress Control Number: 2014955399

Cover illustration: A simulation of magnetic reconnection.

Printed on acid-free paper

Springer is part of Springer Science+Business Media (www.springer.com)

Preface

Astrophysical plasmas are magnetized and turbulent and this presents a serious challenge for studying such a media. For decades turbulent astrophysical magnetic fields were completely enigmatic and this was constraining the progress in understanding key astrophysical processes. In particular, in diffuse media, the processes of cosmic ray propagation, heat transport, formation of a variety of density structures, filaments, molecular clouds, etc. were treated using poorly constrained values of magnetic fields and somewhat ad hoc models of magnetic turbulence. The essential processes related to magnetic fields, for instance, the ability of magnetic fields to change their topology, i.e. magnetic reconnection, were hotly debated with the estimates of the rates used by different researchers varying by many orders of magnitude.

A substantial progress has been made in the field of magnetic fields in diffuse media in the last decade. The new observations allowed to map magnetic fields with higher precision, which affected substantially our understanding of the role of magnetic fields in the interstellar medium and intracluster medium. With better computational abilities it became possible to test and reject theories of key processes in magnetized media. In particular, essential progress has been achieved in understanding the origin and evolution of magnetic fields, in the theory of magnetic field generation, in the physics of magnetic reconnection, acceleration and propagation of cosmic rays in turbulent magnetized media.

Recent research reveals strong synergy between different branches of research of magnetized media. For instance, in some cases, high resolution observation available for interstellar medium makes it an important testing ground for theories related to magnetic fields. These theories can then be applied to a wide variety of magnetic phenomena related to physics of magnetic phenomena in compact sources, gamma ray bursts, stellar activity, galaxies, galaxy clusters, etc.

This volume presents the current knowledge of magnetic fields in diffuse astrophysical media. Starting with an overview of twenty-first century instrumentation to observe astrophysical magnetic fields, the chapters cover observational techniques, origin of magnetic fields, magnetic turbulence, basic processes in magnetized fluids, the role of magnetic fields for cosmic rays, in the interstellar medium and for star

formation. Written by a group of leading experts the book represents an excellent overview of the field. Non-specialists will find sufficient background to enter the field and to be able to appreciate the state of the art.

Madison, WI, USA — Alexander Lazarian
São Paulo, SP, Brazil — Elisabete M. de Gouveia Dal Pino
May 2014 — Claudio Melioli

Contents

Part V MFs in Star Formation Regions

Part I
Current and Forthcoming Observing Facilities

Chapter 1
Future Observations of Cosmic Magnetic Fields with LOFAR, SKA and Its Precursors

Rainer Beck

Abstract Polarization observations with the forthcoming large radio telescopes will open a new era in the observation of magnetic fields and should help to understand their origin. Low-frequency radio synchrotron emission from the Milky Way, galaxies and galaxy clusters, observed with the new Low Frequency Array (LOFAR) and the planned Square Kilometre Array (SKA), traces low-energy cosmic ray electrons and allows us to map the structure of weak magnetic fields in the outer regions and halos of galaxies, in halos and relics of clusters and in the Milky Way. Polarization at higher frequencies (1–10 GHz), to be observed with the SKA and its precursors Australia SKA Pathfinder (ASKAP) and the South African MeerKAT telescopes, will trace magnetic fields in the disks and central regions of galaxies and in cluster relics in unprecedented detail. All-sky surveys of Faraday rotation measures towards a dense grid of polarized background sources with ASKAP (project POSSUM) and the SKA are dedicated to measure magnetic fields in intervening galaxies, clusters and intergalactic filaments, and will be used to model the overall structure and strength of magnetic fields in the Milky Way. Cosmic magnetism is "key science" for LOFAR, ASKAP and the SKA.

1.1 Prospects of Future Magnetic Field Observations

1.1.1 Diffuse Polarized Emission

Synchrotron radiation and Faraday rotation (see also Chap. 3) revealed magnetic fields in our Milky Way, nearby spiral galaxies and in galaxy clusters (see also Chaps. 18 and 20), while little is known about magnetic fields in the intergalactic medium. Furthermore, the origin and evolution of galactic magnetic fields are still mostly unknown. The next-generation radio telescopes will widen the range of observable magnetic phenomena. SKA (Sect. 1.4) and its precursor telescopes ASKAP and MeerKAT (Sect. 1.5) will measure diffuse synchrotron emission from

R. Beck (✉)
Max-Planck-Institut für Radioastronomie, Auf dem Hügel 69, 53121 Bonn, Germany
e-mail: rbeck@mpifr-bonn.mpg.de

A. Lazarian et al. (eds.), *Magnetic Fields in Diffuse Media*, Astrophysics and Space Science Library 407, DOI 10.1007/978-3-662-44625-6_1

the Milky Way, nearby galaxies and nearby clusters of galaxies. As Faraday depolarization increases towards lower frequencies, polarized emission can hardly be detected from the star-forming disks of galaxies at frequencies below about 300 MHz (Arshakian et al. 2011). On the other hand, polarized and unpolarized synchrotron emission at low frequencies should be observable from aging, low-energy electrons that have propagated far away from their places of origin. Hence, LOFAR (Sect. 1.3) is a suitable instrument to search for weak magnetic fields in outer galaxy disks, galaxy halos and halos of galaxy clusters (Anderson et al. 2012). "Relics" in galaxy clusters, probably signatures of huge shock fronts, have steep radio spectra and may become prominent in LOFAR's frequency range (Brunetti et al. 2008).

Deep high-resolution observations at high frequencies, where Faraday effects are small, require a major increase in sensitivity of continuum observations, which can be achieved by the SKA. In this way the detailed structure of the magnetic fields in the ISM of galaxies, in galaxy halos, cluster halos and cluster relics can be observed and the magnetic power spectra measured (Vogt and Enßlin 2005). Direct insight into the interaction between gas and magnetic fields in these objects will become possible. The SKA will also allow measurement of the Zeeman effect of weak magnetic fields in the Milky Way and in nearby galaxies.

Detection of polarized emission from distant, unresolved galaxies can reveal large-scale ordered fields (Stil et al. 2009), to be compared with the predictions of dynamo theory (Arshakian et al. 2009). The SKA should be able to detect Milky-Way type galaxies out to $z \leq 1.5$ (Fig. 1.1) and their polarized emission out to $z \leq 0.5$ (assuming 10 % polarization). Cluster "relics" are highly polarized (van Weeren et al. 2010) and will be detectable at large redshifts.

Bright starburst galaxies are not expected to host ordered fields. Unpolarized synchrotron emission from starburst galaxies, signature of turbulent magnetic fields, should be detected with the SKA out to large redshifts, depending on luminosity and magnetic field strength (Fig. 1.1), and from cluster halos. However, for fields

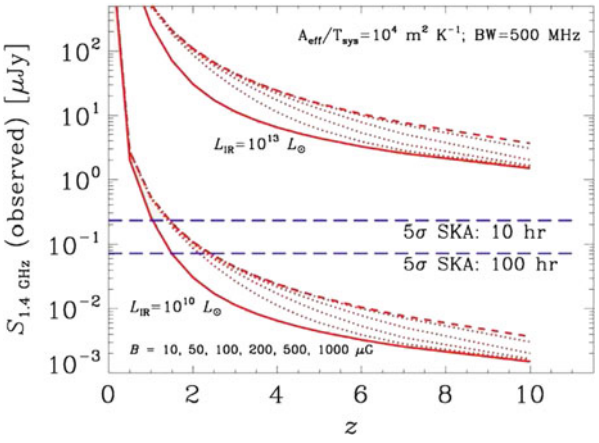

Fig. 1.1 Total synchrotron emission of galaxies at 1.4 GHz as a function of redshift z and magnetic field strength B, and the 5σ detection limits for 10 and 100 h integration time with the SKA (Murphy 2009)

weaker than 3.25 μG $(1+z)^2$, energy loss of cosmic-ray electrons is dominated by the inverse Compton effect with CMB photons, so that the energy appears mostly in X-rays, not in the radio range. On the other hand, for strong fields the energy range of the electrons emitting at a 1.4 GHz drops to low energies, where ionization and bremsstrahlung losses become dominant (Murphy 2009). In summary, the mere detection of synchrotron emission of galaxies at high redshifts would constrain the range of allowed magnetic field strengths.

1.1.2 Rotation Measure Grids

Faraday rotation is another powerful tool to detect cosmic magnetic fields. The Faraday rotation angle $\Delta\chi$ of the polarization plane is proportional to the *Faraday depth (FD)*, defined as the line-of-sight integral over the product of the plasma density and the strength of the field component along the line of sight. If the rotating region is located in front of the emitting region (*Faraday screen*), *RM* and *FD* are identical. Multiple emitting and rotating regions located along the line of sight generate a spectrum of FD components. In such cases, RM Synthesis is needed (Sect. 1.2 and Chap. 3).

If diffuse polarized emission is too weak to be detected, the method of *RM grids* towards background QSOs can still be applied and allows us to determine the field strength and pattern in the intervening objects, such as distant spiral galaxies, clusters and intergalactic filaments. Because the Faraday rotation angle increases with the square of wavelength, low frequencies are also ideal to search for small Faraday rotation measures from weak interstellar and intergalactic fields.

This method can be applied to distances of very distant QSOs ($z \simeq 5$). Regular fields of several μG strength were already detected in distant, intervening galaxies (Bernet et al. 2008, 2013; Kronberg et al. 2008). Mean-field dynamo theory predicts RMs from evolving regular fields with increasing coherence scale at $z \leq 3$ (Arshakian et al. 2009). A reliable model for the field structure of nearby galaxies, cluster halos and cluster relics needs RM values from a large number of polarized background sources, hence large sensitivity and high survey speed (Krause et al. 2009). As the observed RM values are reduced by the redshift dilution factor of $(1+z)^{-2}$, high precision of RM measurements is required (Sect. 1.2).

The *POSSUM* all-sky survey at 1.1–1.4 GHz with the ASKAP telescope (Sect. 1.5) with about 30 deg^2 field of view is expected to measure about 100 RMs of extragalactic sources per square degree within 10 h integration time.

The *SKA Magnetism Key Science Project* plans to observe a wide-field survey (at least 10^4 deg^2) around 1 GHz with 1 h integration per field which should detect sources of 0.5–1 μJy flux density and measure at least 1500 RMs deg^{-2}, or a total of at least 1.5×10^7 RMs from compact polarized extragalactic sources at a mean spacing of $\simeq 90''$ (Gaensler et al. 2004). This survey will be used to model the structure and strength of the magnetic fields in the Milky Way, in intervening

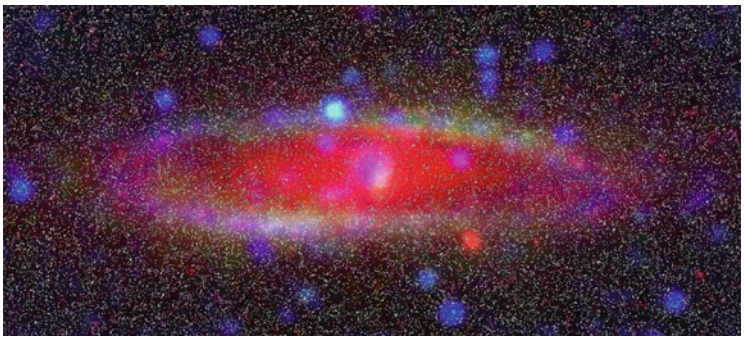

Fig. 1.2 Simulation of RMs towards background sources (*white points*) in the region of M 31 observable with the SKA within 1 h. Optical emission from M 31 is shown in *red*, diffuse radio continuum intensity in *blue* and diffuse polarized intensity in *green* (from Gaensler, priv. comm.)

galaxies and clusters and in the intergalactic medium (Beck and Gaensler 2004). More than 10,000 RM values are expected in the area of the galaxy M 31 and will allow the detailed reconstruction of the 3-D field structure (Fig. 1.2). Simple patterns of regular fields can be recognized out to distances of about 100 Mpc (Stepanov et al. 2008) where the polarized emission is far too low to be mapped. The evolution of field strength in cluster halos can be measured by the RM grid method to redshifts of about one (Krause et al. 2009).

1.1.3 Magnetic Fields of the Milky Way

LOFAR will detect almost all pulsars within 2 kpc of the Sun and discover about 1,000 new nearby pulsars, especially at high latitudes (van Leeuwen and Stappers 2010). Most of these are expected to emit strong, linearly polarized signals at low frequencies. This should allows us to measure their RMs and to derive the Milky Way's magnetic field structure near to the Sun. The SKA pulsar survey should find about 20,000 new pulsars which will mostly be polarized and reveal RMs (Fig. 1.3), suited to map the Milky Way's magnetic field with even higher precision.

The SKA and its precursor telescopes will also map out magnetic fields in gas clouds, HII regions, planetary nebulae and supernova remnants, in the Milky Way, via the Zeeman effect, polarized emission and Faraday rotation.

1.1.4 Intergalactic Filaments

If the filaments of the local Cosmic Web outside clusters contain a magnetic field (Ryu et al. 2008), possibly enhanced by IGM shocks, we hope to detect this field by

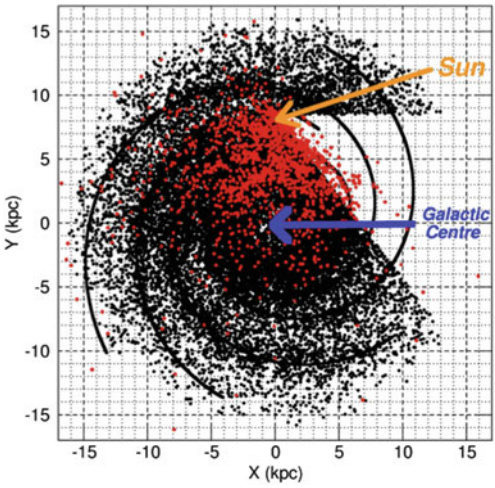

Fig. 1.3 Known pulsars in the Milky Way (*red*) and pulsars expected with the SKA (*black*). Simulation: Michael Kramer, MPIfR Bonn

direct observation of its total synchrotron emission (Keshet et al. 2004) and possibly its polarization, or by Faraday rotation towards background sources. For fields of $\approx 10^{-8}$–10^{-7} G with 1 Mpc coherence length and $n_e \approx 10^{-5}\,\mathrm{cm}^{-3}$ electron density, Faraday rotation measures between 0.1 and 1 rad m^{-2} are expected which will be challenging to detect even with LOFAR. Promising is a statistical analysis like the measurement of the power spectrum of the magnetic field of the Cosmic Web (Kolatt 1998) or the cross-correlation with other large-scale structure indicators like the galaxy density field (Stasyszyn et al. 2010).

If an overall IGM field with a coherence length of a few Mpc existed in the early Universe and its strength varied proportional to $(1+z)^2$, its signature may become evident at redshifts of $z > 3$. Averaging over a large number of RMs is required to unravel the IGM signal. The goal is to detect an IGM magnetic field of 0.1 nG, which needs an RM density of $\approx$ 1,000 sources deg^{-2} (Kolatt 1998), achievable with the SKA. Detection of a general IGM field, or placing stringent upper limits on it, would provide powerful observational constraints on the origin of cosmic magnetism.

1.2 Faraday Rotation Measure Synthesis

Modern radio telescopes are equipped with digital correlators that allow us to record a large number of spectral channels. While radio spectroscopy in total intensity is well-developed, the possibilities of spectropolarimetry in radio continuum have been explored for only a few years. The fundamentals were presented by Burn (1966), the first application to multi-channel polarization data (data cubes) by Brentjens et al. (2005). If the medium has a relatively simple structure, the 3-D structure of the magnetized interstellar medium can be determined (*Faraday tomography*).

Faraday Rotation Measure Synthesis ("RM Synthesis") Fourier-transforms the observed polarized intensity the "Faraday dispersion into function" or, in short, the "Faraday spectrum" $F(\phi)$, which is the (complex-valued) polarized intensity spectrum as a function of "Faraday depth" ϕ (see Chap. 3). As in classical spectroscopy, the interpretation of this spectrum is not straightforward. In particular, there is no simple relation between Faraday depth and geometrical depth. Furthermore, the Faraday spectrum suffers from sidelobes of the main components caused by limited coverage of the wavelength space.

RM Synthesis is characterized by four basic parameters (Beck et al. 2012; Brentjens et al. 2005):

- The resolution $\delta\phi$ in Faraday space, which is inversely proportional to the coverage $\Delta\lambda^2$ in wavelength (λ^2) space;
- the maximum observable $|\phi_{\max}|$ of point-like sources in Faraday space, which is inversely proportional to the width of a single frequency channel;
- the maximum width $|\Delta\phi_{\max}|$ of extended structures in Faraday space (Faraday-rotating *and* synchrotron-emitting regions), which is inversely proportional to the square of the minimum observation wavelength. Wide-band observations at long wavelengths yield high resolution in Faraday space but cannot detect extended structures;
- the ratio of maximum to minimum wavelengths which is crucial to recognize a range of different scales in Faraday space.

Table 1.1 summarizes the properties of the present-day and future radio telescopes. The highest resolution in Faraday space (largest $\Delta\lambda^2$) and hence the highest precision to measure FD components is achieved by LOFAR and SKA, while

Table 1.1 Spectral ranges of various radio telescopes and parameters crucial for RM synthesis

Telescope	λ (m)	$\Delta\lambda^2$ (m^2)	$\lvert\delta\phi\rvert$ (rad/m^2)	$\lvert\Delta\phi_{\max}\rvert$ (rad/m^2)	$(\lambda_{\max}/\lambda_{\min})^2$
LOFAR highband	1.25–2.73	5.9	0.59	2.8	4.8
Westerbork (WSRT) (Netherlands)	0.17–0.23 + 0.77–0.97	0.91[a]	3.8	110	33
GMRT (India)	0.21–0.30 + 0.47–0.52 + 0.87–0.98	0.92[a]	3.8	71	22
DRAO, Parkes, Effelsberg (GMIMS survey)	0.17–0.23 + 0.33–1.0	0.97	3.6	110	35
Parkes (S-PASS survey)	0.12–0.14	0.004	870	220	1.4
Arecibo (GALFACTS)	0.20–0.24	0.021	165	79	1.4
JVLA (USA)	0.025–0.30	0.089	39	5,000	144
ATCA (Australia)	0.03–0.27	0.072	48	3,500	81
ASKAP (POSSUM)	0.21–0.27	0.026	130	71	1.6
SKA	0.021–6	36	0.10	7,100	82,000

[a]High sidelobes in Faraday spectrum expected owing to the large gaps in wavelength coverage

Australia Telescope Compact Array (ATCA), Jansky VLA (JLVA) and SKA provide the largest range of scales in Faraday space (largest $(\lambda_{max}/\lambda_{min})^2$). Until the SKA, the ideal "Faraday telescope", becomes operational, data from telescopes operating in different frequency ranges should be combined to obtain an excellent frequency coverage and hence allow high-precision investigations of cosmic magnetism.

1.3 Low Frequency Array

The meter-wave radio telescope LOFAR (Low Frequency Array), designed by ASTRON, the Netherlands Institute for Radio Astronomy, is the largest connected radio telescope ever built (van Haarlem et al. 2013). LOFAR is a software telescope with no moving parts, steered solely by electronic phase delays. It has a large field of view and can observe towards several directions simultaneously. LOFAR is an interferometric array using about 20,000 small antennas of two different designs, one for the wavelength range 10–80 MHz ("lowband") and one for 110–240 MHz ("highband"). The antennas are aggregated in at least 49 stations with baselines up to more than 1,000 km across Europe. Forty of these stations are distributed across the Netherlands, six stations in Germany, one each in Great Britain, France and Sweden, which are jointly operated as the International LOFAR Telescope (ILT). Another three stations are planned in Poland and further stations may be built in other European countries. The core stations are located about 3 km north of the village of Exloo in the Netherlands (Fig. 1.4). The total effective collecting area is up to approximately 300,000 m^2, depending on frequency and antenna configuration. The angular resolution is between 2″ (at 240 MHz) and 30″ (at 15 MHz) for the

Fig. 1.4 The LOFAR core near Exloo/Netherlands (photo: ASTRON)

Fig. 1.5 International LOFAR station near Tautenburg/Germany. *Left*: dense array of dipole "tiles" for frequencies of 110–240 MHz, *right*: sparse dipole array for 10–80 MHz; *top*: optical Schmidt telescope (copyright: Michael Pluto, Thüringer Landessternwarte)

Dutch stations (up to about 100 km baselines) and can further be improved by about 10x if the international baselines are included (Fig. 1.5). Digital beam forming allows observation towards several directions simultaneously. The data processing is performed by a supercomputer situated at the University of Groningen/Netherlands.

The sensitivities and spatial resolutions attainable with LOFAR will allow several fundamental new studies:

- Search for the signature of the reionization of neutral hydrogen in the distant Universe ($6 < z < 10$), making use of the shift of the 21 cm line into the LOFAR observing window;
- detect the most distant massive galaxies and study the processes of formation of the earliest structures in the Universe: galaxies, galaxy clusters and active galactic nuclei;
- discover about 1,000 new pulsars within a few kiloparsecs from the Sun;
- detect flashes of low-frequency radiation from pulsars and short-lived transient events produced by events such as stellar mergers or black hole accretion, and search for bursts from Jupiter-like extrasolar planets;
- detect ultra-high energy cosmic rays entering the Earth's atmosphere;
- detect coronal mass ejections from the sun and provide large-scale maps of the solar wind;
- map the three-dimensional distribution of magnetic fields in our own and nearby galaxies, in galaxy clusters and in the intergalactic medium (see Sect. 1.1).
- By exploring a new spectral window, LOFAR is likely to make unexpected "serendipitous" discoveries.

First science results of LOFAR were presented in Beck et al. (2013), de Gasperin et al. (2012), van Haarlem et al. (2013), and van Weeren et al. (2012).

1.4 Square Kilometre Array

The Square Kilometre Array (SKA) is the most ambitious radio telescope ever planned. With a collecting area of about one square kilometer, the SKA will be about ten times more sensitive than the largest single dish telescope (305 m diameter) at Arecibo (Puerto Rico), and about 50 times more sensitive than the currently most powerful interferometers. The SKA will continuously cover most of the frequency range accessible from ground, from about 50 MHz to at least 14 GHz. The third major improvement is the enormously wide field of view, ranging from about 100 square degrees at 50 MHz to at least 1 square degree at 1.4 GHz. The speed to survey a large part of the sky, particularly at the lower frequencies, will hence be ten thousand to a million times faster than what is possible today. The SKA is dedicated to constrain fundamental physics on the dark energy, gravitation and magnetism.

1.4.1 Technical Design and Development of the SKA

The SKA will be a radio interferometer and consist of many antennas which are spread over a large area to obtain high the resolving power. The SKA core regions of about 5 km diameter each will contain about 50 % of the total collecting area and comprise dish antennas and aperture arrays. The mid-region out to about 180 km radius from the core comprises dishes (Fig. 1.7) and sparse aperture array antennas (Fig. 1.6) aggregated into stations distributed on a spiral arm pattern. Remote stations with about 20 dish antennas each will spread out to distances of 3,000 km or more from the core and located on continuations of the spiral arm pattern. The overall extent of the array determines the angular resolution, which will be about $0.1''$ at 100 MHz and $0.001''$ at 10 GHz.

The frequency range spanning more than two decades cannot be realized with one single antenna design, so this will be achieved with a combination of different types of antennas. Under investigation are the following technical designs:

1. SKA-low: An aperture array of dipole antennas with wide spacings (a "sparse aperture array") for the low-frequency range (about 50–350 MHz) (Fig. 1.6). This software telescope is an improved version of the LOFAR lowband antennas and also has a large field of view.
2. SKA-mid: An extended array of parabolic dishes of 15 m diameter each for the medium-frequency range, each equipped with a wide-bandwidth single-pixel "feed" and several receiving systems covering about 350 MHz–14 GHz

Fig. 1.6 SKA sparse aperture array station of dipole elements for low frequencies of about 50–350 MHz. Graphics: Swinburne Astronomy Productions and SKA Project Office (SPO)

Fig. 1.7 SKA parabolic dishes for medium frequencies of about 350 MHz–14 GHz. Graphics: Swinburne Astronomy Productions and SPO

(Fig. 1.7). The surface accuracy of these dishes will allow a later receiver upgrade to higher frequencies.

3. SKA-survey: A compact array of parabolic dishes of 12–15 m diameter each for the medium-frequency range, each equipped with a multi-beam, phased-array feed with a huge field of view and several receiving systems covering about 350 MHz–4 GHz. This array will allow fast surveys of the sky.

An additional technology for substantially enhancing the field of view in the 500–1,000 MHz range is under development: aperture arrays of antenna "tiles" with dense spacings, forming an almost circular station 60 m across (Fig. 1.8), similar to the LOFAR highband antennas.

Fig. 1.8 SKA dense aperture array station made up of 3 m x 3 m "tiles" for medium frequencies of about 500 MHz–1 GHz. Graphics: Swinburne Astronomy Productions and SPO

The data from all stations have to be transmitted to a central computer and processed online. Compared to LOFAR with a data rate of about 150 Gb per second and a central processing power of 27 Tflops, the SKA will produce much more data and need much more processing power—by a factor of at least 100. Following "Moore's law" of increasing computing power, a processor with sufficient power should be available by the next decade.

1.4.2 SKA Key Science Projects

Apart from the expected technological spin-offs, five main science questions (Key Science Projects) drive the SKA (Carilli and Rawlings 2004):

- Probing the dark ages: The SKA will use the emission of neutral hydrogen to observe the most distant objects in the Universe and map the detailed structures formed during the Epoch or Reionization out to a redshift of about 27.
- Galaxy evolution, cosmology and dark energy: A deep all-sky SKA survey will detect hydrogen emission from Milky Way-like galaxies out to redshifts of about one, reveal a comprehensive picture of the Universe's expansion history and hence help to distinguish between the various explanations of "dark matter". The same data set will give us unique information about the evolution of galaxies.
- Tests of General Relativity and detection of gravitational waves: Almost all pulsars in the Milky Way will be detected with the SKA (Fig. 1.3) plus several 100 bright pulsars in nearby galaxies. The SKA will search for a radio pulsar orbiting around a black hole, measure time delays in extremely curved space with much higher precision than with laboratory experiments and hence probe the limits of General Relativity. Regular high-precision observations with the

SKA of a network of pulsars with periods of milliseconds opens the way to detect gravitational waves with wavelengths of many parsecs.
- The cradle of life: The SKA will be able to detect the thermal radio emission from centimeter-sized "pebbles" in protoplanetary systems which are thought to be the first step in assembling Earth-like planets. Biomolecules are also observable in the radio range. Finally, the SETI (Search for Extra Terrestrial Intelligence) project will use the SKA to find hints of technological activities.
- Origin and evolution of cosmic magnetism (see Sect. 1.1).

From the five Key Science Projects two major science goals have been identified that drive the technical specifications for the first phase (SKA1):

- Origins: Understanding the history and role of neutral hydrogen in the Universe from the dark ages to the present-day.
- Fundamental Physics: Detecting and timing binary pulsars and spin-stable millisecond pulsars in order to test theories of gravity.

1.4.3 SKA Timeline

The detailed design for low and mid frequencies is ready in 2015. Construction of the SKA is planned to start in 2018. In the first phase (until 2020) about 10 % of the SKA will be erected (SKA1) (Garrett et al. 2010), with completion of construction at the low and mid frequency bands by about 2025 (SKA2), followed by construction at the high band.

The members of the SKA Organisation agreed on a dual site solution for the SKA with two candidate sites fulfilling the scientific and logistical requirements: Southern Africa, extending from South Africa, with a core in the Karoo desert, eastward to Madagascar and Mauritius and northward into the continent, and Australia, with the core in Western Australia. The dishes of SKA1 will be built in South Africa, combined with the MeerKAT telescope. Further dishes for the SKA1-survey array will be added to the Australian SKA Pathfinder (ASKAP) array in Australia. All the dishes and the mid-frequency dense aperture array for SKA2 will be built in Southern Africa. The low-frequency sparse aperture array of dipole antennas for SKA1 and SKA2 will be built in Australia.

1.5 SKA Pathfinder and Precursor Telescopes

Two SKA "pathfinder" telescopes provide examples of low frequency arrays, the European LOFAR (Sect. 1.3) and the Long Wavelength Array (LWA) in the USA. These long-wavelength telescopes are software telescopes steered by electronic phase delays (phased aperture array). Examples of dishes with a single-pixel feed are under development in South Africa (Karoo Array Telescope, MeerKAT).

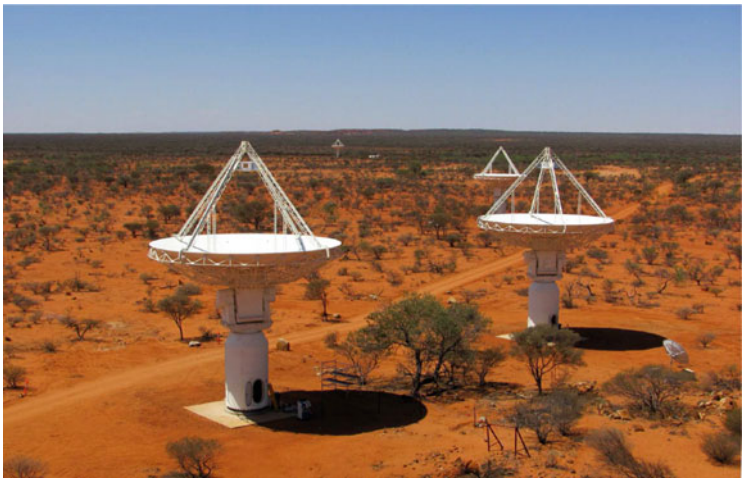

Fig. 1.9 ASKAP antennas (photo: Anthony Schinckel, CSIRO)

Dense aperture arrays comprise up to millions of receiving elements in planar arrays on the ground (Fig. 1.8) which can be phased together to point in any direction on the sky. Due to the large reception pattern of the basic elements, the field of view can be up to 250 square degrees. This technology can also be adapted to the focal plane of parabolic dishes. Prototypes of such wide-field cameras are under construction in Australia (ASKAP), the Netherlands (APERTIF) and in Canada (PHAD).

The Australian SKA Pathfinder (ASKAP), MeerKAT and the Murchison Wide-field Array (MWA) in Australia are SKA "precursor" telescopes at the selected SKA sites and will become part of the SKA array. ASKAP is made up of 36 antennas, each 12 m in diameter (Fig. 1.9) and equipped with a receiving system covering the frequency range 700 MHz–1.8 GHz. ASKAP is currently under construction at the Murchison Radio Astronomy Observatory in Western Australia and started early operations in 2013.

MeerKAT, currently taking shape in South Africa's Karoo region, will consist of 64 dishes of 13.5 m diameter each with an offset Gregorian configuration and equipped with three receiving systems covering the frequency range 580 MHz–14.5 GHz. The KAT-7 precursor array with seven dishes (Fig. 1.10) has been constructed and is being used as an engineering and science prototype. MeerKAT itself will be delivered in three phases. The commissioning will take place in 2014 and 2015, with the array coming online for science operations in 2016.

Fig. 1.10 Antennas of the KAT-7 array (photo: Maik Wolleben, SKA Project South Africa)

References

Anderson, J., Beck, R., Bell, M., et al.: In: Soida, M., et al. (eds.) Magnetic Fields in the Universe: From Laboratory and Stars to Primordial Structures. arXiv:1203.2467 (2012)

Arshakian, T.G., Beck, R.: Mon. Not. R. Astron. Soc. **418**, 2336 (2011)

Arshakian, T.G., Beck, R., Krause, M., Sokoloff, D.: Astron. Astrophys. **494**, 21 (2009)

Beck, R., Gaensler, B.M.: Observations of magnetic fields in the Milky Way and in nearby galaxies with a Square Kilometre Array. In: Carilli, C., Rawlings, S. (eds.) Science with the Square Kilometer Array. New Astronomy Reviews, vol. 48, p. 1289. Elsevier, Amsterdam (2004)

Beck, R., Frick, P., Stepanov, R., Sokoloff, D.: Astron. Astrophys. **543**, A113 (2012)

Beck, R., Anderson, J., Heald, G., et al.: Astronomische Nachr. **334**, 548 (2013)

Bernet, M.L., Miniati, F., Lilly, S.J., et al.: Nature **454**, 302 (2008)

Bernet, M.L., Miniati, F., Lilly, S.J., Astrophys. J. **772**, L28 (2013)

Brentjens, M.A., de Bruyn, A.G.: Astron. Astrophys. **441**, 1217 (2005)

Brunetti, G., Giacintucci, S., Cassano, R., et al., Nature **455**, 944 (2008)

Burn, B.J.: Mon. Not. R. Astron. Soc. **133**, 67 (1966)

Carilli, C., Rawlings, S.: Science with the Square Kilometer Array. New Astronomy Reviews, vol. 48. Elsevier, Amsterdam (2004)

de Gasperin, F., Orru, E., Murgia, M., et al.: Astron. Astrophys. **547**, A56 (2012)

Gaensler, B.M., Beck, R., Feretti, L.: The origin and evolution of cosmic magnetism. In: Carilli, C., Rawlings, S. (eds.) Science with the Square Kilometer Array. New Astronomy Reviews, vol. 48, p. 1003. Elsevier, Amsterdam (2004)

Garrett, M.A., Cordes, J.M., Deboer, D.R., et al.: arXiv:1008.2871 (2010)

Keshet, U., Waxman, E., Loeb, A.: Searching for intergalactic shocks with the Square Kilometre Array. In: Carilli, C., Rawlings, S. (eds.) Science with the Square Kilometer Array. New Astronomy Reviews, vol. 48, p. 1119. Elsevier, Amsterdam (2004)

Kolatt, T.: Astrophys. J. **495**, 564 (1998)

Krause, M., Alexander, P., Bolton, R., et al.: Mon. Not. R. Astron. Soc. **400**, 646 (2009)

Kronberg, P.P., Bernet, M.L., Miniati, F., et al.: Astrophys. J. **676**, 70 (2008)

Murphy, E.: Astrophys. J. **706**, 482 (2009)

Ryu, D., Kang, H., Cho, J., Das, S.: Science **320**, 909 (2008)

Stasyszyn, F., Nuza, S.E., Dolag, K., Beck, R., Donnert, J.: Mon. Not. R. Astron. Soc. **408**, 684 (2010)
Stepanov, R., Arshakian, T.G., Beck, R., Frick, P., Krause, M.: Astron. Astrophys. **480**, 45 (2008)
Stil, J.M., Krause, M., Beck, R., Taylor, A.R.: Astrophys. J. **693**, 1392 (2009)
van Haarlem, M.P., Wise, M.W., Gunst, A.W., et al.: Astron. Astrophys. **556**, A2 (2013)
van Leeuwen, J., Stappers, B.W.: Astron. Astrophys. **509**, A7 (2010)
van Weeren, R.J., Röttering, H.J.A., Brüggen, M., Hoeft, M.: Science **330**, 347 (2010)
van Weeren, R.J., Röttgering, H.J.A., Rafferty, D.A., et al.: Astron. Astrophys. **543**, A43 (2012)
Vogt, C., Enßlin, T.A.: Astron. Astrophys. **434**, 67 (2005)

Chapter 2
Magnetic Fields with the Atacama Large Millimeter/Submillimeter Array

Wouter Vlemmings

Abstract The Atacama Large Millimeter/submillimeter Array (ALMA) is one of the largest radio telescopes and is located at 5,000 m altitude in the Atacama desert in Chile. Its unprecedented sensitivity at extremely high angular and spectral resolution in the (sub-)millimetre wavelength regime, allows for countless advances in astrophysics. One of the areas in which ALMA can make unique contributions, is in that of the study of astrophysical magnetic fields. ALMA is expected to map the magnetic field geometry, and in some cases strength, in a large number of star forming regions, around evolved stars and planetary nebulae, and in nearby galaxies. This chapter provides examples of the amount of improvement ALMA offers the study of magnetic fields based on the current state-of-the-art and shortly introduces new tools that will be available to analyse (sub-)millimetre polarimetric observations.

2.1 The Atacama Large Millimeter/Submillimeter Array

The Atacama Large Millimeter/submillimeter Array (ALMA) is a large international (sub-)millimeter-wavelength radio telescope array in the Atacama Desert of northern Chile. It consists of a total of 66 antennas operating in the wavelength range from 0.4 to 4 mm. Because of its unmatched sensitivity at very high spectral and spatial resolution, ALMA provides new insights into many astrophysical topics, from the formation of stars and planets to the evolution of the most distant galaxies. As ALMA is able to observe in full polarization mode, it can also reveal the magnetic field with a sensitivity and resolution that has not previously been possible.

ALMA is a partnership between Europe, North America (USA and Canada) and East Asia (Japan and Taiwan) in cooperation with the Republic of Chile. The ALMA project is coordinated by the Joint ALMA Office based in Santiago de Chile. The ALMA observatory is operated from the Operation Support Facility (OSF), which is situated at ∼2,900 m altitude. The array itself and the correlator are located at the

W. Vlemmings (✉)
Chalmers University of Technology, Onsala Space Observatory, SE-439 92 Onsala, Sweden
e-mail: wouter.vlemmings@chalmers.se

A. Lazarian et al. (eds.), *Magnetic Fields in Diffuse Media*, Astrophysics and Space Science Library 407, DOI 10.1007/978-3-662-44625-6_2

Fig. 2.1 Several ALMA antennas at the Chajnantor plateau. The 12-m diameter ALMA antennas are seen in the foreground, while in the far left a cluster of smaller 7-m antennas for the ACA are also visible. (Photograph credit: Babak Tafreshi)

Array Operation Site (AOS), at an altitude of 5,000 m (Fig. 2.1). ALMA is rapidly approaching its full operation, and has already observed a number of early science projects in a more limited configuration of ∼16 to 40 antennas.

2.1.1 ALMA Specifications

The main ALMA array consists of 50 antennas with a diameter of 12-m. In addition, 12 antennas with 7-m diameter for interferometry and four 12-m diameter antennas for total power make up the Atacama Compact Array (ACA). This array can be used together with the main ALMA array to improve the imaging capabilities by providing short- and zero-spacing data.

The Atacama desert, at 5,000 m altitude, is one of the driest places on Earth. A typical value for the amount of water in the atmosphere, the precipitable water vapour (pwv), at the ALMA site is ∼1 mm (Fig. 2.2). As a result, the site provides excellent atmospheric transmission over the entire wavelength range covered by ALMA. The ALMA receiver bands and representative numbers are given in Table 2.1. In addition to those listed in the table, band 10 (787–950 GHz) is planned shortly after completion of the array, and band 1 (around 40 GHz) and band 2 (around 80 GHz) might be added in the future. The sensitivity numbers reflect the dynamic scheduling nature of ALMA, with higher pwv allowed at the lower frequencies.

The main ALMA array can be configured with maximum baselines between ∼150 m to ∼16 km. The ACA complements this by providing an array configuration with a diameter of 50 m. At the shortest wavelength (0.4 mm) and largest configuration, ALMA will reach an angular resolution of ∼0.005″, while thanks to the ACA it will still be possible to detect structure at the scale of 10″.

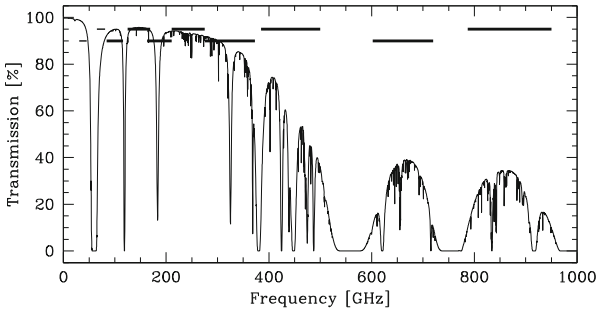

Fig. 2.2 The atmospheric transmission at the ALMA site. The curve shows the transmission for precipitable water vapour of 1.0 mm. The horizontal bars from *left* to *right* indicate the ALMA frequency bands 1–10. Bands 1 and 2 are potential upgrades

Table 2.1 The ALMA receiver bands

Band	Frequency range (GHz)	Wavelength range (mm)	Angular resolution $B_{max} = 150$ m − 16 (″)	Line[a] sensitivity (mJy)	Continuum[b] sensitivity (mJy)	Primary beam (″)	Largest scale (″)
3	84–116	2.6–3.6	4.0–0.038	8.9	0.05	61	37
4	125–169	1.8–2.4	2.7–0.026	9.1	0.06	51	32
5[c]	163–211	1.4–1.8	2.1–0.020	1.3	0.06	33	23
6	211–275	1.1–1.4	1.6–0.015	13	0.10	25	18
7	275–373	0.8–1.1	1.2–0.012	21	0.20	19	12
8	385–500	0.6–0.8	0.9–0.009	63	0.40	14	9
9	602–720	0.4–0.5	0.6–0.006	80	0.64	9.7	6

[a]Sensitivity for 60 s on-source observing time, dual polarization and a spectral resolution of 1 km s^{-1}

[b]Sensitivity for using full continuum setup, with dual polarization, in 60 s on-source time

[c]Initially only available on a limited number of antennas

The ALMA receivers have an instantaneous bandwidth of up to 8 GHz in each of two polarizations that can be divided over four spectral windows of up to 2 GHz each. The ALMA correlator is highly flexible and allows for a combination of multiple spectral modes simultaneously (Escoffier et al. 2007). In the case of full polarization correlation, it is possible to reach a spectral resolution from 976 kHz (1.28 km s^{-1} at 230 GHz) down to 15 kHz (0.02 km s^{-1} at 230 GHz) in spectral line mode. The continuum observing mode produces 64 channels of 31.25 MHz across the full 2 GHz per spectral window.

At the time of writing, the full ALMA polarization capabilities have not yet been commissioned and only continuum observations are planned until 2015. Although depending on the performance in the individual bands, the goal is to reach at least a 0.1 % accuracy, after calibration, in the linear polarization and a maximum *absolute* polarization angle accuracy of 6°. The reachable accuracy of the circular

polarization is not yet determined, but it should, for compact sources, be of similar order.

2.1.2 ALMA Science

ALMA was originally designed with three specific science goals in mind. These goals are:

- The ability to detect spectral line emission from CO or CII in galaxies like the Milky Way at a red-shift of $z = 3$, in less than 24 h.
- The ability to probe the gas kinematics in protostars and protoplanetary disks around young Sun-like stars in molecular clouds out to $\sim$150 pc.
- The ability to provide high dynamic range images at an angular resolution of $0.1''$.

Considering its capabilities, ALMA will also make great strides in numerous other astrophysical topics, by, for example:

- imaging dust emission from galaxies out to $z = 10$;
- studying the kinematics and physical conditions, *including magnetic fields*, in nearby galaxies through (polarimetric) imaging of the dust and molecular gas;
- observations of the gravitational collapse of molecular clouds as well as the formation of disks and jets around low-mass and high-mass protostars, including a study of the role of *magnetic fields*;
- imaging and model refinement of Solar System objects, such as planets, comets, asteroids and Kuiper Belt objects, as well as the Sun itself;
- making a detailed analysis of the dust formation, mass loss, shaping and *magnetic fields* in the circumstellar envelopes of evolved stars and planetary nebulae, as well as around supernovae.

Obviously, the sensitivity of ALMA together with its polarization capabilities provides a significant step beyond the currently available instruments in the ALMA wavelength range. In particular, ALMA will be able to deliver polarization data of scientific interest even when polarimetry is not the primary purpose of the observations. In Sect. 2.3, the potential of magnetic field studies with ALMA will be described compared to the current state-of-the-art in submillimetre and millimetre polarimetric observations.

2.2 ALMA Polarization Calibration

Much of the ALMA polarization science will be focused on linear polarization observations, although circular polarization measurements, in particular those of molecular Zeeman splitting, will also have several interesting applications. ALMA

will be equipped with linearly polarized feeds, which is suboptimal for linear polarization observation (though for band seven quarter wave plates for obtaining dual circular polarization might be available). Assuming, following Cotton (1998), the linear approximation to the polarized antenna feed response and ignoring higher order terms in instrumental and source polarization, the X and Y linear feed cross-correlations between antenna n and m are given by:

$$\begin{aligned} XX &= g_{nX} g^*_{mX}[I + Q\cos 2\chi + U \sin 2\chi] \\ XY &= g_{nX} g^*_{mY}[(d_{nX} - d^*_{mY})I - Q\cos 2\chi + U \sin 2\chi + iV] \\ YX &= g_{nY} g^*_{mX}[(d_{nY} - d^*_{mX})I - Q\cos 2\chi + U \sin 2\chi - iV] \\ YY &= g_{nY} g^*_{mY}[I - Q\cos 2\chi - U \sin 2\chi]. \end{aligned} \tag{2.1}$$

Here the individual antenna polarization gain terms are given by g, which are complex factors representing the effects of the atmosphere and uncorrected electronics. The leakage terms d are also complex factors representing the fraction of the orthogonal polarization corrupting a given feed. The Stokes values are given by I (total intensity), Q and U (linear polarization) and V (circular polarization). Finally, χ is the parallactic angle, which corresponds to the rotation of the antenna feed seen from the source as it is being tracked during the observations.

While first order errors in the relative gains of the polarization feeds X and Y cancel out for calibration of the total intensity I, using a point source in the phase center, additional calibration of the g-terms is needed when interested in polarization. In particular, as seen in Eq. (2.1), any uncorrected phase difference between the two orthogonal polarized feeds, will couple the polarizations. This X-Y phase difference (ϕ_{XY}) cannot be determined by observing an unpolarized source. Uncorrected short term phase fluctuations between the feeds for the different telescopes in the array will further couple the total intensity and polarization and will introduce significant instrumental effects. Using linear feeds, the X-Y phase difference needs to be known to much better than one degree to reach the goal of 0.1 % polarization accuracy.

The exact calibration strategy would depend on how well the calibrator properties are known. One can identify three different possibilities:

1. *Unpolarized calibrator:* Only one observing scan is required for calibration of the d-terms. The antenna d-terms are calibrated and only one unknown complex number remains, which can be determined as part of the g-terms. The phase difference ϕ_{XY} stays unknown.
2. *Polarized calibrator with known polarization:* A single scan will also be sufficient with only a remaining amplitude factor in d_X and d_Y that can be calibrated with the g-terms. The phase difference ϕ_{XY} can be determined from the known polarization characteristics.
3. *Polarized calibrator with unknown polarization:* The calibrator needs to be observed at least three times over a range of 90° or more in parallactic angle.

The d-terms are calibrated with a single remaining complex number absorbed in g, but the phase difference ϕ_{XY} remains unknown.

As is evident from these three cases, the phase difference ϕ_{XY} can only be determined by observing a source with known polarization, while calibration of the d-terms needs either an unpolarized source or one with accurately known polarization. As such sources are rare in the ALMA wavelength range, it is thus likely, that in several cases, the calibration of the d-terms will require observations spanning a sufficient parallactic angle range, making polarization snapshot observations difficult. In any case, the stability in time and frequency of the d-terms and of ϕ_{XY} will be critical but is yet undetermined for ALMA.

An additionally challenging aspect will be the need for an accurate polarization calibration across the entire primary beam, as many sources of interest for ALMA will have extended polarization. The instrumental gain and polarization leakage terms, as well as ϕ_{XY} will depend on the location in the primary beam. Assuming the polarized beam is stable, a correction of these effects will require frequent observations by the ALMA project of a complete Stokes representation of the primary beam pattern.

Finally, the combination of the ACA and total power antennas could be needed for polarization mapping of extended sources. This requires in particular an observing scheme that properly calibrates the polarization of the total power antennas. As single dish calibration of polarization is time consuming and non-trivial, it is potentially possible to calibrate the total power antennas by including them into the full array during calibrator observations.

For the remainder of this chapter, it will be assumed that all calibration is performed optimally and the goal of 0.1 % polarization accuracy is reached in both linear and circular polarization.

2.3 Magnetic Field Observations with ALMA

2.3.1 (Sub-)Millimetre Polarization

It is clear that magnetic fields are ubiquitous throughout the entire Universe and play an important role in a variety of astrophysical environments. A number of these environments, and the details on how polarized emission is generated under the influence of a magnetic field, will be described in other chapters of this book. As is evident from the science topics that its observations will address, ALMA will provide a breakthrough in observational diagnostics of the magnetic field in a number of astrophysical environments. Here, the improvement gained with ALMA in the observations of magnetic fields in Galactic star forming regions and molecular clouds, in nearby galaxies and around evolved stars will be addressed. But in addition, ALMA polarization will be able to provide important constraints on, for

example, maser pumping and radiative transfer theory, galactic dust properties and models of Sgr A*.

2.3.1.1 Linear Polarization

At submillimetre wavelengths, linear polarization can be observed in both continuum dust emission as well as in the radiation originating from certain molecular line transitions. The dust continuum linear polarization, at far-IR and (sub-)millimetre wavelengths, arises from aligned and spinning dust grains. While the exact mechanism involved in the dust alignment is still uncertain (see e.g. Lazarian 2003, and further chapters in this book), all observations to date indicate that the alignment is with respect to the magnetic field. Only in the coldest and densest gas, as found in starless molecular clouds, are there indications that grains are only poorly aligned. The detectable fraction of linear polarization of dust emission is typically of the order of a few percent (e.g. Greaves et al. 1999). If at the same time, one has information on the turbulent velocity in the region probed by the polarization observations, the use of the Chandrasekhar–Fermi method (Chandrasekhar and Fermi 1953) can then provide a measure of the magnetic field strength in the plane of the sky using:

$$B_{\rm pos} = \sqrt{4\pi\rho}\, Q \frac{\delta v_{\rm los}}{\delta\phi}. \tag{2.2}$$

Here ρ is the average mass density, $\delta v_{\rm los}$ is the line of sight velocity dispersion and $\delta\phi$ is the dispersion for the observed magnetic field vectors from the expected magnetic field structure after correcting for observational uncertainties. The dimensionless parameter Q depends on the cloud structure. Turbulent cloud simulations indicate $Q \approx 0.5$ (Ostriker et al. 2001).

Linear polarization of molecular line emission can arise due to the Goldreich–Kylafis effect (Goldreich and Kylafis 1981, 1982). If even a relatively weak magnetic field is present, the molecular gas emission will be linearly polarized when the magnetic sublevels of the rotational states are exposed to anisotropic emission. Alternatively, polarized line emission can arise from molecules that have a preferred rotation axis as the result of strong infrared emission from a nearby source (Morris et al. 1985). Thus, in the presence of a strong IR source, the exact relation between the magnetic field and the linear polarization direction is not immediately clear. Additionally, while the linear polarization of dust emission is always perpendicular to the magnetic field direction, the molecular line linear polarization direction can be perpendicular or parallel to the magnetic field, depending on the direction of the velocity and radiation anisotropy (e.g., Cortes et al. 2005). However, with a careful analysis it is potentially possible to derive the magnetic field orientation from molecular line polarization measurements. The polarization fraction due to the Goldreich–Kylafis effect depends on several factors, such as the anisotropic

radiation field, optical depth and angular momentum of the molecular transition involved, but is typically of the order of 1–10 %.

2.3.1.2 Circular Polarization

Circular polarization is generated in molecular line emission as a result of the Zeeman effect. When the emitting region is permeated by a magnetic field, the Zeeman effect causes a shift of the energy levels involved. This results in a splitting of the molecular line into three Zeeman components, one linearly polarized π component and two oppositely circularly polarized σ components. By measuring the frequency difference between the two circularly polarized components, it is possible to directly determine the magnetic field strength along the line of sight.

The Zeeman effect of different species scales with their magnetic moment. For paramagnetic molecules the magnetic moment is at the level of the Bohr magneton, while for non-paramagnetic molecules it scales with the nuclear magneton. This results in Zeeman splitting approximately three orders of magnitude smaller for non-paramagnetic molecules compared to paramagnetic molecules. For maser transitions from non-paramagnetic molecules, such as H_2O and methanol, the Zeeman splitting has been measured (e.g., Fiebig and Guesten 1989; Vlemmings 2008). However, in the ALMA wavelength range, Zeeman splitting observations of high angular momentum transitions of non-paramagnetic molecules will be unlikely. Still, for several transitions, such as those from the paramagnetic molecules like CN (e.g., Falgarone et al. 2008) and SO, and potentially from atomic radio-recombination lines (e.g., Thum and Morris 1999), Zeeman splitting observations with ALMA will be possible.

2.3.2 Star Formation and Molecular Clouds

The specific importance of magnetic fields during star formation, both in the low-mass and high-mass regime, is still under debate, and will be covered in several of the other chapters. Polarization observations of star forming regions and molecular clouds have been able to probe the magnetic field at various scales and in a wide range of different density regimes. In the higher density regions (hydrogen number densities $n_{H_2} > 10^6\,\mathrm{cm}^{-3}$), close to the protostars, magnetic field measurements have mainly been made using maser observations in the centimeter wavelength regime. The linear and circular polarization maser observations have revealed large scale magnetic fields often aligned with outflows or torus/disc-like structures (e.g., Vlemmings et al. 2010; Surcis et al. 2009, 2012) and consistent with measurements of dust polarization (e.g. Fig. 2.3). The magnetic field strength ranges from a few mG in the less dense OH maser regions to several hundred mG in the shocked H_2O maser regions (e.g., Bartkiewicz et al. 2005; Fish and Reid 2006; Sarma et al. 2001; Vlemmings et al. 2006).

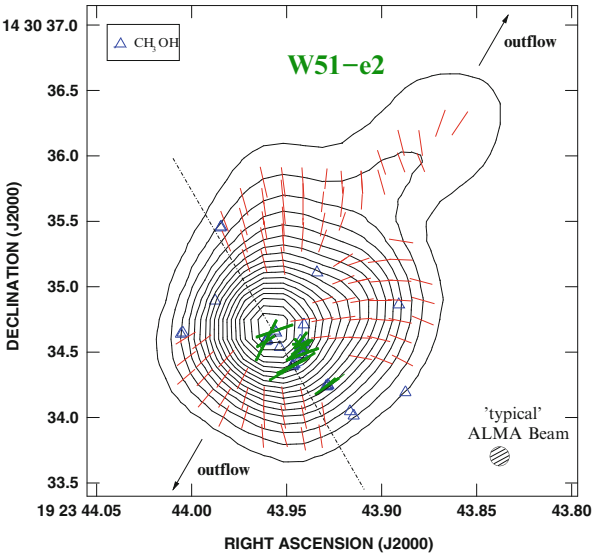

Fig. 2.3 The magnetic field map of core e2 of the massive star forming region W51. The contours are the 330 GHz dust continuum (at $2, 4, 6, 8, 10, 15, 20, \ldots, 60 \times 60$ mJy beam^{-1}) and the *thin line* segments are the $>3\sigma$ magnetic field direction observed with the SMA (Tang et al. 2009). The SMA observations have a angular resolution of $0.7''$, corresponding to ∼4,000 AU. The *triangles* are the 6.7 GHz methanol masers observed at ∼1 mas (∼5 AU) resolution with the European VLBI Network (EVN) (Surcis et al. 2012). The *thick line* segments are the magnetic field direction derived from the methanol maser polarization and agree perfectly with the dust observations. This indicates that the magnetic field maintains its regular structure across several orders of magnitude in scale

The magnetic fields in the lower density molecular clouds and protostellar envelopes have been observed using the Zeeman splitting of HI and non-masing OH transitions, as well as linear polarization from aligned dust grain (e.g., Crutcher et al. 1987, 1996; Girart et al. 2006). Additionally, several observations of CO polarization, attributed to the Goldreich–Kylafis effect, have been carried out (e.g., Girart et al. 1999; Beuther et al. 2010). It is particularly in these last two areas where important steps have been taken over the last few years, and where ALMA will provide significant further progress. A number of Submillimeter Array (SMA) observations have revealed the structure of the magnetic field around protostellar cores in both low-mass and high-mass star forming regions (e.g., Girart et al. 2006, 2009; Tang et al. 2009). These observations have revealed the hour-glass magnetic field morphology that is potential evidence for ambipolar diffusion as discussed in e.g. Mestel and Spitzer (1956). Taking as an example the observations of NGC 1333 IRAS 4A (Girart et al. 2006; Frau et al. 2011; Fig. 2.4) it is possible to estimate the improvements that ALMA will offer.

Example Polarization imaging of the 345 GHz dust emission of NGC 1333 IRAS 4A, originally performed in Girart et al. (2006), was improved with further

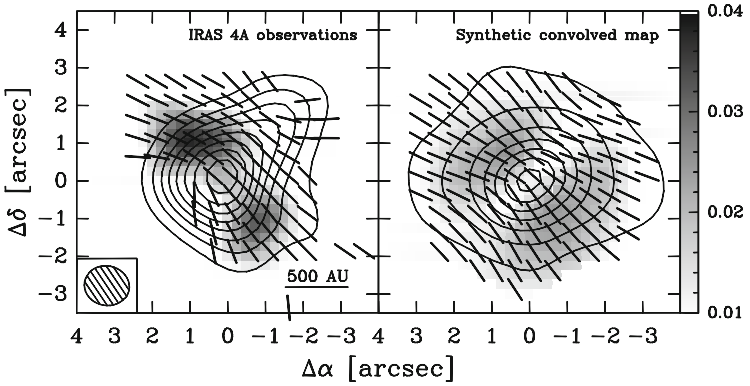

Fig. 2.4 Adapted from Padovani et al. (2012) and Frau et al. (2011). The *left panel* shows the dust polarization of NGC 1333 IRAS 4A using combined SMA sub-compact, compact and extended configuration observations. The contours indicate the 330 GHz continuum emission in steps of 6σ, from 6 to 96σ, where $\sigma = 20$ mJy beam^{-1}. The greyscale is the polarized emission (up to 38.3 mJy beam^{-1} and the line segments indicate the derived magnetic field direction. The panel on the *right* is a synthetic dust polarization map generated with the ARTIST module DustPol (Padovani et al. 2012; Sect. 2.4) produced with the same contour and intensity levels

observations in Frau et al. (2011). The resulting map, made from 8 h SMA tracks in the sub-compact, compact and extended configuration is shown in Fig. 2.4, left. The beam size was $1.24'' \times 1.12''$ (corresponding to 434×392 AU at a distance of $\sim$350 pc). The polarized rms noise was 2.5 mJy beam^{-1} and the peak total intensity and polarized flux were 1.03 ± 0.02 Jy beam^{-1} and 38.2 ± 2.5 mJy beam^{-1}, respectively. To probe the full angular scale across which polarization is detected ($\sim 8''$) at an angular resolution similar to that of the SMA, observations with ALMA at 345 GHz will require the ACA. To reach the rms of 2.5 mJy beam^{-1} per polarization, the main ALMA array would require less than 2 s on source integration time (the ACA would take approximately 3 min, although because of the larger beam ($6''$), the required rms per beam will be less). Alternatively, in approximately 5.5 h on source integration time, ALMA would reach the limiting 0.1 % linear polarization across the entire region where the SMA detected total intensity emission (>20 mJy beam^{-1}).

Thus, ALMA would be able to produce polarization maps of similar quality to that of NGC 1333 IRAS 4A for $\sim$10 sources in one observing track at a significantly improved angular resolution of $\sim 0.2''$ (assuming the settings are such that the polarization calibrator can be shared and observed over sufficient parallactic angle). Consequently, it could also detect the polarization for star forming cores at much larger distances, such as many of the massive star forming regions, or of much smaller mass. In one observing track it could image NGC 1333 IRAS 4A out to beyond 3 kpc or with an order of magnitude smaller dust envelope mass. At the same time, with a spectral window placed on the CO(3-2) line, 0.1 % linear polarization can then be detected in 1 km s^{-1} channels for a line strength of $\sim$1 Jy beam^{-1}.

2.3.3 *Evolved Stars and Planetary Nebulae*

At the end of their evolution, a majority of stars go through a period of high mass loss that is an important source for replenishing interstellar space with processed materials. During the asymptotic giant branch (AGB) phase, this mass loss produces circumstellar envelopes (CSEs), which are found to undergo a major modification during the rapid transition from AGB star to Planetary Nebula (PN). The standard assumption is that the initial slow AGB mass loss in a short time changes into a fast superwind generating shocks and accelerating the surrounding envelope (Kwok et al. 1978). However, a large fraction of PNe have asymmetric shapes, with the majority of the young PNe being bipolar. Thus, at some point during the evolution to a PNe the AGB stars must undergo a process in which the spherically symmetric outflow is altered to produce aspherical PNe morphologies. It has been shown that the energy and momentum contained in the outflows of young bipolar PNe is often orders of magnitude larger than can be provided by radiation pressure (Bujarrabal et al. 2001). The source of this energy has been argued to be magnetic fields, binary or disk interaction or a combination of these (see e.g. Balick and Frank 2002; Frank et al. 2007, and references therein).

As in star forming regions, the main source of magnetic field information around evolved stars has come from maser polarization observations. Ordered magnetic fields with a strength of the order a mG have been detected in the OH maser regions at large distances from the star e.g. Szymczak et al. (1998). Closer in, H_2O masers also indicate the presence of a dynamically important magnetic field, with typical values of a few hundred mG e.g. Vlemmings et al. (2005). Finally, 43 and 86 GHz SiO maser observations reveal field strengths of several Gauss at a distance of only a few stellar radii from the star, assuming a standard Zeeman interpretation (Kemball and Diamond 1997; Herpin et al. 2006). The current measurements are summarized in Fig. 2.5.

Although the exact relation between the magnetic field strength and the distance to the central star remains uncertain, it is likely that the measured fields dynamically influence the shaping of the outflow and, consequently, help shape asymmetric PNe. The magnetic field could also contribute to the stellar mass-loss mechanism (Falceta-Gonçalves et al. 2006). But crucial information on the magnetic field morphology is still lacking. Polarization observations of the masers in the envelope of the supergiant star VX Sgr indicates a large scale magnetic field with its configuration remaining similar from near the star out to several thousands of AU (Vlemmings et al. 2011). However, typically, maser observations only probe a limited number of lines-of-sights through the circumstellar envelope. Observations of thermal molecular line linear polarization, with the different species and transitions tracing different areas of the circumstellar envelope, will thus provide important insight in the relation between the magnetic field and the morphology of the circumstellar environment.

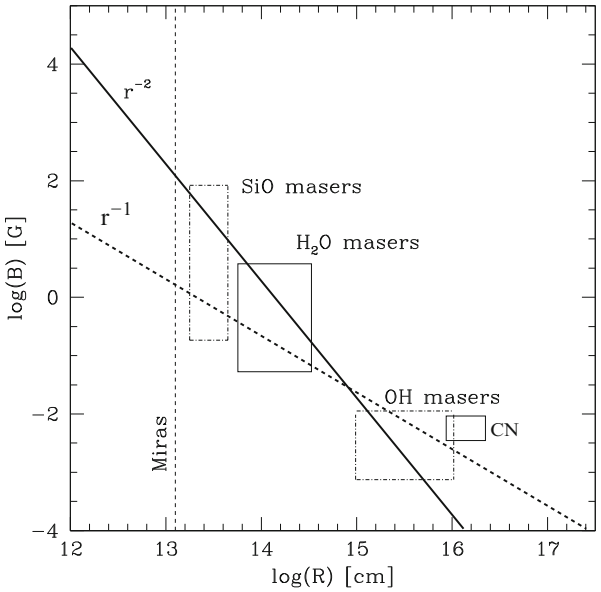

Fig. 2.5 Adapted from Vlemmings et al. (2005). The magnetic field strength vs. radius relation as indicated by current Zeeman splitting observations of the circumstellar environment of evolved stars. The boxes show the range of observed magnetic field strengths derived from the observations of SiO (e.g., Herpin et al. 2006; Amiri et al. 2012), H_2O (e.g., Vlemmings et al. 2005) and OH masers (e.g., Wolak et al. 2012) as well as those from thermal CN circular polarization (Herpin et al. 2009). The *thick solid and dashed lines* indicate an R^{-2} solar-type and R^{-1} toroidal magnetic field configuration. The *vertical dashed line* indicates the stellar surface of a typical AGB star. Thermal molecular line polarization observations with ALMA will probe a wide range of distances (out to several times 10^{17} cm) and can provide not only the morphology at those scales but also a plane-of-the-sky magnetic field strength using the Chandrasekhar–Fermi method

A tentative detection of linear polarization of CS(2-1) in the envelope of the AGB carbon star IRC+10216 was made using single dish observations (Glenn et al. 1997). Later, the first significant detection of linear polarization of CO(2-1) and SiO(5-4) was made in the envelope of IK Tau with the SMA (Vlemmings et al. 2012; Fig. 2.6). This was followed shortly afterwards with the detection of CO(3-2), SiS(19-18) and CS(7-6) linear polarization, again with the SMA, in the envelope of IRC+10216 (Girart et al. 2012). Detailed analysis of radiation and velocity anisotropies, together with multi-level polarization radiative transfer, are needed in order to properly evaluate the relation between the linear polarization and the magnetic field. If the observed polarization is due to the regular Goldreich–Kylafis effect, the observations confirm the presence of a large scale circumstellar magnetic field. In the case of IK Tau this field then appears to be related to the slightly elongated CO envelope morphology (Castro-Carrizo et al. 2010).

Beyond the AGB phase, magnetic field information is even more scarce. A small number of post-AGB and pre-PNe have had their magnetic fields measured, the

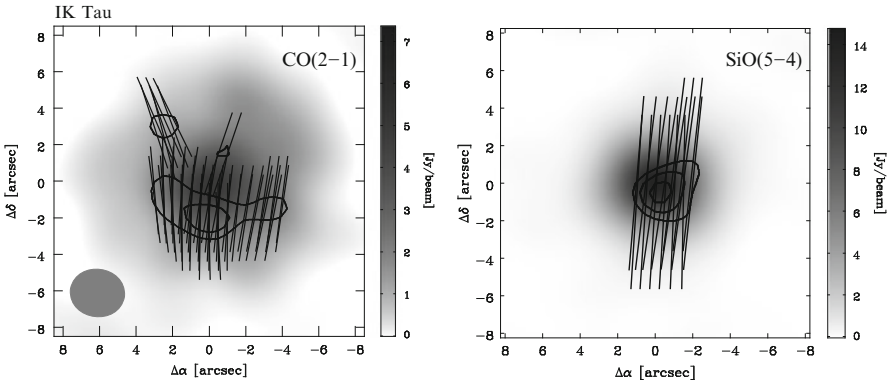

Fig. 2.6 From Vlemmings et al. (2012). The thermal molecular line linear polarization of CO(2-1) at 230 GHz (*left*) and the SiO(5-4) at 217 GHz in the circumstellar envelope of the AGB star IK Tau. The observations were done with the SMA in compact configuration. The contours indicate the 3, 4 and 5σ confidence levels for the polarized emission and the line segments show the linear polarization direction. While the SiO emission originates from closer to the star than the CO emission, the polarization direction is the same. This potentially indicates a preferred field direction throughout the stellar envelope. Due to the 90° ambiguity in the magnetic field direction derived from the polarization vectors, the exact magnetic field orientation is not yet known. However, the preferred direction, either North-South or East-West, could be related to the observed East-West extent in the circumstellar envelope

most notable being the detection of a magnetically collimated jet from the 'water-fountain' pre-PN W43A (Vlemmings et al. 2006). No convincing detections of magnetic fields on PN central stars have yet been made (Leone et al. 2011) and only very few display maser emission that can be used for polarization observations. Thus far, only the young PNe K3-35 has been confirmed to harbour a mG magnetic field in the circumstellar nebula (Gómez et al. 2009). The most convincing evidence for a large scale magnetic field in PNe comes from dust polarization mapping (Sabin et al. 2007).

Depending on the molecule and transition, the observed molecular line linear polarization fractions are between a few and ∼10 %. Those of the dust are of order of a few percent. The SMA can currently only detect such levels for the handful of evolved stars and planetary nebulae with sufficiently bright dust and/or molecular line emission. However, based on the SMA observations of IK Tau, it is clear that ALMA will provide the sensitivity to significantly expand this field of research. In addition, ALMA will allow for measurements of CN circular polarization (e.g. Herpin et al. 2009) in the envelopes of carbon rich AGB stars that host few masers.

Example The linear polarization of CO(2-1) in the envelope of IK Tau was observed with the SMA in a single 9 h track (Vlemmings et al. 2012; Fig 2.6). Despite observing in the compact configuration, a significant amount of flux was lost due to the extent of the CSE. The rms per 5 km s^{-1} channel in the polarization and total intensity images was 35 mJy beam^{-1} and the CO(2-1) peak emission was

7.5 Jy beam^{-1} in a $3.0'' \times 2.6''$ beam. As for the dust polarization measurements in star forming regions, ALMA would be able to reproduce these observations in only a few seconds of observing time. Alternatively, it will produce an improved ($> 10\sigma$) map with higher spatial resolution ($1'' \times 1''$) and better velocity resolution (2 km s^{-1}) within a total observing time of 30 min. Although IK Tau is one of the strongest CO emitting AGB stars, the use of the ACA would allow ALMA to recover more flux and thus observe the thermal molecular line polarization of about a dozen evolved stars out to $\sim$0.5 kpc in a single observing track. Similarly, it will be possible to map individual objects with a CO(2-1) line strength of only $\sim$250 mJy beam^{-1} to a linear polarization of approximately 1 % in a single 8 h observing run. Dust polarization at 230 GHz will simultaneously be detectable at the 0.1 % level for sources with a continuum flux of only $\sim$16 mJy beam^{-1}. This would easily allow for dust polarization mapping of, for example, extended PNe.

2.3.4 Nearby Galaxies

In addition to Galactic magnetic field observations, ALMA will also provide new means of studying the magnetic field in nearby galaxies. Currently, the knowledge of magnetic fields in nearby galaxies mainly comes from observing the polarization of radio synchrotron emission e.g. Beck et al. (2005) and Faraday rotation analysis of local emission as well as that of background sources (e.g., Krause and Beck 1998; Gaensler et al. 2005). These observations and methods, as well as their interpretation, will be covered in other chapters.

The synchrotron polarization typically traces magnetic fields in the diffuse and warm interstellar medium and indicates a field strength ranging from $\sim 5\,\mu$G in radio-faint galaxies to $\sim 100\,\mu$G in starburst galaxies. Such field strengths indicate that magnetic fields are dynamically important. At higher densities, magnetic field probes are more limited. Field strengths up to $\sim$18 mG were detected using OH megamaser emission in a number of starburst galaxies (Robishaw et al. 2008). The megamaser observations probe the magnetic field in dense regions, although it is not clear if these are the generally compressed interstellar medium of the nuclear starburst regions or even more dense molecular clouds.

With ALMA, it will now be possible to probe the magnetic field in the molecular clouds of the nearest galaxies by observing the polarized dust and molecular line emission. Previously, dust polarization of a few percent was observed in the central region of M82 (Greaves et al. 2000), but only very few polarization vectors at $15''$ resolution were mapped. More recently, the CO polarization, attributed to the Goldreich–Kylafis effect, was measured for six giant molecular clouds (GMCs) in M33 (Li and Henning 2011). From these SMA observations it was concluded that there exists a strong relation between the large scale galactic magnetic field and the field found in GMCs. With ALMA similar studies will be possible at higher angular resolution and of much more of the CO emitting molecular gas.

Example The observations of the CO(2-1) polarization of M33 were also performed with the SMA (Li and Henning 2011). Although detailed information about the SMA observations is not available, it is clear from similar arguments presented earlier that ALMA would be able to reproduce the SMA results within a fraction of the time, even considering that the observational setup would require (pointed) mosaics. As an example project, we take the CO observations of the galaxy merger NGC 4194—also known as the Medusa galaxy (Aalto and Hüttemeister 2000), although this particular source is not observable by ALMA. Figure 2.7 shows the CO(1-0) distribution, tracing prominent dust lanes of the merger. The CO is extended over $\sim 25''$, which means that ALMA would be able to map the CO(1-0) in a single pointing, but would need a small mosaic for the higher transitions (where also the ACA is needed to recover the extended emission). Using a single observing track with ALMA, the channel rms in 20 km s^{-1} channels at CO(1-0) is approximately 0.2 mJy beam^{-1}. It would thus be possible to reach the maximum 0.1 % linear polarization accuracy for the inner $\sim 10''$ of CO(1-0) emission shown in the right panel of Fig. 2.7. As the flux in the CO(2-1) transition is 2–3 times larger, and the rms noise in a single track would be similar to that at CO(1-0) in the

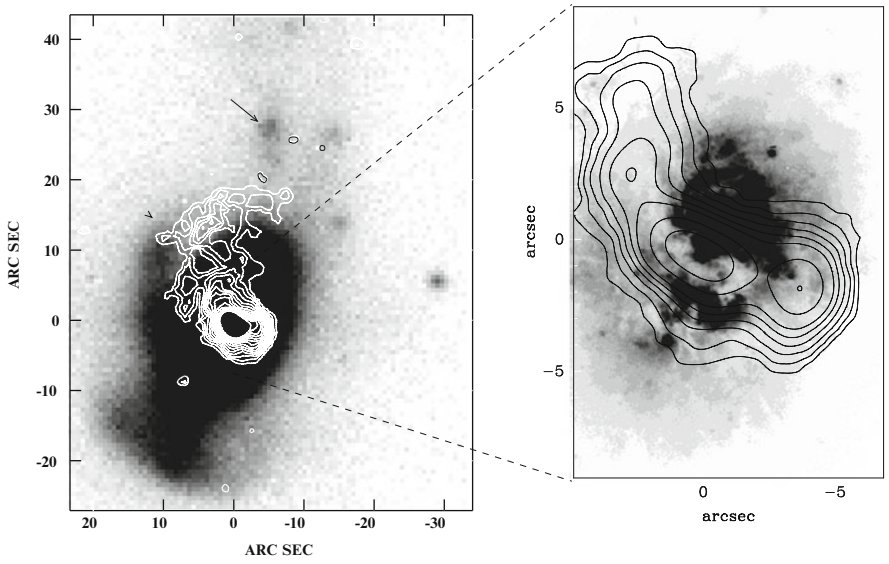

Fig. 2.7 Observations of the CO(1-0) transition at 115 GHz of the "Medusa" merger galaxy NGC 4194 at $D = 39$ Mpc (Aalto and Hüttemeister 2000). The observations were performed using four tracks at the Caltech six-element Owens Valley Radio Observatory (OVRO), providing a beam size of $2.5'' \times 2.0''$ and an rms of 11 mJy beam^{-1} in 20 km s^{-1} channels. The image to the *left* has the integrated CO contours overlayed on an optical R-band image. The image on the *right* displays only the emission from 2,506 to 2,570 km s^{-1} on an HST WFPC2 image. Contour levels are $0.54, 2.6, 2.7, 3.8, \ldots, 31$ Jy beam^{-1} km s^{-1}. The emission extends over a total scale of $25''$. While this source is in the Northern hemisphere, ALMA will be able to detect the CO polarization for similar sources

case of a small mosaic, polarization would be detectable for most of the emission. ALMA will thus be able to map the magnetic field for several nearby galaxies such as NGC 4194.

2.4 ALMA Polarization Analysis Tools: The ARTIST Project

The ARTIST (Adaptable Radiative Transfer Innovations for Submillimeter Telescopes) project[1] was designed as a general model suite for comprehensive multi-dimensional radiative transfer calculations of dust and molecular line emission (Padovani et al. 2011). In addition to the model suite, which is based on the full three-dimensional radiative transfer code LIME (Line Modeling Engine, Brinch and Hogerheijde 2010), the ARTIST project will also provide the tools for modeling polarization at (sub-)millimetre wavelength. As the ARTIST uses a Python-based user interface and produces maps in the FITS format, it can straightforwardly be combined with the Common Astronomy Software Applications package (CASA) that is used for ALMA. In this way it will be possible to directly model the interferometric ALMA response to the polarized emission from model sources produced by the user.

The polarization analysis tools of ARTIST have two components, one for the continuum dust polarization and one for the thermal molecular line polarization. The dust polarization module (DustPol) is described in detail in Padovani et al. (2012). As it is based on LIME, DustPol can be combined with analytical as well as pre-gridded models and output from, e.g., magneto-hydrodynamical (MHD) models. An example of the package capabilities is shown in Fig. 2.8. Here, input from the MHD adaptive mesh refinement code RAMSES (Teyssier 2002; Fromang et al. 2006) is used to produce predictions for polarization observations of a rotating and collapsing core with different mass-to-magnetic flux. The power of DustPol can also be seen in Fig. 2.4, in which the SMA dust polarization observations of NGC 1333 IRAS 4A are compared with a synthetic dust polarization map made with DustPol. The model, with parameters from Frau et al. (2011), corresponds to a collapsing magnetized isothermal toroid as described by Allen et al. (2003).

The second component is the full polarization radiative transfer treatment of thermal molecular lines. The ARTIST line polarization module (LinePol) is mainly aimed at modeling the Goldreich–Kylafis effect on the emission of molecules such as CO (Kuiper et al. in prep.). It thus does not include radiative alignment effects. However, as it uses the multi-level and full three-dimensional radiative transfer capabilities of LIME, LinePol will predict the polarization response of molecular lines in a highly anisotropic radiation field.

[1] http://youngstars.nbi.dk/artist

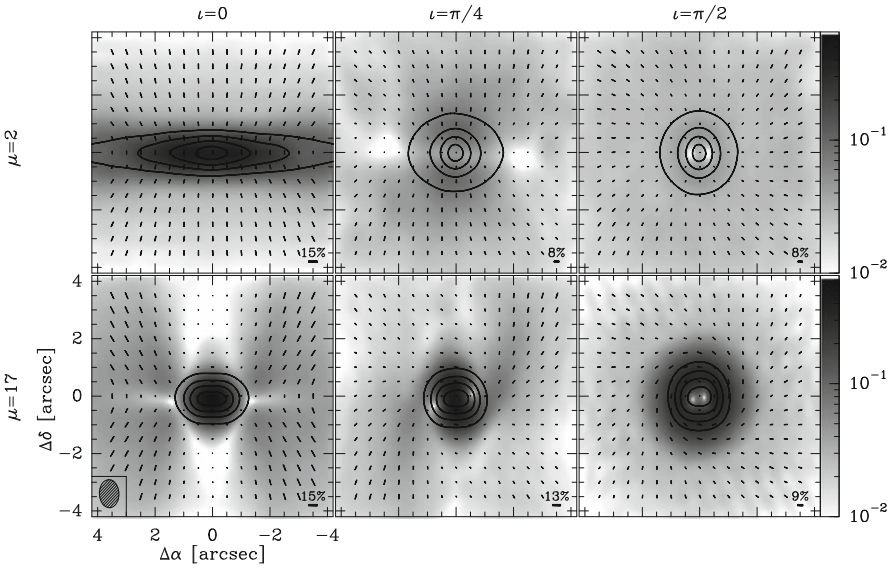

Fig. 2.8 Polarization maps for a collapsing and rotating magnetized core produced with the ARTIST dust polarization module DustPol (Padovani et al. 2012). The models were obtained using the RAMSES code. The *top row* shows the case of a strong magnetic field (mass-to-flux ratio $\mu = 2$) and the *bottom row* that for a weak magnetic field ($\mu = 17$). From *left to right* the inclination varies from edge-on to face-on. The source was assumed to be at $D = 140$ pc with a dust temperature $T_{\rm dust} = 10$ K. The simulated ALMA beam, at 350 GHz, is $0.98'' \times 0.68''$. The simulations show the core at an age of $t = 2.4 \times 10^4$ y with the magnetic field parallel to the rotation axis at $t = 0$. Contours show 30, 50, 70, and 90 % of the peak flux (from *left to right* for $\mu = 2$ the continuum peak flux is 0.43, 0.26, and 0.23 Jy beam^{-1}; for $\mu = 17$ is it 0.62, 0.74, and 0.72 Jy beam^{-1}). ALMA would reach the required 0.1 % linear polarization sensitivity in approximately 5 min on source integration time

Conclusion

ALMA will provide a several orders of magnitude improvement in polarimetric capabilities at the (sub-)millimetre wavelengths compared to the currently available instruments such as the SMA. Not only will the enhanced sensitivity allow for the imaging of magnetic fields in much larger samples of sources, but it will also allow for magnetic field imaging of dense and dusty regions in galaxies besides our own. By imaging the linear polarization of a variety of spectral lines, probing different regions in circumstellar and protostellar envelopes and outflows, it will be possible to generate a detailed picture of the magnetic field morphology. Applying the Chandrasekhar–Fermi method would then allow for measurements of the projected magnetic field strength at various densities. Added to this, circular polarization observations will be

(continued)

possible for a small number of molecules, such as CN, and will provide the line-of-sight magnetic field. Furthermore, ALMA polarization will also be able to constrain, for example, maser pumping models and models for the supermassive black hole Sgr A∗ at the Galactic Center.

The rapid increase in polarization observations that ALMA will produce will also likely provide challenges to several current theoretical models on the generation of polarized dust and line emission itself. Several of these theoretical descriptions are detailed in other chapters of this book, but they include dust alignment as well as the study of dust composition.

Finally, ALMA will be able to produce polarization data products even when this is not the main observational goal. Combined with the new developed analysis tools, such as those from the ARTIST project, the observations of magnetic fields will become increasingly accessible. Thus, ALMA polarization capabilities will usher in an exciting new era in the study of magnetic fields at (sub-)millimeter wavelength.

Acknowledgements WV would like to thank Marco Padovani and Susanne Aalto for providing figures and Daniel Tafoya and Kirsten Kraiberg Knudsen for feedback on the manuscript.

References

Aalto, S., Hüttemeister, S.: Astron. Astrophys. **362**, 42 (2000)
Allen, A., Shu, F.H., Li, Z.-Y.: Astrophys. J. **599**, 351 (2003)
Amiri, N., Vlemmings, W.H.T., Kemball, A.J., van Langevelde, H.J.: Astron. Astrophys. **538**, A136 (2012)
Balick, B., Frank, A.: Ann. Rev.Astron. Astrophys. **40**, 439 (2002)
Bartkiewicz, A., Szymczak, M., Cohen, R.J., Richards, A.M.S.: Mon. Not. R. Astron. Soc. **361**, 623 (2005)
Beck, R., Fletcher, A., Shukurov, A., et al.: Astron. Astrophys. **444**, 739 (2005)
Beuther, H., Vlemmings, W.H.T., Rao, R., van der Tak, F.F.S.: Astrophys. J. Lett. **724**, L113 (2010)
Brinch, C., Hogerheijde, M.R.: Astron. Astrophys. **523**, A25 (2010)
Bujarrabal, V., Castro-Carrizo, A., Alcolea, J., Sánchez Contreras, C. Astron. Astrophys. **377**, 868 (2001)
Castro-Carrizo, A., Quintana-Lacaci, G., Neri, R., et al.: Astron. Astrophys. **523**, A59 (2010)
Chandrasekhar, S., Fermi, E.: Astrophys. J. **118**, 116 (1953)
Cortes, P.C., Crutcher, R.M., Watson, W.D.: Astrophys. J. **628**, 780 (2005)
Cotton, W.D.: MMA Memo 208 (1998)
Crutcher, R.M., Troland, T.H., Kazes, I.: Astron. Astrophys. **181**, 119 (1987)
Crutcher, R.M., Roberts, D.A., Mehringer, D.M., Troland, T.H.: Astrophys. J. Lett. **462**, L79 (1996)
Escoffier, R. P., Comoretto, G., Webber, J.C., et al.: Astron. Astrophys. **462**, 801 (2007)
Falceta-Gonçalves, D., Vidotto, A.A., Jatenco-Pereira, V.: Mon. Not. R. Astron. Soc. **368**, 1145 (2006)
Falgarone, E., Troland, T.H., Crutcher, R.M., Paubert, G.: Astron. Astrophys. **487**, 247 (2008)
Fiebig, D., Guesten, R.: Astron. Astrophys. **214**, 333 (1989)
Fish, V.L., Reid, M.J.: Astrophys. J. Suppl. **164**, 99 (2006)

Frank, A., De Marco, O., Blackman, E., Balick, B.: arXiv:0712.2004 (2007)
Frau, P., Galli, D., Girart, J.M.: Astron. Astrophys. **535**, A44 (2011)
Fromang, S., Hennebelle, P., Teyssier, R.: Astron. Astrophys. **457**, 371 (2006)
Gaensler, B.M., Haverkorn, M., Staveley-Smith, L., et al.: Science **307**, 1610 (2005)
Girart, J.M., Crutcher, R.M., Rao, R.: Astrophys. J. Lett. **525**, L109 (1999)
Girart, J.M., Rao, R., Marrone, D.P.: Science **313**, 812 (2006)
Girart, J.M., Beltrán, M.T., Zhang, Q., Rao, R., Estalella, R.: Science **324**, 1408 (2009)
Girart, J.M., Patel, N., Vlemmings, W., Rao, R.: Astrophys. J. **751**, L20 (2012)
Glenn, J., Walker, C.K., Bieging, J.H., Jewell, P.R.: Astrophys. J. Lett. **487**, L89 (1997)
Goldreich, P., Kylafis, N.D.: Astrophys. J. Lett. **243**, L75 (1981)
Goldreich, P., Kylafis, N.D.: Astrophys. J. **253**, 606 (1982)
Gómez, Y., Tafoya, D., Anglada, G., et al.: Astrophys. J. **695**, 930 (2009)
Greaves, J.S., Holland, W.S., Minchin, N.R., Murray, A.G., Stevens, J.A.: Astron. Astrophys. **344**, 668 (1999)
Greaves, J.S., Holland, W.S., Jenness, T., Hawarden, T.G.: Nature **404**, 732 (2000)
Herpin, F., Baudry, A., Thum, C., Morris, D., Wiesemeyer, H.: Astron. Astrophys. **450**, 667 (2006)
Herpin, F., Baudy, A., Josselin, E., Thum, C., Wiesemeyer, H.: IAU Symp. **259**, 47 (2009)
Kemball, A.J., Diamond, P.J.: Astrophys. J. Lett. **481**, L111 (1997)
Krause, F., Beck, R.: Astron. Astrophys. **335**, 789 (1998)
Kuiper, R., et al.: In prep.
Kwok, S., Purton, C.R., Fitzgerald, P.M.: Astrophys. J. Lett. **219**, L125 (1978)
Lazarian, A.: J. Quant. Spectrosc. Radiative Transf. **79**, 881 (2003)
Leone, F., Martínez González, M.J., Corradi, R.L.M., Privitera, G., Manso Sainz, R.: Astrophys. J. Lett. **731**, L33 (2011)
Li, H.-B., Henning, T.: Nature **479**, 499 (2011)
Mestel, L., Spitzer, L. Jr.: Mon. Not. R. Astron. Soc. **116**, 503 (1956)
Morris, M., Lucas, R., Omont, A.: Astron. Astrophys. **142**, 107 (1985)
Ostriker, E.C., Stone, J.M., Gammie, C.F.: Astrophys. J. **546**, 980 (2001)
Padovani, M., Brinch, C., Girart, J.M., et al.: Astron. Astrophysics. **543**, 16 (2012)
Padovani, M., et al.: IAU Sump. **270**, 451 (2011)
Robishaw, T., Quataert, E., Heiles, C.: Astrophys. J. **680**, 981 (2008)
Sabin, L., Zijlstra, A.A., Greaves, J.S.: Mon. Not. R. Astron. Soc. **376**, 378 (2007)
Sarma, A.P., Troland, T.H., Romney, J.D.: Astrophys. J. Lett. **554**, L217 (2001)
Surcis, G., Vlemmings, W.H.T., Dodson, R., van Langevelde, H.J.: Astron. Astrophys. **506**, 757 (2009)
Surcis, G., Vlemmings, W.H.T., van Langevelde, H.J., Hutawarakorn Kramer, B.: Astron. Astrophys. **541**, A47 (2012)
Szymczak, M., Cohen, R.J., Richards, A.M.S.: Mon. Not. R. Astron. Soc. **297**, 1151 (1998)
Tang, Y.-W., Ho, P.T.P., Koch, P.M., et al.: Astrophys. J. **700**, 251 (2009)
Teyssier, R.: Astron. Astrophys. **385**, 337 (2002)
Thum, C., Morris, D.: Astron. Astrophys. **344**, 923 (1999)
Vlemmings, W.H.T.: Astron. Astrophys. **484**, 773 (2008)
Vlemmings, W.H.T., van Langevelde, H.J., Diamond, P.J.: Astron. Astrophys. **434**, 1029 (2005)
Vlemmings, W.H.T., Diamond, P.J., Imai, H.: Nature, **440**, 58 (2006)
Vlemmings, W.H.T., Diamond, P.J., van Langevelde, H.J., Torrelles, J.M.: Astron. Astrophys. **448**, 597 (2006)
Vlemmings, W.H.T., Surcis, G., Torstensson, K.J.E., van Langevelde, H.J.: Mon. Not. R. Astron. Soc. **404**, 134 (2010)
Vlemmings, W.H.T., Humphreys, E.M.L., Franco-Hernández, R.: Astrophys. J. **728**, 149 (2011)
Vlemmings, W.H.T., Ramstedt, S., Rao, R., Maercker, M.: Astron. Astrophys. **540**, L3 (2012)
Wolak, P., Szymczak, M., Gérard, E.: Astron. Astrophys. **537**, A5 (2012)

Part II
Techniques for Observing Cosmic Magnetic Fields

Chapter 3
Synchrotron Radiation and Faraday Rotation

George Heald

Abstract Synchrotron radiation and its degree of linear polarization are powerful tracers of magnetic fields that are illuminated by cosmic ray electrons. Faraday rotation of the linearly polarized radiation is induced by intervening line-of-sight magnetic fields that are embedded in ionized plasmas. For decades these observational tools have been workhorses for utilizing radio telescopes to study magnetic fields inside and outside the Milky Way. In the modern era they are becoming still more powerful with the advent of broadband receiving systems on the current generation of radio telescopes. In the study of Faraday rotation in particular, rapid development is taking place in techniques to confidently recover the physical conditions of the magnetoionized medium in the Milky Way and extragalactic objects.

3.1 Introduction

Magnetic fields are not directly observable, so their properties must be inferred by their physical effects on matter and radiation. Powerful optical and infrared techniques have been developed for studying magnetic fields, but these are mostly applicable in the very nearby Universe, typically within the Milky Way (see contributions in this volume by Jones and Anderson). Zeeman splitting is a very important radio tracer of magnetic field strengths (see Troland, this volume) but is also used primarily within the Milky Way.

For the study of cosmic magnetism, it is the illumination of magnetic fields by relativistic positrons and electrons (henceforth referred to collectively as electrons) that provides the most powerful and far-reaching information. In this chapter, we briefly overview theoretical aspects of the physics involved, before highlighting some basic techniques using synchrotron radiation that are used to study various aspects of magnetic fields. A strong focus is placed on the still rapidly developing field of Rotation Measure (RM) Synthesis. We conclude with a brief discussion of the capabilities of modern radio telescopes in exploiting these techniques.

G. Heald (✉)
ASTRON, Postbus 2, 7990 AA Dwingeloo, The Netherlands
e-mail: heald@astron.nl

A. Lazarian et al. (eds.), *Magnetic Fields in Diffuse Media*, Astrophysics and Space Science Library 407, DOI 10.1007/978-3-662-44625-6_3

3.2 Synchrotron Radiation

Here we provide a summary of the theory of synchrotron radiation as background for the observational approaches described later in this section. This brief discussion (here and at the beginning of Sect. 3.3) is distilled from the more involved treatments given by Shu (1991), Condon (1992), and Binney and Merrifield (1998), to which the reader is referred for more information.

Magnetic fields accelerate charged particles via the Lorentz force. The acceleration is given by

$$\frac{d}{d\tau}(m\gamma\mathbf{v}) = q\left(\frac{\mathbf{v}}{c}\times\mathbf{B}\right) \tag{3.1}$$

where m is the mass of the particle with charge q, τ is the retarded time, the Lorentz factor $\gamma = (1-v^2/c^2)^{-1/2}$, and $\mathbf{B}$ is the magnetic field. The trajectory of the particle is helical, with a gyration frequency $\omega_B \equiv qB/\gamma mc$ and pitch angle θ (where $\theta = 90°$ for a circular orbit, and $\theta = 0°$ for a particle trajectory parallel to $\mathbf{B}$). The radiated power from the accelerating charge is given (in cgs units) by

$$P = \frac{2}{3}\frac{q^4}{m^2c^5}(\gamma v)^2(B\sin\theta)^2 = 2.37\times10^{-15}\left(\frac{E}{\mathrm{erg}}\right)^2\left(\frac{B\sin\theta}{\mu\mathrm{G}}\right)^2 \tag{3.2}$$

where the final equality is given for electrons in particular, since the dependence on the mass-to-charge ratio means that electrons are by several orders of magnitude dominant over protons or ions in generating synchrotron radiation. The synchrotron power peaks at the characteristic frequency (in Hz),

$$\nu_c = \frac{3}{4\pi}\frac{q}{mc}\gamma^2(B\sin\theta) = 6.26\times10^3\left(\frac{E}{\mathrm{erg}}\right)^2\left(\frac{B\sin\theta}{\mu\mathrm{G}}\right) \tag{3.3}$$

Equation (3.3) tells us that for radio observations (frequencies at or above tens of MHz) and with typical magnetic field strengths of order μG, the observed population of electrons have $\gamma \gg 1$. The radiation is thus highly beamed (width $\sim \gamma^{-1}$) in the direction of the velocity vector. The population of electrons has a power-law energy distribution given by

$$n(\gamma)d\gamma = n_0\gamma^{-p}d\gamma \tag{3.4}$$

where a typical value for the power law index is $p \approx 2.5$. The resulting synchrotron luminosity is thus also a power law,

$$L_\nu \propto \nu^{-(p-1)/2} \equiv \nu^{-\alpha} \tag{3.5}$$

with a typical spectral index $\alpha = 0.75$ for $p = 2.5$. The particles lose energy due to the power emitted in Eq. (3.2), with a characteristic timescale of

$$\tau_{\rm syn} = -\frac{\gamma}{d\gamma/d\tau} = 4\pi \frac{mc}{\sigma_{\rm T}} \gamma^{-1} (B \sin\theta)^{-2} \tag{3.6}$$

where the Thomson cross-section $\sigma_{\rm T} = 8\pi q^4/3m^2c^4$. Since $\tau_{\rm syn}$ is shorter for more energetic electrons (higher γ) the power law in Eq. (3.4) steepens with time (often corresponding to distance from the site of cosmic ray acceleration), therefore increasing the value of α. This is referred to as "synchrotron aging". Substituting Eq. (3.3), we can see that

$$\left(\frac{\tau_{\rm syn}}{\rm yr}\right) = 1.06 \times 10^9 \left(\frac{B \sin\theta}{\mu\rm G}\right)^{-1.5} \left(\frac{\nu_{\rm c}}{\rm GHz}\right)^{-0.5} \tag{3.7}$$

3.2.1 Estimation of Magnetic Field Strength

Given an observation of synchrotron radiation from a celestial object, a natural astrophysical question is the strength of the magnetic field within the emitting source. From Eq. (3.2) it is clear however that the observed synchrotron radio power alone is not sufficient to calculate the strength of the magnetic field that accelerated the cosmic ray electrons. The synchrotron radiation is also dependent on the energy of the emitting particles, which is not necessarily known a priori, although in some cases estimates from γ-ray observations may be available (e.g., Strong et al. 2011; Jaffe et al. 2011; Bringmann et al. 2012; Abdo et al. 2010). A typical approach for dealing with the magnetic field—cosmic ray degeneracy in circumstances where the CR energy is not known is to assume that the magnetic energy density is similar to the cosmic ray energy density. In other words, it is assumed that there is energy *equipartition* of cosmic rays and magnetic fields.[1]

The classical equation for equipartition magnetic field strength can be found in textbooks (e.g., Wilson et al. 2009). Typical results using this scheme to estimate the magnetic field strength in spiral galaxies are summarized by e.g. Beck (2001). The technique is based on numerous subtle assumptions about the distribution and energy spectra of various cosmic ray particles. These assumptions are discussed extensively by Beck and Krause (2005), who also give an updated formula for determining magnetic field strength estimates on the basis of equipartition. The resulting relation allows an estimate of the magnetic field strength, given measurements of the synchrotron intensity and spectral index α, and estimates

[1] Other assumptions, such as pressure equipartition and minimum energy, are also commonly used and may be considered as roughly equivalent; see also the more detailed discussion by Beck and Krause (2005).

of the electron-to-proton ratio and pathlength through the emitting volume. The dependence on all of these parameters except for the synchrotron spectral index is weak, in a powerlaw dependence with index $1/(\alpha + 3)$ as shown by Beck and Krause (2005).

3.3 Polarization and Faraday Rotation

So far, the synchrotron radiation has been treated as if it is fully unpolarized. However, the beamed synchrotron radiation described in Sect. 3.2 is linearly polarized, with the electric vector of the radiation field oriented perpendicular to the component of the magnetic field in the plane of the sky ($B_\perp$, where $\mathbf{B} = \hat{\mathbf{x}}B_\perp + \hat{\mathbf{y}}B_\parallel$ with $\hat{\mathbf{y}}$ pointing along the line of sight). If the field is ordered, the radiation can be linearly polarized up to a maximum fraction

$$\frac{P}{I} = \frac{p+1}{p+7/3} \tag{3.8}$$

meaning that for $p = 2.5$ as discussed in Sect. 3.2, the polarized fraction is up to 72 % for a fully ordered field. Note that synchrotron aging leads to larger values of p, and therefore to somewhat larger values of P/I.

The linear polarization traces ordered fields lying in the plane of the sky. A tangled component to the magnetic field lowers the polarization fraction. So too do Faraday effects, which we now describe.

Radiation passing through a magnetoionized medium suffers propagation effects. This happens because the phase velocity of right-handed circularly (RHC) and left-handed circularly (LHC) polarized light is different in a magnetoionized medium (see, e.g., Jackson 1998). This results in Faraday rotation, a frequency dependent modification of the linear polarization angle,

$$\chi = \chi_0 + \phi\,\lambda^2. \tag{3.9}$$

The proportionality constant, the "Faraday depth" (ϕ), encapsulates the physics of the situation:

$$\phi = 0.81 \int_{\text{source}}^{\text{observer}} n_e \mathbf{B} \cdot d\mathbf{l} \tag{3.10}$$

where n_e is the electron density in cm^{-2}, $\mathbf{B}$ is the magnetic field in μ G, and $\mathbf{l}$ is the line of sight in pc. Classical analysis of polarized synchrotron emission involves measuring χ at a very small number of widely spaced observing frequencies, and fitting a linear slope in Eq. (3.9). In such a situation, ϕ is referred to as the Faraday rotation measure (RM). However, this approximation is only valid if there is a single foreground medium inducing the Faraday rotation (and not emitting its

own polarized synchrotron radiation within the volume), between the background source and the observer. In general, polarized synchrotron radiation may originate from within volumes that induce Faraday rotation, leading to polarized synchrotron emission at a range of ϕ. The "Faraday dispersion function", often referred to as the "Faraday spectrum", describes the complex polarization vector as a function of ϕ, and is written $F(\phi)$. See Brentjens and de Bruyn (2005) and Heald (2009) for examples.

Additional practical complications arise if the Faraday depth is large enough to substantially rotate the polarization vector within the observing bandwidth (an effect known as bandwidth depolarization). This effect can be mitigated with modern multi-channel correlators, as described in Sect. 3.5. Moreover, the individual measurements of χ are only known modulo π (the $n\pi$ ambiguity) making the fitted slope uncertain, as is well illustrated by Rand and Lyne (1994).

Robust recovery of polarized synchrotron radiation and its Faraday rotation in general circumstances is a topic of current study, as described in Sect. 3.4.

3.4 Rotation Measure Synthesis

A robust method for determining the Faraday dispersion function was proposed by Burn (1966). It was little used until its revival by Brentjens and de Bruyn (2005), who coined the phrase "RM Synthesis". The essence of the technique is described here. Further developments and extensions are explained afterward.

Following Burn (1966), we begin by writing the linear polarization vector as a complex quantity,

$$P = Q + iU = P_0 e^{2i\chi} \tag{3.11}$$

Substituting the polarization angle to account for its frequency dependence, and integrating over all possible values of the Faraday depth, we end up with

$$P(\lambda^2) = \int_{-\infty}^{\infty} P_0 e^{2i(\chi_0 + \phi\lambda^2)} d\phi \tag{3.12}$$

or

$$P(\lambda^2) = \int_{-\infty}^{\infty} F(\phi) e^{2i\phi\lambda^2} d\phi \tag{3.13}$$

where $F(\phi)$, the Faraday dispersion function, describes the intrinsic polarized flux as a function of the Faraday depth.

Equation (3.13), which connects the physics of the situation (encapsulated in $F(\phi)$) to the observables (described by $P(\lambda^2)$), takes the form of a Fourier transform. Hence, it can be inverted to yield the Faraday dispersion function as a

function of observable quantities.

$$F(\phi) = \int_{-\infty}^{\infty} P(\lambda^2) e^{-2i\phi\lambda^2} d\lambda^2 \tag{3.14}$$

This can be thought of as a Fourier decomposition of the complex (Q,U) polarization vector's frequency variation into one or more "modes", each of which is the result of a polarized signal at a particular Faraday depth.

Using Eq. (3.13) is not directly possible, however, because the integral requires measurement over all possible values of the square of the observing wavelength λ. This is impossible not merely because radio telescopes cannot cover all wavelengths, but moreover because it is impossible to observe at negative values of λ^2. One option is to make an assumption about the behavior at unsampled values of λ^2; this is addressed in Sect. 3.4.2. For the moment, we will proceed by recasting Eq. (3.14) using a window function, as introduced by Brentjens and de Bruyn (2005). This leads to

$$\tilde{P}(\lambda^2) = W(\lambda^2) P(\lambda^2) = W(\lambda^2) \int_{-\infty}^{\infty} F(\phi) e^{2i\phi\lambda^2} d\phi \tag{3.15}$$

and the inverse is the *reconstructed* Faraday dispersion function

$$\tilde{F}(\phi) = K \int_{-\infty}^{\infty} \tilde{P}(\lambda^2) e^{-2i\phi\lambda^2} d\lambda^2 = F(\phi) \star R(\phi) \tag{3.16}$$

which is the convolution of the actual Faraday dispersion function with the RM Spread Function (RMSF), $R(\phi)$. K is a normalizing factor and is computed as the inverse of the integral of the weight function, namely

$$K = \left(\int_{-\infty}^{\infty} W(\lambda^2) d\lambda^2 \right)^{-1}. \tag{3.17}$$

The RMSF describes the instrumental response based on the wavelength coverage of the observations combined to reconstruct the Faraday dispersion function.

$$R(\phi) \equiv K \int_{-\infty}^{\infty} W(\lambda^2) e^{-2i\phi\lambda^2} d\lambda^2 \tag{3.18}$$

The weight function, $W(\lambda^2)$, can be used to give different relative weights to each of the polarization measurements in each observed frequency channel in order to optimize the RMSF behavior. This can be thought of in analogy to *uv* weighting in synthesis imaging, and is an option that has been little explored to date in the case of RM Synthesis.

Finally, we note that there are two additional features of the RM Synthesis equations. The first takes into account that the integral formulation is still incorrect

in that real observations consist of N discrete samples in frequency space, thus we rewrite as a summation. Second, we use the Fourier shift theorem to add an additional offset factor ($\lambda_0^2 = N^{-1} \sum \lambda^2$) in the exponential, making the variations in the real and imaginary part of the RMSF far less rapid (see Brentjens and de Bruyn 2005 and Appendix A.2 of Heald et al. 2009). This second change is purely cosmetic. Together, we conclude with

$$\tilde{F}(\phi) = K \sum_{c=1}^{N} \tilde{P}_c e^{-2i\phi(\lambda_c^2 - \lambda_0^2)} \tag{3.19}$$

$$R(\phi) = K \sum_{c=1}^{N} W_c e^{-2i\phi(\lambda_c^2 - \lambda_0^2)} \tag{3.20}$$

The formulation in Eq. (3.19) can be thought of as a series of trial RM calculations: if the trial RM is correct, then a substantial (large signal-to-noise) response is observed; if not then no signal is present in the output spectrum.

As written, Eq. (3.19) suggests a calculation for a single line-of-sight. However, the procedure can be done for every pixel of a pair of image cubes (one each of Stokes Q and U). The result of this would be a pair of image cubes, with the third axis corresponding to Faraday depth instead of frequency as in the original cubes.

From the RMSF, there are several quantities of interest that give an indication of the quality of the Faraday dispersion function reconstruction (see Brentjens and de Bruyn 2005; Schnitzeler et al. 2009). These are:

$$\text{FWHM} = \frac{3.8}{\Delta\lambda^2} \tag{3.21}$$

$$\text{max} - \text{scale} = \frac{\pi}{\lambda_{\text{min}}^2} \tag{3.22}$$

$$|\phi_{\text{max}}| = \frac{\sqrt{3}}{\delta\lambda^2} \tag{3.23}$$

Examples of the RMSF are given in Fig. 3.1, illustrating that the metric in Eq. (3.21) is not the only consideration in good recovery of the RM of polarized sources. The left column gives a variety of observational frequency setups, and the right column shows the corresponding RMSF (amplitude only) for each frequency coverage. In the first row, the situation corresponding to two single frequencies is shown. In this case, the two frequencies are 1,150 and 1,450 MHz. The $n\pi$ ambiguity in this case would lead to an ambiguity in RM of

$$\Delta\text{RM} = \frac{\pi}{\Delta\lambda^2} = \frac{\pi}{0.02521\,\text{m}^2} = 124.6\,\text{rad}\,\text{m}^{-2} \tag{3.24}$$

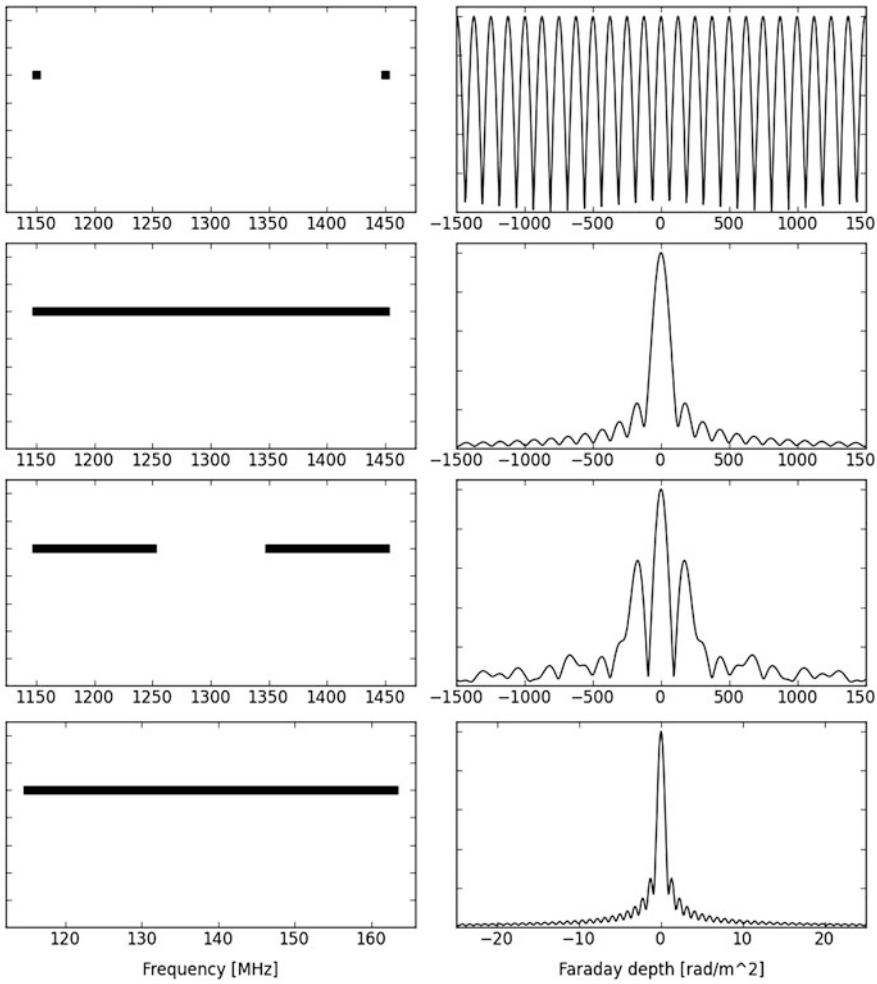

Fig. 3.1 Some examples of frequency coverage (*left panels*) and corresponding RMSF (amplitude only; *right panels*). *Top row*: Two single frequency measurements separated by 300 MHz. The corresponding RMSF is equivalent to the $n\pi$ ambiguity in "classical" RM determination. *Second row*: Broadband (multi-channel) coverage using the same frequency span. The sidelobes of the RMSF have been strongly suppressed. *Third row*: Same coverage but with a gap, as might be produced by RFI flagging. Sidelobe suppression is not as effective, but the width of the central peak remains the same. *Bottom row*: Broadband (multi-channel) coverage at low frequencies as provided by e.g. LOFAR (see the chapter by Beck in this volume). The RM precision is extremely high in such cases. Further details of the different observational setups are discussed in the text

The RMSF in this case clearly has peaks that are found at the same spacing. Hence, RM Synthesis in this case yields the same uncertainty as a normal RM analysis would provide. The situation changes when the frequency span is more uniformly covered with multiple individual measurements. In the second row, three hundred 1 MHz channels are evenly spaced (in frequency) between 1,150 and 1,450 MHz. This case is representative of the type of frequency coverage that will be possible with e.g. APERTIF (Oosterloo et al. 2009) and ASKAP (Johnston et al. 2009), and shows that the sidelobes corresponding to the $n\pi$ ambiguity are significantly suppressed. The suppression of sidelobes is rather different in the third row, where two frequency windows, each consisting of one hundred 1 MHz channels, are separated by 100 MHz. Such a situation might arise due to strong RFI at particular frequencies (between 1,250 and 1,350 MHz in this case), for example. In the given example, all sidelobes except the innermost ones are suppressed. This example can be thought of as similar to the Young double slit experiment: the width of each lobe is related to the full spread in λ^2, but there is an envelope with a width corresponding to the span of each frequency window. In the fourth row, an example is shown at low radio frequencies (240 channels, each of 0.2 MHz), illustrating the substantially better RM resolution. Such a situation is provided by LOFAR (van Haarlem et al. 2013), as shown by Sotomayor-Beltran et al. (2013) (see also the chapter by Beck in this volume).

An intriguing possibility is to include the Fourier transform corresponding to Eq. (3.19) together with the Fourier transform already used to perform the imaging step when dealing with observations of an aperture synthesis radio telescope. This technique, called Faraday synthesis (Bell and Enßlin 2012; see also Pen et al. 2009), transforms directly from visibilities to a three-dimensional Faraday cube, with two angular dimensions (i.e. Right Ascension and Declination) as well as a third corresponding to Faraday depth. Moreover, the deconvolution in Faraday space (described in Sect. 3.4.1) can be implemented together with the image-plane deconvolution. The simulated data that have been used in this technique show great promise: along with improved angular resolution, greater image fidelity is observed in the reconstructed Faraday cubes. An illustration of this is given in Fig. 3.2. The example is based on simulated data. With real data, additional complications will be present. For example, in order to apply Faraday synthesis to wide-field interferometric telescopes such as LOFAR, imaging steps such as w-projection (Cornwell et al. 2008) and A-projection (Bhatnagar et al. 2008) will need to be included in addition to the Faraday synthesis operation along the third axis.

3.4.1 RM Synthesis Deconvolution

The practical application of RM Synthesis must take into account the discrete (and incomplete) nature of the λ^2 coverage in the observations that are used to obtain the measured $\tilde{P}(\lambda^2)$. A major effect that has to be dealt with is the sidelobe response in the RMSF, as illustrated in Fig. 3.1. Cases in which this is essential include

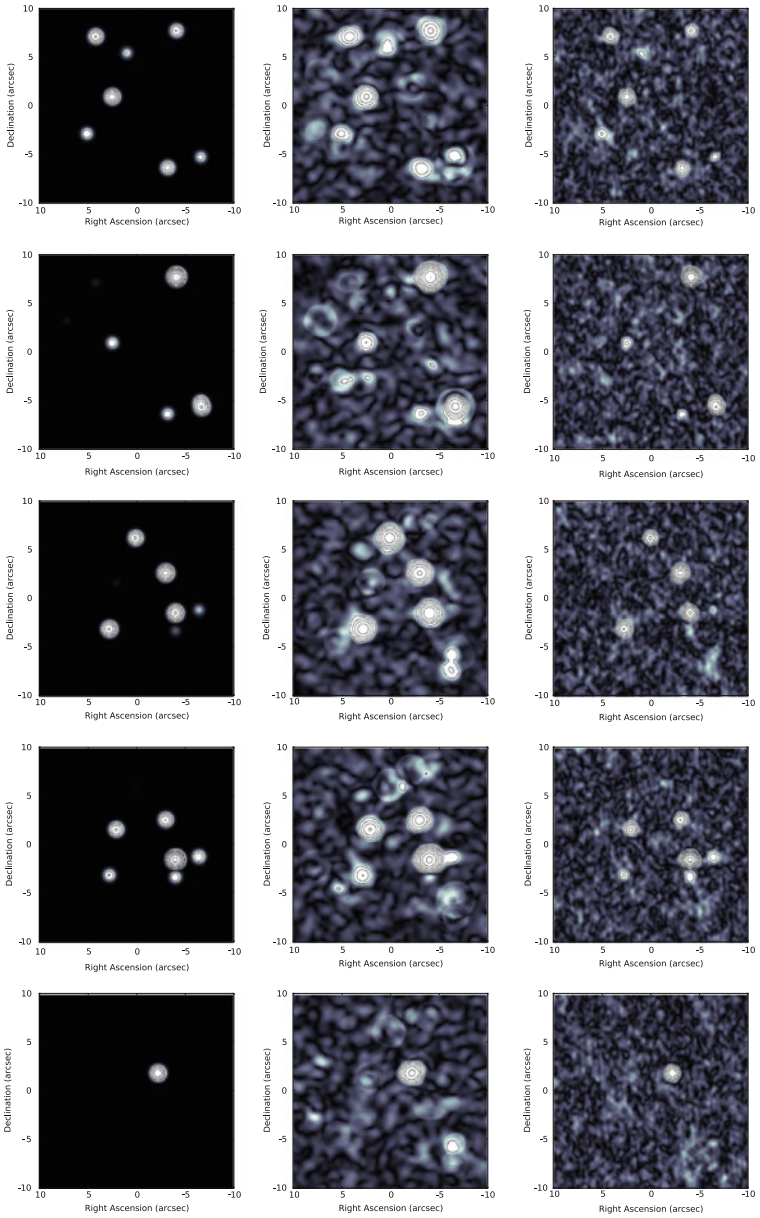

Fig. 3.2 Illustration of Faraday synthesis, reproduced from Bell and Enßlin (2012). The panels show a comparison between an input model of 30 point sources, all at different values of RM, and two reconstructions, at several ϕ values. In each frame, the greyscale varies linearly from 0–50 mJy beam^{-1}, and the contours begin at 50 mJy beam^{-1} with a factor of 2 between each level. *Left*: the model image convolved with an ($0.8'' \times 0.8'' \times 40$ rad m^{-2}) Gaussian. *Middle*: a 2+1D reconstruction (indicating a 2D inversion to an image-plane frequency cube, followed by a 1D RM Synthesis operation along the third axis to Faraday depth space). *Right*: the 3D (Faraday synthesis) reconstruction. *Top to bottom*: $\phi = -205, -160, 200, 230,$ and 395 rad m^{-2}

a polarized source behind a polarized Milky Way screen, and a polarized source (especially at low ϕ) in the presence of instrumental polarization (which tends to have ϕ close to zero). In both cases, the potential sidelobe confusion will decrease the quality of the polarized properties recovered from the reconstructed Faraday dispersion function.

The basic method of deconvolution is based on the analogous procedure developed for image plane deconvolution in aperture synthesis (Högbom 1974). It is described by Brentjens (2007) and Heald et al. (2009). The implementation from the latter paper has been included in the standard MIRIAD (Sault et al. 1995) distribution.

The deconvolution technique consists of the following steps. If the input data are in the form of Faraday cubes, then the technique is performed independently for every spatial pixel in the cube.

1. The most significant peak of the RM spectrum is identified. Typically this is done by simply searching for the peak amplitude of the dirty Faraday spectrum ($|F(\phi)|$). An optional alternative is to cross-correlate the complex Faraday spectrum $F(\phi) = Q(\phi) + iU(\phi)$ with the complex RMSF, and search for the maximum cross-correlation amplitude. This may help to distinguish real peaks in extreme cases of sidelobe confusion, but in practice has not been found to make a substantial improvement in deconvolution quality (Heald et al. 2009).
2. The location along the ϕ axis of the peak identified in step (1) is recorded as ϕ_m.
3. If $|F(\phi_m)|$ is greater than a user-defined threshold, then the RMSF is shifted (to be centered at ϕ_m) and scaled (to $gF(\phi_m)$ where g is a gain factor; typically $g = 0.1$, though note that Macquart et al. (2012) advocate $g = 1.0$ to avoid incomplete recovery of the full polarized signal). This shifted and scaled version of the complex RMSF is subtracted from the current residual spectrum. The value of $gF(\phi_m)$ is recorded and added to a list of clean components to form a clean component spectrum.
4. Once a stop criterion has been reached (maximum number of iterations, or the threshold test in the previous step fails), the clean component spectrum is convolved with a real-valued Gaussian restoring beam and added to the residuals. The output is the cleaned Faraday spectrum.

The deconvolution method described above has some practical limitations. First, depending on the range of frequencies sampled in the observation, extended features in Faraday spectra may not be well recovered (see Eq. (3.22)). Deconvolution of the type described here is not able to recover extended Faraday signals (that were not sampled in the initial observation, just as missing short spacing information in interferometer measurements cannot be recovered through image-plane CLEAN). Moreover the complex nature of the individual components in a Faraday spectrum can cause unexpected interference effects when they are closely spaced (i.e. spaced by less than the FWHM of the RMSF; see Farnsworth et al. 2011). In the worst case, the peak of the Faraday spectrum produced by RM Synthesis can be outside of the ϕ range bounded by the individual sources. This can cause RM-CLEAN to begin

deconvolution at the wrong location ϕ_m in step (1) of the procedure enumerated above. Having started at the wrong ϕ_m, the algorithm cannot recover.

Alternative approaches have been recently developed, which work by minimizing the difference between data and model in the measurement (λ^2) domain. These include the use of the "sparse" technique described by Andrecut et al. (2012) to simultaneously fit a number of individual ϕ components, which can be thin or thick, from an overcomplete dictionary of basis functions. (See also Li et al. 2011 for an earlier and complementary treatment using compressive sensing techniques.) Another possibility is to utilize the maximum likelihood (ML) estimation technique described by Bell et al. (2013), in which an initial guess based on a standard RM-CLEAN is updated through least-squares minimization and merging of nearby clean components (note that a similar but somewhat less general component-merging strategy was adopted by Macquart et al. 2012).

A topic of ongoing research is the robustness of the polarized source properties that can be recovered following the use of RM Synthesis (and RM-CLEAN). Macquart et al. (2012) and George et al. (2012) present detailed analyses of the reliability of polarized features identified in Faraday spectra, finding high confidence in recovered source parameters only above $S/N \approx 7$–8. Meanwhile, Hales et al. (2012) derive an analytical formalism for assessing the threshold for reliable polarized source parameter recovery. An interesting outcome from their analysis indicates that while on the one hand finer channelization leads to the ability to recover polarized sources with higher ϕ (see Eq. (3.23)), on the other hand better reliability in source recovery can be achieved with fewer (wider in λ^2) channels (although note that the improvement is only substantial for a reduction in number of channels by at least about an order of magnitude). This suggests that a balance should be struck in selection of the channelization of future polarization work.

3.4.2 Wavelet Based RM Synthesis

An interesting alternative approach to the standard RM Synthesis technique described above is to recast the basic equations (3.13) and (3.14) as a wavelet transform instead of as a Fourier transform. This is described by Frick et al. (2010), who adopt the constraint that the Faraday dispersion function (or each individual feature therein) should be symmetric with respect to its center,

$$F(2\phi_0 - \phi) = F(\phi) \tag{3.25}$$

where ϕ_0 is the center of a feature of interest in the Faraday spectrum. This assumption leads to the counterpart in the measurement domain that

$$P(-\lambda^2) = e^{-4i\phi_0\lambda^2} P(\lambda^2). \tag{3.26}$$

The antisymmetric case is a straightforward extension of this treatment. However, if more than one feature is present in the Faraday spectrum, then a single point of symmetry is not a correct description. The use of wavelets effectively allows the symmetry condition to be applied for all detected features in the Faraday spectrum.

Frick et al. (2010) show that wavelet-based RM Synthesis can be useful to identify extended structures in Faraday space, and can help to better recover intrinsic properties of the polarized emission. In a followup analysis Frick et al. (2011) investigate further practical aspects of applying wavelet analysis to observational data, and illustrate the ability of the technique to isolate features in the Faraday spectrum which are indicative of underlying physical properties in the observed object.

3.5 Outlook

Ongoing investigations into the analysis of polarized synchrotron emission using RM Synthesis and related techniques are bound to bear fruit in the coming few years. Several new telescopes are being built which provide wide bandwidths and excellent spectral sampling, along with good polarization characteristics. Among these, low frequency telescopes like LOFAR (van Haarlem et al. 2013), the Murchison Widefield Array (MWA; Tingay et al. 2013) and Long Wavelength Array (LWA; Ellingson et al. 2012) will be well suited to detection of Faraday thin sources and extremely high RM precision (see, e.g., Sotomayor-Beltran et al. 2013). Square Kilometre Array (SKA) pathfinder and precursor telescopes operating at 1 GHz frequencies, the Aperture Tile In Focus (APERTIF) upgrade to the Westerbork Synthesis Radio Telescope (WSRT; Oosterloo et al. 2009) and the Australian Square Kilometre Array Pathfinder (ASKAP; Johnston et al. 2009) will collectively provide an all-sky polarization catalog of extragalactic sources. The MeerKAT SKA precursor (Booth and Jonas 2012) will by virtue of its multiband coverage allow high-quality reconstruction of Faraday thick structures. The upgraded Very Large Array (VLA; Perley et al. 2011) goes so far as to cover the complete frequency range from $1 - 50$ GHz, enabling exquisite studies of Faraday structures (see, e.g., Irwin et al. 2012). The future prospects have been summarized in detail by Beck et al. (2012). The techniques described here will certainly provide significant new opportunities for the understanding of cosmic magnetic fields, as is also discussed by Beck (this volume).

Acknowledgements I would like to thank Marijke Haverkorn for reading an early version of the manuscript and for very useful comments.

References

Abdo, A.A., Ackermann, M., Ajello, M., Allafort, A., Atwood, W.B., Baldini, L., Ballet, J., Barbiellini, G., Bastieri, D., Bechtol, K., Bellazzini R., Berenji, B., Blandford, R.D., Bloom, E.D., Bonamente, E., Borgland, A.W., Bouvier, A., Brandt, T.J., Bregeon, J., Brigida, M., Bruel, P., Buehler, R., Burnett, T.H., Buson, S., Caliandro, G.A., Cameron, R.A., Cannon, A., Caraveo, P.A., Casandjian, J.M., Cecchi, C., Çelik, Ö., Charles, E., Chekhtman, A., Chiang, J., Ciprini, S., Claus, R., Cohen-Tanugi, J., Conrad, J., Dermer, C.D., de Angelis, A., de Palma, F., Digel, S.W., Silva, E.D.C.E., Drell, P.S., Drlica-Wagner, A., Dubois, R., Favuzzi, C., Fegan, S.J., Fortin, P., Frailis, M., Fukazawa, Y., Funk, S., Fusco, P., Gargano, F., Germani, S., Giglietto, N., Giordano, F., Giroletti, M., Glanzman, T., Godfrey, G., Grenier, I.A., Grondin, M.H., Guiriec, S., Gustafsson, M., Hadasch, D., Harding, A.K., Hayashi, K., Hayashida, M., Hays, E., Healey, S.E., Jean, P., Jóhannesson, G., Johnson, A.S., Johnson, R.P., Johnson, T.J., Kamae, T., Katagiri, H., Kataoka, J., Kerr, M., Knödlseder, J., Kuss, M., Lande, J., Latronico, L., Lee, S.H., Lemoine-Goumard, M., Longo, F., Loparco, F., Lott, B., Lovellette, M.N., Lubrano, P., Madejski, G.M., Makeev, A., Martin, P., Mazziotta, M.N., Mehault, J., Michelson, P.F., Mitthumsiri, W., Mizuno, T., Moiseev, A.A., Monte, C., Monzani, M.E., Morselli, A., Moskalenko, I.V., Murgia, S., Naumann-Godo, M., Nolan, P.L., Norris, J.P., Nuss, E., Ohsugi, T., Okumura, A., Omodei, N., Orlando, E., Ormes, J.F., Ozaki, M., Paneque, D., Panetta, J.H., Parent, D., Pepe, M., Persic, M., Pesce-Rollins, M., Piron, F., Porter, T.A., Rainò, S., Rando, R., Razzano, M., Reimer, A., Reimer, O., Ritz, S., Romani, R.W., Sadrozinski, H.F.W., Saz Parkinson, P.M., Sgrò, C., Siskind, E.J., Smith, D.A., Smith, P.D., Spandre, G., Spinelli, P., Strickman, M.S., Strigari, L., Strong, A.W., Suson, D.J., Takahashi, H., Takahashi, T., Tanaka, T., Thayer, J.B., Thompson, D.J., Tibaldo, L., Torres, D.F., Tosti, G., Tramacere, A., Uchiyama, Y., Usher, T.L., Vandenbroucke, J., Vianello, G., Vilchez, N., Vitale, V., Waite, A.P., Wang, P., Winer, B.L., Wood, K.S., Yang, Z., Ziegler, M.: Fermi large area telescope observations of local goup galaxies: detection of M 31 and search for M 33. Astron. Astrophys. **523**, L2 (2010). doi:10.1051/0004-6361/201015759. 1012.1952

Andrecut, M., Stil, J.M., Taylor, A.R.: Sparse Faraday rotation measure synthesis. Astron. J. **143**, 33 (2012). doi:10.1088/0004-6256/143/2/33. 1111.4167

Beck, R.: Galactic and extragalactic magnetic fields. Space Sci. Rev. **99**, 243–260 (2001). arXiv:astro-ph/0012402

Beck, R., Krause, M.: Revised equipartition and minimum energy formula for magnetic field strength estimates from radio synchrotron observations. Astronomische Nachrichten **326**, 414–427 (2005). doi:10.1002/asna.200510366. arXiv:astro-ph/0507367

Beck, R., Frick, P., Stepanov, R., Sokoloff, D.: Recognizing magnetic structures by present and future radio telescopes with Faraday rotation measure synthesis. Astron. Astrophys. **543**, A113 (2012). doi:10.1051/0004-6361/201219094. 1204.5694

Bell, M.R., Enßlin, T.A.: Faraday synthesis. The synergy of aperture and rotation measure synthesis. Astron. Astrophys. **540**, A80 (2012). doi:10.1051/0004-6361/201118672. 1112.4175

Bell, M.R., Oppermann, N., Crai, A., Enßlin, T.A.: Improved CLEAN reconstructions for rotation measure synthesis with maximum likelihood estimation. Astron. Astrophys. **551**, L7 (2013). doi:10.1051/0004-6361/201220771. 1211.5105

Bhatnagar, S., Cornwell, T.J., Golap, K., Uson, J.M.: Correcting direction-dependent gains in the deconvolution of radio interferometric images. Astron. Astrophys. **487**, 419–429 (2008). doi:10.1051/0004-6361:20079284. 0805.0834

Binney, J., Merrifield, M.: Princeton, N.J.: Galactic astronomy, Princeton University Press, Princeton series in astrophysics, QB857–B522 (1998)

Booth, R.S., Jonas, J.L.: An overview of the MeerKAT Project. Afr. Skies **16**, 101 (2012)

Brentjens, M.A.: Radio polarimetry in 2.5D. Ph.D. thesis, Rijksuniversiteit Groningen (2007)

Brentjens, M.A., de Bruyn, A.G.: Faraday rotation measure synthesis. Astron. Astrophys. **441**, 1217–1228 (2005). doi:10.1051/0004-6361:20052990. arXiv:astro-ph/0507349

Bringmann, T., Donato, F., Lineros, R.A.: Radio data and synchrotron emission in consistent cosmic ray models. J. Cosmol. Astroparticle Phys. **1**, 049 (2012). doi:10.1088/1475-7516/2012/01/049. 1106.4821

Burn, B.J.: On the depolarization of discrete radio sources by Faraday dispersion. Mon. Not. R. Astron. Soc. **133**, 67 (1966)

Condon, J.J.: Radio emission from normal galaxies. Ann. Rev. Astron. Astrophys. **30**, 575–611 (1992). doi:10.1146/annurev.aa.30.090192.003043

Cornwell, T.J., Golap, K., Bhatnagar, S.: The noncoplanar baselines effect in radio interferometry: the W-projection algorithm. IEEE J. Sel. Top. Signal Process. **2**, 647–657 (2008). doi:10.1109/JSTSP.2008.2005290

Ellingson, S.W., Taylor, G.B., Craig, J., Hartman, J., Dowell, J., Wolfe, C.N., Clarke, T.E., Hicks, B.C., Kassim, N.E., Ray, P.S., Rickard, L.J., Schinzel, F.K., Weiler, K.W.: The LWA1 radio telescope. (2012). arXiv e-prints. 1204.4816

Farnsworth, D., Rudnick, L., Brown, S.: Integrated polarization of sources at $\lambda \tilde{} 1$ m and new rotation measure ambiguities. Astron. J. **141**, 191 (2011). doi:10.1088/0004-6256/141/6/191. 1103.4149

Frick, P., Sokoloff, D., Stepanov, R., Beck, R.: Wavelet-based Faraday rotation measure synthesis. Mon. Not. R. Astron. Soc. **401**, L24–L28 (2010). doi:10.1111/j.1745-3933.2009.00778.x. 0911.0261

Frick, P., Sokoloff, D., Stepanov, R., Beck, R.: Faraday rotation measure synthesis for magnetic fields of galaxies. Mon. Not. R. Astron. Soc. **414**, 2540–2549 (2011). doi:10.1111/j.1365-2966.2011.18571.x. 1102.4316

George, S.J., Stil, J.M., Keller, B.W.: Detection thresholds and bias correction in polarized intensity. Publ. Astron. Soc. Aust. **29**, 214–220 (2012). doi:10.1071/AS11027. 1106.5362

Hales, C.A., Gaensler, B.M., Norris, R.P., Middelberg, E.: Analytic detection thresholds for measurements of linearly polarized intensity using rotation measure synthesis. Mon. Not. R. Astron. Soc. **424**, 2160–2172 (2012). doi:10.1111/j.1365-2966.2012.21372.x. 1205.5310

Heald, G.: The Faraday rotation measure synthesis technique. In: Strassmeier, K.G., Kosovichev, A.G., Beckman, J.E. (eds.) IAU Symposium, IAU Symposium, vol. 259, pp. 591–602 (2009). doi:10.1017/S1743921309031421

Heald, G., Braun, R., Edmonds, R.: The westerbork SINGS survey. II polarization, Faraday rotation, and magnetic fields. Astron. Astrophys. **503**, 409–435 (2009). doi:10.1051/0004-6361/200912240. 0905.3995

Högbom, J.A.: Aperture synthesis with a non-regular distribution of interferometer baselines. Astron. Astrophys. **15**, 417 (1974)

Irwin, J., Beck, R., Benjamin, R.A., Dettmar, R.J., English, J., Heald, G., Henriksen, R.N., Johnson, M., Krause, M., Li, J.T., Miskolczi, A., Mora, S.C., Murphy, E.J., Oosterloo, T., Porter, T.A., Rand, R.J., Saikia, D.J., Schmidt, P., Strong, A.W., Walterbos, R., Wang, Q.D., Wiegert, T.: Continuum halos in nearby galaxies: an EVLA survey (CHANG-ES). I. Introduction to the survey. Astron. J. **144**, 43 (2012). doi:10.1088/0004-6256/144/2/43. 1205.5694

Jackson, J.D.: Classical Electrodynamics, 3rd edn. Wiley, New York (1998)

Jaffe, T.R., Banday, A.J., Leahy, J.P., Leach, S., Strong, A.W.: Connecting synchrotron, cosmic rays and magnetic fields in the plane of the Galaxy. Mon. Not. R. Astron. Soc. **416**, 1152–1162 (2011). doi:10.1111/j.1365-2966.2011.19114.x. 1105.5885

Johnston, S., Feain, I.J., Gupta, N.: Science with the Australian square kilometre array pathfinder (ASKAP). In: Saikia, D.J., Green, D.A., Gupta, Y., Venturi, T. (eds.) The Low-Frequency Radio Universe. Astronomical Society of the Pacific Conference Series, vol 407, p. 446. Astronomical Society of the Pacific, San Francisco (2009). 0903.4011

Li, F., Brown, S., Cornwell, T.J., de Hoog, F.: The application of compressive sampling to radio astronomy. II. Faraday rotation measure synthesis. Astron. Astrophys. **531**, A126 (2011). doi:10.1051/0004-6361/201015890. 1106.1709

Macquart, J.P., Ekers, R.D., Feain, I., Johnston-Hollitt, M.: On the reliability of polarization estimation using rotation measure synthesis. Astrophys. J. **750**, 139 (2012). doi:10.1088/0004-637X/750/2/139. 1203.2706

Oosterloo, T., Verheijen, M.A.W., van Cappellen, W., Bakker, L., Heald, G., Ivashina, M.: Apertif - the focal-plane array system for the WSRT. In: Wide Field Astronomy & Technology for the Square Kilometre Array, Chateau de Limelette, Belgium (2009). 0912.0093

Pen, U.L., Chang, T.C., Hirata, C.M., Peterson, J.B., Roy, J., Gupta, Y., Odegova, J., Sigurdson, K.: The GMRT EoR experiment: limits on polarized sky brightness at 150 MHz. Mon. Not. R. Astron. Soc. **399**, 181–194 (2009). doi:10.1111/j.1365-2966.2009.14980.x. 0807.1056

Perley, R.A., Chandler, C.J., Butler, B.J., Wrobel, J.M.: The expanded very large array: a new telescope for new science. Astrophus. J. **739**, L1 (2011). doi:10.1088/2041-8205/739/1/L1. 1106.0532

Rand, R.J., Lyne, A.G.: New rotation measures of distant pulsars in the inner galaxy and magnetic field reversals. Mon. Not. R. Astron. Soc. **268**, 497 (1994)

Sault, R.J., Teuben, P.J., Wright, M.C.H.: A retrospective view of MIRIAD. In: Shaw, R.A., Payne, H.E., Hayes, J.J.E. (eds.) Astronomical Data Analysis Software and Systems IV. Astronomical Society of the Pacific Conference Series, vol. 77, p. 433. Astronomical Society of the Pacific, San Francisco (1995). arXiv:astro-ph/0612759

Schnitzeler, D.H.F.M., Katgert, P., de Bruyn, A.G.: WSRT Faraday tomography of the galactic ISM at $\lambda \sim 0.86$ m. I. The GEMINI data set at $(l, b) = (181°, 20°)$. Astron. Astrophys. **494**, 611–622 (2009). doi:10.1051/0004-6361:20078912. 0810.4211

Shu, F.H.: The Physics of Astrophysics, vol. 1: Radiation. University Science Books, Mill Valley, CA, p. 446 (1991)

Sotomayor-Beltran, C., Sobey, C., Hessels, J.W.T., de Bruyn, G., Noutsos, A., Alexov, A., Anderson, J., Asgekar, A., Avruch, I.M., Beck, R., Bell, M.E., Bell, M.R., Bentum, M.J., Bernardi, G., Best, P., Birzan, L., Bonafede, A., Breitling, F., Broderick, J., Brouw, W.N., Brüggen, M., Ciardi, B., de Gasperin, F., Dettmar, R.J., van Duin, A., Duscha, S., Eislöffel, J., Falcke, H., Fallows, R.A., Fender, R., Ferrari, C., Frieswijk, W., Garrett, M.A., Grießmeier, J., Grit, T., Gunst, A.W., Hassall, T.E., Heald, G., Hoeft, M., Horneffer, A., Iacobelli, M., Juette, E., Karastergiou, A., Keane, E., Kohler, J., Kramer, M., Kondratiev, V.I., Koopmans, L.V.E., Kuniyoshi, M., Kuper, G., van Leeuwen, J., Maat, P., Macario, G., Markoff, S., McKean, J.P., Mulcahy, D.D., Munk, H., Orru, E., Paas, H., Pandey-Pommier, M., Pilia, M., Pizzo, R., Polatidis, A.G., Reich, W., Röttgering, H., Serylak, M., Sluman, J., Stappers, B.W., Tagger, M., Tang, Y., Tasse, C., ter Veen, S., Vermeulen, R., van Weeren, R.J., Wijers, R.A.M.J., Wijnholds, S.J., Wise, M.W., Wucknitz, O., Yatawatta, S., Zarka, P.: Calibrating high-precision Faraday rotation measurements for LOFAR and the next generation of low-frequency radio telescopes. Astron. Astrophys. **552**, A58 (2013). doi:10.1051/0004-6361/201220728

Strong, A.W., Orlando, E., Jaffe, T.R.: The interstellar cosmic-ray electron spectrum from synchrotron radiation and direct measurements. Astron. Astrophys. **534**, A54 (2011). doi:10.1051/0004-6361/201116828. 1108.4822

Tingay, S.J., Goeke, R., Bowman, J.D., Emrich, D., Ord, S.M., Mitchell, D.A., Morales, M.F., Booler, T., Crosse, B., Wayth, R.B., Lonsdale, C.J., Tremblay, S., Pallot, D., Colegate, T., Wicenec, A., Kudryavtseva, N., Arcus, W., Barnes, D., Bernardi, G., Briggs, F., Burns, S., Bunton, J.D., Cappallo, R.J., Corey, B.E., Deshpande, A., Desouza, L., Gaensler, B.M., Greenhill, L.J., Hall, P.J., Hazelton, B.J., Herne, D., Hewitt, J.N., Johnston-Hollitt, M., Kaplan, D.L., Kasper, J.C., Kincaid, B.B., Koenig, R., Kratzenberg, E., Lynch, M.J., Mckinley, B., Mcwhirter, S.R., Morgan, E., Oberoi, D., Pathikulangara, J., Prabu, T., Remillard, R.A., Rogers, A.E.E., Roshi, A., Salah, J.E., Sault, R.J., Udaya-Shankar, N., Schlagenhaufer, F., Srivani, K.S., Stevens, J., Subrahmanyan, R., Waterson, M., Webster, R.L., Whitney, A.R., Williams, A., Williams, C.L., Wyithe, J.S.B.: The murchison widefield array: the square kilometre array precursor at low radio frequencies. Publ. Astron. Soc. Aust. **30**, e007 (2013). doi:10.1017/pasa.2012.007. 1206.6945

van Haarlem, M.P., Wise, M.W., Gunst, A.W., Heald, G., McKean, J.P., Hessels, J.W.T., de Bruyn, A.G., Nijboer, R., Swinbank, J., Fallows, R., Brentjens, M., Nelles, A., Beck, R., Falcke, H., Fender, R., Hörandel, J., Koopmans, L.V.E., Mann, G., Miley, G., Röttgering, H., Stappers, B.W., Wijers, R.A.M.J., Zaroubi, S., van den Akker, M., Alexov, A., Anderson, J., Anderson, K., van Ardenne, A., Arts, M., Asgekar, A., Avruch, I.M., Batejat, F., Bähren,

L., Bell, M.E., Bell, M.R., van Bemmel, I., Bennema, P., Bentum, M.J., Bernardi, G., Best, P., Bîrzan, L., Bonafede, A., Boonstra, A.J., Braun, R., Bregman, J., Breitling, F., van de Brink, R.H., Broderick, J., Broekema, P.C., Brouw, W.N., Brüggen, M., Butcher, H.R., van Cappellen, W., Ciardi, B., Coenen, T., Conway, J., Coolen, A., Corstanje, A., Damstra, S., Davies, O., Deller, A.T., Dettmar, R.J., van Diepen, G., Dijkstra, K., Donker, P., Doorduin, A., Dromer, J., Drost, M., van Duin, A., Eislöffel, J., van Enst, J., Ferrari, C., Frieswijk, W., Gankema, H., Garrett, M.A., de Gasperin, F., Gerbers, M., de Geus, E., Grießmeier, J.M., Grit, T., Gruppen, P., Hamaker, J.P., Hassall, T., Hoeft, M., Holties, H.A., Horneffer, A., van der Horst, A., van Houwelingen, A., Huijgen, A., Iacobelli, M., Intema, H., Jackson, N., Jelic, V., de Jong, A., Juette, E., Kant, D., Karastergiou, A., Koers, A., Kollen, H., Kondratiev, V.I., Kooistra, E., Koopman, Y., Koster, A., Kuniyoshi, M., Kramer, M., Kuper, G., Lambropoulos, P., Law, C., van Leeuwen, J., Lemaitre, J., Loose, M., Maat, P., Macario, G., Markoff, S., Masters, J., McFadden, R.A., McKay-Bukowski, D., Meijering, H., Meulman, H., Mevius, M., Middelberg, E., Millenaar, R., Miller-Jones, J.C.A., Mohan, R.N., Mol, J.D., Morawietz, J., Morganti, R., Mulcahy, D.D., Mulder, E., Munk, H., Nieuwenhuis, L., van Nieuwpoort, R., Noordam, J.E., Norden, M., Noutsos, A., Offringa, A.R., Olofsson, H., Omar, A., Orrú, E., Overeem, R., Paas, H., Pandey-Pommier, M., Pandey, V.N., Pizzo, R., Polatidis, A., Rafferty, D., Rawlings, S., Reich, W., de Reijer, J.P., Reitsma, J., Renting, G.A., Riemers, P., Rol, E., Romein, J.W., Roosjen, J., Ruiter, M., Scaife, A., van der Schaaf, K., Scheers, B., Schellart, P., Schoenmakers, A., Schoonderbeek, G., Serylak, M., Shulevski, A., Sluman, J., Smirnov, O., Sobey, C., Spreeuw, H., Steinmetz, M., Sterks, C.G.M., Stiepel, H.J., Stuurwold, K., Tagger, M., Tang, Y., Tasse, C., Thomas, I., Thoudam, S., Toribio, M.C., van der Tol, B., Usov, O., van Veelen, M., van der Veen, A.J., ter Veen, S., Verbiest, J.P.W., Vermeulen, R., Vermaas, N., Vocks, C., Vogt, C., de Vos, M., van der Wal, E., van Weeren, R., Weggemans, H., Weltevrede, P., White, S., Wijnholds, S.J., Wilhelmsson, T., Wucknitz, O., Yatawatta, S., Zarka, P., Zensus, A., van Zwieten, J.: LOFAR: The LOw-Frequency ARray. Astron. Astrophys. **556**, A2 (2013). doi:10.1051/0004-6361/201220873. 1305.3550

Wilson, T.L., Rohlfs, K., Hüttemeister, S.: Tools of Radio Astronomy. Springer, Berlin (2009). doi:10.1007/978-3-540-85122-6

Chapter 4
Interstellar Grain Alignment: Observational Status

B-G Andersson

Abstract Interstellar polarization in the optical/infrared has long been known to be due to asymmetrical dust grains aligned with the magnetic field and can potentially provide a resource effective way to probe both the topology and strength of the magnetic-field. However, to do so with confidence, the physics and variability of the alignment mechanisms must be quantitatively understood. The last 15 years has seen major advancements in both the theoretical and observational understanding of this problem. I here review the current state of the observational constraints on the grain alignment physics. While none of the three classes of proposed grain alignment theories: mechanical, paramagnetic relaxation and radiative alignment torque, can be viewed as having been empirically confirmed, the first two have failed some critical observational tests, whereas the latter has recently been given specific observational support and must now be viewed as the leading candidate.

4.1 Introduction

Interstellar optical polarization was discovered in 1949, independently by Hall (1949) and Hiltner (1949a, b). Already in Hiltner's second paper of that year the effect was ascribed to dichroic extinction by asymmetric dust grains aligned with the magnetic field. This is now well established and is supported (Fig. 4.1) by comparing the amount of polarization with the visual extinction, which shows that the upper envelope of the former is linearly correlated with the latter, and by comparing the position angle of the optical/near infrared polarization with the position angle of polarization due to synchrotron radiation, for which a well understood theory exists (e.g. Jackson 1975; Burke and Graham-Smith 1997, 2009).

We can therefore safely assume that the optical/near-infrared (O/IR) polarization observed from the ISM is due to dichroic extinction by asymmetric dust grains aligned with (if not by!) the magnetic field. In the far infrared (FIR), these

B-G Anderson (✉)
SOFIA Science Center, Universities Space Research Association, NASA Ames Research Center, M.S. N232-12, Moffett Field, CA 94035, USA
e-mail: bgandersson@sofia.usra.edu

A. Lazarian et al. (eds.), *Magnetic Fields in Diffuse Media*, Astrophysics and Space Science Library 407, DOI 10.1007/978-3-662-44625-6_4

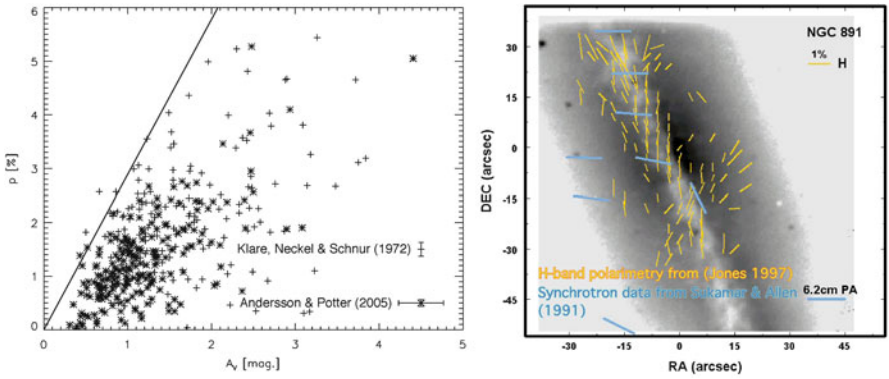

Fig. 4.1 That optical/near-infrared polarization is due to dichroic extinction by asymmetric dust grains aligned with the magnetic field is supported by the fact that (*left*) the upper envelope of the amount of polarization is correlated with the visual extinction (in this case towards a region around the Southern Coalsack; Andersson and Potter (2005)) and (*right*) that the position angles of the polarization agree with the position angles observed from synchrotron radiation (with an offset of 90°, expected for zero pitch-angle electrons, cf. Jackson 1975)

aligned grains give rise to polarized emission, which has been observed, in a number of sources at wavelengths from the far infrared to mm-waves [cf. reviews by Hildebrantd (1996) and summaries by Dotson et al. (2000), Vaillancourt and Matthews (2012), and references therein].

Significant progress has been made over the last two decades in both theory and observations and we are now at a point where quantitative comparisons between theory and observations are being made, and promises to reward us with a predictive, observationally supported theory of interstellar grain alignment within the foreseeable future.

This review will focus on the observational aspects of interstellar grain alignment physics and will only provide a brief summary of the theoretical aspects of the field. Excellent reviews of the latter can be found in e.g. Roberge (1996) and Lazarian (2007).

The main observational constraints on the grain alignment mechanisms come from (in the O/IR) the interstellar extinction and polarization curves (e.g. Fitzpatrick and Massa 1990; Cardelli et al. 1989; Serkowski 1973; Wilking et al. 1980). Based on the theory for scattering of light by small particles ("Mie theory" and its extensions; Mie 1908; Debye 1909; cf. Whittet 2003; Krügel 2003; Draine 2011), complemented by elemental abundance constraints and estimates of the refractive indices for the grain materials, these allow an inversion from the wavelength dependence of the extinction and polarization, respectively, to grains size distributions (by grain material) of the total grain population and the aligned part (Mathis et al. 1977; Kim et al. 1994; Clayton et al. 2003; Mathis 1986; Kim and Martin 1995). The dust is usually modeled as consisting of silicates, amorphous carbon and small graphite particles made up of simple shapes (e.g. spheres, spheroids or cylinders).

The number density of the dust was found to be satisfactorily (Mathis et al. 1977) modeled a power-law size distribution

$$n(a) \propto a^{-q} \tag{4.1}$$

with an exponent of $q \approx 3.5$, and grains at least in the range 0.005–0.25 μm range. Later models extend the upper limit with an exponential decay to larger grains (Kim et al. 1994; Clayton et al. 2003; Draine and Li 2007; Draine and Fraisse 2009). These grain models are—of course—a simplification, which disregards such complications as possibly composite grains or silicate grains with carbonaceous mantles (Duley et al. 1989; Li and Greenberg 1997) or grains of highly complex shapes or structures. In the dark, cold parts of molecular clouds volatile ice mantles form on the refractory grains (Whittet 2003), which can be of substantial relative volume (Hough et al. 2008). In addition to their influence on the extinction and polarization properties of the material it is becoming increasingly clear that these ice mantles are crucial to the understanding of the chemical evolution of molecular clouds (Herbst and van Dishoeck 2009).

The polarized spectrum of MIR absorption and FIR/(sub)mm-wave emission from warm dust provide complementary constraints of the characteristics of the dust in terms of grain shape and refractive indices (e.g. Hildebrantd and Dragovan 1995; Draine and Fraisse 2009) for high column density line of sight.

The most direct probe of the grain alignment is through the fractional polarization (p/A_V). Although this, to first order, measures the fraction of aligned, asymmetric grains, it will, in detail, depend on a number of, often poorly constrained, parameters, including

1. The size distribution of the grains
2. The chemical composition and refractive index of the grains
3. The fraction of asymmetric grains
4. The alignment efficiency of the grains
5. The thermal and radiation field environment of the grains
6. The general orientation of the ordered magnetic field
7. The magnetic field line of sight topology, and level of turbulence

Therefore, these factors, their uncertainties and—possibly—variations along each line of sight, need to be taken into account when comparing observations to theoretical predictions.

Polarization due to dichroic extinction by asymmetric grains aligned with the magnetic field, will only be sensitive to the plane-of-the-sky component of the field. Hence variations in the line-of-sight to plane-of-the-sky ratio of the magnetic field will affect the O/IR fractional polarization. Since both Zeeman splitting (Verchuur 1969; Crutcher et al. 1975; Troland and Crutcher 2008) and Faraday rotation observations (Wolleben and Reich 2004 and references therein) probe the line-of-sight component of the field, direct "cross calibration" between these, nominally more quantitative, methods and O/IR polarimetry are inherently difficult (Andersson and Potter 2009).

To account for the maximum observed polarization at small to moderate opacities of $p/E_{B-V} \leq 9$ % mag^{-1} (Serkowski et al. 1975) efficient alignment of the larger silicate grains is required (Jones 1996 and references therein). Mathis (1986) could reproduce the wavelength dependence of the polarization assuming perfect alignment of the large silicate grains. Kim and Martin (1995), using a combination of extinction and polarization data, showed that even for small axis-ratios, oblate spheroidal silicate grains, combined with a population of spherical (silicate and carbonaceous) grains can reproduce the observed general maximum polarization fraction seen with a high alignment fraction.

Comparisons between the linear and circular polarization observed in the ISM indicates that the dust grains giving rise to the polarization are good dielectrics (Martin 1974; Martin and Angel 1976; Mathis 1986), consistent with silicate, but not with carbonaceous grains. Strong polarization has been detected in the 9.7 and 18 μm silicate spectral features (Smith et al. 2000), whereas the 3.4 μm aliphatic C–H stretch feature, usually associated with carbonaceous dust, does not show detectable polarization (Chiar et al. 2006). For these reasons it is often assumed that large carbonaceous grains are either absent, symmetrical or unaligned. The 2,175 Å extinction "bump" shows associated polarization in 2 out of 30 lines of sight observed (Anderson et al. 1996; Martin et al. 1999). Since this extinction feature is usually thought to be due to small graphite grains it is possible that these can be aligned, at least in some environments, whereas the larger amorphous carbon grains required in some models (Clayton et al. 2003; Draine and Li 2007) might not be alignable.

At large opacities the fractional polarization (p/A_V) drops systematically with opacity (Jones 1989; Jones et al. 1992 (JKD); Goodman et al. 1992, 1995; Gerakines et al. 1995; Whittet et al. 2008), which is usually interpreted in terms of decreasing polarization efficiency. Some of this drop-off is, however, likely due to line-of-sight depolarization where different gas parcels in the cloud have intrinsic magnetic field directions (close to) perpendicular to each other and hence cancel out the polarization from each other.

This phenomenon has been studied by Myers and Goodman (1991), Jones et al. (1992), Ostriker et al. (2001) and Wiebe and Watson (2001). In general it is found that for multiple "decorrelation zones" and a large random field component a limiting behavior of $p \sim A_V^{1/2}$ is predicted, as is appropriate for a random walk process. Observationally, the level of turbulence, and hence the decrease in the fractional polarization, that can be ascribed to a turbulent magnetic field, can be constrained by the fact that even for clouds with large opacities the observed polarization angles are not random (Jones 1996). For the Taurus cloud (observed by Whittet et al. 2008; Fig. 4.3) and even in the deep star-less cores (e.g. Crutcher et al. 2004) ordered magnetic fields are seen.

Figure 4.2 shows the fractional polarization seen towards embedded and field star background sources (Whittet et al. 2008; Jones et al. 2011) overlaid with the predictions from JKD using an equal mix of ordered and random components for the magnetic field with a decorrelation length for the random component of $\tau_K = 0.1$ (Jones et al. 2011). For the lines of sight towards embedded sources, and for $A_V \leq 10$

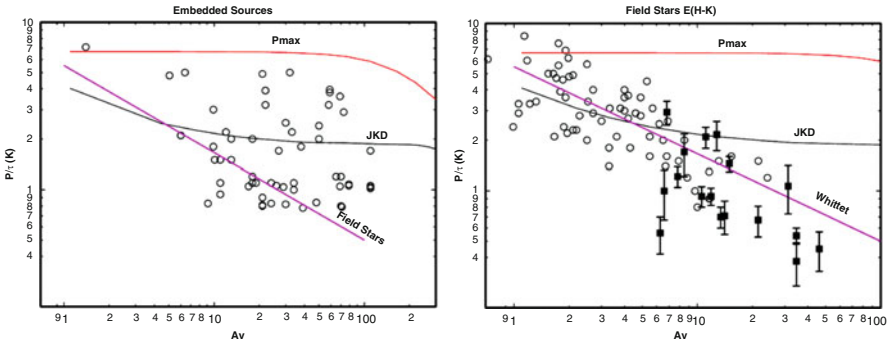

Fig. 4.2 The fractional polarization in the K-band seen towards embedded sources and background field stars (Whittet et al. 2008) are compared with the predictions from a model of polarimetric radiative transfer through a cloud with a turbulent magnetic field. Only at very large opacities without embedded sources does the fractional polarization drop below what can be explained by depolarization due to the random field component (adapted from Jones et al. 2011)

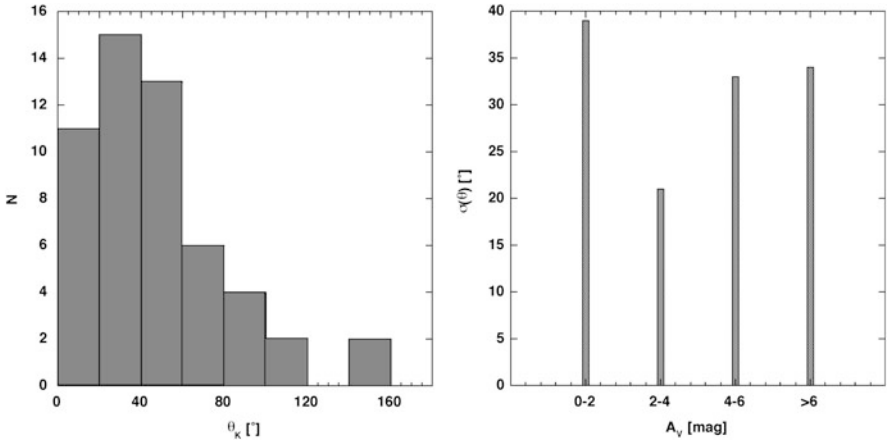

Fig. 4.3 *Left*: The distribution in polarization position angles for the "Field star" sample from Whittet et al. (2008; Fig. 4.2) shows a broad, but non-random distribution, indicating that the decrease in fractional polarization could not be fully ascribed to turbulence in the cloud. The dispersion in the position angles (*right*) shows no systematic variation with opacity

for the field stars, the drop in fractional polarization can be accounted for by the random field's depolarizing effects, while towards even deeper sightline (with these field parameters), additional effects—likely a decrease in the grain alignment efficiency—are required. Figure 4.3 shows the distribution of polarization angles observed for the field star sample of Whittet et al. (2008). While the distribution is broad, it does not allow a depolarization fully dominated by magnetic field turbulence. Note, however, that this result should not be interpreted to mean that grain alignment variations are not present for $A_V < 10$ mag, since the choice of turbulence parameters is not well constrained in detail.

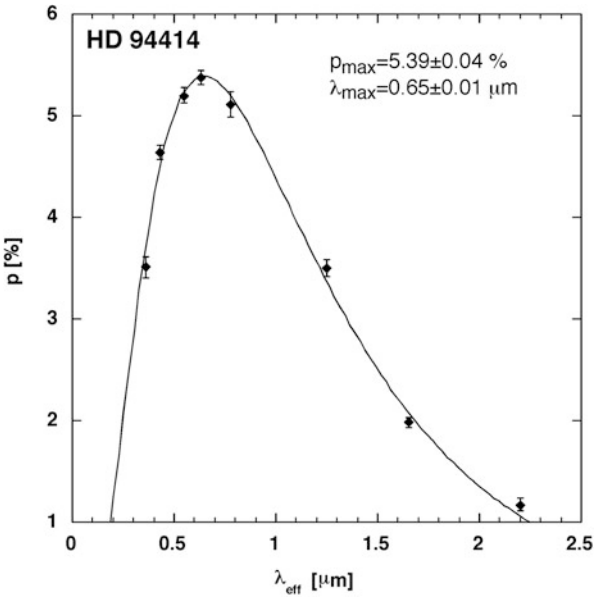

Fig. 4.4 The wavelength dependence of interstellar optical/near infrared polarization follows a universal relation referred to as the Serkowski relation (Eq. (4.2)), here illustrated for the star HD 9441 behind the Chamaeleon I cloud. The data are from Whittet et al. (1992) and the fit uses Eq. (4.3) to relate the K-parameter to λ_{max}

The observed wavelength dependence for interstellar polarization shows a universal shape (Fig. 4.4) with a maximum in the yellow-to-red range and falling off steeply both into the ultraviolet and infrared. The wavelength dependence can be parameterized (Serkowski 1973) by the relation:

$$p(\lambda) = p_{max} \cdot \exp\left\{-K \cdot \ln^2(\lambda_{max}/\lambda)\right\} \tag{4.2}$$

known as the "Serkowski relation", where p_{max} is the maximum amount of polarization seen at wavelength λ_{max}, and K controls the width of the curve. As was realized early on, based on Mie scattering theory (see Whittet 2003), the relatively narrow width of the polarization curve indicates that only a limited grain size distribution contributes to the polarization. More detailed modeling (Mathis 1986; Kim and Martin 1995) shows that the same size distribution can reproduce both the interstellar extinction and polarization curve, but with a larger small-size cut-off for the aligned grains around 0.04–0.05 μm.

Wilking et al. (1980, 1982) and Whittet et al. (1992) showed that K is correlated with λ_{max} such that

$$K = (0.01 \pm 0.05) + (1.66 \pm 0.09) \cdot \lambda_{max} \tag{4.3}$$

Andersson and Potter (2007) showed that a universal (at least for the six interstellar clouds in their study) relation exists between λ_{max} and A_V (Fig. 4.5) of the form

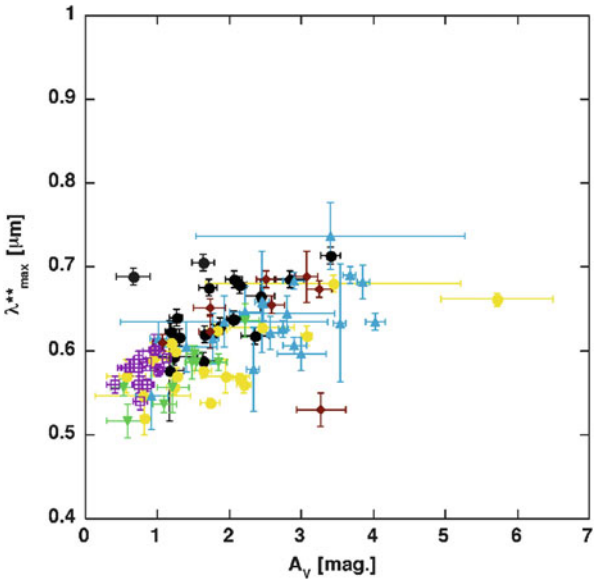

Fig. 4.5 The wavelength of maximum polarization is seen to be linearly correlated with the visual extinction. Different colors correspond to data from different near-by clouds and the raw data have been adjusted to account of different average grains sizes (via $<R_V>$) and star formation rates on the different clouds. See Andersson and Potter (2007) for details

$$\lambda_{max} = (0.166 \pm 0.003) \cdot < R_V > + (0.020 \pm 0.007) \cdot A_V \tag{4.4}$$

where $<R_V>$ is the average total-to-selective extinction in the cloud. Since the grain orientation randomization is assumed to be by gas-grain collisions and since these are more efficient for smaller grains, they interpreted this relationship as indicating radiatively driven grain alignment.

Whittet and van Breda (1978), for a large sample of sightlines, found a correlation between λ_{max} and the ratio of total-to-selective extinction, R_V, such that:

$$R_V = (5.6 \pm 0.3) \cdot \lambda_{max} \tag{4.5}$$

(cf. Whittet et al. (2001) and references therein), which is usually interpreted to indicate grain growth associated with larger values of λ_{max}, as R_V is usually assumed to track the average grain size. Chini and Krügel (1983), however challenged this assumption and Whittet et al. (2001) noted that, for their Taurus sample, very little correlation was seen between λ_{max}, and R_V. Andersson and Potter (2007), expanded on the Whittet et al. results and argued that the derived variation of λ_{max} with R_V is due to the inclusion of different clouds in the same plot and argued that for any given cloud, in their six cloud sample, no clear relation is seen.

The FIR/(sub)mm-wave polarization spectrum shows a broad minimum around 350 μm for lines of sight in star forming cloud cores off of the FIR flux peak (Fig. 4.6).

As shown, originally, by Hildebrand et al. (1999) a single population of grains cannot produce this polarization spectrum. At minimum, a two-component dust population is required with either significantly different grain emissivities or

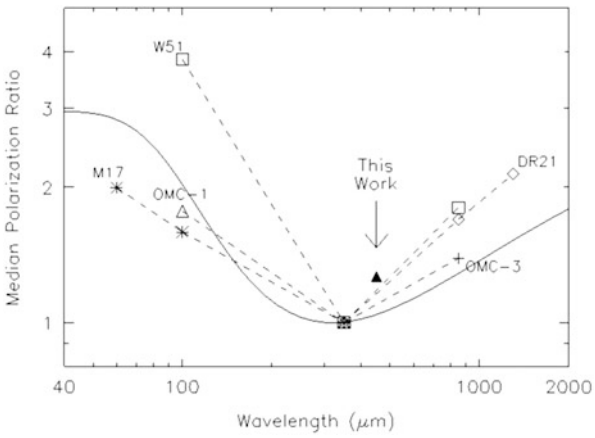

Fig. 4.6 The observed polarization spectrum for a number of molecular cloud cores shows a systematic behavior with a marked minimum in the 350 μm range. Overlaid (*full drawn line*) is an illustrative two-temperature dust model where only the hot component is polarized (Reproduced from Vaillancourt et al. 2008 with permission from the AAS)

temperatures. Their preferred model, yielding the drop in polarization from 60 to 300 μm is one where the components differ in temperature and the warmer dust component is better aligned. As shown by Vaillancourt et al. (2008) the up-turn in the polarization spectrum long ward of 350 mm can, in such a two-component model, be understood as an effect of different grain emissivities.

Hence, grain alignment is seen to vary with environment and in systematic ways, which should provide the observational constraints to allow an understanding of its physics.

4.2 Grain Alignment Theories

Three broad classes of grain alignment theories have been offered to explain ISM polarization: Mechanical alignment (Gold 1952a, b; Lazarian 1994, 1995, 1997a), paramagnetic relaxation alignment (Davis and Greenstein 1951; Jones and Spitzer 1967; Purcell 1979; Mathis 1986) and radiative alignment (Dolginov and Mitrofanov 1976; Draine and Weingartner 1996, 1997; Lazarian and Hoang 2007; Hoang and Lazarian 2008, 2009a, b).

I will only briefly discuss these theories here and refer the interested reader to the above papers, the textbooks by Whittet (2003), Krügel (2003) and Draine (2011) and the review articles by Hildebrantd (1988), Roberge (1996) and Lazarian (2007) for details. While this discussion will focus on the mechanisms aligning the grains, it is crucial to also include the mechanisms randomizing the grain orientation when comparing theoretical predictions to observations. As shown by Draine and Lazarian (1998, their Fig. 4.4), extrapolating to the grain sizes dominating the optical polarization; for neutral material gas-grain collisions are thought to dominate the grain disalignment. For the warm neutral and warm ionized media, infrared

emission, and for dark clouds, plasma drag,[1] may significantly contribute to the slowing of the grain rotation. Hence, variations in the gas density, temperature and ionization rate need to be considered when interpreting polarization data in terms of grain disalignment.

For all alignment theories relying on the grain rotation becoming aligned with the magnetic field (i.e. paramagnetic and radiative alignment) the induced magnetization of a spinning grain, via the Barnett effect (see Draine 2011) assures that the grains have their axis of maximum inertia closely aligned with their angular momentum vector. The magnetization induced by the Barnett effect then causes the grain to Lamor precess about the external magnetic field. For thermally rotating grains at non-zero temperature, this alignment is not perfect (Lazarian and Roberge 1997) and becomes less so with rising grain temperatures, which affects the amount of polarization caused by the grains.

In **Paramagnetic relaxation** alignment, the grains are aligned with the external magnetic field due to the dissipation of internal magnetization energy. The dissipation occurs because the grain rotation makes the magnetic field—as seen by the grain material—vary rapidly enough that the material cannot fully respond to the variations in the applied field. This causes the magnetic susceptibility to become complex and leads to dissipation along those axes not parallel to the field.

The theory can, in turn, be divided into three sub-classes depending on whether (1) the grain magnetic susceptibility is typical for paramagnetic materials (e.g. silicates) and the grain is spun up by gas-grain collisions ("**Davis-Greenstein (DG) alignment**"); whether (2) the magnetic susceptibility is significantly enhanced over that of normal paramagnetic materials, as could result if the paramagnetic grain contained inclusions of ferromagnetic materials ("**Super-paramagnetic alignment**"; Jones and Spitzer 1967; Mathis 1986; Lazarian 1997b); or whether (3) the rotation energy of the grain is well above the thermal energy of the surrounding gas ("**Suprathermal alignment**"; Purcell 1979), as may be the case if the grain rotation is driven by the ejection of photoelectrons or newly formed H_2 molecules.

For any theory where the driving torques are fixed in the grain's coordinate system, a fundamental theoretical issue was raised by Lazarian and Draine (1999a, b). Because of the nuclear Barnett effect, grains at $T \neq 0$, as large as 1 μm are likely to be "thermally trapped" in states with non-suprathermal energies, due to the continued, rapid flipping of the grain induced by the internal thermal excitations of the grain material. For such a grain the systematic torques never have the chance to bring the grain to suprathermal rotations speeds and only thermal alignment mechanisms are available. In all cases of paramagnetic alignment the grain is aligned with its angular momentum parallel to the magnetic field direction and hence the polarization traces out the direction of the projected field.

Mechanical alignment requires a systematic velocity difference between the gas and dust and assumes that gas collisions directly align the grains, somewhat

[1] Plasma drag is caused by the interaction of the grain electrical dipole moment with the surrounding ions.

like a water wheel in a flowing stream. Such alignment results in a grain angular momentum perpendicular to the flow. The original mechanical alignment theory by Gold (1952a, b) assumed no magnetic field and considered the flow to be due to collisions between interstellar clouds oscillating around the galactic mid-plane as the source of the systematic flow motion. Incorporating magnetic fields, flows of charged particles can take place either along the field direction, as ambipolar diffusion across the field or as cyclotron orbits around the field lines. For mechanical alignment by (partially) ionized gas flows we would expect Gold alignment to produce polarization perpendicular to the magnetic field direction.

In recent modifications of the theory (Yan and Lazarian 2003) the magnetic field plays a crucial role also in the acceleration of the dust through a resonance between magneto-hydrodynamic waves and the cyclotron frequency of a charged grain. Since the relative motion of gas and dust grain is now perpendicular to the magnetic field lines, the predicted polarization is here along the projected field.

In mechanical alignment, which relies on collisions which make the grain tumble, the gas-dust flow must be supersonic, since—for sub-sonic flows—isotropic sound waves will tend to keep the grain orientation random (Gold 1952b; Lazarian 2007). Lazarian and Hoang (2007) have discussed mechanical alignment in sub-sonic gas flows where gas collisions with helical grains generates grain spin with the angular momentum along the helicity axis. In parallel to the alignment by radiative torques where, because helicity is invariant under reflection, collisions from opposite sides spins a helical grain up in a common direction, this aligns the grains' spin axis parallel to the flow direction. In the presence of a dynamically important magnetic field, the grains then align with the field and the polarization traces out the field direction.

The major advance in grain alignment theory of the last two decades is the quantitative development of **radiative alignment**, specifically through radiative alignment torque (RAT) theory. Originally proposed by Dolginov and Mitrofanov (1976), the theory proposes that grains with a net helicity can be spun up by the torques imparted by the radiation field as it is scattered off the grain. Because of the grain's helicity, the right- and left-hand circular polarization components of the radiation field have different scattering cross sections off of the grain and for an anisotropic field significant net angular momentum can be built up in the grain. As noted above, because helicity is invariant under reflection, thermal trapping is not a concern in radiative alignment and long duration spin-up can be achieved for an anisotropic radiation field. As the grain acquires a magnetization via the Barnett effect (Purcell 1979) it precesses around the magnetic field and the continued radiative torques during this precession then aligns the grain with the magnetic field. Note that paramagnetic relaxation is not invoked in the alignment in RAT theory. As in the case of paramagnetic alignment, the grain is aligned with its angular momentum vector along the magnetic field and hence RAT alignment, generally, predicts polarization parallel to the magnetic field, as well. Draine and Weingartner (1996, 1997) used numerical calculations based on the DDSCAT code (Purcell and Pennypacker 1973; Draine and Flatau 1994) to show that significant alignment was achievable for a number of grain shapes, many of which were not particularly "cork

screw like" (see Fig. 4.1 of Draine and Weingartner 1997). Lazarian and Hoang (2007; LH07) proposed an analytical model, consisting of a spheroidal grain with an angled, offset, mirror which they showed could closely reproduce the numerical results from Draine and Weingartner. The generality of the analytical model of LH07 has allowed them to extend the theory and provide several specific theoretical predictions.

4.2.1 Theoretical Predictions Amenable to Observational Tests

4.2.1.1 Paramagnetic Relaxation

Davis-Greenstein Alignment

For dust both spun up and randomized by gas-grain collisions it can be shown (e.g. Draine 2011) that the degree of alignment should *decrease* with grain size. The overall grain size distribution can be derived from the interstellar extinction curve (e.g. Mathis et al. 1977; Kim and Martin 1995; Clayton et al. 2003) while that of aligned grains can be determined from the polarization curve (e.g. Kim and Martin 1995).

Jones and Spitzer (1967) used thermodynamic arguments to show that significant alignment of grains with rotation driven by gas-grain collisions can only take place—at least for paramagnetic materials located in magnetic fields with reasonable ISM strengths—if the gas temperature is significantly different from the dust temperature. Since the gas heating at small opacities is dominated by collisions with photoelectrons emitted from small grains (e.g. Hollenbach et al. 2009), and the cooling is dominated by line emission, the gas temperature drops rapidly with increasing opacity. The dust cools through optically thin continuum radiation, so dust temperature varies more slowly with opacity. Comparing observation of FIR dust emission and the line radiation from molecular tracers (e.g. Hotzel et al. 2001), the dust and gas temperatures can be compared. A recent, comprehensive, physical/chemical model of the temperature variations in a dark cloud (Hollenbach et al. 2009) shows that even for a quite elevated radiation field, as the visual extinction reaches A_V 4 mag the gas ($T_g = 22$ K) and dust ($T_d = 15$ K) temperatures rapidly approach each other and by $A_V \approx 10$ mag are within a degree of each other.

- *Are smaller grains better aligned than large ones*?
- *Are grain aligned in environments where the gas and dust temperatures are approximately equal*?

Super-Paramagnetic Alignment

As pointed out by Jones and Spitzer (1967) the thermodynamical constraints on thermally spun up paramagnetic alignment could be overcome if the magnetic susceptibility could be raised by several orders of magnitude. They suggested that this could be accomplished by the inclusion of small ferromagnetic sub grains into the silicate grain bulk consisting of metallic iron, iron-oxides or -sulfates (Jones and Spitzer 1967; Mathis 1986). Mathis (1986) expanded on this suggestion and showed that the observed polarization curve could be reproduced using a standard over-all power-law grain size distribution (Mathis et al. 1977) and with the simple assumption that a silicate grain is aligned if it contains at least one such superparamagnetic (SPM) inclusion. He could also reproduce the observed correlation of the K parameter with λ_{max} (Eq. (4.3)), by assuming that both are driven by an increase in the size of the grains that contains one such SPM inclusion, while keeping the grain size distribution function and its upper cut-off constant. While the observed K vs. λ_{max} behavior could also be accomplished by raising the upper bound on the grain sizes, Mathis argued that this would result in a variable red-to-near infrared extinction law, in contrast to what is observed.

It should be noted, however, that even for super-paramagnetic alignment, Roberge (1996) has argued, based on observational constraints from Hildebrantd and Dragovan (1995) that even in the limit of infinitely large super-paramagnetic aligning torques the gas temperature must still be at least five·T_{dust} for thermally rotating super-paramagnetic grains to be aligned.

- *Do the grains contain super-paramagnetic* (*SPM*) *inclusions*?
- *Do the ISM depletion patterns support the existence of grains with ferromagnetic inclusions*?
  - *If so*, *are grains with more Fe-rich materials better aligned*?
- *Is the K vs.* λ_{max} *relation based on SPM inclusions unique*?

Suprathermal Rotation Alignment

Suprathermal spin-up ("Purcell") alignment requires that energetic particles are ejected from the grain surface in a way that yields a systematic torque. Thus the ejection sites must be localized on the grain surface over times long compared to the gas-grain collisional damping (Lazarian 1995). Purcell discussed three possibilities; inelastic collision with the gas particles, or the ejection of photoelectrons or newly formed H_2 molecules. Of these H_2 formation provides the most promising mechanism. Lazarian (1995) revisited the mechanism, discussing the longevity of the sites of H_2 formation, including the effect of "poisoning" of the active surface sites by oxygen atoms. He estimated that Purcell alignment could be efficient for cold dust grains in gas with significant atomic hydrogen available. For $T_d > 20$ K he finds that the mobility of oxygen atoms leads to rapid poisoning of the active, chemisorption,

sites and hence to short lived spin-up. However, laboratory experiments of H_2 formation (Pirronello et al. 1997, 1999), indicate that the formation under cold interstellar conditions take place through physisorbed particles and is efficient only at 6–10 K for olivine and 13–17 K for amorphous carbon (Katz et al. 1999). Cazaux and Tielens (2004) argued that at higher temperatures the H atoms can access chemisorption sites, which would extend the H_2 formation to higher temperature (cf. Cuppen et al. 2006). Whether the physisorption sites can be localized enough to allow for long-lived "Purcell rockets" is not clear.

In Lazarian's calculations the grain rotation speed drops to thermal values once $n_H/n = 10^{-3}$. In most situations in the ISM we expect the medium to be in a state of detailed balance and hence any formation of H_2 molecules is associated with balancing destructions. Direct photodissociation of H_2 requires a photon of at least 14.5 eV and since this is shortward of the Lyman limit, no such photons are expected to be available in the general ISM. Destruction of the molecule is instead thought to take place through a two-step process initiated by the photo-excitation of the molecule's electronic structure (Field et al. 1966). On the subsequent relaxation into the ground electronic state, the molecule will end up in a vibrational state of $v = 14$ or higher about 15 % of the time which leads to vibrational dissociation (Draine 2011). The initial excitation into the Lyman band requires a photon short ward of 1,108 Å. Assuming a standard interstellar extinction curve for $R_V = 3.1$, $\tau(1{,}108\ \text{Å}) = 1$ is reached already at $A_V \approx 0.24$ mag. The opacity for H_2 photo-destruction is, in addition, strongly enhanced by the self-shielding in the lines, which causes the transition to H_2 to be very rapid (Federman et al. 1979; Viala 1986; van Dishoeck and Black 1986).

While the work function for interstellar grains is not well constrained, Weingartner and Jordan (2008) have estimated a value of 8 eV, corresponding to a photon of $\lambda \approx 1{,}550$ Å. The $\tau(1{,}550\ \text{Å}) = 1$ surface, under the same assumptions, occur at $A_V \approx 0.4$ mag.

Hence, unless the cloud material is highly porous, Purcell alignment should not be active beyond about 1 magnitude of visual extinction. Sorrel (1995) proposed that cosmic ray driven evaporation of grain mantles could drive grains at deeper levels to suprathermal spin velocities. However, Lazarian and Roberge (1997) showed that for this mechanism to work the cosmic ray fluxes has to be six to seven orders of magnitude larger than expected for molecular clouds. Also, as noted above, the discovery of the nuclear Barnett effect (Lazarian and Draine 1999a, b) adds significant doubt to the ability of most interstellar grains to reach suprathermal speeds through a mechanism fixed in the grain's coordinate system because of the effect of thermal trapping where a slowly rotating grain.

– *Is grain alignment seen in environments where the high-energy radiation has been excluded*?
– *Is molecular hydrogen formation associated with enhanced polarization*?

4.2.1.2 Mechanical Alignment

For "classical" mechanical alignment, where the relative gas-dust flow is along the magnetic field lines, the most distinctive prediction of the theory is that the grains will be aligned with their long axis along the field direction and hence cause FIR polarization parallel to it (or perpendicular to the field for O/NIR dichroic extinction). For regions where the magnetic field orientation can be deduced independently and where varying line-of-sight opacities are not an issue, a 90° rotation of the polarization over small scales would indicate a change in alignment mechanism.

As discussed in Li and Houde (2008, and references therein) the velocity dispersion cut-off on small scales in molecular clouds may be used as a probe of the ambipolar diffusing in the material. It should thus, in principle, be possible to probe the suggestion by Lazarian and Hoang (2007) of ambipolar-driven mechanical grain alignment. Whether it can separated from other alignment variations and line-of-sight effects remains to be seen.

- *Is polarization perpendicular to the magnetic field direction observed*?
- *Is the fractional polarization in molecular cloud correlated with the amount of ambipolar diffusion*?

4.2.1.3 Radiative Alignment

RAT alignment predicts that for grain with the required helicity, the radiation field will couple efficiently and, for an anisotropic radiation field, produce alignment as long as $\lambda < 2a$, where λ is the wavelength of the radiation and a is the radius of the grain. This means that a broad range of grain sizes can be aligned under most interstellar conditions, and yields a number of testable predictions.

The size distribution of aligned grains (and hence the polarization curve) can potentially be understood by this simple condition (that grains are aligned for $\lambda < 2a$), as well as some of the observed "anomalies" of interstellar polarization.

In the grain size distributions derived based on maximum entropy method inversions, Kim and Martin (1995) find a smallest aligned grain with a size of $a \approx 0.04$–0.05 μm, half of the wavelength of the Lyman limit $\lambda = 0.0912$ μm. Hence the grain alignment on the small size is potentially simply due to the lack of radiation short ward of the Lyman limit in the general ISM. A closely parallel argument to that of Mathis (1986) can then be made to explain, also under RAT alignment, the correlation between K and λ_{max} in the Serkowski formula. Namely, if the underlying grain size distribution (both total and the asymmetrical fraction) is fixed and the smallest aligned grain is determined by the wavelength cut-off of the available light, then the polarization curve will narrow (K increase) and shift (λ_{max}) to the red, with a reddened radiation field, similarly to the Mathis model.

As the remaining radiation field becomes increasingly reddened, the condition $\lambda < 2a$ should eventually no longer be fulfilled, even for the largest grains. The

large cut-off in the grain size distribution is only weakly constrained by observations (by NIR extinction and total elemental abundances; Mathis 1986; Kim et al. 1994; Clayton et al. 2003), but a steep drop-off in the mass distribution of the silicate grains is usually predicted in the 1–2 μm range. Using the interstellar extinction curve, together with the condition $\lambda < 2a$, to calculate the opacity at which the largest grains are no longer aligned, we find, depending on the value of the total-to-selective extinction and upper grain size limit, of $A_V \approx 7$–24 mag.

Since—for RAT alignment—both the grain heating and the alignment is driven by the radiation field, a correlation between grain temperature and alignment is expected, both at small opacities, driven by the interstellar radiation field—or nearby stars—and in cloud cores, heated by embedded YSOs.

As noted by Hoang and Lazarian (2009a, b) RAT alignment can take advantage of other mechanisms to enhance the alignment efficiency and fraction. Both superparamagnetic grains and suprathermal rotation can be incorporated into the RAT paradigm. "Pin-wheel torques" (H_2 or e^- ejections) can lift grains out of low angular momentum states and enhance the alignment. For radiatively aligned superparamagnetic grains the alignment should be perfect and hence any tertiary alignment drivers (e.g. pinwheel torques) should not be able to further improve the fractional polarization.

A likely unique prediction of RAT theory is that the alignment should vary as the angle between the radiation and magnetic fields (LH07). The exact dependence and sign of the variation depends on the grain characteristics and color of the radiation field, but for "typical" grains in the diffuse galactic field, LH07 predicts enhanced alignment when the radiation field anisotropy is parallel to the magnetic field direction.

- *Does the alignment vary with the color of the radiation field*?
  - *Due to reddening*
  - *Due to the intrinsic SED of the radiation field*?
- *Are the opacities of the "polarization holes" seen in star-less cores consistent with the upper grain size limits derived from extinction and elemental abundance observations*?
- *Can FIR/sub-mm wave polarization from star forming clouds be accounted for*?
- *Does the grain alignment efficiency vary with the angle between the radiation and magnetic fields*?
- *Does H_2 formation enhance the fractional polarization*?

4.3 Observational Considerations

As with any tracer of low to moderate optical depth, polarization measurements are prone to uncertainties due to line-of-sight variations in space density and temperature of both the dust and gas, as well as in other parameters such as the

ionization fraction, grain charge and radiation field. The gas-grain collision rate depends on the gas density and temperature, which disaligns the grains, but may also—for paramagnetic alignment—generate the alignment. For most tracers of these entities, the characteristic depth of the observations (i.e. the depth into the cloud dominating the measurement) is generally not well determined and matching gas and dust temperature to a given gas parcel is difficult. Whereas emission line observations, for instance CO (J = 1–0), are dominated by the $\tau = 1$ surface of the emission line, the opacity of the continuum radiation from the dust is much smaller and usually probes the full line of sight. In a few cases specific (limiting) opacities can be reliably directly sampled. The use of ice mantles on the dust grains provide one such case, where their existence can be used to derive a minimum opacity and tight temperature constraints on the gas and dust (Hollenbach et al. 2009).

If the grain alignment falls with increasing opacity—and assuming that the material is in a gravitationally bound cloud with density increasing toward the center—the line of sight weighting of an observation is complicated. As is the case with other observations of diffuse material, mapping of a cloud can provide the means to a nominal "inversion" of the observations into depth dependence of the characteristics of the gas and dust (e.g. Jones et al. 1992; Whittet et al. 2008), but the sampling density of such maps for optical/NIR polarimetry depends on the density of suitable background sources, which can be a significant problem for high opacity regions with the limited-size telescopes usually available for polarimetric observations. As the ISM extinction curve rises towards the blue, increasingly long wavelength bands need to be employed for larger opacities. However, beyond about K-band (2 μm) the thermal emission (and opacity) of the Earth's atmosphere means that the number of sources bright enough to allow high quality polarimetry becomes much smaller than at shorter wavelengths. FIR/(sub)mm-wave polarization provides a way around the necessity for suitable background targets, but adds the complication of emissivity and dust temperature variations along the line of sight, and has only recently become sensitive enough to probe more than the brightest regions.

In particular if the alignment is directly driven by the radiation field (suprathermal or RAT alignment), it is important to note that the line-of-sight opacity (e.g. A_V) is not necessarily a good measure of the radiation field experienced by the grain. This can be due to the geometry of the cloud (i.e. a sightline in the outskirt of a prolate cloud pointing towards the observer will show a significantly higher A_V than the opacity to the ISRF seen by a grain in that line of sight) or because of near-by bright radiation sources (Fig. 4.7).

Andersson and Potter (2007) discussed various such observational biases and showed e.g. that most of the outliers in plots of λ_{max} vs. A_V could be accounted for by them. The differences in the fractional polarization variations with opacity for background field stars and embedded sources (Whittet et al. 2008) are also likely due to the additional radiation field experienced by the dust from the embedded sources. For FIR polarimetry, internal radiation sources (Vaillancourt 2002; Vaillancourt and Matthews 2012) impose similar considerations and must be accounted for when analyzing the polarization in terms of grain alignment. Given these variations

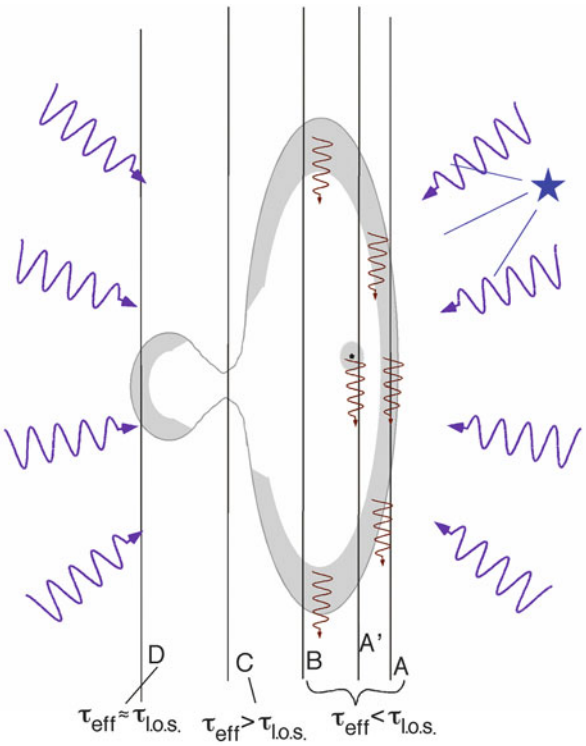

Fig. 4.7 The line of sight (l.o.s.) opacity might not always be a good tracer of the radiation field that a dust grain sees, for non-spherical clouds or clumpy materials. Also, if there are stars near enough to the cloud to be of comparable strength to the diffuse radiation field (*purple*) the use of A_V as indicator of the relative illumination of the dust can lead one astray, (adapted from Andersson and Potter 2007, with permission from the AAS)

in environmental conditions, combining small sample polarization studies from different regions must be done with care.

In addition to these "scalar" line of sight issues, polarization measurements also depend on the topology of the magnetic field. That is, if the inherent polarization *orientation* of successive parcels along the line of sight of the material varies, the total polarization will depend not only on the relative grain alignment, but also on that relative orientation of the field. As discussed in the introduction, the consequences of such variations in the field topology can be difficult to disentangle from variations in the grain alignment efficiency. Detailed modeling of observations incorporating both stochastic magnetic field and alignment efficiency need to be done to evaluate the relative contributions to the loss of fractional polarization observed.

One way of avoiding the uncertainties associated with the depolarization effects, albeit at the cost of requiring observations also of short wavelength (UBV) polarization, is to use the wavelength dependence of the polarization, rather than the (fractional) amount of polarization observed. For optical polarization the Serkowski curve can be shown to trace the characteristic size of the aligned grains. As shown by Kim and Martin (1995) the location of λ_{max} is most sensitive to the smallest

aligned grains. Since these are also the grains most easily disaligned by collisions, we can use this measure as a grain alignment tracer.

4.4 Observational Constraints on Grain Alignment Mechanisms

4.4.1 Davis-Greenstein Alignment

– *Large grains are better aligned than small ones*

Comparing the grain size distribution for all grains to that for the aligned grains required to produce the observed shape and location of the polarization curve and the extinction curve (e.g. Kim and Martin 1995), shows that the large grains (a $\sim$ 0.1 μm) are relatively much better aligned than the smaller ones (a $\sim$ 0.01 μm), in contradiction to the prediction of Davis–Greenstein theory.

– *Grains are aligned also in environments* ($A_V > 5$) *where* $T_{gas} \approx T_{dust}$

Combining H-band polarimetry with FIR continuum observations and CO (J = 1–0) data, Jones et al. (1984) probed the star-less dark core "Tapia's Globule 2" in the Southern Coalsack ($A_V \gtrapprox 12$ mag), and found that, although the derived dust and gas temperatures were almost identical, at around 10 K, the dust in the core is, at least partially, aligned. Magnetic field estimates using the Chandrasekhar–Fermi method (Lada et al. 2004) yield B $\approx$ 25 μG, much less the $\sim$1 mG that would be required to align the grains using Davis–Greenstein alignment (Jones et al. 1984).

A very direct probe of the grain alignment at large opacities is provided by observing the relative polarization seen in solid state spectral features of molecules frozen out onto the grain surfaces. For several ices detected in the ISM, threshold extinctions exist below which no solid-state features are detected (Whittet et al. 1988, 1989; Williams et al. 1992). This threshold extinction varies both by species and from cloud to cloud, but is typically about $A_V \approx 3$ mag for water ice (observable at $\lambda = 3.1$ μm) and $A_V \approx 6$ mag for CO ice (observable at $\lambda = 4.7$ μm). Thus, ice absorption features trace material deep into the clouds where the gas and dust temperatures approach each other. The detection of a significant polarization component in the CO ice line towards background stars, particularly in clouds with no, or only low-mass, star formation directly shows that grains are aligned at a depth into the cloud where the gas and grain temperature approach each other. Observations by Chrysostomou et al. (1996) towards W33A and, particularly, Hough et al. (2008) towards the background star Elias 3–16 probing the Taurus cloud (Fig. 4.8) show strong polarization in the CO ice line and thus put severe doubt on thermal paramagnetic alignment.

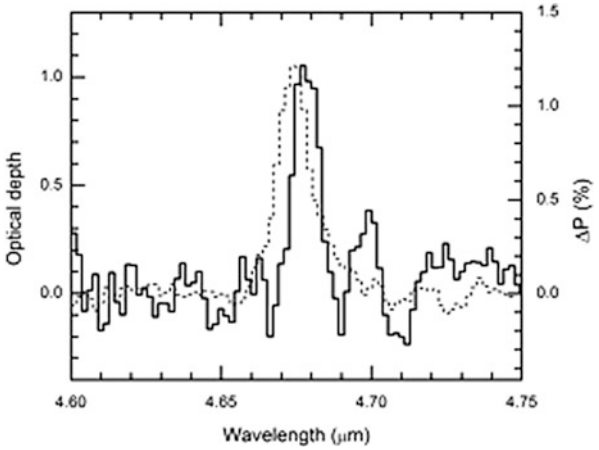

Fig. 4.8 The CO ice line towards the background star Elias 3–16 shows significant polarization, indicating that grains are aligned at $A_V > 6$ mag. The *dashed line* (*left-hand scale*) shows the opacity while the *full line* (*right hand scale*) shows the polarization, with the continuum removed, (reproduced, with permission from Hough et al. 2008)

4.4.2 Super-Paramagnetic Alignment

– *Super-paramagnetic inclusions are seen in Interplanetary Dust Particles* (*IDPs*)

A way to overcome the predicted relatively better alignment efficiency for small grains in thermally spun up grains under paramagnetic alignment was put forward by Mathis (1986), who proposed that a dust grain will be aligned if, and only if, it contains at least one SPM inclusion. Using dust parameters derived from extinction data and the above assumption he could reproduce the polarization curve for $\lambda_{max} = 0.55$ μm, assuming a cut-off in the aligned grains at $a' > 0.09$ μm. Using estimates of the enhancement of the paramagnetism from Jones and Spitzer (1967) he derived a characteristic size of the SMP inclusions of 0.01 μm. Adding UV polarimetry to the constraints, Wolff et al. (1993) modified the cut-off of the aligned grains somewhat to about $0.06 < a < 0.1$ μm. While there is some doubt about how such grains are generated (Martin 1995), the identification of amorphous silicate grains—Glass with Embedded Metals and Sulfides (GEMS)—in interplanetary dust particles from comets (Bradley 1994), lent support to the hypothesis. Goodman and Whittet (1995) argued that the dark patches seen, using transmission electron microscopy, inside these GEMS containing Fe(Ni) metals and iron-rich sulfides, are of the right size and volume-filling factor to match the requirements of Mathis' theory and exhibit super-paramagnetic susceptibilities.

– *The fractional polarization is not correlated with the interstellar solid state iron not included in silicates*

Very recently, Voshchinnikov et al. (2012) cast doubt on the generality of such SPMs in the ISM, by comparing the mineralogy of interstellar dust with its polarizing characteristics. They used an extensive survey of the depletion patterns of Si, Mg and Fe from Voshchinnikov and Henning (2010), combined with new and previously published polarization data to probe for a correlation between

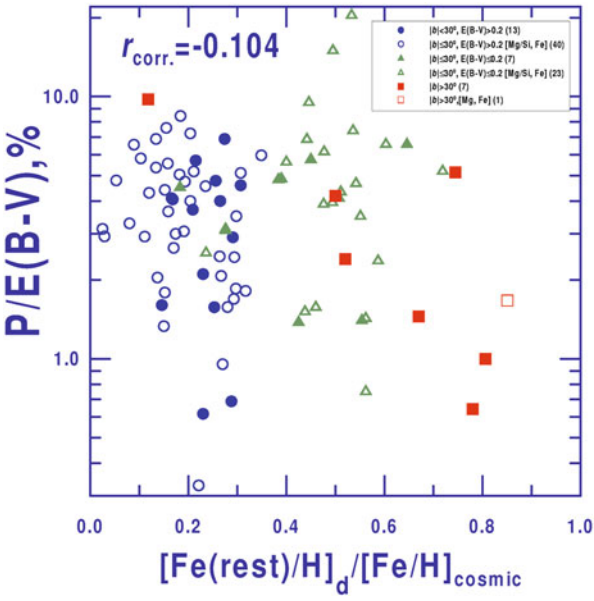

Fig. 4.9 The fractional polarization is plotted against the iron in the solid phase, but not used up in silicates with olivine stoichiometry. If the assumption is made that this "remaining" solid iron is—at least partially—in the form of ferromagnetic compounds, and super-paramagnetic alignment is active, the fractional polarization should increase with the abundance of Fe[rest]. No such increase is seen (reproduced with permission from Voshchinnickov et al. 2012)

ferromagnetic compounds and enhanced polarization. Based on the depletion measurements they calculate the amount of solid phase iron available to make ferromagnetic materials, by assuming that the depleted Silicon and Magnesium are fully used to form minerals with the stoichiometry of Olivine.

They then correlated the "remaining" solid phase iron, where various iron oxides are assumed to dominate, with the fractional polarization ($p/E_{B\text{-}V}$) for 95 lines of sight. No enhanced fractional polarization is seen (Fig. 4.9).

4.4.3 Suprathermal Spin Alignment

– *Grain alignment occurs at opacities where the short wavelength radiation has been excluded*

Whittet et al. (2008) assembled fractional polarization measurements for the Taurus cloud from its surface to $A_V > 20$ mag. and have shown that a single power-law fit ($p/A_V \propto {A_V}^{-b}$) with an exponent of $b = 0.52 \pm 0.07$ can describe the full range for their field star sample. Andersson and Potter (2007) have shown that the wavelength of maximum polarization follows a universal linear relation with A_V (once variations in the average value of R_V between clouds is accounted for) to at least $A_V \approx 4$–5 mag. In neither case are any changes seen in the relations at the opacities where the high-energy photons responsible for H_2 destruction of photoelectric emission have been excluded. It is, however, noteworthy that even though the observed transition from atomic to molecular gas is rapid, it

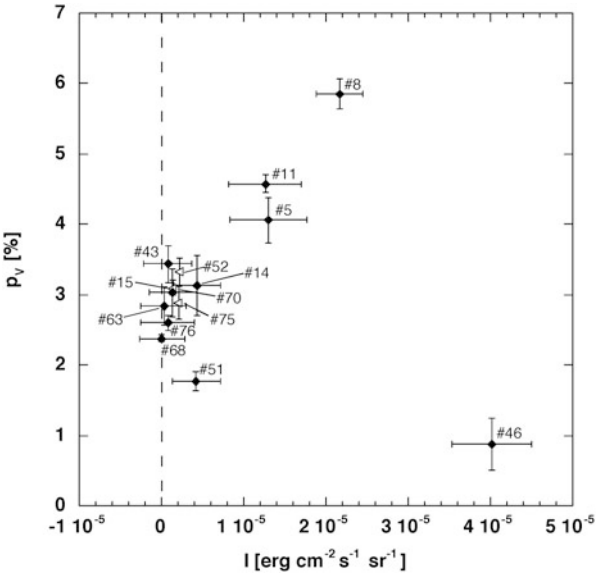

Fig. 4.10 The amount of polarization towards stars behind the reflection nebula IC 63 is correlated with the fluorescent intensity in the H_2 1-0 S(1) line. The fluorescence traces the H_2 destruction and, since the time scales for reformation on the dust grain surfaces is much shorter than the dynamical time scale of the PDR, also the H_2 formation rate. Target #46 is located behind the compression ridge of the nebula where intense collisional disalignment dominates (reproduced from Andersson et al. 2013, with permission from the AAS)

is less abrupt than might be implied by line opacities. In a sample of 23 line of sight observed in H_2 with the Far Ultraviolet Spectroscopic Explorer with visual extinctions up to $A_V \approx 3.4$, Rachford et al. (2002) found no cases of a molecular fraction $f = 2N(H_2)/[2N(H_2) + N(H\ I)] > 0.8$. Hence the transition to fully molecular material is significantly slower than might be expected and atomic hydrogen will be available also at opacities of the order a few.

– *H_2 formation enhanced grain alignment is observationally suggested in the reflection nebula IC 63*

Since the destruction of H_2 in the ISM takes place through a process of line absorption followed by a fluorescent cascade, and the time scale for H_2 formation–destruction cycling is short compared to the dynamical time scales of a photodissociation region (PDR), the NIR fluorescent emission from the molecule traces its formation rate. Andersson et al. (2013) used this argument to search for H_2 formation driven grain alignment in the reflection nebula IC 63. Figure 4.10 shows the measured polarization for the stars probing the nebula as a function of H_2 1–0 S(1) emission. If allowance is made for the strongly enhanced collision rate associated with the compression ridge region in the nebula (probed by target #46 in

the Figure), a statistically significant correlation is seen between H_2 formation and alignment.

4.4.4 Mechanical (Gold) Alignment

– *In some circumstellar environments of high-mass YSOs the polarization seems twist by 90° close to the origin of the outflows.*

High spatial resolution observations of several high-mass young stellar objects (YSO) show complicated position angle structures in the innermost regions around the circumstellar disk and outflows. For instance, Rao et al. (1998) studied the Kleinman-Low object in Orion; Cortes et al. (2006) observed NGC 2071 IR with BIMA and Tang et al. (2009) used the SMA to map G5.89-0.39 in polarized (sub)mm-wave emission. In all cases a (close to) 90° rotation of the polarization is observed when comparing the emission along and across the molecular outflow direction. It is still not clear whether this is better interpreted as evidence of very complicated field geometries or support for mechanical grain alignment. The discovery of synchrotron emission from the jet of a massive YSO (Carrasco-González et al. 2010, 2011) promises to allow an independent tracer of the magnetic field structure and to thus conclusively probe the possibility of mechanical alignment in these sources. As discussed by e.g. Hildebrand et al. (1999), opacity effects can cause polarization angle rotations by 90° with wavelength as the polarization changes over from being dominated by emission to absorption, as seen e.g. towards the Galactic center (Dowell 1997; Novak et al. 1997), but such effects are unlikely to be the cause of the effects seen in high-mass star forming regions.

4.4.5 Radiative Alignment

– *Grain alignment is active at large opacities and varies smoothly with opacity.*

As noted above (Sect. 4. 4.3), the fractional polarization to optical depth much beyond $A_V = 1$ mag. shows a smooth decline with a power-law index of about -0.5, much less than the -1 which would be expected if the polarization was produced only in a relatively thin skin. Similarly the location of λ_{max} varies linearly with A_V to—at least—$A_V = 4$–5 mag.

– *The grain alignment efficiency is correlated with the dust temperature.*

While, as discussed above, the observations of grain alignment in regions where little or no temperature difference exists between the gas and the dust, puts severe doubts on DG alignment, direct variations is the dust temperature should be correlated with the alignment efficiency in RAT alignment since the photons that align he grains will also heat them. Matsumura et al. (2011) have used optical

spectropolarimery to shown that the polarization efficiency is enhanced when the dust temperature is elevated for stars in the Pleiades cluster. A direct correlation between grain alignment and heating is also seen for the dust surrounding HD 97300 in Chamaeleon I (Andersson and Potter 2010).

As discussed above, the polarization spectra in the FIR/(sub)mm-wave regime (Fig. 4.6) requires at least a two-component dust distribution, where the warmer dust is better aligned. Whereas differences in the refractive indices might cause some differences in grain temperature, a more natural explanation, considering the observational data for the O/IR is that the warmer grain component is exposed to a stronger radiation field (Hildebrand et al. 1999; Vaillancourt 2002; Vaillancourt et al. 2008).

– *The "polarizations holes" seen in deep starless clouds are consistent with the loss of alignment of the largest grains.*

At very high opacities in star-less cores a steep drop in the fractional polarization is seen in sub-mm wave polarimetry (e.g. Crutcher et al. 2004) and hinted at in NIR data (Jones et al. 2011; Fig. 4.2) where the slope in the fractional polarization with A_V steepens from a value of about −0.5 (Whittet et al. 2008) to about −1. Jones et al. (2011) have speculated that these "polarization holes" are simply the effect of that the extincted radiation eventually becoming too red to couple to any remaining grains.

– *The grain alignment efficiency depends on the angle between the radiation and magnetic fields*

Andersson and Potter (2010) and Andersson et al. (2011) tested the RAT theory prediction that the grains alignment should depend on the angle between the radiation and magnetic fields by observing the polarization in the Chamaeleon I cloud in the area surrounding the B9 V star HD 97300. Located about 0.3 pc from the near side of the cloud (Jones et al. 1985) the star strongly illuminates the underlying could. For the region of the cloud in which the star dominates the radiation field ($d \approx 0.75°$) a correlation is seen between grain heating and alignment efficiency.

We measured a number of stars at various position angles from the star relative to the magnetic field direction and detect enhanced grain alignment at a 9σ level in the magnetic field direction. We note that, as no position angle rotation was seen, this enhancement is not likely to be due to mechanical alignment. Fitting a toy-model of the grain heating assuming thin "pizza box shaped" grains we found a good fit to the I(60)/I(100) color temperature. The derived fraction of aligned grains is in close agreement with those derived by independent mean by Kim and Martin (1995) (Fig. 4.11).

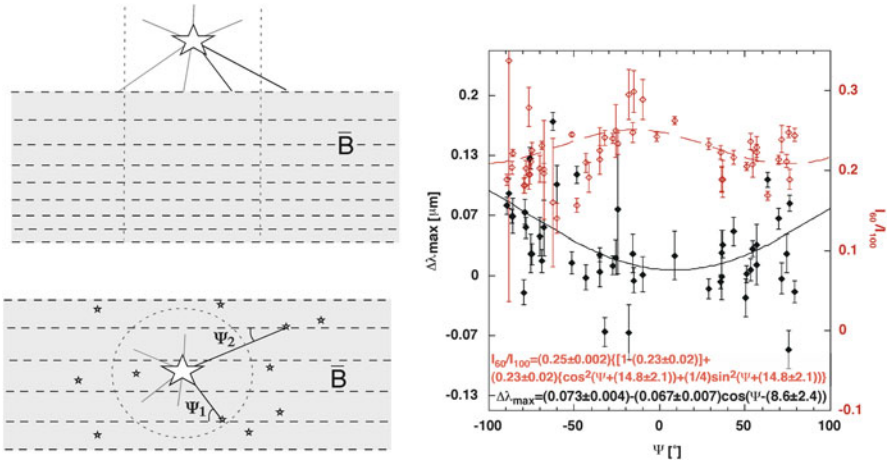

Fig. 4.11 For a star close enough to an interstellar cloud to dominate the radiation field, RAT theory predicts that the alignment should vary with the angle between the magnetic and radiation fields. We can probe this by observing background targets located around the illuminating star (*left*). In accordance with predictions, Andersson et al. (2011) found a maximum in the grain alignment (minimum in $\Delta\lambda_{max}$) at $\Psi = 0$ (*black symbols*). The *red symbols* and *curve* show the color temperature and best fit to a toy model of the differential heating of the aligned grains (see Andersson et al. 2011 for detail)

Summary and Conclusions

Grain alignment is observed to be a universal phenomenon from the diffuse gas to molecular cloud cores (at least those containing star formation). It is seen at large opacities ($A_V \sim 5$–20)—even in clouds without internal heat (or radiation) sources, where the gas and dust temperatures closely approach each other. Most uncontrovertibly this is illustrated by the alignment of the CO ice line towards Elias 3–16 in Taurus (Hough et al. 2008). This would seem to exclude thermal paramagnetic alignment, even for super-paramagnetic grains (Roberge 2004), particularly in light of Voshchinnikov et al. (2012) results that the amount of (presumably) ferromagnetic iron compounds in the dust dues not correlate with the grain alignment.

Combining the JKD/MG depolarization models with the drop-off in the fractional polarization shows that—while the grain alignment falls into the cloud, grains are aligned at large opacities. Using the wavelength of maximum polarization as the tracer of the grain alignment we find a linear relation with A_V to at least $A_V = 4$ and possibly deeper. At these opacities, the energetic photons needed to dissociate the hydrogen molecules or cause photoelectric emission will be excluded. This makes also suprathermal alignment difficult to reconcile with observations for large parts of molecular clouds. However,

(continued)

H_2 formation enhanced alignment might have been observed in the reflection nebula IC 63.

For "classical" mechanical alignment where relative gas-dust flows are along the magnetic field lines, the observed polarization direction in the ISM generally are inconsistent with the alignment predictions. For several high-mass YSOs rapidly rotating polarization field in the inner part of the disk/outflow may however indicate mechanically driven alignment in these environment. For the more recently proposed versions of mechanical alignment (via ambipolar diffusion or through cyclotron resonant acceleration of charged dust grains) the theoretical predictions are either not yet clear enough to provide unambiguous, unique predictions or these have not been tested.

In contrast, radiative alignment torque theory has—over the last decade and a half—partly in response to the difficulties identified for earlier theories, been developed into a self-consistent theory providing specific, testable, predictions. Some of these can explain hitherto puzzling behavior of the observed polarization, while some are new and require specific observations to be performed. The drop in the fractional polarization with depth and the shift λ_{max} to longer wavelength with increasing A_V is a natural consequence of the extinction and reddening of the diffuse Galactic light into the cloud and could also explain the observed K vs. λ_{max} correlation. The relatively good polarization seen in the FIR/(sub)mm-wave for star forming clouds and the contrasting behavior between star forming and starless cores is also consistent with RAT alignment. The fact that grains are heated as well as better aligned next to bright (blue) star also speaks for radiative alignment (Andersson and Potter 2010; Matsumura et al. 2011). The specific, likely unique, prediction that the grain alignment should depend on the angle between the radiation and magnetic fields has been given support though our observations of the polarization surrounding HD 97300, in Chamaeleon.

If confirmed, the hinted at sharp drop-off in fractional polarization beyond $A_V \sim 20$ in starless cores would further support RAT alignment and would provide a unique tool to constrain the size distribution of the large grains. High sampling density polarimetry in environments with varying (but known!) radiation field SEDs (such as where dust can be proved next to very hot stars) could also probe the puzzling polarization behavior of the 2,175 Å extinction bump.

While the lack of polarization of the large carbonaceous grains might seem like a problem for RAT alignment, this may actually be directly understood in the paradigm. While the spin-up of the grains is only dependent on the helicity of the grain and a suitable radiation field, the alignment requires a Barnett magnetization. Since carbon forms diamagnetic materials, carbonaceous grains are not expected to experience Barnett magnetization. Therefore the non-alignment of such grains is an expected in the RAT paradigm.

(continued)

To paraphrase Hildebrand's 1988 review of this subject: While it is necessary to now set aside several of the proposed alignment mechanisms, it is probably not safe to dismiss them altogether. It is likely that each is important somewhere in the universe. It would, however, seem that—as far as the current observational data indicate—RAT theory is the best existing candidate to explain the general interstellar polarization.

Acknowledgments I am grateful to several colleagues for helpful discussions and for comments on early versions of the manuscript. I particular acknowledge many helpful conversations with and helpful suggestions by John Vaillancourt. In addition, Dan Clemens, Terry Jones, Alex Lazarian, Peter Martin and Doug Whittet generously responded to e-mail queries and read early drafts of the manuscript. Any errors or misstatements are, however, mine. The citations quoted in this review are by no means complete, given the long and expansive effort in the field. I apologize in advance to any of my colleagues who might feel slighted by missed or insufficiently strong citations and can only assure them that none of those oversights were intentional. I gratefully acknowledge financial support from the National Science Foundation, through grant AST-1109469.

References

Anderson, C.M., Weitenbeck, A.J., Code, A.D., Nordsieck, K.H., Meade, M.R., Babler, B.L., Zellner, N.E.B., Bjorkman, K.S., Fox, G.K., Johnson, J.J., Sanders, W.T., Lupie, O.L., Edgar, R.J.: AJ **112**, 2726 (1996)

Andersson, B-G, Piirola, V., De Buizer, J., Clemens, D. P., Uomoto, A., Charcos-Llorens, M., Geballe, T. R., Lazarian, A., Hoang, T., & Vornanen, T., ApJ **775**, 84 (2013)

Andersson, B.-G., Potter, S.B.: MNRAS **356**, 1088 (2005)

Andersson, B.-G., Potter, S.B.: ApJ **665**, 369 (2007)

Andersson, B.-G., Potter, S.B.: AIP Conference Proceedings, vol. 1156, pp. 146, 720, 1045 (2009)

Andersson, B.-G., Potter, S.B.: ApJ **720**, 1045 (2010)

Andersson, B.-G., Pintado, O., Potter, S.B., Straižys, V., Charcos-Llorens, M.: A&A **534**, 19 (2011)

Bradley, J.P.: Science **265**, 925 (1994)

Burke, B.F., Graham-Smith, F.: Radio Astronomy. Cambridge University Press, Cambridge (1997)

Burke, B.F., Graham-Smith, F.: An Introduction to Radio Astronomy. Cambridge University Press, Cambridge (2009)

Carrasco-González, C., Rodríguez, L.F., Anglada, G., Martí, J., Torrelles, J.M., Osorio, M.: Science **330**, 1209 (2010)

Carrasco-González, C., Rodríguez, L.F., Osorio, M., Anglada, G., Martí, J., Torrelles, J.M., Galván-Madrid, R., D'Alessio, P.: RMxAC **40**, 229 (2011)

Cardelli, J.A., Clayton, G.C., Mathis, J.S.: ApJ **345**, 245 (1989)

Cazaux, S., Tielens, A.G.G.M.: ApJ **604**, 222 (2004)

Chiar, J.E., Adamson, A.J., Whittet, D.C.B., Chrysostomou, A., Hough, J.H., Kerr, T.H., Mason, R.E., Roche, P.F., Wright, G.: ApJ **651**, 268 (2006)

Chini, R., Krügel, E.: A&A **117**, 289 (1983)

Chrysostomou, A., Hough, J.H., Whittet, D.C.B., Aitken, D.K., Roche, P.F., Lazarian, A.: ApJ **465**, 61 (1996)

Clayton, G.C., Wolff, M.J., Sofia, U.J., Gordon, K.D., Misselt, K.A.: ApJ **588**, 871 (2003)

Cortes, P.C., Crutcher, R.M., Matthews, B.C.: ApJ **650**, 246 (2006)

Crutcher, R.M., Evans, N.J., Troland, T., Heiles, C.: ApJ **198**, 91 (1975)

Crutcher, R.M., Nutter, D.J., Ward-Thompson, D., Kirk, J.M.: ApJ **600**, 279 (2004)
Cuppen, H.M., Morata, O., Herbst, E.: MNRAS **367**, 1757 (2006)
Davis, L.J., Greenstein, J.L.: ApJ **114**, 206 (1951)
Debye, P.: Annalen der Physik **335**, 57 (1909)
Dolginov, A.Z., Mitrofanov, I.G.: Ap&SS **43**, 291 (1976)
Dotson, J.L., Davidson, J., Dowell, C.D., Schleuning, D.A., Hildebrand, R.H.: ApJS **128**, 335 (2000)
Dowell, C.D.: ApJ **487**, 237 (1997)
Draine, B.T., Flatau, P.J.: JOSAA **11**, 1491 (1994)
Draine, B.T., Lazarian, A.: ApJ **508**, 157 (1998)
Draine, B.T., Li, A.: ApJ **657**, 810 (2007)
Draine, B.T., Fraisse, A.A.: ApJ **969**, 1 (2009)
Draine, B.T., Weingartner, J.C.: ApJ **470**, 551 (1996)
Draine, B.T., Weingartner, J.C.: ApJ **480**, 633 (1997)
Draine, B.T.: Physics of the Interstellar and Intergalactic Medium. Princeton University Press, Princeton (2011)
Duley, W.W., Jones, A.P., Williams, D.A.: MNRAS **236**, 709 (1989)
Federman, S.R., Glassgold, A.E., Kwan, J.: ApJ **227**, 466 (1979)
Field, G.B., Summerville, W.B., Dressler, K.: ARA&A **4**, 207 (1966)
Fitzpatrick, E.L., Massa, D.: ApJS **72**, 163 (1990)
Gerakines, P.A., Whittet, D.C.B., Lazarian, A.: ApJ **455**, L171 (1995)
Gold, T.: Nature **169**, 322 (1952a)
Gold, T.: MNRAS **112**, 215 (1952b)
Goodman, A.A., Jones, T.J., Lada, E.A., Myers, P.C.: ApJ **339**, 108 (1992)
Goodman, A.A., Jones, T.J., Lada, E.A., Myers, P.C.: ApJ **448**, 748 (1995)
Goodman, A.A., Whittet, D.C.B.: ApJ **455**, L181 (1995)
Hall, J.S.: Science **109**, 166 (1949)
Herbst, E., van Dishoeck, E.F.: ARAA&A **47**, 427 (2009)
Hildebrantd, R.H.: ApL&C **26**, 263 (1988)
Hildebrantd, R.H.: ASP Conference Series, vol. 97, p. 254 (1996)
Hildebrantd, R.H., Dragovan, M.: ApJ **450**, 663 (1995)
Hildebrand, R.H., Dotson, J.L., Dowell, C.D., Schleuning, D.A., Vaillancourt, J.E.: ApJ **516**, 834 (1999)
Hiltner, W.A.: Science **109**, 165 (1949a)
Hiltner, W.A.: ApJ **109**, 471 (1949b)
Hoang, T., Lazarian, A.: ApJ **695**, 1457 (2008)
Hoang, T., Lazarian, A.: ApJ **697**, 1316 (2009a)
Hoang, T., Lazarian, A.: MNRAS **388**, 117 (2009b)
Hollenbach, D., Kaufman, M.J., Bergin, E.A., Melnick, G.J.: ApJ **690**, 1497 (2009)
Hough, J.H., Aitken, D.K., Whittet, D.C.B., Adamson, A.J., Chrysostomou, A.: MNRAS **387**, 797 (2008)
Hotzel, S., Harju, J., Lemke, D., Mattila, K., Walmsley, C.M.: A&A. **372**, 302 (2001)
Jackson, J.D.: Classical Electrodynamics. Wiley, New York (1975)
Jones, R.V., Spitzer Jr., L.: ApJ **147**, 943 (1967)
Jones, T.J.: AJ **98**, 2062 (1989)
Jones, T.J.: ASP Conference Series, vol. 97, p. 381 (1996)
Jones, T.J., Hyland, A.R., Bailey, L.: ApJ **282**, 675 (1984)
Jones, T.J., Hyland, A.R., Harvey, P.M., Wilking, B.A., Joy, M.: AJ **90**, 1191 (1985)
Jones, T.J., Klebe, D., Dickey, J.M.: ApJ **389**, 602 (1992)
Jones, T.J., Krejny, M., Andersson, B.-G., Bastien, P.: BAAS **217**, 251.22 (2011)
Andersson, B-G, Piirola, V., De Buizer, J., Clemens, D. P., Uomoto, A., Charcos-Llorens, M., Geballe, T. R., Lazarian, A., Hoang, T., Vornanen, T., 2013, ApJ, 775, 84.
Katz, N., Furman, I., Biham, O., Pirronello, V., Vidali, G.: ApJ **522**, 305 (1999)
Kim, S.-H., Martin, P.G.: ApJ **444**, 293 (1995)

Kim, S.-H., Martin, P.G., Hendry, P.D.: ApJ **422**, 164 (1994)
Krügel, E.: The Physics of Interstellar Dust. IoP Publishing, Bristol (2003)
Lada, C.J., Huard, T.L., Crews, L.J., Alves, J.F.: ApJ **610**, 303 (2004)
Lazarian, A.: MNRAS **268**, 713 (1994)
Lazarian, A.: ApJ **451**, 660 (1995)
Lazarian, A.: ApJ **483**, 296 (1997a)
Lazarian, A.: MNRAS **288**, 609 (1997b)
Lazarian, A.: JQSRT **106**, 225 (2007)
Lazarian, A., Draine, B.T.: ApJ **516**, L37 (1999a)
Lazarian, A., Draine, B.T.: ApJ **520**, L67 (1999b)
Lazarian, A., Hoang, T.: MNRAS **378**, 910 (2007) (LH07)
Lazarian, A., Roberge, W.G.: ApJ **484**, 230 (1997)
Li, A., Greenberg, J.M.: A&A **323**, 566 (1997)
Li, H.-B., Houde, M.: ApJ **677**, 1151 (2008)
Martin, P.G.: ApJ **187**, 461 (1974)
Martin, P.G.: ApJ **445**, L63 (1995)
Martin, P.G., Angel, J.R.P.: ApJ **207**, 126 (1976)
Martin, P.G., Clayton, G.C., Wolff, M.J.: ApJ **510**, 905 (1999)
Mathis, J.S., Rumpl, W., Nordsieck, K.H.: ApJ **217**, 425 (1977)
Mathis, J.S.: ApJ **308**, 281 (1986)
Matsumura, M., Kameura, Y., Kawabata, K.S., Akitaya, H., Isogai, M., Seki, M.: PASJ **63**, L43 (2011)
Mie, G.: Annalen der Physik **330**, 377 (1908)
Myers, P.C., Goodman, A.A.: ApJ **373**, 509 (1991)
Novak, G., Dotson, J.L., Dowell, C.D., Goldsmith, P.F., Hildebrand, R.H., Platt, S.R., Schleuning, D.A.: ApJ **487**, 320 (1997)
Ostriker, E.C., Stone, J.M., Gammie, C.F.: ApJ **546**, 980 (2001)
Pirronello, V., Biham, O., Liu, C., Shen, L., Vidali, G.: ApJ **483**, L131 (1997)
Pirronello, V., Liu, C., Roser, J.E., Vidali, G.: A&A **344**, 681 (1999)
Purcell, E.M.: ApJ **231**, 404 (1979)
Purcell, E.M., Pennypacker, C.R.: ApJ **186**, 705 (1973)
Rachford, B.L., Snow, T.P., Tumlinson, J., Shull, J.M., Blair, W.P., Ferlet, R., Friedman, S.D., Gry, C., Jenkins, E.B., Morton, D.C., Savage, B.D., Sonnentrucker, P., Vidal-Madjar, A., Welty, D.E., York, D.E.: ApJ **577**, 221 (2002)
Rao, R., Crutcher, R.M., Plambeck, R.L., Wright, M.C.H.: ApJ **502**, L75 (1998)
Roberge, W.G.: ASP Conference Series, vol. 97, p. 401 (1996)
Roberge, W.G., "Astrophysics of Dust", ASP Conference Series, vol. 309, p. 467 (2004)
Serkowski, K.: In: IAU Symposium 52: "Interstellar Dust and Related Topics", vol. 52, p. 145 (1973)
Serkowski, K., Mathewson, D.S., Ford, V.L.: ApJ **196**, 261 (1975)
Smith, C.H., Wright, C.M., Aitken, D.K., Roche, P.F., Hough, J.H.: MNRAS **312**, 327 (2000)
Sorrel, W.H.: MNRAS **273**, 169 (1995)
Tang, Y.-W., Ho, P.T.P., Girart, J.M., Rao, R., Koch, P., Lai, S.-P.: ApJ **695**, 1399 (2009)
Troland, T., Crutcher, R.M.: ApJ **680**, 457 (2008)
van Dishoeck, E.F., Black, J.H.: ApJS **62**, 109 (1986)
Vaillancourt, J.E.: ApJS **142**, 53 (2002)
Vaillancourt, J.E., Dowell, C.D., Hildebrand, R.H., Kirby, L., Krejny, M.M., Li, H., Novak, G., Houde, M., Shinnaga, H., Attard, M.: ApJ **679**, L25 (2008)
Vaillancourt, J.E., Matthews, B.C.: ApJS **201**, 13 (2012)
Verchuur, G.L.: ApJ **156**, 861 (1969)
Viala, Y.P.: A&AS **64**, 391 (1986)
Voshchinnikov, N.V., Henning, T.: A&A **517**, 45 (2010)
Voshchinnikov, N.V., Henning, T., Prokopjeva, M.S., Das, H.K.: A&A **514**, A52 (2012)
Whittet, D.C.B.: Dust in the Galactic Environment. IoP Publishing, Bristol (2003)

Weingartner, J.C., Jordan, M.E.: ApJ **672**, 382 (2008)
Whittet, D.C.B., van Breda, I.G.: A&A **66**, 57 (1978)
Whittet, D.C.B., Bode, M.F., Longmore, A.J., Adamson, A.J., McFadzean, A.D., Aitken, D.K., Roche, P.F.: MNRAS **233**, 321 (1988)
Whittet, D.C.B., Adamson, A.J., Duley, W.W., Geballe, T.R., McFadzean, A.D.: MNRAS **241**, 707 (1989)
Whittet, D.C.B., Martin, P.G., Hough, J.H., Rouse, M.F., Bailey, J.A., Axon, D.J.: ApJ **386**, 562 (1992)
Whittet, D.C.B., Gerakines, P.A., Hough, J.H., Shenoy, S.S.: ApJ **547**, 872 (2001)
Whittet, D.C.B., Hough, J.H., Lazarian, A., Hoang, T.: ApJ **674**, 304 (2008)
Wiebe, D.S., Watson, W.D.: ApJ **549**, 115 (2001)
Wilking, B.A., Lebofsky, M.J., Kemp, J.C., Martin, P.G., Rieke, G.H.: ApJ **235**, 905 (1980)
Wilking, B.A., Lebofsky, M.J., Rieke, G.H.: AJ **87**, 695 (1982)
Williams, D.A., Hartquist, T.W., Whittet, D.C.B.: MNRAS **258**, 599 (1992)
Wolleben, M., Reich, W.: A&A **427**, 537 (2004)
Wolff, M.J., Clayton, G.C., Meade, M.R.: ApJ **403**, 722 (1993)
Yan, H., Lazarian, A.: ApJ **592**, L33 (2003)

Chapter 5
Magnetic Field Measurement with Ground State Alignment

Huirong Yan and A. Lazarian

Abstract Observational studies of magnetic fields are crucial. We introduce a process "ground state alignment" as a new way to determine the magnetic field direction in diffuse medium. The alignment is due to anisotropic radiation impinging on the atom/ion. The consequence of the process is the polarization of spectral lines resulting from scattering and absorption from aligned atomic/ionic species with fine or hyperfine structure. The magnetic field induces precession and realign the atom/ion and therefore the polarization of the emitted or absorbed radiation reflects the direction of the magnetic field. The atoms get aligned at their low levels and, as the life-time of the atoms/ions we deal with is long, the alignment induced by anisotropic radiation is susceptible to extremely weak magnetic fields ($1\,\mathrm{G} \gtrsim B \gtrsim 10^{-15}\,\mathrm{G}$). In fact, the effects of atomic/ionic alignment were studied in the laboratory decades ago, mostly in relation to the maser research. Recently, the atomic effect has been already detected in observations from circumstellar medium and this is a harbinger of future extensive magnetic field studies. A unique feature of the atomic realignment is that they can reveal the 3D orientation of magnetic field. In this chapter, we shall review the basic physical processes involved in atomic realignment. We shall also discuss its applications to interplanetary, circumstellar and interstellar magnetic fields. In addition, our research reveals that the polarization of the radiation arising from the transitions between fine and hyperfine states of the ground level can provide a unique diagnostics of magnetic fields in the Epoch of Reionization.

H. Yan (✉)
KIAA, Peking University, Beijing 100871, China
e-mail: hryan@pku.edu.cn

A. Lazarian
Astronomy Department, University of Wisconsin-Madison, 475 N. Charter St., Madison, WI 53706, USA
e-mail: lazarian@astro.wisc.edu

A. Lazarian et al. (eds.), *Magnetic Fields in Diffuse Media*, Astrophysics and Space Science Library 407, DOI 10.1007/978-3-662-44625-6_5

5.1 Introduction

Astrophysical magnetic fields are ubiquitous and extremely important, especially in diffuse media, where their energy is comparable or exceed the energy of thermal gas. For instance, in the diffuse interstellar medium (ISM), the magnetic field pressure may exceed the thermal pressure by a factor of ten.

Currently a few techniques are available for the studies of magnetic field in the diffuse medium and each of them has its own area of applicability and limitation. For example, Zeeman splitting of spectral lines can sample only relatively strong magnetic fields in dense and cold clouds (see Crutcher et al. 2010). In most cases, only line of sight component of the field can be obtained. Faraday rotation samples ionized gas and is sensitive to the product of the electron density and the line-of-sight magnetic field. It requires a polarized background source (see Crutcher and Troland 2008) and the disentanglement of magnetic and density variations is non-trivial. Synchrotron polarization traces plane-of-sky magnetic field in the expanses of the low density interstellar media, e.g. galactic halo (see Beck 2011) and in some sense complementary to the dust polarization studies which trace the plane-of-sky magnetic field in denser regions (see Hildebrand 2009). Neither of techniques can provide directly magnetic field strength and the dust polarimetry requires a proper modeling of grain alignment (see Lazarian 2007). In addition, new promising statistical techniques can measure the *average* direction of magnetic field using spectral lines fluctuations (Lazarian et al. 2002; Esquivel and Lazarian 2005, 2011) or synchrotron intensity fluctuations (Lazarian and Pogosyan 2012).

The closest to the technique of ground state alignment (henceforth GSA) are the techniques based on grain alignment and on the Hanle effect and Goldreich–Kulafis effects. It is well known that the extinction and emission from aligned grains reveal magnetic field direction perpendicular to the line of sight (see Hildebrand 2009 for a review). In spite of the progress in understanding of grain alignment (see Lazarian 2007 for a review), the natural variations in grain shapes and compositions introduce uncertainties in the expected degree of polarization. Hanle effect is the modification of polarized resonance-line scattering by magnetic fields. Hanle measurements were proposed for studies of circumstellar magnetic fields but require much higher magnetic fields (Landi Degl'Innocenti and Landolfi 2004). Alignment of the molecules in the excited state subject to radiation flux is the core of the studies based on the Goldreich–Kylafis effect (see Crutcher 2008). The technique is practically applicable to a limited number of molecular species and provides the 90° uncertainty in the determination of magnetic field direction.

We should mention that all techniques suffer from line-of-sight integration, which makes deducing the tomography of magnetic fields difficult. In general, each technique is sensitive to magnetic fields in a particular environment and the synergetic use of the technique is most advantageous. Obviously, the addition of new techniques for determining interstellar magnetic fields is always very valuable development.

Here we discuss a new promising technique to study magnetic fields in diffuse media. These technique is based on the ability of atoms and ions in their *ground state* to be aligned by the flow of photons. As the atoms precess in magnetic field, the alignment reflects the direction of the ambient magnetic field.

As we discuss below, the physical foundations of these technique can be traced back to the laboratory work on atomic alignment in the middle of the previous century (Kastler 1950; Brossel et al. 1952; Hawkins and Dicke 1953; Hawkins 1955; Cohen-Tannoudji et al. 1969; see Yan and Lazarian 2012 for details). Later papers Varshalovich (1971) and Landolfi and Landi Degl'Innocenti (1986) considered isolated individual cases of application of the aligned atoms mostly within toy models (see below for a brief review of the earlier development). Yan and Lazarian (2006, 2007, 2008, 2009) provided detailed calculations of GSA for a number of atoms and through their study identified GSA as a very unique new technique applicable for studying magnetic fields in a variety of environments, from circumstellar regions to the Early Universe. The emission and absorption lines ranging from radio to far UV were discussed. In particular, we identified new ways of study of magnetic fields using *absorption lines* (see Yan and Lazarian 2006), radio lines arising from fine and hyperfine splitting (Yan and Lazarian 2008) and provided extensive calculations of expected polarization degree for a variety of ions and atoms most promising to trace magnetic fields in diffuse interstellar gas, protoplanetary nebula etc.

The GSA technique as it stands now employs spectral-polarimetry and makes use of the ability of atoms and ions to be aligned *in their ground state* by the external anisotropic radiation. The aligned atoms interact with the astrophysical magnetic fields to get realigned. The precession of atoms can trace very weak magnetic field and therefore the technique, which is a big advantage compared to the Zeeman and Hanle techniques (see more in Sect. 5.3.1).

It is important to notice that the requirement for alignment in the atomic ground state is the presence of fine or hyperfine splitting of the ground state. The latter is true for many species present in diffuse astrophysical environments. Henceforth, we shall not distinguish atoms and ions and use word "atoms" dealing with both species. This technique can be used for interstellar,[1] and intergalactic studies as well as for studies of magnetic fields in QSOs and other astrophysical objects.

We would like to stress that the GSA effect is based on well-known physics. In fact, it has been known since 1950s that atoms can be aligned through interactions with the anisotropic flux of resonance emission (or optical pumping, see review Happer 1972 and references therein). Alignment is understood here in terms of orientation of the angular momentum vector **J**, if we use the language of classical mechanics. In quantum terms this means a difference in the population of sublevels corresponding to projections of angular momentum to the quantization axis. There have been a lot of applications of this effect since optical pumping was discovered by Kastler (1950), ranging from atomic clocks, magnetometer, and quantum optics

[1] Here interstellar is understood in a general sense, which, for instance, includes refection nebulae.

to spin-polarized nuclei (see review by Budker and Romalis 2007; book by Cohen-Tannoudji et al. 1969). We will argue in our review that GSA can introduce similar fundamental changes in terms of understanding magnetic fields in diffuse media.

In the review below, we discuss three ways of using aligned atoms to trace the magnetic field direction: (1) absorption lines (2) emission and fluorescent lines and (3) emission and absorption lines related to transitions between the fine structure split states of the ground level.

In addition, we shall discuss below how the information from the lines can be used to derive the 3D structure of the magnetic fields, and, in particular cases, their intensity of magnetic field.

In terms of terminology, we will use "GSA" in the situations where magnetic precession is important and therefore the alignment reveals the magnetic fields. Another possible term for the effect is "atomic magnetic re-alignment", which stresses the nature of the effect that we discuss. However, whenever it does not cause a confusion we prefer to use the term "GSA" in the analogy with the dust alignment which is in most cases caused by radiation and reveals the magnetic field due to dust Larmor precession in external magnetic fields

The polarization arising from GSA is on its way to becoming an accepted tool for interstellar and circumstellar studies. We see some advances in this direction. For instance, polarization of absorption lines arising from GSA was predicted in YL06 and was detected for the polarization of Hα absorption by Kuhn et al. (2007), although they neglected the important realignment effect of the magnetic field in their analysis. Focused on atomic fluorescence, Nordsieck (2012) discussed the observational perspective using pilot spectroscopic observation of NGC as an example. We are sure that further detections of the predicted polarization will follow soon. Therefore we believe that the time is ripe to discuss the status of the GSA in this review in order to attract more attention of both observers and theorists to this promising effect.

In what follows, we describe the earlier work on atomic alignment in Sect. 5.2 and the basic idea of GSA in Sect. 5.3. In Sect. 5.4, we expatiate on absorption polarimetry, which is an exclusive tracer of GSA, we discuss polarimetry of both fine and hyperfine transitions, how to obtain from them 3D magnetic fields, the different regimes of pumping, and circular polarization. Emission polarimetry is presented in Sects. 5.5 and in 5.6, we discuss another window of opportunity in IR and submillimetre based on the fine structure transitions within the aligned ground state. In Sect. 5.7, the additional effect of GSA on abundance study is provided. In Sect. 5.8, we put GSA into the context of a broad view of radiative alignment processes in Astrophysics. In Sect. 5.9, we focus on observational perspectives and present a few synthetic observations with the input data on magnetic field from spacecraft measurements. Summary is provided in Sect. 5.10.

5.2 History on Studies Related to Atomic Alignment

Unlike grain alignment, atomic alignment has long been an established physical phenomena which has solid physical foundations and has been studied and supported by numerous experiments (see review by Happer 1972). The GSA was first proposed by Kastler (1950), who received the Nobel prize in 1966 for pointing out that absorption and scattering of resonant radiation, termed *optical pumping*, can induce imbalances in the ground state. Soon after that, the GSA was observed in experiments (Brossel et al. 1952; Hawkins and Dicke 1953).

It is worth mentioning that atomic realignment in the presence of magnetic field was also studied in laboratory in relation with early-day maser research (see Hawkins 1955). Although our study in YL06 revealed that the mathematical treatment of the effect was not adequate in the original paper,[2] the importance of this pioneering study should not be underestimated. The astrophysical application of the GSA was first discussed in the interstellar medium context by Varshalovich (1968) for an atom with a hyperfine splitting. Varshalovich (1971) pointed out that GSA can enable one to detect the direction of magnetic fields in the interstellar medium, and later in Varshalovich and Chorny (1980) they proposed the alignment of Sodium as a diagnostics of the magnetic field in cometary comae, although the classical approach they used to describe the alignment in the presence of magnetic field is incorrect.

Nearly 20 years after the work by Varshalovich, the case of emission by an idealized fine structure atom subject to a magnetic field and a beam of pumping radiation was discussed by Landolfi and Landi Degl'Innocenti (1986). However, in that case, only a toy model of the process, namely, an idealized two-level atom was considered. In addition, the polarization of the emission from this atom was discussed for a very restricted geometry of observations, namely, a magnetic field direction along the line of sight and both of these perpendicular to the beam of incident light. This made it rather difficult to use the study as a tool for practical mapping of the magnetic fields in various astrophysical environments.

The GSA we deal with in this review should not be confused with the Hanle effect that solar researcher have extensively studied. While both effects are based on similar atomic physics and therefore share some of the quantum electrodynamic machinery for their calculations, the domains of applicability of the effects are very different. In particular, the Hanle effect is the depolarization and rotation of the polarization vector of the resonance scattered lines in the presence of a magnetic field, which happens when the Zeeman splitting becomes comparable to the decay rate of the excited state of an atom. The research into emission line polarimetry resulted in important changes of the views on solar chromosphere (see Landi Degl'Innocenti 1983, 1984, 1998; Stenflo and Keller 1997; Trujillo Bueno and Landi Degl'Innocenti 1997; Trujillo Bueno et al. 2002). However, these studies

[2]Radiative pumping is much slower than magnetic mixing. Radiation was chosen as the quantization axis, nevertheless, which inevitably would lead to the nonzero coherence components. They were neglected in Hawkins (1955), however.

Table 5.1 Relevant rates for GSA

$\nu_L(\mathrm{s}^{-1})$	Larmor precession frequency	$\frac{eB}{m_{ec}}$	$88(B/5\mu$ G)
$\tau_R^{-1}(\mathrm{s}^{-1})$	Radiative pumping rate	$B_{J_l J_u} I$	$7.4\times10^5\left(\frac{R_*}{r}\right)^2$
$\tau_T^{-1}(\mathrm{s}^{-1})$	Emission rate within ground state	A_m	2.3×10^{-6}
$\tau_c^{-1}(\mathrm{s}^{-1})$	Collisional transition rate	$\max(f_{kj}, f_{sf})$	$6.4\left(\frac{n_e}{0.1\mathrm{cm}^{-3}}\sqrt{\frac{8000\mathrm{K}}{T}}\right)\times10^{-9}$

A_m is the magnetic dipole emission rate for transitions among J levels of the ground state of an atom. f_{kj} is the inelastic collisional transition rates within ground state due to collisions with electrons or hydrogens, and f_{sp} is the spin flip rate due to Van der Waals collisions. In the last row, example values for C II are given. τ_R^{-1} is calculated for an O type star, where R_* is the radius of the star radius and r is the distance to the star (from Yan and Lazarian 2006)

correspond to a different setting to the one we consider in the case of GSA. The latter is the weak field regime, for which the Hanle effect is negligible. As we mentioned earlier, in the GSA regime the atoms/ions at ground level are repopulated due to magnetic precession. While the Hanle effect is prominent in the Solar case, it gets too weak for the environments of the interstellar medium, circumstellar regions and plasmas in the Early Universe. These are the areas where the GSA effect is expected to be very important.

The realignment happens, if during the lifetime of an atomic state, more than one Larmor precession happens. The time scale of atomic precession scales as $0.011(5\mu G/B)$ s. As the lifetime of the ground state is typically long (determined by absorption rate, see Table 5.1), even extremely weak magnetic fields can be detected this way. On the contrary, the typical application of the Hanle effect includes excited states with typical life-times of $A^{-1}\gtrsim10^7$.

Full calculations of the alignment of atom and ions in their ground or metastable state in the presence of magnetic field were done in Yan and Lazarian (2006, 2007, 2008). Yan and Lazarian (2006) considers polarization of absorbed light arising from aligned atoms with fine structure, Yan and Lazarian (2007) extends the treatment to emission and atoms with hyperfine, as well as, fine and hyperfine structure. Yan and Lazarian (2008) addresses the issues of radio emission arising from the transitions between the sublevels of the ground state and extended the discussions to the domain of both stronger and weaker magnetic field when the Hanle and ground level Hanle effects are present.

5.3 Basic Physics of GSA

The basic idea of GSA is very simple. The alignment is caused by the anisotropic deposition of angular momentum from photons of *unpolarized* radiation. In typical astrophysical situations the radiation flux is anisotropic[3] (see Fig. 5.1, *right*). As the

[3]Modern theory of dust alignment, which is a very powerful way to study magnetic fields (see Lazarian 2007 and ref. therein) is also appealing to anisotropic radiation as the cause of alignment.

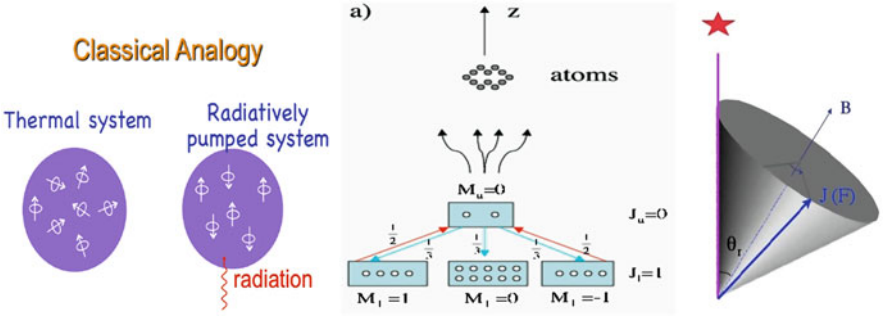

Fig. 5.1 *Upper left*: A carton illustrate classical analogy of the GSA induced by optical pumping; *Lower left*: A toy model to illustrate how atoms are aligned by anisotropic light. Atoms accumulate in the ground sublevel $M = 0$ as radiation removes atoms from the ground states $M = 1$ and $M = -1$; *Upper right*: Typical astrophysical environment where the ground-state atomic alignment can happen. A pumping source deposits angular momentum to atoms in the direction of radiation and causes differential occupations on their ground states. *Lower right*: In a magnetized medium where the Larmor precession rate ν_L is larger than the photon arrival rate τ_R^{-1}, however, atoms are realigned with respect to magnetic field. Atomic alignment is then determined by θ_r, the angle between the magnetic field and the pumping source. The polarization of scattered line also depends on the direction of line of sight, θ and θ_0 (from Yan and Lazarian 2008)

photon spin is along the direction of its propagation, we expect that atoms scattering the radiation from a light beam can become aligned. Such an alignment happens in terms of the projections of the angular momentum onto the direction of the incoming light. To study weak magnetic fields, one should use atoms that can be aligned in the ground state. For such atoms to be aligned, their ground state should have the non-zero angular momentum. Therefore fine (or hyperfine) structure is *necessary* for the alignment that we describe in this review.

Let us first discuss a toy model that provides an intuitive insight into the physics of GSA. Consider an atom with its ground state precessing a total angular momentum $I = 1$ and its upper state having an angular momentum $I = 0$ (Varshalovich 1971). If the projection of the angular momentum to the direction of the incident resonance photon beam is M, the lower state can have values $M = -1$, 0, and 1, while for the upper state $M = 0$ (see Fig.5.1, *left*). The unpolarized beam contains an equal number of left and right hand circularly polarized photons whose projections on the beam direction are 1 and -1. Thus, since the upper state only has $M = 0$, absorption of photons in the lower state will induce transitions from the $M = -1$ and $M = 1$ sublevels. However, the decay from the upper state populates all the three sublevels of the ground state. As the result the atoms accumulate in the $M = 0$ ground sublevel from which no excitations are possible. Accordingly, the optical properties of the media (e.g. absorption cross sections) would change.

This toy model can also illustrate the role of collisions and magnetic field. Without collisions one may expect that all atoms reside eventually at the sublevel of $M = 0$. Collisions, however, redistribute atoms to the different sublevels. Nevertheless, as the randomization of the ground state requires spin flips, it is less efficient

than one might naively imagine (Hawkins 1955). For instance, the experimental study in Kastler (1957) suggests that more than ten collisions with electrons are necessary to destroy an aligned state of sodium. The limited sensitivity of aligned atoms to disorienting collisions makes the effect important for various astrophysical environments.

Owing to precession, the quantum states of the atoms with different projections of the angular momentum will be mixed up. Magnetic mixing happens if the angular momentum precession rate is higher than the rate of the excitation from the ground state, which is true for many astrophysical conditions, e.g., interplanetary medium, ISM, intergalactic medium, etc. As a result, angular momentum is redistributed among the atoms, and the alignment is altered according to the angle between the magnetic field and radiation field θ_r (see Fig. 5.1, *right*). This is the *classical* picture.

In the *quantum* picture, if magnetic precession is dominant, then the natural quantization axis is the magnetic field direction, which in general is different from the symmetry axis of the radiation. The radiative pumping coming from different θ_r results in, then, different alignment.

The classical theory can provide a qualitative interpretation which shall be utilized in this chapter to provide an intuitive picture. However, particularly for emission lines, both the atoms and the radiation have to be described by the density matrices in order to obtain quantitative results. This is because there is coherence among different magnetic sublevels in the upper state.[4]

Our simple considerations above indicate that, in order to be aligned, first, atoms should have enough degrees of freedom: namely, the quantum angular momentum number of the atom must be ≥ 1. Second, the incident flux must be anisotropic. Moreover, the collisional rate should not be too high. While the latter requires special laboratory conditions, it is applicable in many astrophysical environments such as the outer layers of stellar atmospheres, the interplanetary, interstellar, and intergalactic medium.

5.3.1 Timescales

In terms of practical magnetic field studies, the variety of available atomic species is important in many aspects. One of them is the possibility of getting additional information about the environments. Let us illustrate this by considering the various rates (see Table 5.1) involved. These are (1) the rate of the Larmor precession, ν_L, (2) the rate of the optical pumping, τ_R^{-1}, (3) the rate of collisional randomization, τ_c^{-1}, and (4) the rate of the transition within ground state, τ_T^{-1}. In many cases $\nu_L > \tau_R^{-1} > \tau_c^{-1}, \tau_T^{-1}$. Other relations are possible, however. If $\tau_T^{-1} > \tau_R^{-1}$, the transitions

[4]In quantum physics, quantum coherence means that subatomic particles are able to cooperate. These subatomic waves or particles not only know about each other, but are also highly interlinked by bands of shared electromagnetic fields so that they can communicate with each other.

within the sublevels of the ground state need to be taken into account and the relative distribution among them will be modified (see YL06,c). Since emission is isotropic, the angular momentum in the atomic system is preserved and thus alignment persists in this case. In the case $\nu_L < \tau_R^{-1}$, the magnetic field does not affect the atomic occupations and the atoms are aligned with respect to the direction of the radiation. From the expressions in Table 5.1, we see, for instance, that magnetic field can realign CII only at a distance $r \gtrsim 7.7$ AU from an O star if the magnetic field strength is $\sim 5\,\mu$G.

If the Larmor precession rate ν_L is comparable to any of the other rates, the atomic line polarization becomes sensitive to the strength of the magnetic field. In these situations, it is possible to get information about the *magnitude* of magnetic field.

5.3.2 *Different Regimes*

Figure 5.2 illustrates the regime of magnetic field strengths where atomic realignment applies. Atoms are aligned by the anisotropic radiation at a rate of τ_R^{-1}. Magnetic precession will realign the atoms in their ground state if the Larmor precession rate $\nu_L > \tau_R^{-1}$. In contrast, if the magnetic field gets stronger such that the Larmor frequency becomes comparable to the line-width of the upper level, the

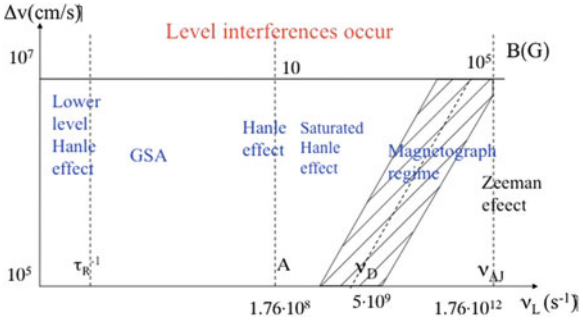

Fig. 5.2 Different regimes divided according to the strength of magnetic field and the Doppler line width. Atomic realignment is applicable to weak field (<1 G) in diffuse medium. Level interferences are negligible unless the medium is substantially turbulent ($\delta v \gtrsim 100$ km/s) and the corresponding Doppler line width becomes comparable to the fine level splitting $\nu_{\Delta J}$. For strong magnetic field, Zeeman effect dominates. When magnetic splitting becomes comparable to the Doppler width, σ and π components (note: we remind the reader that σ is the circular polarization and π represents the linear polarization) can still distinguish themselves through polarization, this is the magnetograph regime; Hanle effect is dominant if Larmor period is comparable to the lifetime of excited level $\nu_L^{-1} \sim A^{-1}$; similarly, for ground Hanle effect, it requires Larmor splitting to be of the order of photon pumping rate; for weak magnetic field (<1 G) in diffuse medium, however, GSA is the main effect provided that $\nu_L = 17.6(B/\mu G)\mathrm{s}^{-1} > \tau_R^{-1}$ (from Yan and Lazarian 2006)

upper level occupation, especially its coherence is modified directly by the magnetic field. This is the domain of Hanle effect, which has been extensively discussed for studies of the solar magnetic field (see Landi Degl'Innocenti and Landolfi 2004 and references therein). When the magnetic splitting becomes comparable to the Doppler line-width v_D, polarization appears. This is the "magnetograph regime" (Landi Degl'Innocenti 1983). For magnetic splitting $v_L \gg v_D$, the energy separation is enough to be resolved, and the magnetic field can be deduced directly from line splitting in this case. If the medium is strongly turbulent with $\delta v \sim 100\,\mathrm{km/s}$ (so that the Doppler line width is comparable to the level separations $v_D \sim v_{\Delta J}$), interferences occur among these levels and should be taken into account.

Long-lived alignable metastable states that are present for some atomic species between upper and lower states may act as proxies of ground states. Absorptions from these metastable levels can therefore also be used as diagnostics for the magnetic field.

The variety of species that are subject to the ground state or metastable state alignment endows the GSA technique with really unique capabilities. Different species are expected to be aligned when the conditions for their existence and their alignment are satisfied. This allows us to study the 3D distribution of magnetic fields, rather than line-average magnetic fields, which are available through most of the alternative techniques.

Most atoms have sublevels in the ground state, among which there are allowed magnetic dipole transitions. Although their transition probabilities are very low, they can be comparable to the optical pumping rate in regions far from any radiation source. Depending on how far away the radiation source is, there can be two regimes divided by the boundary where the magnetic dipole radiation rate A_m is equal to the pumping rate τ_R^{-1}. Inside the boundary, the optical pumping rate is much larger than the M1 transition rate A_m so that we can ignore the magnetic dipole radiations, to a first order approximation. Further out, the magnetic dipole emission is faster than optical pumping, such that it can be assumed that most atoms reside in the lowest energy level of the ground state, and alignment can only occur in this level. The two regimes are demarcated at r_1 (see Fig. 5.3, *left*) defined by

$$\tau_R^{-1} = B_{J_l J_u} I_{BB} (R_*/r_1)^2 = A_m, \tag{5.1}$$

where I_{BB}, R_* are the intensity and radius of the pumping source. For different radiation sources, the distance to the boundary differs. For an O type star, the distance would be $\sim$0.1 pc for species like C II, Si II, while for a shell star ($T_{\mathit{eff}} = 15{,}000\,\mathrm{K}$), it is as close as $\sim$0.003–0.01 pc. For species like C II, Si II the lowest level is not alignable having $J_l = 1/2$, and thus alignment is absent outside the radius $r = r_1$, which ensures that observations constrain the magnetic field topology within this radius.

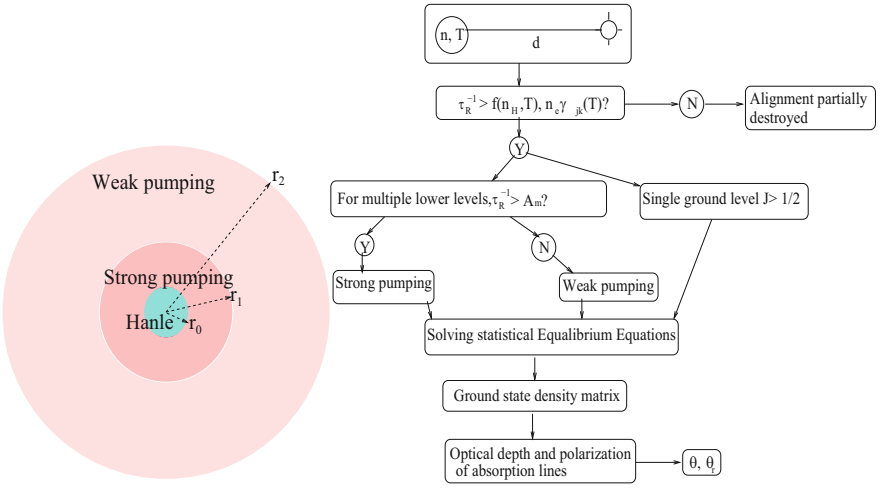

Fig. 5.3 *Left*: A carton illustrating how the atomic pumping changes with distance around a radiation source. For circumsteller region, magnetic field is strong, such that the Hanle effect, which requires $\nu_L \sim A$, dominates. Atomic alignment applies to the much more distant interstellar medium, within r_2, which is defined as the radius where the optical pumping rate τ_R^{-1} is higher than collisional rate. Inside r_2, it can be further divided into two regimes: strong pumping and weak pumping, demarcated at r_1 (see Eq. (5.1)); *right*: whether and how atoms are aligned depends on their intrinsic properties (transitional probabilities and structures) and the physical conditions: density n, temperature T and the averaged radiation intensity from the source I_*. If the pumping rate τ_R^{-1} is less than collisional rates, alignment is partially destroyed. Then for atoms with multiple lower levels, depending on the comparison between the pumping rate and the magnetic dipole radiation rate among the lower levels, the atoms are aligned differently. In the strong pumping case, all the alignable lower levels are aligned; on the contrary, only the ground level can be aligned in the case of weak pumping. From Yan and Lazarian (2006)

5.4 Polarization of Absorption Lines

The use of absorption lines to study magnetic fields with aligned atoms was first suggested by Yan and Lazarian (2006). Below we briefly outline the main ideas of the proposed techniques.

When atomic species are aligned in their ground state, the corresponding absorption from the state will be polarized as a result of the differential absorption parallel and perpendicular to the direction of alignment. The general expression for finite optical depth would be

$$\begin{aligned} I &= (I_0 + Q_0)e^{-\tau(1+\eta_1/\eta_0)} + (I_0 - Q_0)e^{-\tau(1-\eta_1/\eta_0)}, \\ Q &= (I_0 + Q_0)e^{-\tau(1+\eta_1/\eta_0)} - (I_0 - Q_0)e^{-\tau(1-\eta_1/\eta_0)}, \\ U &= U_0 e^{-\tau}, V = V_0 e^{-\tau}, \end{aligned} \tag{5.2}$$

where I_0, Q_0, U_0 are the Stokes parameters of the background radiation, which can be from a weak background source or the pumping source itself. The parameter d refers to the thickness of the medium. There parameters η_0, η_1, η_2 are the corresponding absorption coefficients. In the case of unpolarized background radiation and thin optical depth, the degree of linear polarization is given by

$$P = \frac{Q}{I} = \frac{e^{-(\eta_0+\eta_1)d} - e^{-(\eta_0-\eta_1)d}}{e^{-(\eta_0+\eta_1)d} + e^{-(\eta_0-\eta_1)d}} \approx -\tau \frac{\eta_1}{\eta_0} \tag{5.3}$$

The polarization in this case has a simple relation given by

$$\frac{P}{\tau} = \frac{Q}{I\eta_0 d} \simeq \frac{-\eta_1}{\eta_0} = \frac{1.5\sigma_0^2(J_l,\theta_r)\sin^2\theta w^2_{J_l J_u}}{\sqrt{2} + \sigma_0^2(J_l,\theta_r)(1-1.5\sin^2\theta)w^2_{J_l J_u}}. \tag{5.4}$$

with the alignment parameter $\sigma_0^2 \equiv \frac{\rho_0^2}{\rho_0^0}$, the normalized dipole component of density matrix of ground state, which quantifies the degree of alignment. For instance, for a state of angular momentum 1, the definition of $\rho_0^2 = [\rho(1,1) - 2\rho(1,0) + \rho(1,-1)]$. The general definition of ρ_0^2 can be found in Fano (1957) and D'Yakonov and Perel' (1965). The sign of ρ_0^2 gives the direction of alignment. Since magnetic field is the quantization axis, a positive alignment parameter means that the alignment is parallel to the magnetic field and a negative sign means the alignment is perpendicular to the magnetic field. The angle θ is the angle between the line of sight and magnetic field. $w^2_{J_l J_u}$ defined below, is a parameter determined by the atomic structure

$$w^K_{J_l J_u} \equiv \begin{Bmatrix} 1 & 1 & K \\ J_l & J_l & J_u \end{Bmatrix} / \begin{Bmatrix} 1 & 1 & 0 \\ J_l & J_l & J_u \end{Bmatrix}. \tag{5.5}$$

The values of $w^2_{JJ'}$ for different pairs of J, J' are listed in Table 5.2. We see that it totally depends on the sign of $w^2_{JJ'}$, whether the alignment and polarization

Table 5.2 Numerical values of $w^2_{JJ'}$

J	1			3/2			2		
J'	0	1	2	1/2	3/2	5/2	1	2	3
$w^2_{JJ'}$	1	−0.5	0.1	0.7071	−0.5657	0.1414	0.5916	−0.5916	0.1690
J	5/2			3			7/2		
J'	3/2	5/2	7/2	2	3	4	5/2	7/2	9/2
$w^2_{JJ'}$	0.5292	−0.6047	0.1890	0.4899	−0.6124	0.2041	0.4629	−0.6172	0.2160
J	4			9/2			5		
J'	3	4	5	7/2	9/2	11/2	4	5	6
$w^2_{JJ'}$	0.4432	−0.6205	0.2256	0.4282	−0.6228	0.2335	0.4163	−0.6245	0.2402

J is the J value of the initial level and J' is that of the final level

Table 5.3 Absorption lines of selected alignable atomic species and corresponding transitions

Species	Ground state	Excited state	Wavelength (Å)	P_{max}
S II	$4S^o_{3/2}$	$4P_{1/2,3/2,5/2}$	1,250–1,260	12 %$(3/2 \rightarrow 1/2)$
Cr I	$a7S_3$	$7P^o_{2,3,4}$	3,580–3,606	5 %$(3 \rightarrow 2)$
C II	$2P^o_{1/2,3/2}$	$2S_{1/2}$,$2P_{1/2,3/2}$,$2D_{3/2,5/2}$	1,036.3–1,335.7	15 %$(3/2 \rightarrow 1/2)$
Si II			989.9–1,533.4	7 %$(3/2 \rightarrow 1/2)$
O I	$3P_{2,1,0}$	$3S_1$, $3D_{1,2,3}$	911–1,302.2	29 %$(2 \rightarrow 2)$
S I		$3S_1$,$3P^o_{0,1,2}$, $3D_{1,2,3}$	1,205–1,826	22 %$(1 \rightarrow 0)$
C I			1,115–1,657	18 %$(1 \rightarrow 0)$
Si I	$3P_{0,1,2}$	$3P^o_{0,1,2}$,$3D^o_{1,2,3}$	1,695–2,529	20 %$(2 \rightarrow 1)$
S III			1,012–1,202	24.5 %$(2 \rightarrow 1)$
		$z4G^o_{5/2}$	3,384.74	−0.7 %
Ti II	$a4F_{3/2}$	$z4F^o_{5/2}$	3,230.13	−0.7 %
		$z4F^o_{3/2}$	3,242.93	2.9 %
		$z4D^o_{3/2}$	3,067.25	2.9 %
		$z4D^o_{1/2}$	3,073.88	7.3 %

Note only lines above 912 Å are listed. Data are taken from the Atomic Line List http://www.pa.uky.edu/~peter/atomic/ and the NIST Atomic Spectra Database. The last column gives the maximum polarizations and its corresponding transitions. For those species with multiple lower levels, the polarizations are calculated for shell star (T_{eff} = 15,000 K) in the strong pumping regime; in the weak pumping regime, the maximum polarizations are 19 % for OI transition $(2 \rightarrow 2)$, and 9 % for SI transition $(2 \rightarrow 2)$

are either parallel or orthogonal to each other. Once we detect the direction of polarization of some absorption line, we immediately know the direction of alignment.

The alignment is either parallel or perpendicular to the direction of the symmetry axis of the pumping radiation in the absence of a magnetic field. Real astrophysical fluids, though, are magnetized, and the Larmor precession period is usually larger than the radiative pumping rate, unless, the atom is very close to the radiation source as we noted earlier. In this case, realignment happens and an atomic species can be aligned either parallel or perpendicular to the local magnetic field. The switch between the two cases is always at the Van Vleck angle $\theta_r = 54.7°, 180° - 54.7°$, where θ_r is the angle between the magnetic field and radiation. As a result, the polarization of the absorption line also changes according to Eq. (5.4). *This turnoff at the Van Vleck angle is a generic feature regardless of the specific atomic species as long as the background source is unpolarized and the magnetic field is in the atomic realignment regime.* In practice, this means that once we detect any polarization in absorption line, we get immediate information of the direction of the magnetic field in the plane of sky within 90° degeneracy. If we have two measurables, then according to Eq. (5.4) both θ_r, θ can be determined. With θ_r known, the 90° degeneracy in the pictorial plane can be removed and we can get 3D information of the magnetic field (Table 5.3).

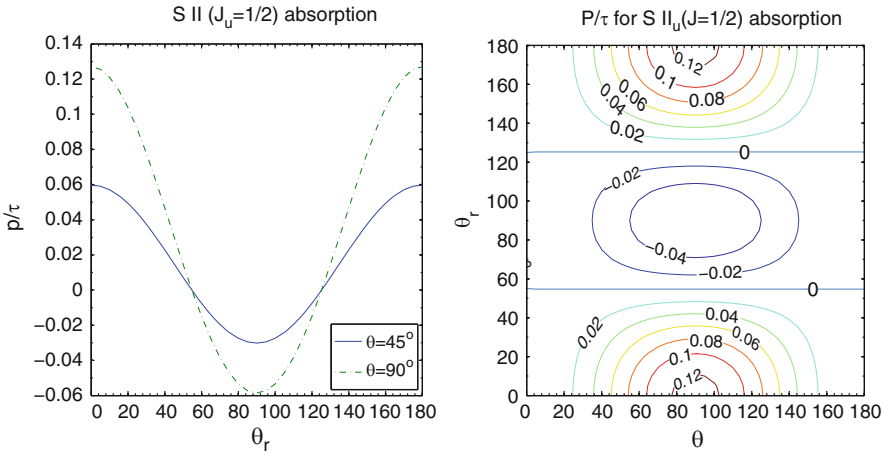

Fig. 5.4 *Left*: Degree of polarization of S II absorption lines vs. θ_r, the angle between magnetic field and direction of pumping source θ, the angle between magnetic field and line of sight. *Right*: The contour graphs of S II polarization. It is determined by the dipole component of density matrix $\sigma_0^2(\theta_r)$ and the direction of observation θ (Eq. (5.4)). From Yan and Lazarian (2006)

Figure 5.4 shows the dependence of the polarization for S II absorption on θ_r, θ, which is representative for all polarized absorption lines. From these plots, a few general features can be identified. At $\theta = 90^o$, the observed polarization reaches a maximum for the same θ_r and alignment, which is also expected from Eq. (5.4). This shows that atoms are indeed realigned with respect to the magnetic field such that the intensity difference is maximized parallel and perpendicular to the field (Fig. 5.1, *right*). At $\theta = 0°, 180°$, the absorption polarization is zero according to Eq. (5.4). Physically this is because the precession around the magnetic field makes no difference in the x, y direction when the magnetic field is along the line of sight (Fig. 5.1, *right*).

We consider a general case where the pumping source does not coincide with the object whose absorption is measured. If the radiation that we measure is also the radiation that aligns the atoms, the direction of pumping source coincides with line of sight, i.e., $\theta = \theta_r$ (Fig. 5.1, *right*).

5.4.1 Is There Any Circular Polarization?

Note that if the incident light is polarized in a different direction than that of the alignment, *circular polarization* can arise due to de-phasing, although this is a second order effect. Consider a background source with a nonzero Stokes

parameter U_0 shining upon atoms aligned in the Q direction.[5] The polarization will be precessing around the direction of alignment and generate a V component representing a circular polarization

$$\frac{V}{I\tau} \simeq \frac{\kappa_Q}{\eta_I}\frac{U_0}{I_0} = \frac{\psi_\nu}{\xi_\nu}\frac{\eta_Q}{\eta_I}\frac{U_0}{I_0} \tag{5.6}$$

where κ is the dispersion coefficient, associated with the real part of the refractory index, whose imaginary part corresponds to the absorption coefficient η. ψ is the dispersion profile and ξ is the absorption profile.

The incident light can be polarized by the source, e.g. synchrotron emission from pulsars, or polarized via the propagation through the interstellar medium, e.g. as a result of selective extinction from the aligned dust grains (see Lazarian 2007). In the latter case, the polarization of the impinging light is usually low and the intensity of circular polarization is expected to be low as well. This should not preclude the detection of the effect as instrumentation improves.

5.5 IR/Submilimetre Transitions Within Ground State

The alignment in the ground state affects not only the optical (or UV) transitions to the excited electronic states, but also the magnetic dipole transitions within the ground state. Similar to HI, other species that have structure within the ground states are also influenced by the optical pumping[6] through the Wouthuysen-Field effect (Wouthuysen 1952; Field 1958). After absorption of a Lyα photon, the hydrogen atom can relax to either of the two hyperfine levels of the ground state, which can induce a HI 21 cm emission if the atom falls onto the ground triplet state (see also Furlanetto et al. 2006 for a review). Recently, the optical pumping oxygen has been proposed as a probe for the intergalactic metals at the epoch of reionization (Hernández-Monteagudo et al. 2007).

However, in these earlier studies, the pumping light has been assumed to be isotropic. This is problematic, particularly for the metal lines whose optical depth is small. During the early epoch of reionization, for instance, the ionization sources are localized, which can introduce substantial anisotropy. The GSA introduced by the anisotropy of the radiation field can play an important role in many circumstances. The earlier oversimplified approach can lead to substantial errors in the predictions. The emissivity and absorption coefficients for the Stokes parameters are modified

[5] To remind our readers, The Stokes parameters Q represents the linear polarization along $\mathbf{e}_1$ minus the linear polarization along $\mathbf{e}_2$; U refers to the polarization along $(\mathbf{e_1} + \mathbf{e_2})/\sqrt{2}$ minus the linear polarization along $(-\mathbf{e_1} + \mathbf{e_2})/\sqrt{2}$ (see Fig. 5.1, *right*).

[6] To clarify, we do not distinguish between pumping by optical lines or UV lines, and name them simply "optical pumping".

Table 5.4 The polarization of forbidden lines

Lines	Lower level	Upper level	Wavelength (μm)	P_{max} (%)
$[C\ I]$	$3P_0$	$3P_1$	610	20
$[O\ I]$	$3P_2$	$3P_1$	63.2	24
$[C\ II]$	$3P_{1/2}$	$3P_{3/2}$	157.7	2.7
$[Si\ II]$	$3P_{1/2}$	$3P_{3/2}$	34.8	4
$[S\ IV]$	$3P_{1/2}$	$3P_{3/2}$	610	10.5

due to the alignment effect. The ratio of the corresponding optical depth, to that without alignment, is

$$\tilde{\tau} = \frac{\tau}{\tau_0} = \frac{\tilde{\eta} - \tilde{\eta}_{s,i} \exp(-T_*/T_s)}{1 - \exp(-T_*/T_s)}, \tag{5.7}$$

where T_* is the equivalent temperature of the energy separation of the metastable and ground levels, and T_s is the spin temperature.

The ratios of absorption and stimulated emission coefficients with and without alignment are given by

$$\tilde{\eta}_i = \eta_1/\eta_1^0 = 1 + w_{0l}\sigma_0^2(J_l^0)\mathscr{J}_0^2(i,\Omega), \tag{5.8}$$

$$\tilde{\eta}_{s,i} = \tilde{\epsilon}_i = \epsilon_i/\epsilon_i^0 = 1 + w_{l0}\sigma_0^2(J_l)\mathscr{J}_0^2(i,\Omega) \tag{5.9}$$

where $\mathscr{J}_0^2(i,\Omega)$ are the irreducible tensors for the Stokes parameters (see, e.g. Yan and Lazarian 2006). Since both the upper (metastable) level, and the lower levels are long lived and can be realigned by the weak magnetic field in a diffuse medium, the polarization of *both emission and absorption* between them is polarized either parallel or perpendicular to the magnetic field like the case of all the absorptions from the ground state, and can be described by Eq. (5.4). In the case of emission, the dipole component of the density matrix in Eq. (5.4) should be replaced by that of the metastable level. In Fig. 5.11, we show an example of our calculation of the polarization of the [C I] 610 μm line, which can be detected in places like PDRs.

We discussed pumping of the hyperfine lines [H I] 21 cm and [N V] 70.7 mm in Yan and Lazarian (2007) and the fine structure line [O I] 63.2 μm here. This effect exists in all atoms with some structure in ground state, e.g., Na I, K I, fine structure lines of [C I], [C II], [Si II], [N II], [N III], [O II], [O III],[S II], [S III], [S IV], [Fe II], etc. (see Table 4.1 in Lequeux 2005). The example lines we have calculated are listed in Table 5.4. Many atomic radio lines are affected in the same way and they can be utilized to study physical conditions, especially in the early universe: abundances, the extent of reionization through the anisotropy (or localization) of the optical pumping sources, and *magnetic fields*, etc.

5.6 Atoms with Hyperfine Structure

Although the energy of hyperfine interaction is negligible, the hyperfine interaction should be accounted for atoms with nuclear spins. This is because for these angular momentum instead of energy is the determinative factor. Hyperfine coupling increases the total angular momentum and the effects are twofold. For species with fine structure ($J > 1/2$), the hyperfine interaction reduces the degree of alignment since, in general, the more complex the structure is, the less alignment there is. This is understandable, as polarized radiation arises mostly from the sublevels with the largest axial angular momentum, which constitutes a smaller percentage in atoms with more sublevels. For species without fine structure ($J < 1/2$) like alkali atoms, the hyperfine interaction enables alignment by inducing more sublevels[7] (see Fig. 5.5).

Note that the alignment mechanism of alkali atoms is different from that illustrated in the cartoon (depopulation pumping) since the excitation rates from different sublevels in the ground state are equal. In other words, atoms from all the sublevels have equal probabilities to absorb photons. For the same reason, the absorption from alkali atoms is not polarized.[8] The actual alignment is due to another mechanism: repopulation pumping. The alkali atoms are repopulated as a result of spontaneous decay from a polarized upper level (see Happer 1972). Upper level becomes polarized because of differential absorption rates to the levels.

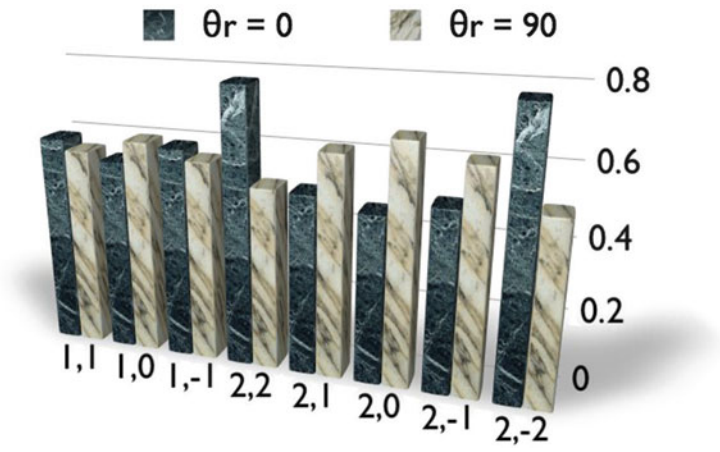

Fig. 5.5 The occupation in ground sublevels for Na. It is modulated by the angle between magnetic field and the radiation field θ_r

[7]There are no energy splittings among them, the effect is only to provide more projections of angular momentum (see Yan and Lazarian 2007).

[8]Only if hyperfine structure can be resolved, polarization can occur.

5.7 Polarization of Resonance and Fluorescence Lines

When the magnetic precession rate becomes less than the emission rate of the upper level, the direct effect of the magnetic field on the upper level is negligible. The only influence of the magnetic field is on the ground state through the alignment of atoms. This is the effect that was the focus of our studies in Yan and Lazarian (2006, 2007, 2008). The atoms are aligned either parallel or perpendicular to the magnetic field as we discussed before.

The differential occupation in the ground state (see Fig. 5.5) can be transferred to the upper level of an atom through excitation. The emission from such a differentially populated state is therefore polarized. The corresponding emission coefficients of the Stokes parameters are given in Landi Degl'Innocenti (1984), Yan and Lazarian (2008) for fine structure transitions and Yan and Lazarian (2007) for transitions involving hyperfine structures. Indeed emission line can be polarized without GSA. This corresponds the textbook description of polarization of scattered lines. It can be shown that if the dipole and other higher order components of the ground state density matrix $\rho^2_{q'}$ are zeros, we recover the classical result in the optically thin case

$$\epsilon_2 = \epsilon_3 = 0,\ P = \frac{\epsilon_1}{\epsilon_0} = \frac{3E_1 \sin^2\alpha}{4 - E_1 + 3E_1\cos^2\alpha} \tag{5.10}$$

where α is the scattering angle.[9] The polarizability is actually given by

$$E_1 = \frac{w^2_{J_u J_l} r_{20}}{p_0} \tag{5.11}$$

for transitions in atoms with fine structure. If we account for the alignment by radiation, but ignore the magnetic field, i.e., $\theta_r = 0$, then

$$E_1 = \frac{w^2_{J_u J_l}\left[r_{20} + r_{22}\sigma_0^2(J_l) + \sqrt{2}p_2\sigma_0^2(J_l)\right]}{\sqrt{2}p_0 + r_{02}\sigma_0^2} \tag{5.12}$$

For the optically thin case, the linear polarization degree is given by $p = \sqrt{Q^2+U^2}/I = \sqrt{\epsilon_2^2+\epsilon_1^2}/\epsilon_0$, and the positional angle $\chi = \frac{1}{2}\tan^{-1}(U/Q) = \frac{1}{2}\tan^{-1}(\epsilon_2/\epsilon_1)$.

Since the weak magnetic field does not have a direct influence on the upper level, there is no general simple geometrical correspondence between the polarization and

[9] Since there is no alignment on the ground state and we can choose the direction of radiation as the quantization axis, $\alpha = \theta$.

Table 5.5 The maximum polarizations expected for a few example of emission lines and their corresponding transitions

Species	Lower state	Upper state	Wavelength (Å)	$\lvert P_{max}\rvert$
S II	$4S^o_{3/2}$	$4P_{3/2}$	1,253.81	30.6 %
		$4P_{5/2}$	1,259.52	31.4 %
	$3P_0$	$3S^o$	1,306	16 %
	$3P_1$	$3S^o$	1,304	8.5 %
O I	$3P_2$	$3S^o$	1,302	1.7 %
	$3P$	$3S^o$	5,555, 6,046, 7,254	2.3 %
	$3P_0$	$3D^o$	1,028	4.29 %
	$3P_1$	$3D^o$	1,027	7.7 %
	$3P_2$	$3D^o$	1,025	10.6 %
	$3P$	$3D^o$	5,513, 5,958, 7,002	1.3 %
H I	$1S_{1/2}$	$2P_{3/2}$	912–1,216	26 %
Na I	$1S_{1/2}$	$2P_{3/2}$	5891.6	20 %
K I	$1S_{1/2}$	$2P_{3/2}$	7,667, 4,045.3	21 %
N V	$1S_{1/2}$	$2P_{3/2}$	1238.8	22 %
P V	$1S_{1/2}$	$2P_{3/2}$	1117.977	27 %
N I	$4S^o_{3/2}$	$4P_{1/2}$	1,200	5.5 %
Al II	$1S_0$	$1P^o_1$	8,643	20 %

the magnetic field as in the case of absorption, except the special case where the scattering angle is small (see 5.8 and Shangguan and Yan 2012 for details). In fact, from the discussions above (Eq. (5.10)), we see that the polarization is either parallel or perpendicular to the radiation field in the absence of GSA. The effect of GSA is to introduce coherence on the upper level through the radiative excitation, which is then transferred to the emission. To obtain the direction of the magnetic field, one needs quantitative measurements of at least two lines. The lines for which we have calculated the polarizations are listed in Table 5.5.

In the case that the direction of optical pumping is known, e.g., in planetary system and circumstellar regions, magnetic realignment can be identified if the polarization is neither perpendicular or parallel to the incident radiation (see Eqs. (5.10), (5.12)). As an example, we here show a polarization map for a spherical system with a poloidal magnetic field (Yan and Lazarian 2009), e.g., a circumstellar envelope. The polarization would be spherically symmetric without accounting for the effect of the magnetic field. With magnetic realignment however, the pattern of the polarization map is totally different, see Fig. 5.9. *In practice, one can remove the uncertainty by measuring polarization from both alignable and non-alignable species, the latter of which do not trace the magnetic field.*

5.8 Influence of Magnetic field on Polarization and Line Intensity

The influence of the magnetic field on the polarization of scattered lines can be illustrated by contour maps of the position angle as a function of the magnetic field direction for a fixed scattering angle. The geometry of the maps is defined in Fig. 5.6, *left*.

When the scattering angle is relatively large ($\theta_0 \gtrsim 20°$), quasi-symmetry is maintained and ϕ_B corresponding to the symmetric axis equals to the scattering angle (or to $\theta_0 + 180°$) (see dash lines in Fig. 5.7, *right*). χ on the quasi-symmetric axis are zero. This means that when the projection of the magnetic field on the scattering plane is parallel to the line of sight, the vector of polarization also lies in the same plane. In general, the position angle reduces with decreasing scattering angles. *When the scattering angle is small, the direction of polarization generally directly traces the magnetic field direction in the pictorial plane (see Fig. 5.7, left).* In addition, the polarization is the same for θ_0 and $(180° - \theta_0)$ because of the symmetry.

The magnetic field alters not only the direction of polarization of scattered lines, but also the degree of polarization (see Fig. 5.6, *right*). Owing to averaging due to magnetic mixing the magnetic field decreases the polarization degree at large scattering angles and increases the polarization at small scattering angles. In the classical description, there is some similarity to the Hanle process as discussed

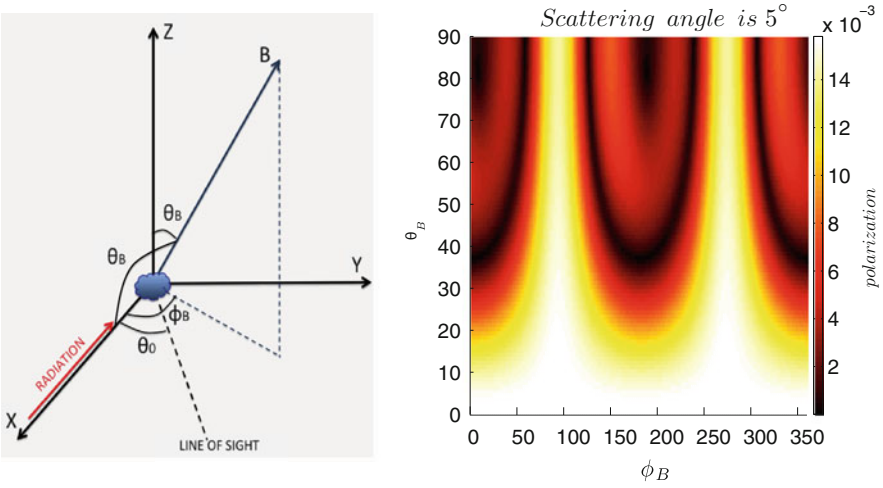

Fig. 5.6 *Left*: The magnetic field (θ_B, ϕ_B) was measured in the reference frame where x-axis points to the radiation source, z-axis is perpendicular to the scattering plane. Scattering angle, θ_0 is fixed; *right*: the contour map of the polarization degree as a function of the direction of magnetic field. The scattering angle is fixed at 5°. (θ_B, ϕ_B) is the solid angle of the magnetic field s defined in Fig. 5.6. From Shangguan and Yan (2012)

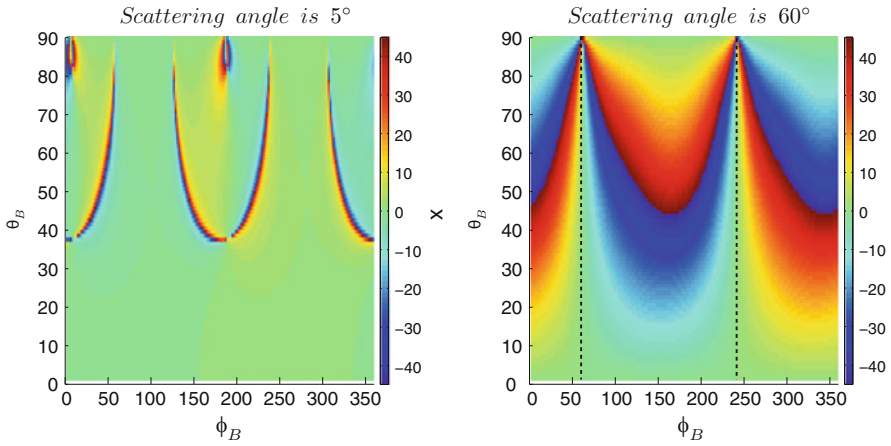

Fig. 5.7 The contour map of position angle, χ, as a function of the direction of magnetic field. The scattering angles are set to be 5° (*left*) and 60° (*right*). In the *right panel*, the *dashed lines* are two quasi-symmetry axes corresponding to $\phi_B = 60°$ and 240°, respectively. θ_B and ϕ_B are defined in Fig. 5.6. From Shangguan and Yan (2012)

in Kastler (1973) and House (1974). The difference is that magnetic coherence is transferred to the upper state indirectly from the ground state through absorption (see details in Shangguan and Yan 2012).

5.9 Observational Perspective

5.9.1 Interstellar Absorption and 3D Magnetic Field Measurement

In contrast to the case of emission, GSA is a unique mechanism for polarizing absorption lines, as first proposed by Yan and Lazarian (2006). As illustrated above, the 2D magnetic field in the plane of sky can be easily obtained from the direction of the polarization. If we have quantitative measurements, we can get the 3D magnetic field.

The resonance absorption lines in Table 5.2 appropriate for studying magnetic fields in diffuse, low column density ($A_V \sim$ few tenths) neutral interstellar clouds are those of N I, O I, S II, Mn II, and Fe II. These are all in the ultraviolet.

At higher column densities, the above lines become optically thick, and lines of lower abundance, as well as excited states of the above lines become available. Significantly, some of these lines (from Ti II, Fe I) are in the visible. An interesting region, where the degenerate case (pumping along the line of sight) should hold is the "Orion Veil" (Abel et al. 2006), a neutral cloud with $A_V \sim 1.5$, and $N \sim 1{,}000$,

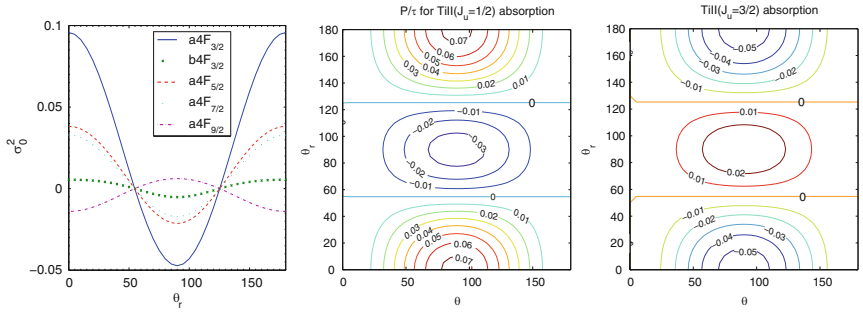

Fig. 5.8 *Left*: The alignment of the ground state $a4F$ and metastable level $b4F_{3/2}$ of Ti II; *middle* and *right*: the contour of equal degree of polarization of Ti II absorption lines ($J_l = 1/2 \rightarrow J_u = 1/2, 3/2$). θ_r and θ are the angles of incident radiation and line of sight from the magnetic field (see Fig. 5.2, *right*). In the case of pumping source coincident with the background source, we have the degeneracy and polarization will be determined by one parameter $\theta_r = \theta$. From Yan and Lazarian (2008)

which is 1–2 parsec in the foreground of the Orion Nebula. The Orion Veil should be pumped by the Trapezium. This region is of particular interest for magnetic field studies, since it is one of the only places where maps exist of the H I 21 cm Zeeman effect, which provides the sign and magnitude of the magnetic field along the line of sight. The magnetic realignment diagnostic, on the other hand, gives the orientation of the magnetic field lines in 3D, which is exactly complimentary information: combination of the two yields a complete 3D magnetic field map.

The Ti II lines provide a fairly accessible test of the magnetic alignment diagnostic, although there are not enough strongly polarized lines in the visible to be useful by themselves: observation of an effect for Ti II, with moderate resolution, would motivate a serious study of the pumping of the much more numerous Fe I lines, and the construction of more advanced instrumentation. Table 5.3 shows the five strongest Ti II lines, all from the J = 3/2 ground state of the ion (see also Fig. 5.8). The polarization depends only on the J value of the upper state, regardless of the other quantum numbers. We have assumed "weak pumping" for this calculation, such that the rate of decay from the excited states of the ground term exceeds the pumping rate. The most strongly polarized line, at 3,074 Å, is unfortunately difficult to observe from the ground, and the strongest line, at 3,384 Å, is only weakly polarized. The 3,243 Å line is the most favorable for observations. It is estimated that for a line with $\tau \sim 1$ and a width of 20 km/s, this effect would be detectable at 10σ for all stars brighter than V = 8 with the spectropolarimeter at SALT with a resolution R = 6,000 (Nordsieck, private communications).

As a first step, with low resolution measurement, 2D magnetic field in the pictorial plane can be easily obtained from the direction of polarization modulo a 90° degeneracy, similar to the case of grain alignment and the Goldreich-Kylafis effect. Different from the case of emission, any polarization, if detected in absorption lines, would be a unique indicator of alignment, and tracer of the

magnetic field since no other mechanisms can induce polarization in absorption lines. The polarization in Hα absorption reported by Kuhn et al. (2007) was, in fact, due to the GSA as predicted in Yan and Lazarian (2006) for general absorptions.

If we have two measurable, we can solve Eq. (5.4) and obtain both θ_r and θ. With θ_r known, the 90° degeneracy can be removed since we can decide whether the polarization is parallel or perpendicular to the magnetic field in the plane of the sky. Combined with θ, the angle between the magnetic field and the line of sight, we get the 3D direction of the magnetic field.

5.9.2 Circumstellar Absorption

The Be star ζ Tau illustrates one application of the diagnostic for circumstellar matter. A number of absorption lines from the metastable level of Si II $2P_{3/2}$ are seen, along with the O I and S II lines already discussed. This provides for a large number of different species. In this case the absorption is likely being formed in a disk atmosphere, absorbing light from the disk and pumped by light from the star. The net polarization signal is integrated across the disk, and depends just on the magnetic field geometry and the inclination of the disk. In this case, the inclination is known from continuum polarization studies to be 79° (Carciofi et al. 2005). The FUSP (The Far Ultraviolet SpectroPolarimeter, PI: K. Nordsieck) sounding rocket should be sensitive to these effects: ζ Tau is one of the brightest UV sources in the sky.

A second interesting circumstellar matter case is that for planetary disks around pre-main sequence stars. In this case, pumping conditions are similar to those for comets in the Solar System: with pumping rates on the order of 0.1–1 Hz, and realignment for fields greater than 10–100 mGauss. Conditions here are conducive to substantial populations in CNO metastable levels above the ground term: Roberge et al. (2002) find strong absorption in the FUV lines (1,000–1,500 Å) of O I (1D) and N I and S II (2D), apparently due to dissociation of common ice molecules in these disks (these are also common in comet comae). Since these all have $J_l > 1$, they should be pumped, and realigned. This presents an exciting possibility for detecting the magnetic geometry in planetary disks and monitoring them with time. Since these are substantially fainter sources, this will require a satellite facility.

5.9.3 Fluorescence from Reflection Nebulae

The magnetic realignment diagnostic can also be used in fluorescently scattered lines. This is because the alignment of the ground state is partially transferred to the upper state in the absorption process. There are a number of fluorescent lines in emission nebulae which are potential candidates (see Nordsieck 2012). Although such lines have been seen in the visible in H II regions (Grandi 1975a,b) and

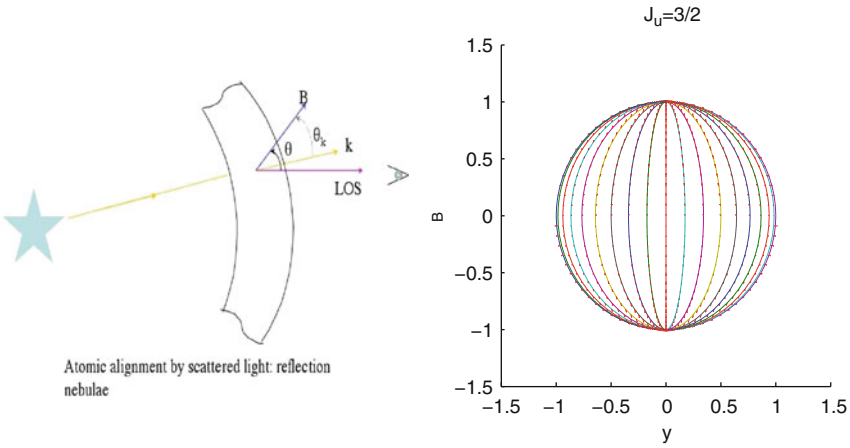

Fig. 5.9 *Left*: Schematics of GSA by circumstellar scattering; *right*: polarization vectors of O I emission in a circumstellar region with alignment by uniform magnetic field. The inclination of magnetic field is 45° from the light of sight. The magnetic field is in the y direction in the plane of sky (from Yan and Lazarian 2009)

planetary nebulae (Sharpee et al. 2004), we suggest that reflection nebulae would be a better place to test the diagnostic, since the lack of ionizing flux limits the number of levels being pumped, and especially since common fluorescent ions like N I and O I would not be ionized, eliminating confusing recombination radiation. Realignment should make itself evident in a line polarization whose position angle is not perpendicular to the direction to the central star. This deviation depends on the magnetic geometry and the scattering angle. The degree of polarization also depends on these two parameters. It will be necessary to compare the polarization of several species with different dependence on these factors to separate the effects. This situation is an excellent motivation for a pilot observation project (Fig. 5.9).

5.9.4 Magnetic Field in PDR Regions

Most fine structure FIR lines arise from photon dominated (PDR) regions, which represent the transition region between fully ionized material and molecular clouds illuminated by a stellar source of UV radiation. The line ratio of the brightest ones, e.g., [C II] 158 μm, [O I] 63, 145 μm, are used to infer physical parameters, including density and UV intensity based on the assumption that they are collisionally populated. Recent observations of UV absorption by Sterling et al. (2005), however, find that the population ratio in $3P_{1,0}$ state, the originating levels of [O I] 63, 145 μm is about twice the LTE value in the planetary nebula (PN) SwSt 1, and fluorescence excitation by stellar continuum is concluded to be the dominant excitation mechanism. In this case, the alignment is bound to happen on

the two excited levels $3P_{1,0}$ because of the anisotropy of the pumping radiation field, resulting polarizations in the [O I] 63, 145 μm lines.

The high spatial resolution of SOFIA, for instance, is advantageous in zooming into PDRs and resolving the lines. Moreover, in highly turbulent environment, we expect that the magnetic field to be entangled. The higher resolution then means less averaging in the signals from atoms aligned with the magnetic field. The high sensitivity of the upgraded HAWC++ also provides us with the possibility of doing precise quantitative measurement of the spectral polarizations, which can resolve the ambiguity of the 90° degeneracy and enables a 3D topology of the magnetic field, which cannot be obtained from any other present magnetic diagnostics.

5.10 Observational Tests

Here we demonstrate a synthetic observation of polarization of the sodium D lines, which can reveal the magnetic fields of Jupiter and the solar wind that interacts with the comet, via magnetic alignment. The advantage of direct studies of magnetic perturbations by spacecrafts has been explored through many important missions. However, the spacecraft measurements are rather expensive. Are there any other cost-effective ways to study magnetic turbulence in interplanetary medium?

Comets are known to have sodium tails and sodium is an atom that can be aligned by radiation and realigned by solar wind magnetic fields. This opens an opportunity of studying magnetic fields in the solar wind from the ground, by tracing the polarization of the Sodium line. We simulated the degree of polarization and its variations arising from resonant scattering from the Na line in a magnetized comet wake (Yan and Lazarian 2007; Yan 2009). The study has been extended to comet Halley and Jupiter's satellite Io, based on the magnetic field data from Vega1&2 during the encounter with comet Halley in 1986 and the Galileo's mission to Jupiter, respectively (see details in Shangguan and Yan 2012).

Although the abundance of sodium in comets is very low, its high efficiency in scattering sunlight makes it a good tracer (Thomas 1992). As discussed in Yan and Lazarian (2007), the gaseous sodium atoms in the comet's tail acquire angular momentum from the solar radiation, i.e. they are aligned. Resonant scattering from these aligned atoms is therefore polarized. Collision rates in the coma of comets are very low, less than once/day beyond a few 1,000 km from the nucleus, so that fluorescent alignment should be rapidly established in the outflowing sodium from the comet (Harris et al. 1997).

As shown in Fig. 5.10, the geometry of the scattering is well defined, i.e., the scattering angle θ_0 is known. The alignment is modulated by the local magnetic field. The polarization of the sodium emission thus provides unique information on the magnetic field in the interplanetary medium. Depending on its direction, the embedded magnetic field alters the degree of alignment and therefore the polarization of the light scattered from the aligned atoms. Figure 5.10 illustrates the trajectory of a comet along which the magnetic field varies and the polarization of

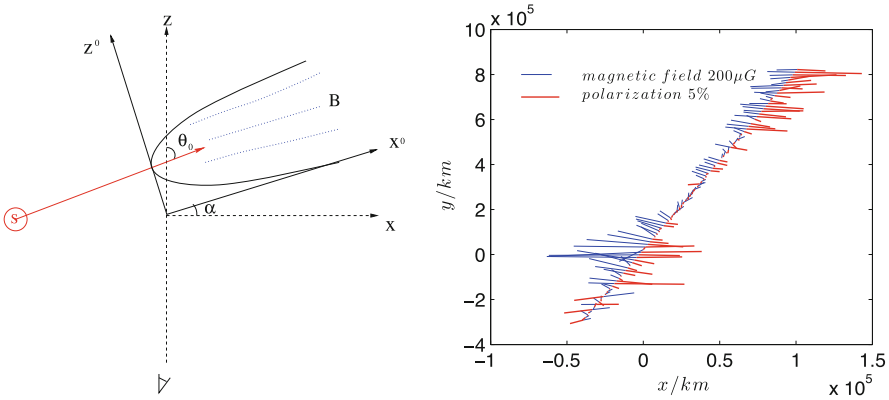

Fig. 5.10 *Left*: Schematics of the resonance scattering of sunlight by the sodium in comet wake. The sodium tail points in the direction opposite to the Sun. The observer on the Earth sees the stream at the angle θ_0. Magnetic field realigns atoms via fast Larmor precession. Thus the polarization traces the interplanetary magnetic fields. *Right*: the magnetic field and polarization along the trajectory of Vega1 encountering the comet Halley (from Shangguan and Yan 2012)

Sodium D2 emission changes accordingly. By comparing observations with them, we can cross-check our model and determine the structure of the magnetic field in the heliosphere with similar observations. One can investigate not only spatial, but also *temporal* variations of the magnetic fields. Since alignment happens at a time scale τ_R, magnetic field variations on this time scale will be reflected. This can allow for a cost-effective way of studying interplanetary magnetic turbulence at different scales.

GSA provides us a unique opportunity to detect the magnetic field that is beyond the reach of space probes. The polarization direction traces directly the orientation of the magnetic field, especially when the scattering angle is small. We can, accurately, acquire complete information about the magnetic field with two or more lines from alignable species. Since the alignment happens on a very short timescale (inverse of photo-excitation rate), instantaneous tomography of the magnetic field can be realized through GSA.

5.11 GSA and Cosmological Studies

5.11.1 Magnetic Field in the Epoch of Reionization?

The issue of the characteristics of magnetic field at the epoch of reionization is a subject of significant controversy. The fact that the levels of the O I ground state can be aligned through anisotropic pumping suggest the possibility of using GSA to diagnose whether magnetic field existed at that early epoch.

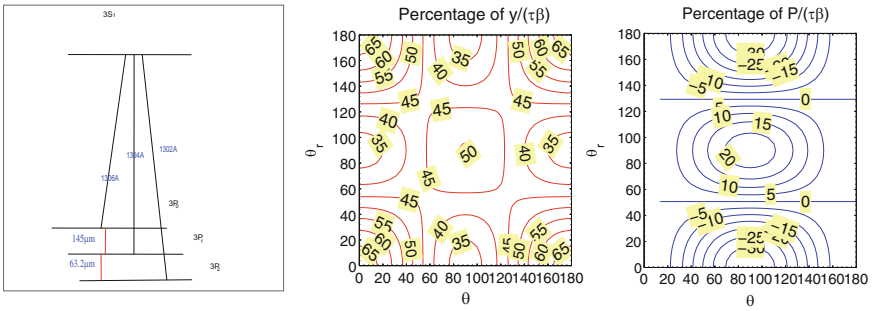

Fig. 5.11 *Left*: The schematics of fluorescence pumping of [O I] line; *middle* and *right*: $y/(\tau\beta)$, $P/(\tau\beta)$ of [OI] line in early universe. θ_r, θ are respectively the angles of the incident radiation and l.o.s. from the magnetic field. From YL08

The degree of polarization in the optically thin case can be obtained in a similar way to above by replacing $\tilde{\eta}_0, \tilde{\epsilon}_0$ by $\tilde{\eta}_1, \tilde{\epsilon}_1$. In the alignment regime, the Stokes parameters, U = 0, and therefore,

$$
\begin{aligned}
P = \frac{Q_\nu}{B_\nu(T_{CMB})} &= \tau \left\{ \frac{\tilde{\epsilon}_1[\exp(T_*/T_{CMB}) - 1]}{\tilde{\eta}_1 \exp(T_*/T_s) - \tilde{\epsilon}_1} - 1 \right\} \\
&\simeq \tau_0[\tilde{\epsilon}_1(1 + y_{iso}/\tau_0) - \frac{\tilde{\eta}_1 - \tilde{\epsilon}_1}{1 - \exp(-T_*/T_s)}] \\
&= \tilde{\epsilon}_1 y_{iso} - \tau_0 \frac{1.5 \sin^2\theta[w_{l0}\sigma_0^2(J_l) - w_{0l}\sigma_0^2(J_l^0)]/\sqrt{2}}{1 - \exp(-T_*/T_s)} \qquad (5.13)
\end{aligned}
$$

In the case of a nonzero magnetic field, the density matrices are determined by θ_r, the angle between the magnetic field and pumping radiation, as well as the parameter β. Similar to y, the degree of polarization is also proportional to β. In Fig. 5.11, we show the dependence of the ratios $y/(\tau\beta)$, $P/(\tau\beta)$ on θ_r and θ. Since U = 0, the line is polarized either parallel ($P > 0$) or perpendicular ($P < 0$) to the magnetic field. The switch between the two cases happen at $\theta_r = \theta_V = 54.7°, 180 - 54.7°$, which is a common feature of polarization from aligned level (see Yan and Lazarian 2006, 2008 for detailed discussions).

5.11.2 *Influence on Abundance Studies*

The GSA not only induces/influences the polarization of spectral lines, but also modulate the line intensity. This can cause substantial error in the estimates of chemical abundances, if the effect is not accounted for. This has been shown in the last section on the pumping of [O I] line in early universe. The same also happens with permitted absorption and emission lines (see Fig. 5.12).

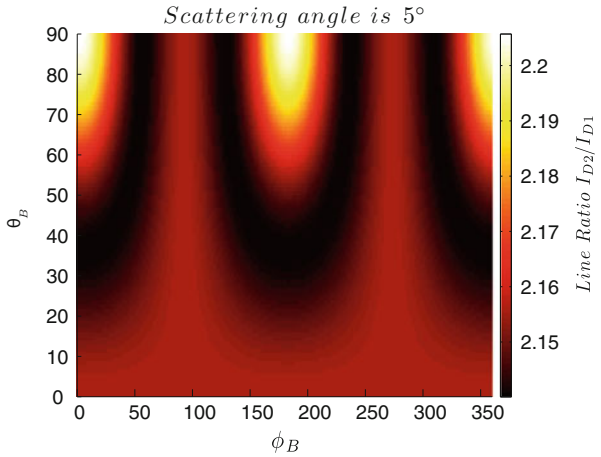

Fig. 5.12 The contour map of line ratio, I_{D2}/I_{D1} as a function of the direction of magnetic field. The scattering angle is also set to be 5°. From Shangguan and Yan (2012)

5.11.3 Metal Detection in Early Universe

For instance, the distortion of the CMB due to the optical pumping calculated, accounting for the anisotropy of the optical/UV radiation field for the optically thin case, differs from the result without the anisotropy included (Yan and Lazarian 2009):

$$\begin{aligned} y = \frac{\Delta I_\nu}{B_\nu(T_{CMB})} &= \tau \left\{ \frac{\tilde{\epsilon}_1[\exp(T_*/T_{CMB}) - 1]}{\tilde{\eta}\exp(T_*/T_s) - \tilde{\eta}_s} - 1 \right\} \\ &= \tau_0 \left[\frac{\tilde{\epsilon}_1[\exp(T_*/T_{CMB}) - 1]}{\exp(T_*/T_s) - 1} - \tilde{\tau} \right] \\ &\simeq \tau_0[\tilde{\epsilon}_1(1 + y_{iso}/\tau_0) - \tilde{\tau}] \\ &= \tilde{\epsilon}_1 y_{iso} + \tau_0 \frac{[w_{l0}\sigma_0^2(J_l) - w_{0l}\sigma_0^2(J_l^0)](1 - 1.5\sin^2\theta)/\sqrt{2}}{1 - \exp(-T_*/T_s)} \end{aligned} \tag{5.14}$$

where y_{iso} is the distortion neglecting the anisotropy of the radiation field and GSA (see Hernández-Monteagudo et al. 2007). Indeed if alignment is not accounted, then

$$y = y_{iso} = \tau_0 \frac{T_*}{T_s}\frac{\Delta T}{T_{cmb}} = \tau_0 \frac{T_{cmb}}{T_s} \exp\left(\frac{T_*}{T_{cmb}}\right) \left[1 - \frac{A(J_l^0)}{\sum_{J_l} A(J_l)}\right] \frac{[J_l^0]\beta B_m I_m}{[J_l](A_m + B_m^s I_m)}, \tag{5.15}$$

where A_m, B_m, B_m^s are the Einstein coefficients for the magnetic dipole transitions within the ground state, and I_m is the corresponding line intensity, $\beta \equiv BI_\nu / B_m I_m$. Both $\tilde{\eta}_s$ and $\tilde{\tau}$ depend on the line of sight and the GSA (Eqs. (5.7), (5.9)), the resulting distortion in radiation is thus determined by the angle θ as well as the UV intensity of the O I line I_ν (or β, see Fig. 5.11). Since both of the two terms on the right hand side of Eq. (5.14) are proportional to β, the resulting distortion y is also proportional to β.

In some sense, this study is made for the case of weak pumping regimes discussed in Yan and Lazarian (2006). But we take into account in addition the absorption and stimulated emission within the ground state.

5.12 Feasibility of GSA Studies

The GSA is a subtle effect that is described by a complex quantum electrodynamics formalism. Therefore it is important to stress that this does not translates into the effect being difficult to measure. Indeed, as we mentioned earlier, the effect was first studied successfully in the laboratory many years ago. The predicted polarization effects, as we shown in the text, can be quite substantial. Moreover, different species show different degrees of alignment (including zero alignment) and this allows separation of the GSA-induced polarization from polarization of instrumental origin.

We have also discussed that effects related to GSA, but in a different regime of magnetic saturation, have been successfully studied in the solar atmosphere.This vividly supports our claim that the GSA effect is not only measurable in laboratory, but also under astrophysical conditions.[10] In fact, the polarization observed by Kuhn et al. (2007) in an circumstellar envelope already indicate the effect of the GSA polarization of absorption lines, as predicted in Yan and Lazarian (2006).

In terms of observational studies, one should remember that it usually takes some time for the technique to get accepted. One may recall a long history of attempts at measuring of the Goldreich-Kylafis effect. However, now the technique is routinely used. We feel that a similar process is takeing place with the practical usage of the GSA effect. We hope that this review can accelerate the observational work towards practical use of GSA.

[10]Incidentally, these studies induced a local revolution in understanding of the solar spectra. We expect even deeper impact of the GSA studies. Indeed, the domain of the applicability of the GSA is really extensive and the consequences of the magnetic field and abundance studies are extremely important.

5.13 Summary

GSA is an important effect, the potential of which for magnetic field studies has not been yet tapped by the astrophysical community. The alignment itself is an effect well studied in the laboratory. The effects arise due to the ability of atoms/ions with fine and hyperfine structure to get aligned in the ground/metastable states. Due to the long life of the atoms in such states the Larmor precession in an external magnetic field imprints the direction of the field onto the polarization of emitting and absorbing species. This provides a unique tool for studies of magnetic fields using polarimetry of UV, optical and radio lines. The range of objects suitable for studies is extremely wide and includes magnetic fields in the early universe, in the interplanetary medium, in the interstellar medium, and in circumstellar regions. Apart from this, the consequences of alignment should be taken into account for the correct determination of the abundances of alignable species.

As astrophysical magnetic fields cover a large range of scales, it is important to have techniques to them at different scales. In this respect atomic realignment fits a unique niche as it reveals small scale structure of the magnetic field. For instance, we have discussed the possibility of studying magnetic fields in the interplanetary medium. This can be done without the conventional, expensive, probes by studying the polarization of spectral lines. In some cases the spreading of small amounts of sodium or other alignable species can produce detailed magnetic field maps of a particular regions of interplanetary space, e.g. the Earth magnetosphere.

Acknowledgements HY acknowledges the support from 985 grant from Peking University and the "Beyond the Horizons" grant from Templeton foundation as well as the visiting professorship at the International Institute of Physics (Brazil). AL's research is supported by the NSF AST 1109295 and the NSF Center for Magnetic Self-Organization (CMSO). He also acknowledges the Humboldt Award and related productive stay at the Universities of Bochum and Cologne.

References

Abel, N.P., Ferland, G.J., O'Dell, C.R., Shaw, G., Troland, T.H.: Astrophys. J. **644**, 344 (2006)
Beck, R.: 25th Texas Symposium on Relativistic Astrophysics (Texas 2010). In: Aharonian, F.A., Hofmann, W., Rieger, F.M. (eds.) American Institute of Physics Conference Series, vol. 1381, pp. 117–136 (2011)
Brossel, J., Kastler, A., Winter, J.: J. Phys. Radium **13**, 668 (1952)
Budker, D., Romalis, M.: Nat. Phys. **3**, 227 (2007)
Carciofi, A.C., Bjorkman, J.E., Bjorkman, K.S.: In: Adamson, A., Aspin, C., Davis, C., Fujiyoshi, T. (eds.) Astronomical Polarimetry: Current Status and Future Directions. Astronomical Society of the Pacific Conference Series, vol. 343, p. 417. Astronomical Society of the Pacific, San Francisco (2005)
Cohen-Tannoudji, C., Dupont-Roc, J., Haroche, S., Laloë, F.: Phys. Rev. Lett. **22**, 758 (1969)
Crutcher, R.M.: Astrophys. Space Sci. **313**, 141 (2008)
Crutcher, R.M., Troland, T.H.: Astrophys. J. **685**, 281 (2008)
Crutcher, R.M., Hakobian, N., Troland, T.H.: Mon. Not. R. Astron. Soc. **402**, L64 (2010)

D'Yakonov, M.I., Perel', V.I.: Sov. J. Exp. Theor. Phys. **21**, 227 (1965)
Esquivel, A., Lazarian, A.: Astrophys. J. **631**, 320 (2005)
Esquivel, A., Lazarian, A.: Astrophys. J. **740**, 117 (2011)
Fano, U.: Rev. Mod. Phys. **29**, 74 (1957)
Field, G.: Proc. IRE **46**, 240 (1958)
Furlanetto, S.R., Oh, S.P., Briggs, F.H.: Phys. Rep. **433**, 181 (2006)
Grandi, S.A.: Astrophys. J. **199**, L43 (1975a)
Grandi, S.A.: Astrophys. J. **196**, 465 (1975b)
Happer, W.: Rev. Mod. Phys. **44**, 169 (1972)
Harris, W.M., Nordsieck, K.H., Scherb, F., Mierkiewicz, E.J.: AAS/division for planetary sciences meeting abstracts. Bull. Am. Astron. Soc. **29**, 1034 (1997)
Hawkins, W.B.: Phys. Rev. **98**, 478 (1955)
Hawkins, W.B., Dicke, R.H.: Phys. Rev. **91**, 1008 (1953)
Hernández-Monteagudo, C., Rubiño-Martín, J.A., Sunyaev, R.A.: Mon. Not. R. Astron. Soc. **380**, 1656 (2007)
Hildebrand, R.H.: In: Lis, D.C., Vaillancourt, J.E., Goldsmith, P.F., Bell, T.A., Scoville, N.Z., Zmuidzinas, J. (eds.) Submillimeter Astrophysics and Technology: A Symposium Honoring Thomas G. Phillips. Astronomical Society of the Pacific Conference Series, vol. 417, p. 257 (2009)
House, L.L.: Publ. Astron. Soc. Aust. **86**, 490 (1974)
Kastler, A.: J. Phys. Radium **11**, 255 (1950)
Kastler, A.: J. Opt. Soc. Am. (1917–1983), **47**, 460 (1957)
Kastler, A.: Nucl. Instrum. Methods **110**, 259 (1973)
Kuhn, J.R., Berdyugina, S.V., Fluri, D.M., Harrington, D.M., Stenflo, J.O.: Astrophys. J. **668**, L63 (2007)
Landi Degl'Innocenti, E.: Solar Phys. **85**, 3 (1983)
Landi Degl'Innocenti, E.: Solar Phys. **91**, 1 (1984)
Landi Degl'Innocenti, E.: Nature **392**, 256 (1998)
Landi Degl'Innocenti, E., Landolfi, M. (eds.) Polarization in Spectral Lines. Astrophysics and Space Science Library, vol. 307. Kluwer Academic Publishers, Dordrecht (2004)
Landolfi, M., Landi Degl'Innocenti, E.: Astron. Astrophys. **167**, 200 (1986)
Lazarian, A.: J. Quant. Spectrosc. Radiative Transf. **106**, 225 (2007)
Lazarian, A., Pogosyan, D.: Astrophys. J. **747**, 5 (2012)
Lazarian, A., Pogosyan, D., Esquivel, A.: In: Taylor, A.R., Landecker, T.L., Willis, A.G. (eds.) Seeing Through the Dust: The Detection of HI and the Exploration of the ISM in Galaxies. Astronomical Society of the Pacific Conference Series, vol. 276, p. 182 (2002)
Lequeux, J.: The Interstellar Medium. Springer, Berlin (2005)
Nordsieck, K.: Astronomical Polarimetry 2008. In: Bastien, P., Manset, N., Clemens, D. P., St-Louis, N (eds). ASP Conference Series, vol. 449, p. 139. San Francisco: Astronomical Society of the Pacific (2012)
Roberge, A., Feldman, P. D., Lecavelier des Etangs, A., Vidal-Madjar, A., Deleuil, M., Bouret, J.-C., Ferlet, R., Moos, H. W.: Astrophys. J. **568**, 343 (2002)
Shangguan, J., Yan, H.: Astrophys. Space Sci. **343,335** (2012)
Sharpee, B., Baldwin, J.A., Williams, R.: Astrophys. J. **615**, 323 (2004)
Stenflo, J.O., Keller, C.U.: Astron. Astrophys. **321**, 927 (1997)
Sterling, N.C., Dinerstein, H.L., Bowers, C.W., Redfield, S.: Astrophys. J. **625**, 368 (2005)
Thomas, N.: Surv. Geophys. **13**, 91 (1992)
Trujillo Bueno, J., Landi Degl'Innocenti, E.: Astrophys. J. **482**, L183 (1997)
Trujillo Bueno, J., Landi Degl'Innocenti, E., Collados, M., Merenda, L., Manso Sainz, R.: Nature **415**, 403 (2002)
Varshalovich, D.A.: Astrofizika **4**, 519 (1968)
Varshalovich, D.A.: Sov. Phys. Uspekhi **13**, 429 (1971)
Varshalovich, D.A., Chorny, G.F.: Icarus **43**, 385 (1980)
Wouthuysen, S.A.: Astron. J. **57**, 31 (1952)

Yan, H.: Mon. Not. R. Astron. Soc. **397**, 1093 (2009)
Yan, H., Lazarian, A.: Astrophys. J. **653**, 1292 (2006)
Yan, H., Lazarian, A.: Astrophys. J. **657**, 618 (2007)
Yan, H., Lazarian, A.: Astrophys. J. **677**, 1401 (2008)
Yan, H., Lazarian, A.: In: Revista Mexicana de Astronomia y Astrofisica Conference Series, vol. 36, pp. 97–105 (2009)
Yan, H., Lazarian, A.: J. Quant. Spectrosc. Radiative Transf. **113**, 1409 (2012)

Part III
MF in Turbulent Media

Chapter 6
Kinetic Turbulence

Gregory G. Howes

Abstract The weak collisionality typical of turbulence in many diffuse astrophysical plasmas invalidates an MHD description of the turbulent dynamics, motivating the development of a more comprehensive theory of kinetic turbulence. In particular, a kinetic approach is essential for the investigation of the physical mechanisms responsible for the dissipation of astrophysical turbulence and the resulting heating of the plasma. This chapter reviews the limitations of MHD turbulence theory and explains how kinetic considerations may be incorporated to obtain a kinetic theory for astrophysical plasma turbulence. Key questions about the nature of kinetic turbulence that drive current research efforts are identified. A comprehensive model of the kinetic turbulent cascade is presented, with a detailed discussion of each component of the model and a review of supporting and conflicting theoretical, numerical, and observational evidence.

6.1 Introduction

The study of turbulence in astrophysical plasmas has almost exclusively employed a magnetohydrodynamic (MHD) description of the turbulent dynamics, treating the magnetized plasma as a single fluid, an approximation valid for large-scale, low-frequency dynamics in the strongly collisional limit. Yet, the plasmas in a wide variety of turbulent astrophysical environments often violate one or more of the conditions required by the MHD approximation, particularly on the small scales at which dissipation mechanisms act to damp the turbulent fluctuations, ultimately leading to heating of the plasma. The study of the turbulent dynamics at small scales and of the physical mechanisms responsible for the dissipation of the turbulence generally requires a kinetic treatment. Thus, it is necessary to leave behind the comfortable surroundings of the theory of MHD turbulence and enter the uncharted territory of the evolving theory of *kinetic turbulence*.

G.G. Howes (✉)
Department of Physics and Astronomy, University of Iowa, Iowa City, IA 52242, USA
e-mail: gregory-howes@uiowa.edu

A. Lazarian et al. (eds.), *Magnetic Fields in Diffuse Media*, Astrophysics and Space Science Library 407, DOI 10.1007/978-3-662-44625-6_6

6.1.1 Quantitative Characterization of Plasma Turbulence

Turbulent systems are typically described theoretically by a spectral decomposition of the broadband spatial fluctuations into a sum of plane wave modes, each characterized by its three dimensional wavevector, phase, and amplitude. An energy spectrum of the turbulent fluctuations therefore provides a useful quantitative description of the turbulent system. In a magnetized plasma, the three-dimensional wavevector space can be reduced to two dimensions by assuming axial symmetry about the direction of the equilibrium magnetic field, requiring only the specification of the turbulent power with respect to the cylindrical components of the wavevector, $k_\perp$ and $k_\parallel$. The nature of the dynamics in the different ranges of the kinetic turbulent cascade can be quantitatively characterized by two properties: (1) the *one-dimensional magnetic energy spectrum* in perpendicular wavenumber, $E_B(k_\perp)$; and (2) the *wavevector anisotropy*, or the distribution of turbulent power in wavevector space. Here $E_B(k_\perp)$ is defined such that the total magnetic energy is given by $E_B = \int dk_\perp E_B(k_\perp)$. For Alfvénic turbulence that is driven isotropically at the outer-scale wavenumber k_0, the conjecture of critical balance implies that the turbulent power fills a region of the cylindrical wavevector space satisfying $k_\parallel \lesssim k_0^{1-q} k_\perp^q$. Specification of the scaling of the boundary of this region, $k_\parallel \propto k_\perp^q$, is sufficient to completely characterize the anisotropic distribution of turbulent power.

6.1.2 Limits of MHD Treatment of Astrophysical Turbulence

The limitations of an MHD treatment of astrophysical turbulence can be illuminated by considering the domain of applicability of MHD turbulence theory within the broader context of plasma turbulence. Beginning with the general theory of the turbulent cascade of kinetic energy in hydrodynamic systems, we consider the modifications required to describe the turbulent energy cascade in the magnetized plasma systems relevant to astrophysical environments.

6.1.2.1 From Fluid to Kinetic Models of the Turbulent Cascade

The limitations of MHD turbulence theory can be illustrated most clearly by a qualitative comparison of the features of nonlinear cascade of energy in hydrodynamic turbulence, MHD turbulence, and kinetic turbulence (see also the chapter by Beresnyak and Lazarian in this volume).

In hydrodynamic systems, turbulent motions are driven at some large scale L, denoting the driving or energy injection scale. Nonlinear interactions serve to transfer the turbulent kinetic energy to motions at ever smaller scales, until reaching a small scale l_ν at which dissipation via viscous damping is sufficient to terminate the turbulent cascade. For typical hydrodynamic systems, a large dynamic range

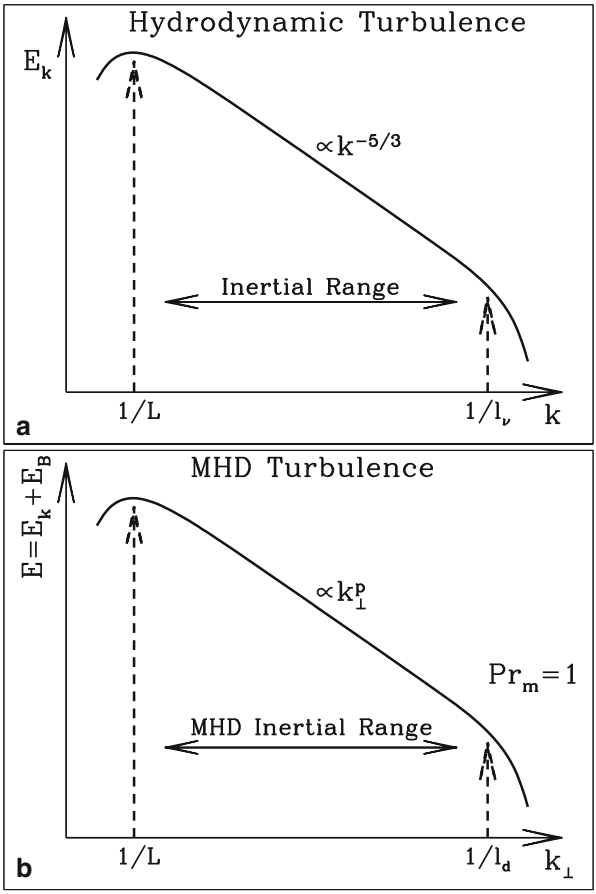

Fig. 6.1 (**a**) Wavenumber spectrum for kinetic energy in hydrodynamic turbulence, from the driving scale, L, through the inertial range, to the viscous dissipation scale, l_ν. (**b**) Perpendicular wavenumber spectrum for total energy $E = E_k + E_B$ in MHD turbulence with $\mathrm{Pr}_m = 1$, from the driving scale, L, through the inertial range, to the viscous and resistive dissipation scale, $l_d = l_\nu = l_\eta$

exists between the driving and dissipation scales, $L/l_\nu \gg 1$. In that case, one may define an *inertial range* of scales l within which the effects of the driving and dissipation are negligible, $L \gg l \gg l_\nu$. Within the inertial range, there exists no particular characteristic length scale, so the dynamics of the turbulence in the inertial range is found to be self-similar, and a simple application of dimensional analysis is sufficient to describe accurately the steady-state hydrodynamic turbulent cascade of energy (Kolmogorov 1991). A qualitative diagram of the kinetic energy wavenumber spectrum for the hydrodynamic turbulence cascade is shown in Fig. 6.1a.

In magnetohydrodynamic systems, the turbulence theory must be modified in three important ways. First, the dynamics of two turbulent fields, the velocity and the magnetic field, must be described, so the cascade of both kinetic and magnetic energy is mediated by nonlinear turbulent interactions. Second, fluctuations of the two turbulent fields are dissipated by distinct mechanisms, viscosity for the velocity and resistivity for the magnetic field. The characteristic length scales of viscous dissipation l_ν and resistive dissipation l_η need not be equal, and their ratio is characterized by the magnetic Prandtl number $\mathrm{Pr}_m \equiv l_\nu / l_\eta$. Third, the magnetic field in the plasma establishes a preferred direction, leading to distinct dynamics in the direction parallel to the magnetic field and in the plane perpendicular to the magnetic field. In addition, the magnetic tension provided by the magnetic field supports a type of linear wave, the Alfvén wave, which has no counterpart in the hydrodynamic case, transforming the nature of the turbulent motions from hydrodynamic vortices to magnetohydrodynamic waves. This third complication is the most significant change from hydrodynamic turbulence, and leads to the inherent anisotropy of MHD turbulence, where turbulent energy is transferred more rapidly to small perpendicular scales $l_\perp$ than to small parallel scales $l_\parallel$. Nonetheless, despite these significant differences, the overall qualitative picture of the turbulent energy cascade in MHD turbulence bears a striking resemblance to the hydrodynamic case.

Consider, in particular, the simplified case of MHD turbulence in a $\mathrm{Pr}_m = 1$ plasma, so there exists a single dissipation scale $l_d = l_\nu = l_\eta$. One may define an MHD inertial range, $L \gg l_\perp \gg l_d$, directly analogous to the hydrodynamic case. Due to the anisotropy of the turbulent energy transfer, the turbulent dynamics are optimally described with respect to the perpendicular scale $l_\perp$. The evolution of the parallel scale is determined in terms of the perpendicular scale by the condition of *critical balance* (Goldreich and Sridhar 1995), so that $l_\parallel \propto l_\perp^q$. The exponent q describes the *scale-dependent anisotropy* of the MHD turbulent cascade, where $q = 2/3$ in the Goldreich–Sridhar model (Goldreich and Sridhar 1995), and $q = 1/2$ in the Boldyrev model (Boldyrev 2006). Similar to the hydrodynamic case, in the MHD inertial range, there exists no characteristic length scale, so the dynamics of MHD turbulence is found to be self-similar as well. Therefore, for the $\mathrm{Pr}_m = 1$ case, the MHD turbulence theory appears nearly the same as the hydrodynamic turbulence theory, with a few minor changes: (1) the turbulent cascade is described by the perpendicular scale $l_\perp$ rather than an isotropic scale l; (2) there exists a scale-dependent anisotropy due to the parallel scaling $l_\parallel \propto l_\perp^q$; and (3) the exponent p in the self-similar power law solution for the one-dimensional energy spectrum $E \propto k_\perp^p$ may differ quantitatively from the hydrodynamic solution. But the general qualitative picture—a self-similar MHD turbulent cascade of energy from the driving scale L, through an inertial range, to the dissipative scale l_d—remains essentially the same as the hydrodynamic cascade, as is evident by comparing the diagram of the wavenumber spectrum for total energy $E = E_k + E_B$ in the MHD turbulent cascade in Fig. 6.1b to the hydrodynamic case in Fig. 6.1a.

In kinetic plasma systems, this simple qualitative model of the turbulent cascade changes dramatically due to the existence of three characteristic length scales and new physics associated with each of these scales. The three characteristic length

scales that come into play in typical conditions for turbulent astrophysical plasmas are the ion mean free path λ_i, the ion Larmor radius ρ_i, and the electron Larmor radius ρ_e. The MHD approximation requires the following four conditions:

1. Nonrelativistic conditions, $v_{ts}/c \ll 1$
2. Strongly collisional conditions, $\lambda_i / l \ll 1$
3. Large-scale motions, $\rho_i / l \ll 1$
4. Low-frequency dynamics, $\omega / \Omega_i \ll 1$

Here $v_{ts} = \sqrt{2T_s/m_s}$ is the thermal velocity[1] of species s, ω is the typical frequency of the turbulent fluctuations, and Ω_i is the ion cyclotron frequency. It is clear that, in the MHD approximation, all three of the characteristic scales above are assumed to be infinitesimal compared to the typical scale of the turbulent motions, l. However, in astrophysical plasmas of interest, the turbulent dynamics frequently violate conditions (2) and (3) above.[2] Therefore, it is important to examine more closely how these characteristic scales enter into the dynamics of the turbulent cascade in astrophysical plasmas, leading to a violation of the MHD approximation and requiring the transition to a kinetic description of the turbulent dynamics.

6.1.2.2 Violation of the MHD Approximation

Spacecraft measurements of turbulence in the solar wind provide invaluable guidance for the construction of a theoretical model that describes the energy spectrum of the kinetic turbulent cascade. Recent measurements of solar wind turbulence with unprecedented temporal resolution enable us to probe the turbulent dynamics down to the scale of the electron Larmor radius (Sahraoui et al. 2009; Kiyani et al. 2009; Alexandrova et al. 2009; Chen et al. 2010; Sahraoui et al. 2010; Alexandrova et al. 2012). Therefore, we now have a fairly complete observational picture of the kinetic turbulent cascade in the solar wind over a dynamic range of 10^6 from the large energy injection scale at $L \sim 10^6$ km down to the scale of the electron Larmor radius at $\rho_e \sim 1$ km. From the large body of turbulence measurements in the solar wind (Sahraoui et al. 2009; Kiyani et al. 2009; Alexandrova et al. 2009; Chen et al. 2010; Sahraoui et al. 2010; Alexandrova et al. 2012), we can construct a general diagram for the perpendicular wavenumber spectrum of the magnetic energy in turbulent astrophysical plasmas, shown in Fig. 6.2a. It is important to emphasize here that, although the general form of the magnetic energy spectrum is well established from observations, the interpretation of this spectrum in terms of the characteristic plasma scales requires significant input from plasma kinetic theory, and many of the features of Fig. 6.2a remain topics of active research.

[1] Here T_s is expressed in units of energy, absorbing the Boltzmann constant.

[2] Note that condition (4) is not generally independent of condition (3). For MHD Alfvén waves, the condition $\omega \ll \Omega_i$ may be alternatively written $\rho_i / l_\parallel \ll \sqrt{\beta_i}$, where the ion plasma beta is $\beta_i = 8\pi n_i T_i / B^2$. Thus, if $\sqrt{\beta_i} \sim \mathcal{O}(1)$, then condition (4) is roughly equivalent to condition (3).

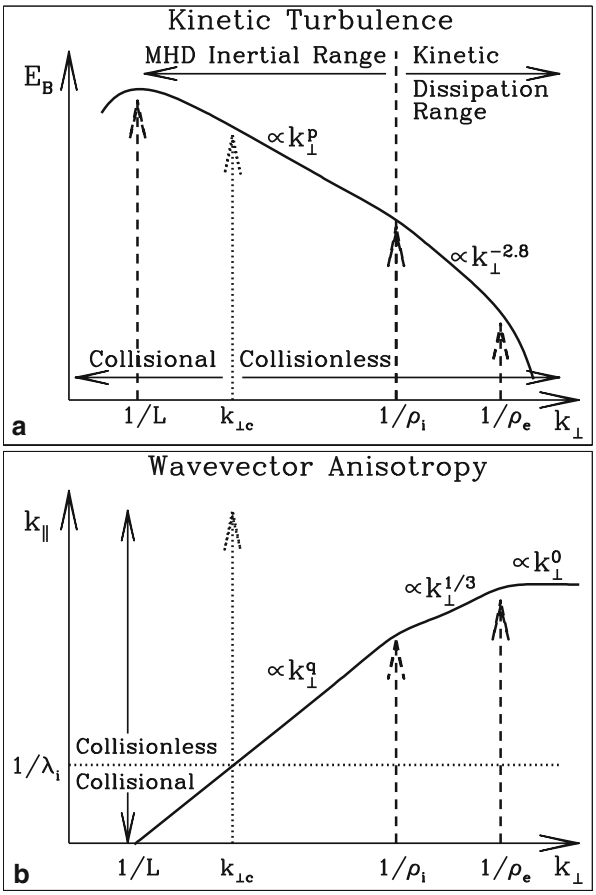

Fig. 6.2 (**a**) Perpendicular wavenumber spectrum for magnetic energy in kinetic turbulence, from the driving scale, L, through the MHD inertial range to the ion Larmor radius ρ_i, where the turbulent cascade enters the kinetic dissipation range, and down to the electron Larmor radius ρ_e. The transition from collisional to collisionless dynamics occurs at $k_{\perp c}$. (**b**) Wavevector anisotropy in kinetic turbulence, scaling as $k_\perp^q$ in the MHD inertial range, $k_\perp^{1/3}$ in the kinetic dissipation range, and $k_\perp^0$ (no parallel cascade) beyond electron scales. The transition from collisional to collisionless dynamics occurs at $k_\parallel \rho_i \sim 1$

In Fig. 6.2a, the plasma turbulence is driven at some large scale $L \gg \rho_i$. It is generally assumed, in the absence of arguments to the contrary, that the turbulence is driven isotropically with respect to the magnetic field, so that the perpendicular and parallel components of the driving wavevector $\mathbf{k}_0$ are equal, $k_{\parallel 0} \sim k_{\perp 0} \sim k_0 \sim 1/L$. If the plasma conditions at the driving scale satisfy the MHD approximation, then the large scale end of the turbulent cascade is described by MHD turbulence theory. Although the turbulent fluctuations in an MHD plasma may, in general, be composed of a mixture fast, Alfvén, and slow waves, observational and numerical

evidence suggests that Alfvén waves dominate the turbulent dynamics in typical astrophysical plasmas (this point is discussed further below). For the Alfvénic turbulent cascade, the one-dimensional magnetic energy spectrum as a function of perpendicular wavenumber $k_\perp$ scales as $E_B \propto k_\perp^p$, where the spectral index is $p = -5/3$ in the Goldreich–Sridhar model (Goldreich and Sridhar 1995) or $p = -3/2$ in the Boldyrev model (Boldyrev 2006). The wavevector anisotropy of the anisotropic Alfvénic cascade scales as $k_\parallel \propto k_\perp^q$, where the values for q are given in Sect. 6.1.2.1; this anisotropic cascade of energy through wavevector space is depicted in Fig. 6.2b.

As the MHD turbulent cascade transfers energy to smaller scales (higher wavenumber), it eventually reaches the one of the characteristic length scales λ_i, ρ_i, or ρ_e, at which point the MHD approximation is violated. Here we focus on exploring how these length scales enter into the model for kinetic turbulence and what effect they have on the turbulent dynamics. For typical conditions in astrophysical plasmas, the characteristic length scales are ordered by $\lambda_i > \rho_i > \rho_e$, so the ion mean free path λ_i is usually reached first.

The ion mean free path λ_i characterizes the collisionality for the motion of plasma particles parallel to the magnetic field,[3] so it must be compared to the parallel wavenumber $k_\parallel$. For $k_\parallel \lambda_i \ll 1$, the plasma is strongly collisional; for $k_\parallel \lambda_i \gg 1$, the plasma is weakly collisional. Fluid approximations, such as hydrodynamics or MHD, break down for plasma conditions $k_\parallel \lambda_i \gtrsim 1$, so kinetic theory is formally required to describe the plasma dynamics in moderately to weakly collisional regimes.

As depicted in Fig. 6.2b, at some point in the MHD inertial range, the parallel scales may reach the scale of the ion mean free path, $k_\parallel \lambda_i \sim 1$, marking the transition from collisional dynamics that is well described by MHD at $k_\parallel \lambda_i \ll 1$ to collisionless dynamics that requires a kinetic description at $k_\parallel \lambda_i \gg 1$. The condition of critical balance determines the relation between the parallel and perpendicular wavenumbers of strong MHD turbulence (Goldreich and Sridhar 1995), so we may define the perpendicular wavenumber $k_{\perp c}$ that corresponds to the transition of collisionality at $k_\parallel \lambda_i \sim 1$. This transition in the perpendicular wavenumber spectrum typically occurs at perpendicular scales larger than the ion Larmor radius, $k_{\perp c} \rho_i < 1$, as shown in Fig. 6.2a. For perpendicular wavenumbers $k_\perp \ll k_{\perp c}$, the strongly collisional dynamics is well described by MHD, and for $k_\perp \gg k_{\perp c}$ the weakly collisional dynamics require a kinetic description, as depicted in Fig. 6.2a.

For the weakly collisional range $k_\perp \gg k_{\perp c}$, it has been shown rigorously from kinetic theory that the Alfvénic turbulent fluctuations remain essentially fluid in nature (Schekochihin et al. 2009). The Alfvénic turbulent cascade continues to be

[3]The Lorentz force limits the perpendicular motion of plasma particles to the particle Larmor radius. Since typical astrophysical conditions yield $\rho_i \ll \lambda_i$, the plasma is essentially always collisionless in the perpendicular direction. Note, however, that because plasma particles cannot move beyond the Larmor radius in the perpendicular direction from the magnetic field, this embodies the large-scale *perpendicular* motions, $l_\perp \gg \rho_i$, with a fluid-like behavior, even under weakly collisional conditions.

accurately described by the equations of reduced MHD (Strauss 1976) and remains undamped down to the perpendicular scale of the ion Larmor radius, $k_\perp \rho_i \sim 1$ (Schekochihin et al. 2009). Therefore, although the MHD approximation is formally violated at scales $k_\perp \gtrsim k_{\perp c}$, the MHD description of the anisotropic Alfvénic cascade remains applicable, regardless of whether the dynamics is collisional or collisionless, for all scales larger than the ion Larmor radius, $k_\perp \rho_i \ll 1$. Therefore, we denote the range of scales $L \gg l_\perp \gg \rho_i$ in the *kinetic* turbulent cascade as the *MHD inertial range*.

MHD Inertial Range: The range of perpendicular scales from the large scale of energy injection to the scale of the ion Larmor radius, $L \gg l_\perp \gg \rho_i$, including both collisional and collisionless regimes.

On the other hand, compressible turbulent fluctuations associated with the MHD fast and slow waves in the MHD inertial range require a kinetic description at all moderately to weakly collisional scales, $k_\parallel \lambda_i \gtrsim 1$ or $k_\perp \gtrsim k_{\perp c}$. These modes are damped both collisionally by ion viscosity at $k_\parallel \lambda_i \sim 1$ (Braginskii 1965) and collisionlessly by ion Landau damping at $k_\parallel \lambda_i \gg 1$ (Barnes 1966). Therefore, it is expected that the damped compressible modes will play at most a subdominant role relative to the undamped Alfvénic fluctuations in turbulent astrophysical plasmas. In the weakly collisional solar wind, for example, compressible fluctuations generally contribute less than 10 % of the turbulent magnetic energy (Tu and Marsch 1995; Bruno and Carbone 2005) in the MHD inertial range. Therefore, we turn our attention back to the dynamics of the dominant Alfvénic turbulent fluctuations.

When the Alfvénic turbulent cascade reaches the perpendicular scale of the ion Larmor radius, $k_\perp \rho_i \sim 1$, the MHD description of the Alfvénic fluctuations breaks down completely for two reasons. First, finite Larmor radius effects lead to a decoupling of the ions from the turbulent electromagnetic fluctuations at perpendicular wavenumbers $k_\perp \rho_i \gtrsim 1$. The result is that the non-dispersive Alfvén wave in the limit $k_\perp \rho_i \ll 1$ undergoes transitions to the dispersive kinetic Alfvén wave in the limit $k_\perp \rho_i \gg 1$. The dispersive nature of the Alfvénic fluctuations accelerates the rate of the turbulent nonlinear energy transfer, leading to a steepening of the magnetic energy spectrum, with a break in the spectrum at the $k_\perp \rho_i \sim 1$, as shown in Fig. 6.2a. Second, collisionless damping of the electromagnetic fluctuations occurs due to the Landau resonance with the ions, with a peak in the ion damping rate around $k_\perp \rho_i \sim 1$. In addition, electron Landau damping can also contribute significantly for all scales $k_\perp \rho_i \gtrsim 1$. The combined effect of the ion and electron collisionless damping can lead to a further steepening of the spectrum for scales $k_\perp \rho_i \gtrsim 1$ (Howes et al. 2011a,b). Finally, the cascade reaches the perpendicular scale of the electron Larmor radius, $k_\perp \rho_e \sim 1$, where collisionless damping becomes sufficiently strong to terminate the turbulent cascade, leading to an exponential drop off of the magnetic energy spectrum (Terry et al. 2012;

Alexandrova et al. 2012; Tenbarge et al. 2013b). MHD turbulence theory cannot describe the dispersive wave behavior or the dissipation that occurs via kinetic mechanisms at scales $k_\perp \rho_i \gtrsim 1$. Therefore, we denote the range of scales $l_\perp \lesssim \rho_i$ in the kinetic turbulent cascade as the *kinetic dissipation range*.

Kinetic Dissipation Range: The range of perpendicular scales at or below the scale of the ion Larmor radius, $l_\perp \lesssim \rho_i$, where wave dispersion and collisionless dissipation play important roles.

6.1.3 Importance of Kinetic Turbulence

Of fundamental importance in the study of astrophysical turbulence is to determine the pathway by which the energy of turbulent motions is ultimately converted to plasma heat. Astrophysical turbulence is generally driven by violent events or instabilities at large scales, but fluctuations are dissipated strongly only at scales of order or smaller than the ion Larmor radius. A kinetic turbulent cascade arises to transfer energy via nonlinear couplings from the large energy injection scales, through the MHD inertial range, down to the scale of the ion Larmor radius. The turbulent fluctuations begin to be damped when the cascade reaches the scale of the ion Larmor radius, marking the entry into the kinetic dissipation range. Since the dynamics within the kinetic dissipation range is typically weakly collisional, the dissipation of the turbulent electromagnetic fluctuations must be accomplished via collisionless mechanisms governed by plasma kinetic theory. The energy thus removed from the turbulent fluctuations ultimately leads to thermal heating of the protons, electrons, and minority ions in the plasma. The observational signature of astrophysical objects depends strongly on the nature of the plasma heating, so to interpret observational data requires a detailed characterization of the small-scale, kinetic plasma turbulence.

For example, as matter in an accretion disk spirals slowly into a black hole, it converts a tremendous amount of gravitational potential energy into heat. Several physical mechanisms contribute to this process. First, the magnetorotational instability (Balbus and Hawley 1991, 1998) taps free energy from the differential rotation of the accretion disk to drive turbulence on the scale height of the disk, $L \sim H$. The turbulence effectively transports angular momentum outward in the disk, enabling accretion disk plasma to fall down the gravitational potential and mediating the conversion of gravitational potential energy into kinetic and magnetic energy of the MHD turbulent fluctuations. The high temperatures characteristic of the plasma in a black hole accretion disk lead to a collisional mean free path $\lambda_i \sim H$, so the turbulent dynamics is weakly collisional. A kinetic turbulent cascade is responsible for the transfer of turbulent energy through the MHD inertial range down to the

scale of the ion Larmor radius, where the turbulent electromagnetic fluctuations are damped via collisionless mechanisms in the kinetic dissipation range. An entropy cascade ultimately mediates the final conversion of this turbulent free energy into plasma heat. Therefore, the radiation that is emitted from the hot, magnetized plasma is a strong function of the black hole properties and of the character of the small-scale plasma fluctuations, where the plasma heating occurs. To interpret observational data from the Chandra X-ray Observatory, for example, one must unravel the details of the kinetic turbulent cascade.

Developing a mature model of the kinetic turbulent cascade is critical to understanding the turbulent dynamics of the kinetic dissipation range, the physical mechanisms responsible for the damping of the turbulent fluctuations, and the resulting heating of the plasma species. The ultimate goal is to develop a predictive capability to estimate accurately the heating of the protons, electrons, and minority ions in the plasma based on the plasma parameters and the characteristics of the turbulent driving.

6.2 Key Questions About Kinetic Turbulence

The unprecedented availability of high temporal resolution solar wind turbulence measurements from current spacecraft missions has enabled the observational characterization of the kinetic turbulent cascade from the large scales of energy injection down to the scale of the electron Larmor radius. This has spurred the heliospheric physics community to engage actively the topic of the turbulence in the dissipation range of the solar wind, and has engendered considerable controversy about a number of significant issues related to the fundamental character of kinetic turbulence. In particular, the nature of both the turbulent fluctuations in this regime and the physical mechanisms responsible for their dissipation remains highly contested within the scientific community. Four key questions relevant to the study of the dissipation range of solar wind turbulence are

1. What are the limits of validity of using a fluid description of the turbulence in the dissipation range, and which aspects of the turbulence require a kinetic description?
2. Are the linear plasma wave properties relevant to the turbulent fluctuations of the dissipation range?
3. What are the characteristic dynamics of the dissipation range fluctuations?
4. What physical mechanisms are responsible for the dissipation of the turbulent fluctuations and the ultimate conversion of their energy to plasma heat?

Although these significant questions about the nature of kinetic turbulence remain controversial, a promising model of the kinetic turbulent cascade (Howes 2008; Howes et al. 2008a; Schekochihin et al. 2009; Howes et al. 2011a) has been developed that appears to be broadly consistent with most observations of solar wind turbulence. This model involves an anisotropic cascade of Alfvénic fluctuations

beginning as a cascade of Alfvén waves in the MHD inertial range and transitioning to a cascade of kinetic Alfvén waves subject to collisionless damping in the kinetic dissipation range. Yet the cascade of energy from large to small scales described by this kinetic turbulence model may not explain all of the fluctuations observed in the solar wind. For example, fluctuations can be generated by the action of kinetic temperature anisotropy instabilities (Bale et al. 2009) that are driven by the spherical expansion of the solar wind, an effect beyond the scope of this model. Plausible arguments exist that suggest some of these additional effects may coexist peacefully with the kinetic turbulence, proceeding without being significantly affected by or significantly affecting the kinetic turbulent cascade. The remainder of this chapter aims to describe in detail the model of the kinetic turbulent cascade and to discuss the supporting and conflicting theoretical, observational, and numerical evidence.

6.3 A Model of the Kinetic Turbulent Cascade

A basic theoretical model of the kinetic turbulent cascade in astrophysical plasmas has been developed with the aim to describe completely the flow of energy from the large driving scales of the turbulence to its ultimate fate as thermal heat of the plasma (Howes 2008; Howes et al. 2008a; Schekochihin et al. 2009; Howes et al. 2011a). We present here a brief outline of this model, before delving into a detailed description of each component of the model and a discussion of supporting and conflicting evidence.

Violent events or instabilities first drive turbulent fluctuations of the magnetic field and plasma at some large scale, generating a mixture of finite amplitude fast, Alfvén, and slow waves. If the fluctuations are driven isotropically with velocities approximately equal to the Alfvén velocity in the plasma, a cascade of strong compressible MHD turbulence will mediate the transfer of the turbulent kinetic and magnetic energy to smaller scales. The fast waves cascade to smaller scales isotropically, while the critically balanced Alfvén wave cascade produces an anisotropic distribution of Alfvén and slow wave fluctuations in this collisional part of the MHD inertial range. The parallel scales of the turbulent fluctuations eventually reach the ion collisional mean free path, marking the transition from strongly to weakly collisional dynamics. The compressible fast and slow wave fluctuations suffer collisional damping at the moderately collisional scale of the transition, and collisionless damping at the smaller, weakly collisional scales. The incompressible Alfvénic fluctuations remain undamped through this transition, so the damped fast and slow waves are expected to contribute subdominantly to the turbulence compared to the Alfvén waves. The Alfvén waves continue their cascade undamped through the collisionless remainder of the MHD inertial range until their perpendicular scales reach the ion Larmor radius, marking the transition to the kinetic dissipation range.

The anisotropic Alfvénic fluctuations at this transition transfer energy into a cascade of kinetic Alfvén waves at perpendicular scales below the ion Larmor radius. In addition, collisionless wave-particle interactions via the Landau resonance with the ions lead to a peak in the ion kinetic damping at the ion Larmor radius, dissipating some fraction of the turbulent electromagnetic fluctuation energy. The undamped remainder of the turbulent energy continues as a cascade of kinetic Alfvén waves to smaller perpendicular scales, forming the kinetic dissipation range at all scales below the ion Larmor radius. Throughout this range, electron Landau damping may cause significant collisionless damping of the turbulent fluctuations, with the strength of the damping increasing as the perpendicular scale decreases. At the perpendicular scale of the electron Larmor radius, the electron Landau damping becomes sufficiently strong to terminate the cascade, leading to an exponential decay of the turbulent energy spectrum at the electron scale.

Thermodynamically, the transfer of free energy from the kinetic and magnetic energy of the turbulent electromagnetic fluctuations to free energy in velocity space structure of the particle distribution functions is not equivalent to irreversible thermal heating of the plasma. Irreversible plasma heating, and the associated increase of entropy, ultimately requires collisions. This is accomplished in a weakly collisional plasma by the ion and electron entropy cascades, dual cascades in physical and velocity space that drive fluctuations to small enough velocity-space scales that arbitrarily weak collisions are sufficient to achieve irreversibility. This final process marks the thermodynamic end of the kinetic turbulent cascade, completing the conversion of large-scale turbulent fluctuation energy to thermal heat of the plasma.

This model of the kinetic turbulent cascade implies certain answers to the questions posed in Sect. 6.2, so we elucidate those answers here:

1. A fluid description is applicable for all turbulent fluctuations at scales larger than the collisional transition, and for the Alfvénic dynamics at all scales larger than the ion Larmor radius. The dynamics and kinetic damping of the compressible fluctuations at all moderately to weakly collisional scales, and of the Alfvénic fluctuations at the scales of the ion Larmor radius and below, require a kinetic description.
2. The properties of the turbulent fluctuations at scales sufficiently below the driving scale are related to the characteristics of the linear kinetic plasma waves.
3. The dissipation range fluctuations are kinetic Alfvén waves.
4. Ion and electron Landau damping are the physical mechanisms by which the turbulent electromagnetic fluctuations are damped, and the ion and electron entropy cascades mediate the irreversible transition of free energy in the particle distribution functions to thermal heat.

In the following sections, we describe in detail all of the facets of this model of the kinetic turbulent cascade, providing supporting theoretical, observational, and numerical evidence and reviewing findings in conflict with this model. A general diagram of the magnetic energy spectrum and the distribution of turbulent power in wavevector space is shown in Fig. 6.3.

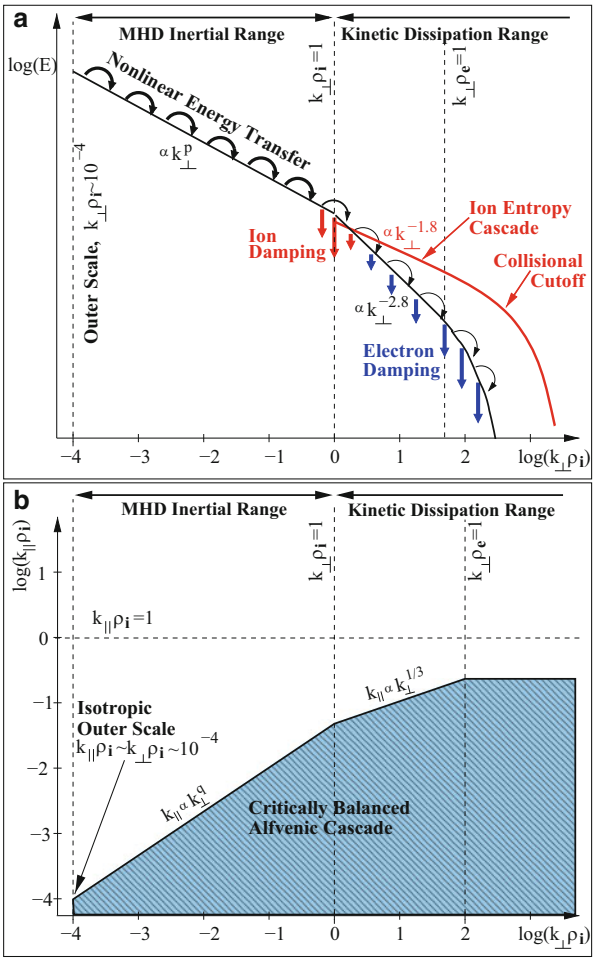

Fig. 6.3 (**a**) Diagram of the magnetic energy spectrum and ion entropy cascade in kinetic turbulence. (**b**) Anisotropic distribution of power in $(k_\perp, k_\parallel)$ wavevector space in kinetic turbulence

6.3.1 MHD Inertial Range: From Driving Scales to the Collisional Transition

The turbulence in astrophysical environments is typically driven by some external mechanism, often a violent event or large-scale instability, that generates plasma motions at some large scale, $L \gg \rho_i$. This energy injection scale, often denoted the outer scale of the turbulence, is an important characteristic of any turbulent astrophysical system, and is conveniently parameterized by the wavenumber, $k_0 \sim 1/L$. For the investigation of kinetic turbulence, a convenient dimensionless measure of the driving scale is the *driving wavenumber*, $k_0\rho_i$, where $k_0\rho_i \ll 1$ indicates that the

turbulence is driven at large scale compared to the ion Larmor radius. It is generally assumed, in the absence of arguments to the contrary, that the turbulence is driven isotropically with respect to the magnetic field, so that the perpendicular and parallel components of the driving wavevector are equal, $k_{\parallel 0} \sim k_{\perp 0} \sim k_0$.

If the MHD approximation is satisfied for the turbulent dynamics of the plasma at the driving scale, then the large scale section of the MHD inertial range is described by MHD turbulence theory (Sridhar and Goldreich 1994; Goldreich and Sridhar 1995; Galtier et al. 2000; Lithwick and Goldreich 2001; Boldyrev 2006) (see also the chapter by Beresnyak and Lazarian in this volume). If the amplitude of the driven turbulent velocities are comparable to the Alfvén velocity in the magnetized plasma, then a cascade of strong MHD turbulence arises to transfer energy nonlinearly to higher wavenumbers; for smaller amplitudes, weak MHD turbulence will be generated (Sridhar and Goldreich 1994; Goldreich and Sridhar 1995). Since most turbulent astrophysical environments are believed to be driven strongly, and weak turbulence eventually transits to strong turbulence as the cascade progresses (Sridhar and Goldreich 1994), we focus here on the case of strong MHD turbulence. In general, the finite-amplitude turbulent fluctuations may be considered to be a mixture of the three propagating MHD wave modes, the incompressible Alfvén waves and compressible fast and slow waves, as well as the non-propagating entropy mode. The nature of the turbulent cascades of these various characteristic fluctuations have been elucidated by numerical simulations of MHD turbulence: the fast waves cascade isotropically in wavevector space, while the Alfvén waves, slow waves and entropy mode fluctuations cascade anisotropically according to the condition of critical balance (Maron and Goldreich 2001; Cho and Lazarian 2003).

The fast wave cascade produces an isotropic one-dimensional magnetic energy spectrum $E_B(k) \propto k^{-3/2}$, as observed in simulations (Cho and Lazarian 2003). Two competing models exist that describe the nature of strong MHD turbulence for Alfvén waves, the Goldreich–Sridhar model (Goldreich and Sridhar 1995) and the Boldyrev model (Boldyrev 2006). The magnetic energy spectrum of the Alfvénic turbulent cascade is predicted to scale as $E_B \propto k_\perp^p$, where the spectral index is $p = -5/3$ in the Goldreich–Sridhar model (Goldreich and Sridhar 1995) and $p = -3/2$ in the Boldyrev model (Boldyrev 2006). The anisotropy of the Alfvénic cascade, for isotropic driving at wavenumber k_0, is given by $k_\parallel = k_0^{1-q} k_\perp^q$, where $q = 2/3$ in the Goldreich–Sridhar model (Goldreich and Sridhar 1995), and $q = 1/2$ in the Boldyrev model (Boldyrev 2006). The slow waves and entropy modes are passively cascaded by the Alfvén waves, and therefore adopt the same spectrum and anisotropic distribution of power as the Alfvén waves (Maron and Goldreich 2001; Lithwick and Goldreich 2001). For anisotropic turbulent fluctuations with $k_\perp \gg k_\parallel$, the frequencies of the fast wave fluctuations, which scale as $\omega \propto k$, are generally much higher than the frequencies of the Alfvén and slow wave fluctuations, which scale as $\omega \propto k_\parallel$, so the dynamics of the fast wave cascade are expected to decouple from the dynamics of the Alfvén and slow wave cascades (Lithwick and Goldreich 2001; Howes et al. 2012).

The turbulent cascade transfers energy nonlinearly to higher wavenumber fluctuations, as dictated by the MHD turbulence theory, until the parallel wavenumber

reaches the transition from collisional to collisionless dynamics, $k_\parallel \lambda_i \sim 1$. The perpendicular wavenumber, $k_{\perp c}$, that corresponds to $k_\parallel \lambda_i \sim 1$, differs for the anisotropic Alfvén wave cascade and the isotropic fast wave cascade. For the anisotropic Alfvénic cascade, the perpendicular wavenumber of this transition is given by $k_{\perp c} \sim k_0 (k_0 \lambda_i)^{-1/q}$, whereas, for the isotropic fast wave cascade, it is given by $k_{\perp c} \sim k_0 (k_0 \lambda_i)^{-1}$, or more simply $k_{\perp c} \lambda_i \sim 1$. Since $q < 1$, this means that the fast wave cascade reaches the collisional transition first, at a smaller wavenumber than the Alfvén wave cascade.

For many astrophysical plasmas, the transition for both fast and Alfvén waves occurs within the MHD inertial range, $k_{\perp c} \rho_i < 1$. The compressible fast waves, slow waves, and entropy modes undergo strong collisional damping by ion viscosity (Braginskii 1965) in the moderately collisional conditions at $k_\perp \sim k_{\perp c}$. Any energy in the compressible turbulent fluctuations that passes through this transition is expected to be transferred nonlinearly to the kinetic counterparts of the MHD fast and slow waves (Klein et al. 2012) in the weakly collisional conditions at wavenumbers $k_\perp \gg k_{\perp c}$ (Schekochihin et al. 2009). The Alfvén waves are incompressible, involving no motions parallel to the magnetic field, so they are essentially unaffected by the transition in collisionality, and the Alfvén wave cascade continues unabated to higher wavenumbers, $k_\perp \gg k_{\perp c}$.

6.3.2 *MHD Inertial Range: From the Collisional Transition to the Ion Larmor Radius*

Critical balance predicts a scale-dependent wavevector anisotropy given by $k_\perp / k_\parallel = (k_\perp / k_0)^{1-q}$, where $q < 1$ for either the Goldreich–Sridhar or Boldyrev models. Therefore, at perpendicular wavenumbers within the MHD inertial range sufficiently higher than the driving wavenumber, $k_\perp \gg k_0$, the Alfvénic fluctuations become anisotropic in the sense that $k_\perp \gg k_\parallel$. In the limit of the MHD inertial range $k_\perp \rho_i \ll 1$, the kinetic dynamics of these anisotropic Alfvénic fluctuations is described rigorously by the equations of reduced MHD (Strauss 1976), and the Alfvén wave cascade remains undamped down to the perpendicular scale of the ion Larmor radius, $k_\perp \rho_i \sim 1$ (Schekochihin et al. 2009). It has also been shown that the slow wave and Alfvén wave cascades do not exchange energy in the MHD inertial range (Schekochihin et al. 2009), and the fast waves likewise are not expected to exchange energy with the Alfvén waves due to the mismatch in frequency, as discussed in Sect. 6.3.1. Therefore, the dynamics of the Alfvénic cascade throughout the MHD inertial range is correctly described by the MHD turbulence theory, even at the weakly collisional scales, $k_\perp \gg k_{\perp c}$.

The magnetic energy spectrum in the solar wind seems to bear this out. Spacecraft measurements in the super-Alfvénic solar wind are generally interpreted by assuming the Taylor hypothesis (Taylor 1938), that frequency of measured temporal fluctuations is directly related to the wavenumber of spatial variations that

are swept past the spacecraft. At the frequencies $f \lesssim 0.4\,\mathrm{Hz}$, corresponding to spatial scales larger than the ion Larmor radius, the magnetic energy spectrum in the solar wind has a spectral index of approximately $-5/3$ (Goldstein et al. 1995), apparently consistent with the prediction of the Goldreich–Sridhar theory for strong MHD turbulence. It is worth noting, however, that the velocity spectrum was found to have a spectral index closer to $-3/2$ (Podesta et al. 2007), in conflict with the Goldreich–Sridhar model. Recent work on the evolution of the residual energy, $E_r = E_k - E_B$, in MHD turbulence, however, suggests that these spectral indices may indeed be consistent with the Boldyrev theory, and that the difference in the spectral indices of the kinetic and magnetic energy spectra is an inherent property of the MHD turbulent cascade (Boldyrev et al. 2011, 2012).

The cascade of compressible turbulent fluctuations that passes through the collisional transition will suffer moderate to strong collisionless damping by the Landau resonance with the ions (Barnes 1966) at all higher wavenumbers, $k_\perp \gg k_{\perp c}$. The damping of the compressible fluctuations in the moderate to weakly collisional regimes at $k_\perp \gtrsim k_{\perp c}$ leads to the theoretical prediction that compressible fluctuations will play a subdominant role relative to the undamped Alfvénic fluctuations in turbulent astrophysical plasmas. Studies of interstellar scintillation (Armstrong et al. 1981, 1995) show evidence for a power-law spectrum of density fluctuations over 12 orders of magnitude in the interstellar medium, suggesting that compressible fluctuations are not entirely damped. But it is not possible from remote astrophysical observations to deduce the relative contributions of compressible and incompressible components of the turbulence.

In situ spacecraft measurements of turbulent fluctuations in the solar wind, however, allow a direct determination. The entire turbulent cascade in the solar wind, including the driving scales, is weakly collisional, $\lambda_i/L \gg 1$, so spacecraft measurements constrain the role of compressible fluctuations in collisionless conditions, $k_\perp \gg k_{\perp c}$. Measurements show that the turbulent fluctuations in the MHD inertial range appear to be dominantly incompressible (Tu and Marsch 1995; Bruno and Carbone 2005), where the incompressible motions have been shown to be Alfvénic in nature (Belcher and Davis 1971). The compressible fluctuations generally contribute less than 10 % of the turbulent magnetic energy (Tu and Marsch 1995; Bruno and Carbone 2005). These compressible fluctuations have typically been interpreted as a possible mixture of fast MHD waves and pressure balanced structures (PBSs) (Tu and Marsch 1995; Bruno and Carbone 2005), where the latter are equivalent to non-propagating slow mode fluctuations with $k_\parallel = 0$ (Tu and Marsch 1994; Kellogg and Horbury 2005). Note, however, that a recent study using a novel method of synthetic spacecraft data (Klein et al. 2012) suggests that these compressible fluctuations are not associated with the kinetic counterpart of the fast MHD wave, but rather consist of an anisotropic distribution of kinetic slow wave fluctuations. Clearly, more investigation of the kinetic physics of compressible turbulent fluctuations in astrophysical environments, including their damping via collisional and collisionless mechanisms and the resulting plasma heating, is needed. Nonetheless, since only a small fraction of the turbulent energy appears to be associated with the compressible fluctuations, we focus our attention henceforth

on the dominant Alfvénic turbulent fluctuations, as they reach the perpendicular scale of the ion Larmor radius, $k_\perp \rho_i \sim 1$.

6.3.3 Transition at the Ion Larmor Radius

Spacecraft measurements of turbulence in the solar wind demonstrate that the $-5/3$ scaling of the magnetic energy spectrum in the MHD inertial range breaks at a frequency around $f \sim 0.4\,\mathrm{Hz}$, leading to a steeper spectrum at higher frequencies in the kinetic dissipation range. Numerous observational studies have attempted to correlate the position of the break with a characteristic plasma time or length scale, such as the ion cyclotron frequency, the ion Larmor radius, or the ion inertial length (Goldstein et al. 1994; Leamon et al. 1998, 1999, 2000; Smith et al. 2001; Perri et al. 2010; Smith et al. 2012; Bourouaine et al. 2012), but contradictory results have been found. Establishing a convincing correlation has likely been elusive because three competing effects may contribute to the dynamics at this transition between the MHD inertial range and kinetic dissipation range: (1) the transition from non-dispersive to dispersive linear wave physics as the ions decouple from the turbulent electromagnetic fluctuations; (2) a peak in the ion kinetic damping; and (3) the possible role of kinetic instabilities, such as temperature anisotropy instabilities (Bale et al. 2009), in generating electromagnetic fluctuations at this scale.

Based on theoretical considerations of the kinetic plasma physics, the kinetic turbulence model presented here predicts that the transition between the relatively well understood MHD inertial range and the significantly more controversial kinetic dissipation range occurs at the perpendicular scale of the ion Larmor radius, $k_\perp \rho_i \sim 1$ (Howes 2008; Howes et al. 2008a; Schekochihin et al. 2009; Howes et al. 2011a). The boundary conditions (in wavevector space) for the nonlinear transfer of energy into the kinetic dissipation range are given by the nature of the turbulent fluctuations at the end of the MHD inertial range. At this transition at $k_\perp \rho_i \sim 1$, the wavevector anisotropy of Alfvénic turbulent fluctuations is given by $k_\perp / k_\parallel \sim (k_0 \rho_i)^{q-1}$, so for a sufficiently large MHD inertial range, $k_0 \rho_i \ll 1$, this implies $k_\perp \gg k_\parallel$ since $q < 1$ (Goldreich and Sridhar 1995; Boldyrev 2006). This significant wavevector anisotropy at the transition is supported by multi-spacecraft measurements of turbulence in the near-earth Solar wind (Sahraoui et al. 2010). It follows that, beyond this transition, the characteristic wavevector of the fluctuations satisfies $k_\perp \rho_i \gtrsim 1$ and $k_\parallel \rho_i \ll 1$; the Alfvénic solution of linear kinetic theory with such a wavevector is the kinetic Alfvén wave (Hasegawa and Sato 1989; Stix 1992). Therefore, the Alfvén waves of the MHD inertial range are predicted to transfer their energy, via nonlinear interactions at the transition $k_\perp \rho_i \sim 1$, to kinetic Alfvén waves (Leamon et al. 1998; Gruzinov 1998; Leamon et al. 1999; Quataert and Gruzinov 1999; Howes et al. 2008a; Schekochihin et al. 2009). Nonlinear gyrokinetic simulations of this transition appear to support this hypothesis (Howes et al. 2008b), reproducing the qualitative changes in the electric and magnetic field

energy spectra measured in the solar wind at the scale of the spectral break (Bale et al. 2005).

Another important effect that occurs at the transition at $k_\perp \rho_i \sim 1$ is a peak in the collisionless damping rate of the electromagnetic fluctuations due to the Landau resonance with the ions (Leamon et al. 1998, 1999, 2000; Howes et al. 2008a, 2011a; Howes 2008; Schekochihin et al. 2009). This ion kinetic damping becomes increasingly strong as the ion plasma beta increases, and is generally non-negligible for plasmas with beta of order unity or larger, $\beta_i \gtrsim 1$, leading to a significant fraction of the dissipated turbulent energy heating the ions (Howes 2010, 2011), in approximate agreement with empirical estimates of the plasma heating in the solar wind (Cranmer et al. 2009; Breech et al. 2009). Some measurements of the magnetic energy spectrum in the dissipation range of the solar wind show a significant steepening to a slope of approximately -4 at the ion scales, flattening to -2.8 spectrum further into the dissipation range (Sahraoui et al. 2010), evidence suggesting significant ion kinetic damping.

In a steady-state kinetic turbulent cascade, the turbulent energy reaching the transition at $k_\perp \rho_i \sim 1$ that is not damped at that scale will carry on, launching a turbulent cascade of kinetic Alfvén waves in the kinetic dissipation range at $k_\perp \rho_i \gtrsim 1$. Although the Alfvén and slow wave cascades do not exchange energy in the MHD inertial range, they may exchange energy at this transition (Schekochihin et al. 2009), so it is possible that the kinetic Alfvén wave cascade can gain energy that is transferred nonlinearly from compressible fluctuations in the MHD inertial range.

6.3.4 *Kinetic Dissipation Range: Between the Ion and Electron Larmor Radius*

Although direct spacecraft measurements of the kinetic dissipation range of turbulence in the near-Earth solar wind have been possible for more than a decade, the nature of the turbulent fluctuations in this regime remains a controversial topic. Characterizing these fluctuations is one of the key goals in heliospheric physics today, especially because the relevant physical dissipation mechanisms that ultimately lead to heating of the plasma depend strongly on the nature of the turbulent fluctuations themselves.

Many early investigations of the dissipation range in solar wind turbulence implicitly assumed that the turbulent fluctuations in the dissipation range are related to the linear wave modes in the plasma. Two main hypotheses have been proposed, that the turbulence is composed of either kinetic Alfvén waves (Leamon et al. 1998; Gruzinov 1998; Leamon et al. 1999; Quataert and Gruzinov 1999; Howes et al. 2008a; Schekochihin et al. 2009) or whistler waves (Stawicki et al. 2001; Gary et al. 2010; Narita and Gary 2010). Although these two possibilities generally remain the leading candidates, several other possibilities have been suggested: ion Bernstein waves (Sahraoui et al. 2012), ion cyclotron waves (Jian et al. 2009), non-propagating

pressure balanced structures (PBSs), or inherently nonlinear structures, particularly highly intermittent coherent structures and current sheets (Servidio et al. 2011).

Direct spacecraft measurements of turbulence in the solar wind at the frequencies $f \gtrsim 1\,\mathrm{Hz}$, corresponding to the kinetic dissipation range, provide important constraints on the nature of the turbulent fluctuations. A number of recent studies employing high temporal resolution spacecraft measurements have found a nearly power-law scaling of the magnetic energy spectrum between the ion and electron scales with a spectral index of approximately -2.8 (Sahraoui et al. 2009; Kiyani et al. 2009; Alexandrova et al. 2009; Chen et al. 2010; Sahraoui et al. 2010). These observations of the turbulence over the dissipation range scales raise two important questions that any model for kinetic turbulence must answer: (1) What causes the magnetic energy spectrum to steepen in the dissipation range; and (2) Does significant dissipation of the turbulent fluctuations occur between the ion and electron scales?

In the model of the kinetic turbulent cascade, the boundary conditions in wavevector space determined by the anisotropic Alfvénic cascade through the MHD inertial range suggest that the turbulent energy is transferred nonlinearly to a cascade of kinetic Alfvén waves in the kinetic dissipation range, as discussed in Sect. 6.3.3. Here we describe the properties of the kinetic Alfvén wave cascade at perpendicular scales below the ion Larmor radius, $k_\perp \rho_i \gtrsim 1$.

Although MHD Alfvén waves are non-dispersive, kinetic Alfvén waves become dispersive due to the averaging of the ion response over the finite ion Larmor radius, a physical effect that increasingly decouples the ions from the electromagnetic fluctuations with wavevectors satisfying $k_\perp \rho_i \gtrsim 1$ (Hollweg 1999; Schekochihin et al. 2009). A useful formula combining the linear frequency in the Alfvén and kinetic Alfvén wave regimes (Howes et al. 2006; Schekochihin et al. 2009) is given by

$$\omega = k_\parallel v_A \sqrt{1 + \frac{(k_\perp \rho_i)^2}{\beta_i + 2/(1 + T_e/T_i)}} \tag{6.1}$$

In addition, the kinetic Alfvén wave is significantly compressible, generating a non-zero parallel magnetic field fluctuation, $\delta B_\parallel$, particularly in the limit of low to moderate plasma beta, $\beta_i \lesssim 1$ (Hollweg 1999; Tenbarge et al. 2012b).

The model for kinetic turbulence predicts the quantitative scaling of the magnetic energy spectrum and the wavevector anisotropy for the kinetic Alfvén wave cascade. The Kolmogorov hypothesis—that the energy transfer rate is constant due to local (in wavenumber space) nonlinear interactions—can be used to predict the magnetic energy spectrum for the kinetic Alfvén wave cascade in the absence of significant dissipation. For $k_\perp \rho_i \gg 1$, the linear wave frequency increases due to dispersion, yielding a scaling $\omega \propto k_\parallel k_\perp$. This leads to more rapid nonlinear energy transfer, steepening the magnetic energy spectrum to a predicted scaling $E_B \propto k_\perp^{-7/3}$ when dissipation is neglected (Biskmap et al. 1999; Cho and Lazarian 2004; Krishan and Mahajan 2004; Shaikh and Zank 2005; Galtier 2006; Howes et al. 2008a;

Schekochihin et al. 2009). Extending the concept of critical balance—that the linear wave frequency and nonlinear energy transfer frequency remain in balance—to the kinetic Alfvén wave regime leads to a predicted wavevector anisotropy given by $k_\parallel \propto k_\perp^{1/3}$ (Cho and Lazarian 2004; Howes et al. 2008a; Schekochihin et al. 2009).

In addition to the effects of wave dispersion, collisionless damping via wave-particle interactions can also play an important role in kinetic turbulence for all scales $k_\perp \rho_i \gtrsim 1$. In addition to the peak in ion Landau damping at $k_\perp \rho_i \sim 1$ discussed in Sect. 6.3.3, electron Landau damping may also play a significant role for all scales $k_\perp \rho_i \gtrsim 1$, becoming increasingly strong as the perpendicular wavenumber increases (Howes et al. 2008a). Although early models of the turbulent energy cascade in the kinetic dissipation range suggested that such strong collisionless Landau damping would lead to an exponential cutoff of the spectrum before reaching the perpendicular scale of the electron Larmor radius, $k_\perp \rho_e \sim 1$ (Howes et al. 2008a; Podesta et al. 2010), subsequent solar wind observations called this prediction into question (Sahraoui et al. 2009; Kiyani et al. 2009; Alexandrova et al. 2009; Chen et al. 2010; Sahraoui et al. 2010) and recent kinetic numerical simulations have demonstrated that this idea is incorrect (Howes et al. 2011b).

In addition to collisionless damping via the Landau resonance, if the kinetic Alfvén wave frequency reaches the ion cyclotron frequency, $\omega \to \Omega_i$, collisionless damping may occur via the cyclotron resonance with the ions. However, the very large MHD inertial range typical of astrophysical plasma turbulence leads to highly anisotropic fluctuations at small scales, $k_\parallel \ll k_\perp$, so the kinetic Alfvén wave frequency typically remains very small compared to the ion cyclotron frequency, $\omega \ll \Omega_i$. Therefore, ion cyclotron damping is not predicted to play a strong role in the dissipation of astrophysical turbulence (Howes et al. 2008a), with a few exceptions, such as the inner heliosphere (Howes 2011).

There is significant evidence accumulating in support of a kinetic Alfvén wave cascade at the perpendicular scales between the electron and ion Larmor radius, but there also remains observational evidence that appears to be unexplained by this model. The scaling predictions for the kinetic Alfvén wave cascade in the absence of dissipation have been corroborated by simulations using electron MHD, a fluid limit which describes the dynamics of kinetic Alfvén waves in the limit $k_\parallel \ll k_\perp$, but does not resolve the physics of collisionless dissipation. Specifically, these simulations reproduce the predicted magnetic energy scaling, $E_B \propto k_\perp^{-7/3}$ (Biskmap et al. 1999; Cho and Lazarian 2004, 2009; Shaikh and Zank 2009), and wavevector anisotropy, $k_\parallel \propto k_\perp^{1/3}$ (Cho and Lazarian 2004, 2009). The magnetic energy spectrum from these fluid simulations, however, is not consistent with the observed spectral index of approximately -2.8 (Sahraoui et al. 2009, 2010; Kiyani et al. 2009; Alexandrova et al. 2009; Chen et al. 2010).

It has been recently suggested that the combined effects of collisionless dissipation and nonlocal energy transfer can lead to a further steepening of the magnetic energy spectrum beyond $k_\perp^{-7/3}$ for scales $k_\perp \rho_i \gtrsim 1$ (Howes et al. 2011a). For a hydrogenic plasma of protons and electrons, the dynamic range between the ion and electron Larmor radius for unity temperature ratio is $\rho_i/\rho_e \simeq 43$, so there is little

room for an asymptotic range of perpendicular scales satisfying the requirements $1/\rho_i \ll k_\perp \ll 1/\rho_e$. Therefore, it should come as no surprise that a self-similar spectrum with a spectral index of $-7/3$ is not observed—throughout the range of perpendicular scales between the ion and electron Larmor radius, the transition at $k_\perp \rho_i \sim 1$ and strong kinetic dissipation at $k_\perp \rho_e \sim 1$ may significantly affect the turbulent dynamics.

Nonlinear gyrokinetic simulations of turbulence in the kinetic dissipation range seem to bear this out. A simulation over the entire range of scales from the ion to the electron Larmor radius, which resolves the physics of collisionless ion and electron damping, produces a nearly power-law magnetic energy spectrum with a spectral index of -2.8, in remarkable quantitative agreement with the solar wind measurements (Howes et al. 2011b). Additional gyrokinetic simulations support the predicted scaling of the wavevector anisotropy, $k_\parallel \propto k_\perp^{1/3}$ (Tenbarge et al. 2013b; Tenbarge and Howes 2012c). Direct spacecraft measurements of dissipation range turbulence in the solar wind have yielded other lines of evidence in support of or in conflict with the model of a kinetic Alfvén wave cascade. A k-filtering analysis of multi-spacecraft data from the Cluster mission establishes that the plasma-frame fluctuation frequencies are consistent with linear dispersion relation of the kinetic Alfvén wave and inconsistent with that of the whistler wave (Sahraoui et al. 2010). A study combining measurements of the ratio of electric to magnetic field fluctuation amplitudes and of the magnetic compressibility have shown that the small-scale fluctuations agree well with predictions for kinetic Alfvén waves and are inconsistent with that for whistler waves (Salem et al. 2012). An examination of the compressibility of turbulent fluctuations in the weakly collisional plasma in the MHD inertial range finds evidence of negligible energy in the fast wave mode, suggesting that all large-scale turbulent energy is transferred, via the anisotropic Alfvénic cascade, to kinetic Alfvén waves, with little energy coupling to whistler waves (Klein et al. 2012). Investigations of the magnetic helicity of turbulent fluctuations as a function of the angle of the wavevector with respect to the local magnetic field direction finds a broad region of positive helicity at oblique angles (He et al. 2011; Podesta and Gary 2011), as expected for kinetic Alfvén waves (Howes and Quataert 2010), but a small region corresponding to nearly parallel wavevectors that is consistent with either ion cyclotron waves or whistler waves (He et al. 2011; Podesta and Gary 2011).

The presence of either ion cyclotron or whistler waves with nearly parallel wavevectors is not explained by the model for kinetic Alfvén wave turbulence, but these fluctuations may be driven by the action of kinetic temperature anisotropy instabilities in the spherically expanding solar wind (Bale et al. 2009). These instabilities typically generate relatively isotropic fluctuations (with respect to the local mean magnetic field direction), having wavevector components $k_\perp \rho_i \sim k_\parallel \rho_i \sim 1$. Since the anisotropic Alfvénic cascade produces fluctuations with $k_\parallel \ll k_\perp$, and since Alfvénic frequencies in Eq. (6.1) scale linearly with the parallel component, $\omega \propto k_\parallel$, these anisotropy-driven fluctuations are expected to have a much higher frequency and to occupy a different regime of wavevector space than turbulent

fluctuations of the turbulent cascade. Therefore, it is reasonable to expect that any kinetic-instability-driven fluctuations may persist without significantly affecting, or being significantly affected by, the turbulent fluctuations of the anisotropic Alfvénic cascade.

In conclusion, although the nature of the kinetic turbulence at the perpendicular scales between the electron and ion Larmor radius has not been established conclusively, there appears to significant evidence for an anisotropic cascade of kinetic Alfvén waves in the kinetic dissipation range. Collisionless dissipation via the Landau resonance with the electrons appears to be play a non-negligible role in steepening the magnetic energy spectrum beyond the dissipationless prediction. But this damping is not strong enough to halt the cascade, so the kinetic turbulence continues down to the perpendicular scale of the electron Larmor radius, at which point strong kinetic dissipation can effectively terminate the turbulent cascade.

6.3.5 *Kinetic Dissipation Range: Termination at Electron Larmor Radius*

Ultimately, the kinetic turbulent cascade reaches the perpendicular scale of the electron Larmor radius, $k_\perp \rho_e \sim 1$. At this scale, the linear collisionless damping rate due to electron Landau damping reaches a value $\gamma/\omega \sim 1$, sufficiently strong that the turbulent magnetic energy cascade is terminated. A simplified analytical treatment of the turbulent cascade undergoing this dissipation suggests the spectrum will develop an exponential fall-off $E_B \propto k_\perp^{-2.8} \exp(-k_\perp \rho_e)$ setting in at the perpendicular scale of the electron Larmor radius, $k_\perp \rho_e \sim 1$ (Terry et al. 2012). As the amplitudes of the turbulent fluctuations are diminished by damping, the strong kinetic Alfvén wave turbulence eventually drops below critical balance and becomes weak dissipating kinetic Alfvén wave turbulence (Howes et al. 2011a). It has been conjectured that the transition back to weak turbulence leads to an inhibition of the parallel cascade, so the parallel number of the fluctuations remains constant (Howes et al. 2011a), as shown in Fig. 6.2b.

A recent study of a sample of 100 solar wind magnetic energy spectra at the electron scales shows that all of these spectra may be fit by an empirical form $E_B \propto k_\perp^\alpha \exp(-k_\perp \rho_e)$, where $-2.5 \geq \alpha \geq -2.8$ (Alexandrova et al. 2012). A nonlinear gyrokinetic simulation of the turbulence over the range $0.12 \leq k_\perp \rho_e \leq 2.5$ yields an energy spectrum demonstrating an exponential fall-off that is quantitatively fit by $E_B \propto k_\perp^{-2.8} \exp(-k_\perp \rho_e)$, further supporting the model of the kinetic turbulent cascade (Tenbarge et al. 2013b). A refined model of the turbulent cascade (Howes et al. 2011a)—incorporating the weakening of the nonlinear turbulent energy transfer due to dissipation, the effect of nonlocal energy transfer, and the linear collisionless damping via the Landau resonance—fits the shape of the spectrum well. This provides compelling evidence that collisionless damping is the dominant mechanism for the dissipation of the kinetic turbulent cascade, marking the end of the kinetic dissipation range (Tenbarge et al. 2013b).

A number of recent works have suggested instead that dissipation in current sheets is the dominant dissipation mechanism for plasma turbulence, based on fluid simulations using MHD (Dmitruk et al. 2004; Servidio et al. 2009, 2010, 2011) and Hall MHD (Dmitruk and Matthaeus 2006), hybrid simulations with kinetic ions and fluid electrons (Parashar et al. 2009, 2010; Markovskii and Vasquez 2011; Servidio et al. 2012), and observational studies of large-scale discontinuities in the solar wind (Osman et al. 2011a,b). However, all the numerical work upon which this conclusion has been based employ a fluid description of the electrons which does not resolve the dominant collisionless dissipation mechanism of Landau damping. In a collisionless plasma, current sheets supporting small-scale reconnection with a guiding magnetic field are expected to form at the perpendicular scale of the electron Larmor radius, $k_\perp \rho_e \sim 1$ (Birn and Priest 2006). A recent gyrokinetic simulation over the range of electron scales $0.12 \leq k_\perp \rho_e \leq 2.5$, which resolves both collisionless electron Landau damping and the formation of current sheets at $k_\perp \rho_e \sim 1$, finds dissipation via current sheets to be sub-dominant compared to linear collisionless damping (Tenbarge and Howes 2013a).

These results establish fairly secure observational and numerical grounds that the electromagnetic fluctuations of the kinetic turbulent cascade are dissipated at the perpendicular scale of the electron Larmor radius, $k_\perp \rho_e \sim 1$. Further work is ongoing to identify the dominant physical mechanisms for the dissipation of these turbulent electromagnetic fluctuations. Although this dissipation terminates the kinetic dissipation range of electromagnetic fluctuations at electron scales, there remains the final matter of identifying the physical mechanism mediating the conversion of this turbulent fluctuation energy irreversibly to thermodynamic heat in a weakly collisional astrophysical plasma.

6.3.6 *Irreversible Heating Via the Ion and Electron Entropy Cascades*

At the perpendicular scales of the ion and electron Larmor radius, collisionless wave-particle interactions via the Landau resonance damp the turbulent electromagnetic fluctuations. In the absence of collisions, this process conserves a generalized energy, generating nonthermal structure in velocity space of the corresponding plasma particle distribution functions (Howes 2008; Schekochihin et al. 2009; Plunk et al. 2010). Boltzmann's H-theorem dictates that, in a kinetic plasma, collisions are required to increase the entropy and therefore achieve irreversible thermodynamic heating (Howes et al. 2006). In the weakly collisional plasmas of astrophysical environments, an *entropy cascade*—a nonlinear phase mixing process (Dorland and Hammett 1993) that drives a dual cascade in physical and velocity space—mediates the transfer, at sub-Larmor radius scales, of the nonthermal free energy in the particle distribution functions to sufficiently small scales in velocity space that arbitrarily weak collisions can manifest irreversibility, increasing the entropy

and thermodynamically heating the plasma (Schekochihin et al. 2009; Plunk et al. 2010). This inherently kinetic physical mechanism represents the final element of the kinetic turbulent cascade, governing the final transition of the turbulent energy to its ultimate fate as plasma heat.

The ion entropy cascade in two-dimensional plasma systems (in the plane perpendicular to the local mean magnetic field) has been thoroughly examined theoretically (Schekochihin et al. 2009; Plunk et al. 2010) and verified in gyrokinetic numerical simulations (Tatsuno et al. 2009; Plunk and Tatsuno 2011). In the inherently three-dimensional system of Alfvénic plasma turbulence (Howes et al. 2011b), the effects of the ion entropy cascade in generating structure in the perpendicular component of velocity space (Howes 2008) and in manifesting ion heating at physical scales well below the peak in the collisionless ion damping (Howes et al. 2011b) have been identified numerically. Yet, a thorough analysis of the ion and electron entropy cascades in kinetic turbulence remains to be undertaken.

Conclusion

Turbulence is found ubiquitously throughout the universe, playing a governing role in the conversion of the energy of large-scale motions to astrophysical plasma heat. Extending our understanding of astrophysical turbulence from the limited theory of MHD turbulence to the more comprehensive theory of kinetic turbulence opens up the possibility of ultimately achieving a predictive capability to determine the plasma heating due to the dissipation of turbulence. This chapter has outlined a theoretical model of the kinetic turbulent cascade describing the flow of energy from the large driving scales, through the MHD inertial range, to the transition at the ion Larmor radius, and into the kinetic dissipation range, where the energy is ultimately converted to plasma heat. Although significant progress has already been made, much research remains to be done to refine the kinetic turbulence model and test its predictions using numerical simulations and observational data.

Since kinetic turbulence includes a number of the physical processes that are inherently kinetic—such as collisionless wave-particle interactions and the entropy cascade—kinetic numerical simulations will play an essential role in testing the predictions of this model. The higher dimensionality of kinetic systems—in general, requiring three dimensions in physical space and three dimensions in velocity space—demands a huge investment of computational resources to perform numerical simulations. It is tempting to reduce the dimensionality in physical space to two-dimensions to lower the computational costs, but doing so fundamentally limits the applicability of the results to turbulent astrophysical plasmas. The reason is because the anisotropic Alfvénic turbulence dominating the kinetic turbulent cascade is inherently three-dimensional in physical space: the dominant nonlinearity

(continued)

responsible for the turbulent cascade requires both dimensions perpendicular to the magnetic field, and Alfvénic fluctuations require variation in the parallel dimension (Howes et al. 2011b). Therefore, kinetic simulation results can only be directly compared to astrophysical systems if physical space is modeled in three dimensions.

Observational tests of the kinetic turbulence model should exploit intuition from kinetic plasma theory to unravel the dependence of the turbulent properties on the plasma parameters. The suitably normalized MHD linear dispersion relation depends only on two dimensionless parameters, $\hat{\omega}_{\rm MHD} = \omega/(kv_A) = \hat{\omega}_{\rm MHD}(\beta, \theta)$: the plasma beta β, and the angle between the wavevector and the magnetic field θ (Klein et al. 2012). In contrast, the linear physics of Vlasov–Maxwell kinetic theory depends on five dimensionless parameters, $\tilde{\omega}_{\rm VM} = \omega/\Omega_i = \tilde{\omega}_{\rm VM}(k_\parallel \rho_i, k_\perp \rho_i, \beta_i, T_i/T_e, v_{ti}/c)$: the normalized parallel wavenumber $k_\parallel \rho_i$, the normalized perpendicular wavenumber $k_\perp \rho_i$, the ion plasma beta β_i, the ion-to-electron temperature ratio T_i/T_e, and the ratio of the ion thermal velocity to the speed of light v_{ti}/c (Stix 1992; Howes et al. 2006).[4] The dynamical behavior of the kinetic plasma—for example, the frequencies, collisionless damping rates, and eigenfunctions of the fluctuations—varies as these dimensionless parameters are changed. Therefore, since the kinetic plasma physics depends on these parameters, observational investigations of kinetic turbulence should strive to analyze measurements in terms of the ion plasma beta β_i, the ion-to-electron temperature ratio T_i/T_e, and length scales normalized to a characteristic plasma kinetic length scale, such as the ion Larmor radius or ion inertial length.

Finally, we conclude this chapter on kinetic turbulence with a schematic diagram that depicts the salient features of the kinetic turbulent cascade, as shown in Fig. 6.3 for the case of turbulence in the near-Earth solar wind (the relevant panel is noted in parentheses in the description below). The turbulence is driven isotropically at a large scale, corresponding to a normalized wavenumber $k_0 \rho_i \sim 10^{-4}$ (a,b). Nonlinear interactions serve to transfer the energy from this low driving wavenumber to higher wavenumber through the MHD inertial range, generating a magnetic energy spectrum scaling as $E_B \propto k_\perp^p$, where $p = -5/3$ or $-3/2$ (a). This cascade is anisotropic in wavevector space, such that turbulent fluctuations fill the shaded region below $k_\parallel \propto k_\perp^q$, where $q = 2/3$ or $1/2$ (b). The Alfvénic turbulence transitions from the MHD inertial range to the kinetic dissipation range at a perpendicular

(continued)

[4] In the limit that the turbulent astrophysical fluctuations satisfy the gyrokinetic approximation, $k_\parallel \ll k_\perp$ and $\omega \ll \Omega_i$ (Frieman and Chen 1982; Howes et al. 2006; Schekochihin et al. 2009), the linear physics depends on only three dimensionless parameters, $\overline{\omega}_{\rm GK} = \omega/(k_\parallel v_A) = \overline{\omega}_{\rm GK}(k_\perp \rho_i, \beta_i, T_i/T_e)$ (Howes et al. 2006).

wavenumber $k_\perp \rho_i \sim 1$, a scale at which collisionless ion Landau damping peaks (a). The energy transferred via wave-particle interactions to the ion distribution function feeds the ion entropy cascade at wavenumbers $k_\perp \rho_i \gtrsim 1$, a dual cascade in physical and velocity space that mediates the transfer of nonthermal structure to sufficiently small scales in velocity space that weak collisions can thermalize the energy (a). The remaining turbulent energy that is not collisionlessly damped at $k_\perp \rho_i \sim 1$ is transferred nonlinearly to a kinetic Alfvén wave cascade in the kinetic dissipation range, $k_\perp \rho_i \gtrsim 1$, leading to a magnetic energy spectrum $E_B \propto k_\perp^{-2.8}$ (a) and a wavevector anisotropy $k_\parallel \propto k_\perp^{1/3}$ (b). In addition, electron Landau damping becomes stronger as the wavenumber increases over the entire range $k_\perp \rho_i \gtrsim 1$ (a). Finally, electron Landau damping becomes sufficiently strong to terminate the kinetic turbulent cascade, leading to an exponential fall-off of the magnetic energy spectrum at $k_\perp \rho_e \sim 1$ (a), inhibiting the transfer of energy to higher parallel wavenumber (b), and possibly launching an electron entropy cascade (not shown).

Acknowledgements I would like to thank Steve Cowley, Bill Dorland, and Eliot Quataert for their invaluable guidance, steering my career toward the study of turbulence in kinetic astrophysical plasmas. Alex Schekochihin, Tomo Tatsuno, Ryusuke Numata, and Jason TenBarge have contributed tremendously to my efforts to understand kinetic turbulence. Financial support has been provided by NSF grant PHY-10033446, NSF CAREER Award AGS-1054061, and NASA grant NNX10AC91G.

References

Alexandrova, O., Saur, J., Lacombe, C., Mangeney, A., Mitchell, J., Schwartz, S.J., Robert, P.: Universality of solar-wind turbulent spectrum from MHD to electron scales. Phys. Rev. Lett. **103**(16), 165003 (2009)

Alexandrova, O., Lacombe, C., Mangeney, A., Grappin, R., Maksimovic, M.: Solar wind turbulent spectrum at plasma kinetic scales. Astrophys. J. **760**, 121 (2012)

Armstrong, J.W., Cordes, J.M., Rickett, B.J.: Density power spectrum in the local interstellar medium. Nature **291**, 561–564 (1981)

Armstrong, J.W., Rickett, B.J., Spangler, S.R.: Electron density power spectrum in the local interstellar medium. Astrophys. J. **443**, 209–221 (1995)

Balbus, S.A., Hawley, J.F.: A powerful local shear instability in weakly magnetized disks. i. Linear analysis. Astrophys. J. **376**, 214–222 (1991)

Balbus, S.A., Hawley, J.F.: Instability, turbulence, and enhanced transport in accretion disks. Rev. Mod. Phys. **70**, 1–53 (1998)

Bale, S.D., Kellogg, P.J., Mozer, F.S., Horbury, T S., Reme, H.: Measurement of the electric fluctuation spectrum of magnetohydrodynamic turbulence. Phys. Rev. Lett. **94**(21):215002 (2005)

Bale, S.D., Kasper, J.C., Howes, G.G., Quataert, E., Salem, C., Sundkvist, D.: Magnetic fluctuation power near proton temperature anisotropy instability thresholds in the solar wind. Phys. Rev. Lett. **103**(21), 211101 (2009)

Barnes, A.: Collisionless damping of hydromagnetic waves. Phys. Fluids **9**, 1483–1495 (1966)
Belcher, J.W., Davis, L.: Large-amplitude Alfvén waves in the interplanetary medium, 2: J. Geophys. Res. **76**, 3534–3563 (1971)
Birn, J., Priest, E.R.: Reconnection of Magnetic Fields. Cambriodge University Press, Cambriodge (2006)
Biskmap, D., Schwarz, E., Zeiler, A., Celani, A., Drake, J.F.: Electron magnetohydrodynamic turbulence. Phys. Plasmas **6**, 751–758 (1999)
Boldyrev, S.: Spectrum of magnetohydrodynamic turbulence. Phys. Rev. Lett. **96**(11), 115002 (2006)
Boldyrev, S., Perez, J.C., Borovsky, J.E., Podesta, J.J.: Spectral scaling laws in magnetohydrodynamic turbulence simulations and in the solar wind. Astrophys. J. Lett. **741**, L19 (2011)
Boldyrev, S., Perez, J.C., Wang, Y.: Residual energy in weak and strong MHD turbulence. (2012). ArXiv e-prints
Bourouaine, S., Alexandrova, O., Marsch, E., Maksimovic, M.: On spectral breaks in the power spectra of magnetic fluctuations in fast solar wind between 0.3 and 0.9 AU. Astrophys. J. **749**, 102 (2012)
Braginskii, S.I.: Transport processes in a plasma. Rev. Plasma Phys. **1**, 205 (1965)
Breech, B., Matthaeus, W.H., Cranmer, S.R., Kasper, J.C., Oughton, S.: Electron and proton heating by solar wind turbulence. J. Geophys. Res. (Space Phys.), **114**(A13), 9103 (2009)
Bruno, R., Carbone, V.: The solar wind as a turbulence laboratory. Living Rev. Solar Phys. **2**, 4 (2005)
Chen, C.H.K., Horbury, T.S., Schekochihin, A.A., Wicks, R.T., Alexandrova, O., Mitchell, J.: Anisotropy of solar wind turbulence between ion and electron scales. Phys. Rev. Lett. **104**(25), 255002 (2010)
Cho, J., Lazarian, A.: Compressible magnetohydrodynamic turbulence: mode coupling, scaling relations, anisotropy, viscosity-damped regime and astrophysical implications. Mon. Not. Roy. Astron. Soc. **345**, 325–339 (2003)
Cho, J., Lazarian, A.: The anisotropy of electron magnetohydrodynamic turbulence. Astrophys. J. Lett. **615**, L41–L44 (2004)
Cho, J., Lazarian, A.: Simulations of electron magnetohydrodynamic turbulence. Astrophys. J. **701**, 236–252 (2009)
Cranmer, S.R., Matthaeus, W.H., Breech, B.A., Kasper, J.C.: Empirical constraints on proton and electron heating in the fast solar wind. Astrophys. J. **702**, 1604–1614 (2009)
Dmitruk, P., Matthaeus, W.H.: Test particle acceleration in three-dimensional Hall MHD turbulence. J. Geophys. Res. (Space Phys.) **111**, 12110 (2006)
Dmitruk, P., Matthaeus, W.H., Seenu, N.: Test particle energization by current sheets and nonuniform fields in magnetohydrodynamic turbulence. Astrophys. J. **617**, 667–679 (2004)
Dorland, W., Hammett, G.W.: Gyrofluid turbulence models with kinetic effects. Phys. Fluids B **5**, 812–835 (1993)
Frieman, E.A., Chen, L.: Nonlinear gyrokinetic equations for low-frequency electromagnetic waves in general plasma equilibria. Phys. Fluids **25**, 502–508 (1982)
Galtier, S.: Wave turbulence in incompressible Hall magnetohydrodynamics. J. Plasma Phys. **72**, 721–769 (2006)
Galtier, S., Nazarenko, S.V., Newell, A.C., Pouquet, A.: A weak turbulence theory for incompressible magnetohydrodynamics. J. Plasma Phys. **63**, 447–488 (2000)
Gary, S.P., Saito, S., Narita, Y.: Whistler turbulence wavevector anisotropies: particle-in-cell simulations Astrophys. J. **716**, 1332–1335 (2010)
Goldreich, P., Sridhar, S.: Toward a theory of interstellar turbulence II. Strong Alfvénic turbulence. Astrophys. J. **438**, 763–775 (1995)
Goldstein, M.L., Roberts, D.A., Fitch, C.A.: Properties of the fluctuating magnetic helicity in the inertial and dissipation ranges of solar wind turbulence. J. Geophys. Res. **99**, 11519–11538 (1994)
Goldstein, M.L., Roberts, D.A., Matthaeus, W.H.: Magnetohydrodynamic turbulence in the solar wind. Ann. Rev. Astron. Astrophys. **33**, 283–326 (1995)

Gruzinov, A.V.: Radiative efficiency of collisionless accretion. Astrophys. J. **501**, 787 (1998)
Hasegawa, A., Sato, T.: Space plasma physics. 1. Stationary processes. *Physics and Chemistry in Space*, vol. 16. Springer-Verlag: Berlin (1989)
He, J., Marsch, E., Tu, C., Yao, S., Tian, H.: Possible evidence of Alfvén-cyclotron waves in the angle distribution of magnetic helicity of solar wind turbulence. Astrophys. J. **731**, 85 (2011)
Hollweg, J.V.: Kinetic Alfvén wave revisited. J. Geophys. Res. **104**, 14811–14820 (1999)
Howes, G.G.: Inertial range turbulence in kinetic plasmas. Phys. Plasmas **15**(5), 055904 (2008)
Howes, G.G.: A prescription for the turbulent heating of astrophysical plasmas. Mon. Not. R. Astron. Soc. **409**, L104–L108 (2010)
Howes, G.G.: Prediction of the proton-to-total turbulent heating in the solar wind. Astrophys. J. **738**, 40 (2011)
Howes, G.G., Quataert, E.: On the interpretation of magnetic helicity signatures in the dissipation range of solar wind turbulence. Astrophys. J. Lett. **709**, L49–L52 (2010)
Howes, G.G., Cowley, S.C., Dorland, W., Hammett, G.W., Quataert, E., Schekochihin, A.A.: Astrophysical gyrokinetics: basic equations and linear theory. Astrophys. J. **651**, 590–614 (2006)
Howes, G.G., Cowley, S.C., Dorland, W., Hammett, G.W., Quataert, E., Schekochihin, A.A.: A model of turbulence in magnetized plasmas: Implications for the dissipation range in the solar wind. J. Geophys. Res. **113**(A12), A05103 (2008)
Howes, G.G., Dorland, W., Cowley, S.C., Hammett, G.W., Quataert, E., Schekochihin, A.A., Tatsuno, T.: Kinetic simulations of magnetized turbulence in astrophysical plasmas. Phys. Rev. Lett. **100**(6), 065004 (2008)
Howes, G.G., Tenbarge, J.M., Dorland, W.: A weakened cascade model for turbulence in astrophysical plasmas. Phys. Plasmas **18**(10), 102305 (2011)
Howes, G.G., TenBarge, J.M., Dorland, W., Quataert, E., Schekochihin, A.A. Numata, R., Tatsuno, T.: Gyrokinetic simulations of solar wind turbulence from ion to electron scales. Phys. Rev. Lett. **107**(3), 035004 (2011)
Howes, G.G., Bale, S.D., Klein, K.G., Chen, C.H.K., Salem, C.S., TenBarge, J.M.: The slow-mode nature of compressible wave power in solar wind turbulence. Astrophys. J. Lett. **753**, L19, (2012)
Jian, L.K., Russell, C.T., Luhmann, J.G., Strangeway, R.J., Leisner, J.S., Galvin, A.B.: Ion cyclotron waves in the solar wind observed by STEREO near 1 AU. Astrophys. J. Lett. **701**, L105–L109 (2009)
Kellogg, P.J., Horbury, T.S.: Rapid density fluctuations in the solar wind. Ann. Geophys. **23**, 3765–3773 (2005)
Kiyani, K.H., Chapman, S.C., Khotyaintsev, Y.V., Dunlop, M.W., Sahraoui, F.: Global scale-invariant dissipation in collisionless plasma turbulence. Phys. Rev. Lett. **103**, 075006 (2009)
Klein, K.G., Howes, G.G., TenBarge, J.M., Bale, S.D., Chen, C.H.K., Salem, C.S.: Using synthetic spacecraft data to interpret compressible fluctuations in solar wind turbulence. Astrophys. J. **755**, 159 (2012)
Kolmogorov, A.N.: The local structure of turbulence in incompressible viscous fluid for very large reynolds numbers. Dokl. Akad. Nauk SSSR **30**, 9– (1941). [English Translation: Proc. R. Soc. London A **434**, 9 (1991)]
Krishan, V., Mahajan, S.M.: Magnetic fluctuations and Hall magnetohydrodynamic turbulence in the solar wind. J. Geophys. Res. **109**(A18), A11105 (2004)
Leamon, R.J., Smith, C.W., Ness, N.F., Matthaeus, W.H., Wong, H.K.: Observational constraints on the dynamics of the interplanetary magnetic field dissipation range. J. Geophys. Res. **103**, 4775–4787 (1998)
Leamon, R.J., Smith, C.W., Ness, N.F., Wong, H.K.: Dissipation range dynamics: Kinetic alfvén waves and the importance of β_e. J. Geophys. Res. **104**, 22331–22344 (1999)
Leamon, R.J., Matthaeus, W.H., Smith, C.W., Zank, G.P., Mullan, D.J., Oughton, S.: MHD-driven kinetic dissipation in the solar wind and corona. Astrophys. J. **537**, 1054–1062 (2000)
Lithwick, Y., Goldreich, P.: Compressible magnetohydrodynamic turbulence in interstellar plasmas. Astrophys. J. **562**, 279–296 (2001)

Markovskii, S.A., Vasquez, B.J.: A short-timescale channel of dissipation of the strong solar wind turbulence. Astrophys. J. **739**, 22 (2011)
Maron, J., Goldreich, P.: Simulations of incompressible magnetohydrodynamic turbulence. Astrophys. J. **554**, 1175–1196 (2001)
Narita, Y., Gary, S.P.: Inertial-range spectrum of whistler turbulence. Ann. Geophys. **28**, 597–601 (2010)
Osman, K.T., Matthaeus, W.H., Greco, A., Servidio, S.: Evidence for inhomogeneous heating in the solar wind. Astrophys. J. Lett. **727**, L11+ (2011)
Osman, K.T., Matthaeus, W.H., Wan, M., Rappazzo, A.F.: Intermittent dissipation and local heating in the solar wind. ArXiv e-prints (2011)
Parashar, T.N., Shay, M.A., Cassak, P.A., Matthaeus, W.H.: Kinetic dissipation and anisotropic heating in a turbulent collisionless plasma. Phys. Plasmas **16**(3), 032310 (2009)
Parashar, T.N., Servidio, S., Breech, B., Shay, M.A., Matthaeus, W.H.: Kinetic driven turbulence: Structure in space and time. Phys. Plasmas **17**(10), 102304 (2010)
Perri, S., Carbone, V., Veltri, P.: Where does fluid-like turbulence break down in the solar wind? Astrophys. J. Lett. **725**, L52–L55 (2010)
Plunk, G.G., Tatsuno, T.: Energy transfer and dual cascade in kinetic magnetized plasma turbulence. Phys. Rev. Lett. **106**(16), 165003 (2011)
Plunk, G.G., Cowley, S.C., Schekochihin, A.A., Tatsuno T.: Two-dimensional gyrokinetic turbulence. J. Fluid Mech. **664**, 407–435 (2010)
Podesta, J.J., Gary, S.P.: Magnetic helicity spectrum of solar wind fluctuations as a function of the angle with respect to the local mean magnetic field. Astrophys. J. **734**, 15 (2011)
Podesta, J.J., Roberts, D.A., Goldstein, M.L.: Spectral exponents of kinetic and magnetic energy spectra in solar wind turbulence. Astrophys. J. **664**, 543–548 (2007)
Podesta, J.J., Borovsky, J.E., Gary, S.P.: A kinetic Alfvén wave cascade subject to collisionless damping cannot reach electron scales in the solar wind at 1 AU. Astrophys. J. **712**, 685–691 (2010)
Quataert, E., Gruzinov, A.: Turbulence and particle heating in advection-dominated accretion flows. Astrophys. J. **520**, 248–255 (1999)
Sahraoui, F., Goldstein, M.L., Robert, P., Khotyaintsev, Y.V.: Evidence of a cascade and dissipation of solar-wind turbulence at the electron gyroscale. Phys. Rev. Lett. **102**(23), 231102 (2009)
Sahraoui, F., Goldstein, M.L., Belmont, G., Canu, P., Rezeau, L.: Three dimensional anisotropic k spectra of turbulence at subproton scales in the solar wind. Phys. Rev. Lett. **105**(13), 131101 (2010)
Sahraoui, F., Belmont, G., Goldstein, M.L.: New insight into short-wavelength solar wind fluctuations from vlasov theory. Astrophys. J. **748**, 100 (2012)
Salem, C.S., Howes, G.G, Sundkvist, D., Bale, S.D., Chaston, C.C., Chen, C.H.K., Mozer, F.S.: Identification of kinetic Alfvén wave turbulence in the solar wind. Astrophys. J. Lett. **745**, L9 (2012)
Schekochihin, A.A., Cowley, S.C., Dorland, W., Hammett, G.W., Howes, G.G., Quataert, E., Tatsuno, T.: Astrophysical gyrokinetics: kinetic and fluid turbulent cascades in magnetized weakly collisional plasmas. Astrophys. J. Supp. **182**, 310–377 (2009)
Servidio, S., Matthaeus, W.H., Shay, M.A., Cassak, P.A., Dmitruk, P.: Magnetic reconnection in two-dimensional magnetohydrodynamic turbulence. Phys. Rev. Lett. **102**(11), 115003 (2009)
Servidio, S., Matthaeus, W.H., Shay, M.A., Dmitruk, P., Cassak, P.A., Wan, M.: Statistics of magnetic reconnection in two-dimensional magnetohydrodynamic turbulence. Phys. Plasmas **17**(3), 032315 (2010)
Servidio, S., Dmitruk, P., Greco, A., Wan, M., Donato, S., Cassak, P.A., Shay, M.A., Carbone, V., Matthaeus, W.H.: Magnetic reconnection as an element of turbulence. Nonlin. Proc. Geophys. **18**, 675–695 (2011)
Servidio, S., Valentini, F., Califano, F., Veltri, P.: Local kinetic effects in two-dimensional plasma turbulence. Phys. Rev. Lett. **108**(4), 045001 (2012)
Shaikh, D., Zank, G.P.: Driven dissipative whistler wave turbulence. Phys. Plasmas **12**(12), 122310 (2005)

Shaikh, D., Zank. G.P.: Spectral features of solar wind turbulent plasma. Mon. Not. R. Astron. Soc. **400**, 1881–1891 (2009)

Smith, C.W., Mullan, D.J., Ness, N.F., Skoug, R.M., Steinberg, J.: Day the solar wind almost disappeared: magnetic field fluctuations, wave refraction and dissipation. J. Geophys. Res. **106**, 18625–18634 (2001)

Smith, C.W., Vasquez, B.J., Hollweg, J.V.: Observational constraints on the role of cyclotron damping and kinetic alfvén waves in the solar wind. Astrophys. J. **745**, 8 (2012)

Sridhar, S., Goldreich, P.: Toward a theory of interstellar turbulence I. Weak Alfvénic turbulence. Astrophys. J. **433**, 612–621 (1994)

Stawicki, O., Gary, S.P., Li, H.: Solar wind magnetic fluctuation spectra: dispersion versus damping. J. Geophys. Res. **106**, 8273–8282 (2001)

Stix, T.H. : Waves in Plasmas. American Institute of Physics, New York (1992)

Strauss, H.R.: Nonlinear, three-dimensional magnetohydrodynamics of noncircular tokamaks. Phys. Fluids **19**, 134–140 (1976)

Tatsuno, T., Schekochihin, A.A., Dorland, W., Plunk, G., Barnes, M.A., Cowley, S.C., Howes, G.G.: Nonlinear phase mixing and phase-space cascade of entropy in gyrokinetic plasma turbulence. Phys. Rev. Lett. **103**(1), 015003 (2009)

Taylor, G.I.: The spectrum of turbulence. Proc. R. Soc. A **164**, 476–490 (1938)

TenBarge, J.M., Howes, G.G.: Current sheets and collisionless damping in kinetic plasma turbulence. Astrophys. J. **771**, L27 (2013a)

TenBarge, J.M., Podesta, J.J., Klein, K.G., Howes, G.G.: Interpreting magnetic variance anisotropy measurements in the solar wind. Astrophys. J. **774**, 139 (2013b)

Tenbarge, J.M., Howes, G.G.: Evidence of critical balance in kinetic Alfvén wave turbulence simulations. Phys. Plasmas **19**, 055901 (2012c)

TenBarge, J.M., Podesta, J.J., Klein, K.G., Howes, G.G.: Interpreting magnetic variance anisotropy measurements in the solar wind. Astrophys. J. **753**, 107 (2012b)

Terry, P.W., et al.: Dissipation range turbulent cascades in plasmas. Phys. Plasmas **19**, 055906 (2012)

Tu, C.-Y., Marsch, E.: On the nature of compressive fluctuations in the solar wind. J. Geophys. Res. **99**, 21481 (1994)

Tu, C.-Y., Marsch, E.: MHD structures, waves and turbulence in the solar wind: observations and theories. Space Sci. Rev. **73**, 1–2 (1995)

Chapter 7
Interstellar Polarization and Magnetic Turbulence

Terry Jay Jones

Abstract Polarimetry of starlight observed through dust and observations of polarized thermal emission from this dust are some of the few ways to observe the presence of magnetic fields in the interstellar medium. Not only is the strength and overall geometry of the magnetic field important in physical processes in the ISM, the turbulent component to the field also plays an important role. Turbulence in the field is directly tied to turbulence in the gas and consequently to the dynamics of the gas, on both large and small scales. Using interstellar polarization to measure parameters relating to turbulence in the magnetic field is necessarily an indirect process. In this chapter we explore several techniques and results for using polarimetry to explore the turbulent component of the magnetic field in the Galaxy.

7.1 Polarization in Transmission and Emission

Dust in the interstellar medium contains a component that is made up of large silicates that are asymmetric and aligned with the interstellar magnetic field (see the chapter by B-G Andersson on grain alignment in this volume and references therein). Transmission of starlight through these aligned dust grains will cause the light to be polarized due to differential extinction by the dust. The strength of the fractional polarization will, in general, grow with increasing extinction. For perfect alignment with no variations in the magnetic field geometry, we have $P = \tanh(\beta\tau)$ (e.g. Jones 1989) where β is the fractional polarization per unit optical depth. Even for a completely random magnetic field geometry along the line of sight, the fractional polarization will still increase with $P \propto \sqrt{\tau}$. Consider $Q = I_P \cos 2\theta$ and $U = I_P \sin 2\theta$, where I_P is the polarized intensity. To first order, this can be thought of as a random walk in the $Q/I - U/I$ diagram, where the distance from the origin is $P = \sqrt{(Q/I)^2 + (U/I)^2}$, and the distance increases by the square root of the number of steps (in optical depth). Note that for the pure random case, the position angle on the sky is completely undetermined.

T.J. Jones (✉)
Minnesota Institute for Astrophysics, 116 Church St. SE, Minneapolis, MN 55455, USA
e-mail: tjj@astro.umn.edu

A. Lazarian et al. (eds.), *Magnetic Fields in Diffuse Media*, Astrophysics and Space Science Library 407, DOI 10.1007/978-3-662-44625-6_7

For dust in emission, a different behavior of P with τ is found. The aligned dust grains causing extinction can also produce emission in the Far-Infrared and millimeter (MM) waves. For this case, the polarization will be high at small optical depths if there is very little fluctuation in the magnetic field down the column of emitting dust. Fluctuations in the magnetic field geometry that are likely to be found along longer (and denser) lines of sight will decrease the polarization from maximum (e.g. Hildebrand et al. 2000; Jones 2003). Thus, in the optical and Near-Infrared, interstellar polarization will generally increase with increasing optical depth, but in the FIR and MM, it will generally decrease with increasing optical depth. Keeping these differences in mind, both polarimetry in transmission and in emission can be used to explore the turbulent component to the magnetic field in molecular clouds and the very diffuse ISM.

The efficiency of grain alignment is also a major factor in determining the observed fractional polarization. Even if the magnetic field is perpendicular to the line of sight and nearly constant in direction, poor grain alignment will result in a low fractional polarization compared to the case with perfect alignment. Evidence is strong that in the very diffuse ISM grain alignment is nearly perfect. Mie theory computations by Mathis (1986) could reproduce the wavelength dependence of the polarization (Wilking et al. 1980) assuming perfect alignment of the large silicate grains. Using the observed trend of polarization with extinction in the optical (Serkowski et al. 1975) and the wavelength dependence of the polarization, Kim and Martin (1995) found that a high alignment fraction was necessary for the large silicate grains to produce the observed polarization. Jones et al. (1992) found that the trend in polarization with extinction in the diffuse ISM and along lines of sight to embedded luminous YSOs could be explained by turbulence alone, without any variation in grain alignment.

However, in dense, dark clouds, with no internal source of radiation, there is growing evidence that grain alignment decreases significantly. This was noted by Goodman et al. (1995) and has been explored by several other researchers since Gerakines et al. (1995) and Whittet et al. (2008). The question of grain alignment efficiency is covered in detail in the chapter by Andersson in this volume. For the purposes of this chapter, one must keep in mind that grain alignment is probably a serious issue in dense molecular clouds with high extinction ($A_V > 20$).

7.2 Turbulence and the Field Strength

When Hall (1949) and Hiltner (1949) began searching for intrinsic polarization in distant OB stars, they found that a clearly coherent pattern of position angles was present across the sky in several directions in the Milky Way. The pattern could not be due to the intrinsic polarization of the individual stars, since their rotation axes were likely to be randomly distributed over the sky. Some other, global, mechanism must be responsible for the strong correlation in position angle from star-to-star.

This coherent pattern was not perfectly smooth or smoothly varying. There were wiggles present on top of mean direction of the position angles. We now recognize, at least for the very diffuse ISM, that the galactic magnetic field defines the pattern (e.g. Jones 1996, chapter by B-G Andersson on grain alignment in this volume). The wiggles in the polarization pattern must, then, be due to wiggles in the magnetic field geometry as projected on the plane of the sky. Since the gas in the ISM is highly conducting, these wiggles in the polarization vectors must be tied motions in the gas.

Chandrasekhar and Fermi (1953), hereafter CF, developed a method that uses the observed dispersion in polarization position angle, the local gas density, and the local gas velocity dispersion to estimate the magnetic field strength. For a somewhat idealized case, they found:

$$B = \sqrt{\frac{4}{3}\pi\rho}\frac{\sigma_V}{\alpha}[\mu G] \tag{7.1}$$

where B is the magnetic field strength in the plane-of-the-sky, ρ is the volume mass density (in $\mathrm{g\,cm^{-3}}$), σ_V is the gas velocity dispersion (in $\mathrm{cm\,s^{-1}}$) and α is the dispersion in the polarization vectors in radians. A physical understanding of this formula is simple, a small dispersion in position angles with a large velocity dispersion in the gas requires that the magnetic field be very stiff.

Although at first glance the CF method appears quite powerful, the somewhat ideal case considered by CF is never actually found in observations. For interstellar polarization of stars in extinction, the aligned dust grains in a pencil beam along the line of sight to the star all contribute to the net polarization. The observed position angle is an average of the projected magnetic field, weighted by the dust density along the line of sight (assuming perfect grain alignment). Polarization in emission from the dust in the thermal infrared is observed in a finite beam size. So, not only is the magnetic field geometry along the line of sight being averaged, it is also being averaged across the beam.

This averaging will, in general, narrow the dispersion in position angle compared to what one would measure for a thin sheet of dust observed with a very narrow beam. Direct application of the CF to these types of observations leads to a measured dispersion of the position angles on the sky that is too small, hence, calculated field strengths that are too large (Itoh et al. 1999; Morris et al. 1992). Some sort of calibration of the CF method for application to real world observations is needed.

A promising approach to test this method is to create synthetic plane-of-the-sky maps from numerical simulations. In the simulations, the field strength, field geometry and gas turbulence are all known. Synthetic observations of interstellar polarization, both in transmission and emission, and the magnetic field characteristics they infer, can then be compared to the intrinsic values. Ostriker et al. (2001) performed 3D-MHD simulations, and obtained 2D polarization maps and that could be used for the application of the CF method. They showed that the CF method gives reasonable results for highly magnetized media with a modest dispersion in polarization position angle. For most applications, a simple numerical factor of 0.5 can applied to the field strength given in Eq. (7.1).

This work was extended by Falceta-Gonçalves et al. (2009) for a wider range of simulations. Their results include the probability distribution function, the power spectrum, and the structure function of the polarization angles from polarization in emission. Their statistical analysis revealed strong differences depending on whether the gas is sub/supersonic or sub/super-Alfvénic. They also proposed revised formulae for the CF expression, based on their simulations. This study leads to the ability to more fully characterize the dynamics of molecular clouds from polarimetric observations. They also present a modified CF method to determine the magnetic field strength (see also Poidevin et al. 2013).

Although in the most diffuse ISM, grain alignment appears to be very efficient (Kim and Martin 1994; Jones 1996; Roberge 1996), there is strong evidence that the polarizing efficiency decreases at large optical depths in dark clouds (Goodman et al. 1995; Whittet et al. 2008). Whether or not this is due to turbulence alone (Wiebe and Watson 2001) or to physics of the grain alignment mechanism (see the chapter by Andersson volume) in addition to turbulence is still not clear. If the alignment mechanism is at least partly to blame, then the dispersion in position angle across the plane of the sky is weighted more to the field geometry around the periphery of the cloud, and will not necessarily reflect the field strength associated with the total dust column density (extinction).

Keeping these caveats in mind, application of the CF method can still prove quite powerful. Marchwinski et al. (2012), for example, use results from the GPIPS survey (Clemens et al. 2012) to study the polarization vectors for interstellar polarization in transmission from stars shining through from behind the quiescent molecular cloud GRSMC 45.60+0.30 (Fig. 7.1). GPIS is a survey of the Galacitc plane in $H(1.65\,\mu\mathrm{m})$ band that will target all stars within the observation fields. Combining

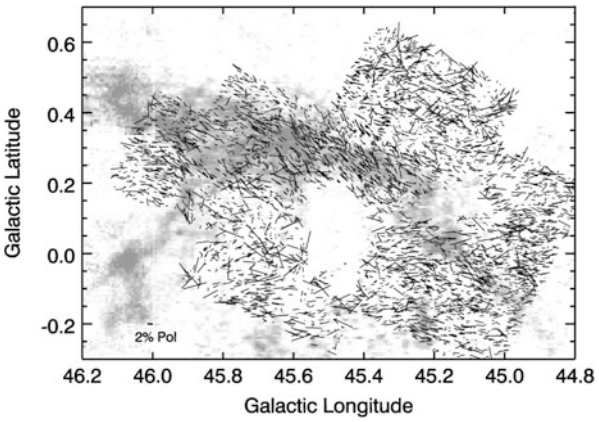

Fig. 7.1 GPIPS (Clemens et al. 2012) H band polarization vectors overlaid on an integrated ^{13}CO grey scale map of GRSMC 45.60 + 0.30. Marchwinski et al. (2012) used the statistics of the fluctuations in position angles to study the magnetic field strength in the cloud. The extinction through the cloud itself is relatively low, a few A_V, so grain alignment should be efficient

the polarimetry with ^{13}CO spectral line widths, they find that there are local regions of higher field strength within the cloud. They find sub critical mass-to-flux ratios for these regions, implying their magnetic fields continue to suppress star formation.

7.3 Turbulence and the Position Angle Structure Function

Another problem using the CF method is distinguishing between smooth variations in the position angle of the threaded component with the random component (wiggles along these slowly varying field lines). Making assumptions about the larger scale structure for the morphology of the magnetic field (derived from a polarization map), may still lead to imprecise values for the turbulent component. Hildebrand et al. (2009) developed a technique where a structure function of the polarization angle with angular separation is used to estimate the turbulent component of the field without making any assumptions on the morphology of the large-scale magnetic field.

Consider the difference between position angles separated by ℓ angular units on the sky (given by position x). Compute the following square root of the structure function (see Kobulnicky et al. 1994; Hildebrand et al. 2009):

$$\Theta_{rms}(\ell) = \left\langle \Delta\theta^2(\ell) \right\rangle^{1/2} = \left[\frac{1}{N} \sum_{1}^{N} (\theta(x) - \theta(x-\ell))^2 \right]^{1/2} \tag{7.2}$$

Hildebrand et al. (2009) refer to this as the Dispersion Function. If the magnetic field has exactly the same geometry across the region being studied with no turbulence, Θ_{rms} will be zero. If the constant component to the magnetic field is smoothly varying across the region, $\Theta_{rms}(\ell)$ should increase with angular distance scale. For the random component, the contribution to $\Theta_{rms}(\ell)$ should vary from near zero at very small separation to a maximum when the largest angular scale for the random component is reached. It is assumed that the scale length for the random component is smaller than for the constant component. Also note that it is assumed the constant and random components are statistically independent. An idealized trend for $\Theta_{rms}(\ell)$ is shown in Fig. 7.2.

This technique was used by Hildebrand et al. (2009) to analyze far-infrared polarimetry of several star forming regions. Houde et al. (2009) expanded on this work by better taking into account integration down along the line of sight (the dust emission is optically thin in the FIR). They applied their improved technique to OMC-1, where they find a scale length for the random component of $\delta \approx 0.016$ pc and equal strength in the random and constant components.

A similar, but less sophisticated analysis was made using R (optical) band polarimetry in transmission toward the Cyg OB2 association by Kobulnicky et al. (1994). They found that the constant component had a scale length of about 0.7° (Fig. 7.3). This is evident by the leveling off of the measured structure function with

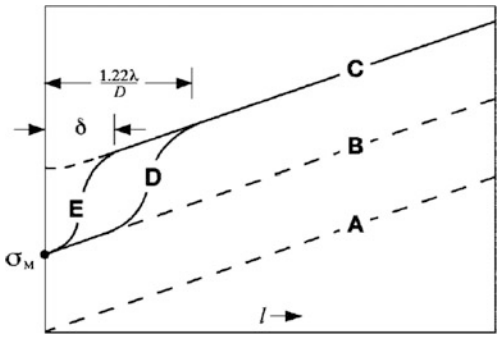

Fig. 7.2 Idealized trend in the Dispersion Function $\Theta_{rms}(\ell)$ (vertical axis) for five simplified cases. A: noiseless data with no turbulence. B: data with noise σ_M, but no turbulence. C: same, but with turbulence. E: showing the scale length of the random component δ. D: including the effects of beam size. Taken from Hildebrand et al. (2009)

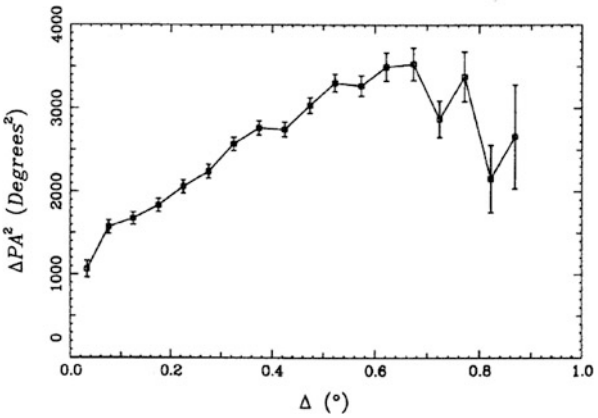

Fig. 7.3 Structure function of polarization position angle for 118 Cyg OB2 members from Kobulnicky et al. (1994)

angular separation beyond 0.7°. There is a hint of a drop in the structure function for the smallest angular bin, but there were too few star separations on this scale to accurately measure the random component.

7.4 Global Statistics

Measuring and using turbulence to study the physical conditions in individual dark clouds will reflect both general trends and the individual characteristics of the dark clouds themselves. There are large data sets of interstellar polarization of the

very diffuse ISM that can be used to analyze large scale statistical properties of the magnetic field in the Milky Way as a whole. Future data sets, in particular polarization plots of the Galactic Plane from the high frequency Planck observations will further enhance this knowledge.

As a starting point, one could use large data sets of optical and Near-Infrared polarimetry in transmission (e.g. Heiles 2000; Clemens et al. 2012). Without turbulence and a magnetic field geometry primarily in the plane of the sky, the strength of interstellar polarization in extinction should be strongly correlated with optical depth, in the sense that more extinction results in higher fractional polarization. In their seminal study, Serkowski et al. (1975) found that there was an upper limit to the magnitude of the fractional polarization for any given extinction, but there was a very wide range in polarization values below this upper limit. This suggested that variations in the magnetic field geometry and grain alignment efficiency essentially erased an overall trend.

By extending this work to longer wavelengths, which penetrate deeper into the ISM, Jones (1989) found the polarization of stars in the general ISM and luminous young stars embedded in dense molecular clouds (but NOT background stars shining through quiescent, dense molecular clouds) was correlated with extinction. This correlation was not linear, however, but rather could be fit by a power law trend where the polarization at K (2.2 μm) is:

$$P_K = 2.2\tau_K^{0.75}(\%) \tag{7.3}$$

Jones (1989) was able to explain this trend by a mixture of random and constant components to the magnetic field. This work was extended by Jones et al. (1992) who, using a very simple model, found that a 50/50 mix of random and constant components could best explain the overall trend. This result is equivalent to equating the velocity dispersion in the gas and the Alfvén velocity (see also Chandrasekhar and Fermi 1953; Zweibel 1990; Myers and Goodman 1991). The model trend is shown as the solid line in Fig. 7.4.

The ratio of unity between the field strength in the turbulent, or random component and the constant, or threaded, component to the Galactic field is a bit higher, but consistent with radio synchrotron statistics (e.g. Beck 2001) and a detailed analysis of Galactic foreground emission in the WMAP polarization data (Miville-Deschênes et al. 2008). Jones et al. (1992) found that the scale 'length' of the turbulence (the random component) corresponded to $\tau_K \approx 0.1$, or ≈ 500 pc in the diffuse ISM. Note that interstellar polarization in transmission is sensitive to only the largest scale length for the random component (Zweibel 1996). Turbulence on smaller scales will tend to 'average out' when integrated along a line of sight. In denser regions, the physical scale length may be shorter, but possibly still tied to the optical depth (Jones et al. 1992).

Using a larger optical polarimetry data set, Fosalba et al. (2002) present a statistical analysis of Galactic interstellar polarization. They find a somewhat larger contribution from the random component $B_{cnst} = 0.8 B_{rand}$. The also find a very similar relationship between the fractional polarization and optical depth to that

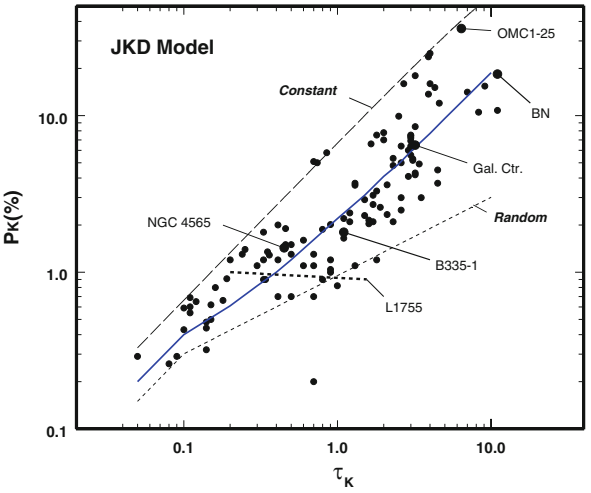

Fig. 7.4 Trend in fractional polarization at K with optical depth and the JKD model fit (Jones et al. 1992) for a 50/50 mix of constant and random components to the Galactic magnetic field. The scale 'length' for the random component is $\tau_K = 0.1$. Note that the quiescent dark cloud, L1755, does not follow the trend

found for the K band data in Jones et al. (1992). With the advent of the GPIPS catalog (Clemens et al. 2012), which contains polarimetry in the H band ($1.65\mu m$), a similar detailed statistical analysis can be done for greater dust column depths than is possible with the optical data.

7.5 Future Work

Both observations, analysis, and theoretical modeling continue to advance. There are now numerical simulations of star forming regions that create synthetic polarimetric observations for use with and comparison to observational data. The GPIPS (Clemens et al. 2012) survey will produce high quality H (1.65 μm) band polarimetry of several hundred thousand field stars in the Galactic Plane. Planck (Tauber 2004) will have a polarimetric capability and in the higher frequency channels which will be able to make maps of polarized dust emission in the Galactic plane at $\approx 5'$ angular resolution (Bernard 2012). This corresponds to tens of thousands of data points with fractional polarization and position angle for the entire Galactic plane. Our challenge is to use these huge data sets to explore the nature of turbulence in the magnetic field in both local regions such as molecular clouds and larger regions, up to the entire Galaxy in volume.

A key component to our ability to extract physically useful information from observations of interstellar polarization is the role of grain alignment. A better understanding of grain alignment, in particular how grain alignment is a function of local environment, is crucial to the study of turbulence in the ISM using interstellar polarization. This may not be so important in the very diffuse ISM sampled by Planck, but GPIPS, BlastPol (Pascale 2013), ALMA (Henning et al. 2002), and the

SMA (Rao 2008) will probe more narrow columns through denser molecular gas with highly variable local conditions. Understanding the role of magnetic turbulence on these scales, which correspond to the earliest stages of star formation, will require a viable grain alignment model.

References

Beck, R.: Space Sci. Rev. **99**, 243 (2001)
Bernard, J.-P.: 39th COSPAR Scientific Assembly, **39**, 149 (2012)
Chandrasekhar, S., Fermi, E.: Astrophys. J. **118**, 116 (1953)
Clemens, D.P., Pinnick, A.F., Pavel, M.D., Taylor, B.W.: Astrophys. J. Suppl. **200**, 19 (2012)
Falceta-Gonçalves, D., Lazarian, A., Kowal, G.: Revista Mexicana de Astronomia y Astrofisica Conference Series, **36**, 37 (2009)
Fosalba, P., Lazarian, A., Prunet, S., Tauber, J.A.: Astrophys. J. **564**, 762 (2002)
Gerakines, P.A., Whittet, D.C.B., Lazarian, A.: Astrophys. J. Lett. **455**, L171 (1995)
Goodman, A.A., Jones, T.J., Lada, E.A., Myers, P.C.: Astrophys. J. **448**, 748 (1995)
Hall, J.S.: Science **109**, 166 (1949)
Heiles, C.: Astron. J. **119**, 923 (2000)
Henning, T., Launhardt, R., Stecklum, B., Wolf, S.: The Origin of Stars and Planets: The VLT View, **79** (2002)
Hildebrand, R.H., Davidson, J.A., Dotson, J.L., et al.: Publ. Astron. Soc. Pac. **112**, 1215 (2000)
Hildebrand, R.H., Kirby, L., Dotson, J.L., Houde, M., Vaillancourt, J.E.: Astrophys. J. **696**, 567 (2009)
Hiltner, W.A.: Science, **109**, 165 (1949)
Houde, M., Vaillancourt, J.E., Hildebrand, R.H., Chitsazzadeh, S., Kirby, L.: Astrophys. J. **706**, 1504 (2009)
Itoh, Y., Chrysostomou, A., Burton, M., Hough, J.H., Tamura, M.: Mon. Not. R. Astron. Soc. **304**, 406 (1999)
Jones, T.J.: Astrophys. J. **346**, 728 (1989)
Jones, T.J.: Polarimetry of the Interstellar Medium, vol. 97, p. 381 (1996)
Jones, T.J.: New Astron. Rev. **47**, 1123 (2003)
Jones, T.J., Klebe, D., Dickey, J.M.: Astrophys. J. **389**, 602 (1992)
Kim, S.-H., Martin, P.G.: Astrophys. J. **431**, 783 (1994)
Kim, S.-H., Martin, P.G.: Astrophys. J. **444**, 293 (1995)
Kobulnicky, H.A., Molnar, L.A., Jones, T.J.: Astron. J. **107**, 1433 (1994)
Marchwinski, R.C., Pavel, M.D., Clemens, D.P.: Astrophys. J. **755**, 130 (2012)
Mathis, J.S.: Astropys. J. **308**, 281 (1986)
Miville-Deschênes, M.-A., Ysard, N., Lavabre, A., et al.: Astron. Astrophys. **490**, 1093 (2008)
Morris, M., Davidson, J.A., Werner, M., et al.: Astrophys. J. Lett. **399**, L63 (1992)
Myers, P.C., Goodman, A.A.: Astrophys. J. **373**, 509 (1991)
Ostriker, E.C., Stone, J.M., Gammie, C.F.: Astrophys. J. **546**, 980 (2001)
Pascale, E.: IAU Symp. **288**, 154 (2013)
Poidevin, F., Falceta-Gonçalves, D., Kowal, G., de Gouveia Dal Pino, E.M., Magalhães, A.M.: Astrophys. J. **777**, 112 (2013)
Rao, R.: Cosmic Agitator: Magnetic Fields in the Galaxy (2008)
Roberge, W.G.: Polarimetry of the Interstellar Medium, vol. 97, p. 401 (1996)
Serkowski, K., Mathewson, D.S., Ford, V.L.: Astrophys. J. **196**, 261 (1975)
Tauber, J.A.: The Magnetized Interstellar Medium, p. 191 (2004)
Whittet, D.C.B., Hough, J.H., Lazarian, A., Hoang, T.: Astrophys. J. **674**, 304 (2008)

Wiebe, D.S., Watson, W.D.: Astrophys. J. Lett. **549**, L115 (2001)
Wilking, B.A., Lebofsky, M.J., Kemp, J.C., Martin, P.G., Rieke, G.H.: Astrophys. J. **235**, 905 (1980)
Zweibel, E.G.: Astrophys. J. **362**, 545 (1990)
Zweibel, E.G.: Polarimetry of the Interstellar Medium, vol. 97, p. 486 (1996)

Chapter 8
MHD Turbulence, Turbulent Dynamo and Applications

Andrey Beresnyak and Alex Lazarian

Abstract MHD Turbulence is common in many space physics and astrophysics environments. We first discuss the properties of incompressible MHD turbulence. A well-conductive fluid amplifies initial magnetic fields in a process called small-scale dynamo. Below equipartition scale for kinetic and magnetic energies the spectrum is steep (Kolmogorov $-5/3$) and is represented by critically balanced strong MHD turbulence. In this Chapter we report the basic reasoning behind universal nonlinear small-scale dynamo and the inertial range of MHD turbulence. We measured the efficiency of the small-scale dynamo $C_E = 0.05$, Kolmogorov constant $C_K = 4.2$ and anisotropy constant $C_A = 0.63$ for MHD turbulence in high-resolution direct numerical simulations. We also discuss so-called imbalanced or cross-helical MHD turbulence which is relevant for in many objects, most prominently in the solar wind. We show that properties of incompressible MHD turbulence are similar to the properties of Alfvénic part of MHD cascade in compressible turbulence. The other parts of the cascade evolve according to their own dynamics. The slow modes are being cascaded by Alfvénic modes, while fast modes create an independent cascade. We show that different ways of decomposing compressible MHD turbulence into Alfvén, slow and fast modes provide consistent results and are useful in understanding not only turbulent cascade, but its interaction with fast particles.

8.1 Introduction

Historically, most of the turbulence studies were concerned with non-conductive fluids, described by the Navier–Stokes equations. This is because most fluids present on Earth are non-conductive. In the context of a larger Cosmos, this situation is not a rule but rather an exception. Indeed, space is filled with ionizing radiation and only

A. Beresnyak (✉)
Ruhr-Universität Bochum, 44780 Bochum, Germany
e-mail: andrey.at.astro@gmail.com

A. Lazarian
University of Wisconsin-Madison, Madison, WI, USA
e-mail: lazarian@astro.wisc.edu

A. Lazarian et al. (eds.), *Magnetic Fields in Diffuse Media*, Astrophysics and Space Science Library 407, DOI 10.1007/978-3-662-44625-6_8

the protection of our atmosphere, which is very dense by astronomical standards, allows us to have a big volumes of insulating fluids, such as the atmosphere and the oceans. In contrast, most of the ordinary matter in the Universe is ionized, i.e. in a state of plasma. The description of ionized, well-conductive fluids must include the Lorentz force and the induction equation for the magnetic field. As it turned out, turbulent conductive fluids tend to quickly generate their own magnetic fields in the process known as dynamo. On the other hand, the presence of the dynamically important magnetic field could be considered an observational fact. In spiral galaxies magnetic field has a regular component, usually along the arms and a random turbulent component of the same order. The value of the magnetic field, around 5 μG, roughly suggests equipartition between magnetic and kinetic forces.

Observations of magnetized turbulence in the interstellar medium, galaxy clusters and the solar wind have confirmed that turbulence is indeed ubiquitous in astrophysical flows and has been detected in almost all astrophysical and space environments, see, e.g., Goldstein et al. (1995), Armstrong et al. (1995), Chepurnov et al. (2010). The Reynolds numbers of astrophysical turbulence are, typically, very high, owing to astrophysical scales which are enormous compared to dissipative scales. Recent years have been marked by new understanding of the key role that turbulence plays in a number of astrophysical processes (Cho et al. 2003; Elmegreen and Scalo 2004). Most notably, turbulence has drastically changed the paradigms of interstellar medium and molecular cloud evolution (Stone et al. 1998; Ostriker et al. 2001; Vázquez-Semadeni et al. 2007), see also review McKee et al. (2007). While small scale, kinetic turbulence has been probed by a variety of approaches such as gyrokinetics, Hall MHD and electron MHD (Howes et al. 2006; Schekochihin and Cowley 2007; Cho and Lazarian 2004), in this review we concentrate mostly on the fluid-scale MHD turbulence which is the most important for star formation and interaction with cosmic rays.

The theoretical understanding of magnetized turbulence can be roughly subdivided in two big domains: MHD dynamo and the inertial range of MHD turbulence. In the first part of this review we will explain small-scale dynamo, which is fast, universal mechanism to wind up magnetic fields. The second half is devoted to the properties of the inertial range cascades of incompressible and compressible MHD turbulence. In particular we discuss both the spectrum of fundamental MHD modes and the intermittency properties of turbulence. The third part is devoted to applications of our knowledge of MHD cascades, which includes turbulent reconnection, cosmic ray propagation (Beresnyak et al. 2011) and damping of instabilities (Beresnyak and Lazarian 2008).

8.2 Astrophysical Dynamo

One of the central processes of MHD dynamics is how conductive fluid generates its own magnetic field, a process known broadly as “dynamo”. Turbulent dynamo has been subdivided into “large-scale/mean-field dynamo” and “small-scale/fluctuation

dynamo" depending on whether magnetic fields are amplified on scales larger or smaller than outer scale of turbulence.

Although several "no-dynamo" theorems have been proved for flows with symmetries, a generic turbulent flow, which possesses no exact symmetry, was expected to amplify magnetic field by stretching, due to the particle separation in a turbulent flow. For the large-scale dynamo, a "twist-stretch-fold" mechanism was introduced (Vainshtein and Zeldovich 1972). Turbulent flow possessing perfect statistical isotropy can not generate large-scale field, so the observed large-scale fields, such as in the disk galaxies, are generated when statistical symmetries of turbulence are broken by large-scale asymmetries of the system, such as stratification, rotation and shear, see, e.g., Vishniac et al. (2001), Käpylä et al. (2009). Large-scale dynamo is often investigated using so-called mean field theory, see, e.g. Krause and Raedler (1980), where the magnetic and velocity field are decomposed into mean and fluctuating parts and the equations for the mean field are closed using statistical or volume averaging over the fluctuating turbulent part.

The studies of large-scale dynamo are very rich and diverse due to the variety of conditions in astrophysical flows in different objects, one of the most ambitious goals is to explain the solar cycle, see, e.g., Brandenburg and Subramanian (2005). In this review we decided to concentrate on the small-scale dynamo as it is fast and generic and almost always generate magnetic fluctuations with energy of the order of the kinetic energy (so-called equipartition). Magnetic fluctuations could be subsequently ordered by slower large-scale dynamo and produce large-scale magnetic fields. Some objects, such as galaxy clusters, are dominated by small-scale dynamo, however.

Most studied was so-called kinematic regime of small-scale dynamo, which ignores the backreaction of the magnetic field (Kazantsev 1968; Kraichnan and Nagarajan 1967; Kulsrud et al. 1992). However, from these models it was not clear whether magnetic energy will continue to grow after the end of kinematic regime. In astrophysical objects with very large Re it becomes inapplicable at very short timescales. Also magnetic spectrum of kinematic dynamo, possessing positive spectral index, typically 3/2, is incompatible with observations in galaxy clusters (Laing et al. 2008). These observations clearly indicate steep spectrum with negative power index at small scales. In fact, from theoretical viewpoint, kinematic dynamo is inapplicable in most astrophysical environment, because the Alfvén speed is typically many orders of magnitude higher than the Kolmogorov velocity.

The understanding of nonlinear small-scale dynamo was developing slowly and was influenced by analytical kinematic studies. For a long time a popular belief was that after becoming nonlinear the small-scale dynamo will saturate in one way or another. If we assume that the magnetic energy indeed saturates as soon as the dynamo become nonlinear. The saturation level in this case will be $\rho v_\eta^2/2$, where v_η is a Kolmogorov velocity scale. This is a factor of $Re^{-1/2}$ smaller than the kinetic energy density and is completely unimportant in high-Re astrophysical environments. The price tag to discover what will happen in the nonlinear regime was, therefore, fairly high. The early work by Schlüter and Biermann (1950)

suggested that the dynamo will continue to grow and will saturate on each subsequent scale by its dynamical time. The true revival of small-scale dynamo happened relatively recently due to availability of direct numerical simulations. First simulations were concerned with saturated state of small scale dynamo and produced steep spectrum at small scales and significant outer-scale fields, and the saturated state seems to be only weakly dependent on *Re* and *Pr* as long as *Re* is large, see, e.g, Haugen et al. (2004). Furthermore it was suggested in Schekochihin and Cowley (2007), Cho et al. (2009), Ryu et al. (2008), Beresnyak et al. (2009), Beresnyak (2012) that there is a linear growth stage. In subsequent sections we will follow the argumentation of Beresnyak (2012), who provided sufficient analytical and numerical argumentation behind the universality of the nonlinear small-scale dynamo.

8.2.1 Universal Nonlinear Small-Scale Dynamo

We assume that the spectra of magnetic and kinetic energies at a particular moment of time are similar to what is presented on Fig. 8.1. Magnetic and kinetic spectra cross at some "equipartition" scale $1/k^*$, below which both spectra are steep due to MHD cascade (Goldreich et al. 1995; Beresnyak 2011). This assumption is suggested by both numerical evidence (Beresnyak et al. 2009a; Cho et al. 2009) and observations of magnetic fields in clusters of galaxies (Laing et al. 2008). Also, if we start with assuming $Pr = 1$ and magnetic energy very small and follow standard kinematic dynamo calculations, e.g. Kulsrud et al. (1992) the magnetic energy will grow exponentially till the magnetic spectrum intersect kinetic spectrum

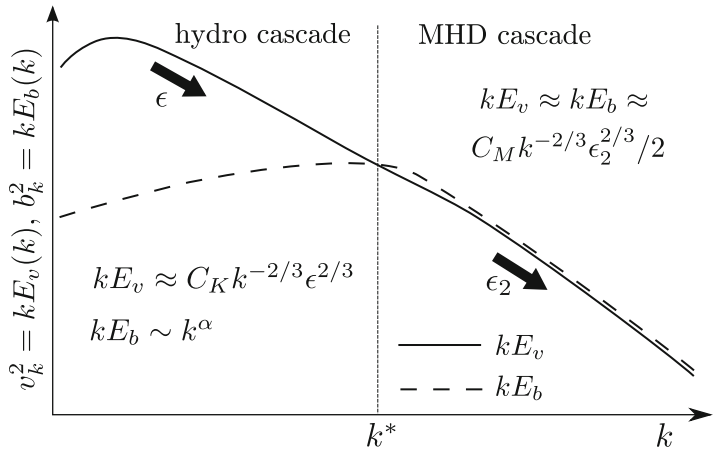

Fig. 8.1 A cartoon of kinetic and magnetic spectra in small-scale dynamo, at a particular moment of time when equipartition wavenumber is k^*

at the viscous scales. This will roughly correspond to the beginning of the nonlinear regime with equipartition scale equal to the dissipation scale.

At larger scales magnetic spectrum is shallow, k^{α}, $\alpha > 0$, while kinetic spectrum is steep due to the hydro cascade. Most of the magnetic energy is concentrated at scale $1/k^*$. We designate C_K and C_M as Kolmogorov constants of hydro and MHD respectively. The hydrodynamic cascade rate is ϵ and the MHD cascade rate as ϵ_2. Due to the conservation of energy in the inertial range, magnetic energy will grow at a rate $\epsilon - \epsilon_2$. We will designate $C_E = (\epsilon - \epsilon_2)/\epsilon$ as an "efficiency of the small-scale dynamo" and will argue that this is a true constant, since: (a) turbulent dynamics is local in scale in the inertial range; (b) neither ideal MHD nor Euler equations contain any scale explicitly. Magnetic energy, therefore, grows linearly with time if $\epsilon = const$. The equipartition scale $1/k^*$ will grow with time as $t^{3/2}$ (Beresnyak et al. 2009). This is equivalent to saying that small-scale dynamo saturates at several dynamical times at scale $1/k^*$ and proceeds to a twice larger scale (Schekochihin and Cowley 2007). If magnetic energy grows approximately till equipartition (Haugen et al. 2004; Cho et al. 2009), the whole process will take around several dynamical timescales of the system, or more quantitatively, $(C_K^{3/2}/C_E)(L/v_L)$.

8.2.2 Locality of the Small-Scale Dynamo

We will use "smooth filtering" approach with dyadic-wide filter in k-space (Aluie and Eyink 2010). We designate a filtered vector quantity as $\mathbf{a}^{[k]}$ where k is a center of a dyadic Fourier filter in the range of wave numbers $[k/2, 2k]$. The actual logarithmic width of this filter is irrelevant to further argumentation, as long as it is not very small. We will assume that the vector field $\mathbf{a}$ is Hölder-continuous, i.e., $|\mathbf{a}(\mathbf{x}) - \mathbf{a}(\mathbf{y})| < |\mathbf{x} - \mathbf{y}|^{\mathbf{h}}$ with exponent $0 < h < 1$ and designate $a_k = \langle |\mathbf{a}^{[k]}|^3 \rangle^{1/3}$ (angle brackets are averages over ensemble), which is expected to scale as $a_k \sim k^{\sigma_3}$, e.g., $k^{-1/3}$ for velocity in Kolmogorov turbulence. The energy cascade rate is $\epsilon = C_K^{-3/2} k v_k^3$, where we defined Kolmogorov constant C_K by third order, rather than second order quantities. We will keep this designation, assuming that traditional Kolmogorov constant could be used instead. We use spectral shell energy transfer functions such as $T_{vv}(p,k) = -\langle \mathbf{v}^{[k]}(\mathbf{v}\cdot\nabla)\mathbf{v}^{[p]} \rangle$, $T_{w^+w^+}(p,k) = -\langle \mathbf{w}^{+[k]}(\mathbf{w}^-\cdot\nabla)\mathbf{w}^{+[p]} \rangle$ Alexakis et al. (2005), applicable to incompressible ideal MHD equations, where $w^{\pm}$ are Elsässer variables and v, b and $w^{\pm}$ are measured in the same Alfvénic units. Using central frequency k and studying "infrared" (IR) transfers from $p \ll k$, and "ultraviolet" (UV) transfers, from $q \gg k$, we will provide absolute bounds on $|T|$, in units of energy transfer rate as in Aluie and Eyink (2010), Eyink (2005), and *relative* volume-averaged bounds which are divided by the actual energy rate and are dimensionless. We will consider three main k intervals presented on Fig. 8.1: $k \ll k^*$ ("hydro cascade"), $k \sim k^*$ ("dynamo") and $k \gg k^*$ ("MHD cascade").

Table 8.1 Transfers and upper limits

Transfers			$p \ll k$	$q \gg k$
$T_{vv}(p,k)$	=	$-\langle \mathbf{v}^{[k]}(\mathbf{v}\cdot\boldsymbol{\nabla})\mathbf{v}^{[p]}\rangle$	$pv_p v_k^2$	$kv_k v_q^2$
$T_{bb}(p,k)$	=	$-\langle \mathbf{b}^{[k]}(\mathbf{v}\cdot\boldsymbol{\nabla})\mathbf{b}^{[p]}\rangle$	$pb_p v_k b_k$	$kb_k v_q b_q$
$T_{vb}(p,k)$	=	$\langle \mathbf{b}^{[k]}(\mathbf{b}\cdot\boldsymbol{\nabla})\mathbf{v}^{[p]}\rangle$	$pv_p b_k^2$	$kb_k v_q b_q$
$T_{bv}(p,k)$	=	$\langle \mathbf{v}^{[k]}(\mathbf{b}\cdot\boldsymbol{\nabla})\mathbf{b}^{[p]}\rangle$	$pb_p v_k b_k$	$kv_k b_q^2$
$T_{w^+w^+}(p,k)$	=	$-\langle \mathbf{w}^{+[k]}(\mathbf{w}^-\cdot\boldsymbol{\nabla})\mathbf{w}^{+[p]}\rangle$	$pw_p w_k^2$	$kw_k w_q^2$

8.2.3 MHD Cascade, $k \gg k^*$

The only energy cascades here are Elsässer cascades and, by the design of our problem, w^+ and w^- have the same statistics, so we will drop $\pm$. For an exchange with $p \ll k$ band, for $|T_{ww}|$, using Hölder inequality and wavenumber conservation we get an upper bound of $pw_p w_k^2$ and for $q \gg k$ band it is $kw_q^2 w_k$, these bounds are asymptotically small. For the full list of transfers and limits refer to Table 8.1. The relative bound should be taken with respect to $C_M^{-3/2} k w_k^3$, where C_M is a Kolmogorov constant for MHD, from which we get that most of the energy transfer with the $[k]$ band should come from $[kC_M^{-9/4}, kC_M^{9/4}]$ band, see Beresnyak (2011). The global transfers between kinetic and magnetic energy must average out in this regime, nevertheless, the pointwise IR and UV transfers can be bounded by $pb_p v_k b_k$ and $kb_q^2 v_k$ and are small (Eyink 2005).

8.2.4 Hydro Cascade, $k \ll k^*$

Despite having some magnetic energy at these scales, most of the energy transfer is dominated by velocity field. Indeed, $|T_{vv}|$ is bounded by $pv_p v_k^2$ for $p \ll k$ and by $kv_q^2 v_k$ for $q \gg k$. Compared to these, $|T_{bv}|$ transfers are negligible: $pb_p v_k b_k$ and $kb_q^2 v_k$. For magnetic energy in $p \ll k$ case we have $|T_{vb}|$ and $|T_{bb}|$ transfers bounded by $pv_p b_k^2$, $pb_p v_k b_k$ and for $q \gg k$ case $|T_{vb}|$ and $|T_{bb}|$ are bounded by $kb_k v_q b_q$. Out of these three expressions the first two go to zero, while the third goes to zero if $\alpha - 2/3 < 0$ or have a maximum at $q = k^*$ if $\alpha - 2/3 > 0$. This means that for the transfer to magnetic energy we have IR locality, but not necessarily UV locality. Note that magnetic energy for $k \ll k^*$ is small compared to the total, which is dominated by $k = k^*$. We will assume that $\alpha - 2/3 > 0$ and that the spectrum of b_k for $k < k^*$ is formed by nonlocal $|T_{vb}|$ and $|T_{bb}|$ transfers from k^*, namely magnetic structures at k are formed by stretching of magnetic field at k^* by velocity field at k. Magnetic spectrum before k^* is, therefore, nonlocal and might not be a power-law, but our further argumentation will only require that $b_k < v_k$ for $k < k^*$.

8.2.5 Dynamo Cascade $k = k^*$

In this transitional regime our estimates of Elsässer UV transfer and kinetic IR transfer from two previous sections will hold. We are interested how these two are coupled together and produce observed magnetic energy growth. IR $p \ll k^*$ $|T_{vb}|$ and $|T_{bb}|$ transfers will be bounded by $pv_p b_{k^*}^2$ and $pb_p v_{k^*} b_{k^*}$, which go to zero, so there is a good IR locality. Ultraviolet transfers will be bounded by $k^* b_{k^*} b_q v_q$. This quantity also goes to zero as q increases, so there is an UV locality for this regime as well. Let us come up with bounds of relative locality. Indeed, the actual growth of magnetic energy was defined as $\epsilon_B = \epsilon - \epsilon_2 = C_E C_K^{-3/2} k v_k^3$. So, $p \ll k^*$ IR bound is $k^* C_E^{3/2} C_K^{-9/4}$ and UV bound is $k^* C_E^{-3/2} C_M^{9/4}$. We conclude that most of the interaction which result in magnetic energy growth must reside in the wavevector interval of $k^*[C_E^{3/2} C_K^{-9/4}, C_E^{-3/2} C_M^{9/4}]$. Numerically, if we substitute $C_K = 1.6$, $C_M = 4.2$, $C_E = 0.05$ we get the interval of $k^*[0.004, 2000]$. So, despite being asymptotically local, small-scale dynamo can be fairly nonlocal in practice.

Summarizing, the kinetic cascade at large scales and the MHD cascade at small scales are dominated by local interactions. The transition between the kinetic cascade and the MHD cascade is also dominated by local interactions, and since ideal MHD equations do not contain any scale explicitly, the efficiency of small-scale dynamo C_E is a true universal constant. Note that C_E relates energy fluxes, not energies, so this claim is unaffected by the presence of intermittency. Magnetic spectrum at $k \ll k^*$ is dominated by nonlocal triads that reprocess magnetic energy from $k = k^*$ but, since this part of the spectrum contains negligible magnetic energy, our universality claim is unaffected by this nonlocality.

8.2.6 Numerical Results

We performed numerical simulations of statistically homogeneous isotropic small-scale dynamo by solving MHD equations with stochastic non-helical driving and explicit dissipation with $Pr_m = 1$. The details of the code and driving are described in detail in our earlier publications (Beresnyak et al. 2009a,b) and Table 8.2 shows simulation parameters. We started each simulation from previously well-evolved

Table 8.2 Three-dimensional MHD dynamo simulations

Run	n	N^3	Dissipation	$\langle\epsilon\rangle$	Re	C_E
M1-6	6	256^3	$-7.6 \cdot 10^{-4} k^2$	0.091	1,000	0.031 ± 0.002
M7-9	3	512^3	$-3.0 \cdot 10^{-4} k^2$	0.091	2,600	0.034 ± 0.004
M10-12	3	$1{,}024^3$	$-1.2 \cdot 10^{-4} k^2$	0.091	6,600	0.041 ± 0.005
M13	1	$1{,}024^3$	$-1.6 \cdot 10^{-9} k^4$	0.182	–	0.05 ± 0.005
M14	1	$1{,}536^3$	$-1.5 \cdot 10^{-15} k^6$	0.24	–	0.05 ± 0.005

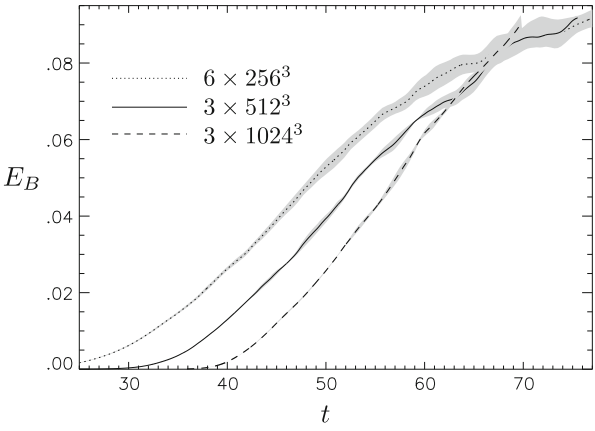

Fig. 8.2 Magnetic energy growth vs. time in code units, observed in simulations M1-6 ($\tau_\eta = 0.091$ in code units), M7-9 ($\tau_\eta = 0.057$) and M10-12 ($\tau_\eta = 0.036$). We used sample averages which greatly reduced fluctuations and allowed us to measure C_E with sufficient precision

driven hydro simulation by seeding low level white noise magnetic field. We ran several statistically independent simulations in each group and obtained growth rates and errors from sample averages. In all simulations, except M14, the energy injection rate was controlled. Figure 8.2 shows sample-averaged time evolution of magnetic energy. Growth is initially exponential and smoothly transition into the linear stage. Note, that scatter is initially small, but grows with time, which is consistent with the picture of magnetic field growing at progressively larger scales and having progressively less independent realizations in a single datacube.

8.2.7 On the Efficiency of Small-Scale Dynamo

Our C_E is much smaller than unity. One would expect a quantity of order unity because this is a universal number, determined only by strong interaction on equipartition scale. If we refer to the ideal incompressible MHD equations, written in terms of Elsässer variables, $\partial_t \mathbf{w}^{\pm} + \hat{S}(\mathbf{w}^{\mp} \cdot \nabla)\mathbf{w}^{\pm} = 0$, the dynamo could be understood as decorrelation of $\mathbf{w}^{\pm}$ which are originally equal to each other in the hydrodynamic cascade. In our case this decorrelation is happening at the equipartition scale $1/k^*$. Being time-dependent, it propagates upscale, while ordinarily energy cascade goes downscale. The small value of C_E might be due to this. As opposed to picture with multiple reversals and dissipation due to microscopic diffusivity, typical for kinematic case, in our picture we appeal to *turbulent diffusion* which helps to create large-scale field. Both stretching and diffusion depend on turbulence at the same designated scale $1/k^*$, so in the asymptotic regime of large Re one of these processes must dominate. As C_E is small, stretching and diffusion are close to canceling each other.

8.3 MHD Turbulence in the Inertial Range

Inertial range of turbulence was introduced by Kolmogorov (1941) as a range of spatial scales where driving and dissipation are unimportant and perturbations exist due to energy transfer from one scale to another. In the inertial range of MHD turbulence perturbations of both velocity and magnetic field will be much smaller than the local Alfvénic velocity $v_A = B/\sqrt{4\pi\rho}$, due to the turbulence spectrum being steeper than k^{-1}, therefore local mean magnetic field will strongly affect dynamics in this range (Iroshnikov 1964; Kraichnan 1965). Furthermore, the large-scale dynamo we mentioned in Sect. 8.2 will operate in such objects as spiral galaxies and provide the mean field for the MHD turbulence in the interstellar medium (ISM).

As in the case of hydrodynamics, the study of MHD turbulence began with weakly compressible and incompressible cases which are directly applicable to many environments, such as stellar interiors, ICM and hot phases of the ISM. Later it was realized that many features of incompressible MHD turbulence are still present even in supersonic dynamics, due to the dominant effect of Alfvénic shearing (Cho and Lazarian 2003; Beresnyak et al. 2005). It had been pointed out by Goldreich et al. (1995) that strong mean field incompressible turbulence is split into the cascade of Alfvénic mode, described by Reduced MHD or RMHD (Kadomtsev and Pogutse 1974; Strauss 1976) and the passive cascade of slow (pseudo-Alfvén) mode. In the strong mean field case it was sufficient to study only the Alfvénic dynamics, as it will determine all statistical properties of turbulence, such as spectrum or anisotropy. This decoupling was also observed in numerics. Luckily, being the limit of very strong mean field, RMHD has a two-parametric symmetry, which we will discuss further in Sect. 8.3.1, which, under certain conditions, makes universal cascade with power-law energy spectrum possible.

Interaction of Alfvénic perturbations propagating in a strong mean field is unusual due to a peculiar dispersion relation of Alfvénic mode, $\omega = k_\parallel v_A$, where $k_\parallel$ is a wavevector parallel to the mean magnetic field. This results in a tendency of MHD turbulence to create "perpendicular cascade", where the flux of energy is preferentially directed perpendicular to the magnetic field. This tendency enhances the nonlinearity of the interaction, described by $\xi = \delta v k_\perp / v_A k_\parallel$, which is the ratio of the mean-field term to the nonlinear term, and results in development of essentially strong turbulence. As turbulence becomes marginally strong, $\xi \sim 1$, the cascading timescales become close to the dynamical timescales $\tau_{\rm casc} \sim \tau_{\rm dyn} = 1/wk_\perp$ and the perturbation frequency ω has a lower bound due to an uncertainty relation $\tau_{\rm casc}\omega > 1$ (Goldreich et al. 1995). This makes turbulence being "stuck" in the $\xi \sim 1$ regime, which is known as "critical balance". There is another lower bound on ω, due to the *directional* uncertainty of the $\mathbf{v}_A$, which was discovered in Beresnyak et al. (2008). In the case of balanced MHD turbulence, which we consider in the next few sections, this two bounds coincide. We consider more general imbalanced case in Sect. 8.4.

Goldreich–Sridhar (1995, henceforth GS95) model is predicting a $k^{-5/3}$ energy spectrum with anisotropy[1] described as $k_\parallel \sim k_\perp^{2/3}$. Numerical studies (Cho et al. 2000, 2002; Maron et al. 2001) confirmed steep spectrum and scale-dependent anisotropy, but (Maron et al. 2001; Müller and Grappin 2005) claimed a shallower than $-5/3$ spectral slope in the strong mean field case, which was close to $-3/2$. This motivated adjustments to the GS95 model (Galtier et al. 2005; Boldyrev 2005; Gogoberidze 2007). A model with so called "dynamic alignment" (Boldyrev 2005, 2006) became popular after the scale-dependent alignment was discovered in numerical simulations (Beresnyak and Lazarian 2006). This model is based on the idea that the alignment between velocity and magnetic perturbations decreases the strength of the interaction scale-dependently, and claims that the alignment goes as $k^{-1/4}$. This would, as they argue, modify the spectral slope of MHD turbulence from the $-5/3$ Kolmogorov slope to the observed $-3/2$ slope. It also claims (Boldyrev 2006) that there is a self-consistent turbulent mechanism that produces such an alignment. Below we examine both the alignment and the spectrum.

8.3.1 Basic Equations

Ideal MHD equations describe the dynamics of ideally conducting inviscid fluid with magnetic field and can be written in Heaviside and $c = 1$ units as

$$\partial_t \rho + \nabla\cdot(\rho \mathbf{v}) = 0, \tag{8.1}$$

$$\rho(\partial_t + \mathbf{v}\cdot\nabla)\mathbf{v} = -\nabla P + \mathbf{j}\times\mathbf{B}, \tag{8.2}$$

$$\nabla\cdot\boldsymbol{B} = 0, \tag{8.3}$$

$$\partial_t \mathbf{B} = \nabla\times(\mathbf{v}\times\mathbf{B}), \tag{8.4}$$

with current $\mathbf{j} = \nabla\times\mathbf{B}$ and vorticity $\boldsymbol{\omega} = \nabla\times\mathbf{v}$. This should be supplanted with energy equation and a prescription for pressure P. The incompressible limit assumes that the pressure is so high that the density is constant and velocity is purely solenoidal ($\nabla\cdot\mathbf{v} = 0$). This does not necessarily refer to the ratio of outer scale kinetic pressure to molecular pressure, but could be interpreted as scale-dependent condition. Indeed, if we go to the frame of the fluid, local perturbations of velocity will diminish with scale and will be much smaller than the speed of sound. In this situation it will be possible to decompose velocity into low-amplitude sonic waves and essentially incompressible component of $\mathbf{v}$, as long as we are not in the vicinity

[1]The anisotropy should be understood in terms of local magnetic field direction, i.e. the magnetic field direction at the given scale. The original treatment, e.g. the closure relations employed, in the Goldreich–Sridhar paper uses the global frame of reference which was noticed later in Lazarian et al. (1999) and used in the numerical works that validated the theory (Cho et al. 2000, 2002; Maron et al. 2001).

of a shock. The incompressible component, bound by $\nabla\cdot\mathbf{v} = 0$, will be described by much simpler equations:

$$\partial_t \mathbf{v} = \hat{S}(-\boldsymbol{\omega}\times\mathbf{v} + \mathbf{j}\times\mathbf{b}), \tag{8.5}$$

$$\partial_t \mathbf{b} = \nabla\times(\mathbf{v}\times\mathbf{b}), \tag{8.6}$$

where we renormalized magnetic field to velocity units $\mathbf{b} = \mathbf{B}/\rho^{1/2}$ (the absence of 4π is due to Heaviside units) and used solenoidal projection operator $\hat{S} = (1 - \nabla\Delta^{-1}\nabla)$ to get rid of pressure. Finally, in terms of Elsässer variables $\mathbf{w}^{\pm} = \mathbf{v} \pm \mathbf{b}$ this could be rewritten as

$$\partial_t \mathbf{w}^{\pm} + \hat{S}(\mathbf{w}^{\mp}\cdot\nabla)\mathbf{w}^{\pm} = 0. \tag{8.7}$$

This equation resembles incompressible Euler's equation. Indeed, hydrodynamics is just a limit of $b = 0$ in which $\mathbf{w}^{+} = \mathbf{w}^{-}$. This resemblance, however, is misleading, as the local mean magnetic field could not be excluded by the choice of reference frame and, as we noted earlier, will strongly affect dynamics on all scales. We can explicitly introduce local mean field as $\mathbf{v_A}$, assuming that it is constant, so that $\delta\mathbf{w}^{\pm} = \mathbf{w} \pm \mathbf{v}_A$:

$$\partial_t \boldsymbol{\delta}\mathbf{w}^{\pm} \mp (\mathbf{v_A}\cdot\nabla)\delta\mathbf{w}^{\pm} + \hat{S}(\delta\mathbf{w}^{\mp}\cdot\nabla)\delta\mathbf{w}^{\pm} = 0. \tag{8.8}$$

In the linear regime of small δw's they represent perturbations, propagating along and against the direction of the magnetic field, with nonlinear term describing their interaction. As we noted earlier, due to the resonance condition of Alfvénic perturbations they tend to create more perpendicular structure, making MHD turbulence progressively more anisotropic. This was empirically known from tokamak experiments and was used in so-called reduced MHD approximation, which neglected parallel gradients in the nonlinear term (Kadomtsev and Pogutse 1974; Strauss 1976). Indeed, if we denote $\parallel$ and $\perp$ as directions parallel and perpendicular to $\mathbf{v}_A$, the mean field term $(v_A\nabla_{\parallel})\delta w^{\pm}$ is much larger than $(\delta w_{\parallel}^{\mp}\nabla_{\parallel})\delta w^{\pm}$ and the latter could be ignored in the inertial range where $\delta w^{\pm} \ll v_A$. This will result in Eq. (8.8) being split into

$$\partial_t \boldsymbol{\delta}\mathbf{w}_{\parallel}^{\pm} \mp (\mathbf{v_A}\cdot\nabla_{\parallel})\delta\mathbf{w}_{\parallel}^{\pm} + \hat{S}(\delta\mathbf{w}_{\perp}^{\mp}\cdot\nabla_{\perp})\delta\mathbf{w}_{\parallel}^{\pm} = 0, \tag{8.9}$$

$$\partial_t \boldsymbol{\delta}\mathbf{w}_{\perp}^{\pm} \mp (\mathbf{v_A}\cdot\nabla_{\parallel})\delta\mathbf{w}_{\perp}^{\pm} + \hat{S}(\delta\mathbf{w}_{\perp}^{\mp}\cdot\nabla_{\perp})\delta\mathbf{w}_{\perp}^{\pm} = 0, \tag{8.10}$$

which, physically represent a limit of very strong mean field where $\boldsymbol{\delta}\mathbf{w}_{\parallel}^{\pm}$ is a slow (pseudo-Alfvén) mode and $\boldsymbol{\delta}\mathbf{w}_{\perp}^{\pm}$ is the Alfvén mode and Eq. (8.9) describes a passive dynamics of slow mode which is sheared by the Alfvén mode, while Eq. (8.10) describes essentially nonlinear dynamics of the Alfvén mode and is known as reduced MHD. For our purposes, to figure out asymptotic behavior in the inertial range, it is sufficient to study Alfvénic dynamics and slow mode can be always added later, because it will have the same statistics.

It turns out that reduced MHD is often applicable beyond incompressible MHD limit, in a highly collisionless environments, such as tokamaks or the solar wind. This is due to the fact that Alfvén mode is transverse and does not require pressure support. Indeed, Alfvénic perturbations rely on magnetic tension as a restoring force and it is sufficient that charged particles be tied to magnetic field lines to provide inertia (Schekochihin et al. 2009).

A remarkable property of RMHD is that it has a precise two-parametric symmetry: $\mathbf{w} \rightarrow \mathbf{w}A,\ \lambda \rightarrow \lambda B,\ t \rightarrow tB/A,\ \Lambda \rightarrow \Lambda B/A$. Here λ is a perpendicular scale, Λ is a parallel scale, A and B are arbitrary parameters of the transformation. This is similar to the symmetry in Euler equation ($\mathbf{B} = \mathbf{0}$ limit of MHD), except for a different prescription for parallel scale Λ which now scales as time. It is due to this precise symmetry and the absence of any designated scale, that we can hypothesize universal regime, similar to hydrodynamic cascade of Kolmogorov (1941). In nature, the universal regime for MHD can be achieved with $\delta w^{\pm} \ll v_A$. In numerical simulations, we can directly solve RMHD equations, which have precise symmetry already built in. From practical viewpoint, the statistics from the full MHD simulation with $\delta w^{\pm} \sim 0.1 v_A$ is virtually indistinguishable from RMHD statistics and even $\delta w^{\pm} \sim v_A$ is still fairly similar to the strong mean field case (Beresnyak et al. 2009b).

8.3.2 Basic Scalings in the Balanced Case

As was shown in a rigorous perturbation study of weak MHD turbulence, it has a tendency of becoming *stronger* on smaller scales (Galtier et al. 2000). Indeed, if $k_{\parallel}$ is constant and $k_{\perp}$ is increasing, $\xi = \delta w k_{\perp}/v_A k_{\parallel}$ will increase, due to $\delta w \sim k_{\perp}^{-1/2}$ in this regime. This will naturally lead to strong turbulence, where ξ will stuck around unity due to two competing processes: (1) increasing interaction by perpendicular cascade and (2) decrease of interaction due to the uncertainty relation $\tau_{\rm casc}\omega > 1$, where $\tau_{\rm casc}$ is a cascading timescale. Therefore, MHD turbulence will be always marginally strong in the inertial range, which means that cascading timescale is associated with dynamical timescale $\tau_{\rm casc} \sim \tau_{\rm dyn} = 1/\delta w k_{\perp}$ (Goldreich et al. 1995). In this case, assuming that energy transfer is local in scale and, therefore, depend only on perturbations amplitude on each scale, we can write Kolmogorov-type phenomenology as

$$\epsilon^{+} = \frac{(\delta w_{\lambda}^{+})^2 \delta w_{\lambda}^{-}}{\lambda}, \quad \epsilon^{-} = \frac{(\delta w_{\lambda}^{-})^2 \delta w_{\lambda}^{+}}{\lambda}, \tag{8.11}$$

where $\epsilon^{\pm}$ is an energy flux of each of the Elsässer variables and $\delta w_{\lambda}^{\pm}$ is a characteristic perturbation amplitude on a scale λ. Such an amplitude can be obtained by Fourier filtering with a dyadic filter in k-space, see, e.g., Beresnyak (2012).

Since we consider so-called balanced case with both w's having the same statistical properties and energy fluxes, one of these equations is sufficient. This will result in a $\delta w \sim \lambda^{1/3}$, where λ is a perpendicular scale, or, in terms of energy spectrum $E(k)$,

$$E(k) = C_K \epsilon^{2/3} k^{-5/3}, \tag{8.12}$$

where C_K is known as Kolmogorov constant. We will be interested in Kolmogorov constant for MHD turbulence. This scaling is supposed to work until dissipation effects kick in. In our further numerical argumentation dissipation scale will play a big role, but not from a physical, but rather from a formal point of view. We will introduce an idealized scalar dissipation term in a RHS of Eq. (8.7) as $-\nu_n(-\nabla^2)^{n/2}\mathbf{w}^{\pm}$, where n is an order of viscosity and $n = 2$ correspond to normal Newtonian viscosity, while for $n > 2$ it is called hyperviscosity. The dissipation scale for this GS95 model is the same as the one for Kolmogorov model, i.e. $\eta = (\nu_n^3/\epsilon)^{1/(3n-2)}$. This is a unique combination of ν_n and ϵ that has units of length. Note that Reynolds number, estimated as vL/ν_2, where L is an outer scale of turbulence, is around $(L/\eta)^{4/3}$.

Furthermore, the perturbations of w will be strongly anisotropic and this anisotropy can be calculated from the critical balance condition $\xi \approx 1$, so that $k_\parallel \sim k_\perp^{2/3}$. Interestingly enough this could be obtained directly from units and the symmetry of RMHD equations from above. Indeed, in the RMHD limit, $k_\parallel$ or $1/\Lambda$ must be in a product with v_A, since only the product enters the original RMHD equations. We already assumed above that turbulence is local and each scale of turbulence has no knowledge of other scales, but only the local dissipation rate ϵ. In this case the only dimensionally correct combination for the parallel scale Λ, corresponding to perpendicular scale λ is

$$\Lambda = C_A v_A \lambda^{2/3} \epsilon^{-1/3}, \tag{8.13}$$

where we introduced a dimensionless "anisotropy constant" C_A. Equations (8.12) and (8.13) roughly describe the spectrum and anisotropy of MHD turbulence. Note, that GS95's $-5/3$ is a basic scaling that should be corrected for intermittency. This correction is negative due to structure function power-law exponents being a concave function of their order (Frisch 1995) and is expected to be small in three-dimensional case. This correction for hydrodynamic turbulence is around -0.03. Such a small deviation should be irrelevant in the context of debate between $-5/3$ and $-3/2$, which differ by about 0.17.

A modification of the GS95 model was proposed by Boldyrev (2005, 2006, henceforth B06) who suggested that the original GS95 scalings can be modified by a scale dependent factor that decreases the strength of the interaction, so that RHS of the Eq. (8.11) is effectively multiplied by a factor of $(l/L)^{1/4}$, where L is an outer scale. In this case the spectrum will be expressed as $E(k) = C_{K2}\epsilon^{2/3}k^{-3/2}L^{1/6}$. Note that this spectrum is the only dimensionally correct spectrum with $k^{-3/2}$

scaling, which does not contain dissipation scale η. The absence of L/η, is due to so-called zeroth law of turbulence which states that the amplitude at the outer scale should not depend on the viscosity. This law follows from the locality of energy transfer has been know empirically to hold very well. The dissipation scale of B06 model is different from that of the GS95 model and can be expressed as $\eta' = (v_n^3/\epsilon)^{1/(3n-1.5)} L^{0.5/(3n-1.5)}$.

8.3.3 Structure Functions and Spectra

Structure and correlation functions (SF and CF) has been traditionally used in turbulence research for a long time. In theory these are quantities statistically averaged over ensemble, while in numerics the averaging is usually over time and volume using homogeneity and stationarity. The typical quantity people use in isotropic hydrodynamic turbulence is an isotropic second order structure function of velocity:

$$SF^2(l) = \langle (v(\mathbf{r}-\mathbf{l}) - v(\mathbf{r}))^2 \rangle_{\mathbf{r}}. \tag{8.14}$$

This is a difference in velocity between two points separated by vector $\mathbf{l}$, squared and averaged over the volume, i.e. the vector $\mathbf{r}$. This quantity could be represented by the sum of the "longitudinal" and "transverse" components with velocity decomposed into a direction perpendicular and parallel to $\mathbf{l}$. The longitudinal structure function is important in experimental research of hydrodynamic turbulence, since this is the primary quantity measured by the heated wire technique.

MHD turbulence is not isotropic, therefore, there is a wider variety of structure functions that one can possibly measure. However, in the RMHD limit there is a particular structure function which plays the similar role as the isotropic SF in hydrodynamics, the perpendicular SF

$$SF_\perp^2(l) = \langle (w^\pm(\mathbf{r} - l\,\mathbf{n}) - w^\pm(\mathbf{r}))^2 \rangle_{\mathbf{r}}, \tag{8.15}$$

where $\mathbf{n}$ is a vector perpendicular to the magnetic field. Power spectra, on the other hand, are produced by obtaining a Fourier transform $\hat{\mathbf{v}}(\mathbf{k})$ of original quantity $\mathbf{v}(\mathbf{r})$ and taking the product $\frac{1}{2}\mathbf{v_i}(\mathbf{k})\mathbf{v_i^*}(\mathbf{k})$, where $*$ is a complex conjugate. Relations between spectra and structure functions are well-known, see, e.g. Monin and Iaglom (1975).

A number of exact relations for structure functions are known both for hydro and MHD, see, e.g., Biskamp (2003). The famous Kolmogorov $-4/5$ law relates a parallel signed structure function for velocity in the inertial range with the dissipation rate:

$$SF_{3\|h}(l) = \langle (\delta v_{l\|})^3 \rangle = -\frac{4}{5}\epsilon l. \tag{8.16}$$

Another exact relation, similar to the Yaglom's $-4/3$ law for incompressible hydro exists for axially symmetric MHD turbulence:

$$SF_{3\|}(l) = \langle \delta w_{l\|}^{\mp} (\delta w_l^{\pm})^2 \rangle = -2\epsilon l, \tag{8.17}$$

where l is taken perpendicular to the axis of statistical symmetry—the direction of the mean magnetic field **B** (Politano and Pouquet 1998). One can measure SFs above and argue about influence of dissipation and driving in each particular simulation. Figure 8.3 shows several structure functions, compensated by various powers of l and the ratio of parallel third order structure function and full third order SF, $SF_3 = \langle |v(\mathbf{r}-\mathbf{l}) - v(\mathbf{r})|^3 \rangle$.

Normally, the inertial range in a simulation is defined as a range of scales where $-SF_{3\|}/l$ is closest to its theoretical value, i.e. the influence of energy injection from driving and energy dissipation from viscous term is minimized. Another test for the inertial range is the test for turbulence self-similarity, in particular one can take the above ratio of the unsigned and signed third order SFs. This ratio must be constant as long as turbulence is self-similar. Figure 8.3 shows that hydrodynamic turbulence is rather self-similar and the scaling of the second-order structure function in the inertial range is around $l^{0.7}$, i.e. close to the Kolmogorov scaling. In the MHD simulation the self-similarity is broken and although one can argue that the scaling is closer to the $l^{2/3}$ in the point where $-SF_{3\|}/l\epsilon$ is closest to its theoretical value of 2, claiming a certain scaling based on these data would be an overstatement. In the

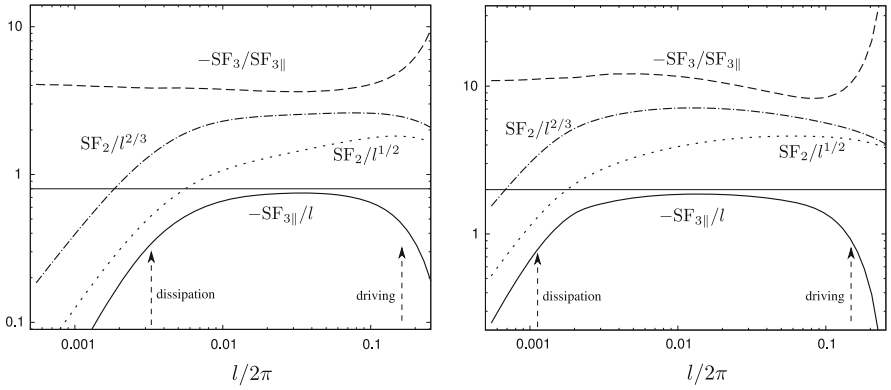

Fig. 8.3 Different structure functions vs the distance l, measured in hydrodynamic (*left*) and MHD (*right*) simulations. *Solid lines* show $-SF_{3\|}/l\epsilon$. The influence of driving and dissipation is minimized in the point where $-SF_{3\|}/l\epsilon$ is closer to its theoretical value. The *dashed line* indicates the ratio of the third order SF, defined in the text to the parallel third order SF. This ratio is a test for turbulence self-similarity, as long as this ratio is constant, the turbulence is well self-similar. Finally, *dotted and dash-dotted lines* indicate the same second order structure functions, compensated by $l^{1/2}$ and $l^{2/3}$ correspondingly, in arbitrary units. Here $l^{2/3}$ is the Richardson–Kolmogorov scaling and $l^{1/2}$ is the scaling that appears in Kraichnan DIA model for hydrodynamics, Iroshnikov–Kraichnan model for MHD and B06 model

next section we will describe a rigorous method to claim a certain scaling based on numerical convergence in a series of simulations.

Power spectra are the measures, complimentary to second order structure functions. In particular, so-called one-dimensional power spectrum P_k is a Fourier transform of the SF_2. This function is popular in the satellite measurements of the solar wind turbulence, where a particular quantity, $\mathbf{v}$ or $\mathbf{B}$ is measured as a function of time. It is then interpreted as an instant measurement along a line in a turbulent realization (so-called Taylor hypothesis). The power spectra from many samples like this are averaged to obtain P_k for either velocity or magnetic field. Another experimental measure is the so-called parallel power spectrum $P_{\|k}$. It is obtained in the measurements of hydrodynamic turbulence by heated wire technique. A scalar quantity is measured in this technique, which is the velocity perturbation parallel to the average flow velocity. Similarly this is interpreted as a measurement in space by using Taylor frozen flow hypothesis. Finally, there is a power spectrum favored by numerics, which is a three-dimensional spectrum $E(k)$. This spectrum is obtained from full three-dimensional power spectrum $\frac{1}{2}\mathbf{v}(\mathbf{k})\cdot\mathbf{v}^*(\mathbf{k})$ by integrating over the solid angle in $\mathbf{k}$ space, so that $E(k)$ is only a function of scalar k. In statistically isotropic hydro and MHD turbulence the integration is in spherical shells, while in RMHD, the parallel wavenumber is infinitely small compared to other wavenumbers, so the integration is, effectively, along all $k_\|$ and the circle in $\mathbf{k}_\perp$ space, i.e. the isotropic spectrum is equivalent to the perpendicular spectrum. Three spectra $P(k)$, $P_\|(k)$ and $E(k)$ of the solenoidal vector field are related by the following expressions, see, e.g., Monin and Iaglom (1975):

$$P(k) = \int_k^\infty E(k_1)\frac{dk_1}{k_1}, \tag{8.18}$$

$$P_\|(k) = \int_k^\infty E(k_1)\left(1-\frac{k^2}{k_1^2}\right)\frac{dk_1}{k_1}, \tag{8.19}$$

Figure 8.4 shows three types of spectra from the simulation. The primary spectrum was E_k and the two other spectra were calculated by the above expressions. All three spectra have different shapes. If one would want to claim a particular scaling by qualitatively estimating the scaling from numerical spectrum, the estimate will depend on the type of the spectrum and the chosen range of k used for fitting the scaling. Based on Fig. 8.4 one can claim any spectral slope between $-5/3$ and $-3/2$. This further reiterates the need of rigorous quantitative measurement based on numerical convergence, presented in the next section.

8.3.4 The Numerical Scaling Argument

As was noted before, turbulence with very long range of scales is common in astrophysics. Numerics, however, is not only unable to reproduce such range, but

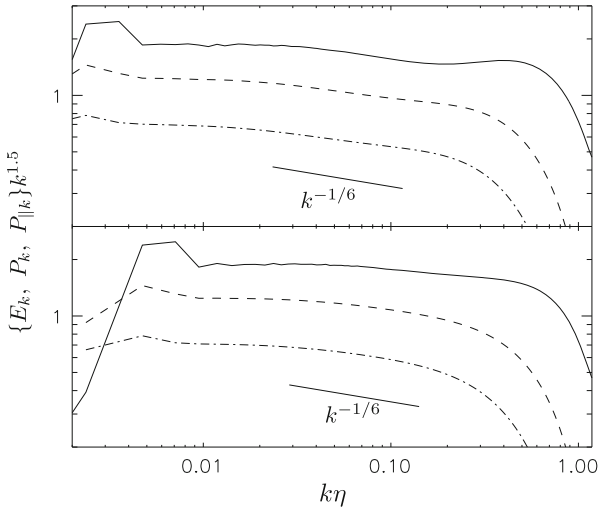

Fig. 8.4 Three types of spectra from a numerical simulations R1, R4. E_k—*solid*, P_k—*dashed*, $P_{\|k}$—*dash-dotted*. In a simulation with limited resolution all three spectra have different shapes

actually struggles to obtain any good "inertial range". In this situation a rigorous quantitative arguments have to be invented to investigate asymptotic scalings.

Suppose we performed several simulations with different Reynolds numbers. If we believe that turbulence is universal, and the scale separation between forcing scale and dissipation scale is large enough, the properties of small scales should not depend on how turbulence was driven and on the scale separation itself. This is because neither MHD nor hydrodynamic equations explicitly contain any scale, so simulation with a smaller dissipation scale could be considered, due to symmetry from above, as a simulation with the same dissipation scale, but larger driving scale. For example, the small scale statistics in a $1{,}024^3$ simulation should look the same as small-scale statistics in 512^3, if the physical size of the elementary cell is the same and the dissipation scale is the same. Naturally, this scaling argument in numerics require that the geometry of the elementary cells are the same and the actual numerical scheme used to solve the equations is the same. Also, numerical equations should not contain any scale explicitly, but this is normally satisfied. What scaling argument does not require is a high precision on the dissipation scale or a particular form of dissipation, whether explicit or numerical. This is because we need that the statistics on small scales is similar in two simulations, which is the case when numerics is the same on dissipation scale and the influence of the outer scale is small by assumption of turbulence locality.

In practice the scaling argument or a resolution study is done in a following way: the averaged spectra in two simulations are expressed in dimensionless units corresponding to the expected scaling, for example a $E(k)k^{5/3}\epsilon^{-2/3}$ is used for hydrodynamics, and plotted versus dimensionless wavenumber $k\eta$, where

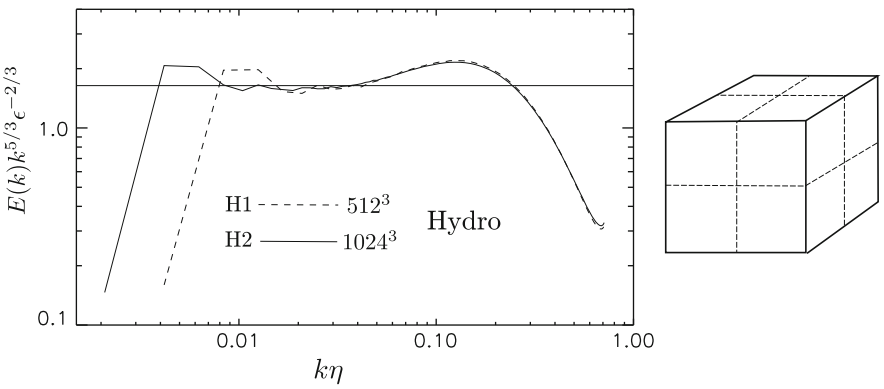

Fig. 8.5 The spectra from hydrodynamic simulations illustrate the numerical scaling argument. The large cube on the *right* can be split into smaller cubes with the same small scale statistics. Therefore as long as turbulence is scale-local and the effects of large scales could be neglected, the smaller simulation demonstrate the same statistics, as evident from convergence of dimensionless spectra on the *left*

dissipation scale η correspond to the same model, e.g. $\eta = (\nu^3/\epsilon)^{1/4}$ is used for scalar second order viscosity ν and Kolmogorov phenomenology. Plotted this way the two spectra should collapse onto the same curve on the viscous scales, see, e.g., Fig. 8.5. This method has been used in hydrodynamics since long time ago, see, e.g., Yeung and Zhou (1997), Gotoh et al. (2002), Kaneda et al. (2003). Although for hydrodynamics good convergence on the dissipation scale has been observed starting with rather moderate resolutions, which signifies that hydrodynamic cascade has good, narrow locality, the larger the resolution, the better the convergence should be. Note that in Kaneda et al. (2003), which had very high resolution even the intermittency correction to the spectrum has been captured. So, the optimal strategy for MHD would be to perform the largest resolution simulations possible and do a resolution study with particular models in mind.

8.3.5 *Numerical Experiments*

We will briefly explain the numerical setup and methods used in Beresnyak et al. (2009b,a), Beresnyak and Lazarian (2010), Beresnyak (2011, 2012). For further detail the reader is referred to these publications. We used pseudospectral dealiased code to solve RMHD equations. Same code was used earlier for RMHD, incompressible MHD and incompressible hydrodynamic simulations. The RHS of Eq. (8.10) was complemented by an explicit dissipation term $-\nu_n(-\nabla^2)^{n/2}\mathbf{w}^{\pm}$ and forcing term $\mathbf{f}$. Diffusive terms with $n = 2$ are referred to as normal viscosity and with $n > 2$ are referred to as hyperviscosity. Table 8.3 shows the parameters of the balanced simulations. The Kolmogorov scale is defined as $\eta = (\nu_n^3/\epsilon)^{1/(3n-2)}$,

Table 8.3
Three-dimensional RMHD balanced simulations

Run	$n_x \cdot n_y \cdot n_z$	Dissipation	$\langle\epsilon\rangle$	L/η
R1	$256 \cdot 768^2$	$-6.82 \cdot 10^{-14} k^6$	0.073	200
R2	$512 \cdot 1536^2$	$-1.51 \cdot 10^{-15} k^6$	0.073	400
R3	$1024 \cdot 3072^2$	$-3.33 \cdot 10^{-17} k^6$	0.073	800
R4	768^3	$-6.82 \cdot 10^{-14} k^6$	0.073	200
R5	1536^3	$-1.51 \cdot 10^{-15} k^6$	0.073	400
R6	$384 \cdot 1024^2$	$-1.70 \cdot 10^{-4} k^2$	0.081	280
R7	$768 \cdot 2048^2$	$-6.73 \cdot 10^{-5} k^2$	0.081	560
R8	768^3	$-1.26 \cdot 10^{-4} k^2$	0.073	350
R9	1536^3	$-5.00 \cdot 10^{-5} k^2$	0.073	700

the integral scale $L = 3\pi/4E \int_0^\infty k^{-1} E(k)\, dk$ (which was approximately 0.79 for R1-3). Dimensionless ratio L/η could serve as a "length of the spectrum", although spectrum is actually significantly shorter for n=2 viscosity and somewhat shorter for n=6 hyperviscosity.

Since we would like to use this review to illustrate the resolution study argument we used a variety of resolution, dissipation and driving schemes. There are four schemes, presented in Table 8.2, and used in simulations R1-3, R4-5, R6-7 and R8-9. In some of the simulations the resolution in the direction parallel to the mean magnetic field, n_x, was reduced by a factor compared to perpendicular resolution. This was deemed possible due to an empirically known lack of energy in the parallel direction in k-space and has been used before (Müller and Grappin 2005). The R4-5 and R8-9 groups of simulations were fully resolved in parallel direction. One would expect that roughly the same resolution will be required in parallel and perpendicular direction (Beresnyak et al. 2009b). In all simulation groups time step was strictly inversely proportional to the resolution, so that we can utilize the scaling argument.

Driving had a constant energy injection rate for all simulations except R6-7, which had fully stochastic driving. All simulations except R8-9 had Elsässer driving, while R8-9 had velocity driving. All simulations were well-resolved and R6-7 were over resolved by a factor of 1.6 in scale (a factor of 2 in Re). The anisotropy of driving was that of a box, while injection rate was chosen so that the amplitude was around unity on outer scale, this roughly corresponds to critical balance on outer scale. Indeed, as we will show in subsequent section, since anisotropy constant is smaller than unity, our driving with $\lambda \sim \Lambda \sim 1$ and $\delta w \sim 1$ on outer scale is somewhat over-critical, so Λ decreases after driving scale to satisfy uncertainty relation (see Fig. 8.9). This is good for maintaining critical balance over wide range of scales as it eliminates possibility for weak turbulence.

In presenting four groups of simulations, with different geometries of elementary cell, different dissipation terms and different driving, our intention is to show that the scaling argument works irrespective of numerical effects, but rather relies on scale separation and the assumption of universal scaling. Simulations R1-3 are the same as those presented in Beresnyak (2011).

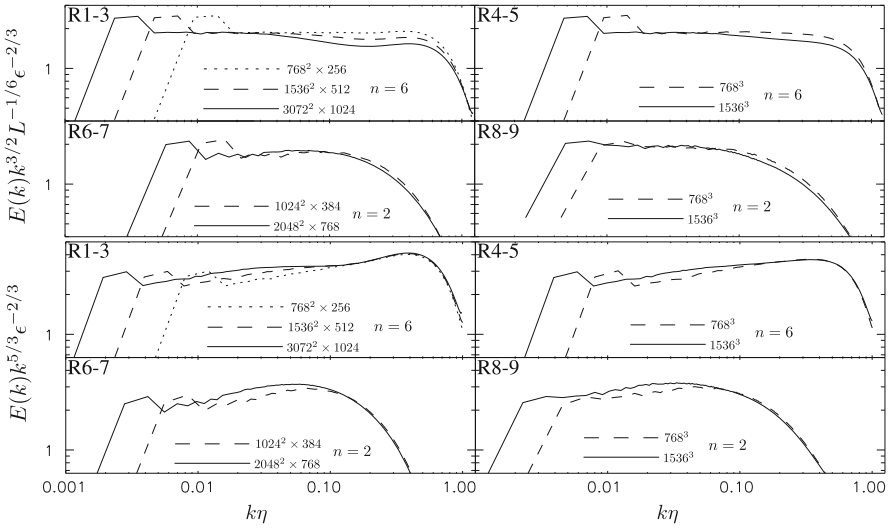

Fig. 8.6 Numerical convergence of spectra in all simulations. Two *upper rows* are used to study convergence assuming B06 model and two *bottom rows*—assuming GS95 model. Note that definition of dissipation scale η depends on the model, this difference is tiny in hyperviscous simulations R1-5, but significant in viscous simulations R6-9. Numerical convergence require that spectra will be similar on small scales, including the dissipation scale, see, e.g. Gotoh et al. (2002). As we see from the plots, numerical convergence is absent for B06 model. For GS95 model the convergence is reached only at the dissipation scale. Higher-resolution simulations are required to demonstrate convergence in the inertial range

8.3.6 Resolution Study for Balanced Spectra

Figure 8.6 presents a resolution study all simulations. The upper rows assume B06 scaling, while the bottom rows assume GS95 scaling. Reasonable convergence on small scales was achieved only for GS95 scaling. The normalized amplitude at the dissipation scale for two upper rows of plots systematically goes down with resolution, suggesting that $-3/2$ is not an asymptotic scaling. The flat part of the normalized spectrum on R1-3 plots was fit to obtain Kolmogorov constant of $C_{KA} = 3.27 \pm 0.07$ which was reported in Beresnyak (2011). The total Kolmogorov constant for both Alfvén and slow mode in the above paper was estimated as $C_K = 4.2 \pm 0.2$ for the case of isotropically driven turbulence with zero mean field, where the energy ratio of slow and Alfvén mode C_s is between 1 and 1.3. This larger value $C_K = C_{KA}(1 + C_s)^{1/3}$ is due to slow mode being passively advected and not contributing to nonlinearity. The measurement of C_{KA} had relied on an assumption that the region around $k\eta \approx 0.07$ represent asymptotic regime. Recently, we performed simulations with resolution up to $4{,}096^3$, which also confirmed the $-5/3$ spectrum (Beresnyak 2014). Furthermore, it appears from these simulations that the residual energy, $E_B - E_v$ have the same spectral slope as the total energy, i.e.

there is a constant fraction of residual energy in the inertial range. This fraction was measured in Beresnyak (2014) to be around 0.15. Previously, the most popular model (Müller and Grappin 2005) suggested that the spectrum of the residual energy follows k^{-2} scaling, which is problematic both conceptually and theoretically. We confirmed that the residual energy is a fraction of the total energy in the inertial range and made explanations suggesting different scalings for magnetic and kinetic energies unnecessary.

8.3.7 Dynamic Alignment: Theories vs Measurements

Recent simulations, as we discussed earlier, support GS95 model and therefore it can be considered correct in the zeroth approximation. However, we are far from believing that we understand all the effects of MHD turbulence. For instance, it is not clear how different alignment effects that we considered in Sect. 8.3.6 may affect the basic properties of MHD turbulence at the limited range of scales when they exhibit scale-dependent properties.

An attempt to construct a model for such a behavior taking into account *DA* was done in Boldyrev (2005). There it was proposed that $\mathbf{w}^+$ and $\mathbf{w}^-$ eddies are systematically aligned and therefore, GS95 model should be amended and the inertial range scaling should be modified. As we discussed earlier, this suggestion is not supported by either resolution studies or studies of the alignment/polarization effects that we performed. For instance, the original alignment idea was investigated numerically in Beresnyak and Lazarian (2006) and no significant alignment was found for the averaged angle between $\mathbf{w}^+$ and $\mathbf{w}^-$, $AA = \langle|\delta\mathbf{w}^+_\lambda \times \delta\mathbf{w}^-_\lambda|/|\delta\mathbf{w}^+_\lambda||\delta\mathbf{w}^-_\lambda|\rangle$, but when this angle was weighted with the amplitude $PI = \langle|\delta\mathbf{w}^+_\lambda \times \delta\mathbf{w}^-_\lambda|\rangle/\langle|\delta\mathbf{w}^+_\lambda||\delta\mathbf{w}^-_\lambda|\rangle$, some alignment was found. Later Boldyrev (2006) proposed the alignment between $\mathbf{v}$ and $\mathbf{b}$ and Mason et al. (2006) suggested a particular amplitude-weighted measure, $DA = \langle|\delta\mathbf{v}_\lambda \times \delta\mathbf{b}_\lambda|\rangle/\langle|\delta\mathbf{v}_\lambda||\delta\mathbf{b}_\lambda|\rangle$. We note that *DA* is similar to PI but contain two effects: alignment and local imbalance. The latter could be measured with $IM = \langle|\delta(w^+_\lambda)^2 - \delta(w^-_\lambda)^2|\rangle/\langle\delta(w^+_\lambda)^2 + \delta(w^-_\lambda)^2\rangle$, (Beresnyak et al. 2009a).

In this section we check the assertion of Boldyrev (2005, 2006) that alignment depends on scale as $\lambda^{1/4}$, by using *DA* which is, by some reason, favored by aforementioned group. We did a resolution study of *DA*, assuming suggested scaling, which is presented on Fig. 8.7. Convergence was absent in all simulations. It appears that the claims of Boldyrev (2006) were not substantiated by a proper resolution study. In general, a result from a single isolated simulation could be easily contaminated by the effects of outer scale, since it is not known a-priori how local MHD turbulence is and what resolution is sufficient to get rid of such effects. On the contrary, the resolution study offers a systematic approach to this problem.

Figure 8.7 also shows "dynamic alignment" slope for all simulations. Although there similar to the previous plot there is no convergence, it is interesting to note that alignment slope decreases with resolution. This suggests that most likely the asymptotic state for the alignment slope is zero, i.e. alignment is scale-independent

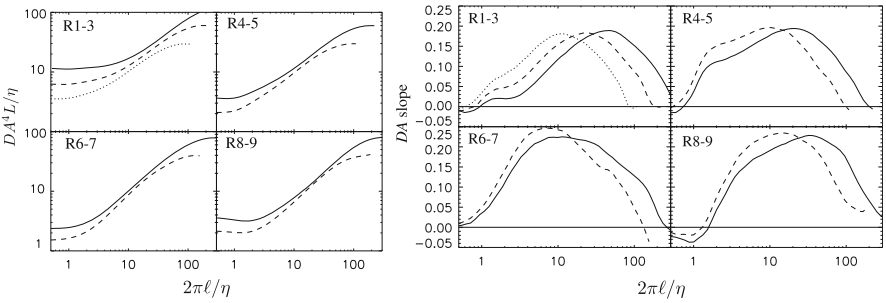

Fig. 8.7 *Left*: resolution study for "dynamic alignment", assuming B06 scaling. Both axis are dimensionless, solid is higher resolution and *dashed* is lower resolution. Convergence is absent for all simulations. This suggests that $l^{0.25}$ is not a universal scaling for alignment. *Right*: *DA* slope, defined as $l/DA\partial DA/\partial l$, solid is higher resolution and *dashed* is lower resolution. Dynamic alignment slope does not converge and has a tendency of becoming smaller in higher-resolution simulations. This may indicate that the asymptotic alignment slope is zero, which will correspond to the GS95 model

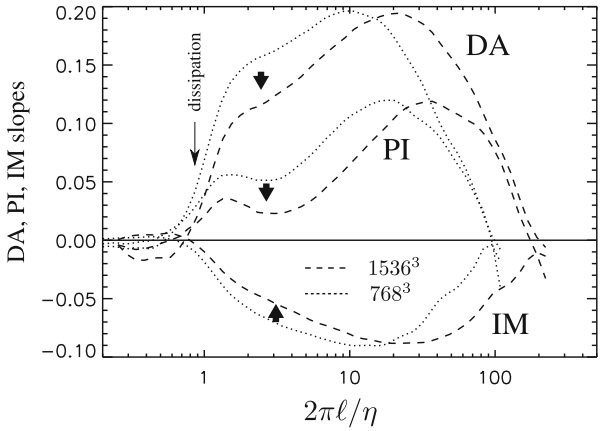

Fig. 8.8 Slopes of several alignment measures vs scale in R4-5 (for definitions see the text). Each measure follows its own scaling, however there are indications that they are all tied to the outer scale, due to the maximum of alignment being a fraction of the outer scale, which is an indication that their scale-dependency is of transient nature

and GS95 model is recovered. Also, alignment from simulations R1-5 seems to indicate that the maximum of the alignment slope is tied to the outer scale, therefore alignment is a transitional effect.

In our earlier studies (Beresnyak and Lazarian 2006; Beresnyak et al. 2009a) we measured several types of alignment and found no evidence that all alignment measures follow the same scaling, see, e.g., Fig. 8.8. As one alignment measure, PI, has been already known to be well scale-dependent (Beresnyak and Lazarian 2006) prior to *DA*, it appears that a particular measure of the alignment in Mason

et al. (2006) was hand-picked for being most scale-dependent and no thorough explanation was given why it was preferred.

We are not aware of any convincing physical argumentation explaining why alignment should be a power-law of scale. Boldyrev (2006) argues that alignment will tend to increase, but will be bounded by field wandering, i.e. the alignment on each scale will be created independently of other scales and will be proportional to the relative perturbation amplitude $\delta B/B$. But this violates two-parametric symmetry of RMHD equations mentioned above, which suggests that field wandering can not destroy alignment or imbalance. Indeed, a perfectly aligned state, e.g., with $\delta \mathbf{w}^- = 0$ is a precise solution of MHD equations and it is not destroyed by its own field wandering. The alignment measured in simulations of strong MHD turbulence with different values of $\delta B_L/B_0$ showed very little or no dependence on this parameter (Beresnyak et al. 2009a).

Some alignment measures are scale-dependent over about one order of magnitude in scale. The origin of this scale-dependency was not yet clearly identified. However, the most plausible explanation is the combinations of two facts: (a) MHD turbulence is less local than hydro turbulence (Beresnyak et al. 2009a; Beresnyak and Lazarian 2010; Beresnyak 2011) and (b) the driving used in MHD turbulence does not particularly well reproduce the statistical properties of the inertial range. Thus transition to asymptotic statistics of the inertial range takes larger scale separation than in the hydrodynamic case.

The contribution to energy flux from different k wavebands is important to understand, since most cascade models assume locality, or rather to say the very term "cascade" assumes locality. An analytical upper bound on locality suggests that the width of the energy transfer window can scale as $C_K^{9/4}$ (Beresnyak 2012), however, in practice turbulence can be more local. The observation of Beresnyak et al. (2009a) that MHD simulations normally lack bottleneck effect, even with high-order dissipation, while hydrodynamic simulations always have bottleneck, which is especially dramatic with high-order dissipation, is consistent with above conjecture on locality, since bottleneck effect relies on locality of energy transfer. As locality constraint depends on the efficiency of the energy transfer, so that the efficient energy transfer must be local, while inefficient one could be nonlocal (Beresnyak and Lazarian 2010; Beresnyak 2011, 2012). As we observe larger C_K in MHD turbulence compared to hydrodynamic turbulence, the former could be less local than the latter, which is consistent with our earlier findings.

8.3.8 Dynamic Alignment: Relation to Spectra

The papers (Boldyrev 2006; Mason et al. 2006) and subsequent papers assert that the particular measure of alignment, DA in our notation, is weakening interaction scale-dependently, so that the energy spectral slope is modified. In particular, the above papers claim that if $DA \sim \lambda^\alpha$, then the spectrum $E(k) \sim k^{-5/3+2/3\alpha}$ which,

in the case of $\alpha = 1/4$ will result in $E(k) \sim k^{-3/2}$. Numerics does not show flat spectra if one compensates $E(k)$ slope with $2/3$ of *DA* slope, however. Let us critically examine the claim $E(k) \sim k^{-5/3+2/3\alpha}$ from the theoretical viewpoint. The exact relation describing energy flux through scales is given by Eq. (8.17). Let us analyze this statistical average for a "+" component at a particular value of l: $\langle \delta w_{l\|}^{-} (\delta w_l^{+})^2 \rangle$. Indeed, it appears that the anti-correlation of δw_l^{-} and δw_l^{+} could result in a reduction of the above statistical average, as (Boldyrev 2006) seems to allege. There are three arguments against this, however.

Firstly, the *DA* does not describe such an anti-correlation, and something different, such as *IM* should be taken instead. So, the assumption of the interaction weakening rely on the claim that alignment measures scale similarly. As we see from Fig. 8.8, the slopes of *DA* and *IM* are quite different and if *DA* reaches the maximum slope of 0.2, the *IM* only reaches the maximum slope of 0.09 and this value does not increase with resolution. This is far from 0.25, required in B06 model. The numerical analysis of Mason et al. (2006) and subsequent papers, however, dealt exclusively with *DA* and the earlier publication (Beresnyak and Lazarian 2006) that reported several different alignment measures, which scaled differently, was ignored and the strong claim of interaction weakening was made nevertheless. However, with present numerics reported so far, even assuming an anti-correlation argument, one can not deduce that the interaction is weakened by a factor of $l^{1/4}$.

Secondly, the *DA* is based on a second order measure, while $\langle \delta w_{l\|}^{-} (\delta w_l^{+})^2 \rangle$ is third-order. We also know that *AA* which is based on zeroth order (sin of the alignment angle) is very weakly scale-dependent (Beresnyak and Lazarian 2006), we can extrapolate to "third-order alignment" having $\sim \lambda^{3\alpha/2}$ dependence and the spectral slope will be $E(k) \sim k^{-5/3+\alpha}$. This is actually more numerically consistent with the data than $E(k) \sim k^{-5/3+2/3\alpha}$, because α is typically below 0.2 and the spectral slope is often flatter than $-3/2$ close to the driving scale.

Thirdly, and most importantly, there is no rigorous argumentation that could suggest that the discussed anti-correlation necessarily reduces the above statistical average. Indeed, the $\delta w_{l\|}^{-}$ is a signed quantity, and so is the whole expression under the statistical average. Therefore, the value of the statistical average is not necessarily related to the RMS value of the expression, but rather depend on the *skewness* of the PDF of the expression. This is most obviously indicated by the Fig. 8.3 where the ratio of unsigned to signed statistical average is about 10. In fact, this ratio could be arbitrarily large, e.g. in weak MHD turbulence, where taking larger B_0 will result in decreased energy rates, the above PDF becoming closer to Gaussian and its skewness going to zero. It is only the GS95 similarity hypothesis for the case of strong MHD turbulence, which is similar to Kolmogorov hypothesis, that asserts that the skewness is independent on scale, allows us to derive the $k^{-5/3}$ spectrum. When one wants to explore a different similarity relations, as (Boldyrev 2005, 2006) did, it is necessary to argue in favor of the scale-independent skewness again. In MHD turbulence, which has fluctuations of the imbalance ratios, it is not clear what self-similarity prescription should be adopted. In a more detailed treatment of the imbalanced turbulence below we argue that is it very likely

that the skewness of $\delta w_{l\parallel}^{-}(\delta w_l^{+})^2$ and $\delta w_{l\parallel}^{+}(\delta w_l^{-})^2$ could be very different in the imbalanced case, due to the fact that the stronger component is cascaded weakly, i.e. $\langle \delta w_{l\parallel}^{-}(\delta w_l^{+})^2 \rangle$ is not the constant fraction of $\langle |\delta w_l^{-}|(\delta w_l^{+})^2 \rangle$, but could be much smaller.

To summarize, the assertion that the interaction is weakened by the *DA* factor is at best heuristic and could be seriously questioned by both numerical data and theoretical argumentation. Apart from this, we reiterate the arguments of previous sections that the numerical evidence strongly suggests that *DA* and other alignment measures become constant in the inertial range and that the asymptotic inertial-range scaling for MHD turbulence is closer to $-5/3$.

8.3.9 Anisotropy: Balanced Case

In Sect. 8.3 we suggested that anisotropy should be universal in the inertial range and expressed as $\Lambda = C_A v_A \lambda^{2/3} \epsilon^{-1/3}$, where C_A is an anisotropy constant to be determined from the numerical experiment or observation. Note, that both Alfvénic and slow modes should have the same anisotropy. This is because they have the same ratio of propagation to nonlinear timescales. Figure 8.9 shows anisotropy for the two best resolved groups R1-3 and R4-5. We used a model independent method of minimum parallel structure function, described in detail in Beresnyak et al. (2009b). Alternative definitions of local mean field give comparable results, as long as they are reasonable. From R1-3 we obtain $C_A = 0.63$. Note, that the conventional definition of critical balance involve the amplitude, rather than

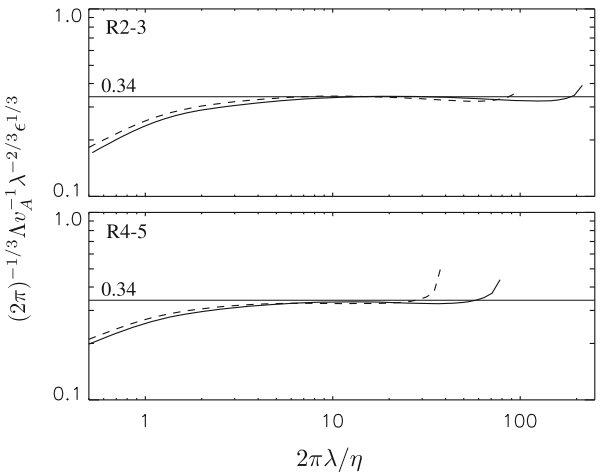

Fig. 8.9 The scaling study for anisotropy shows moderately good convergence to a universal anisotropy $\Lambda = C_A v_A \lambda^{2/3} \epsilon^{-1/3}$ with anisotropy constant C_A of around 0.63

$(\epsilon\lambda)^{1/3}$, so the constant in this classical formulation will be $C_A C_K^{1/2} \approx 1.1$, which is closer to unity. Together with energy spectrum this is a full description of universal axisymmetric two-dimensional spectrum of MHD turbulence in the inertial range.

8.3.10 Basic Properties of Balanced MHD Turbulence

In this review we argue that the properties of Alfvén and slow components of MHD turbulence in the inertial range will be determined only by the Alfvén speed v_A, dissipation rate ϵ and the scale of interest λ. The energy spectrum and anisotropy of Alfvén mode will be expressed as

$$E(k) = C_K \epsilon^{2/3} k^{-5/3}, \tag{8.20}$$

$$\Lambda/\lambda = C_A v_A (\lambda\epsilon)^{-1/3}, \tag{8.21}$$

with $C_K = 3.3$ and $C_A = 0.63$. If the slow mode is present, its anisotropy will be the same, and it will contribute to both energy and dissipation rate. Assuming the ratio of slow to Alfvén energies between 1 and 1.3, the latter was observed in statistically isotropic high resolution MHD simulation with no mean field, we can use $C_K = 4.2$ for the total energy spectrum (Beresnyak 2011).

Anisotropy of MHD turbulence is an important property that affects such processes as interaction with cosmic rays, see, e.g., Yan and Lazarian (2002). Since cosmic ray pressure in our Galaxy is of the same order as dynamic pressure, their importance should not be underestimated. Another process affected is the three-dimensional turbulent reconnection, see, e.g., Lazarian et al. (1999).

Previous measurements of the energy slope relied on the highest-resolution simulation and fitted the slope in the fixed k-range close to the driving scale, typically between $k = 5$ and $k = 20$. We argue that such a fit is unphysical unless a numerical convergence has been demonstrated. We can plot the spectrum vs dimensionless $k\eta$ and if we clearly see a converged dissipation range and a bottleneck range, we can assume that larger scales, in terms of $k\eta$ represent inertial range. In fitting fixed k-range at low k we will never get rid of the influence of the driving scale. In fitting a fixed $k\eta$ range, the effects of the driving will diminish with increasing resolution.

Since we still have trouble transitioning into the inertial range in large mean field simulations, for now it is impossible to demonstrate inertial range in statistically isotropic simulations similar to once presented in Müller and Grappin (2005). This is because we do not expect a universal power-law scaling in transAlfvénic regime, due to the absence of appropriate symmetries and the transitioning to subAlfvénic regime, where such scaling is possible, will require some extra scale separation. These two transitions require numerical resolution that is even higher than the highest resolution presented in this Chapter and for now seem computationally impossible.

Full compressible MHD equations contain extra degrees of freedom, which, in a weakly compressible case, entails the additional cascade of the fast MHD mode, possibly of weak nature. Supersonic simulations with moderate Mach numbers (Cho and Lazarian 2003) show that Alfvénic cascade is pretty resilient and is not much affected by compressible motions. The models of the "universal" supersonic turbulence covering supersonic large scales and effectively subsonic small scales are based mainly on simulations with limited resolution and unlikely to hold true. This is further reinforced by the results presented in this chapter which demonstrated that even a much simpler case of sub-Alfvénic turbulence require fairly high resolutions to obtain an asymptotic scaling (see, e.g., Figs. 8.3,8.6).

8.4 Imbalanced MHD Turbulence

While hydrodynamic turbulence have only one energy cascade, the incompressible MHD turbulence has two, due to the exact conservation of the Elsässer (oppositely going wave packets') "energies". This can be also formulated as the conservation of total energy and cross-helicity.[2] The situation of zero total cross-helicity, which we considered in previous sections has been called "balanced" turbulence as the amount of oppositely moving wavepackets balance each other, the alternative being "imbalanced" turbulence. Most of the above studies concentrated on the balanced case, and, without exception, the GS95 model, which is the strong cascading model with critical balance, can only be kept self-consistent assuming balanced case.

The real MHD turbulence, however, is often imbalanced, such as in situations when the mean magnetic field is present and we have a strong localized source of perturbations. The perfect example is the solar wind, where satellite measurements discovered strong correlations between $\mathbf{v}$ and $\mathbf{B}$ since long time ago. These correlations actually correspond to the imbalanced turbulence with the dominant component propagating away from the Sun. If the mean magnetic field of the Parker spiral is directed locally outwards the Sun then the dominant component will be $\mathbf{w}^-$, otherwise it'll be $\mathbf{w}^+$. For visualization of simulated imbalanced turbulence, see Fig. 8.10.

Certainly, we expect similar phenomena happen in the active galactic nuclei (AGN), where the jet has a strong large mean magnetic field component and the perturbations will propagate primarily away from the central engine, where they will be excited by either Blandford–Znajek mechanism, for the inside jet, or by the motions of the magnetic field footpoints, embedded into the turbulent accretion disk. Another example is the interstellar medium (ISM) turbulence in spiral galaxies. Indeed, in spiral galaxies, due to the action of the large-scale dynamo there is a large-scale component of the magnetic field, spanning the radius of the disk itself. The ISM turbulence, however, is inhomogeneous, due to the energy sources for

[2]The latter, $\int \mathbf{v} \cdot \mathbf{B}\, d^3x$ is a quantity conserved in the absence of dissipation.

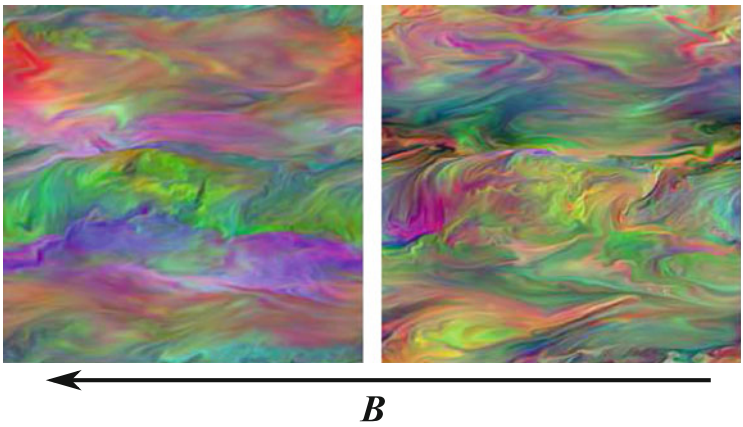

Fig. 8.10 The slices of $\mathbf{w}^+ = \mathbf{v} + \mathbf{B}/\sqrt{4\pi\rho}$ (*left*) and $\mathbf{w}^- = \mathbf{v} - \mathbf{B}/\sqrt{4\pi\rho}$ (*right*) from the three-dimensional MHD simulation with strong mean magnetic field and imbalance

turbulence (supernovas and stellar winds) distributed unevenly in the disk. This will create imbalanced turbulence, which might properties different from the balanced one, which has implications for ISM heating, cosmic ray propagation and many other physical processes in the ISM.

Finally, from the theoretical viewpoint, it is impossible to fully understand balanced turbulence by itself, if the more general imbalanced case is not treated. This is due to the fact that turbulence is a stochastic phenomena with all quantities fluctuating and every piece of turbulence at any given time can have imbalance in it. In this respect, while the mean-field Kolmogorov model can be expanded to include fluctuations of the dissipation rate in the volume, the mean field GS95 model can not.

Imbalanced turbulence, or "turbulence with non-zero cross-helicity" has been discussed long ago by a number of authors (Dobrowolny et al. 1980; Matthaeus and Montgomery 1980; Grappin et al. 1983; Pouquet et al. 1988). This work testified that the non-zero cross-helicity modifies the turbulence. Although these studies correctly reproduced separate cascades for energy and cross-helicity, they were based on then-popular models of MHD turbulence and later it became evident that these are problematic. For example, the closure theory of isotropic MHD turbulence (Pouquet et al. 1976), which reproduced Iroshnikov–Kraichnan model can be criticized on the basis that the ad-hoc term for "relaxation of triple correlations", happen to be larger than real physical nonlinear interaction and makes MHD turbulence, effectively, isotropic. Numerics, however, show that strong MHD turbulence is locally anisotropic, as we demonstrated in previous sections. Another class of models were based on so-called two-dimensional MHD turbulence that, as we demonstrated in previous sections, is unable to reproduce basic properties of the real three-dimensional turbulence, such as strong interaction with critical balance.

8.4.1 Theoretical Considerations

As we explain in the previous sections, the MHD cascade is primarily perpendicular and as it proceeds to small scales, the applicability of weak interaction breaks down, and Alfvénic turbulence becomes strong. In this situation GS95 assumed that the frequency of the wavepacket can not be smaller than the inverse lifetime of the wavepacket, estimated from nonlinear interaction. In the GS95 closure model there is an explicit ad-hoc term that allows for the increase of the wave frequency. Unlike previous models this term is scale-dependent and is based on the assumption of turbulence locality, i.e. that there is one characteristic amplitude of perturbation pertaining to each scale and that this perturbation determines the strength of the interaction and finally renormalization of frequencies. However, as was realized as early as in the original GS95 paper in the imbalanced case we have two characteristic amplitudes, w^+, w^-, and the choice for frequency renormalization becomes unclear.[3] Any theory of strong imbalanced turbulence, must deal with this difficulty.

Let us first demonstrate that a straightforward generalization of GS95 for the imbalanced case does not work. If we assume that the frequency renormalization for one wavepacket is determined by the shear rate of the oppositely moving wavepacket, the wave with small amplitude (say, w^-) may only weakly perturb large amplitude wave w^+ and the frequency of cascaded w^+ will conserve. On the other hand, w^+ may strongly perturb w^- and w^-'s frequency will be determined as w_l^+/l.[4] This mismatch in frequencies creates an inconsistency in the paradigm of scale-local cascade where both wavepackets must have both parallel and perpendicular wavenumbers comparable. As the cascade proceeds to small scales this mismatch only increases, making the cascade nonlocal and inefficient. Such shutdown of the cascade on small scales is unacceptable, since in the stationary case it must carry a constant energy flux for both components. In order to deal with this fundamental difficulty, one must assume something extra to the original GS95 critical balance.

Currently there were several propositions how to deal with strong anisotropic imbalanced MHD turbulence. In Lithwick et al. (2007), the authors proposed that the parallel scale for both components is determined by the shear rate of the stronger component. This model predicts the same anisotropy for both components. In Beresnyak et al. (2008) the authors proposed a new formulation for critical balance

[3] We assume that imbalanced turbulence is "strong" as long as the applicability of weak Alfvénic turbulence breaks down. This requires that at least one component is perturbed strongly. In the imbalanced turbulence the amplitude of the dominant component is larger, so that in the transition to strong regime the applicability of weak cascading of the subdominant component breaks down first.

[4] Throughout this Chapter we assume that w^+ is the larger-amplitude wave. This choice, however, is purely arbitrary and corresponds to the choice of positive versus negative total cross-helicity.

for the stronger component. In Chandran (2008) an advection-diffusion model of cascading was adopted, where advection was describing perpendicular cascade and diffusion was describing the increase of frequencies. These three models clearly state the difficulty described above and try to resolve it with the new physical argumentation that goes beyond the original GS95 critical balance. These three models smoothly transition to the balanced theory of GS95 in the limit of small imbalance. Several other models has been suggested, advocating a different picture, in particular the influence of so-called dynamic alignment. In Perez and Boldyrev (2009) the authors argued that the dynamic alignment will effectively lead to the same nonlinear timescale for both components. This has been criticized as grossly inconsistent with numerics (Beresnyak et al. 2009b; Beresnyak and Lazarian 2010) and having no meaningful physical limit for large imbalances.

8.4.2 *Lithwick, Goldreich and Sridhar (Lithwick et al. 2007) Model, LGS07*

LGS07 argue that the strong wave w^+ is also cascaded strongly and its frequency is equal to the frequency of the weak wave, i.e. the critical balance for strong wave uses the amplitude of the strong wave itself ($w^+\Lambda = v_A\lambda$). In this case the anisotropies of the waves are identical. The formulas for energy cascading are strong cascading formulas, i.e.

$$\epsilon^{\mp} = \frac{(w^{\mp}(\lambda))^2 w^{\pm}(\lambda)}{\lambda}. \tag{8.22}$$

This lead to the prediction $w^+/w^- = \epsilon^+/\epsilon^-$. In terms of energy spectra the model predicts

$$E_k^{\pm} = C_K(\epsilon^{\pm})^{4/3}(\epsilon^{\mp})^{-2/3}k^{5/3}, \tag{8.23}$$

where the Kolmogorov constant C_K must be the same for the theory to have a limit of standard balanced MHD turbulence.

8.4.3 *Beresnyak and Lazarian (Beresnyak and Lazarian 2008) Model, BL08*

BL08a relaxes the assumption of local cascading for the strong component w^+, while saying the w^- is cascaded in a GS95-like way. In BL08a picture the waves have different anisotropies (see Fig. 8.11) and the w^+ wave actually have smaller

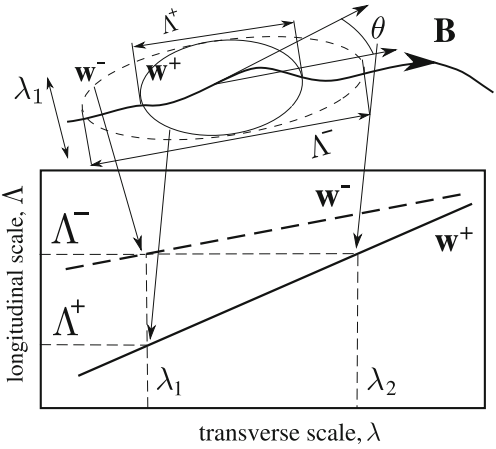

Fig. 8.11 *Upper*: a $\mathbf{w}^+$ wavepacket, produced by cascading by $\mathbf{w}^-$ wavepacket is aligned with respect to $\mathbf{w}^-$ wavepacket, but misaligned with respect to the local mean field on scale λ_1, by the angle θ. *Lower*: the longitudinal scale Λ of the wavepackets, as a function of their transverse scale, λ; Λ^+, Λ^-, λ_1, λ_2 are the notations used in this Chapter. From Beresnyak and Lazarian model (Beresnyak et al. 2008)

anisotropy than w^-, which is opposite to what a naive application of critical balance would predict. The anisotropies of the waves are determined by

$$w^+(\lambda_1)\Lambda^-(\lambda_1) = v_A\lambda_1, \tag{8.24}$$

$$w^+(\lambda_2)\Lambda^+(\lambda^*) = v_A\lambda_1, \tag{8.25}$$

where $\lambda^* = \sqrt{\lambda_1\lambda_2}$, and the energy cascading is determined by weak cascading of the dominant wave and strong cascading of the subdominant wave:

$$\epsilon^+ = \frac{(w^+(\lambda_2))^2 w^-(\lambda_1)}{\lambda_1} \cdot \frac{w^-(\lambda_1)\Lambda^-(\lambda_1)}{v_A\lambda_1} \cdot f(\lambda_1/\lambda_2), \tag{8.26}$$

$$\epsilon^- = \frac{(w^-(\lambda_1))^2 w^+(\lambda_1)}{\lambda_1}. \tag{8.27}$$

One of the interesting properties of BL08a model is that, unlike LGS07 and C08, it does not produce self-similar (power-law) solutions when turbulence is driven with the same anisotropy for w^+ and w^- on the outer scale. BL08a, however, claim that, on sufficiently small scales, the initial non-power-law solution will transit into asymptotic power law solution that has $\Lambda_0^-/\Lambda_0^+ = \epsilon^+/\epsilon^-$ and $\lambda_2/\lambda_1 = (\epsilon^+/\epsilon^-)^{3/2}$. The range of scales for the transition region was not specified by BL08a, but it was assumed that larger imbalance will require larger transition region.

8.4.4 *Perez and Boldyrev (2009) Model, PB09*

Unlike the models described above PB09 employs dynamic alignment which decreases without limit to smaller scales as $l^{1/4}$ and claims the 3/2 spectral slope

Table 8.4 Three-dimensional RMHD imbalanced simulations

Run	Resolution	f	Dissipation	ϵ^+/ϵ^-	$(w^+)^2/(w^-)^2$
I1	$512 \cdot 1024^2$	$w^\pm$	$-1.9 \cdot 10^{-4} k^2$	1.187	1.35 ± 0.04
I2	768^3	$w^\pm$	$-6.8 \cdot 10^{-14} k^6$	1.187	1.42 ± 0.04
I3	$512 \cdot 1024^2$	$w^\pm$	$-1.9 \cdot 10^{-4} k^2$	1.412	1.88 ± 0.04
I4	768^3	$w^\pm$	$-6.8 \cdot 10^{-14} k^6$	1.412	1.98 ± 0.03
I5	$1024 \cdot 1536^2$	$w^\pm$	$-1.5 \cdot 10^{-15} k^6$	2	5.57 ± 0.08
I6	$1024 \cdot 1536^2$	$w^\pm$	$-1.5 \cdot 10^{-15} k^6$	4.5	45.2 ± 1.5

for both components. In this respect it is similar to Boldyrev (2005, 2006). It does, however, a big step beyond these papers by claiming that alignment will effectively result in the same nonlinear timescales for both components, which effectively lead to $(w^+)^2/(w^-)^2 = \epsilon^+/\epsilon^-$. It could be rephrased that PB09 predicts turbulent viscosity which is equal for both components. It is not clear, however, how this could be made consistent with the limit of large imbalances, where the weak component will not be able to produce any sizable turbulent viscosity.

8.4.5 Imbalanced Simulations

Table 8.4 summarizes our high-resolution experiments with imbalanced driving. All experiments were conducted to reproduce stationary turbulence. We started our high resolution simulations with earlier lower-resolution runs that were evolved for a long time, typically hundreds Alfvénic times and reached stationary state. The imbalanced runs were evolved for longer times, up to 40 dynamical times, due to longer cascading timescales for the stronger component. The energy injection rates were kept constant in I1-6 and the fluctuating dissipation rate was within few percent of the former.

8.4.6 Nonlinear Cascading and Dissipation Rate

Compared to spectral slopes, dissipation rates are robust quantities that require much smaller dynamical range and resolution to converge. Figure 8.12 shows energy imbalance $(w^+)^2/(w^-)^2$ versus dissipation rate imbalance ϵ^+/ϵ^- for simulations I2, I4, I5 and I6. We also use two data points from our earlier simulations with large imbalances, A7 and A5 from BL09a. I1 and I3 are simulations with normal viscosity similar to I2 and I4. They show slightly less energy imbalances than I2

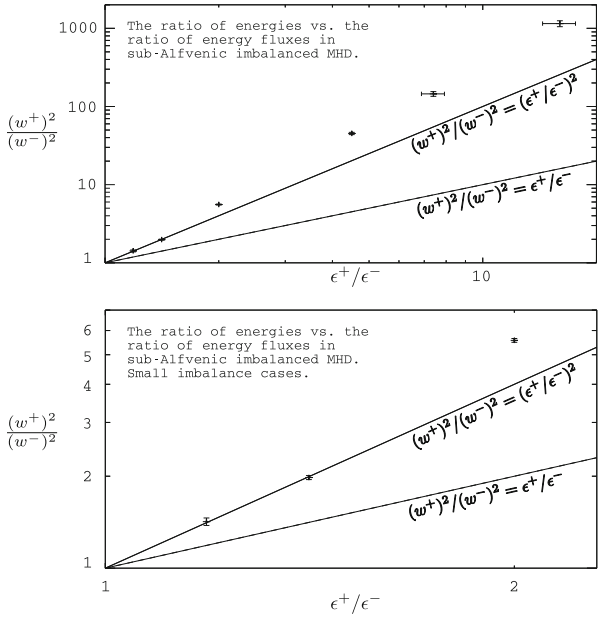

Fig. 8.12 Energy imbalances versus dissipation rate imbalance. *Lower panel* shows a magnified portion of the *upper panel*. *Solid line*: LGS07 prediction, dashed line: a formula from PB09, this also is a prediction for purely viscous dissipation. The point indicate measurements from simulations, where errorbars indicate fluctuation in time. I1 and I3 are simulations with normal viscosity which have slightly lower energy imbalance than I2 and I4. This is an indication that in these simulations viscosity was affecting outer scales. Two high imbalance points are taken from Beresnyak et al. (2009b). For a fixed dissipation ratio the energy imbalance has a tendency to only *increase* with resolution

and I4. We see that most data points are above the prediction of LGS07, which is consistent with BL08. In other words, numerics strongly suggest that

$$\frac{(w^+)^2}{(w^-)^2} \geq \left(\frac{\epsilon^+}{\epsilon^-}\right)^2. \tag{8.28}$$

Although there is a tentative correspondence between LGS07 and the data for small degrees of imbalance, the deviations for large imbalances are significant. The important lesson, however, that in the case of small imbalances the cascading smoothly transition to the balanced case, i.e. the prediction of GS95 model. This is an important verification that the exactly balanced case is not a special case, in a sense.

In the case of strong imbalance it suggests that the strong component cascading rate is smaller than what is expected from strong cascading. As to PB09 prediction, it is inconsistent with data for all degrees of imbalance including those with small imbalance and normal viscosity, i.e. I1 and I3.

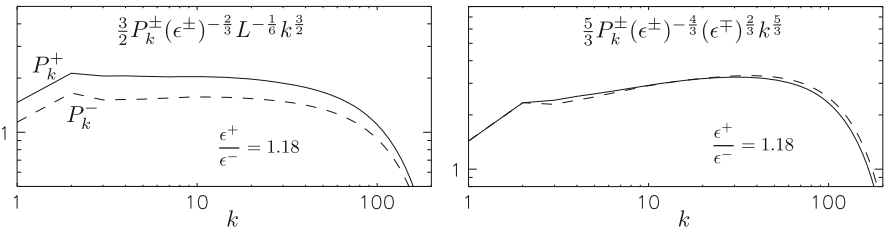

Fig. 8.13 Energy spectra for w^+ (*solid*) and w^- (*dashed*) from simulation I2, compensated by factors that correspond to PB09 (*upper panel*) and LGS07 (*lower panel*). Either theory is confirmed for this low-imbalanced case if the spectra for w^+ and w^- collapse onto the same curve. We see that the collapse is much better for the LGS07 model

8.4.7 Imbalanced Spectra

Figure 8.13 shows spectra from low-imbalance simulation I2, compensated by the predictions of PB09 and LGS07. We see that the collapse of two curves for w^+ and w^- is much better for the LGS07 model, however the spectral slope is much closer to $-3/2$ than to $-5/3$. The issue of spectral slope was discussed in previous section with respect to the balanced simulations. We were arguing that MHD cascade is less local than hydro cascade and is being influenced by driving on a larger range of scales, more importantly the statistical properties of driving is different than asymptotic regime of MHD cascade, which results in a transition range of scales of about one order of magnitude. We expect the same effect to operate in the imbalanced case. Indeed, if we neglect the part of the spectrum with k between 2 and 20, the spectrum could be considered flat on the lower panel of Fig. 8.13. In this deviation of spectral slope from $-5/3$ we do not see any significant differences between the balanced case, which was discussed extensively in the previous sections and the low-imbalance case.

Figure 8.14 shows spectra from all I1-6 simulations, compensated by the prediction of LGS07. For lower imbalances the collapse is reasonably good and become progressively worse for larger imbalances. This deviation, however, does not fully follow the prediction of the asymptotic power-law solutions from BL08, which will predict that the solid curve will go above C_{KA} and the dashed curve—below it. This is possibly explained by the fact that asymptotic power law solutions were not reached in these limited resolution experiments, this is also observed for anisotropies which we consider in the next section.

8.4.8 Imbalanced Anisotropies

We measured parallel and perpendicular structure functions in simulations I1-I6 in order to quantify anisotropies of eddies. The perpendicular structure function

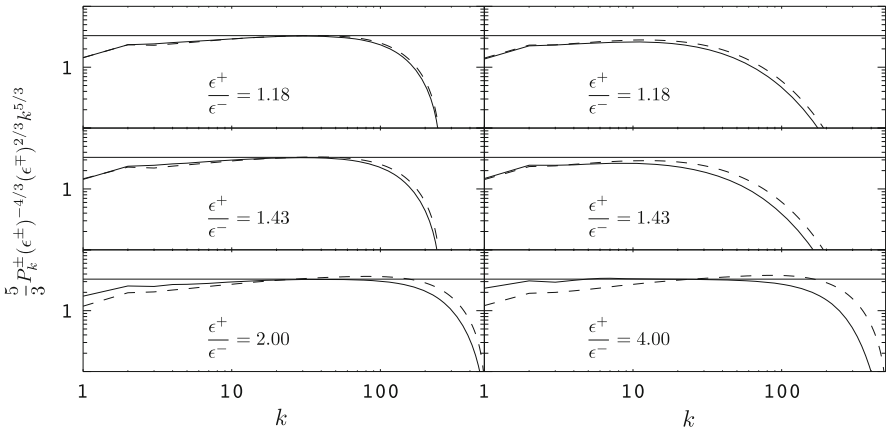

Fig. 8.14 Energy spectra for w^+ (*solid*) and w^- (*dashed*) for simulations I1-I6, compensated by factors that correspond to LGS07. The *thin solid line* corresponds to Kolmogorov constant for Alfvénic turbulence $C_{KA} = 3.27$. The factor $5/3$ is introduced due to the difference between P_k and E_k

was defined above. In the RMHD case which physically correspond to the case of very strong mean field the perpendicular structure function must be calculated with respect to the global mean field. The same is not true for the parallel structure function. Indeed, measuring parallel SF with respect to the global field will destroy scale-dependent anisotropy, even in the case of very strong field. If we have $\delta B_L/B_0 \ll 1$, the field line wandering will be of the order of $B_0/\delta B_L$, while the GS95 anisotropy on the scale l will be much higher, $\sim B_0/\delta B_l$, by a factor of B_L/B_l. The direction of the mean field will deviate from the direction of the local field by the angle which is much larger than the angle of GS95 anisotropy. This will result in an incorrect estimation of the parallel structure function which will be contaminated by contribution from perpendicular direction. Therefore, one must measure anisotropy with respect to local mean field, as was realized in Cho et al. (2000, 2002), Beresnyak et al. (2009a).

For the parallel structure function we will use the model-independent method suggested in Beresnyak et al. (2009a) or "minimum method", namely

$$SF^2_{\parallel}(\Lambda) = \min_{\lambda}\langle(w^{\pm}(\mathbf{r} - \Lambda\mathbf{b}_{\lambda}/b_{\lambda}) - w^{\pm}(\mathbf{r}))^2\rangle_{\mathbf{r}}. \tag{8.29}$$

Where $\mathbf{b}_{\boldsymbol{\lambda}}$ is the magnetic field smoothed on scale λ with Gaussian kernel. It turns out that this method gives very close results to the previously suggested methods of choosing the local mean field, most prominently in the balanced case. We choose this method as it does not contain any arbitrary assumptions as previous methods.

As long as we know both parallel and perpendicular structure functions, the mapping $\Lambda(\lambda)$ is obtained from the equation $SF^2_{\parallel}(w^{\pm}, \Lambda) = SF^2_{\perp}(w^{\pm}, \lambda)$. Phys-

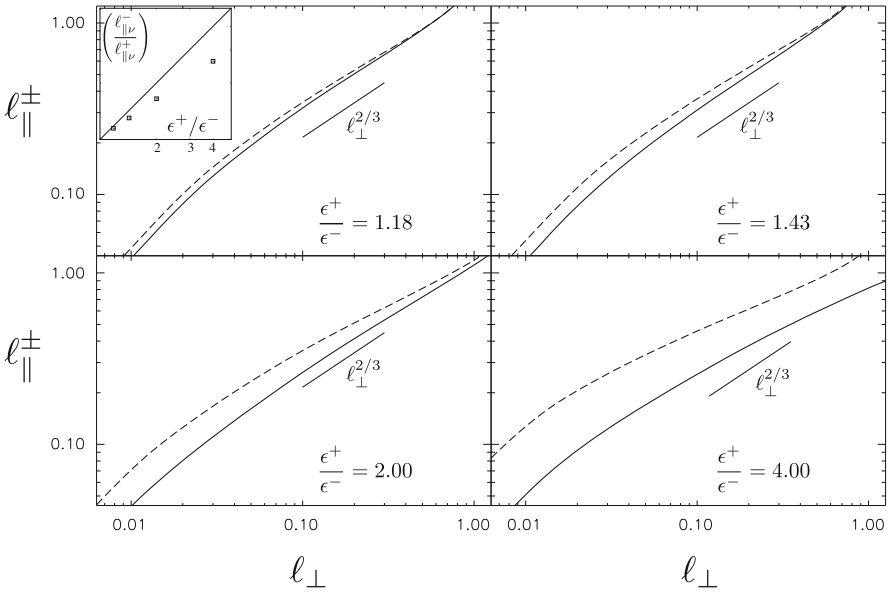

Fig. 8.15 Anisotropies for w^+ (*solid*) and w^- (*dashed*), simulations I1-I6. The relation between parallel scale Λ and perpendicular scale λ is obtained by second order structure functions, as explained in the text. The *small upper inset* shows the ratio of anisotropies on smallest scales vs the prediction of BL08 for the asymptotic power-law solution, which is ϵ^+/ϵ^-

ically this correspond to measurement of the parallel eddy size Λ, whose energy is concentrated on scales λ.

Figure 8.15 shows anisotropies for I1-6 simulations. All simulations were driven by the same anisotropies on the outer scale, which is unfavorable for obtaining the asymptotic power law solutions of BL08, which have an anisotropy ratio which is constant through scales and equal to ϵ^+/ϵ^-. It is, however, favorable to the LGS07 model, which predicts the same w^+ and w^- anisotropies for all scales. Therefore, these simulations are a sensitive test between LGS07 and BL08 models, both of which are roughly consistent in terms of energy ratios and spectra for small imbalances. If LGS07 was true, starting with the same anisotropies on outer scale, this should be preserved by the cascade on smaller scales, but this is not what is observed on Fig. 8.15, where anisotropies start to diverge on smaller scales. The ratio of anisotropies is roughly consistent with BL08 asymptotic power-law solutions for small imbalances and falls short for larger imbalances. This is explained by the fact that it is harder to get to the asymptotic power-law solutions for larger imbalances, as was also observed for the case of power spectra.

8.5 Compressibility in MHD Turbulence

Our discussion so far was centered at the incompressible MHD turbulence. From the astrophysical point of view compressibility is an essential property that cannot be ignored. This calls for studies to what extend our earlier description survives in realistic set ups and what additional properties are gained by compressible MHD turbulence.

Kolmogorov turbulence is known to be applicable to compressible non-magnetized fluids and therefore one should expect that some properties of GS95 model should persist at least for low Mach number magnetic turbulence. At the same time, new modes are excited in MHD in the presence of compressibility. In particular, if MHD turbulence in the incompressible limit can be decomposed into Alfvén and pseudo-Alfvén modes, in the case of compressible MHD turbulence, three modes, namely, Alfvén, slow and fast are present. While the pseudo-Alfvén modes are a limiting case of the slow modes for compressibility going to zero, the fast modes present a new type of motion intrinsic for compressible media.[5]

8.5.1 Decomposition into Fundamental Modes

The original procedure of decomposition of MHD simulations into different modes was proposed by (Cho and Lazarian 2002, 2003 henceforth CL02, CL03, respectively). Unlike earlier discussions which dealt with small perturbations the aforementioned papers demonstrated the decomposition of the transAlfvénic turbulence, i.e. the turbulence with substantial amplitudes. The procedure of decomposition is performed in the Fourier space by a simple projection of the velocity Fourier components $\hat{\mathbf{u}}$ on the direction of the displacement vector for each mode (see Fig. 8.16). The directions of the displacement vectors $\hat{\boldsymbol{\xi}}_s$, $\hat{\boldsymbol{\xi}}_f$, and $\hat{\boldsymbol{\xi}}_A$ corresponding to the slow mode, fast and Alfvén modes, respectively, are defined by their unit vectors

$$\hat{\boldsymbol{\xi}}_s \propto (-1+\alpha-\sqrt{D})k_\parallel \hat{\mathbf{k}}_\parallel + (1+\alpha-\sqrt{D})k_\perp \hat{\mathbf{k}}_\perp\,, \tag{8.30}$$

$$\hat{\boldsymbol{\xi}}_f \propto (-1+\alpha+\sqrt{D})k_\parallel \hat{\mathbf{k}}_\parallel + (1+\alpha+\sqrt{D})k_\perp \hat{\mathbf{k}}_\perp\,, \tag{8.31}$$

$$\hat{\boldsymbol{\xi}}_A = -\hat{\boldsymbol{\varphi}} = \hat{\mathbf{k}}_\perp \times \hat{\mathbf{k}}_\parallel\,, \tag{8.32}$$

where $\mathbf{k}_\parallel$ and $\mathbf{k}_\perp$ are the parallel and perpendicular to $\mathbf{B}_{\rm ext}$ components of wave vector, respectively, $D = (1+\alpha)^2 - 4\alpha\cos^2\theta$, $\alpha = a^2/V_A^2$, θ is the angle between $\mathbf{k}$ and $\mathbf{B}_{\rm ext}$, and $\hat{\boldsymbol{\varphi}}$ is the azimuthal basis in the spherical polar coordinate system.

[5] In the limiting case of compressibility going to zero, the fast modes are sound waves with phase speed going to infinity.

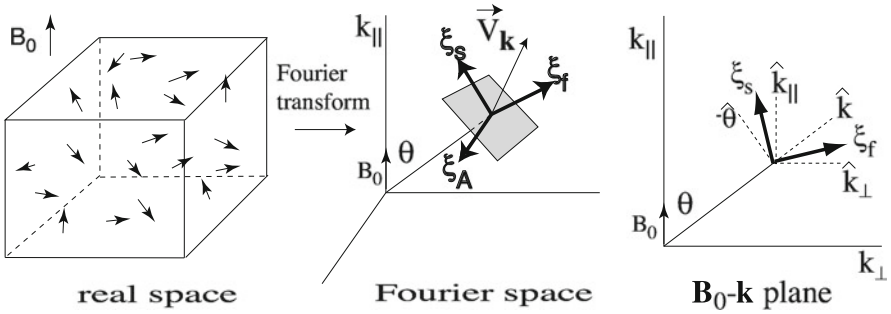

Fig. 8.16 Graphical representation of the mode separation method. We separate the Alfvén, slow and fast modes by the projection of the velocity Fourier component $\mathbf{v}_k$ on the bases $\hat{\boldsymbol{\xi}}_A$, $\hat{\boldsymbol{\xi}}_s$ and $\hat{\boldsymbol{\xi}}_f$, respectively. From CL03

The Fourier components of each mode can be directly used to calculate spectra. For other measures, such as structure functions, transforms back to the real space were used.

The results of CL02 and CL03 revealed several important properties of MHD turbulence. For the cases studied, they revealed that GS95 scaling is valid for *Alfvén modes*:

$$\text{Alfvén}: \quad E^A(k) \propto k^{-5/3}, \quad k_\parallel \propto k_\perp^{2/3}.$$

Slow modes also follows the GS95 model for both high β and mildly supersonic low β cases:

$$\text{Slow}: \quad E^s(k) \propto k^{-5/3}, \quad k_\parallel \propto k_\perp^{2/3}.$$

For the highly supersonic low β case, the kinetic energy spectrum of slow modes tends to be steeper, which may be related to the formation of shocks.

Fast mode spectra are compatible with acoustic turbulence scaling relations:

$$\text{Fast}: \quad E^f(k) \propto k^{-3/2}, \text{ isotropicspectrum.}$$

The super-Alfvénic turbulence simulations suggested that the picture above was true at sufficiently small scales at which Alfvén speed V_A was larger than the turbulent velocity v_l.

Figure 8.17 illustrate that even in highly supersonic regime, where it was customary to claim that the modes were completely blended, the decomposition reveals a regular structure of MHD modes that corresponds to the expectation of the compressible extension of the GS95 theory.

Surely, one can debate whether the adopted technique is reliable. Indeed, the technique above is statistical in nature. That is, we separate each MHD mode with

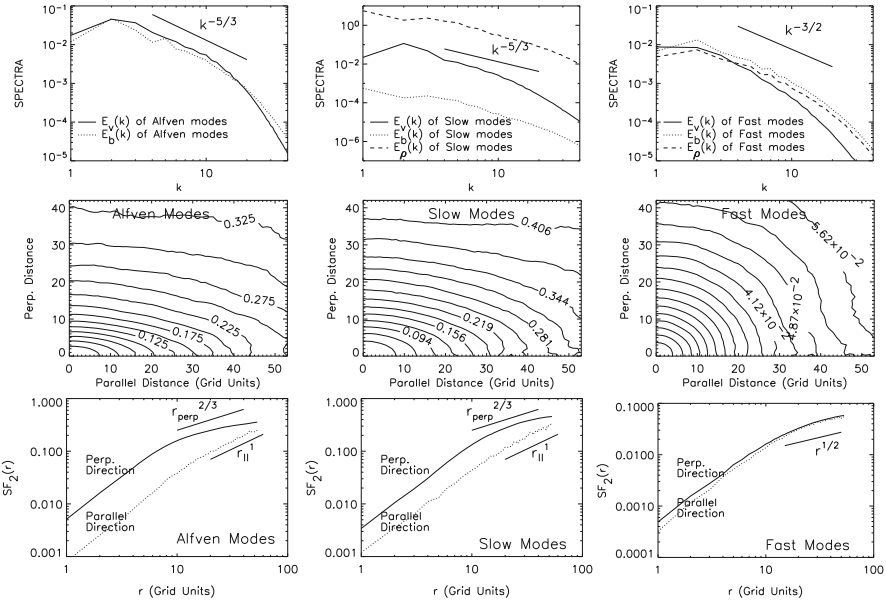

Fig. 8.17 Highly supersonic low β ($\beta \sim 0.02$ and $M_s \sim 7$). $V_A \equiv B_0/\sqrt{4\pi\rho} = 1$. a (sound speed) $= 0.1$. $\delta V \sim 0.7$. Alfvén modes follow the GS95 scalings. Slow modes follow the GS95 anisotropy. But velocity spectrum of slow modes is uncertain. Fast modes are isotropic

respect to the *mean* magnetic field $\mathbf{B}_0$. This procedure is affected by the wandering of large scale magnetic field lines, as well as density inhomogeneities.[6]

Nevertheless, CL03 demonstrated that the technique gave statistically correct results. For instance, in low β regime, the velocity of a slow mode is nearly parallel to the *local* mean magnetic field. Therefore, for low β plasmas, we can obtain velocity statistics for slow modes in real space as follows. First, the direction of the *local* mean magnetic field was measured using the local magnetic field. Second, the calculation of the second order structure function for slow modes was defined by the formula $\mathrm{vSF}_2(\mathbf{r}) =< |(\mathbf{v}(\mathbf{x}+\mathbf{r}) - \mathbf{v}(\mathbf{x})) \cdot \hat{\mathbf{B}}_l|^2 >$, where $\hat{\mathbf{B}}_l$ is the unit vector along the *local* mean field.

Figure 8.18a shows the contours obtained by the method for the high sonic Mach number run. In Fig. 8.18b, we compare the result obtained this way (dashed lines) and using CL03 technique. A similar plot for the mildly supersonic case is presented in Fig. 8.18c.

[6]One way to remove the effect by the wandering of field lines is to drive turbulence anisotropically in such a way as $k_{\perp,L}\delta V \sim k_{\parallel,L} V_A$, where $k_{\perp,L}$ and $k_{\parallel,L}$ stand for the wavelengths of the driving scale and δV is the r.m.s. velocity. By increasing the $k_{\perp,L}/k_{\parallel,L}$ ratio, we can reduce the degree of mixing of different wave modes.

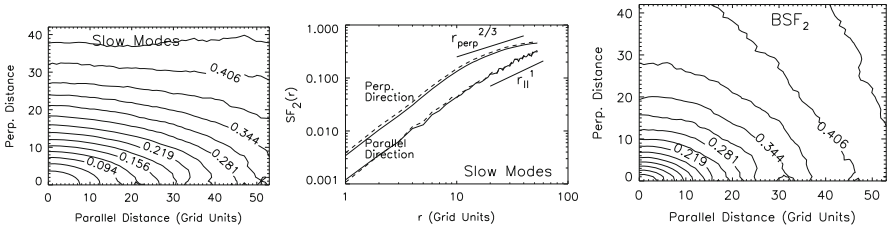

Fig. 8.18 Comparison between Fourier space method and real space method. (**a**) *Left:* From real space calculation. $M_s \sim 7$. (**b**)*middle: Solid*: Fourier space. *Dashed*: real space. $M_s \sim 7$. (**c**)*right:* Similar plot for $M_s \sim 2.3$

How physical is this decomposition? If the coupling between the modes is strong in MHD turbulence one cannot talk about three different energy cascades. Indeed, the compressible MHD turbulence is a highly non-linear phenomenon and it has been thought that Alfvén, slow and fast modes are strongly coupled. Nevertheless, one may question whether this is true. A remarkable feature of the GS95 model is that Alfvén perturbations cascade to small scales over just one wave period, while the other non-linear interactions require more time. Therefore one might expect that the non-linear interactions with other types of waves should affect Alfvénic cascade only marginally. Moreover, since the Alfvén waves are incompressible, the properties of the corresponding cascade may not depend on the sonic Mach number.

The generation of compressible motions (i.e. *radial* components in Fourier space) from Alfvénic turbulence is a measure of mode coupling. How much energy in compressible motions is drained from Alfvénic cascade? According to closure calculations (Zank and Matthaeus 1993), the energy in compressible modes in *hydrodynamic* turbulence scales as $\sim M_s^2$ if $M_s < 1$. CL03 conjectured that this relation can be extended to MHD turbulence if, instead of M_s^2, we use $\sim (\delta V)_A^2/(a^2 + V_A^2)$. (Hereinafter, we define $V_A \equiv B_0/\sqrt{4\pi\rho}$, where B_0 is the mean magnetic field strength.) However, since the Alfvén modes are anisotropic, this formula may require an additional factor. The compressible modes are generated inside the so-called GS95 cone, which takes up $\sim (\delta V)_A/V_A$ of the wave vector space. The ratio of compressible to Alfvénic energy inside this cone is the ratio given above. If the generated fast modes become isotropic (see below), the diffusion or, "isotropization" of the fast wave energy in the wave vector space increase their energy by a factor of $\sim V_A/(\delta V)_A$. This results in

$$\frac{\delta E_{comp}}{\delta E_{Alf}} \approx \frac{\delta V_A V_A}{V_A^2 + c_s^2}, \tag{8.33}$$

where δE_{comp} and δE_{Alf} are energy of compressible and Alfvén modes, respectively. Equation (8.33) suggests that the drain of energy from Alfvénic cascade is marginal when the amplitudes of perturbations are weak, i.e. $(\delta V)_A \ll V_A$. Results of

numerical calculations shown in CL02 support these theoretical considerations. This justifies[7] our treating modes separately.

8.5.2 Other Ways of Decomposition into Fundamental Modes

Kowal and Lazarian (2010, henceforth KL10) extended the CL03 technique by introducing an additional step before the Fourier separation, in which we decompose each component of the velocity field into orthogonal wavelets using discrete wavelet transform:

$$\mathbf{U}(a, \mathbf{w}_{lmn}) = a^{-N/2} \sum_{\mathbf{x}_{ijk}} \psi \left(\frac{\mathbf{x}_{ijk} - \mathbf{w}_{lmn}}{a} \right) \mathbf{u}(\mathbf{x}_{ijk}) \Delta^N \mathbf{x}, \tag{8.34}$$

where $\mathbf{x}_{ijk}$ and $\mathbf{w}_{lnm}$ are N-dimensional position and translation vectors, respectively, a is the scaling parameter, $\mathbf{u}(\mathbf{x}_{ijk})$ is the velocity vector field in the real space, $\mathbf{U}(\mathbf{x}_{ijk})$ is the velocity vector field in the wavelet space, and ψ is the orthogonal analyzing function called wavelet. The sum in the equation is taken over all position indices. KL10 use Daubechies wavelet as an analyzing function and fast discrete version of the wavelet transform, as a result they obtained a finite number of wavelet coefficients. After the wavelet transform of the velocity the Fourier representation of each wavelet coefficient was calculated and perform individual separation into the MHD modes was performed in the Fourier space using the CL03 method and then update the Fourier coefficients of all MHD waves iterating over all wavelets. In this way KL06 obtained a Fourier representation of the Alfvén, slow and fast waves. The final step is the inverse Fourier transform all wave components.

This additional step allows for important extension of the CL03 method, namely, allows for the local definition of the mean magnetic field and density used to calculate α and D coefficients. Since the individual wavelets are defined locally both in the real and Fourier spaces, the averaging of the mean field and density is done only within the space of each wavelet.

The study in KL10 provided results consistent with the CL03 and it extended the decomposition to new physical cases. For instance, Fig. 8.19 shows the anisotropy for subAlfvénic turbulence which agrees well with that obtained in CL03.

Another way to decompose into modes using structure functions has been recently proposed and tested by one of the authors (AB). In this method the separation vector $\mathbf{l}$ of the structure function plays the role of the wavenumber, because there is a correspondence relation between one-dimensional structure function along the certain line and the power spectrum along the same line.

[7] A claim in the literature is that a strong coupling of incompressible and compressible motions is required to explain simulations that show fast decay of MHD turbulence. There is not true. The incompressible motions decay themselves in just one Alfvén crossing time.

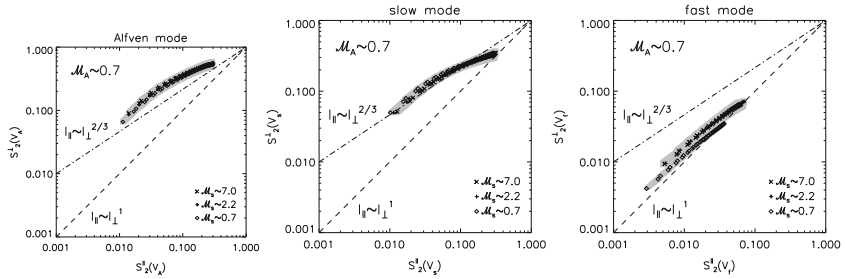

Fig. 8.19 Anisotropy of the Alfvén, slow and fast modes. To show the anisotropy we use the 2nd-order total structure functions, parallel and perpendicular to the local mean magnetic field. Points correspond to the mean profiles of the structure functions averaged over several snapshots. The *gray* areas under points correspond to the degree of departures of the structure functions in time. From KL10

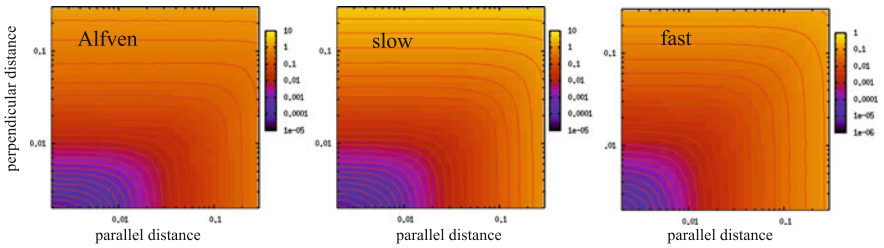

Fig. 8.20 Anisotropy of the Alfvén, slow and fast modes as evidenced by the contours of the second order structure function. Here we used the new SF decomposition method. The Alfvén and slow mode exhibit scale-dependent anisotropy, while the fast mode is almost isotropic

Figure 8.20 shows the contours of the structure function corresponding to each mode obtained in datacubes from $M_s = 10$ supersonic simulations used earlier in Beresnyak et al. (2005) (see also Sect. 8.5.4). The anisotropies of each mode show the same behavior as in the earlier discussed global decomposition method, see Fig. 8.17. There are two advantages in using the new decomposition method. First, it is computationally efficient, as the structure functions can be calculated by the Monte-Carlo method which samples only a fraction of data points. This way, the very high resolution simulations can be processed in a reasonable time. The second advantage is that the structure function is a local measurement, so we can measure spectral characteristics of the modes in a highly inhomogeneous situations. This method has been applied to the decomposition of MHD turbulence obtained in high-resolution cosmological simulation of a galaxy cluster (Beresnyak et al. 2013). The cluster environments has been notoriously difficult to analyze due to the strong dependence of all quantities on the distance to the center. The new method was used to calculate the SFs in concentric shells around the cluster center. Among other things the aforementioned paper estimated the fraction of the fast mode to around 0.25, which is fairly high for subsonic to trans-sonic cluster environment.

We hypothesized that this is due to the way the cluster turbulence is driven—through mergers, which are essentially compressible trans-sonic motions.

8.5.3 Decomposition into Solenoidal and Potential Modes

KL10 also used a different decomposition of the velocity field. Using the Hodge generalization of the Helmholtz theorem we can split an arbitrary vector field $\mathbf{u}$ into three components:

$$\mathbf{u} = \mathbf{u}_p + \mathbf{u}_s + \mathbf{u}_l, \tag{8.35}$$

where each component has specific properties:

(a) Potential component ($\mathbf{u}_p$)—it is curl-free component, i.e. $\nabla \times \mathbf{u}_p = 0$, so it stems from a scalar potential ϕ:

$$\mathbf{u}_p = \nabla\phi. \tag{8.36}$$

The scalar potential ϕ is not unique. It is defined up to a constant. This component describes the compressible part of the velocity field.

(b) Solenoidal component ($\mathbf{u}_s$)—it is divergence-free component, i.e. $\nabla \cdot \mathbf{u}_s = 0$, so it stems from a vector potential $\mathscr{A}$:

$$\mathbf{u}_s = \nabla \times \mathscr{A}. \tag{8.37}$$

The vector potential $\mathscr{A}$ also is not unique. It is defined only up to a gradient field. In the case of velocity this component describes the incompressible part of the field.

(c) Laplace component ($\mathbf{u}_l$)—it is both divergence-free and curl-free. Laplace component comes from a scalar potential which satisfies the Laplace differential equation $\Delta\phi = 0$.

Thus the decomposition can be rewritten in the form:

$$\mathbf{u} = \nabla \times \mathscr{A} + \nabla\phi + \mathbf{u}_l. \tag{8.38}$$

The results of this decomposition are illustrated in Fig. 8.21

It is clear that the compressible components of velocity correspond to shocks, while the incompressible part is dominated by GS95-type motions.

Table 8.5 illustrates how the percentage of energy changes within different components of the flow. It is clear from the table that even for highly compressible magnetized supersonic flows most of the energy is residing in the incompressible motions. In terms of fundamental modes the Alfvén modes dominate. However, the role of the fast modes increases with the increase of the sonic Mach number.

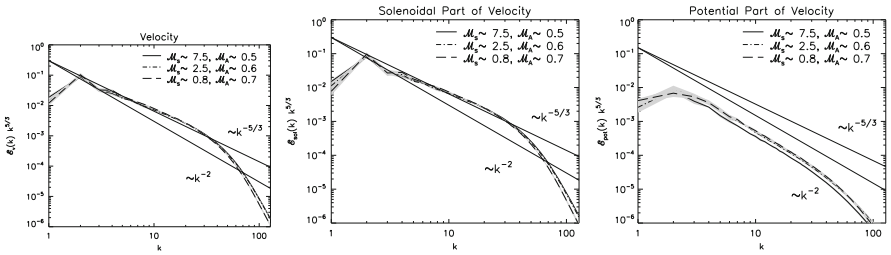

Fig. 8.21 Spectra of the solenoidal and potential parts of velocity for subAlfvénic turbulence. From KL10

Table 8.5 Percentage amount of the kinetic energy contained within each velocity component

$\mathscr{M}_s$	$\mathscr{M}_A$	$V_{\text{incomp.}}$	$V_{\text{comp.}}$	V_A	V_s	V_f
~ 0.7	~ 0.7	$96.5^{\pm 0.8}$	$3.3^{\pm 0.8}$	$58^{\pm 4}$	$37^{\pm 3}$	$4.8^{\pm 0.7}$
~ 2.2	~ 0.7	$93^{\pm 2}$	$7^{\pm 2}$	$58^{\pm 5}$	$33^{\pm 4}$	$9^{\pm 2}$
~ 7.0	~ 0.7	$92^{\pm 2}$	$7^{\pm 2}$	$56^{\pm 4}$	$36^{\pm 4}$	$8.0^{\pm 0.7}$
~ 0.7	~ 7.4	$95^{\pm 2}$	$5^{\pm 2}$	$52^{\pm 4}$	$42^{\pm 4}$	$6.2^{\pm 0.8}$
~ 2.3	~ 7.4	$86^{\pm 1}$	$14^{\pm 2}$	$47^{\pm 3}$	$37^{\pm 4}$	$16^{\pm 2}$
~ 7.1	~ 7.1	$84^{\pm 2}$	$16^{\pm 2}$	$47^{\pm 4}$	$33^{\pm 4}$	$20^{\pm 2}$

Errors correspond to a measure of the time variation

8.5.4 Density Scalings

The properties of density in supersonic ISM turbulence has always been of interest to astronomers due to its applications to star formation. The density is thought be associated primarily with the slow mode, since this is the mode that perturb density the most in low-beta supersonic fluid. However, the structure function of density was generally observed to be very different from the structure function of the velocity of the slow mode. In particular, while slow mode show well-pronounced scale-dependent anisotropy, see Fig. 8.17, the structure function of density was almost isotropic, see Fig. 8.22. This mysterious difference has made applications of our knowledge of supersonic MHD turbulence to the case of star formation difficult.

However, Beresnyak et al. (2005) proposed a simple picture which both unraveled the mystery and further shed light on the dynamics of density in supersonic MHD. It turned out that the second-order structure function method work appropriately only if the quantity in question has a Gaussian distribution. If we use it on density, which distributed approximately log-normally and has high-density tail, this greatly favor high-density regions or clumps. The apparent isotropy, therefore, is an artifact of these clumps being distributed randomly in space. Furthermore, the flat spectrum of density comes from the same effect, namely, high-density clumps act as a delta-functions and produce flat spectrum. When we use log-density instead of density, the spectra become steeper and the second-order structure function shows remarkable scale-dependent anisotropy, see Fig. 8.22.

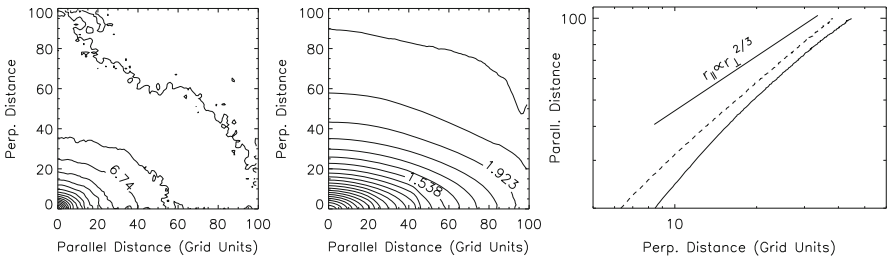

Fig. 8.22 Contours of the structure function of density (*left*), log-density (*center*) and the anisotropy of log-density (*right*). From Beresnyak et al. (2005)

So it turned out that while the perturbations of density and its log-normal PDF are created by random slow shocks, the structure of density has an imprint from Alfvénic driving, the same imprint the structure of slow mode velocity has.

8.5.5 Viscosity-Dominated Regime of MHD Turbulence

In this section, we focus on the effects of viscosity. In strong hydrodynamic turbulence energy is injected at a scale L, and cascades down to smaller scales without significant viscous losses until it reaches the viscous damping scale l_{dv}. The Kolmogorov energy spectrum applies to the inertial range, i.e. all scales between L and l_{dv}. This simple picture becomes more complicated when we deal with MHD turbulence because there are two dissipation scales—the velocity damping scale l_{dv} and the magnetic diffusion scale l_{dm}, where magnetic structures are dissipated. In fully ionized collisionless plasmas (e.g. the hottest phases of the ISM), l_{dv} is less than an order of magnitude larger than l_{dm}, but both scales are very small. However, in partially ionized plasmas (e.g. the warm or cold neutral phase of the ISM), the two dissipation scales are very different and $l_{dv} \gg l_{dm}$. In the Cold Neutral Medium (see Draine et al. 1999 for a list of the ISM phases) neutral particle transport leads to viscous damping on a scale which is a fraction of a parsec. In contrast, in these same phases $l_{dm} \sim 100\,km$.

This has a dramatic effect on the energy cascade model in a partially ionized medium. When the energy reaches the viscous damping scale l_{dv}, kinetic energy will dissipate there, but the magnetic energy will not. In the presence of dynamically important magnetic field (Cho et al. 2002; hereafter CLV02b), reported a completely new regime of turbulence below the scale at which viscosity damps kinetic motions of fluids. They showed that magnetic fluctuations extend below the viscous damping scale and form a shallow spectrum $E_b(k) \sim k^{-1}$. This spectrum is similar to that of the viscous-convective range of a passive scalar in hydrodynamic turbulence.

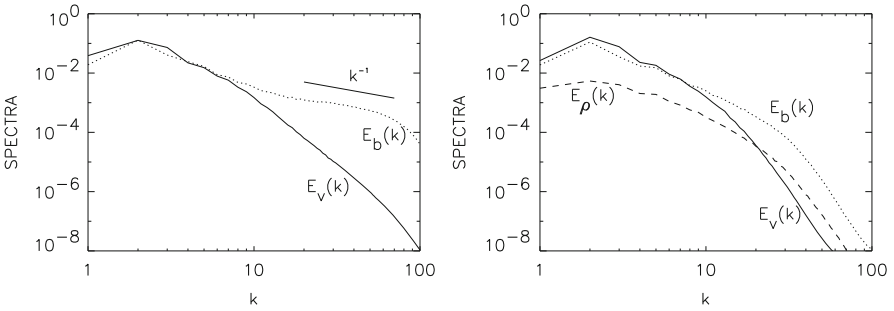

Fig. 8.23 Viscous damped regime (viscosity > magnetic diffusivity). Due to large viscosity, velocity damps after $k \sim 10$. (**a**) *Left*: Incompressible case with 384^3 grid points. Magnetic spectra show a shallower slope ($E_b(k) \propto k^{-1}$) below the velocity damping scale. We achieve a very small magnetic diffusivity through the use hyper-diffusion. From CLV02b. (**b**) *Right*: Compressible case with 216^3 grid points. Magnetic and density spectra show structures below the velocity damping scale at $k \sim 10$. The structures are less obvious than the incompressible case because it is relatively hard to achieve very small magnetic diffusivity in the compressible run. From CL03

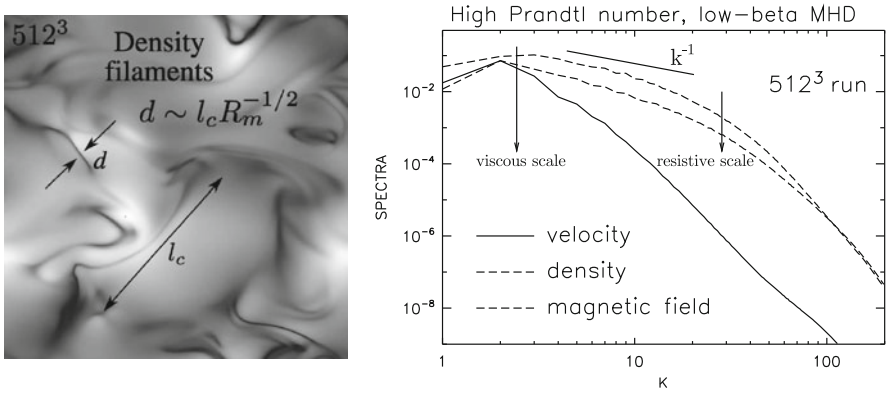

Fig. 8.24 Simulations of supersonic, viscously damped MHD turbulence, with high viscosity emulating high drag from ambipolar diffusion in molecular clouds. *Left*: Filaments of density created by magnetic compression of the gas in this regime. Darker regions correspond to higher density. The viscous damping scale l_c is much larger than the current sheet thickness d. This creates large observed density contrasts. *Right*: The spectra of density, velocity and magnetic field in this case. While the density and magnetic spectra are similar, the velocity spectrum has a cutoff due to high viscosity. Note that the resistive scale in this regime is not L/Rm but $LRm^{-1/2}$

A further numerical study of the viscosity-damped MHD turbulence was presented in CL03 and Cho et al. (2003). Figure 8.23 compares the results for this regime obtained for compressible and incompressible MHD turbulence.

Figure 8.24 show structures and spectra in supersonic viscous MHD simulations, emulating conditions in the molecular clouds, where high ambipolar diffusion could result in drag and damping of kinetic motions. Remarkably, the kinetic and magnetic spectra are very similar to the incompressible and weakly compressible cases.

However, the structures, observed in the datacubes are completely different. The supersonic structures are completely dominated by the current sheets, which are also density sheets. This is because currents sheets has low magnetic pressure and this has to be compensated by gas pressure.

The theoretical study of weakly compressible viscously damped case was performed in Lazarian, Vishniac and Cho (2004, henceforth LVC04). Below we present a brief summary of the theory. Following the usual treatment of ordinary strong MHD turbulence, we define the wavenumbers $k_\parallel$ and $k_\perp$ as the components of the wavevector measured along the *local* mean magnetic field and perpendicular to it, respectively. Here the local mean magnetic field is the direction of the locally averaged magnetic field, which depends not only on the location but also the volume over which the average is taken. See Cho et al. (2000, 2002) for details.

Lazarian, Vishniac, and Cho (2004, henceforth LVC04) proposed a theoretical model for viscosity-damped MHD turbulence. We summarize the model as follows.

Since there is no significant velocity fluctuation below l_{dv}, the time scale for the energy cascade below l_{dv} is fixed at the viscous damping scale. Consequently the energy cascade time scale t_{cas} is scale-independent below l_{dv} and the requirement for a scale independent energy transfer rate b_l^2/t_{cas} yields

$$b_l \sim \text{constant, or} \quad E_b(k) \sim k^{-1}, \tag{8.39}$$

where $kE_b(k) \sim b_l^2$.

In LVC04, we assume that the curvature of the magnetic field lines changes slowly, if at all, in the cascade:

$$k_\parallel \sim \text{constant}. \tag{8.40}$$

This is consistent with a picture in which the cascade is driven by repeated shearing at the same large scale. It is also consistent with the numerical work described in CLV02b, which yielded a constant $k_\parallel$ throughout the viscously damped nonlinear cascade. A corollary is that the wavevector component in the direction of the perturbed field is also approximately constant, so that the increase in k is entirely in the third direction.

The kinetic spectrum depends on the scaling of intermittency. In LVC04, we define a filling factor ϕ_l, which is the fraction of the volume containing strong magnetic field perturbations with a scale $l \sim k^{-1}$. We denote the velocity and perturbed magnetic field inside these sub-volumes with a "^" so that

$$v_l^2 = \phi_l \hat{v}_l^2, \tag{8.41}$$

and

$$b_l^2 = \phi_l \hat{b}_l^2. \tag{8.42}$$

We can balance viscous and magnetic tension forces to find

$$\frac{\nu}{l^2}\hat{v}_l \sim \max[\hat{b}_l k_c, B_0 k_{\parallel,c}]\hat{b}_l \sim k_c \hat{b}_l^2, \tag{8.43}$$

where $k_c \sim 1/l_{dv}$ and $k_{\parallel,c}$ is the parallel component of the wave vector corresponding to the perpendicular component k_c. We used the GS95 scaling ($B_0 k_{\parallel,c} \sim b_l k_c$) and $\hat{b}_l \geq b_l$ to evaluate the two terms in the square braces. Motions on scales smaller than l_{dv} will be continuously sheared at a rate τ_s^{-1}. These structures will reach a dynamic equilibrium if they generate a comparable shear, that is

$$\frac{\hat{v}_l}{l} \sim \tau_s^{-1} \sim \text{constant}. \tag{8.44}$$

Combining this with Eq. (8.43), we get

$$\phi_l \sim k_c l \tag{8.45}$$

and

$$E_v(k) \sim k^{-4}. \tag{8.46}$$

Note that Eq. (8.43) implies that kinetic spectrum would be $E_v(k) \sim k^{-5}$ if ϕ_l=constant.

8.5.6 *Application of Results to Collisionless Fluids*

Some astrophysical magnetized fluids are collisionless, meaning the typical collision frequency is lower than the gyrofrequency. It is important to understand to what extend the results obtained for MHD can also be applied to such environments. The effective collisionality of the medium depends on the collective effects of magnetic scattering of ions. For instance, gyroresonance instability induced by large scale compressions produces small scale perturbations that induce efficient scattering of charged particles (Schekochihin and Cowley 2006; Lazarian and Beresnyak 2006; Schekochihin et al. 2008). Thus the free energy of turbulent environment makes plasmas, effectively, much more collisional. Another example of this is a collisionless shock which excite plasma waves and lead to effective particle thermalization.

Furthermore, some subsets of MHD equations, such as reduced or Alfvénic MHD, which we studied in great detail in Sects. 8.3 and 8.4, are actually applicable to fully collisionless plasmas, because Alfvénic motions are essentially [**E** × **B**] drift motions, rely only on magnetic tension and do not require collisions, see, e.g., Schekochihin et al. (2009).

A recent study in Santos-Lima et al. (2014), using a closure for anisotropic plasma pressure, showed that for a reasonable choice of the relaxation term the collisionless fluids behave similar to MHD. Thus we expect that both MHD turbulence scaling relations and the results of turbulent dynamo that we discussed in above are applicable to collisionless turbulent astrophysical plasmas above the effective collisional scale. The measurements in the solar wind indicate that the effective MHD scales could be as low as the ion skip depth or the ion Larmor radius.

8.5.7 Outlook on Relativistic Turbulence

When electromagnetic energy density is much larger than the rest mass energy density of matter, the electromagnetic fields becomes essentially force-free, which is described with the so-called relativistic force-free approximation. The examples of such environments include electron-positron pulsar magnetospheres and the inner parsec-scale AGN jets.

Numerical simulations of force-free MHD turbulence by Cho (2005) reported anisotropic Goldreich–Sridhar scalings, similar to the ones observed in Alfvénic turbulence, which was earlier conjectured by Thompson and Blaes (1998). More recently a challenging numerical work of studying imbalanced relativistic turbulence was performed in Cho and Lazarian (2014, henceforth CL14). Figure 8.25 shows the energy densities and energy spectra of the dominant and subdominant components.

The results of this study agree with the predictions of the Beresnyak–Lazarian (Beresnyak et al. 2008) model for non-relativistic imbalanced turbulence that we discussed in Sect. 8.4. In fact, CL14 concluded that the magnetic spectrum of dominant waves is steeper than that of sub-dominant waves and the dominant waves exhibit anisotropy which is weaker than predicted in Goldreich et al. (1995) while the sub-dominant waves exhibit stronger than GS95 anisotropy. In addition,

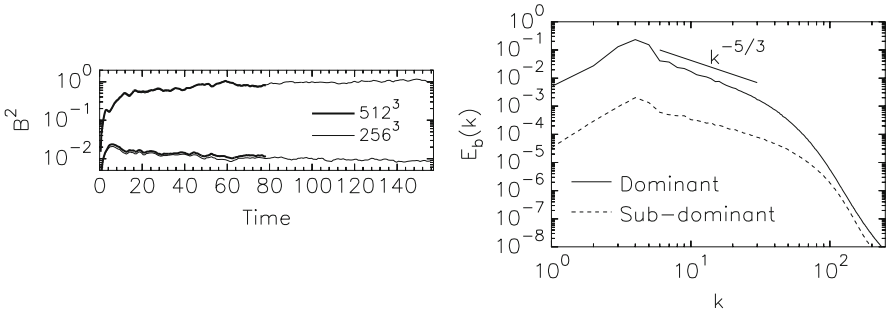

Fig. 8.25 *Left panel*: The time dependence of energy densities for the dominant and subdominant waves. *Right panel*: Energy spectra of the dominant and subdominant waves. The spectrum of the subdominant flux is shallower that for the dominant wave. From CL14

CL14 showed that The energy density ratio of the dominant to subdominant waves scales in proportion to the ratio of the energy injection rates to the power of n, i.e. $(\epsilon_+/\epsilon-)^n$, where $n > 2$, which is also consistent with the Beresnyak–Lazarian Beresnyak et al. (2008) predictions.

The work on imbalanced and balanced relativistic turbulence strongly indicate that the nature of turbulence does not significantly change with the transfer to the relativistic regime. This conclusion is suggestive that the models based on the Goldreich–Sridhar turbulence, e.g. the turbulent reconnection model (Lazarian et al. 1999) can be extended to relativistic phenomena (see discussion in Lyutikov and Lazarian 2013).

8.6 Intermittency of MHD Turbulence

8.6.1 General Considerations

So far our focus in the review was on the turbulence self-similarity. This property, which is also called scale-invariance, implies that fluid turbulence can be reproduced by the magnification of some part of it.

At the dissipation scales the self-similarity is known to fail with turbulence forming non-Gaussian dissipation structures as exemplified, e.g. in Biskamp (2003). Interestingly enough, present-day research shows that self-similarity is not exactly true even along the inertial range. Instead the fluctuations tend to get increasingly sparse in time and space at smaller scales. This property is called *intermittency* (see also the Chapter by Falgarone et al. in this volume). Note, that the power-law scaling does not guarantee the scale-invariance or absence of intermittency.

One way to do such studies is to investigate the scaling powers of longitudinal velocity fluctuations, i.e. $(\delta V)^p$, where $\delta V \equiv (\mathbf{V}(\mathbf{x}+\mathbf{r}) - \mathbf{V}(\mathbf{x}))\mathbf{r}/r$. The infinite set of various powers of $S^p \equiv \langle(\delta V)^p\rangle$, where $\langle..\rangle$ denote ensemble[8] averaging, is equivalent to the p.d.f. of the velocity increments. For those powers one can write $S^p(r) = a_p r_p^{\xi}$ to fully characterize the isotropic turbulent field in the inertial range. While the scaling coefficients a_p are given by the values of the function S^p e.g. at the injection scale, the scaling exponents ξ_p are very non-trivial. It is possible to show that for a self-similar flow the scaling exponents are linear function of n, i.e. $\xi_p \sim p$, which for Kolmogorov model $S^1 \sim v_l \sim l^{1/3}$ gives $\xi_p = p/3$. Experimental studies, however, give different results which shows that the Kolmogorov model is an oversimplified one.

MHD turbulence, unlike hydro turbulence, deals not only with velocity fluctuations, but also with the magnetic ones. The intermittencies of the two fields can be different. In addition, MHD turbulence is anisotropic as magnetic field affects

[8] In astrophysics spatial or temporal averaging is used.

motions parallel to the local direction of **B** very different. This all makes it more challenging to understand the properties of MHD intermittency more interesting.

An interesting and yet not understood property of structure functions, however, helps to extend the range over which S^p can be studied. Benzi et al. (1995) reported that for hydrodynamic turbulence the functions $S^p(S^3)$ exhibit much broader power-law range compared to $S^p(r)$. While for the inertial range a similarity in scaling of the two functions stem from the Kolmogorov scaling $S^3 \sim r$, the power-law scaling of $S^p(S^3)$ protrudes well beyond the inertial range into the dissipation range.[9] This observation shows that the dissipation "spoils" different orders of S in the same manner. Therefore there is no particular need to use the third moment, but one can use any other moment $S^m \sim r^m$ and obtain a good power law of the function $S^p \sim (S^m)^{\xi_p/\xi_m}$ (see Biskamp 2003).

8.6.2 She-Leveque Model of Intermittency

A successful model to reproduce both experimental hydro data and numerical simulations is She-Leveque (1994) model. According to Dubrulle (1994) this model can be derived assuming that the energy from large scale is being transferred to $f < 1$ less intensive eddies and $1 - f$ of more intensive ones. The scaling relations suggested in She and Leveque (1994) related ζ_p to the scaling of the velocity $V_l \sim l^{1/g}$, the energy cascade rate $t_l^{-1} \sim l^{-x}$, and the co-dimension of the dissipative structures C:

$$\zeta_p = \frac{p}{g}(1-x) + C\left(1 - (1 - x/C)^{p/g}\right). \tag{8.47}$$

For incompressible turbulence these parameters are $g = 3$, $x = 2/3$, and $C = 2$, implying that dissipation happens over 1D structures (e.g. vortices). So far the She-Leveque scaling has done well in reproducing the intermittency of incompressible hydrodynamic turbulence.

8.6.3 Intermittency of Incompressible Turbulence

In their pioneering study Müller and Biskamp (2000) applied the She-Leveque model to incompressible MHD turbulence and attracted the attention of the MHD researchers to this tool. They used Elsässer variables and claimed that their results are consistent with dissipation within 2D structures (e.g. 2D current sheets). The

[9] In practical terms this means that instead of obtaining S^p as a function of r, one gets S^p as a function of S^3, which is nonlinear in a way to correct for the distortions of S^p.

consequent study (Cho et al. 2002) used velocities instead of Elsässer variables and provided a different answer, namely, that the dimension of dissipation structures is the same as in incompressible hydro, i.e. the dissipation structures are 1D. The difference between the two results was explained in Cho, Lazarian and Vishniac (2003, henceforth CLV03). They noted that, first of all, the measurements in Müller and Biskamp (2000) were done in the reference frame related to the *mean* magnetic field, while the measurements in Cho et al. (2002) were done in the frame related to the *local* magnetic field. We believe that the latter is more physically motivated frame, as it is the local magnetic field is the field that is felt by the eddies. It is also in this reference frame that the scale-dependent anisotropy predicted in the GS95 model is seen. Computations in CLV03 confirmed that the dissipation structures that can be identified as velocity vortices in the local magnetic field reference frame can also be identified with two dimensional sheets in terms of Elsässer variables in the mean magnetic field reference frame. This, first of all, confirms a mental picture where motions perpendicular to magnetic field lines are similar to hydrodynamic eddies. More importantly, it sends a warning message about the naive interpretation of the She-Leveque scalings in the MHD turbulence.

8.6.4 Intermittency of Compressible Turbulence

Intermittency in compressible MHD turbulence was discussed in Boldyrev (2002) who assumed that the dissipation there happens in shocks[10] and therefore the dimension of the dissipation structures is 2. The idea of the dominance of shock dissipation does not agree well with the numerical simulations in CL02, CL03, where the dominance of the vortical motions in *subAlfvénic* turbulence (i.e. magnetic pressure is larger than the gaseous one) was reported. Nevertheless, numerical simulations in Padoan et al. (2004) showed that for *superAlfvénic* turbulence (i.e. magnetic pressure is less than the gas pressure) the dimension of the dissipation structures was gradually changing from one to somewhat higher than two as the Mach number was increasing from 0.4 to 9.5. The very fact that the superAlfvénic turbulence, which for most of the inertial scale resolvable by simulations does not have a dynamically important magnetic field is different from subAlfvénic is not surprising. The difference between the results in Padoan et al. (2004) at low Mach number and the incompressible runs in Müller and Biskamp (2000) deserves a discussion, however. First of all, the results in Padoan et al. (2004) are obtained for the velocity,

[10]The cited paper introduces the model of compressible turbulence which it calls Kolmogorov–Burgers model. Within this model turbulence goes first along the Kolmogorov scaling and then, at small scales forms shocks. The model was motivated by the numerical measurements of the turbulence spectrum that indicated the index of supersonic turbulence close to $-5/3$. This however was shown to be an artifact of numerical simulations with lower resolution. Simulations in Kritsuk et al. (2007) showed that the slope with $-5/3$ is the result of the numerical bottleneck and the actual slope of the highly compressible turbulence is -2, as was expected earlier.

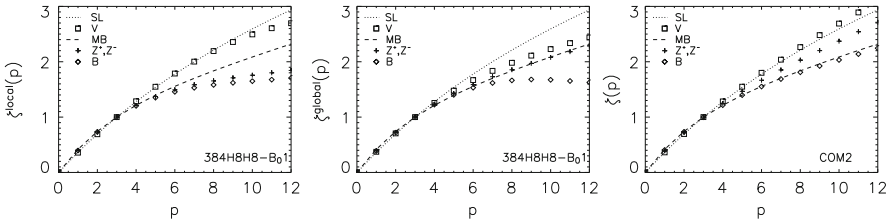

Fig. 8.26 *Left panel*: Intermittency exponents for incompressible MHD turbulence in perpendicular directions in the local frame. The velocity exponents show a scaling similar to the She-Leveque model. The magnetic field shows a different scaling. *Central panel*: Intermittency exponents for incompressible MHD turbulence in the global frame. Note that the result for $z^{\pm}$ is very similar to the Müller–Biskamp model Müller and Biskamp (2000). *Right panel*: Intermittency exponents for superAlfvénic compressible turbulence in the global frame. From CLV03

while the results in Müller and Biskamp (2000) are obtained for the Elsässer variables. CLV03 has shown that the magnetic field and velocity have different intermittencies. Indeed, it is clear from Fig. 8.1 that $\zeta^{\rm magnetic} < \zeta^{\rm velocity}$ which means that magnetic field is more intermittent than velocity. An interesting feature of superAlfvénic simulations in Fig. 8.26 is that the velocity follows the She-Leveque hydro scaling with vortical dissipation, while magnetic field exhibits a pronounced dissipation in current sheets. Both features are expected if magnetic field is not dynamically important and the turbulence stays essentially hydrodynamic. We also see that the dynamically important magnetic field does changes the intermittency. The flattening of magnetic field scaling is pronounced in Fig. 8.26.

A more recent study of intermittency of the velocity field of compressible turbulence was performed in KL10. In Fig. 8.27 we show scaling exponents for the velocity and all its parts and waves calculated in the global reference frame. In the top left plot of Fig. 8.27 we see that for the subAlfvénic turbulence the scaling exponents of velocity follow the She-Lévêque scaling with $D = 1$. Supported by the theoretical considerations we can say that most of the dissipative structures are one-dimensional. Even though the scalings are not perfectly independent of the value of $\mathscr{M}_s$, since we see somewhat lower values of ζ for higher p, the differences between these values for models with different sonic Mach numbers are within their error bars, thus it is relatively difficult to state that the scalings are completely independent or only weakly dependent of the values of $\mathscr{M}_s$. Looking in the corresponding plot for models with a weak magnetic field we clearly see that the spread of curves for different sonic Mach numbers is much higher than in the previous case. For subsonic model the scaling exponents of velocity follow very well the theoretical curve defined by the S-L scaling with parameter D corresponding to one-dimensional structures. The model with $\mathscr{M}_s \sim 2.3$, however, follows perfectly the S-L scaling with $D = 2$ corresponding to the two-dimensional dissipative structures. Moreover, models with even higher values of the sonic Mach number have the scaling exponents for $p > 3$ somewhat below the S-L scaling with $D = 2$. These observations suggest that the scaling exponents of the velocity change with

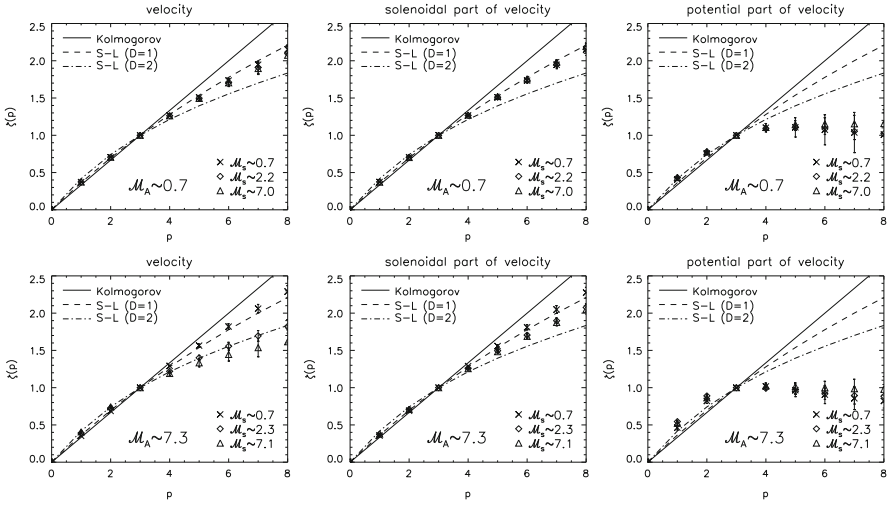

Fig. 8.27 Scaling exponents of the velocity (*left column*) and its incompressible and compressible parts (*middle and right columns*, respectively) for experiments with different sonic Mach numbers in two regimes: subAlfvénic (*upper row*) and superAlfvénic (*lower row*). From KL10

the sonic Mach number but only in the case of weak magnetic field turbulence. The presence of a strong magnetic field significantly reduces these changes and preserves the generation of the dissipative structures of higher than one dimensions.

After the decomposition of velocity into its incompressible and compressible parts we also calculate their scaling exponents. In the middle and right columns of Fig. 8.27 we show the incompressible and compressible parts of the velocity field, respectively. The incompressible part it strong. It constitutes most of the velocity field thus it is not surprising that its scaling exponents are very similar to those observed in velocity. This is true in the case of subAlfvénic models, because all curves in the middle left plot in Fig. 8.27 are tightly covering the S-L scaling with $D = 1$. The similarity between the velocity and its solenoidal part is also confirmed in the case of superAlfvénic models but only for subsonic case, when the role of shocks is strongly diminished. Two supersonic models show exponents following a scaling more closer to the S-L one with $D = 1$, yet still with lower values for $p > 3$.

8.6.5 Intermittency of Viscosity-Damped Turbulence

For the extreme intermittency of the magnetic field suggested in LVC04 the higher moments of structure functions $S_p \sim \hat{b_l}^p \phi_l$ which means that $S_p \sim l^{1-p/2}$. The concentration of magnetic field in thin filaments gives rise to resistive loses that should eventually make $\xi_p = 0$ for sufficiently large p. In Fig. 8.28 we see this

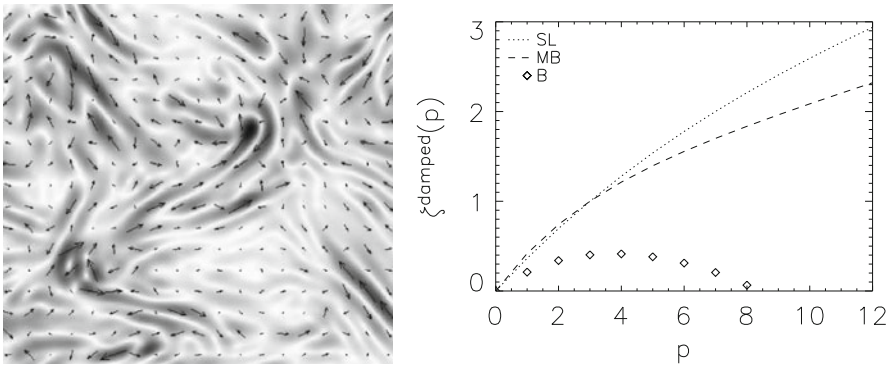

Fig. 8.28 The incompressible viscously damped simulations: *Left*: magnetic reversals (in the plane $\perp$ to mean $\langle \mathbf{B} \rangle$) that create current layers and makes turbulence highly intermittent. Darker regions correspond to higher magnetic field. *Right*: intermittency indexes

general tendency for high p. For the absence of the more precise correspondence we may blame (a) our crude model for estimating ξ, (b) numerical effects, and (c) LVC04 model itself. Addressing the issue (b), we would say that the compelling arguments in the model provide k^{-1} spectrum and this would provide $\xi(2) = 0$ in accordance with the intermittency model above. However, due to numerical effects identified in LVC04 the spectrum of magnetic fluctuations is slightly steeper.

8.7 Selected Implications of MHD Turbulence and Turbulent Dynamo

Astrophysical fluids are turbulent and therefore one must take into account properties of turbulence while describing astrophysical processes. We have discussed various implications in recent reviews, e.g. in Lazarian et al. (2012). Below is provided a brief summary of selected applications of the scalings obtained.

8.7.1 Magnetic Reconnection in the Presence of MHD Turbulence

Magnetic reconnection is a long standing problem. Is it associated with the fundamental ability of magnetic flux tubes to change their topology, while being submerged within conducting fluids (Biskamp 2000; Priest and Forbes 2000). Lazarian and Vishniac (1999, henceforth LV99) considered turbulence as the agent that makes magnetic reconnection fast (see Fig. 8.29). The scheme proposed in LV99 there differs appreciably from the earlier attempts to enhance reconnection

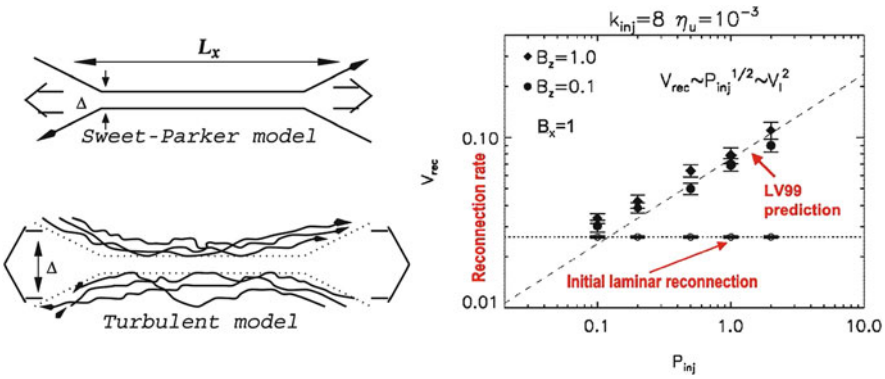

Fig. 8.29 *Left*: *upper panel*. Sweet–Parker reconnection. Δ is limited by resistivity and is small. *Lower panel*: reconnection according to the LV99 model. Δ is determined by turbulent field wandering and can be large. From Lazarian et al. (2004). *Right*: testing of LV99 model with numerical simulations in Kowal et al. (2009). The dependence on the power of turbulent driving is shown

via turbulence, (Speiser 1970; Jacobson and Moses 1984; Matthaeus and Lamkin 1985, 1986), see Eyink et al. (2011) for a detailed comparison. The LV99 model relies on opening of reconnection region via magnetic field wandering, and for the Alfvénic turbulence model that was discussed in this review provide the scaling that are of reconnection velocity V_{rec} being proportional to square root of the injection power P_{inj}. Figure 8.29 shows a good relation of the numerical testing in Kowal et al. (2009, 2012) and the predictions.

A study in Eyink, Lazarian and Vishniac (2011, henceforth ELV11) reveals a very deep relation between MHD turbulence and magnetic reconnection. In fact, it was shown back in LV99 that the predicted reconnection rates are necessary to make the GS95 model self-consistent, i.e. to resolve magnetic knots that emerge as eddy-like motions perpendicular to the direction of local magnetic field twist magnetic field lines. ELV11 demonstrates that the Lagrangian properties of MHD turbulence require the violation[11] of magnetic flux being frozen in and re-derives the predictions of LV99 model from this established properties. As magnetic flux frozenness is a corner stone of major astrophysical theories its violation in turbulent fluids has deep consequences. For instance, the change of our understanding of diffusion out of star forming clouds in the presence of turbulence was recently discussed in Lazarian et al. (2012), Lazarian (2014). The numerical confirmation of the violation of magnetic field flux freezing in turbulent fluids was reported in Eyink et al. (2013). We also note that magnetic field wandering described in LV99

[11]The violation of frozen in condition in turbulence is implicit in LV99. It was stated explicitly in Vishniac et al. (1999) and discussed in terms of star formation in Lazarian (2005). The first formal quantitative study was performed in Eyink (2011).

is applicable not only to reconnection, but also to the problem of heat transfer (see Lazarian 2006).

8.7.2 Turbulence and Particle Acceleration

MHD turbulence plays an important role in accelerating energetic particles. First of all, the second order Fermi acceleration can arise directly from the scattering of particles by turbulence, see, e.g., Melrose (1980). Properties of MHD turbulence that we discussed above are essential to understanding this process. If turbulence is injected at large scales, the anisotropy of Alfvénic modes at small scales makes them inefficient for scattering and acceleration of cosmic rays (Chandran 2000; Yan and Lazarian 2002). In this situation, fast modes were identified in Yan and Lazarian (2002) as the major scattering and acceleration agent for cosmic rays and energetic particles in interstellar medium (see also Yan et al. 2004, 2008). This conclusion was extended for solar environments in Petrosian, Yan & Lazarian (2006) and intracluster medium in Brunetti and Lazarian (2007).

Turbulent magnetic field in the pre-shock and post-shock environment are important for the first order Fermi acceleration associated with shocks (Schlickeiser 2002). In particular, magnetic field enhancement compared to its typical interstellar values is important in the pre-shock region for the acceleration of high energy particles. Turbulent dynamo that we discussed in Sect. 8.2 can provide a way of generating magnetic field in the precursor of the shock. In Beresnyak et al. (2009) it was shown that the interactions of the density inhomogeneities pre-existing in the interstellar medium with the precursor generate strong magnetic fields in the shock precursor, which allows particle acceleration up to the energy of 10^{16} eV.

In addition, fast magnetic reconnection of turbulent magnetic field can itself induce the first order Fermi acceleration (de Gouveia Dal Pino and Lazarian 2005; Lazarian 2005). Recent numerical simulations in Kowal et al. (2012), demonstrate the efficiency of this process.

8.7.3 Thin Structures in the Interstellar Medium

The viscosity-dominated regime of turbulence can be responsible for the formation of structures in interstellar medium and other astrophysical environments. The magnetic pressure compresses the gas as demonstrated in Fig. 8.24. More importantly, extended current sheets that naturally emerge as magnetic field fluctuates in the plane perpendicular to the mean magnetic field. It was speculated in Lazarian (2007) that these current sheets can account for the origin of the small ionized and neutral structures (SINS) on AU spatial scales (Heiles 1997; Stanimirović et al. 2004).

Goldreich and Sridhar (2006) appealed to the generation of the magnetic field in the high *Pt* turbulent plasma (Schekochihin et al. 2004) to account for the high

amplitude, but small scale fluctuations of plasma density observed in the direction of the Galactic center. They argued that the plasma viscosity parallel to magnetic field can act in the same way as the normal viscosity of unmagnetized fluids. Lazarian et al. (2009) argued that the regime of dynamo in Schekochihin et al. (2004) and the turbulence in Lazarian et al. (2004) have similarities in terms of the density enhancement that are created. Although in the case of magnetic turbulence with sufficiently strong mean magnetic field, global reversals, that (Goldreich and Sridhar 2006) appeal to in compressing plasma, do not happen, the reversals of the magnetic field direction occur in the direction perpendicular to the mean magnetic field. As the mean magnetic field goes to zero, the two regimes get indistinguishable as far as the density enhancements are concerned. Thus high intensity fluctuations of plasma density towards the Galactic center may also be the result of viscosity-damped turbulence.

8.7.4 *Intermittent Turbulent Heating of Interstellar Gas*

E. Falgarone and her collaborators (Falgarone et al. 2005; Falgarone 2007; Hily-Blant and Falgarone 2007; Hily-Blant et al. 2008) (see also the Chapter by Falgarone et al. in this volume) attracted the attention of the interstellar community to the potential important implications of intermittency. A small and transient volume with high temperatures or violent turbulence can have significant effects on the net rates of processes within the ISM. For instance, many interstellar chemical reactions (e.g., the strongly endothermic formation of CH^+) might take place within very intensive intermittent vortices. The aforementioned authors claimed the existence of the observational evidence for such reactions and heating.

The bottom part of Fig. 8.30 shows our calculations for the volume fractions of various dissipation rates (i.e., heating). While the temperatures achieved will

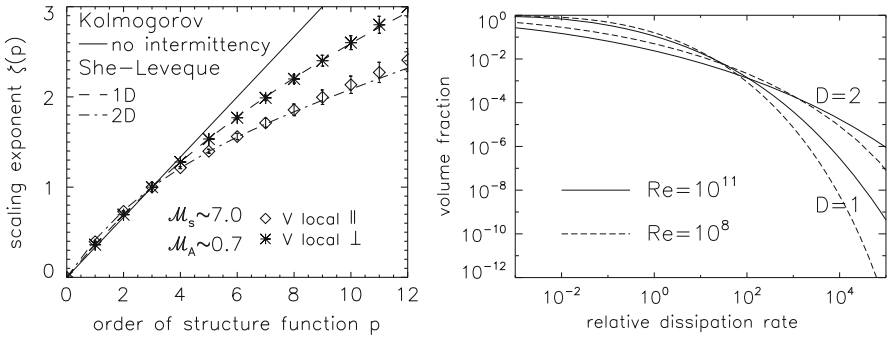

Fig. 8.30 *Left Panel*: the intermittencies of velocities in the subAlfvénic, $M_A = 0.7$ supersonic $M_s = 7$ MHD simulations. From Kowal et al. (2007). *Right Panel*: volume fraction with the dissipation rate is higher than the mean rate for the She-Leveque model of intermittency with $D = 1$ and 2

depend upon the cooling functions, some important conclusions are available from the analysis of Fig. 8.30. Indeed, the model of chemical reactions by Falgarone et al. requires that a substantial part of the turbulent cascade energy dissipate in the very intermittent structures. Figure 8.30 shows that the bulk of the energy dissipates within structures where the dissipation rate is higher than the mean value less than the factor of 100, provided that the She-Leveque model is valid. This provides stringent constraints on what chemistry we could expect to be induced by intermittent turbulent heating.

Interestingly enough, the case of intermittency studies supports our point of the futility of the "brute force" numerical approach. For instance, for a typical ISM injection scale of 50 pc, the Reynolds number can be as high as $\mathrm{Re} = 10^{11}$. In comparison, numerical simulations can only reach $\mathrm{Re} \leq 10^5$ for the present record resolution of $4,096^3$.

8.7.5 *Suppression of Instabilities by Alfvenic Turbulence*

Alfvenic turbulence can suppress instabilities, in particular, streaming instability that arises as energetic particles stream in one direction along magnetic field lines (Yan et al. 2004; Farmer et al. 2004; Beresnyak and Lazarian 2008). The effect is based on cascading of slab waves induced as a result of the instability development by the ambient turbulence. Thus the effect is not limited by suppressing of streaming instability. For instance, in Lazarian and Beresnyak (2006) and Yan et al. (2011) the suppression of gyroresonance instability by turbulence was considered.

The thorough numerical study of the suppression of the slab waves by Alfvenic turbulence was performed in Beresnyak and Lazarian (2008), see Fig. 8.31, not only

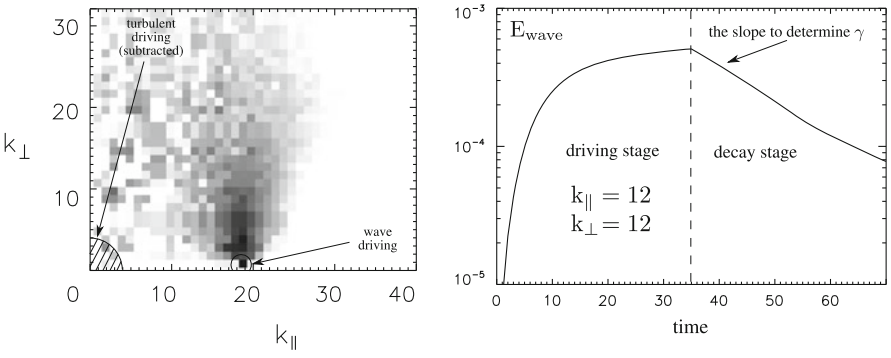

Fig. 8.31 The wave perturbation excited on top of existing turbulence exhibit exponential decay, as one expects a linear decay for a test perturbation in such perturbation simulation, despite the turbulence itself is strongly nonlinear. This linear decay rate is independent of amplitude, unlike nonlinear damping, so turbulence does not result in saturation of an instability but rather damps it completely or not. From Beresnyak and Lazarian (2008)

for the slab waves moving parallel to magnetic field, but also for waves moving at arbitrary angles to the mean magnetic field. The numerical simulations confirmed the theoretical expectations in the paper.

Turbulent damping is also likely to be important in suppressing instabilities, such as tearing, in current sheets, after turbulent reconnection sets in, see section 8.7.1 and the Chapter by Lazarian et al in this book.

8.7.6 Turbulent Dynamo and High Redshift Physics

Magnetic turbulent dynamo that we discussed in Sect. 8.2 is essential for understanding magnetic field in the early Universe. Indeed, as long as the Universe becomes ionized and highly conductive, the viscosity is also greatly reduced due to ions scattering in the magnetic fields (Schekochihin and Cowley 2006; Schekochihin et al. 2008). This creates high-Re environment which naturally produces turbulence. Despite a lot of discussion if early dynamo is concentrated on the initial field generation mechanisms, such as Biermann battery and its modifications (Lazarian 1992), we now understand that in the limit of very high Re the level of the initial field is not very important. Instead, around 5 % of the energy of the turbulent cascade is deposited into magnetic energy due to high-Re small-scale dynamo. The magnetic field, therefore, could get dynamically important at high redshifts. This will change the nature of many processes, for example we expect that magnetic field should be important in the process of formation of the first stars. These possibility is discussed in Schober et al. (2012, 2013), but we believe that the relative role of non-linear dynamo is even more important than it was presented in the latter study (Xu and Lazarian 2014).

Acknowledgements AB was supported by Humboldt Fellowship. AL acknowledges the support of the NSF grant AST-1212096, the Vilas Associate Award as well as the support of the NSF Center for Magnetic Self- Organization. In addition, AL thanks the International Institute of Physics (Natal, Brazil) and the Observatoire de Nice for its hospitality during writing this review. Discussions with Ethan Vishniac and Greg Eyink are acknowledged. We thank Siyao Xu for reading the manuscript.

References

Alexakis, A., Mininni, P.D., Pouquet, A: Phys. Rev. E **72**(4), 046301 (2005).: doi10.1103/PhysRevE.72.046301

Aluie, H., Eyink, G.L.: Phys. Rev. Lett. **104**(8), 081101 (2010). doi:10.1103/PhysRevLett.104.081101

Armstrong, J.W., Rickett, B.J., Spangler, S.R.: Astrophys. J. **443**, 209 (1995). doi:10.1086/175515

Benzi, R., Struglia, M.V., Tripiccione, R.: eprint arXiv:chao-dyn/9509018, p. 9018 (1995)

Beresnyak, A.: Phys. Rev. Lett. **106**(7), 075001 (2011). doi:10.1103/PhysRevLett.106.075001

Beresnyak, A.: Phys. Rev. Lett. **108**(3), 035002 (2012). doi:10.1103/PhysRevLett.108.035002

Beresnyak, A.: Mon. Not. R. Astron. Soc. **422**, 3495 (2012). doi:10.1111/j.1365-2966.2012.20859.x
Beresnyak, A.: (2014). ArXiv e-prints
Beresnyak, A., Lazarian, A., Astrophys. J. **640**, L175 (2006). DOI 10.1086/503708
Beresnyak, A., Lazarian, A.: Astrophys. J. **678**, 961 (2008). doi:10.1086/587052
Beresnyak, A., Lazarian, A.: Astrophys. J. **682**, 1070 (2008). doi:10.1086/589428
Beresnyak, A., Lazarian, A.: Astrophys. J. **702**, 1190 (2009). doi:10.1088/0004-637X/702/2/1190
Beresnyak, A., Lazarian, A.: Astrophys. J. **702**, 460 (2009). doi:10.1088/0004-637X/702/1/460
Beresnyak, A., Lazarian, A.: Astrophys. J. **722**, L110 (2010). doi:10.1088/2041-8205/722/1/L110
Beresnyak, A., Jones, T.W., Lazarian, A.: Astrophys. J. **707**, 1541 (2009). doi:10.1088/0004-637X/707/2/1541
Beresnyak, A., Lazarian, A., Cho, J.: Astrophys. J. **624**, L93 (2005). doi:10.1086/430702
Beresnyak, A., Yan, H., Lazarian, A.: Astrophys. J. **728**, 60 (2011). doi:10.1088/0004-637X/728/1/60
Beresnyak, A., Xu, H., Li, H., Schlickeiser, R.: Astrophys. J. **771**, 131 (2013). doi:10.1088/0004-637X/771/2/131
Biskamp, D.: Magnetic Reconnection in Plasmas. Cambridge University Press, Cambridge (2000)
Biskamp, D.: Magnetohydrodynamic Turbulence. Cambridge University Press, Cambridge (2003)
Boldyrev, S.: Astrophys. J. **569**, 841 (2002). doi:10.1086/339403
Boldyrev, S.: Astrophys. J. **626**, L37 (2005). doi:10.1086/431649
Boldyrev, S.: Phys. Rev. Lett. **96**(11), 115002 (2006). doi:10.1103/PhysRevLett.96.115002
Brandenburg, A., Subramanian, K.: Phys. Rep. **417**, 1 (2005). doi:10.1016/j.physrep.2005.06.005
Brunetti, G., Lazarian, A.: Mon. Not. R. Astron. Soc. **378**, 245 (2007). doi:10.1111/j.1365-2966.2007.11771.x
Chandran, B.D.G: Phys. Rev. Lett. **85**, 4656 (2000). doi:10.1103/PhysRevLett.85.4656
Chandran, B.D.G.: Astrophys. J. **685**, 646 (2008). doi:10.1086/589432
Chepurnov, A., Lazarian, A.: Astrophys. J. **710**, 853 (2010). doi:10.1088/0004-637X/710/1/853
Cho, J.: Astrophys. J. **621**, 324 (2005). doi:10.1086/427493
Cho, J., Lazarian, A.: Phys. Rev. Lett. **88**(24), 245001 (2002). doi:10.1103/PhysRevLett.88.245001
Cho, J., Lazarian, A.: Mon. Not. R. Astron. Soc. **345**, 325 (2003). doi:10.1046/j.1365-8711.2003.06941.x
Cho, J., Lazarian, A.: Astrophys. J. **615**, L41 (2004). doi:10.1086/425215
Cho, J., Lazarian, A.: Astrophys. J. **780**, 30 (2014). doi:10.1088/0004-637X/780/1/30
Cho, J., Vishniac, E.T.: Astrophys. J. **539**, 273 (2000). doi:10.1086/309213
Cho, J., Vishniac, E.T.: Astrophys. J. **538**, 217 (2000). doi:10.1086/309127
Cho, J., Lazarian, A., Vishniac, E.T.: Astrophys. J. **564**, 291 (2002). doi:10.1086/324186
Cho, J., Lazarian, A., Vishniac, E.T.: Astrophys. J. **566**, L49 (2002). doi:10.1086/339453
Cho, J., Lazarian, A., Vishniac, E.T.: Astrophys. J. **595**, 812 (2003). doi:10.1086/377515
Cho, J., Lazarian, A., Vishniac, E.T.: In: Falgarone, E., Passot, T. (eds.) Turbulence and Magnetic Fields in Astrophysics. Lecture Notes in Physics, vol. 614, pp. 56–98. Springer, Berlin (2003)
Cho, J., Vishniac, E.T., Beresnyak, A., Lazarian, A., Ryu, D.: Astrophys. J. **693**, 1449 (2009). doi:10.1088/0004-637X/693/2/1449
Dobrowolny, M., Mangeney, A., Veltri, P.: Phys. Rev. Lett. **45**, 144 (1980). doi:10.1103/PhysRevLett.45.144
Draine, B.T., Lazarian, A.: Astrophys. J. **512**, 740 (1999). doi:10.1086/306809
Dubrulle, B.: Phys. Rev. Lett. **73**, 959 (1994). doi:10.1103/PhysRevLett.73.959
de Gouveia Dal Pino, E.M., Lazarian, A.: Astron. Astrophys. **441**, 845 (2005). doi:10.1051/0004-6361:20042590
Elmegreen, B.G., Scalo, J.: Ann. Rep. Astron. Astrophys. **42**, 211 (2004). doi:10.1146/annurev.astro.41.011802.094859
Eyink, G.L.: Physica D Nonlinear Phenomena **207**, 91 (2005). doi:10.1016/j.physd.2005.05.018
Eyink, G.L.: Phys. Rev. E **83**(5), 056405 (2011). doi:10.1103/PhysRevE.83.056405
Eyink, G.L., Lazarian, A., Vishniac, E.T.: Astrophys. J. **743**, 51 (2011). doi:10.1088/0004-637X/743/1/51

Eyink, G., Vishniac, E., Lalescu, C., Aluie, H., Kanov, K., Bürger, K., Burns, R., Meneveau, C., Szalay, A.: Nature **497**, 466 (2013). doi:10.1038/nature12128
Falgarone, E.: In: Star Formation, Then and Now (2007)
Falgarone, E., Pineau Des Forêts, G., Hily-Blant, P., Schilke, P.: In: IAU Symposium, vol. 235, p. 143P (2005)
Farmer, A.J., Goldreich, P.: Astrophys. J. **604**, 671 (2004). doi:10.1086/382040
Frisch, U.: Turbulence. The legacy of A. N. Kolmogorov. Cambridge University Press, Cambridge (1995)
Galtier, S., Nazarenko, S.V., Newell, A.C., Pouquet, A.: J. Plasma Phys. **63**, 447 (2000). doi:10.1017/S0022377899008284
Galtier, S., Pouquet, A., Mangeney, A.: Phys. Plasmas **12**(9), 092310 (2005). doi:10.1063/1.2052507
Gogoberidze, G.: Phys. Plasmas **14**(2), 022304 (2007). doi:10.1063/1.2437753
Goldreich, P., Sridhar, S.: Astrophys. J. **438**, 763 (1995). doi:10.1086/175121
Goldreich, P., Sridhar, S.: Astrophys. J. **640**, L159 (2006). doi:10.1086/503668
Goldstein, B.E.,Smith, E.J., Balogh, A., Horbury, T.S., Goldstein, M.L., Roberts, D.A.: Geophys. Res. Lett. **22**, 3393 (1995). doi:10.1029/95GL03183
Gotoh, T., Fukayama, D., Nakano, T.: Phys. Fluids **14**, 1065 (2002)
Grappin, R., Leorat, J., Pouquet, A.: Astron. Astrophys. **126**, 51 (1983)
Haugen, N.E., Brandenburg, A., Dobler, W.: Phys. Rev. E **70**(1), 016308 (2004). doi:10.1103/PhysRevE.70.016308
Heiles, C.: Astrophys. J. **481**, 193 (1997). doi:10.1086/304033
Hily-Blant, P., Falgarone, E., Astron. Astrophys. **469**, 173 (2007). doi:10.1051/0004-6361:20054565
Hily-Blant, P., Falgarone, E., Pety, J.: Astron. Astrophys. **481**, 367 (2008). doi:10.1051/0004-6361:20078423
Howes, G.G., Cowley, S.C., Dorland, W., Hammett, G.W., Quataert, E., Schekochihin, A.A.: Astrophys. J. **651**, 590 (2006). doi:10.1086/506172
Iroshnikov, P.: Sov. Astron. **7**, 566 (1964)
Jacobson, A.R., Moses, R.W.: Phys. Rev. A **29**, 3335 (1984). doi:10.1103/PhysRevA.29.3335
Kadomtsev, B.B., Pogutse, O.P.: Sov. J. Exp. Theor. Phys. **38**, 283 (1974)
Kaneda, Y., Ishihara, T., Yokokawa, M., Itakura, K., Uno, A.: Phys. Fluids **15**, L21 (2003). doi:10.1063/1.1539855
Käpylä, P.J., Korpi, M.J., Brandenburg, A.: Astron. Astrophys. **500**, 633 (2009). doi:10.1051/0004-6361/200811498
Kazantsev, A.P.: Sov. J. Exp. Theor. Phys. **26**, 1031 (1968)
Kolmogorov, A.: Akademiia Nauk SSSR Doklady **30**, 301 (1941)
Kowal, G., Lazarian, A.: Astrophys. J. **720**, 742 (2010). doi:10.1088/0004-637X/720/1/742
Kowal, G., Lazarian, A., Beresnyak, A.: Astrophys. J. **658**, 423 (2007). doi:10.1086/511515
Kowal, G., Lazarian, A., Vishniac, E.T., Otmianowska-Mazur, K.: Astrophys. J. **700**, 63 (2009). doi:10.1088/0004-637X/700/1/63
Kowal, G., Lazarian, A., Vishniac, E.T., Otmianowska-Mazur, K.: Nonlinear Process. Geophys. **19**, 297 (2012). doi:10.5194/npg-19-297-2012
Kowal, G., de Gouveia Dal Pino, E.M., Lazarian, A.: Phys. Rev. Lett. **108**(24), 241102 (2012). doi:10.1103/PhysRevLett.108.241102
Kraichnan, R.: Phys. Fluids **8**, 1385 (1965)
Kraichnan, R.H., Nagarajan, S: Phys. Fluids **10**, 859 (1967). doi:10.1063/1.1762201
Krause, F., Raedler, K.H.: Mean-Field Magnetohydrodynamics and Dynamo Theory. Pergamon Press, Oxford (1980)
Kritsuk, A.G., Norman, M.L., Padoan, P., Wagner, R.: Astrophys. J. **665**, 416 (2007). doi:10.1086/519443
Kulsrud, R.M., Anderson, S.W.: Astrophys. J. **396**, 606 (1992). doi:10.1086/171743
Laing, R.A., Bridle, A.H., Parma, P., Murgia, M.: Mon. Not. R. Astron. Soc. **391**, 521 (2008). doi:10.1111/j.1365-2966.2008.13895.x

Lazarian, A.: Astron. Astrophys. **264**, 326 (1992)
Lazarian, A.: Astrophys. J. **645**, L25 (2006). doi:10.1086/505796
Lazarian, A.: In: Haverkorn, M., Goss, W.M. (eds.) SINS - Small Ionized and Neutral Structures in the Diffuse Interstellar Medium. Astronomical Society of the Pacific Conference Series, vol. 365, p. 324 (2007)
Lazarian, A.: In: de Gouveia dal Pino, E.M., Lugones, G., Lazarian, A. (eds.) Magnetic Fields in the Universe: From Laboratory and Stars to Primordial Structures. American Institute of Physics Conference Series, vol. 784, pp. 42–53 (2005). doi:10.1063/1.2077170
Lazarian, A.: Space Sci. Rev. **181**, 1 (2014).
Lazarian, A., Beresnyak, A.: Mon. Not. R. Astron. Soc. **373**, 1195 (2006). doi:10.1111/j.1365-2966.2006.11093.x
Lazarian, A., Opher, M.: Astrophys. J. **703**, 8 (2009). doi:10.1088/0004-637X/703/1/8
Lazarian, A., Vishniac, E.T.: Astrophys. J. **517**, 700 (1999). doi:10.1086/307233
Lazarian, A., Vishniac, E.T., Cho, J.: Astrophys. J. **603**, 180 (2004). doi:10.1086/381383
Lazarian, A., Esquivel, A., Crutcher, R., Astrophys. J. **757**, 154 (2012). doi:10.1088/0004-637X/757/2/154
Lazarian, A., Vlahos, L., Kowal, G., Yan, H., Beresnyak, A., de Gouveia Dal Pino, E.M.: Space Sci. Rev. **173**, 557 (2012).
Lithwick, Y., Goldreich, P., Sridhar, S.: Astrophys. J. **655**, 269 (2007). doi:10.1086/509884
Lyutikov, M., Lazarian, A.: Soc. Sci. Res. **178**, 459 (2013). doi:10.1007/s11214-013-9989-2
Maron, J., Goldreich, P.: Astrophys. J. **554**, 1175 (2001). doi:10.1086/321413
Mason, J., Cattaneo, F., Boldyrev, S.: Phys. Rev. Lett. **97**(25), 255002 (2006). doi:10.1103/PhysRevLett.97.255002
Matthaeus, W.H., Lamkin, S.L.: Phys. Fluids **28**, 303 (1985). doi:10.1063/1.865147
Matthaeus, W.H., Lamkin, S.L.: Phys. Fluids **29**, 2513 (1986). doi:10.1063/1.866004
Matthaeus, W.H., Montgomery, D.: Ann. N Y Acad. Sci. **357**, 203 (1980). doi:10.1111/j.1749-6632.1980.tb29687.x
McKee, C.F., Ostriker, E.C.: Ann. Rep. Astron. Astrophys. **45**, 565 (2007). doi:10.1146/annurev.astro.45.051806.110602
Melrose, D.B.: Plasma Astrohysics. Nonthermal processes in Diffuse Magnetized Plasmas - vol. 1: The Emission, Absorption and Transfer of Waves in Plasmas; vol. 2: Astrophysical Applications. Gordon and Breach, New York (1980)
Monin, A.S., Iaglom, A.M.: Statistical Fluid Mechanics: Mechanics of Turbulence, vol. 2 /rev. and enlarged edn. MIT Press, Cambridge (1975)
Müller, W.C., Biskamp, D.: Phys. Rev. Lett. **84**, 475 (2000). doi:10.1103/PhysRevLett.84.475
Müller, W.C., Grappin, R.: Phys. Rev. Lett. **95**(11), 114502 (2005). doi:10.1103/PhysRevLett.95.114502
Ostriker, E.C., Stone, J.M., Gammie, C.F.: Astrophys. J. **546**, 980 (2001). doi:10.1086/318290
Padoan, P., Jimenez, R., Juvela, M., Nordlund, A.A.: Astrophys. J. **604**, L49 (2004). doi:10.1086/383308
Perez, J.C., Boldyrev, S.: Phys. Rev. Lett. **102**(2), 025003 (2009). doi:10.1103/PhysRevLett.102.025003
Petrosian, V., Yan, H., Lazarian, A.: Astrophys. J. **644**, 603 (2006).
Politano, H., Pouquet, A.: Phys. Rev. E **57**, R21 (1998). doi:10.1103/PhysRevE.57.R21. URL http://link.aps.org/doi/10.1103/PhysRevE.57.R21
Pouquet, A., Frisch, U., Léorat, J.: J. Fluid Mech. **77**(02), 321 (1976)
Pouquet, A., Sulem, P.L., Meneguzzi, M.: Phys. Fluids **31**, 2635 (1988). doi:10.1063/1.866541
Priest, E., Forbes, T.: Cambridge University Press, Cambridge (2000)
Ryu, D., Kang, H., Cho, J., Das, S.: Science **320**, 909 (2008). doi:10.1126/science.1154923
Santos-Lima, R., de Gouveia Dal Pino, E.M., Kowal, G., Falceta-Gonçalves, D., Lazarian, A., Nakwacki, M.S.: Astrophys. J. **781**, 84 (2014). doi:10.1088/0004-637X/781/2/84
Schekochihin, A.A., Cowley, S.C.: Phys. Plasmas **13**(5), 056501 (2006). doi:10.1063/1.2179053
Schekochihin, A.A., Cowley, S.C.: Turbulence and Magnetic Fields in Astrophysical Plasmas, p. 85–+. Springer, Berlin (2007)

Schekochihin, A.A., Cowley, S.C., Taylor, S.F., Maron, J.L., McWilliams, J.C.: Astrophys. J. **612**, 276 (2004). doi:10.1086/422547
Schekochihin, A.A. , Cowley, S.C., Kulsrud, R.M., Rosin, M.S., Heinemann, T.: Phys. Rev. Lett. **100**(8), 081301 (2008). doi:10.1103/PhysRevLett.100.081301
Schekochihin, A.A., Cowley, S.C., Dorland, W., Hammett, G.W., Howes, G.G., Quataert, E., Tatsuno, T.: Astrophys. J. **182**, 310 (2009). doi:10.1088/0067-0049/182/1/310
Schlickeiser, R.: Cosmic Ray Astrophysics. Springer, Berlin (2002)
Schlüter, A., Biermann, I.: Zeitschrift Naturforschung Teil A **5**, 237 (1950)
Schober, J., Schleicher, D., Federrath, C., Glover, S., Klessen, R.S., Banerjee, R.: Astrophys. J. **754**, 99 (2012). doi:10.1088/0004-637X/754/2/99
Schober, J., Schleicher, D.R.G., Klessen, R.S.: Astron. Astrophys. **560**, A87 (2013). doi:10.1051/0004-6361/201322185
She, Z.S., Leveque, E.: Phys. Rev. Lett. **72**, 336 (1994). doi:10.1103/PhysRevLett.72.336
Speiser, T.W.: Plan. Space Sci. **18**, 613 (1970). doi:10.1016/0032-0633(70)90136-4
Stanimirović, S., Weisberg, J.M., Hedden, A., Devine, K., Green, T., Anderson, S.B.: Astrophys. Space Sci. **292**, 103 (2004). doi:10.1023/B:ASTR.0000045005.36554.36
Strauss, H.R.: Phys Fluids **19**(1), 134 (1976). doi:10.1063/1.861310. URL http://link.aip.org/link/?PFL/19/134/1
Stone, J.M., Ostriker, E.C., Gammie, C.F.: Astrophys. J. **508**, L99 (1998). doi:10.1086/311718
Thompson, C., Blaes, O.: Phys. Rev. D **57**, 3219 (1998). doi:10.1103/PhysRevD.57.3219
Vázquez-Semadeni, E., Gómez, G.C., Jappsen, A.K., Ballesteros-Paredes, J., González, R.F., Klessen, R.S.: Astrophys. J. **657**, 870 (2007). doi:10.1086/510771
Vainshtein, S., Zeldovich, Y.: Physics-Uspekhi **15**(2), 159 (1972)
Vishniac, E.T., Cho, J.: Astrophys. J. **550**, 752 (2001). doi:10.1086/319817
Vishniac, E.T., Lazarian, A.: Astrophys. J. **511**, 193 (1999). doi:10.1086/306643
Xu, S., Lazarian, A.: (2014). In preparation
Yan, H., Lazarian, A.: Phys. Rev. Lett. **89**, 281102 (2002). doi:10.1103/PhysRevLett.89.281102
Yan, H., Lazarian, A.: Astrophys. J. **614**, 757 (2004). doi:10.1086/423733
Yan, H., Lazarian, A.: Astrophys. J. **677**, 1401 (2008). doi:10.1086/533410
Yan, H., Lazarian, A.: Astrophys. J. **731**, 35 (2011). doi:10.1088/0004-637X/731/1/35
Yan, H., Lazarian, A., Draine, B.T.: Astrophys. J. **616**, 895 (2004). doi:10.1086/425111
Yeung, P.K., Zhou, Y.: Phys. Rev. E **56**, 1746 (1997). doi:10.1103/PhysRevE.56.1746
Zank, G.P., Matthaeus, W.H.: Phys. Fluids **5**, 257 (1993). doi:10.1063/1.858780

Chapter 9
The Intermittency of ISM Turbulence: What Do the Observations Tell Us?

Edith Falgarone, Giorgos Momferratos, and Pierre Lesaffre

Abstract The interstellar medium is highly turbulent, but this medium, a partially ionized plasma, is also multi-phase, compressible and magnetized, hence the complexity of its turbulence extends beyond theoretical grasp. Turbulence being with gravity a key player in the star formation process, it is anticipated that its dissipation is a key process too. A fundamental property of turbulent dissipation is its space-time intermittency, studied mostly in hydrodynamical turbulence. After an overview of our limited knowledge of intermittency based on laboratory experiments, theory and numerical simulations, this chapter gathers the set of observations, now made possible by the new capabilities of molecular spectroscopy and polarimetry, that may be seen as signatures of intermittency in the magnetized turbulent interstellar medium. It includes powerful statistical approaches of the interstellar velocity field, the detection of large velocity-shears at very small scales, and chemical and radiative diagnostics of intermittent dissipation. Models of magnetized dissipation bursts, either in the form of coherent vortices or low velocity C-shocks are also presented and confronted to observations, as well as results on the regions of most intense dissipation in spectral simulations of magneto-hydrodynamical (MHD) and non-ideal turbulence.

9.1 The Turbulent Interstellar Medium

The interstellar medium (ISM) contributes to less that 1 % to the mass of our Galaxy (and in most galaxies of the present day universe) and yet it is the reservoir of gas that still allows the formation of new stars. It is paradoxical that this medium plays such a critical role in the cycle of cosmic matter and yet contributes such a small fraction of the galaxy masses. It is part of an open cycle that drives baryons from dying stars to new stars, at a rate of a few $M_\odot$ year^{-1} in our Galaxy, comparable to the rate of gas infall from the extragalatic environment. The warmest phases of the ISM are fully ionized. Its neutral and coldest phases, which comprise the bulk of its

E. Falgarone (✉) • G. Momferratos • P. Lesaffre
Ecole Normale Supérieure, 24 rue Lhomond, 75005 Paris, France
e-mail: edith.falgarone@ens.fr; giorgos.momferratos@ens.fr; pierre.lesaffre@ens.fr

A. Lazarian et al. (eds.), *Magnetic Fields in Diffuse Media*, Astrophysics and Space Science Library 407, DOI 10.1007/978-3-662-44625-6_9

mass, consist in two main phases, the cold neutral medium (CNM) at $\sim$100 K and the warm neutral medium (WNM) at $\sim 10^4\,K$, approximately in thermal pressure equilibrium (Field et al. 1969).

Because it sits in the gravitational potential of the Galaxy and it extends up to 1 kpc or more above the plane, the ISM has to be supported by a pressure that is about ten times its thermal pressure, $P_{tot} = 3 \times 10^{-12}$ dynes cm^{-2}, or $P_{tot}/k_B \sim 2 \times 10^4$ K cm^{-3} (Cox 2005). The non-thermal contributions to the total pressure are due to supersonic turbulence and magnetic fields, in rough equipartition, as shown by measurements of magnetic field intensity (Crutcher et al. 2010) and HI linewidths (Haud and Kalberla 2007). The distribution of thermal pressures in the Solar Neighbourhood, inferred from [CI] fine-structure absorption lines towards nearby stars (Jenkins and Tripp 2011) peaks at about $P_{th}/k_B \sim 3 \times 10^3$ K cm^{-3}, with large fluctuations, up to a few 10^4 K cm^{-3}. It is noteworthy that the total non-thermal pressure in the Galactic plane is of the same order as the largest thermal pressure fluctuations observed, suggesting that the non-thermal energy eventually and occasionally degrades into thermal energy.

Interstellar turbulence has been advocated very early (von Weizsäcker 1951) but the nature, origin and properties of turbulence in the ISM are still highly debated and controversial issues in spite of dedicated observational and numerical efforts. Moreover, the gas suprathermal motions might just be random motions if a full turbulent cascade does not have time to develop in the violent ISM. We recall here a few definitions.

The definition of turbulence is built on experiment. Turbulence is an instability of laminar flows. Their velocity field $\mathbf{u}$ satisfying the incompressibility condition $\nabla \cdot \mathbf{u} = 0$ is solution of the Navier–Stokes equation

$$\partial_t \mathbf{u} + (\mathbf{u} \cdot \nabla)\mathbf{u} = -\frac{\nabla p}{\rho} + \nu \nabla^2 \mathbf{u} \tag{9.1}$$

where p is the pressure and ν is the kinematic viscosity. This instability develops as soon as the inertial $\mathbf{u} \cdot \nabla \mathbf{u}$ accelerations greatly exceed the viscous $\nu \Delta \mathbf{u}$ ones (ν is the kinematic viscosity) i.e. when the Reynolds number $Re = l u_l / \nu$, at a scale l of characteristic velocity u_l, exceeds a few hundreds. This instability at scale l is at the origin of an energy transfer to smaller scales, that eventually become unstable too and transfer their kinetic energy to still smaller scales, etc... This is the turbulent cascade that develops between the integral scale, L, at which energy is injected, and the dissipation scale l_D, close to the particle mean-free-path, where energy is dissipated into heat due to the particle viscosity. The timescale for the growth of this instability is of the order of the turnover time $\tau_l = l/u_l$ at each length scale l. Kolmogorov (1941) (hereafter K41) predicted the self-similar behavior of the velocity field in incompressible turbulence by postulating a dissipationless cascade characterized by a transfer rate of kinetic energy independent of scale, $\epsilon_l \propto u_l^2/\tau_l = u_l^3/l$, hence the well-known scaling $u_l \propto l^{1/3}$. It is easy to demonstrate that this assumption leads to an energy spectrum $E(k) \propto k^{-5/3}$ known as the Kolmogorov spectrum. $E(k)$ has the dimension of a kinetic energy per unit mass and

Table 9.1 Characteristics of the turbulence observed in various components of the interstellar medium (Solar Neighborhood). ϵ_l is expressed in $L_\odot/M_\odot$ for comparison with the energy provided by stellar radiation

		CNM	Molecular clouds	Low-mass dense cores
$\overline{n}$	cm^{-3}	30	200	10^4
l	pc	10	3	0.1
T	K	100	20	10
σ_l	$km\ s^{-1}$	≈ 3.5	1	0.1
B	μG	10	20	100
$\mathbf{v}_A$	$km\ s^{-1}$	3.4	2	1.4
$\epsilon_l = \frac{1}{2}u_l^3/l$	$L_\odot/M_\odot$	10^{-3}	10^{-4}	10^{-6}
$\epsilon_\rho = \frac{1}{2}\overline{\rho}u_l^3/l$	$erg\ cm^{-3}s^{-1}$	2×10^{-25}	1.7×10^{-25}	2.5×10^{-25}
Λ	$erg\ cm^{-3}s^{-1}$	5×10^{-24}	4×10^{-24}	3×10^{-24}
$P_{turb} = \frac{1}{3}\overline{\rho}u_l^2$	$erg\ cm^{-3}$	3×10^{-11}	2×10^{-11}	10^{-11}
$\nu = \frac{1}{3}\lambda u_{th}$	$cm^2\ s^{-1}$	2.2×10^{17}	1.5×10^{16}	2.1×10^{14}
$l_d = (\nu^3/\epsilon_l)^{1/4}$	AU	3.2	0.8	0.1
$Re = l u_l/\nu$		7.6×10^7	9.6×10^7	2.3×10^7

unit wavenumber because the average specific kinetic energy at scale $l = 2\pi/k$ is $\langle u_l^2 \rangle = \int_k^\infty E(k')dk'$. In Kolmogorov turbulence, the turnover timescale τ_l therefore decreases towards small-scales while the velocity gradient $u_l/l \propto l^{-2/3}$ increases. In the case of the ISM, the Reynolds numbers in the neutral ISM (see Table 9.1) are $\sim 10^8$ and the turnover timescale of the largest scales (300 pc, the thickness of the HI disk, and $6\,km\,s^{-1}$, the cloud velocity dispersion) is of the order of 50 Myr. It may be seen as the largest time required for the turbulent cascade to develop. We thus consider that in the bulk of the ISM (far from regions actively forming young stars) a turbulent cascade has time to develop and the gas motions are truly turbulent. Interestingly, the energy spectrum of mildly supersonic turbulence (rms sonic Mach numbers ~ 1) has a slope comparable to that of the Kolmogorov spectrum, and this holds for decaying (Porter et al. 1998), driven (Porter et al. 2002) hydrodynamic turbulence, as well as MHD turbulence (Vestuto et al. 2003). This is so because, after a few turnover times, the power in compressible modes drops below that in solenoidal (or shear) modes, whatever the initial conditions, amounting to no more than $\sim 10\,\%$ of the total power. In MHD turbulence, the relative power of shear to compressible modes increases as the magnetic field intensity increases (Vestuto et al. 2003).

The difficulty at characterizing interstellar turbulence is due in part to the huge range of scales separating those of the energy injection, at the Galaxy scale and even beyond when extragalactic infall is taken into account (see de Avillez and Breitschwerdt 2005), from those where it is dissipated, presumably below the milliparsec scale. It is also due to the fact that the turbulence is compressible, magnetized and multi-phase. It is critical, though, to unravel the properties of interstellar turbulence because turbulence and magnetic fields are the main contributions to the pressure of the ISM and the main stabilizing support of molecular clouds against

their self-gravity. Turbulent dissipation is therefore a key process among those leading to the formation of molecular clouds, star formation, and therefore galaxy evolution (see the reviews of Elmegreen and Scalo 2004; Scalo and Elmegreen 2004; Hennebelle and Falgarone 2012).

Studies of a turbulent velocity field are by nature statistical and in the case of the ISM have to rely on the analysis of line shapes observed at high spectral resolution. Early works were conducted on large samples of absorption lines observed against nearby stars. The λ 21 cm line of atomic hydrogen is hard to interpret because of the mixture of emission from the WNM and self-absorption by the CNM. However, a remarkable Kolmogorov spectrum covering two orders of magnitude in scales has been obtained in a high-latitude region where the HI emission arises primarily in the CNM (Miville-Deschênes et al. 2003a). The high optical depth of the ^{12}CO(1-0) line has opened new fields of investigation of the turbulence within molecular clouds. Molecular clouds, as seen in this line, have the remarkable property that their CO line emission is "clumpy" at all scales, i.e. the CO line intensity highly fluctuates in space and velocity, a property likely due to the underlying turbulence. The pioneering Larson's study (1981) who ascribed to turbulence the power-law increase $\propto l^{0.38}$ of the internal velocity dispersion of clouds of size l has now been extended to larger samples of molecular clouds and tracers. We refer to Hennebelle and Falgarone (2012) for references and a critical review of these results.

CO(1-0) observations provide a measurement of the kinetic energy transfer rate per unit volume $\epsilon_\rho = \frac{1}{2}\rho u_l^3/l$ where ρ and $u_l = 1.6\sigma_l$ are the mean gas density and mean velocity of scale l, respectively. The large fluctuations of this quantity in a population of molecular clouds traced by ^{12}CO(1-0) are in sharp contrast with the fact that its *average* value stays the same from structures of 0.01 pc to giant molecular clouds (GMC) of 100 pc and has the value observed in the atomic gas (Haud and Kalberla 2007) (see Fig. 6 in Hennebelle and Falgarone 2012). This suggests that ϵ_ρ is an invariant of the hierarchy of molecular clouds traced by CO(1-0) and that these clouds are part of the same turbulent cascade as the atomic ISM. The energy spectrum in molecular gas is therefore expected to differ from the Kolmogorov spectrum. Note however that the average density between the smallest (10^{-2} pc) and largest (100 pc) scales increase only by a factor of 20. The Kolmogorov spectrum obtained in the nearby CNM (Miville-Deschênes et al. 2003a) is due to the fact that the CNM density does not fluctuate much: its thermal pressure is well defined (Jenkins and Tripp 2011) alike its temperature $T_K \sim 80$ K inferred from HI absorption measurements.

The characteristics of interstellar turbulence as observed in the diffuse medium (HI in emission), molecular clouds and dense cores (see Table 9.1) are such that the possible invariant of the cascade, the energy transfer rate ϵ_ρ, encompasses the warm neutral medium and the coldest and densest structures of low-mass ($M \leq$ a few $M_\odot$). If we assume that the energy transfer rate equals the average dissipation rate in the cascade, the comparison of $\epsilon_\rho \sim 10^{-25}$ erg cm^{-3}s^{-1} and Λ, the average cooling rate, in Table 9.1, shows that turbulent dissipation is too low, on average, to be a dominant source of heating of the ISM, in comparison with that provided by starlight ($> 1\ L_\odot/M_\odot$). Turbulent dissipation may however become a dominant

heating source locally, if it is concentrated in bursts that fill only a small subset of space. This is the property of space-time intermittency of turbulence that is discussed in this chapter.

9.2 Intermittency in Hydrodynamical Incompressible Turbulence

9.2.1 Definitions and Statistical Signatures

For half a century now, turbulence has been recognized to be intermittent i.e. the smaller the scale, the larger the spatio-temporal velocity fluctuations, relative to their average value. Turbulent energy is not evenly distributed in space and time by the turbulent cascade: at each step of the cascade, the active sub-scales do not fill space so that the subset of space on which the active scales are distributed has a multifractal geometry (see the review of Anselmet et al. 2001 and the book of Frisch 1996). The statistical properties of the velocity fluctuations have been widely studied experimentally in laboratory and atmospheric flows: in all cases, the statistics of *velocity derivative and increments* signals are found to be non-Gaussian, with large departures from the average more frequent than for a Gaussian distribution. The probability distribution function (*pdf*) of the turbulent velocity field, in turn, remains Gaussian. Moreover, the departure of the *velocity increments pdf*s from a Gaussian distribution increases as the lag over which the increments are measured decreases. All the functions of the velocity involving a spatial derivative have therefore non-Gaussian *pdf*s: the velocity shears ($\partial_j u_i$) and, accordingly, the rate-of-strain $S_{ij} = \partial_j u_i + \partial_i u_j$ and the dissipation rate in incompressible turbulence $\epsilon_D = \frac{\nu}{2}\Sigma_{ij}(\partial_j u_i + \partial_i u_j)^2$, with non-Gaussian wings more pronounced at small scale.

The quantitative signature of intermittency appears in the behavior of the high-order structure functions of the longitudinal velocity field measured over a lag s, $\langle[\delta u_x(s)]^p\rangle \propto s^{\zeta_p}$. This relation is statistical, not deterministic, and the brackets hold for an average over an "appropriate" volume with respect to s^3. The anomalous scaling of the exponents $\zeta_p \neq p/3$ characterizes the degree of intermittency and provides the multifractal dimension of the most singular structures, i.e. that of the subset of space where the smallest active regions, and turbulent dissipation, are distributed (Anselmet et al. 2001). In incompressible turbulence, the so-called *active small scales* are those of largest vorticity or velocity shear. Various models have been proposed for the values of ζ_p. The most successful is certainly the one proposed by She and Lévêque (1994) who infer the relation

$$\zeta_p = \frac{-\gamma + 1}{3} p + \gamma \frac{1 - \beta^{p/3}}{1 - \beta}, \tag{9.2}$$

where γ is the exponent of the dissipation rate scaling in regions containing the most intermittent structures and β is related to the co-dimension C of the strongest dissipation structures $\gamma/(1-\beta) = C$. For incompressible hydrodynamical turbulence, the dissipative structures tend to be filamentary with co-dimension $C = 3-1 = 2$ while $\gamma = 2/3$ is assumed to be valid for the most dissipative structures. In compressible turbulence, where dissipation occurs in shocks (Boldyrev et al. 2002), and magnetized turbulence where it occurs in current sheets (Politano and Pouquet 1995; Müller and Biskamp 2000), the most intense dissipative structures are two-dimensional, so that the co-dimension $C = 1$ while $\beta = 1/3$ (see Pan et al. 2008).

Another essential facet of turbulent intermittency is that the most active small scales are not randomly distributed in space but are organized into coherent structures—*the sinews of turbulence*, as qualified by Moffatt et al. (1994). In incompressible turbulence, the structures of largest vorticity and weak rate-of-strain ($S_{ij} = \partial_j u_i + \partial_i u_j$) tend to be filamentary, while those of highest rate-of-strain and dissipation are rather in the form of sheets or ribbons, following the analysis of numerical simulations (Roux et al. 1999; Moisy and Jiménez 2004). These structures are remarkable in the sense that they are both large scales, i.e. their length is comparable to the integral scale of turbulence, and small scale structures, i.e. they have substructure down to the dissipation scale. The coupling between the largest and smallest scales operated by turbulence is now well established in simulations, as shown by Mininni, Alexakis and Pouquet who find that small-scale intermittency is more pronounced in turbulent fields where the large-scale shear is larger (Mininni et al. 2006a).

9.2.2 Open Questions

The above section has not addressed some fundamental facets of intermittency: the multifractal nature of the subset of space on which turbulent dissipation is concentrated, the link between intermittency of the velocity and that of the dissipation, and the duality of the Eulerian and Lagrangian descriptions of intermittency. These facets have been studied in incompressible hydrodynamical (HD) flows and, interestingly, the results point towards the existence of a universal behaviour. In their analysis of laboratory experiments monitoring the fluctuations of pressure in a turbulent flow, Roux et al. (1999) have shown that once they have removed the strong signals associated with intense vorticity filaments the multifractal nature of the background pressure fluctuation persists, providing strong experimental support to the multifractal distribution of the pressure fluctuations. In a joint analysis of the best available laboratory and numerical experiments at high Reynolds numbers, Arnéodo and his team (Arnéodo et al. 2008) show that the multifractal description captures intermittency at all scales, including the dissipative range, with only a few parameters independent of Re. They provide a unifying description of the scalings of the Lagrangian and Eulerian velocity structure functions. Chevillard et al. (2013) further develop the phenomenology of intermittency in the Lagrangian context,

using new experimental and numerical results. They find that the multifractal formalism captures the universality of intermittency, down to the dissipative scales and in the Eulerian and Lagrangian frames.

Whether or not the universality of HD turbulence in a broad range of Re numbers is relevant to more complex turbulent fields, such as ISM turbulence, is an open question. It is encouraging though that the Lagrangian velocity fluctuations are found to be highly intermittent too because, as will be seen below, it strengthens the possibility that intermittent dissipation of turbulence impacts the chemistry of the gas phase.

9.3 Intermittency in the ISM: The Observers Perspective

Searches for non-Gaussian statistics in the ISM velocity field have been conducted for many years now and some results are presented below. Measurements of the departure of the moments of order p of the velocity structure functions from the $\zeta_p = p/3$ prediction of the K41 model are extremely difficult in practice because the number of independent measurements needed to compute S_p grows as $\sim 10^{p/2}$. Access to $p = 8$, for instance, therefore requires 10^4 independent measurements. In the ISM, only recently has this been accessible.

9.3.1 Signatures of the Intermittency in the Velocity Field of Molecular Clouds

9.3.1.1 Parsec-Scale Coherent Structures of Intense Velocity-Shear

Identifying regions of intermittency in interstellar turbulence is challenging for several independent reasons. Firstly, these regions are non-space filling and correspond to rare events in time and space: their finding requires the analysis of large homogeneous statistical samples of the velocity field. This means observations at high spectral and spatial resolution of large regions of interstellar material. Secondly, observations do not provide the full velocity field, but only its line-of-sight (*los*) projection provided by the Doppler-shift of a molecular line, so statistical analysis similar to those performed in laboratory flows or in the solar wind are not possible. However, measurements of the spectrum of molecular lines with a frequency resolution finer than the sound speed in cold H_2 provide information on the suprathermal velocity field. The ^{12}CO(1-0) line has turned out to be a most useful tool for this search.[1] Thirdly, only spatial variations of the *los* velocity in the plane-

[1] under the restriction that only diffuse molecular gas of low to moderate line opacity be studied, to avoid complications due to radiative transfer.

of-the-sky (*pos*) are provided by observations. Therefore, the velocity variations are by essence cross-variations $\partial_j u_i$. Finally, the line emission being integrated along a *los*, the velocity information at a given position is the full line profile and its moments, the first moment being the line centroid velocity C. The statistics of the velocity increments are built through those of the line centroid velocity increments (CVI) δC_l measured between two positions separated by a lag l in the *pos*. The CVIs have been shown by Lis et al. (1996) to be a proxy of extrema of vorticity, being the *los* average of the *pos* projection of the vorticity. This is because the vorticity is a signed quantity. In the *los* integration, the vorticity fluctuations cancel out and the result is dominated by a few large values, when they exist.

Thanks to the improved efficiency of observations at high spectral resolution in the millimeter wave domain, it is now possible to map large fields at high spectral and spatial resolutions with a high sensitivity in a reasonable amount of observing time. An example, drawn from observations in the Polaris Flare carried out at the IRAM-30 m telescope in the ^{12}CO($J = 2 - 1$) line, is shown in Fig. 9.1 (Hily-Blant and Falgarone 2009). The $\sim 10^5$ independent spectra sample homogeneous turbulence in diffuse molecular gas. The CVI-*pdf*s in that field have the anticipated non-Gaussian wings that increase as the lag over which the increment is measured decreases (Fig. 9.2, left). The locus of the extreme CVIs (the E-CVIs) that build

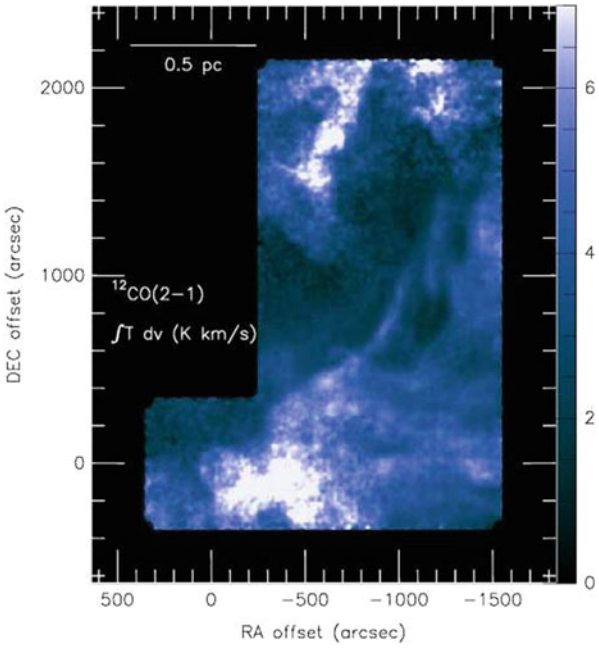

Fig. 9.1 Map of the ^{12}CO(J=2-1) integrated intensity (in K km s^{-1}) over a $40' \times 30'$ area located in the Polaris Flare. The number of independent spectra is $\sim 10^5$. The spatial resolution is 11 arcsec or 8 mpc at the distance of the field, d=150 pc

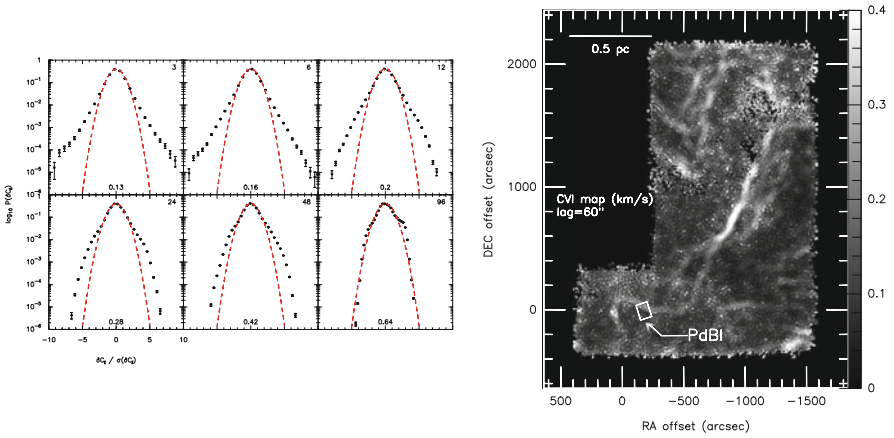

Fig. 9.2 *Left*: Normalized *pdf*s of line centroid velocity increments δC_l measured over variable lags, expressed in units of 15 arcsec (numbers in the *upper right* corners), and computed within the field of Fig. 9.1. The Gaussians of same dispersion $\sigma(\delta C_l)$ (given in km s^{-1} at the *bottom* of each panel) are also drawn. The non-Gaussian wings of the *pdf*s increase as the lag decreases. Note that, as expected, a probability of 10^{-5} is reached in the most extreme bins. *Right*: In the same field, locus of the positions populating the non-Gaussian wings of the *pdf* for a lag of 60 arcsec. The wedge is in km s^{-1}. The rectangle locates the area observed with the IRAM-PdBI. From Hily-Blant and Falgarone (2009)

up the non-Gaussian wings of the *pdf*s is an elongated narrow structure ($\sim$0.03 pc thick), almost straight over more than one parsec and surrounded by an ensemble of weaker, shorter structures (Fig. 9.2, right). As expected, the lane of largest E-CVIs coincides with the region where the velocity-shears are the largest, 40 km s^{-1} pc^{-1} (see Hily-Blant and Falgarone 2009). Most interestingly, it also coincides with a lane of weak ^{12}CO(2-1) emission and one of the weakest filaments of dust thermal emission detected at 250 μm in that field with *Herschel*/SPIRE (Miville-Deschênes et al. 2010). Last, two low-mass dense cores lie at the South-East tip of the E-CVIs locus (Heithausen et al. 2002). All these suggest a *causal link* between extrema of turbulent dissipation, the formation of CO molecule, the formation of tenuous dense filaments and that of low-mass dense cores.

A similar analysis has been performed in a cloud edge of the Perseus–Taurus–Auriga giant molecular complex. The field has the same total hydrogen column density as that in the Polaris Flare, but is less turbulent (half the pc-scale rms velocity dispersion). The CVI-*pdf*s show departures from a Gaussian distribution with an amplitude 2.5 times smaller than in the Polaris Flare (Hily-Blant et al. 2008). This result is in agreement with the theoretical predictions of Mininni et al. (2006a) and further supports the fact that these observations are manifestations of intermittency.

These properties taken together, (1) the increasing departure of CVI-*pdf*s from a Gaussian distribution as the scale decreases, (2) the spatial coherent structures of E-CVIs and (3) the link between the large-scale properties of turbulence and the magnitude of the small-scale E-CVIs, all suggest that the ^{12}CO(2-1) E-CVIs

trace the intermittency of turbulence in diffuse molecular clouds. The multifractal geometry of the E-CVIs structures in the Polaris Flare probed by the non-linear dependence of ζ_p with p up to $p = 6$ discussed in Hily-Blant et al. (2008) is now confirmed, up to higher orders, by the analysis of this larger data set. Unexpectedly, the ζ_p departure from a linear dependence agrees, within the error bars, with the predictions for incompressible turbulence (She and Lévêque 1994). Hily–Blant, Falgarone and Pety also show the sharp increase of the flatness (or kurtosis) of the velocity field, defined here as $\frac{\langle \delta C_l^4 \rangle}{\langle \delta C_l^2 \rangle^2}$ as the scale l decreases (Hily-Blant et al. 2008).

9.3.1.2 Milliparsec-Scale Observations: Approaching the Dissipation Scales

A step further towards small-scales is provided by IRAM Plateau de Bure Interferometer (PdBI) ^{12}CO(1-0) line observations of the small field shown in Fig. 9.2 (right) at a resolution of ∼4 arcsec or 3 mpc (Falgarone et al. 2009). These observations are unique so far: the lines detected are very weak, but the spatial dynamic range of the map is large enough to allow the detection of eight elongated structures with thickness as small as ≈3 mpc (600 AU) and length up to 70 mpc, set indeed by the size of the field. They are *not filaments* because once merged with short-spacing data, the PdBI-structures appear to be the sharp edges of more extended CO emission. Moreover, six out of eight form pairs of quasi-parallel structures at different velocities. Statistically, this cannot be due to chance alignment. Velocity-shears estimated for the three pairs include the largest values ever measured in non-star-forming regions, up to 780 km s^{-1} pc^{-1}. Other cases of CO(1-0) milliparsec-scale structures forming elongated patterns with large velocity-shear (up to ∼180 km s^{-1} pc^{-1}) have been found in diffuse gas (Heithausen 2006, 2004). Finally, the PdBI-structures are almost straight and their different position angles, cover a broad range of values, from $PA = 60°$ to 165°, an unexpected result given the small size of the field. The scatter of their PAs is therefore as large within that small field of ∼70 mpc than it is for the coherent structure in the parsec-scale field (Fig. 9.2).

9.3.1.3 Polarization Measurements of Starlight in the Polaris Flare

Dust absorption polarizes starlight and the direction of the polarization turns out to be that of the *pos* projection of the magnetic field, B_{pos}, because dust grains are aligned by the magnetic field by processes that we do not detail here (see the chapter of Andersson, this volume, for a review). The sampling of the field direction is therefore uneven and dictated by the position of the background stars bright enough to allow measurements of polarized light that amounts to only a few % of the star luminosity. The Polaris Flare has been observed in the visible (Mohan et al., in prep.) with the "Beauty and the Beast" spectro-polarimeter at Mt Megantic (Manset and

Bastien 1995) over a large field of ∼30 pc, providing 45 sensitive measurements, the polarization fractions measured being as low as 0.3 %. The distribution of the *PA*s of the polarization at large scale is broad, with values distributed from 10° to 150°. In the near-IR, observations have been carried out with the Mimir imaging polarimeter (Clemens et al. 2012) at the Perkins telescope of two $10' \times 10'$ (or 0.45 pc) fields encompassing the PdBI-field and the area of largest E-CVIs (Fig. 9.2, right). The number of detected polarizations barely exceeds ten because at these high latitudes the number of stars bright enough to perform polarization measurements is low. However, the scatter of the *PA*s is as large as that observed at the 30 pc-scale and there is a trend for the *pos* projection of the magnetic field to be aligned with the intense velocity-shears. Yet, any statistically meaningful comparison of the orientation of B_{pos} with the structures of most intense velocity shears has to rely on more observations.

These results on intense velocity-shears and starlight polarization do not provide a full three-dimensional view of the magnetic fields in regions of velocity-shear extrema, but they carry promising information. The regions of intense velocity-shears are straight structures in projection in the *pos* at the arcmin-scale (∼0.05 pc) (Falgarone et al. 2009). They have to be straight also in real space and therefore be part of sheets that are straight in at least one direction. This is reminiscent of the findings of Mininni, Pouquet and Montgomery regarding the formation of parallel current and vortex sheets in MHD turbulence that destabilize, fold and roll up along directions parallel to the magnetic fields (Mininni et al. 2006b). We put these results in perspective of pseudo-spectral numerical simulations of non-ideal magnetized turbulence in Sect. 9.5.

9.3.2 *Signatures of Intermittency: Hot Glitters in the Cold Medium*

A resilient and major puzzle has long been the existence in the diffuse ISM of molecular species that have a formation endothermicity far above the available thermal energy: their large observed abundances cannot be reproduced by state-of-the-art chemistry models driven by UV photons and cosmic-rays only (Le Petit et al. 2006). This has been known for 70 years in the case of CH^+ that was among the first molecular species discovered in space by absorption spectroscopy against nearby stars. Not only does this cation form through the highly endothermic reaction $C^+ + H_2$ ($\Delta E/k = 4940$ K) but it is also rapidly destroyed by collisions with H_2. The puzzle has been recently deepened and extended to the whole Galaxy by *Herschel*/HIFI observations of the $CH^+(J = 1 - 0)$ transition in absorption against the dust continuum emission of remote star forming regions (Falgarone et al. 2010a,b), confirming the very high abundance of this cation in the diffuse ISM. Similarly, SH^+, that has a formation endothermicity almost twice as large as CH^+, is also observed to be abundant in the diffuse ISM (Menten et al. 2011; Godard et al. 2012).

Another outstanding and more recent puzzle is the origin of the H_2 pure rotational line emission of the diffuse ISM. Its discovery dates back to the ISO-SWS detection of the four lowest rotational transitions across a large pathlength of diffuse gas in the Galactic plane, $N_H \sim 10^{22}$ cm^{-2}, equivalent to 16 mag (Falgarone et al. 2005). Given the high energy of the upper level of these transitions, 510 K for the S(0) line, up to 2,540 K for the S(3) line, and the absence of intense UV radiation field able to excite these levels by fluorescence, a non-thermal excitation of some kind is required. This Galactic emission was modelled by advocating heating of the gas by turbulent dissipation. The dissipation regions, distributed along the line of sight, were either hundreds of low velocity magneto-hydrodynamical (MHD) shocks (8–12 km s^{-1}) or thousands tiny regions of intense velocity-shears, heating the gas by ion-neutral friction and/or viscous dissipation. The interesting new result of these models was that a fraction as small as a few percent of warm gas, heated by dissipation of mechanical energy, was sufficient to reproduce the observed line intensities, and their line ratios. New detections of these lines have been performed by *Spitzer*/IRS, in the diffuse gas around supernova remnants (Hewitt et al. 2009), at an edge of the Taurus molecular complex (Goldsmith et al. 2010), and in several diffuse clouds (Ingalls et al. 2011). In all these studies, UV excitation cannot explain the H_2 line intensities and non-thermal excitation, likely fed by turbulent dissipation, is required.

Last, large fluctuations of the CO emission of diffuse gas at small scale have been observed that cannot be ascribed to UV-shielding fluctuations (see references in Hennebelle and Falgarone 2012). This sharp variability is primarily due to CO chemistry, a point that cannot be understood in the framework of UV-driven chemistry and is discussed in the next section.

9.4 Intermittency in the ISM: The Theoretical Chemistry Perspective

Models of non-equilibrium chemistry have attempted to capture the essence of the coupling between the impulsive heating due to intermittent turbulent dissipation and the warm chemistry it triggers. They have focussed on the diffuse ISM because it is there that the very first steps of chemistry in space take place with the formation of the light hydrides, formed by reaction of the most abundant heavy elements (C, O, N, S, Si) with H_2. It is there too that the high observed abundances of these light hydrides cannot be understood. This is so because many of the formation reactions of these hydrides are so highly endothermic that they are blocked at the temperature of the cold diffuse ISM that contains the traces of H_2 indispensable for the chemistry to be initiated. Table 9.2 gives the broad range of energy barriers that the chemistry of light hydrides offers. The presence of these species in the cold ISM can thus be used as diagnostics of intermittent dissipation of turbulence. Two different frameworks have been adopted for the dissipative structures: either small-scale magnetized vortices (Joulain et al. 1998; Godard et al. 2009) or magnetized low-

Table 9.2 Non-exhaustive list of bottleneck reactions for molecule formation with their temperature barrier or endothermicity

Reaction	Temperature barrier (K)
$O+H_2 \rightarrow OH+ H$	2,980
$C^+ + H_2 \rightarrow CH^+ + H$	4,640
$S+ H_2 \rightarrow SH+ H$	9,620
$S^+ + H_2 \rightarrow SH^+ + H$	9,860
$C+ H_2 \rightarrow CH+ H$	14,100
$Si^+ + H_2 \rightarrow SiH^+ + H$	14,310
$N+ H_2 \rightarrow NH+ H$	14,600
H_2 dissociation energy	52,000

velocity shocks (Falgarone et al. 2005; Lesaffre et al. 2013). They are discussed below.

9.4.1 Non-Equilibrium Chemistry in a Magnetized Burgers Vortex

The TDR model (for Turbulent Dissipation Regions model Godard et al. 2009, 2012, 2014), is based on the fact that turbulent dissipation that involves $\nabla \cdot \mathbf{u}$ and $\nabla \times \mathbf{u}$ is an intermittent quantity. It is built on an analytical solution of the Helmholtz equation for the vorticity, the Burgers vortex. In addition to the traditional parameters of chemistry models, the density $n_{\rm H}$ and UV shielding characterized by the visual extinction A_V, the free parameters of the TDR model are constrained by the known large-scale properties of turbulence in the diffuse medium (see Joulain et al. 1998): the rate-of-strain a—a quantity homogeneous to s^{-1}—(see definition in Sect.9.2) and the maximum orthoradial gas velocity in the vortex, set by the turbulent velocity dispersion at large scale. The rate-of-strain and the equilibrium radius of the vortex are related by $r_0^2 = 4\nu/a$. A hydrodynamical steady-state of a (slightly modified) magnetized Burgers vortex of finite length is computed. The gas density is low enough that the neutral component decouples from the ions and magnetic field in the layers where the orthoradial velocity is the largest. The thermal and chemical evolution of a fluid cell crossing the steady-state vortex is computed in a Lagrangian frame. The dissipation is due to (1) viscous dissipation in the layers of intense velocity-shear at the vortex outer boundary and (2) ion-neutral friction induced by the decoupling of the ionized and neutral flows in the central regions.

Since the diffuse medium has a low density, its chemical and thermal inertia are large. The TDR model takes into account the long-lasting relaxation period that follows the end of any dissipative burst. The vortex lifetime, i.e. the duration of the burst of dissipation, is set by energetic considerations (see Godard et al. 2009, 2014) and is as short as a few hundred years. A random line of sight through the medium therefore samples three kinds of gas: thousands of active vortices occupying at most a few percent of any random line of sight across the medium, many more relaxation

phases and the ambient medium. The relaxation times of the different species cover a broad range, from 200 year for CH^+ up to 5×10^4 year for CO. This introduces a potentially untractable complexity in the comparison of the abundances of different species.

A large number of models have been run to explore the parameter space varying the density ($30 < n_H < 500$ cm^{-3}), the visual extinction ($0.1 < A_V < 2$ mag), the rate-of-strain ($10^{-12} < a < 10^{-10}$ s^{-1}) and the average turbulent energy transfer rate, ϵ, assumed to be equal to the average dissipation rate $\overline{\epsilon}_D$.

The main results are as follows (Godard et al. 2014):

1. The CH^+ abundance is found to increase linearly with $\overline{\epsilon}_D$, which makes this radical a specific tracer of the dissipation of suprathermal energy in the ISM. The observed abundances of CH^+ and SH^+ are well reproduced for the conditions prevailing in the diffuse ISM in the Galaxy, including the inner Galaxy.
2. The efficient formation of CH^+ opens a new branch of chemical reactions by producing CH_3^+, a daughter species of CH^+. CH_3^+ is very reactive and for instance, by reaction with O, forms HCO^+, a parent species of CO. The warm chemistry driven by turbulent dissipation therefore produces many daughter-species and significantly contributes to the formation of CO in the diffuse turbulent medium.
3. The observed abundances tend to favor low rates-of-strain, i.e. models in which dissipation is dominated by ion-neutral friction rather than viscous dissipation. Remarkably, the pc-scale velocity shear of 40 km s^{-1} pc^{-1} observed in the Polaris Flare would correspond to a straining field from the large scales $a = 1.5 \times 10^{-12}$ s^{-1}, while the intense small-scale shear of 780 km s^{-1} pc^{-1} detected at the mpc-scale is 20 times larger. Both rates-of-strain are in the range of a values consistent with chemical observations.
4. Only a few percent of the gas heated by turbulent dissipation are sufficient to trigger the warm chemistry consistent with observations.
5. The last interesting prediction of the TDR model is the intensity of the radiative cooling during the thermal relaxation phase. It is dominated by the H_2 pure rotational lines, as long as the gas temperature is above $\sim$500 K, then, as the gas cools down, the fine-structure [CII] and OI lines take over. It is remarkable that the total energy radiated by H_2 and C^+ during the relaxation phase is about the same, the latter being about ten times weaker on average over a duration ten times larger. The [CII] emission from a gas component heated by turbulent dissipation rather than by UV photons is predicted to be a possible significant fraction of the total [CII] emission of the diffuse medium.

9.4.2 Non-equilibrium Chemistry in Magnetized Shocks

Another dissipative process in supersonic turbulence occurs in shocks. Shocks are anticipated to be part of the grand pattern of intermittent dissipation of

ISM turbulence. We discuss below models of the non-equilibrium chemistry that develops in low-velocity C-type shocks. They have specific features that can be used to estimate the degree of magnetization of the medium for instance.

When two parcels of fluid collide with relative velocities greater than the information propagation speed, a shock is born. From a large scale point of view, the shock looks like a thin sheet, or working surface, where the relative kinetic energy between the fluid parcels is converted to magnetic, radiative, thermal and internal energy. The surge of thermal energy at the working surface can trigger chemical reactions otherwise blocked by thermal barriers. In the reference frame of the working surface, the gas flows into the shock from one side (the pre-shock) and flows out from the other side (the post-shock side). The entrance velocity of the shock is defined as the velocity of the fluid in the pre-shock side relative to the speed of the working surface. In a magnetized and partially ionised gas such as the ISM, two information speeds are relevant. The fastest speed is the magnetosonic speed in the ionized fluid and the slowest is the Alfvén speed in the neutral gas.

When the shock speed is greater than both these speeds, a J-type shock occurs where ions and neutrals remain coupled at all times. The fine structure of the shock inside the working surface is as follows (see Fig. 9.3). At the shock entrance, kinetic energy is converted on a few mean free paths (i.e. the viscous length) by viscous friction into heat and internal energy. Gradual cooling ensues which depends on the chemical composition of the gas. This converts thermal energy into radiation and the decrease of temperature leads to an increase of density. Indeed, because of the increased temperature, the sound speed is now very large, and the working surface is very nearly uniform in pressure, so density and temperature are related. This

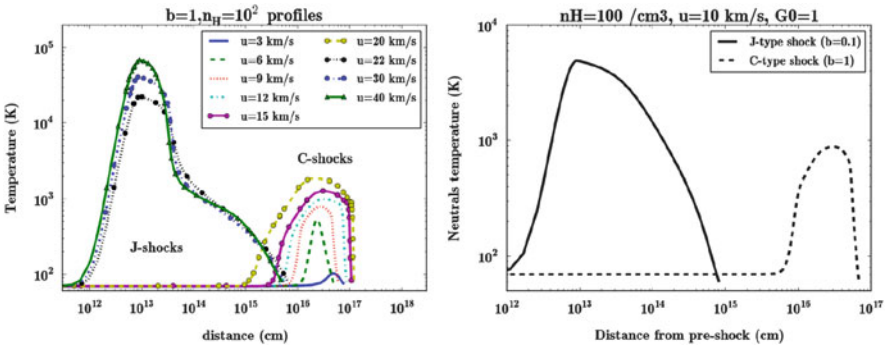

Fig. 9.3 *Left*: Temperature profiles for highly magnetized shocks ($b = 1$) of different velocities u. Here $b = B/n_{\rm H}^{-0.5}$ with B expressed in μG and $n_{\rm H}$ in cm^{-3}. The fluid flows from *left to right* with the preshock on the *left* and post-shock on the *right*. Only J-type shocks are present for the lowest values of the b/u ratio. *Right*: Temperature profiles for two different magnetizations ($b = 0.1$ and 1) and one shock velocity. It displays the relevant lengthscales: the viscous length that extends to $d = 10^{13}$ cm from pre-shock, the cooling length that ends at $d = 10^{15}$ cm, which is roughly the thickness of the J-type shock, the ion-neutral coupling length $d = 5 \times 10^{16}$ cm at which ions and neutrals start to recouple and the heating due to ion-neutral friction starts to drop. From Lesaffre et al. (2013)

compression leads to field lines compression and part of the input energy through the shock is converted into magnetic energy.

When the shock speed is greater than the Alfvén speed in the neutrals but lower than the magnetosonic speed in the ions, ions and neutrals experience the shock differently. The information propagates faster than the shock speed in the ions, which just experience a wave, whereas the neutrals experience a shock. The resulting structure at the beginning is a J-type shock with a continuous magnetic precursor upstream. The relative speed between the ions and neutrals leads to friction which tends to recouple the two fluids and in most cases, the J-type shock eventually disappears to leave only a continuous structure known as a C-type shock. Across the working surface, friction between ions and neutrals now mediates the conversion of kinetic energy into heat. In this case the heating, the cooling and magnetic compression all happen at the same time. The resulting temperature is lower than for corresponding J-type shocks, with lower final compression factors, but the thickness of the working surface is much greater than for a J-type shock. Indeed, the length of a J-type shock is controlled by the cooling length of the gas, whereas in a C-type shock the gas cannot cool until the ion and neutral velocities are recoupled (see Fig. 9.3, right), and it is the much longer ion-neutral coupling lengthscale which dictates the width of the shock. As a result, the total column-densities across C-type shocks are usually higher than for J-type shocks. Hence, the impact on some chemical tracers in the gas can actually be much greater and each type of shock has its own specific chemical signature (Lesaffre et al. 2013; Flower and Pineau des Forêts 2012).

The components of the magnetic field relevant for the computation of the above information speeds are the components which lay in the shock surface. In a turbulent medium it is likely that the orientation of the field with respect to the normal of the shock surface can be arbitrary and both types of shocks are likely to co-exist. Moreover, the velocity vector is not necessarily orthogonal to the working surface, thus leading to oblique shocks. Oblique shocks lead to a rotation of the transverse component of the magnetic field when crossing the working surface (Pilipp and Hartquist 1994). To conclude, although the orientation of both the velocity and the magnetic fields vectors with respect to the shock surface both matter, it is nevertheless hard to infer any correlations between the shock orientation and the magnetic fields.

The chemical yields from magnetized shocks may be attributed to several factors. First, the increase of temperature due to the dissipation which helps to increase the chemical rates: it does so drastically when the reactions are subject to thermal barriers comparable to the temperature obtained in these shocks (see Table 9.2). Second, the compression which increases the collisional rates and shortens the chemical time-scales. Third, the drift velocity which provides additional energy in the reference frame for the ion-neutral reactions. The first factor acts in both types of shocks, the second one operates mainly in J-type shocks and the third one exclusively in C-type shocks. This diversity of factors implies a variety of chemical signatures for J-type and C-type shocks (see Lesaffre et al. 2013). For example, CO, OH and H_2O are enhanced in both types of shock, but require higher

velocities for C-type shocks than J-type shocks. Conversely, CH^+ relies on ion-neutral reactions and its abundance is increased more in C-type shocks than in J-type shocks.

9.5 Intermittency in MHD and Non-ideal Turbulence: The Theorist and Numericist Perspectives

Turbulence in a magnetized ionized fluid exhibits fundamentally different dynamics from that in neutral fluids. There is not even agreement among theorists on the energy spectrum of MHD turbulence. The discussions in Wan et al. (2012), Beresnyak (2011), Mason et al. (2012) illustrate recent advances in this controversy (see also the chapter by Beresnyak and Lazarian in this volume). Yet, intermittency has been advocated in a number of magnetized turbulent environments. For example, Schmidt et al. (2010) have shown that the treatment of intermittency in supernovae explosions may play a crucial role. In another context, the formation of chondrules in meteorites requires an intermittent heating which may be a signature of the turbulent state of the Solar Nebulae at the time (King and Pringle 2010). Below, we recall some fundamental properties of magnetized turbulence. We also report on ongoing numerical efforts at characterizing dissipation in spectral simulations of MHD and non-ideal turbulence by Momferratos et al. (2014).

9.5.1 Energy Spectrum

The incompressible MHD equations read

$$\partial_t \mathbf{u} + (\mathbf{u}\cdot\nabla)\,\mathbf{u} = -\frac{\nabla p}{\rho} + \mathbf{j}\times\mathbf{b} + \nu\nabla^2\mathbf{u} \tag{9.3}$$

$$\partial_t \mathbf{b} + \nabla\times(\mathbf{u}\times\mathbf{b}) = \eta\nabla^2\mathbf{b} \tag{9.4}$$

where $\mathbf{u}$ is the velocity field satisfying $\nabla\cdot\mathbf{u} = 0$, $\mathbf{b} = \mathbf{B}/\sqrt{4\pi\rho}$ is the Alfvén velocity in a fluid of density ρ satisfying $\nabla\cdot\mathbf{b} = 0$, p is the pressure, $\mathbf{j} = \nabla\times\mathbf{b}$ is the current density, ν is the kinematic viscosity and η is the magnetic diffusivity. If $\nu = \eta = 0$, the above system conserves total energy $E = 1/2\langle\mathbf{u}^2\rangle + 1/2\langle\mathbf{b}^2\rangle$, cross-helicity $H_c = \langle\mathbf{u}\cdot\mathbf{b}\rangle$ and magnetic helicity $H_m = \langle\mathbf{a}\cdot\mathbf{b}\rangle$ where $\mathbf{a}$ is the vector potential, $\mathbf{b} = \nabla\times\mathbf{a}$.

In the presence of a mean magnetic field $\mathbf{B}_0$, the introduction of the Elsässer variables $\mathbf{z}^\pm = \mathbf{u}\pm\mathbf{b}$ leads to the following symmetric form of the MHD equations

$$\partial_t\mathbf{z}^\pm \mp (\mathbf{v}_A\cdot\nabla)\mathbf{z}^\pm + \left(\mathbf{z}^\mp\cdot\nabla\right)\mathbf{z}^\pm = -\nabla p^* + \nu^+\nabla^2\mathbf{z}^\pm + \nu^-\nabla^2\mathbf{z}^\mp \tag{9.5}$$

where $\mathbf{v}_A = \mathbf{B}_0/\sqrt{4\pi\rho}$ is the Alfvén velocity of the mean field, $p^* = p/\rho + b^2/2$ is the total pressure and $2\nu^{\pm} = \nu \pm \eta$. The second term on the left hand side represents counter-propagating Alfvén waves. The difference in sign between the two equations implies that the mean magnetic field cannot be canceled by a Galilean transformation, and is thus dynamically important at all scales. The next term corresponds to nonlinear interaction of Alfvén waves through collisions.

Total energy and cross-helicity can be expressed in terms of the Elsässer variables as $E = \langle \left(\mathbf{z}^+\right)^2 \rangle$ and $H_c = \langle (\mathbf{z}^-)^2 \rangle$. This implies that two colliding Alfvén waves are deformed by the non-linear term in such a way that the above quantities remain constant, since they are only dissipated by the diffusive terms.

This property allowed Iroshnikov and Kraichnan (IK) (Iroshnikov 1963; Kraichnan 1965) to construct a phenomenological theory of the inertial range. If the Alfvén wave amplitude at a scale λ is δu_λ, during a collision of two waves it changes by the magnitude of the nonlinear term $\delta u_\lambda^2/\lambda$ multiplied by the interaction time λ/v_A: $\Delta\delta u_\lambda = \delta u_\lambda^2/\mathrm{v}_A$. If one further assumes that collisions change the energy of the waves as a random walk, the number of collisions required to deform each wave considerably is $N = (\delta u_\lambda/\Delta\delta u_\lambda)^2 = (\mathrm{v}_A/\delta u_\lambda)^2$. The timescale of the cascade is $\tau_{IK} = N\lambda/\mathrm{v}_A = (\lambda \mathrm{v}_A)/\delta u_\lambda^2$. Assuming a constant energy flux through the inertial range $\varepsilon = \delta u_\lambda^2/\tau_{IK}$, one obtains the scaling $\delta u_\lambda \propto \lambda^{1/4}$. The energy spectrum $E(k) \propto \mid \delta u_k^2 \mid k^2$ scales as $k^{-3/2}$ in the inertial range.

In the IK theory, the energy spectrum is isotropic. Goldreich and Sridhar (GS) (Goldreich and Sridhar 1995) introduced the assumption of critical balance: the Alfvén term $\mp(\mathbf{v}_A \cdot \nabla)\mathbf{z}^{\pm}$ is of the same order as the nonlinear term $(\mathbf{z}^{\mp} \cdot \nabla)\mathbf{z}^{\pm}$. This implies $\mathrm{v}_A/l \sim \delta b_\lambda/\lambda$ with l the longitudinal scale of the wave and λ its transverse scale. l is equal to the product of the Alfvén velocity v_A and the eddy turnover time $\tau_{GS} = \lambda/\delta u_\lambda$, implying $\delta u_\lambda \sim \delta b_\lambda$. τ_{GS} is chosen as the timescale of the cascade, and the constancy of the energy flux $\delta u_\lambda^2/\tau_{GS}$ gives $\delta u_\lambda \sim \delta b_\lambda \propto \lambda^{1/3}$ in the inertial range. This scaling is identical to K41, except that the scale λ is perpendicular to the magnetic field, resulting in an anisotropic energy spectrum $E(k_\perp) \propto k_\perp^{-5/3}$. In fact, critical balance implies $l \propto \lambda^{2/3}$, so that the cascade becomes increasingly anisotropic at small scales.

9.5.2 *Intermittency in MHD Turbulence*

In MHD turbulence, the energy dissipation rate

$$\varepsilon = \frac{\nu}{2} \sum_{i,j=1}^{3} \left(\partial_i u_j + \partial_j u_i\right)^2 + \eta \left(\nabla \times \mathbf{b}\right)^2 \tag{9.6}$$

includes the Ohmic dissipation in addition to the viscous dissipation. It is found to be concentrated largely on two-dimensional structures. These sheets of dissipation are observed in spectral simulations of incompressible MHD turbulence (Fig. 9.4,

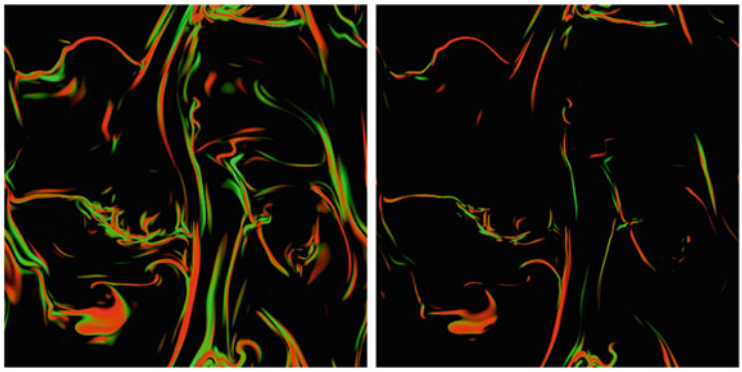

Fig. 9.4 Color maps of dissipation field at the temporal peak of total dissipation for the ABC initial conditions and two different ranges of the total dissipation (see Fig. 9.5): between the mean value μ and $\mu + \sigma$ (*left panel*) and between $\mu + \sigma$ and $\mu + 3\sigma$ (*right panel*). The subset of space on which dissipation is concentrated is much less space-filling for the higher dissipation rates. *Red*: Ohmic dissipation, *green*: viscous dissipation. From Momferratos et al. (2014)

Momferratos et al. 2014). Spectral methods are known to be of very high accuracy and well-suited for the study of small-scale structure (Canuto and Funaro 1988). The simulation is a freely decaying solution of Eqs. (9.3) and (9.4) with a null mean magnetic field. Two different initial conditions were considered for the large scale flow: one based on the Arnol'd–Beltrami–Childress (ABC) flow and the other based on the Orszag–Tang (OT) vortex. In the case of the ABC initial conditions, the non-dimensional cross-helicity

$$H_c = \frac{2\langle \mathbf{u} \cdot \mathbf{b} \rangle}{\sqrt{\langle \mathbf{u}^2 \rangle \langle \mathbf{b}^2 \rangle}} \tag{9.7}$$

is $\sim 2 \times 10^{-3}$, corresponding to a low initial correlation between the velocity field and the magnetic field. The mean magnetic helicity

$$H_m = \langle \mathbf{a} \cdot \mathbf{b} \rangle \tag{9.8}$$

where $\mathbf{a}$ is the vector potential with $\mathbf{b} = \nabla \times \mathbf{a}$, is considerable, $H_m \sim 0.2 u_0^2 l_0$. Here, l_0 and u_0 are typical length and velocity scales of the simulations. In the case of the OT initial conditions, the non-dimensional cross-helicity is ~ 0.1 while the mean magnetic helicity is almost zero, $H_m \sim 1 \times 10^{-9} u_0^2 l_0$. Thus, these two different initial conditions represent evolution under different constraints. Yet, the dissipation fields, such as that shown in Fig. 9.4 for the ABC initial conditions, are qualitatively very similar. The *pdf* of the total dissipation exhibits a log-normal core and a power-law tail that corresponds to extreme heating events. It is shown in Fig. 9.5 for the ABC initial conditions.

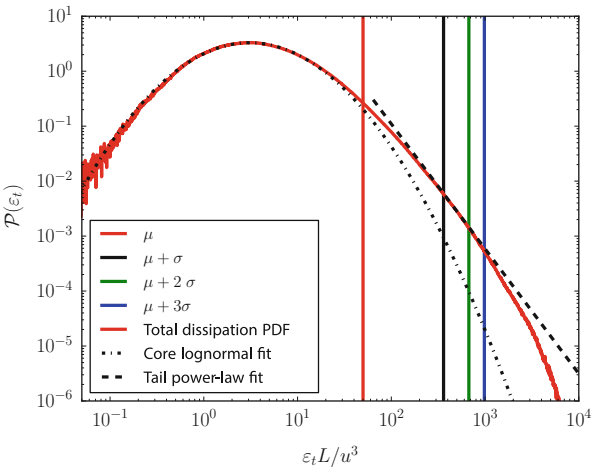

Fig. 9.5 *Pdf* of the total dissipation rate for the ABC initial conditions at the temporal peak of total dissipation rate. μ is the mean and σ the standard deviation. From Momferratos et al. (2014)

Just as in HD turbulence, intermittency can be quantified by the deviation of the scaling exponents of the velocity field and magnetic field structure functions from the K41 values. In the inertial range $l_D \ll r \ll L$, they scale as $S_p^{\{u,b\}}(r) \propto r^{\zeta_p^{\{u,b\}}}$. The intermittency model of She and Lévêque (1994) was generalized by Politano and Pouquet (1995) taking into account different possibilities for the co-dimension of the structures of high dissipation C and the scaling exponent of the increments in the inertial range $\delta u_\lambda \sim \delta b_\lambda \propto \lambda^{1/g}$

$$\zeta_p^{GSL}(g, C) = \frac{p}{g}\left(1 - \frac{2}{g}\right) + C\left(1 - \left(1 - \frac{2}{gC}\right)\right)^{\frac{p}{g}} \tag{9.9}$$

where GSL stands for the generalized She-Lévêque model. The co-dimension $C = 1$ for sheets, while the scaling parameter g is 3 for K41 and 4 for IK.

The method of extended self-similarity (ESS) introduced by Benzi et al. (1993) facilitates the estimation of structure function exponents from experimental or numerical data by extending the range of scales where their value is constant. This method considers the relative exponent

$$\frac{\zeta_p^u}{\zeta^*} = \frac{d\,\log(S_u^p(r))}{d\,\log(S^*(r))} \tag{9.10}$$

where the scaling of the structure function $S^*(r)$ is known from theory. In MHD, $S^*(r)$ is provided by the four-thirds law of Politano and Pouquet (1998)

$$S_3^{\pm}(r) = \langle \delta \mathbf{z}_\parallel^{\pm} (\delta \mathbf{z}^{\mp})^2 \rangle = -\frac{4}{3}\langle \varepsilon^{\pm} \rangle r, \quad l_D \ll r \ll L \tag{9.11}$$

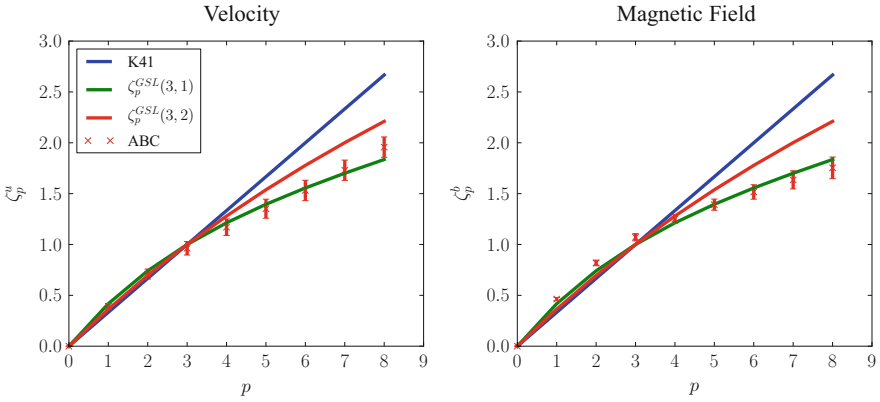

Fig. 9.6 Velocity and magnetic field structure function exponents for the ABC initial condition, calculated using extended self-similarity. The curves corresponding to two cases of the generalized She-Lévêque model, labelled by the scaling parameter g and the co-dimension C are drawn as well as the K41 linear dependence

where ε^+ is the energy dissipation and ε^- is the cross-helicity dissipation. This is an exact statistical result which follows from the MHD equations under the assumptions of statistical homogeneity, isotropy, stationarity and zero magnetic helicity (Politano and Pouquet 1998). Figure 9.6 displays the structure function exponents for the same ABC simulation, calculated up to order eight using ESS. The results agree quite well with the generalized She-Lévêque model, under the assumptions that the structures of high dissipation are sheets and that in the inertial range the scaling exponent of the increments is $1/3$. The magnetic field is found to be more intermittent than the velocity field, its exponents having a larger deviation from the K41 non-intermittent prediction.

The tail of the *pdf* of the total dissipation, shown in Fig. 9.5, corresponds to extreme dissipation events that have a complex geometrical structure. Following Uritsky et al. (2010), Momferratos et al. (2014) have defined the structures of high dissipation as connected sets of points each having a local value of the total dissipation above a prescribed threshold. The structures of high dissipation exhibit varied geometrical complexity, but are overall quasi two-dimensional, i.e. sheet-like. A statistical analysis shows that their geometric and dynamical characteristics exhibit power-law scaling, with different exponents in the inertial and dissipative ranges (Uritsky et al. 2010; Momferratos et al. 2014).

As a last illustration of the high degree of spatial intermittency observed in simulations of MHD turbulence, Momferratos et al. (2014) show that the curve giving the fraction of total dissipation contained in structures that take up a given volume fraction rises very steeply near the origin. As a result, 30 % of the total dissipation is contained in less than 3 % of the total volume.

9.5.3 *Intermittency in Non-ideal Turbulence: Ambipolar Diffusion*

In the diffuse interstellar medium, the partially ionized state of the gas can have significant effects on the turbulent motions. The most complete description of the motion of a partially ionized gas is the two fluid model (see the chapter of Zweibel, this volume). In the diffuse ISM however, for low ionization fractions, ρ_i/ρ_n, one can neglect ion inertia, pressure and viscosity and assume that in the ion momentum equation, the friction force due to the ion-neutral drift is balanced by the Lorentz force. If one further assumes incompressibility, the equations of ambipolar diffusion MHD reduce to the following system:

$$\partial_t \mathbf{u} + (\mathbf{u}\cdot\nabla)\,\mathbf{u} = -\frac{1}{\rho}\nabla p + \mathbf{j}\times\mathbf{b} + \nu\nabla^2\mathbf{u} \tag{9.12}$$

$$\partial_t \mathbf{b} = \nabla\times(\mathbf{u}\times\mathbf{b}) + (\gamma\rho_i)^{-1}\nabla\times\big((\mathbf{j}\times\mathbf{b})\times\mathbf{b}\big) + \eta\nabla^2\mathbf{b} \tag{9.13}$$

where $\mathbf{b} = \mathbf{B}/\sqrt{4\pi\rho}$ is the Alfvén velocity defined in terms of the total density $\rho = \rho_n + \rho_i$ and γ is the coefficient of ion-neutral friction.

Equations (9.12) and (9.13) were simulated using the same spectral method as in the pure MHD case described in the previous section by Momferratos et al. (2014), with identical initial conditions to compare the evolution with and without ambipolar diffusion.

Ambipolar diffusion has a significant effect on the spatial structure of the dissipation field. In a partially ionized gas, in addition to viscous and Ohmic dissipation, total energy is also dissipated by ambipolar diffusion (or more correctly, by the friction between the ions and the neutrals) at the rate

$$\varepsilon_a = (\gamma\rho_i)^{-1}\,((\mathbf{j}\times\mathbf{b})\times\mathbf{b})^2 \tag{9.14}$$

The intermittent spatial structure of the dissipation field in the case of ambipolar diffusion is shown in Fig. 9.7 where two ranges of the total dissipation rate are selected: the larger the dissipation rate, the smaller the volume filling factor of the subset of space on which dissipation is distributed. Ambipolar diffusion contributes a more diffuse component to the dissipation field, that has the tendency to surround the sheets of Ohmic and viscous dissipation (see Momferratos et al. 2014 for a quantitative discussion). This is reminiscent of the early findings of Brandenburg and Zweibel (1994). The dissipation due to ion-neutral friction i.e. ambipolar diffusion) contributes significantly to extreme heating events because the power-law tail in the *pdf* of total dissipation is more pronounced in the case with ambipolar diffusion.

Last, Fig. 9.8 is an attempt at reproducing the quantities observable in the ISM with their unavoidable projections. A proxy of viscous dissipation, the contribution due to the *pos* projection of the vorticity is shown in the top panel. This quantity is close to the increments of the line centroid velocity that are accessible to

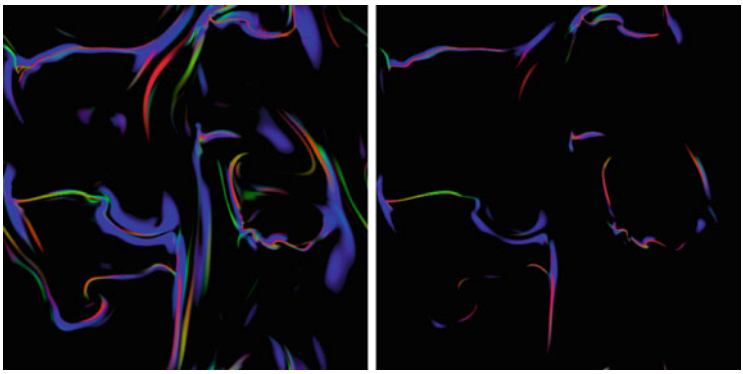

Fig. 9.7 Maps of the dissipation field in the ABC run with ambipolar diffusion, at the temporal peak of total dissipation. The same dissipation ranges as in Fig. 9.4 are shown: between the mean value μ and $\mu+\sigma$ (*left panel*) and between $\mu+\sigma$ and $\mu+3\sigma$ (*right panel*). *Red*: Ohmic dissipation, *green*: viscous dissipation, *blue*: dissipation due to ambipolar diffusion. The latter is distributed in thicker structures than those due to ohmic dissipation (*red*) and viscous dissipation (*green*)

observations (Sect. 9.3.1). The *pos* projection of the magnetic field is also shown. This projection is that provided by the measurements of the polarization angle of either the dust thermal emission (in which case the field direction is perpendicular to that of the polarization) or the absorbed starlight in the visible or near-IR (in which case the field direction is parallel to that of the polarization). The bottom panel displays $\Delta\Psi$, the increment of the orientation of B_{pos} averaged over annuli of ten resolution elements in radius. The comparison of the patterns visible in these figures with those of Fig. 9.7 shows that the largest *pos* projections of the vorticity and the largest $\Delta\Psi$ at small scale delineate structures that tend to follow those of the most intense dissipation, although it is not a one-to-one correspondence, due to projection effects. The same is true for the alignment of B_{pos} and the projected vorticity.

9.6 Summary and Perspectives

In spite of the theoretical and experimental challenges it poses, even in incompressible turbulence, and in spite of the lack of predictions in magnetized compressible turbulence, intermittency seems to be present in the ISM. It manifests itself by non-Gaussian statistics of the velocity field that are more salient at small scales and by the existence of coherent structures of velocity-shears over a broad range of scales (from pc to mpc scales). An indirect facet of its existence is the impact of intermittent turbulent dissipation that locally heats the ISM and opens chemical routes that are blocked by highly endothermic reactions in the cold ISM . These reactions have thresholds that span an extended range in energy so that chemistry

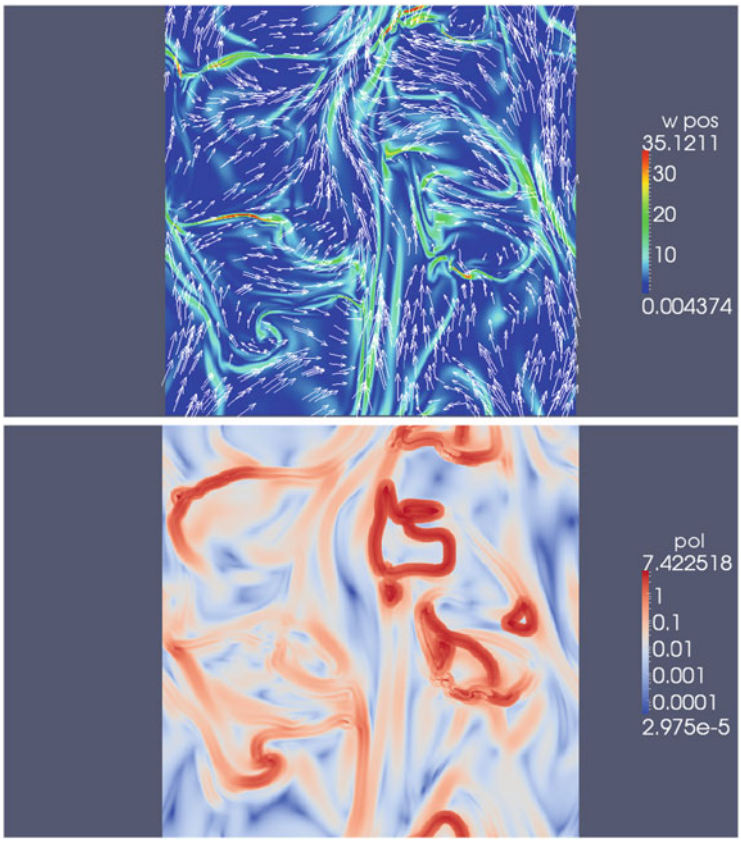

Fig. 9.8 Comparison of two proxies of observables of the dissipation field in the ABC simulation with weak ambipolar diffusion: the *pos* projection of the vorticity, a proxy of the line velocity centroid increments (see Sect. 9.3.1) (*top*), the small scale increments of the direction of the *pos* projection of the magnetic field, a proxy of the variations of the polarization angle of the dust thermal emission (*bottom*). The *pos* projections of the magnetic field are superposed in the *top panel*

could be envisioned as a test of the multifractal nature of intermittency: the molecular species with the highest barriers would be the tracers of the fractal set of smallest fractal dimension and largest local dissipation. From these signatures of intermittency in the chemistry of the diffuse ISM, we infer that Lagrangian intermittency is indeed present. Lagrangian intermittency would also impact the mixing of dynamical, thermal and dynamical properties of the gas and hence the transport processes.

As far as the magnetic field is concerned, only very few measurements are presently available in the field where the velocity field has been investigated with large enough statistics at small scales. There is, however, a possible trend of alignment of the vorticity and magnetic field in the plane-of-the-sky which needs

to be put on a firmer statistical basis. The topology of the smallest scale structures accessible to observations still escapes numerical grasp but the perspectives in the field of observations are bright.

Last, intermittency seems to be a universal phenomenon, present as soon as the Reynolds number is high enough, and it is likely to have an impact in a broad variety of astrophysical media ranging from the most dilute intergalactic medium to the densest stellar interiors, including all phases of the interstellar medium, protoplanetary discs and supernovae.

Acknowledgements This work was partly funded by the grant ANR-09-BLAN-0231-01 from the French Agence Nationale de la Recherche (ANR) as part of the SCHISM project. The numerical work was granted access to the HPC resources of MesoPSL financed by the Région Ile-de-France and the ANR project Equip@Meso (Reference ANR-10-EQPX-29-01). We also acknowledge granted time on the national facilities at CINES and IDRIS.

References

Anselmet, F., Antonia, R., Danaila, L.: Planet Space Sci. **49**, 1177 (2001)
Arnéodo, A., Benzi, R., Berg, J., et al.: Phys. Rev. Lett. **100**, 4504A (2008)
Benzi, R., Ciliberto, S., Baudet, C., Ruiz Chavarria, G., Tripiccione, R.: Phys. Rev. Lett. **48**, 29 (1993)
Beresnyak, A.: Phys. Rev. Lett. **106**, 075001 (2011)
Boldyrev, S., Nordlund, A., Padoan, P.: Astrophys. J. **573**, 678 (2002)
Brandenburg, A., Zweibel, E.G.: Astrophys. J. **427**, L91 (1994)
Canuto, C., Funaro, D.: SJNA, **25**, 24 (1988)
Chevillard L., Castaing, B., Arnéodo, A., Lévêque, E., Pinton J.-F., Roux, S.: CR Phy. **13**, 899C (2013)
Clemens, D.P., Pinnick, A.F., Pavel, M.D.: Astrophys. J. Suppl. **200**, 20 (2012)
Cox, D.: Ann. Rev. Astron. Astrophys. **43**, 337 (2005)
Crutcher, R., Wandelt, B., Heiles, C., Falgarone, E., Troland, T.: Astrophys. J. **725**, 466 (2010)
de Avillez, M., Breitschwerdt, D.: Astron. Astrophys. **436**, 585 (2005)
Elmegreen, B., Scalo, J.: Ann. Rev. Astron. Astrophys. **42**, 211 (2004)
Falgarone, E., Verstraete, L., Pineau Des Forêts, G., Hily-Blant, P.: Astron. Astrophys. **433**, 997 (2005)
Falgarone, E., Pety, J., Hily-Blant, P.: Astron. Astrophys. **507**, 355 (2009)
Falgarone, E., Ossenkopf, V., Gerin, M., et al. Astron. Astrophys. **518**, L118 (2010)
Falgarone, E., Godard, B., Cernicharo, J., et al.: Astron. Astrophys. **521**, L15 (2010)
Field G., Goldsmith, D., Habing, H.: Astrophys. J. **155**, 149 (1969)
Flower, D., Pineau des Forêts, G.: Mon. Not. R. Astron. Soc. **421**, 2786 (2012)
Frisch, U.: Turbulence. Turb. book. Cambridge, UK, Cambridge University Press, (1996)
Godard, B., Falgarone, E., Pineau des Forêts, G.: Astron. Astrophys. **495**, 847 (2009)
Godard, B., Falgarone, E., Gerin, M., et al.: Astron. Astrophys. **540**, 87 (2012)
Godard, B., Falgarone, E., Pineau des Forêts, G.: Astron. Astrophys. (2014, in press). arXiv1408.3716G
Goldreich, P., Sridhar, S.: Astrophys. J. **438**, 763 (1995)
Goldsmith, P., Velusamy, T., Li, D., Langer, W.: Astrophys. J. **715**, 1370 (2010)
Haud, U., Kalberla, P.: Astron. Astrophys. **466**, 555 (2010)
Heithausen, A.: Astron. Astrophys. **606**, L13 (2004)
Heithausen, A.: Astron. Astrophys. **450**, 193 (2006)

Heithausen, A., Bertoldi, F., Bensch, F.: Astron. Astrophys. **383**, 591 (2002)
Hennebelle P., Falgarone, E.: Astron. Astrophys. Rev. **20**, 55 (2012)
Hewitt, J.W., Rho, J., Andersen, M., Reach, W.T.: Astrophys. J. **694**, 1266 (2009)
Hily-Blant, P., Falgarone, E.: Astron. Astrophys. **500**, L59 (2009)
Hily-Blant, P., Falgarone, E., Pety, J.: Astron. Astrophys. **481**, 367 (2008)
Ingalls, J., Bania, T., Boulanger, F., Draine, B., Falgarone, E., Hily-Blant, P.: Astrophys. J. **743**, 174 (2011)
Iroshnikov, P.: Sov. Astron. **7**, 566 (1963)
Jenkins, E., Tripp, T.: Astrophys. J. **734**, 65 (2011)
Joulain, K., Falgarone, E., Pineau des Forêts, G., Flower, D.: Astron. Astrophys. **340**, 241 (1998)
King, A.R., Pringle, J.E.: Mon. Not. R. Astron. Soc. **404**, 1903 (2010)
Kolmogorov A.N.: Proc. R. Soc. Lon. Ser. A **434**, Reprinted in 1991 (1941)
Kraichnan, R.: Phys. Fluids **8**, 1385 (1965)
Larson, R.: Mon. Not. R. Astron. Soc. **194**, 809 (1981)
Le Petit, F., Nehmé, C., Le Bourlot, J., Roueff, E.: Astrophys. J. Suppl. **164**, 506 (2006)
Lesaffre, P., Pineau des Forêts, G., Godard, B., et al.: Astron. Astrophys. **550**, A106 (2013)
Lis, D., Pety, J., Phillips, T., Falgarone, E.: Astrophys. J. **463**, L623 (1996)
Manset, N., Bastien, P.: Publ. Astron. Soc. Pac. **107**, 83 (1995)
Mason, J., Perez, J.C., Boldyrev, S., Cattaneo, F.: Phys. Plasmas **19**, 055902 (2012)
Menten, K., Wyrowski, F., Belloche, A., Güsten, R., Dedes, L., Müller, H.: Astron. Astrophys. **525**, 77 (2011)
Mininni, P.D., Alexakis, A., Pouquet, A.: Phys. Rev. Lett. **74**, 6303M (2006)
Mininni, P.D., Pouquet, A., Montgomery, D.C.: Phys. Rev. Lett. **97**, 4503M (2006)
Miville-Deschênes, M.-A., Joncas, G., Falgarone, E., Boulanger, F.: Astron. Astrophys. **411**, 109 (2003a)
Miville-Deschênes, M.-A., Martin, P., Abergel, A.: Astron. Astrophys. **518**, L104 (2010)
Moffatt, H., Kida, S., Ohkitani, K.: J. Fluid Mech. **259**, 241 (1994)
Moisy, F., Jiménez, J.: J. Fluid Mech. **513**, 111 (2004)
Momferratos, G., Lesaffre P., Falgarone, E., Pineau des Forêts, G.: Mon. Not. R. Astron. Soc. **443**, 86 (2014)
Müller, C., Biskamp, D.: Phys. Rev. Lett. **84**, 475 (2000)
Pan, L., Wheeler, J., Scalo, J.: Astrophys. J. **681**, 470 (2008)
Pilipp, W., Hartquist T.W.: Mon. Not. R. Astron. Soc. **267**, 801 (1994)
Politano, H., Pouquet, A.: Phys. Rev. Lett. **52**, 636 (1995)
Politano, H., Pouquet, A.: Phys. Rev. Lett. **57**, 21 (1995)
Porter, D.H., Woodward, P.R., Pouquet, A.: Phys. Fluids **10**, 237 (1998)
Porter, D.H., Pouquet, A., Woodward, P.R.: Phys. Rev. Lett. **66**, 6301 (2002)
Roux, S., Muzy J.-F., Arnéodo, A.: Eur. Phys. J. B **8**, 301 (1999)
Scalo, J., Elmegreen, B.: Ann. Rev. Astron. Astrophys. **42**, 275 (2004)
Schmidt, W., Ciaraldi-Schoolmann, F., Niemeyer, J.C., Röpke, F.K., Hillebrandt, W.: Astrophys. J. **710**, 1683 (2010)
She, Z.-S., Lévêque, E.: Phys. Rev. **72**, 336 (1994)
Uritsky, V.M., Pouquet, A., Rosenberg, D., Mininni, P.D., Donovan, E.F.: Phys. Rev. E **82**, e6326 (2010)
Vestuto, J.G., Ostriker, E.C., Stone, J.M.: Astrophys. J. **590**, 858 (2003)
von Weizsäcker, C.F.: Astrophys. J. **114**, 165 (1951)
Wan, M., Oughton, S., Servidio, S., Matthaeus, W.H.: J. Fluid Mech. **697**, 296 (2012)

Chapter 10
Cosmic Ray Transport in Turbulent Magnetic Field

Huirong Yan

Abstract Cosmic ray (CR) transport and acceleration are determined by the properties of magnetic turbulence. Recent advances in MHD turbulence call for revisions in the paradigm of cosmic ray transport. We use the models of magnetohydrodynamic turbulence that were tested in numerical simulation, in which turbulence is injected at large scale and cascades to small scales. We shall address the issue of the transport of CRs, both parallel and perpendicular to the magnetic field. Both normal diffusion on large scales and superdiffusion on small scales shall be addressed. We shall demonstrate compressible fast modes are the dominant cosmic ray scatterer from both quasilinear and nonlinear theories. We shall also show that the self-generated wave growth by CRs is constrained by preexisting turbulence and discuss the process in detail in the context of shock acceleration at supernova remnants and their implications. In addition, we shall dwell on the nonlinear growth of kinetic gyroresonance instability of cosmic rays induced by large scale compressible turbulence. The feedback of the instability on large scale turbulence should be included in future simulations.

10.1 Introduction

The propagation and acceleration of cosmic rays (CRs) are governed by their interactions with magnetic fields. Astrophysical magnetic fields are turbulent and, therefore, the resonant and non-resonant (e.g. transient time damping, or TTD) interaction of cosmic rays with MHD turbulence is the accepted principal mechanism to scatter and isotropize cosmic rays (see Schlickeiser 2002). In addition, efficient scattering is essential for the acceleration of cosmic rays. For instance, scattering of cosmic rays back into the shock is a vital component of the first order Fermi acceleration (see Longair 1997). At the same time, stochastic acceleration by

H. Yan (✉)
KIAA, Peking University, Beijing 100871, China
e-mail: hryan@pku.edu.cn

A. Lazarian et al. (eds.), *Magnetic Fields in Diffuse Media*, Astrophysics and Space Science Library 407, DOI 10.1007/978-3-662-44625-6_10

turbulence is entirely based on scattering. The dynamics of cosmic rays in MHD turbulence holds the key to all high energy astrophysics and related problems.

We live in an exciting era when we are starting to test fundamental processes taking place at the beginning of the Universe, at the event horizon of black holes, when the nature of dark matter and dark energy is being probed etc. Using computers many researchers make sophisticated complex models to confront the observations in unprecedented details. In the mean time, with the launching of the new facilities, we have much more observational data available than ever before. For instance, CHANDRA observations of supernova remnants provide a strong constraint to diffusion coefficients and/or magnetic fields near the shock (see, e.g. Bamba et al. 2005; Pohl et al. 2005); the diffuse gamma-ray measurements from Fermi from the Galactic disc have been successfully used to phenomenologically constrain numerical modeling of cosmic rays, e.g., with GALPROP (Ackermann et al. 2012); observations of solar energetic particles (SEP) have been also fruitful over the past decades and lead to better understanding of transport in the solar wind (see a review by Horbury et al. 2005; and references therein). These developments make it urgent that we understand the key physical processes underlying astrophysical phenomena, can parameterize them and, if necessary, use as a subgrid input in our computer models.

At present, the propagation of the CRs is an advanced theory, which makes use both of analytical studies and numerical simulations. However, these advances have been done within the turbulence paradigm which is being changed by the current research in the field. Instead of the empirical 2D+slab model of turbulence, numerical simulations suggest anisotropic Alfvénic modes following (Goldreich and Sridhar 1995; GS95) scalings (an analog of 2D, but not an exact one, as the anisotropy changes with the scale involved) + fast modes (Cho and Lazarian 2002). These progresses resulted in important revisions on the theory of cosmic ray transport (see a review by Lazarian et al. 2008; and references therein). The GS95 turbulence injected on large scales and its extensions to compressible medium is less efficient in scattering of CRs compared to the estimates made assuming that magnetic turbulence consists of plane waves moving parallel to magnetic field (Chandran 2000; Yan and Lazarian 2002). Fast compressible modes, on the other hand, are demonstrated as the dominant scattering agent in spite of various damping processes they are subjected to (Yan and Lazarian 2002, 2004, 2008)

At the same time, one should not disregard the possibilities of generation of additional perturbations on small scales by CR themselves. For instance, the slab Alfvénic perturbation can be created, e.g., via streaming instability (see Wentzel 1974; Cesarsky 1980). Instabilities induced by anisotropic distribution of CRs were also suggested as a possibility to scatter CRs (Lerche 1967; Melrose 1974). Particularly at shock front, studies of instabilities have been one of the major efforts since the acceleration efficiency is essentially determined by the confinement at the shock front and magnetic field amplifications. Examples of the new developments in the field include, current driven instability (Bell 2004), vorticity generation at curved shock (Giacalone and Jokipii 2007), through Baroclinic effect (Inoue et al.

2009), through precursor (Beresnyak et al. 2009), etc. This field is rich in its own and we shall not dwell upon it in this chapter.

In fact, the small scale instabilities and large scale turbulence are not independent of each other. *First* of all, the instability generated waves can be damped through nonlinear interaction with the large scale turbulence (Yan and Lazarian 2002, 2004; henceforth YL02, YL04). In the case of anisotropic GS95 turbulence, the efficiency is reduced (Farmer and Goldreich 2004). Nonetheless, owing to the non-linear damping, the instabilities can only grow in a limited range, e.g., $\sim$<100 GeV in interstellar medium for the streaming instability (Farmer and Goldreich 2004; Yan and Lazarian 2004). *Secondly*, the large scale compressible turbulence also generate small scale waves through firehose, gyroresonance instability, etc. (Schekochihin and Cowley 2006; Lazarian and Beresnyak 2006; Yan and Lazarian 2011; Santos-Lima et al. 2013).

Propagation of CRs perpendicular to mean magnetic field is another important problem for which one needs to take into account both large and small scale interactions in tested models of turbulence. Indeed, if one takes only the diffusion along the magnetic field line and field line random walk (FLRW Jokipii 1966; Jokipii and Parker 1969; Forman et al. 1974), compound (or subdiffusion) would arise. Whether the subdiffusion is realistic in fact depends on the models of turbulence chosen (Yan and Lazarian 2008, 2012). In this chapter we review current understandings to this question within the domain of numerically tested models of MHD turbulence.

In what follows, we introduce the basic mechanisms for the interactions between particles and turbulence in Sect. 10.2. We discuss the cosmic ray transport in large scale turbulence, including both analytical and numerical studies in Sect. 10.3. Applications to cosmic ray propagation is presented in Sect. 10.4 In Sect. 10.5, we consider the perpendicular transport of cosmic rays on both large and small scales. We shall also discuss the issue of super-diffusion and the applicability of sub-diffusion. In Sect. 10.6, we concentrate on the issue of self-confinement in the presence of preexisting turbulence and dwell on, in particular, the streaming instability at supernova remnant shocks and its implication for CR acceleration. Section 10.7, we address the issue of gyroresonance instability of CRs and its feedback on large scale compressible turbulence. Summary is provided in Sect. 10.8.

10.2 Interactions Between Turbulence and Particles

Basically there are two types of resonant interactions: gyroresonance acceleration and transit acceleration (henceforth TTD). The resonant condition is $\omega - k_\parallel v\mu = n\Omega$ ($n = 0, \pm 1, 2\ldots$), where ω is the wave frequency, $\Omega = \Omega_0/\gamma$ is the gyrofrequency of relativistic particle, $\mu = \cos\xi$, where ξ is the pitch angle of particles. TTD formally corresponds to $n = 0$ and it requires compressible perturbations.

The Fokker–Planck equation is generally used to describe the evolvement of the gyrophase-averaged distribution function f,

$$\frac{\partial f}{\partial t} = \frac{\partial}{\partial \mu}\left(D_{\mu\mu}\frac{\partial f}{\partial \mu} + D_{\mu p}\frac{\partial f}{\partial p}\right) + \frac{1}{p^2}\frac{\partial}{\partial p}\left[p^2\left(D_{\mu p}\frac{\partial f}{\partial \mu} + D_{pp}\frac{\partial f}{\partial p}\right)\right],$$

where p is the particle momentum. The Fokker–Planck coefficients $D_{\mu\mu}, D_{\mu p}, D_{pp}$ are the fundamental physical parameters for measuring the stochastic interactions, which are determined by the electromagnetic fluctuations (see Schlickeiser and Miller 1998):

Gyroresonance happens when the Doppler shifted wave frequency matches the Larmor frequency of a particle. In quasi-linear theory (QLT), the Fokker–Planck coefficients are given by (see Schlickeiser and Miller 1998; Yan and Lazarian 2004)

$$\begin{aligned}\begin{pmatrix} D_{\mu\mu} \\ D_{pp} \end{pmatrix} = \frac{\pi\Omega^2(1-\mu^2)}{2}\int_{\mathbf{k_{min}}}^{\mathbf{k_c}} dk^3\delta(k_\parallel v_\parallel - \omega \pm \Omega)\begin{bmatrix} \left(1+\frac{\mu V_{ph}}{v\zeta}\right)^2 \\ m^2V_A^2 \end{bmatrix} \times \\ \times\left\{\left[J_2^2\left(\frac{k_\perp v_\perp}{\Omega}\right) + J_0^2\left(\frac{k_\perp v_\perp}{\Omega}\right)\right]\begin{bmatrix} M_{\mathscr{R}\mathscr{R}}(\mathbf{k}) + M_{\mathscr{L}\mathscr{L}}(\mathbf{k}) \\ K_{\mathscr{R}\mathscr{R}}(\mathbf{k}) + K_{\mathscr{L}\mathscr{L}}(\mathbf{k}) \end{bmatrix}\right. \\ \left. -2J_2\left(\frac{k_\perp v_\perp}{\Omega}\right)J_0\left(\frac{k_\perp v_\perp}{\Omega}\right)\left[e^{i2\phi}\begin{bmatrix} M_{\mathscr{R}\mathscr{L}}(\mathbf{k}) \\ K_{\mathscr{R}\mathscr{L}}(\mathbf{k}) \end{bmatrix} + e^{-i2\phi}\begin{bmatrix} M_{\mathscr{L}\mathscr{R}}(\mathbf{k}) \\ K_{\mathscr{L}\mathscr{R}}(\mathbf{k}) \end{bmatrix}\right]\right\},\end{aligned} \tag{10.1}$$

where $\zeta = 1$ for Alfvén modes and $\zeta = k_\parallel/k$ for fast modes, $k_{min} = L^{-1}$, $k_c = \Omega_0/v_{th}$ corresponds to the dissipation scale, $m = \gamma m_H$ is the relativistic mass of the proton, $v_\perp$ is the particle's velocity component perpendicular to $\mathbf{B}_0$, $\phi = \arctan(k_y/k_x)$, $\mathscr{L}, \mathscr{R} = (x \pm iy)/\sqrt{2}$ represent left and right hand polarization. M_{ij} and K_{ij} are the correlation tensors of magnetic and velocity fluctuations.

From the resonance condition, we know that the most important interaction occurs at $k_\parallel = k_{\parallel,res} = \Omega/v_\parallel$. This is generally true except for small μ (or scattering near 90°).

TTD happens due to the resonant interaction with parallel magnetic mirror force. Particles can be accelerated by when they are in phase with the waves either by interacting with oscillating parallel electric field (Landau damping), or by moving magnetic mirrors (TTD). When particles are trapped by moving in the same speed with waves, an appreciable amount of interactions can occur between waves and particles. Since head-on collisions are more frequent than that trailing collisions, particles gain energies. Different from gyroresonance, the resonance function of TTD is broadened even for CRs with small pitch angles. The formal resonance peak $k_\parallel/k = V_{ph}/v_\parallel$ favors quasi-perpendicular modes. However, these quasi-perpendicular modes cannot form an effective mirror to confine CRs because the gradient of magnetic perturbations along the mean field direction $\nabla_\parallel \mathbf{B}$ is small.

As we will show later in Sect. 10.3.3, the resonance is broadened in nonlinear theory (see Yan and Lazarian 2008).

10.3 Scattering of Cosmic Rays

10.3.1 Scattering by Alfvénic Turbulence

As we discussed in Sect. 10.2, Alfvén modes are anisotropic, eddies are elongated along the magnetic field, i.e., $k_\perp > k_\parallel$. The scattering of CRs by Alfvén modes is suppressed first because most turbulent energy goes to $k_\perp$ due to the anisotropy of the Alfvénic turbulence so that there is much less energy left in the resonance point $k_{\parallel,res} = \Omega/v_\parallel \sim r_L^{-1}$. Furthermore, $k_\perp \gg k_\parallel$ means $k_\perp \gg r_L^{-1}$ so that cosmic ray particles have to be interacting with lots of eddies in one gyro period. This random walk substantially decreases the scattering efficiency. The scattering by Alfvén modes was studied in YL02. In case that the pitch angle ξ not close to 0, the analytical result is

$$\left[\begin{array}{c} D_{\mu\mu} \\ D_{pp} \end{array}\right] = \frac{v^{2.5}\mu^{5.5}}{\Omega^{1.5}L^{2.5}(1-\mu^2)^{0}.5}\Gamma[6.5, k_c^{-\frac{2}{3}}k_{\parallel,res}L^{\frac{1}{3}}]\left[\begin{array}{c} 1 \\ m^2V_A^2 \end{array}\right], \tag{10.2}$$

where $\Gamma[a, z]$ is the incomplete gamma function. The presence of this gamma function in our solution makes our results orders of magnitude larger than those[1] in Chandran (2000), who employed GS95 ideas of anisotropy, but lacked the quantitative description of the eddies. However, the scattering frequency,

$$\nu = 2D_{\mu\mu}/(1-\mu^2), \tag{10.3}$$

are nearly 10^{10} times lower than the estimates for isotropic and slab model (see Fig. 10.1, *left*). *It is clear that for most interstellar circumstances, the scattering by Alfvénic turbulence is suppressed.* As the anisotropy of the Alfvén modes is increasing with the decrease of scales, the interaction with Alfvén modes becomes more efficient for higher energy cosmic rays. When the Larmor radius of the particle becomes comparable to the injection scale, which is likely to be true in the shock region as well as for very high energy cosmic rays in diffuse ISM, Alfvén modes get important.

[1]The comparison was done with the resonant term in Chandran (2000) as the nonresonant term is spurious.

10.3.2 Cosmic Ray Scattering by Compressible MHD Turbulence

As we mentioned earlier, numerical simulations of MHD turbulence supported the GS95 model of turbulence, which does not have the "slab" Alfvénic modes that produced most of the scattering in the earlier models of CR propagation. Can the turbulence that does not appeal to CRs back-reaction (see Sect. 10.4) produce efficient scattering?

In the models of ISM turbulence (Armstrong et al. 1995; McKee and Ostriker 2007), where the injection happens at large scale, fast modes were identified as a scattering agent for cosmic rays in interstellar medium (Yan and Lazarian 2002, 2004). These works made use of the quantitative description of turbulence obtained in Cho and Lazarian (2002) to calculate the scattering rate of cosmic rays.

Different from Alfvén and slow modes, fast modes are isotropic (Cho and Lazarian 2002). Indeed they are subject to both collisional and collisionless damping. The studies in Yan and Lazarian (2002, 2004) demonstrated, nevertheless, that the scattering by fast modes dominates in most cases in spite of the damping[2] (see Fig. 10.1, *right*). More recent studies of cosmic ray propagation and acceleration that explicitly appeal to the effect of the fast modes include Cassano and Brunetti

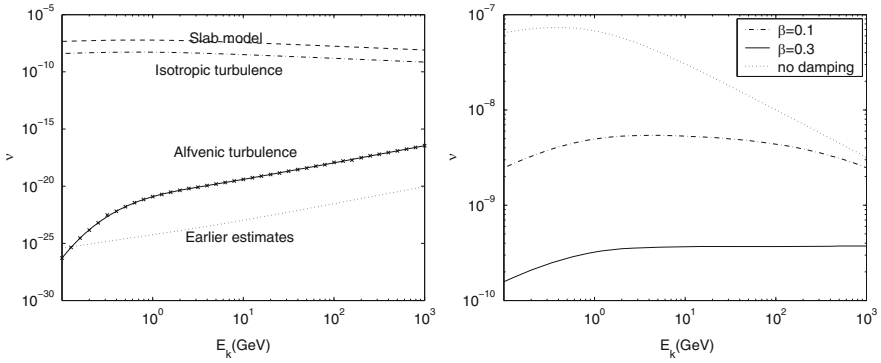

Fig. 10.1 *Left:* Rate of CR scattering by Alfvén waves versus CR energy. The *lines* at the *top* of the figure are the accepted estimates obtained for Kolmogorov turbulence. The *dotted curve* is from Chandran (2000). The analytical calculations are given by the *solid line* with our numerical calculations given by crosses; *Right:* the scattering by fast modes, *dashed line* represents the case without damping for fast modes included, the *solid* and *dash-dot line* are the results taking into account collisionless damping

[2]On the basis of weak turbulence theory, Chandran (2005) has argued that high-frequency fast waves, which move mostly parallel to magnetic field, generate Alfvén waves also moving mostly parallel to magnetic field. We expect that the scattering by thus generated Alfvén modes to be similar to the scattering by the fast modes created by them. Therefore we expect that the simplified approach adopted in Yan and Lazarian (2004) and the papers that followed to hold.

(2005), Brunetti and Lazarian (2007), Yan and Lazarian (2008) and Yan et al. (2008). Incidentally, fast modes have been also identified as primary agents for the acceleration of charged dust particles (Yan and Lazarian 2003; Yan et al. 2004).

10.3.3 Nonlinear Theory of Diffusion

While QLT allows easily to treat the CR dynamics in a local magnetic field system of reference, a key assumption in QLT, that the particle's orbit is unperturbed, makes one wonder about the limitations of the approximation. Indeed, while QLT provides simple physical insights into scattering, it is known to have problems. For instance, it fails in treating 90° scattering (see Völk 1973; Voelk 1975; Jones et al. 1973, 1978; Owens 1974; Goldstein 1976; Felice and Kulsrud 2001) and perpendicular transport (see Kóta and Jokipii 2000; Matthaeus et al. 2003).

Indeed, many attempts have been made to improve the QLT and various non-linear theories have been attempted (see Dupree 1966; Völk 1973; Voelk 1975; Jones et al. 1973; Goldstein 1976). Currently we observe a surge of interest in finding way to go beyond QLT. Examples include the nonlinear guiding center theory (see Matthaeus et al. 2003), second-order quasilinear theory (Shalchi 2005; Qin 2007; le Roux and Webb 2007), etc. Most of the analysis were limited to traditional 2D+slab models of MHD turbulence. An important step was taken in Yan and Lazarian (2008), where non-linear effect was accounted for in treating CR scattering in the type of MHD turbulence that are supported by numerical simulations. The results have been applied to both solar flares (Yan et al. 2008) and grain acceleration (Hoang et al. 2012). Below, we introduce the nonlinear theory and their applications to both particle transport and acceleration in incompressible and compressible turbulence based on the results from Yan and Lazarian (2008).

The basic assumption of the quasi-linear theory is that particles follow unperturbed orbits. In reality, particle's pitch angle varies gradually with the variation of the magnetic field due to conservation of adiabatic invariant $v_\perp^2/B$, where B is the total strength of the magnetic field (see Landau and Lifshitz 1975). Since B is varying in turbulent field, so are the projections of the particle speed $v_\perp$ and $v_\parallel$. This results in broadening of the resonance. The variation of the velocity is mainly caused by the magnetic perturbation $\delta B_\parallel$ in the parallel direction. This is true even for the incompressible turbulence we discussion in this section. For the incompressible turbulence, the parallel perturbation arises from the pseudo-Alfvén modes. The perpendicular perturbation $\delta B_\perp$ is higher order effect, which we shall neglect here.

The propagation of a CR can be described as a combination of a motion of its guiding center and CR's motion about its guiding center. Because of the dispersion of the pitch angle $\Delta\mu$ and therefore of the parallel speed $\Delta v_\parallel$, the guiding center is perturbed about the mean position $< z >= v\mu t$ as they move along the field lines. As a result, the perturbation $\delta B(\mathbf{x}, t)$ that the CRs view when moving along the field gets a different time dependence. The characteristic phase function $e^{ik_\parallel z(t)}$ of

the perturbation $\delta B(\mathbf{x}, t)$ deviates from that for plane waves. Assuming the guiding center has a Gaussian distribution along the field line,

$$f(z) = \frac{1}{\sqrt{2\pi}\sigma_z} e^{-\frac{(z-<z>)^2}{2\sigma_z^2}}, \tag{10.4}$$

one gets by integrating over z,

$$\int_{-\infty}^{\infty} dz e^{ik_\parallel z} f(z) = e^{ik_\parallel <z>} e^{-k_\parallel^2 \sigma_z^2/2}. \tag{10.5}$$

The first adiabatic invariant gives us

$$\sigma_z^2 =< \Delta v_\parallel^2 > t^2 = \frac{v^4}{v_\parallel^2} \left(\frac{< \delta B_\parallel^2 >}{B_0^2} \right) t^2. \tag{10.6}$$

Insert Eq. (10.5) into the expression of $D_{\mu\mu}$ (see Voelk 1975; Yan and Lazarian 2004), we obtain

$$D_{\mu\mu} = \frac{\Omega^2(1-\mu^2)}{B_0^2} \int d^3k \sum_{n=0}^{\infty} R_n(k_\parallel v_\parallel - \omega \pm n\Omega) \left[I^A(\mathbf{k}) \frac{n^2 J_n^2(w)}{w^2} + \frac{k_\parallel^2}{k^2} J_n'^2(w) I^M(\mathbf{k}) \right], \tag{10.7}$$

Following are the definitions of the parameters in the above equation. Ω, μ are the Larmor frequency and pitch angle cosine of the CRs. J_n represents Bessel function, and $w = k_\perp v_\perp/\Omega = k_\perp LR\sqrt{1-\mu^2}$, where $R = v/(\Omega l)$ is the dimensionless rigidity of the CRs, L is the injection scale of the turbulence. $k_\perp, k_\parallel$ are the components of the wave vector $\mathbf{k}$ perpendicular and parallel to the mean magnetic field, ω is the wave frequency. $I^A(\mathbf{k})$ is the energy spectrum of the Alfvén modes and $I^M(\mathbf{k})$ represents the energy spectrum of magnetosonic modes. In QLT, the resonance function $R_n = \pi\delta(k_\parallel v_\parallel - \omega \pm n\Omega)$. Now due to the perturbation of the orbit, it should be

$$\begin{aligned} & R_n(k_\parallel v_\parallel - \omega \pm n\Omega) \\ &= \Re \int_0^{\infty} dt e^{i(k_\parallel v_\parallel + n\Omega - \omega)t - \frac{1}{2}k_\parallel^2 <\Delta v_\parallel^2> t^2} \\ &= \frac{\sqrt{\pi}}{|k_\parallel \Delta v_\parallel|} \exp\left[-\frac{(k_\parallel v\mu - \omega + n\Omega)^2}{k_\parallel^2 \Delta v_\parallel^2} \right] \\ &\simeq \frac{\sqrt{\pi}}{|k_\parallel| v_\perp \sqrt{M_A}} \exp\left[-\frac{(k_\parallel v\mu - \omega + n\Omega)^2}{k_\parallel^2 v_\perp^2 M_A} \right] \end{aligned} \tag{10.8}$$

where $M_A \equiv \delta V/v_A = \delta B/B_0$ is the Alfvénic Mach number and v_A is the Alfvén speed. We stress that Eqs. (10.7), (10.8) are generic, and applicable to both incompressible and compressible medium.

For gyroresonance ($n = \pm 1, 2, \ldots$), the result is similar to that from QLT for $\mu \gg \Delta\mu = \Delta v_\parallel/v$. In this limit, Eq. (10.7) represents a sharp resonance and becomes equivalent to a δ-function when put into Eq. (10.7). In general, the result is different from that of QLT, especially at $\alpha \to 90°$, the resonance peak happens at $k_{\parallel,res} \sim \Omega/\Delta v$ in contrast to the QLT result $k_{\parallel,res} \sim \Omega/v_\parallel \to \infty$. We shall show below, that due to the anisotropy, the scattering coefficient $D_{\mu\mu}$ is still very small if the Alfvén and the pseudo-Alfvén modes are concerned.

On the other hand, the dispersion of the $v_\parallel$ means that CRs with a much wider range of pitch angle can be scattered by the compressible modes through TTD ($n = 0$), which is marginally affected by the anisotropy and much more efficient than the gyroresonance. In QLT, the projected particle speed should be comparable to phase speed of the magnetic field compression according to the δ function for the TTD resonance. This means that only particles with a specific pitch angle can be scattered. For the rest of the pitch angles, the interaction is still dominated by gyroresonance, which efficiency is negligibly small for the Alfvénic anisotropic turbulence (see Sect. 10.3.1). With the resonance broadening, however, wider range of pitch angle can be scattered through TTD, including 90°.

10.3.4 Results from Test Particle Simulations

We live in an era when we can test various processes in astrophysics and numerical studies have become an important part of theoretical efforts. Test particle simulation has been used to study CR scattering and transport (Giacalone and Jokipii 1999; Mace et al. 2000). The aforementioned studies, however, used synthetic data for turbulent fields, which have several disadvantages. Creating synthetic turbulence data which has scale-dependent anisotropy with respect to the local magnetic field (as observed in Cho and Vishniac 2000; Maron and Goldreich 2001) is difficult and has not been realized yet. Also, synthetic data normally uses Gaussian statistics and delta-correlated fields, which is hardly appropriate for description of strong turbulence.

Using the results of direct numerical MHD simulations as the input data, Beresnyak et al. (2011) and Xu and Yan (2013) performed test particle simulations. Their results show good correspondence with the analytical predictions. We briefly summarize the results here. As shown in Fig. 10.2, particles' motion is diffusive both along the magnetic field (x direction) and across the field (y direction). Moreover, the scattering coefficient shows the same pitch angle dependence as that predicted in Yan and Lazarian (2008), namely the scattering is most efficient for large pitch angles due to the TTD mirror interaction (see Fig. 10.2, *left*).

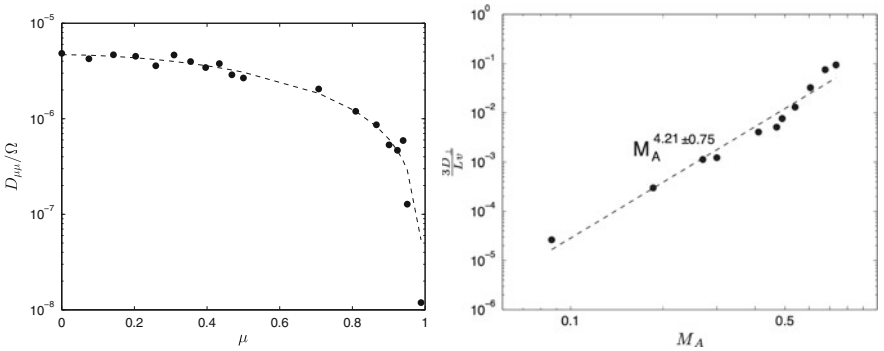

Fig. 10.2 *Left*: Dimensionless CR scattering coefficient $D_{\mu\mu}/\Omega$ vs the pitch angle μ. It is dominated by TTD resonant mirror interaction with compressible modes; *right:* diffusive behavior of the particles displayed in the tracing simulations. Both the parallel and perpendicular transport are normal diffusion, and the ratio of their diffusion coefficients is $\sim M_A^4$, consistent with the analytical prediction in Yan and Lazarian (2008) (from Xu and Yan 2013)

Table 10.1 The parameters of idealized ISM phases and relevant damping

ISM	Halo	HIM	WIM	WNM	CNM	DC
T(K)	2×10^6	1×10^6	8,000	6,000	100	15
c_S(km/s)	130	91	8.1	7	0.91	0.35
n(cm^{-3})	10^{-3}	4×10^{-3}	0.1	0.4	30	200
l_{mfp}(cm)	4×10^{19}	2×10^{18}	6×10^{12}	8×10^{11}	3×10^6	10^4
L(pc)	100	100	50	50	50	50
B(μG)	5	2	5	5	5	15
β	0.28	3.5	0.11	0.33	0.42	0.046
Damping	Collisionless	Collisional	Collisional	Neutral-ion	Neutral-ion	Neutral-ion

The dominant damping mechanism for turbulence is given in the last line
HIM hot ionized medium, *CNM* cold neutral medium, *WNM* warm neutral medium, *WIM* warm ionized medium, *DC* dark cloud

10.4 Cosmic Ray Propagation in Galaxy

The scattering by fast modes is influenced by the medium properties as the fast modes are subject to linear damping, e.g., Landau damping. Using the approach above we revisit the problem of the CR propagation in the selected phases of the ISM (see Table 10.1 for a list of fiducial parameters appropriate for the idealized phases[3]) assuming that turbulence is injected on large scales.

[3]The parameters of idealized interstellar phases are a subject of debate. Recently, even the entire concept of the phase being stable entities has been challenged (see Gazol et al. 2007; and ref. therein). Indeed different parts of interstellar medium can exhibit variations of these parameters (see Wolfire et al. 2003; and ref. therein).

10.4.1 Halo

In Galactic halo (see Table 10.1), the Coulomb collisional mean free path is $\sim$10 pc, the plasma is thus in a collisionless regime. The cascading rate of the fast modes is (Cho and Lazarian 2002)

$$\tau_k^{-1} = (k/L)^{1/2}\delta V^2/V_{ph}. \tag{10.9}$$

By equating it with the collisionless damping rate

$$\Gamma_c = \frac{\sqrt{\pi\beta}\sin^2\theta}{2\cos\theta}kv_A \times \left[\sqrt{\frac{m_e}{m_i}}\exp\left(-\frac{m_e}{\beta m_i\cos^2\theta}\right) + 5\exp\left(-\frac{1}{\beta\cos^2\theta}\right)\right], \tag{10.10}$$

we obtain the turbulence truncation scale k_c:

$$k_c L \simeq \frac{4M_A^4 m_i\cos^2\theta}{\pi m_e\beta\sin^4\theta}\exp\left(\frac{2m_e}{\beta m_i\cos^2\theta}\right). \tag{10.11}$$

where $\beta = P_{gas}/P_{mag}$.

The scale k_c depends on the *wave pitch angle* θ, which makes the damping anisotropic. As the turbulence undergoes cascade and the waves propagate in a turbulent medium, the angle θ is changing. As discussed in YL04 the field wandering defines the spread of angles. During one cascading time, the fast modes propagate a distance $v\tau_{cas}$ and see an angular deviation $\tan\delta\theta \simeq \sqrt{\tan^2\delta\theta_\parallel + \tan^2\delta\theta_\perp}$, which is

$$\tan\delta\theta \simeq \sqrt{\frac{M_A^2\cos\theta}{27(kL)^{1/2}} + \left(\frac{M_A^2\sin^2\theta}{kL}\right)^{1/3}} \tag{10.12}$$

As evident, the damping scale given by Eq. (10.11) varies considerably especially when $\theta \to 0$ and $\theta \to 90°$. For the quasi-parallel modes, the randomization ($\propto (kL)^{-1/4}$) is negligible since the turbulence cascade continues to very small scales. On small scales, most energy of the fast modes is contained in these quasi-parallel modes (Yan and Lazarian 2004; Petrosian et al. 2006).

For the quasi-perpendicular modes, the damping rate (Eq. (10.10)) should be averaged over the range $90° - \delta\theta$ to 90°. Equating Eqs. (10.9) and (10.10) averaged over $\delta\theta$, we get the averaged damping wave number (see Fig. 10.3, *left*). The field line wandering has a marginal effect on the gyroresonance, whose interaction with the quasi-perpendicular modes is negligible (YL04). However, TTD scattering rates of moderate energy CRs ($<$ 10 TeV) will be decreased owing to the increase of the damping around the 90° (see Fig. 10.3, *left*). For higher energy CRs, the influence of damping is marginal and so is that of field line wandering.

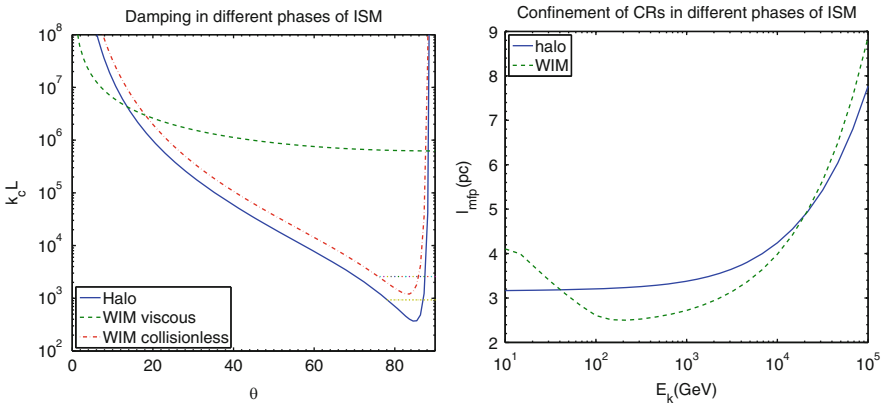

Fig. 10.3 *Left*: The turbulence truncation scales in Galactic halo and warm ionized medium (WIM). The damping curves flattens around 90° due to field line wandering (*dotted lines*, see Yan and Lazarian 2004; Lazarian et al. 2004); For WIM, both viscous and collisionless damping are applicable; *right*: the mean free paths in two different phases of ISM: halo (*solid line*) and WIM (*dashed line*). At lower energies ($\sim< 100$ GeV), the different dependence in WIM is owing to the viscous damping (from Yan and Lazarian 2008)

The QLT result on gyroresonance in the range $\mu > \Delta\mu$ provides a good approximation to the non-linear results (Yan and Lazarian 2008). For CRs with sufficiently small rigidities, the resonant fast modes ($k_{res} \approx 1/(R\mu)$) are on small scales with a quasi-slab structure (see Fig.10.3, *left*). For the scattering by these quasi-parallel modes, the analytical result that follows from QLT approximation (see Yan and Lazarian 2004) for the gyroresonance is[4]

$$\begin{bmatrix} D^G_{\mu\mu} \\ D^G_{pp} \end{bmatrix} = \frac{\pi v \mu^{0.5}(1-\mu^2)}{4LR^{0.5}} \begin{bmatrix} \frac{1}{7}[1+(R\mu)^2]^{-\frac{7}{4}} - (\tan^2\theta_c + 1)^{-\frac{7}{4}} \\ \frac{m^2V_A^2}{3}\left\{[1+(R\mu)^2]^{-\frac{3}{4}} - (\tan^2\theta_c+1)^{-\frac{3}{4}}\right\} \end{bmatrix} \tag{10.13}$$

where $\tan\theta_c = k_{\perp,c}/k_{\parallel,res}$.

Once we know the functional form of the $D_{\mu\mu}$, we can obtain the corresponding mean free path (Earl 1974):

$$\lambda_\parallel/L = \frac{3}{4}\int_0^1 d\mu \frac{v(1-\mu^2)^2}{(D^T_{\mu\mu} + D^G_{\mu\mu})L}, \tag{10.14}$$

where $D^T_{\mu\mu}$ is the contribution from TTD interaction and can be obtained using the nonlinear theory (see Yan and Lazarian 2008 and also Sect. 10.3.3) with the inertial

[4]It can be shown that the QLT result follows from our more general results (see Eqs. (10.7), (10.8)) if we put $\Delta\mu \to 0$. This justifies our use of the analytical approximation.

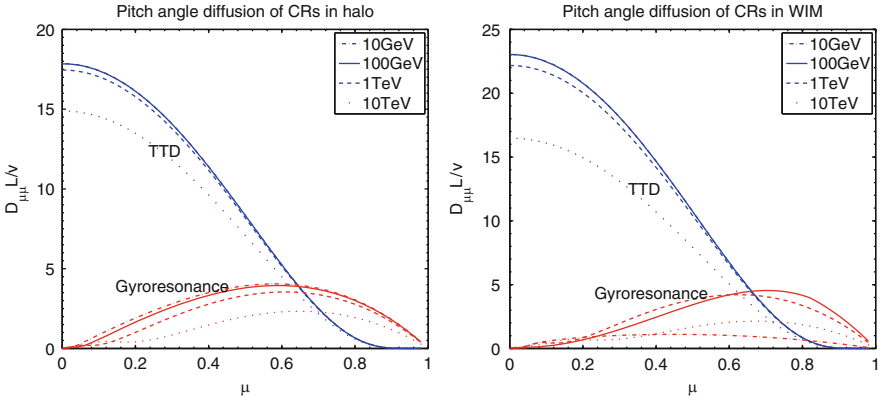

Fig. 10.4 Pitch angle diffusion coefficients in halo and WIM. *Upper lines* in the plots represent the contribution from TTD and *lower lines* are for gyroresonance (from Yan and Lazarian 2008)

range of fast modes determined for the local medium (see, e.g., 10.11 in the case of collisionless damping).

The mean free path is sensitive to the scattering by gyroresonance at small pitch angles, due to the influence of damping on the fast modes on small scales. Figure 10.4 shows the pitch angle diffusion of CRs with different energies due to the TTD and gyroresonance.

The weak dependence of the mean free path (see Fig. 10.3, *right*) of the moderate energy (e.g. <1 TeV) CRs in halo results from the fact that gyroresonance changes marginally with the CR energy (see Fig. 10.4). This is associated with the damping in collisionless medium. We expect that similar flat dependence can happen in any collisionless medium. This can be a natural explanation of the puzzling "Palmer Concensus" (Palmer 1982), the same trend observed in solar wind.

10.4.2 Warm Ionized Medium

In warm ionized medium, the Coulomb collisional mean free path is $l_{mfp} = 6 \times 10^{12}$ cm and the plasma $\beta \simeq 0.11$. Suppose that the turbulence energy is injected from large scale, then the compressible turbulence is subjected to the viscous damping besides the collisionless damping. By equating the viscous damping rate with the cascading rate (Eq. (10.9)), we obtain the following truncation scale,

$$k_c L = x_c \begin{cases} (1-\xi^2)^{-\frac{2}{3}} & \beta \ll 1 \\ (1-3\xi^2)^{-\frac{4}{3}} & \beta \gg 1 \end{cases} \tag{10.15}$$

where $x_c = \left[\frac{6\rho\delta V^2 L}{\eta_0 V_A}\right]^{\frac{2}{3}}$, η_0 is the longitudinal viscosity. In the low β regime, the motions are primarily perpendicular to the magnetic field so that $\partial v_x/\partial x = \dot{n}/n \sim \dot{B}/B$. The longitudinal viscosity enters here as the result of distortion of the Maxiwellian distribution (see Braginskii 1965). The transverse energy of the ions increases during compression because of the conservation of adiabatic invariant $v_\perp^2/B$. If the rate of compression is faster than that of collisions, the ion distribution in the momentum space is bound to be distorted from the Maxiwellian isotropic sphere to an oblate spheroid with the long axis perpendicular to the magnetic field. As a result, the transverse pressure gets greater than the longitudinal pressure, resulting in a stress $\sim \eta_0 \partial v_x/\partial x$. The restoration of the equilibrium increases the entropy and causes the dissipation of energy.

The viscous damping scale is compared to collisionless cutoff scale (Eq. (10.11)) in Fig. 10.3, *left*. As shown there, both viscous damping and collisionless damping are important in WIM. Viscous damping is dominant for small θ and collisionless damping takes over for large θ except for $\theta = 90°$. This is because collisionless damping increases with θ much faster than the viscous damping. For sufficiently small wave pitch angles, the viscous damping is too small to prevent the fast modes to cascade down to scales smaller than the mean free path l_{mfp}. Because of the similar quasi-slab structure on small scales, Eq. (10.13) can be also applied in WIM. The results are illustrated in Fig. 10.4. Compared to the case in halo, we see that the qualitative difference stands in the gyroresonance. This is because gyroresonance is sensitive to the quasi-slab modes whose damping differs in halo and WIM.

10.4.3 Other Phases

In hot ionized medium (HIM), the plasma is also in collisionless regime, but the density is higher and the plasma beta is larger than 1. The damping by protons thus becomes substantial especially at small pitch angles. The damping truncates the turbulence at much larger scales than the gyroscales of the CRs of the energy range we consider. No gyroresonance can happen and some other mechanisms are necessary to prevent CRs streaming freely along the field. The turbulence injected from small scales might play an important role (see Sect. 10.6).

In partially ionized gas one should take into account an additional damping that arises from ion-neutral collisions (see Kulsrud and Pearce 1969; Lithwick and Goldreich 2001; Lazarian et al. 2004). In the latter work a viscosity-damped regime of turbulence was predicted at scales less the scale $k_{c,amb}^{-1}$ at which the ordinary magnetic turbulence is damped by ionic viscosity. The corresponding numerical work, e.g., Cho et al. (2002) testifies that for the viscosity-damped regime the parallel scale stays equal to the scale of the ambipolar damping, i.e., $k_\parallel = k_{c,amb}$, while $k_\perp$ increases. In that respect, the scattering by such magnetic fluctuations is analogous to the scattering induced by the weak turbulence (see Sect. 2.3, Yan and Lazarian 2008). The difference stems from the spectrum of $k_\perp$ is shallower

than the spectrum of the weak turbulence. The predicted values of the spectrum for the viscosity-damped turbulence $E(k_\perp) \sim k_\perp^{-1}$ (Lazarian et al. 2004) are in rough agreement with simulations. More detailed studies of scattering in partially ionized gas will be necessary.

10.5 Perpendicular Transport

In this section we deal with the diffusion perpendicular to *mean* magnetic field.

Propagation of CRs perpendicular to the mean magnetic field is another important problem in which QLT encounters serious difficulties. Compound diffusion, resulting from the convolution of diffusion along the magnetic field line and diffusion of field line perpendicular to mean field direction, has been invoked to discuss transport of cosmic rays in the Milky Way (Getmantsev 1963; Lingenfelter et al. 1971; Allan 1972). The role of compound diffusion in the acceleration of CRs at quasi-perpendicular shocks were investigated by Duffy et al. (1995) and Kirk et al. (1996).

Indeed, the idea of CR transport in the direction perpendicular to the mean magnetic field being dominated by the field line random walk (FLRW, Jokipii 1966; Jokipii and Parker 1969; Forman et al. 1974) can be easily justified only in a restricted situation where the turbulence perturbations are small and CRs do not scatter backwards to retrace their trajectories. If the latter is not true, the particle motions are subdiffusive, i.e., the squared distance diffused growing as not as t but as t^α, $\alpha < 1$, e.g., $\alpha = 1/2$ (Kóta and Jokipii 2000; Mace et al. 2000; Qin et al. 2002). If true, this could indicate a substantial shift in the paradigm of CR transport, a shift that surely dwarfs a modification of magnetic turbulence model from the 2D+slab to a more simulation-motivated model that we deal here.

It was also proposed that with substantial transverse structure, i.e., transverse displacement of field lines, perpendicular diffusion is recovered (Qin et al. 2002). Is it the case of the MHD turbulence models we deal with?

How realistic is the subdiffusion in the presence of turbulence? The answer for this question apparently depends on the models of turbulence chosen.

Compound diffusion happens when particles are restricted to the magnetic field lines and perpendicular transport is solely due to the random walk of field line wandering (see Kóta and Jokipii 2000). In the three-dimensional turbulence, field lines are diverging away due to shearing by the Alfvén modes (see Lazarian and Vishniac 1999; Narayan and Medvedev 2001; Lazarian 2006). Since the Larmor radii of CRs are much larger than the minimum scale of eddies $l_{\perp,min}$, field lines within the CR Larmor orbit are effectively diverging away owing to shear by the Alfvénic turbulence. The cross-field transport thus results from the deviations of field lines at small scales, as well as field line random walk at large scale ($>\min[L/M_A^3, L]$).

Both observation of Galactic CRs and solar wind indicate that the diffusion of CRs perpendicular to magnetic field is normal diffusion (Giacalone and Jokipii 1999; Maclennan et al. 2001). Why is that?

Most recently the diffusion in magnetic fields was considered for thermal particles in Lazarian (2006), for cosmic rays in Yan and Lazarian (2008). In what follows we present the results based on the studies in Yan and Lazarian (2008).

10.5.1 Perpendicular Diffusion on Large Scale

For perpendicular diffusion, the important issue is the reference frame. We emphasize that we consider the diffusion perpendicular to the *m*ean field direction in the global reference of frame.

High M_A turbulence: High M_A turbulence corresponds to the field that is easily bended by hydrodynamic motions at the injection scale as the hydro energy at the injection scale is much larger than the magnetic energy, i.e. $\rho V_L^2 \gg B^2$. In this case magnetic field becomes dynamically important on a much smaller scale, i.e. the scale $l_A = L/M_A^3$ (see Lazarian 2006). If the parallel mean free path of CRs $\lambda_\parallel \ll l_A$, the stiffness of B field is negligible so that the perpendicular diffusion coefficient is the same as the parallel one, i.e., $D_\perp = D_\parallel \sim 1/3\lambda_\parallel v$. If $\lambda_\parallel \gg l_A$, the diffusion is controlled by the straightness of the field lines, and $D_\perp = D_\parallel \approx 1/3 l_A v$. The diffusion is isotropic if scales larger than l_A are concerned.

Low M_A turbulence: In the magnetically dominated case, i.e. the field that cannot be easily bended at the turbulence injection scale, individual magnetic field lines are aligned with the mean magnetic field. The diffusion in this case is anisotropic. If turbulence is injected at scale L it stays weak for the scales larger than LM_A^2 and it is strong at smaller scales. Consider first the case of $\lambda_\parallel > L$. The time of the individual step is $L/v_\parallel$, then $D_\perp \approx 1/3 L v M_A^4$. This is similar to the case discussed in the FLRW model (Jokipii 1966). However, we obtain the dependence of M_A^4 instead of their M_A^2 scaling. In the opposite case of $\lambda_\parallel < L$, the perpendicular diffusion coefficient is $D_\perp \approx D_\parallel M_A^4$, which coincides with the result obtained for the diffusion of thermal electrons in magnetized plasma (Lazarian 2006). This is due to the anisotropy of the Alfvénic turbulence.

10.5.2 Superdiffusion on Small Scales

The diffusion of CR on the scales $\ll L$ is different and it is determined by how fast field lines are diverging away from each other. The mean deviation of a field in a distance δx is proportional to $[\delta z]^{3/2}$ (Lazarian and Vishniac 1999; Lazarian 2006), same as Richardson diffusion in the case of hydrodynamic turbulence (see Eyink et al. 2011). Following the argument, we showed in Yan and Lazarian (2008) that the cosmic ray perpendicular transport is superdiffusive. The reason is that there is no random walk on small scales up to the injection scale of strong MHD turbulence (LM_A^2 for $M_A < 1$ and l_A for $M_A > 1$). This can well explain the recently observed super-diffusion in solar wind (Perri and Zimbardo 2009). Superdiffusion can have

important implications for shock acceleration as discussed in details in Lazarian and Yan (2013).

10.5.3 Is There Subdiffusion?

The diffusion coefficient $D_{\parallel} M_A^4$ we obtained in the case of $M_A < 1$, means that the transport perpendicular to the dynamically strong magnetic field is a normal diffusion, rather than the subdiffusion as discussed in a number of recent papers. This is also supported by test particle simulations (Beresnyak et al. 2011; Xu and Yan 2013; see Fig. 10.2, *right*). Let us clarify this point by obtaining the necessary conditions for the subdiffusion to take place.

The major implicit assumption in subdiffusion (or compound diffusion) is that the particles trace back their trajectories in x direction on the scale δz. When is it possible to talk about retracing of particles? In the case of random motions at a single scale *only*, the distance over which the particle trajectories get uncorrelated is given by the Rechester and Rosenbluth (1978) model. Assuming that the damping scale of the turbulence is larger that the CR Larmor radius, the Rechester and Rosenbluth (1978) model, when generalized to anisotropic turbulence provides (Narayan and Medvedev 2001; Lazarian 2006) $L_{RR} = l_{\parallel,min} \ln(l_{\perp,min}/r_{Lar})$ where $l_{\parallel,min}$ is the parallel scale of the cut-off of turbulent motions, $l_{\perp,min}$ is the corresponding perpendicular scale, r_{Lar} is the CR Larmor radius. The assumption of $r_{Lar} < l_{\perp,min}$ can be valid, for instance, for Alfvénic motions in partially ionized gas. However, it is easy to see that, even in this case, the corresponding scale is rather small and therefore subdiffusion is not applicable for the transport of particles in Alfvénic turbulence over scales $\gg l_{\parallel,min}$.

If $r_{Lar} > l_{\perp,min}$, as it is a usual case for Alfvén motions in the phase of ISM with the ionization larger than $\approx 93\,\%$, where the Alfvénic motions go to the thermal particle gyroradius (see estimates in Lithwick and Goldreich 2001; Lazarian et al. 2004), the subdiffusion of CR is not an applicable concept for Alfvénic turbulence. This does not preclude subdiffusion from taking place in particular models of magnetic perturbations, e.g. in the slab model considered in Kóta and Jokipii (2000), but we believe in the omnipresence of Alfvénic turbulence in interstellar gas (see Armstrong et al. 1995).

10.6 Streaming Instability in the Presence of Turbulence

When cosmic rays stream at a velocity much larger than Alfvén velocity, they can excite by gyroresonance MHD modes which in turn scatter cosmic rays back, thus increasing the amplitude of the resonant mode. This runaway process is known as streaming instability. It was claimed that the instability could provide confinement for cosmic rays with energy less than $\sim 10^2\,\mathrm{GeV}$

(Cesarsky 1980). However, this was calculated in an ideal regime, namely, there was no background MHD turbulence. In other words, it was thought that the self-excited modes would not be appreciably damped in fully ionized gas.[5] This is not true for turbulent medium, however. Yan and Lazarian (2002) pointed out that the streaming instability is partially suppressed in the presence of background turbulence (see more in Lazarian et al. 2003). More recently, detailed calculations of the streaming instability in the presence of background Alfvénic turbulence were presented in Farmer and Goldreich (2004). The growth rate of the modes of wave number k is (Longair 1997).

$$\Gamma_{cr}(k) = \Omega_0 \frac{N(\geq E)}{n_p}(-1 + \frac{v_{stream}}{V_A}), \tag{10.16}$$

where $N(\geq E)$ is the number density of cosmic rays with energy $\geq E$ which resonate with the wave, n_p is the number density of charged particles in the medium. The number density of cosmic rays near the sun is $N(\geq E) \simeq 2 \times 10^{-10}\,(E/\mathrm{GeV})^{-1.6}\,\mathrm{cm}^{-3}\mathrm{sr}^{-1}$ (Wentzel 1974).

Interaction with fast modes was considered by Yan and Lazarian (2004). Such an interaction happens at the rate $\tau_k \sim (k/L)^{-1/2} V_{ph}/V^2$. By equating it with the growth rate Eq. (10.16), we can find that the streaming instability is only applicable for particles with energy less than

$$\gamma_{max} \simeq 1.5 \times 10^{-9} [n_p^{-1} (V_{ph}/V)(Lv\Omega_0/V^2)^{0.5}]^{1/1.1}, \tag{10.17}$$

which for HIM, provides ~20 GeV if taking the injection speed to be $V \simeq 25$ km/s. Similar result was obtained with Alfvén modes by Farmer and Goldreich (2004).

Magnetic field itself is likely to be amplified through an inverse cascade of magnetic energy at which perturbations created at a particular k diffuse in k space to smaller k thus inducing inverse cascade. As the result, the magnetic perturbations at smaller k get larger than the regular field. Consequently, even if the instability is suppressed for the growth rate given by Eq. (10.16) it gets efficient due to the increase of perturbations of magnetic field stemming from the inverse cascade. The precise picture of the process depends on yet not completely clear details of the inverse cascade of magnetic field.

Below, we present the application of the current understanding of the interaction between the streaming instability and the background turbulence to the modeling of the gamma ray emission from molecular clouds near SNRs (see more details in Yan et al. 2012). We shall treat the problem in a self-consistent way by comparing the streaming level that is allowed by the preexisting turbulence and the required diffusion for the CRs.

[5] We neglect the nonlinear Landau damping, which is suppressed in turbulence due to decrease of mean free path.

10.6.1 Application to CR Acceleration at the Shocks

Diffusive shock acceleration of energetic CR particles relies on the crucial process of amplification of MHD turbulence so that particles can be trapped at the shock front long enough to be accelerated to the high energy observed. One of the most popular scenarios that has been adopted in the literature is the streaming instability generated by the accelerated particles. However, in the highly nonlinear regime the fluctuations of magnetic field arising from the streaming instability get large and the classical treatment of the streaming instability is not applicable. We circumvent the problem by proposing that the field amplification we consider does not arise from the streaming instability, but is achieved earlier through other processes, e.g. the interaction of the shock precursor with density perturbations preexisting in the interstellar medium (Beresnyak et al. 2009). Due to the resonant nature of the streaming instability, the perturbations δB arising from it are more efficient in scattering CRs compared to the large scale fluctuations produced by non-resonant mechanisms, e.g. the one in Beresnyak et al. (2009). Therefore in this chapter, we limit our discussions to the regime of $\delta B \sim< B_0$, where B_0 is the magnetic field that has already been amplified in the precursor region.[6] Notations used in this subsection are provided in Table 10.2.

When particles reach the maximum energy at a certain time, they escape and the growth of the streaming instability stops. Therefore we can obtain the maximum energy by considering the stationary state of the evolution. The steady state energy density of the turbulence $W(k)$ at the shock is determined by

$$(U \pm v_A)\nabla W(k) = 2(\Gamma_{cr} - \Gamma_d)W(k), \tag{10.18}$$

where U is the shock speed, and the term on the l.h.s. represents the advection of turbulence by the shock flow. $v_A \equiv B_0/\sqrt{4\pi nm}$ and n are the Alfvén speed and the ionized gas number density of the precursor region, respectively. The plus sign represents the forward propagating Alfvén waves and the minus sign refers to the backward propagating Alfvén waves. The terms on the r.h.s. describes the wave amplification by the streaming instability and damping with Γ_d as the corresponding damping rate of the wave. The distribution of accelerated particles at strong shocks is $f(p) \propto p^{-4}$. If taking into account the modification of the shock structure by the accelerated particles, the CR spectrum becomes harder. Assume the distribution of CRs at the shock is $f_0(p) \propto p^{-4+a}$ (see table 10.3). The nonlinear growth was studied by Ptuskin and Zirakashvili (2005).

[6]The effective B_0 is therefore renormalized and can be much larger than the typical field in ISM (see, e.g., Diamond and Malkov 2007).

Table 10.2 The notation we used in Sect. 10.6.1

A	Normalized wave amplitude $\delta B/B_0$
a	Hardening of the CR spectrum at the shock front
B_0	Mean magnetic field at the shock in the later Sedov phase
B_{cav}	Intercloud magnetic field strength
δB	Wave amplitude
c	Light speed
d	Distance of the molecular cloud from observer
D	Diffusion coefficient of CRs
E	CR energy
E_{SN}	Supernova explosion
f	Distribution function of CRs
f_π	Fraction of energy transferred from parent protons to pions
k	Wave number
K(t)	Normalization factor of CR distribution function
L	The injection scale of background turbulence
m	Proton rest mass
M_c	Cloud mass
n	Intercloud number density
N_γ	γ ray flux
p	CR's momentum
p_{max}	The maximum momentum accelerated at the shock front
P_{CR}	CR pressure
q	Charge of the particle
r	Distance from SNR centre
R_c	The distance of the molecular cloud from the SNR centre
r_g	Larmor radius of CRs
R_d	diffusion distance of CRs
R_{sh}	Shock radius
R_{esp}, t_{esp}	The escaping distance/time of CRs
s	1D spectrum index of CR distribution
t	Time since supernova explosion
t_{age}	The age of SNR
t_{sed}	The time at which SNR enters the Sedov phase
U	Shock speed
U_i	Initial shock velocity
v	Particle speed
v_s	Streaming speed of CRs
W	Wave energy
α	Power index of D with respect to particle momentum p

(continued)

Table 10.2 (continued)

χ	Reduction factor of D with respect to D_{ISM}
δ	Power index of p_{max} with respect to t
η	Fraction of SN energy converted into CRs
Γ_{cr}	The growth rate of streaming instability
Γ_d	Wave damping rate
κ	Ratio of diffusion length to shock radius
Ω_0	The Larmor frequency of non-relativistic protons
σ_{pp}	Cross section for pp collision
ξ	The ratio of CR pressure to fluid ram pressure

Table 10.3 Model parameters adopted

a	χ	η	κ	ξ	α
0.1∼ 0.3	∼0.05	∼ 0.3	0.04 ∼ 0.1	0.2 ∼0.4	0.5

The generalized growth rate of streaming instability is

$$\Gamma_{cr} = \frac{12\pi^2 q^2 v_A \sqrt{1+A^2}}{c^2 k} \times \int_{p_{res}}^{\infty} dpp \left[1 - \left(\frac{p_{res}}{p}\right)^2\right] D \left|\frac{\partial f}{\partial x}\right|, \tag{10.19}$$

where q is the charge of the particle, c is the light speed, $p_{res} = ZeB_0\sqrt{1+A^2}/c/k_{res}$ is the momentum of particles that resonate with the waves. $A = \delta B/B_0$ is wave amplitude normalized by the mean magnetic field strength B_0.

$$D = \sqrt{1+A^2} v r_g/3/A^2(> k_{res}) \tag{10.20}$$

is the diffusion coefficient of CRs, v and r_g are the velocity and Larmor radius of the CRs. In the planar shock approximation, one gets the following growth rate of the upstream forward moving wave at x=0,

$$\Gamma_{cr}(k) = \frac{C_{cr}\xi U^2 (U + v_A) k^{1-a}}{(1+A^2)^{(1-a)/2} c v_A \phi(p_{max}) r_0^a} \tag{10.21}$$

where $C_{cr} = 4.5/(4-a)/(2-a)$, $r_0 = mc^2/q/B_0$, where ξ measures the ratio of CR pressure at the shock and the upstream momentum flux entering the shock front, m is the proton rest mass, and p_{max} is the maximum momentum accelerated at the shock front. $H(p)$ is the Heaviside step function.

The linear damping is negligible since the medium should be highly ionized. In fully ionized gas, there is nonlinear Landau damping, which, however, is suppressed due to the reduction of particles' mean free path in the turbulent medium (see Yan

and Lazarian 2011). We therefore neglect this process here. Background turbulence itself can cause nonlinear damping to the waves (Yan and Lazarian 2002). Unlike hydrodynamical turbulence, MHD turbulence is anisotropic with eddies elongated along the magnetic field. The anisotropy increases with the decrease of the scale (Goldreich and Sridhar 1995). Because of the scale disparity, $k_\parallel > k_\perp \gg k_\parallel^t$, the nonlinear damping rate in MHD turbulence is less than the wave frequency $k_\parallel v_A$, and it is given by Farmer and Goldreich (2004), Yan and Lazarian (2004)

$$\Gamma_d \sim \sqrt{k/L} v_A, \tag{10.22}$$

where L is the injection scale of background turbulence, and the k is set by the resonance condition $k \sim k_\parallel \sim 1/r_L$.

There are various models for the diffusive shock acceleration. We consider here the escape-limited acceleration. In this model, particles are confined in the region near the shock where turbulence is generated. Once they propagate far upstream at a distance l from the shock front, where the self-generated turbulence by CRs fades away, the particles escape and the acceleration ceases. The characteristic length that particles penetrate into the upstream is $D(p)/U$. The maximum momentum is reached when $D(p)/U \simeq l/4$.[7] Assuming $l = \kappa R_{sh}$, where $\kappa < 1$ is a numerical factor, one can get

$$\frac{p_{max}}{mc} = \frac{3\kappa A^2 U R_{sh}}{\sqrt{1+A^2} v r_0}. \tag{10.23}$$

In particular, for $A < 1$

$$\frac{p_{max}}{mc} = \left[\left(-v_A \sqrt{\frac{1}{r_0 L}} + \sqrt{\frac{v_A^2}{r_0 L} + \frac{2C_{cr} a \xi U^3 (U+v_A)}{\kappa r_0 R_{sh} c v_A}} \right) \left(\frac{\kappa R_{sh}}{U} \right) \right]^2,$$

$$A = \frac{p_{max} r_0}{\sqrt{18} \kappa m U R_{sh}} \sqrt{1 + \sqrt{1 + 36 \left(\frac{\kappa m U R_{sh}}{p_{max} r_0} \right)^2}}, \tag{10.24}$$

In the limit of low shock velocity,

$$v_A \ll U \ll c \left[\left(\frac{v_A}{c} \right)^3 \frac{\kappa R_{sh}}{2LC_{cr} a \xi} \right]^{1/4}, \tag{10.25}$$

[7] The factor 1/4 arises from the following reason. As pointed out by Ostrowski and Schlickeiser (1996), the spectrum is steepened for small l, i.e., $lU/D(p) \sim< 4$.

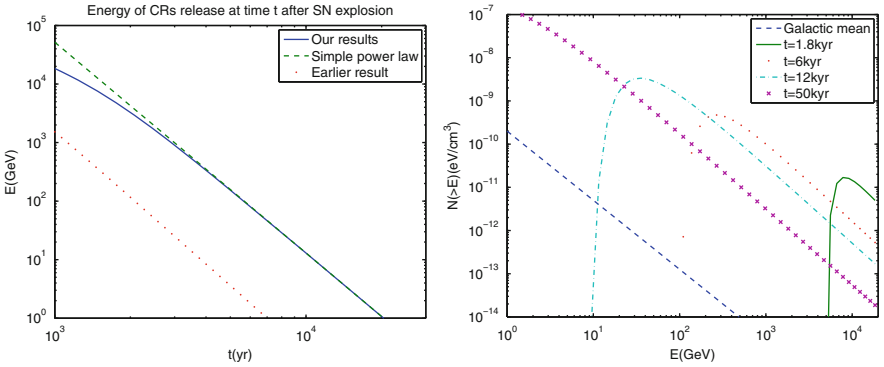

Fig. 10.5 *Left*: The energy of CRs that are released at the shock at time t in the Sedov phase. Our result shows that the often assumed power law solution (see Gabici et al. 2009; Ohira et al. 2010) is only realized in asymptotic regime as described in Eqs. (10.25), (10.26). It is also larger than the earlier result (*dotted line*) in Ptuskin and Zirakashvili (2005) where the damping of the waves by background turbulence is overestimated. *Right*: the spectrum of CRs at a distance $r = 12\,\mathrm{pc}$ after 1,800 (*solid line*), 6,000 (*dotted line*), 12,000 (*dashdot line*), 50,000 years (*cross line*). The Galactic mean is plotted as a reference (*dashed line*). From Yan et al. (2012)

we get

$$\frac{p_{max}}{mc} = (C_{cr}\xi U^3)^2 \frac{a^2 L}{r_0 c^2 v_A^4} \tag{10.26}$$

for the Sedov phase ($t > t_{sed} \equiv 250(E_{51}/(n_0 U_9^5))^{1/3}\mathrm{yr}$), where $E_{51} = E_{SN}/10^{51}\mathrm{erg}$ and $U_9 = U_i/10^9\,\mathrm{cm/s}$ are the total energy of explosion and the initial shock velocity. In Fig. 10.5, we plot the evolution of $p_{max}/(mc)$ during the Sedov phase. The solid line represents the results from Eq. (10.24). As we see, at earlier epoch when advection and streaming instability are both important, the evolution of p_{max} does not follow a power law. For comparison, we also put a power law evolution in the same figure as depicted by Eq. (10.26) (dashed line).

Our result is also larger than that obtained by Ptuskin and Zirakashvili (2005) since the wave dissipation rate is overestimated in their treatment.

10.6.2 Enhanced Scattering and Streaming Instability Near SNRs

The result from Yan et al. (2012) show that the local scattering of CRs has to be enhanced by an order of magnitude $\chi = 0.05$ in order to produce the amount of γ ray emission observed. A natural way to increase the scattering rate is through the streaming instability. The enhanced flux of the CRs are demonstrated to generate

strong enough instability to overcome nonlinear damping by the background turbulence (Yan et al. 2012). The growth rate in the linear regime is

$$\Gamma_{gr} = \Omega_0 \frac{N(\geq E)}{n} \left(\frac{v_s}{v_A} - 1 \right), \tag{10.27}$$

where v_s is the streaming speed of CRs. The growth rate should overcome the damping rate (Eq. (10.22)) for the instability to operate. The condition $\Gamma_{gr} > \Gamma_d$ leads to

$$v_s > v_A \left(1 + \frac{n v_A}{N \Omega_0 \sqrt{r_{gL}}} \right) \tag{10.28}$$

The spatial diffusion coefficient adopted here, $D \approx v_s L = \chi D_{ISM}$, satisfies this requirement. The growth and damping rates are compared in Fig. 10.6, *right*. We see that the streaming instability works in the energy range needed to produce the observed γ ray emission, proving that our results are self-consistent.

Note that the case we consider here is different from the general interstellar medium discussed in Yan and Lazarian (2004) and Farmer and Goldreich (2004), namely, the local cosmic ray flux near SNRs is much enhanced (see Fig. 10.5, *right*). Consequently, the growth rate of the streaming instability becomes high enough to overcome the damping rate by the preexisting turbulence in the considered energy range Fig. 10.6.

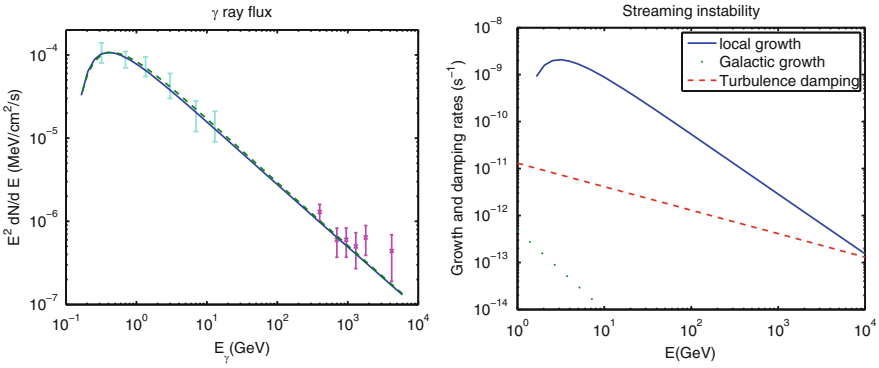

Fig. 10.6 *Left*: The spectrum of Gamma ray emission from W28. The Fermi data are shown as *dotted points* (Abdo et al. 2010), and the H.E.S.S. data are plotted as 'x' points (Aharonian et al. 2008) with error bars. *Solid line* is our result. *Right*: The growth and nonlinear damping rates of streaming instability. With the locally enhanced flux, the growth rate of streaming instability becomes much larger than the mean Galactic value so that it can overcome the nonlinear damping by turbulence for a wide energy range. This is consistent with our earlier treatment in which streaming instability plays an essential role in the cosmic ray diffusion near SNRs. From Yan et al. (2012)

10.7 Gyroresonance Instability of CRs in Compressible Turbulence

Until recently, test particle approximation was assumed in most of earlier studies in which turbulence cascade is established from large scales and no feedback of CRs is included. This may not reflect the reality as we know the energy of CRs is comparable to that in turbulence and magnetic field (see Kulsrud 2005). It was suggested by Lazarian and Beresnyak (2006) that the gyroresonance instability of CRs can drain energy from the large scale turbulence and cause instability on small scales by the turbulence compression induced anisotropy on CRs (see Fig. 10.7, *left*). And the wave generated on the scales, in turn, provides additional scattering to CRs. In Yan and Lazarian (2011), quantitative studies was provided based on the nonlinear theory of the growth of the instability and the feedback of the growing waves on the distributions of CRs.

In the presence of background compressible turbulence, the CR distribution is bound to be anisotropic because of the conservation of the first adiabatic invariant $\mu \equiv v_\perp^2/B$. Such anisotropic distribution is subjected to various instabilities. Waves are generated through the instabilities, enhancing the scattering rates of the particles, their distribution will be relaxed to the state of marginal state of instability even in

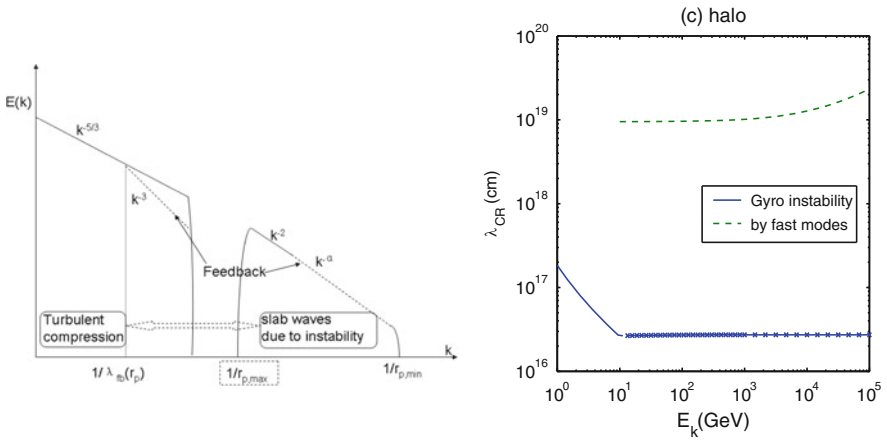

Fig. 10.7 *Left*: The spectral energy density of slab waves that is transferred from the large scale compressible turbulence via the gyroresonance instability of CRs. In the case that the instability grows up to the maximum energy rate allowed by the turbulence cascade, large scale turbulence is truncated at λ_{fb} and the wave amplitude $E(k)dk \sim \epsilon_N^u$ is given by Eq. (10.30). Note that the picture is different from LB06, namely, the feedback on the large scale turbulence occurs only in some cases when the scattering is not sufficient to prevent the waves from growing to the maximum values (Yan and Lazarian 2011); *right*: CR scattering is dominated by compressible modes. For high energy CRs ($>\sim$10 GeV), the scattering is due to direct interaction with fast modes; For low energy CRs, the interaction is mainly due to the gyroresonance instability induced by compression of magnetic fields

the collisionless environment. While the hydrodynamic instability requires certain threshold, the kinetic instability can grow very fast with small deviations from isotropy. Here, we focus on the gyroresonance instability. Both the qualitative and quantitative studies in Yan and Lazarian (2011) show that the isotropization rate is roughly $\tau_{scatt}^{-1} \sim \frac{\Gamma_{gr}\epsilon_N}{\beta_{CR}A}$, where Γ_{cr}, ϵ_N are the instability growth rate and the wave energy normalized by magnetic energy, respectively. β_{CR} is the ratio of CR pressure to magnetic pressure, A is the degree of anisotropy of the CR momentum distribution.

By balancing the rate of decrease in anisotropy due to scattering and the growth due to compression, one can get

$$\epsilon_N \sim \frac{\beta_{CR}\omega\delta v}{\Gamma_{gr}v_A}, \quad \lambda_{CR} = r_p/\epsilon_N., \tag{10.29}$$

where v_A is the Alfvén speed, $\omega, \delta v$ are the wave frequency and amplitude at the scale that effectively compresses the magnetic field and create anisotropy in CRs' distribution (Yan and Lazarian 2011). Since the growth rate decreases with energy, the instability only operates for low energy CRs ($\sim<$ 100 GeV, see Fig. 10.7, *right*) due to the damping by the preexisting turbulence (Yan and Lazarian 2011) .

10.7.1 Bottle-Neck for the Growth of the Instability and Feedback on Turbulence

The creation of the slab waves through the CR resonant instability is another channel to drain the energy of large scale turbulence. This process, on one hand, can damp the turbulence. On the other hand, it means that the growth rate is limited by the turbulence cascade. The energy growth rate cannot be larger than the turbulence energy cascading rate, which is $1/2\rho V_L^4/v_A/L$ for fast modes in low β medium and $\rho v_A^3/l_A$ for slow modes in high β medium. This places a constraint on the growth, thus the upper limit of wave energy is given by

$$\epsilon_N^u = \begin{cases} M_A^2 L_i/(LA)\gamma^{\alpha-1}, & \beta < 1 \\ L_i/(l_{AA})\gamma^{\alpha-1}, & \beta > 1, \end{cases} \tag{10.30}$$

where γ is the Lorentz factor and $L_i \simeq 6.4 \times 10^{-7}(B/5\mu\mathrm{G})(10^{-10}\,\mathrm{cm}^3/n_{cr})\,\mathrm{pc}$. The growth is induced by the compression at scales $\sim< \lambda_{CR}$. Therefore, in the case that $\Gamma_{gr}\epsilon$ reaches the energy cascading rate, fast modes are damped at the corresponding maximum turbulence pumping scale $\lambda_{fb} = r_p/\epsilon_N$ (see Fig. 10.7, *left*). If λ_{fb} is larger than the original damping scale l_c, then there is a feedback on the large scale compressible turbulence. This shows that test particle approach is not adequate and feedback should be included in future simulations.

10.8 Summary

In this chapter, we reviewed recent development on cosmic ray transport theories based on modern understanding of MHD turbulence. The main conclusions from both analytical study and test particle simulations in MHD turbulence are:

- Compressible fast modes are most important for CR scattering. CR transport therefore varies from place to place.
- Nonlinear mirror interaction is essential for pitch angle scattering (including 90°).
- Cross field transport is diffusive on large scales and super-diffusive on small scales.
- Subdiffusion does not happen in 3D turbulence.
- Self-generated waves are subject to damping by preexisting turbulence
- Small scale waves can be generated in compressible turbulence by gyroresonance instability. Feedback of CRs on turbulence need to be included in future simulations.

References

Abdo, A.A., Ackermann, M., Ajello, M., et al.: Astrophys. J. **718**, 348 (2010)
Ackermann, M., et al.: Astrophys. J. **750**, 3 (2012)
Aharonian, F., Akhperjanian, A.G., Bazer-Bachi, A.R., et al.: Astron. Astrophys. **481**, 401 (2008)
Allan, H.R.: Astrophys. Lett. **12**, 237 (1972)
Armstrong, J.W., Rickett, B.J., Spangler, S.R.: Astrophys. J. **443**, 209 (1995)
Bamba, A., Yamazaki, R., Yoshida, T., Terasawa, T., Koyama, K.: Astrophys. J. **621**, 793 (2005)
Bell, A.R.: Mon. Not. R. Astron. Soc. **353**, 550 (2004)
Beresnyak, A., Jones, T.W., Lazarian, A.: Astrophys. J. **707**, 1541 (2009)
Beresnyak, A., Yan, H., Lazarian, A.: Astrophys. J. **728**, 60 (2011)
Braginskii, S.I.: Rev. Plasma Phys. **1**, 205 (1965)
Brunetti, G., Lazarian, A.: Mon. Not. R. Astron. Soc. **378**, 245 (2007)
Cassano, R., Brunetti, G.: Mon. Not. R. Astron. Soc. **357**, 1313 (2005)
Cesarsky, C.J.: Ann. Rev. Astron. Astrophys. **18**, 289 (1980)
Chandran, B.D.G.: Phys. Rev. Lett. **85**, 4656 (2000)
Chandran, B.D.G.: Phys. Rev. Lett. **95**, 265004 (2005)
Cho, J., Lazarian, A.: Phys. Rev. Lett. **88**, 245001 (2002)
Cho, J., Vishniac, E.T.: Astrophys. J. **539**, 273 (2000)
Cho, J., Lazarian, A., Vishniac, E.T.: Astrophys. J. **566**, L49 (2002)
Diamond, P.H., Malkov, M.A.: Astrophys. J. **654**, 252 (2007)
Duffy, P., Kirk, J.G., Gallant, Y.A., Dendy, R.O.: Astron. Astrophys. **302**, L21 (1995)
Dupree, T.H.: Phys. Fluids **9**, 1773 (1966)
Earl, J.A.: Astrophys. J. **193**, 231 (1974)
Eyink, G.L., Lazarian, A., Vishniac, E.T.: Astrophys. J. **743**, 51 (2011)
Farmer, A.J., Goldreich, P.: Astrophys. J. **604**, 671 (2004)
Felice, G.M., and Kulsrud, R.M.: Astrophys. J. **553**, 198 (2001)
Forman, M.A., Jokipii, J.R., Owens, A.J.: Astrophys. J. **192**, 535 (1974)
Gabici, S., Aharonian, F.A., Casanova, S.: Mon. Not. R. Astron. Soc. **396**, 1629 (2009)

Gazol, A., Kim, J., Vázquez-Semadeni, E., Luis, L.: In: Haverkorn, M., Goss, W.M. (eds.) SINS - Small Ionized and Neutral Structures in the Diffuse Interstellar Medium. Astronomical Society of the Pacific Conference Series, vol. 365, p. 154. Astronomical Society of the Pacific, San Francisco (2007)
Getmantsev, G.G.: Sov. Astron. **6**, 477 (1963)
Giacalone, J., Jokipii, J.R.: Astrophys. J. **520**, 204 (1999)
Giacalone, J., Jokipii, J.R.: Astrophys. J. **663**, L41 (2007)
Goldreich, P., Sridhar, S.: Astrophys. J. **438**, 763 (1995)
Goldstein, M.L.: Astrophys. J. **204**, 900 (1976)
Hoang, T., Lazarian, A., Schlickeiser, R.: Astrophys. J. **747**, 54 (2012)
Horbury, T.S., Forman, M.A., Oughton, S.: Plasma Phys. Control. Fusion **47**, B703 (2005)
Inoue, T., Yamazaki, R., Inutsuka, S.-i.: Astrophys. J. **695**, 825 (2009)
Jokipii, J.R.: Astrophys. J. **146**, 480 (1966)
Jokipii, J.R., Parker, E.N.: Astrophys. J. **155**, 777 (1969)
Jones, F.C., Birmingham, T.J., Kaiser, T.B.: Astrophys. J. **180**, L139 (1973)
Jones, F.C., Birmingham, T.J., Kaiser, T.B.: Phys. Fluids **21**, 347 (1978)
Kirk, J.G., Duffy, P., Gallant, Y.A.: Astron. Astrophys. **314**, 1010 (1996)
Kóta, J., Jokipii, J.R.: Astrophys. J. **531**, 1067 (2000)
Kulsrud, R.M.: Plasma Physics for Astrophysics. Kulsrud, R.M. (ed.) Princeton University Press, Princeton (2005)
Kulsrud, R., Pearce, W.P.: Astrophys. J. **156**, 445 (1969)
Landau, L.D., Lifshitz, E.M.: The Classical Theory of Fields. Elsevier, Amsterdam (1975)
Lazarian, A.: Astrophys. J. **645**, L25 (2006)
Lazarian, A., Beresnyak, A.: Mon. Not. R. Astron. Soc.: **373**, 1195 (2006)
Lazarian, A., Vishniac, E.T.: Astrophys. J. **517**, 700 (1999)
Lazarian, A., Yan, H.: Astrophys. J. **784**, 38 (2014)
Lazarian, A., Cho, J., Yan, H.: Recent Res. Dev. Astrophys. Res. Signpost **1**, 297 (2003)
Lazarian, A., Vishniac, E.T., Cho, J.: Astrophys. J. **603**, 180 (2004)
Lazarian, A., Beresnyak, A., Yan, H., Opher, M., Liu, Y.: Space Sci. Rev. **143**, 387 (2009)
le Roux, J.A., Webb, G.M.: Astrophys. J. **667**, 930 (2007)
Lerche, I.: Astrophys. J. **147**, 689 (1967)
Lingenfelter, R.E., Ramaty, R., Fisk, L.A.: Astrophys. Lett. **8**, 93 (1971)
Lithwick, Y., Goldreich, P.: Astrophys. J. **562**, 279 (2001)
Longair, M.S.: High Energy Astrophysics, vol. 2: Stars, the Galaxy and the Interstellar Medium. Cambridge University Press, Cambridge (1994) [1997]
Mace, R.L., Matthaeus, W.H., Bieber, J.W.: Astrophys. J. **538**, 192 (2000)
Maclennan, C.G., Lanzerotti, L.J., Hawkins, S.E.: In: International Cosmic Ray Conference, vol. 8, p. 3265 (2001)
Maron, J., Goldreich, P.: Astrophys. J. **554**, 1175 (2001)
Matthaeus, W.H., Qin, G., Bieber, J.W., Zank, G.P.: Astrophys. J. **590**, L53 (2003)
McKee, C.F., Ostriker, E.C.: Ann. Rev. Astron. Astrophys. **45**, 565 (2007)
Melrose, D.B.: Solar Phys. **37**, 353 (1974)
Narayan, R., Medvedev, M.V.: Astrophys. J. **562**, L129 (2001)
Ohira, Y., Murase, K., Yamazaki, R.: Astron. Astrophys. **513**, A17 (2010)
Ostrowski, M., Schlickeiser, R.: Solar Phys. **167**, 381 (1996)
Owens, A.J.: Astrophys. J. **191**, 235 (1974)
Palmer, I.D.: Rev. Geophys. Space Phys. **20**, 335 (1982)
Perri, S., Zimbardo, G.: Adv. Space Res. **44**, 465 (2009)
Petrosian, V., Yan, H., Lazarian, A.: Astrophys. J. **644**, 603 (2006)
Pohl, M., Yan, H., Lazarian, A.: Astrophys. J. **626**, L101 (2005)
Ptuskin, V.S., Zirakashvili, V.N.: Astron. Astrophys. **429**, 755 (2005)
Qin, G.: Astrophys. J. **656**, 217 (2007)
Qin, G., Matthaeus, W.H., Bieber, J.W.: Astrophys. J. **578**, L117 (2002)
Rechester, A.B., Rosenbluth, M.N.: Phys. Rev. Lett. **40**, 38 (1978)

Santos-Lima, R., de Gouveia Dal Pino, E.M., Kowal, G., Falceta-Gonçalves, D., Lazarian, A., Nakwacki, M.S.: Mon. Not. R. Astron. Soc. **429**, 3371 (2013)
Schekochihin, A.A., Cowley, S.C.: Phys. Plasmas **13**, 056501 (2006)
Schlickeiser, R.: In: Schlickeiser, R. (ed.) Cosmic Ray Astrophysics. Springer, Berlin (2002)
Schlickeiser, R., Miller, J.A.: Astrophys. J. **492**, 352 (1998)
Shalchi, A.: Phys. Plasmas **12**, 052905 (2005)
Voelk, H.J.: Rev. Geophys. Space Phys. **13**, 547 (1975)
Völk, H.J.: Astrophys. Space Sci. **25**, 471 (1973)
Wentzel, D.G.: Ann. Rev. Astron. Astrophys. **12**, 71 (1974)
Wolfire, M.G., McKee, C.F., Hollenbach, D., Tielens, A.G.G.M.: Astrophys. J. **587**, 278 (2003)
Xu, S., Yan, H.: Astrophys. J. **779**, 140 (2013)
Yan, H., Lazarian, A.: Phys. Rev. Lett. **89**, B1102+ (2002)
Yan, H., Lazarian, A.: Astrophys. J. **592**, L33 (2003)
Yan, H., Lazarian, A.: Astrophys. J. **614**, 757 (2004)
Yan, H., Lazarian, A.: Astrophys. J. **673**, 942 (2008)
Yan, H., Lazarian, A.: Astrophys. J. **731**, 35 (2011)
Yan, H., Lazarian, A.: In: Pogorelov, N.V., Font, J.A., Audit, E., Zank, G.P. (eds.) Numerical Modeling of Space Plasma Slows (ASTRONUM 2011). Astronomical Society of the Pacific Conference Series, vol. 459, p. 40 San Francisco: Astronomical Society of the Pacific (2012)
Yan, H., Lazarian, A., Draine, B.T.: Astrophys. J. **616**, 895 (2004)
Yan, H., Lazarian, A., Petrosian, V.: Astrophys. J. **684**, 1461 (2008)
Yan, H., Lazarian, A., Schlickeiser, R.: Astrophys. J. **745**, 140 (2012)

Part IV
Diffusion, Reconnection and Acceleration in Astrophysical Plasmas

Chapter 11
Ambipolar Diffusion

Ellen G. Zweibel

Abstract When magnetic forces are present in a partially ionized medium, the plasma drifts with respect to the neutrals. This plasma—neutral drift, which is known as ambipolar diffusion, occurs in all partially ionized astrophysical systems, including portions of the interstellar medium, protostellar accretion disks, and the chromosphere of the Sun and other cool stars. Ambipolar drift redistributes magnetic flux, which can trigger star formation. It affects short wavelength interstellar turbulence, the structure of interstellar shocks, flow driven instabilities, and the nature of magnetic reconnection. Energy dissipated by ion-neutral friction can be an important source of heat. This chapter reviews ambipolar drift as a process and discusses some of the implications.

11.1 Introduction

Ambipolar diffusion is a key process in several of the great problems in plasma astrophysics: how magnetic fields are transported, how magnetic fields influence the stability of their host medium, and how magnetic fields affect the transformation of ordered energy to heat.

The term "ambipolar diffusion" was introduced to astrophysics by Mestel and Spitzer (1956). It is present in virtually all partially ionized gases with embedded magnetic fields, because the Lorentz force acts directly only on the charged component, not the neutral component. In the absence of any frictional coupling, these two components would therefore follow different dynamics. But friction is always present, and tends to establish a steady state in which the plasma drifts relative to the neutrals at a rate such that electromagnetic force on the plasma balances collisional drag by the neutrals. Thus, ambipolar diffusion is a momentum redistribution mechanism that allows magnetic forces to act on neutral particles. Inevitably, the residual drift transports magnetic field relative to the neutrals (even

E.G. Zweibel (✉)
Department of Astronomy, University of Wisconsin-Madison, Madison, WI, USA

Department of Physics, University of Wisconsin-Madison, Madison, WI, USA
e-mail: zweibel@astro.wisc.edu

A. Lazarian et al. (eds.), *Magnetic Fields in Diffuse Media*, Astrophysics and Space Science Library 407, DOI 10.1007/978-3-662-44625-6_11

when the field is frozen to the plasma). And, being a frictional process, the drift also heats the ambient gas.

In Mestel and Spitzer (1956), ambipolar diffusion was applied to the problem of star formation: a self gravitating cloud threaded by a magnetic field will not collapse if its mass to magnetic flux ratio is less than a critical value of order $(\pi\sqrt{6G})^{-1/2}$. Ambipolar drift allows neutral material to slip inward, leaving the plasma and magnetic field behind. Once the mass to flux ratio exceeds the critical value, collapse ensues and star formation can proceed.

Ambipolar diffusion, or ambipolar drift, applies to a wide range of other problems. At about the same time as Mestel and Spitzer (1956), it was shown that ambipolar drift is an important dissipation mechanism for hydromagnetic waves and turbulence (Piddington 1956). Later, it was shown that it can play a major role in determining the structure of interstellar shocks, that it can affect the rate and onset of magnetic reconnection, and magnetic instabilities, and that it is an even more effective magnetic flux transport mechanism in the presence of turbulence. At the same time, the original application to star formation has receded somewhat as evidence has accumulated that the early picture in which isolated clouds evolve from magnetically subcritical to magnetically supercritical under quiescent conditions is probably too simple (for example see Nakano 1998; Crutcher 1999; Mac Low and Klessen 2004; McKee and Ostriker 2007; Klessen et al. 2011; or Crutcher 2012).

More recently, ambipolar drift has been taken beyond single fluid magneto-hydrodynamics (MHD) and into the Hall regime, where electrons and ions—or, more broadly, positive and negative charge carriers—do not behave as a single fluid, but follow different dynamics. Hall effects are important in protostellar and protoplanetary disks and in dense molecular clouds where dust grains contribute to the charge balance. Ion-neutral coupling makes the Hall effect relevant at much larger scales than in an electron-ion plasma, and the Hall effect, in turn, modifies important dynamical processes such as magnetic reconnection and the magnetorotational instability. Hall dynamics is thought to be especially important in protostellar and protoplanetary accretion disks, and in the last stages of cloud collapse during star formation.

Ambipolar drift occurs in many settings: weakly ionized interstellar gas, weakly ionized accretion disks, the solar chromosphere and similar stellar envelopes, planetary ionospheres, comets, and neutron stars. Ion-neutral coupling is also studied in the laboratory.[1] This chapter will focus primarily on diffuse media and on interstellar applications, including star and planet formation, but the basic material may be of interest to researchers in other fields.

The organization of the chapter is as follows: Sect. 11.2 discusses basic formulations of ambipolar drift and its properties, Sect. 11.3 discusses interactions between ambipolar drift, waves, and turbulence, Sect. 11.4 reviews the role of ambipolar drift

[1] In laboratory plasma physics, the term "ambipolar diffusion" typically refers not to plasma-neutral drift, but to diffusion of electrons and ions at the geometric mean of their single species diffusion rates due to electrostatic coupling.

in MHD shocks and thermal fronts, Sect. 11.5 treats the effects of ambipolar drift on flow driven instabilities, Sect. 11.6 discusses the role of ambipolar drift in magnetic reconnection, and Sect. 11.7 is a summary. Due to the large number of papers in this field it is impossible to give a comprehensive reference list, but at least a few citations are provided for each topic as an introduction to the literature.

11.2 Basics

11.2.1 Fluid Dynamical Approach

Consider a partially ionized gas with plasma mass density ρ_p, flow velocity $\mathbf{u}_p$, pressure P_p, and corresponding neutral quantities ρ_n, $\mathbf{u}_n$, P_n, with an embedded magnetic field $\mathbf{B}$ and plasma current density $\mathbf{J}$ in a gravitational field $\mathbf{g}$. For simplicity we assume only one ion species and one neutral species are present. The continuity and momentum equations for the plasma and neutrals[2] are

$$\frac{\partial \rho_p}{\partial t} = -\nabla \cdot \rho_p \mathbf{u}_p - R_{rec}\rho_p^2 + R_i \rho_n, \tag{11.1}$$

$$\frac{\partial \rho_n}{\partial t} = -\nabla \cdot \rho_n \mathbf{u}_n + R_{rec}\rho_p^2 - R_i \rho_n, \tag{11.2}$$

$$\rho_p \left(\frac{\partial}{\partial t}\mathbf{u}_p + \mathbf{u}_p \cdot \nabla \mathbf{u}_p \right) = -\nabla P_p + \frac{\mathbf{J} \times \mathbf{B}}{c} + \rho_p \mathbf{g} - \rho_p \rho_n \gamma_{pn} \left(\mathbf{u}_p - \mathbf{u}_n \right), \tag{11.3}$$

$$\rho_n \left(\frac{\partial}{\partial t}\mathbf{u}_n + \mathbf{u}_n \cdot \nabla \mathbf{u}_n \right) = -\nabla P_n - \rho_n \mathbf{g} + \rho_p \rho_n \gamma_{pn} \left(\mathbf{u}_n - \mathbf{u}_p \right), \tag{11.4}$$

where $R_{rec}\rho_p^2$ represents two body recombination, R_{ion} represents ionization, and $\gamma_{pn} \equiv \langle \sigma v \rangle_{in}/(m_i + m_n)$ is the collision rate coefficient. We assume here that the most important collisions are between ions and neutrals, with electrons contributing relatively little to momentum balance. In cases where several types of collision are important, possibly involving different ion and neutral species, $\langle \sigma v \rangle$ and γ_{pn} should be computed by combining all relevant processes. In cases where the drift velocity $\mathbf{u}_D \equiv \mathbf{u}_p - \mathbf{u}_n$ exceeds about 19 km s^{-1}, u_D replaces v in the rate coefficient.

In the numerical examples given here we use

$$\langle \sigma v \rangle_{in} = 1.9 \times 10^{-9} \mathrm{cm}^3 \mathrm{s}^{-1}, \tag{11.5}$$

[2] In most treatments of ambipolar drift, "ion" is used in place of "plasma". This is accurate in the sense that the electrons contribute little to momentum exchange. In this paper, we use "plasma" when the electrons and ions can be treated as a single fluid, as distinguished from situations in which the Hall effect is important and the charged species must be treated as multiple fluids.

for cool to cold interstellar gas where the ions are metals or metallic molecules (Draine et al. 1983). Expressions for the solar chromosphere, where the gas is warmer and protons can be the dominant ion species, are given in De Pontieu et al. (2001).

Adding Eqs. (11.1) and (11.2) yields a continuity equation for the combined fluids

$$\frac{\partial \rho}{\partial t} = -\nabla \cdot \rho \mathbf{u}, \tag{11.6}$$

where $\rho \equiv \rho_p + \rho_n$ is the mass density and $\mathbf{u} \equiv (\rho_p \mathbf{u}_p + \rho_n \mathbf{u}_n)/\rho$ is the velocity of the center of mass.

Adding Eqs. (11.3) and (11.4) shows that the collision term conserves the total momentum of the system, but taking the scalar products of Eqs. (11.3) and (11.4) with $\mathbf{u}_p$, and $\mathbf{u}_n$ respectively and adding the result shows that the collision term converts kinetic energy to heat at the rate

$$H_{pn} = \rho_p \rho_n \gamma_{pn} \left(\mathbf{u}_p - \mathbf{u}_n\right)^2. \tag{11.7}$$

11.2.1.1 The One Fluid Approximation

On large lengthscales and long timescales, the plasma and neutrals are well coupled dynamically and thermally, and close to ionization equilibrium. If the medium is also weakly ionized, so that the inertia of the plasma is negligible, it is possible to treat the medium as a single fluid.

With the assumption that plasma inertia can be neglected, Eq. (11.3) reduces to

$$\mathbf{u}_D = \frac{\mathbf{J} \times \mathbf{B}}{\rho_p \rho_n \gamma_{pn} c} = \frac{(\nabla \times \mathbf{B}) \times \mathbf{B}}{4\pi \rho_p \rho_n \gamma_{pn}}, \tag{11.8}$$

where in the last step we have used Ampere's Law. Equation (11.8) shows that the drift velocity is just the rate of acceleration by the Lorentz force, multiplied by the ion-neutral collision time. An example is sketched in Fig. 11.1.

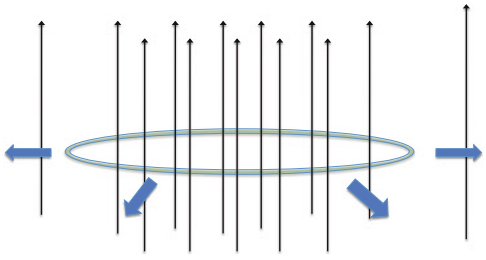

Fig. 11.1 Sketch of ambipolar drift. The magnetic field inside the contour is stronger than the field outside, so the drift is outward, down the magnetic pressure gradient

Evaluating $\mathbf{u}_D$ requires both ρ_n and ρ_p. Since $\rho_p/\rho_n \ll 1$, $\rho_n \approx \rho$ and $\mathbf{u} \approx \mathbf{u}_n$. Therefore we derive ρ_n from Eq. (11.6). But for ρ_i, we have to make another assumption, such as that the medium is close to ionization equilibrium. This holds if the ionization and recombination terms in Eqs. (11.1) and (11.2) are much larger than the dynamical terms.

Adding Eqs. (11.3) and (11.4) gives the momentum equation for the total fluid

$$\rho\left(\frac{\partial}{\partial t}\mathbf{u} + \mathbf{u}\cdot\nabla\mathbf{u}\right) = -\nabla P + \frac{\mathbf{J}\times\mathbf{B}}{c} + \rho\mathbf{g}. \tag{11.9}$$

Equation (11.9) is just the momentum equation for a conducting fluid of density ρ.

In order to see what Eq. (11.8) implies for magnetic flux transport, we write down the magnetic induction equation, omitting resistivity

$$\frac{\partial}{\partial t}\mathbf{B} = \nabla\times\left(\mathbf{u}_p\times\mathbf{B}\right) \tag{11.10}$$

and express $\mathbf{u}_p$ as $\mathbf{u}_D + \mathbf{u}_n \approx \mathbf{u}_D + \mathbf{u}$. We then rewrite Eq. (11.10) as

$$\frac{\partial}{\partial t}\mathbf{B} = \nabla\times(\mathbf{u}\times\mathbf{B}) + \nabla\times(\mathbf{u}_D\times\mathbf{B})\,. \tag{11.11}$$

Equations (11.8), (11.9), and (11.11) together are sometimes called the "strong coupling approximation" (Shu 1983). The plasma and neutrals follow almost the same dynamics, but the field is not perfectly frozen to the medium because of ambipolar drift. This can be quantified by revisiting one of the standard proofs of the frozen flux theorem (Spitzer 1962). We consider an element of surface S with boundary C and normal $\hat{\mathbf{n}}$. The magnetic flux $\Phi(t)$ threading S at time t is

$$\Phi(t) \equiv \int \mathbf{B}\cdot\hat{\mathbf{n}}\,dS. \tag{11.12}$$

If S moves with the bulk fluid (not the plasma), then differentiating Eq. (11.12) with respect to time, using Eq. (11.11), and accounting for the motion of S, leads to

$$\frac{\partial}{\partial t}\Phi = \int_C \mathbf{B}\cdot(\mathbf{u}_D\times\mathbf{dl})\,. \tag{11.13}$$

Equation (11.13) shows that magnetic flux is transported across C at a rate proportional to the component of $\mathbf{u}_D$ normal to C, while if $\mathbf{u}_D \equiv 0$, Φ is constant in time. It's important to emphasize, however, that although the fieldlines are not frozen to the bulk fluid, they are frozen to the plasma. Breaking and reconnecting the fieldlines requires additional physical effects, such as Ohmic resistivity or an anisotropic electron pressure tensor. We pursue this point in Sects. 11.2.2 and 11.6. As an example of ambipolar drift, let us use Eq. (11.8) to estimate the ambipolar drift time τ_{AD} for a magnetically supported, self gravitating cloud. Setting $\mathbf{J}\times\mathbf{B}/c =$

$\rho_n \mathbf{g} \sim GM\rho/R^2 \sim 4\pi G\rho^2/3$, where R is the mean radius, using the definition of γ_{pn}, assuming the ion mass m_i much exceeds the neutral mass m_n, as is typical in molecular clouds, and defining the ionization fraction $x_i \equiv n_i/n_n$, we find

$$u_D \sim \frac{4\pi G m_n R}{3 x_i \langle \sigma v \rangle}. \tag{11.14}$$

The corresponding ambipolar diffusion timescale τ_{AD} is

$$\tau_{AD} \sim \frac{R}{u_D} \sim \frac{3 x_i \langle \sigma v \rangle}{4\pi G m_n}. \tag{11.15}$$

Thus, magnetic flux is removed from a magnetically supported cloud on a timescale that depends only on physical constants and on the ionization state of the cloud. We can estimate this timescale; taking $\langle \sigma v \rangle$ from Eq. (11.5), setting $m_n = 3.9 \times 10^{-24}$ g (appropriate for a gas in which H is molecular and 10 % of the atoms are He) we find $\tau_{AD} \sim 5.5\, 10^{13} x_i$ year. In dense molecular cores, $x_i \sim 10^{-7}$, suggesting that the cores lose significant magnetic support over several Myr. More refined calculations give similar estimates (Nakano 1984; Fiedler and Mouschovias 1992, 1993; McKee et al. 1993 and references therein).

11.2.1.2 The Ambipolar Reynolds Number

It is useful to have an order of magnitude estimate for the importance of ambipolar drift relative to advection of the magnetic field with the bulk flow. If we introduce a magnetic lengthscale L such that $|\nabla \times \mathbf{B}| \sim B/L$, then to order of magnitude

$$u_D \sim \frac{v_A^2 \tau_{ni}}{L}, \tag{11.16}$$

where $v_A \equiv B/\sqrt{4\pi\rho}$ is the Alfvén speed in the bulk medium and $\tau_{ni} \equiv (\rho_p \gamma_{pn})^{-1}$ is the neutral-ion collision time. The quantity $v_A^2 \tau_{ni}$ has the dimensions of diffusivity; we call it λ_{AD}.

$$\lambda_{AD} \equiv \frac{v_A^2}{\rho_p \gamma_{pn}}. \tag{11.17}$$

The drift speed u_D defined in Eq. (11.8) can then be interpreted as a diffusive flux. Replacing gradients by L^{-1} in Eq. (11.11), we see that the characteristic ambipolar diffusion time $\tau_{AD} \sim L^2/\lambda_{AD}$, while the characteristic advection time $\tau_{ADV} \sim L/u$. By analogy with resistive MHD, we define the ambipolar Reynolds number R_{AD} (Zweibel and Brandenburg 1997)

$$R_{AD} \equiv \frac{\tau_{AD}}{\tau_{ADV}} = \frac{Lu}{\lambda_{AD}}. \tag{11.18}$$

We expect that if $R_{AD} \gg 1$ the field is effectively frozen to the bulk fluid, while if $R_{AD} \ll 1$, the field is decoupled from the flow. The strong coupling approximation requires $R_{AD} \gg 1$; if $R_{AD} < 1$, a multiple fluid theory is required. In Li et al. (2008), R_{AD} is shown to be a useful parameter for classifying regimes of partially ionized turbulence.

11.2.1.3 Multiple Fluid Approach

The one fluid approximation described in Sect. 11.2.1.1 is suited to large scale, low frequency phenomena for which $R_{AD} \gg 1$, $\rho_p/\rho_n \ll 1$, and the medium is close to ionization equilibrium. There is a single continuity equation (Eq. (11.6)) and a momentum equation for the center of mass (Eq. (11.9)). All the dynamical effects of ambipolar drift are subsumed into the induction equation (Eq. (11.11)). The thermal effects appear through the heating term (Eq. (11.7)), evaluated from Eq. (11.8).

For small scale, high frequency phenomena with $R_{AD} \leq 1$ it is necessary to resort to multiple fluid theory, the simplest being two fluid (plasma and neutrals). Examples of phenomena that require multiple fluid theory are high frequency waves (Sect. 11.3.1), small scale turbulence and turbulent dynamos (Sect. 11.3), shocks (Sect. 11.4), and magnetic reconnection (Sect. 11.6). It is also necessary to take a multifluid approach to track the abundances of individual species (Ciolek and Mouschovias 1994), in problems where the ionization balance is important (Ciolek and Mouschovias 1998), or where one wishes to study chemical reaction rates. A very general set of equations for multiple fluids, allowing for chemical reactions, is given in Draine (1986). Note that in some cases, dust grains are an important charged species.

Whether the plasma can be treated as a single fluid or whether electrons and ions follow their own dynamics is a separate issue, and is discussed in Sects. 11.2.2 and 11.3.1.2.

11.2.1.4 Numerical Implementation of Ambipolar Drift

Ambipolar drift has been studied in the one fluid approximation by many authors. An elegant 1D Lagrangian implementation was given in Shu (1983), while Mac Low et al. (1994) were the first to incorporate it into a general purpose MHD code. A one fluid treatment in an adaptive mesh refinement (AMR) code is presented in Duffin and Pudritz (2008).

Ambipolar drift can also be captured by solving coupled equations for multiple fluids, such as Eqs. (11.1)–(11.4) supplemented by energy equations, or the more general equations given in Draine (1986). This approach is more fundamental, but there is a practical difficulty: for $\rho_p/\rho_n \ll 1$, the characteristic MHD speed v_{Ap} for the plasma component is much larger than any other speed in the problem (for example, in a weakly ionized molecular cloud, v_{Ap} can be hundreds of km/s while bulk flow velocities are only a few km/s). This means that accurately resolving both independent plasma and neutral flows can be very expensive. Ionization and

recombination times can also be short, and add a another source of stiffness to the problem.

The problem of disparate timescales has been dealt with in three ways. One is to simply assume that ρ_p/ρ_n is not too small. Ratios as low as 10^{-2} have been treated in many studies. This regime includes the solar chromosphere, but not interstellar molecular or cold atomic gas.

A second approach, the so-called heavy ion approximation, was introduced by Li et al. (2006). In the heavy ion approximation, the mass density of the plasma is artificially increased while the plasma-neutral collision rates are decreased so as to keep their product constant. This means that important scales, such as the plasma-neutral decoupling scale, can be given the values they would have in a medium with much lower ρ_p/ρ_n. The heavy ion approximation is suitable for problems in which the plasma-neutral coupling is quite strong, such as studies of large scale turbulence in dense molecular clouds. It is expected to be less successful for weakly coupled problems in which the plasma and neutrals follow their own dynamics. For example, in molecular clouds, the ratio of plasma pressure to magnetic pressure is much smaller than assumed in the heavy ion approximation. Therefore, waves and turbulence below the plasma-neutral decoupling scale would not be modeled accurately in the heavy ion approximation.

A third approach is to develop numerical methods to extend the range of ρ_p/ρ_n that can be treated with the full two-fluid equations. Ionization fractions as low as 10^{-6} by mass have been achieved in Tilley and Balsara (2008) for isothermal equations of state and Tilley et al. (2012) with a full energy equation. With the growth of computing power, such treatments are becoming more accessible.

11.2.2 Tensor Conductivity Approach

An alternative approach to magnetic phenomena in weakly ionized gases is based on the tensor conductivity formalism, and was pioneered by Cowling in Cowling (1956) and significantly extended in Wardle and Ng (1999) to describe ambipolar drift in media which are so weakly ionized that collisions between charged particles can be neglected and the plasma inertia is completely negligible. This approach is especially useful in situations where there are multiple charge carriers, such as electrons, ions, and charged dust grains, and where the Hall effect can be important.

In the tensor conductivity approach, Faraday's Law is written

$$\frac{\partial}{\partial t}\mathbf{B} = -c\boldsymbol{\nabla}\times\mathbf{E} = \boldsymbol{\nabla}\times(\mathbf{u}\times\mathbf{B}) - c\boldsymbol{\nabla}\times\mathbf{E}', \tag{11.19}$$

where $\mathbf{E}'$ is the electric field in the frame of the bulk fluid, which moves at velocity $\mathbf{u}$. The electric current density

$$\mathbf{J} \equiv \sum_j Z_j e \mathbf{u}_j, \tag{11.20}$$

where the summation is over charged species j, is related to $\mathbf{E}'$ through a conductivity tensor $\boldsymbol{\sigma}$ by $\mathbf{J} = \boldsymbol{\sigma} \cdot \mathbf{E}'$. Since $\mathbf{J} = c\nabla \times \mathbf{B}/(4\pi)$, Eq. (11.19) is an equation for $\mathbf{B}$ and $\mathbf{u}$ alone.

In computing $\mathbf{J}$, it is assumed that the plasma is cold, and that inertial effects are negligible compared to collisional effects, so that the momentum equation for each charged species j is given in the $'$ frame by

$$Z_j e \left(\mathbf{E}' + \frac{\mathbf{u}_j}{c} \times \mathbf{B} \right) - m_j \gamma_{jn} \rho \mathbf{u}_j . \tag{11.21}$$

Equation (11.21) can be solved for the $\mathbf{u}_j$ in terms of $\mathbf{E}'$, the results substituted into Eq. (11.20), and the results for $\boldsymbol{\sigma}$ read off. It is convenient to adopt a coordinate system with unit vectors $\hat{\mathbf{e}}_1 = \hat{\mathbf{B}} \times \hat{\mathbf{E}}$, $\hat{\mathbf{e}}_2 = \hat{\mathbf{E}}$, $\hat{\mathbf{e}}_3 = \hat{\mathbf{B}} \equiv \hat{\mathbf{e}}_\parallel$. Then the components of $\boldsymbol{\sigma}$ are

$$\sigma_1 = \frac{ec}{B} \sum_j \frac{Z_j n_j}{1 + \beta_j^2}, \tag{11.22}$$

$$\sigma_2 = \frac{ec}{B} \sum_j \frac{Z_j n_j \beta_j}{1 + \beta_j^2} \tag{11.23}$$

$$\sigma_\parallel = \frac{ec}{B} \sum_j Z_j n_j \beta_j \tag{11.24}$$

where $\beta_j \equiv Z_j eB/(m_j \rho \gamma_{jn} c)$ is the so-called Hall parameter for particles of type j. When $\beta_j \gg 1$, the particles are nearly frozen to the fluid (the MHD approximation). In this regime, Hall effects are negligible and it can be shown that $c^2/(4\pi\sigma_2)$ is equivalent to λ_{AD}, the ambipolar diffusivity introduced below Eq. (11.16). The quantity σ_2 is also called the Pedersen or Cowling conductivity. For $\beta_j \sim 1$, particles no longer follow the fieldlines and the Hall effect comes into play. In fully ionized plasmas, the ions detach on scales comparable to their gyroradius or to the ion skin depth (the gyroradius of an ion moving at the Alfvén speed), whichever is larger. The electrons stay magnetized down to much shorter scales. When collisions with neutrals are sufficiently strong, the effective inertia of the ions is increased by $\sqrt{\rho/\rho_i}$, so the scale on which they detach from the fieldlines (in the cold plasma regime) is larger by the same factor.

11.3 Waves and Turbulence

11.3.1 Waves

Moving beyond the basics, we begin with waves because one can develop some intuition about ion-neutral drift by studying how it affects waves.

Ambipolar drift is an important damping mechanism for waves. The rate at which waves are damped in molecular clouds has been used to set limits on their lifetimes and on the wavelengths that can be present (Arons and Max 1975; Zweibel and Josafatsson 1983; Myers and Khersonsky 1995; Williams et al. 1998). Ion-neutral friction is the main damping mechanism for the fluctuations that scatter cosmic rays in the primarily neutral phases of the interstellar medium (Kulsrud and Pearce 1969), and for hydromagnetic waves in stellar chromospheres (De Pontieu et al. 2001).

Wave damping can be calculated from either the fluid dynamical approach (Sect. 11.2.1) or the tensor conductivity approach (Sect. 11.2.2); we use the former because it is easily implemented for both strong and weak plasma-neutral coupling.

11.3.1.1 MHD Waves

For simplicity, we consider small amplitude shear Alfvén waves with wavenumber $k_\parallel$ parallel to the unperturbed magnetic field $\mathbf{B}$ (for a more general discussion of hydromagnetic waves including compressibility effects and nonparallel propagation, see Ferrière et al. 1988; for the effects of self gravity, ionization, and recombination, see Mouschovias et al. 2011). We linearize Eqs. (11.3), (11.4), and (11.10), keeping inertial terms, and assume the perturbations go as $e^{i(\mathbf{k}\cdot\mathbf{x}-\omega t)}$. This leads to the dispersion relation

$$\omega^2\left[1+\frac{\rho_n\gamma_{pn}}{\rho_p\gamma_{pn}-i\omega}\right]=-k_\parallel^2 v_{Ap}^2, \tag{11.25}$$

where $v_{Ap}\equiv B/\sqrt{4\pi\rho_p}$ is the Alfvén speed in the plasma.

Equation (11.3.1) is easily solved in two limits. If $\omega/(\rho_p\gamma_{pn})\gg 1$, the dispersion relation is approximately

$$\omega\approx k_\parallel v_{Ap}-i\frac{\rho_n\gamma_{pn}}{2}. \tag{11.26}$$

In this high frequency limit, the plasma and neutrals are not well coupled. The wave speed is determined by plasma inertia, and there is collisional damping at half the ion-neutral collision rate. The hydromagnetic waves generated by streaming of GeV cosmic rays, for example, are usually in this regime. If $\omega/(\rho_p\gamma_{pn})\ll 1$, the dispersion relation is approximately,

$$\omega\approx k_\parallel v_A-i\frac{k_\parallel^2\lambda_{AD}}{2}, \tag{11.27}$$

where we have used Eq. (11.17). In deriving Eq. (11.27), we have assumed that $\rho_p/\rho_n\ll 1$. In this low frequency limit, the plasma and neutrals are strongly coupled, the wave speed is determined by the inertia of the bulk medium, and the waves are damped diffusively, with λ_{AD} as the appropriate diffusion constant.

Hydromagnetic disturbances in the interstellar medium and the solar chromosphere can usually be treated in the low frequency approximation.

At intermediate wavelengths

$$k_l \equiv \frac{2\rho_p \gamma_{pn}}{v_A} < k_\parallel < k_u \equiv \frac{\rho_n \gamma_{pn}}{2v_{Ap}} \tag{11.28}$$

the dissipation is strong and the waves do not propagate. Note that if we set $L^{-1} = k_l$ and $u = v_A$ in Eq. (11.18) and use Eq. (11.17), the ambipolar Reynolds number for the critically damped wave is $R_{AD} = 1/2$. Using Eq. (11.5) and typical densities, ionization fractions, and magnetic fieldstrengths, we find that in the dense cores of molecular clouds, the lower cutoff wavelength $2\pi/k_l$ is typically tenths to hundredths of pc, and tens of km in the solar chromosphere. The theory presented here is valid at wavelengths longer than a mean free path. On shorter scales, kinetic theory must be used to calculate the damping.

11.3.1.2 Hall Waves

Up to now, we have not considered separate momentum equations for electrons and ions.[3] The electron momentum equation is

$$\rho_e \left(\frac{\partial}{\partial t}\mathbf{u}_e + \mathbf{u}_e \cdot \nabla \mathbf{u}_e\right) = -\nabla P_e - e n_e \left(\mathbf{E} + \frac{\mathbf{u}_e}{c} \times \mathbf{B}\right) - \rho_e \nu_{en}(\mathbf{u}_e - \mathbf{u}_n) - \rho_e \nu_{ei}(\mathbf{u}_e - \mathbf{u}_i), \tag{11.29}$$

where ν_{en} and ν_{ei} are the electron-neutral and electron-ion collision frequencies, respectively, and we are ignoring gravity. Neglecting electron inertia and writing $\mathbf{u}_e - \mathbf{u}_i = -\mathbf{J}/(en_e)$, $\mathbf{u}_e - \mathbf{u}_n = -\mathbf{J}/(en_e) + \mathbf{u}_D$, we can rewrite Eq. (11.29) as

$$\mathbf{E} + \frac{\mathbf{u}_i}{c} \times \mathbf{B} = \frac{\mathbf{J} \times \mathbf{B}}{en_e c} - \frac{\nabla P_e}{en_e} + \frac{m_e(\nu_{en} + \nu_{ei})}{e^2 n_e}\mathbf{J} - \frac{m_e \nu_{en}}{e}\mathbf{u}_D. \tag{11.30}$$

Equation (11.30) is Ohm's Law. The second term on the left hand side gives flux freezing to the plasma if the other terms are negligible (the plasma center of mass velocity $\mathbf{u}_p \sim \mathbf{u}_i$). The first term on the right hand side is the Hall term; it represents differences between $\mathbf{u}_i$ and $\mathbf{u}_e$. The second term represents the force arising from the electron pressure gradient. If P_e and ρ_e have the same level surfaces, this term is curl free and does not contribute to magnetic induction; if the isobaric and isochoric surfaces differ, the resulting induction is known as Biermann's Battery. The third

[3] We can assume quasineutrality, $n_e \sim Z n_i$, where Z is the ion charge, as long as the lengthscales of interest are much longer than the electron Debye length, $7(T_e/n_e)^{1/2}$ cm; this allows us to solve a single continuity equation.

term represents resistivity due to electron-ion and electron-neutral collisions. We have neglected it in our treatment so far. The fourth term represents additional electron collisional momentum loss to the neutrals.

We now consider the Hall effect for the same problem we treated in Sect. 11.3.1.1: transverse electromagnetic waves propagating parallel to the ambient magnetic field in a weakly ionized medium, with one species of singly charged ions. As in Sect. 11.3.1.1 we linearize Eqs. (11.3) and (11.4) and express the plasma velocity perturbation $\delta \mathbf{u}_p$ in terms of the current perturbation $\delta \mathbf{J}$

$$\delta \mathbf{u}_p = i \frac{\delta \mathbf{J} \times \mathbf{B}}{\omega n_i m_{eff} c}, \tag{11.31}$$

where m_{eff} is the effective ion mass

$$m_{eff} = m_i \left[1 + \frac{\rho_n \gamma_{pn}}{\rho_p \gamma_{pn} - i\omega} \right]. \tag{11.32}$$

If $\omega \gg \rho_n \gamma_{pn}$, $m_{eff} \sim m_i$, while if $\omega \ll \rho_p \gamma_{pn}$, $m_{eff} \sim m_i \rho_n / \rho_p$.

Comparing the first two terms on the right hand side of Eq. (11.30), we see that than the Hall term is larger than the inductive term if

$$\frac{eB}{m_{eff} c} < \omega. \tag{11.33}$$

In fully ionized gases, the Hall effect is important for $\omega > \omega_{ci}$. The same criterion holds for weakly ionized gases if $\omega > \rho_n \gamma_{pn}$. But if $\omega < \rho_i \gamma_{pn}$, the Hall effect is important for $\omega > \omega_{ci}(\rho_p/\rho)$, i.e. the Hall effect becomes important at lower frequencies. This effect can only occur if $\omega_{ci} \rho_p / \rho_n < \omega < \rho_p \gamma_{pn}$, which requires that the ion Hall parameter β_i introduced in Sect. 11.2.2 be less than one.

These results can be recast in terms of lengthscales. The characteristic wavenumber above which the Hall effect is important in a fully ionized plasma is $\omega_{ci} v_{Ap}$; we call this the inverse ion skin depth d_i^{-1}, or inverse ion inertial length (it represents the lengthscale below which the ions have too much inertia to $\mathbf{E} \times \mathbf{B}$ drift). In the limit of strong collisions, $m_{eff}/m_i \sim \rho/\rho_p$, d_i is increased by a factor of $(\rho/\rho_p)^{1/2}$.

11.3.2 Effect of Ambipolar Drift on Turbulence

Ion-neutral drift also affects MHD turbulence. We have in mind the standard picture in which turbulence is driven at a large scale at wavenumber k_{dr} and cascades nonlinearly to smaller scales. Dissipation is assumed to be unimportant at the driving scale and to increase with decreasing scale until at some wavenumber, k_{diss}, the dissipation rate exceeds the nonlinear transfer rate $k\delta v_k$. The range $k_{dr} < k < k_{diss}$ is called the inertial range. The nonlinear transfer rate increases with decreasing

scale, but δv_k decreases with increasing k, so that the turbulent energy density is dominated by the power at large scales.

In a neutral fluid, viscosity is the most important dissipation mechanism. The viscous diffusivity λ_ν is of order $v_n^2 \tau_{nn}$, where v_n^2 is the thermal velocity of the neutrals and τ_{nn} is the neutral–neutral collision time. Using Eq. (11.17), we see that the ratio of viscous to ambipolar diffusivity is

$$\frac{\lambda_\nu}{\lambda_{AD}} \sim \frac{v_n^2}{v_A^2} \frac{n_i}{n_n} \frac{m_i}{m_n + m_i} \frac{\langle \sigma v \rangle_{in}}{\langle \sigma v_{nn}}. \tag{11.34}$$

In the cold atomic and molecular interstellar gas, $v_n/v_A < 1$, $m_i/(m_n + m_i) \sim 1$, and $\langle \sigma v \rangle_{nn}$ is typically a few times 10^{-10} cm^{3}s^{-1}. Using Eq. (11.5), we see that for the low ionization fraction typical of this gas—$n_i/n_n < 10^{-2}$ - $\lambda_\nu/\lambda_{AD} << 1$. Therefore, ion-neutral friction becomes important on scales much longer than the viscous scale. Friction will damp the ion motion on the scale at which the ambipolar Reynolds number $R_{AD} \sim 1$ (Eq. (11.18)) while the cascade in the neutrals is sustained down to smaller scales by inertial forces. This may be an explanation for the trend toward lower turbulent broadening of ion species relative to neutral species in some molecular clouds (Li and Houde 2008; Falceta-Goncalves et al. 2010; Hezareh et al. 2010; Tilley and Balsara 2010; Li et al. 2012a); these authors have combined observations and simulations to estimate the lengthscale at which ion-neutral damping becomes dominant. A theoretical description of such turbulence is given in Lazarian et al. (2004). In the solar chromosphere, $\lambda_{nu}/\lambda_{AD} < 1$ as well, but the ratio is less extreme because of the higher ionization fraction.

Turbulent damping by ion-neutral friction is also a significant source of heating. Heating by ambipolar drift of the *laminar* field was originally estimated in Scalo (1977) and used to bound the magnetic fieldstrengths in molecular clouds. Heating by ambipolar drift of the turbulent field was calculated in numerical simulations by Padoan et al. (2000) in the one fluid (strong coupling) approximation (Sect. 11.2.1.1) and found to be large, but overestimated due to a normalization error. Frictional heating was calculated in the heavy ion approximation (Sect. 11.2.1.4) by Li et al. (2012b). When the results of Padoan et al. (2000) are normalized correctly, the two calculations are in reasonably good agreement.

It might be argued that in a steady state, turbulence is always dissipated by one mechanism or another, so that the heating rate is simply the same as the driving rate. This is true in a global sense, but the spatial and intensity distribution of dissipation rates are of interest too. Ion-neutral friction tends to create thin sheets (Sect. 11.6.2) where much of the heating is concentrated.

11.3.3 Effect of Turbulence on Ambipolar Drift

Turbulent diffusion is frequently invoked in astrophysics. It is a hybrid process which depends on both dynamics and diffusivity: if some property of a system varies

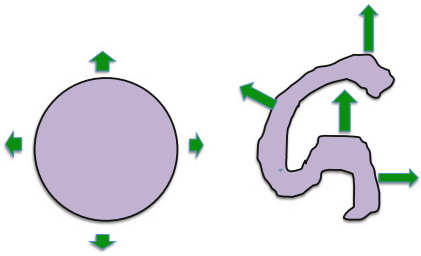

Fig. 11.2 Sketch of turbulent diffusion. Slow diffusion of a quantity with a regular gradient is show on the *left*. Faster diffusion of the same quantity after fluid motions have drawn it into an irregular shape is shown on the *right*

on a large scale, turbulent motions within the system will bring parcels of fluid with different attributes into close proximity, creating small scale gradients. Microscopic diffusion will then act to irreversibly smooth the gradients. While the microscopic diffusivity D_m scales with particle mean free path l_{mfp} and thermal velocity v_{th} ($D_m \sim l_{mfp} v_{th}$), the turbulent diffusivity D_{turb} scales with the turbulent eddy size l_{turb} and turbulent velocity v_{turb} ($D_{turb} \sim l_{turb} v_{turb}$). If this sounds abstract, consider a pile of red, wet socks placed next to a pile of blue, wet socks. Assume the socks were made cheaply, and their color dissolves in water. The interface between the piles will then slowly turn purple. If one waits long enough, and keeps the socks wet, both piles will eventually turn completely purple. But this takes a very long time, for even the cheapest socks. On the other hand, if the socks are not sorted initially into red and blue, but mixed together in a single heap, they will turn purple much more quickly. In this analogy, the red and blue piles of socks are comingled by turbulence, and the new color, purple, is created by microscopic diffusion.[4]

The first investigations of ambipolar diffusion in the presence of turbulence (Zweibel 2002; Fatuzzo and Adams 2002; Kim and Diamond 2002) used the one fluid approximation (Sect. 11.2.1.1) together with some form of averaging to show that a large scale magnetic field can diffuse at close to the eddy rate D_{turb} in the presence of prescribed, small scale turbulent flow. More insight into the mechanism is provided in Heitsch et al. (2004), who prescribed the neutral flow but calculated the plasma flow explicitly, accounting for magnetic forces, friction with the neutrals, and plasma inertia. The resulting drift of plasma and magnetic field relative to the neutrals results in diffusion of the large scale magnetic field relative to the matter at nearly the eddy rate (Fig. 11.2).

All four of the foregoing studies took the magnetic fieldlines to be straight and the fluctuations to lie in a plane perpendicular to the field. This geometry captures (but exaggerates) the anisotropic, quasi-2D nature of turbulence in a strong magnetic field, and has the advantage that magnetic flux transport is easy to measure. Enhancement of the ambipolar drift rate in the presence of fully 3D,

[4]Note, however, that a pile of red and blue socks, observed from a distance, may simply look like a pile of purple socks, and that even after the colors have run together it might be possible to separate individual molecules of red and blue dye and restore the socks to their original states. The true origin of irreversibility in statistical mechanics is a subtle problem, far beyond the scope of this chapter.

highly compressible turbulence was also reported by Li et al. (2012a). They showed that the density weighted mean ion-neutral drift speed (as computed in the heavy ion approximation) increases with increasing ambipolar Reynolds number (Eq. 11.18), qualitatively confirming the predictions of Zweibel (2002) and Kim and Diamond (2002).

11.4 Shocks and Fronts

11.4.1 Shocks

Shocks occur in many astrophysical contexts. They are an important mechanism for compressing fluid, quickly accelerating or decelerating it, transforming bulk kinetic energy to heat, and, under sufficiently collisionless conditions, accelerating a tiny minority of particles to high energies. An excellent review of interstellar shocks is presented in Draine and McKee (1993).

In single fluid, MHD, a compressive disturbance which propagates perpendicular to the magnetic field forms a shock if the propagation speed exceeds the magnetoacoustic speed $v_{ms} \equiv \sqrt{v_A^2 + v_S^2}$, where $v_S \equiv (\partial P/\partial\rho)^{1/2}$ is the adiabatic sound speed.[5] If the shock is stationary in some reference frame, the density, flow speed, magnetic field strength, and temperature downstream can be calculated from upstream quantities by the so-called Rankine–Hugoniot conditions, which are derived by idealizing the shock transition layer as infinitesimally thin and integrating the steady state fluid equations across it. The thickness of the shock is set by the dissipation mechanism; in a collisional, neutral fluid it is approximately the particle mean free path, which is the minimum lengthscale on which bulk kinetic energy can be converted to random motions.

The basic physics of shocks in partially ionized gases was first laid out by Mullan (1971) and Draine (1980). In weakly ionized gas, v_{ms} is typically much larger for the plasma component than for the neutrals. If there were no plasma-neutral friction, there would be a range of speeds over which the neutral fluid would shock but the plasma would not. As we established in Sect. 11.3, in both the interstellar medium and the solar chromosphere, the neutral viscous scale is typically much less than the ion-neutral decoupling scale. This allows a plasma precursor to develop. The precursor is a spatially extended layer in which the plasma properties and magnetic field vary smoothly. The plasma flow remains sub-magnetosonic with respect to the plasma Alfvén and sound speeds. The neutral flow, which far upstream is supersonic, cannot have the same velocity profile as the plasma, so a large plasma-

[5] Disturbances which propagate parallel to the magnetic field are not directly affected by it, and shock formation requires only that the propagation speed exceed v_S. At intermediate angles, "fast", "slow", and possibly intermediate shocks can develop. Since the qualitative effects of ambipolar drift appear in the perpendicular case we restrict ourselves to that.

neutral drift is set up in the neighborhood of the shock. The resulting friction transfers momentum between the species and dissipates flow energy as heat. If the heating does not raise the neutral temperature enough to effect a transition from supersonic to subsonc flow, the neutral profiles are smooth and broad, and the shock is termed C-type. If the neutral gas temperature is increases enough for the flow to become subsonic, the transition in the neutrals can either be mediated by a thin viscous layer—termed a J-type shock, or by ion-neutral heating in a broader layer, a so-called C^* shock.

A new ingredient was added to the problem by Blasi et al. (2012). These authors showed that a population of fast neutrals can be created by charge exchange downstream of the shock. If these neutrals stream back across the shock they deposit energy and momentum upstream, effectively creating a precursor which reduces the Mach number of the shock. The effect of this modified shock structure on cosmic ray acceleration is discussed in Morlino et al. (2012).

Ambipolar diffusion mediated shocks are subject to a corrugational instability that was first explained by Wardle (1990). However, in Falle et al. (2009) it was shown that if ionization equilibrium is sufficiently rapid, the instability is suppressed, because the plasma density is slaved to the neutral density.

The evolution in time of ambipolar diffusion mediated shocks (in one dimension) was recently considered by Chen and Ostriker (2012). They argued that because momentum transfer from ions to neutrals is required to sustain a steady C-type shock, there must be an initial phase, before friction has time to act, when the neutrals are strongly compressed. During this stage, the magnetic field follows the plasma, and ratio of magnetic flux to mass decreases, possibly leading to the formation of magnetically supercritical clouds.

11.4.2 Fronts

Magnetized transition layers between the cool and warm phases in the neutral interstellar medium Field et al. (1969), Draine (2010) display some of the same properties as shocks in partially ionized gas. At the so-called saturation pressure, heating and cooling exactly balance and the layer is static. Below the saturation pressure, cool gas warms and evaporates; above the saturation pressure, warm gas cools and condenses. The natural thickness of these layers is approximately the Field length (Field 1965), the length at which the heat conduction rate balances the radiative cooling rate.

In the interstellar medium, the thermal and viscous diffusivities are about the same; thus, as we saw from Eq. (11.34), the ambipolar diffusivity λ_{AD} is much larger than either. Therefore, the magnetic field is not compressed with the gas across a condensation front, but diffuses back into the warm gas. This is one possible mechanism for producing the flat fieldstrength—density correlation observed in the neutral interstellar medium (Stone and Zweibel 2010).

11.5 Instabilities in a Weakly Ionized Medium

11.5.1 Flow Driven Instabilities

Shear flows occur in many astrophysical situations, and are often unstable. Two important examples are the Kelvin–Helmholtz instability (KHI) and the magnetorotational instability (MRI). The KHI, which can occur with or without magnetic fields, operates at the transition layer between planar layers of fluid in relative motion; for example, it can excite waves when wind blows over the surface of water. It creates a turbulent boundary layer which entrains and mixes the unstable fluid. The MRI, which as the name implies requires a magnetic field, operates in rotating fluids in which the angular rotation rate $\Omega(r)$ decreases outward.

11.5.1.1 Kelvin–Helmholtz Instability

The basic setup for the KHI is a shear flow of the form $\mathbf{u} = \hat{x}U(z)$. The growth rate can be found analytically if $U(z)$ changes discontinuously by an amount ΔU at some location z. The fastest growing modes are 2D, incompressible chains of vortices. The growth rate for modes of wavenumber k is $k\Delta U(\rho_1\rho_2)^{1/2}/(\rho_1 + \rho_2)$, where $\rho_{1,2}$ are the densities on either side of the velocity discontinuity. These results, and many others pertinent to the KHI, are derived in Drazin and Reid (1981).

A magnetic field $\mathbf{B} = \hat{x}B$ parallel to the flow can be either stabilizing or destabilizing. If the flow is subalfvenic everywhere then it is stabilized by magnetic tension. For examples of superalfvenic flows which are destabilized by magnetic fields see Kent (1968); for a discussion of the destabilization mechanism see Lecoanet et al. (2010). A field which is too weak to stabilize the flow dramatically affects the nonlinear stage of the instability, however. As the field is wound up by the vortices it exerts small scale forces which spawn rich secondary structure (Malagoli et al. 1996; Frank et al. 1996; Palotti et al. 2008). The effect of a magnetic field on the discontinuous velocity profile is always stabilizing, however. The dispersion relation is derived in Chandrasekhar (1961).

In a weakly ionized gas with a fairly strong magnetic field, such as a molecular cloud, the plasma Alfvèn speed v_{Ap} can be hundreds of km/s, much faster than any flows, such as protostellar jets, that happen to be present. On the other had, the neutrals are not acted upon directly be the magnetic field at all. This suggests that a weakly ionized gas is always unstable to the KHI, and that the instability will reside primarily in the neutrals, with only minor perturbations to the plasma and magnetic field. This was shown by Watson et al. (2004) for discontinuous velocity profiles. The effects of continuous shear and the Hall term were followed into the nonlinear regime by Jones and Downes (2011) (recall from Sect. 11.3.1.2 that in a sufficiently collisional, weakly ionized medium, the Hall scale is enhanced above its plasma value by $\sqrt{\rho/\rho_i}$). These authors found that in the nonlinear stage,

ion-neutral friction efficiently converts turbulent energy to heat, potentially damping out a turbulent boundary layer.

11.5.1.2 Magnetorotational Instability

The MRI is believed to be a key mechanism for transporting angular momentum outward in astrophysical accretion disks. It may drive turbulent motions in galactic disks, and may amplify and regenerate magnetic fields. The instability was first discussed in the context of astrophysical disks in Balbus and Hawley (1991) and its properties were reviewed in Balbus and Hawley (1998). It is driven by the tendency of magnetic fields to enforce uniform rotation along a fieldline, and is most simply explained if the magnetic field is parallel to the rotation axis. Then if two magnetically connected fluid elements initially at the same radius are displaced, one inward and one outward, magnetic forces increase the angular momentum of the outer one and decrease the angular momentum of the inner one. This amplifies the original displacements. The maximum growth rate of the instability occurs at the wavenumber k at which the Alfvén frequency kv_A is of order the rotation frequency Ω. The corresponding wavelength must be less than the thickness of the disk. Since the disk scale height H and sound speed v_s are related by $v_s \sim \Omega H$, this imposes a limit on the magnetic fieldstrength at which the MRI can exist; $v_A/v_s \leq 1$. The amplification rate of maximally unstable perturbations is typically of order Ω.

The effect of partial ionization on this picture was first considered by Blaes and Balbus (1994). First, suppose that the neutral - ion collision rate $\rho_p \gamma_{pn}$ is much less than the radial oscillation frequency κ of particles in the disk (the epicyclic frequency). In this case the plasma and the neutrals are decoupled, and the most unstable wavenumber is of order Ω/v_{Ap}. These modes can only satisfy vertical boundary conditions if the magnetic field is extremely weak. On the other hand, if $\rho_p \gamma_{pn}/\kappa \gg 1$, plasma-neutral coupling is good and the disk behaves like a plasma with v_A computed from the full mass density.

As we have already seen, plasma-neutral collisional effects and Hall effects are coupled due to the increase in the Hall scale when plasma-neutral collisions are frequent, as they are in protostellar disks. The role of the Hall effect in the MRI was first examined by Wardle (1999) for a vertical magnetic field, and later by Balbus and Terquem (2001) for arbitrarily oriented magnetic fields. The Hall effect imparts net helicity to magnetic perturbations, which become right hand circularly polarized Whistler waves in the limit that the ion response is negligible. This broadens the possible parameter space in which instability exists. The maximum growth rate remains of order Ω, and is thus very fast compared to typical evolutionary timescales.

11.5.1.3 Gravitational Instability

The characteristic timescale for gravitational instability of a self-gravitating body is of order the dynamical timescale $\tau_D \sim (G\rho)^{-1/2}$, and in interstellar molecular

clouds is typically much faster than the ambipolar diffusion timescale introduced in Eq. (11.15). In the absence of diffusion, magnetically subcritical bodies are stable against gravitational collapse.

Ambipolar drift, however, provides a mechanism for releasing gravitational binding energy and destabilizing the cloud (Langer 1978). A characteristic timescale $\tau \sim (\tau_{AD}\tau_D^2)^{1/3}$ for this process was identified in Zweibel (1998); it holds for magnetically subcritical, self gravitating sheets that are within about 30 % of critical. A nonlinear simulation of the process showed that an unstable sheet breaks up into fragments in relative motion (Indebetouw and Zweibel 2000).

The linear stability problem was revisited in Ciolek and Basu (2006). The 2D geometry was retained (an idealization of a highly flattened cloud) but finite thickness was assumed and external pressure was included. Numerical models which follow the instability to finite amplitude show that ambipolar drift can have an important effect on the fragmentation, and on the properties of the fragments (Basu et al. 2009a,b).

11.6 Ambipolar Drift and Magnetic Reconnection

Magnetic reconnection is the topological rearrangement of magnetic field on timescales much faster than the resistive diffusion time. It is an important process in astrophysics. Irreversible topological change is necessary for magnetic dynamos. Rapid conversion of magnetic energy to plasma energy is behind astrophysical flares. Reconnection is very important in laboratory plasmas as well; it affects energy balance, transport, and plasma confinement. For a review of magnetic reconnection in astrophysical and laboratory plasmas, see Zweibel and Yamada (2009).

Although ambipolar drift transports the magnetic field with respect to the neutrals, it preserves the topology of the magnetic field with respect to the plasma (or, in cases where the Hall effect is important, to the electrons), and thus is not a reconnection process. However, it affects the reconnection process itself, and can promote its onset. For a recent review of partial ionization effects in reconnection see Zweibel et al. (2011).

The default picture of reconnection is the Sweet–Parker model (Sweet 1958; Parker 1957). The setup is sketched in Fig. 11.3. It is 2D, incompressible, and steady. Opposing magnetic fields $\pm B$ are brought together by an inflow v_{in} over a length L and reconnected by Ohmic diffusion in a thin layer of width δ_{SP}. The conversion of magnetic to thermal energy, and the magnetic tension in the reconnected field, expel the magnetic field and plasma at the Alfvén speed v_A. The reconnection rate v_{in} and layer width δ can be solved for in terms of v_A and L by equating the mass fluxes in and out of the region

$$\rho v_{in} L = \rho v_A \delta_{SP} \tag{11.35}$$

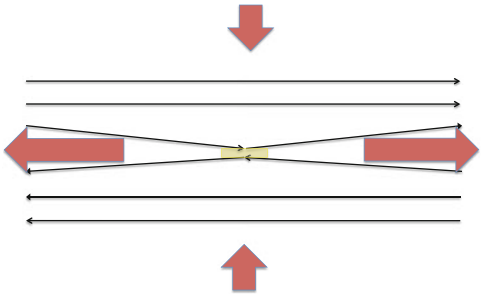

Fig. 11.3 In Sweet–Parker reconnection, opposing magnetic fields (*black lines*) are brought together over a length L by a flow (*short red arrows*). Ohmic resistivity reconnects them at a highly flattened X-point (*yellow region*), and the plasma and reconnected field are expelled at the Alfvén speed (*long red arrows*) by pressure and magnetic tension along thin magnetic channels

and assuming the electric field is determined inductively everywhere except in the reconnection region, where it is Ohmic

$$\frac{v_{in}}{c}B = \eta J \sim \frac{\eta c B}{4\pi \delta_{SP}} \tag{11.36}$$

Rearranging Eqs. (11.35) and (11.36) we can show that $\delta_{SP} = L/\sqrt{S}$ and

$$v_{in} = \frac{v_A}{\sqrt{S}}, \tag{11.37}$$

where $S \equiv 4\pi L v_A/\eta c^2$ is the Lundquist number. Typically $S \sim 10^{8-10}$ for solar problems and $S \sim 10^{15-20}$ for interstellar problems, so Sweet-Parker theory predicts very slow reconnection. Reconnection is slow because the outflow region must be thin enough to be resistive while the outflow speed itself cannot exceed v_A. This limits the flow of mass into the reconnection region. The incompatibility of the Sweet–Parker reconnection rate with the rapid energization observed in solar flares and other heliospheric phenomena led to a quest for faster reconnection mechanisms that has led to great progress in this field.

11.6.1 Strongly and Weakly Coupled Reconnection

Which Alfvén speed, v_A or v_{Ap}, should be used in computing the reconnection rate in a weakly ionized medium? Roughly speaking, we would expect v_A to be the relevant speed if reconnection is slow enough that the neutrals have time to be accelerated by the neutrals, while v_{Ap} holds in the opposite limit. This was first shown in Zweibel (1989), both for Sweet–Parker reconnection and for resistive instabilities known as

tearing modes (Furth et al. 1963), which grow at a rate proportional to $v_{A,Ap}^{2/5}$. Thus, the Sweet–Parker reconnection rate and the resistive tearing mode growth rate can be enhanced by factors of $(\rho/\rho_p)^{1/4}$, and $(\rho/\rho_p)^{1/5}$, respectively. This goes in the right direction, but does not enhance the reconnection rate by more than 1–2 orders of magnitude, even in dense molecular gas.

Significant enhancement of the reconnection rate may come about, however, if we go beyond the standard MHD model. It has been known for some time that the Hall effect can accelerate the reconnection rate (see Drake et al. 2008 for a summary of the arguments). In Sect. 11.3.1.2 we showed that the Hall effect is important on scales below the ion skin depth d_i. Thus, slow Sweet–Parker reconnection transitions to fast Hall-mediated reconnection when δ_{SP} drops below d_i. We also saw in Sect. 11.3.1.2 that d_i can be increased by a factor of ρ/ρ_p when ion-neutral collisions are strong. It was shown in Malyshkin and Zweibel (2011) that a similar effect occurs for magnetic reconnection. The expression for effective particle mass m_{eff} is slightly more complicated than Eq. (11.32) however; if the ratio of the plasma flow time along the current sheet to the ion-neutral collision time is less than ρ/ρ_p then m_{eff}/m_i is simply one plus the ratio of these times. The main point, however, is that the ambipolar drift can promote the onset of Hall-mediated reconnection by increasing the effective inertia of the ions.

11.6.2 Current Sheet Formation: Triggering Rapid Reconnection

Magnetic fieldlines are triggered to reconnect where the current density is high. Ambipolar drift can concentrate the current. Consider the situation shown in Fig. 11.4. A uniformly oriented magnetic field $\hat{z}B(x,t)$ has an initially linear profile; $B(x,0) = B_0 x/l$. Assume the neutral pressure is very large and nearly constant, so the motion of the neutrals can be ignored. The plasma, on the other hand, is accelerated down the magnetic pressure gradient toward the null point $B = 0$. This reshapes the magnetic field profile. We can analyze this mathematically using Eq. (11.11), which in this simple geometry becomes a nonlinear diffusion equation for B

$$\frac{\partial B}{\partial t} = \frac{\partial}{\partial x}\frac{B^2}{4\pi\gamma_{pn}\rho_p\rho_n}\frac{\partial B}{\partial x}. \tag{11.38}$$

The steady state solution of Eq. (11.38) which fits the boundary condition $B(l) = B_0$ is $B(x) = B_0(x/l)^{1/3}$. The current density corresponding to this solution is infinite at $x = 0$. It was shown in Brandenburg and Zweibel (1994) that an initially linear profile evolves towards the singular profile. Resistivity, however, prevents this singular state from being attained. Instead, magnetic flux is annihilated in a thin

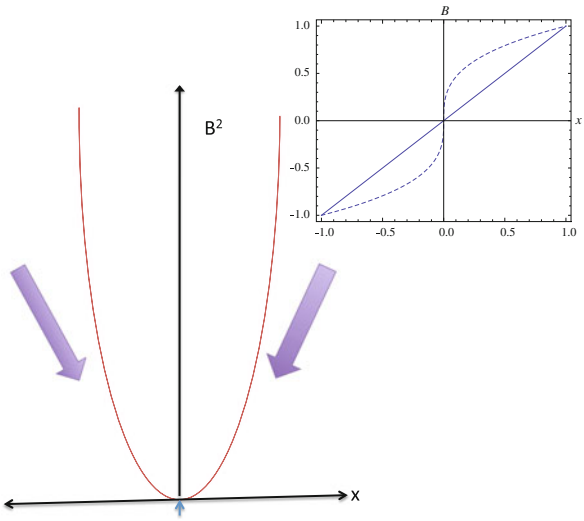

Fig. 11.4 Magnetic pressure profile in the neighborhood of a magnetic neutral sheet. The *thick arrows* symbolize acceleration of the plasma down the magnetic pressure gradient. The *inset* shows the evolution of an initially linear magnetic profile (*solid line*) to a state of constant ambipolar diffusive flux (*dashed line*)

layer where the magnetic field reverses, and it is interesting to ask how fast this can happen.

The rate of merging is not determined by resistivity alone (Vishniac and Lazarian 1999; Heitsch and Zweibel 2003a). The flow of plasma toward the neutral line tends to build up a large ion pressure peak. In deriving the singular solution to Eq. (11.38) it is assumed that recombination is fast enough to remove this peak, and maintain ionization equilibrium. Thus, the continuity equation is satisfied by recombination rather than by advection. In Vishniac and Lazarian (1999) and Heitsch and Zweibel (2003a) it is shown that there is a fast recombination regime of 1D magnetic reconnection in which the outflow time L/v_A is replaced by the ion recombination time. Recently the MHD problem has been studied rather comprehensively in 2D simulations by Leake et al. (2012). This reference assesses the regimes of validity of the 1D and semianalytical results as well as the stability of the steady state solutions.

11.7 Summary

The study of ion-neutral drift in astrophysical systems has expanded far beyond solution of the magnetic flux problem in star formation, the context in which it was originally conceived. In the chapter we have introduced the basic analytical tools and numerical considerations for studying ion-neutral drift. We have shown some of the ways in which it interacts with waves and turbulence, how it modifies shocks and fronts, its role in gravitational instabilities and shear flow instabilities with and without rotation, and its effects on magnetic reconnection. We anticipate that ion-

neutral drift will remain an important part of astrophysical gas dynamics from the mesoscales at which the drifts become appreciable down to the microscales where the neutrals simply introduce dissipation.

Acknowledgements I am grateful to the many colleagues and collaborators with whom I have discussed ambipolar diffusion over the years. This work was partially supported by NSF Grant PHY 0821899, which funds the Center for Magnetic Self-Organization.

References

Arons, J., Max, C.E.: Astrophys. J. **196**, L77 (1975)
Balbus, S.A., Hawley, J.F.: Astrophys. J. **376**, 214 (1991)
Balbus, S.A., Hawley, J.F.: Rev. Mod. Phys. **70**, 1 (1998)
Balbus, S.A., Terquem, C.: Astrophys. J. **552**, 235 (2001)
Basu, S., Ciolek, G.E., Dapp, W.B., Wurster, J.: New A **14**, 483 (2009a)
Basu, S., Ciolek, G.E., Wurster, J.: New A **14**, 221 (2009b)
Blaes, O.M., Balbus, S.A.: Astrophys. J. **412**, 163 (1994)
Blasi, P., Morlino, G., Bandiera, R., Amato, E., Caprioli, D.: Astrophys. J. **755**, article id. 121 (2012)
Brandenburg, A., Zweibel, E.G.: Astrophys. J. **427**, L91 (1994)
Chandrasekhar, S.: Hydrodynamic & Hydromagnetic Stability. Clarendon Press, Oxford (1961)
Chen, C-Y., Ostriker, E.C.: Astrophys. J. **744**, 124 (2012)
Ciolek, G.E., Basu, S.: Astrophys. J. **652**, 542 (2006)
Ciolek, G.E., Mouschovias, T.C.: Astrophys. J. **425**, 142 (1994)
Ciolek, G.E., Mouschovias, T.C.: Astrophys. J. **504**, 280 (1998)
Cowling, T.G.: Mon. Not. Roy. Ast. Soc. **116**, 114 (1956)
Crutcher, R.M.: Astrophys. J. **520**, 706 (1999)
Crutcher, R.M.: Ann. Rev. Astron. Astrophys. **50**, 29 (2012)
De Pontieu, B., Martens, P.C.H., Hudson, H.S.: Astrophys. J. **558**, 859 (2001)
Draine, B.T.: Astrophys. J. **241**, 1021 (1980)
Draine, B.T.: Mon. Not. Roy. Ast. Soc. **220**, 133 (1986)
Draine, B.T.: Physical Processes in the Interstellar and Intergalactic Medium. Princeton University Press, Princeton (2010)
Draine, B.T., McKee, C.F.: ARRA **31**, 373 (1993)
Draine, B.T., Roberge, W.D., Dalgarno, A.: Astrophys. J. **264**, 485 (1983)
Drake, J.F., Shay, M.A., Swisdak, M.: Phys. Plasmas **15**, 042306 (2008)
Drazin, P.G., Reid, W.H.: Hydrodynamic Stability. Cambridge University Press, Cambridge (1981)
Duffin, D.F., Pudritz, R.E.: Mon. Not. R. Astron. Soc. **391**, 1659 (2008)
Falceta-Goncalves, D., Lazarian, A., Kowal, G.: Astrophys. J. **679**, 537 (2010)
Falle, S.A.E.G., Hartquist, T.W., van Loo, §. In: Pogorlov, N.V., Audit, E., Colella, P., Zank, G.P. (eds.) Numerical Modeling of Space Plasma Flows, p. 80. Astronomical Society of the Pacific (2009)
Fatuzzo, M., Adams, F.C.: Astrophys. J. **570**, 210 (2002)
Ferrière, K.M., Zweibel, E.G., Shull, J.M.: Astrophys. J. **332**, 984 (1988)
Fiedler, R.A., Mouschovias, T.C.: Astrophys. J. **391**, 199 (1992)
Fiedler, R.A., Mouschovias, T.C.: Astrophys. J. **415**, 680 (1993)
Field, G.B.: Astrophys. J. **142**, 531 (1965)
Field, G.B., Goldsmith, D.W., Habing, H.J.: Astrophys. J. **155**, L149 (1969)
Frank, A., Jones, T.W., Ryu, D., Gaalaas, J.B.: Astrophys. J. **460**, 777 (1996)
Furth, H.P., Killeen, J., Rosenbluth, M.N.: Phys. Fl. **6**, 459 (1963)

Heitsch, F., Zweibel, E.G.: Astrophys. J. **583**, 229 (2003a)
Heitsch, F., Zweibel, E.G., Slyz, A.D., Devriendt, J.E.G.: Astrophys. J. **603**, 165 (2004)
Hezareh, T., Houde, M., McCoey, C., Li, H-B.: Astrophys. J. **720**, 603 (2010)
Indebetouw, R., Zweibel, E.G.: Astrophys. J. **532**, 361 (2000)
Jones, A.C., Downes, T.P.: Mon. Not. Roy. Ast. Soc. **418**, 390 (2011)
Kent, A.: J. Plasma Phys. **2**, 543 (1968)
Kim, E-J., Diamond, P.H.: Astrophys. J. **578**, L113 (2002)
Klessen, R.S., Krumholz, M.R., Heitsch, F.: Adv. Sci. Lett. **4**, 258 (2011)
Kulsrud, R.M., Pearce, W.P.: Astrophys. J. **156**, 445 (1969)
Langer, W.D.: Astrophys. J. **225**, 95 (1978)
Lazarian, A., Vishniac, E.T., Cho, J.: Astrophys. J. **603**, 180 (2004)
Leake, J.E., Lukin, V.S., Linton, M.G., Meier, E.T.: Astrophys. J. **760**, article id. 109 (2012)
Lecoanet, D., Zweibel, E.G., Townsend, R.H.D., Huang, Y-M.: Astrophys. J. **712**, 1116 (2010)
Li, H-B., Houde, M.: Astrophys. J. **677**, 1151 (2008)
Li, P.S., McKee, C.F., Klein, R.I.: Astrophys. J. **653**, 1280 (2006)
Li., P.S., McKee, C.F., Klein, R.I., Fisher, R.T.: Astrophys. J. **684**, 380 (2008)
Li, P.S., McKee, C.F., Klein, R.I.: Astrophys. J. **744**, 73 (2012)
Li, P.S., Myers, A., McKee, C.F.: Astrophys. J. **760**, article id. 33 (2012)
Mac Low, M-M., Klessen, R.S.: Rev. Mod. Phys. **76**, 125 (2004)
Mac Low, M-M., Norman, M.L., Konigl, A., Wardle, M.: Astrophys. J. **442**, 726 (1994)
Malagoli, A., Bodo, G., Rosner, R.: Astrophys. J. **456**, 708 (1996)
Malyshkin, L.M., Zweibel, E.G.: Astrophys. J. **739**, article id. 72 (2011)
McKee, C.F., Ostriker, E.C.: Ann. Rev. Astron. Astrophys. **45**, 565 (2007)
McKee, C.F., Zweibel, E.G., Heiles, C., Goodman, A.A. In: Levy, E.H., Lunine, J. (eds.) Protostars & Planets III, p. , 327. University of Arizona Press, Tucson (1993)
Mestel, L., Spitzer, L.: Mon. Not. Roy. Ast. Soc. **116**, 503 (1956)
Morlino, G., Blasi, P., Bandiera, R., Amato, E., Caprioli, D. (2012). arXiv:1211.6148
Mouschovias, T.C., Ciolek, G.E., Morton, S.A.: Mon. Not. R. Astron. Soc. **415**, 1751 (2011)
Mullan, D.J.: Mon. Not. R. Astron. Soc. **153**, 145 (1971)
Myers, P.C., Khersonsky, V.K.: Astrophys. J. **442**, 186 (1995)
Nakano, T.: Fund. Cosmic Phys. **9**, 139 (1984)
Nakano, T.: Astrophys. J. **494**, 587 (1998)
Padoan, P., Zweibel, E.G., Nordlund, A.: Astrophys. J. **540**, 332 (2000)
Palotti, M.L., Heitsch, F., Zweibel, E.G., Huang, Y-M.: Astrophys. J. **678**, 234 (2008)
Parker, E.N.: JGR **62**, 509 (1957)
Piddington, J.H.: Mon. Not. Roy. Ast. Soc. **116**, 314 (1956)
Scalo, J.M.: Astrophys. J. **213**, 705 (1977)
Shu, F.H.: Astrophys. J. **273**, 202 (1983)
Spitzer, L.: Physics of Fully Ionized Gases. Wiley Interscience, New York (1962)
Stone, J.M., Zweibel, E.G.: Astrophys. J. **724**, 131 (2010)
Sweet, P.A.: Electromagnetic Phenomena in Cosmical Physics, p. 123. Cambridge University Press, Cambridge (1958)
Tilley, D.A., Balsara, D.S.: Mon. Not. R. Astron. Soc. **389**, 1058 (2008)
Tilley, D.A., Balsara, D.S.: Mon. Not. R. Astron. Soc. **406**, 1201 (2010)
Tilley, D.A., Balsara, D.S., Meyer, C.: New Ast. **17**, 368 (2012)
Vishniac, E.T., Lazarian, A.: Astrophys. J. **511**, 193 (1999)
Wardle, M.: Mon. Not. Roy. Ast. Soc. **246**, 98 (1990)
Wardle, M.: Mon. Not. Roy. Ast. Soc. **307**, 849 (1999)
Wardle, M., Ng, C.: Mon. Not. Roy. Ast. Soc. **303**, 239 (1999)
Watson, C., Heitsch, F., Zweibel, E.G., Churchwell, E.: Astrophys. J. **608**, 274 (2004)
Williams, J.P., Bergin, E.A., Caselli, P., Myers, P.C., Plume, R.: Astrophys. J. **503**, 689 (1998)
Zweibel, E.G.: Astrophys. J. **350**, 550 (1989)
Zweibel, E.G.: Astrophys. J. **499**, 746 (1998)
Zweibel, E.G.: Astrophys. J. **567**, 962 (2002)

Zweibel, E.G., Brandenburg, A.: Astrophys. J. **478**, 563 (1997)
Zweibel, E.G., Josafatsson, K.: Astrophys. J. **270**, 511 (1983)
Zweibel, E.G., Yamada, M.: Ann. Rev. Astron. Astrophys. **47**, 291 (2009)
Zweibel, E.G., Lawrence, E., Yoo, J., Ji, H., Yamada, M., Malyshkin, L.: Phys. Plasmas **18**, 111211 (2011)

Chapter 12
Magnetic Reconnection in Astrophysical Environments

Alex Lazarian, Gregory L. Eyink, Ethan T. Vishniac, and Grzegorz Kowal

Abstract Magnetic reconnection is a process that changes magnetic field topology in highly conducting fluids. Traditionally, magnetic reconnection was associated mostly with solar flares. In reality, the process must be ubiquitous as astrophysical fluids are magnetized and motions of fluid elements necessarily entail crossing of magnetic frozen in field lines and magnetic reconnection. We consider magnetic reconnection in realistic 3D geometry in the presence of turbulence. This turbulence in most astrophysical settings is of pre-existing nature, but it also can be induced by magnetic reconnection itself. In this situation turbulent magnetic field wandering opens up reconnection outflow regions, making reconnection fast. We discuss Lazarian and Vishniac (1999) model of turbulent reconnection, its numerical and observational testings, as well as its connection to the modern understanding of the Lagrangian properties of turbulent fluids. We show that the predicted dependences of the reconnection rates on the level of MHD turbulence make the generally accepted Goldreich and Sridhar (1995) model of turbulence self-consistent. Similarly, we argue that the well-known Alfvén theorem on flux freezing is not valid for the turbulent fluids and therefore magnetic fields diffuse within turbulent volumes. This is an element of magnetic field dynamics that was not accounted by earlier theories. For instance, the theory of star formation that was developing assuming

A. Lazarian (✉)
Department of Astronomy, University of Wisconsin, 475 North Charter Street, Madison, WI 53706, USA
e-mail: lazarian@astro.wisc.edu

G.L. Eyink
Department of Applied Mathematics and Statistics, The Johns Hopkins University, Baltimore, MD 21218, USA
e-mail: eyink@jhu.edu

E.T. Vishniac
Department of Physics and Astronomy, McMaster University, 1280 Main Street West, Hamilton, ON L8S 4M1, Canada
e-mail: ethan@mcmaster.ca

G. Kowal
Escola de Artes, Ciências e Humanidades, Universidade de São Paulo, Av. Arlindo Béttio, 1000 Ermelino Matarazzo, CEP 03828-000, São Paulo, Brazil
e-mail: g.kowal@iag.usp.br

A. Lazarian et al. (eds.), *Magnetic Fields in Diffuse Media*, Astrophysics and Space Science Library 407, DOI 10.1007/978-3-662-44625-6_12

that it is only the drift of neutrals that can violate the otherwise perfect flux freezing, is affected and we discuss the consequences of the turbulent diffusion of magnetic fields mediated by reconnection. Finally, we briefly address the first order Fermi acceleration induced by magnetic reconnection in turbulent fluids.

12.1 Introduction

Magnetic fields modify fluid dynamics and it is generally believed that magnetic fields embedded in a highly conductive fluid retain their topology for all time due to the magnetic fields being frozen-in Alfvén (1942); Parker (1979). Nevertheless, highly conducting ionized astrophysical objects, like stars and galactic disks, show evidence of changes in topology, i.e. "magnetic reconnection", on dynamical time scales (Parker 1970; Lovelace 1976; Priest and Forbes 2002). Historically, magnetic reconnection research was motivated by observations of the solar corona (Innes et al. 1997; Yokoyama and Shibata 1995; Masuda et al. 1994) and this influenced attempts to find peculiar conditions conducive for flux conservation violation, e.g. special magnetic field configurations or special plasma conditions. For instance, much work has concentrated on showing how reconnection can be rapid in plasmas with very small collision rates (Shay et al. 1998; Drake 2001; Drake et al. 2006; Daughton et al. 2006). However, it is clear that reconnection is a ubiquitous process taking place in various astrophysical environments, e.g. magnetic reconnection can be inferred from the existence of large-scale dynamo activity inside stellar interiors (Parker 1993; Ossendrijver 2003), as well as from the eddy-type motions in magnetohydrodynamic turbulence. Without fast magnetic reconnection magnetized fluids would behave like Jello or felt, rather than as a fluid.

In fact, solar flares (Sturrock 1966) are just one vivid example of reconnection activity. Some other reconnection events, e.g. γ-ray bursts (Zhang and Yan 2011; Lazarian et al. 2004; Fox et al. 2005; Galama et al. 1998) also occur in collisionless media, while others take place in collisional media. Thus attempts to explain only collisionless reconnection substantially limits astrophysical applications of the corresponding reconnection models. We also note that magnetic reconnection occurs rapidly in computer simulations due to the high values of resistivity (or numerical resistivity) that are employed at the resolutions currently achievable. Therefore, if there are situations where magnetic fields reconnect slowly, numerical simulations do not adequately reproduce astrophysical reality. This means that if collisionless reconnection is the only way to make reconnection rapid, then numerical simulations of many astrophysical processes, including those of the interstellar medium (ISM), which is collisional, are in error. Fortunately, this scary option is not realistic, as recent observations of the collisional parts of the solar atmosphere indicate fast reconnection (Shibata and Magara 2001).

What makes reconnection enigmatic is that it is not possible to claim that reconnection must always be rapid empirically, as solar flares require periods of

flux accumulation time, which correspond to slow reconnection. Thus magnetic reconnection should have some sort of trigger, which should not depend on the parameters of the local plasma. In this review we argue that the trigger is turbulence.

We may add that some recent reviews dealing with turbulent magnetic reconnection include Browning and Lazarian (2013); Karimabadi and Lazarian (2013). The first one analyzes the reconnection in relation to solar flares, the other provides the comparison of the PIC simulations of the reconnection in collisionless plasmas with the reconnection in turbulent MHD regime.

In the review below we provide a simple description of the basics of magnetic reconnection and astrophysical turbulence in Sect. 12.2, present the theory of magnetic reconnection in the presence of turbulence and its testing in Sects. 12.3 and 12.4, respectively. Observational tests of the magnetic reconnection are described in Sect. 12.5 while the extensions of the reconnection theory are discussed in Sect. 12.6 and its astrophysical implications are summarized in Sect. 12.7. In Sect. 12.8 we present a discussion and summary of the review.

12.2 Basics of Magnetic Reconnection and Astrophysical Turbulence

12.2.1 Models of Laminar Reconnection

Turbulence is usually not a welcome ingredient in theoretical modeling. Turbulence carries an aura of mystery, especially magnetic turbulence, which is still a subject of ongoing debates. Thus, it is not surprising that researchers prefer to consider laminar models whenever possible.

The classical Sweet–Parker model, the first analytical model for magnetic reconnection, was proposed by Parker (1957); Sweet (1958).[1] Sweet–Parker reconnection has the virtue that it relies on a robust and straightforward geometry (see Fig. 12.1). Two regions with uniform *laminar* magnetic fields are separated by thin current sheet. The speed of reconnection is given roughly by the resistivity divided by the sheet thickness, i.e.

$$V_{rec1} \approx \eta/\Delta. \tag{12.1}$$

One might incorrectly assume that by decreasing the current sheet thickness one can increase the reconnection rate. In fact, for *steady state reconnection* the plasma in the current sheet must be ejected from the edge of the current sheet at the Alfvén speed, V_A. Thus the reconnection speed is

[1]The basic idea of the model was first discussed by Sweet and the corresponding paper by Parker refers to the model as "Sweet model".

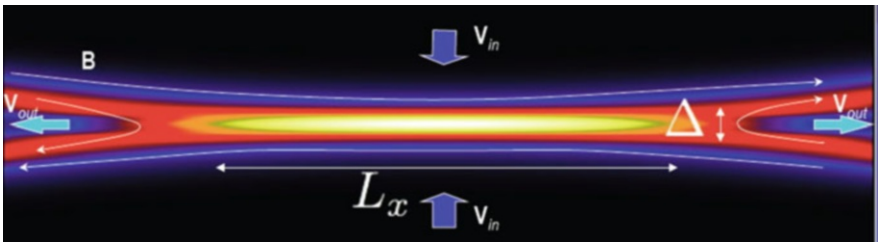

Fig. 12.1 Sweet–Parker reconnection. Simulations of laminar reconnection from Kowal et al. (2009) are used. The current sheet has L_x extension, while the ejection of matter and shared component of magnetic field happens through Δ. The cross-section of the reconnection is shown. Generically, the shared component of magnetic field is directed perpendicular to the picture plane. This component should be also ejected through Δ

$$V_{rec2} \approx V_A \Delta / L, \tag{12.2}$$

where L is the length of the current sheet, which requires Δ to be large for a large reconnection speed.

In other words, we face two contradictory requirements on the outflow thickness, namely, Δ should be large so as to not constrain the outflow of plasma and Δ should be small for the Ohmic diffusivity to do its job of dissipating magnetic field lines. As a result, the steady state Sweet–Parker reconnection rate is a compromise between the two contradictory requirements. If Δ becomes small, the reconnection rate V_{rec1} increases, but the insufficient outflow of plasma from the current sheet will lead to an increase in Δ and slow down the reconnection process. If Δ increases, the outflow will speed up but the oppositely directed magnetic field lines get further apart and V_{rec1} drops. The slow reconnection rate limits the supply of plasma into the outflow and decreases Δ. This self regulation ensures that in the steady state $V_{rec1} = V_{rec2}$ which determines both the steady state reconnection rate and the steady state Δ. As a result, the overall reconnection speed is reduced from the Alfvén speed by the square root of the Lundquist number, $S \equiv L_x V_A / \eta$, i.e.

$$V_{rec,SP} = V_A S^{-1/2}. \tag{12.3}$$

For astrophysical conditions the Lundquist number S may easily be 10^{16} and larger. The corresponding Sweet–Parker reconnection speed is negligible. If this sets the actual reconnection speed then we should expect magnetic field lines in the fluid not to change their topology, which in the presence of chaotic motions should result in a messy magnetic structure with the properties of Jello. On the contrary, the fast reconnection suggested by solar flares, dynamo operation etc. requires that the dependence on S be erased.

A few lessons can be learned from the analysis of the Sweet–Parker reconnection. First of all, it is a self-regulated process. Second, even with the Sweet–Parker scheme the instantaneous rates of reconnection are not restricted. Indeed, under the

external forcing the Ohmic annihilation rate given by V_{rec1} can be arbitrary large, which, nevertheless does not mean that the time averaged rate of reconnection is also large. This should be taken into account when the probability distribution functions of currents are interpreted in terms of magnetic reconnection (see Sect. 12.4.5).

The low efficiency of the Sweet-Parker reconnection arises from the disparity of the scales of Δ, which is determined by microphysics, i.e. depends on η, and L_x that has a huge, i.e. astronomical, size. The introduction of plasma effects does not change this problem as in this case Δ should be of the order of the ion Larmor radius, which is $\ll L_x$. There are two ways to make the reconnection speed faster. One way is to reduce L_x, by changing the geometry of reconnection region, e.g. making magnetic field lines come at a sharp angle rather than in a natural Sweet–Parker way. This is called X-point reconnection. The most famous example of this is Petschek reconnection (Petschek 1964) (see Fig. 12.2). The other way is to extend Δ and make it comparable to L_x. Obviously, a factor different from resistivity should be involved. In this review we provide evidence that turbulence can do the job of increasing Δ. However, before focusing on this process, we shall first discuss very briefly the Petschek reconnection model, which for a few decades served as the default model of fast reconnection.

Figure 12.2 illustrates the Petschek model of reconnection. The model suggests that extended magnetic bundles come into contact over a tiny area determined by the Ohmic diffusivity. This configuration differs dramatically from the expected generic configuration when magnetic bundles try to press their way through each other. Thus the first introduction of this model raised questions of dynamical self-consistency. An X-point configuration has to persist in the face of compressive bulk forces.

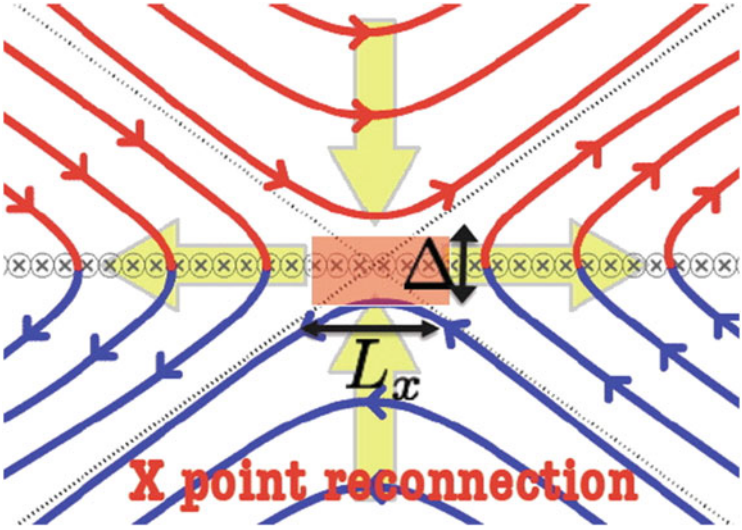

Fig. 12.2 Petschek reconnection is an X-point reconnection where due to the formation of shocks the magnetic field lines are bent sharply towards the reconnection "point" with $L_x \sim \Delta$

However, numerical simulations have shown that an initial X-point configuration of magnetic field reconnection is unstable in the MHD limit for small values of the Ohmic diffusivity (Biskamp 1996) and the magnetic field will relax to a Sweet–Parker configuration. The physical explanation for this effect is simple. In the Petschek model shocks are required in order to maintain the geometry of the X-point. These shocks must persist and be supported by the flows driven by fast reconnection. The simulations showed that the shocks fade away and the contact region spontaneously increases.

X-point reconnection can be stabilized when the plasma is collisionless. Numerical simulations (Shay et al. 1998, 2004) have been encouraging in this respect and created the hope that there was at last the solution of the long-standing problem of magnetic reconnection. However, there are several important issues that remain unresolved. First, it is not clear that this kind of fast reconnection persists on scales greater than the ion inertial scale (Bhattacharjee et al. 2003). Several numerical studies (Wang et al. 2001; Smith et al. 2004; Fitzpatrick 2004) have found large scale reconnection speeds which are not fast in the sense that they show dependence on resistivity. There are countervailing analytical studies (Malyshkin 2008; Shivamoggi 2011) which suggest that Hall X-point reconnection rates are independent of resistivity or other microscopic plasma mechanisms of line slippage, but the rates determined in these studies become small when the ion inertial scale is much less than L_x. Second, in many circumstances the magnetic field geometry does not allow the formation of X-point reconnection. For example, a saddle-shaped current sheet cannot be spontaneously replaced by an X-point. The energy required to do so is comparable to the magnetic energy liberated by reconnection, and must be available beforehand. Third, the stability of the X-point is questionable in the presence of the external random forcing, which is common, as we discuss later, for most of the astrophysical environments. Finally, the requirement that reconnection occurs in a collisionless plasma restricts this model to a small fraction of astrophysical applications. For example, while reconnection in stellar coronae might be described in this way, stellar chromospheres can not. This despite the fact that we observe fast reconnection in those environments (Shibata and Magara 2001). More generally, Yamada (2007) estimated that the scale of the reconnection sheet should not exceed about 40 times the electron mean free path. This condition is not satisfied in many environments which one might naively consider to be collisionless, among them the interstellar medium. The conclusion that stellar interiors and atmospheres, accretion disks, and the interstellar medium in general does not allow fast reconnection is drastic and unpalatable.

Petschek reconnection requires an extended X-point configuration of reconnected magnetic fluxes and Ohmic dissipation concentrated within a microscopic region. As we discuss in this review (see Sect. 12.5), neither of these predictions were supported by solar flare observations. This suggests that neither Sweet–Parker nor Petschek models present a universally applicable mechanism of astrophysical magnetic reconnection. This does not preclude that these processes are important in particular special situations. In what follows we argue that Petschek-type reconnection may be applicable for magnetospheric current sheets or any collisionless plasma

systems, while Sweet–Parker can be important for reconnection at small scales in partially ionized gas.

12.2.2 Turbulence in Astrophysical Fluids

Neither of these models take into account turbulence, which is ubiquitous in astrophysical environments. Indeed, plasma flows at high Reynolds numbers are generically turbulent, since laminar flows are then prey to numerous linear and finite-amplitude instabilities. This is sometimes driven turbulence due to an external energy source, such as supernova in the ISM (Norman and Ferrara 1996; Ferrière 2001), merger events and AGN outflows in the intercluster medium (ICM) (Subramanian et al. 2006; Enßlin and Vogt 2006; Chandran 2005), and baroclinic forcing behind shock waves in interstellar clouds. In other cases, the turbulence is spontaneous, with available energy released by a rich array of instabilities, such as the MRI in accretion disks (Balbus and Hawley 1998), the kink instability of twisted flux tubes in the solar corona (Galsgaard and Nordlund 1997; Gerrard and Hood 2003), etc. Whatever its origin, observational signatures of astrophysical turbulence are seen throughout the universe. The turbulent cascade of energy leads to long "inertial ranges" with power-law spectra that are widely observed, e.g. in the solar wind (Leamon et al. 1998; Bale et al. 2005), and in the ICM Schuecker et al. (2004); Vogt and Enßlin (2005).

Figure 12.3 illustrates the so-called "Big Power Law in the Sky" of the electron density fluctuations. The original version of the law was presented by Armstrong et al. Armstrong et al. (1995) for electron scattering and scintillation data. It was later extended by Chepurnov et al. (Chepurnov and Lazarian 2010) who used Wisconsin Hα Mapper (WHAM) electron density data. We clearly see the power law extending over many orders of spatial scales and suggesting the existence of turbulence in the interstellar medium. With more surveys, with more developed techniques we are getting more evidence of the turbulent nature of astrophysical fluids. For instance, for many years non-thermal line Doppler broadening of the spectral lines was used as an evidence of turbulence.[2] The development of new techniques, namely, Velocity Channel Analysis (VCA) and Velocity Correlation Spectrum (VCS) in a series of papers by Lazarian and Pogosyan (2000, 2004, 2006, 2008) enabled researchers to use HI and CO spectral lines to obtain the power spectra of turbulent velocities (see Lazarian (2009) for a review and references therein).

As turbulence is known to change dramatically many processes, in particular, diffusion and transport processes, it is natural to pose the question to what extent

[2]The power-law ranges that are universal features of high-Reynolds-number turbulence can be inferred to be present from enhanced rates of dissipation and mixing (Eyink 2008) even when they are not seen.

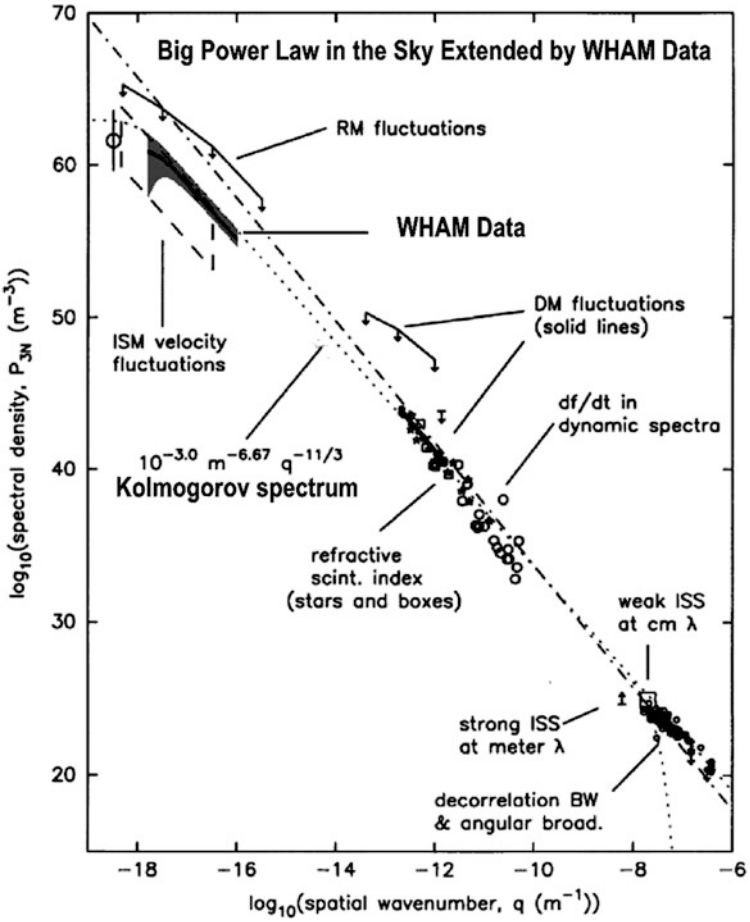

Fig. 12.3 Turbulence in the interstellar gas of the Milky Way as revealed by electron density fluctuations. "Big Power Law in the Sky" Armstrong et al. (1995) extended using WHAM data. The slope corresponds to that of Kolmogorov turbulence. From Chepurnov and Lazarian (2010)

the theory of astrophysical reconnection must take into account the pre-existing turbulent environment. We note that even if the plasma flow is initially laminar, kinetic energy release by reconnection due to some slower plasma process is expected to generate vigorous turbulent motion in high Reynolds number fluids.

12.2.3 MHD Description of Plasma Motions

Turbulence in plasma happens at many scales, from the largest to those below the proton Larmor radius. The effect of turbulence on magnetic reconnection is different for different types of turbulence. For instance, micro turbulence can

change the microscopic resistivity of plasmas and induce anomalous resistivity effects (see Vekshtein et al. (1970)). In this review we advocate the idea that for solving the problem of magnetic reconnection in most astrophysical important cases the approach invoking MHD rather than plasma turbulence is adequate. To provide an initial support for this point, we shall reiterate a few known facts about the applicability of MHD approximation (Kulsrud 1983; Eyink et al. 2011). Below we argue that MHD description is applicable to many settings that include both collisional and collisionless plasmas, provided that we deal with plasmas at sufficiently large scales. To describe magnetized plasma dynamics one should deal with three characteristic length-scales: the ion gyroradius ρ_i, the ion mean-free-path length $\ell_{mfp,i}$ arising from Coulomb collisions, and the scale L of large-scale variation of magnetic and velocity fields.

One case of reconnection that is clearly not dealt with by the popular models of collisionless reconnection (see above) is the "strongly collisional" plasma with $\ell_{mfp,i} \ll \rho_i$. This is the case e.g. of star interiors and most accretion disk systems. For such "strongly collisional" plasmas a standard Chapman–Enskog expansion provides a fluid description of the plasma (Braginsky 1965), with a two-fluid model for scales between $\ell_{mfp,i}$ and the ion skin-depth $\delta_i = \rho_i/\sqrt{\beta_i}$ and an MHD description at scales much larger than δ_i. This is the most obvious case of MHD description for plasmas.

Hot and rarefied astrophysical plasmas are often "weakly collisional" with $\ell_{mfp,i} \gg \rho_i$. Indeed, the relation that follows from the standard formula for the Coulomb collision frequency (e.g. see Fitzpatrick 2011, Eq. 1.25) is

$$\frac{\ell_{mfp,i}}{\rho_i} \propto \frac{\Lambda}{\ln \Lambda} \frac{V_A}{c}, \tag{12.4}$$

where $\Lambda = 4\pi n \lambda_D^3$ is the plasma parameter, or the number of particles within the Debye screening sphere, which indicates that Λ can be very large. Typical values for some weakly coupled cases are shown in Table 12.1 Eyink et al. (2011).

For the "weakly collisional" but well magnetized plasmas one can invoke the expansion over the small ion gyroradius. This results in the "kinetic MHD equations" for lengths much larger than ρ_i. The difference between these equations and the MHD ones is that the pressure tensor in the momentum equation is anisotropic, with the two components $p_\parallel$ and $p_\perp$ of the pressure parallel and perpendicular to the local magnetic field direction (Kulsrud 1983). "Weakly collisional", i.e. $L \gg \ell_{mfp,i}$., and collisionless, i.e. $\ell_{mfp,i} \gg L$ systems have been studied recently (Kowal et al. 2011; Santos-Lima et al. 2013). While the direct collisions are infrequent, compressions of the magnetic field induces anisotropies, as a consequence of the adiabatic invariant conservation, in the phase space particle distribution. This induces instabilities that act upon plasma causing particle scattering (Schekochihin and Cowley 2006; Lazarian and Beresnyak 2006). Thus instead of Coulomb collisional frequency a new frequency of scattering is invoked. In other words, particles do not interact between each other, but each particle interacts with the ensemble of small scale perturbations induced by instabilities in the compressed

Table 12.1 Representative parameters for some weakly-coupled astrophysical plasmas (from Eyink et al. 2011)

Parameter	Warm ionized ISM[a]	Post-CME current sheets[b]	Solar wind at magnetosphere[c]
Density n, cm^{-3}	0.5	7×10^7	10
Temperature T, eV	0.7	10^3	10
Plasma parameter Λ	4×10^9	2×10^{10}	5×10^{10}
Ion thermal velocity $v_{th,i}$, cm/s	10^6	3×10^7	5×10^6
Ion mean-free-path $\ell_{mfp,i}$, cm	6×10^{11}	10^{10}	7×10^{12}
Magnetic diffusivity λ, cm^2/s	10^7	8×10^2	6×10^5
Magnetic field B, G	10^{-6}	1	10^{-4}
Plasma beta β	14	3	1
Alfvén speed V_A, cm/s	3×10^5	3×10^7	7×10^6
Ion gyroradius ρ_i, cm	10^8	3×10^3	6×10^6
Large-scale velocity U, cm/s	10^6	4×10^6	5×10^6
Large length scale L, cm	10^{20}	5×10^{10}	10^8
Lundquist number $S_L = \frac{V_{AL}}{\lambda}$	3×10^{18}	2×10^{15}	10^9
Resistive length* $\ell_\eta^\perp$, cm	5×10^5	1	20

[a]Norman and Ferrara (1996); Ferrière (2001)
[b]Bemporad (2008)
[c]Zimbardo et al. (2010)
*This nominal resistive scale is calculated from $\ell_\eta^\perp \simeq L(V_A/U)S_L^{-3/4}$, assuming GS95 turbulence holds down to that scale, and should not be taken literally when $\ell_\eta^\perp < \rho_i$

magnetized plasmas. By adopting the in-situ measured distribution of particles in the collisionless solar wind Santos-Lima et al. (2013) showed numerically that the dynamics of such plasmas is identical to that of MHD.

Even without invoking instabilities, one can approach "weakly collisional" plasmas solving for the magnetic field using an ideal induction equation, if one ignores all collisional effects. In many cases, e.g. in the ISM and the magnetosphere (see Table 12.1) the resistive length-scale $\ell_\eta^\perp$ is much smaller than both ρ_i and $\rho_e \approx \frac{1}{43}\rho_i$. Magnetic field-lines are, at least formally, well "frozen-in" on these scales. [3] In the "weakly collisional" case the"kinetic MHD" description can be simplified at scales greater than $\ell_{mfp,i}$ by including the Coulomb collision operator and making a Chapman-Enskog expansion. This reproduces a fully MHD description at those large scales. The idealized warm ionized phase of ISM represents "weakly collisional" plasmas in Table 12.1.

We can also note that additional simplifications that justify the MHD approach occur if the turbulent fluctuations are small compared to the mean magnetic field, and having length-scales parallel to the mean field much larger than perpendicular

[3]In Sect. 12.7.1 we discuss the modification of the frozen in concept in the presence of turbulence. This is not important for the present discussion, however.

length-scales. Treating wave frequencies that are low compared to the ion cyclotron frequency we enter the domain of "gyrokinetic approximation" which is commonly used in fusion plasmas. This approximation was advocated for application in astrophysics by Schekochihin et al. (2007, 2009).

For the "gyrokinetic approximation" at length-scales larger than the ion gyroradius ρ_i the incompressible shear-Alfvén wave modes get decoupled from the compressive modes and can be described by the simple "reduced MHD" (RMHD) equations. As we argue later in the review, the shear-Alfvén modes are the modes that induce fast magnetic reconnection, while the other modes are of auxiliary importance for the process.

All in all, our considerations in this part of the review support the generally accepted notion that the MHD approximation is adequate for most astrophysical fluids at sufficiently large scales. A lot of work on reconnection is concentrated on the small scale dynamics, but if magnetic reconnection is determined by large scale motions, as we argue in this review, then the MHD description of magnetic reconnection is appropriate.

12.2.4 Modern Understanding of MHD Turbulence

Within this volume MHD turbulence is described in the chapter by Beresnyak and Lazarian (see also a description of MHD turbulence in the star formation context in the chapter by H. Vazquez-Semadeni). Therefore in presenting the major MHD turbulence results that are essential for our further derivation in the review, we shall be very brief. We will concentrate on Alfvénic modes, while disregarding the slow and fast magnetosonic modes that in principle contribute to MHD turbulence (Cho and Lazarian 2002, 2003; Kowal and Lazarian 2010). The interaction between the modes is in many cases not significant, which allows the separate treatment of Alfvén modes (Cho and Lazarian 2002; Goldreich and Sridhar 1995; Lithwick and Goldreich 2001).

While having a long history of competing ideas, the theory of MHD turbulence has become testable recently due to the advent of numerical simulations (see Biskamp 2003) which confirmed the prediction of magnetized Alfvénic eddies being elongated in the direction of the local magnetic field (see Shebalin et al. 1983; Higdon 1984) and provided results consistent with the quantitative relations for the degree of eddy elongation obtained in the fundamental study by Goldreich and Sridhar (1995) (henceforth GS95).

The relation between the parallel and perpendicular dimensions of eddies in GS95 picture are presented by the so called critical balance condition, namely,

$$\ell_{\parallel}^{-1} V_A \sim \ell_{\perp}^{-1} \delta u_{\ell}, \tag{12.5}$$

where δu_ℓ is the eddy velocity, while $\ell_\parallel$ and $\ell_\perp$ are, respectively, eddy scales parallel and perpendicular to the *local* direction of magnetic field. The *local* system of reference is that determined by the direction of magnetic field at the scale in the vicinity of the eddy. It should be definitely distinguished from the mean magnetic field reference frame (Lithwick and Goldreich 2001; Lazarian and Vishniac 1999; Cho and Vishniac 2000; Maron and Goldreich 2001; Cho et al. 2002), where no universal relations between the eddy scale exist. This is very natural, as small scale turnover eddies can be influenced only by the magnetic field around these eddies.

The motions perpendicular to the local magnetic field are essentially hydrodynamic. Therefore, combining (12.5) with the Kolmogorov cascade notion, i.e. that the energy transfer rate is $\delta u_\ell^2/(\ell_\perp/\delta u_\ell) = const$ one gets $\delta u_\ell \sim \ell_\perp^{1/3}$, which coincides with the known Kolmogorov relation between the turbulent velocity and the scale. For the relation between the parallel and perpendicular scales one gets

$$\ell_\parallel \propto L_i^{1/3} \ell_\perp^{2/3}, \tag{12.6}$$

where L_i is the turbulence injection scale. Note that recent measurements of anisotropy in the solar wind are consistent with Eq. (12.6) (Podesta 2010; Wicks et al. 2010, 2011).

In its original form the GS95 model was proposed for energy injected isotropically with velocity amplitude $u_L = V_A$. If the turbulence is injected at velocities $u_L \ll V_A$ (or anisotropically with $L_{i,\parallel} \ll L_{i,\perp}$), then the turbulent cascade is weak and $\ell_\perp$ decreases while $\ell_\parallel = L_i$ stays the same (Lazarian and Vishniac 1999; Montgomery and Matthaeus 1995; Galtier et al. 2000; Ng and Bhattacharjee 1996). In other words, as a result of the weak cascade the eddies become thinner, but preserve the same length along the local magnetic field. It is possible to show that the interactions within weak turbulence increase and transit to the regime of the strong MHD turbulence at the scale

$$l_{trans} \sim L_i (u_L/V_A)^2 \equiv L_i M_A^2 \quad M_A < 1 \tag{12.7}$$

and the velocity at this scale is $v_{trans} = u_L M_A$, with $M_A = u_L/V_A \ll 1$ being the Alfvénic Mach number of the turbulence (Lazarian and Vishniac 1999; Lazarian 2006). Thus, weak turbulence has a limited, i.e. $[L_i, L_i M_A^2]$ inertial range and at small scales it transits into the regime of strong turbulence.[4]

Table 12.2 illustrates different regimes of MHD turbulence both when it is injected isotropically at superAlfvénic and subAlfvénic velocities. Naturally, superAlfvénic turbulence at large scales is similar to the ordinary hydrodynamic

[4]We should stress that weak and strong are not the characteristics of the amplitude of turbulent perturbations, but the strength of non-linear interactions (see more discussion in Cho et al. (2003)) and small scale Alfvénic perturbations can correspond to a strong Alfvénic cascade.

Table 12.2 Regimes and ranges of MHD turbulence

Type of MHD turbulence	Injection velocity	Range of scales	Motion type	Ways of study
Weak	$u_L < V_A$	$[L_i, L_i M_A^2]$	Wave-like	Analytical
Strong subAlfvénic	$u_L < V_A$	$[L_i M_A^2, l_{min}]$	Eddy-like	Numerical
Strong superAlfvénic	$u_L > V_A$	$[l_A, l_{min}]$	Eddy-like	Numerical

L_i and l_{min} are injection and dissipation scales, respectively $M_A \equiv u_L/V_A$

turbulence, as weak magnetic fields cannot strongly affect turbulent motions. However, at the scale

$$l_A = L_i (V_A/u_L)^3 = L_i M_A^{-3} \quad M_A > 1 \tag{12.8}$$

the motions become Alfvénic.

In this review we address the reconnection mediated by turbulence. For this the regime of weak, i.e. wave-like, perturbations can be an important part of the dynamics. A description of MHD turbulence that incorporates both weak and strong regimes was presented in Lazarian and Vishniac (1999) (henceforth LV99). In the range of length-scales where turbulence is strong, this theory implies that

$$\ell_\parallel \approx L_i \left(\frac{\ell_\perp}{L_i}\right)^{2/3} M_A^{-4/3} \tag{12.9}$$

$$\delta u_\ell \approx u_L \left(\frac{\ell_\perp}{L_i}\right)^{1/3} M_A^{1/3}, \tag{12.10}$$

when the turbulence is driven isotropically on a scale L_i with an amplitude u_L. These are equations that we will use further to derive the magnetic reconnection rate.

Here we do not discuss attempts to modify GS95 theory by adding concepts like "dynamical alignment", "polarization", "non-locality" (Boldyrev 2006; Beresnyak and Lazarian 2006, 2009; Gogoberidze 2007). First of all, those do not change the nature of turbulence to affect the reconnection of the weakly turbulent magnetic field. Indeed, in LV99 the calculations were provided for a wide range of possible models of anisotropic Alfvénic turbulence and provided fast reconnection. Moreover, more recent studies (Beresnyak and Lazarian 2010; Beresnyak 2011, 2012) support the GS95 model. A more detailed discussion of MHD turbulence can be found in the recent review (e.g. Brandenburg and Lazarian 2013) and in Beresnyak and Lazarian's Chapter in this volume.

GS95 presents a model of 3D MHD turbulence that exists in our 3D world. Historically, due to computational reasons, many MHD related studies were done in 2D. The problem of such studies in application to magnetic turbulence is that shear Alfvén waves that play the dominant role for 3D MHD turbulence are entirely lacking in 2D. Furthermore, all magnetized turbulence in 2D is transient, because the dynamo mechanism required to sustain magnetic fields is lacking in 2D (Zeldovich 1957). Thus the relation of 2D numerical studies invoking MHD turbulence, e.g. magnetic reconnection in 2D turbulence, and the processes in the actual 3D geometry is not clear. A more detailed discussion of this point can be found in Eyink et al. (2011).

12.3 Magnetic Reconnection in the Presence of Turbulence

12.3.1 Initial Attempts to Invoke Turbulence to Accelerate Magnetic Reconnection

The first attempts to appeal to turbulence in order to enhance the reconnection rate were made more than 40 years ago. For instance, some papers have concentrated on the effects that turbulence induces on the microphysical level. In particular, Speiser (1970) showed that in collisionless plasmas the electron collision time should be replaced with the electron retention time in the current sheet. Also Jacobson (Jacobson and Moses 1984) proposed that the current diffusivity should be modified to include the diffusion of electrons across the mean field due to small scale stochasticity. However, these effects are insufficient to produce reconnection speeds comparable to the Alfvén speed in most astrophysical environments.

"Hyper-resistivity" (Strauss 1986; Bhattacharjee and Hameiri 1986; Hameiri and Bhattacharjee 1987; Diamond and Malkov 2003) is a more subtle attempt to derive fast reconnection from turbulence within the context of mean-field resistive MHD. The form of the parallel electric field can be derived from magnetic helicity conservation. Integrating by parts one obtains a term which looks like an effective resistivity proportional to the magnetic helicity current. There are several assumptions implicit in this derivation. The most important objection to this approach is that by adopting a mean-field approximation, one is already assuming some sort of small-scale smearing effect, equivalent to fast reconnection. Furthermore, the integration by parts involves assuming a large scale magnetic helicity flux through the boundaries of the exact form required to drive fast reconnection. The problems of the hyper-resistivity approach are discussed in detail in Eyink et al. (2011).

A more productive development was related to studies of instabilities of the reconnection layer. Strauss (1988) examined the enhancement of reconnection through the effect of tearing mode instabilities within current sheets. However, the resulting reconnection speed enhancement is roughly what one would expect based

simply on the broadening of the current sheets due to internal mixing.[5] Waelbroeck (1989) considered not the tearing mode, but the resistive kink mode to accelerate reconnection. The numerical studies of tearing have become an important avenue for more recent reconnection research (Loureiro et al. 2009; Bhattacharjee et al. 2009). As we discuss later in realistic 3D settings tearing instability develops turbulence (Karimabadi et al. 2013; Beresnyak 2013)) which induces a transfer from laminar to turbulent reconnection.[6]

Finally, a study of 2D magnetic reconnection in the presence of external turbulence was done by Matthaeus and Lamkin (1985, 1986). An enhancement of the reconnection rate was reported, but the numerical setup precluded the calculation of a long term average reconnection rate. As we discussed in Sect. 12.2.1 bringing in the Sweet–Parker model of reconnection magnetic field lines closer to each other one can enhance the instantaneous reconnection rate, but this does not mean that averaged long term reconnection rate increases. This, combined with the absence of the theoretical predictions of the expected reconnection rates makes it difficult to make definitive conclusions from the study. Note that, as we discussed in Sect. 12.2.4, the nature of turbulence is different in 2D and 3D. Therefore, the effects accelerating magnetic reconnection mentioned in the study, i.e. formation of X-points, compressions, may be relevant for 2D set ups, but not relevant for the 3D astrophysical reconnection. These effects are not invoked in the model of the turbulent reconnection that we discuss below. We also may note that a more recent study along the approach in Matthaeus and Lamkin (1985) is one in Watson et al. (2007), where the effects of small scale turbulence on 2D reconnection were studied and no significant effects of turbulence on reconnection were reported for the setup chosen by the authors.

In a sense, the above study is the closest predecessor of LV99 work that we deal below. However, there are very substantial differences between the approach of LV99 and Matthaeus and Lamkin (1985). For instance, LV99, as is clear from the text below, uses an analytical approach and, unlike Matthaeus and Lamkin (1985), (a) provides analytical expressions for the reconnection rates; (b) identifies the broadening arising from magnetic field wandering as the mechanism for inducing fast reconnection; (c) deals with 3D turbulence and identifies incompressible Alfvénic motions as the driver of fast reconnection.

[5] In a more recent work Shibata and Tanuma (2001) extended the concept suggesting that tearing may result in fractal reconnection taking place on very small scales.

[6] Also earlier works suggest such a transfer (Dahlburg et al. 1992; Dahlburg and Karpen 1994; Dahlburg 1997; Ferraro and Rogers 2004).

12.3.2 Model of Magnetic Reconnection in Weakly Turbulent Media

As we discussed earlier, considering astrophysical reconnection in laminar environments is not normally realistic. As a natural generalization of the Sweet-Parker model it is appropriate to consider 3D magnetic field wandering induced by turbulence as in LV99. The corresponding model of magnetic reconnection is illustrated by Fig. 12.4.

Like the Sweet-Parker model, the LV99 model deals with a generic configuration, which should arise naturally as magnetic flux tubes try to make their way one through another. This avoids the problems related to the preservation of wide outflow which plagues attempts to explain magnetic reconnection via Petscheck-type solutions. In this model if the outflow of reconnected flux and entrained matter is temporarily slowed down, reconnection will also slow down, but, unlike Petscheck solution, will not change the nature of the solution.

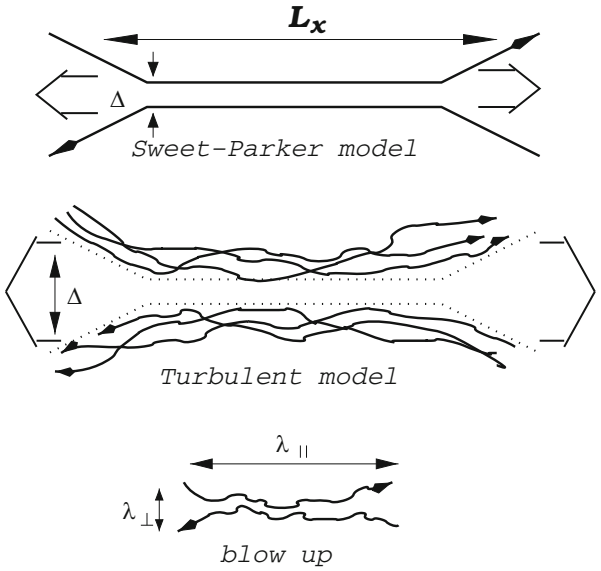

Fig. 12.4 *Upper plot*: Sweet-Parker model of reconnection. The outflow is limited to a thin width δ, which is determined by Ohmic diffusivity. The other scale is an astrophysical scale $L \gg \delta$. Magnetic field lines are assumed to be laminar. *Middle plot*: turbulent reconnection model that accounts for the stochasticity of magnetic field lines. The stochasticity introduced by turbulence is weak and the direction of the mean field is clearly defined. The outflow is limited by the diffusion of magnetic field lines, which depends on macroscopic field line wandering rather than on microscales determined by resistivity. *Low plot*: An individual small scale reconnection region. The reconnection over small patches of magnetic field determines the local reconnection rate. The global reconnection rate is substantially larger as many independent patches reconnect simultaneously. Conservatively, the LV99 model assumes that the small scale events happen at a slow Sweet-Parker rate. Following Lazarian et al. (2004)

The major difference between the Sweet-Parker model and the LV99 model is that while in the former the outflow is limited by microphysical Ohmic diffusivity, in the latter model the large-scale magnetic field wandering determines the thickness of outflow. Thus LV99 model does not depend on resistivity and, depending on the level of turbulence, can provide both fast and slow reconnection rates. This is a very important property for explaining observational data related to reconnection flares.

For extremely weak turbulence, when the range of magnetic field wandering becomes smaller than the width of the Sweet-Parker layer $LS^{-1/2}$, the reconnection rate reduces to the Sweet-Parker rate, which is the ultimate slowest rate of reconnection. As a matter of fact, this slow rate holds only for Lundquist numbers less than S_c, the critical value for tearing mode instability of the Sweet-Parker solution. At higher Lundquist numbers, self-generated turbulence will be the inevitable outcome of unstable breakdown of the Sweet-Parker current sheet and this will yield the minimal reconnection rate in an otherwise quiet environment (see, in particular, Beresnyak 2013).

We note that LV99 does not appeal to a chaotic field created within a hydrodynamic weakly magnetized turbulent flow. On the contrary, the model considers the case of a large scale, well-ordered magnetic field, of the kind that is normally used as a starting point for discussions of reconnection. In the presence of turbulence one expects that the field will have some small scale 'wandering' and this effect changes the nature of magnetic reconnection.

Ultimately, the magnetic field lines will dissipate due to microphysical effects, e.g. Ohmic resistivity. However, it is important to understand that in the LV99 model only a small fraction of any magnetic field line is subject to direct Ohmic annihilation. The fraction of magnetic energy that goes directly into heating the fluid approaches zero as the fluid resistivity vanishes. In addition, 3D Alfvénic turbulence enables many magnetic field lines to enter the reconnection zone simultaneously, which is another difference between 2D and 3D reconnection.

12.3.3 Opening Up of the Outflow Region Via Magnetic Field Wandering

To get the reconnection speed one should calculate the thickness of the outflow Δ that is determined by the magnetic field wandering. This was done in LV99, where the scaling relations for the wandering field lines were established.

The scaling relations for Alfvénic turbulence discussed in Sect. 12.2.4 allow us to calculate the rate of magnetic field spreading. A bundle of field lines confined within a region of width y at some particular point spreads out perpendicular to the mean magnetic field direction as one moves in either direction following the local magnetic field lines. The rate of field line diffusion is given by

$$\frac{d\langle y^2\rangle}{dx} \sim \frac{\langle y^2\rangle}{\lambda_\parallel}, \tag{12.11}$$

where $\lambda_{\parallel}^{-1} \approx \ell_{\parallel}^{-1}$, $\ell_{\parallel}$ is the parallel scale and the corresponding transversal scale, $\ell_{\perp}$, is $\sim \langle y^2 \rangle^{1/2}$, and x is the distance along an axis parallel to the magnetic field. Therefore, using equation (12.9) one gets

$$\frac{d\langle y^2 \rangle}{dx} \sim L_i \left(\frac{\langle y^2 \rangle}{L_i^2} \right)^{2/3} \left(\frac{u_L}{V_A} \right)^{4/3} \tag{12.12}$$

where we have substituted $\langle y^2 \rangle^{1/2}$ for $\ell_{\perp}$. This expression for the diffusion coefficient will only apply when y is small enough for us to use the strong turbulence scaling relations, or in other words when $\langle y^2 \rangle < L_i^2 (u_L / V_A)^4$. Larger bundles will diffuse at the rate of $L_i^2 (u_L / V_A)^4$, which is the maximal rate. For $\langle y^2 \rangle$ small, Eq. (12.12) implies that a given field line will wander perpendicular to the mean field line direction by an average amount

$$\langle y^2 \rangle^{1/2} \approx \frac{x^{3/2}}{L_i^{1/2}} \left(\frac{u_L}{V_A} \right)^2 \quad x < L_i \tag{12.13}$$

in a distance x. The fact that the rms perpendicular displacement grows faster than x is significant. It implies that if we consider a reconnection zone, a given magnetic flux element that wanders out of the zone has only a small probability of wandering back into it. We also note that y proportional to $x^{3/2}$ is a consequence of the process of Richardson diffusion that we discuss below.

When the turbulence injection scale is less than the extent of the reconnection layer, i.e. $Lx \gg L_i$ magnetic field wandering obeys the usual random walk scaling with L_x / L_i steps and the mean squared displacement per step equal to $L_i^2 (u_L / V_A)^4$. Therefore

$$\langle y^2 \rangle^{1/2} \approx (L_i x)^{1/2} (u_L / V_A)^2 \quad x > L_i \tag{12.14}$$

Using Eqs. (12.13) and (12.14) one can derive the thickness of the outflow Δ (see Fig. 12.1) and obtain (LV99):

$$V_{rec} \approx V_A \min \left[\left(\frac{L_x}{L_i} \right)^{1/2}, \left(\frac{L_i}{L_x} \right)^{1/2} \right] M_A^2, \tag{12.15}$$

where $V_A M_A^2$ is proportional to the turbulent eddy speed. This limit on the reconnection speed is fast, both in the sense that it does not depend on the resistivity, and in the sense that it represents a large fraction of the Alfvén speed when L_i and L_x are not too different and M_A is not too small. At the same time, Eq. (12.15) can lead to rather slow reconnection velocities for extreme geometries or small turbulent velocities. This, in fact, is an advantage, as this provides a natural explanation for flares of reconnection, i.e. processes which combine both periods of slow and fast magnetic reconnection. The parameters in Eq. (12.15) can change in the process

of magnetic reconnection, as the energy injected by the reconnection will produce changes in M_A and L_i. In fact, we claim that in the process of magnetic reconnection and the energy injection that this entails for magnetically dominated plasmas, one can expect both $L_i \to L_x$ and $M_A \to 1$, which will induce efficient reconnection with $V_{rec} \sim V_A$.

12.3.4 Richardson Diffusion and LV99 Model

It is well known that at scales larger than the turbulence injection scale the fluid exhibits diffusive properties. At the same time, at scales less than the turbulence injection scale the properties of diffusion are different. Since the velocity difference increases with separation, one expects that accelerated diffusion, or super diffusion should take place. This process was first described by Richardson for hydrodynamic turbulence. A similar effect is present for MHD turbulence (see Eyink and Benveniste 2013 and references therein).

Richardson diffusion can be illustrated with a simple model. Consider the growth of the separation between two particles $dl(t)/dt \sim v(l)$, which for Kolmogorov turbulence is $\sim \alpha_t l^{1/3}$, where α_t is proportional to the energy cascading rate, i.e. $\alpha_t \approx V_L^3/L$ for turbulence injected with superAlvénic velocity V_L at the scale L. The solution of this equation is

$$l(t) = [l_0^{2/3} + \alpha_t (t - t_0)]^{3/2}, \tag{12.16}$$

which at late times leads to Richardson diffusion or $l^2 \sim t^3$ compared with $l^2 \sim t$ for ordinary diffusion.

Richardson diffusion provides explosive separation of magnetic field lines. It is clear from Eq. (12.16) that the separation of magnetic field lines does not depend on the initial separation l_0 after sufficiently long intervals of time t. Potentially, one can make l_0 very small, but, realistically, l_0 should not be smaller than the scale of the marginally damped eddies l_{damp}, as the derivation of the Richardson diffusion assumes the existence of inertial-range turbulence at the scales under study. At scales less than l_{damp} diffusion is determined by the shearing by the marginally damped eddies. This is known to result in Lagrangian chaos and Lyapunov exponential separation of the points. Separation at long times in this regime does depend on the initial separation of points. In other words, in realistic turbulence up to the scale of l_{damp} the distance between the points preserves the memory of the initial separation of points, while at scales larger than l_{damp} this dependence is washed out.

Richardson diffusion is important in terms of spreading magnetic fields. In fact, the magnetic field line spread as a function of the distance measured along magnetic field lines, which we discussed in the previous subsection, is also a manifestation of

Richardson diffusion, but in space rather than in time. Below, we, however, use the time dependence of Richardson diffusion to re-derive the LV99 results.

Sweet-Parker reconnection can serve again as our guide. There we deal with Ohmic diffusion. The latter induces the mean-square distance across the reconnection layer that a magnetic field-line can diffuse by resistivity in a time t given by

$$\langle y^2(t)\rangle \sim \lambda t. \tag{12.17}$$

where $\lambda = c^2/4\pi\sigma$ is the magnetic diffusivity. The field lines are advected out of the sides of the reconnection layer of length L_x at a velocity of order V_A. Therefore, the time that the lines can spend in the resistive layer is the Alfvén crossing time $t_A = L_x/V_A$. Thus, field lines that can reconnect are separated by a distance

$$\Delta = \sqrt{\langle y^2(t_A)\rangle} \sim \sqrt{\lambda t_A} = L_x/\sqrt{S}, \tag{12.18}$$

where S is Lundquist number. Combining Eqs. (12.2) and (12.18) one gets again the well-known Sweet-Parker result, $v_{rec} = V_A/\sqrt{S}$.

Below, following Eyink et al. (2011) (henceforth ELV11) we provide a different derivation of the reconnection rate within the LV99 model. We make use of the fact that in Richardson diffusion (Kupiainen 2003) the mean squared separation of particles $\langle|x_1(t)-x_2(t)|^2\rangle \approx \epsilon t^3$, where t is time, ϵ is the energy cascading rate and $\langle\ldots\rangle$ denote an ensemble averaging. For subAlfvénic turbulence $\epsilon \approx u_L^4/(V_A L_i)$ (see LV99) and therefore analogously to Eq. (12.18) one can write

$$\Delta \approx \sqrt{\epsilon t_A^3} \approx L(L/L_i)^{1/2} M_A^2 \tag{12.19}$$

where it is assumed that $L < L_i$. Combining Eqs. (12.2) and (12.19) one gets

$$v_{rec,LV99} \approx V_A(L/L_i)^{1/2} M_A^2. \tag{12.20}$$

in the limit of $L < L_i$. Similar considerations allow to recover the LV99 expression for $L > L_i$, which differs from Eq. (12.20) by the change of the power $1/2$ to $-1/2$. These results coincide with those given by Eq. (12.15).

12.3.5 Role of Plasma Effects for Magnetic Reconnection

In the LV99 model the outflow is determined by turbulent motions that are determined by the motions on the small scales. The small scale physics in this situation gets irrelevant if the level of turbulence is fixed. Following Eyink et al. (2011) it is possible to define the criterion for the Hall effect to be important within the LV99 reconnection model.

Using the GS95 model one can estimate the pointwise ratio of the Hall electric field to the MHD motional field as

$$\frac{J/en}{u_L} \simeq \frac{c\delta B(\ell_\eta^\perp)/4\pi ne\ell_\eta^\perp}{u_L} \simeq \frac{\delta_i}{L_i} M_A S_L^{1/2} \tag{12.21}$$

where $S_L = V_A L_i/\lambda$ is the Lundquist number based on the forcing length-scale of the turbulence and $M_A = u_L/V_A$ is the Alfvénic Mach number, $\ell_\eta^\perp$ is the resistive cutoff length, J current density, and n electron density. This can be expressed as a ratio $(J/en)/u_L \simeq \delta_i/\delta_T$ of ion skin depth to the turbulent Taylor scale

$$\delta_T = L_i M_A^{-1} S_L^{-1/2}, \tag{12.22}$$

which can be interpreted heuristically as the current sheet thickness of small-scale Sweet-Parker reconnection layers. If the magnetic diffusivity in the definition of the Lundquist number is assumed to be that based on the Spitzer resistivity, given by $\lambda = \delta_e^2 v_{th,e}/\ell_{ei}$ where δ_e is the electron skin depth, $v_{th,e}$ is the electron thermal velocity, and ℓ_{ei} is the electron mean-free-path length for collisions with ions, then $S_L = \left(\frac{m_e}{m_i}\right)^{1/2} \beta^{-1/2} \left(\frac{\ell_{ei}}{\delta_e}\right)^2 \left(\frac{L_i}{\ell_{ei}}\right)$, with $\beta = v_{th,i}^2/V_A^2$ the plasma beta. Substituting into (12.21) provides

$$\frac{\delta_i}{\delta_{SP}} \simeq \left(\frac{m_i}{m_e}\right)^{1/4} (v_{th,i}/u_*)\beta^{1/4} \left(\frac{\ell_{ei}}{L_i}\right)^{1/2}, \tag{12.23}$$

which coincides precisely with the ratio defined by Yamada et al. (2006) (see their Eq. (12.6)), who proposed a ratio $\delta_i/\delta_{SP} > 1$ as the applicability criterion for Hall reconnection rather than Sweet-Parker. However, satisfaction of this criterion does not imply that the LV99 model is inapplicable! Eq.uation (12.23) states only that small scale reconnection occurs via collisionless effects and the structure of local, small-scale reconnection events should be strongly modified by Hall or other collisionless effects, possibly with an X-type structure, an ion layer thickness $\sim \delta_i$, quadrupolar magnetic fields, etc. However, these local effects do not alter the resulting reconnection velocity. See Eyink et al. (2011), Appendix B, for a more detailed discussion.

The LV99 model assumes that the thickness Δ of the reconnection layer is set by turbulent MHD dynamics (line-wandering and Richardson diffusion). Thus, self-consistency requires that the length-scale Δ must be within the range of scales where shear-Alfvén modes are correctly described by incompressible MHD. This implies a criterion for collisionless reconnection in the presence of turbulence

$$\rho_i \geq \Delta \tag{12.24}$$

with Δ calculated from Eq. (12.19) and ρ_i the ion cyclotron radius. Since $\Delta \propto L_x$, the large length-scale of the reconnecting flux structures, this criterion is far from

being satisfied in most astrophysical settings. For example, in the three cases of Table 12.1, one finds using $\Delta = LM_A^2$ that $\rho_i/\Delta \simeq 10^{-13}$ for the warm ISM, $\simeq 10^{-6}$ for post-CME sheets, and $\simeq .1$ for the magnetosphere. In the latter case the criterion (12.24) implies that the effect of collisionless plasmas are important. This is not a typical situation, however. To what extent turbulence below the Larmor radius should be accounted for is an interesting open issue that we address only very briefly in Sect. 12.5.

12.4 Numerical Testing of Theory Predictions

12.4.1 Approach to Numerical Testing

Numerical studies have proven to be a very powerful tool of the modern astrophysical research. However, one must admit their limits. The dimensionless ratios that determine the importance of Ohmic resistivity are the Lundquist and magnetic Reynolds numbers. The difference between the two numbers is not big and they are usually of the same order. Indeed, the magnetic Reynolds number, which is the ratio of the magnetic field decay time to the eddy turnover time, is defined using the injection velocity v_l as a characteristic speed instead of the Alfvén speed V_A, as in the Lundquist number. Therefore for the sake of simplicity we shall be talking only about the Lundquist number.

As we discussed in Sect. 12.2.1 because of the very large astrophysical length-scales L_x involved, astrophysical Lundquist numbers are huge, e.g. for the ISM they are about 10^{16}, while present-day MHD simulations correspond to $S < 10^4$. As the numerical resource requirements scale as N^4, where N is the ratio between the maximum and minimum scales resolved in a computational model, it is feasible neither at present nor in the foreseeable future to have simulations with realistically large Lundquist numbers. In this situation, numerical results involving magnetic reconnection cannot be directly related to astrophysical situation and a brute force approach is fruitless.

Fortunately, numerical approach is still useful for testing theories and the LV99 theory presents clear predictions to be tested for the moderate Lundquist numbers available with present-day computational facilities. Below we present the results of theory testing using this approach.

12.4.2 Numerical Simulations

To simulate reconnection a code that uses a higher-order shock-capturing Godunov-type scheme based on the essentially non oscillatory (ENO) spatial reconstruction and Runge-Kutta (RK) time integration was used to solve isothermal

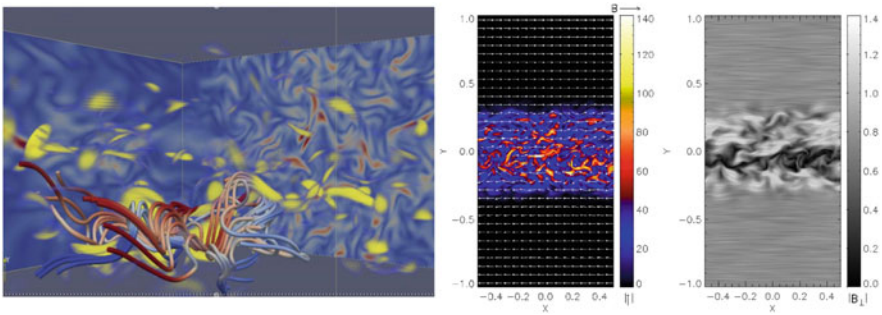

Fig. 12.5 Visualization of reconnection simulations in Kowal et al. (2009, 2012). *Left panel*: magnetic field in the reconnection region. Large perturbations of magnetic field lines arise from reconnection rather than driving; the latter is subAlfvénic. The color corresponds to the polarization of magnetic component B_x. *Central panel*: current intensity and magnetic field configuration during stochastic reconnection. We show a slice through the middle of the computational box in the xy plane after twelve dynamical times for a typical run. The guide field is perpendicular to the page. The intensity and direction of the magnetic field is represented by the length and direction of the arrows. The color bar gives the intensity of the current. The reversal in B_x is confined to the vicinity of y=0 but the current sheet is strongly disordered with features that extend far from the zone of reversal. *Right panel*: representation of the magnetic field in the reconnection zone with textures

non-ideal MHD equations. For selected simulations plasma effects were simulated using accepted procedures (Kowal et al. 2009).

The driving of turbulence was performed using wavelets in Kowal et al. (2009) and in real space in Kowal et al. (2012). In both cases the driving was supposed to simulate pre-existing turbulence. The visualization of simulations is provided in Fig. 12.5.

12.4.3 Dependence on Resistivity, Turbulence Injection Power and Turbulence Scale

As we show below, simulations in Kowal et al. (2009, 2012) provided very good correspondence to the LV99 analytical predictions for the dependence on resistivity, i.e. no dependence on resistivity for sufficiently strong turbulence driving, and the injection power, i.e. $V_{rec} \sim P_{inj}^{1/2}$. The corresponding dependence is shown in Fig. 12.6.

The measured dependence on the turbulence scale was a bit more shallow compared to the LV99 predictions (see Fig. 12.7). This may be due to the existence of an inverse cascade that changes the driving from the idealized assumptions in LV99 theory.

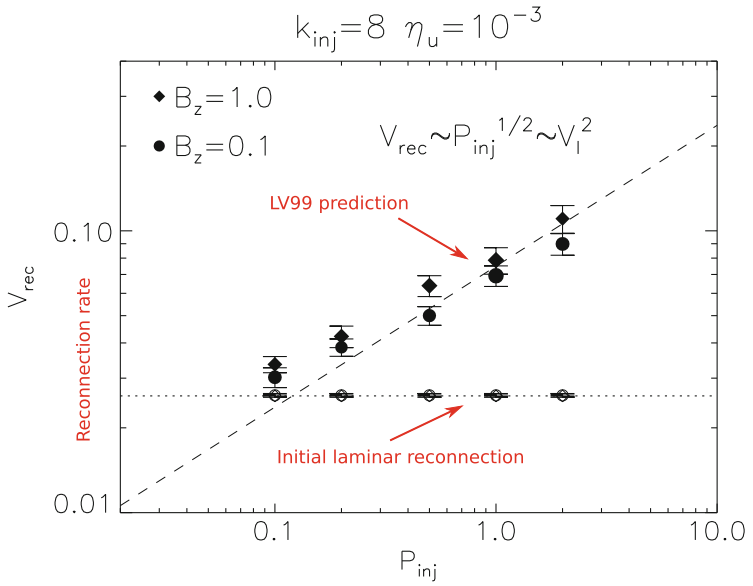

Fig. 12.6 The dependence of the reconnection velocity on the injection power for different simulations with different drivings. The predicted LV99 dependence is also shown. P_{inj} and k_{inj} are the injection power and scale, respectively, B_z is the guide field strength, and η_u the value of uniform resistivity coefficient. From Kowal et al. (2012)

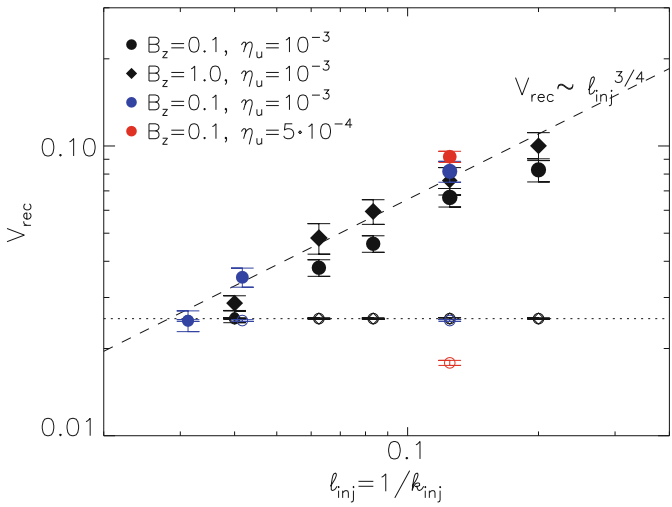

Fig. 12.7 The dependence of the reconnection velocity on the injection scale. From Kowal et al. (2012)

12.4.4 Dependence on Guide Field Strength, Anomalous Resistivity and Viscosity

The simulations did not reveal any dependence on the strength of the guide field B_z (see Fig. 12.6). This raises an interesting question. In the limit where the parallel wavelength of the strong turbulent eddies is less than the length of the current sheet, we can rewrite the reconnection speed as

$$V_{rec} \approx \left(\frac{PL_x}{V_{Ax}}\right)^{1/2} \frac{1}{k_\parallel V_A}. \tag{12.25}$$

Here P is the power in the strong turbulent cascade, L_x and V_{Ax} are the length scale and Alfvén velocity in the direction of the reconnecting field, and V_A is the total Alfvén velocity, including the guide field. The parallel wavenumber, $k_\parallel$, is characteristic of the large scale strongly turbulent eddies. We have assumed that such eddies are smaller than the size of the current sheet. The point of rewriting the reconnection speed in this way is that it is insensitive to assumptions about the connection between the input power and driving scale and the parameters of the strongly turbulent cascade.

In a physically realistic situation, the dynamics that drive the turbulence, whatever they are, provide a characteristic frequency and input power. Since the guide field enters only in the combination $k_\parallel V_A$, i.e. through the eddy turn over rate, this implies that varying the guide field will not change the reconnection speed. However, in the numerical simulations cited above the driving forces are independent of time scale, and sensitive to length scale, so getting the physically realistic scaling is unexpected. Further complicating matters, we note that the dependence on length scale, described in the previous section, is roughly what we expect if $k_\parallel$ is given by the forcing wavenumber.

This is the only clear discrepancy between the simulations and our predictions. It is clearly important to understand its nature. One possibility is that the transfer of energy from the weak turbulence driven by isotropic forcing to the strongly turbulent eddies does not proceed in the expected manner. This may be due to the effect of the strong magnetic shear when a guide field is present. Alternatively, the periodicity of the box, or the possibility that some wave modes may leave the computational box faster than the nonlinear decay rate, may skew the weakly turbulent spectrum. The latter possibilities can be tested by simulating strong turbulence and comparing the results with equation (12.25). The former will require a more detailed theoretical and computational study of the nature of the strong turbulence in the presence of strong magnetic shear.

The left panel of Fig. 12.8 shows the dependence of the reconnection rate on viscosity. This can be explained as the effect of the finite inertial range of turbulence. For an extended range of motions, LV99 does not predict any viscosity dependence. However, for numerical simulations the range of turbulent motions is very limited

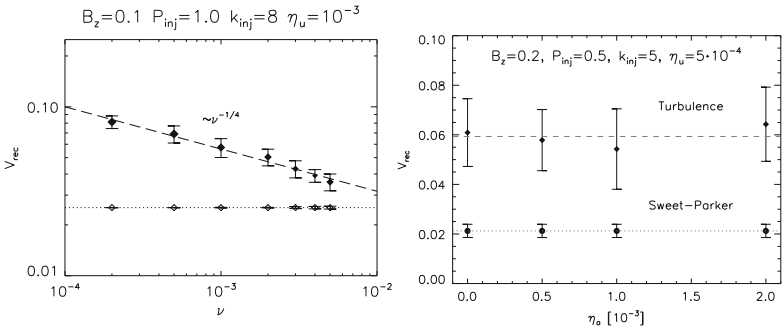

Fig. 12.8 *Left panel*. the dependence of the reconnection velocity on viscosity. From Kowal et al. (2012). *Right panel*. the dependence of reconnection velocity on anomalous resistivity. From Kowal et al. (2009)

and any additional viscosity decreases the resulting velocity dispersion and therefore the field wandering.

LV99 predicted that in the presence of sufficiently strong turbulence, plasma effects should not play a role. The accepted way to simulate plasma effects within MHD code is to use anomalous resistivity. The results of the corresponding simulations are shown in the right panel of Fig. 12.8 and they confirm that the change of the anomalous resistivity does not change the reconnection rate.

12.4.5 Structure of the Reconnection Region

The internal structure of the reconnection region is important, both for the role it plays in determining the overall reconnection speed, and for what it tells us about the nature of local electric currents. We can imagine two extreme pictures. First, the magnetic shear might be concentrated in a narrow, albeit highly distorted sheet, whose width is determined by microphysics. In this case the outflow region would be much broader than the current sheet and particle acceleration would take place in a nearly two dimensional, and highly singular, region. The electric field in the current sheet would be very large, much larger than one would be able to simulate directly. At the other extreme, the current sheet and the outflow zone may roughly coincide. In this case the current sheet is broad and the currents are distributed widely within a three dimensional volume. The electric fields would be roughly similar to what we expect in homogeneous turbulence. In the former case the turbulence within the current sheet is difficult to estimate. In the latter case, it would be similar to the turbulence within a statistically homogeneous volume, of the sort that we can simulate. This would imply that the basic derivation of reconnection speeds in LV99 is valid and particle acceleration takes place in a broad volume. While both of these models are caricatures, they give a good sense of the basic issues at stake.

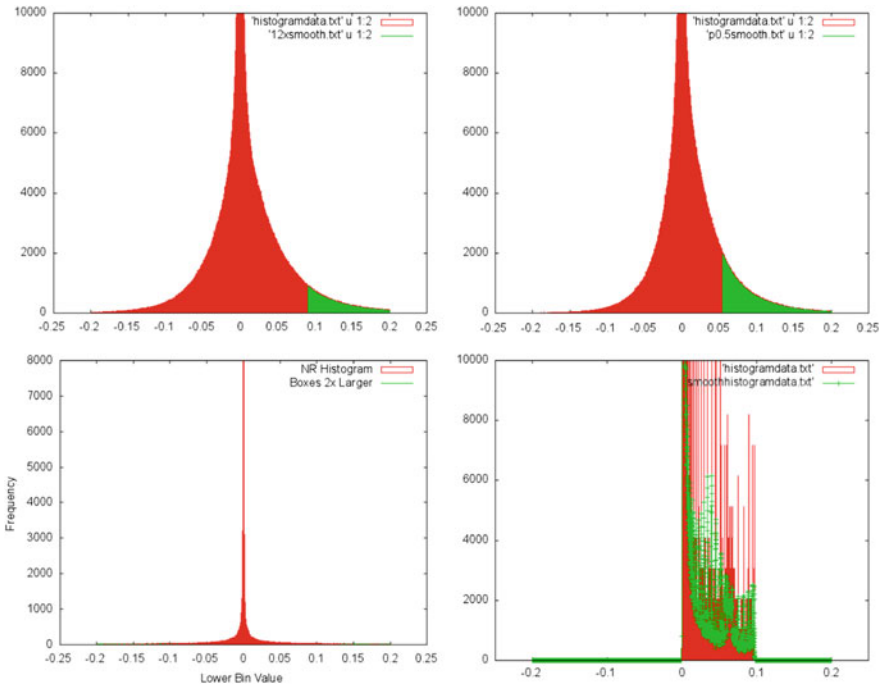

Fig. 12.9 These figures show histograms of the gradient of the reversing component of the large scale magnetic field in the direction normal to the unperturbed current sheet, i.e. $\partial_y B_x$. *Upper left panel* is for the highest power simulation, P=1. *Upper right panel* is for P=0.5. *Lower left* is for P=1 but with no large scale magnetic field reversal, i.e. simply locally driven strong turbulence. Bins with twice the number of cells as the corresponding bin with the opposite sign of $\partial_y B_x$ are shown in *green*. *Lower right* shows the first simulation in the absence of turbulent forcing. From Vishniac et al. (2012)

The structure of the reconnection region was analyzed by Vishniac et al. (2012) based on the numerical work by Kowal et al. (2009). While this paper only examined simulations with relatively large forcing, the results seem to favour the latter picture, in which the reconnection region is broad, the magnetic shear is more or less coincident with the outflow zone, and the turbulence within it is broadly similar to turbulence in a homogeneous system. In particular, this analysis showed that peaks in the current were distributed throughout the reconnection zone, and that the width of these peaks were not a strong function of their strength. The single best illustration of the results is shown in Fig. 12.9 which shows histograms of magnetic field gradients in the simulations with strong and moderate driving power, with no magnetic field reversal but with driven turbulence, and with no driven turbulence at all, but a passive magnetic field reversal (i.e. Sweet-Parker reconnection). A few features stand out in this figure. First, all the simulations with driven turbulence have a roughly gaussian distribution of magnetic field gradients. In the case with no field reversal (panel c) the peak is narrow and symmetric around zero. In the presence of a

large scale field reversal the peak is slightly broadened, and skewed. (The simulation without reconnection was run at a lower resolution, so the total number of cells is smaller by a factor of 8.) Finally, the last panel shows a very spiky distribution of points to the right of the origin. The spikiness is an artifact of the numerical grid. In the absence of turbulence the same values tend to repeat. That occupied bins are all for positive magnetic field gradients is a trivial consequence of the background solution and the laminar nature of Sweet-Parker reconnection.

It is striking that turbulent reconnection does not produce any strong feature corresponding to a preferred value of the magnetic field gradient. Instead one sees a systematic bias towards large positive values. We conclude from the lack of coherent features within the outflow zone, and the broad distribution of values of the gradient of the magnetic field, that the second picture is best. The current sheet and the outflow zone are roughly coincident and this volume is filled with turbulent structures.

One weakness of this analysis is that it has been tested only for relatively strong magnetic turbulence. Although the driven turbulence in these simulations was subalfvenic, they were not very weak. We can expect that the skew in Fig. 12.9 will become stronger at as the turbulent velocities are turned down. At some point the mean gradient should begin to affect the turbulent spectrum.

12.4.6 Testing of Magnetic Richardson Diffusion

As we discussed, the LV99 model is intrinsically related to the concept of Richardson diffusion in magnetized fluids. Thus by testing the Richardson diffusion of magnetic field, one also provides tests for the theory of turbulent reconnection.

The first numerical tests of Richardson diffusion were related to magnetic field wandering predicted in LV99 (Maron et al. 2004; Lazarian et al. 2004; Beresnyak 2013). In Fig. 12.10 we show the results obtained in Lazarian et al. (2004). There we clearly see different regimes of magnetic field diffusion, including the $y \sim x^{3/2}$ regime. This is a manifestation of the spatial Richardson diffusion.

A direct testing of the temporal Richardson diffusion of magnetic field-lines was performed recently in Eyink et al. (2013). For this experiment, stochastic fluid trajectories had to be tracked backward in time from a fixed point in order to determine which field lines at earlier times would arrive to that point and be resistively "glued together". Hence, many time frames of an MHD simulation were stored so that equations for the trajectories could be integrated backward. The results of this study are illustrated in Fig. 12.10. The left panel shows the trajectories of the arriving magnetic field-lines, which are clearly widely dispersed backward in time, more resembling a spreading plume of smoke than a single "frozen-in" line. Quantitative results are presented in the right panel, which plots the root-mean-square line dispersion in directions both parallel and perpendicular to the local mean magnetic field. Times are in units of the resistive time $1/j_{rms}$ determined by the rms current value and distances in units of the resistive length λ/j_{rms}. The

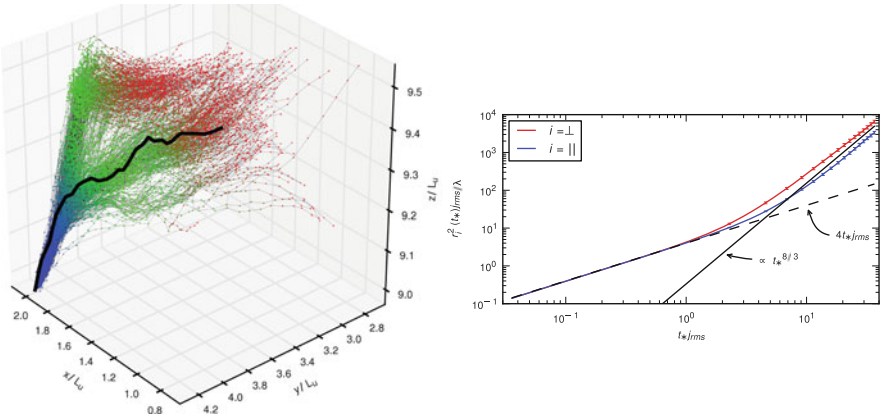

Fig. 12.10 *Left panel* stochastic trajectories that arrive at a fixed point in the archived MHD flow, color-coded *red*, *green*, and *blue* from earlier to later times. From Eyink et al. (2013). *Right panel*. mean-square dispersion of field-lines backwards in time, with *red* for direction parallel and *blue* for direction perpendicular to the local magnetic field. From Eyink et al. (2013)

dashed line shows the standard diffusive estimate $4\lambda t$, while the solid line shows the Richardson-type power-law $t^{8/3}$. Note that this simulation exhibited a $k^{-3/2}$ energy spectrum (or Hölder exponent 1/4) for the velocity and magnetic fields, similar to other MHD simulations at comparable Reynolds numbers, and the self-consistent Richardson scaling is with exponent 8/3 rather 3. Although a $t^{8/3}$ power-law holds both parallel and perpendicular to the local field direction, the prefactor is greater in the parallel direction, due to backreaction of the magnetic field on the flow via the Lorentz force. The implication of these results is that standard diffusive motion of field-lines holds for only a very short time, of order of the resistive time, and is then replaced by super-diffusive, explosive separation by turbulent relative advection. This same effect should occur not only in resistive MHD but whenever there is a long power-law turbulent inertial range. Whatever plasma mechanism of line-slippage holds at scales below the ion gyroradius— electron inertia, pressure anisotropy, etc.—will be accelerated and effectively replaced by the ideal MHD effect of Richardson dispersion.

12.5 Observational Consequences and Tests

Historically, studies of reconnection were motivated by observations of Solar flares. There we deal with the collisionless turbulent plasmas and it is important to establish whether plasma microphysics or LV99 turbulent dynamics determine the observed solar reconnection.

Qualitatively, one can argue that there is observational evidence in favor of the LV99 model. For instance, observations of the thick reconnection current outflow

regions observed in the Solar flares (Ciaravella and Raymond 2008) were predicted within LV99 model at the time when the competing plasma Hall term models were predicting X-point localized reconnection. However, as plasma models have evolved to include tearing and formation of magnetic islands (see Drake et al. 2010) it is necessary to get to a quantitative level to compare the predictions from the competing theories and observations.

To be quantitative one should relate the idealized model LV99 turbulence driving to the turbulence driving within solar flares. In LV99 the turbulence driving was assumed isotropic and homogeneous at a distinct length scale L_{inj}. A general difficulty with observational studies of turbulent reconnection is the determination of L_{inj}. One possible approach is based on the relation $\varepsilon \simeq u_L^4/V_A L_{inj}$ for the weak turbulence energy cascade rate. The mean energy dissipation rate ε is a source of plasma heating, which can be estimated from observations of electromagnetic radiation (see more in ELV11). However, when the energy is injected from reconnection itself, the cascade is strong and anisotropic from the very beginning. If the driving velocities are sub-Alfvénic, turbulence in such a driving is undergoing a transition from weak to strong at the scale LM_A^2 (see Sect. 12.3.4). The scale of the transition corresponds to the velocity $M_A^2 V_A$. If turbulence is driven by magnetic reconnection, one can expect substantial changes of the magnetic field direction corresponding to strong turbulence. Thus it is natural to identify the velocities measured during the reconnection events with the strong MHD turbulence regime. In other words, one can use:

$$V_{rec} \approx U_{obs,turb}(L_{inj}/L_x)^{1/2}, \tag{12.26}$$

where $U_{obs,turb}$ is the spectroscopically measured turbulent velocity dispersion. Similarly, the thickness of the reconnection layer should be defined as

$$\Delta \approx L_x(U_{obs,turb}/V_A)(L_{inj}/L_x)^{1/2}. \tag{12.27}$$

Naturally, this is just a different way of presenting LV99 expressions, but taking into account that the driving arises from reconnection and therefore turbulence is strong from the very beginning (see more in Eyink et al. 2013. The expressions given by Eqs. (12.26) and (12.27) can be compared with observations in (Ciaravella and Raymond 2008). There, the widths of the reconnection regions were reported in the range from $0.08L_x$ up to $0.16L_x$ while the observed Doppler velocities in the units of V_A were of the order of 0.1. It is easy to see that these values are in a good agreement with the predictions given by Eq. (12.27). We note, that if we associate the observed velocities with isotropic driving of turbulence, which is unrealistic for the present situation, then a discrepancy with Eq. (12.27) would appear. Because of that Ciaravella and Raymond (2008) did not get quite as good quantitative agreement between observations and theory as we did, but still within observational uncertainties. In Sych et al. (2009), authors explaining quasi-periodic pulsations in observed flaring energy releases at an active region above the sunspot,

proposed that the wave packets arising from the sunspots can trigger such pulsations. This is exactly what is expected within the LV99 model.

As we discussed in Sect. 12.3.5 the criterion for the application of LV99 theory is that the outflow region is much larger than the ion Larmor radius $\Delta \gg \rho_i$. This is definitely satisfied for the solar atmosphere where the ratio of Δ to ρ_i can be larger than 10^6. Plasma effects can play a role for small scale reconnection events within the layer, since the dissipation length based on Spitzer resistivity is ~ 1 cm, whereas $\rho_i \sim 10^3$ cm (Table 12.1). However, as we discussed earlier, this does not change the overall dynamics of turbulent reconnection.

Reconnection throughout most of the heliosphere appears similar to that in the Sun. For example, there are now extensive observations of reconnection jets (outflows, exhausts) and strong current sheets in the solar wind (Gosling 2012). The most intense current sheets observed in the solar wind are very often not observed to be associated with strong (Alfvénic) outflows and have widths at most a few tens of the proton inertial length δ_i or proton gyroradius ρ_i (whichever is larger). Small-scale current sheets of this sort that do exhibit observable reconnection have exhausts with widths at most a few hundreds of ion inertial lengths and frequently have small shear angles (strong guide fields) (Gosling et al. 2007; Gosling and Szabo 2008). Such small-scale reconnection in the solar wind requires collisionless physics for its description, but the observations are exactly what would be expected of small-scale reconnection in MHD turbulence of a collisionless plasma (Vasquez et al. 2007). Indeed, LV99 predicted that the small-scale reconnection in MHD turbulence should be similar to large-scale reconnection, but with nearly parallel magnetic field lines and with "outflows" of the same order as the local, shear-Alfvénic turbulent eddy motions. It is worth emphasizing that reconnection in the sense of flux-freezing violation and disconnection of plasma and magnetic fields is required at every point in a turbulent flow, not only near the most intense current sheets. Otherwise fluid motions would be halted by the turbulent tangling of frozen-in magnetic field lines. However, except at sporadic strong current sheets, this ubiquitous small-scale turbulent reconnection has none of the observable characteristics usually attributed to reconnection, e.g. exhausts stronger than background velocities, and would be overlooked in observational studies which focus on such features alone.

However, there is also a prevalence of very large-scale reconnection events in the solar wind, quite often associated with interplanetary coronal mass ejections and magnetic clouds or occasionally magnetic disconnection events at the heliospheric current sheet (Phan et al. 2009; Gosling 2012). These events have reconnection outflows with widths up to nearly 10^5 of the ion inertial length and appear to be in a prolonged, quasi-stationary regime with reconnection lasting for several hours. Such large-scale reconnection is as predicted by the LV99 theory when very large flux-structures with oppositely-directed components of magnetic field impinge upon each other in the turbulent environment of the solar wind. The "current sheet" producing such large-scale reconnection in the LV99 theory contains itself many ion-scale, intense current sheets embedded in a diffuse turbulent background of weaker (but still substantial) current. Observational efforts addressed to proving/disproving the LV99 theory should note that it is this broad zone of more

diffuse current, not the sporadic strong sheets, which is responsible for large-scale turbulent reconnection. Note that the study (Eyink et al. 2013) showed that standard magnetic flux-freezing is violated at general points in turbulent MHD, not just at the most intense, sparsely distributed sheets. Thus, large-scale reconnection in the solar wind is a very promising area for LV99. The situation for LV99 generally gets better with increasing distance from the sun, because of the great increase in scales. For example, reconnecting flux structures in the inner heliosheath could have sizes up to $\sim$100 AU, much larger than the ion cyclotron radius $\sim 10^3$ km (Lazarian and Opher 2009).

The magnetosphere is another example that is under active investigation by the reconnection community. The situation there is different, as $\Delta \sim \rho_i$ is the general rule and we expect plasma effects to be dominant. Turbulence of whistler waves, e.g. electron MHD (EMHD) turbulence may play its role, however. For instance, Huang et al. (2012) reported a magnetotail event in which they claim that turbulent electromotive force is responsible for reconnection. The turbulence at those scales is not MHD. We may speculate that the LV99 can be generalized for the case of EMHD and apply to such events. This should be the issue of further studies.

It may be worth noting that the possibility of in-situ measurements of magnetospheric reconnection make it a very attractive subject for the reconnection community. Upcoming missions like the Magnetospheric Multiscale Mission (MMS), set to launch in 2014, will provide detailed observations of reconnection diffusion regions, energetic particle acceleration, and micro-turbulence in the magnetospheric plasma. In addition to the exciting prospect of better understanding of the near-Earth space environment, the hope has been expressed that this mission will provide insight into magnetic reconnection in a very wide variety of astrophysical and terrestrial plasmas. We believe that magnetospheric observations may indeed shed light on magnetic reconnection in man-made settings such as fusion machines (tokamaks or spheromaks) and laboratory reconnection experiments, which also involve collisionless plasmas and overall small length scales. However, magnetospheric reconnection is a rather special, non-generic case in astrophysics, with Δ of the order or less than ρ_i, while the larger scales involved in most astrophysical processes imply that $\Delta \gg \rho_i$. We claim that this is the domain where turbulence and the broadening of Δ that it entails must be accounted for. Thus, magnetospheric reconnection, in the opinion of the present reviewers, is a special case which will provide insight mainly into micro-scale aspects of reconnection, which are of more limited interest in general astrophysical environments. Reconnection elsewhere in the solar system, including the sun, its atmosphere, and the larger heliosphere (solar wind, heliosheath, etc.) are better natural laboratories for observational study of generic astrophysical reconnection in both collisionless and collisional environments.

12.6 Extending LV99 Theory

12.6.1 Reconnection in Partially Ionized Gas

Turbulence in the partially ionized gas is different from that in fully ionized plasmas. One of the critical differences arises from the viscosity caused by neutrals atoms. This results in the media viscosity being substantially larger than the media resistivity. The ratio of the former to the latter is called the Prandtl number and in what follows we consider high Prandtl number turbulence. In reality, MHD turbulence in the partially ionized gas is more complicated as decoupling of ions and neutrals and other complicated effects occur at sufficiently small scale. The discussion of these regimes is given in Lazarian et al. (2004). However, for the purposes of reconnection, we believe that a simplified discussion below is adequate, as follows from the fact that we discussed earlier, namely, that the LV99 reconnection is determined by the dynamics of large scales of turbulent motions.

The high Prandtl number turbulence was studied numerically in Cho et al. (2002, 2003); Schekochihin et al. (2004) and theoretically in Lazarian et al. (2004). What is important for our present discussion is that for scales larger than the viscous damping scale the turbulence follows the usual GS95 scaling, while it develops a shallow power law magnetic tail and steep velocity spectrum below the viscous damping scale $\ell_{\perp,crit}$. The existence of the GS95 scaling at sufficiently large scales means that our considerations about Richardson diffusion and magnetic reconnection that accompany it should be valid at these scales. Thus, our goal is to establish the scale of current sheets starting from where the Richardson diffusion will induce the accelerated separation of magnetic field lines.

In high Prandtl number media the GS95-type turbulent motions decay at the scale $l_{\perp,crit}$, which is much larger than the scale at which Ohmic dissipation becomes important. Thus over a range of scales less than $l_{\perp,crit}$ to some much smaller scale magnetic field lines preserve their identity. These magnetic field lines are being affected by the shear on the scale $l_{\perp,crit}$, which induces a new regime of turbulence described in Cho et al. (2002); Lazarian et al. (2004).

To establish the range of scales at which magnetic fields perform Richardson diffusion one can observe that the transition to the Richardson diffusion is expected to happen when field lines get separated by the perpendicular scale of the critically damped eddies $l_{\perp,crit}$. The separation in the perpendicular direction starts with the scale r_{init} following the Lyapunov exponential growth with the distance l measured along the magnetic field lines, i.e. $r_{init}\exp(l/l_{\parallel,crit})$, where $l_{\parallel,crit}$ corresponds to critically damped eddies with $l_{\perp,crit}$. It seems natural to associate r_{init} with the separation of the field lines arising from the action of Ohmic resistivity on the scale of the critically damped eddies

$$r_{init}^2 = \eta l_{\parallel,crit}/V_A, \tag{12.28}$$

where η is the Ohmic resistivity coefficient.

The problem of magnetic line separation in turbulent fluids was considered for chaotic separation in smooth, with large scale motions at a single large scale flows by Rechester and Rosenbluth (1978) and for superdiffusive separation in turbulent plasmas with arbitrary Alfvenic Mach number in (see Lazarian (2006); Lazarian and Yan (2014)). Following the logic in the paper and taking into account that the largest shear arises from the critically damped eddies, it is possible to determine the distance to be covered along magnetic field lines before the lines separate by the distance larger than the perpendicular scale of viscously damped eddies is equal to

$$L_{RR} \approx l_{\parallel,crit} \ln(l_{\perp,crit}/r_{init}) \tag{12.29}$$

Taking into account Eq. (12.28) and that

$$l^2_{\perp,crit} = \nu l_{\parallel,crit}/V_A, \tag{12.30}$$

where ν is the viscosity coefficient. Thus Eq. (12.29) can be rewritten

$$L_{RR} \approx l_{\parallel,crit} \ln Pt \tag{12.31}$$

where $Pt = \nu/\eta$ is the Prandtl number.

If the current sheets are much longer than L_{RR}, then magnetic field lines undergo Richardson diffusion and according to Eyink et al. (2011) the reconnection follows the laws established in LV99. In other words, on scales significantly larger than the viscous damping scale LV99 reconnection is applicable. At the same time on scales less than L_{RR} magnetic reconnection may be slow.[7] This small scale reconnection regime requires further studies. For instance, results of laminar reconnection in the partially ionized gas obtained analytically in Vishniac and Lazarian (1999) and studied numerically by Heitsch and Zweibel (2003) can be applicable. This approach has been recently used by Leake et al. (2012) to explain chromospheric reconnection that takes place in weakly ionized plasmas. In this review we, however, are interested at reconnection at large scales and therefore do not dwell on small scale phenomena.

For the detailed structure of the reconnection region in the partially ionized gas the study in Lazarian et al. (2004) is relevant. There the magnetic turbulence below the scale of the viscous dissipation is accounted for. However, those magnetic structures on the small scales cannot change the overall reconnection velocities.

[7]Incidentally, this can explain the formation of density fluctuations on scales of thousands of Astronomical Units, that are observed in the ISM.

12.6.2 Development of Turbulence Due to Magnetic Reconnection

Astrophysical fluids are generically turbulent. However, even if the initial magnetic field configuration is laminar, magnetic reconnection ought to induce turbulence due to the outflow (LV99, Lazarian and Vishniac 2009). This effect was confirmed by observing the development of turbulence both in recent 3D Particle in Cell (PIC) simulations (Karimabadi et al. 2013) and 3D MHD simulations (Beresnyak 2013; Kowal et al. in prep.).

Earlier on, the development of chaotic structures due to tearing was reported in Loureiro et al. (2009) as well as in subsequent publications (see Bhattacharjee et al. 2009). However, we should stress that there is a significant difference between turbulence development in 2D and 3D simulations. As we discussed in Sect. 12.3.2 the very nature of turbulence is different in 2D and 3D. In addition, the effect of the outflow is very different in simulations with different dimentionality. For instance, in 2D the development of the Kelvin-Hemholtz instability is suppressed by the field that is inevitably directed parallel to the outflow. On the contrary, the outflow can induce this instability in the generic 3D configuration. In general, we do expect realistic 3D systems to be more unstable and therefore prone to development of turbulence. This corresponds well to the results of 3D simulations that we refer to.

Beresnyak (2013) studied the properties of reconnection-driven turbulence and found its correspondence to those expected for MHD turbulence (see Sect. 12.3.2). The difference with isotropically driven turbulence is that magnetic energy is observed to be dominant compared with kinetic energy. The periodic boundary conditions adopted in Beresnyak (2013) limits the time span over which magnetic reconnection can be studied and therefore the simulations focus on the process of establishing reconnection. Nevertheless, as the simulations reveal a nice turbulence power law behavior, one can apply the approach of turbulent reconnection and closely connected to it, Richardson diffusion (see Sect. 12.3.4).

Beresnyak (2013, private communication) used LV99 approach and obtained expressions describing the evolution of the reconnection layer in the transient regime of turbulence development that he observes. Below we provide our theoretical account of the results in Beresnyak (2013) using our understanding of turbulent reconnection also based on LV99 theory. However, we get expressions which differ from those by Beresnyak.

The logic of our derivation is really simple. As the magnetic fluxes get into contact the width of the reconnection layer Δ is growing. The rate at which this happens is limited by the mixing rate induced by the eddies at the scale Δ, i.e.

$$\frac{1}{\Delta}\frac{d\Delta}{dt} \approx g\frac{V_\Delta}{\Delta} \tag{12.32}$$

with a factor g which takes into account possible inefficiency in the diffusion process. As V_Δ is a part of the turbulent cascade, i.e. the mean value of $V_\Delta^2 \approx \int \Phi(k_1) dk_1$, where

$$\Phi = C_k \epsilon^{2/3} k_1^{-5/3}, \tag{12.33}$$

and C_k is a Kolmogorov constant, which for ordinary MHD turbulence is calculated in Beresnyak (2012), but in our special case may be different. If the energy dissipation rate ε were time-independent, then the layer width would be implied by Eqs. (12.32) and (12.33) to grow according to Richardson's law $\Delta^2 \sim \varepsilon t^3$. However, in the transient regime considered, energy dissipation rate is evolving. If the y-component of the magnetic field is reconnecting and the cascade is strong, then the mean value of the dissipation rate ϵ is

$$\epsilon \approx \beta V_{Ay}^2 / (\Delta / V_\Delta), \tag{12.34}$$

where β is another coefficient measuring the efficiency of conversion of mean magnetic energy into turbulent fluctuations. This coefficient can be obtained from numerical simulations.

The ability of the cascade to be strong from the very beginning follows from the large perturbations of the magnetic fields by magnetic reconnection, while magnetic energy can still dominate the kinetic energy. The latter factor that can be experimentally measured is given by a parameter r_A. With this factor and making use of Eqs. (12.33) and (12.34), the expression for V_Δ can be rewritten in the following way:

$$V_\Delta \approx C_k r_A (V_{Ay}^2 V_\Delta \beta)^{2/3} \tag{12.35}$$

where the dependences on $k_1 \sim 1/\Delta$ cancel out.

This provides the expression for the turbulent velocity at the injection scale V_Δ

$$V_\Delta \approx (C_K r_A)^{3/4} V_{Ay} \beta^{1/2} \tag{12.36}$$

as a function of the experimentally measurable parameters of the system. Thus the growth of the turbulent reconnection zone is according to Eq. (12.32)

$$\frac{d\Delta}{dt} \approx g \beta^{1/2} (C_K r_A)^{3/4} V_{Ay} \tag{12.37}$$

which predicts the nearly constant growth of the outflow region as seen in Fig. 12.3 in Beresnyak (2013).

Using the values of the numerical constants provided to us by Beresnayk we get a fair correspondence with the results of simulations in Beresnyak (2013). However, we feel that further testings are necessary.

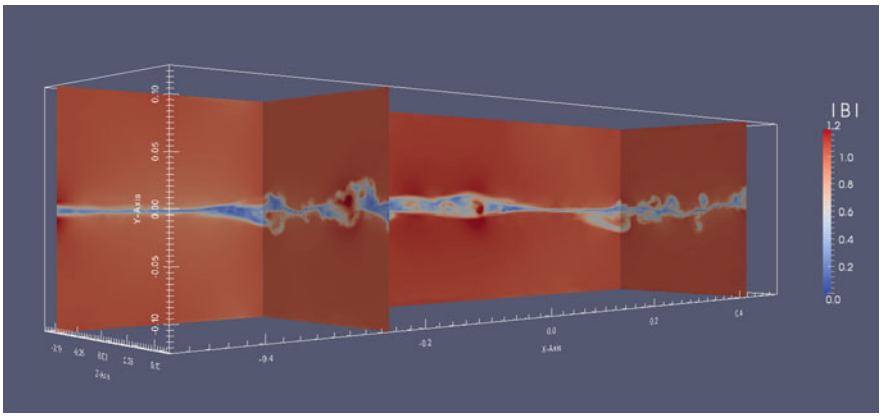

Fig. 12.11 Visualization of the model of turbulence generated by the seed reconnection from Kowal et al. (in prep.). Three different cuts (one XY plane at Z=-0.1 and two YZ-planes at X=-0.25 and X=0.42) through the computational domain show the strength of magnetic field $|\mathbf{B}|$ at the evolution time $t = 1.0$. Kelvin-Helmholtz-type structures are well seen in the planes perpendicular to the reconnecting magnetic component B_x. In the Z direction, the Kelvin-Helmholtz instability is slightly suppressed by the guide field of the strength $B_z = 0.1B_x$ (with $B_x = 1.0$ initially). The initial current sheet is located along the XZ plane at Y=0.0. A weak ($E_{kin} \approx 10^{-4} E_{mag}$) random velocity field was imposed initially in order to seed the reconnection

As the reconnection gets into the steady state regime, one expects the outflow to play an important role and therefore the reconnection rate gets modified. This regime cannot be studied in periodic box simulations like those in Beresnyak (2013) as they require studies for more than one Alfven crossing time. Studies with open boundary conditions are illustrated by Fig. 12.11 from our new study.

The equations for the reconnection rate were obtained in LV99 for the isotropic injection of energy. For the case of anisotropic energy injection of turbulence we should apply the approach in Sect. 12.5. Using Eq. (12.27) and identifying V_Δ with the total velocity dispersion, which is similar to the use of $U_{obs,turb}$ in Eq. (12.26) one can get

$$V_{rec} \approx V_\Delta (\Delta / L_x)^{1/2} \tag{12.38}$$

where the mass conservation condition provides the relation $V_{rec} L_x \approx V_{Ay} \Delta$. Using the latter condition one gets

$$V_{rec} \approx V_{Ay} (C_K r_A)^{3/2} \beta \tag{12.39}$$

which somewhat slower than the rate at which the reconnection layer was growing initially. The latter behavior of reconnection is also present for the Sweet-Parker

reconnection, since the reconnection rate can be faster even before the formation of steady state current sheet (see Kowal et al. 2009).

We are going to compare the prediction given by Eq. (12.39) against the results of recent simulations illustrated by Fig. 12.11. The figure shows a few slices of the magnetic field strength $|\mathbf{B}|$ through the three-dimensional computational domain with dimensions $L_x = 1.0$ and $L_y = L_z = 0.25$. The simulation was done with the resolution $2048 \times 512 \times 512$. Open boundary conditions along the X and Y directions allowed studies of steady state turbulence. At the presented time $t = 1.0$ the turbulence strength increased by two orders of magnitude from its initial value of $E_{kin} \approx 10^{-4} E_{mag}$. Initially, only the seed velocity field at the smallest scales was imposed (a random velocity vector was set for each cell). We expect that most of the injected energy comes from the Kelvin-Helmholtz instability induced by the local interactions between the reconnection events, which dominates in the Z-direction, along which a weak guide field is imposed ($B_z = 0.1 B_x$). As seen in the planes perpendicular to B_x in Fig. 12.11, Kelvin-Helmholtz-like structures are already well developed at time $t = 1.0$. Turbulent structures are also observed within the XY-plane, which probably are generated by the strong interactions of the ejected plasma from the neighboring reconnection events. More detailed analysis of the spectra of turbulence and efficiency of the Kelvin-Helmholtz instability as the turbulent injection mechanism are presented in Kowal et al. (in prep.).

12.6.3 Effect of Energy Dissipation in the Reconnection Layer

In the original LV99 paper it was argued that only a small fraction of the energy stored in the magnetic field is lost during large-scale reconnection and the magnetic energy is instead converted nearly losslessly to kinetic energy of the outflow. This can only be true, however, when the Alfvénic Mach number $M_A = u_L / V_A$ is small enough. If M_A becomes too large, then it was argued in ELV11 that energy dissipation in the reconnection layer becomes non-negligible compared to the available magnetic energy and there is a consequent reduction of the outflow velocity. Note that even if M_A is initially small, reconnection may drive stronger turbulence (see previous subsection) and increase the fluctuation velocities u_L in the reconnection layer. This scenario may be relevant to post-CME reconnection, for example, where there is empirical evidence that the energy required to heat the plasma in the reconnection layer ("current sheet") to the observed high temperatures is from energy cascade due to turbulence generated by the reconnection itself (Susino et al. 2013). In addition, V_A within the reconnection layer will be smaller than the upstream values, because of annihilation of the anti-parallel components, which will further increase the Alfvénic Mach number. If M_A rises to a sufficiently large value, then the energy dissipated becomes large enough to cause a reduction in the outflow velocity v_{out} below the value V_A assumed in LV99 and the predictions of the theory must be modified. We consider here briefly the modification proposed in ELV11 and some of its consequences.

The effect of turbulent dissipation can be estimated from steady-state energy balance in the reconnection layer:

$$\frac{1}{2}v_{out}^3\Delta = \frac{1}{2}V_A^2 v_{ren}L_x - \varepsilon L_x\Delta, \tag{12.40}$$

where kinetic energy carried away in the outflow is balanced against magnetic energy transported into the layer minus the energy dissipated by turbulence. Here we estimate the turbulent dissipation using the formula $\varepsilon = u_L^4/V_A L_i$ for sub-Alfvénic turbulence (Kraichnan 1965). If one divides (12.40) by $\Delta = L_x v_{rec}/v_{out}$, one gets

$$v_{out}^3 = V_A^2 v_{out} - 2\frac{u_L^4}{V_A}\frac{L_x}{L_i}, \tag{12.41}$$

which is a cubic polynomial for v_{out}. The solutions are easiest to obtain by introducing the ratios $f = v_{out}/V_A$ and $r = 2M_A^4(L_x/L_i)$ which measure, respectively, the outflow speed as a fraction of V_A and the energy dissipated by turbulence in units of the available magnetic energy, giving

$$r = f - f^3. \tag{12.42}$$

When $r = 0$, the only solution of (12.42) with $f > 0$ is $f = 1$, recovering the LV99 estimate $v_{out} = V_A$ for $M_A \ll 1$. For somewhat larger values of r, $f \simeq 1 - (r/2)$, in agreement with the formula $f = (1-r)^{1/2}$ that follows from Eq.(65) in ELV11, implying a slight decrease in v_{out} compared with V_A. Note that formula (12.42) cannot be used to determine f for too large r, because it has then no positive, real solutions! This is easiest to see by considering the graph of r vs. f. The largest value of r for which a positive, real f exists is $r_{max} = 2/\sqrt{27} \approx 0.385$ and then f takes on its minimum value $f_{min} = 1/\sqrt{3} \approx 0.577$. This implies that the LV99 approach is limited to M_A sufficiently small, because of the energy dissipation inside the reconnection layer and the consequent reduction of the outflow velocity. This is not a very stringent limitation, however, because r is proportional to M_A^4. If one assumes $L_x \simeq L_i$, one may consider values of M_A up to 0.662. Given the neglect of constants of order unity in the above estimate, we may say only that the LV99 approach is limited to $M_A \lesssim 1$. At the extreme limit of applicability of LV99, v_{out} is still a sizable fraction of V_A, i.e. 0.577, not a drastically smaller value.

The effect of the reduced outflow velocity may be, somewhat paradoxically, to *increase* the reconnection rate. The reason is that field-lines now spend a time L_x/v_{out} exiting from the reconnection layer, greater than assumed in LV99 by a factor of $1/f$. This implies a thicker reconnection layer Δ due to the longer time-interval of Richardson diffusion in the layer, greater than LV99 by a factor of $(1/f)^{3/2}$. The net reconnection speed $v_{rec} = v_{out}\Delta/L_x$ is thus larger by a factor of $(1/f)^{1/2}$. The increased width Δ more than offsets the reduced outflow velocity v_{out}. However, this effect can give only a very slight increase, at most by a factor of $3^{1/4} \simeq 1.31$ for $f_{min} = 1/\sqrt{3}$. We see that for the entire regime

$M_A \lesssim 1$ where LV99 theory is applicable, energy dissipation in the reconnection layer implies only very modest corrections. It is worth emphasizing that "large-scale reconnection" in super-Alfvénic turbulence with $M_A > 1$ is a very different phenomenon, because magnetic fields are then so weak that they are easily bent and twisted by the turbulence. Any large-scale flux tubes initially present will be diffused by the turbulence through a process much different than that considered by LV99.

12.6.4 Relativistic Reconnection

Magnetic turbulence in a number of astrophysical highly magnetized objects, accretion disks near black holes, pulsars, gamma ray bursts may be in the relativistic regime when the Alfvén velocity approaches that of light. The equations that govern magnetized fluid in this case look very different from the ordinary MHD equations. However, studies by Cho (2005); Cho and Lazarian (2014) show that for both balanced and imbalanced turbulence, the turbulence spectrum and turbulence anisotropies are quite similar in this regime and the non-relativistic one. This suggests that the Richardson diffusion and related processes of LV99-type magnetic reconnection should carry on to the relativistic case (see Lazarian and Yan 2012). This prediction was confirmed by the recent numerical simulations who with his relativistic code adopted the approach in Kowal et al. (2009) and showed that the rate of 3D relativistic magnetic reconnection gets independent of resistivity.

The suggestion that LV99 is applicable to relativistic reconnection motivated the use of the model for explaining gamma ray bursts in Lazarian et al. (2003); Zhang and Yan (2011) studies (see also Sect. 12.7.2) and in accretion disks around black holes and pulsars studies (de Gouveia dal Pino and Lazarian 2005; Giannios 2013). Now, as the extension of the model to relativistic case has be confirmed these and other cases where the relativistic analog of LV99 process was discussed to be applicable (see Lyutikov and Lazarian 2013) are given numerical support.

Naturally, more detailed studies of both relativistic MHD turbulence and relativistic magnetic reconnection are required (see also chapter by de Gouveia Dal Pino and Kowal in this volume and references therein). It is evident that in magnetically-dominated, low-viscous plasmas turbulence is a generic ingredient and thus it must be taken into account for relativistic magnetic reconnection. As we discuss elsewhere in the review the driving of turbulence may by external forcing or it can be driven by reconnection itself.

12.7 Implications of Fast Reconnection in Turbulent Fluids

12.7.1 Flux Freezing in Astrophysical Fluids

Since the concept was first proposed by Hannes Alfvén in 1942, the principle of frozen-in field lines has provided a powerful heuristic which allows simple, back-of-the-envelope estimates in place of full solutions (analytical or numerical) of the MHD equations (Parker 1979; Kulsrud 2005). As such, the flux-freezing principle has been applied to gain insight into diverse processes, such as star formation, stellar collapse, magnetic dynamo, solar wind magnetospheric interactions, etc. However, it has long been understood that magnetic flux-conservation, if strictly valid, would forbid magnetic reconnection, because field-lines frozen into a continuous plasma flow cannot change their topology. Thus, the flux-freezing principle is in apparent contradiction with numerous observations of fast reconnection in high-conductivity plasmas.

Quite apart from these serious empirical difficulties, the flux-freezing principle has recently been shaken by a fundamental theoretical problem. Standard mathematical proofs of flux-freezing in MHD always assume, implicitly, that velocity and magnetic fields remain smooth as $\eta \to 0$. However, MHD solutions with small resistivities and viscosities (high magnetic and kinetic Reynolds numbers) are generally turbulent. These solutions exhibit long ranges of power-law spectra corresponding to very non-smooth or "rough" magnetic and velocity fields. Fluid particle (Lagrangian) trajectories in such rough flows are known to be non-unique and stochastic (see Bernard et al. 1998; Gawędzki and Vergassola 2000; E and vanden-Eijnden 2000a,b, 2001b; Chaves et al. 2003, and, for reviews, Kupiainen 2003; Gawędzki 2008). In fact, it is possible to show that, in the limit of infinite Reynolds number, there is an infinite random ensemble of particle motions for the same initial conditions! This remarkable phenomenon has been called *spontaneous stochasticity*. It view of the above, it is immediately clear as a consequence that standard flux-freezing cannot hold in turbulent plasma flows. After all, the usual idea is that magnetic field-lines at high conductivity are tied to the plasma flow and follow the fluid motion. However, if the latter is non-unique and stochastic, then which fluid element will the field-line follow?

The phenomenon of spontaneous stochasticity in magnetic field was shown to be inseparably related to LV99 reconnection theory in ELV11. It provides, however, a new outlook on the problem of magnetic field in turbulent fluids. The notion of the violation of the flux conservation Alfvén theorem is implicit in LV99 (but it is expressed explicitly in Vishniac and Lazarian (1999)). At the moment we can definitively assert that the domain of the Alfvén theorem on flux freezing is limited to laminar fluids only.

In view of the longstanding misconceptions about the general validity of magnetic flux-conservation for high-conductivity MHD, it is worth making a few more detailed remarks. The standard textbook proofs of flux-conservation (e.g. Chandrasekhar 1961) all make implicit assumptions that are violated in turbulent

flow. The proofs typically start with the ideal induction equation

$$\partial_t \mathbf{B} = \nabla \times (\mathbf{u} \times \mathbf{B})$$

and consider a material surface $S(t)$ advected by velocity $\mathbf{u}$. Then the time-derivative of the flux integral becomes

$$\frac{d}{dt}\int_{S(t)} \mathbf{B}(t) \cdot d\mathbf{A} = \int_{S(t)} \partial_t \mathbf{B}(t) \cdot d\mathbf{A} + \int_{C(t)} \mathbf{B}(t) \cdot (\mathbf{u} \times d\mathbf{x}).$$

The first term from the evolution of $\mathbf{B}$ and the second term from the motion of the surface cancel identically, implying constant flux through the surface. Of course, in reality, there is always a finite conductivity σ, however large, and the induction equation is

$$\partial_t \mathbf{B} = \nabla \times (\mathbf{u} \times \mathbf{B}) + \lambda \triangle \mathbf{B},$$

with $\lambda = c^2/4\pi\sigma$. The last term represents a diffusion of magnetic field lines in or out of the surface element, so that flux is no longer exactly conserved.

For a laminar velocity field, this diffusion effect is small. It is not hard to see that a pair of field lines will attain a displacement $\mathbf{r}(t)$ apart under the combined effect of advection and diffusion obeying

$$\frac{d}{dt}\langle r^2 \rangle = 12\lambda + 2\langle \mathbf{r} \cdot \delta\mathbf{u}(\mathbf{r}) \rangle$$

where $\delta\mathbf{u}(\mathbf{r})$ is the relative advection velocity at separation $\mathbf{r}$. Thus,

$$\frac{d}{dt}\langle r^2 \rangle \leq 12\lambda + 2\|\nabla \mathbf{u}\| \langle r^2 \rangle,$$

where $\|\nabla \mathbf{u}\|$ is the maximum value of the velocity-gradient $\nabla \mathbf{u}$. It follows that two lines initially at the same point, by time t can have separated at most

$$\langle r^2(t) \rangle \leq 6\lambda \frac{e^{2\|\nabla \mathbf{u}\| t} - 1}{\|\nabla \mathbf{u}\|}. \tag{12.43}$$

If we thus consider a smooth laminar flow with a fixed, finite value of $\|\nabla \mathbf{u}\|$, then $\langle r^2(t) \rangle \to 0$ as $\lambda \to 0$. Under such an assumption, magnetic field lines do not diffuse a far distance away from the solution of the deterministic ordinary differential equation $d\mathbf{x}/dt = \mathbf{u}(\mathbf{x}, t)$, and the magnetic line-diffusion becomes a negligible effect. In that case, magnetic flux is conserved better as λ decreases.

However, in a turbulent flow, the above argument fails! The inequality (12.43) still holds, of course, but it no longer restricts the dispersion of field-lines under the joint action of resistivity and advection. As is well-known, a longer and longer

inertial range of power-law spectrum $E(k)$ occurs as viscosity ν decreases and the maximum velocity gradient $\|\nabla \mathbf{u}\|$ becomes larger and larger. In fact, energy dissipation $\varepsilon = \nu \|\nabla \mathbf{u}\|^2$ is observed to be non-vanishing as $\nu \to 0$ in turbulent flow, requiring velocity gradients to grow unboundedly. Estimating $\|\nabla \mathbf{u}\| \sim (\varepsilon/\nu)^{1/2}$, the upper bound (12.43) becomes

$$\langle r^2(t) \rangle \leq 6\lambda (\nu/\varepsilon)^{1/2} [\exp(2t(\varepsilon/\nu)^{1/2}) - 1]. \tag{12.44}$$

This bound allows unlimited diffusion of field-lines. Consider first the case $\lambda = \nu$ or $Pt = 1$, for simplicity, where Richardson's theory implies that

$$\langle r^2(t) \rangle \sim 12\lambda t + \varepsilon t^3. \tag{12.45}$$

The rigorous upper bound always lies strictly above Richardson's prediction and, in fact, goes to infinity as $\nu = \lambda \to 0$! The case of large Prandtl number is just slightly more complicated, as previously discussed in Sect. 12.6.1. When $Pt \gg 1$, the inequality (12.44) holds as an equality for times $t \ll t_{trans}$ with

$$t_{trans} = \frac{\ln(Pt)}{2(\varepsilon/\nu)}. \tag{12.46}$$

This is then followed by a Richardson diffusion regime

$$\langle r^2(t) \rangle \sim 6(\nu^3/\varepsilon)^{1/2} + \varepsilon (t - t_{trans})^3, \qquad t \gg t_{trans}, \tag{12.47}$$

assuming that the kinetic Reynolds number is also large and a Kolmogorov inertial range exists at scales greater than the Kolmogorov length $(\nu^3/\varepsilon)^{1/4}$. Once again, the upper bound (12.44) is much larger than Richardson's prediction and, at times longer than t_{trans}, the dispersion of field lines is independent of resistivity.

The textbook proofs of magnetic flux-freezing for ideal MHD are therefore based on unstated assumptions which are explicitly violated in turbulent flows. They are mathematically valid derivations with appropriate assumptions, but physically inapplicable in typical astrophysical systems with plasma turbulence at MHD scales. It is worth emphasizing that any attempt to obtain fast reconnection (independent of resistivity) within a similar hydromagnetic description must likewise account for flux-freezing violation. For example, it has been conjectured (Mandt et al. 1994; Shay and Drake 1998) that reconnection rates are independent of resistivity in Hall MHD X-point reconnection. This proposal faces the same a priori theoretical difficulty as MHD-based theories, since magnetic field-lines remain frozen-in to the electron fluid in ideal Hall MHD. The conjectured failure of flux-freezing in Hall MHD X-point reconnection even as $\lambda \to 0$ must therefore be explained. Analytical studies of Hall reconnection indicate that the mechanism may be mathematically similar to the turbulent LV99 case, in that gradients of the electron fluid velocity $\mathbf{u}^e$ in the direction of the outgoing reconnection jets are predicted to diverge proportional to S, the Lundquist number (Malyshkin 2008; Shivamoggi 2011).

The Hall effects discussed above, as well as other microscopic plasma effects, are not expected to modify the Richardson diffusion of magnetic field lines at length scales much greater than the ion Larmor radius (see Appendix B of ELV11 and Sect. 12.3.5 of this review). However, one may worry that additional *hydrodynamic* effects at large scales may fundamentally alter Richardson diffusion. For example, in the Kraichnan-Kazantsev turbulence model (Kraichnan 1965), where "spontaneous stochasticity" was first predicted, it was shown that a sufficiently high degree of compressibility may eliminate Richardson dispersion entirely and replace it with instead a coalescence of fluid particles (Gawędzki and Vergassola 2000; E and vanden-Eijnden 2001a). If such effects were found in compressible MHD turbulence, then they could strongly alter the quantitative predictions of LV99, at the very least. This is a particular source of concern because most astrophysical plasmas are compressible, with Mach numbers ranging from a bit less than unity (subsonic) to very large (hypersonic). Note that the numerical tests of Richardson dispersion reported in Sect. 12.4.6 were for incompressible MHD turbulence. Could compressible MHD turbulence be fundamentally different?

There is at this time no complete theory of Richardson dispersion for MHD turbulence (or, for that matter, for hydrodynamic turbulence), but there are several reasons to believe that compressibility effects will be minimal on the turbulent motion of field lines relevant to reconnection. First, very high degrees of compressibility are required in the Kraichnan model (Kraichnan 1965) to eliminate spontaneous stochasticity. In 3D the kinetic energy in the potential part of the flow must be ten times greater than in the solenoidal part! Such extreme compressibility is rare in astrophysics. Of course, the Kraichnan model velocity is Gaussian and contains no compressible coherent structures like shocks, which may magnify the compressibility effects. It is well-known that the simple Burgers model, which is entirely potential flow, exhibits no spontaneous stochasticity but instead coalescence of particles in shocks (Bauer and Bernard 1999). However, Burgers differs in another crucial respect from the Kraichnan model in that it is time-irreversible. As discussed in Eyink (2011) and ELV11, it is the Richardson dispersion of magnetic field lines *backward in time* which is relevant to breakdown of flux-freezing. As shown in Eyink et al. (2013), the Burgers model does exhibit spontaneous stochasticity backward in time and field lines will thus not be "frozen-in" for vanishing resistivities. This is completely unlike the Kraichnan model for pure potential flow in which fluid particles coalesce backward in time as well as forward. In the Burgers model, therefore, magnetic field lines which arrive together at the shock become glued together to produce a resultant magnetic field at the shock. This is the same thing that happens at each point in incompressible MHD turbulence! Our second argument is thus that micro-scale shocklets in compressible MHD turbulence will probably glue field lines together in a manner almost indistinguishable from the surrounding "sea" of rough turbulence with continuous velocities. Finally, we note that the compressible MHD wave modes (slow and fast magnetosonic waves) are found in numerical simulations to decouple dynamically from the solenoidal shear-Alfvén modes, which exhibit turbulence characteristics very similar to those of incompressible MHD (Cho and Lazarian 2002, 2003). Since shear-Alfvén

waves produce the dominant fluid motions normal to the direction of the mean magnetic field, they will be the principal drivers of magnetic field-line diffusion across a turbulent reconnection layer. While more research into compressible MHD turbulence is desirable, the above facts support the view that compressibility effects will not strongly alter turbulent magnetic reconnection.

12.7.2 Solar Flares and Gamma Ray Bursts

Preexisting turbulence is a rule for astrophysical systems. However, for sufficiently low M_A the LV99 reconnection rates may be quite small. Would this mean that the reconnection will stay slow? LV99 model predicts *reconnection instability* that can drive reconnection in a bursty fashion in low β plasmas. If initially M_A is very small, the magnetic field wandering is small and therefore the reconnection is going to proceed at a slow pace. However, the system of two highly magnetized flux tubes being in contact is unstable to the development of turbulence arising from magnetic reconnection. Indeed, if the outflow gets turbulent, turbulence should, first of all, increase the magnetic field wandering thus increasing the width of the outflow Δ. Second, the increase of Δ increases the energy injection in the system via the increase of V_{rec}. Both factors drive up the level of turbulence in the system[8] inducing a positive feedback which in magnetically dominated media will lead to explosive reconnection.

A characteristic feature of this reconnection instability is that it has a threshold and therefore it can allow the accumulation of the flux prior to reconnection. In other words, as remarked before, LV99 model predicts that the reconnection can be both fast and slow, which is the necessary requirement of bursty reconnection frequently observed in nature, e.g. in solar flares. This process may be related to the bursts of reconnection observed in simulations in Lapenta (2008). In addition, LV99 predicted the process of *triggered reconnection* when reconnection in one part of the volume sends perturbations that initiate reconnection in adjacent volumes. Such process was, as we mentioned earlier, also reported recently in the observations of Sych et al. (2009).

The value of the threshold for initiating the burst depends on the system. For instance, tearing instability associated with magnetic reconnection (see Loureiro et al. 2009; Bhattacharjee et al. 2009) in 3D should create turbulence in agreement with the numerical simulations that we discussed in Sect. 12.4. This shows how the tearing and turbulent mechanisms may be complementary, with tearing triggering turbulent reconnection. Note that, once turbulence develops, the LV99 mechanism can provide much faster reconnection compared to tearing and tearing becomes a subdominant process. Depending on the value of the Reynolds number of the

[8]For instance, the increase of Δ increases the Reynolds number of the outflow, making the outflow more turbulent.

outflow, the emerging turbulence may completely supplant the tearing instability as the driver of reconnection. We believe that such flares of turbulent reconnection can explain a wide variety of astrophysical processes ranging from solar flares to gamma ray bursts as well as bursty reconnection in the pulsar winds (eg. de Gouveia dal Pino and Lazarian 2005).

A simple quantitative model of flares was presented in Lazarian and Vishniac (2009). There it is assumed that since stochastic reconnection is expected to proceed unevenly, with large variations in the thickness of the current sheet, one can expect that some unknown fraction of this energy will be deposited inhomogeneously, generating waves and adding energy to the local turbulent cascade.

For the sake of simplicity, the plasma density is assumed to be uniform so that the Alfvén speed and the magnetic field strength are interchangeable. The nonlinear dissipation rate for waves is

$$\tau_{nonlinear}^{-1} \sim \max\left[\frac{k_\perp^2 v_{wave}^2}{k_\parallel V_A}, k_\perp^2 VL\right], \tag{12.48}$$

where the first rate is the self-interaction rate for the waves and the second is the dissipation rate induced by the ambient turbulence (see Beresnyak and Lazarian 2008). The important point here is that $k_\perp$ for the waves falls somewhere in the inertial range of the strong turbulence. Eddies at that wavenumber will disrupt the waves in one eddy turnover time, which is necessarily less than L/V_A. Therefore, the bulk of the wave energy will go into the turbulent cascade before escaping from the reconnection zone.

An additional simplification is achieved by assuming that some fraction ϵ of the energy liberated by stochastic reconnection is fed into the local turbulent cascade. The evolution of the turbulent energy density per area is

$$\frac{d}{dt}\left(\Delta V^2\right) = \epsilon V_A^2 V_{rec} - V^2 \Delta \frac{V_A}{L_x}, \tag{12.49}$$

where the loss term covers both the local dissipation of turbulent energy, and its advection out of the reconnection zone. Since $V_{rec} \sim v_{turb}$ and $\Delta \sim L_x(V/V_A)$, it is possible to rewrite this by defining $\tau \equiv tV_A/L_x$ so that

$$\frac{d}{d\tau} M_A^3 \approx \epsilon M_A - M_A^3. \tag{12.50}$$

If ϵ is a constant then

$$V \approx V_A \epsilon^{1/2}(1 - e^{-2\tau/3})^{1/2}. \tag{12.51}$$

This implies that the time during which reconnection rate rises to $\epsilon^{1/2}V_A$ is comparable to the ejection time from the reconnection region ($\sim L_x/V_A$).

Within this toy model ϵ is not defined. Its value can be constrained through observations. Given that reconnection events in the solar corona seem to be episodic, with longer periods of quiescence, this is suggestive that ϵ is very small, for example, depends strongly on the ratio of the thickness of the current sheet to L_x. In particular, if it scales as M_A to some power greater than two then initial conditions dominate the early time evolution.

Another route by which magnetic reconnection might be self-sustaining via turbulence injection would be in the context of a series of topological knots in the magnetic field, each of which is undergoing reconnection. For simplicity, one can assume that as each knot undergoes reconnection it releases a characteristic energy into a volume which has the same linear dimension as the distance to the next knot. The density of the energy input into this volume is roughly $\epsilon V_A^2 V/L_x$, where here ϵ is defined as the efficiency with which the magnetic energy is transformed into turbulent energy. Thus one gets

$$\epsilon \frac{V_A^2 V}{L_x} \sim \frac{v'^3}{L_k}, \tag{12.52}$$

where L_k is the distance between knots and v' is the turbulent velocity created by the reconnection of the first knot. This process will proceed explosively if $v' > V$ or

$$V_A^2 L_k \epsilon > V^2 L_x. \tag{12.53}$$

The condition above is easy to fulfill. The bulk motions created by reconnection can generate turbulence as they interact with their surrounding, so ϵ should be of order unity. Moreover the length of any current sheet should be at most comparable to the distance to the nearest distinct magnetic knot. The implication is that each magnetic reconnection event will set off its neighbors, boosting their reconnection rates from V_L, set by the environment, to $\epsilon^{1/2} V_A (L_k/L_x)^{1/2}$ (as long as this is less than V_A). The process will take a time comparable to the crossing time L_x/V_L to begin, but once initiated will propagate through the medium with a speed comparable to speed of reconnection in the individual knots. The net effect can be a kind of modified sandpile model for magnetic reconnection in the solar corona and chromosphere. As the density of knots increases, and the energy available through magnetic reconnection increases, the chance of a successfully propagating reconnection front will increase.

This picture is broadly supported by current observations and numerical simulations of solar flares and Coronal Mass Ejections or CME's. For example, simulations by Lynch et al. (2008) of the "breakout model" of CME initiation show that an extremely complex magnetic line structure develops in the ejecta during and after the initial breakout reconnection phase, even under the severe numerical resolution constraints of such simulations. In the very high Lundquist-number solar environment, this complex field must correspond to a strongly turbulent state, within which the subsequent "anti-breakout reconnection" and post-CME current sheet occur. Direct observations of such current sheets (Ciaravella and Raymond 2008;

Bemporad 2008) verify the presence of strong turbulence and greatly thickened reconnection zones, consistent with the LV99 model. In the numerical simulations, the "trigger" of the initial breakout reconnection is numerical resistivity and there is no evidence of turbulence or complex field-structure during the eruptive flare onset. This is very likely to be a result of the limitations on resolution, however, and we expect that developing turbulence will accelerate reconnection in this phase of the flare as well.

While the details of the physical processes discussed above can be altered, it is clear that LV99 reconnection induces bursts in highly magnetized plasmas. This can be applicable not only to the solar environment but also to more exotic environments, e.g. to gamma ray bursts. The model of gamma ray bursts based on LV99 reconnection was suggested in Lazarian et al. (2003). It was elaborated and compared with observations in Zhang and Yan (2011). Currently, the latter model is considered promising and it attracts a lot of attention of researchers. Flares of reconnection that we described above can also be important for compact sources, like pulsars and black holes in microquasars and AGNs (de Gouveia dal Pino and Lazarian 2005). They seem like a more natural way of explaining the observed phenomenon compared to e.g. individual plasmoids (cf. Giannios 2013).

12.7.3 Reconnection Diffusion and Star Formation

Star formation theory was formulated several decades ago with an explicit assumption that the fully ionized gas and magnetic field are coupled to very high degree. Therefore, the source of the decoupling was identified with the presence of neutral atoms which do not directly feel magnetic fields, but interact with ions that tend to follow magnetic field lines. The slippage of matter in respect to magnetic field was called ambipolar diffusion and became the textbook explanation for the processes of star formation in magnetized gas (see also the Chapters of E. Zweibel and of Lizano and Galli in this volume).

Naturally, fast magnetic reconnection changes the situation dramatically. It is clear that in turbulent astrophysical media the dynamics of matter and gas are different from the idealized picture above and this presents a serious shift in the conventional paradigm of star formation.

The process of moving of matter in respect to magnetic field was identified in Lazarian (2005) (see also Lazarian and Vishniac 2009) and successfully tested in the subsequent publications for the case of molecular clouds and protostellar disks, e.g. Santos-Lima et al. (2010, 2012, 2013); de Gouveia Dal Pino et al. (2012); Leão et al. (2013). The theory of transporting matter in turbulent magnetized medium is discussed at length in Lazarian (2011a); Lazarian et al. (2012); Lazarian (2014) and we refer our reader to these publications. The process was termed "reconnection diffusion" to stress the importance of reconnection in the diffusive transport.

The peculiarity of reconnection diffusion is that it requires nearly parallel magnetic field lines to reconnect, while the textbook description of reconnection is usually associated with anti-parallel description of magnetic field lines. One

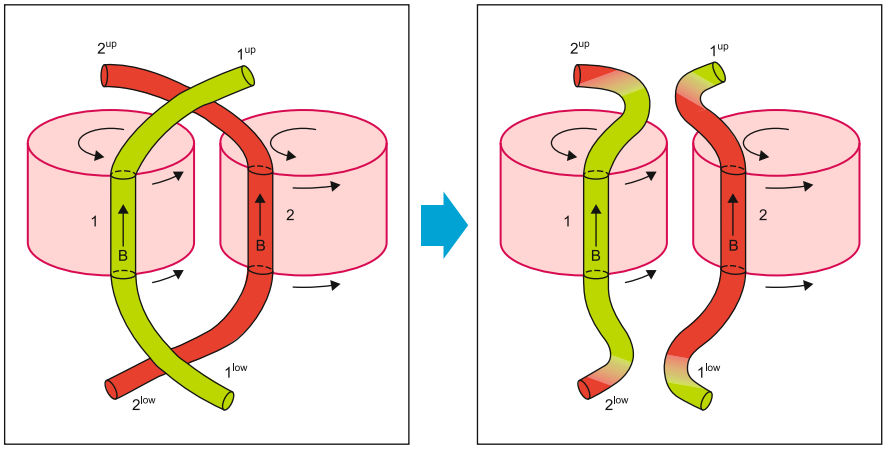

Fig. 12.12 Reconnection diffusion: exchange of flux with entrained matter. Illustration of the mixing of matter and magnetic fields due to reconnection as two flux tubes of different eddies interact. Only one scale of turbulent motions is shown. In real turbulent cascade such interactions proceed at every scale of turbulent motions. From Lazarian (2011a)

should understand that the configuration shown in Fig. 12.4 is just a cross section of the magnetic fluxes depicting the anti-parallel components of magnetic field. Generically, in 3D reconnection configurations the sheared component of magnetic field is present. The process of reconnection diffusion is closely connected with the reconnection between adjacent Alfvénic eddies (see Fig. 12.12). As a result, adjacent flux tubes exchange their segments with entrained plasmas and flux tubes of different eddies get connected. This process involves eddies of all the sizes along the cascade and ensures fast diffusion which has similarities with turbulent diffusion in ordinary hydrodynamic flows.

Finally, a number of studies attempted to understand the role of joint action of turbulence and ambipolar diffusion. For instance, Heitsch et al. (2004) (henceforth HX04) performed 2.5D simulations of turbulence with two-fluid code and examined the decorrelation of neutrals and magnetic field in the presence of turbulence (see also the Chapter by Zweibel in this volume). The study reported an enhancement of diffusion rate compared to the ambipolar diffusion in a laminar fluid. HX04 correctly associated the enhancement with turbulence creating density gradients that are being dissolved by ambipolar diffusion (see also Zweibel 2002). However, in 2.5D simulations of HX04 the numerical set-up precluded reconnection from taking place as magnetic field was perpendicular to the plane of 2D mixing and therefore magnetic field lines were absolutely parallel to each other. This will not happen in realistic astrophysical situations where reconnection will be an essential part of the physical picture. Therefore, we claim that a treatment of "turbulent ambipolar diffusion" without addressing the reconnection issue is of academic interest.

Incidentally, the authors of HX04 reported an enhanced rate that is equal to the turbulent diffusion rate LV_L. The fact that ambipolar diffusion rate does not enter

the result in HX04 suggests that ambipolar diffusion is irrelevant for the diffusion of matter in the presence of turbulence. This is another reason not to call the observed process "turbulent ambipolar diffusion" .[9]

Therefore we believe that HX04 captured in their simulations a special degenerate case of 2.5D turbulent diffusion where due to a special set up the reconnection is avoided and magnetic field lines do not intersect. We also note that, in the presence of turbulence, the independence of the gravitational collapse from the ambipolar diffusion rate was reported in numerical simulations by Balsara et al. (2001), although further higher resolution studies are still missing..

A comprehensive review dealing with reconnection diffusion is presented in Lazarian (2014).

12.7.4 Heat and Cosmic Ray Transport in the Presence of Reconnection

Magnetic reconnection is a very fundamental basic process that happens in all magnetized fluids. As we discussed in Sect. 12.3 magnetic reconnection is closely related to the turnover processes of magnetic eddies as well as magnetic field wandering. The former is essential for the heat advection via turbulent mixing of magnetized gas. The process was invoked by Cho et al. (2003) to explain the suppression of cooling flows in galaxy clusters. Fast LV99 magnetic reconnection was invoked to justify the existence of magnetic eddies for the very high Lundquist number plasmas (see more Lazarian 2009, 2011b).

Heat transport is also possible in magnetized plasma if electrons are streaming along meandering magnetic field lines. In Lazarian (2006) the heat transfer by electron streaming was compared with that induced by turbulent eddies and it was concluded that in typical clusters of galaxies the latter dominates.

Transport of cosmic rays along meandering magnetic field was invoked to solve the problem of perpendicular diffusion in Milky Way in classical studies (Jokipii 1973). For the propagation of cosmic rays the dynamics of turbulent magnetized plasmas is not important as c/V_A is usually large. However, the formation of the complicated web of the wandering magnetic field lines that is consistent with the Kolmogorov-type scaling of turbulence statistics does necessarily require fast magnetic reconnection.

[9] A similar process takes place in the case of molecular diffusivity in turbulent hydrodynamic flows. The result for the latter flows is well known: in the turbulent regime, molecular diffusivity is irrelevant for the turbulent transport. The process is called therefore "turbulent diffusivity" without adding the superfluous and inappropriate word "molecular".

12.7.5 Reconnection and First-Order Fermi Acceleration

The process of LV99 reconnection invokes shrinking magnetic loops. (see Lazarian 2005; Lazarian et al. 2011). This process that naturally follows from the LV99 model was invoked by de Gouveia dal Pino and Lazarian (2005) to predict efficient First-Order Fermi acceleration of cosmic rays in the reconnection regions (see also Lazarian 2005). The latter are traditionally associated with the acceleration of particles in shocks.[10]. Later research revealed the high promise of the process for explaining various physical processes. Recently, the acceleration of cosmic rays in reconnection has been invoked to explain results on the anomalous cosmic rays obtained by Voyager spacecrafts (Lazarian and Opher 2009; Drake et al. 2010), the local anisotropy of cosmic rays (Lazarian and Desiati 2010) and the acceleration of cosmic rays in clusters of galaxies (Lazarian and Brunetti 2011), as well as in the surrounds of compact sources and black holes (de Gouveia dal Pino and Lazarian 2005) and relativistic jets (Giannios 2013). Naturally, the process of acceleration is much more widespread and not limited to the explored examples.

In addition to the acceleration of cosmic rays parallel to magnetic field, acceleration perpendicular to the magnetic field is also possible, as discussed in Lazarian et al. (2012). The advantage of such a perpendicular acceleration is that the gain of energy is taking place every Larmor period of the cosmic ray. The efficiency of perpendicular acceleration was observed in simulations of Kowal et al. (2012), where the simulations of turbulent reconnection were used to study the acceleration of cosmic rays (see more details in de Gouveia Dal Pino and Kowal's chapter in this volume).

12.7.6 Dissipation of Turbulence in Current Sheets

MHD turbulence cascade does not depend on the details of microphysics. However, at sufficiently small scales current sheets are formed and those may dissipate a substantial part of the turbulent cascade. As we discussed in Sect. 12.3 within LV99 model small scale reconnection events may happen due to ordinary Ohmic or plasma effects. In particular, the small scale current sheets can be in the collisionless regime. Therefore it is not easy to distinguish the nature of magnetic reconnection by studying the processes of electron and proton heating.

[10]The First-Order Fermi acceleration is a process in which the energy gain is proportional to the first order of the ratio of the shock velocity to that of light. It should be distinguished from the stochastic Second-Order Fermi acceleration which is proportional to the square of this ratio.

12.8 Discussion

12.8.1 Interrelation of LV99 Reconnection and Modern Understanding of MHD Turbulence

MHD turbulence has advanced considerably in the last 20 years. It is easy to understand that strong Alfvénic turbulence that induces Richardson diffusion does require fast reconnection. Indeed, eddy type motions that are produced by such turbulence can happen only if the magnetic field of the eddies relaxes on the time scale of eddy turnover. Calculations in LV99 showed that the GS95 theory Goldreich and Sridhar (1995) is self-consistent when the small-scale magnetic reconnection between adjacent turbulent eddies happens with the LV99 predicted rate.[11] This result also follows from the Richardson diffusion that we discussed in the chapter by a factor . This rate varies from $\sim V_A$ for largest eddies in transAlfvénic turbulence to a small fraction of V_A for the smallest eddies. Obviously, no mechanism that produces a fixed reconnection rate, e.g. the rate of $0.1V_A$ that for decades was a sort of Holy Grail rate for the researchers attempting to explain Solar flares, can make modern theories of MHD turbulence, both the GS95 and its existing modifications, self-consistent. At the same time, ELV11 showed that the Lagrangian dynamics of turbulent fluids do require fast magnetic reconnection. Or, reversing the role of cause and effect, the Lagrangian phenomenon of Richardson dispersion produces a breakdown in the standard form of flux-freezing for a turbulent MHD flow. The reconnection rates that are dictated by the well-established process of Richardson diffusion coincide with those predicted by LV99.

In other words, LV99 reconnection is an intrinsic and inseparable element of MHD turbulence. There can be other types of magnetic reconnection, that are important in particular circumstances, but in turbulent fluids the LV99 type seems inevitable.

[11] Indeed, within the GS95 picture the reconnection happens with nearly parallel lines with magnetic pressure gradient $V_A^2/l_\parallel$ being reduced by a factor $l_\perp^2/l_\parallel^2$, since only reversing component is available for driving the outflow. At the same time the length of the contracted magnetic field lines is also reduced from $l_\perp$ but $l_\perp^2/l_{\parallel|}$. Therefore the acceleration is $\tau_{eject}^{-2} l_\perp^2/l_{\parallel|}$. As a result, the Newtons' law gives $V_A^2 l_\perp^2/l_\parallel^3 \approx \tau_{eject}^{-2} l_\perp^2/l_{\parallel|}$. This provides the result for the ejection rate $\tau_{eject}^{-1} \approx V_A/l_\parallel$. The length over which the magnetic eddies intersect is $l_\perp$ and the rate of reconnection is $V_{rec}/l_\perp$. For the stationary reconnection this gives $V_{rec} \approx V_A l_\perp/l_\parallel$, which provides the reconnection rate $V_A/l_\parallel$, which is exactly the rate of the eddy turnovers in GS95 turbulence.

12.8.2 Suggestive Evidence on Fast Reconnection

A study of tearing instability of current sheets in the presence of background 2D turbulence that observed the formation of large-scale islands was performed in Politano et al. (1989). While one can argue that observed long-lived islands are the artifact of adopted 2D geometry, the authors present evidence for *fast energy dissipation* in 2D MHD turbulence and show that this result does not change as they change the resolution. A more recent work of Mininni and Pouquet (2009) provides evidence for *fast dissipation* also in 3D MHD turbulence. This phenomenon is consistent with the idea of fast reconnection, but cannot be treated as a direct evidence of the process. Although related, fast dissipation and fast magnetic reconnection are rather different physical processes, dealing with decrease of energy on the one hand and decrease of magnetic flux on the other.

Works by Galsgaard and Nordlund, in particular (Galsgaard and Nordlund 1997), could also be interpreted as an indirect support for fast reconnection. The authors showed that in their simulations they could not produce highly twisted magnetic fields. One possible interpretation of this result could be the fast relaxation of magnetic field via reconnection. In this case, these observations could be related to the numerical finding of Lapenta and Bettarini (2011) which shows that reconnecting magnetic configurations spontaneously get chaotic and dissipate, which, as discussed in Lapenta and Lazarian (2012), may be related to the LV99 model. However, in view of many uncertainties of the numerical studies, this relation is unclear. The highest resolution simulations of Galsgaard and Nordlund (1997) were only 136^3 and with Reynolds number so small that they could not allow a turbulent inertial-range.

12.8.3 Convergence of Different Approaches to Fast Reconnection

The LV99 model of magnetic reconnection in the presence of weakly stochastic magnetic fields was proposed more than a decade ago. In fact, LV99 and the idea of collisionless X-point reconnection mediated by the Hall effect are essentially coeval. At the same time, due to a few objective factors, it met less enthusiasm in the community than the X-point collisionless reconnection. One can speculate what were the factors responsible for this slow start. For one thing, the collisionless X-point reconnection was initiated and supported by numerical simulations, while the numerical testing of LV99 became possible only recently. In addition, the acceptance of the idea of astrophysical fluids generically being in turbulent state was only taking roots in 1999 (but see Chandrasekhar 1949!) and at that time it had much less observational support. By now we have much more evidence which justifies the claim that models ignoring pre-existent turbulence have little relevance to astrophysics. Finally, the analytical solutions of LV99 were based on the use and

extension of the GS95 model of turbulence. However, the GS95 theory was far from being universally accepted at the time LV99 was published.[12]

The situation has changed substantially by now. With GS95, as we discussed earlier, being widely accepted, with more observational evidence of ubiquitous turbulence in astrophysical environments and with the successful testing of the LV99 model, it is more difficult to argue against the importance of turbulence for astrophysical reconnection. Moreover, the LV99 model has received more support from solar observations Sect. 12.5, which both showed that magnetic reconnection can be fast in collisional media, where the aforementioned collisionless reconnection does not work. Solar observations also confirmed LV99 predictions on the thickness of reconnection regions and on triggering reconnection by the neighboring reconnection events. Last, but not the least, a very important development took place, namely, the LV99 model was connected to the modern developments in the Lagrangian description of magnetized fluids and the equivalence of the approach in LV99 and that based on spontaneous stochasticity was established (see Sects. 12.3 and 12.4).

One can argue that we have observed the convergence of LV99 with other directions of reconnection research. In particular, recent models of collisionless reconnection have acquired several features in common with the LV99 model. In particular, they have moved to consideration of volume-filling reconnection (see Drake et al. 2006). While much of the discussion may still be centered around 2D magnetic islands produced by reconnection, in three dimensions these islands are expected to evolve into contracting 3D loops or ropes (Daughton et al. 2008), which is broadly similar to what is depicted in Fig. 12.11, at least in the sense of introducing stochasticity to the reconnection zone. Moreover, it is more and more realized that the 3D geometry of reconnection is essential and that the 2D physics is not adequate and may be misleading. This essentially means the end of the epoch of the dominance of collisionless X-point reconnection. The interest of the models alternative to LV99 shifted to chaotically broadened extended Y-shaped outflow regions, which were advocated in LV99 and confirmed by observations.

The departure from the concept of laminar reconnection and the introduction of magnetic stochasticity is also apparent in a number of recent papers appealing to the tearing mode instability to drive fast reconnection (see Loureiro et al. 2009; Bhattacharjee et al. 2009). These studies showed that tearing modes do not require collisionless environments and thus collisionality is not a necessary ingredient of fast reconnection.[13] Finally, the reported development of turbulence in 3D numerical simulations clearly testifies that the reconnection induces turbulence

[12]In fact, this unsatisfactory situation with the theory of turbulence motivated some of us to work seriously on testing turbulence models (see Cho and Vishniac 2000; Cho et al. 2002; Cho and Lazarian 2002, 2003)

[13]The largest-scale Hall MHD simulations performed to date (Huang et al. 2011) do show somewhat higher reconnection rates for laminar X-point solutions than for plasmoid unstable regimes, but the X-point solutions lose stability and seem to have lower reconnection rates with decreasing ratios δ_i / L_x.

even if the initial reconnection conditions are laminar. Naturally, one should expect that turbulence modifies tearing instability and induces its own laws for reconnection thus making for many situations the tearing modes only the trigger to self-supported turbulent reconnection. If this is the case, the final non-linear stage of the reconnection should allow a theoretical description based on the LV99 model.

All in all, in the last decade, the models competing with LV99 have undergone a substantial evolution, from 2D collisionless X-point reconnection based mostly on Hall effect to 3D reconnection where the collisionless condition is no more required, Hall effect is not employed, but magnetic stochasticity and turbulence play an important role in the thick Y-shaped reconnection regions. In other words, a remarkable convergence has taken place.

Saying all the above, we want to stress that collisionless X-point reconnection may nevertheless be suitable for the description of reconnection when the reconnecting flux-structures are comparable with the ion gyro scale, which is the case of the reconnection studied situ in the magnetosphere (see Table 12.1). However, this is a special case of magnetic reconnection with, we argue, atypical features compared with most astrophysical reconnection.

12.8.4 Recent Attempts to Relate Turbulence and Reconnection

Guo et al. (2012) proposed a model based on the earlier idea of mean field approach suggested initially in Kim and Diamond (2001). In the latter paper the author concluded that the reconnection rate should be always slow in the presence of turbulence. On the contrary, models in Guo et al. (2012) invoke hyperresistivity and get fast reconnection rates. Similarly, invoking the mean field approach Higashimori and Hoshino (2012) presented their model of turbulent reconnection.

The mean field approach invoked in the aforementioned studies was critically analyzed by Eyink (2011), and below we briefly present some arguments from that study. The principal difficulty is with the justification of using the mean field approaches to explain fast magnetic reconnection. In such an approach effects of turbulence are described using parameters such as anisotropic turbulent magnetic diffusivity and hyper-resistivity experienced by the fields once averaged over ensembles. The problem is that it is the lines of the full magnetic field that must be rapidly reconnected, not just the lines of the mean field. ELV11 stress that the former implies the latter, but not conversely. No mean-field approach can claim to have explained the observed rapid pace of magnetic reconnection unless it is shown that the reconnection rates obtained in the theory are strictly independent of the length and timescales of the averaging. More detailed discussion of the conceptual problems of the hyper-resistivity concept and mean field approach to magnetic reconnection is presented in Lazarian et al. (2004) and ELV11.

12.8.5 Reconnection and Numerical Simulations

As discussed in section Sect. 12.4.1, a brute force numerical approach to astrophysical reconnection is impossible. Therefore our numerical studies of reconnection diffusion in Santos-Lima et al. (2010, 2012, 2013); Leão et al. (2013) deal with a different domain of Lundquist numbers and the theoretical justification why *for the given problem* the Lundquist number regime is not essential. For the case of reconnection diffusion simulations, LV99 theory predicts that the dynamics of reconnection is independent from the Lundquist number and therefore the reconnection in the computer simulations *in the presence of turbulence* adequately represents the astrophysical process.

The above numerical results explored the consequences of reconnection diffusion. Similarly, as numerical studies of ambipolar diffusion do not "prove" the very concept of ambipolar diffusion, our studies were not intended to "prove" the idea of reconnection diffusion. Our goal was to demonstrate that, *in agreement with the theoretical expectations*, the process of reconnection diffusion is important for a number of astrophysical set-ups relevant to star formation.

12.8.6 Plasma Physics and Reconnection

We have been primarily interested in this review in reconnection phenomena at scales much larger than the ion gyro-radius ρ_i. We have also made the claim— which may appear paradoxical to some—that these phenomena can be explained by hydrodynamical processes in turbulent MHD regimes. Microscopic plasma processes do play a role, however, which should be briefly explained. Consider a collisionless turbulent plasma, such as the solar wind, in which the MHD description of the cascade terminates at the ion gyro radius. At scales smaller than ρ_i but larger than ρ_e, the plasma is described by an ion kinetic equation and a system of "electron reduced MHD" (ERMHD) equations for kinetic Alfvén waves (Schekochihin et al. 2007, 2009). This system exhibits the "Hall effect", with distinct ion and electron mean flow velocities and magnetic field-lines frozen-in to the electron fluid. The ERMHD equations (or the more general "electron MHD" or EMHD equations) produce the typical features of "Hall reconnection" such as quadrupolar magnetic fields in the reconnection zone (Uzdensky and Kulsrud 2006).[14] At length scales smaller than ρ_e, kinetic equations are required to describe

[14]Because the Hall MHD equations have played a prominent role in magnetic reconnection research of the past decade (Shay et al. 1998, 1999; Wang et al. 2000; Birn et al. 2001; Drake 2001; Malakit et al. 2009; Cassak et al. 2010), it is worth remarking that those equations are essentially never applicable in astrophysical environments. A derivation of Hall MHD based on collisionality requires that the ion skin-depth δ_i must satisfy the conditions $\delta_i \gg L \gg \ell_{mfp,i}$. The second inequality is needed so that a two-fluid description is valid at the scales L of interest, while

both the ions and the electrons. It is at these scales that the magnetic flux finally "unfreezes" from the electron fluid, due to effects such as Ohmic resistivity, electron inertia, finite electron gyroradius, etc. However, as we have discussed at length in this review, these weak effects are vastly accelerated by turbulent advection and manifested, in surprising ways, at far larger length scales.

Acknowledgements A.L. research is supported by the NSF grant AST 1212096, Vilas Associate Award as well as the support 1098 from the NSF Center for Magnetic Self-Organization. The research is supported by the Center for Magnetic Self-Organization in Laboratory and Astrophysical Plasmas. Stimulating environment provided by Humboldt Award at the Universities of Cologne and Bochum, as well as a Fellowship at the International Institute of Physics (Brazil) is acknowledged. G.K. acknowledges support from FAPESP (projects no. 2013/04073-2 and 2013/18815-0). Part of the computations were performed using supercomputer RANGER (Teragrid AST080005N, TACC, USA, https://www.xsede.org/tg-archives/), supercomputer GALERA (ACK TASK, Poland, http://www.task.gda.pl/), and supercomputer ALPHACRUCIS (LAi, IAG-USP, Brazil, http://lai.iag.usp.br/). We thank Andrey Beresnyak for useful discussions of the generation of turbulence in the process of magnetic reconnection.

References

Alfvén, H.: Ark. Mat., Astron. o. Fys. **29B**, 1 (1942)
Armstrong, J.W., Rickett, B.J., Spangler, S.R.: Astrophys. J. **443**, 209 (1995)
Balbus, S.A., Hawley, J.F.: Rev. Mod. Phys. **70**, 1 (1998)
Bale, S.D., Kellogg, P.J., Mozer, F.S., Horbury, T.S., Reme, H.: Phys. Rev. Lett. **94**, 215002 (2005)
Balsara, D.S., Crutcher, R.M., Pouquet, A.: Astrophys. J. **557**, 451 (2001)
Bauer, M., Bernard, D.: J. Phys. A Math. Gen. **32**, 5179 (1999)
Bemporad, A.: Astrophys. J. **689**, 572 (2008)
Beresnyak, A.: Astrophys. J. Lett. **767**, L39 (2013)
Beresnyak, A.: Phys. Rev. Lett. **106**, 075001 (2011)
Beresnyak, A.: Mon. Not. R. Astron. Soc. **422**, 3495 (2012)
Beresnyak, A.: (2013). arXiv:1301.7424
Beresnyak, A., Lazarian, A.: Astrophy. J. Lett. **640**, L175 (2006)
Beresnyak, A., Lazarian, A.: Astrophys. J. **682**, 1070 (2008)
Beresnyak, A., Lazarian, A.: Astrophys. J. **702**, 1190 (2009)
Beresnyak, A., Lazarian, A.: Astrophys. J. Lett. **722**, L110 (2010)

---

the first inequality is needed so that the Hall term remains significant at those scales. However, substituting $\delta_i = \rho_i / \sqrt{\beta_i}$ into (12.4) yields the result

$$\frac{\ell_{mfp,i}}{\delta_i} \propto \frac{\Lambda}{\ln \Lambda} \frac{v_{th,i}}{c}.$$

The ratio $v_{th,i}/c$ is generally small in astrophysical plasmas, but the plasma parameter Λ is usually large by even much, much more (see Table 12.1). Thus, it is usually the case that $\ell_{mfp,i} \gg \delta_i$, unless the ion temperature is extremely low. A collisionless derivation of Hall MHD from gyrokinetics requires also a restrictive condition of cold ions (Schekochihin et al. 2009, Appendix E). Thus, Hall MHD is literally valid only for cold, dense plasmas like those produced in some laboratory experiments, such as the MRX reconnection experiment (Yamada 1999; Yamada et al. 2010).

Bernard, D., Gawędzki, K., Kupiainen, A.: J. Stat. Phys., **90**, 519 (1998)
Bhattacharjee, A., Hameiri, E.: Phys. Rev. Lett. **57**, 206 (1986)
Bhattacharjee, A., Ma, Z.W., Wang, X.: Lecture Notes in Physics, vol. 614, p. 351 (2003)
Bhattacharjee, A., Huang, Y.-M., Yang, H., Rogers, B.: Phys. Plasmas **16**, 112102 (2009)
Birn, J., et al.: J. Geophys. Res. **106**, 3715 (2001)
Biskamp, D.: Astrophys. Space Sci. **242**, 165 (1996)
Biskamp, D.: Biskamp, D. (ed.) Magnetohydrodynamic Turbulence, pp. 310. Cambridge University Press, Cambridge (2003). ISBN 0521810116
Boldyrev, S: Phys. Rev. Lett. **96**, 115002 (2006)
Brandenburg, A., Lazarian, A.: Space Sci. Rev. **178**, 163 (2013)
Braginsky, S.I.: Rev. Plasma Phys. **1**, 205 (1965)
Browning, P., Lazarian, A.: Space Sci. Rev. **178**, 325 (2013)
Cassak, P.A., Shay, M.A., Drake, J.F.: Phys. Plasmas **17**, 062105 (2010)
Chandran, B.D.G.: Astrophys. J. **632**, 809 (2005)
Chandrasekhar, S.: Astrophys. J. **110**, 329 (1949)
Chandrasekhar, S.: Hydrodynamic and Hydromagnetic Stability, Oxford University Press, Oxford (1961)
Chaves, M., Gawędzki, K., Horvai, P., Kupiainen, A., Vergassola, M.: J. Stat. Phys. **113**, 643 (2003)
Chepurnov, A., Lazarian, A.: Astrophys. J. **710**, 853 (2010)
Cho, J.: Astrophys. J. **621**, 324 (2005)
Cho, J., Lazarian, A.: Phys. Rev. Lett. **88**, 245001 (2002)
Cho, J., Lazarian, A.: Mon. Not. R. Astron. Soc. **345**, 325 (2003)
Cho, J., Lazarian, A.: Astrophys. J. **780**, 30 (2014)
Cho, J., Vishniac, E.T.: Astrophys. J. **539**, 273 (2000)
Cho, J., Lazarian, A., Vishniac, E.T.: Astrophys. J. **564**, 291 (2002)
Cho, J., Lazarian, A., Vishniac, E.T.: Turbulence Magn. Fields Astrophys. **614**, 56 (2003)
Ciaravella, A., Raymond, J.C.: Astrophys. J. **686**, 1372 (2008)
Dahlburg, R.B.: J. Plasma Phys. **57**, 35 (1997)
Dahlburg, R.B., Karpen, J.T.: Space Sci. Rev. **70**, 93 (1994)
Dahlburg, R.B., Antiochos, S.K., Zang, T.A.: Phys. Fluids B **4**, 3902 (1992)
Daughton, W., Scudder, J., Karimabadi, H.: Phys. Plasmas **13**, 072101 (2006)
Daughton, W., Roytershteyn, V., Albright, B.J., Bowers, K., Yin, L., Karimabadi, H.: AGU Fall Meeting Abstracts, A1705 (2008)
de Gouveia dal Pino, E.M., Lazarian, A.: Astron. Astrophys. **441**, 845 (2005)
de Gouveia Dal Pino, E.M., Leão, M.R.M., Santos-Lima, R., Guerrero, G., Lazarian, A.: Phys. Scripta **86**, 018401 (2012)
Diamond, P.H., Malkov, M.: Phys. Plasmas **10**, 2322 (2003)
Drake, J.F.: Nature **410**, 525 (2001)
Drake, J.F., Swisdak, M., Che, H., Shay, M.A.: Nature **443**, 553 (2006)
Drake, J.F., Opher, M., Swisdak, M., Chamoun, J.N.: Astrophys. J. **709**, 963 (2010)
Enßlin, T.A., Vogt, C.: Astron. Astrophys. **453**, 44 (2006)
Eyink, G.L.: Phys. D Nonlinear Phenomena **237**, 1956 (2008)
Eyink, G.L.: Phys. Rev. E **83**, 056405 (2011)
Eyink, G.L., Benveniste, D.: Phys. Rev. E **88**, 041001 (2013)
Eyink, G.L., Lazarian, A., Vishniac, E.T.: Astrophys. J. **743**, 51 (2011)
Eyink, G.L., Vishniac, E.T., Lalescu, C., Aluie, H., Kanov, K., Bürger, K., Burns, R., Meneveau, C., Szalay, A.: Nature, **497**, 466 (2013)
Ferraro, N.M., Rogers, B.N.: Phys. Plasmas **11**, 4382 (2004)
Ferrière, K.M.: Rev. Mod. Phys. **73**, 1031 (2001)
Fitzpatrick, R.: Phys. Plasmas **11**, 937 (2004)
Fitzpatrick, R.: Introduction to Plasma Physics. Online Lecture Notes. http://farside.ph.utexas.edu/teaching/plasma/plasma.html (2011)
Fox, D.B., et al.: Nature **437**, 845 (2005)
Galama, T.J., et al.: Nature **395**, 670 (1998)

Galsgaard, K., Nordlund, A.A.: J. Geophys. Res. **102**, 219 (1997)
Galsgaard, K., Nordlund, A.A.: J. Geophys. Res. **102**, 231 (1997)
Galtier, S., Nazarenko, S.V., Newell, A.C. Pouquet, A.: J. Plasma Phys. **63**, 447 (2000)
Gawędzki, K.: (2008). arXiv:0806.1949
Gawędzki, K., Vergassola, M.: Physica D, **138**, 63 (2000)
Gerrard, C.L., Hood, A.W.: Solar Phys. **214**, 151 (2003)
Giannios, D.: Mon. Not. R. Astron. Soc. **431**, 355 (2013)
Gogoberidze, G.: Phys. Plasmas **14**, 022304 (2007)
Goldreich, P., Sridhar, S.: Astrophys. J. **438**, 763 (1995)
Gosling, J.T.: Space Sci. Rev. **172**, 187 (2012)
Gosling, J.T., Szabo, A.: J. Geophys. Res. **113**, A10103 (2008)
Gosling, J.T., Phan, T.D., Lin, R.P., Szabo, A.: Geophys. Res. Lett. **34**, L15110 (2007)
Guo, Z.B., Diamond, P.H., Wang, X.G.: Astrophys. J. **757**, 173 (2012)
Hameiri, E., Bhattacharjee, A.: Phys. Fluids **30**, 1743 (1987)
Heitsch, F., Zweibel, E.G.: Astrophys. J. **583**, 229 (2003)
Heitsch, F., Zweibel, E.G., Slyz, A.D., Devriendt, J.E.G.: Astrophys. J. **603**, 165 (2004)
Higashimori, K., Hoshino, M.: J. Geophys. Res. (Space Phys.) **117**, 1220 (2012)
Higdon, J.C.: Astrophys. J. **285**, 109 (1984)
Huang, Y.-M., et al.: Phys. Plasmas **18**, 072109 (2011)
Huang, S.-Y., et al.: Geophys. Res. Lett. **39**, L11104 (2012)
Innes, D.E., Inhester, B., Axford, W.I., Wilhelm, K.: Nature **386**, 811 (1997)
Jacobson, A.R., Moses, R.W.: Phys. Rev. A **29**, 3335 (1984)
Jokipii, J.R.: Astrophys. J. **183**, 1029 (1973)
Karimabadi, H., Lazarian, A.: Phys. Plasmas **20**, 112102 (2013)
Karimabadi, H., Roytershteyn, V., Wan, M., et al.: Phys. Plasmas **20**, 012303 (2013)
Kim, E.-j., Diamond, P.H.: Astrophys. J. **556**, 1052 (2001)
Kowal, G., Lazarian, A.: Astrophys. J. **720**, 742 (2010)
Kowal, G., Lazarian, A., Falceta-Gonçalves, D.A., Vishniac, E.T.: (2009, in preparation)
Kowal, G., Lazarian, A., Vishniac, E.T., Otmianowska-Mazur, K.: Astrophys. J. **700**, 63 (2009)
Kowal, G., Falceta-Gonçalves, D.A., Lazarian, A.: New J. Phys. **13**, 053001 (2011)
Kowal, G., Lazarian, A., Vishniac, E.T., Otmianowska-Mazur, K.: Nonlinear Process. Geophys. **19**, 297 (2012)
Kowal, G., de Gouveia Dal Pino, E.M., Lazarian, A.: Phys. Rev. Lett. **108**, 241102 (2012)
Kraichnan, R.H.: Phys. Fluids **8**, 1385 (1965)
Kulsrud, R.: Princeton University Press, Princeton (2005)
Kulsrud, R.: Rosenbluth, M.N., Sagdeev, R.Z. (eds.) Handbook of Plasma Physics. North Holland, New York (1983)
Kupiainen, A.: Ann. Henri Poincaré **4**(Suppl. 2), S713 (2003)
Lapenta, G.: Phys. Rev. Lett. **100**, 235001 (2008)
Lapenta, G., Bettarini, L.: (2011). arXiv:1102.4791
Lapenta, G., Lazarian, A.: Nonlinear Process. Geophys. **19**, 251 (2012)
Lazarian, A.: Magnetic Fields in the Universe: From Laboratory and Stars to Primordial Structures, 784, 42 (2005)
Lazarian, A.: Astrophys. J. Lett. **645**, L25 (2006)
Lazarian, A.: Space Sci. Rev. **143**, 357 (2009)
Lazarian, A.: (2011a). arXiv:1108.2280
Lazarian, A.: (2011b). arXiv:1111.0694
Lazarian, A.: Space Sci. Rev. **181**, 1 (2014)
Lazarian, A., Beresnyak, A.: Mon. Not. R. Astron. Soc. **373**, 1195 (2006)
Lazarian, A., Brunetti, G.: Memorie della Societa Astronomica Italiana **82**, 636 (2011)
Lazarian, A., Desiati, P.: Astrophys. J. **722**, 188 (2010)
Lazarian, A., Petrosian, V., Yan, H., Cho, J.: (2003). arXiv:astro-ph/0301181
Lazarian, A., Pogosyan, D.: Astrophys. J. **537**, 720 (2000)
Lazarian, A., Pogosyan, D.: Astrophys. J. **616**, 943 (2004)

Lazarian, A., Pogosyan, D.: Astrophys. J. **652**, 1348 (2006)
Lazarian, A., Pogosyan, D.: Astrophys. J. **686**, 350 (2008)
Lazarian, A., Opher, M.: Astrophys. J. **703**, 8 (2009)
Lazarian, A., Vishniac, E.T.: Astrophys. J. **517**, 700 (1999)
Lazarian, A., Vishniac, E.T., Cho, J.: Astrophys. J. **603**, 180 (2004)
Lazarian, A., Vishniac, E.T.: Revista Mexicana de Astronomia y Astrofisica Conference Series, 36, 81 (2009)
Lazarian, A., Kowal, G., Vishniac, E., de Gouveia Dal Pino, E.: Planet. Space Sci. **59**, 537 (2011)
Lazarian, A., Vlahos, L., Kowal, G., Yan, H., Beresnyak, A., de Gouveia Dal Pino, E.M.: Space Sci. Rev. **173**, 557 (2012)
Lazarian, A., Esquivel, A., Crutcher, R.: Astrophys. J. **757**, 154 (2012)
Lazarian, A., Yan, H.: American Institute of Physics Conference Series, **1505**, 101 (2012)
Lazarian, A., Yan, H.: Astrophys. J. **784**, 38 (2014)
Leake, J.E., Lukin, V.S., Linton, M.G., Meier, E.T.: Astrophys. J. **760**, 109 (2012)
Leamon, R.J., Smith, C.W., Ness, N.F., Matthaeus, W.H., Wong, H.K.: J. Geophys. Res. **103**, 4775 (1998)
Leão, M.R.M., de Gouveia Dal Pino, E.M., Santos-Lima, R., Lazarian, A.: Astrophys. J. **777**, 46L (2013)
Lithwick, Y., Goldreich, P.: Astrophys. J. **562**, 279 (2001)
Loureiro, N.F., Uzdensky, D.A. , Schekochihin, A.A., Cowley, S.C. Yousef, T.A.: Mon. Not. R. Astron. Soc. **399**, L146 (2009)
Lovelace, R.V.E.: Nature **262**, 649 (1976)
Lynch, B.J., et al.: Astrophys. J. **683**, 1192 (2008)
Lyutikov, M., Lazarian, A.: Space Sci. Rev., **178**, 459 (2013)
Malakit, K., Cassak, P.A., Shay, M.A., Drake, J.F.: Geophys. Rev. Lett. **36**, 7107 (2009)
Malyshkin, L.M.: Phys. Rev. Lett. **101**, 225001 (2008)
Mandt, M.E., Denton, R.E., Drake, J.F.: Geophys. Res. Lett. **21**, 73 (1994)
Maron, J., Goldreich, P.: Astrophys. J. **554**, 1175 (2001)
Maron, J., Chandran, B.D., Blackman, E.: Phys. Rev. Lett. **92**, 045001 (2004)
Masuda, S., Kosugi, T., Hara, H., Tsuneta, S., Ogawara, Y.: Nature **371**, 495 (1994)
Matthaeus, W.H., Lamkin, S.L.: Phys. Fluids **28**, 303 (1985)
Matthaeus, W.H., Lamkin, S.L.: Phys. Fluids **29**, 2513 (1986)
Mininni, P.D., Pouquet, A.: Phys. Rev. E **80**, 025401 (2009)
Montgomery, D., Matthaeus, W.H.: Astrophys. J. **447**, 706 (1995)
Norman, C.A., Ferrara, A.: Astrophys. J. **467**, 280 (1996)
Ng, C.S., Bhattacharjee, A.: Astrophys. J. **465**, 845 (1996)
Ossendrijver, M.: Astron. Astrophys. Rev. **11**, 287 (2003)
Parker, E.N.: J. Geophys. Res. **62**, 509 (1957)
Parker, E.N.: Astrophys. J. **162**, 665 (1970)
Parker, E.N.: Cosmic Magnetism, Clarendon Press/Oxford University Press, Oxford/New York, 858 p. (1979)
Parker, E.N.: Astrophys. J. **408**, 707 (1993)
Petschek, H.E.: Hess, W.H. (ed.) Physics of Solar Flares, AAS-NASA Symposium (NASA SP-50), (Greenbelt, MD: NASA), 425 (1964)
Phan, T.D., Gosling, J.T., Davis, M.S.: Geophys. Res. Lett. **36**, L09108 (2009)
Podesta, J.J.: Twelfth International Solar Wind Conference, 1216, 128 (2010)
Politano, H., Pouquet, A., Sulem, P.L.: Phys. Fluids B **1**, 2330 (1989)
Priest, E.R., Forbes, T.G.: Astron. Astrophys. Rev. **10**, 313 (2002)
Rechester, A.B., Rosenbluth, M.N.: Phys. Rev. Lett. **40**, 38 (1978)
Santos-Lima, R., Lazarian, A., de Gouveia Dal Pino, E.M., Cho, J.: Astrophys. J. **714**, 442 (2010)
Santos-Lima, R., de Gouveia Dal Pino, E.M., Lazarian, A.: Astrophys. J. **747**, 21 (2012)
Santos-Lima, R., de Gouveia Dal Pino, E.M., Kowal, G., Falceta-Gonçalves, D.A., Lazarian, A., Nakwacki, M.S.: Mon. Not. R. Astron. Soc. **429**, 3371 (2013)
Schekochihin, A.A., Cowley, S.C.: Phys. Plasmas **13**, 056501 (2006)

Schekochihin, A.A., Cowley, S.C., Maron, J.L., McWilliams, J.C.: Astrophys. J. **612**, 276 (2004)
Schekochihin, A.A., Cowley, S.C., Dorland, W.: Plasma Phys. Control. Fusion **49**, 195 (2007)
Schekochihin, A.A., Cowley, S.C., Dorland, W., Hammett, G.W., Howes, G.G., Quataert, E., Tatsuno, T.: Astrophys. J. **182**, 310 (2009)
Schuecker, P., Finoguenov, A., Miniati, F., Böhringer, H., Briel, U.G.: Astron. Astrophy. **426**, 387 (2004)
Shay, M.A., Drake, J.F.: Geophys. Rev. Lett. **25**, 3759 (1998)
Shay, M.A., Drake, J.F., Denton, R.E., Biskamp, D.: J. Geophys. Res. **103**, 9165 (1998)
Shay, M.A., Drake, J.F., Swisdak, M.M.: Phys. Plasmas **11**, 2199 (2004)
Shay, M.A., Drake, J.F., Rogers, B.N., Denton, R.E.: Geophys. Rev. Lett. **26**, 2163 (1999)
Shebalin, J.V., Matthaeus, W.H., Montgomery, D.: J. Plasma Phys. **29**, 525 (1983)
Shibata, K., Magara, T.: Living Rev. Solar Phys. **8**, 6 (2001)
Shibata, K., Tanuma, S.: Earth Planets Space **53**, 473 (2001)
Shivamoggi, B.K.: Phys. Plasmas **18**, 052304 (2011)
Smith, D., Ghosh, S., Dmitruk, P., Matthaeus, W.H.: Geophys. Res. Lett. **31**, L02805 (2004)
Speiser, T.W.: Planet. Space Sci. **18**, 613 (1970)
Strauss, H.R.: Phys. Fluids **29**, 3668 (1986)
Strauss, H.R.: Astrophys. J. **326**, 412 (1988)
Sturrock, P.A.: Nature **211**, 695 (1966)
Subramanian, K., Shukurov, A., Haugen, N.E.L.: Mon. Not. R. Astron. Soc. **366**, 1437 (2006)
Susino, R., Bemporad, A., Kruker, S.: (2013). arXiv:1310.2853v1 [astro-ph.SR]
Sweet, P.A.: Bo Lehnert (ed.) Proceedings from IAU Symposium no. 6. Cambridge University Press, Cambridge, p. 123 (1958)
Sych, R., Nakariakov, V.M., Karlicky, M., Anfinogentov, S.: Astron. Astrophys. **505**, 791 (2009)
Uzdensky, D.A., Kulsrud, R.M.: Phys. Plasmas **13**, 062305 (2006)
Vasquez, B.J., Abramenko, V.I., Haggerty, D.K., Smith, C.W.: J. Geophys. Res. **112**, A11102 (2007)
Vekshtein, G.E., Ryutov, D.D., Sagdeev, R.Z.: Sov. J. Exp. Theor. Phys. Lett. **12**, 291 (1970)
Vishniac, E., Lazarian, A.: In: Ostrowski, M., Schlickeiser, R. (eds.) Plasma Turbulence and Energetic Particles in Astrophysics. Proceedings of the International Conference, Cracow, Poland, 5–10 September, 1999 Obserwatorium Astronomiczne, Uniwersytet Jagielloński, Kraków (1999)
Vishniac, E.T., Pillsworth, S., Eyink, G.L., Kowal, G., Lazarian, A., Murray, S.: Nonlinear Process. Geophys. **19**, 605 (2012)
Vogt, C., Enßlin, T.A.: Astron. Astrophys. **434**, 67 (2005)
Waelbroeck, F.L.: Phys. Fluids B **1**, 2372 (1989)
Wang, X., Bhattacharjee, A., Ma, Z.W.: J. Geophys. Res. **105**, 27 633 (2000)
Wang, X., Bhattacharjee, A., Ma, Z.W.: Phys. Rev. Lett. **87**, 265003 (2001)
Watson, P.G., Oughton, S., Craig, I.J.D.: Phys. Plasmas **14**, 032301 (2007)
Weinan, E., Vanden-Eijnden, E.: Phys. Fluids **12**, 149 (2000a)
Weinan, E., Vanden-Eijnden, E.: Proc. Natl. Acad. Sci. USA **97**, 8200 (2000b)
Weinan, E., vanden-Eijnden, E.: Physica D **152/153**, 636 (2001)
Weinan, E., Vanden-Eijnden, E.: Phys. D Nonlinear Phenomena **152**, 636 (2001)
Wicks, R.T., Horbury, T.S., Chen, C.H.K. Schekochihin, A.A.: Mon. Not. R. Astron. Soc. **407**, L31 (2010)
Wicks, R.T., Horbury, T.S., Chen, C.H.K., Schekochihin, A.A.: Phys. Rev. Lett. **106**, 045001 (2011)
Yamada, M.: J. Geophys. Res. **104**, 14529 (1999)
Yamada, M.: Phys. Plasmas **14**, 058102 (2007)
Yamada, M., Ren, Y., Ji, H., Breslau, J., Gerhardt, S., Kulsrud, R., Kuritsyn, A.: Phys. Plasmas **13**, 052119 (2006)
Yamada, M., Kulsrud, R., Ji, H.: Rev. Mod. Phys. **82**, 603 (2010)
Yokoyama, T., Shibata, K.: Nature **375**, 42 (1995)
Zeldovich, Ya B.: J. Exp. Theor. Phys **4**, **460** (1957)

Zhang, B., Yan, H.: Astrophys. J. **726**, 90 (2011)
Zimbardo, G., Greco, A., Sorriso-Valvo, L., Perri, S., Vörös, Z., Aburjania, G., Chargazia, K., Alexandrova, O.: Space Sci. Rev. **156**, 89 (2010)
Zweibel, E.G.: Astrophys. J. **567**, 962 (2002)

Chapter 13
Particle Acceleration by Magnetic Reconnection

Elisabete M. de Gouveia Dal Pino and Grzegorz Kowal

Abstract Observational data require a rich variety of mechanisms to accelerate fast particles in astrophysical environments operating under different conditions. The mechanisms discussed in the literature include varying magnetic fields in compact sources, stochastic processes in turbulent environments, and acceleration behind shocks. An alternative, much less explored mechanism involves particle acceleration within magnetic reconnection sites. In this chapter we discuss this mechanism and show that particles can be efficiently accelerated by magnetic reconnection through a first order Fermi process within large scale current sheets (specially when in the presence of local turbulence which speeds up the reconnection and make the acceleration region thicker) and also through a second order Fermi process in pure MHD turbulent environments.

13.1 Introduction

Energetic particles are ubiquitous in astrophysical environments and their acceleration still challenges the researchers. For instance, the origin of the ultra high energy cosmic rays (UHECRs) is unknown yet. Their spectrum is consistent with an origin in extragalactic astrophysical sources and candidates range from the birth of compact objects to explosions related to gamma-ray bursts (GRBs), or events in active galaxies (AGNs) (Kotera and Olinto 2011), however, the mechanism(s) that produce(s) them is(are) still not fully understood. Similarly, recent very high energy observations with the Fermi and Swift satellites and ground based gamma ray observatories (HESS, VERITAS and MAGIC) of AGNs and GRBs have been challenging the current particle acceleration theories which have to explain how

E.M. de Gouveia Dal Pino (✉)
Instituto de Astronomia, Geofísica e Ciências Atmosféricas, Universidade de São Paulo, Rua do Matão 1226, Cidade Universitária, 05508-090 São Paulo, SP, Brazil
e-mail: dalpino@iag.usp.br

G. Kowal
Escola de Artes, Ciências e Humanidades, Universidade de São Paulo, Av. Arlindo Béttio, 1000 Ermelino Matarazzo, 03828-000 São Paulo, Brazil
e-mail: g.kowal@iag.usp.br

A. Lazarian et al. (eds.), *Magnetic Fields in Diffuse Media*, Astrophysics and Space Science Library 407, DOI 10.1007/978-3-662-44625-6_13

particles are accelerated to TeV or larger energies in regions relatively small compared to the fiducial scale of their sources (Sol et al. 2013).

The mechanisms frequently discussed in the literature for accelerating energetic particles include varying magnetic fields in compact sources (e.g., de Gouveia Dal Pino and Lazarian 2000, 2001; Melrose 2009), stochastic processes in turbulent environments (Melrose 2009), and acceleration behind shocks. The latter, in particular, has been extensively discussed in the literature (Sironi and Spitkovsky 2009; Melrose 2009; Kotera and Olinto 2011) An alternative, much less explored mechanism so far, involves particle acceleration within magnetic reconnection sites.

Magnetic reconnection occurs when two magnetic fluxes of opposite polarity encounter each other (see middle panel of Fig. 13.7). In the presence of finite magnetic resistivity, the converging magnetic field lines annihilate at the discontinuity surface and a current sheet forms there.

Traditionally, particle acceleration in reconnection sites has been regarded as a linear process due to the advective electric field (also referred as the reconnection electric field) that develops along the current sheet, in the normal direction to the magnetic field ($\epsilon = V_R B/c$, where V_R is the reconnection velocity) (e.g., Speiser 1965; Litvinenko 1996; Zenitani and Hoshino 2001; Giannios 2010). While describing a betatron-like orbit (also often called Speiser orbit) along this direction, particles are continuously accelerated by the electric field with its energy increasing linearly with the distance (z) travelled along the current sheet or reconnection layer ($E \sim eV_R Bz/c$) (Speiser 1965).

In 2005, de Gouveia Dal Pino and Lazarian (2005) (henceforth GL05) proposed a mechanism to accelerate particles to relativistic velocities within the reconnection layer, in a similar way to the first-order Fermi process that occurs in shocks, which is also able to increase their energy exponentially. It is known from shock acceleration theory that particles are injected upstream and allowed to convect into the shock, while diffusing in space so as to undergo multiple shock crossings, and thereby gaining energy through a first order Fermi process (Fermi 1949). Similarly, GL05 (de Gouveia Dal Pino and Lazarian 2005) proposed that trapped charged particles may bounce back and forth several times and gain energy due to head-on collisions with the two converging magnetic fluxes of opposite polarity that move to each other at the reconnection velocity (V_R). They found that the particle energy gain after each round trip is $\Delta E/E \propto V_R/c$. Under *fast* magnetic reconnection conditions, e.g. induced by turbulence (Lazarian and Vishniac 1999), V_R can be of the order of the local Alfvén speed V_A (see below and also the Chapter by Lazarian et al. in this volume). At the surroundings of relativistic sources, for instance, $V_R \simeq v_A \simeq c$, so that the mechanism can be rather efficient. GL05 (de Gouveia Dal Pino and Lazarian 2005) have also shown that the accelerated particles have a power-law distribution and a corresponding electron synchrotron radio power-law spectrum which is compatible with the observed radio flares of galactic black hole binaries (microquasars). Though that study was specifically applied to microquasars, it can be far more general in astrophysical systems, as we discuss below.

Afterwards, Drake et al. (2006) invoked a similar process, but within a collisionless reconnection scenario (see the chapter by Lazarian et al. in this volume). In their model, the contraction of two-dimensional magnetic loops is controlled by

the firehose instability that arises in a particle-in-cell (PIC) domain (Lyubarsky and Liverts 2008; Drake et al. 2010). Other processes of acceleration, e.g. due to turbulence arising as a result of reconnection (La Rosa et al. 2006) were shown to be less dominant.

Magnetic reconnection is very frequent and therefore, it should be expected to induce acceleration of particles in a wide range of galactic and extragalactic environments. Originally discussed predominantly in the context of electrons in solar flares (Drake et al. 2006, 2009; Gordovskyy et al. 2010; Gordovskyy and Browning 2011; Zharkova and Siversky 2011), it was later applied to explain the origin of anomalous cosmic ray protons (Lazarian and Opher 2009; Drake et al. 2010), and the anisotropies in the direction of solar system magnetotail (Lazarian and Desiati 2010). It also has been gaining importance beyond the solar system, in more extreme astrophysical environments and sources, such as in the production of ultra high energy cosmic rays (Giannios 2010; Kotera and Olinto 2011), in particle acceleration in jet-accretion disk systems (de Gouveia Dal Pino and Lazarian 2005; de Gouveia Dal Pino et al. 2010a,b; Giannios 2010; del Valle et al. 2011), and in the general framework of compact sources, as AGNs and GRBs (Lazarian et al. 2003; Zenitani and Hoshino 2001; Zenitani et al. 2009; de Gouveia Dal Pino et al. 2010b, 2011; Giannios 2010; Zhang and Yan 2011; Uzdensky 2011; Uzdensky and McKinney 2011), and even in pulsar nebulae, like Crab (Cerutti et al. 2013).

The applications above, however, still require extensive study of particle acceleration in magnetic reconnection sites, as well as on its connection with magnetohydrodynamical (MHD) turbulence and $fast$ magnetic reconnection.

In particular, a way to probe the analytical results above is through numerical simulations. So far, most of the numerical studies of particle acceleration by magnetic reconnection have been performed for two-dimensional, collisionless pair plasmas by means of particle-in-cell (PIC) simulations (e.g., Drake et al. 2006, 2010; Zenitani and Hoshino 2001; Cerutti et al. 2013). However, these apply to kinetic scales of only a few hundred plasma inertial lengths ($\sim 100 c/\omega_p$, where ω_p is the plasma frequency). The generally much larger scales of the astrophysical systems (pulsars, AGNs, GRBs, etc.) frequently require a collisional MHD description of reconnection.

Some progress in this direction has been achieved recently (de Gouveia Dal Pino et al. 2010b, 2011; Lazarian et al. 2011; Kowal et al. 2011, 2012) where the model of GL05 (de Gouveia Dal Pino and Lazarian 2005) was tested successfully by means of two (2D) and three dimensional (3D) MHD simulations. Kowal, de Gouveia Dal Pino and Lazarian (2011, henceforth LGK11) (Kowal et al. 2011), in particular, have shown that the acceleration of particles inserted in MHD domains of reconnection without including kinetic effects produces results similar to those found in particle-in-cell (PIC) (collisionless) simulations where particle acceleration is controlled by kinetic effects such as the firehose instability (Zenitani and Hoshino 2001; Drake et al. 2006, 2010). This demonstrated that the acceleration in reconnection regions is a universal process which is not determined by the details of the plasma physics and can be also very efficient in collisional gas. They have also shown that particle acceleration in 3D MHD reconnection behaves quite differently from the acceleration in 2D domains since the increase in the acceleration component parallel

to the magnetic field is not constrained by the production or size of contracting islands, as in the 2D case. These results call for focusing on realistic 3D geometries of reconnection.

Other concomitant studies have also explored test particle acceleration in MHD domains (Gordovskyy et al. 2010; Gordovskyy and Browning 2011). Gordovskyy et al. (2010), for instance, focussed on 2D models with time-dependent reconnection, while (Gordovskyy and Browning 2011), aiming the study of particle acceleration in small solar flares, examined a somewhat different scenario, with the acceleration of test particles by magnetic reconnection induced by kink instabilities in 3D twisted magnetic loops. Although they have obtained results for the particle energy distributions which are compatible with field-aligned acceleration as in the studies above, they did not explore the nature of the mechanism accelerating the particles.

Kowal, de Gouveia Dal Pino and Lazarian (2012, henceforth KGL12) (Kowal et al. 2012) have, in turn, injected test particles in different 3D collisional MHD reconnection and compared the particle spectrum and acceleration rates in these different domains. When considering a single Sweet-Parker topology (Sweet 1958; Parker 1957) (subject to large artificial magnetic resistivity to allow fast reconnection), they have found that particles accelerate predominantly through a first-order Fermi process, as predicted in GL05 (de Gouveia Dal Pino and Lazarian 2005). When turbulence is induced within the current sheet, the acceleration is highly enhanced. This is due to the fact that reconnection becomes fast in a natural way (and independent of magnetic resistivity) in the presence of turbulence (Lazarian and Vishniac 1999; Kowal et al. 2009) and allows the formation of a thick volume filled with multiple simultaneously reconnecting magnetic fluxes. Besides, reconnection is intrinsically 3D in this case (see also the chapter by Lazarian et al. in this volume for more details of the fast reconnection process in the presence of turbulence). The particles trapped within this volume suffer several head-on scatterings with the contracting magnetic fluctuations, which significantly increase the acceleration rate and the amount of particles which are accelerated through a first-order Fermi process. They have also tested the acceleration of particles in pure MHD turbulence, where particles suffer collisions both with approaching and receding magnetic irregularities. The acceleration rate is smaller in this case and suggests that the dominant process is a second order Fermi.

In this chapter, we discuss these acceleration mechanisms in magnetic reconnection sites in detail and review the recent analytical and numerical results in this regard.

13.2 Analytical Model for First Order Fermi Particle Acceleration Within Magnetic Reconnection Sites

We first discuss an analytical model for acceleration of particles within reconnection sites which was originally introduced by GL05 de Gouveia Dal Pino and Lazarian (2005) (see also Lazarian 2005; de Gouveia Dal Pino et al. 2010a, 2014). Figure 13.1 illustrates the simplest realization of the acceleration within a large scale

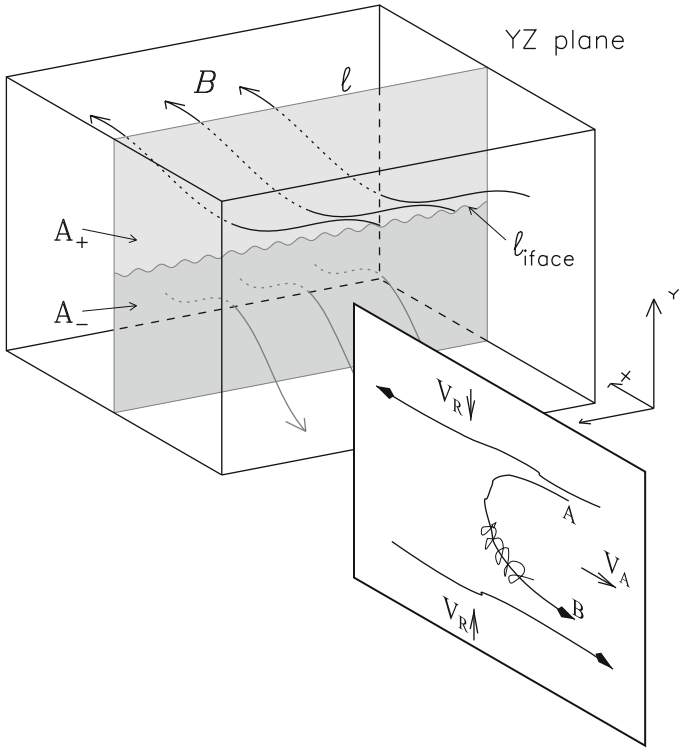

Fig. 13.1 Particle acceleration in a reconnection site where two magnetic field fluxes of opposite polarity move to each other. *Top left*: three-dimensional view of a magnetic reconnection sheet. *Bottom right*: detail of a particle being accelerated within the reconnection site. It spirals about a reconnected magnetic field line and bounces back and forth between points A and B. The reconnected regions move towards each other with the reconnection velocity V_R. Particles gain energy due to "collisions" with the magnetic irregularities within the two converging fluxes, just like in the first-order Fermi process in shock fronts (see GL05 de Gouveia Dal Pino and Lazarian 2005). Bouncing between the points A and B happens either because of streaming instability induced by energetic particles or by magnetic turbulence in the reconnection region (as discussed in Lazarian and Vishniac 1999). In particular, when turbulence is present, the acceleration region is filled in by several oppositely moving reconnected flux tubes which collide and repeat on smaller and smaller scales the pattern of the larger scale reconnection making the process very fast and therefore, the particle acceleration very efficient. Since in such a case the reconnection is naturally a three-dimensional process, particle acceleration as shown in the *bottom right panel* may occur in all directions within the current sheet and is not restricted to the direction depicted in the figure. (Adapted from Kowal et al. 2009; Lazarian et al. 2011; see also de Gouveia Dal Pino et al. 2014)

reconnection region. As described in the Figure, as a particle bounces back and forth between two converging magnetic fluxes of opposite polarity, it gains energy through a first-order Fermi acceleration.

In order to derive the energy spectrum of the accelerated particles one can invoke a similar procedure to the one employed in the calculation of the first order Fermi

acceleration in shocks (see, e.g., Bell 1978; Longair 2011; Lazarian et al. 2011). Let us consider the acceleration of M_0 particles with an initial energy E_0. If a particle acquires an energy $E = \beta E_0$ after a collision, its energy after m collisions will $\beta^m E_0$. At the same time if the probability of a particle to remain within the acceleration region is P, after m collisions the number of accelerated particles will be $M = P^m M_0$. Therefore, $\ln(M/M_0)/\ln(E/E_0) = \ln P/\ln\beta$ or

$$\frac{M}{M_0} = \left(\frac{E}{E_0}\right)^{\ln P/\ln\beta} \tag{13.1}$$

Since some of these M particles will be further accelerated before escaping the system, the equation above implies that the number $N(E)$ of particles accelerated to energies equal to or larger than E is given by:

$$N(E)dE = const \times E^{-1+(\ln P/\ln\beta)}dE \tag{13.2}$$

To compute P and β within the reconnection site we may consider the following process. The particles from the upper reconnection region will "see" the lower reconnection region moving towards them with the velocity $2V_R$ (see Fig. 13.1). If a particle from the upper region enters at an angle θ with respect to the direction of V_R into the lower region then the expected energy gain of the particle is $\delta E/E = 2V_R\cos\theta/c$. For an isotropic distribution of particles their probability function is $p(\theta) = 2\sin\theta\cos\theta d\theta$ and therefore the average energy gain per crossing of the reconnection region is

$$\langle \delta E/E\rangle = \frac{V_R}{c}\int_0^{\pi/2} 2\cos^2\theta\sin\theta d\theta = 4/3\frac{V_R}{c} \tag{13.3}$$

Particles will complete a full acceleration cycle when they return back to the upper reconnection region. Similarly, if they are in the lower reconnection region they will see the upper reconnection region moving towards them with the speed $2V_R$. As a result, a full acceleration cycle provides an energy increase $\langle \delta E/E\rangle_{cycle} = 8/3(V_R/c)$ and thus [1]

$$\beta = E/E_0 = 1 + 8/3(V_R/c) \tag{13.4}$$

Let us assume that the particle diffusion velocity is much smaller than V_R. In analogy to particle acceleration in a shock front, for simplicity, we further assume that the total number of particles crossing the boundaries of the upper and lower magnetic fluxes is $2 \times 1/4(nc)$, where n is the number density of particles. If the

[1] We note that Giannios (2010) re-derived the relation above in the limit when the reconnection velocity itself approaches the light speed and obtained an expression that naturally recovers the form of Eq. (13.4) in the non-relativistic regime.

particles are advected to outside of the reconnection region with the magnetized plasma outflow then, the loss of the energetic particles will be given approximately by $2V_R n$. Therefore the fraction of energetic particles which are lost in a cycle will be $V_R n/[1/4(nc)] = 4V_R/c$ and

$$P = 1 - 4V_R/c. \tag{13.5}$$

Combining Eqs. (13.2), (13.4), and (13.5) one obtains

$$N(E)dE = const_1 E^{-5/2} dE, \tag{13.6}$$

which is the spectrum of accelerated energetic particles for the case when the plasma back-reaction is negligible (de Gouveia Dal Pino and Lazarian 2005; Lazarian et al. 2011). We note that the power-law index obtained above is independent of the reconnection velocity V_R. This is in part due to the simplified assumptions in the derivation above. Nonetheless, we will see below that in the much more realistic numerical simulations of the acceleration of test particles in non-relativistic MHD reconnection sites, the acceleration rate and power spectrum are not very much sensitive to the reconnection speed (del Valle et al. 2014).

In recent work, Drury (2012) tried to improve the analytical model above by considering two additional effects. First, he took into account the energy losses due to the outflow from the reconnection region (which is associated with a divergence of the flow field) and second, he relaxed the assumption considered above (GL05) that the escape rate is the same as that from a shock. Then, he repeated the calculation above and obtained a power law spectral index which is the same as in shock acceleration if expressed in terms of the compression ratio in the system $r = \rho_2/\rho_1$, where ρ_1 and ρ_2 are the plasma densities at the inflow and the outflow regions of the reconnection site, respectively. In other words, he obtained:

$$f(p) \propto p^{\frac{-3r}{r-1}}, \tag{13.7}$$

where $f(p)$ is the particles distribution function as a function of their momentum p. Considering that only little energy is used to heat the plasma and the conversion is essentially one of magnetic energy into kinetic energy, then the reconnection can be very compressive, unless the outflow is significantly over pressured relative to the environment. But, for a strongly magnetized inflow this is a very weak constraint (Drury 2012). Thus one can expect in general large values of the compression ratio, possibly larger than the value four usually assumed for adiabatic shocks. For large values of r one finds $f(p) \propto p^{-3}$, or:

$$N(E) \propto E^{-1} \tag{13.8}$$

which is a power-law spectrum much harder than the one obtained above by GL05, but confirms their prediction that a rather efficient first-order Fermi particle acceleration process can take place in magnetic reconnection sites.

The considerations above also allow one to estimate the acceleration time-scale due to reconnection, which is a straightforward generalization of the result for shock acceleration as well.

The simplest way to evaluate the acceleration time is by setting the energy of the accelerated particle E equal to $e(V_R/c)Bz$, where z is the distance travelled by the particle along the current sheet (normal to the magnetic field direction) while being accelerated by the effective electric field $(V_R/c)B$. The acceleration time is, therefore (e.g. Speiser 1965; Giannios 2010)

$$t_{acc} \simeq z/c \simeq \frac{E}{eV_R B}. \tag{13.9}$$

This acceleration time scale is similar to that for shock acceleration, and the constraints on maximum energy due to the finite age and size of the reconnection region will thus be comparable to those in shock acceleration.

A simple way to estimate the maximum energy that a particle can achieve is by realizing that it can no longer be confined within the reconnection region when its Larmor radius becomes larger than the thickness of the reconnection layer l_{rec}. This implies that:

$$E_{max} \simeq ecl_{rec}B \tag{13.10}$$

It should be noticed that Drury's model above (Drury 2012) predicts that the acceleration within reconnection sites requires, as in shocks, a large compression ratio in order to be efficient. However, according to the discussion in the previous section (see also the following sections), the requirement for the magnetic reconnection acceleration process to proceed efficiently is to keep the accelerated particles within contracting magnetic loops. This requires constraints on the particle diffusivity specially perpendicular to the magnetic field direction. The subtlety of this point is related to the fact that while in the first-order Fermi acceleration in shocks compression is important, the acceleration via reconnection is applicable also to incompressible fluids. Thus, unlike shocks, not the entire volume has to shrink by compression in order to the acceleration to occur, but the volume of the magnetic flux tube. If the perpendicular diffusion of the particles to the magnetic field is large they may decouple from the magnetic field. Indeed, it is easy to see that as long as the particles in the magnetic flux rope, as depicted in Fig. 13.1, bounce back and forth between the converging mirrors they will be accelerated. However, if these particles leave the flux rope too fast, they may start bouncing between the magnetic fields of different flux ropes which may sometimes decrease their energy, thus favouring a second order rather than a first-order Fermi process. Thus it is important that the particle diffusion parallel and perpendicular to the magnetic field stays different. Particle anisotropy which arises from particle preferentially being accelerated in the parallel direction must be significant. In the next section where we depict results of numerical simulations of particle acceleration by magnetic

reconnection, the evolution of both particles' velocity components is tracked separately in order to stress this point.

In the case of laminar reconnection sites (i.e., with no turbulence), as in a Sweet-Parker model for reconnection (or as in the model above; see also Sect. 13.3.4), the scales can be much smaller compared to shock structures. This will lead to lower maximum energies (the dominant limiting loss process being diffusion out of the sides of the reconnection region). This means that the models developed above apply only if the particle diffusion length scale in the inflow is small compared to its lateral extent. Thus they may only apply in a restricted energy range which should be contrasted with the case of shock acceleration where the scale separation is, in general, much larger. Nevertheless, when turbulence is present within the reconnection site, this will make the reconnection volume much larger (Lazarian and Vishniac 1999; Kowal et al. 2009, 2011, 2012) and therefore, this process can be competitive to shock acceleration, as we will see below.

13.3 Particle Acceleration in Reconnection Sites: Numerical Studies

As discussed in the previous section, magnetic reconnection results in shrinking of magnetic loops between two converging magnetic fluxes of opposite polarity and the charged particles entrained over the magnetic loops are accelerated (see Fig. 13.1). In this section we discuss the results of numerical studies that confirm these predictions.

In what follows, we consider different domains of magnetic reconnection which were modelled by solving the isothermal MHD equations numerically in a uniform mesh using a Godunov-type scheme (Kowal et al. 2009, 2011, 2012).

In order to integrate the test particle trajectories a data cube obtained from the MHD models is frozen in time and then 10,000 test particles are injected in the domain with random initial positions and directions and with an initial thermal distribution. For each particle the relativistic equation of motion is solved

$$\frac{d}{dt}(\gamma m u) = q\,(E + u \times B)\,, \tag{13.11}$$

where m, q and u are the particle mass, electric charge and velocity, respectively, E and B are the electric and magnetic fields, respectively, $\gamma \equiv \left(1 - u^2/c^2\right)^{-1}$ is the Lorentz factor, and c is the speed of light. The electric field E is taken from the MHD simulations

$$E = -v \times B + \eta J, \tag{13.12}$$

where v is the plasma velocity, $J \equiv \nabla \times B$ is the current density, and η is the Ohmic resistivity coefficient. The resistive term above can be neglected because its effect on

particle acceleration is negligible (Kowal et al. 2011). These studies do not include the particle energy losses, so that particles gain or loose energy only through the interactions with the moving magnetized plasma.

We note that since we are focusing on the acceleration process only, very simple domains can be considered which represent only small periodic boxes of entire magnetic reconnection or turbulent sites. For this reason, the typical crossing time through the box of an injected thermal particle is very small and it has to re-enter the computational domain several times before gaining significant energy by multiple scatterings. Thus, whenever a particle reaches the box boundary it re-enters in the other side to continue scattering (Kowal et al. 2012).

13.3.1 Particle Acceleration in 2D Domains

Figure 13.2 presents an evolved 2D MHD configuration with eight Harris current sheets in a periodic box (Kowal et al. 2011) (see also Drake et al. 2010). The initial density profile is such that the total (gas plus magnetic) pressure is uniform. Random

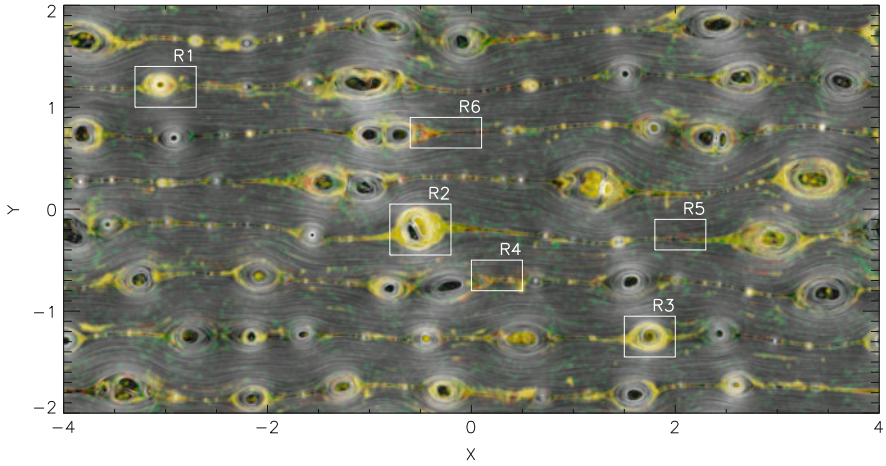

Fig. 13.2 Topology of the magnetic field represented as a gray texture with semi-transparent color maps representing locations where the parallel and perpendicular particle velocity components are accelerated for a 2D model with $B_z = 0.0$ at time 6.0 in the code units. The *red and green* colors correspond to regions where either parallel or perpendicular acceleration occurs, respectively, while the *yellow* color shows locations where both types of acceleration occur. The parallel component increases in the contracting islands and in the current sheets as well, while the perpendicular component increases mostly in the regions between current sheets. White boxes show regions that are more carefully analyzed in Kowal et al. (2011) paper. The simulation was performed with the resolution 8,192 × 4,096. Ten thousand test particles were injected in this snapshot with the initial thermal distribution with a temperature corresponding to the sound speed of the MHD model. (From Kowal et al. 2011)

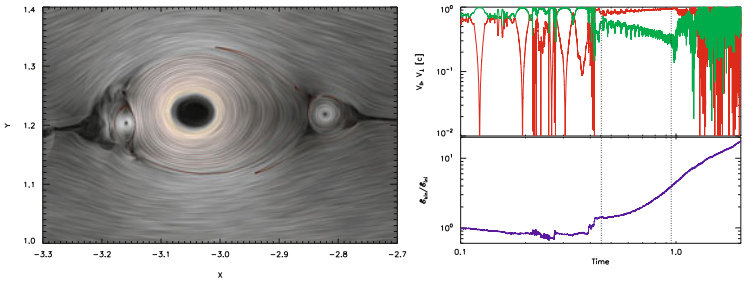

Fig. 13.3 The case of a shrinking island where the particles accelerate efficiently. It corresponds to region R1 of Fig. 13.2. The *left panel* shows the trajectory of a single test proton trapped in this contracting island. We see two small magnetic islands on both sides of the central elongated island which are merging with it. This process results in the contraction of the central island. The *right panel* shows the exponential increase of the particle energy. The proton orbiting around the center of the magnetic island increases its energy increment after each orbit. (Extracted from Kowal et al. 2011)

weak velocity fluctuations were imposed to this environment in order to enable spontaneous reconnection events and the development of the magnetic islands.

Figure 13.2 clearly shows the merging of islands in some locations and the resulting stretching or shrinking which provides appropriate conditions for particle acceleration. KGL11 (Kowal et al. 2011) find that an increase of the parallel velocity component is mostly observed within shrinking islands and in current sheets (see the red and yellow zones in Fig. 13.2), while the increase of the perpendicular component is observed mostly near and within stretching islands and between current sheets (see the green and yellow zones in Fig. 13.2). This complex behavior is related to the degree of island deformation and the particle direction and speed. Within contracting magnetic islands or current sheets the particles accelerate predominantly through the first order Fermi process, as previously described, while outside of the current sheets and the islands the particles experience mostly drift acceleration due to magnetic fields gradients (Kowal et al. 2011). In Fig. 13.3 the first of these effects is zoomed in an example of a single test proton which is trapped in a shrinking island and is accelerated. Its parallel speed increases while the gyro rotation slows down. This results in an exponential growth of the kinetic energy of the particle (as shown in the right panel).

Similar results were found in 2D collisionless pair plasma PIC simulations (Drake et al. 2010; Zenitani and Hoshino 2001; Cerutti et al. 2013). In such cases, reconnection is fast because it is facilitated by the two-fluid (Hall) effects and/or anomalous resistivity and exhibit a Petschek-like (1964) structure (Birn et al. 2001; Yamada et al. 2010, 2006; Shay et al. 1998, 2004).

This implies that the first-order Fermi acceleration process within shrinking islands is not restricted to collisionless physics or kinetic effects as previously suggested and described by PIC simulations (e.g. Drake et al. 2006, 2010 and references therein). This acceleration mechanism in reconnection sites works also

in collisional plasmas, under the MHD approximation, as shown above and, in fact, MHD codes present an easier way to study the physics of particle acceleration numerically.

13.3.2 Acceleration Near and Within Current Sheets

In the current sheet zones (regions R4–R6 of Fig. 13.2) we can also identify a first order Fermi acceleration due to simple particle scattering between the converging flows entering both sides of the current sheet (or even in merging/shrinking islands which are just forming there), as described in de Gouveia Dal Pino and Lazarian (2005).

In zones above and below the current sheets particles possibly experience predominantly a drift acceleration driven by non-uniformities of the magnetic field (e.g., Melrose 2009). Generally, this effect is less efficient than the first order Fermi process in merging/contracting islands and results in smaller acceleration rates. The origin of this effect is due to the net work done on a charge by the Lorentz force (Eq. (13.12)) in a zone of non-uniform large scale magnetic field. The principal equation governing this is the scalar product of the particle velocity (or momentum) and the acceleration by the convective electric field, $-v \times B$. In uniform magnetic fields, the energy gain and loss acquired during a gyroperiod exactly cancel, so in result no net work is done, $\Delta W = 0$.

Figure 13.4 zooms in the details of the acceleration of a test particle near and within a single (Sweet-Parker shaped; see also Sect. 13.3.4) current sheet. Before the particle reaches the current sheet discontinuity it is drifted by the plasma inflow

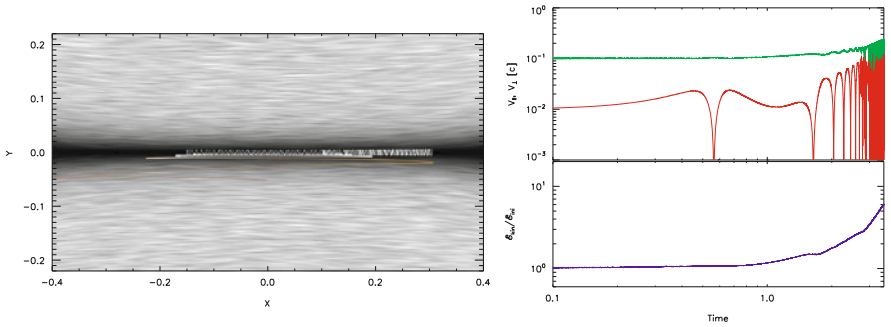

Fig. 13.4 The case of acceleration near and within a single current sheet with a Sweet–Parker configuration like region (R6 in Fig. 13.2). The *left panel* shows the trajectory of a test proton approaching the diffusion region. The color of the trajectory corresponds to the particle energy (which increases from *red to yellow* and then finally to *white* when the particle reaches the current sheet). The *right panel* shows the evolution of the particle energy. In the model of Sweet–Parker reconnection presented in this figure we used explicit large resistivity coefficient $\eta = 10^{-3}$ in order to make reconnection fast. The grid size in the model was set to $\Delta x = 1/1024$. (Extracted from Kowal et al. 2011)

and the increasing gradient of B as it approaches the current sheet. When it enters the discontinuity (the white part of the trajectory in the left panel), it bounces back and forth several times and gains energy (which increases exponentially as shown in the right panel of Fig. 13.4) due to head-on collisions with the converging flow, on both sides of the magnetic discontinuity, in a first order Fermi process, as described in GL05 degouveia05. At the same time it drifts along the magnetic lines which eventually allow it to escape from the acceleration region. Therefore, we see two mechanisms: a drift acceleration (dominating outside of the current sheet) and first order Fermi acceleration inside the current sheet. These processes naturally depend on the initial particle gyroradius, since it determines the amount of time the particle remains in the acceleration zone before escaping.

13.3.3 2D Versus 3D simulations

The results presented in the previous sections were obtained for 2D models without a guide field. This means that in this case the magnetic lines creating the islands are closed and a charged particle can be trapped indefinitely in such an island. The presence of a guide field normal to the plane of Fig. 13.2 opens the magnetic loops and allows the charged particles to travel freely in the out-of-plane direction. Moreover, the islands evolve much slower in the presence of a strong guide field.

Figure 13.5 depicts the time evolution of the kinetic energy of the particles which have their parallel and perpendicular (red and blue points, respectively) velocity components accelerated for three models of reconnection. The kinetic energy is normalized by the proton rest mass value, i.e., it is actually $\gamma - 1$) that is plotted, where γ is the Lorentz factor. In the 2D model without a guide field (as in the models studied in the previous section) there is an exponential growth of energy mostly due to the acceleration of the parallel component which stops after the energy reaches values of 10^3–10^4. From that level on, particles accelerate their perpendicular component only with smaller linear rate in a log–log diagram. In the 2D model with a weak guide field $B_z = 0.1$ normal to the plane of Fig. 13.2, there is also an exponential acceleration of the parallel velocity component, but due to the presence of the weak guide field, this component accelerates further to higher energies at a similar rate as the perpendicular one. This implies that the presence of a guide field removes the restriction seen in the 2D model without a guide field and allows the particles to increase their parallel velocity components as they travel along the guide field, in open loops rather than in confined 2D islands. This result is reassured by the 3D model in Fig. 13.5, where no guide field is necessary as the MHD domain is fully three-dimensional. In this case, we clearly see a continuous increase of both components, which suggests that the particle acceleration behavior changes significantly when 3D effects are considered, i.e. where open loops replace the closed 2D reconnecting islands.

With the parametrization considered, the gyroradius of a proton becomes comparable to the size of the box domain when its Lorentz factor reaches a value of a

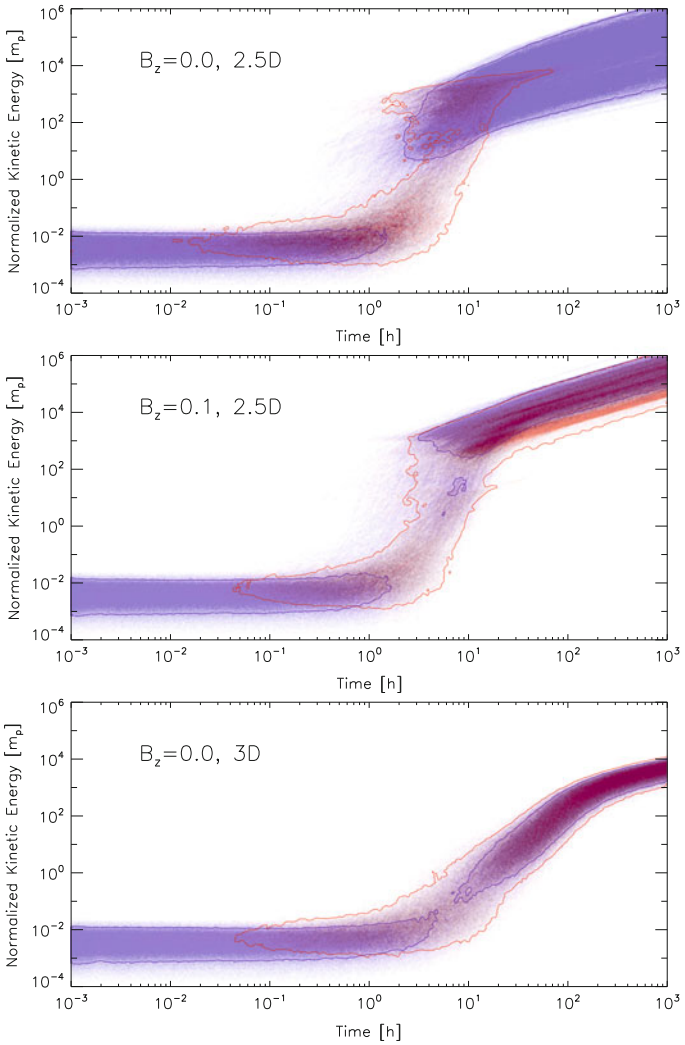

Fig. 13.5 Kinetic energy evolution of a group of 10^4 protons in 2D models of reconnection with a guide field strength B_z=0.0 and 0.1 (*top and middle panels*, respectively). In the *bottom panel* a fully 3D model with initial B_z=0.0 is presented. The colors show how the parallel (*red*) and perpendicular (*blue*) components of the particle velocities increase with time. The contours correspond to values 0.1 and 0.6 of the maximum number of particles for the parallel and perpendicular accelerations, respectively. The energy is normalized by the rest proton mass energy. The background magnetized flow with multiple current sheet layers is at time 4.0 in Alfvén time units ($t = L/V_A$, where L is the size of the computational domain and V_A is the Alfvén speed corresponding to the initial magnetic field in the system) for all models. (From Kowal et al. 2011)

few times 10^4. The largest islands in the system can have sizes of a few tenths of the size of the box. These rough estimates help us to understand the energy evolution in Fig. 13.5. In the case with no guide field (top panel of Fig. 13.5), the exponential parallel acceleration stops right before the energy value 10^4 is reached. After this, the rate of acceleration significantly decreases. This occurs because the Larmor radius of the particles has become larger than the sizes of biggest islands. Therefore, from this level on the particles cannot be confined anymore within the islands and the first order Fermi acceleration ceases. After that, there is a much slower drift acceleration (of the perpendicular component only) caused by the gradients of the large scale magnetic fields and acceleration between islands. If a guide field is inserted in such a system (as in the model of the middle panel of Fig. 13.5), the picture is very similar. However, since the particles are now able to travel along the guide field, their parallel velocity component also continues to increase after the 10^4 threshold. Of course, in the 3D model, the particles follow the same trend (bottom panel of Fig. 13.5).

While in two dimensional MHD models without a guide field the parallel acceleration saturates at some level, in the presence of an out-of-plane guide field or in three dimensional models this saturation effect is removed.

13.3.4 Acceleration in 3D Sweet-Parker Reconnection

In the Sweet–Parker model of reconnection of two large scale magnetic fluxes of opposite polarity (Sweet 1958; Parker 1957), the speed of reconnection, i.e. the speed at which two inflowing magnetic field lines annihilate by ohmic dissipation, is roughly η/Δ, where Δ is the width of the current sheet discontinuity (Fig. 13.1) and η is the Ohmic magnetic resistivity. The entrained plasma follows the local field lines and exits through the edges of the current sheet at roughly the Alfvén speed, $V_A \equiv B/(4\pi\rho)^{1/2}$, where ρ is the local density. Thus using momentum flux conservation it is easy to demonstrate that the resulting reconnection speed is a tiny fraction of the Alfvén speed, or $V_R \approx V_A S^{-1/2}$, where $S = LV_A/\eta$ is the Lundquist number and L is the length of the current sheet. Due to the typically huge astrophysical sizes of the reconnection sites, S is also huge for Ohmic diffusivity values (e.g., for the interstellar medium, $S \sim 10^{16}$) and this makes the Sweet–Parker reconnection very slow. However, observations require a reconnection speed close to V_A in several circumstances (e.g., in solar flares). A way to speed up reconnection is to invoke plasma instabilities, as for instance, the stream instability which makes resistivity anomalously large in the relation above (Parker 1979). Another way is to consider the presence of turbulence in the current sheet (Lazarian and Vishniac 1999), a process that will be described in Sect. 13.3.5.

In the model shown in the top of Fig. 13.6, KGL12 (Kowal et al. 2012) investigated the acceleration of thousands of particles in a Sweet–Parker current sheet but, in order to make reconnection fast, they employed a diffusivity coefficient

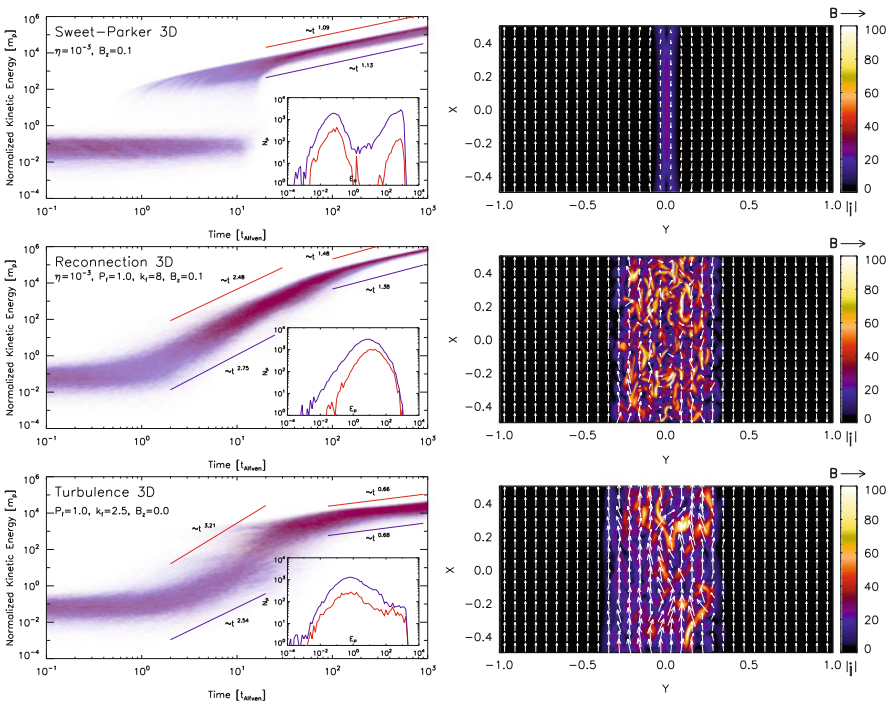

Fig. 13.6 *Left column*: Particle kinetic energy distributions for 10,000 protons injected in the Sweet–Parker reconnection (*top*), fast magnetic reconnection (*middle*), and purely turbulent (*bottom*) domains. The colors indicate which velocity component is accelerated (*red or blue* for parallel or perpendicular, respectively). The energy is normalized by the rest proton energy. Subplots show the particle energy distributions at $t = 5.0$. *Right column*: XY cuts through the domain at $Z = 0$ of the absolute value of current density $|\mathbf{J}|$ overlapped with the magnetic vectors for the Sweet–Parker reconnection (*top*), fast reconnection (*middle*), and purely turbulent domains (*bottom*). For the *top and middle* models with large scale current sheets it was employed $B_{0z} = 0.1$, $\eta = 10^{-3}$, and a resolution $256 \times 512 \times 256$, while for the *bottom* pure turbulent model it was employed $B_{0z} = 0.2$ and a resolution $128 \times 256 \times 128$. (From Kowal et al. 2012)

$\eta = 10^{-3}$ expressed in code units which, due to the numerical diffusivity, is several orders of magnitude larger than the typical Ohmic diffusivity in astrophysical environments and besides, makes the Sweet–Parker reconnection in the simulation efficient. The time evolution of the energy distribution for the accelerating particles is shown for this model in the top left panel of Fig. 13.6. Initially, the perpendicular acceleration dominates, because the volume in which particles are injected is much larger than the current sheet. The perpendicular acceleration, due to a drift of the magnetic flux, starts before the particles reach the reconnection region (Kowal et al. 2011). The distribution of particles does not change significantly until $t = 1.0$. Then, a rapid increase in energy by roughly four orders of magnitude appears for a fraction of particles. We observe a big gap between the energy levels before and after these acceleration events, which is also evident in the particle energy spectrum depicted

in the subplot of the same diagram. The events are spread in time because particles gain substantial energy at different instants when crossing the current sheet. The energy growth during this stage is exponential. This is clearly due to the first-order Fermi acceleration process, as stressed before (de Gouveia Dal Pino and Lazarian 2005; Kowal et al. 2011, 2012) and already shown in Fig. 13.4. We note that, as in Fig. 13.5, the particles accelerate at smaller rates after reaching the energy level $\sim 10^4$, because the thickness of the acceleration region becomes smaller than their Larmor radii and this is consistent with the predictions of Eq. (13.11).

Although the Sweet–Parker model with an artificially enhanced resistivity results in a predominantly first-order Fermi acceleration, only a small fraction of the injected particles is trapped and efficiently accelerated in the current sheet (see the energy spectrum of the accelerated particles in the bottom right of Fig. 13.6). This is because the acceleration zone is very thin.

13.3.5 Acceleration in 3D Reconnection Sites with Turbulence

As remarked before, Lazarian and Vishniac (1999) (see also the **Chapter by Lazarian** in this book) proposed a model for fast reconnection that does not depend on the magnetic diffusivity (see also Eyink et al. 2011). Given the fact that MHD turbulence is ubiquitous in astrophysical environments, this may be a universal trigger of fast reconnection. The predictions of this model have been tested successfully by numerical simulations (Kowal et al. 2009, 2012) which confirmed that the reconnection speed is of the order of the Alfvén speed and independent of resistivity. An important consequence of fast reconnection by turbulent magnetic fields is the formation of a thick volume filled with small scale magnetic fluctuations. In order to test the acceleration of particles within such a domain, KGL12 (Kowal et al. 2012) introduced turbulence within a current sheet with a Sweet–Parker configuration (as described in the previous paragraph) and followed the trajectories of 10,000 protons injected in this domain.

The middle left panel of Fig. 13.6 shows the evolution of the kinetic energy of the particles in this case. After injection, a large fraction of test particles accelerates and the particle energy growth occurs earlier than in the Sweet–Parker case (see also the energy spectrum at $t = 5$ in the detail at the bottom right of the same diagram). This is explained by a combination of two effects: the presence of a large number of converging small scale current sheets and the broadening of the acceleration region due to the turbulence. Here, we do not observe the gap seen in the Sweet-Parker reconnection, because particles are continually accelerated by encounters with several small and intermediate scale current sheets randomly distributed in the thick volume. The acceleration process is clearly still a first order Fermi process, as in the Sweet–Parker case, but more efficient as it involves larger number of particles, since the size of the acceleration zone and the number of scatterers have been naturally increased by the presence of turbulence.

An inspection of the particle spectrum in the subplot of the middle panel of Fig. 13.6 at t=5 c.u. reveals already the formation of a power law spectrum $N(E) \sim E^{-1}$ in the energy range $E/m_p c^2 \sim 10 - 10^3$, where m_p is the proton mass. This power law index is compatible with former results obtained from collisionless PIC simulations (e.g., Zenitani and Hoshino 2001).

13.3.6 Acceleration by Reconnection in Pure 3D Turbulent Environments

The bottom left panel of Fig. 13.6 shows the kinetic energy evolution of accelerated particles in a domain with turbulence only, i.e., without large scale magnetic flux tubes and thus no large scale current sheet. This could be the situation in typical diffuse MHD environments like the interstellar, the intracluster and intergalactic media. One of the fundamental points of the Lazarian & Vishniac theory (Lazarian and Vishniac 1999) is the fact that whenever there is MHD turbulence, there will be fast reconnection of the turbulent magnetic field lines from the injection to the dissipation scales of the turbulence (Lazarian et al. 2011; Santos-Lima et al. 2010, xxxx,x; Leão et al. 2013). Therefore, particles will be able to accelerate while trapped within these multiple current sheets at all scales.

We see in Fig. 13.6 that the acceleration is less efficient at the beginning and a much smaller fraction of particles is accelerated than when a large scale current sheet is present, as in the middle panel of Fig. 13.6. In the later case, the converging flow on both sides of the large scale current sheet brings approaching scattering centres that undergo only head-on collisions with the particles allowing a continuous growth of the particle energy until the saturation level. In pure turbulence, however, the absence of a large scale converging flow results in a random particle scattering into both approaching and receding small scale magnetic fluctuations (although at a smaller rate), so that the overall acceleration is possibly a second-order Fermi process.

It should be also remarked that earlier studies of particle acceleration in pure 3D MHD turbulent environments have already identified the development of stochastic acceleration and a power-law tail in the energy spectrum of the accelerated particles (see e.g., Dmitruk et al. 2003).

13.4 Discussion and Conclusions

Advances both in the understanding of magnetic reconnection in the MHD regime and improvement on high energy observations have lately motivated the studies of particle acceleration in reconnection sites of astrophysical sources and environments.

In this Chapter, we reviewed particle acceleration in 2D and 3D (collisional) MHD domains of magnetic reconnection. It has been shown that particles can be efficiently accelerated by reconnection through a first order Fermi process within large scale current sheets (built up by large scale converging magnetic fluxes), specially when local turbulence is present. The later makes the reconnection fast (Lazarian and Vishniac 1999) and the volume of the accelerating zone thick (Kowal et al. 2011, 2012). The particles trapped within the current sheet suffer several head-on scatterings with the contracting magnetic fluctuations as originally predicted by GL05 (de Gouveia Dal Pino and Lazarian 2005) (see also Drake et al. 2006) and undergo an exponential growth in their kinetic energy, as demonstrated numerically by KGL11 (Kowal et al. 2011) and KGL12 (Kowal et al. 2012). In a Sweet–Parker configuration (with the reconnection speed made artificially large by numerical diffusion) the acceleration rate is slightly smaller because of the thinner current sheet, but it is also a first-order Fermi process. In contrast, in pure 3D turbulent environments (with no large scale current sheets), particles with gyroradii smaller than the injection scale of the turbulence are accelerated through a second order Fermi process while interacting with both approaching and receding small scale turbulent current sheets. This process can be particularly important for cosmic ray acceleration in diffuse turbulent environments like the interstellar, intracluster and intergalctic media, while the first order Fermi acceleration in large scale current sheets can be relevant particularly in stellar coronae, compact sources (like the accretion disk coronae in AGNs, microquasars, etc.; see Fig. 13.7 as an illustrative example), and highly magnetized flows (like AGN, microquasar and GRB jets).

It has been also shown that the acceleration within fast reconnection sites works both, in collisionless and collisional (especially in the presence of turbulence)

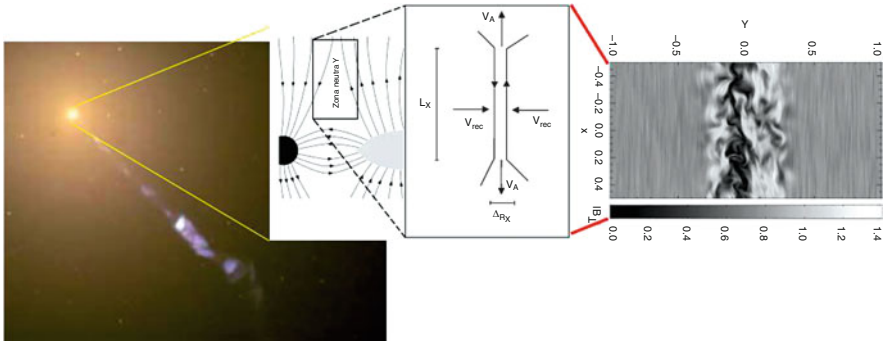

Fig. 13.7 From *left to right* the figure shows: the HST image of M87 AGN; a schematic representation of the expected magnetic field structure around the accretion disk and the central black hole (as in de Gouveia Dal Pino and Lazarian 2005); a schematic representation of the reconnection zone with the two converging magnetic fluxes of opposite polarity as in a Sweet–Parker configuration approaching each other with a reconnection speed $V_R = V_{rec}$, and a 3D MHD simulation of magnetic reconnection with turbulence injected within the current sheet to make reconnection fast (as in Kowal et al. 2012)

environments. The acceleration by magnetic reconnection in the 2D collisional MHD regime (Kowal et al. 2011, 2012) successfully reproduces the results obtained with (collisionless) 2D PIC codes (e.g. Drake et al. 2010). This proved that the acceleration in reconnection regions is a universal process which is not determined by details of the plasma physics or kinetic effects. However, in the collisional case, only the injected particles with Larmor radii near the MHD scales are effectively accelerated. This injection problem can be solved using hybrid codes able to resolve both the kinetic and the MHD scales.

It should be noticed that Onofri et al. (2006) also investigated particle acceleration in MHD reconnection regimes. However, they concluded that MHD would not be a good approximation to describe the process of acceleration by reconnection. This is because their 3D numerical simulations were performed in a fully resistive MHD regime. Therefore, they obtained an efficient particle acceleration due to the high electric field induced by the resistivity term only (see Eq. 13.11) and an absorption of most of the available magnetic energy by the electrons in a very small fraction of the characteristic time of the MHD simulation. This led them to conclude that resistive MHD codes are unable to represent the full extent of particle acceleration in 3D reconnection. KGL11 and KGL12 (Kowal et al. 2011, 2012) on the other hand, explored particle acceleration in a nearly ideal MHD regime where only small numerical resistivity was present. In this case, the contribution of a resistivity induced electric field is negligible when compared to the advection component, namely, the electric field resulting from the plasma motion in the magnetized medium, $-v \times B$.

It has been also demonstrated that the acceleration of energetic particles in 2D and 3D reconnection domains shows substantial differences (Kowal et al. 2011). This calls for focusing on realistic 3D geometries of reconnection. The numerical studies (Kowal et al. 2011, 2012) have also revealed that apart from the first order Fermi acceleration, additional less efficient acceleration processes, like drift acceleration due to non-uniform magnetic fields and second order Fermi, also interfere in the process (see also Dmitruk et al. 2003).

All these numerical studies of particle acceleration have neglected the time evolution of the MHD environment. This is in general valid since this is much longer than the particle time scales. In fact, when considering, for instance, the acceleration within large scale current sheets with turbulence, particles are accelerated by magnetic fluctuations in the turbulent field and interact resonantly with larger and larger structures as their energy increases due to the scatterings. In a steady state turbulent environment, as considered here, particles will see on average the same sort of fluctuation distribution, so that after several Alfvén times, one should expect no significant changes in the particle spectrum due to the evolution of the large scale MHD environment (del Valle et al. 2014). Nonetheless, this evolution may be important when considering more realistic non-steady environments and when calculating real spectra and loss effects (e.g. Lehe et al. 2009; Khiali et al. 2014). It may be also relevant when considering the (second order Fermi) acceleration in pure turbulent environments (as in Fig. 13.6, bottom panel). In this case, electric fields arising from slow modes (betatron acceleration) can be relevant to the acceleration

process making it twice as larger since the betatron term $\partial B/\partial t$ contributes as much as the electric field term (Eq. (13.11)) in the second order process. In forthcoming studies when considering more realistic non-steady environments, MHD data cubes varying in time should be used specially in pure turbulent studies.

It should be remarked also that the collisional MHD simulations shown here focussed on proton acceleration. Although applicable to electrons too, the numerical integration of the electron trajectories is much longer. Nevertheless, such tests are also needed. In particular, it has been suggested that in electron-positron plasmas the pairs could annihilate in compressed reconnection sheets (Drury 2012), so that this could influence the acceleration by reconnection, e.g., in pulsar winds and relativistic jets in general.

13.4.1 Analytical Predictions Versus Numerical Simulations

It has been seen that analytical studies of the first order Fermi process in large scale current sheets predict that (de Gouveia Dal Pino and Lazarian 2005; Drury 2012): (1) the acceleration rate is similar to that for shock acceleration; and (2) the energy power law spectrum of the accelerated particles can be even harder (Drury 2012) than the one predicted for shock acceleration and independent on the reconnection velocity (de Gouveia Dal Pino and Lazarian 2005). These predictions, although based on very simplified assumptions can be, in principle, tested with numerical simulations. However, a larger parametric space considering, e.g., different ratios between the initial Alfvén (or reconnection) speed and the light speed, and different amplitudes of the injected turbulence (which speeds up reconnection within the large scale current sheet) must be still performed in order to assess the sensitivity of both the acceleration rate and the particle spectrum to the physical conditions in the reconnection domain. Results from collisional MHD numerical simulations with injection Alfvén velocities in the range $v_A/c \sim 1/1000 - 1/5$ (Kowal et al. 2011, 2012; del Valle et al. 2014), indicate that the acceleration time is nearly independent of the initial Alfvén (and reconnection) speed and is given by $t_{acc} \sim E^{0.4}$ (this is directly derived from diagrams as in Figs. 13.5 and 13.6). This is initially longer than the estimated time by Eq. (13.9), but becomes comparable to it as the particles approach the maximum energy value that they can reach in the acceleration zone (del Valle et al. 2014). As we have seen, this maximum energy is attained when the particle Larmour radius becomes comparable to the size of the acceleration zone.

The determination of the dependence of the energy spectral index and the fraction of accelerated particles at high energies with the initial and the boundary conditions is more complex (see Fig. 13.6) and requires further numerical studies, particularly considering the effects of particle feedback. So far, the results of particle acceleration in 3D MHD reconnection sites indicate a hard power law spectrum $N(E) \sim E^{-1}$ (Kowal et al. 2011, 2012; see Sect. 3). This is comparable with results obtained from 2D collisionless PIC simulations considering merging islands (for which an energy power-law index $\sim (-1.5)$ has been found; Drake et al. 2010),

or X-type Petschek's configurations (e.g., Zenitani and Hoshino 2001, for which an energy power-law index $\sim (-1)$ has been obtained).

13.4.2 Particle Acceleration in Relativistic Domains of Reconnection

In this review, we discussed mostly Fermi acceleration considering non-relativistic reconnection environments, that is, generally assuming V_R smaller than the light speed. This seems to be appropriate in the solar (or stellar) corona and wind and in the Earth magnetotail where this mechanism has been more extensively explored. However, in systems like, e.g, the very near surrounds of black holes and pulsars, $v_A \sim c$ and thus, since in fast reconnection V_R must approach v_A, reconnection itself may become relativistic in such domains. There has been some advancement in relativistic reconnection studies too. The theoretical grounds have been established by a number of authors (Romanova and Lovelace 1992; Blackman and Field 1994; Lyubarsky 2005; Lyutikov 2003; Jaroschek et al. 2004; Hesse and Zenitani 2007; Zenitani and Hoshino 2008; Zenitani et al. 2009; Komissarov 2007; Coroniti 1990; Lyubarsky and Kirk 2001; see also Uzdensky (2011) and references therein for a review and the chapter by Lazarian et al. in this volume). Essentially, it has been realized that Sweet–Parker reconnection in the relativistic regime is slow, as in the non-relativistic regime, while 2D X-point Petschek's reconnection predicts a fast rate as in the non-relativistic domain (Lyubarsky 2005). The numerical advances in relativistic reconnection have been performed so far only for 2D collisionless X-point Petschek's configurations by means of PIC simulations of pair plasmas, but have confirmed the results of the analytical theory. In such relativistic collisionless electron-positron pair plasmas, the investigation of relativistic particle acceleration is almost straightforward. Studies by, e.g., Zenitani and Hoshino (2001) have revealed results which are compatible with those of acceleration in non-relativistic reconnection.

However, studies of particle acceleration in the collisional relativistic MHD regime (RMHD) are still in their childhood. As an example, Fig. 13.8 shows very preliminary results of simulations of 10,000 test particles injected in a 2D relativistic MHD jet system as in (Kowal et al. 2012). The colors highlight the regions where particles are being accelerated, mostly through first order Fermi, to relativistic energies both behind shocks and within magnetic reconnection islands. The comparison between the acceleration rate diagrams on the right hand side of this figure suggests that both mechanisms are competitive.

These results are encouraging and may have rather important consequences on particle acceleration and high energy emission processes in microquasars, pulsar winds, AGNs, and GRBs and demand further extensive investigation. The assessment of the role of this mechanism in modelling flares in the spectrum of compact sources is also in order (de Gouveia Dal Pino and Lazarian 2005;

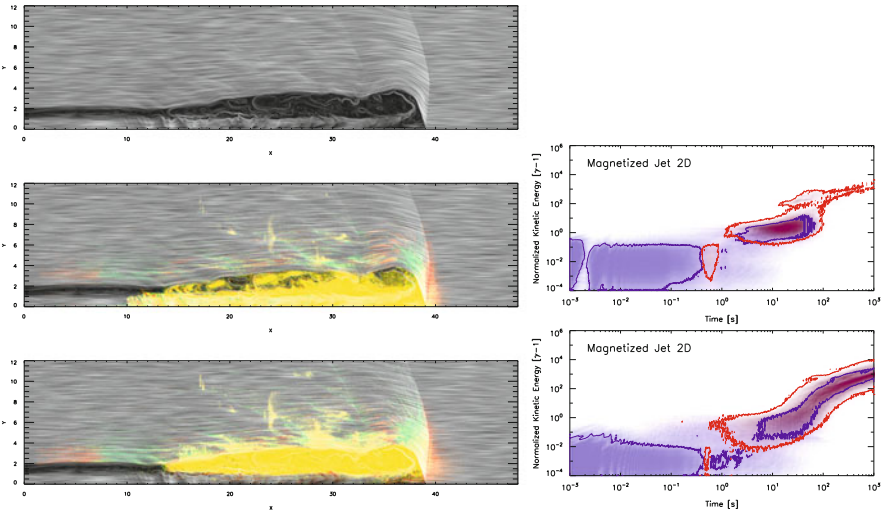

Fig. 13.8 Two-dimensional relativistic-MHD jet. *Left diagrams*: *top panel* depicts the topology of the magnetic field represented as gray texture for a 2D relativistic jet at $t = 80.0$ in code units with initial uniform longitudinal magnetic field corresponding to a ratio between the gas pressure and the magnetic pressure $\beta = 1/300$, a density ratio between the jet and the ambient medium 0.01; a jet Mach number $M_j = 6.0$, and a Lorentz factor $\Gamma = 10.0$. The *left middle and bottom panels* show the same diagram but with superimposed semi-transparent color maps representing locations where the parallel and perpendicular particle velocity components are accelerated. The *red and green colors* correspond to regions where either parallel or perpendicular acceleration occurs, respectively, while the *yellow color* shows locations where both types of acceleration occur. The *top left panel* clearly depicts the large scale features typically seen in 2D jet simulations, i.e., the bow shock at the head where the light jet beam impacts supersonically a much denser environment, and internal shocks (or knots) all along the beam which are driven by the pinch mode of the Kelvin–Helmholtz (K-H) instability. We also identify a more turbulent cocoon enveloping the beam which is formed by the mixing of the shocked ambient and jet gas. Magnetic islands can be clearly distinguished in this region. The *left middle panel* depicts only the accelerated particles within the beam and in the bow shock region, while the *bottom left panel* depicts the particles which are accelerated mostly in the surrounding cocoon. The *right diagrams* show the acceleration rates: the *top* one corresponds to the *middle left panel*, i.e., to the acceleration regions within the beam and the bow shock and therefore, is dominated by first order Fermi acceleration behind shocks; and the *bottom right panel* corresponds to the *bottom left panel*, i.e., to the acceleration mostly in magnetic islands and thus is dominated by first order Fermi due to magnetic reconnection. The simulation was performed with a resolution $8{,}192 \times 4{,}096$. Ten thousand test particles were injected in this snapshot with an initial thermal distribution with a temperature corresponding to the sound speed of the relativistic-MHD model

de Gouveia Dal Pino et al. 2010a,b; Drury 2012). For instance, in recent work Cerutti et al. (2013) performed 2D PIC collisionless reconnection simulations of ultra-relativistic pair plasmas considering the effects of radiation reaction on the particles. They detected several features of first order Fermi particle acceleration in their simulations that had been already revealed in non-relativistic simulations (e.g. Kowal et al. 2011, 2012), but were also able to reproduce the observed

spectral energy distribution of the Crab nebula flares. Another recent study have demonstrated that the acceleration by magnetic reconnection can be more efficient than shock acceleration in the surrounds of galactic black holes (microquasars) and reproduce the observed high energy spectral distribution of sources like Cyg X-1 and Cyg X-3 (Khiali et al. 2014). In fact, acceleration by magnetic reconnection seems to have a major role in the surrounds of a broad range of black hole sources (from microquasars to low luminous AGNs) (de Gouveia Dal Pino et al. 2010a; Kadowaki and de Gouveia Dal Pino 2014).

Finally, particles accelerated in domains of reconnection, particularly in pure turbulent regions, may be available as seed populations for further first order Fermi shock or magnetic reconnection acceleration in these different systems.

To summarize, magnetic reconnection is now recognized as an essential process not only in the solar system but also beyond it, in a large number of astrophysical sources, including turbulent environments which in turn, are ubiquitous. In this situation the acceleration of particles by reconnection may play a vital role, the importance of which should be evaluated with further extensive research.

Acknowledgements E.M.G.D.P. acknowledges partial support from the Brazilian agencies FAPESP (grant no. 2006/50654-3 and CNPq (grant no. 300083/94-7) and G.K. also acknowledges support from FAPESP (grant 2009/50053-8). The authors are also in debt to Alex Lazarian for fruitful and joyful collaboration in this work. Part of the simulations presented here have been carried out in LAI (Astrophysical Laboratory of Informatics at IAG-USP).

References

Bell, A.R.: Mon. Not. R. Astron. Soc. **182**, 147 (1978)
Birn, J., Drake, J.F., Shay, M.A., Rogers, B.N., Denton, R.E., Hesse, M., Kuznetsova, M., Ma, Z.W., Bhattacharjee, A., Otto, A., Pritchett, P.L.: J. Geophys. Res. **106**, 3715 (2001)
Blackman, E.G., Field, G.B.: Phys. Rev. Lett. **72**, 494 (1994)
Cerutti, B., Werner, G.R., Uzdensky, D.A., Begelman, M.C.: Astrophys. J. **770**, 147 (2013)
Coroniti, F.V.: Astrophys. J. **349**, 538 (1990)
de Gouveia Dal Pino, E.M., Lazarian, A.: Astrophys. J. Lett. **536**, L31 (2000)
de Gouveia Dal Pino, E.M., Lazarian, A.: Astrophys. J. **560**, 358 (2001)
de Gouveia Dal Pino, E.M., Lazarian, A.: Astron. Astrophys. **441**, 845 (2005)
de Gouveia Dal Pino, E.M., Piovezan, P.P., Kadowaki, L.H.S.: Astron. Astrophys. **518**, A5 (2010a)
de Gouveia Dal Pino, E.M., Kowal, G., Kadowaki, L.H.S., Piovezan, P., Lazarian, A.: Int. J. Mod. Phys. D **19**, 729 (2010b)
de Gouveia Dal Pino, E.M., Kowal, G.,Lazarian, A., Santos-Lima, R. (2011). Procs. of Science, in AGN Physics in the CTA Era, PoS(AGN 2011)031 (2011). arXiv: 1107.26742
de Gouveia Dal Pino, E.M., Kowal, G., Lazarian, A. In: Highlight Review in 33rd International Cosmic Ray Conference, Brazilian Journal Physics. Special issue (2014, submitted)
del Valle, M.V., Romero, G.E., Luque-Escamilla, P.L., Martí, J., Ramón Sánchez-Sutil, J.: Astrophys. J. **738**, 115 (2011)
del Valle, M.V., de Gouveia Dal Pino, E.M., Kowal, G. (2014, in preparation)
Dmitruk, P., Matthaeus, W.H., Seenu, N., Brown, M.R.: Astrophys. J. Lett. **597**, L81 (2003)
Drake, J.F., Swisdak, M., Schoeffler, K.M., Rogers, B.N., Kobayashi, S.: Geophys. Res. Lett. **33**, 13105 (2006)

Drake, J.F., Cassak, P.A., Shay, M.A., Swisdak, M., Quataert, E.: Astrophys. J. Lett. **700**, L16 (2009)
Drake, J.F., Opher, M., Swisdak, M., Chamoun, J.N.: Astrophys. J. **709**, 963 (2010)
Drury, L.O.: Mon. Not. R. Astron. Soc. **422**, 2474 (2012)
Eyink, G.L., Lazarian, A., Vishniac, E.T.: Astrophys. J. **743**, 51 (2011)
Fermi, E.: Phys. Rev. **75**, 1169 (1949)
Giannios, D.: Mon. Not. R. Astron. Soc. **408**, L46 (2010)
Gordovskyy, M., Browning, P.K., Vekstein, G.E.: Astrophys. J. **720**, 1603 (2010)
Gordovskyy, M., Browning, P.K.: Astrophys. J. **729**, 101 (2011)
Hesse, M., Zenitani, S.: Phys. Plasmas **14**(11), 112102 (2007)
Jaroschek, C.H., Treumann, R.A., Lesch, H., Scholer, M.: Phys. Plasmas **11**, 1151 (2004)
Kadowaki, L., de Gouveia Dal Pino, E.M., Singh, C. (2014, submitted)
Khiali, B., de Gouveia Dal Pino, E.M., Kowal, G., del Valle (2014, submitted). arXiv:1406.5664
Komissarov, S.S.: Mon. Not. Roy. Astron. Soc. **382**, 995 (2007)
Kotera, K., Olinto, A.V.: Ann. Rev. Astron. Astrophys. **49**, 119 (2011)
Kowal, G., Lazarian, A., Vishniac, E.T., Otmianowska-Mazur, K.: Astrophys. J. **700**, 63 (2009)
Kowal, G., de Gouveia Dal Pino, E.M., Lazarian, A.: Astrophys. J. **735**, 102 (2011)
Kowal, G., de Gouveia Dal Pino, E.M., Lazarian, A.: Phys. Rev. Lett. 108, 241102 (2012)
Kowal, G., Lazarian, A., Vishniac, E.T., Otmianowska-Mazur, K.: Nonlinear Process. Geophys. **19**, 297 (2012)
La Rosa, T.N., Shore, S.N., Joseph, T., Lazio, W., Kassim, N.E.: J. Phys. Conf. Ser. **54**, 10 (2006)
Lazarian, A. In: de Gouveia dal Pino, E.M., Lugones, G., Lazarian, A. (eds.) Magnetic Fields in the Universe: From Laboratory and Stars to Primordial Structures. AIP Conference Proceedings Series, vol. 784, p. 42. American Institute of Physics, Melville (2005)
Lazarian, A., Desiati, P.: Astrophys. J. **722**, 188 (2010)
Lazarian, A., Opher, M.: Astrophys. J. **703**, 8 (2009)
Lazarian, A., Vishniac, E.T.: Astrophys. J. **517**, 700 (1999)
Lazarian, A., Petrosian, V., Yan, H., Cho, J.: Review at the NBSI workshop "Beaming and Jets in Gamma Ray Bursts", Copenhagen, 12–30 August 2002 (2003). arXiv:astro-ph/0301181
Lazarian, A., Kowal, G., Vishniac, E., de Gouveia Dal Pino, E.M.: Planet. Space Sci. **59**, 537 (2011)
Leão, M.R.M., de Gouveia Dal Pino, E.M., Santos-Lima, R., Lazarian, A.: Astrophys. J. **777**, 46 (2013)
Lehe, R., Parrish, I.J., Quataert, E.: Astrophys. J. **707**, 404 (2009)
Litvinenko, Y.E.: Astrophys. J. **462**, 997 (1996)
Longair, M.S. In: Malcolm S.L. (ed.) High Energy Astrophysics. Cambridge University Press, Cambridge (2011). ISBN: 9780521756181
Lyubarsky, Y.E.: Mon. Not. Roy. Astron. Soc. **358**, 113 (2005)
Lyubarsky, Y., Kirk, J.G.: Astrophys. J. **547**, 437 (2001)
Lyubarsky, Y., Liverts, M.: Astrophys. J. **682**, 1436 (2008)
Lyutikov, M.: Mon. Not. Roy. Astron. Soc. **346**, 540 (2003)
Melrose, D.B.: In: Robert Meyers (ed.) Encyclopedia of complexity and systems science, Springer review (2009). arXiv:astro-ph.SR/0902.1803
Onofri, M., Isliker, H., Vlahos, L.: Phys. Rev. Lett. **96**, 151102 (2006)
Parker, E.: Cosmical Magnetic Fields: Their Origin and their Activity. International Series of Monographs on Physics. Oxford University Press, New York (1979). ISBN-10: 0198512902
Parker, E.N.: J. Geophys. Res. **62**, 509 (1957)
Petschek, H.E: Magnetic Field Annihilation. In: Hess,W.N. (ed.) The Physics of Solar Flares, p. 425. Oxford University Press, New York (1964)
Romanova, M.M., Lovelace, R.V.E.: Astron. Astrophys. **262**, 26 (1992)
Santos-Lima, R., Lazarian, A., de Gouveia Dal Pino, E.M., Cho, J.: Astrophys. J. **714**, 442 (2010)
Santos-Lima, R., de Gouveia Dal Pino, E.M., Lazarian, A.: Astrophys. J. **747**, 21 (2010)
Santos-Lima, R., de Gouveia Dal Pino, E.M., Lazarian, A.: Mon. Not. Roy. Astron. Soc. **429**, 3371 (2010)

Shay, M.A., Drake, J.F., Denton, R.E., Biskamp, D.: J. Geophys. Res. **103**, 9165 (1998)
Shay, M.A., Drake, J.F., Swisdak, M.M.: Phys. Plasmas **11**, 2199 (2004)
Sironi, L., Spitkovsky, A.: Astrophys. J. **698**, 1523 (2009)
Sol, H., Zech, A., Boisson, C., et al.: Astroparticle Phys. **43**, 215 (2013)
Speiser, T.W.: J. Geophys. Res. **70**, 4219 (1965)
Sweet, P.A. In: Lehnert, B. (ed.) Electromagnetic Phenomena in Cosmical Physics, p. 123. Conference Proceedings of IAU Symposium 6. Cambridge University Press, Cambridge (1958)
Uzdensky, D.A.: Space Sci. Rev. **101**, 45 (2011)
Uzdensky, D.A., McKinney, J.C.: Phys. Plasams **18**, 042105 (2011)
Yamada, M., Ren, Y., Ji, H., Breslau, J., Gerhardt, S., Kulsrud, R., Kurisyn, A.: Phys. Plasmas **13**, 0521229 (2006)
Yamada, M., Kulsrud, R., Ji, H.: Rev. Mod. Phys. **82**, 603 (2010)
Zhang, B., Yan, H.: Astrophys. J. **726**, 90 (2011)
Zharkova, V.V., Siversky, T. In: Bonanno, A., de Gouveia Dal Pino, E.M., Kosovichev, A. (eds.) AIP Conference Proceedings Series. Advances in Plasma Astrophysics: IAU 274th Meeting. Cambridge University Press/AIP, New York (2011)
Zenitani, S., Hoshino, M.: Astrophys. J. **562**, L63 (2001)
Zenitani, S., Hoshino, M.: Astrophys. J. **677**, 530 (2008)
Zenitani, S., Hesse, M., Klimas, A.: Astrophys. J. **696**, 1385 (2009)

Part V
MFs in Star Formation Regions

Chapter 14
Interstellar MHD Turbulence and Star Formation

Enrique Vázquez-Semadeni

Abstract This chapter reviews the nature of turbulence in the Galactic interstellar medium (ISM) and its connections to the star formation (SF) process. The ISM is turbulent, magnetized, self-gravitating, and is subject to heating and cooling processes that control its thermodynamic behavior, causing it to behave approximately isobarically, in spite of spanning several orders of magnitude in density and temperature. The turbulence in the warm and hot ionized components of the ISM appears to be trans- or subsonic, and thus to behave nearly incompressibly. However, the neutral warm and cold components are highly compressible, as a consequence of both thermal instability (TI) in the atomic gas and of moderately-to-strongly supersonic motions in the roughly isothermal cold atomic and molecular components. Within this context, we discuss: (1) the production and statistical distribution of turbulent density fluctuations in both isothermal and polytropic media; (2) the nature of the clumps produced by TI, noting that, contrary to classical ideas, they in general accrete mass from their environment in spite of exhibiting sharp discontinuities at their boundaries; (3) the density-magnetic field correlation (and, at low densities, lack thereof) in turbulent density fluctuations, as a consequence of the superposition of the different wave modes in the turbulent flow; (4) the evolution of the mass-to-magnetic flux ratio (MFR) in density fluctuations as they are built up by dynamic compressions; (5) the formation of cold, dense clouds aided by TI, in both the hydrodynamic (HD) and the magnetohydrodynamic (MHD) cases; (6) the expectation that star-forming molecular clouds are likely to be undergoing global gravitational contraction, rather than being near equilibrium, as generally believed, and (7) the regulation of the star formation rate (SFR) in such gravitationally contracting clouds by stellar feedback which, rather than keeping the clouds from collapsing, evaporates and disperses them while they collapse.

E. Vázquez-Semadeni (✉)
Centro de Radioastronomía y Astrofísica, Universidad Nacional Autónoma de México, Campus Morelia, P.O. Boz 3-72 (Xangari), Morelia, Michoacán 58089, México
e-mail: e.vazquez@crya.unam.mx

A. Lazarian et al. (eds.), *Magnetic Fields in Diffuse Media*, Astrophysics and Space Science Library 407, DOI 10.1007/978-3-662-44625-6_14

14.1 Introduction

The interstellar medium (ISM) of our galaxy (the Milky Way, or simply, The Galaxy) is a mixture of gas, dust, cosmic rays, and magnetic fields that occupy the volume in-between stars (e.g., Ferrière 2001). The gaseous component, with a total mass $\sim 10^{10} M_\odot$, may be in either ionized, neutral atomic or neutral molecular forms, spanning a huge range of densities and temperatures, from the so-called hot ionized medium (HIM), with densities $n \sim 10^{-2}\,\mathrm{cm}^{-3}$ and temperatures $T \sim 10^6$ K, through the warm ionized and neutral (atomic) media (WIM and WNM, respectively, both with $n \sim 0.3\,\mathrm{cm}^{-3}$ and $T \sim 10^4$ K) and the cold neutral (atomic) medium (CNM, $n \sim 30\,\mathrm{cm}^{-3}$, $T \sim 100$ K), to the *giant molecular clouds* (GMCs, $n \gtrsim 100\,\mathrm{cm}^{-3}$ and $T \sim 10$–20 K). These span several tens of parsecs across, and, in turn, contain plenty of substructure, which is commonly classified into *clouds* ($n \sim 10^3\,\mathrm{cm}^{-3}$, size scales L of a few parsecs), *clumps* ($n \sim 10^4\,\mathrm{cm}^{-3}$, $L \sim 1$ pc), and *cores* ($n \gtrsim 10^5\,\mathrm{cm}^{-3}$, $L \sim 0.1$ pc). It is worth noting that the temperature of most molecular gas is remarkably uniform, $\sim 10 - 30$ K.

Moreover, the ISM is most certainly turbulent, as typical estimates of the Reynolds number (R_e) within it are very large. For example, in the cold ISM, $R_\mathrm{e} \sim 10^5$–10^7 (Elmegreen and Scalo 2004; Sect. 4.1). This is mostly due to the very large spatial scales involved in interstellar flows. Because the temperature of the ISM varies so much from one type of region to another, so does the sound speed, and therefore the turbulent velocity fluctuations are often moderately or even strongly supersonic (e.g., Heiles and Troland 2003; Elmegreen and Scalo 2004; and references therein). In these cases, the flow is significantly compressible, inducing large-amplitude (nonlinear) density fluctuations. The density enhancements thus formed constitute dense clouds and their substructure (e.g., Sasao 1973; Elmegreen 1993; Ballesteros-Paredes et al. 1999a).

In addition to being turbulent, the ISM is subject to a number of additional physical processes, such as gravitational forces exerted by the stellar and dark matter components as well as by its own self-gravity, magnetic fields, cooling by radiative microscopic processes, and radiative heating due both to nearby stellar sources as well as to diffuse background radiative fields. It is within this complex and dynamical medium that stars are formed by the gravitational collapse of certain gas parcels.

In this chapter, we focus on the interaction between turbulence, the effects of radiative heating and cooling, which effectively enhance the compressibility of the flow, the self-gravity of the gas, and magnetic fields. Their complex interactions have a direct effect on the star formation process. The plan of the chapter is as follows: in Sect. 14.2 we briefly recall the effects that the net heating and cooling have on the effective equation of state of the flow and, in the case of thermally unstable flows, on its tendency to spontaneously segregate in distinct phases. Next, in Sect. 14.3 we discuss a few basic notions about turbulence and the turbulent production of density fluctuations in both the hydrodynamic (HD) and magnetohydrodynamic cases, to then discuss, in Sect. 14.4, the evolution and

properties of clouds and clumps formed by turbulence in multiphase media. In Sect. 14.5, we discuss the likely nature of turbulence in the diffuse (warm and hot) components of the ISM, as well as in the dense, cold atomic and molecular clouds, suggesting that in the latter, at least during the process of forming stars, the velocity field may be dominated by gravitational contraction. Next, in Sect. 14.6 we discuss the regulation of star-formation (SF) in gravitationally contracting molecular clouds (MCs), in particular whether it is accomplished by magnetic support, turbulence, or stellar feedback, and how. Finally, in section "Summary and Conclusions" we conclude with a summary and some final remarks.

14.2 ISM Thermodynamics: Thermal Instability

The ISM extends essentially over the entire disk of the Galaxy and, when considering a certain dense subregion of it, such as a cloud or cloud complex, it is necessary to realize that any such subregion constitutes an open system, whose interactions with its environment need to be taken into account. A fundamental form of interaction with the surroundings, besides dynamical interactions, is through the exchange of heat, which occurs mostly through heating by the UV background radiation produced by distant massive stars, local heating when nearby stellar sources (OB star ionization heating and supernova explosions), cosmic ray heating, and cooling by thermal and line emission from dust and gas, respectively (see, e.g., Dalgarno and McCray 1972; Wolfire et al. 1995).

Globally, and as a first approximation, the ISM is roughly isobaric, as illustrated in Fig. 14.1. As can be seen there, most types of regions, either dilute or dense, lie within an order of magnitude from a thermal pressure $P \sim 3{,}000\ \mathrm{K\,cm^{-3}}$. The largest deviations from this pressure uniformity are found in HII regions, which are the ionized regions around massive stars due to their UV radiation output, and in molecular clouds, which, as we shall see in Sect. 14.5.5, are probably pressurized by gravitational compression.

The peculiar thermodynamic behavior of the ISM is due to the functional forms of the radiative heating and cooling functions acting on it, which depend on the density, temperature, and chemical composition of the gas. The *left* panel of Fig. 14.2 shows the temperature dependence of the cooling function Λ (Dalgarno and McCray 1972). One well-known crucial consequence of this general form of the cooling is that the atomic medium is *thermally unstable* (Field 1965) in the density range $1 \lesssim n \lesssim 10\ \mathrm{cm^{-3}}$ (corresponding to $5000 \gtrsim T \gtrsim 300$ K), meaning that the medium tends to spontaneously segregate into two stable *phases*, one warm and diffuse, with $n \sim 0.3\ \mathrm{cm^{-3}}$ and $T \sim 8{,}000\,\mathrm{K}$, and the other cold and dense, with $n \sim 30\ \mathrm{cm^{-3}}$ and $T \sim 80\,\mathrm{K}$, both at a pressure $P/k \sim 2{,}500\mathrm{K\,cm^{-3}}$ (Field et al. 1969; Wolfire et al. 1995; see also the reviews by Meerson 1996; Vázquez-Semadeni et al. 2003b; Vázquez-Semadeni 2012), as illustrated in the *right* panel of Fig. 14.2. The cold gas is expected to form small clumps, since the fastest growing mode of the instability occurs at vanishingly small scales in the absence of thermal

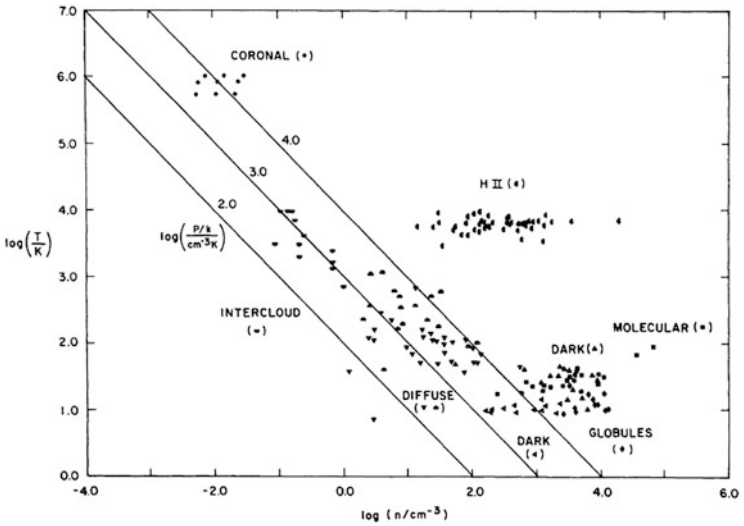

Fig. 14.1 Thermal pressure in various types of interstellar regions. The points labeled *coronal* correspond essentially to what we refer to as the HIM in the text; *intercloud* regions refer to the WIM and WNM; *diffuse*, to CNM clouds, and *dark, globule* and *molecular* to molecular gas. From Myers (1978)

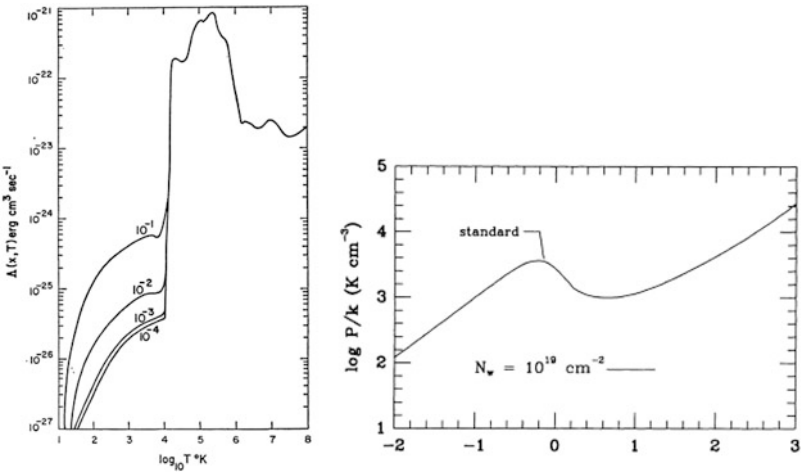

Fig. 14.2 *Left*: Temperature dependence of the cooling function Λ. The labels indicate values of the ionization fraction (per number) of the gas. From Dalgarno and McCray (1972). *Right*: Thermal-equilibrium pressure $P_{\rm eq}$ as a function of number density for "standard" conditions of metallicity and background UV radiation for the atomic medium. The horizontal axis gives $\log_{10}(n/\mathrm{cm}^3)$. From Wolfire et al. (1995)

conductivity, or at scales ~ 0.1 pc for the estimated thermal conductivity of the ISM (see, e.g., Field 1965; Audit and Hennebelle 2005). Because the atomic gas in the ISM has two stable phases, it is often referred to as a *thermally bistable* medium.

It is important to note that, even if the medium is *not* thermally unstable, the balance between heating and cooling implies a certain functional dependence of $P_{\rm eq}(\rho)$, which is often approximated by a *polytropic* law of the form $P_{\rm eq} \propto \rho^{\gamma_{\rm e}}$ (e.g., Elmegreen 1991; Vázquez-Semadeni et al. 1996), where $\gamma_{\rm e}$ is the *effective polytropic exponent*. In general, $\gamma_{\rm e}$ is *not* the ratio of specific heats for the gas in this case, but rather a free parameter that depends on the functional forms of Λ and Γ. The isobaric mode of thermal instability (TI) corresponds to $\gamma_{\rm e} < 0$. A flow is sometimes said to be *softer* as the parameter $\gamma_{\rm e}$ becomes smaller.

14.3 Compressible Polytropic MHD Turbulence

14.3.1 Equations

In the previous section we have discussed thermal aspects of the ISM, whose main dynamical effect is the segregation of the medium into the cold and warm phases. Let us now discuss dynamics. As was mentioned in Sect. 14.1, the ISM is in general turbulent and magnetized, and therefore it is necessary to understand the interplay between turbulence, magnetic fields, and the effects of the net cooling ($n\Lambda - \Gamma$), which affects the compressibility of the gas (Vázquez-Semadeni et al. 1996).

The dynamics of the ISM are governed by the fluid equations, complemented by self-gravity, the heating and cooling terms in the energy equation, and the equation of magnetic flux conservation (e.g., Shu 1992):

$$\frac{\partial \rho}{\partial t} + \mathbf{u}\cdot\nabla\rho = -\rho\nabla\cdot\mathbf{u}, \tag{14.1}$$

$$\frac{\partial \mathbf{u}}{\partial t} + \mathbf{u}\cdot\nabla\mathbf{u} = -\frac{\nabla P}{\rho} - \nabla\varphi + \nu\left[\nabla^2\mathbf{u} + \frac{\nabla(\nabla\cdot\mathbf{u})}{3}\right] + \frac{1}{4\pi\rho}(\nabla\times\mathbf{B})\times\mathbf{B}, \tag{14.2}$$

$$\frac{\partial e}{\partial t} + \mathbf{u}\cdot\nabla e = -(\gamma-1)e\nabla\cdot\mathbf{u} + \Gamma - n\Lambda, \tag{14.3}$$

$$\frac{\partial \mathbf{B}}{\partial t} + \nabla\times(\mathbf{B}\times\mathbf{u}) = -\nabla\times(\eta\nabla\times\mathbf{B}) + \nabla\times\left\{\frac{\mathbf{B}}{4\pi\gamma_{\rm c}\rho_{\rm n}\rho_{\rm i}}\times[\mathbf{B}\times(\nabla\times\mathbf{B})]\right\}, \tag{14.4}$$

$$\nabla^2\varphi = 4\pi G\rho, \tag{14.5}$$

where $\rho = \mu_{\rm m} m_{\rm H} n$ is the mass density, $\mu_{\rm m}$ is the mean particle mass, $m_{\rm H}$ is the hydrogen mass, $\mathbf{u}$ is the velocity vector, e is the internal energy per unit mass, $\mathbf{B}$ is the magnetic field strength vector, φ is the gravitational potential, ν is the kinematic

viscosity, η is the electrical resistivity, and γ_c is the collisional coupling constant between neutrals and ions in a partially ionized medium. Equation (14.1) represents mass conservation, and is also known as the *continuity equation*. Equation (14.2) is the momentum conservation, or *Navier–Stokes* equation per unit mass, with additional source terms representing the gravitational force $\nabla\varphi/\rho$ and the Lorentz force. In turn, the gravitational potential is given by *Poisson's equation*, Eq. (14.5). Equation (14.3) represents the conservation of internal energy, with Γ being the heating function and Λ the cooling function. The combination $n\Lambda - \Gamma$ is usually referred to as the *net cooling*, and the condition $n\Lambda = \Gamma$ is known as the *thermal equilibrium* condition. Finally, Eq. (14.4) represents the conservation of magnetic flux (see below). Equations (14.1)–(14.5) are to be solved simultaneously, given some initial and boundary conditions.

A brief discussion of the various terms in the momentum and flux conservation equations is in order. In Eq. (14.2), the second term on the left is known as the *advective* term, and represents the transport of i-momentum by the j component of the velocity, where i and j represent any two components of the velocity. It is responsible for *mixing*. The pressure gradient term (first term on the right-hand side [RHS]) in general acts to counteract pressure, and therefore density, gradients across the flow. The term in the brackets on the RHS, the *viscous* term, being of a diffusive nature, tends to erase velocity gradients, thus tending to produce a uniform flow. Finally, the last term on the RHS is the Lorentz force.

On the other hand, Eq. (14.4), assuming $\eta = 0$ (i.e., zero electrical resistivity, or equivalently, infinite conductivity) and $\gamma_c \to \infty$ (i.e., perfect coupling between neutrals and ions), implies that the magnetic flux Φ through a Lagrangian cross-sectional area A, given by

$$\Phi \equiv \int_A \mathbf{B} \cdot \hat{n}\, \mathrm{d}A, \tag{14.6}$$

remains constant in time as the area moves with the flow. This is the property known as *flux freezing*, and implies that the gas can slide freely along field lines, but drags the field lines with it when it moves perpendicularly to them. Note that this condition is often over-interpreted as to imply that the magnetic and the density fields must be correlated, but this is an erroneous notion. Only motions perpendicular to the magnetic field lines produce a correlation between the two fields, while motions parallel to the lines leave the magnetic field unaffected, while the density field can fluctuate freely. We discuss this at more length in Sect. 14.3.4.

The first term on the RHS of Eq. (14.4) represents dissipation of the magnetic flux by electrical resistivity, and gives rise to the phenomenon of *reconnection* of field lines (see, e.g., the book by Shu 1992, and the review by Lazarian 2012). The second term on the RHS of Eq. (14.4) represents *ambipolar diffusion* (AD), the deviation from the perfect flux-freezing condition that occurs for the neutral particles in the flow due to their slippage with respect to the ions in a partially ionized medium. We will further discuss the role of AD in the process of star formation (SF) in Sects. 14.3.4.3 and 14.5.5.2.

14.3.2 Governing Non-Dimensional Parameters

Turbulence develops in a flow when the ratio of the advective term to the viscous term becomes very large. That is,

$$\frac{\mathscr{O}\left[\mathbf{u}\cdot\nabla\mathbf{u}\right]}{\mathscr{O}\left[\nu\left(\nabla^2\mathbf{u}+\frac{\nabla(\nabla\cdot\mathbf{u})}{3}\right)\right]}\sim\frac{U^2}{L}\left[\nu\frac{U}{L^2}\right]^{-1}\sim\frac{UL}{\nu}\equiv R_\mathrm{e}\gg 1, \tag{14.7}$$

where R_e is the *Reynolds number*, U and L are characteristic velocity and length scales for the flow, and $\mathscr{O}$ denotes "order of magnitude". This condition implies that the mixing action of the advective term overwhelms the velocity-smoothing action of the viscous term.

On the other hand, noting that the advective and pressure gradient terms contribute comparably to the production of density fluctuations, we can write

$$1\sim\frac{\mathscr{O}\left(\mathbf{u}\cdot\nabla\mathbf{u}\right)}{\mathscr{O}\left(\nabla P/\rho\right)}\sim\frac{U^2}{L}\left[\frac{\Delta P}{L\rho}\right]^{-1}\sim U^2\left(\frac{c_\mathrm{s}^2\Delta\rho}{\rho}\right)^{-1}\equiv M_\mathrm{s}^2\left(\frac{\Delta\rho}{\rho}\right)^{-1}, \tag{14.8}$$

$$\Rightarrow\frac{\Delta\rho}{\rho}\sim M_\mathrm{s}^2, \tag{14.9}$$

where $M_\mathrm{s}\equiv U/c_\mathrm{s}$ is the *sonic Mach number*, $\Delta\rho/\rho$ is the *density jump*, and we have made the approximation that $\Delta P/\Delta\rho\sim c_\mathrm{s}^2$, where c_s is the sound speed. Equation (14.9) then implies that strong compressibility requires $M_\mathrm{s}\gg 1$. Conversely, flows with $M_\mathrm{s}\ll 1$ behave incompressibly, even if they are gaseous. Such is the case, for example, of the Earth's atmosphere. In the incompressible limit, $\rho=$ cst., and thus Eq. (14.1) reduces to $\nabla\cdot\mathbf{u}=0$. Note, however, that the requirement $M_\mathrm{s}\gg 1$ for strong compressibility applies for flows that behave nearly isothermally, for which the approximation $\Delta P/\Delta\rho\sim c_\mathrm{s}^2$ is valid, while "softer" (cf. Sect. 14.2) flows have much larger density jumps at a given Mach number. For example, Vázquez-Semadeni et al. (1996) showed that polytropic flows of the form $P\propto\rho^{\gamma_\mathrm{e}}$ with $\gamma_\mathrm{e}\to 0$, have density jumps of the order $e^{M_\mathrm{s}^2}$.

A trivial, but often overlooked, fact is that, in order to produce a density enhancement in a certain region of the flow, the velocity at that point must have a negative divergence (i.e., a *convergence*), as can be seen by rewriting Eq. (14.1) as

$$\frac{\mathrm{d}\rho}{\mathrm{d}t}=-\rho\nabla\cdot\mathbf{u}, \tag{14.10}$$

where $\mathrm{d}/\mathrm{d}t\equiv\partial/\partial t+\mathbf{u}\cdot\nabla$ is the *total*, *material*, or *Lagrangian* derivative. However, it is quite common to encounter in the literature discussions of pre-existing density enhancements ("clumps") in hydrostatic equilibrium. It should be kept in mind that these can only exist in multi-phase media, where a dilute, warm phase can have the same pressure as a denser, but colder, clump. But even in this case, the *formation*

of that clump must have initially involved the convergence of the flow towards the cloud, and the hydrostatic situation is applicable in the limit of very long times after the formation of the clump, when the convergence of the flow has subsided.

Finally, two other important parameters determining the properties of a magnetized flow are the *Alfvénic Mach number*, $M_{\rm A} \equiv U/\upsilon_{\rm A}$ and the *plasma beta*, $\beta \equiv P_{\rm th}/P_{\rm mag}$ where $\upsilon_{\rm A} = B/\sqrt{4\pi\rho}$ is the *Alfvén speed*. Similarly to the non-magnetic case, large values of the Alfvénic Mach number are required in order to produce significant density fluctuations through compressions *perpendicular* to the magnetic field. However, it is important to note, as mentioned in Sect. 14.3.1, that compressions *along* the magnetic field lines are not opposed at all by magnetic forces. Note that, in the isothermal case, $\beta = 2c_{\rm s}^2/\upsilon_{\rm A}^2$.

14.3.3 Production of Density Fluctuations. The Non-Magnetic Case

As mentioned in the previous sections, strongly supersonic motions, or the ability to cool rapidly, allow the production of large-amplitude density fluctuations in the flow. Note, however, that the nature of turbulent density fluctuations in a single-phase medium[1] (such as, for example, a regular isothermal or adiabatic flow) is very different from that of the cloudlets formed by TI (cf. Sect. 14.2). In a single-phase turbulent medium, turbulent density fluctuations must be transient, because in this case a higher density generally implies a higher pressure,[2] and therefore the fluctuations must re-expand (in roughly a sound-crossing time) after the compression that produced them has subsided.

Note that the above result includes the case with self-gravity, since in single-phase media, although hydrostatic equilibrium solutions do exist, they are generally unstable. Specifically, the singular isothermal sphere is known to be unstable (Shu 1977), and non-singular configurations such as the Bonnor-Ebert (BE) spheres (Ebert 1955; Bonnor 1956) need to be truncated so that the central-to-peripheral density ratio is smaller than a critical value ~ 14 in order to be stable. Such stable configurations, however, need to be confined by some means to prevent their expansion. Generally, the confining agent is assumed to consist of a dilute, warm phase that provides pressure without adding additional weight. However, such a warm phase is not available in single-phase flows, and the only way to confine the BE sphere is to continuously extend it to infinity, in which case the central-

[1] Thermodynamically, a *phase* is a region of space throughout which all physical properties of a material are essentially uniform (e.g., Modell and Reid 1974). A *phase transition* is a boundary that separates physically distinct phases, which differ in most thermodynamic variables except one (often the pressure). See Vázquez-Semadeni (2009) for a discussion on the nature of phases and phase transitions in the ISM.

[2] An exception would be a so-called Burgers' flow, which is characterized by the absence of the pressure gradient term (Burgers 1974), and can be thought of as the transitional regime from thermal stability to instability.

to-peripheral density ratio also tends to infinity, and the configuration is unstable (Vázquez-Semadeni et al. 2005a).

Instead, in *multiphase* flows, abrupt density variations may exist between different phases even though they may be at roughly the same thermal pressure, and therefore, the dense clumps do not tend to re-expand. In the remainder of this section we discuss the probability distribution of the density fluctuations, the nature of the resulting clumps and their interfaces with their environment, the correlation between the magnetic and density fields, and the evolution of the mass-to-magnetic flux ratio as the clumps are assembled by turbulent compressions.

14.3.3.1 The Probability Distribution of Density Fluctuations. The Non-Magnetic Case

For astrophysical purposes it is important to determine the distribution of the density fluctuations, as they may constitute, or at least provide the seeds for, what we normally refer to as "clouds" in the ISM. In single-phase media, however, due to the transient nature of turbulent density fluctuations, this distribution refers to a time-stationary population of fluctuations, even though the fluctuations themselves will appear and disappear on timescales of the order of their crossing time at the speed of the velocity fluctuations that produce them.

The probability density function (PDF) of the density field in turbulent isothermal flows was initially investigated through numerical simulations. Vázquez-Semadeni (1994) found that, in the isothermal case, the PDF posesses a lognormal form. A theory for the emergence of this functional form was later proposed by Passot and Vázquez-Semadeni (1998), in which the production of density fluctuations was assumed to arise from a succession of random compressive or expansive waves, each one acting on the value of the density left by the previous one. The amplitude of each wave can then be described as a random variable, characterized by some probability distribution. Because the medium contains a unique distribution of (compressible) velocity fluctuations, and because the density jumps in isothermal flow depend only on Mach number but not on the local density, the density fluctuations belong all to a unique distribution as well, yet each one can be considered independent of the others if the global time scales considered are much longer than the autocorrelation time of the velocity divergence (Blaisdell et al. 1993). Finally, because the density jumps are multiplicative in the density (cf. Eq. 14.9), then they are additive in $s \equiv \ln \rho$. Under these conditions, the Central Limit Theorem can be invoked for the increments in s, implying that s will be normally distributed, independently of the distribution of the waves. In consequence, ρ will have a lognormal PDF.

In addition, Passot and Vázquez-Semadeni (1998) also argued that the variance of the density fluctuations should scale linearly with M_s, a suggestion that has been investigated further by other groups (Padoan et al. 1997; Federrath et al. 2008). In particular, using numerical simulations of compressible turbulence driven by either

solenoidal (or "vortical") or compressible (or "potential") forces, the latter authors proposed that the variance of s is given by

$$\sigma_s = \ln(1 + bM_s^2), \tag{14.11}$$

where b is a constant whose value depends on the nature of the forcing, taking the extreme values of $b = 1/3$ for purely solenoidal forcing, and $b = 1$ for purely compressible forcing. The lognormal density PDF for the one-dimensional, isothermal simulations of Passot and Vázquez-Semadeni (1998), with its dependence on M_s, is illustrated in the *left* panel of Fig. 14.3. Finally, Passot and Vázquez-Semadeni (1998; see also Nordlund and Padoan 1999) also investigated the case where the flow behaves as a polytrope (cf. Sect. 14.2) with arbitrary values of γ_e, by noting that in this case the sound speed is not constant, but rather depends on the density as $c_s \propto \rho^{(\gamma_e-1)/2}$, implying that the local Mach number of a fluid parcel now depends on the local density besides its dependence on the value of the flow velocity. Introducing this dependence of M_s on ρ in the expression for the lognormal PDF, Passot and Vázquez-Semadeni (1998) concluded that the density PDF should develop a power-law tail, at high densities when $\gamma_e < 1$, and at low densities when $\gamma_e > 1$. This result was then confirmed by numerical simulations of polytropic turbulent flows (Fig. 14.3, *right* panel). Physically, the cause for the deviation of the PDF from the lognormal shape is that, for $\gamma_e > 1$, the sound speed increases with increasing density, and therefore, high-density regions can re-expand and disappear quickly, while "voids", with a lower sound speed, last for long times. For $\gamma_e < 1$, the sound speed *decreases* for increasing density, and the behavior is reversed: large-amplitude density peaks have lower sound speeds and therefore last for longer times, while the voids have higher sound speeds and disappear quickly. The resulting topology of the density field is illustrated in the one-dimensional case in Fig. 14.4.

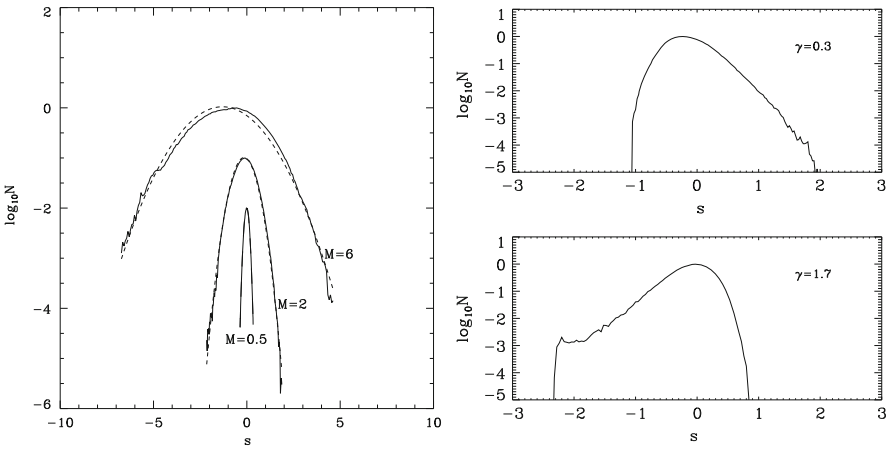

Fig. 14.3 *Left*: Lognormal density PDFs for isothermal one-dimensional simulations at various Mach numbers, indicated by the labels. The independent variable is $s \equiv \ln \rho$. *Right*: Density PDFs for polytropic cases (i.e., with $P \propto \rho^{\gamma_e}$), with effective polytropic exponent $\gamma_e = 0.3$ (*top*) and $\gamma_e = 1.7$ (*bottom*). From Passot and Vázquez-Semadeni (1998)

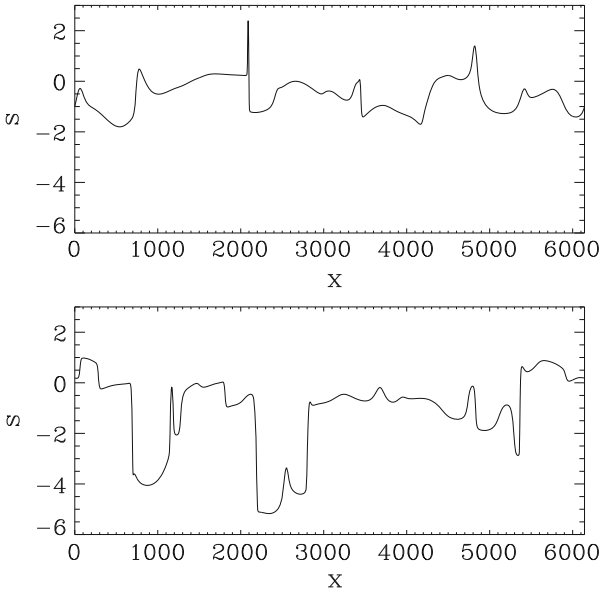

Fig. 14.4 Plots of $s = \ln \rho$ of the density field in one-dimensional simulations of polytropic flows with a resolution of 6,144 grid points by Passot and Vázquez-Semadeni (1998). *Top*: A simulation with $\gamma_e = 0.5$, exhibiting high-amplitude, narrow density peaks, due to the low sound speed at high density. *Bottom*: A simulation with $\gamma_e = 1.5$, exhibiting low-amplitude, extended density peaks and deep "voids" due to the high values of the sound speed at high densities, and low values at low densities

14.3.3.2 The Nature of Turbulent Clumps

The Ambiguity of Clump Boundaries and Masses

The clumps produced as turbulent density fluctuations are precisely that: fluctuations in a continuum. Besides, there is in general a mass and energy flux through any fixed boundary we choose to define around the local density maximum (Ballesteros-Paredes et al. 1999a). This is especially true in isothermal flows, where no transition from a diffuse phase to a dense one with the same pressure can occur, so that the only density discontinuities possible are those produced by shocks. In this case, the density fluctuations produced by turbulent compressions (a transient event of elevated ram pressure[3]) must always be transients, and must eventually re-expand or collapse (see Sect. 14.3.3). In thermally bistable media, the "boundaries"

[3]By "ram" or "hydrodynamic" pressure, we refer to the pressure exerted by the coherent motion, at speed υ, of a fluid of density ρ, and is given by $\rho\upsilon^2$. A familiar example of this is the pressure exerted by a water jet coming out of a fireman's hose.

are somewhat better defined, although there is still mass flux through them (see Sect. 14.4.2.1).

The elusiveness of the notion of clump boundaries implies that we must rethink some of our dearest notions about clumps. First of all, the mass of a cloud or clump is not well defined, and additionally must evolve in time. It is ill-defined because the clump boundary itself is. Several procedures exist for "extracting" clumps from observational maps or from numerical simulations. One of the most widely employed algorithms for locating clumps is *Clumpfind* (Williams et al. 1994), which works by locating local peaks in the field being examined and then following the field down its gradient until another clump profile is met, at which point an arbitrary boundary is defined between the two. However, this procedure, by construction, is uncapable of recognizing "hierarchical", or "nested", structures, where one coherent "parent" clump contains other equally coherent "child" ones. Moreover, not surprisingly, it has been shown that the clump sets obtained from application of this algorithm depend sensitively on the parameters chosen for the definition of the clumps (Pineda et al. 2009). Conversely, a technique that, by definition, *is* capable of detecting "parent" structures, is based on "structure trees", or "dendrograms" (e.g., Houlahan and Scalo 1992; Rosolowsky et al. 2008), which works by thresholding an image at successive intensity levels, and following the "parent"-"child" relationship between the structures identified at the different levels. Clearly, the two techniques applied to the same data produce very different sets of clumps and, in consequence, different clump mass distributions.

This variety of procedures for defining clumps illustrates the ambiguity inherent in defining a finite *object* that is actually part of a continuum, and implies that the very concept of the mass of a clump carries with it a certain level of inherent uncertainty.

Clump Masses Evolve in Time

A turbulent density fluctuation is a local density enhancement produced by a velocity field that at some moment in time is locally convergent, as indicated by Eq. (14.10). This process accumulates mass in a certain region of space ("the clump"), with the natural consequence that the mass of the clump must increase with time, at least initially, if the clump is defined, for example, as a connected object with density above a certain threshold. This definition corresponds, for example, to clumps defined as compact objects observed in a particular molecular tracer, since such tracers require the density to be above a certain threshold to be excited.

The growth of the clump's density (and mass) lasts as long as the total pressure within the clump (which may include thermal, turbulent and magnetic components) is smaller than the ram pressure from the compression. However, in a single-phase medium, once the turbulent compression subsides, the clump, which is at higher density than its surroundings, and therefore also at a higher pressure, must therefore begin to re-expand, unless it manages to become gravitationally unstable and proceed to collapse (Vázquez-Semadeni et al. 2005a; Gómez et al. 2007; see

also Sect. 14.3.3). Therefore, the mass above the clump-defining density threshold may begin to decrease again. (Again, see Sect. 14.4.2.1 for the case of clumps forming in multi-phase media.) As we shall see in Sect. 14.3.4.3, the fact that clumps' masses evolve in time has direct implications for the amount of magnetic support that the clump may have against its self-gravity.

14.3.4 Production of Density Fluctuations. The Magnetic Case

In the magnetized case, the problem of density fluctuation production becomes more complex, as the turbulent velocity field also produces magnetic field fluctuations. In this section, we discuss two problems of interest in relation to SF: The correlation of the density and magnetic fluctuations, and the effect of the magnetic field on the PDF of density fluctuations.

14.3.4.1 Density-Magnetic Field Correlation

This is a highly relevant issue in relation to SF, as the "standard" model of magnetically-regulated SF (hereafter SMSF; see, e.g., the reviews by Shu et al. 1987; Mouschovias 1991) predicted that magnetic fields should provide support for the density fluctuations ("clumps") against their self-gravity, preventing collapse, except for the material that, through AD, managed to lose its support (see the discussion in Sect. 14.5.5.2). Thus, the strength of the magnetic field induced in the turbulent density fluctuations is an important quantity to determine.

Under perfect field-freezing conditions, the simplest scenario of a fixed-mass clump threaded by an initially uniform magnetic field, and undergoing an isotropic gravitational contraction implies that the field should scale as $B \propto \rho^{2/3}$ (Mestel 1966), since the density scales as $\rho \propto R^{-3}$, where R is the radius of the clump, while the flux-freezing condition implies that $B \propto R^{-2}$. The assumption that the clump is instead oblate, or disk-like, with the magnetic field providing support in the radial direction and thermal pressure providing support in the direction perpendicular to its plane, gives the scaling $B \propto \rho^{1/2}$ (Mouschovias 1976, 1991).

In a turbulent flow, however, the situation becomes more complicated. "Clumps" are not fixed-mass entities, but rather part of a continuum that possesses random, chaotic motions. In principle, unless the magnetic energy is *much* larger than the turbulent kinetic energy, the compressive motions that form a clump can have any orientation with respect to the local magnetic field lines, and thus the resulting density enhancement may or may not be accompanied by a corresponding magnetic field enhancement (cf. Sect. 14.3.1). In particular, Passot and Vázquez-Semadeni (2003; hereafter, PV03) studied this problem analytically in the isothermal case, by decomposing the flow into nonlinear, so-called "simple" waves (e.g., Landau and Lifshitz 1959), which are the nonlinear extensions of the well known linear MHD waves (e.g., Shu 1992), having the same three well-known modes: fast, slow,

and Alfvén (Mann 1995). For illustrative purposes, note that compressions along the magnetic field lines are one instance of the *slow* mode, while compressions perpendicular to the field lines (i.e., *magnetosonic* waves) are an instance of the *fast* mode. As is well known, Alfvén waves are transverse waves propagating along field lines, and carry no density enhancement. However, they can exert pressure, and the dependence of this pressure on the density has been investigated by McKee and Zweibel (1995) and PV03.

For simplicity and insight, PV03 considered the so-called "1+2/3-dimensional" case, also known as "slab geometry", meaning that all three components of vector quantities are considered, but their variation is studied with respect to only one spatial dimension. For the Alfvén waves, they performed a linear perturbation analysis of a circularly polarized wave. They concluded that each of the modes is characterized by a different scaling between the magnetic pressure ($\propto B^2$) and the density, as follows:

$$B^2 \propto c_1 - \beta\rho \qquad \text{slow,} \tag{14.12}$$

$$B^2 \propto \rho^2 \qquad \text{fast,} \tag{14.13}$$

$$B^2 \propto \rho^{\gamma_m} \qquad \text{Alfvén,} \tag{14.14}$$

where c_1 is a constant, and γ_m is a parameter that can take values in the range (1/2,2) depending on the Alfvénic Mach number (see also McKee and Zweibel 1995). Note that Eq. (14.12) implies that for $\rho > c_1/\beta$ the slow mode disappears (Mann 1995), so that only the fast and Alfvén modes remain. Conversely, note that, at low density, the magnetic pressure due to the fast and Alfvén modes becomes negligible in comparison with that due to the slow mode, which approaches a constant. This implies that a log-log plot of B vs. ρ will exhibit an essentially constant value of B at very small values of the density. In other words, *at low values of the density, the domination of the slow mode implies that the magnetic field exhibits essentially no correlation with the density.*

PV03 were able to test these results numerically by taking advantage of the slab geometry, which allowed to set up waves propagating at well-defined angles with respect to the mean magnetic field, and therefore being able to isolate, or nearly isolate, the three different wave modes. The *left* panel of Fig. 14.5 shows the distribution of points in the B^2-s space for a simulation dominated by the slow mode, exhibiting the behavior outlined above, corresponding to Eq. (14.12). In contrast, the *right* panel of Fig. 14.5 shows the distribution of points in the same space for a simulation dominated by the fast mode, exhibiting the behavior indicated by Eq. (14.13).

The most important conclusion from Eqs. (14.12)–(14.14) is that, in a turbulent flow in which all modes are active, the net, average scaling of the magnetic field with the density will arise from the combined effect of the various modes. Moreover, since at low densities the values of B produced by the fast and Alfvén modes are also small, while the field strengths produced by the slow mode remain roughly constant, the field fluctuations will be dominated by the latter mode at low

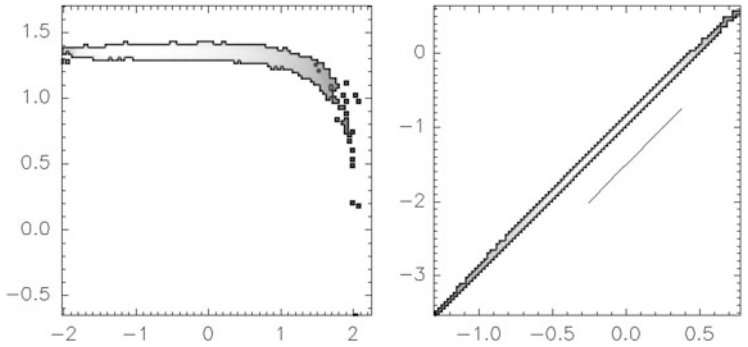

Fig. 14.5 Two-dimensional histograms of the grid cells in numerical simulations in the $\ln B^2$ (vertical axis)-$\ln \rho$(horizontal axis) space. The gray scale indicates the density of points in this space. *Left*: A slab-geometry numerical simulation by PV03 dominated by the slow mode, exhibiting the behavior indicated by Eq. (14.12). *Right*: Same as the *left* panel, but for a numerical simulation dominated by the fast mode, exhibiting the behavior indicated by Eq. (14.13)

densities, and a roughly density-independent field strength is expected. Conversely, at high densities, the slow mode disappears, while the contribution from the fast and Alfvén modes will dominate, producing a field strength that increases with increasing density. Finally, because each mode produces a different dependence of the magnetic field strength with the density, we expect that the instantaneous value of the density at a certain location in physical space is not enough to determine the value of the magnetic field strength there. Instead, this value depends on the *history of modes* of the nonlinear waves that have passed through that location, naturally implying that, within a large cloud, a large scatter in the measured values of the magnetic field is expected. The expected net scaling of the field strength with the density is illustrated in the *left* panel of Fig. 14.6. These results are in qualitative agreement with detailed statistical analyses of the magnetic field distribution in the ISM (Crutcher et al. 2010), as illustrated in the *right* panel of Fig. 14.6.

14.3.4.2 Effect of the Magnetic Field on the Density PDF

According to the discussion in Sect. 14.3.3.1, the dependence of the pressure on density determines the shape of the density PDF, being a lognormal for the isothermal case, $\gamma_e = 1$. In the presence of a magnetic field, it would be natural to expect that the magnetic pressure, which in general does not need to behave as an isothermal polytrope, might cause deviations from the lognormal density PDF associated to isothermal turbulent flows.

However, the discussion above on the density-magnetic field correlation (or rather, lack thereof), implies that the magnetic pressure does not have a systematic effect on density fluctuations of a given amplitude, as the value of the magnetic field is not uniquely determined by the local value of the density. PV03 concluded

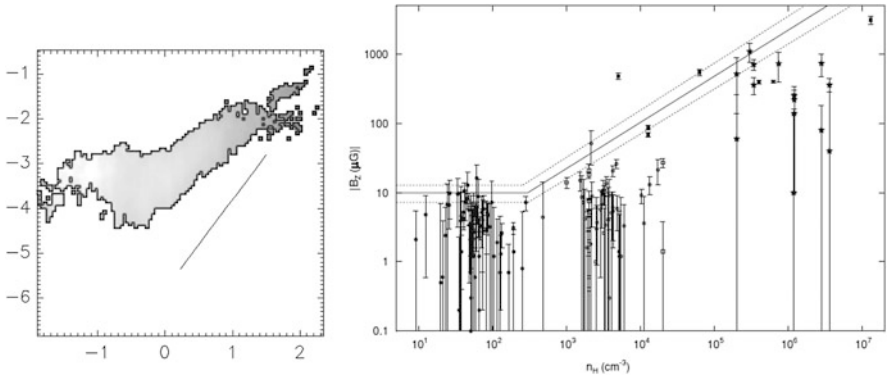

Fig. 14.6 *Left*: Two-dimensional histogram of the grid cells in the B^2-n space from a numerical simulation by PV03 in which both the slow and the fast modes are active. At low densities, the slow mode causes a density-independent magnetic field strength, while at higher densities, the fast mode produces a positive correlation. The straight-line segment has a slope of 2. *Right*: Magnetic field strength determinations by Zeeman splitting observations in molecular clouds, as compiled by Crutcher et al. (2010). The rising straight line segment has a slope ≈ 0.65, implying $B^2 \propto n^{1.3}$, in qualitative agreement with the numerical result

that the effect of the magnetic pressure was more akin to a random forcing in the turbulent flow than to a systematic pressure gradient that opposes compression. As a consequence, the underlying density PDF determined by the functional form of the thermal pressure did not appear to be significantly affected by the presence of the magnetic field, except under very special geometrical setups in slab geometry, and that in fact are unlikely to persist in a more general three-dimensional setup. The persistence of the underlying PDF dictated by the thermodynamics in the presence of the magnetic field is in agreement with numerical studies of MHD turbulent flows that indeed have found approximately lognormal PDFs in the isothermal case (e.g., Nordlund and Padoan 1999; Ostriker et al. 1999, 2001; Vázquez-Semadeni and García 2001; Beresnyak et al. 2005), and bimodal density PDFs in thermally-bistable flows (Gazol et al. 2009), which we discuss in Sect. 14.4.1.

14.3.4.3 Evolution of the Mass-to-Magnetic Flux Ratio

The discussion in Sect. 14.3.3.2 implies that the mass deposited in a clump by turbulent compressions is a somewhat ill-defined quantity, depending on where and how one chooses to define the "boundaries" of the clump, and on the fact that its mass is time-dependent. This has important implications for the so-called mass-to-flux ratio (MFR) of the clump, and therefore, for the ability of the magnetic field to support the clump against its self-gravity.

As is well known (Mestel and Spitzer 1956), a virial balance analysis implies that, for a cloud of mass M threaded by a uniform field B, gravitational collapse can only occur if its MFR satisfies

$$\frac{M}{\Phi} > \left(\frac{M}{\Phi}\right)_{\rm crit} \equiv \left(\alpha\pi^2 G\right)^{-1/2}, \tag{14.15}$$

where α is a constant of order unity whose precise value depends on the shape and mass distribution in the cloud (see, e.g., Mestel and Spitzer 1956; Nakano and Nakamura 1978; Shu 1992). Otherwise, the cloud is absolutely supported by the magnetic field, meaning that the support holds irrespective of the density of the cloud. In what follows, we shall denote the MFR, normalized to this critical value, by λ. Regions with $\lambda > 1$ are called *magnetically supercritical*, while those with $\lambda < 1$ are termed *magnetically subcritical*. Traditionally, it has been assumed that the mass of the cloud is well defined. However, our discussions above (Sect. 14.3.3.2) suggest that it may be convenient to revisit these notions.

When considering density enhancements ("cores") formed by turbulent compressions within a cloud of size L, it is convenient to assume that the initial condition for the cloud is one with uniform density and magnetic field, and that the turbulence produces local fluctuations in the density and the magnetic field strength. A simple argument advanced by Vázquez-Semadeni et al. (2005a) then shows that the MFR of a core of size ℓ and MFR λ_ℓ, must be within the range

$$\lambda_0 \frac{\ell}{L} < \lambda_\ell < \lambda_0, \tag{14.16}$$

where λ_0 is the MFR of the whole cloud. The lower limit applies for the case when the "core" is actually simply a subregion of the whole cloud of size L, with the same density and magnetic field strength. Since the density and field strength are the same, the mass of the core simply scales as $(\ell/L)^3$, while the magnetic flux scales as $(\ell/L)^2$. Therefore, the MFR of a subregion of size ℓ scales as (ℓ/L). Of course, this lower-limit extreme, corresponding to the case of a "core" of the same density and field strength as the whole cloud, is an idealization, since observationally such a structure cannot be distinguished from its parent cloud. Nevertheless, as soon as some compression has taken place, the core will be observationally distinguishable from the cloud (for example, by using a tracer that is only excited at the core's density), and the measurement of the MFR *in the core* will be bounded from below by this limit.

On the other hand, the upper limit corresponds simply to the case where the entire cloud of size L has been compressed isotropically to a size ℓ, since in this case both the mass and the magnetic flux are conserved, and so is the MFR.

This reasoning has the implication that the MFR that is *measured* in a core within a cloud must be smaller than that measured for the whole cloud, as long as the condition of flux-freezing holds. Note that one could argue that this is only an observational artifact, and that the physically relevant mass is that associated to the whole flux tube the core belongs to, but this is only reflecting the ambiguity

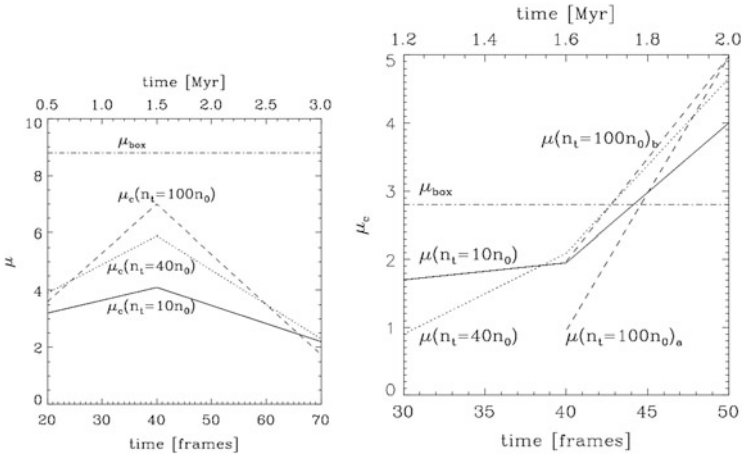

Fig. 14.7 Evolution of the mass-to-flux ratio (MFR, denoted μ in these plots), normalized to the critical value, in cores formed in numerical simulations of continuously driven MHD isothermal turbulence by Vázquez-Semadeni et al. (2005a). The cores are defined as connected sets of grid cells with density above a density threshold n_t, and are followed over time. Three values of n_t are used, illustrating how the value of the MFR depends and evolves as successively more internal regions of the density fluctuation are considered. *Left*: Evolution of λ in a core that does not collapse. At all values of n_t, the MFR first increases and then decreases again. *Right*: A core that does collapse. In this panel, two lines are shown at the largest value of n_t, because the parent clump splits into two cores at this threshold. In both panels, the rate of variation of λ is larger for larger values of n_t, and λ for the innermost region ($n_t = 100n_0$, where n_0 is the mean density of the simulation) is seen to start *lower* than that of the envelope, and to overtake it as the degree of mass concentration is increased, in this case as a consequence of numerical diffusion, which plays a role analogous to that of AD

discussed above concerning the masses of clumps. In practice, *the physically relevant mass for the computation of the MFR is the one responsible for the local gravitational potential well against which the magnetic field is providing the support*, and this mass is precisely the mass of the core, not the mass along the entire flux tube, especially when phase transitions are involved.

Note also that, as discussed in Sect. 14.3.3.2, the mass of the clump must be evolving in time. If the compression is occurring mostly along field lines (since in this direction the magnetic field presents no resistance to it), then the magnetic flux remains roughly constant, while the mass increases at first, and later it possibly decreases if the clump begins to re-expand. Otherwise, if the core becomes massive enough that it becomes gravitationally unstable *and* supercritical, it must begin to collapse gravitationally (Fig. 14.7). At this point, the rapid density enhancement at the core in turn enhances the action of AD (e.g., Shu et al. 1987; Mouschovias 1991;

see also Sect. 14.3.1), causing the magnetic flux to escape the core,[4] so that the latter eventually acquires a larger value of λ than its envelope. Thus, the prediction from this dynamic scenario of core formation is that cores in early stages of evolution should exhibit smaller values of the MFR than their envelopes, while cores at more advanced stages should exhibit larger values of the MFR than their envelopes. Evidence in this direction has begun to be collected observationally (Crutcher et al. 2009), as well as through synthetic observations of numerical simulations (Lunttila et al. 2009).

Before closing this section, an important remark is in order. Recent numerical and observational evidence (cf. Sect. 14.5.5) suggests that the "turbulence" in star-forming molecular clouds may actually consist of a hierarchy of gravitational contraction motions, rather than of random, isotropic turbulence. In such a case, the physical processes discussed in this section are still applicable, noting that the converging flows that produce the clumps may be driven by larger-scale gravitational collapse rather than by random turbulent compressions, and the only part of the previous discussion that ceases to be applicable is the possibility that some cores may fail to collapse and instead re-expand. If the motions all have a gravitational origin, then essentially all cores must be on their way to collapse. It is worth pointing out that in this case, what drives the collapse of an apparently subcritical core is the collapse of its parent, supercritical structure.

14.4 Turbulence in the Multiphase ISM

In the previous sections we have separately discussed two different kinds of physical processes operating in the ISM: radiative heating and cooling, and compressible MHD turbulence in the special case of isothermality. However, since both operate simultaneously in the atomic ISM, it is important to understand how they interact with each other, especially because the mean density of the Galactic ISM at the Solar galactocentric radius, $\langle n \rangle \sim 1$ cm^{-3}, falls precisely in the thermally unstable range. This problem has been investigated numerically by various groups (e.g., Hennebelle and Pérault 1999, 2000; Walder and Folini 2000; Koyama and Inutsuka 2000, 2002; Vázquez-Semadeni et al. 2000, 2003a, 2006, 2007, 2011; Hennebelle etal. 2008; Banerjee et al. 2009; Gazol et al. 2001, 2005, 2009; Kritsuk and Norman 2002; Sánchez-Salcedo et al. 2002; Piontek and Ostriker 2004, 2005; Audit and Hennebelle 2005, 2010; Heitsch et al. 2005; Hennebelle and Audit 2007), and in this section we review their main results.

[4] Note that this "escape" is meant in a Lagrangian sense, i.e., following the flow. That is, considering a certain fluid parcel as it contracts, AD causes the flux to be "left behind" from the fluid particles that make up the parcel. Conversely, in an Eulerian sense, the magnetic flux remains fixed, but the fluid parcel increases its mass in this frame.

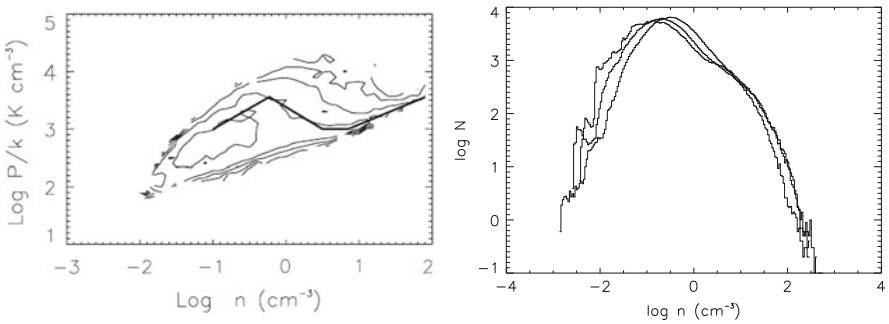

Fig. 14.8 *Left*: Two-dimensional histogram of the grid cells in the pressure-density diagram for a two-dimensional simulation of turbulence in the thermally-bistable atomic medium, with *rms* velocity dispersion of 9 km s^{-1}, a numerical box size of 100 pc, and the turbulent driving applied at a scale of 50 pc. *Right*: Density PDF in simulations like the one on the *left* panel, but with three different values of the *rms* velocity: 4.5 km s^{-1} (*solid line*), 9 km s^{-1} (*dotted line*), and 11.3 km s^{-1} (*dashed line*). The bimodality of the PDF is seen to become less pronounced as the rms velocity increases, with a single power-law tail developing in the density range between the values where the peaks would be otherwise located. From Gazol et al. (2005)

14.4.1 Density PDF in the Multiphase ISM

A key parameter controlling the interaction between turbulence and net cooling is the ratio $\eta \equiv \tau_c/\tau_t$, where $\tau_c \sim kT/(n\Lambda)$ is the cooling time, with k being the Boltzmann constant, and $\tau_t \sim L/U$ is the turbulent crossing time. The remaining symbols have been defined above. In the limit $\eta \gg 1$, the dynamical evolution of the turbulent compressions occurs much more rapidly than they can cool, and therefore the compressions behave nearly adiabatically. Conversely, in the limit $\eta \ll 1$, the fluctuations cool down essentially instantaneously while the turbulent compression is evolving, and thus they tend to reach the thermal equilibrium pressure P_{eq} as soon as they are produced[5] (Elmegreen 1991; Passot et al. 1995; Sánchez-Salcedo et al. 2002; Vázquez-Semadeni et al. 2003a; Gazol et al. 2005). Because in a turbulent flow velocity fluctuations of a wide range of amplitudes and size scales are present, the resulting density fluctuations in general span the whole range between those limits, and the actual thermal pressure of a fluid parcel is not uniquely determined by its density, but rather depends on the details of the velocity fluctuation that produced it. This causes a scatter in the values of the pressure around the thermal-equilibrium value in the pressure-density diagram (Fig. 14.8, *left* panel), and also produces

[5]It is often believed that fast cooling directly implies isothermality. However, this is a misconception. While it is true that fast cooling is a necessary condition for approximately isothermal behavior, the reverse implication does not hold. Fast cooling only implies an approach to the thermal equilibrium condition, but this need not be isothermal. The precise form of the effective equation of state depends on the details of the functional dependence of the heating and cooling functions on the density and temperature.

significant amounts of gas (up to nearly half of the total mass) with densities and temperatures in the classically forbidden thermally unstable range (Gazol et al. 2001; de Avillez and Breitschwerdt 2005; Audit and Hennebelle 2005; Mac Low et al. 2005), a result that has been encountered by various observational studies as well (e.g., Dickey et al. 1978; Heiles 2001). In any case, the tendency of the gas to settle in the stable phases still shows up as a multimodality of the density PDF, which becomes less pronounced as the *rms* turbulent velocity increases (Fig. 14.8, *right* panel).

14.4.2 The Formation of Dense, Cold Clouds and Clumps

14.4.2.1 The Non-Magnetic Case

A very important consequence of the interaction of turbulence (or, more generally, large-scale coherent motions of any kind) and TI is that the former may *nonlinearly* induce the latter. Indeed, Hennebelle and Pérault (1999; see also Koyama and Inutsuka 2000) showed that transonic (i.e., with $M_s \sim 1$) compressions in the WNM can compress the medium and bring it sufficiently far from thermal equilibrium that it can then undergo a phase transition to the CNM (Fig. 14.9, *left* panel). This process amounts then to producing a cloud with a density up to 100× larger than that of the WNM by means of only moderate, transonic compressions. This is in stark contrast with the process of producing density fluctuations by pure supersonic compressions in, say, an isothermal medium, in which such density contrasts would require Mach numbers $M_s \sim 10$. It is worth noting that the turbulent velocity dispersion of $\sim$ 8–11 km s^{-1} in the warm Galactic ISM (Kulkarni and Heiles 1987; Heiles and Troland 2003) is, precisely, transonic.

Moreover, the cold clouds formed by this mechanism have typical sizes given by the size scale of the compressive wave in the transverse direction to the compression, rather than having to be of the same size scale as the fastest growing mode of TI, which is very small ($\lesssim$ 0.1 pc; cf. Sect. 14.2). The initial stages of this process may produce thin CNM sheets (Vázquez-Semadeni et al. 2006), which are in fact observed (Heiles and Troland 2003). However, such sheets are quickly destabilized, apparently by a combination of nonlinear thin shell (NTSI; Vishniac 1994), Kelvin–Helmholtz and Rayleigh–Taylor instabilities (Heitsch et al. 2005), fragmenting and becoming turbulent. This causes the clouds to become a complex mixture of cold and warm gas, where the cold gas is distributed in an intrincate network of sheets, filaments and clumps, possibly permeated by a dilute, warm background. An example of this kind of structure is shown in the *right* panel of Fig. 14.9.

A noteworthy feature of the clouds and clumps formed by TI is that, contrary to the case of density fluctuations in single-phase media, they can have more clearly defined and long-lasting boundaries. This is because their boundaries may be defined by the locus of the interface between the cold and warm phases, which, once formed, tends to persist over long timescales compared to the dynamical

time, because the two phases are essentially at the same pressure. *Under quasi-hydrostatic conditions*, these boundaries would have little or no mass flux across them (i.e., they are *contact discontinuities*; see, e.g., Shu 1992). Any mass exchange that managed to happen would be due to evaporation or condensation, occurring when the thermal pressure differs from the saturation value between the phases (e.g., Zel'Dovich and Pikel'Ner 1969; Penston and Brown 1970; Nagashima et al. 2005; Inoue et al. 2006). The latter two papers have in fact proposed that such evaporation may contribute to the driving of interstellar turbulence, although the characteristic velocities they obtained ($\lesssim 1$ km s^{-1}) appear to be too small for this to be the dominant mechanism for driving the large scale ISM turbulence, with characteristic speeds of ~ 10 km s^{-1}.

However, in the presence of large-scale (> 10 pc) and large-amplitude ($\gtrsim 10$ km s^{-1}) motions, corresponding either to the supernova-driven global ISM turbulence, to larger-scale instabilities, such as the magneto-Jeans (e.g., Kim and Ostriker 2001) or magneto-rotational (Balbus and Hawley 1991) ones, or simply to the passage of spiral arms, the *nonlinear* triggering of TI implies that the fronts bounding the clouds and clumps are not contact discontinuities, but rather *phase transition fronts*—structures analogous to shocks, with large density, temperature and velocity jumps, but without the need for locally supersonic velocities. Across such fronts, a substantial mass flux occurs (Vázquez-Semadeni et al. 2006; Banerjee et al. 2009). This is mechanism is illustrated in Fig. 14.10, which clearly shows the rapid growth of a clump by accretion of diffuse material in a numerical simulation. This is in stark

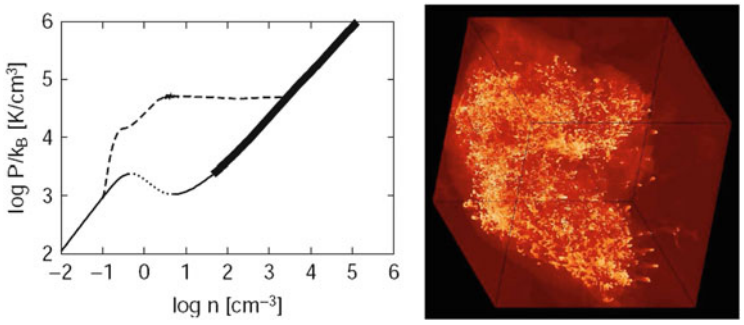

Fig. 14.9 *Left*: Evolutionary path (*dashed line*) in the P vs. ρ diagram of a fluid parcel initially in the WNM after suffering a transonic compression that nonlinearly triggers TI. The *solid* and *dotted lines* show the locus of $P_{\rm eq}(\rho)$, the solid sections corresponding to linear stability and the dotted ones to linear instability. The solid section to the left of the *dotted line* corresponds to the WNM and the one at the right, to the CNM. The perturbed parcel evolves from *left to right* along the *dashed line*. From Koyama and Inutsuka (2000). *Right*: Projected (or *column*) density structure of the resulting GMC in a numerical simulation of its formation by colliding WNM streams, and its subsequent evolution. The numerical box has a size of 15 pc on a side, and the resolution is 1200^3 grid cells. The "GMC" is seen to consist of the agglomeration of a huge number of small clumps, which have formed by fragmentation caused by the action of combined instabilities in the compressed gas. From Audit and Hennebelle (2010)

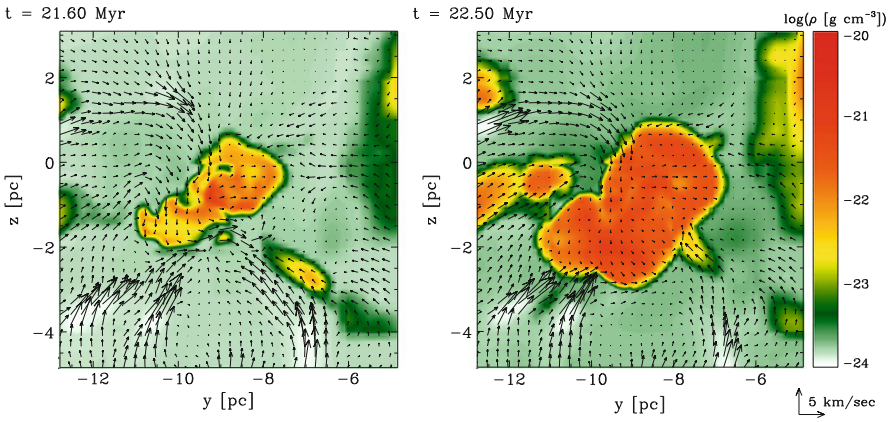

Fig. 14.10 Density cuts through the plane $x = 2.5$ pc in an adaptive-mesh refinement (AMR) numerical simulation of molecular cloud formation by Banerjee et al. (2009), illustrating the clump growth mechanism. The numerical box size is 256 pc, and the maximum resolution is 0.06 pc. The arrows show the projection of the velocity field on this plane. *Left*: The clump at time $t = 21.6$ Myr. *Right*: The clump at $t = 22.5$ Myr. Comparing the two times the growth of the clump is evident. The velocity field is seen to generally point towards the clump, indicating that material from the diffuse external medium is entering the clump, causing its growth

contrast with early ideas that the clumps grew by coagulation of tiny cloudlets on very long timescales ($\sim$ 100 Myr; e.g., Kwan 1979).

It should be emphasized, however, that the density does not necessarily always present a sharp jump between the clump and its surroundings. As discussed in Sect. 14.4.1, the presence of turbulence in the diffuse medium also implies a certain degree of mixing, and the existence of a certain fraction of the mass that is traversing the unstable range. In Fig. 14.10 this can be observed as the greenish regions, especially near the right edge of the *left* panel.

We conclude then that, although in thermally bistable flows clump boundaries are in general better defined than in turbulent isothermal flows because of the density jumps induced by the thermal bistability, this does not imply that they are impenetrable boundaries that restrict the flow of the medium. Rather, the clumps are formed and then grow by accretion of diffuse material across these phase transition fronts.

Finally, it is important to note that, in the scenario of GMC formation described above, the compressions in the WNM tend to initially form thin sheets of CNM (Vázquez-Semadeni et al. 2006), in agreement with observations of CNM clouds (Heiles and Troland 2003). These sheets, however, grow by accretion of diffuse gas, fragmenting and becoming turbulent due to the combined action of various instabilities (Vázquez-Semadeni et al. 2006; Heitsch et al. 2006), so that GMCs may actually consist of huge conglomerates of small clumps, as illustrated in the *right* panel of Fig. 14.9. This is consistent with the observed clumpy structure of GMCs (Blitz 1993; sect. VII).

14.4.2.2 The Magnetic Case

In the presence of a magnetic field, the process of cloud formation by phase transitions to the cold phase requires further considerations. First, the orientation of the compressive motion relative to that of the magnetic field strongly influences the ability of the compression to trigger a transition to the dense phase. Hennebelle and Pérault (2000) investigated this problem by means of numerical simulations with slab (1+1/2D) geometry, finding that, for a certain value of the magnetic field strength, and a given sonic Mach number of the compression, there exists a maximal angle between the direction of compression and the direction of the magnetic field beyond which no phase transition is induced. They found this angle to typically lie between 20° and 40°, for typical values of the warm neutral medium.

Hennebelle and Pérault (2000) also found that, when the formation of a cloud does occur, either the field is re-oriented along the compression (in the case of weak fields), or the flow is re-oriented along field lines (in the case of stronger fields), and the accumulation of gas to form the clump ends up being aligned with the magnetic field. In addition, Inoue and Inutsuka (2008) have found that compressions perpendicular to the magnetic field strongly inhibit the formation of dense, molecular-type clouds, and that, in this case, only diffuse HI clouds manage to form. As a consequence, the discussion of cloud formation can be made in terms of compressions parallel to the magnetic field without loss of generality. We will take up this problem again in Sect. 14.5.5, when we discuss the onset of gravitational collapse of the clouds.

14.5 The Nature of the Turbulence in the Various ISM Components

14.5.1 Generalities

As discussed in the previous sections, the ionized and atomic components of the ISM consist of gas in a wide range of temperatures, from $T \sim 10^6$ K for the HIM, to $T \sim 40$ K for the CNM. In particular, Heiles and Troland (2003) report temperatures in the range $500 < T < 10^4$ K for the WNM, and in the range $10 < T < 200$ K for the CNM. The WIM is expected to have $T \sim 10^4$ K. This implies that the adiabatic sound speed, given by (e.g., Landau and Lifshitz 1959)

$$c_\mathrm{s} = \sqrt{\frac{\gamma kT}{\mu_\mathrm{m} m_\mathrm{H}}} \approx 10.4 \text{ km s}^{-1} \left(\frac{T}{10^4 \mathrm{K}}\right)^{1/2}, \tag{14.17}$$

will also exhibit large fluctuations in the medium. In the second equality, we have used $\mu_{\rm m} = 1.27$. In the following sections we discuss the implications of these ranges for the various ISM components.

14.5.2 The Hot Ionized medium

At temperatures $T \sim 10^6$ K, the sound speed in the HIM is ~ 100 km s^{-1}, much larger than the velocity dispersion in the general ISM, ~ 10 km s^{-1}. Thus, except in the immediate vicinity of supernova explosions, where the velocities can reach thousands of km s^{-1}, the HIM in general is expected to behave nearly incompressibly. Moreover, because the density is very low ($\lesssim 10^{-2}$ cm^{-3}), the cooling time ($\tau_{\rm c} \sim kT/n\Lambda$; cf. Sect. 14.4.1) is very long (a few tens of Myr), and the medium is then expected to behave roughly adiabatically, at least up to scales of a few hundred parsecs.

14.5.3 The Warm Ionized Medium

Collecting measurements of interstellar scintillation (fluctuations in amplitude and phase of radio waves caused by scattering in the ionized ISM) from a variety of observations, Armstrong et al. (1995) estimated the power spectrum of density fluctuations in the WIM, finding that it is consistent with a Kolmogorov (1941) spectrum, a result expected for weakly compressible flows (Bayly et al. 1992), on scales $10^8 \lesssim L \lesssim 10^{15}$ cm.

More recently, using data from the Wisconsin Hα Mapper Observatory, Chepurnov and Lazarian (2010) have been able to extend the spectrum to scales $\sim 10^{19}$ cm, suggesting that the WIM behaves as an incompressible turbulent flow over size scales spanning more than ten orders of magnitude. This suggestion is supported also by the results of Hill et al. (2008) who, by measuring the distribution of Hα emission measures in the WIM, and comparing with numerical simulations of turbulence at various Mach numbers, concluded that the sonic Mach number of the WIM should be $\sim$ 1.4–2.4. Although the WIM is ionized, and thus should be strongly coupled to the magnetic field, the turbulence then being magnetohydrodynamic (MHD), Kolmogorov scaling should still apply, according to the theory of incompressible MHD fluctuations (Goldreich and Sridhar 1995). The likely sources of kinetic energy for these turbulent motions are stellar energy sources such as supernova explosions (see, e.g., Mac Low and Klessen 2004).

14.5.4 The Atomic Medium

In contrast to the relatively simple and clear-cut situation for the ionized ISM, the turbulence in the neutral (atomic and molecular) gas is more complicated. According to the discussion in Sect. 14.5.1, the temperatures in the atomic gas may span a continuous range from a few tens to several thousand degrees. Additionally, Heiles and Troland (2003) report column density-weighted *rms* velocity dispersions $\sigma_v \sim 11$ km s^{-1} for the WNM, and typical internal motions of $M_s \sim 3$ for the CNM. It is thus clear that the WNM is transonic ($M_s \sim 1$), while the CNM is moderately supersonic. This occurs because the atomic gas is thermally bistable, and because transonic compressions in the WNM can nonlinearly induce TI and thus a phase transition to the CNM (Sect. 14.4.1). Thus, the neutral atomic medium is expected to consist of a complex mixture of gas spanning over two orders of magnitude in density and temperature.

It is worth noting that early pressure-equilibrium models (e.g., Field et al. 1969; McKee and Ostriker 1977) proposed that the unstable phases were virtually nonexistent in the ISM, but the observational and numerical results discussed in Sect. 14.4.1 suggest that a significant fraction of the atomic gas mass lies in the unstable range, transiting between the stable phases. Also, numerical simulations of such systems suggest that the velocity dispersion *within* the dense clumps is subsonic, but that the velocity dispersion of the clumps within the diffuse substrate is supersonic with respect to their internal sound speed (although subsonic with respect to the warm gas; Koyama and Inutsuka 2002; Heitsch et al. 2005).

14.5.5 The Molecular Gas

14.5.5.1 Molecular Clouds: Supersonically Turbulent, or Collapsing?

The evidence

Molecular clouds (MCs) have long been known to be strongly self-gravitating (e.g., Goldreich and Kwan 1974; Larson 1981). In view of this, Goldreich and Kwan (1974) initially proposed that MCs should be in a state of gravitational collapse, and that the observed motions in MCs (as derived by the non-thermal linewidths of molecular lines) corresponded to this collapse. However, shortly thereafter, Zuckerman and Palmer (1974) argued against this possibility by noting that, if all the molecular gas in the Galaxy, with mean density $n \sim 100\,\mathrm{cm}^{-3}$ and total mass $M_{\rm mol} \sim 10^9 M_\odot$, were in free-fall, then a simple estimate of the total SF rate (SFR) in the Galaxy, given by SFR $\sim M_{\rm mol}/\tau_{\rm ff} \sim 200\ M_\odot\ \mathrm{yr}^{-1}$, where $\tau_{\rm ff} = \sqrt{3\pi/32G\rho}$ is the free-fall time, would exceed the observed rate of $\sim 2\ M_\odot$ year^{-1} (e.g., Chomiuk and Povich 2011) by about two orders of magnitude. Moreover, Zuckerman and Evans (1974) argued that, if clouds were undergoing large-scale radial motions (a regime which they assumed would include the case of a

global gravitational contraction), then the star formation activity, and the HII regions associated with it, would tend to be concentrated at the center of the cloud. Under these conditions, the H_2CO absorption lines seen on the spectra of the HII regions, produced by the surrounding, infalling gas, should be redshifted with respect to the CO lines produced by the cloud as a whole, an effect which Zuckerman and Evans (1974) showed does not occur. They also argued that such a "radial-motion" flow regime is inconsistent with the fact that clouds contain multiple HII regions, clusters, and dense clumps. A related notion, which still persists today, is that, if a cloud is undergoing global collapse, the largest linewidths should occur near the collapse center, as the infall velocities should be at a maximum there, contrary to the observation that the largest velocity dispersions occur at the largest scales (Larson 1981).

These objections prompted the suggestion (Zuckerman and Evans 1974) that the non-thermal motions in MCs corresponded instead to *small-scale* (in comparison to the sizes of the clouds) random turbulent motions. The need for these motions to be confined to small scales arose from the need to solve the absence of a systematic shift between the H_2CO absorption lines of HII regions and the CO lines from their parent molecular clouds noted by those authors. But such a small-scale nature also had the advantage that the turbulent (*ram*) pressure could provide an approximately isotropic pressure that could counteract the self-gravity of the clouds at large, thus providing a suitable mechanism for keeping the clouds from collapsing and maintaining them in near virial equilibrium (Larson 1981). On the other hand, because turbulence is known to be a dissipative phenomenon (e.g., Landau and Lifshitz 1959), research then focused on finding suitable sources for driving the turbulence and avoiding rapid dissipation. The main driving source was considered to be energy injection from stars (e.g., Norman and Silk 1980; McKee 1989; Li and Nakamura 2006; Nakamura and Li 2007; Krumholz et al. 2006; Carroll et al. 2009, 2010; Wang et al. 2010; see also the reviews by Mac Low and Klessen 2004 and Vázquez-Semadeni 2010), and reduction of dissipation was proposed to be accomplished by having the turbulence being MHD, and consisting mostly of Alfvén waves, which were thought not to dissipate as rapidly (e.g., Shu et al. 1987), and which could provide an isotropic pressure (McKee and Zweibel 1995).

However, in the last decade several results have challenged the turbulent pressure-support scenario: (1) Turbulence is known to be characterized by having the largest velocity differences occurring at the largest scales, and MCs are no exception, exhibiting scaling relations between velocity dispersion and size which suggest that the largest velocity differences occur at the largest scales (Larson 1981; Heyer and Brunt 2004; Brunt et al. 2009; Fig. 14.11, *left* and *middle* panels). This is inconsistent with the small-scale requirement for turbulent support. (2) It was shown by several groups that MHD turbulence dissipates just as rapidly as hydrodynamic turbulence (Mac Low et al. 1998; Stone et al. 1998; Nordlund and Padoan 1999), dismissing the notion of reduced dissipation in "Alfvén-wave turbulence", and thus making the presence of strong driving sources for the turbulence an absolute necessity. (3) Clouds with very different contributions from various turbulence-driving mechanisms, including those with little or no SF activity,

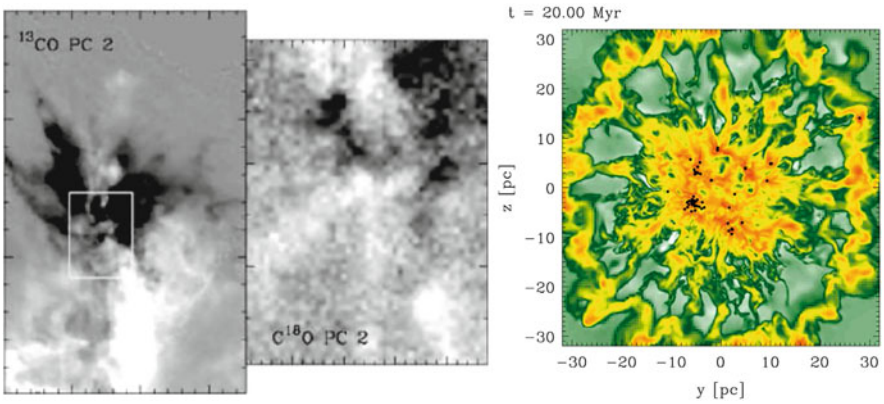

Fig. 14.11 *Left and middle panels:* Second eigenimages obtained by Principal Component Analysis of spectroscopic data of the star-forming region NGC 1333, showing the main contribution to the linewidth of molecular emission in this region (Brunt et al. 2009). The *middle image* shows the region enclosed in the rectangle in the *left* image. *Black and white* colors represent oppositely-signed components of the velocity. Brunt et al. (2009) describe the pattern as a "dipole", in which large-scale patches of alternating velocity direction are observed. This is seen in both the large-scale (*left*) and the small-scale (*middle*) images. *Right panel:* Image of the projected density field of a 3D numerical simulation with cooling, self-gravity, and magnetic fields, representing the formation of a dense atomic cloud by the collision of WNM streams in the direction perpendicular to the plane of the figure. The time shown is 20 Myr after the start of the simulation. The black dots denote "sink" particles, which replace local collapsing zones in the simulation. The whole cloud is also collapsing, although its collapse is not completed yet by the end of the simulation, at $t = 31$ Myr. From Vázquez-Semadeni et al. (2011)

such as the so-called *Maddalena's cloud* (Maddalena and Thaddeus 1985), show similar turbulence characteristics (Williams et al. 1994; Schneider et al. 2011), suggesting that stellar energy injection may not be the main source of turbulence in MCs.

Moreover, simulations of dense cloud formation in the nonmagnetic case have shown that, once a large cold CNM cloud forms out of a collision of WNM streams, it quickly acquires a large enough mass that it can begin to collapse gravitationally in spite of it being turbulent (Vázquez-Semadeni et al. 2007, 2010; Heitsch and Hartmann 2008; Heitsch et al. 2008a). This happens because, as the atomic gas transitions from the warm to the cold phase, its density increases by roughly two orders of magnitude, while the temperature drops by the same factor. Thus, the Jeans mass in the gas, proportional to the product $n^{-1/2}T^{3/2}$, drops by a factor $\sim 10^4$, implying that the cold cloud assembled by the compression can rapidly exceed its Jeans mass.

In turn, the gravitational contraction very effectively enhances the column density of the gas, promoting the formation of molecular hydrogen (H_2) (Hartmann et al. 2001; Bergin et al. 2004; Heitsch and Hartmann 2008), and so it appears that the formation of a *molecular* cloud may involve some previous gravitational contraction (see also McKee 1989). In addition, according to the discussion in

Sects. 14.4.2 and 14.5.4, the CNM clouds formed by converging WNM flows should be born turbulent and clumpy. This turbulent nature of the clouds may further promote the formation of molecular hydrogen (Glover and Mac Low 2007a). The simulations (Vázquez-Semadeni et al. 2007, 2010; Heitsch and Hartmann 2008) show that the nonlinear, turbulent density fluctuations can locally complete their collapse *before* the global collapse of the cloud is completed (Fig. 14.11, *right* panel), both because their densities are large enough that their free-fall time is significantly shorter than that of the whole cloud (Heitsch and Hartmann 2008; Pon et al. 2011), and because clouds in general have flattened or filamentary shapes (e.g., Bally et al. 1989; de Geus et al. 1990; Heiles and Troland 2003; Molinari et al. 2010; André et al. 2010). Interestingly, the free-fall time for these geometries may be much larger than the standard free-fall time, $\tau_{\rm ff} = \sqrt{3\pi/32G\rho}$, which is applicable to a spherically symmetric structure (Toalá et al. 2012; Pon et al. 2012). Thus, an approximately spherical clump of the same volume density within a flattened or elongated structure can collapse much earlier than the non-spherical cloud in which it is immersed.

In addition, the turbulent velocities initially induced in the clouds by the converging flows in the simulations are observed to be relatively small (only moderately supersonic [$M_{\rm s} \sim 3$] with respect to the dense gas). Strongly supersonic ($M_{\rm s} \sim 10$) velocities like those observed in real molecular clouds only develop later in the simulations, due to the ensuing gravitational contraction (Vázquez-Semadeni et al. 2007). This is in agreement with the fact that CNM clouds are observed to typically have moderately supersonic ($M_{\rm s} \sim 3$) velocity dispersions (Heiles and Troland 2003), while GMCs are observed to have much larger turbulent rms Mach numbers, $M_{\rm s} \sim 10$–20 (Wilson et al. 1970). Finally, Banerjee et al. (2009) noted that, in their numerical simulations, the clumps with highest internal velocity dispersions were those that had already formed collapsed objects ("sink" particles), even though energy feedback from the sinks was not included. This again suggested that the largest velocities develop by the action of self-gravity.

Do Observations Rule Out Global Gravitational Contraction in Star-Forming Molecular Clouds?

It is very important to note that the possibility of MCs being in gravitational collapse is not in contradiction with any observed properties of MCs. First, as noted by Ballesteros-Paredes et al. (2011a), the magnitudes of the virial and free-fall velocities for a self-gravitating object are observationally indistinguishable. Thus, the interpretation of cloud energetics in terms of virial equilibrium is completely interchangeable by an interpretation of collapse.

Also, one important argument against the possibility of gravitational collapse of MCs is the argument by Zuckerman and Palmer (1974) that it would lead to exceedingly large SFRs. We discuss the possible resolution of this conundrum in Sect. 14.6.2. Another frequent argument against the global gravitational contraction scenario is that such a regime should produce readily observable signatures, such as

the systematic shift between the CO lines from the clouds and the absorption lines seen towards HII regions proposed by Zuckerman and Evans (1974), as discussed at the beginning of this section. However, it should be noted that the argument by ZE74 against large-scale motions in the clouds would also apply to turbulent motions as we presently understand them, since turbulent flows in general have the largest velocity differences across the largest velocity separations, as discussed above in relation to the left and middle panels of Fig. 14.11. The only kind of turbulence that would not be invalidated by ZE74's argument would be microscopic turbulence, in which the largest turbulent scale should be much smaller than the size of the cloud, but, as already discussed above, this is clearly not the case in molecular clouds, as illustrated by the *left* and *middle* panels of Fig. 14.11.

Moreover, the above arguments against global collapse in clouds are based on the assumptions that the cloud has a roughly spherical symmetry, and that the collapse is monolithic, meaning that there is a single, dominant flow, aimed at a major, localized collapse center. Actually, numerical simulations of cloud formation and evolution show that this is not the case. As mentioned above, the clouds are far from having a spherical symmetry, and instead tend to have flattened or filamentary shapes. In addition, the clouds are born turbulent, and therefore they contain nonlinear density fluctuations, which have shorter free-fall times than the average in the cloud, and thus collapse earlier. Thus, multiple collapse centers arise in the cloud before the global collapse is completed, and, as a consequence, there is no single, evident, dominant collapse center, possibly resolving the concerns of Zuckerman and Evans (1974). Essentially, the cloud fragments gravitationally, with the local collapse centers accreting from filaments that in turn accrete from the bulk of the cloud (Gómez and Vázquez-Semadeni 2014), in agreement with the velocity structure of clumps and their surrounding filaments (Myers 2009; André et al. 2010; Palmeirim et al. 2013; Kirk et al. 2013; Peretto et al. 2014). Towards the end of the evolution, the locally collapsing regions formed earlier tend to merge to form a massive region then acquires large densities and velocities, typical of massive-star forming regions (Vázquez-Semadeni et al. 2009). This flow regime has been termed *hierarchical, chaotic gravitational fragmentation* (Vázquez-Semadeni et al. 2009; Ballesteros-Paredes et al. 2011a).

Note, however, that all of the above arguments in favor of gravitational contraction motions in MCs probably apply mostly to clouds in the early-to-intermediate stages of their evolution; that is, from their formation to their strongly star-forming stages. Nevertheless, after strong stellar feedback has disrupted the clouds, it is likely that shreds may remain in a relatively quiescent stage, perhaps supported by the magnetic field, without forming stars, and perhaps even being on their way to dispersal (Elmegreen 2007; Vázquez-Semadeni et al. 2011).

All of the above evidence suggests that the observed supersonic nonthermal motions in MCs may evolve from being dominated by random turbulence in the early evolutionary stages of the (mostly atomic) clouds, to being infall-dominated at more advanced (mostly molecular) stages, characterized by large densities, velocities, and star formation rates. Note, however, that the turbulent component

may be maintained or even somewhat amplified by the collapse (Vázquez-Semadeni et al. 1998; Robertson and Goldreich 2012).

In this scenario of hierarchical gravitational fragmentation, the main role of the truly turbulent (i.e., fully random) motions is to provide the nonlinear density fluctuation seeds that will collapse locally once the global contraction has caused their density to increase sufficiently for them to become locally gravitationally unstable (Clark and Bonnell 2005). Evidence for such multi-scale collapse has recently begun to be observationally detected (Galván-Madrid et al. 2009; Schneider et al. 2010).

14.5.5.2 The Molecular Gas. Results Including the Magnetic Field

According to the discussion in Sect. 14.4.2.2, the formation of a cold, dense *atomic* cloud can be accomplished by the compression of warm material along magnetic field lines, which nonlinearly triggers a phase transition to the cold phase. However, as discussed in the previous section, the formation of a *molecular* cloud probably requires the gravitational contraction of the atomic cloud previously formed by the compression. Thus, in the presence of the magnetic field, this requires an understanding of the role of magnetic support; that is, of the evolution of the mass-to-flux ratio (MFR).

As is well known, and was reviewed in Sect. 14.3.4.3, there exists a critical value of the MFR below which the magnetic field is able to support the cloud against its own self-gravity. Along the direction of the field lines, the criticality condition in terms of the mass column density $\Sigma = \rho L$ and the field strength B_0 for a cylindrical geometry is (Nakano and Nakamura 1978),

$$(\Sigma/B_0)_{\rm crit} = (4\pi^2 G)^{-1/2} \approx 0.16\, G^{-1/2}, \tag{14.18}$$

where ρ is the mass density and L is the cylinder length. This condition gives the accumulation length, in terms of fiducial values representative of the ISM in the solar neighborhood, as (Hartmann et al. 2001)

$$L_{\rm c} \approx 470 \left(\frac{B_0}{5\lambda {\rm G}}\right) \left(\frac{n}{1\ {\rm cm}^{-3}}\right)^{-1}\ {\rm pc}, \tag{14.19}$$

where we have assumed $\mu_{\rm m} = 1.27$. In principle, if the Galactic field is primarily azimuthal, then the Galactic ISM at large is magnetically supercritical in general, because field lines circle around the entire Galactic disk, and thus sufficiently long distances are always available along them.[6] Thus, *the MFR of a system is not a*

[6]Note, however, that supercriticality does not necessarily imply collapse, since the gas may be thermally or otherwise supported, as is likely the case for the diffuse warm medium at scales of hundreds of parsecs.

uniquely defined, absolute parameter, but rather depends on where the boundaries of the system are drawn. Also, recall that the critical value of the MFR depends on the local geometry of the system being considered. For instance, a system with spherical symmetry has a critical value of $(\Sigma/B_0)_{\rm crit} = (6\pi^2 G)^{-1/2} \approx 0.13\, G^{-1/2}$ (e.g. Shu 1992), somewhat smaller than that given by Eq. (14.18).

Now consider a cloud or clump that is formed by the accumulation of gas along field lines in general.[7] In the rest of this discussion, we will generically refer to the resulting density enhancement as a "cloud", referring to either a cloud, a clump, or a core. Although redistribution of matter along field lines does not in principle affect the *total* MFR along the full "length" of a flux tube, this length is a rather meaningless notion, since the flux tube may extend out to arbitrarily long distances. What is more meaningful is the MFR *of the dense gas that makes up the cloud*, since the cloud is denser than its surroundings, and thus it is the main source of the self-gravity that the field has to oppose. In fact, for the formation of a cloud out of flow collisions in the WNM, the density of the cloud is $\sim$ 100 times larger than that of the WNM (Field et al. 1969; Wolfire et al. 1995), and so the self-gravity of the latter is negligible. Thus, in this problem, natural boundaries for the cloud are provided by the locus of the phase transition front between the dense and the diffuse gas, allowing a clear working definition of the MFR.

However, contrary to the very common assumption of a constant cloud mass, the formation of clouds by converging gas streams implies that the mass of the cloud is a (generally increasing) function of time (cf. Sect. 14.3.3.2), a conclusion that has recently been reached observationally as well (Fukui et al. 2009). This means that, *within the volume of the cloud, the MFR is also an increasing quantity*, since the flux remains constant if the flow is along field lines, while the mass increases (see also Shu et al. 2007). If the cloud starts from essentially zero mass, this in turn implies that the MFR of a cloud is expected to start out strongly subcritical (when the cloud is only beginning to appear), and to evolve towards larger values at later times. Rewriting Eq. (14.19) for the column density, we see that the cloud becomes supercritical when (Vázquez-Semadeni et al. 2011)

$$N_{\rm cr} \approx 1.5 \times 10^{21} \left(\frac{B_0}{5\mu {\rm G}}\right)\ {\rm cm}^{-2}, \tag{14.20}$$

where $N \equiv \Sigma/\mu_{\rm m} m_H$ is the *number* column density, and is to be measured along the field lines. The critical column density for magnetic criticality given by Eq. (14.20) turns out to be very similar, at least for solar neighbourhood conditions, to the critical column density of hydrogen atoms necessary for cold atomic gas to become molecular, $N_{\rm H} \sim 1$–2×10^{21} cm^{-2} (e.g., Franco and Cox 1986; van

[7] Since compressions perpendicular to the magnetic field cannot induce collapse of an initially subcritical region, as they do not change the MFR, and compressions oblique to the field can produce collapse by reorienting the directions of the flow and the field lines (Hennebelle and Pérault 2000), our assumed configuration involves no loss of generality.

Dishoeck and Black 1988; van Dishoeck and Blake 1998; Hartmann et al. 2001; Glover and Mac Low 2007a,b; Glover et al. 2010).

Moreover, the critical column density given by Eq. (14.20) is also very similar to that required for rendering cold gas gravitationally unstable, which is estimated to be

$$N_{\rm grav} \approx 0.7 \times 10^{21} \left(\frac{P/k}{3000\ K\ {\rm cm}^{-3}} \right)^{1/2}\ {\rm cm}^{-2} \tag{14.21}$$

(Franco and Cox 1986; Hartmann et al. 2001). Thus, *the evolution of a cloud is such that it starts out as an atomic, unbound, and subcritical diffuse cloud (Vázquez-Semadeni et al. 2006) and, as it continues to accrete mass from the warm atomic medium, it later becomes molecular, supercritical, and collapsing, at roughly the same time* (Hartmann et al. 2001). This is fully consistent with the observation that diffuse atomic clouds are in general strongly subcritical (Heiles and Troland 2005) and not strongly self-gravitating, while GMCs are approximately critical or moderately supercritical (Crutcher 1999; Bourke et al. 2001; Troland and Crutcher 2008), and are generally gravitationally bound (e.g., Blitz 1993).

It is important to note that this is in stark contrast to the SMSF (see, e.g., the reviews by Shu et al. 1987; Mouschovias 1991), where it was considered that the magnetic criticality of a cloud was the main parameter determining whether it would form only low-mass stars and at a slow pace (in the case of subcritical clouds), or form clusters, including high-mass stars, and at a fast pace (supercritical clouds). This constituted a bimodal scenario of SF, and sub- and supercritical clouds constituted two separate classes.

Instead, in the evolutionary scenario for MCs described above, clouds are expected to *evolve* from being simultaneously atomic, subcritical and not strongly self-gravitating to being molecular, supercritical and strongly self-gravitating. Next, the roughly simultaneous transition to self-gravitating and supercritical suggests that, in general, GMCs should be in a state of gravitational contraction, at least initially, even in the presence of typical magnetic field strengths in the Galactic disk. Of course, significant scatter in the MFR is expected, both intrinsically (see Sect. 14.3.4.1) and as a consequence of observational uncertainties (e.g., Crutcher 1999), and thus a certain fraction of the GMCs may remain subcritical up to significantly evolved stages, or even throughout their entire evolution. This case is discussed further below.

The formation and evolution of molecular clouds in the magnetic case has been investigated recently using numerical simulations of GMC formation by compressions in the WNM aligned with the magnetic field (Hennebelle etal. 2008; Banerjee et al. 2009; Vázquez-Semadeni et al. 2011). The latter authors in particular included self-gravity and AD, and considered three cases: one supercritical, with $\lambda = 1.3$, and two subcritical, with $\lambda = 0.9$ and 0,7, corresponding to mean field strengths of 2, 3, and 4 μG, respectively. The initial magnetic field was considered uniform. In all cases, the mean density was 1 cm^{-3} and the temperature

$T = 5{,}000\,\mathrm{K}$. The compressions consisted of two oppositely-directed streams of gas at the mean density, and of length 112 pc, immersed in a 256-pc box.

The evolution of the subcritical cases is worth discussing in detail, as it differs somewhat from simple expectations. These simulations produced a dense cloud that quickly began to contract gravitationally, similarly to non-magnetic simulations. This occurred because a uniform magnetic field does not provide any support, since the latter requires the existence of a magnetic gradient. Support builds up gradually as the field lines are bent. The clouds thus contracted for a few tens of Myr, until the magnetic tension was large enough to halt the collapse, at which point they re-expanded, and entered an oscillatory regime, around the equilibrium configuration. However, due to the existence of diffusion (both numerical and from AD), local collapse events managed to occur, in agreement with the notions from the SMSF (see also McKee 1989). The notable difference with that model, though, occurred in the fact that the clouds only formed stars during the global contraction phase, especially at maximum compression, and essentially shut off in the re-expanding phase. This is in contrast to the SMSF, in which the GMCs at large were assumed to be in equilibrium and forming stars continuously, albeit slowly.

The above discussion suggests that the possibility of *star-forming* molecular clouds being in a state of gravitational contraction may hold even if they have subcritical MFRs. The subsequent re-expansion of these clouds (or their remnants) may lead to a star-formation-inactive and quiescent phase, perhaps on their way to dispersal, if the clouds are exiting the spiral arms by that time, as proposed by Elmegreen (2007).

14.6 Star Formation in the Turbulent ISM

14.6.1 Does Molecular Cloud "Turbulence" Provide Support for Molecular Clouds?

In the previous sections we have discussed how large-scale compressions in the general ISM produce density fluctuations, in particular by nonlinearly inducing phase transitions from the cold to the warm medium. Because the largest dimensions of the clouds thus formed are as large as the transverse dimension of the compression that formed them, and because of the large drop in the local Jeans mass upon the phase transition (cf. Sect. 14.5.5.1), they can soon find themselves being strongly gravitationally unstable and proceed to collapse. It is important to note that the large-scale compression forming the clouds may (and in fact, is likely to) have an origin different from the general turbulence in the ISM, such as, for example, large-scale instabilities like the magneto-Jeans one (e.g. Kim and Ostriker 2001), or simply the passage of the stellar spiral-arm potential well.

In fact, it is worth noting that just the turbulence driven by supernovae does not seem to be able to sustain itself, since the mass driven into a Jeans-unstable

regime per unit time by the turbulence is not enough to maintain the same supernova rate that drives the turbulence (Joung and Mac Low 2006). This conclusion is also supported by the fact that successive generations of triggered SF do not appear to be able to form stars as massive as in the previous generation (Deharveng and Zavagno 2011). Thus, it appears safe to conclude that the main driver of star formation is gravity at the largest scales.

During the last decade, the main role of interstellar turbulence has been thought to be the *regulation* of SF, mainly on the basis of the assumption that the turbulent velocity dispersion contributes to the support of molecular clouds against their self-gravity, analogously to the role of the thermal velocity dispersion, and perhaps including a scale-dependent amplitude (Chandrasekhar 1951; Bonazzola et al. 1987; Bertoldi and McKee 1992; Vazquez-Semadeni and Gazol 1995; Mac Low and Klessen 2004; Krumholz and McKee 2005; Hennebelle and Chabrier 2008, 2011; Padoan and Nordlund 2011). Thus, turbulence has been thought to provide support to clouds as a whole, while simultaneously inducing small-scale density fluctuations (clumps) within the clouds that may undergo gravitational collapse if they are compressed enough for their Jeans mass to become smaller than their actual mass (Vázquez-Semadeni et al. 2003b; Ballesteros-Paredes et al. 2007). In this manner, global collapse of the clouds could be prevented, avoiding the Zuckerman and Palmer (1974) conundrum that the global collapse of molecular clouds would cause an excessively large SFR (see Sect. 14.5.5.1), while at the same time allowing for the collapse of a small fraction of the mass, brought to instability by the local supersonic turbulent compressions. However, this last notion was challenged by Clark and Bonnell (2005), who argued that the turbulence only provides the seed density fluctuations for subsequent gravitational fragmentation, without significant local reductions in the Jeans mass induced by the turbulence.

Moreover, Heitsch and Hartmann (2008) showed that the fraction of mass with short free-fall times ($\lesssim 1$ Myr) in the clouds increases monotonically over time in the presence of self-gravity, indicating a secular evolution towards higher densities, while simulations with no self-gravity exhibited a stationary fraction of mass with short free-fall times, as would be the case in clouds supported against collapse by the turbulence (Fig. 14.12).

Finally, the simulations have also shown that the fraction of molecular gas also increases in time, so that the cloud would indeed be classified as atomic in its early phases, and as molecular in later ones (Heitsch and Hartmann 2008; Clark et al. 2012). In particular, the latter authors have shown that the formation of CO-dominated regions only occurs ~ 2 Myr before SF starts, although significant amounts of H_2 can appear earlier.

All of the above evidence suggests that the strongly supersonic motions observed in MCs may be a *manifestation* of the gravitational contraction occurring in the clouds, rather than truly turbulent (i.e., random) motions, of a separate origin, that can counteract the gravitational contraction of the clouds. It is worth noting here that Klessen and Hennebelle (2010) have recently shown that, in general, the accretion power at scales from entire Galactic disks to protostellar disks, passing through the GMC scale, is more than enough to drive the turbulence observed in these systems.

However, it should be noted that, in the case of GMCs, this suggestion differs qualitatively from the nature of the motions discussed above. Rather than accretion *driving* turbulent motions in the clouds which can then support them, the discussion above suggests that the observed motions in the clouds *are* the infall itself, with only a small, subdominant, truly random turbulent component superposed on them. In this case, these motions cannot provide support against the self-gravity of the clouds.

14.6.2 Regulation of Star Formation Via Stellar Feedback

All of the above evidence strongly suggests that interstellar clouds undergo a secular evolution, starting their existence as moderately supersonic, magnetically subcritical, sheet-like atomic clouds, and evolving towards becoming supercritical, molecular, gravitationally contracting objects. However, in this case, the Zuckerman and Palmer (1974) SF conundrum (cf. Sect. 14.5.5.1) must be addressed. That is, if MCs are essentially in free-fall, how to prevent the SFR from being two orders of magnitude larger than it is observed to be in the Galaxy?

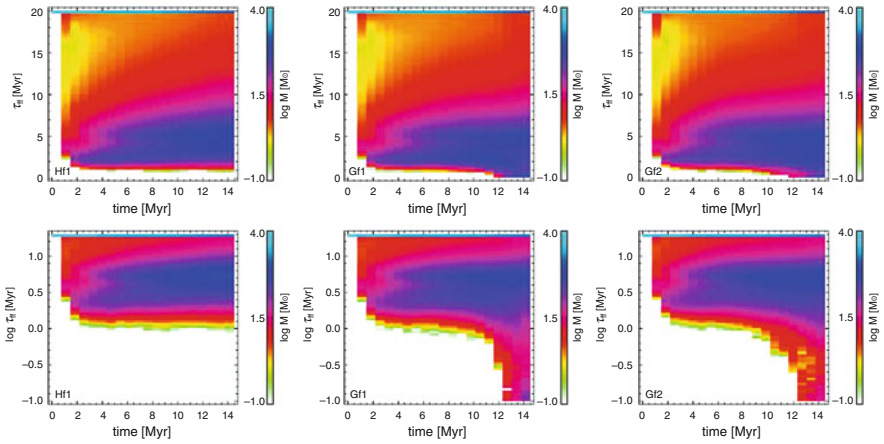

Fig. 14.12 Time evolution of the mass (indicated by the color scale) at a given free-fall time (vertical axis) in numerical simulations of cloud formation and evolution by Heitsch and Hartmann (2008). The *top* row shows the free-fall time in a linear scale, while the *bottom* row shows it in logarithmic scale. The panels on the *left* show a simulation with no self-gravity, while the *middle* and *right* panels show two different simulations with self-gravity. In the case with no self-gravity, the fraction of mass at a given free-fall time is seen to remain nearly constant, and the minimum free-fall time to remain at $\sim$ 1 Myr, while in the cases with self-gravity, the minimum free-fall time decreases secularly. Note that, in these plots, $\tau_{\rm ff}$ is simply a proxy for the density, since $\tau_{\rm ff} \propto \rho^{-1/2}$, and so it can be evaluated even if gravity is not included in the simulations

Early studies proposed that ionizing radiation from massive stars should be able to disperse a cloud as early as when only $\sim$ 10 % of the cloud's mass has been converted to stars (see, e.g., Sect. 4 of Field 1970), so that the remaining 90 % would be prevented from forming any more stars. This suggestion, however, was challenged by Mouschovias (1976), who argued that those estimates were based on the assumption of unrealistically low mean densities for the clouds ($\sim$ 10 cm^{-3}), and that using more realistic values ($\sim$ 10^5 cm^{-3}) would result in a grossly insufficient amount of ionization in the cloud, thus invalidating the mechanism as a suitable one for dispersing the clouds. As an alternative, Mouschovias (1976) proposed the basic notions for the SMSF: that the MCs should be magnetically subcritical in general, so that their envelopes would remain supported by the magnetic tension, while only the central core would be able to proceed to collapse through AD (cf. Sects. 14.3.1 and 14.3.4.1). However, observational evidence from the last decade has suggested that most MCs are likely to be at least moderately magnetically supercritical (e.g., Bourke et al. 2001; Troland and Crutcher 2008; Crutcher et al. 2010), a conclusion also reached by theoretical arguments (see Sect. 14.5.5.2 and references therein).

Another alternative was the proposal that MCs could be supported by turbulence, either hydrodynamical or MHD. However, since turbulence needs to be continuously driven, two variants have been considered for the driving: either it might be due to feedback from stellar sources internal to the clouds (cf. Sect. 14.5.5.1), or else to external driving sources such as supernova shocks. However, as discussed in Sects. 14.4.2.1 and 14.5.5.2, the role of external turbulence seems more likely to be the driving of MC *formation*, rather than the driving of the strongly supersonic internal turbulence of the GMCs, because the turbulence induced in the forming clouds is only moderately supersonic, rather than strongly so (cf. Sect. 14.6.1).

The possibility of driving the turbulence by stellar feedback from inside the clouds has been extensively studied, both analytically and numerically (e.g., Norman and Silk 1980; McKee 1989; Li and Nakamura 2006; Nakamura and Li 2007; Carroll et al. 2009, 2010; Wang et al. 2010). In most such studies, it has been concluded that this feedback can maintain the clumps within GMCs in near virial equilibrium. Studies of the SFR and the SFE under these conditions have often idealized the turbulence as being simply randomly driven, and have shown that in this case the SFE can be maintained at levels of a few percent, comparable to the observed ones (e.g., Klessen et al. 2000; Vázquez-Semadeni et al. 2003a, 2005b).

However, as discussed in the review by Vázquez-Semadeni (2010), numerical simulations of the momentum feedback from protostellar outflows have only considered numerical boxes at the parsec (clump) scale, neglecting the infall from the environment of the clump, which has been observed in GMC formation simulations. This adds a large amount of infall onto the system not included in those simulations. Thus, it seems that outflows cannot provide sufficient feedback to prevent the collapse of entire GMCs.

The role of massive-star ionization feedback in the support of GMCs has been investigated semi-analytically by Krumholz et al. (2006) and Goldbaum et al. (2011) considering the time-dependent virial theorem in the presence of feedback, and of

feedback and infall, respectively, concluding that the clouds may oscillate around the virial equilibrium state for several Myr, until they are finally dispersed. However, full numerical simulations of this problem (Vázquez-Semadeni et al. 2010) suggest that the infall is not suppressed, and instead that the regulation of the SFR occurs because most of the infalling material is evaporated before it can form further stars, except in the case of the most massive ($\sim 10^6 M_\odot$) GMCs (Dale et al. 2012), where supernova feedback and/or radiation pressure may also be required to accomplish the dispersal of the clouds.

Thus, it appears that the resolution of the Zuckerman and Palmer (1974) conundrum lies not in the prevention of the global contraction of star-forming GMCs, but rather on the effect of the feedback, and that this effect is, after all, essentially as initially suggested by Field (1970). The resolution of the objection by Mouschovias (1976), in turn, appears to lie in that the fraction of mass that is at very high densities ($> 10^5$ cm^{-3}) is very small (see, e.g., Blitz 1993; Sects. VII and IX) and inhomogeneously distributed, so that eventually HII regions may break out from the densest regions and ionize the rest of the MC (see, e.g., Peters et al. 2010).

Summary and Conclusions

In this contribution, we have briefly reviewed the role and interaction between the main physical processes present in the ISM: radiative heating and cooling, magnetic fields, self-gravity, and turbulence, and their implications for the SF process. The presence of radiative heating and cooling implies in general that the gas behaves in a non-isentropic (i.e., non-adiabatic) way, and in particular it may become *thermally unstable* in certain regimes of density and temperature, where low-amplitude (i.e., *linear*) perturbations can cause runaway heating or cooling of the gas that only stops when the gas exits that particular regime. This in turn causes the gas to avoid those unstable density and temperature ranges, and to settle in the stable ones, thus tending to segregate the gas into different phases of different densities and/or temperatures. In classical models of the ISM, only the stable phases were expected to exist in significant amounts.

We then discussed some compressible MHD turbulence basics, and the production, nature and evolution of turbulent density fluctuations in polytropic (i.e., of the form $P \propto \rho^{\gamma_e}$) flows, discussing in particular the probability density function (PDF) of the density fluctuations, which takes a lognormal form in isothermal regimes, and develops power-law tails in polytropic ones. We also discussed the correlation (and, at low densities, lack thereof) between the magnetic field and the density as a consequence of the superposition of the different MHD wave modes, and the evolution of the mass-to-magnetic flux ratio (MFR) as density enhancements are assembled by turbulent fluctuations.

(continued)

We next discussed turbulence in the multi-phase ISM, noting that, since turbulence is an inherently mixing phenomenon, it opposes the segregating effect of thermal instability, causing the production of gas parcels in the classically forbidden unstable regimes, which may add up to nearly half the mass of the ISM, although the density PDF in general still exhibits some multimodality due to the preference of the gas to settle in the stable regimes. The existence of gas in the unstable ranges has been established by various observational studies.

Next, we discussed the nature of the turbulence in the different ranges of density and temperature of the gas, noting that in the diffuse ionized regions, where the flow is transonic (i.e., with Mach numbers $M_s \sim 1$), the gas appears to behave in an essentially incompressible way, exhibiting Kolmogorov scalings over many orders of magnitude in length scale. However, in the neutral atomic component, where the gas is thermally bistable, the flow is expected to exhibit large density and temperature fluctuations, by up to factors ~ 100, thus being highly fragmented. We also pointed out that large-scale compressions in the warm neutral gas, which may be triggered by either random turbulent motions, or by yet larger-scale instabilities, may nonlinearly induce the formation of large regions of dense, cold gas; much larger, in particular, than the most unstable scales of TI, which have sizes ~ 0.1 pc, thus forming large cold atomic clouds that may be the precursors of giant molecular clouds (GMCs). This is because these clouds are expected to become molecular, gravitationally unstable, and magnetically supercritical at approximately the same time, so that when they reach a mostly molecular stage, they are likely to be undergoing generalized gravitational contraction.

The clouds are born internally turbulent and clumpy, and the resulting nonlinear density fluctuations ("clumps") eventually become locally gravitationally unstable during the contraction of the whole large-scale cloud. Because they are denser, they have shorter free-fall times, and can complete their local collapses before the global one does, thus producing a regime of *hierarchical gravitational fragmentation*, with small-scale, short-timescale collapses occurring within larger-scale, longer-timescale ones. It is thus quite likely that the flow regime in the dense molecular clouds corresponds to a dominant multi-scale gravitational contraction, with smaller-amplitude random (turbulent) motions superposed on it.

The local collapses cause star formation (SF) that begins before the global collapse is concluded, and the ionizing feedback from the massive stars that form during this stage appears to be sufficient to erode and disperse the clouds before the entire mass of the clouds is converted to stars, thus avoiding the objection by Zuckerman and Palmer (1974) to free-falling GMCs, that they would form stars at a rate much larger than the observed Galactic rate. They do so, but only for short periods of time, before most of their mass gets dispersed.

(continued)

We conclude that turbulence in the magnetized, multi-phase, self-gravitating ISM is an extremely rich and complex phenomenon, but whose (thermo)dynamics is beginning to be understood, together with its relation to the star formation process.

Acknowledgements This work has been funded in part by CONACYT grant 102488.

References

André, P., Men'shchikov, A., Bontemps, S., et al.: Astron. Astrophys. **518**, L102 (2010)
Armstrong, J.W., Rickett, B.J., Spangler, S.R.: Astrophys. J. **443**, 209 (1995)
Audit, E., Hennebelle, P.: Astron. Astrophys. **433**, 1 (2005)
Audit, E., Hennebelle, P.: Astron. Astrophys. **511**, A76 (2010)
Balbus, S.A., Hawley, J.F.: Astrophys. J. **376**, 214 (1991)
Ballesteros-Paredes, J., Hartmann, L., Vázquez-Semadeni, E.: Astrophys. J. **527**, 285 (1999)
Ballesteros-Paredes, J., Klessen, R.S., Mac Low, M.-M., Vazquez-Semadeni, E.: Protostars Planets **V**, 63 (2007)
Ballesteros-Paredes, J., Hartmann, L.W., Vázquez-Semadeni, E., Heitsch, F., Zamora-Avilés, M.A.: Mon. Not. R. Astron. Soc. **411**, 65 (2011)
Bally, J., Stark, A.A., Wilson, R.W., Langer, W.D. In: The Physics and Chemistry of Interstellar Molecular Clouds - mm and Sub-mm Observations in Astrophysics, vol. 331, p. 81 (1989)
Banerjee, R., Vázquez-Semadeni, E., Hennebelle, P., Klessen, R.S.: Mon. Not. R. Astron. Soc. **398**, 1082 (2009)
Bayly, B.J., Levermore, C.D., Passot, T.: Phys. Fluids **4**, 945 (1992)
Beresnyak, A., Lazarian, A., Cho, J.: Astrophys. J. Lett. **624**, L93 (2005)
Bergin, E.A., Hartmann, L.W., Raymond, J.C., Ballesteros-Paredes, J.: Astrophys. J. **612**, 921 (2004)
Bertoldi, F., McKee, C.F.: Astrophys. J. **395**, 140 (1992)
Blaisdell, G.A., Mansour, N.N., Reynolds, W.C.: J. Fluid Mech. **256**, 443 (1993)
Blitz, L.: Protostars Planets **III**, 125 (1993)
Bonazzola, S., Heyvaerts, J., Falgarone, E., Perault, M., Puget, J.L.: Astron. Astrophys. **172**, 293 (1987)
Bonnor, W.B.: Mon. Not. R. Astron. Soc. **116**, 351 (1956)
Bourke, T.L., Myers, P.C., Robinson, G., Hyland, A.R.: Astrophys. J. **554**, 916 (2001)
Brunt, C.M., Heyer, M.H., Mac Low, M.: Astron. Astrophys. **504**, 883 (2009)
Burgers, J.M.: The Nonlinear Diffusion Equation. Reidel, Dordrecht (1974)
Carroll, J.J., Frank, A., Blackman, E.G., Cunningham, A.J., Quillen, A.C.: Astrophys. J. **695**, 1376 (2009)
Carroll, J.J., Frank, A., Blackman, E.G.: Astrophys. J. **722**, 145 (2010)
Chandrasekhar, S.: R. Soc. Lon. Proc. Ser. A **210**, 26 (1951)
Chepurnov, A., Lazarian, A.: Astrophys. J. **710**, 853 (2010)
Chomiuk, L., Povich, M.S.: Astrophys. J. **142**, 197 (2011)
Clark, P.C., Bonnell, I.A.: Mon. Not. R. Astron. Soc. **361**, 2 (2005)
Clark, P.C., Glover, S.C.O., Klessen, R.S., Bonnell, I.A.: Mon. Not. R. Astron. Soc. **424**, 2599 (2012)
Crutcher, R.M.: Astrophys. J. **520**, 706 (1999)
Crutcher, R.M., Hakobian, N., Troland, T.H.: Astrophys. J. **692**, 844 (2009)

Crutcher, R.M., Wandelt, B., Heiles, C., Falgarone, E., Troland, T.H.: Astrophys. J. **725**, 466 (2010)
Dale, J.E., Ercolano, B., Bonnell, I.A.: Mon. Not. R. Astron. Soc. **424**, 377 (2012)
Dalgarno, A., McCray, R.A.: Ann. Rev. Astron. Astrophys. **10**, 375 (1972)
de Avillez, M.A., Breitschwerdt, D.: Astron. Astrophys. **436**, 585 (2005)
de Geus, E.J., Bronfman, L., Thaddeus, P.: Astron. Astrophys. **231**, 137 (1990)
Deharveng, L., Zavagno, A. In: Alves, J., et al. (eds.) Computational Star Formation, IAU Symposium, vol. 270, p. 239 (2011)
Dickey, J.M., Terzian, Y., Salpeter, E.E.: Astrophys. J. Suppl. **36**, 77 (1978)
Ebert, R.: Zeitschrift für Astrophysik **36**, 222 (1955)
Elmegreen, B.G. In: NATO ASIC Proceeding 342: The Physics of Star Formation and Early Stellar Evolution, vol. 35 (1991)
Elmegreen, B.G.: Astrophys. J. Lett. **419**, L29 (1993)
Elmegreen, B.G.: Astrophys. J. **668**, 1064 (2007)
Elmegreen, B.G., Scalo, J.: Ann. Rev. Astron. Astrophys. **42**, 211 (2004)
Federrath, C., Klessen, R.S., Schmidt, W.: Astrophys. J. Lett. **688**, L79 (2008)
Ferrière, K.M.: Reviews. Mod. Phys. **73**, 1031 (2001)
Field, G.B.: Astrophys. J. **142**, 531 (1965)
Field, G.B.: Memoires of the Societe Royale des Sciences de Liege **19**, 29 (1970)
Field, G.B., Goldsmith, D.W., Habing, H.J.: Astrophys. J. Lett. **155**, L149 (1969)
Franco, J., Cox, D.P.: Publ. Astron. Soc. Pac. **98**, 1076 (1986)
Fukui, Y., et al.: Astrophys. J. **705**, 144 (2009)
Galván-Madrid, R., Keto, E., Zhang, Q., et al.: Astrophys. J. **706**, 1036 (2009)
Gazol, A., Vázquez-Semadeni, E., Sánchez-Salcedo, F.J., Scalo, J.: Astrophys. J. Lett. **557**, L121 (2001)
Gazol, A., Vázquez-Semadeni, E., Kim, J.: Astrophys. J. **630**, 911 (2005)
Gazol, A., Luis, L., Kim, J.: Astrophys. J. **693**, 656 (2009)
Glover, S.C.O., Mac Low, M.-M.: Astrophys. J. **659**, 1317 (2007a)
Glover, S.C.O., Mac Low, M.-M.: Astrophys. J. Suppl. **169**, 239 (2007)
Glover, S.C.O., Federrath, C., Mac Low, M.-M., Klessen, R.S.: Mon. Not. R. Astron. Soc. **404**, 2 (2010)
Goldbaum, N.J., Krumholz, M.R., Matzner, C.D., McKee, C.F.: Astrophys. J. **738**, 101 (2011)
Goldreich, P., Kwan, J.: Astrophys. J. **189**, 441 (1974)
Goldreich, P., Sridhar, S.: Astrophys. J. **438**, 763 (1995)
Gómez, G.C., Vázquez-Semadeni, E., Shadmehri, M., Ballesteros-Paredes, J.: Astrophys. J. **669**, 1042 (2007)
Gómez, G.C., Vázquez-Semadeni, E.: Astrophys. J. **791**, 124 (2014)
Hartmann, L., Ballesteros-Paredes, J., Bergin, E.A.: Astrophys. J. **562**, 852 (2001)
Heiles, C.: Astrophys. J. Lett. **551**, L105 (2001)
Heiles, C., Troland, T.H.: Astrophys. J. **586**, 1067 (2003)
Heiles, C., Troland, T.H.: Astrophys. J. **624**, 773 (2005)
Heitsch, F., Hartmann, L.: Astrophys. J. **689**, 290 (2008)
Heitsch, F., Burkert, A., Hartmann, L.W., Slyz, A.D., Devriendt, J.E.G.: Astrophys. J. Lett. **633**, L113 (2005)
Heitsch, F., Slyz, A.D., Devriendt, J.E.G., Hartmann, L.W., Burkert, A.: Astrophys. J. **648**, 1052 (2006)
Heitsch, F., Hartmann, L.W., Slyz, A.D., Devriendt, J.E.G., Burkert, A.: Astrophys. J. **674**, 316 (2008)
Hennebelle, P., Audit, E.: Astron. Astrophys. **465**, 431 (2007)
Hennebelle, P., Chabrier, G.: Astrophys. J. **684**, 395 (2008)
Hennebelle, P., Chabrier, G.: Astrophys. J. Lett. **743**, L29 (2011)
Hennebelle, P., Pérault, M.: Astron. Astrophys. **351**, 309 (1999)
Hennebelle, P., Pérault, M.: Astron. Astrophys. **359**, 1124 (2000)
Hennebelle, P., Banerjee, R., Vázquez-Semadeni, E., Klessen, R.S., Audit, E.: Astron. Astrophys. **486**, L43 (2008)

Heyer, M.H., Brunt, C.M.: Astrophys. J. Lett. **615**, L45 (2004)
Hill, A.S., Benjamin, R.A., Kowal, G., et al.: Astrophys. J. **686**, 363 (2008)
Houlahan, P., Scalo, J.: Astrophys. J. **393**, 172 (1992)
Inoue, T., Inutsuka, S.-I.: Astrophys. J. **687**, 303 (2008)
Inoue, T., Inutsuka, S.-I., Koyama, H.: Astrophys. J. **652**, 1331 (2006)
Joung, M.K.R., Mac Low, M.-M.: Astrophys. J. **653**, 1266 (2006)
Kim, W.-T., Ostriker, E.C.: Astrophys. J. **559**, 70 (2001)
Kirk, H., Myers, P.C., Bourke, T.L., Gutermuth, R.A., Hedden, A., Wilson, G.: Astrophys. J. **766**, 115 (2013)
Klessen, R.S., Hennebelle, P.: Astron. Astrophys. **520**, A17 (2010)
Klessen, R.S., Heitsch, F., Mac Low, M.-M.: Astrophys. J. **535**, 887 (2000)
Kolmogorov, A.: Akademiia Nauk SSSR Doklady **30**, 301 (1941)
Koyama, H., Inutsuka, S.-I.: Astrophys. J. **532**, 980 (2000)
Koyama, H., Inutsuka, S.-I.: Astrophys. J. Lett. **564**, L97 (2002)
Kritsuk, A.G., Norman, M.L.: Astrophys. J. Lett. **569**, L127 (2002)
Krumholz, M.R., McKee, C.F.: Astrophys. J. **630**, 250 (2005)
Krumholz, M.R., Matzner, C.D., McKee, C.F.: Astrophys. J. **653**, 361 (2006)
Kulkarni, S.R., Heiles, C.: Interstellar Process. **134**, 87 (1987)
Kwan, J.: Astrophys. J. **229**, 567 (1979)
Landau, L.D., Lifshitz, E.M.: Course of Theoretical Physics. Fluid Mechanics. Pergamon Press, Oxford (1959)
Larson, R.B.: Mon. Not. R. Astron. Soc. **194**, 809 (1981)
Li, Z.-Y., Nakamura, F.: Astrophys. J. Lett. **640**, L187 (2006)
Lunttila, T., Padoan, P., Juvela, M., Nordlund, Å.: Astrophys. J. Lett. **702**, L37 (2009)
Mac Low, M.-M., Klessen, R.S.: Rev. Mod. Phys. **76**, 125 (2004)
Mac Low, M.-M., Klessen, R.S., Burkert, A., Smith, M.D.: Phys. Rev. Lett. **80**, 2754 (1998)
Mac Low, M.-M., Balsara, D.S., Kim, J., de Avillez, M.A.: Astrophys. J. **626**, 864 (2005)
Maddalena, R.J., Thaddeus, P.: Astrophys. J. **294**, 231 (1985)
Mann, G.: J. Plasma Phys. **53**, 109 (1995)
McKee, C.F.: Astrophys. J. **345**, 782 (1989)
McKee, C.F., Ostriker, J.P.: Astrophys. J. **218**, 148 (1977)
McKee, C.F., Zweibel, E. G.: Astrophys. J. **440**, 686 (1995)
Meerson, B.: Rev. Mod. Phys. **68**, 215 (1996)
Mestel, L.: Mon. Not. R. Astron. Soc. **133**, 265 (1966)
Mestel, L., Spitzer, L., Jr.: Mon. Not. R. Astron. Soc. **116**, 503 (1956)
Modell, M., Reid, R.C.: Thermodynamics and its Applications. Prentice-Hall, Englewood Cliffs (1974)
Molinari, S., Swinyard, B., Bally, J., et al.: Astron. Astrophys. **518**, L100 (2010)
Mouschovias, T.C.: Astrophys. J. **207**, 141 (1976)
Mouschovias, T.C. In: NATO ASIC Proceedings 342: The Physics of Star Formation and Early Stellar Evolution, p. 449 (1991)
Myers, P.C.: Astrophys. J. **225**, 380 (1978)
Myers, P.C.: Astrophys. J. **700**, 1609 (2009)
Nagashima, M., Koyama, H., Inutsuka, S.-I.: Mon. Not. R. Astron. Soc. **361**, L25 (2005)
Nakamura, F., Li, Z.-Y.: Astrophys. J. **662**, 395 (2007)
Nakano, T., Nakamura, T.: Publ. Astron. Soc. Jpn. **30**, 671 (1978)
Nordlund, Å, Padoan, P.: Interstellar Turbulence, **218** (1999)
Norman, C., Silk, J.: Astrophys. J. **238**, 158 (1980)
Ostriker, E.C., Gammie, C.F., Stone, J.M.: Astrophys. J. **513**, 259 (1999)
Ostriker, E.C., Stone, J.M., Gammie, C.F.: Astrophys. J. **546**, 980 (2001)
Padoan, P., Nordlund, Å.: Astrophys. J. **526**, 279 (1999)
Padoan, P., Nordlund, Å.: Astrophys. J. **730**, 40 (2011)
Padoan, P., Nordlund, A., Jones, B.J.T.: Mon. Not. R. Astron. Soc. **288**, 145 (1997)
Palmeirim, P., André, P., Kirk, J., et al.: Astron. Astrophys. **550**, A38 (2013)

Passot, T., Vázquez-Semadeni, E.: Phys. Rev. E **58**, 4501 (1998)
Passot, T., Vázquez-Semadeni, E.: Astron. Astrophys. **398**, 845(PV03) (2003)
Passot, T., Vazquez-Semadeni, E., Pouquet, A.: Astrophys. J. **455**, 536 (1995)
Penston, M.V., Brown, F.E.: Mon. Not. R. Astron. Soc. **150**, 373 (1970)
Peretto, N., Fuller, G. A., André, Ph., Arzoumanian, D., Rivilla, V. M., Bardeau, S., Duarte Puertas, S., Guzmán Fernaandez, J. P., Lenfestey, C., Li, G.-X., Olguin, F. A., Rö ck, B. R., de Villiers, H., Williams, J.: A&A, **561A**, 83 (2014)
Peters, T., Banerjee, R., Klessen, R.S., et al.: Astrophys. J. **711**, 1017 (2010)
Pineda, J.E., Rosolowsky, E.W., Goodman, A.A.: Astrophys. J. Lett. **699**, L134 (2009)
Piontek, R.A., Ostriker, E.C.: Astrophys. J. **601**, 905 (2004)
Piontek, R.A., Ostriker, E.C.: Astrophys. J. **629**, 849 (2005)
Pon, A., Johnstone, D., Heitsch, F.: Astrophys. J. **740**, 88 (2011)
Pon, A., Toalá, J.A., Johnstone, D., et al.: Astrophys. J. (2012, in press). arXiv:1207.3078
Robertson, B., Goldreich, P.: Astrophys. J. Lett. **750**, L31 (2012)
Rosolowsky, E.W., Pineda, J.E., Kauffmann, J., Goodman, A.A.: Astrophys. J. **679**, 1338 (2008)
Sánchez-Salcedo, F.J., Vázquez-Semadeni, E., Gazol, A.: Astrophys. J. **577**, 768 (2002)
Sasao, T.: Publ. Astron. Soc. J. **25**, 1 (1973)
Schneider, N., Csengeri, T., Bontemps, S., et al.: Astron. Astrophys. **520**, A49 (2010)
Schneider, N., Bontemps, S., Simon, R., et al.: Astron. Astrophys. **529**, A1 (2011)
Shu, F.H.: Astrophys. J. **214**, 488 (1977)
Shu, F.H.: Physics of Astrophysics, vol. II, by Frank H. Shu. University Science Books, Mill Valley (1992)
Shu, F.H., Adams, F.C., Lizano, S.: Ann. Rev. Astron. Astrophys. **25**, 23 (1987)
Shu, F.H., Allen, R.J., Lizano, S., Galli, D.: Astrophys. J. Lett. **662**, L75 (2007)
Stone, J.M., Ostriker, E.C., Gammie, C.F.: Astrophys. J. Lett. **508**, L99 (1998)
Toalá, J.A., Vázquez-Semadeni, E., Gómez, G.C.: Astrophys. J. **744**, 190 (2012)
Troland, T.H., Crutcher, R.M.: Astrophys. J. **680**, 457 (2008)
van Dishoeck, E.F., Black, J.H.: Astrophys. J. **334**, 771 (1988)
van Dishoeck, E.F., Blake, G.A.: Ann. Rev. Astron. Astrophys. **36**, 317 (1998)
Vázquez-Semadeni, E.: Astrophys. J. **423**, 681 (1994)
Vázquez-Semadeni, E. In: de Avillez, M. (ed.) The Role of Disk-Halo Interaction in Galaxy Evolution: Outflow vs. Infall? EAS Publications Series, vol. 56, p. 39. EDP Sciences, Les Ulis (2009)
Vázquez-Semadeni, E. In: Alves, J., et al. (eds.) Computational Star Formation, IAU Symposium, vol. 270, p. 275. Cambridge (2010)
Vázquez-Semadeni, E. In: Klapp, J., Medina, A., Cros, A., Vargas, C. (eds.) Fluid Dynamics in Physics, Engineering and Environmental Applications. Springer, Berlin (2012)
Vázquez-Semadeni, E., García, N.: Astrophys. J. **557**, 727 (2001)
Vazquez-Semadeni, E., Gazol, A.: Astron. Astrophys. **303**, 204 (1995)
Vázquez-Semadeni, E., Passot, T., Pouquet, A.: Astrophys. J. **473**, 881(VPP96) (1996)
Vázquez-Semadeni, E., Cantó, J., Lizano, S.: Astrophys. J. **492**, 596 (1998)
Vázquez-Semadeni, E., Gazol, A., Scalo, J.: Astrophys. J. **540**, 271 (2000)
Vázquez-Semadeni, E., Ballesteros-Paredes, J., Klessen, R.S.: Astrophys. J. Lett. **585**, L131 (2003)
Vázquez-Semadeni, E., Gazol, A., Passot, T., et al. In: Turbulence and Magnetic Fields in Astrophysics. Lecture Notes in Physics, vol. 614, p. 213. Springer, New York (2003)
Vázquez-Semadeni, E., Kim, J., Ballesteros-Paredes, J.: Astrophys. J. Lett. **630**, L49 (2005)
Vázquez-Semadeni, E., Kim, J., Shadmehri, M., Ballesteros-Paredes, J.: Astrophys. J. **618**, 344 (2005)
Vázquez-Semadeni, E., Ryu, D., Passot, T., González, R.F., Gazol, A.: Astrophys. J. **643**, 245 (2006)
Vázquez-Semadeni, E., Gómez, G.C., Jappsen, A.K., et al.: Astrophys. J. **657**, 870 (2007)
Vázquez-Semadeni, E., Gómez, G.C., Jappsen, A.-K., Ballesteros-Paredes, J., Klessen, R.S.: Astrophys. J. **707**, 1023 (2009)

Vázquez-Semadeni, E., Colín, P., Gómez, G.C., Ballesteros-Paredes, J., Watson, A.W.: Astrophys. J. **715**, 1302 (2010)
Vázquez-Semadeni, E., Banerjee, R., Gómez, G.C., et al.: Mon. Not. R. Astron. Soc. **414**, 2511 (2011)
Vishniac, E.T.: Astrophys. J. **428**, 186 (1994)
Walder, R., Folini, D.: Astrophy. Space Sci. **274**, 343 (2000)
Wang, P., Li, Z.-Y., Abel, T., Nakamura, F.: Astrophys. J. **709**, 27 (2010)
Williams, J.P., de Geus, E.J., Blitz, L.: Astrophys. J. **428**, 693 (1994)
Wilson, R.W., Jefferts, K.B., Penzias, A.A.: Astrophys. J. Lett. **161**, L43 (1970)
Wolfire, M.G., Hollenbach, D., McKee, C.F., Tielens, A.G.G.M., Bakes, E.L.O.: Astrophys. J. **443**, 152 (1995)
Zel'Dovich, Y.B., Pikel'Ner, S.B.: Sov. J. Exp. Theor. Phys. **29**, 170 (1969)
Zuckerman, B., Evans, N.J.: Astrophys. J. **192**, L149 (1974)
Zuckerman, B. Palmer, P.: Ann. Rev. Astron. Astrophys. **12**, 279 (1974)

Chapter 15
Observations of Magnetic Fields in Molecular Clouds: Testing Star Formation Theory

Richard M. Crutcher

Abstract This chapter reviews Zeeman observations of magnetic fields in molecular clouds and their use in testing star formation theory. The result is that while ambipolar diffusion driven star formation appears to be inconsistent with observations, reconnection diffusion seems to be consistent.

15.1 Introduction

One of the major issues in star formation theory is the magnetic flux problem—stars would have orders of magnitude stronger magnetic fields if flux freezing held during the formation process. A way to solve this problem during the early stages has for many years been considered to be almost the "standard model" for at least low-mass star formation. In this model self-gravitating clouds form that are magnetically subcritical. That is, the magnetic field is sufficiently strong to support clouds against gravitational contraction. However, flux freezing is not perfect. Gravity drives neutrals through the magnetic field and the ions toward the gravitational center, building up mass in the central region until the core becomes supercritical—the magnetic field in the core is not sufficiently strong to prevent the augmented core mass from contracting more rapidly. The contraction now drags in both the magnetic field and the ions. This process is called ambipolar diffusion, and results in a relatively slow, quasi-static, inefficient star formation process (e.g., Mouschovias and Ciolek 1999). However, in recent years the roles played by turbulence have drawn increasing attention. Convergent turbulent flows can build up mass in small volumes, forming self-gravitating clouds. Some of these clouds may initially be supercritical, due possibly to flows primarily along flux tubes so mass but not magnetic flux increases. Such clouds may then form stars on relatively short time scales. Other clouds may be formed that are subcritical, and will not form stars unless the mass to magnetic flux ratio M/Φ can be increased. One way to do this is of course the relatively slow ambipolar diffusion

R.M. Crutcher (✉)
University of Illinois, Urbana, IL 61801, USA
e-mail: crutcher@illinois.edu

A. Lazarian et al. (eds.), *Magnetic Fields in Diffuse Media*, Astrophysics and Space Science Library 407, DOI 10.1007/978-3-662-44625-6_15

process. However, another physical process has recently been suggested—magnetic reconnection. Turbulence can greatly increase the magnetic reconnection rate so that it can dominate ambipolar diffusion as the primary process for solving the magnetic flux problem during the early stages of star formation (Santos-Lima et al. 2010, 2012, 2013; Lazarian et al. 2012; Leão et al. 2013).

Ambipolar diffusion theory has self-gravitating clouds originally being subcritical, with their cores becoming supercritical through the action of ambipolar diffusion, while the envelopes remain subcritical. This is because the ambipolar diffusion rate is much faster in the smaller, denser and shielded inner region of a cloud, where the fractional ionization is lower. The reconnection diffusion rate does not depend on ionization but on the strength of the turbulence. Because turbulence is stronger in the lower density envelopes of clouds and in diffuse H I clouds, the reconnection diffusion rate will be faster in diffuse regions and in envelopes of molecular clouds, the opposite of the ambipolar diffusion case.

Although the role played by magnetic fields in the star formation process remained unclear in spite of many years of observational effort, recent work has significantly clarified the picture and made it possible to test the two magnetic diffusion processes briefly discussed above. This Chapter covers the same ground as a very recent review by the present author of magnetic fields in molecular clouds published in the 2012 edition of Annual Reviews of Astronomy and Astrophysics (Crutcher 2012), and the reader is referred to that article for a somewhat broader and more comprehensive review than the present chapter. However, that article was completed in November 2011, before the possible importance of reconnection diffusion in star formation had been appreciated and explored. The present Chapter therefore extends and updates the Annual Reviews article.

In this chapter I very briefly review the observational techniques available for studying magnetic fields in molecular clouds, describe results that are directly applicable to testing the ambipolar diffusion and reconnection diffusion processes, and discuss the state of the observational testing. I focus primarily on Zeeman results in this chapter; discussion of results from other techniques may be found in Crutcher (2012).

15.2 Observations of Magnetic Field Strengths

Interstellar magnetic fields may be observed by mapping linearly polarized emission or absorption from dust and spectral lines. Crutcher (2012) reviewed such observations in detail. These techniques give information about the morphology of magnetic fields, but they do not directly give magnetic field strengths, which provide the most definitive tests of theory. There are statistical methods that allow inference of the mean magnetic field strength based on the assumption that the observed dispersion in polarization position angles over a source may be related to the strength of turbulence, which is inferred from the volume density and the width of a molecular line. However, such methods give only the mean field strength in the plane of the

sky over an area and are subject to very significant uncertainties. For this reason, I focus here on Zeeman observations, which do give direct measurements of magnetic field strengths.

Zeeman data also have significant limitations. Although the Zeeman effect in principle yields all three components of the magnetic vector **B**, in quasi-thermal (non maser) spectral lines the linearly polarized Stokes Q and U Zeeman signals are too weak to detect. Hence, only measurement of the circularly polarized Stokes V spectra are available, which yield only the line-of-sight component B_{los} of **B**. Much of the uncertainty about the role of magnetic fields in star formation comes from this limitation.

Because a strong Zeeman effect requires that atoms and molecules have an unpaired electron, unambiguous detections in the interstellar medium (excluding masers) have to date been in only three species: H I, OH, and CN. However, since the spectral lines of these species sample complementary densities ($n_H \sim 1 - 10^2, 10^3 - 10^4$, and $10^5 - 10^6$ cm^{-3}, respectively), it is possible to observe magnetic field strengths throughout the density range necessary to test the role of magnetic fields in the early stages of star formation. The Zeeman data give B_{los} averaged over the telescope beam and over the density regime sampled by the spectral line, and can distinguish different B_{los} in different (even blended) velocity components, so individual clouds or subregions can be studied. Figure 15.1 shows

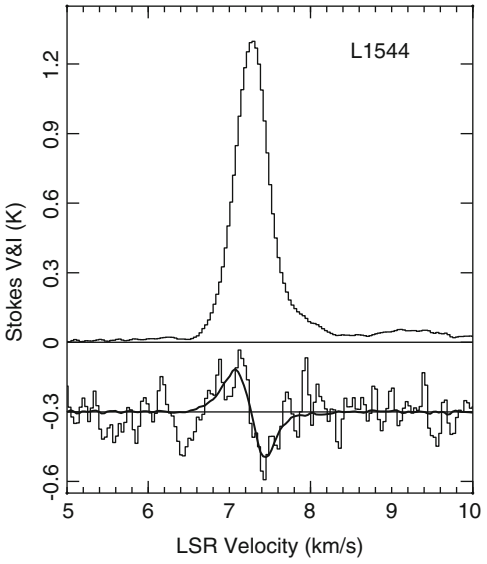

Fig. 15.1 Example of molecular cloud Zeeman data, for the starless core L1544. The OH 1,665 and 1,667 MHz line data were averaged to show the combined sensitivity. The *top and bottom panels* show the Stokes I and V spectra, respectively; the Stokes V data have been scaled up by a factor of 10 for display. To obtain B_{los}, dI/dv, which is proportional to B_{los}, is fitted by least squares to the observed Stokes V spectrum. The fit shown by the heavy line superposed on the Stokes V spectrum is for $B_{los} = +10.8 \pm 1.7\,\mu$G. The plus sign indicates that B_{los} points away from us

an example of molecular cloud Zeeman data, and illustrates the difficulty and hence the sparseness of Zeeman results for molecular clouds. The result for L1544 required 16 h of integration time with the Arecibo telescope.

The Zeeman data that will be discussed here are from the compilation by Crutcher (1999) and from the five later major Zeeman surveys of H I (Heiles and Troland 2004), OH (Bourke et al. 2001; Troland and Crutcher 2008; Thompson and Troland 2014), and CN (Falgarone et al. 2008).

15.3 Testing Magnetic Diffusion Theory

The two theories mentioned above for solving the magnetic flux problem at early stages are ambipolar diffusion and reconnection diffusion. Each makes different predictions that may be tested with Zeeman observations. I discuss five tests: (1) whether there are magnetically supported, self-gravitating clouds, (2) the variation of the mass to magnetic flux ratio with cloud radius, (3) the variation of field strength with density, (4) the range of field strengths among clouds of the same density, and (5) complete models of individual clouds.

An important parameter is the ratio of the gravitational and magnetic forces, which is proportional to the ratio of mass to magnetic flux, M/Φ. A widely used expression for the critical value at which the two forces are in balance is $(M/\Phi)_{crit} = 1/2\pi\sqrt{G}$ (Nakano and Nakamura 1978). Clouds with $M/\Phi > (M/\Phi)_{crit}$ are supercritical (mass too large to be supported by the magnetic field), while clouds with $M/\Phi < (M/\Phi)_{crit}$ are subcritical. Because $M/\Phi \propto N/B$, where N is the column density and B is the magnetic field strength, it is possible to measure M/Φ in interstellar clouds. Normalized by the above critical $(M/\Phi)_{crit}$, $(M/\Phi)_{obs} = 3.8 \times 10^{-21}\, N_H/B$, where $N_H = N(HI) + 2N(H_2)$ is in cm^{-2} and B is in μG. Henceforth, all observed $(M/\Phi)_{obs}$ that are discussed will have been normalized, so $(M/\Phi)_{obs} > 1$ is supercritical, $(M/\Phi)_{obs} < 1$ is subcritical.

15.3.1 Subcritical Molecular Clouds

To form clouds, ambipolar diffusion theory starts with mass flowing along magnetic field lines, building up mass in a disk-like structure that eventually becomes self gravitating and magnetically supported. Hence, the theory predicts that there should be a population of subcritical, self-gravitating molecular clouds. Whether such clouds are observed is a test of the theory. On the other hand, reconnection diffusion acts rapidly and efficiently during the early, diffuse stage where physical scales are large and turbulence is strong. The rate is sufficiently fast that self-gravitating molecular clouds need never be subcritical.

Figure 15.2 shows B_{los} versus N_H; the direction of B_{los} has been suppressed, so only the magnitude is plotted. Although an individual Zeeman measurement gives

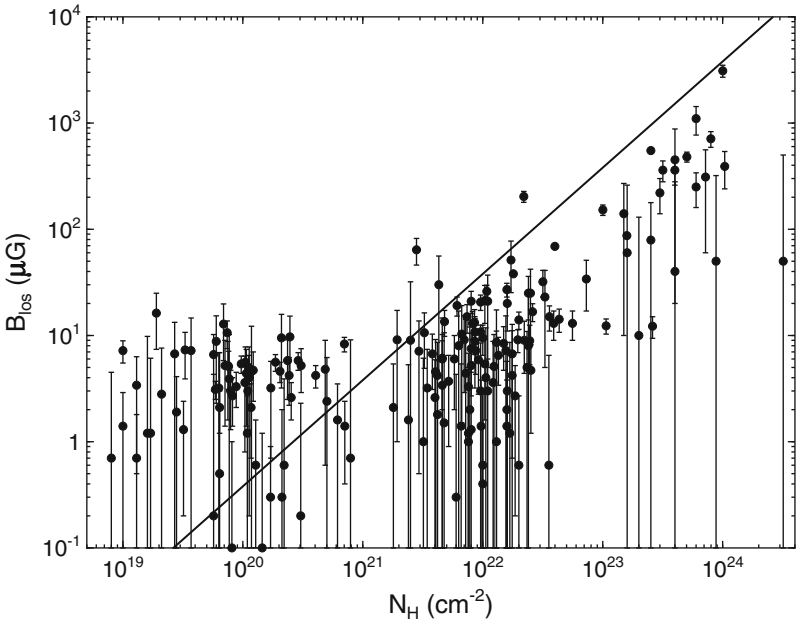

Fig. 15.2 H I, OH, and CN Zeeman measurements of the magnitude of B_{los} versus N_H. The *straight line* is for a critical $M/\Phi = 3.8 \times 10^{-21} N_H/B$. Clouds above this line are subcritical, those below are supercritical

B_{los} (hence only an upper limit to M/Φ), the upper envelope of the B_{los} in Fig. 15.2 defines the total field strength B_{tot} at each N_H, since for some fraction of the clouds **B** should point approximately along the line of sight.

At first glance this figure may seem to show exactly what the ambipolar diffusion theory predicts. For $N_H \lesssim 10^{21}$ cm^{-2}, the M/Φ are subcritical; these clouds are lower density H I clouds. For $N_H \gtrsim 10^{21}$ cm^{-2}, the M/Φ are overwhelmingly supercritical; these clouds are higher density molecular clouds and cores. Hence, the data appear consistent with the theory, with neutrals gravitationally contracting while leaving the magnetic flux behind and hence increasing M/Φ in the higher density molecular gas. However, there are problems with this picture. The H I clouds in the Arecibo Millinium Survey (Heiles and Troland 2004, 2005) are in approximate pressure equilibrium with the warm interstellar medium and are not self-gravitating, so they could not gravitationally collapse through the magnetic field to form supercritical cores. Heiles and Troland (2003) showed that the structure of the H I diffuse clouds must generally be sheet-like.

So where are the self-gravitating, subcritical clouds? For $N_H \gtrsim 10^{21}$ cm^{-2} most of the points in Fig. 15.2 are molecular clouds that are generally self-gravitating, so this should be the region of transition from subcritical to supercritical clouds. Yet there are zero definite cases of subcritical clouds for $N_H > 10^{21}$ cm^{-2}! The two points which seem to be significantly above the critical line are both from a

survey (Bourke et al. 2001) of OH in absorption toward H II regions, and neither is claimed as a definite detection by these authors. Polarized maser emission within the absorption lines led to inconsistencies and uncertainties in the fit for B_{los} that were not reflected in the formal uncertainties. Hence, there are no clear observational cases of self-gravitating, subcritical clouds, which must exist in the ambipolar diffusion theory.

15.3.2 Variation of M/Φ with Cloud Radius

The ambipolar diffusion theory of star formation predicts and requires that M/Φ increase from the envelope to core region of a cloud. Crutcher, Hakobian and Troland (hereinafter CHT) (Crutcher et al. 2009) directly tested this prediction. Their experiment measured $\mathscr{R} \equiv (M/\Phi)_{core}/(M/\Phi)_{envelope}$. The idealized ambipolar diffusion theory of core formation requires $\mathscr{R}$ to be approximately equal to the inverse of the original (before evolution driven by ambipolar diffusion) subcritical M/Φ, or $\mathscr{R} > 1$. The test used OH Zeeman observations to determine the line-of-sight magnetic field B_{los} and the column density N_{OH} in each of four dark cloud cores and envelopes. The central assumption of this test was that the angle θ between the line of sight and the magnetic field was approximately the same in core and envelope. Then the measured $B_{los} = B_{tot}\cos\theta$ would have the same θ in the numerator and denominator of $\mathscr{R}$, and the dependence on the unknown θ would disappear. Therefore, $\mathscr{R} = (N_{OH}/B_{los})_{core}/(N_{OH}/B_{los})_{envelope}$, all directly measurable quantities.

Because cloud cores with the strongest measured B_{los} were selected for the test, it is likely that $B_{los} \approx B_{tot}$ with $\theta \sim 0$, so $\cos\theta \approx 1$ and small changes in θ between core and envelope would not affect $\mathscr{R}$ very much. Supporting this assumption of the experiment is the fact that published models of core formation driven by ambipolar diffusion have strong, regular magnetic field morphology such that the unknown angle θ between **B** and the line of sight is approximately the same in core and envelope regions. From maps of polarized dust emission, field morphologies in cores and envelopes are found to be correlated in direction (Li et al. 2009).

With measurements of B_{los} and $N(OH)$ toward each core and envelope, it was possible to calculate $\mathscr{R}$ and its uncertainty toward each cloud. Because B_{los} was not detected (at the 3σ level) toward any of the four cloud envelopes, in no case was the calculated value of $\mathscr{R}$ significantly (3σ) different from 0. But the astrophysical question is not whether $\mathscr{R}$ is significantly different from 0, it is whether the $\mathscr{R}$ were significantly different from 1, since the ambipolar diffusion theory requires that $\mathscr{R} > 1$. The results for the four clouds (with the significance with respect to $\mathscr{R} = 1$ in parentheses) were: $\mathscr{R}$(L1448CO) = 0.02 ± 0.36 (2.7σ), $\mathscr{R}$(B217-2) = 0.15 ± 0.43 (2.0σ), $\mathscr{R}$(L1544) = 0.42 ± 0.46 (1.3σ), and $\mathscr{R}$(B1) = 0.41 ± 0.20 (3.0σ). Hence, in all four cases, the experiment found $\mathscr{R} < 1$, not $\mathscr{R} > 1$ as the theory predicts.

Proponents of the ambipolar diffusion theory of star formation strongly attacked the CHT results and conclusions, with the two strongest objections being that (1) motion of cores through surrounding more diffuse gas could lead to **B** in cores and their envelopes not being essentially parallel and (2) that since B_{los} was not detected in the envelopes only upper limits should be considered (Mouschovias and Tassis 2009, 2010). Crutcher et al. (2010) responded to the objections. The first objection is certainly possible, although it would require that all four cores move nearly in the plane of the sky so the envelope fields would be dragged into the plane of the sky and thus invisible to Zeeman observations. Also, as mentioned above, evidence from linear polarization mapping that directions in cores and surrounding gas are strongly correlated argues against this morphology. On the second objection, it is certainly true that at the 3σ upper-limit level, $\mathscr{R} = 1$ is consistent with the data for each cloud individually. Hence, Mouschovias and Tassis argue that the observations are consistent with ambipolar diffusion. However, the assumption of the ambipolar diffusion theory that clouds initially are subcritical implies not that $\mathscr{R} = 1$ but that $\mathscr{R} > 1$, so the significance of the individual observational results for ambipolar diffusion is larger than given by comparison with $\mathscr{R} = 1$. Moreover, while the observational results for each cloud individually can be argued to be (marginally) consistent with the prediction of ambipolar diffusion, one must also consider that a sample of four clouds was observed. If in fact $\mathscr{R} > 1$ in all four clouds, one would expect observational noise to sometimes produce an observed $\mathscr{R}$ greater than the "true" value, not always smaller. While the sample size of four clouds is not large, the observations reported by CHT certainly suggest a problem with the idea that ambipolar diffusion was responsible for the formation of cores in all four clouds. Indeed, the purely statistical probability that all four of the clouds have $\mathscr{R} > 1$ is 3×10^{-7}.

Lunttila et al. (2008) computed synthetic Zeeman profiles for their super-Alfvénic simulations of molecular clouds and cores formed by turbulence in an initially uniform interstellar medium. They did not explicitly include magnetic reconnection. They numerically performed the same observations on their simulated cores as the real observations of CHT. They found that $\mathscr{R}$ had a large scatter among their cores, $0.08 \leq \mathscr{R} \leq 1.6$, with the PDF favoring values less than 1. Since CHT observed only four clouds, the simulations are consistent with the observations.

How do the CHT results compare with the predictions of reconnection diffusion? Lazarian et al. (2012) argue that reconnection diffusion is inevitable in turbulent media. Because reconnection diffusion depends on the strength of turbulence and not on the degree of ionization, it will be stronger in the larger scale, more turbulent envelopes of clouds than in the smaller, less turbulent cores. Their toy models based on mean parameters of the four clouds observed by CHT showed that removal of magnetic field is less efficient in the cores than in the envelopes, and that agreement with the CHT measurements of $\mathscr{R}$ would result. The time scale of 200 kyr is much faster than the ambipolar diffusion time scale. With ambipolar diffusion magnetic flux is conserved and frozen into the envelope matter, producing a disagreement with the CHT observations. With reconnection diffusion magnetic flux is destroyed much more efficiently in the envelope than in the core, producing agreement with CHT observations of the radial dependance of M/Φ.

15.3.3 Bayesian Analysis of Total Magnetic Field Strength

Although the above two tests were possible with only the line-of-sight component of the magnetic field strength, further tests require knowledge of the total magnetic field strength. It is possible to infer information about the total magnetic field strength by a statistical analysis of surveys of Zeeman data. One assumes for the sample of clouds that the angle θ between the line of sight and **B** is random, and also assumes various forms for the PDF of B_{tot}, $P(B_{tot})$. The analysis can then give the $P(B_{tot})$ that is most consistent with the data. Crutcher et al. (2010) employed a Bayesian statistical technique in order to investigate $P(B_{tot})$. They used the four data sets (Crutcher 1999; Heiles and Troland 2004; Troland and Crutcher 2008; Falgarone et al. 2008) that had information about the volume density n_H. The model assumed was that the maximum B_{tot} was independent of n_H up to some value of density n_0, with $B_{tot,max} = B_0$. For $n_H > n_0$, the maximum B_{tot} was assumed to have a power-law increase, $B_{tot,max} = B_0(n_H/n_0)^{\alpha}$. A model of $P(B_{tot})$, taken to be the same function at every n_H, was assumed that used a parameter f to characterize $P(B_{tot})$. For $f = 1$, $P(B_{tot})$ would be a delta function, while if $f = 0$, $P(B_{tot})$ would be a flat PDF, with B_{tot} ranging uniformly between 0 and $B_{tot,max}$ at each n_H. Intermediate values of f were allowed in the analysis. Figure 15.3 shows the data and inferred maximum value of the total magnetic field strength versus density. The

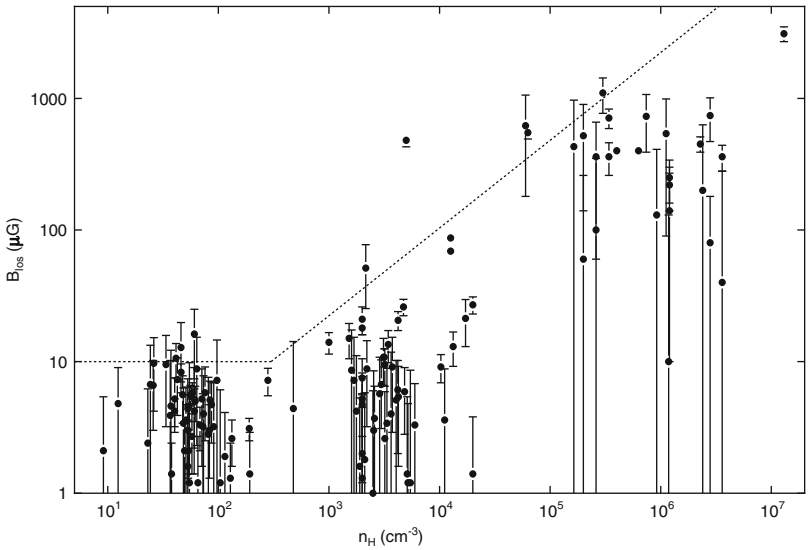

Fig. 15.3 H I, OH, and CN Zeeman measurements of the magnitude of B_{los} versus n_H. The dashed line segments show the most probable model from the Bayesian analysis for the maximum total magnetic field strength at each density. The total field strength of an individual cloud lies between this maximum and essentially 0, with a flat distribution between 0 and the maximum

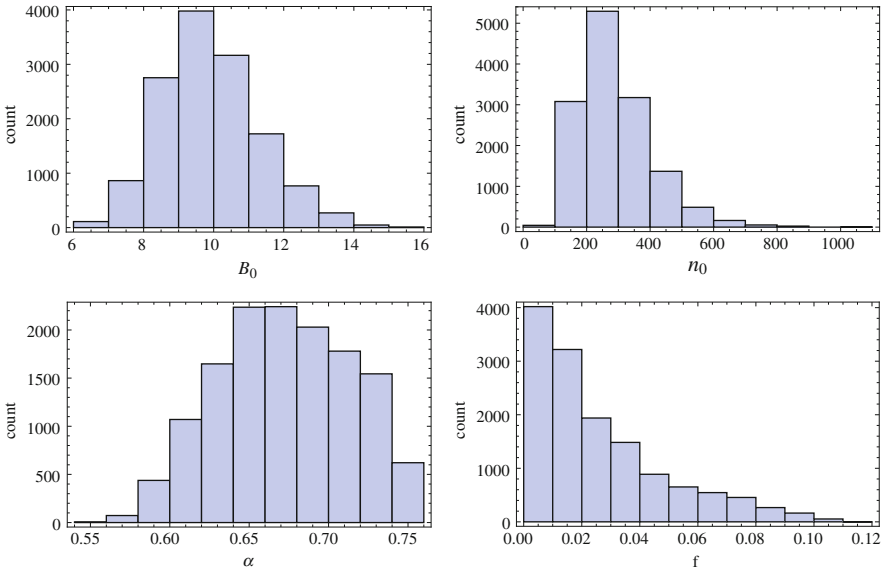

Fig. 15.4 The PDFs for each of the four parameters in the Bayesian analysis. B_0 is the maximum total field strength for densities less than n_0, α is the power-law scaling exponent for the maximum total field strength for densities greater than n_0, and f is the fraction of the flat PDF of the total B cut from the complete flat PDF

PDFs of the four parameters (n_0, B_0, α, f) inferred by the Bayesian analysis are shown in Fig. 15.4.

15.3.3.1 Range of Field Strengths Among Clouds of the Same Density

The typical molecular clouds is supercritical, with mean $M/\Phi \sim 3$. The Bayesian result gives further information about the variation in B_{tot} among clouds with the same n_H. The result for the range of field strengths among clouds of the same density was that the PDF is flat, with total field strength among these clouds varying linearly (from one cloud to another) from the maximum value $B_{tot,max}$ at that density shown by the dashed line in Fig. 15.3 down to $f \times B_{tot,max}$. Figure 15.4 shows that f is very small, so some high-density clouds have very small total magnetic field strengths. The ambipolar diffusion theory does not directly forbid molecular clouds with very weak magnetic fields, since the field strength is an input to the theory. Such clouds could have formed in regions of low magnetic field. However, such clouds would not be magnetically supported and ambipolar diffusion would not be relevant to their collapse. On the other hand, reconnection diffusion will act to bring the magnetic field strengths in molecular clouds into equilibrium with the surrounding interstellar medium. Depending on the age and history of a cloud, it may have a magnetic field strength close to the mean value ($\sim$6 μG) of the diffuse interstellar

medium, or very much stronger, if the cloud is relatively young or if it is collapsing faster than the reconnection time scale (see next section).

15.3.3.2 Variation of Field Strength with Density

For a $B \propto \rho^{\alpha}$ parameterization of the variation of field strength with density, the power law exponent $\alpha \approx 0.65$, with an extremely low probability that $\alpha < 0.6$ (see Fig. 15.4). Ambipolar diffusion theory predicts $\alpha \lesssim 0.5$. The observed value agrees best with the value $\alpha = 2/3$ found by Mestel (1966) for magnetic fields too weak to affect the morphology of gravitational contraction. Reconnection diffusion can reduce magnetic field strengths to the levels where they are too weak to significantly affect gravitational contraction. Although a detailed calculation of the time scale for reconnection diffusion depends on uncertain parameters such as the injection scale of turbulence, Lazarian et al. (2012) did show at densities $n_H \gtrsim 10^4$ cm^{-3}, reconnection diffusion is faster than the free-fall contraction rate (see also Leão et al. 2013). Hence, at higher densities gravitational collapse would increase the field strength faster than reconnection diffusion could decrease it. The Bayesian analysis gave $n_0 \sim 300$ cm^{-3} (see Fig. 15.4) as the n_H at which magnetic field strength starts to increase with density. However, Fig. 15.3 shows few clouds with B greater than the diffuse H I values at $n_H < 10^4$ cm^{-3}, and the reconnection diffusion calculation involves a simple model and uncertain input parameters.

15.4 Complete Models of Individual Clouds

Ambipolar diffusion models have been calculated specifically for two clouds, for comparison with observational data including OH Zeeman detections. Crutcher et al. (1994) discussed a model for the B1 cloud; it had an initial $B_{tot} = 43\,\mu$G, and an initial $M/\Phi = 0.42$ of critical. The model assumed that the cloud was a disk whose minor axis was at an angle $\theta = 70°$ to the line of sight; all observed properties of B1 available at that time were given accurately by the model. In particular, the present-day ambipolar-diffusion evolved central $B_{los} = 29\,\mu$G; the observed value is $B_{los} = 27\,\mu$G. The prediction of this model would be $\mathscr{R} \approx 1/0.42 = 2.4$, a factor of ~6 larger than the CHT result above (Sect. 3.2) for B1; that CHT result differs from 2.4 by 10σ! Moreover, now that the (Troland and Crutcher 2008) survey of dark cloud cores has shown that B1 has the greatest B_{los} of any core with a detected B_{los}, it seems more likely that **B** is nearly along the line of sight, and that the true central B_{tot} is close to the observed $B_{los} = 27\,\mu$G and not the model result $B = 85\,\mu$G, which implied $B_{los} = 85\,\mu\text{G} \cos 70° = 29\,\mu$G. When B1 was among a very small number of dark clouds with sensitive OH Zeeman observations, it was not unreasonable to hypothesize that its field lay nearly in the plane of the sky. However, other clouds similar to B1 with similar total field strengths should

have **B** nearly along the line of sight, yielding $B_{los} \sim 85\,\mu$G; these are not found in the Arecibo OH dark cloud survey (Troland and Crutcher 2008) results.

Ciolek and Basu (2000) computed a model for the L1544 cloud. They assumed $\theta \approx 74°$, again a very large angle between **B** and the line of sight, which was necessary in order to have the required large central field strength agree with the small observed value of B_{los}. The initial M/Φ was 0.8 of critical. This would imply $\mathscr{R} \approx 1.25$, which differs from the measurement (Sect. 3.2) of $\mathscr{R} = 0.42 \pm 0.46$, although not by a significant amount. However, as for B1, the large value for θ is possible for a particular cloud, but the large θs for both clouds require that both be special cases, with large B_{tot} but much smaller observable B_{los}.

Although Lazarian et al. (2012) presented toy models for the mean parameters of the four clouds studied by CHT, these models did not evolve density with time and hence are not complete models that can be compared in detail with observations of individual clouds. Such detailed models are necessary for further tests of reconnection diffusion. In fact, we refer to recent successful numerical modeling of magnetic flux transport by turbulent reconnection diffusion in different stages of star formation, from cloud core collapse to protostellar disk formation by Santos-Lima et al. (2010, 2012, 2013) and Leão et al. (2013).

Conclusion

Zeeman observations of molecular clouds have advanced sufficiently that meaningful tests of the predictions of ambipolar diffusion and reconnection diffusion can be made. Conclusions from five tests discussed here are the following:

- If ambipolar diffusion theory is relevant for star formation, there should be a relatively long-lived phase of self-gravitating, magnetically subcritical clouds. None are observed to exist. Reconnection diffusion is sufficiently fast that weaker magnetic fields and hence supercritical molecular clouds are predicted, in agreement with the data.
- The observed M/Φ is not found to increase between the envelope and core regions of dark clouds, contrary to the prediction of ambipolar diffusion. Reconnection diffusion is faster in the larger scale, more high turbulent envelope regions than in cores, reducing magnetic field strength and hence increasing M/Φ in envelopes, as is observed (see also recent numerical studies of turbulent clouds evolution which seem to confirm this trend Leão et al. 2013).
- The observed power law scaling of field strength with density has exponent $\alpha \approx 0.6$–0.7. Ambipolar diffusion predicts $\alpha \lesssim 0.5$. Reconnection diffusion reduces field strengths such that at higher densities gravitational collapse may be close to the weak field theoretical value of $\alpha = 2/3$

(continued)

- The statistically preferred PDF of the total field strengths in molecular clouds is flat, i.e., there are as many molecular clouds at a given density with very small magnetic field strengths as there are with the maximum strengths observed at that density. Reconnection diffusion reduces field strengths, such that with sufficient time they approach equilibrium with the diffuse H I medium. Ambipolar diffusion does not directly address this issue, since the initial magnetic field strength of molecular clouds is an input to the theory. However, ambipolar diffusion would be irrelevant if self-gravitating molecular clouds were supercritical when formed.
- Detailed ambipolar diffusion models of two clouds require strong total field strengths that are nearly in the plane of the sky in order to match the much smaller, observed line-of-sight field strengths. All magnetic fields cannot be nearly in the plane of the sky. Detailed reconnection models of cloud evolution have yet to be calculated. In fact, important steps in this direction have been recently performed by means of 3D MHD numerical simulations of turbulent clouds by Santos-Lima et al. (2010) and Leão et al. (2013).

Magnetic reconnection appears to be compatible with all of the Zeeman observations of molecular clouds, while the predictions of ambipolar diffusion models have a number of serious disagreement with observations. However, the set of Zeeman observations remains quite sparse, especially at the higher densities sampled by CN. ALMA observations may lead to increased spatial resolution and sensitivity that will enable further tests of the star formation theory and the role played by magnetic fields.

Acknowledgements The author's research on the role of magnetic fields in star formation is supported by the National Science Foundation under grant AST1007713.

References

Bourke, T.L., Myers, P.C., Robinson, G., Hyland, A.R.: Astrophys. J. **554**, 916–932 (2001)
Ciolek, G.E., Basu, S.: Astrophys. J. **529**, 925–931 (2000)
Crutcher, R.M.: Astrophys. J. **520**, 706–713 (1999)
Crutcher, R.M.: Ann. Rev. Astron. Astrophys. **50**, 29–63 (2012)
Crutcher, R.M., Mouschovias, T.C., Troland, T.H., Ciolek, G.E.: Astrophys. J. **427**, 839–847 (1994)
Crutcher, R.M., Hakobian, N., Troland, T.H.: Astrophys. J. **692**, 844–855 (2009)
Crutcher, R.M., Hakobian, N., Troland, T.H.: Mon. Not. R. Astron. Soc. **402**, L64–L66 (2010)
Crutcher, R.M., Wandelt, B., Heiles, C., Falgarone, E., Troland, T.H.: Astrophys. J. **725**, 466–479 (2010)
Falgarone, E., Troland, T.H., Crutcher, R.M., Paubert, G.: Astron. Astrophys. **487**, 247–252 (2008)
Heiles, C., Troland, T.H.: Astrophys. J. **586** 1067–1093 (2003)
Heiles, C., Troland, T.H.: Astrophys. J. Suppl. **151**, 271–297 (2004)
Heiles, C., Troland, T.H.: Astrophys. J. **624**, 773–793 (2005)
Lazarian, A., Esquivel, A., Crutcher: Astrophys. J. **757**, 154 (2012)

Li, H., Dowell, C.D., Goodman, A., Hildebrand, R., Novak, G.: Astrophys. J. **704**, 891–897 (2009)
Leão, M.R.M., de Gouveia Dal Pino, E.M., Santos-Lima, R., Lazarian, A.: Astrophys. J. **777**, 46L (2013)
Lunttila, T., Padoan, P., Juivela, M., Nordlund, Å: Astrophys. J. Lett. **686**, L91–L94 (2008)
Mestel, L.: Mon. Not. R. Astron. Soc. **133**, 265–284 (1966)
Mouschovias, T.C., Ciolek, G.E. In: Lada, C.J., Kylafis, N.D. (eds.) The Origin of Stars and Planetary Systems, pp. 305–339. Kluwer, Dordrecht (1999)
Mouschovias, T.C., Tassis, K.: Mon. Not. R. Astron. Soc. **400**, L15–L19 (2009)
Mouschovias, T.C., Tassis, K.: Mon. Not. R. Astron. Soc. **409**, 801–809 (2010)
Nakano, T., Nakamura, T.: Publ. Astron. Soc. J. **30**, 671–679 (1978)
Santos-Lima, R., Lazarian, A., de Gouveia Dal Pino, E.M., Cho, J.: Astrophys. J. **714**, 442 (2010)
Santos-Lima, R., de Gouveia Dal Pino, E.M., Lazarian, A.: Astrophys. J. **747**, 21 (2012)
Santos-Lima, R., de Gouveia Dal Pino, E.M., Lazarian, A.: Mon. Not. R. Astron. Soc. **429**, 3371 (2013)
Thompson, K.L., Troland, T.H. (2014, in preparation)
Troland, T.H., Crutcher, R.M.: Astrophys. J. **680**, 457–465 (2008)

Chapter 16
Gravitational Collapse and Disk Formation in Magnetized Cores

Susana Lizano and Daniele Galli

Abstract We discuss the effects of the magnetic field observed in molecular clouds on the process of star formation, concentrating on the phase of gravitational collapse of low-mass dense cores, cradles of sunlike stars. We summarize recent analytic work and numerical simulations showing that a substantial level of magnetic field diffusion at high densities has to occur in order to form rotationally supported disks. Furthermore, newly formed accretion disks are threaded by the magnetic field dragged from the parent core during the gravitational collapse. These disks are expected to rotate with a sub-Keplerian speed because they are partially supported by magnetic tension against the gravity of the central star. We discuss how sub-Keplerian rotation makes it difficult to eject disk winds and accelerates the process of planet migration. Moreover, magnetic fields modify the Toomre criterion for gravitational instability via two opposing effects: magnetic tension and pressure increase the disk local stability, but sub-Keplerian rotation makes the disk more unstable. In general, magnetized disks are more stable than their nonmagnetic counterparts; thus, they can be more massive and less prone to the formation of giant planets by gravitational instability.

16.1 Introduction

The goal of this review is to summarize recent theoretical work addressing the role of magnetic fields in the process of star formation, and, in particular, on the formation of circumstellar disks. In fact, the interstellar magnetic field dragged in the star plus disk system by the collapse of the parent cloud affects, in the first place, the process of disk formation itself (Sect. 16.3.1), but also provides a natural mechanism for disk viscosity and resistivity via the MRI instability

S. Lizano (✉)
Centro de Radioastronomía y Astrofísica, UNAM, Apartado Postal 3-72, 58089 Morelia, Michoacán, Mexico
e-mail: s.lizano@crya.unam.mx

D. Galli
INAF-Osservatorio Astrofisico di Arcetri, Largo E. Fermi 5, 50125 Firenze, Italy
e-mail: galli@arcetri.astro.it

A. Lazarian et al. (eds.), *Magnetic Fields in Diffuse Media*, Astrophysics and Space Science Library 407, DOI 10.1007/978-3-662-44625-6_16

(Sect. 16.4.1), affects the rotation curve of the disk (Sect. 16.4.2), its stability properties (Sect. 16.4.3), and the migration of planets (Sect. 16.4.4). Unfortunately, the detection of magnetic fields in circumstellar disks is still an observational challenge (Sect. 16.3.2). For recent comprehensive reviews see, e.g., Königl and Salmeron (2011) for the role of magnetic fields in the process of disk formation, and Armitage (2011) for the evolution of protoplanetary disks.

16.2 Magnetic Fields in Molecular Clouds

Theoretical considerations (Chandrasekhar and Fermi 1953; Mestel and Spitzer 1956) show that a cloud of mass M enclosing a magnetic flux Φ can be supported by the magnetic field against its self-gravity provided its non-dimensional mass-to-flux ratio λ expressed in units of $(2\pi G^{1/2})^{-1}$ where G is the gravitational constant, is less than unity,

$$\lambda \equiv 2\pi G^{1/2} \left(\frac{M}{\Phi} \right) < 1. \tag{16.1}$$

Subcritical clouds with $\lambda < 1$ evolve on a timescale that characterizes the diffusion of the magnetic field (e.g., Nakano 1979). On the other hand, supercritical clouds with $\lambda > 1$ cannot be supported by the magnetic field alone, even if the field were perfectly frozen in the gas. These clouds would collapse on a magnetically diluted free-fall timescale.

A large number of measurements of the intensity of the magnetic field has been obtained for different ISM conditions with various techniques (see e.g. Crutcher 2012 and the chapter by Crutcher, this volume). The available measurements of magnetic field strength in molecular clouds support the conclusion that on average, clouds are close to the critical value $\lambda \approx 1$. OH Zeeman measurements at cloud densities $\sim 10^3$ cm^{-3} give mean mass-to-flux ratios $\lambda \sim 2$–3 (Crutcher and Troland 2008). In dense cores, the mean value of the mass-to-flux ratio from CN Zeeman observations is $\lambda \sim 2$. Nevertheless, due to uncertainties in the measurement of the gas column densities of a factor ~ 2, a possible range of mass-to-flux ratios is $\lambda \sim 1$–4 (Falgarone et al. 2008). As we discuss below, these observed magnetic fields are dynamically important for the cloud evolution and gravitational collapse to form stars. In fact, these fields are well ordered on the large scales of molecular clouds (e.g., Goldsmith et al. 2008).

Thanks to the presence in the ISM of aspherical dust grains aligned with the field, polarization maps of the thermal emission of molecular clouds at submillimeter wavelengths have made possible to determine the field geometry and the relative importance of the ordered and turbulent components of the magnetic field. At the core scales, recent SMA maps of polarized dust continuum emission show the hourglass morphology expected for a magnetically controlled collapse rather than a disordered field dominated by important levels of turbulent motions (e.g.,

Girart et al. 2006, 2009; Gonçalves et al. 2008; Tang et al. 2009). Moreover, the statistical analysis of submillimeter polarization maps based on the dispersion function method, shows that the ratio of the rms turbulent component of the magnetic field to the mean value is of the order of 0.1–0.5 (Hildebrand et al. 2009; Houde et al. 2009). Thus, turbulent motions do not dominate the large scale well ordered magnetic field.

As a first approximation, the magnetic field in molecular clouds can be considered frozen to the gas. Even though the gas is lightly ionized, with an ionization fraction $\sim 10^{-8}$–10^{-7} (see e.g. Caselli et al. 1998), collisions between charged particles and neutrals efficiently transmit the Lorentz force to the largely neutral gas. In these conditions, the relevant mechanism of field diffusion is ambipolar diffusion (hereafter AD), originally proposed by Mestel and Spitzer (1956), a process by which the fluid of charged particles attached to the magnetic field can slowly drift with respect to the fluid of neutral particles (see chapter by Zweibel in this volume). The field is then left behind with respect to the neutral gas and the mass-to-flux ratio increases as the cloud condenses under the influence of its self-gravity. Thus, an initially magnetically subcritical region of mass sufficiently high for its self-gravity to overcome the support provided by thermal pressure and turbulent motions, evolves under this process toward a centrally condensed core with supercritical mass-to-flux ratio, $\lambda \geq 1$ that eventually collapses and fragments (e.g., Lizano and Shu 1989; Tomisaka et al. 1990). These authors showed that, for typical conditions of molecular clouds (densities $\sim 10^3\,\mathrm{cm}^{-3}$, magnetic fields $B \sim 30\,\mu\mathrm{G}$), the AD timescale for core formation was a few $\times 10^6$ year. Once the dense cores are formed, with densities of $\sim 3 \times 10^4\,\mathrm{cm}^{-3}$, they quickly evolve toward the stage of gravitational collapse in a few $\times 10^5$ year, of the order of the free-fall timescale. The mass-to-flux ratio increases little in this condensation process of core formation, thus, the major phase of flux loss occurs at higher densities. At core densities, also Ohmic losses are far too small to significantly reduce the magnetic field strength. For example, for an ionization fraction $\sim 10^{-8}$ and density $\sim 10^5\,\mathrm{cm}^{-3}$, the Ohmic dissipation time of a magnetic field extending on a length scale of ~ 0.1 pc is of the order of 10^{15} year. In contrast, at higher density, $n \sim 10^{11}\,\mathrm{cm}^{-3}$, characteristic of circumstellar disk formation, the field can be effectively removed from the system by processes like Ohmic diffusion and the Hall effect (see, e.g. Pinto et al. 2008; Pinto and Galli 2008). At some point in the star formation process magnetic field removal is necessary to prevent the formation of stars with MG fields, as would be the case under field freezing conditions. This has been called the "magnetic flux" problem by Mestel and Spitzer (1956). Current observations show that at the surface of young stars the fields have magnitudes of kG (e.g., Johns-Krull et al. 1999, 2004), they are likely to be generated by dynamo action, rather than being fossil fields.

It has been under debate whether the formation and evolution of the dense cores is controlled by magnetic fields as discussed above (e.g., Mouschovias and Ciolek 1999; Adams and Shu 2007; Nakamura and Li 2008) or by gravo-turbulent fragmentation driven by supersonic turbulence (e.g., Padoan et al. 2001; Klessen et al. 2005; Vázquez-Semadeni et al. 2005), or by hierarchical gravitational collapse of a cloud as a whole (e.g., Ballesteros-Paredes et al. 2011a,b and chapter by

Vázquez–Semadeni in this volume). We favor the first process because the large scale magnetic fields dominate over their turbulent components and they are strong enough to contribute to the support of a cloud core against its self-gravity if λ is of order unity. Furthermore, as we will discuss below, these fields influence the dynamics of the gravitational collapse and they are difficult to get rid of.

The process of gravitational collapse therefore separates logically into two phases: (a) how cloud cores that were initially sub-critical evolve to a state of being super-critical, and (b) how cloud cores of both low and high mass that are super-critical subsequently gravitationally collapse and possibly fragment once they pass beyond the threshold of stability. In this chapter we will focus on the second problem, the phase of gravitational collapse of a super-critical magnetized rotating core to form a star-disk system.

16.3 Gravitational Collapse of Magnetized Cores

16.3.1 Catastrophic Magnetic Braking and Disk Formation

Recently, several studies have addressed the gravitational collapse of a magnetized rotating cloud core to form a protostar plus disk system. These studies have considered the ideal magnetohydrodynamic (MHD) regime where the magnetic flux is frozen to the fluid, and the non-ideal MHD regime where several diffusive processes are taken into account. In particular, in their seminal work, Allen et al. (2003) considered the ideal MHD collapse of a core threaded by a large scale poloidal field, taking as an initial state a singular isothermal uniformly rotating toroid (Li and Shu 1996). They found a pseudo-disk predicted by Galli and Shu (1993a,b), a non-equilibrium flattened structure formed around the star by the tendency of the gas to flow along field lines and by the pinching Lorentz force resulting from the bending of the field dragged to the central star. These simulations also produced the slow outflows (with velocities of few km s^{-1}) found in previous numerical studies (e.g, Tomisaka 2002). Nevertheless, the simulations did not show the formation of a rotationally supported disk (RSD). Allen et al. argued that RSDs do not form in the ideal MHD regime because the enhanced strength and increased lever arm of the magnetic field dragged into the center of collapse results in a very efficient transfer of angular momentum from the accretion region to the cloud envelope. Subsequent numerical simulations confirmed that RSDs naturally form if $B = 0$ but do not form in strongly magnetized clouds (e.g., Price and Bate 2007; Fromang et al. 2006; Duffin and Pudritz 2009). In fact, the process of magnetic braking was known to provide a way to remove the cloud angular momentum and to allow the formation of disks and binary stars (e.g., Mouschovias and Paleologou 1980). However, the braking found in these simulations of the gravitational collapse phase was too efficient and prevented altogether the formation of a disk.

Galli et al. (2006) studied the self-similar collapse of an axisymmetric isothermal magnetized rotating cloud in the ideal MHD regime and found an analytic solution that asymptotically approaches free fall onto a central mass point, with an angular distribution that depends on the mass loading of magnetic field lines. They found that, independent on the details of the starting state, the magnetic field acquires a split-monopole configuration where the magnetic field is almost radial and directed in opposite directions above and below the mid plane. In this configuration the radial magnetic field strength increases as the inverse square of the distance r from the origin,

$$|B_r| = \phi_* \frac{c_s^3 t}{G^{1/2} r^2}, \tag{16.2}$$

where ϕ_* is the non-dimensional magnetic flux trapped in the central source, c_s is the sound speed and t is the time since the onset of collapse. This strong field produces a very efficient magnetic braking that prevents the formation of a RSD. The azimuthal velocity of the infalling gas decreases to zero at the center as $u_\varphi \propto -jr^{1/2}$, where j is the specific angular momentum of the gas in the envelope. Thus, the gas spirals into the star with velocity approaching free-fall, $u_r \propto r^{-1/2}$. The negative sign in the azimuthal velocity indicates that the magnetic braking is so efficient as to enforce counter rotation in the infalling gas, very close to the protostar. This counter rotation of the innermost parts of the accretion flow has also been found in numerical simulations (Mellon and Li 2009; Krasnopolsky et al. 2010). The azimuthal component of the magnetic field decreases as $B_\varphi \propto r^{-1}$ that increases with decreasing radius more slowly than the poloidal component given by Eq. (16.2). Thus, the winding of the field goes to zero near the protostar. Figure 16.1 illustrates the velocity field of the accretion flow in the equatorial plane of a magnetized rotating cloud. In this figure the inner solution of Galli et al. (2006) has been matched ad hoc to the outer rotating flow. The flow shows counter rotation at the center, before the gas falls onto the star.

Summarizing, in the absence of magnetic torques, the angular momentum of infalling fluid elements is conserved and a RSD is formed inside a radius r_d, where the azimuthal velocity, increasing as r^{-1}, becomes equal to the Keplerian velocity around the protostar, increasing like $r^{-1/2}$. Instead, when magnetic braking dominates over angular momentum conservation, the azimuthal velocity goes to zero at small radii, and no RSD is formed. Galli et al. named this process "catastrophic magnetic braking" and concluded that the dissipation of dynamically important levels of magnetic field is a fundamental requisite for the formation of protoplanetary disks around young stars.

Several numerical simulations addressed the question of determining the maximum level of magnetization required to allow disk formation under field-freezing conditions. These studies have found that disk formation is possible only for clouds with mass-to-flux ratios $\lambda > 10-80$ (Mellon and Li 2008; Hennebelle and Fromang 2008; Seifried et al. 2011), or $\lambda > 3$ for misaligned magnetic and rotation axis (Hennebelle and Ciardi 2009; Joos et al. 2012). Nevertheless, misalignment alone is

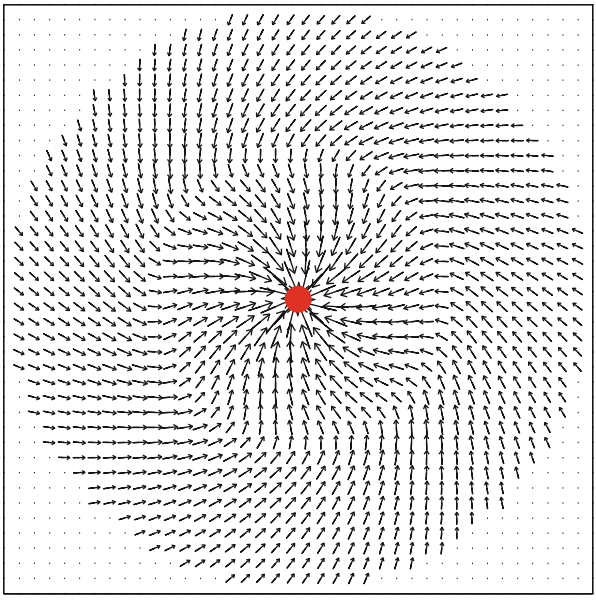

Fig. 16.1 Illustration of the velocity field of the accretion flow in the equatorial plane of a magnetized rotating cloud. In this figure the inner solution of Galli et al. (2006) has been matched to the outer rotating flow. Because the azimuthal velocity decreases as $u_\varphi \propto -jr^{1/2}$ for $r \to 0$, where j is the gas specific angular momentum at large distance, no rotationally supported disk is formed. The flow shows a counter rotation at the center, before the gas falls into the star. The magnetic field lines coincide with the streamlines outlined by the *arrows*

unlikely to solve the problem of catastrophic magnetic braking at least for cores with $\lambda \approx 2$ (Li et al. 2013). Krumholz et al. (2013) recently proposed that a combination of misalignment *and* weakness of the magnetic field may lead to the formation of disks in agreement with the observed fraction of disks around embedded protostars. However, since the mass-to-flux ratio in molecular clouds is $\lambda \sim 1$–4 as discussed in Sect. 16.1, it is clear the constraint of ideal MHD must be relaxed at some point to allow the formation of rotationally (rather than magnetically) supported disks.

Shu et al. (2006) solved analytically the problem of gravitational collapse of a magnetized cloud with a uniform resistivity η, in the kinematic approximation, i.e. neglecting the back reaction of the magnetic field on the motion of the gas (Fig. 16.2). Under this simplifying assumption, dissipation of the magnetic field occurs inside a sphere with radius $r_{\rm Ohm}$, that is inversely proportional to the instantaneous stellar mass $M_*(t)$, and proportional to the square of the electrical resistivity η, which may include Ohmic dissipation and AD:

$$r_{\rm Ohm} \equiv \frac{\eta^2}{2GM_*} \approx 10 \left(\frac{\eta}{10^{20}\ {\rm cm^2\ s^{-1}}} \right)^2 \left(\frac{M_*}{M_\odot} \right)^{-1} {\rm AU}. \qquad (16.3)$$

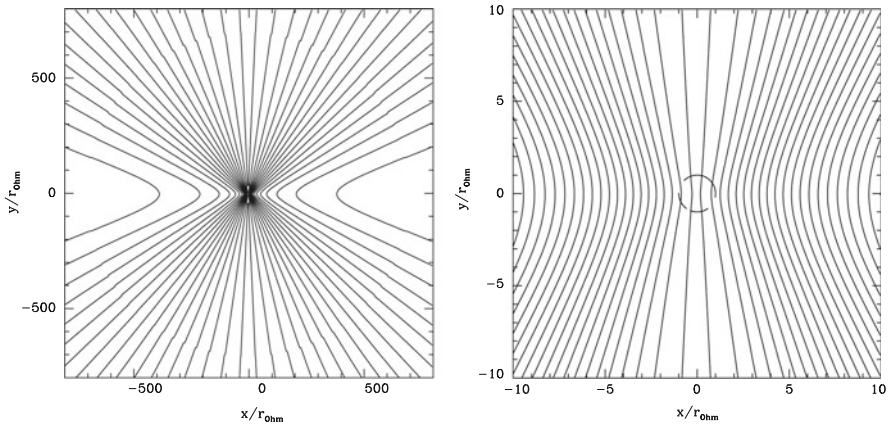

Fig. 16.2 Magnetic field configuration in the meridional plane for magnetized cloud collapse with uniform resistivity. Distances are measured in units of the Ohm radius $r_{\rm Ohm}$. The *left panel* shows the field lines at large distance from the central source, inside the region of radius $\leq 500\, r_{\rm Ohm}$. The *right panel* shows the field lines inside a region of radius $\leq 10\, r_{\rm Ohm}$ from the center. The *dashed circle* has a radius equal to $r_{\rm Ohm}$ (figure from Galli et al. 2009)

Shu et al. showed that for values of $\eta \sim 10^{20}\,{\rm cm^2\,s^{-1}}$, the strength of the uniform magnetic field around the accreting protostar is $B \sim 1$ G, of the order of the measured values in meteorites. This anomalous resistivity is a few orders of magnitude larger than the microscopic resistivity found by Nakano et al. (2002) for the densities and ionization conditions of pseudo-disks (see also Li et al. 2011). Krasnopolsky et al. (2010) performed axisymmetric numerical simulations of resistive MHD relaxing the kinematic approximation, and found that lower values of the resistivity $\eta \sim 10^{19}\,{\rm cm^2\,s^{-1}}$ were enough to allow the formation of RSDs. Shu et al. also pointed out that the luminosity resulting from the Ohmic dissipation of the electric current can be very large,

$$L_{\rm Ohm} \sim 300\,\lambda^{-2} \left(\frac{M_*}{M_\odot}\right)^5 \left(\frac{\eta}{10^{20}\,{\rm cm^2\,s^{-1}}}\right)^{-5} L_\odot. \tag{16.4}$$

In fact, the resistivity cannot be much smaller than the values quoted above, without violating the constraints on the observed protostellar luminosity.

Krasnopolsky and Königl (2002) and Braiding and Wardle (2012) studied self-similar 1-D models of the gravitational collapse of a flattened rotating, magnetized cloud. Krasnopolsky and Königl found that magnetic flux piles up at the so-called "AD shock" increasing the efficiency of magnetic braking. Braiding and Wardle included also the Hall effect and found that RSDs could form for appropriate values of the Hall coefficient and orientation of the magnetic field, since the Hall diffusion is not invariant under field reversal. However, in these self-similar models the diffusion coefficients scale as $c_s^2 t$. Thus, at typical times, $t \sim 10^{4-5}$ yr, and for

$c_s \sim 0.2\,\mathrm{km\ s^{-1}}$, they have values $\sim 10^{20}$–$10^{21}\,\mathrm{cm^2\ s^{-1}}$, larger than the expected microscopic values, in agreement with Shu et al. (2006).

In recent years, several MHD simulations have been carried out that include different non-ideal processes: Ohmic dissipation, AD, and the Hall effect (see, e.g., Mellon and Li 2009; Krasnopolsky et al. 2010, 2011; Li et al. 2011). These simulations find that, for realistic levels of cloud magnetization and cosmic ionization rates, flux redistribution by AD is not enough to allow the formation of a RSD; and, as discussed above, in some cases, AD can even enhance the magnetic braking. They also require anomalous Ohmic resistivity to form RSDs, and find that the Hall effect can spin up the gas even in the case of an initially non-rotating cloud, although the disks formed this way are sub-Keplerian. These authors conclude that the combined effects of these diffusion mechanisms may weaken the magnetic braking enough to form RSDs.

Machida et al. (2011) performed 3-D resistive MHD simulations of the collapse of strongly magnetized clouds ($\lambda \approx$1–3). Keeping the magnetic field anchored in the cloud's envelope, they found that the efficiency of magnetic braking depends on disk/envelope mass ratio: magnetic braking is very efficient during the main accretion phase when the envelope is much more massive than the forming disk and the disk radius remains $\sim$10 AU or less; magnetic braking then becomes largely ineffective when most of the envelope mass has been accreted by the star/disk system. As a consequence, the disk expands to a radius of $\sim$ 100 AU during the late accretion phase, when the residual envelope mass is reduced to $\sim$ 70–80 % of the initial value (for a low-mass core). This work suggests that Class 0 sources would have small disks, while older sources would develop the observed hundred AU disks, a prediction that could be tested by the new generation interferometer ALMA. In contrast with all other ideal MHD simulations, Machida et al. also found the formation of a RSD in the ideal MHD regime. A convergence study is necessary to asses the possible influence of numerical diffusion in this result. Also Dapp and Basu (2010) and Dapp et al. (2012) find that Ohmic dissipation with normal microscopic values is effective at high densities and RSDs can form. Nevertheless, their simulations address very early times, when the disk has a size of only several stellar radii around a protostar with mass $\sim 10^{-2}\,M_\odot$. In particular, their simulations are stopped when the expansion wave is only 15 AU away. This is too early in the protostellar evolution process to determine the possibility that the disk can survive through all the accretion phase.

Another diffusion mechanism that has been proposed recently is the reconnection diffusion of the magnetic field in a turbulent medium (Lazarian and Vishniac 1999). Santos-Lima et al. (2012) performed collapse simulations to study this process and find a disk that is rotationally supported at radii between $\sim$ 65–120 AU. However, large levels of turbulence were injected in the simulation such that the turbulent Mach number produced in this way starts at four and increases with time. This is in contrast with the observations that indicate that dense cores are quiescent with the presence of only subsonic turbulence (e.g., Pineda et al. 2010). Moreover, since this process relies on numerical diffusion to mimic the process of field reconnection,

a convergence study is needed to establish the physical properties of the disks produced this way. Seifried et al. (2012) also included turbulence in ideal MHD simulations and claimed that this effect alone can lead to the formation of RSDs, without the requirement of magnetic flux loss. These authors acknowledge a very high numerical diffusion in the region of disk formation that, as discussed above, probably accounts for the field dissipation and the weakening of the magnetic braking. Furthermore, Santos-Lima et al. (2013) argued that their apparent constant mass-to-flux ratio is due to their averaging over a large volume which can mask the flux loss.

It is interesting to notice that several numerical simulations have found that the efficient braking and extra support provided by magnetic fields inhibit cloud fragmentation (e.g., Hosking and Whitworth 2004; Hennebelle and Teyssier 2008; Duffin and Pudritz 2009; Commerçon et al. 2010, Commerçon et al. 2011). Also, the MHD numerical simulations that have been carried out to study the problem of magnetic field diffusion assume in general an isothermal equation of state and do not compute the energy released by field dissipation. This power could be appreciable (see Eq. (16.4)), and would be available to heat the gas and the dust and increase the ionization.

In conclusion, how observed RSDs are formed around protostars is still an open question. The answer is probably a combination of diffusive processes at high densities plus the dissipation of the core envelope where the angular momentum is deposited by magnetic braking.

16.3.2 Measurements of Mass-to-Flux Ratios in Protostellar Disks

It is possible to estimate the values of the mass-to-flux ratio of some star-disk systems and compare them to the measured values in molecular cloud cores. This comparison provides an observational constraint on the amount of magnetic flux dragged by the disk. At very large disk radii, magnetic field strengths of the order of a few mG have been measured by Zeeman splitting in OH maser rings associated to high-mass protostars (see Table 16.1 for references). These ringlike configurations have radii of order 10^3 AU, are elongated in the direction perpendicular to the outflow, and are usually characterized by a linear velocity gradient, suggestive of rotation or accelerated expansion (see Cesaroni et al. 2007 for a review). In general, these observations suggest that, at these radii, the field is mostly poloidal, although the presence of reversals might indicate the presence of a toroidal component probably generated by rotation. Assuming that these measurements actually probe a disk field and that it is possible to estimate the system mass from the observed kinematics of the maser rings, one can obtain the mass-to-flux ratio of the system. If the vertical component of the field B_z scales with radius like $B_z(\varpi) \propto \varpi^{-(1+\alpha)}$, with $\alpha \approx 3/8$ (Shu et al. 2007; see also discussion in Sect. 16.3), most of the

Table 16.1 Estimates of the mass-to-flux ratio λ_{sys} in circumstellar disks around massive stars from OH Zeeman measurements

Source	u_φ (km s^{-1})	B_z (mG)	ϖ (10^3 AU)	λ_{sys}	Reference
W57N	6	7	3	2.7	Hutawarakorn et al. (2002)
IRAS20126	3	11	0.85	1.5	Edris et al. (2007)
G35.2–0.74N	5	5	2.6	3.1	Hutawarakorn and Cohen (1999)
AFGL2591	5	4	0.75–1.5	6.7–13	Hutawarakorn and Cohen (2005)

disk magnetic flux Φ_d is at large radii, $\Phi_d = 2/(1-\alpha)B_z(\varpi)\varpi^2$. The enclosed mass of disk plus star can be estimated from the observed rotation, such that $G(M_d + M_*) \approx u_\varphi^2(\varpi)\varpi$. With these assumptions, the mass-to-flux ratio of the system is

$$\lambda_{sys} = \frac{2\pi G^{1/2}(M_* + M_d)}{\Phi_d} \approx (1-\alpha)\frac{u_\varphi^2(\varpi)}{G^{1/2}B_z(\varpi)\varpi}. \tag{16.5}$$

Inserting the values of B_z, u_φ, and ϖ measured in OH maser rings around a few high-mass protostars (see Table 16.1), we obtain values of λ_{sys} in the range 2–13. Comparing these values of λ_{sys} to the values $\lambda \approx 2$ typical of protostellar cores, we conclude that the mass-to-flux ratio of circumstellar disks around massive stars is somewhat larger, but not by a large factor, than the mass-to flux ratio of the parent cloud. In other words, the magnetic flux trapped in circumstellar disks around stars of mass $M_* \approx 10\ M_\odot$ is only a factor of a few smaller than the flux that would be trapped in the system under field-freezing. These results, if confirmed, suggest that the solution to the catastrophic magnetic braking problem discussed in Sect. 16.3.1 does not require a strong annihilation of magnetic field in the circumstellar region (by, e.g., reconnection and/or turbulence), but rather a redistribution of the field (by a microscopic or macroscopic process) towards a quasi-force-free configuration. In this respect, it will be very important to obtain the mass-to-flux ratios also in disks around low-mass stars, an endeavor that ALMA will make possible in the near future (see chapter by Vlemmings in this volume).

16.4 Magnetized Accretion Disks

16.4.1 Viscosity and Resistivity

As discussed in the previous section, the RSDs drag a fraction of the magnetic flux from the parent core during the gravitational collapse. Once the accretion has stopped, the magnetized disk will evolve subject to two diffusive processes: viscosity, ν, due to turbulent and magnetic stresses, that produces accretion toward

the star and transfer of angular momentum outside; and resistivity, η, due to microscopic collisions and the magnetorotational instability (MRI; see, e.g., review of Balbus and Hawley 1998), which allows matter to slip across field lines. The MRI is considered responsible for the disk "anomalous" viscosity needed to explain the disks lifetimes of ∼few $\times 10^6$ yr (Haisch et al. 2001; Sicilia-Aguilar et al. 2004). As pointed out by Shu et al. (2007), even in the case of a strong poloidal field, magnetized accretion disks can develop the MRI instability.

In these disks, the dragging of field lines by accretion is balanced by the outward field diffusion only if the ratio $\eta/\nu \sim z_0/\varpi \ll 1$, where z_0 is the vertical half disk thickness and ϖ is the radial cylindrical coordinate (Lubow et al. 1994). This result is at variance with the usual assumption of a magnetic Prandtl number $\nu/\eta \sim 1$ in magnetized disks. Moreover, the magnetic tension due to the poloidal magnetic field threading the disk will produce sub-Keplerian rotation (Shu et al. 2007).

In near field freezing conditions, the accretion flow generates a mean radial field from the mean vertical field. This mean radial field has two important consequences: First, it changes the radial force balance and causes sub-Keplerian rotation of the gas. If one neglects the disk self-gravity and gas pressure, the force balance equation is

$$\varpi \Omega^2 = -\frac{B_z B_\varpi^+}{2\pi\Sigma} + \frac{GM_*}{\varpi^2}, \tag{16.6}$$

where Ω is the rotation rate, Σ is the disk mass surface density, B_z is the component of the magnetic field threading vertically through the disk, and B_ϖ^+ is the radial component of the magnetic field just above the disk that responds to the radial accretion flow. The rotation rate, given by the solution of the above equation, is smaller than the Keplerian value $\left(GM_*/\varpi^3\right)^{1/2}$, because of the extra support of the magnetic tension against gravity,

$$\Omega = f\left(\frac{GM_*}{\varpi^3}\right)^{1/2}, \quad \text{with the sub-Keplerian factor } f < 1. \tag{16.7}$$

Note that the field lines are bent because the sources of the disk magnetization are currents at infinity anchoring magnetic field lines to the parent cloud. Second, the stretching of the poloidal field by differential rotation produces an azimuthal field in the disk that, coupled with the radial field, exerts a mean stress and torques the gas, allowing the disk viscous evolution. In the absence of numerical simulations of the MRI that are both global and have a non-zero net magnetic flux, Shu et al. (2007) proposed a functional form of the viscosity based on mixing length arguments,

$$\nu = D\frac{B_z^2 z_0}{2\pi\Sigma\Omega}, \tag{16.8}$$

where $D \leq 1$ is a dimensionless coefficient. Since, as discussed above, the resistivity η is related to viscosity in steady state, for f = constant, Shu et al.

were able to construct full radial models of disks around young stars. They find that the disk masses, sizes and magnetic field strengths are consistent with the observations. The coefficient D should acquire small values if there are substantial "dead zones", where the ionization is too low to couple to magnetic fields except, possibly, for thin surface layers (as could be the case in disks around T Tauri stars). They propose that rapid transport of mass and magnetic fluctuations across strong mean field lines can occur through the reconnection of small magnetic loops, twisted and bent by the turbulent flow, this process being the source of the disk viscous and resistive diffusivities. Since the microscopic disk resistivities drop at large radii ($\varpi > 10-20$ AU; see, e.g., Sano et al. 2000), Shu et al. conclude that the MRI has to provide the anomalously large value of the resistivity in the outer disk in order to allow accretion to continue to the central star.

For a disk model with standard flaring ($z_0 \propto \varpi^{5/4}$) Eq. (16.6) can be recast in the form

$$1 - f^2 = \frac{0.5444}{\lambda_{\rm sys}^2} \left(\frac{M_*}{M_d} \right). \tag{16.9}$$

For a closed star plus disk system in which infall has ceased, the mass-to-flux ratio $\lambda_{\rm sys}$ remains constant. Then, since disk accretion decreases the disk mass M_d relative to stellar mass M_*, the departure from Keplerian rotation, $(1 - f^2)$, must grow with time. This happens because viscosity drains mass from the disk onto the star, while resistivity can only cause the redistribution of flux within the disk but cannot change the total flux, making f decrease with time. Thus, the disk becomes more sub-Keplerian and magnetized with time.

16.4.2 Sub-Keplerian Disk Rotation

Accretion disks threaded by a poloidal magnetic field lines as shown in Fig. 16.3, bent with respect to the vertical by angles larger than 30°, are candidates to produce disk winds (Blandford and Payne 1982; for a recent review on disk winds, see, e.g. Pudritz et al. 2007). In fact, in the models of magnetized disks of Shu et al. (2007) this criterion is comfortably satisfied (see their Table 16.1). Nevertheless, sub-Keplerian rotation of the gas in accretion disks poses a problem to disk wind models. In order to launch winds, sub-Keplerian disk either have to be warm to overcome the potential barrier, or they need a dynamically fast diffusion across the magnetic field lines (Shu et al. 2008).

In the case of thermal launching, given the fractional deviation from Keplerian rotation $f < 1$, the gas needs to climb the local potential barrier in order to be ejected magnetocentrifugally along field lines. Thus, the gas requires a thermal speed

$$c_s^2 \approx \frac{1}{4}(1 - f^2)\frac{GM_*}{\varpi}. \tag{16.10}$$

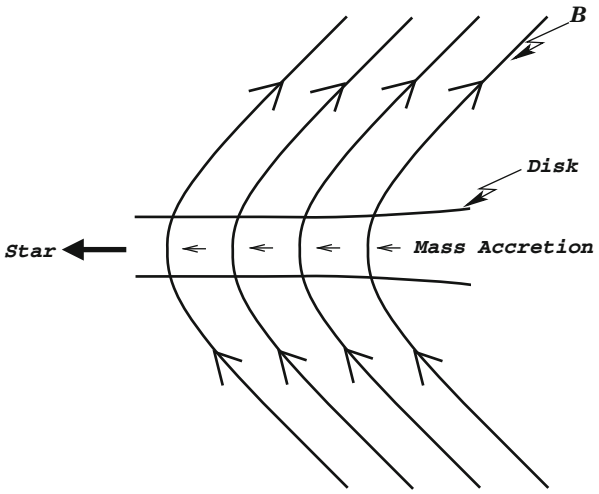

Fig. 16.3 Sketch of a magnetized disk where the field lines are dragged by the accretion flow onto the star (from Shu et al. 2007)

One can write this condition as a constraint for the gas temperature in terms of the local escape speed, $u_{esc} = \sqrt{2GM_*/\varpi}$,

$$T \approx 1.4 \times 10^6 \left(1 - f^2\right) \left(\frac{u_{\rm esc}}{200\,{\rm km\,s^{-1}}}\right) K. \tag{16.11}$$

Thus, for a deviation from Keplerian rotation as small as $f = 0.95$, typical of protostellar disks, the gas temperature need to be as large as $T \sim 1.4 \times 10^5\, K$ to eject a disk wind that can reach typical protostellar speeds of $\sim$200 km s^{-1}. Since the disks around young stars are cold ($T < 1{,}000$ K; e.g., D'Alessio et al. 1999) thermal launching is not a viable mechanism for magnetocentrifugal disk winds.

Resistive launching is in fact used by current disk wind models that use large resistivities that allow the gas to diffuse vertically across magnetic field lines to the launching point where $f = 1$ (see, e.g., Fig. 5 of Ferreira and Pelletier 1995 showing f as a function of height). Nevertheless, fast diffusion also occurs radially, and, as a result, these models have accretion speeds of the order of the sound speed, $u_\varpi \sim c_s$. Such large speeds imply too short accretion timescales

$$\tau_{\rm acc} = \frac{\varpi}{u_\varpi} \sim 2,400 \left(\frac{\varpi}{100\,{\rm AU}}\right) \left(\frac{c_s}{0.2\,{\rm km\,s^{-1}}}\right)^{-1} {\rm yr}, \tag{16.12}$$

i.e., these models have too short disk lifetimes (see Sect. 16.4.1).

Therefore, magnetocentrifugally-driven, cold, disk wind models need to face the challenge imposed by the sub-Keplerian gas rotation due to the support provided by

magnetic tension by a dynamically important poloidal field: disk winds cannot be launched thermally and diffusive launching makes the disks short lived.

16.4.3 Stability and Planet Formation

Gravitational instabilities in accretion disks around young stars can grow in the nonlinear regime and produce secondary bodies within the disk, such as brown dwarfs and giant planets. On the other hand, if the growing perturbations saturate, the gravitational torques can lead to redistribution of angular momentum and disk accretion. In non magnetic disks, both processes require the onset of gravitational instability, which, for axisymmetric perturbations, is determined by the value of the Toomre parameter Q_T,

$$Q_T \equiv \frac{c_s \kappa}{\pi G \Sigma}\,, \tag{16.13}$$

where $\kappa = \varpi^{-1}[\partial(\varpi^2\Omega)^2/\partial\varpi]^{1/2}$ is the epicyclic frequency (Toomre 1964).

In the presence of magnetic fields, however, the condition of gravitational instability is modified. The modification to the Toomre criterion for a magnetized disk has been discussed previously in the Galactic context by several authors (e.g., see Elmegreen 1994). However the magnetic field in the Galaxy is likely to be dynamo-generated and mostly toroidal (see chapter by Beck, this volume), whereas in a circumstellar disk the magnetic field is expected to be mostly poloidal and dragged from the parent cloud. From a linear stability analysis, Lizano et al. (2010) derived the modified Toomre Q_M parameter for a disk threaded by a poloidal magnetic field, which provides the boundary of stability for axisymmetric ($m = 0$) perturbations, given by

$$Q_M = \frac{\Theta^{1/2} a \kappa}{\pi \epsilon G \Sigma_0}\,, \tag{16.14}$$

where

$$\Theta \equiv 1 + \frac{B_z^2 z_0}{2\pi \Sigma c_s^2} \quad \text{and} \quad \epsilon \equiv 1 - \frac{1}{\lambda^2}\,, \tag{16.15}$$

and $\lambda = 2\pi G^{1/2}\Sigma/B_z$ is the local value of the mass-to-flux ratio in the disk. For $Q_M < 1$, perturbations with wavenumber between $k_\pm = k_{\max}(1 \pm \sqrt{1 - Q_M^2})$ are unstable, with $k_{\max} = (\epsilon/\Theta)k_J$ being the wavenumber of maximum growth, and $k_J = \pi G \Sigma / c_s^2$ the Jeans wavenumber. Since $\epsilon/\Theta < 1$, the effect of the magnetic field is to increase the length scale of the gravitational instability with respect to the Jeans length scale.

Another important factor that determines Q_M in Eq. (16.14) is the epicyclic frequency. As discussed in Sect. 16.4.1, magnetized disks around young stars rotate at sub-Keplerian speeds because magnetic tension modifies the force balance equation, then $\kappa = f\Omega_K$. Therefore, the inclusion of magnetic fields produces competing effects on the instability parameter Q_M: the strong fields enforce sub-Keplerian flow, which reduces Q_M and leads to greater instability; on the other hand, both magnetic pressure and magnetic tension act to increase Q_M and lead to enhanced stability. For typical disks around low- and high-mass stars, the stabilizing effect wins in the inner regions, as shown in Fig. 16.4. Thus, stable magnetized disks can be more massive than their non-magnetized counterparts. The two panels in Fig. 16.4 show the values of the parameters Q_T, Q_M and the local mass-to-flux ratio λ, for the disk models of Shu et al. (2007) as function of the normalized disk radius ϖ/R_d. Since Q_M is always larger than Q_T, the magnetic field has a stabilizing effect against gravity, and the radius of the stable region increases by $\sim$ 20–30 %

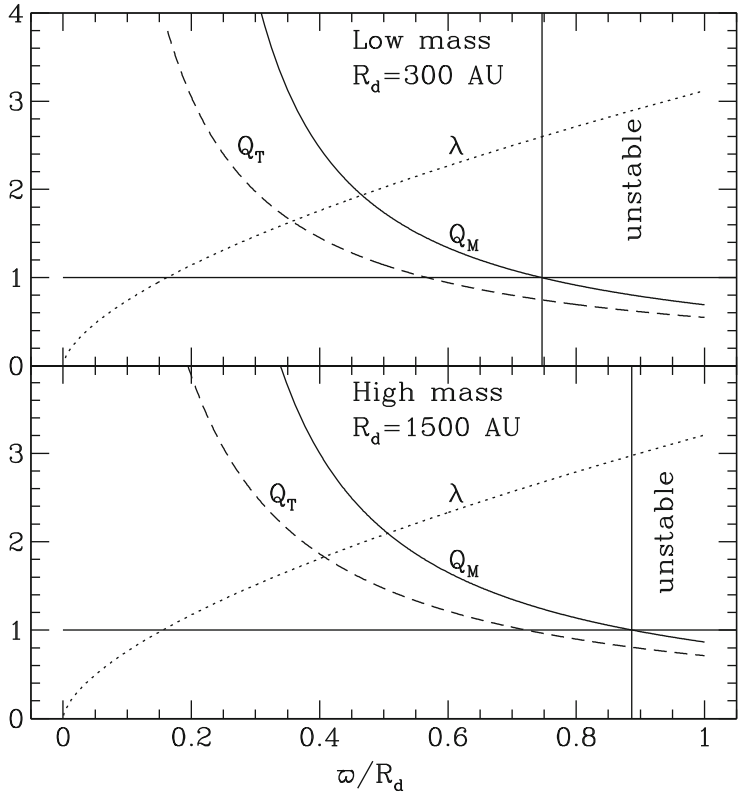

Fig. 16.4 Radial profiles of the Toomre stability parameter Q_T, the magnetic stability parameter Q_M, and the local mass-to-flux ratio λ in typical disks around high-mass stars (*lower panel*) and low-mass stars (*upper panel*). These profiles are obtained from the disk models of Shu et al. (2007) with an aspect ratio $\propto \varpi^{1/4}$. The radial coordinate is normalized to the disk radius R_d

with respect to a nonmagnetic disk. Correspondingly, the fraction of stable enclosed disk mass, $m(\varpi)/M_d$, where M_d is the total disk mass, increases by $\sim$ 30–40 %. Also, the unstable region is magnetically supercritical ($\lambda > 1$), as required to allow local gravitational collapse.

The increased stability of magnetized disks against gravitational perturbations poses an obstacle to the formation of giant planets, or somewhat larger secondary bodies such as brown dwarfs, by this process. As discussed by Lizano et al. (2010), the formation of giant planets in the outer parts of disks where $Q_M < q_* \approx 2$ has to satisfy, in addition, the condition of short cooling time $\tau_{\rm cool}$, and the rapid loss of an appreciable amount of magnetic flux. The coupled constraints on Q_M and $\tau_{\rm cool}$ result in a condition for the Minimum Mass Solar Nebula (MMSN) disk, on the minimum radius outside which giant planet formation can occur,

$$\varpi > 1100\,(f\mathscr{F})^2 \ {\rm AU}, \tag{16.16}$$

where $\mathscr{F} \approx 0.5$ is a nondimensional quantity that depends on the mass-to-flux ratio λ. The condition on the magnetic flux loss gives a constraint on the disk resistivity

$$\eta > 2.5 \times 10^{18}\,{\rm cm^2\,s^{-1}}, \tag{16.17}$$

larger than the microscopic resistivity.

Therefore, magnetic fields stabilize protoplanetary disks, and make it more difficult to form giant planets via gravitational instability. At any rate, this process can occur only at large radii.

16.4.4 Implications of Disk Magnetization for Planet Migration

Protoplanets experience orbital migration due to angular momentum exchange by tidal interactions with the disk material. There are several types of tidal interactions that occur through wave excitation or advected disk material: Type I migration applies to embedded protoplanets; Type II migration occurs when the protoplanet is massive enough to open a gap; and Type III migration is driven by coorbital torques (see review Papaloizou and Terquem 2006). In magnetized disks, sub-Keplerian rotation results in a new migration mechanism for embedded proto-planets (Adams et al. 2009). These bodies rotating at Keplerian speed, $\Omega_K = (GM_*/r^3)^{1/2}$, where r is the planet semi-major axis, experience a headwind against the magnetically controlled gas that rotates at sub-Keplerian speeds. The drag force drives their inward migration. The relative speed between the gas and the proto-planet is $u_{\rm rel} = (1-f)\Omega_K r$, and the torque is

$$T = C_D \pi R_P^2 r \rho_g u_{\rm rel}^2 = \frac{\pi}{2} C_D\,(1-f)^2\,\Omega_K^2 r^3 R_P^2 \left(\frac{\Sigma}{z_0}\right), \tag{16.18}$$

where $C_D \sim 1$ is the drag coefficient, R_P is the planet radius, $\rho_g = \Sigma/2z_0$ is the gas density, and z_0 is the disk scale height. Assuming circular orbits, the time change of the planet's angular momentum gives the time evolution of r

$$\frac{1}{r}\frac{dr}{dt} = \frac{2T}{m_P \Omega_K r^2}, \tag{16.19}$$

that implies a migration timescale $t_M \sim 70{,}000$ year for an Earth-like planet in a MMSN disk with $f \sim 0.66$.

This mechanism dominates over Type I migration for sufficiently small planets with masses $m_P \leq 1 M_{\rm Earth}$, and/or close orbits $r < 1$ AU. Taking into account both mechanisms, the total migration time t_M moderately decreases due to the sub-Keplerian torques, but the mass accreted by planetary cores during the migration epoch changes more substantially, as shown in Fig. 16.5. Furthermore, Paardekooper (2009) showed that disk-planet interactions in Type I migration are affected by the degree of disk sub-Keplerian rotation because the position of the Lindblad and corotation resonances change with the sub-Keplerian factor f. Paardekooper concluded that migration in sub-Keplerian disks, in general, will be directed inwards and will be sped up compared to Keplerian disks. In general, Type I migration is very fast, with timescales of the order of 10^5 year, implying that low-mass planets have a hard time surviving in gaseous disks; thus, they would need to form at later times,

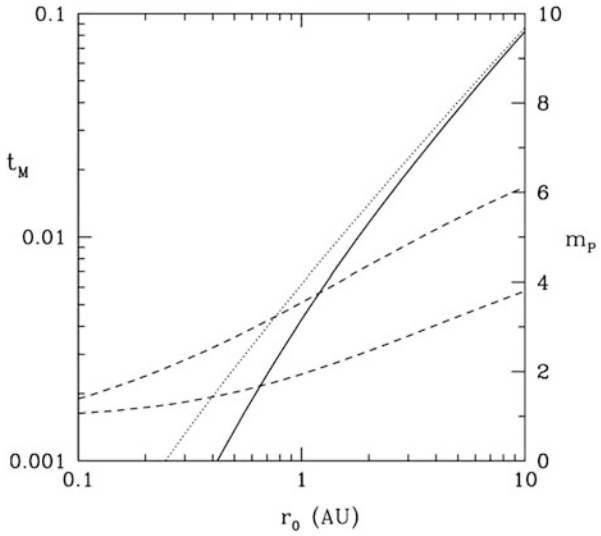

Fig. 16.5 Migration time and final core mass versus starting radius, r_0. The *solid curve* shows migration time t_M in Myr (left axis) including sub-Keplerian and Type I torques. The *dotted curve* shows t_M for Type I torques only. The *dashed curves* show the final core mass m_P in $M_{\rm Earth}$ (right axis) for migration with both torques (*bottom*) and Type I torques only (*top*) (from Adams et al. 2009)

when the gas has been accreted or dispersed. Moreover, as discussed by Papaloizou and Terquem (2006), even the survival of the rocky cores of giant planets would be compromised unless this type of migration is somehow suppressed or modified by, for example, eccentricity effects (Papaloizou 2002), large scale toroidal magnetic fields (Terquem 2003), stocastic torques due to the presence of turbulence (Nelson and Papaloizou 2004; Laughlin et al. 2004; Adams and Bloch 2009); or by disk opacity effects (Menou and Goodman 2004; Paardekooper and Mellema 2006).

Conclusion

Magnetic fields are dynamically important for star formation. The measured levels of cloud magnetization, $\lambda = 1-4$, imply that the clouds are close to the critical value of the mass-to-flux ratio to provide support against gravitational collapse. Also, observations of polarized dust emission and statistical analysis of polarization maps strongly suggest that the field is well ordered on pc scales, and has only a relatively small turbulent component.

Although it has been believed since the 1970s that magnetic braking is responsible for the loss of angular momentum in cloud cores, an unexpected result has been the theoretical finding that in an ideal MHD flow the magnetic braking becomes so efficient as to prevent the formation of centrifugally supported disks. Therefore, magnetic field diffusion and/or dissipation in the high density regime of gravitational collapse is needed to avoid catastrophic braking. Field dissipation was also advocated to solve the magnetic flux problem in newly born stars. Several non ideal MHD diffusion processes, able to redistribute the magnetic field brought by gravity in the collapse region, have been studied in analytic and numerical simulations to alleviate the catastrophic magnetic braking, but all of them have been found relatively inefficient. Thus, at the moment, the problem has not yet been resolved. Conversely, solutions based on magnetic reconnection may require high levels of turbulence, which are generally not observed in dense cloud cores.

Once the centrifugally supported disks form, they are expected to have important levels of magnetization due to the incomplete diffusion and/or dissipation of the magnetic field dragged during the gravitational collapse. The strong poloidal field produces sub-Keplerian rotation of the gas because magnetic tension provides support against gravity. This slower rotation poses a local potential barrier that disk winds have to overcome, either by thermal pressure or by fast diffusivity, to reach the launching point where magnetocentrifugal acceleration can take place. Since thermal launching is not possible in cold disks around low-mass stars, disk wind models rely on fast diffusion of the gas across field lines. However, this fast diffusion also produces accretion flows with velocities of the order of the sound speed, that will empty the disk into the star in very short timescales, of only several thousand years. Up to

(continued)

now, no solution has been proposed to this conundrum. Sub-Keplerian rotation of the gas in the disk also produces a headwind on forming proto-planets that move at Keplerian speeds, making them lose angular momentum and migrate faster toward the central star.

Finally, the magnetic fields modify the disk stability by two opposing effects: magnetic pressure and tension support the gas against gravitational collapse, but sub-Keplerian rotation makes the gas locally more unstable. The resulting magnetically modified Toomre stability parameter, Q_M, is in general larger than its nonmagnetic counterpart in accretion disks around young stars. Thus, stable magnetized disks can be more massive that nonmagnetic disks. The region of instability is pushed at larger radii, making it more difficult to form giant planets via gravitational instability.

In the near future, ALMA will be able to measure magnetic fields and disk rotation curves with unprecedented spatial resolution and test the theoretical models discussed here. BLAST-pol will map the magnetic field direction of a large sample of molecular clouds and determine the relative strength of the large scale versus the turbulent magnetic field components testing the importance of magnetic fields in cloud support and evolution.

Acknowledgements S. L. and D. G. acknowledge support from the Scientific Cooperation Agreement Mexico-Italy MX11M07: "The formation of disks and planets around young stars". S. L. also acknowledges support from PAPIIT-UNAM IN100412. The authors thank Fred C. Adams, Anthony Allen, Michael J. Cai, Alfred E. Glassgold, and Frank H. Shu for a longtime enjoyable collaboration, and an anonymous referee for a detailed and thoughtful report.

References

Adams, F.C., Bloch, A.M.: Astrophys. J. **701**, 1381 (2009)
Adams, F.C., Shu, F.H.: Astrophys. J. **671**, 497 (2007)
Adams, F.C., Cai, M.J., Lizano, S.: Astrophys. J. Lett. **702**, L182 (2009)
Allen, A., Shu, F.H., Li, Z.-Y.: Astrophys. J. **599**, 351 (2003)
Armitage, P.J.: Ann. Rev. Astron. Astrophys. **49**, 195 (2011)
Balbus, S.A., Hawley, J.F.: Rev. Mod. Phys. **70**, 1 (1998)
Ballesteros-Paredes, J., Hartmann, L.W., Vázquez-Semadeni, E., Heitsch, F., Zamora-Avilés, M.A.: Mon. Not. R. Astron. Soc. **411**, 65 (2011a)
Ballesteros-Paredes, J., Vázquez-Semadeni, E., Gazol, A., et al.: Mon. Not. R. Astron. Soc. **416**, 1436 (2011b)
Blandford, R.D., Payne, D.G.: Mon. Not. R. Astron. Soc. **199**, 883 (1982)
Braiding, C.R., Wardle, M.: Mon. Not. R. Astron. Soc. **422**, 261 (2012)
Caselli, P., Walmsley, C.M., Terzieva, R., Herbst, E.: Astrophys. J. **499**, 234 (1998)
Cesaroni, R., Galli, D., Lodato, G., Walmsley, C.M., Zhang, Q.: Protostars and Planets, vol. 197. University of Arizona Press, Tucson (2007)
Chandrasekhar, S., Fermi, E.: Astrophys. J. **118**, 113 (1953)

Commerçon, B., Hennebelle, P., Audit, E., Chabrier, G., Teyssier, R.: Astron. Astrophys., **510**, L3 (2010)
Commerçon, B., Hennebelle, P., Henning, T.: Astrophys. J. Lett. **742**, L9 (2011)
Crutcher, R.M.: Ann. Rev. Astron. Astrophys. **50**, 29 (2012)
Crutcher, R.M., Troland, T.H.: Astrophys. J. **685**, 281 (2008)
D'Alessio, P., Calvet, N., Hartmann, L., Lizano, S., Cantó, J.: Astrophys. J. **527**, 893 (1999)
Dapp, W.B., Basu, S.: Astron. Astrophys. **521**, L56 (2010)
Dapp, W.B., Basu, S., Kunz, M.W.: Astron. Astrophys. **541**, A35 (2012)
Duffin, D.F., Pudritz, R.E.: Astrophys. J. Lett. **706**, L46 (2009)
Edris, K.A., Fuller, G.A., Cohen, R.J.: Astron. Astrophys. **46**, 865 (2007)
Elmegreen, B.G.: Astrophys. J. **433**, 39 (1994)
Falgarone, E., Troland, T.H., Crutcher, R.M., Paubert, G.: Astron. Astrophys. **487**, 247 (2008)
Ferreira, J., Pelletier, G.: Astron. Astrophys. **295**, 807 (1995)
Fromang, S., Hennebelle, P., Teyssier, R.: Astron. Astrophys. **457**, 371 (2006)
Galli, D., Shu, F.H.: Astrophys. J. **417**, 220 (1993a)
Galli, D., Shu, F.H.: Astrophys. J. **417**, 243 (1993b)
Galli, D., Lizano, S., Shu, F.H., Allen, A.: Astrophys. J. **647**, 374 (2006)
Galli, D., Cai, M., Lizano, S., Shu, F.H.: RevMxAA(SC) **36**, 143 (2009)
Girart, J.M., Rao, R., Marrone, D.P.: Science **313**, 812 (2006)
Girart, J.M., Beltrán, M.T., Zhang, Q., Rao, R., Estalella, R.: Science **324**, 1408 (2009)
Goldsmith, P.F., Heyer, M., Narayanan, G., et al.: Astrophys. J. **680**, 428 (2008)
Gonçalves, J., Galli, D., Girart, J.M.: Astron. Astrophys. **490**, 2008 (2008)
Haisch, K.E., Jr., Lada, E.A., Lada, C.J.: Astrophys. J. Lett. **553**, L153 (2001)
Hennebelle, P., Ciardi, A.: Astron. Astrophys. **506**, L29 (2009)
Hennebelle, P., Fromang, S.: Astron. Astrophys. **477**, 9 (2008)
Hennebelle, P., Teyssier, R.: Astron. Astrophys. **477**, 25 (2008)
Hildebrand, R.H., Kirby, L., Dotson, J.L., Houde, M., Vaillancourt, J.E.: Astrophys. J. **696**, 567 (2009)
Hosking, J.G., Whitworth, A.P.: Mon. Not. R. Astron. Soc. **347**, 3 (2004)
Houde, M., Vaillancourt, J.E., Hildebrand, R.H., Chitsazzadeh, S., Kirby, L.: Astrophys. J. **706**, 1504 (2009)
Hutawarakorn, B., Cohen, R.J.: Mon. Not. R. Astron. Soc. **303**, 845 (1999)
Hutawarakorn, B., Cohen, R.J.: Mon. Not. R. Astron. Soc. **357**, 338 (2005)
Hutawarakorn, B., Cohen, R.J., Brebner, G.C.: Mon. Not. R. Astron. Soc. **330**, 349 (2002)
Johns-Krull, C.M., Valenti, J., Koresko, C.: Astrophys. J. **516**, 900 (1999)
Johns-Krull, C.M., Valenti, J.A., Saar, S.H.: Astrophys. J. **617**, 1204 (2004)
Joos, M., Hennebelle, P., Ciardi, A.: (2012). arXiv:1203.1193
Klessen, R.S., Ballesteros-Paredes, J., Vázquez-Semadeni, E., Durán-Rojas, C.: Astrophys. J. **620**, 786 (2005)
Königl, A., Salmeron, R.: In: Paulo J. V. Garcia (ed.) Physical Processes in Circumstellar Disks around Young Stars, vol. 283. University of Chicago Press, Chicago (2011)
Krasnopolsky, R., Königl, A.: Astrophys. J. **580**, 987 (2002)
Krasnopolsky, R., Li, Z.-Y., Shang, H.: Astrophys. J. **716**, 1541 (2010)
Krasnopolsky, R., Li, Z.-Y., Shang, H.: Astrophys. J. **733**, 54 (2011)
Krumholz, M.R., Crutcher, R.M., Hull, C.L.H.: Astrophys. J. Lett. **767**, L11 (2013)
Laughlin, G., Steinacker, A., Adams, F.C.: Astrophys. J. **608**, 489 (2004)
Lazarian, A., Vishniac, E.T.: Astrophys. J. **517**, 700 (1999)
Li, Z.-Y., Shu, F.H.: Astrophys. J. **472**, 211 (1996)
Li, Z.-Y., Krasnopolsky, R., Shang, H.: Astrophys. J. **738**, 180 (2011)
Li, Z.-Y., Krasnopolsky, R., Shang, H.: (2013). arXiv:1301.6545
Lizano, S., Shu, F.: Astrophys. J. **342**, 834 (1989)
Lizano, S., Galli, D., Cai, M.J., Adams, F.C.: Astrophys. J. **724**, 1561 (2010)
Lubow, S.H., Papaloizou, J.C.B., Pringle, J.E.: Mon. Not. R. Astron. Soc. **267**, 235 (1994)
Machida, M.N., Inutsuka, S.-I., Matsumoto, T.: Publ. Astron. Soc. Jpn. **63**, 555 (2011)

Mellon, R.R., Li, Z.-Y.: Astrophys. J. **681**, 1356 (2008)
Mellon, R.R., Li, Z.-Y.: Astrophys. J. **698**, 922 (2009)
Menou, K., Goodman, J.: Astrophys. J. **606**, 520 (2004)
Mestel, L., Spitzer, L.: Mon. Not. R. Astron. Soc. **116**, 503 (1956)
Mouschovias, T.C., Ciolek, G.E.: The Origin of Stars and Planetary Systems. NATO ASIC Proc., vol. 540, p. 305 (1999)
Mouschovias, T.C., Paleologou, E.V.: Astrophys. J., **237**, 877 (1980)
Nakamura, F., Li, Z.-Y.: Astrophys. J. **687**, 354 (2008)
Nakano, T.: Publ. Astron. Soc. Jpn. **31**, 697 (1979)
Nakano, T., Nishi, R., Umebayashi, T.: Astrophys. J. **573**, 199 (2002)
Nelson, R.P., Papaloizou, J.C.B.: Mon. Not. R. Astron. Soc. **350**, 849 (2004)
Paardekooper, S.-J.: Astron. Astrophys. **506**, L9 (2009)
Paardekooper, S.-J., Mellema, G.: Astron. Astrophys. **459**, L17 (2006)
Padoan, P., Juvela, M., Goodman, A.A., Nordlund, A.A.: Astrophys. J. **553**, 227 (2001)
Papaloizou, J.C.B.: Astron. Astrophys. **388**, 615 (2002)
Papaloizou, J.C.B., Terquem, C.: Rep. Prog. Phys. **69**, 119 (2006)
Pineda, J.E., Goodman, A.A., Arce, H.G., et al.: Astrophys. J. Lett. **712**, L116 (2010)
Pinto, C., Galli, D.: Astron. Astrophys. **484**, 17 (2008)
Pinto, C., Galli, D., Bacciotti, F.: Astron. Astrophys. **484**, 1 (2008)
Price, D.J., Bate, M.R.: Mon. Not. R. Astron. Soc. **377**, 77 (2007)
Pudritz, R.E., Ouyed, R., Fendt, C., Brandenburg, A.: Protostars and Planets vol. 277. University of Arizona Press, Tucson (2007)
Sano, T., Miyama, S.M., Umebayashi, T., Nakano, T.: Astrophys. J. **543**, 486 (2000)
Santos-Lima, R., de Gouveia Dal Pino, E.M., Lazarian, A.: Astrophys. J. **747**, 21 (2012)
Santos-Lima, R., de Gouveia Dal Pino, E.M., Lazarian, A.: Mon. Not. R. Astron. Soc. **429**, 3371 (2013)
Seifried, D., Banerjee, R., Klessen, R.S., Duffin, D., Pudritz, R.E.: Mon. Not. R. Astron. Soc. **417**, 1054 (2011)
Seifried, D., Banerjee, R., Pudritz, R.E., Klessen, R.S.: Mon. Not. R. Astron. Soc. **423**, L40 (2012)
Shu, F.H., Galli, D., Lizano, S., Cai, M.J.: Astrophys. J. **647**, 382 (2006)
Shu, F.H., Galli, D., Lizano, S., Glassgold, A.E., Diamond, P.H.: Astrophys. J. **665**, 535 (2007)
Shu, F.H., Lizano, S., Galli, D., Cai, M.J., Mohanty, S.: Astrophys. J. **682**, L121 (2008)
Sicilia-Aguilar, A., Hartmann, L.W., Briceño, C., Muzerolle, J., Calvet, N.: AJ **128**, 805 (2004)
Tang, Y.-W., Ho, P.T.P., Koch, P.M., Girart, J.M., Lai, S.P., Rao, R.: Astrophys. J. **700**, 251 (2009)
Terquem, C.E.J.M.L.J.: Mon. Not. R. Astron. Soc. **341**, 1157 (2003)
Toomre, A.: Astrophys. J. **139**, 1217 (1964)
Tomisaka, K.: Astrophys. J. **575**, 306 (2002)
Tomisaka, K., Ikeuchi, S., Nakamura, T.: Astrophys. J. **362**, 202 (1990)
Vázquez-Semadeni, E., Kim, J., Shadmehri, M., Ballesteros-Paredes, J.: Astrophys. J. **618**, 344 (2005)

Part VI
MF in Galaxies and Beyond

Chapter 17
Magnetic Fields in the Milky Way

Marijke Haverkorn

Abstract This chapter presents a review of observational studies to determine the magnetic field in the Milky Way, both in the disk and in the halo, focused on recent developments and on magnetic fields in the diffuse interstellar medium. I discuss some terminology which is confusingly or inconsistently used and try to summarize current status of our knowledge on magnetic field configurations and strengths in the Milky Way. Although many open questions still exist, more and more conclusions can be drawn on the large-scale and small-scale components of the Galactic magnetic field. The chapter is concluded with a brief outlook to observational projects in the near future.

17.1 Introduction

The Milky Way is a dynamic environment, much of which (partially) consists of plasma: stars, jets, objects such as H II regions or supernova remnants, and the general interstellar medium (ISM). No wonder that magnetic fields are ubiquitous throughout the Galaxy, in almost all astrophysical objects from strong fields in pulsar atmospheres to weak fields on scales of many kiloparsecs, threading the whole Galaxy. The importance of these magnetic fields is manifold: in the energy balance of the Milky Way, transport of angular momentum, acceleration and propagation of charged particles, gas dynamics, etc. All interstellar matter but the densest, coldest clouds is sufficiently ionized (even with an ionization degree of only 10^{-4} to 10^{-3}) for the neutral gas component to remain coupled to the ionized gas, and therefore be efficiently frozen into the magnetic field (Ferrière 2001). Equipartition of magnetic and turbulent gas density (Heiles and Haverkorn 2012) indicates that dynamical feedback of the magnetic field on the gas plays an important role.

M. Haverkorn (✉)
Department of Astrophysics/IMAPP, Radboud University Nijmegen, P.O. Box 9010, 6500 GL Nijmegen, The Netherlands

Leiden Observatory, Leiden University, P.O. Box 9513, 2300 RA Leiden, The Netherlands
e-mail: m.haverkorn@astro.ru.nl

A. Lazarian et al. (eds.), *Magnetic Fields in Diffuse Media*, Astrophysics and Space Science Library 407, DOI 10.1007/978-3-662-44625-6_17

Fully characterizing the strength, direction, and structure of the extended Galactic magnetic field threading the entire Milky Way is an extremely daunting task. This field can be regarded as a combination of a large-scale field threading the Galaxy, probably maintained by the Galactic dynamo, and a small-scale field. The small-scale field is caused by and interacts with interstellar turbulence, supernova explosions and remnants and other shock waves, and is altered by gas dynamics, magnetic reconnection, turbulence effects etc. In addition, the available observational methods detect either one component of the magnetic field (strength or direction, parallel or perpendicular to the line of sight) and/or in one particular tracer (ionized gas, dense cold gas, dense dust, diffuse dust). Lastly, some of the difficulty of determining the Galactic magnetic field stems from our vantage point inside the Milky Way. Creating a three-dimensional picture from mostly two-dimensional tracers necessitates many assumptions about the magnetic field, as well as about the thermal and cosmic ray electron distributions, and about the (local) interstellar objects and processes influencing these.

Despite the difficulties, attempts to detect and determine the Galactic magnetic field have been many in recent (and not so recent) years. This is not only because magnetic fields influence so many physical processes in the ISM, but also because of its importance to other fields in astronomy and astrophysics. For instance, the Cosmic Microwave Background (CMB) community has shown a keen interest in the Galactic magnetic field, since it produces Galactic polarized synchrotron emission which acts as a strong foreground for CMB polarization. Also, astroparticle physicists studying sources and propagation of Galactic and extragalactic cosmic rays profit from detailed magnetic field models, which predict distributions of arrival directions of (high energy) cosmic rays. In addition, high-precision cosmological studies of the Epoch of Reionization need a detailed understanding of Galactic polarization to be able to understand and subtract any polarization leaking into their extremely sensitive measurements of highly redshifted H I.

It is not possible to cover all observations of magnetic fields in the Milky Way in this review. Fortunately, I can refer to a number of complementing reviews. For observations of magnetic fields in dense clouds and their relation to star formation, see various chapters in this Volume. For a historical review on magnetic field observations in the Milky Way, see Wielebinski (2005) or Wielebinski and Beck (2010), and Ferrière (2009) provides an excellent treatise on magnetic fields in the Galactic Center. I refer to e.g., Frisch (2007) for a review on the very local ISM, including magnetic fields, and to Noutsos (2012) for a recent review on Galactic magnetic fields from Faraday rotation of pulsars and extragalactic sources. Haverkorn and Heesen (2012) published a recent review about magnetic fields in galactic haloes. I will focus here on work mostly in the last decade. For earlier reviews, see Han (2001), Wielebinski (2005), Noutsos (2012) and Heiles and Haverkorn (2012).

This chapter starts with a brief description of some terminology used in literature in Sect. 17.2. Sections 17.3–17.5 describe current knowledge of magnetic field observations in the Galactic disk, in the Galactic halo and in the combined disk-halo system, respectively. A short summary and conclusions are stated in Sect. 17.6,

and finally, Sect. 17.7 describes some recent, progressing and future observational projects which are important for the investigation of Galactic magnetic fields.

17.2 Terminology

17.2.1 Large-Scale vs Small-Scale Fields

The description of large-scale and small-scale galactic magnetic fields in the literature is often confusing, with different authors using different terminology for the same magnetic field configurations or the same words for different field structure. Here I give an overview over these different magnetic field configurations and ways to describe them.

Traditionally, galactic magnetic fields have been divided up in small-scale and large-scale fields. The term "large-scale" fields (also called regular, uniform or coherent fields) indicates the component of magnetic field that is coherent on length scales of the order of a galaxy, usually assumed to follow the spiral arms or to be ring-shaped. "Small-scale magnetic fields" (also called random, tangled, or turbulent) describe the magnetic field component connected to the turbulent ISM. The small-scale field is usually simply assumed to follow a power law with a certain outer scale, where energy is injected, which then cascades down to smaller turbulent scales until energy dissipates at the dissipation scale. Small-scale magnetic field fluctuations connected to discrete objects such as H II regions or supernova remnants warrant their own review paper and are usually treated separately from the "Galactic magnetic field", although interaction between these fields and the general Galactic magnetic field is of course pervasive.

However, lately, a third component of the magnetic field starts to be included in Galactic magnetic field studies, as it has for some time in magnetic field studies of external galaxies (see R. Beck's chapter in this volume). This component is a field of which the direction varies on small scales, but the orientation does not. Such a field can arise when a turbulent field structure is compressed into a two-dimensional structure by e.g., supernova remnant shocks, spiral arm density waves, or galactic shear. This field component is often referred to as anisotropic random, but is also called ordered random (Beck 2007) or striated (Jansson and Farrar 2012a).[1] A clear explanation of these components is given in Fig. 17.1, reproduced from Jaffe et al. (2010). The cartoons illustrate the morphology of the three components and indicate the differences between the tracers total intensity I, polarized intensity PI and rotation measures RM for different lines of sight towards these three components. Combination of these tracers makes it possible to distinguish between the three field components.

As Fig. 17.1 shows, studies using RMs alone cannot distinguish between ordered random and isotropic random field components, which are often grouped together in a "random" field. Similarly, investigations using synchrotron emission cannot

[1] Note that Jaffe et al. (2010) refer to this component as 'ordered'.

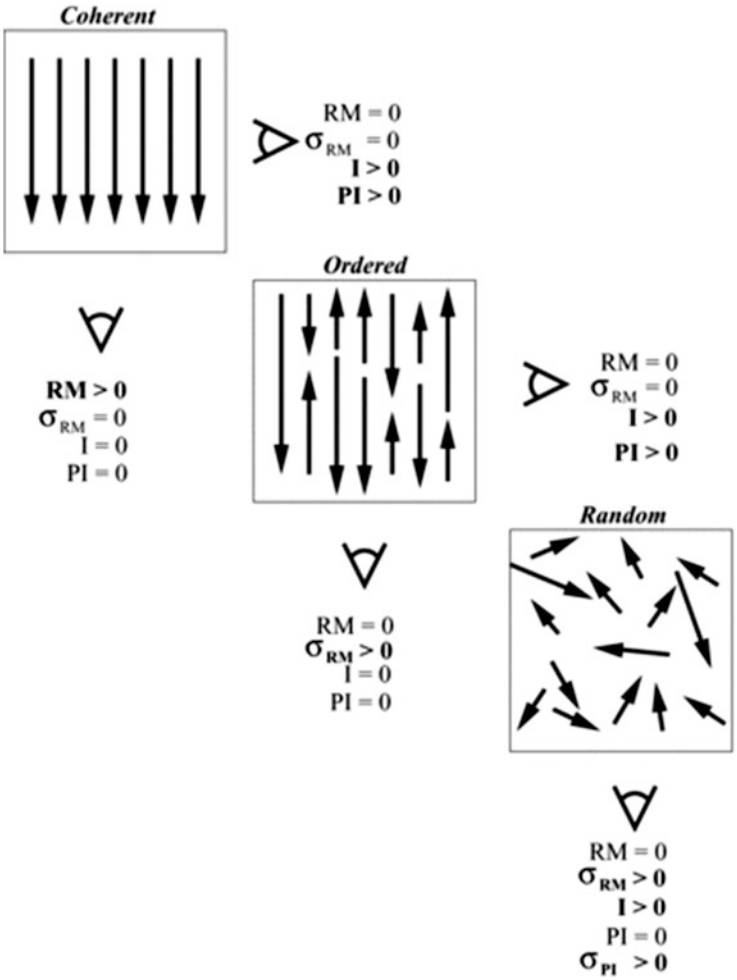

Fig. 17.1 Sketch illustrating the three components of galactic magnetic fields. For consistency in the literature, the component labeled "ordered" here should be called "ordered random" and the component labeled "random" should be "isotropic random". The three observables for these magnetic fields are total intensity I, polarized intensity PI and rotation measure RM. Image reproduced from Jaffe et al. (2010)

distinguish between coherent and ordered random field, due to which these two components are often assembled into one "ordered" component.

17.2.2 Configurations of Large-Scale Galactic Magnetic Fields

A number of fairly simple configurations have been explored for the coherent magnetic field in the Milky Way. These configurations are based on rotational

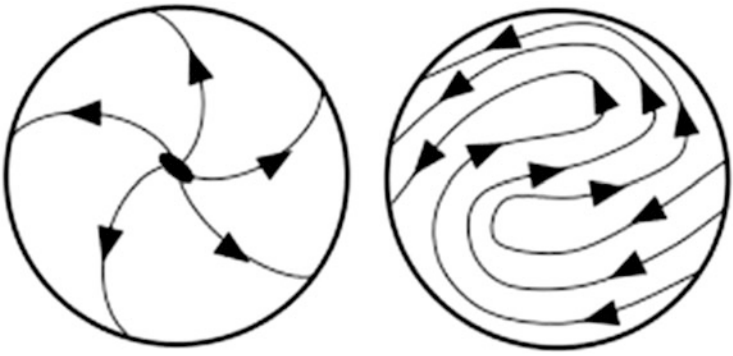

Fig. 17.2 Magnetic field configurations of the disk field: bird's-eye view of a galaxy with axisymmetric (*left*) versus bisymmetric (*right*) spiral magnetic field lines in the galactic disk. Image adapted from Brown (2010) and Zweibel and Heiles (1997)

symmetry around the Galactic Center, and on mirror symmetry with respect to the Galactic plane.

The two simplest disk configurations are an *axisymmetric*[2] and *bisymmetric* spiral structure, which denote magnetic fields oriented along the spiral arms. In the axisymmetric situation, magnetic field lines all point inwards or outwards. Bisymmetric fields are antisymmetric with respect to the spin axis of the galaxy. Therefore, the bisymmetric situation includes field reversals in the azimuthal direction (see Fig. 17.2). Axisymmetric fields are denoted by azimuthal mode $m = 0$, bisymmetric fields are $m = 1$. Higher azimuthal modes m or a mix of modes may be present, e.g., the $m = 2$ or *quadri-symmetric* mode.

The field can also be described in terms of its symmetry with respect to the Galactic plane. A *symmetric or even-parity* field has a mirrored magnetic field configuration (see Fig. 17.3). Note that this indicates a reversal of the vertical magnetic field direction across the Galactic plane, and that the toroidal component of the magnetic field points in the same direction above and below the plane. An *anti-symmetric or odd-parity* field has field lines that run through the Galactic plane, and toroidal fields that reverse direction above and below the plane.

This symmetric and anti-symmetric mirror symmetry is often denoted with S and A, respectively. This classification is followed by a number which gives the azimuthal mode number m. So, e.g., an $A0$ field configuration has an axisymmetric field, the horizontal component of which is directed in opposite directions above and below the Galactic plane.

A slightly more complex field configuration is the Disk-Even-Halo-Odd (DEHO) configuration, consisting of two independent field components for the Galactic disk and halo; as the name indicates, the vertical symmetry of this magnetic field

[2]Sometimes called *disymmetric* (Jansson et al. 2009).

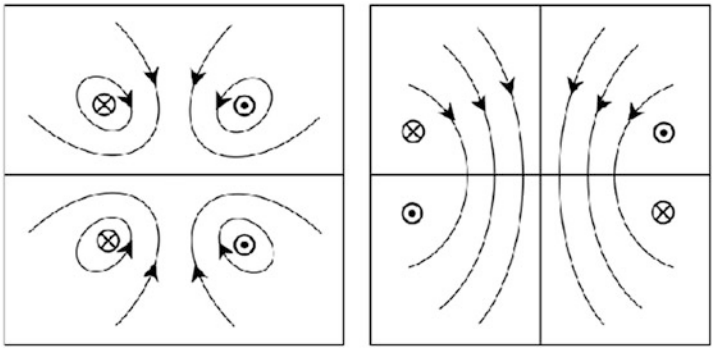

Fig. 17.3 Magnetic field configurations of the halo field: edge-on view of a galaxy with symmetric, even field configuration (*left*) or anti-symmetric, odd field configuration. Image reproduced from Haverkorn and Heesen (2012)

configuration is even in the Galactic disk, but odd in the halo. I mention this morphology here, since it is preferred in several observational studies of all-sky magnetic field configurations, discussed in Sect. 17.5.

17.2.3 Pitch Angle Definition

The pitch angle of a spiral magnetic field is defined as

$$p = \tan^{-1} \frac{B_r}{B_\phi} \tag{17.1}$$

where B_r is the radial component of the magnetic field and B_ϕ its azimuthal component. For a trailing spiral, B_r and B_ϕ have opposite signs, so that the pitch angle is negative, also described in the literature as "radially inward". Note that Page et al. (2007) use a deviating definition of their angle ψ_0 as $\psi_0 = \tan^{-1} B_\phi / B_r$.

17.3 Magnetic Fields in the Galactic Disk

17.3.1 Large-Scale Magnetic Field Strength

The strength of the local large-scale magnetic field as obtained from Faraday rotation of pulsars and extragalactic sources is typically around 1.5–2 μG. These estimates mostly result from RM and Dispersion Measure (DM) data from pulsars (Manchester 1974; Han et al. 2006), from wavelet analysis (Frick et al. 2001) or

fitting RM data to large-scale models of Galactic magnetic fields (as discussed extensively below).

The total field strength in the Solar neighborhood is estimated to be around 6 μG, from observed synchrotron emissivities and assumed equipartition between cosmic rays and magnetic fields (Strong et al. 2000; Beck 2001). This is in agreement with magnetic field strength estimates in Galactic H I regions from Zeeman splitting ($B \approx 2$–$10\,\mu$G, Crutcher et al. 2010).

Towards the Galactic center, the magnetic field strength increases. Estimates from synchrotron emission give a total field strength of about 10 μG at a Galactocentric radius of 3 kpc (Beck 2001), the pulsar study by Han et al. (2002) concludes a regular field strength of $4.4 \pm 0.9\,\mu$G in the Norma arm, and also large-scale magnetic field modeling generally finds stronger total magnetic field strength towards the Galactic center (e.g., Brown et al. 2007; Strong et al. 2000; Nota and Katgert 2010). The extensive study by Heiles (1995), using various tracers, concludes that $B_{tot} \approx 7.6$–$11.2\,\mu$G at a Galactocentric radius of 4 kpc.

The magnetic field strength is independent of density for low densities in the diffuse ISM ($n \lesssim 300\,\mathrm{cm}^{-3}$), indicating infall along magnetic field lines (Crutcher et al. 2010). Only for dense clouds and molecular clouds, magnetic field strengths increase roughly as the square root of density.

17.3.2 Large-Scale Magnetic Field Structure

The configuration of the large-scale magnetic field in the Milky Way disk is still a matter of hot debate. Some features meet with reasonable or total agreement: the magnetic fields seem to roughly follow the spiral arms, which is in agreement with all external spiral galaxies observed (Beck 2001), and even ring galaxies (Chyży and Buta 2008) (however, see Vallée 2008). This conclusion is drawn not only from polarized radio synchrotron and Faraday rotation measurements, but is also supported by starlight polarization measurements (Heiles 1996; Nishiyama et al. 2010), submm dust polarization (Bierman et al. 2011) and Zeeman splitting observations in hydroxyl masers (Green et al. 2012). Even young H II regions (Pavel and Clemens 2012) and molecular clouds (Han and Zhang 2007) seem to have magnetic fields aligned with a large-scale field along the Galactic plane .

Also, one large-scale reversal of the magnetic field near the Sun towards the Galactic Center has been known for decades (Thomson and Nelson 1980; Simard-Normandin and Kronberg 1980) and is confirmed by the rotation measure studies discussed here, but also by magnetic field directions in massive star-forming regions as probed by Zeeman splitting of OH masers (Fish et al. 2003). However, the exact number and location of large-scale reversals, pitch angles, characteristics of the turbulent magnetic field as a function of location and properties of the magnetic field close to the Galactic Center are still under discussion.

The past decade has seen a surge in studies using ad-hoc Galactic magnetic field models such as axisymmetric, bisymmetric or ring-shaped magnetic fields

to fit to observational data. The goal is to determine free fit parameters such as magnetic field configuration, pitch angle and strength. Table 17.1 shows a brief and necessarily incomplete summary of these models and some of their properties, as an attempt to make the differences between these models insightful, and to draw conclusions from this large body of work by many authors. Many of these models contain complexities that cannot all be captured in a simple table, e.g., models include radially declining magnetic field strengths or use different ways to incorporate large-scale magnetic field reversals. Also, the models use various models of thermal and/or cosmic ray electron densities, which we do not discuss here at all. The range of conclusions in these papers is much wider than noted in the table; here we focus on modeling results about the magnetic field strength and structure only.

It is highly non-trivial to compare the results from these models since they are so heterogeneous: most models use different input configurations for magnetic fields, thermal electron density and cosmic ray density, and use the various magnetic field parameters as either input or output parameters. However, some consensus seems to appear: most models tend to favor axisymmetric magnetic field models with one reversal just inside the Solar circle (Brown et al. 2007; Sun et al. 2008; Jansson et al. 2009; Jaffe et al. 2010). These best fit configurations (sometimes with some embellishments) have been taken as fixed input in subsequent papers, in order to determine e.g., out-of-plane magnetic fields (Jansson and Farrar 2012a), or the pitch angle and synchrotron spectral index (Fauvet et al. 2011). However, careful analysis of pulsar RMs by Men et al. (2008) proved that none of the three widely used magnetic field models (axisymmetric, bisymmetric, ring) are consistent with the data. These authors conclude that the magnetic field of the Milky Way must be more complex than one simple dynamo mode, possibly a combination of modes, as observed in some external galaxies (see R. Beck's chapter, this volume).

One notable difference in results can be seen in models based mostly on pulsars and models based mostly on extragalactic sources. RMs of extragalactic sources average magnetic field and density fluctuations over the complete line of sight through the whole Galaxy. Pulsar RMs only probe the line of sight to the individual pulsar, or even the path length between two pulsars in close projected proximity on the sky, which is a shorter distance and much more variable over small coordinate differences. In addition, RMs from extragalactic sources tend to be averaged over some region in the sky in order to diminish contributions from their intrinsic RM and from the turbulent Galactic ISM. Therefore, RMs measured from pulsars tend to show much more influence of the small-scale magnetic field component. Good examples of this are presented in Han et al. (2006), who used RMs from pulsars. They did not use any model but constructed a magnetic field configuration by looking at sign reversals of pulsar RMs in arms or interarms. Their data confirmed a counter-clockwise field in the Carina-Sagittarius spiral arm and suggest a counter-clockwise field in the Perseus. They find an abundance of small-scale structure in RM sign, which they interpret as clockwise magnetic fields in the interarm regions and counter-clockwise magnetic fields in the spiral arms, indicating large-scale magnetic field reversals at every arm-interarm boundary. Magnetic field modeling

Table 17.1 Table summarizing models comparing Milky Way magnetic field configurations to various observational tracers

Refs.	Tracer[a]	D/H	Models[b]	Model results	p
Brown et al. (2007)	149 EGS RMs 120 pulsar RMs	Q4[c] disk	spiral	one reversal	$-11.5°$
Fauvet et al. (2011)	WMAP5 I 23 GHz; ARCHEOPS 353 GHz I 408 MHz	all	modified log spiral $B_z + B_{ran}$	$B_z = 0.4\ \mu$G	$-30°$
Jaffe et al. (2010)	I 408 MHz WMAP P 23 GHz 269 EGS RMs	disk	ASS, log spiral, B_{ran}, compression	$B_{reg} : B_{ran} : B_{ani} = 1 : 5 : 4$ Field config as in model 1	$-11.5°$ IN
Jansson et al. (2009)	WMAP5 PI 23 GHz 1433 EGS RMs	disk	BSS/ASS -S/-A, ring, lit. models	no good models, disk and halo separate	$+35°$
Jansson and Farrar (2012a)	WMAP7 PI 23 GHz $\gtrsim$37000 EGS RMs	all	spiral, B_{ran}, B_{ani}, B_z	one reversal $B_{ani} = 1.7B_{reg}$, $B_z = 4.6\ \mu$G at GC[d]	$-11.5°$ IN
Men et al. (2008)	482 pulsar RMs	disk	ASS, BSS, ring	no good models, slight preference for ASS	
Miville-Deschênes et al. (2008)	I 408 MHz WMAP PI 23 GHz	halo	BSS, B_{ran}	$B_{ran} = 0.57B_{reg}$	$-8.5°$
Nota and Katgert (2010)	133 pulsar RMs 107 EGS RMs	Q4[d] disk	log spirals	QSS/many reversals preferred	
Page et al. (2007) Pshirkov et al. (2011)	WMAP3 PI 23 GHz $\gtrsim$37000 EGS RMs	halo all	log spirals, B_z ASS, BSS, ring	B_z at 25° tilt ASS best in disk; odd in halo	$-55°$ [d] $-5°$
Ruiz-Granados et al. (2010)	WMAP5 PI 23 GHz	halo	ASS, BSS, ring, bi-toroidal, B_z	ASS preferred, $B_z = 1/muG$	$-24°$[e]

(continued)

Table 17.1 (continued)

Refs.	Tracer[a]	D/H	Models[b]	Model results	p
Sun et al. (2008)	I 408 MHz WMAP PI 23 GHz $I + PI$ 1.4 GHz	all	ASS, BSS, ring	ASS best in disk, odd in halo	$-12°$ IN
Vallée (2005)	354 pulsar RMs	disk	rings with p	one reversal only	$-12°$ IN
Van Eck et al. (2011)	1373 EGS RMs 557 pulsar RMs	disk	ASS, BSS, ring combinations	no single model for complete Galaxy	$0°$ or $-11.5°$ IN

Note the incredible range of possible data, models, fixed parameters and output parameters. Column 1 gives the reference to the paper, column 2 details the used tracers and column 3 notes whether the model pertains to the Galactic disk, the halo, or both ('all'). Column 4 summarizes the ad-hoc models used for each paper, and Column 6 (some of) the main results. Column 7 gives the pitch angle of the *disk* field, where 'IN' is added if this pitch angle was a fixed input value. Symbols are as defined in the text

[a] I total intensity, *PI* polarized intensity, *EGS* extragalactic sources, *WMAPi* Wilkinson Microwave Anisotropy Probe data over i years

[b] *ASS* axisymmetric spiral, *BSS* bisymmetric spiral, *QSS* quadrisymmetric spiral, *-A/-S* (anti-)symmetric with respect to Galactic plane

[c] *Qi* ith quadrant of the Milky Way, *GC* Galactic Center

[d] Taking into account their deviating definition of pitch angle, see Sect. 17.2.3

[e] Actually given as $p = +24°$ in the paper, but with the opposite definition of azimuth direction

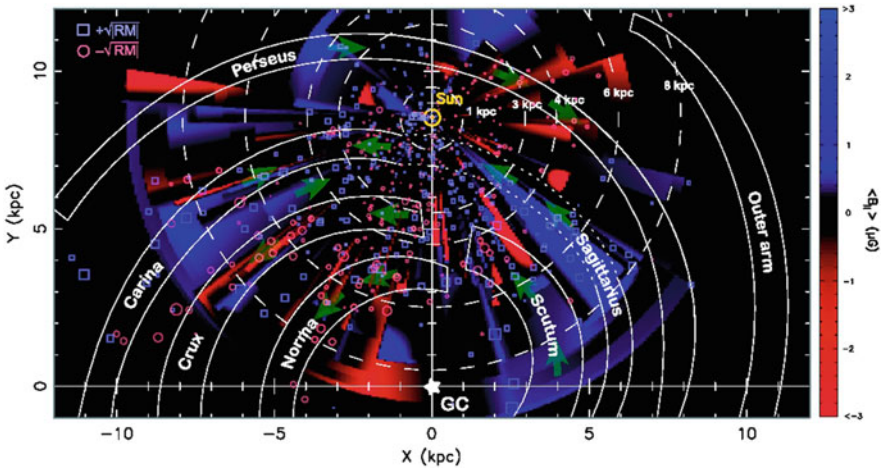

Fig. 17.4 Bird's-eye view of the Milky Way, where the *blue squares* (*red circles*) denote the location of a pulsar with a positive (negative) RM. The size of the symbol is proportional to the square root of RM. Magnetic field strengths derived and interpolated from these pulsar data are given in *red-blue color* scale (where $B > 3$ μG is saturated). The *green arrows* give the predominant direction of parallel magnetic field in a certain region. Image reproduced from Noutsos (2012)

by Nota and Katgert (2010) confirm reversals at every arm-interarm boundary, but find results at $>3\sigma$ only for the Crux and Norma arms and the interarm region in between.

Figure 17.4, reproduced from Noutsos (2012), nicely illustrates the intermediate-scale structure in RMs from pulsars, which are interpreted in the literature as reversals along spiral arm directions (Han et al. 2006) or as intermediate-scale fluctuations in the field (Noutsos 2012). As an example of the difference with modeling results including extragalactic sources, I mention Van Eck et al. (2011), who analyzed the Milky Way's magnetic field RM data of pulsars and extragalactic sources combined. They divide up the Galactic disk in three separate longitude ranges and concluded that there is no simple configuration which fits the whole Galactic plane sufficiently well, see Fig. 17.5. They also conclude that not more than one large-scale field reversal is needed to explain the data.

One way to decrease the influence of small-scale structure on pulsar RM measurements is by averaging these data as well before analysis of the structure. This can be done e.g., by wavelet analysis (Stepanov et al. 2002), using pulsar RMs. Using this method, Frick et al. (2001) only obtained reliable results a few kpc from the Sun due to sparsity of data beyond. However, these authors found evidence for one magnetic field reversal at a distance of $0.6 - 1$ kpc towards the Galactic center, and an other reversal between the Perseus and (local) Orion arm, in agreement with some earlier studies (Rand and Kulkarni 1989; Clegg et al. 1992). However, Mitra et al. (2003) show that the anomalous RMs interpreted as a large-scale reversal

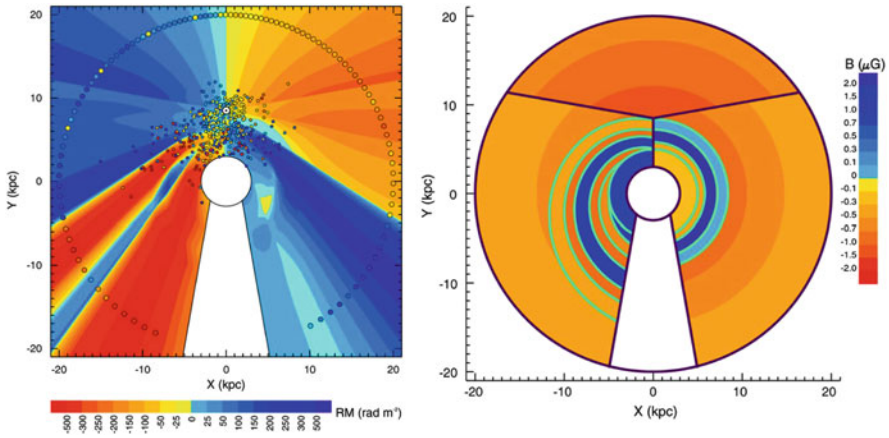

Fig. 17.5 *Left*: Bird's-eye view of the Milky Way, where the Galactic Center is at $(X, Y) = (0, 0)$ and the Sun is at $(X, Y) = (0, 8.5)$ kpc. The *small circles* within the Galaxy denote observed pulsar RMs, *large circles* around the Galaxy show observed extragalactic source RMs in the Galactic plane, boxcar-averaged over 9° in longitude with a step size of 3°. The *background color* scale presents predicted RMs at each location according to the model in the *right hand figure*. *Right*: Model of Galactic magnetic field in which the Galaxy is divided up into three regions. *Color* denotes magnetic field strength. Outer Galaxy: logarithmic spiral with $p = -11.5°$; fourth Galactic quadrant: model from Brown et al. (2007); first quadrant: ASS+RING model from Sun et al. (2008). Image reproduced from Van Eck et al. (2011)

towards the Perseus arm can be explained by anomalous RMs due to the influence of H II regions along the line of sight.

There is some evidence to suggest that the one well-determined large-scale reversal in the disk magnetic field does not follow the Sagittarius-Carina arm exactly, but slices through it (Brown et al. 2007; Van Eck et al. 2011 see also Fig. 17.5), a phenomenon that has been seen in the nearby spiral galaxy M51 as well (Fletcher et al. 2011; Heald et al. 2009). In addition, the magnetic field towards the outer Galaxy $l \sim 180°$ may be closer to circular rather than spiral (Rae and Brown 2010; Van Eck et al. 2011).

Also, many studies provide evidence for a dominant even symmetry of the local regular field in the disk with respect to the Galactic plane (Frick et al. 2001; Jansson et al. 2009; Pshirkov et al. 2011; Mao et al. 2012).

17.3.3 The Pitch Angle of the Magnetic Spiral Arms

Estimates of the pitch angle of the Milky Way's magnetic spiral arms are widely varying, depending on the tracer used to determine this angle. Vallée (1995, 2002) collected pitch angle estimates from 1980 to 2001, obtained from H I and H II gas, pulsars, dust, CO, rotation measures and O stars, which vary from −5° to −21°. His

weighted average is $p = -12° \pm 1°$. Polarized starlight indicates a pitch angle of $p = -7.2° \pm 4.1°$ (Heiles 1996), consistent with the other estimates.

The magnetic field models in Table 17.1 based on RM data give pitch angles in the range $p \sim -5°$ to $-15°$, while models fitting to high-frequency (mostly WMAP) polarized synchrotron emission data tend to find much higher pitch angles $p \sim -25°$ to $-30°$ (except for Miville-Deschênes et al. 2008, who find $p = -8.5°$ based on the WMAP degree of polarization, modeling a BSS spiral field and adding a turbulent component to match the observed depolarization). As a notable exception, Jansson et al. (2009) finds a high (and oppositely directed!) pitch angle $p = +35°$, based on RMs, but warns that this result is "highly model dependent". Indeed, they describe that fixing the pitch angle at $p = -12°$ in their best-fit model only decreases the fitting quality slightly.

Using the straightforward method of comparing longitude-dependences of RMs of extragalactic sources in the first and fourth quadrants, Kronberg and Newton-McGee (2011) conclude that the Milky Way has a bisymmetric structure towards the inner disk and an axisymmetric pattern towards the outer disk with an "inward spiral pitch angle" of $5.5° \pm 1°$. However, their pitch angle calculation assumes that the sign changes in RM in the first and fourth quadrant are due to the same spiral arm, which would actually indicate a pitch angle of $p = +5.5°$, i.e. a trailing instead of a leading spiral. The longitudes of the changes in RM sign in the first and fourth quadrants are more plausibly due to the Local Arm in the first quadrant and the Carina arm in the fourth, in which case their pitch angle estimate is based on an incorrect assumption.

17.3.4 Turbulent Magnetic Fields in the Disk

The strength of the random, turbulent magnetic field component can be estimated from RM fluctuations, combined with an estimate of thermal electron density.[3] Gaensler et al. (2001) performed this analysis in a small region in the Galactic plane in the 4th quadrant and found a random field strength of $B_{ran} \gtrsim 1.3\ \mu$G. Large-scale magnetic field models that include the turbulent magnetic field as a free parameter find $B_{ran} \sim 3-4\ \mu$G (e.g., Jaffe et al. 2010; Sun et al. 2008). However, the estimates for the regular and total magnetic field strengths would suggest a slightly larger value for the turbulent component, i.e. $B_{ran} = \sqrt{B_{tot}^2 - B_{reg}^2} \approx 5.5\ \mu$G.

Under the assumption of a Faraday screen, Schnitzeler et al. (2007) find that $B_{ran}/B_{reg,\perp} \lesssim 2$ in a relatively small field of view at the anti-center at Galactic latitude $b = 20°$, based on synchrotron depolarization. In two other relatively small fields out of the Galactic plane, Haverkorn et al. (2004a) find $B_{ran} \approx 1-3\ \mu$G and

[3] Since RM fluctuations and synchrotron depolarization trace the isotropic random field and the parallel component of the ordered random field (see Fig. 17.1), the strengths cited are a combination of these two components.

an unusually low ratio of random to regular magnetic field components $B_{ran}/B_{reg} = 0.7 \pm 0.5$. However, both these regions are located in the extended, high-polarization Fan region, which is thought to have a higher contribution of the regular magnetic field than the average ISM (Wolleben et al. 2006). This unusually low value of magnetic field ratio agrees with the higher-frequency synchrotron polarization study of Miville-Deschênes et al. (2008), which however includes the anisotropic random field component in their regular field strength calculation, plausibly explaining the low random-to-regular magnetic field ratio.

The power spectrum of magnetic field is difficult to measure directly, but information about the field can be derived from power spectra or structure functions of RM, assuming some distribution of thermal electron density fluctuations. RM fluctuations follow a power law, although the slope tends to be flatter than Kolmogorov (Simonetti and Cordes 1986; Clegg et al. 1992). Early studies covering large parts of the sky conclude that the outer scale of the turbulent magnetic field, connected to the energy injection scale of the dominant source, is $\sim$100 pc (Lazaryan and Shutenkov 1990; Ohno and Shibata 1993). However, when distinguishing spiral arms and interarm regions explicitly, the turbulent outer scale in spiral arms seems to be much smaller, only a few parsecs (Haverkorn et al. 2004b, 2006, 2008). Small outer scale estimates like this are also found from anisotropies in TeV cosmic ray nuclei (Malkov et al. 2010), and from analysis of fluctuations in radio synchrotron emission in the Fan region (Iacobelli et al. 2013).

Finally, there is evidence for an anti-correlation between small-scale magnetic field structure and density, at least in the denser ISM: denser components display more disordered magnetic field structure in submm BICEP data in the Galactic plane (Bierman et al. 2011).

17.4 Magnetic Fields in the Galactic Halo

The strength of the magnetic field in the Galactic halo[4] is estimated to be between $2 - 12$ μG from the best-fit models in Table 17.1. The field in the halo is thought to be fairly uniform: the average line of sight component of the magnetic field at high latitudes (where the $\sin(b)$ dependence has been taken into account) has a standard deviation $\sigma_B \lesssim 0.4$ μG (Schnitzeler 2010). Using equipartition arguments, Mao et al. (2010) derived $B_{ran} \approx 1$ μG in the halo, indeed smaller than in the disk.

The scale height derived from synchrotron emissivity under the assumption of equipartition between cosmic rays and magnetic fields is about 5–6 kpc (Cox 2005). Using hydrostatic balance, including kinetic, magnetic and cosmic-ray pressures,

[4]Two separate definitions of the Galactic halo with respect to the thick disk cause some confusion: The Galactic halo is regularly referred to as the region above the thick disk. However, in a second common use of the term Galactic halo it is equal to the thick disk. We use here the second definition, where the halo is equal to the thick disk.

Boulares and Cox (1990) find an almost linearly decreasing field strength from about 5 μG in the plane to 1 − 2.5 μG at 3 kpc height above the disk. Han and Qiao (1994) used pulsar RMs to derive a magnetic field scale height of 1.5 kpc—the discrepancy with earlier estimates may be due to the fact that pulsar RMs only sample the large-scale, regular component of the field while equipartition estimates also take into account the turbulent component.

The northern and southern hemisphere have different properties. The RM variance is a factor of 2 higher toward the South Galactic Pole than toward the North Galactic Pole (Stil et al. 2011). RM data also show a north-south asymmetry in RMs (Frick et al. 2001), emphasized by Mao et al. (2012), who studied extragalactic source RMs in two distinct parts of the sky towards the outer Galaxy ($100° < l < 117°$ and $|b| > 15°$). They concluded that the observations cannot be reproduced by symmetric exponential or double-toroidal Galactic halo fields as used in the literature. They find a higher halo field strength in the south ($B_H \approx 7$ μG) than in the north ($B_H \approx 2$ μG), and suggest that magnetic spiral arms might exist in the halo as well.

A large-scale vertical magnetic field at the Solar radius is small, if it exists at all. Mao et al. (2010) find from extragalactic source RMs towards the northern and southern Galactic pole at $|b| > 70°$ that there is no evidence for a large-scale vertical magnetic field component at the Solar radius in the northern hemisphere, while $\langle B_z \rangle \approx 0.3$ μG in the south. This is not necessarily due to an asymmetry in the large-scale vertical field, but can be due to differences in nearby structure in the two hemispheres. Taylor et al. (2009) evaluated the vertical magnetic field from RMs from all NVSS[5] sources. Their conclusion that $\langle B_z \rangle = 0.3 \pm 0.03$ μG agrees with Mao et al. (2010) in the southern hemisphere, but they also find a small vertical magnetic field of $\langle B_z \rangle = -0.14 \pm 0.02$ μG in the northern hemisphere. Mao et al. (2010) attribute this difference to the North Polar Spur, which they removed from their data and Taylor et al. (2009) did not. Han and Qiao (1994) found a vertical magnetic field $B_z = 0.2 - 0.3$ μG from south to north; however, they forced the direction of the field to be south-north or north-south and only fitted the field strength. Therefore, it is not possible to say whether their data would agree with the above conclusions. Small and varying vertical magnetic field strengths found in a field of view at $l = 153°$, $0.5° < b < 18°$ by Schnitzeler et al. (2007) and at high Galactic latitudes $b = 70°$ (de Bruyn et al. 2006) probably reflect smaller-scale magnetic field fluctuations and not the large-scale field.

17.5 Magnetic Fields in the Entire Disk + Halo System

Most models in Table 17.1 do not only discuss the Galactic disk or halo but simultaneously fit both the disk and the halo, allowing for different configurations in disk and halo magnetic fields. Jansson et al. (2009) tried to unify models of the

[5]NRAO VLA Sky Survey (Condon et al. 1998).

Galactic disk and halo, using a number of different models from the literature. They concluded that the magnetic field structure in the Galactic disk and halo were different and cannot be captured by scaled-up versions of the same magnetic field configuration. Their best-fit model is a disk-even halo-odd (DEHO) field, which was shown to be theoretically possible if one attributes an important role to the Galactic wind in the dynamo process (Moss et al. 2010). The conclusion of a best-fit DEHO field was also reached by Sun et al. (2008). These authors fitted 22.8 GHz synchrotron data from the Wilkinson Microwave Anisotropy Probe (WMAP, Hinshaw et al. 2007) and rotation measures from 1090 extragalactic point sources to their models and argued that none of the available models were a good fit to the data. However, they could conclude that a disk magnetic field which was symmetric with respect to the Galactic plane was strongly favored. For the halo, a toroidal field which is anti-symmetric with respect to the plane was preferred. Indeed, this anti-symmetric structure in the rotation measure sky with respect to the Galactic Center ("butterfly pattern"), only existent in the inner Galaxy, was already noticed decades ago (Simard-Normandin and Kronberg 1980). This has been interpreted as an $A0$ dynamo (Han et al. 2006), i.e. a dynamo causing an $A0$ field configuration (see Sect. 17.2.1), but has also been attributed to local structure (Wolleben et al. 2010a; Stil et al. 2011). $A0$ dynamo models are also strongly inconsistent with modeling comparing near-infrared starlight polarization measurements, based on discrepancies in the Galactic disk. However, adding an even disk-component to these models (DEHO field) makes them inconsistent with observed degrees of polarization of near-infrared starlight (Pavel et al. 2012).

Jaffe et al. (2010) included an ordered (anisotropic random) component to the regular (coherent) and random Galactic magnetic field components in their model. Due to the large number of free parameters (22), some of which are degenerate, they choose to constrain some parameters using one observational data set only, and keeping these fixed while constraining other parameters. Due to these degeneracies and the large number of unknowns, the authors caution to not attach too much value to the absolute numbers they find for field strengths. They do argue that their ratio of the three field components regular:random:anisotropic random, of 1:5:3, is relatively robust. So they conclude that the anisotropic random field is stronger than the regular field component. In Jaffe et al. (2011), these authors use a more realistic cosmic ray distribution in the Galaxy and find that the random component is even larger with respect to the coherent component.

At the moment, the latest all-inclusive modeling attempt is presented in Jansson and Farrar (2012a,b). Jansson and Farrar (2012a) include two new components for the magnetic field: a vertical, out-of-plane component similar to the X-shaped fields seen in external galaxies (e.g., Haverkorn and Heesen 2012); and a contribution by anisotropic random magnetic fields. The latter is degenerate with an increased intensity of cosmic ray electrons over the usually quoted values (Strong et al. 2007), but generally comparable in strength to the regular field. A random component for the magnetic field is added in Jansson and Farrar (2012b), which is allowed to vary in strength in 8 spiral regions. This complex magnetic field model now has 36 free

parameters, making it exceedingly difficult to be confident that the true minimum in 36-dimensional parameter space has been found.

The set of papers which fit magnetic field models to radio polarization data at high frequencies ($\geq$22 GHz WMAP data) (Ruiz-Granados et al. 2010; Fauvet et al. 2011) tend to find a higher pitch angle than rotation measure studies of $\sim$24 – 30°. Planck all-sky maps will provide additional observational constraints, which simulations show suggest the same high pitch angles (Fauvet et al. 2012). A non-negligible vertical magnetic field component is needed in these models as well, currently at odds with conclusions from rotation measure analyses (Sect. 17.4).

It may be possible in the near future to derive Galactic magnetic field structure from observations of arrival directions of Ultra-High Energy Cosmic Rays (UHECRs), but currently the sources and composition of UHECRs are too uncertain to constrain any Galactic magnetic field models (Golup et al. 2009).

17.6 Summary and Conclusions

In this section, I present a short summary of observational knowledge of magnetic fields in the Milky Way, neglecting all subtleties discussed above. I will also try to draw some conclusions.

The strength of the magnetic field in the Solar neighborhood is fairly well determined. The regular, large-scale component $B_{reg} \approx 2\,\mu$G, while the total magnetic field is $B_{tot} \approx 6\,\mu$G. Estimates of the isotropic random magnetic field from magnetic field modeling of $B_{ran} \approx 3-4\,\mu$G suggest that there exists also an anisotropic random field component of comparable strength to the random component. The magnetic field strength increases towards the inner Galaxy, and is independent of density for the diffuse interstellar gas.

The magnetic field direction in the Galactic disk most likely roughly follows the spiral arms. This is not always the case, since pitch angle estimates from modeling still vary, and there are concrete indications at several locations in the Galactic disk that the magnetic field direction does not coincide with the stellar or gaseous arms. The disk magnetic field is symmetric (even) with respect to the Galactic plane.

There is one large-scale magnetic reversal close to the Sun towards the inner Galaxy, but the existence and location(s) of more reversals is still under debate. The studies that rely mostly or totally on pulsar data indicate magnetic fields with more intermediate-scale structure (reversals) than studies (also) including extragalactic source RMs. This difference is likely due to the intrinsic differences in the data: extragalactic source RMs are averaged over the entire line of sight through the Galaxy and often over a patch of the plane of the sky as well, which washes out smaller scale structure partially. Fitting pulsar data would retrieve this smaller scale structure. However, pulsars with known RMs are concentrated in a few kpc from the Sun and their distances can be quite uncertain. Therefore, it is quite possible that what is interpreted as reversals along spiral arms are actually other intermediate scale structures caused by e.g., superbubbles.

The pitch angle of the magnetic field is roughly $p \approx -5°$ to $-15°$, depending on tracer (rotation measure, starlight polarization, gas, CO, etc). A notable exception is modeling of high-frequency (i.e. Planck/WMAP frequencies and higher) synchrotron emission, studies of which consistently show higher pitch angles of $p \approx -25°$ to $-30°$. The random magnetic field component shows a turbulent power spectrum with an outer scale of turbulence that is a few parsecs in the disk, possibly only the spiral arms, and up to $\sim$100 pc in the Galactic halo.

The magnetic field strength in the gaseous halo, or thick disk, is comparable to that in the disk, with an uncertainty of a factor 2 – 3. The scale height is many kiloparsecs ($\sim$5 – 6 kpc), possibly smaller for the regular field component. There is a pronounced north-south asymmetry across the Galactic disk: the magnetic field variance is higher in the south. There is a small large-scale vertical magnetic field component towards the south $B_z \approx 0.3\,\mu$G, while a small vertical magnetic field component towards the north could be attributed to the North Polar Spur.

The complete disk-halo system has been extensively modeled in the past decade, using a wide variety of observational tracers, magnetic field configurations and components, thermal and cosmic ray density models, and input and output parameters. One property that all models share is that none of them gives a satisfactory fit to all the data. This is not surprising, seeing the immense complexity of the magnetic and gaseous structures observed in the Milky Way. Large loops of radio emission such as the North Polar Spur or Loop I to IV (Berkhuijsen 1971) show influence of magnetic fields (Spoelstra 1973; Stil et al. 2011), created by supernovae blowing bubbles in the ionized interstellar gas, dragging the magnetic field with them. The named Loops are giant structures in the sky because they are located very close to the Sun and are therefore conspicuous on the sky. However, hundreds or even thousands more of these structures should exist in the rest of the Milky Way, all affecting the large-scale structure of the magnetic field. These and other local structures are virtually impossible to include in modeling and therefore often omitted. This is especially clear towards the Galactic anti-center, where the regular magnetic field is directed almost perpendicular to the line of sight and therefore has a negligible RM contribution in this direction. As Pshirkov et al. (2011) note, any regular magnetic field model with a small pitch angle severely underestimates the amount of RM fluctuations observed in this direction. These local structures, combined with the location-dependent turbulent nature of the magneto-ionized medium, make this modeling a daunting enterprise.

The variety in conclusions from Galactic magnetic field models using different tracers and methods, indicates a large role of small-scale position-dependent turbulence, discrete structures, significant changes in pitch angle along a spiral arm, or—most likely—all of these. Variable pitch angles are also suggested by simulations of density waves including magnetic fields (Gómez and Cox 2004). This explanation does make it more plausible why a ring-like magnetic field model gives fit results of comparable quality as the spiral arm models, or why deviations of magnetic field directions from gaseous and stellar pitch angles are found.

17.7 Epilogue

A number of recent technological and computational developments make a large expansion in parameter space related to studies of cosmic magnetic fields possible: Phased Array Feeds allow deep surveys of large parts of the sky in reasonable observing times; low frequency polarimetry is becoming possible thanks to sufficient computer power and technological expertise to build software telescopes, and finally large-scale galactic (but also extragalactic, intracluster) magnetic fields can be probed in (almost) three dimensions using Rotation Measure Synthesis (Brentjens and de Bruyn 2005).

This has sparked renewed interest in the field of cosmic magnetism, as evidenced by the *Cosmic Magnetism Key Science Project* (MKSP, Anderson et al. 2012) for the LOw-Frequency ARray LOFAR; the *Polarisation Sky Survey of the Universe's Magnetism* (POSSUM, Gaensler et al. 2010) for the Australian Square Kilometre Array Pathfinder (ASKAP), and cosmic magnetism studies as part of the WODAN project (Röttgering et al. 2011) using the APERTIF Phased Array Feeds on the Westerbork Synthesis Radio Telescope (WSRT). These are all exciting innovative telescopes and/or instruments currently under construction. For details on magnetism studies with LOFAR, SKA, Planck and ALMA see the Chapters by R. Beck and W. Vlemmings in this volume. I will discuss other important future and ongoing initiatives below.

17.7.1 Galactic Magnetism with Existing Instrumentation

A number of large radio polarimetric surveys have recently been done or are in progress, with the aim of studying the magnetized ISM of the Milky Way, at a variety of frequencies.

Several surveys with the ALFA seven feed array on the Arecibo telescope are being performed, among which the Galactic ALFA Continuum Transit Survey (GALFACTS, Taylor and Salter 2010). GALFACTS will survey the whole Arecibo sky (declinations $-1.33° < \delta < 38.03°$) in the frequency range 1,225–1,525 MHz down to a sensitivity of 90 μJy. Its main science goals are exploration of the Milky Way's magnetic field and the properties of the magnetized ISM. Observations have been progressing for 4 years and has been completed in 2013.

The lower Faraday rotation (and therefore more distant polarization horizon) at higher frequencies was the reason for the 6-cm Sino-German survey of the Galactic plane ($10° < l < 230°$, $|b| < 5°$) with the Urumqi 25-m single dish (Sun et al. 2007, 2011; Gao et al. 2010; Xiao et al. 2011). This survey is mostly focused on the detection of discrete magnetized objects such as H II regions, supernova remnants and Faraday screens. At even higher frequencies of 5 GHz, the C-Band All-Sky Survey (C-BASS) will provide an all-sky polarimetric survey. Although its main science goal is providing characterization of foregrounds for Cosmic Microwave

Background (CMB) polarization studies, it will also explore Galactic magnetic fields. Data acquisition is ongoing.

The S-Band Polarization All-Sky Survey (S-PASS) is a radio polarimetric study of the entire southern sky at 2,307 MHz in a 184 MHz bandwidth, performed with the Parkes 64 m single dish telescope with a polarization sensitivity better than 1 mJy/beam. The science goals of the survey are two-fold: characterizing polarized foregrounds for measurements of the B-mode of CMB Polarization, and exploration of Galactic magnetic fields. The survey observations are completed and first science results are being published (Carretti et al. 2013a,b; Sun et al. 2013). The Southern Twenty-centimeter All-sky Polarization Survey (STAPS) was observed commensally with S-PASS and data processing is ongoing.

The largest ongoing project to map Galactic magnetism using existing instrumentation is the Global Magneto-Ionic Medium Survey (GMIMS, Wolleben et al. 2009). This project consists of a series of polarimetric surveys in the northern and southern hemispheres, from ∼300 to ∼1,800 MHz. Data acquisition for the southern-sky survey spanning 287 – 870 MHz with the Parkes telescope is completed and data processing in progress, while the STAPS survey described above will function as the high-band (1,300 – 1,800 MHz) southern-sky survey for GMIMS. For the high-band survey in the north (1,277 – 1,740 MHz), performed with the DRAO 26-m single dish (Wolleben et al. 2010b), observations have finished and data reduction is nearing completion, with first science results discussed in Wolleben et al. (2010a). Options for observing the remaining GMIMS surveys are being considered.

With an angular resolution of $30 - 60'$ and a frequency resolution of at least 1 MHz, GMIMS will provide the first spectro-polarimetric data set of the large-scale polarized emission over the entire sky, observed with single-dish telescopes. The broad frequency coverage is of great importance for high resolution and broad sensitivity of Rotation Measure Synthesis. Therefore, the combined surveys with a 1,500 MHz bandwidth will give unprecedented maps of Faraday depth over the whole sky, revolutionizing studies of the magneto-ionized ISM in the Galaxy using this method.

17.7.2 Galactic Magnetism with Next-Generation Instrumentation

The WSRT is being upgraded with phased array feeds named APERture Tile In Focus (APERTIF, Oosterloo et al. 2010) with a 300 MHz bandwidth in the range of 1.0–1.7 GHz. This upgrade will increase Westerbork's field of view with a factor 25 to about 8 square degrees, making it a wonderful survey instrument.

One of the key surveys to be performed with APERTIF is the Westerbork Observations of the Deep APERTIF Northern-Sky (WODAN, Röttgering et al. 2011). WODAN aims to image the whole northern sky down to 10 μJy rms with a broad bandwidth around 1,400 MHz, and part of the sky a factor two deeper.

It is mostly geared towards cosmology and other extragalactic science, with an observational aim to detect 30 million radio sources including 100,000 clusters, 10 million starbursting galaxies at $z > 1$ and virtually all radio loud AGN in the Universe. However, many of these sources will emit polarized emission at this wavelength, which will be Faraday rotated by the Galactic magnetized ISM. This will provide an observational data set for Galactic magnetism studies far surpassing the currently available NVSS rotation measure data base (Taylor et al. 2009).

Similarly to WODAN in the northern sky, the southern sky will be surveyed by several projects on the Australian SKA Pathfinder (ASKAP, Johnston et al. 2008). WODAN's sister survey is called Evolutionary Map of the Universe (EMU, Norris 2010), but the data obtained is shared between EMU and a project dedicated to cosmic magnetism, named Polarization Sky Survey of the Universe's Magnetism (POSSUM, Gaensler et al. 2010). POSSUM aims to measure the Faraday rotation of 3 million extragalactic radio sources over 30,000 square degrees, which will allow major steps in characterizing the large-scale and turbulent components of the Galactic magnetic field, but also test (dynamo) theories for the origin and evolution of the Milky Way's magnetic field.

Finally, the Murchison Widefield Array (MWA, Whitney et al. 2011), under development in Western Australia at the moment is a low-frequency radio interferometer at 80–300 MHz—analogous to LOFAR in the north but smaller; however, with an excellent uv-coverage on small baselines. Although its main science goals are the Epoch of Reionization, solar and ionospheric science and transients, it can also be used to provide detailed rotation measure synthesis maps of low-magnetic-field areas in the southern sky.

Acknowledgements The author wants to express her sincere thanks to Katia Ferrière and George Heald for critically reading and commenting on the manuscript, to Philip Kronberg for discussion about details of spiral arms pitch angles, to Jo-Anne Brown, Tess Jaffe, Aris Noutsos, and Cameron van Eck for kindly giving permission to use their figures and useful comments and discussion. This work is part of the research programme 639.042.915, which is (partly) financed by the Netherlands Organisation for Scientific Research (NWO).

References

Anderson, J., Beck, R., Bell, M., et al.: arXiv:1203.2467 (2012)
Beck, R.: Space Sci. Rev. **99**, 243 (2001)
Beck, R.: Astron. Astrophys. **470**, 539 (2007)
Berkhuijsen, E.M.: Astron. Astrophys. **14**, 359 (1971)
Bierman, E.M., Matsumura, T., Dowell, C.D., et al.: Astrophys. J. **741**, 81 (2011)
Boulares, A., Cox, D.P.: Astrophys. J. **365**, 544 (1990)
Brentjens, M.A., de Bruyn, A.G.: Astron. Astrophys. **441**, 1217 (2005)
Brown, J.C.: Astron. Soc. Pac. Conf. Ser. **438**, 216 (2010)
Brown, J.C., Haverkorn, M., Gaensler, B.M., et al.: Astrophys. J. **663**, 258 (2007)
Carretti, E., Crocker, R.M., Staveley-Smith, L., et al.: Nature, **493**, 66 (2013a)
Carretti, E., Brown, S., Staveley-Smith, L., et al.: MNRAS, **430**, 1414 (2013b)
Chyży, K.T., Buta, R.J.: Astrophys. J. Lett. **677**, L17 (2008)

Clegg, A.W., Cordes, J.M., Simonetti, J.M., Kulkarni, S.R.: Astrophys. J. **386**, 143 (1992)
Condon, J.J., Cotton, W.D., Greisen, E.W., et al.: Astron. J. **115**, 1693 (1998)
Cox, D.P.: Annu. Rev. Astron. Astrophys. **43**, 337 (2005)
Crutcher, R.M., Wandelt, B., Heiles, C., Falgarone, E., Troland, T.H.: Astrophys. J. 725, 466 (2010)
de Bruyn, A.G., Katgert, P., Haverkorn, M., Schnitzeler, D.H.F.M.: Astron. Nachrichten **327**, 487 (2006)
Fauvet, L., Macías-Pérez, J.F., Aumont, J., et al.: Astron. Astrophys. **526**, A145 (2011)
Fauvet, L., Macías-Pérez, J.F., Jaffe, T.R., et al.: Astron. Astrophys. **540**, A122 (2012)
Ferrière, K.: Rev. Mod. Phys. **73**, 1031 (2001)
Ferrière, K.: Astron. Astrophys. **505**, 1183 (2009)
Fish, V.L., Reid, M.J., Argon, A.L., Menten, K.M.: Astrophys. J. **596**, 328 (2003)
Fletcher, A., Beck, R., Shukurov, A., Berkhuijsen, E.M., Horellou, C.: Mon. Notices R. Astron. Soc. **412**, 2396 (2011)
Frick, P., Stepanov, R., Shukurov, A., Sokoloff, D.: Mon. Notices R. Astron. Soc. **325**, 649 (2001)
Frisch, P.C.: Space Sci. Rev. **130**, 355 (2007)
Gaensler, B.M., Dickey, J.M., McClure-Griffiths, N.M., et al.: Astrophys. J. **549**, 959 (2001)
Gaensler, B.M., Landecker, T.L., Taylor, A.R., POSSUM Collaboration: Bull. Am. Astron. Soc. **42**, #470.13 (2010)
Gao, X.Y., Reich, W., Han, J.L., et al.: Astron. Astrophys. **515**, A64 (2010)
Golup, G., Harari, D., Mollerach, S., Roulet, E.: Astropart. Phys. **32**, 269 (2009)
Gómez, G.C., Cox, D.P.: Astrophys. J. **615**, 758 (2004)
Green, J.A., McClure-Griffiths, N.M., Caswell, J.L., Robishaw, T., Harvey-Smith, L.: Mon. Notices R. Astron. Soc. **425**, 2530 (2012)
Han, J.L.: Astrophys. Space Sci. **278**, 181 (2001)
Han, J.L., Qiao, G.J.: Astron. Astrophys. **288**, 759 (1994)
Han, J.L., Zhang, J.S.: Astron. Astrophys. **464**, 609 (2007)
Han, J.L., Manchester, R.N., Lyne, A.G., Qiao, G.J.: Astrophys. J. Lett. **570**, L17 (2002)
Han, J.L., Manchester, R.N., Lyne, A.G., Qiao, G.J., van Straten, W.: Astrophys. J. **642**, 868 (2006)
Haverkorn, M., Heesen, V.: Space Sci. Rev. **166**, 133 (2012)
Haverkorn, M., Katgert, P., de Bruyn, A.G. Astron. Astrophys. **427**, 169 (2004)
Haverkorn, M., Gaensler, B.M., McClure-Griffiths, N.M., Dickey, J.M., Green, A.J.: Astrophys. J. **609**, 776 (2004)
Haverkorn, M., Gaensler, B.M., Brown, J.C., Bizunok, N.S., McClure-Griffiths, N.M., Dickey, J.M., Green, A.J.: Astrophys. J. Lett. **637**, 33 (2006)
Haverkorn, M., Brown, J.C., Gaensler, B.M., McClure-Griffiths, N.M.: Astrophys. J. **680**, 362 (2008)
Heald, G., Braun, R., Edmonds, R.: Astron. Astrophys. **503**, 409 (2009)
Heiles, C.: The Physics of the Interstellar Medium and Intergalactic Medium, ASP Conference Series, vol. 80, eds A. Ferrara, C.F. McKee, C. Heiles, P.R. Shapiro. Publisher, Astronomical Society of the Pacific, San Francisco, California, **80**, 507 (1995)
Heiles, C.: Astrophys. J. **462**, 316 (1996)
Heiles, C., Haverkorn, M.: Space Sci. Rev. **166**, 293 (2012)
Hinshaw, G., Nolta, M.R., Bennett, C.L., et al.: Astrophys. J. Suppl. **170**, 288 (2007)
Iacobelli, M., Haverkorn, M., Orru, E. et al.: Astron. Astrophys. **558**, 72 (2013)
Jaffe, T.R., Leahy, J.P., Banday, A.J., et al.: Mon. Notices R. Astron. Soc. **401**, 1013 (2010)
Jaffe, T.R., Banday, A.J., Leahy, J.P., Leach, S., Strong, A.W.: Mon. Notices R. Astron. Soc. **416**, 1152 (2011)
Jansson, R., Farrar, G.R.: Astrophys. J. Lett. **761**, L11 (2012)
Jansson, R., Farrar, G.R.: Astrophys. J. **757**, 14 (2012)
Jansson, R., Farrar, G.R., Waelkens, A.H., Enßlin, T.A.: J. Cosmol. Astropart. Phys. **7**, 21 (2009)
Johnston, S., Taylor, R., Bailes, M., et al.: Exp. Astron. **22**, 151 (2008)
Kronberg, P.P., Newton-McGee, K.J.: Publ. Astron. Soc. Aust. **28**, 171 (2011)

Lazaryan, A.L., Shutenkov, V.P. SvAL **16**, 297L (1990)
Malkov M.A., Diamond P.H., Drury L., Sagdeev R.Z.: Astrophys. J. **721**, 750 (2010)
Manchester, R.N.: Astrophys. J. **188**, 637 (1974)
Mao, S.A., Gaensler, B.M., Haverkorn, M., et al.: Astrophys. J. **714**, 1170 (2010)
Mao, S.A., McClure-Griffiths, N.M., Gaensler, B.M., et al.: Astrophys. J. **755**, 21 (2012)
Men, H., Ferrière, K., Han, J.L.: Astron. Astrophys. **486**, 819 (2008)
Mitra, D., Wielebinski, R., Kramer, M., Jessner, A.: Astron. Astrophys. **398**, 993 (2003)
Miville-Deschênes, M.-A., Ysard, N., Lavabre, A., et al.: Astron. Astrophys. **490**, 1093 (2008)
Moss, D., Sokoloff, D., Beck, R., Krause, M.: Astron. Astrophys. **512**, A61 (2010)
Nishiyama, S., Hatano, H., Tamura, M., et al.: Astrophys. J. Lett. **722**, L23 (2010)
Norris, R.: Bull. Am. Astron. Soc. **36**, #604.05 (2010)
Nota, T., Katgert, P.: Astron. Astrophys. **513**, A65 (2010)
Noutsos, A.: Space Sci. Rev. **166**, 307 (2012)
Ohno, H., Shibata, S.: Mon. Notices R. Astron. Soc. **262**, 953 (1993)
Oosterloo, T., Verheijen, M., van Cappellen, W.: ISKAF2010 Science Meeting (2010)
Page, L., Hinshaw, G., Komatsu, E., et al.: Astrophys. J. Suppl. **170**, 335 (2007)
Pavel, M.D., Clemens, D.P.: Astrophys. J. **760**, 150 (2012)
Pavel, M.D., Clemens, D.P., Pinnick, A.F.: Astrophys. J. **749**, 71 (2012)
Pshirkov, M.S., Tinyakov, P.G., Kronberg, P.P., Newton-McGee, K.J.: Astrophys. J. **738**, 192 (2011)
Rae, K.M., Brown, J.C.: Astron. Soc. Pac. Conf. Ser. **438**, 229 (2010)
Rand, R.J., Kulkarni, S.R.: Astrophys. J. **343**, 760 (1989)
Röttgering, H., Afonso, J., Barthel, P., et al.: J. Astrophys. Astron. **32**, 557 (2011)
Ruiz-Granados, B., Rubiño-Martín, J.A., Battaner, E.: Astron. Astrophys. **522**, A73 (2010)
Schnitzeler, D.H.F.M.: Mon. Notices R. Astron. Soc. **409**, L99 (2010)
Schnitzeler, D.H.F.M., Katgert, P., de Bruyn, A.G.: Astron. Astrophys. **471**, L21 (2007)
Schnitzeler, D.H.F.M., Katgert, P., Haverkorn, M., de Bruyn, A.G.: Astron. Astrophys. **461**, 963 (2007)
Simard-Normandin, M., Kronberg, P.P.: Astrophys. J. **242**, 74 (1980)
Simonetti, J.H., Cordes, J.M.: Astrophys. J. **310**, 160 (1986)
Spoelstra, T.A.T.: Astron. Astrophys. **24**, 149 (1973)
Stepanov, R., Frick, P., Shukurov, A., Sokoloff, D.: Astron. Astrophys. **391**, 361 (2002)
Stil, J.M., Taylor, A.R., Sunstrum, C.: Astrophys. J. **726**, 4 (2011)
Strong, A.W., Moskalenko, I.V., Reimer, O.: Astrophys. J. **537**, 763 (2000)
Strong, A.W., Moskalenko, I.V., Ptuskin, V.S.: Ann. Rev. Nucl. Particle Sci. **57**, 285 (2007)
Sun, X.H., Han, J.L., Reich, W., et al.: Astron. Astrophys. **469**, 1003 (2007)
Sun, X.H., Reich, W., Waelkens, A., Enßlin, T.A.: Astron. Astrophys. **477**, 573 (2008)
Sun, X.H., Reich, W., Han, J.L., et al.: Astron. Astrophys. **527**, A74 (2011)
Sun, X.H., Gaensler, B.M., Carretti, E., et al.: Mon. Notices R. Astron. Soc. 2804 (2013)
Taylor, A.R., Salter, C.J.: Astron. Soc. Pac. Conf. Ser. **438**, 402 (2010)
Taylor, A.R., Stil, J.M., Sunstrum, C.: Astrophys. J. **702**, 1230 (2009)
Thomson, R.C., Nelson, A.H.: Mon. Notices R. Astron. Soc. **191**, 863 (1980)
Vallee, J.P.: Astrophys. J. **454**, 119 (1995)
Vallée, J.P.: Astrophys. J. **566**, 261 (2002)
Vallée, J.P.: Astrophys. J. **619**, 297 (2005)
Vallée, J.P.: Astrophys. J. **681**, 303 (2008)
Van Eck, C.L., Brown, J.C., Stil, J.M., et al.: Astrophys. J. **728**, 97 (2011)
Whitney, A., Booler, T., Bowman, J., et al.: Bull. Am. Astron. Soc. #132.07 (2011)
Wielebinski, R.: Cosmic Magn. Fields, Lecture Notes in Physics, eds. R. Wielebinski, R. Beck **664**, 89 (2005)
Wielebinski, R., Beck, R.: Galaxies and their Masks, by D.L. Block, K.C. Freeman, I. Puerari, Springer Science+Business Media (2010)
Wolleben, M., Landecker, T.L., Reich, W., Wielebinski, R.: Astron. Astrophys. **448**, 411 (2006)

Wolleben, M., Landecker, T.L., Carretti, E., et al.: IAU Symposium, vol. 259, p. 89 (2009)
Wolleben, M., Fletcher, A., Landecker, T.L., et al.: Astrophys. J. Lett. **724**, L48 (2010)
Wolleben, M., Landecker, T.L., Hovey, G.J., et al.: Astron. J. **139**, 1681 (2010)
Xiao, L., Han, J.L., Reich, W., et al.: Astron. Astrophys. **529**, A15 (2011)
Zweibel, E.G., Heiles, C.: Nature **385**, 131 (1997)

Chapter 18
Magnetic Fields in Galaxies

Rainer Beck

Abstract The origin and evolution of cosmic magnetic fields, their strength and structure in intergalactic space, their first occurrence in young galaxies, and their dynamical importance for galaxy evolution remain widely unknown. Radio synchrotron emission, its polarization and its Faraday rotation are powerful tools to study the strength and structure of magnetic fields in galaxies. Unpolarized radio synchrotron emission traces isotropic turbulent fields which are strongest in spiral arms and bars (20–30 μG) and in central starburst regions (50–100 μG). Such fields are dynamically important; they can affect gas flows and drive gas inflows in central regions. Polarized radio emission traces ordered fields which can be regular or anisotropic turbulent, generated from isotropic turbulent fields by compression or shear. The strongest ordered fields of 10–15 μG strength are generally found in interarm regions and follow the orientation of adjacent gas spiral arms. In galaxies with strong density waves, ordered (anisotropic turbulent) fields are also observed at the inner edges of the spiral arms. Ordered fields with spiral patterns exist in grand-design, barred and flocculent galaxies, and in central regions of starburst galaxies. Ordered fields in interacting galaxies have asymmetric distributions and are an excellent tracer of past interactions between galaxies or with the intergalactic medium. Irregular galaxies host isotropic turbulent fields often of similar strength as in spiral galaxies, but only weak ordered fields. Faraday rotation measures (RM) of the diffuse polarized radio emission from the disks of several galaxies reveal large-scale spiral patterns that can be described by the superposition of azimuthal modes; these are signatures of regular fields generated by a mean-field $\alpha - \Omega$ dynamo. So far no indications were found in external galaxies of large-scale field reversals, like the one in the Milky Way. Ordered magnetic fields are also observed in radio halos around edge-on galaxies out to large distances from the plane, with X-shaped patterns. In the outflow cone above a starburst region of NGC 253, RM data indicate a helical magnetic field.

R. Beck (✉)
Max-Planck-Institut für Radioastronomie, Auf dem Hügel 69, 53121 Bonn, Germany
e-mail: rbeck@mpifr-bonn.mpg.de

A. Lazarian et al. (eds.), *Magnetic Fields in Diffuse Media*, Astrophysics and Space Science Library 407, DOI 10.1007/978-3-662-44625-6_18

18.1 Introduction

Magnetic fields are a major agent in the interstellar medium and control the density and distribution of cosmic rays. Cosmic rays accelerated in supernova remnants can provide the pressure to drive galactic outflows and buoyant loops of magnetic fields via the Parker instability. Outflows from starburst galaxies in the early Universe may have magnetized the intergalactic medium.

The detection with the AUGER observatory of ultrahigh-energy cosmic rays (UHECRs) reaching the Earth and the possibly anisotropic distribution of their arrival directions (Abreu 2010) calls for a proper model of particle propagation. As UHECR particles are deflected by large-scale regular fields and scattered by turbulent fields, the structure and the extent of the fields in the disk and halo of the Milky Way are necessary parameters for a propagation model, but our present knowledge does not allow safe conclusions. The view onto external spiral galaxies can help.

18.2 Origin of Magnetic Fields

The origin of the first magnetic fields in the Universe is a mystery (Widrow 2002). *Seed fields* may be "primordial", generated during a phase transition in the early Universe (Caprini et al. 2009), or may originate from the time of cosmological structure formation by the Weibel instability (Lazar et al. 2009), or from injection by the first stars or jets generated by the first black holes (Rees 2005), or from the Biermann mechanism in the first supernova remnants (Hanayama et al. 2005), or from plasma fluctuations (Schlickeiser 2012). The non-detection of GeV γ-ray emission with the FERMI satellite from blazars, which were observed at TeV energies with the HESS observatory, may indicate that the secondary particles are deflected by intergalactic fields of least 10^{-16} G strength and a high volume filling factor (Dolag et al. 2011).

The most promising mechanism to sustain magnetic fields in the interstellar medium of galaxies is the dynamo (Beck et al. 1996). A small-scale dynamo in protogalaxies may have amplified seed fields to several μG strength (the energy level of turbulence) within less than 10^8 year (Schleicher et al. 2010). To explain the generation of large-scale fields in galaxies, the mean-field $\alpha - \Omega$ dynamo has been developed. It is based on turbulence, differential rotation and helical gas flows (α-*effect*), driven by supernova explosions (Gressel et al. 2008). The $\alpha - \Omega$ dynamo generates large-scale helicity with a non-zero mean in each hemisphere. As total helicity is a conserved quantity, the dynamo is quenched by the small-scale fields with opposite helicity unless these are removed from the system (Shukurov et al. 2006). Outflows are essential for effective $\alpha - \Omega$ dynamo action. The mean-field approximation got support from high-resolution MHD modeling (Gent et al. 2013).

Dynamo-type fields are described by modes with different azimuthal symmetries in the disk plane and two different vertical symmetries (even or odd parity) perpendicular to the disk plane. Several modes can be excited in the same object. In flat, rotating objects like galaxy disks, the strongest mode S0 consists of a toroidal field of *axisymmetric spiral* shape within the disk, without sign reversals across the equatorial plane, and a weaker poloidal field of even-symmetry structure. The $\alpha - \Omega$ dynamo in galaxy disks predicts that within a few 10^9 year large-scale regular fields are generated from μG turbulent fields (Arshakian et al. 2009). Field reversals from the early phases may survive until today (Moss et al. 2012). Global numerical models of galaxies (Gissinger et al. 2009; Hanasz et al. 2009) confirmed the basic results of the $\alpha - \Omega$ dynamo. Dynamo modes can be identified observationally from the pattern of polarization angles and of RMs of the diffuse polarized emission of galaxy disks (see Sect. 18.6.1).

18.3 Measuring Magnetic Fields in Galaxies

Magnetic fields need illumination to be detectable. *Polarized emission* at optical, infrared, submillimeter and radio wavelengths holds the clue to measure magnetic fields in galaxies. Optical linear polarization is a result of extinction by elongated dust grains in the line of sight which are aligned in the interstellar magnetic field (the *Davis-Greenstein effect*). The B-vector (E + 90°) runs perpendicular to the field. Starlight polarization yields the orientation of large-scale magnetic fields in the Milky Way (Fosalba et al. 2002). However, light can also be polarized by scattering, a process unrelated to magnetic fields and hence a contamination that is difficult to subtract from diffuse polarized emission from galaxies, e.g. in the spiral galaxy M 51 (Scarrott et al. 1987).

Linearly polarized emission from elongated dust grains at infrared and submillimeter wavelengths is not affected by polarized scattered light. The B-vector is parallel to the magnetic field. The field structure can be mapped in gas clouds of the Milky Way and in galaxies, e.g. in the halo of the galaxy M 82 (Greaves et al. 2000).

Most of what we know about interstellar magnetic fields comes through the detection of radio waves. *Zeeman splitting* of radio spectral lines directly measures the field strength in gas clouds of the Milky Way (Crutcher et al. 2010) and in starburst galaxies (Robishaw et al. 2008). The intensity of *synchrotron emission* (Chap. 3; examples in Figs. 18.1 and 18.5) is a measure of the number density of cosmic-ray electrons in the relevant energy range and of the strength of the total magnetic field component in the sky plane. The assumption of energy equipartition between these two components allows us to calculate the total magnetic field strength from the synchrotron intensity (Sect. 18.4.1).

Linearly polarized synchrotron emission (examples in Figs. 18.4 and 18.6) emerges from ordered fields in the sky plane. As polarization "vectors" are ambiguous by 180°, they cannot distinguish *regular (coherent) fields*, defined to have a constant direction within the telescope beam, from *anisotropic turbulent fields*,

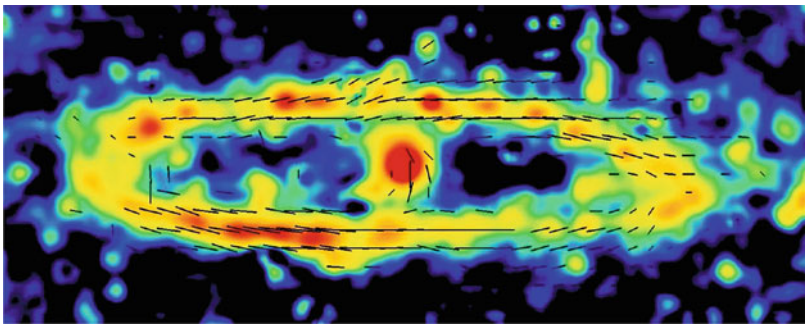

Fig. 18.1 Total radio intensity (colors) and B-vectors (corrected for Faraday rotation) in the Andromeda galaxy (M 31), observed at 6 cm with the Effelsberg telescope (from Berkhuijsen et al. 2003)

which are generated from isotropic turbulent fields by compressing or shearing gas flows and reverse their direction within the telescope beam. Unpolarized synchrotron emission indicates *isotropic turbulent (random) fields* which have random directions in 3-D and have been amplified by turbulent gas flows.

The intrinsic degree of linear polarization of synchrotron emission is about 75%. The observed degree of polarization is smaller due to the contribution of unpolarized thermal emission, which may dominate in star-forming regions, by *Faraday depolarization* along the line of sight and across the beam (Sokoloff et al. 1999), and by geometrical depolarization due to variations of the field orientation within the beam.

The polarization vector is rotated in a magnetized thermal plasma by *Faraday rotation*. As the rotation angle is sensitive to the sign of the field direction, only regular fields give rise to Faraday rotation, while the Faraday rotation contributions of turbulent fields cancel along the line of sight. Measurements of the Faraday rotation from multi-wavelength observations (Figs. 18.15 and 18.16) yield the strength and direction of the average regular field component along the line of sight. If Faraday rotation is small (in galaxies typically at wavelengths shorter than a few centimeters), the B-vector of polarized emission gives the intrinsic field orientation in the sky plane, so that the magnetic pattern can be mapped directly (Beck 2005).

The Faraday rotation angle $\Delta\chi$ is proportional to the square of the wavelength λ and to the *Faraday depth (FD)*,[1] different from the *rotation measure (RM)*.[2] If one or more rotating regions are located in front of the emitting region (*Faraday screen*), *RM* and *FD* are identical. Distinct emitting and rotating regions located along the line of sight generate a spectrum of FD components, and RM varies with λ^2. In such

[1] $FD = 0.81 \int B_\parallel \, n_e \, dl$, where FD is measured in rad m^{-2}, the line-of-sight magnetic field $B_\parallel$ in μG, the thermal electron density n_e in cm^{-3}, and the line of sight l in pc.

[2] RM is the slope of the function $\Delta\chi\,(\lambda^2)$, $RM = \Delta\chi/\Delta\lambda^2$, and hence varies with λ^2 if $\Delta\chi$ is a nonlinear function of λ^2.

cases, multi-channel spectro-polarimetric radio data are needed that can be Fourier-transformed into Faraday space, called *RM Synthesis* (Chap. 3). If the medium has a relatively simple structure, the 3-D structure of the magnetized interstellar medium can be determined (*Faraday tomography*).

A grid of RM measurements of polarized background sources is another powerful tool to study magnetic field patterns in galaxies (Stepanov et al. 2008), but a large number of background sources is required to recognize the field patterns, to separate the Galactic foreground contribution and to account for intrinsic RMs of the background sources.

18.4 Total Magnetic Fields

18.4.1 Field Strengths

The typical average *equipartition strength* of the total magnetic field (Beck and Krause 2005) in spiral galaxies is about 10 μG, assuming energy equipartition between cosmic rays and magnetic fields. The equipartition assumption is valid on scales of larger than about 1 kpc (Stepanov et al. 2014). Radio-faint galaxies like M 31 (Fig. 18.1) and M 33 have weaker total magnetic fields (about 6 μG), while gas-rich spiral galaxies with high star-formation rates, like M 51 (Fig. 18.5), M 83 (Fig. 18.6) and NGC 6946, have total field strengths of 20–30 μG in their spiral arms. The strongest total fields of 50–100 μG are found in starburst galaxies, like M 82 (Adebahr et al. 2013) and the "Antennae" NGC 4038/9 (Chyży and Beck 2004), and in nuclear starburst regions, like in NGC 253 (Heesen et al. 2011a), and in barred galaxies (Beck et al. 2005).

If energy losses of cosmic-ray electrons are significant, especially in starburst regions or massive spiral arms, the equipartition values are lower limits (Beck and Krause 2005) and are probably underestimated in starburst galaxies by a factor of a few (Thompson et al. 2006). Field strengths of 0.5–18 mG were detected in starburst galaxies by the Zeeman effect in the OH megamaser emission line at 18 cm wavelength (Robishaw et al. 2008). These values refer to highly compressed gas clouds and are not typical of the diffuse interstellar medium.

The relative importance of various competing forces in the interstellar medium can be estimated by comparing the corresponding *energy densities*. The mean energy densities of the total (mostly turbulent) magnetic field and the cosmic rays in NGC 6946 (Fig. 18.2) and M 33 are $\simeq 10^{-11}$ erg cm^{-3} and $\simeq 10^{-12}$ erg cm^{-3}, respectively (Beck 2007; Tabatabaei et al. 2008), similar to that of the turbulent gas motions across the whole star-forming disk, but about 10 times larger than that of the ionized gas. Magnetic fields are dynamically important. The total magnetic energy density may even dominate in the outer galaxy where the equipartition field strength is an underestimate due to energy losses of the cosmic-ray electrons. The energy density of the regular magnetic field decreases even more slowly than that

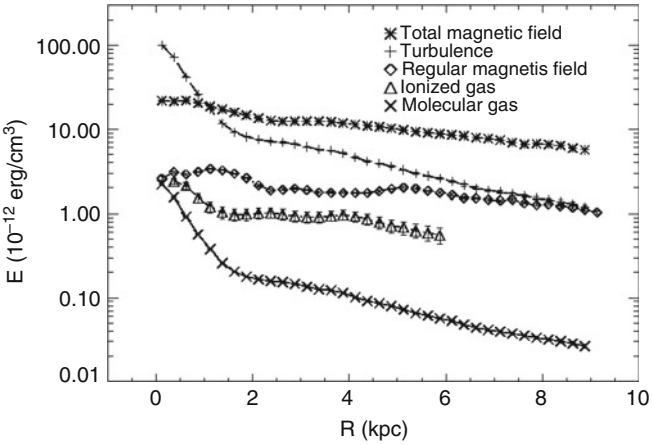

Fig. 18.2 Radial variation of the energy densities in NGC 6946: total magnetic field E_B ($B_t^2/8\pi$), regular magnetic field ($B_{reg}^2/8\pi$), turbulent motion of the neutral gas E_{turb} ($0.5\,\rho_n\,v_{turb}^2$, where $v_{turb} \approx 7$ km/s), thermal energy of the ionized gas E_{th} ($0.5\,n_e\,k\,T_e$) and thermal energy of the molecular gas E_n ($0.5\,\rho_n\,k\,T_n$), determined from observations of synchrotron and thermal radio continuum and the CO and HI line emissions (from Beck 2007)

of the total field. Although the star-formation activity is low in the outer disk, the magneto-rotational instability (MRI) may serve as the source of turbulence required for dynamo action (Sellwood and Balbus 1999; Elstner et al. 2014).

In the case of energy equipartition, the radial scale length of the total field in the disk of mildly inclined galaxies, or the vertical scale height in the halo of edge-on galaxies, is at least $(3-\alpha)$ times larger than the synchrotron scale length of typically 4 kpc (Basu and Roy 2013) (where $\alpha \simeq -1$ is the synchrotron spectral index). The resulting value of $\simeq 16$ kpc is a lower limit because the cosmic-ray electrons lose their energy with distance from the star-forming disk and the equipartition assumption yields too small values for the field strength. The galactic fields probably extend far out into intergalactic space, but at GHz frequencies the measured extent of the radio disks of galaxies is limited by energy loss of cosmic-ray electrons. Measurements at low frequencies (where energy losses are smaller) are needed, e.g. with LOFAR (Chap. 1). Faraday rotation towards polarized background sources may allow us to measure weak fields to even larger distances from the star-forming disks. A large radial scale length may mean that magnetic fields affect the global rotation of the gas in the outer parts of spiral galaxies (Jałocha et al. 2012; Ruiz-Granados et al. 2010), but this cannot explain the flat rotation curves (Elstner et al. 2014).

18.4.2 The Radio–Infrared Correlation

The integrated luminosity of the total radio continuum emission at centimeter wavelengths (frequencies of a few GHz), which is mostly of nonthermal synchrotron origin, and the far-infrared (FIR) luminosity of star-forming galaxies are tightly correlated. This correlation is one of the tightest correlations known in astronomy. It extends over five orders of magnitude (Bell 2003) and is valid in starburst galaxies to redshifts of at least 3 (Seymour et al. 2008). Hence the total radio emission can serve as a tracer of magnetic fields and of star formation out to large distances. The correlation requires that total (mostly turbulent) magnetic fields and star formation are connected, so that the field strength exceeds several 100 μG in distant galaxies (Murphy 2009). The tightness needs multiple feedback mechanisms that are not yet understood (Lacki et al. 2010).

The total radio and far-infrared (FIR) intensities *within* galaxies are also highly correlated. The exponent of the correlation in M 51 was found to be different in the central region, spiral arms and interarm regions (Dumas et al. 2011; Basu et al. 2012). The magnetic field and its structure play an important role to understand the correlation (Tabatabaei et al. 2013a,b). The radio–infrared correlation can be presented as a correlation between turbulent field strength and star-formation rate (Fig. 18.3, Tabatabaei et al. 2013a; Heesen et al. 2014). In contrast, the ordered field is either uncorrelated with the star-formation rate, or anticorrelated in galaxies where the ordered field is strongest in interarm regions with low star formation (Fig. 18.4). A wavelet cross-correlation analysis for M 33 showed that the radio–

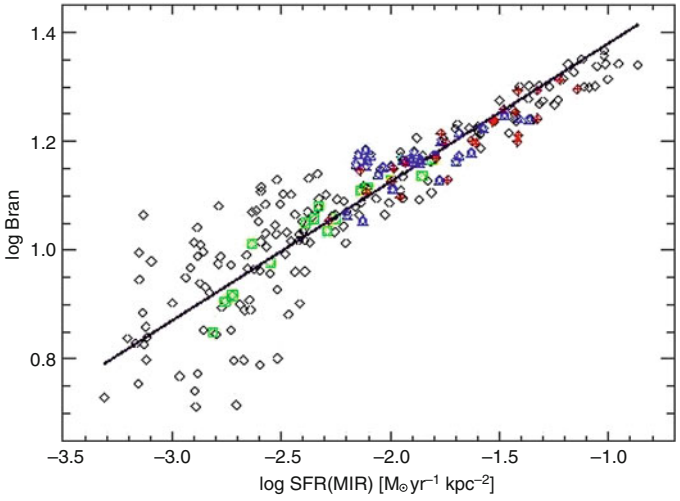

Fig. 18.3 Correlation between the strength of the total equipartition field (dominated by the turbulent field) and star-formation rate per area (determined from the 24 μm infrared intensities) within the galaxy NGC 4254 (from Chyży 2008)

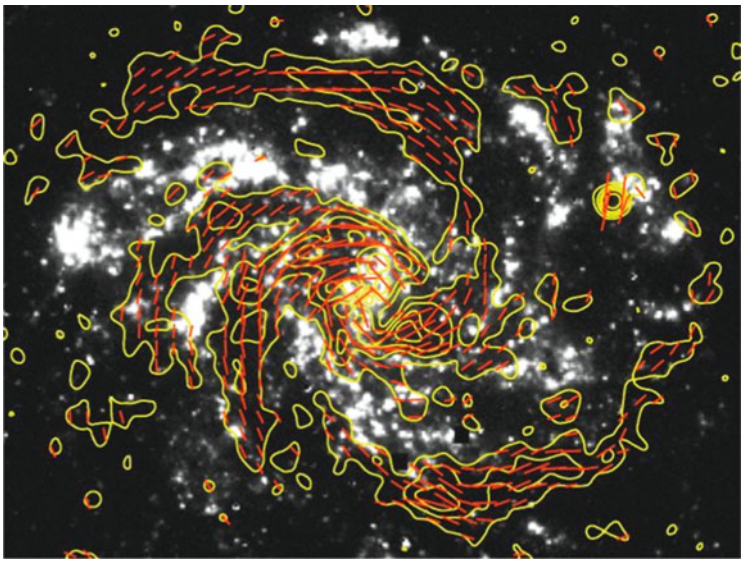

Fig. 18.4 Polarized radio emission (contours) and B-vectors of NCC 6946, combined from observations at 6 cm wavelength with the VLA and Effelsberg telescopes and smoothed to 15″ resolution (from Beck 2007), overlaid onto an Hα image from Anne Ferguson (Copyright: MPIfR Bonn and *Sterne und Weltraum*)

FIR correlation holds at scales <1 kpc (Tabatabaei et al. 2007). The correlation in the Large Magellanic Cloud (LMC) breaks down below scales of about 50 pc (Hughes et al. 2006). The propagation of cosmic-ray electrons away from their sources in star-forming regions is probably responsible for the breakdown scale, and the propagation length depends on the field structure (Tabatabaei et al. 2013b).

18.5 Structure of Ordered Magnetic Fields

18.5.1 Spiral Galaxies

Ordered (regular and/or anisotropic) field traced by polarized synchrotron emission form spiral patterns in almost every galaxy (Beck 2005), even in galaxies with a star-forming ring (Chyży and Buta 2008), in flocculent galaxies without massive spiral arms (Soida et al. 2002), in the central regions of galaxies and in circumnuclear gas rings of barred galaxies (Beck et al. 2005). Ordered fields are generally strongest (10–15 μG) in the regions *between* the optical spiral arms and oriented parallel to the adjacent spiral arms, in some galaxies forming *magnetic arms*, like in

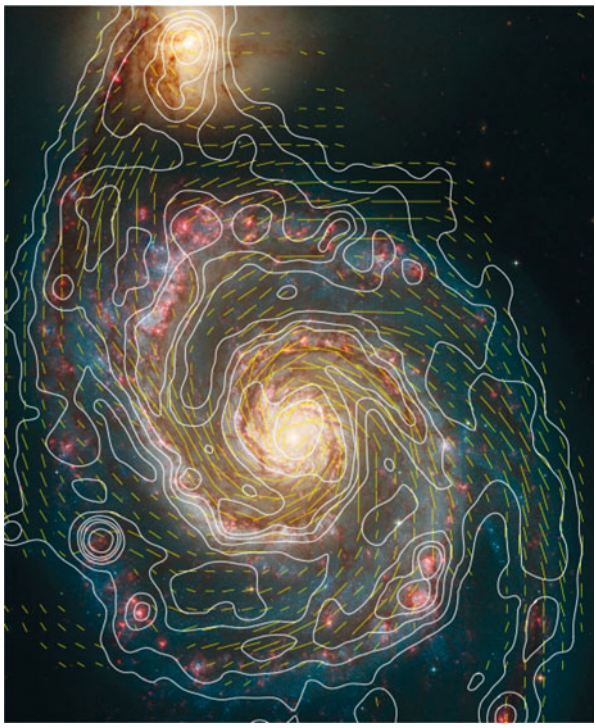

Fig. 18.5 Total radio emission (contours) and B-vectors of M 51, combined from observations at 6 cm wavelength with the VLA and Effelsberg telescopes and smoothed to 15″ resolution (from Fletcher et al. 2011), overlaid onto an optical image from the HST (Copyright: MPIfR Bonn and *Hubble Heritage Team*. Graphics: magazine *Sterne und Weltraum*)

IC 342 (Krause 1993) and NGC 6946 (Fig. 18.4), with exceptionally high degrees of polarization (up to 50%). These are probably generated by a large-scale dynamo (Sect. 18.2). In galaxies with strong density waves like M 51 (Fig. 18.5) and M 83 (Fig. 18.6) enhanced ordered (anisotropic turbulent) fields occur at the inner edges of the inner optical arms, in the interarm regions and in the outer optical arms. From an analysis of dispersions of the radio polarization angles at 6 cm in M 51, the ratio of the correlation lengths parallel and perpendicular to the local ordered magnetic field is about 2 (Houde et al. 2013).

The observed smooth spiral patterns with radially decreasing pitch angles (Fletcher 2010) indicate a general decoupling between magnetic fields and the gas flow, as predicted by $\alpha - \Omega$ dynamo action. At present, no other model can explain the magnetic spiral patterns in the many types of galaxies.

The typical degree of radio polarization within the spiral arms is only a few percent; hence the field in the spiral arms must be mostly tangled or randomly oriented within the telescope beam, the width of which corresponds to a few 100 pc. Turbulent fields in spiral arms are probably generated by turbulent gas motions related to star formation activity (small-scale dynamo).

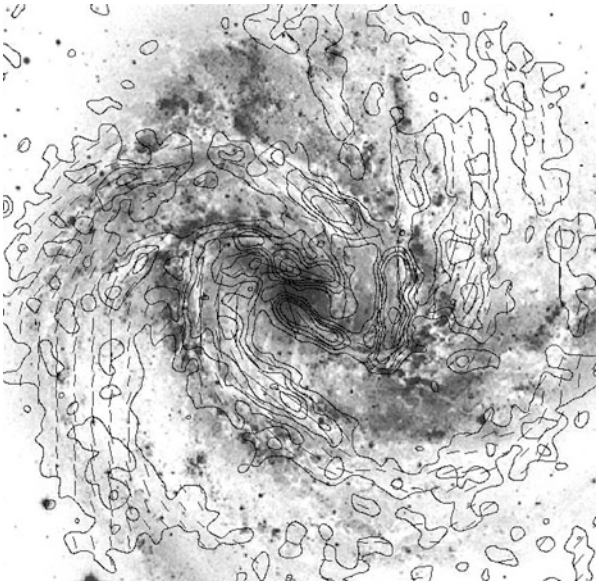

Fig. 18.6 Polarized radio emission (contours) and B-vectors of M 83, combined from observations at 6 cm wavelength with the VLA and Effelsberg telescopes and smoothed to 15″ resolution (from Beck, unpublished), overlaid onto an optical image from Dave Malin, Anglo Australian Observatory (Copyright: MPIfR Bonn and AAO)

At wavelengths of around 20 cm, most of the polarized emission from the far side of the disk and halo is Faraday-depolarized and the emission from the front side dominates. A striking asymmetry of the polarized emission occurs along the major axis of 12 spiral galaxies with inclinations of less than about 60°, observed with sufficiently high sensitivity. The emission is always much weaker around the kinematically receding side (positive radial velocities) of the major axis (Braun et al. 2010; Vollmer et al. 2013). This asymmetry is still visible at 11 cm wavelength, but disappears at smaller wavelengths where the emission from the far side becomes observable. In strongly inclined galaxies, both sides of the major axis become Faraday-depolarized at around 20 cm. Modeling shows that a combination of disk and halo fields, as predicted by $\alpha - \Omega$ dynamo models (Sect. 18.2), can explain the asymmetry (Braun et al. 2010).

18.5.2 Barred Galaxies

In galaxies with massive bars the field lines follow the gas flow (Fig. 18.7). As the gas rotates faster than the bar pattern of a galaxy, a shock occurs in the cold gas, which has a small sound speed, while the flow of warm, diffuse gas is only slightly

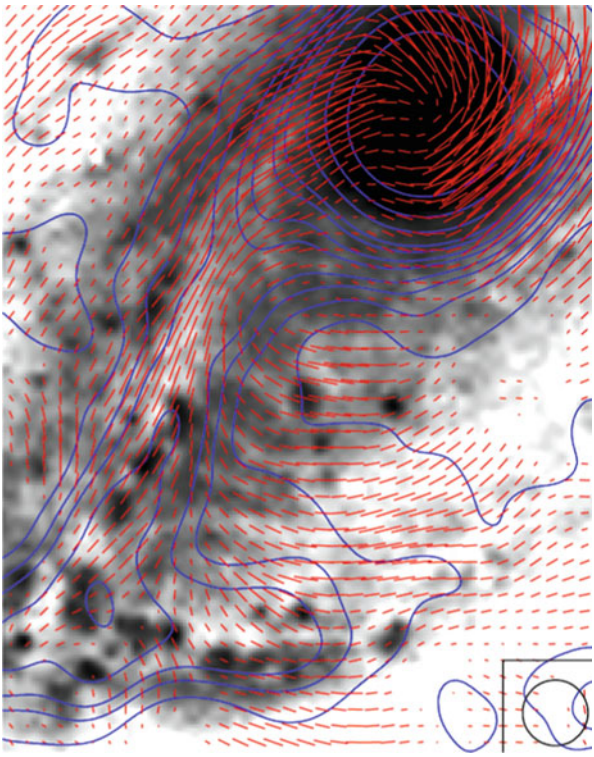

Fig. 18.7 Total radio emission (contours) and B-vectors of the barred galaxy NGC 1097, observed at 6 cm wavelength with the VLA and smoothed to 10″ resolution (from Beck et al. 2005). The background optical image is from Halton Arp (Copyright: MPIfR Bonn and Cerro Tololo Observatory)

compressed but sheared. The ordered field is also hardly compressed, probably coupled to the diffuse gas and strong enough to affect its flow (Beck et al. 2005). The ordered field is also strong in the upstream region (south of the center in Fig. 18.7), oriented almost perpendicular to the bar. The polarization pattern in barred galaxies can be used as a tracer of shearing gas flows in the sky plane and complements spectroscopic measurements of radial velocities.

The central regions of barred galaxies are often sites of ongoing intense star formation and strong magnetic fields that can affect gas flows. NGC 1097 hosts a bright ring with about 1.5 kpc diameter and an active nucleus in its center (Fig. 18.8). The ordered field in the ring has a spiral pattern and extends to the nucleus. The orientation of the innermost spiral field agrees with that of the spiral dust filaments visible on optical images. Magnetic stress in the circumnuclear ring due to the strong total magnetic field (about 50 μG) can drive gas inflow (Balbus and Hawley 1998) at a rate of several solar masses per year, which is sufficient to fuel the activity of the nucleus (Beck et al. 2005).

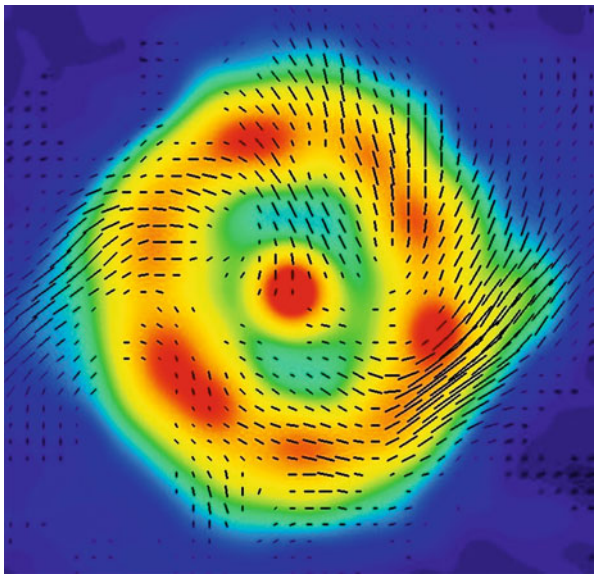

Fig. 18.8 Total radio intensity and B-vectors in the circumnuclear ring of the barred galaxy NGC 1097, observed at 3.5 cm wavelength with the VLA at 3″ resolution (from Beck et al. 2005)

18.5.3 Flocculent and Irregular Galaxies

Flocculent galaxies have disks but no grand-design spiral structure. Nevertheless, spiral magnetic patterns are observed in all flocculent galaxies, indicating that the $\alpha - \Omega$ dynamo works independently of density waves. Ordered magnetic fields with strengths similar to those in grand-design spiral galaxies have been detected in the flocculent galaxies M 33, NGC 3521, NGC 5055 and in NGC 4414 (Soida et al. 2002), and also the mean degree of polarization (corrected for the differences in spatial resolution) is similar in grand-design and flocculent galaxies (Knapik et al. 2000).

Radio continuum maps of irregular, slowly rotating galaxies may reveal strong total magnetic fields, e.g. in the Magellanic-type galaxy NGC 4449 (Fig. 18.9), with a partly ordered field of about 7 μG strength and a spiral pattern (Chyży et al. 2000). Faraday rotation shows that this ordered field is mostly regular and the $\alpha - \Omega$ dynamo is operating. Dwarf irregular galaxies with almost chaotic rotation do not have any regular fields and only spots of faint polarized emission (Heesen et al. 2011b) (see also Fig. 18.10). The turbulent field strengths are generally smaller than in spiral galaxies (Chyży et al. 2011), except for starburst dwarfs, e.g. NGC 1569 with 10–15 μG field strength (Kepley et al. 2010), where star formation activity is sufficiently high for the operation of the small-scale dynamo.

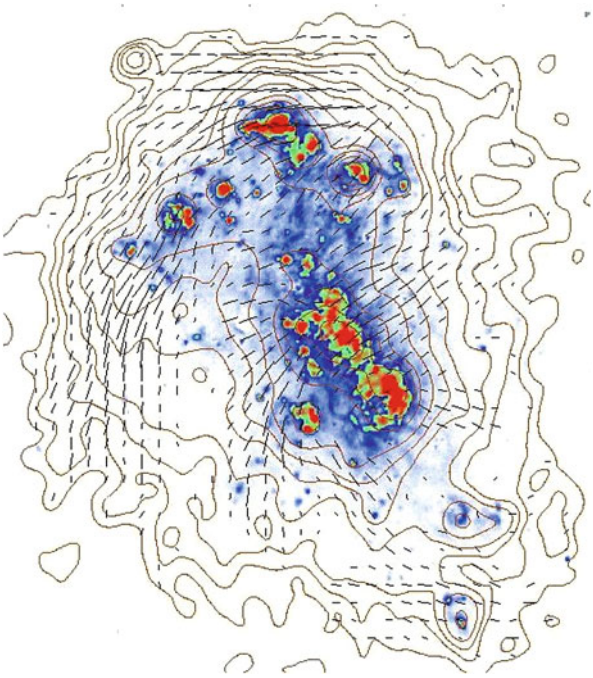

Fig. 18.9 Total radio intensity (contours) and B-vectors of the dwarf irregular galaxy NGC 4449, observed at 3.6 cm with the VLA (from Chyży et al. 2000). The background Hα image is from Dominik Bomans (Bochum University)

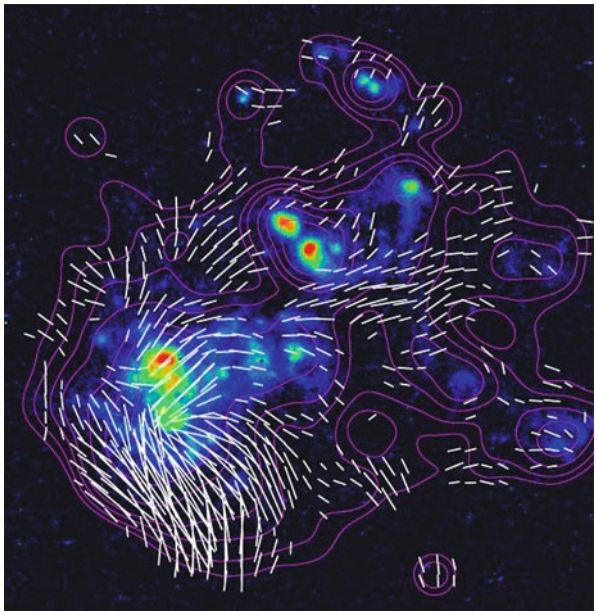

Fig. 18.10 Total radio intensity (contours) and B-vectors of the dwarf irregular galaxy IC 10, observed at 6 cm with the VLA (from Chyży et al., in prep). The background Hα image is from Dominik Bomans (Bochum University)

18.5.4 Interacting Galaxies

Gravitational interaction between galaxies leads to asymmetric gas flows, compression, shear, enhanced turbulence and outflows. Magnetic fields can become aligned along the compression front or perpendicular to the velocity gradients. Such gas flows make turbulent fields highly anisotropic.

The classical interacting galaxy pair is NGC 4038/39, the "Antennae" (Chyży and Beck 2004). It shows bright, extended radio emission filling the whole system. In the interaction region between the galaxies, where star formation did not yet start, and at the northeastern edge of the system, the magnetic field is partly ordered, probably the result of compression and shearing motions along the tidal tail. Particularly strong, almost unpolarized emission comes from a region of violent star formation, hidden in dust. The average total magnetic field is stronger than in normal spirals, but the mean degree of polarization is unusually low, implying that the fields are tangled.

Interaction with a dense intergalactic medium also imprints unique signatures onto magnetic fields and thus the radio emission. The Virgo cluster is a location of especially strong interaction effects (Figs. 18.11 and 18.12), and almost all cluster galaxies observed so far show asymmetries of their polarized emission because the outer magnetic fields were compressed (Vollmer et al. 2007, 2013; Weżgowiec et al. 2007, 2012). Ordered fields are an excellent tracer of past interactions between galaxies or with the intergalactic medium.

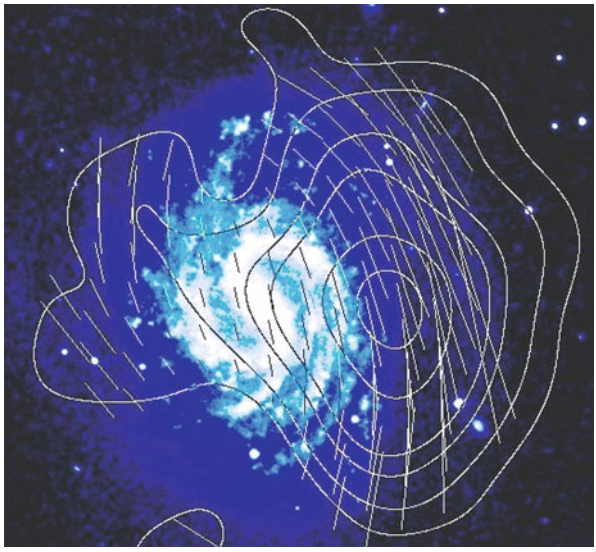

Fig. 18.11 Polarized radio intensity (contours) and B-vectors of the Virgo galaxy NGC 4535, observed at 6 cm with the Effelsberg telescope (from Weżgowiec et al. 2007). The background optical image is from the Digital Sky Survey

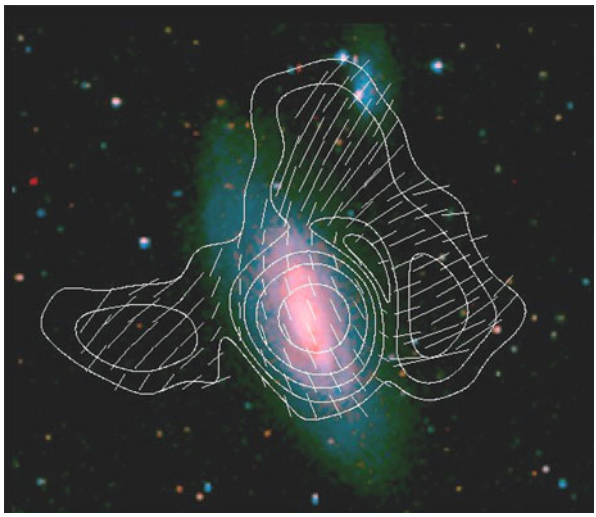

Fig. 18.12 Polarized radio intensity (contours) and B-vectors of the Virgo galaxy NGC 4569, observed at 6 cm with the Effelsberg telescope (from Chyży et al. 2006). The background optical image is from the Digital Sky Survey

18.5.5 Halos Around Edge-on Galaxies

Nearby galaxies seen *edge-on* generally show a disk-parallel field near the disk plane (Dumke et al. 1995). As a result, polarized emission can also be detected from distant, unresolved galaxies if the inclination is larger than about 20° (Stil et al. 2009). This opens a new method to search for ordered fields in distant galaxies. High-sensitivity radio polarization observations of edge-on galaxies like NGC 253 (Heesen et al. 2009b), NGC 891 (Fig. 18.13) and NGC 5775 (Fig. 18.14) revealed vertical field components in the halo forming an X-shaped pattern which may be related to dynamo action (Moss et al. 2010) or to outflows.

The stronger magnetic field in the central regions leads to larger synchrotron loss, leading to the "dumbbell" shape of many radio halos, e.g. in NGC 253 (Heesen et al. 2009a). From the radio scale heights at several frequencies and the corresponding lifetimes of cosmic-ray electrons (due to synchrotron, IC and adiabatic losses) a transport speed of about 300 km/s was measured for the electrons in the halo of NGC 253 (Heesen et al. 2009a). Most edge-on galaxies observed so far have radio scale heights of about 2 kpc. Because the average field strengths and hence electron lifetimes are different in these galaxies, this indicates that the outflow speed of the electrons increases with the average field strength in order to achieve similar scale heights (Krause 2009). The average field strength is related to the average gas density and star-formation rate.

In the exceptionally large radio halos around the irregular and interacting galaxies M 82 (Adebahr et al. 2013; Reuter et al. 1994) and NGC 4631 (Golla and Hummel 1994; Irwin et al. 2012; Mora and Krause 2013) a few magnetic spurs could be resolved, connected to star-forming regions. These observations support the idea of a strong galactic outflow that is driven by regions of star formation in the inner disk.

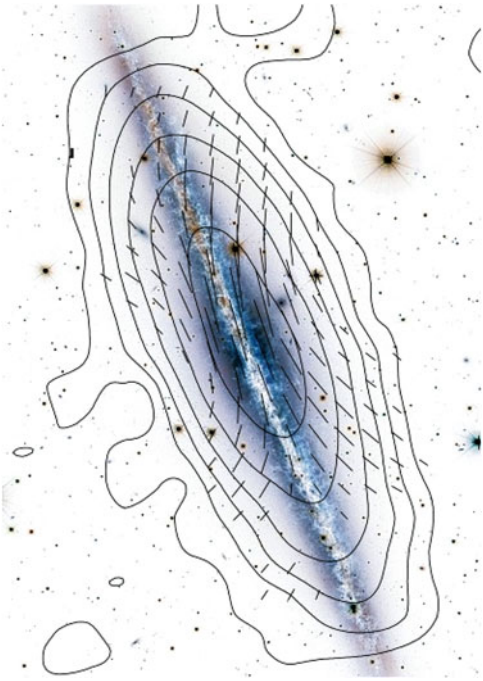

Fig. 18.13 Total radio emission (84″ resolution) and B-vectors of the edge-on galaxy NGC 891, a galaxy similar to the Milky Way, observed at 3.6 cm with the Effelsberg telescope (from Krause 2009). The background optical image is from the CFHT

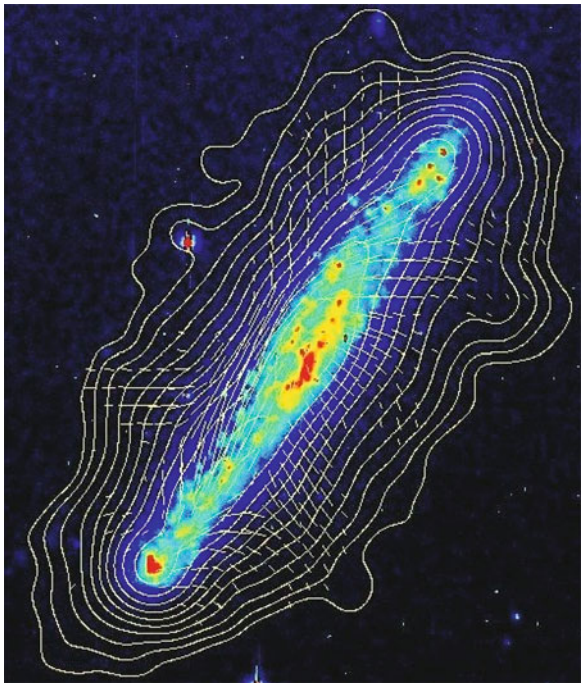

Fig. 18.14 Total radio intensity and B-vectors of the edge-on galaxy NGC 5775, observed at 6 cm wavelength with the VLA at 17″ resolution (from Tüllmann et al. 2000)

18.5.6 Early-Type and Spheroidal Galaxies

Spiral galaxies of type Sa and S0 and elliptical galaxies without an active nucleus have very little star formation and hence hardly produce cosmic rays that could emit synchrotron emission. The only deep observation of a Sa galaxy, M 104 with a prominent dust ring, revealed weak, ordered magnetic fields (Krause et al. 2006). Large-scale regular magnetic fields may exist in differentially rotating galaxies without star formation because turbulence can be generated by the magneto-rotational instability (MRI) (Sellwood and Balbus 1999). Their detection may become possible via RM grids of background sources with future radio telescopes (Chap. 1).

The search for synchrotron emission from nearby dwarf spheroidal galaxies without star formation is an attractive possibility to detect decaying weakly interactive massive particles (WIMPs), candidates of dark matter (Colafrancesco et al. 2007).

18.6 Regular Magnetic Fields

18.6.1 Large-Scale Fields in Galaxy Disks

Spiral fields are generated by compression, by shear in interarm regions, or by dynamo action (Sect. 18.2). Large-scale patterns of Faraday rotation measures (RM) are signatures of regular fields generated by the $\alpha - \Omega$ dynamo and can be identified from diffuse polarized emission of the galaxy disks (Krause 1990) or from RM data of polarized background sources (Stepanov et al. 2008). If several dynamo modes are superimposed, a Fourier analysis of the RM variation with azimuthal angle is needed. The resolution of present-day observations is sufficient to identify 2–3 modes.

The disks of about a dozen nearby spiral galaxies reveal large-scale RM patterns. The Andromeda galaxy M 31 (Fig. 18.1) is the prototype of a dynamo-generated axisymmetric spiral disk field (Fletcher et al. 2004). Other candidates for a dominating axisymmetric disk field (dynamo mode $m = 0$) are the nearby spirals IC 342 (Krause et al. 1989a) and NGC 253 (Heesen et al. 2009b). The axisymmetric field in the irregular Large Magellanic Cloud (LMC) is almost azimuthal (small pitch angle) (Mao et al. 2012). Dominating bisymmetric spiral fields (dynamo mode $m = 1$) are rare, as predicted by dynamo models, but possibly exists in M 81 (Krause et al. 1989b). Faraday rotation in NGC 6946 (Fig. 18.15) and in other similar galaxies with magnetic arms can be described by a superposition of two azimuthal dynamo modes ($m = 0$ and $m = 2$) with about equal amplitudes where the quadrisymmetric ($m = 2$) spiral mode is phase shifted with respect to the density wave (Beck 2007). For several other galaxies, three modes ($m = 0$, 1 and 2) are necessary to describe the data (Fletcher 2010).

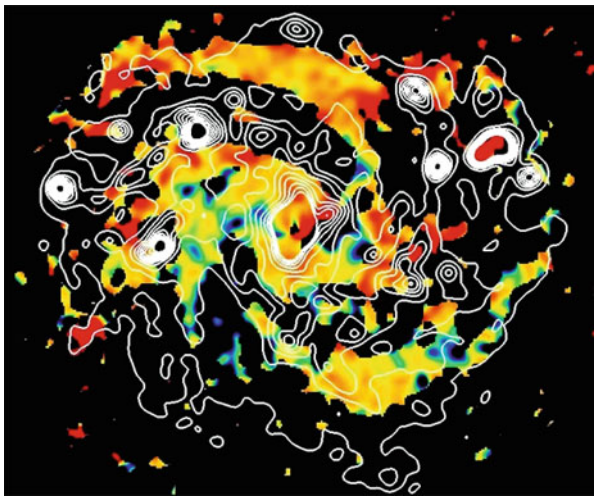

Fig. 18.15 Total radio intensity at 6 cm wavelength (contours) and Faraday rotation measures between 3.6 and 6 cm wavelengths (colors) in NGC 6946, derived from combined observations with the VLA and Effelsberg telescopes at 15″ resolution (from Beck 2007). The color scale ranges from $-75\,\mathrm{rad/m^2}$ to $+175\,\mathrm{rad/m^2}$. The average rotation measure of about $+50\,\mathrm{rad/m^2}$ is caused by the foreground medium in the Milky Way

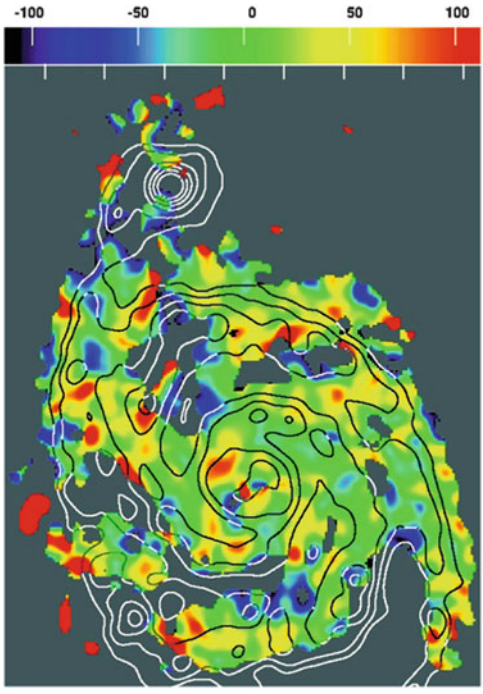

Fig. 18.16 Total radio intensity at 6 cm wavelength (contours) and Faraday rotation measures between 3.6 and 6 cm wavelengths in M 51, derived from combined observations with the VLA and Effelsberg telescopes at 15″ resolution (from Fletcher et al. 2011). The color scale ranges from $-120\,\mathrm{rad/m^2}$ to $+120\,\mathrm{rad/m^2}$

However, the spiral pattern of magnetic fields cannot be solely the result of $\alpha - \Omega$ dynamo action. If the beautiful spiral pattern of M 51 seen in radio polarization (Fig. 18.5) were only due to a regular field in the disk, its line-of sight component should generate a conspicuous large-scale pattern in RM, which is not observed (Fig. 18.16). This means that a large amount of the ordered field is

anisotropic turbulent and probably generated by compression and shear of the non-axisymmetric gas flows in the density-wave potential. The anisotropic turbulent field is strongest at the positions of the prominent dust lanes on the inner edge of the inner gas spiral arms, due to compression of turbulent fields in the density-wave shock. Regular fields (dynamo modes $m = 0$ and $m = 2$) also exist in the disk of M 51, but are much weaker than the anisotropic turbulent field (Fletcher et al. 2011).

In the disks of many other galaxies no clear patterns of Faraday rotation were found. Either several high dynamo modes are superimposed and cannot be distinguished with the limited sensitivity and resolution of present-day telescopes, or the timescale for the generation of large-scale modes is longer than the galaxy's lifetime (Arshakian et al. 2009), or field injection by strong star-formation activity perturbs the generation of the large-scale regular field (Moss et al. 2012).

By comparing the signs of the RM distribution and the velocity field on both sides of a galaxy's major axis, the inward and outward directions of the radial component of the axisymmetric spiral field can be distinguished (Krause and Beck 1998). Dynamo models predict that both signs have the same probability, which is confirmed by observations. The axisymmetric fields of M 31, IC 342, NGC 253 and the axisymmetric field component in NGC 6946 point inwards, while those of NGC 4254, NGC 5775 and the axisymmetric component of the disk field in M 51 point outwards.

18.6.2 Large-Scale Fields in Galaxy Halos

While the azimuthal symmetry of the magnetic field is known for many galaxies, the vertical symmetry (even or odd) is harder to determine. The field of odd symmetry reverses its sign above and below the galactic plane. In mildly inclined galaxies the RM patterns of diffuse polarized emission from even and odd-symmetry fields are similar, while the RMs of background sources are different: strong for odd and small for even symmetry. Background RMs in the Large Magellanic Cloud field indicate an even-symmetry field (Mao et al. 2012). The symmetry type is best visible in strongly inclined galaxies, via the RM sign above and below the plane. Indication for an even-symmetry field was found in NGC 253 (Heesen et al. 2009b).

With help of high-resolution RM mapping, an outwards-directed helical field of about 20 μG strength, extending to at least 1 kpc height, could be identified in the gas outflow cone of NGC 253 (Heesen et al. 2011a). This field may help to confine the outflow.

18.6.3 Field Reversals

Large-scale field reversals at certain radial distances from a galaxy's center, like that observed in the Milky Way (Van Eck et al. 2011; Chap. 17), have not

Table 18.1 Typical field structures in nearby galaxies (where "turbulent" means "isotropic turbulent")

Galaxy type	Magnetic field structure	Regular (dynamo) field
Sc galaxy with strong density wave	Ordered spiral field at inner arm edge and in interarm regions, turbulent field in arms	Moderate
Sb or Sc galaxy with weak or moderate density wave	Ordered spiral field in interarm regions, turbulent + ordered field in arms	Strong
Barred Sc galaxy	Ordered + turbulent field along bar, spiral field outside bar	Moderate
Flocculent Sc or Sd galaxy	Spiral + turbulent field in disk	Weak
Irregular galaxy	Turbulent field in star-forming regions + segments of ordered field	Weak
Starburst dwarf galaxy	Turbulent field in star-forming regions	Not detected
Spheroidal dwarf galaxy	Not detected	Not detected
Sa galaxy	Ordered + turbulent fields	Not detected
S0 galaxy	Not detected	Not detected
E galaxy (non-active nucleus)	Not detected	Not detected

been detected in external galaxies, although high-resolution RM maps of Faraday rotation are available for many spiral galaxies. In M 81 the dominating bisymmetric spiral field implies two large-scale reversals (Krause et al. 1989b). In the barred galaxy NGC 7479, where a jet serves as a bright polarized background and where high-resolution observations were possible with high signal-to-noise ratio, several reversals on 1–2 kpc scale were detected in the foreground disk of the galaxy (Laine and Beck 2008). A field reversal extending over 0.6 kpc scale and coinciding with a hole in neutral hydrogen was detected in NGC 6946 (Heald 2012).

The typical magnetic field structures observed in nearby galaxies are summarized in Table 18.1.

18.7 Outlook

Future high-resolution, high-sensitivity observations at medium and high frequencies with the *Jansky Very Large Array* (JVLA) and the planned *Square Kilometre Array* (SKA) (Chap. 1) will directly map the detailed field structure in galaxies and the interaction with the gas. The recently opened low-frequency radio telescope *Low Frequency Array* (LOFAR) and the *Murchison Widefield Array* (MWA) are suitable instruments to search for extended synchrotron radiation at the lowest possible levels in outer galaxy disks and halos and the transition to intergalactic space. We are entering a golden era of magnetic field observations in galaxies.

References

Abreu, P.: The Pierre Auger Collaboration. Astroparticle Phys. **34**, 314 (2010)
Adebahr, B., Krause, M., Klein, U., et al.: Astron. Astrophys. **555**, A23 (2013)
Arshakian, T.G., Beck, R., Krause, M., Sokoloff, D.: Astron. Astrophys. **494**, 21 (2009)
Balbus, S.A., Hawley, J.F.: Rev. Mod. Phys. **70**, 1 (1998)
Basu, A., Roy, S.: Mon. Notices R. Astron. Soc. **433**, 1675 (2013)
Basu, A., Roy, S., Mitra, D.: Astrophys. J. **756**, 141 (2012)
Beck, R.: In: Wielebinski, R., Beck, R. (eds.) Cosmic Magnetic Fields, p. 41. Springer, Berlin (2005)
Beck, R.: Astron. Astrophys. **470**, 539 (2007)
Beck, R., Brandenburg, A., Moss, D., Shukurov, A., Sokoloff, D.: Ann. Rev. Astron. Astrophys. **34**, 155 (1996)
Beck, R., Krause, M.: Astron. Nachr. **326**, 414 (2005)
Beck, R., Fletcher, A., Shukurov, A., et al.: Astron. Astrophys. **444**, 739 (2005)
Bell, E.F.: Astrophys. J. **586**, 794 (2003)
Berkhuijsen, E.M., Beck, R., Hoernes, P.: Astron. Astrophys. **398**, 937 (2003)
Braun, R., Heald, G., Beck, R.: Astron. Astrophys. **514**, A42 (2010)
Caprini, C., Durrer, R., Fenu, E.: J. Cosmol. Astroparticle Phys. **11**, 001 (2009)
Chyży, K.T.: Astron. Astrophys. **482**, 755 (2008)
Chyży, K.T., Beck, R.: Astron. Astrophys. **417**, 541 (2004)
Chyży, K.T., Buta, R.J.: Astrophys. J. **677**, L17 (2008)
Chyży, K.T., Beck, R., Kohle, S., Klein, U., Urbanik, M.: Astron. Astrophys. **356**, 757 (2000)
Chyży, K.T., Soida, M., Bomans, D.J., et al.: Astron. Astrophys. **447**, 465 (2006)
Chyży, K.T., Weżgowiec, M., Beck, R., Bomans, D.J.: Astron. Astrophys. **529**, A94 (2011)
Colafrancesco, S., Profumo, S., Ullio, P.: Phys. Rev. D **75**, 023513 (2007)
Crutcher, R.M., Wandelt, B., Heiles, C., Falgarone, E., Troland, T.H.: Astrophys. J. **725**, 466 (2010)
Dolag, K., Kachelriess, M., Ostapchenko, S., Tomas, R.: Astrophys. J. **727**, L4 (2011)
Dumas, G., Schinnerer, E., Tabatabaei, F.S., et al.: Astron. J. **141**, 41 (2011)
Dumke, M., Krause, M., Wielebinski, R., Klein, U.: Astron. Astrophys. **302**, 691 (1995)
Elstner, D., Beck, R., Gressel, O.: Astron. Astrophys. **568**, A104 (2014)
Fletcher, A.: In: Kothes, R., et al. (eds.) The Dynamic Interstellar Medium. ASP Conference Series, vol. 438, p. 197. Astr. Soc. of the Pacific, San Francisco (2010)
Fletcher, A., Berkhuijsen, E.M., Beck, R., Shukurov, A.: Astron. Astrophys. **414**, 53 (2004)
Fletcher, A., Beck, R., Shukurov, A., Berkhuijsen, E.M., Horellou, C.: Mon. Notices R. Astron. Soc. **412**, 2396 (2011)
Fosalba, P., Lazarian, A., Prunet, S., Tauber, J.A.: Astrophys. J. **546**, 762 (2002)
Gent, F.A., Shukurov, A., Sarson, G.R., Fletcher, A., Mantere, M.J.: Mon. Notices R. Astron. Soc. **430**, L40 (2013)
Gissinger, C., Fromang, S., Dormy, E.: Mon. Notices R. Astron. Soc. **394**, L84 (2009)
Golla, G., Hummel, E.: Astron. Astrophys. **284**, 777 (1994)
Greaves, J.S., Holland, W.S., Jenness, T., Hawarden, T.G.: Nature **404**, 732 (2000)
Gressel, O., Elstner, D., Ziegler, U., Rüdiger, G.: Astron. Astrophys. **486**, L35 (2008)
Hanasz, M., Wóltański, D., Kowalik, K.: Astrophys. J. **706**, L155 (2009)
Hanayama, H., Takahashi, K., Kotake, K., et al.: Astrophys. J. **633**, 941 (2005)
Heald, G.: Astrophys. J. **754**, L35 (2012)
Heesen, V., Beck, R., Krause, M., Dettmar, R.-J.: Astron. Astrophys. **494**, 563 (2009a)
Heesen, V., Krause, M., Beck, R., Dettmar, R.-J.: Astron. Astrophys. **506**, 1123 (2009b)
Heesen, V., Beck, R., Krause, M., Dettmar, R.-J.: Astron. Astrophys. **535**, A79 (2011a)
Heesen, V., Rau, U., Rupen, M.P., Brinks, E., Hunter, D.A.: Astrophys. J. **739**, L23 (2011b)
Heesen, V., Brinks, E., Leroy, A.K., et al.: Astron. J. **147**, 103 (2014)
Houde, M., Fletcher, A., Beck, R., et al.: Astrophys. J. **766**, 49 (2013)
Hughes, A., Wong, T., Ekers, R., et al.: Mon. Notices R. Astron. Soc. **370**, 363 (2006)

Irwin, J., Beck, R., Benjamin, R.A., et al.: Astrophys. J. **144**, 44 (2012)
Jałocha, J., Bratek, Ł., Pękala, J., Kutschera, M.: Mon. Notices R. Astron. Soc. **421**, 2155 (2012)
Kepley, A.A., Mühle, S., Everett, J., et al.: Astrophys. J. **712**, 536 (2010)
Knapik, J., Soida, M., Dettmar, R.-J., Beck, R., Urbanik, M.: Astron. Astrophys. **362**, 910 (2000)
Krause, M.: In: Beck, R., et al. (eds.) Galactic and Intergalactic Magnetic Fields, p. 187. Kluwer, Dordrecht (1990)
Krause, M.: In: Krause, F., et al. (eds.) The Cosmic Dynamo, p. 303. Kluwer, Dordrecht (1993)
Krause, M.: Rev. Mex. AyA **36**, 25 (2009)
Krause, F., Beck, R.: Astron. Astrophys. **335**, 789 (1998)
Krause, M., Hummel, E., Beck, R.: Astron. Astrophys. **217**, 4 (1989a)
Krause, M., Beck, R., Hummel, E.: Astron. Astrophys. **217**, 17 (1989b)
Krause, M., Wielebinski, R., Dumke, M.: Astron. Astrophys. **448**, 133 (2006)
Lacki, B.C., Thompson, T.A., Quataert, E.: Astrophys. J. **717**, 1 (2010)
Laine, S., Beck, R.: Astrophys. J. **673**, 128 (2008)
Lazar, M., Schlickeiser, R., Wielebinski, R., Poedts, S.: Astrophys. J. **693**, 1133 (2009)
Mao, S.A., McClure-Griffiths, N.M., Gaensler, B.M., et al.: Astrophys. J. **759**, 25 (2012)
Mora, S.C., Krause, M.: Astron. Astrophys. **560**, A42 (2013)
Moss, D., Sokoloff, D., Beck, R., Krause, M.: Astron. Astrophys. **512**, A61 (2010)
Moss, D., Stepanov, R., Arshakian, T.G., et al.: Astron. Astrophys. **537**, A68 (2012)
Murphy, E.: Astrophys. J. **706**, 482 (2009)
Rees, M.J.: In: Wielebinski, R., Beck, R. (eds.) Cosmic Magnetic Fields, p. 1. Springer, Berlin (2005)
Reuter, H.-P., Klein, U., Lesch, H., Wielebinski, R., Kronberg, P.P.: Astron. Astrophys. **282**, 724 (1994)
Robishaw, T., Quataert, E., Heiles, C.: Astrophys. J. **680**, 981 (2008)
Ruiz-Granados, B., Rubiño-Martín, J.A., Florido, E., Battaner, E.: Astrophys. J. **723**, L44 (2010)
Scarrott, S.M., Ward-Thompson, D., Warren-Smith, R.F.: Mon. Notices R. Astron. Soc. **224**, 299 (1987)
Schleicher, D.R.G., Banerjee, R., Sur, S., et al.: Astron. Astrophys. **522**, A115 (2010)
Schlickeiser, R.: Phys. Rev. Lett. **109**, 261101 (2012)
Sellwood, J.A., Balbus, S.A.: Astrophys. J. **511**, 660 (1999)
Seymour, N., Dwelly, T., Moss, D., et al.: Mon. Notices R. Astron. Soc. **386**, 1695 (2008)
Shukurov, A., Sokoloff, D., Subramanian, K., Brandenburg, A.: Astron. Astrophys. **448**, L33 (2006)
Soida, M., Beck, R., Urbanik, M., Braine, J.: Astron. Astrophys. **394**, 47 (2002)
Sokoloff, D., Bykov, A.A., Shukurov, A., et al.: Mon. Notices R. Astron. Soc. **299**, 189 (1998). Erratum in Mon. Notices R. Astron. Soc. **303**, 207 (1999)
Stepanov, R., Arshakian, T.G., Beck, R., Frick, P., Krause, M.: Astron. Astrophys. **480**, 45 (2008)
Stepanov, R., Shukurov, A., Fletcher, A., et al.: Mon. Notices R. Astron. Soc. **437**, 2201 (2014)
Stil, J.M., Krause, M., Beck, R., Taylor, A.R.: Astrophys. J. **693**, 1392 (2009)
Tabatabaei, F., Beck, R., Krause, M., et al.: Astron. Astrophys. **466**, 509 (2007)
Tabatabaei, F., Krause, M., Fletcher, A., Beck, R.: Astron. Astrophys. **490**, 1005 (2008)
Tabatabaei, F.S., Schinnerer, E., Murphy, E.J., et al.: Astron. Astrophys. **552**, A19 (2013a)
Tabatabaei, F.S., Berkhuijsen, E.M., Frick, P., Beck, R., Schinnerer, E.: Astron. Astrophys. **557**, A129 (2013b)
Thompson, T.A., Quataert, E., Waxman, E., Murray, N., Martin, C.L.: Astrophys. J. **645**, 186 (2006)
Tüllmann, R., Dettmar, R.-J., Soida, M., Urbanik, M., Rossa, J.: Astron. Astrophys. **364**, L36 (2000)
Van Eck, C.L., Brown, J.C., Stil, J.M., et al.: Astrophys. J. **728**, 97 (2011)
Vollmer, B., Soida, M., Beck, R., et al.: Astron. Astrophys. **464**, L37 (2007)
Vollmer, B., Soida, M., Beck, R., et al.: Astron. Astrophys. **553**, A116 (2013)
Weżgowiec, M., Urbanik, M., Vollmer, B., et al.: Astron. Astrophys. **471**, 93 (2007)
Weżgowiec, M., Urbanik, M., Beck, R., et al.: Astron. Astrophys. **545**, A69 (2012)
Widrow, L.M.: Rev. Mod. Phys. **74**, 775 (2002)

Chapter 19
Simulations of Galactic Dynamos

Axel Brandenburg

Abstract We review our current understanding of galactic dynamo theory, paying particular attention to numerical simulations both of the mean-field equations and the original three-dimensional equations relevant to describing the magnetic field evolution for a turbulent flow. We emphasize the theoretical difficulties in explaining non-axisymmetric magnetic fields in galaxies and discuss the observational basis for such results in terms of rotation measure analysis. Next, we discuss nonlinear theory, the role of magnetic helicity conservation and magnetic helicity fluxes. This leads to the possibility that galactic magnetic fields may be bi-helical, with opposite signs of helicity and large and small length scales. We discuss their observational signatures and close by discussing the possibilities of explaining the origin of primordial magnetic fields.

19.1 Introduction

We know that many galaxies harbor magnetic fields. They often have a large-scale spiral design (for a review, see the Chapter by Haverkorn in this volume). Understanding the nature of those fields was facilitated by an analogous problem in solar dynamo theory, where large-scale magnetic fields on the scale of the entire Sun were explained in terms of mean-field dynamo theory. Competing explanations in terms of primordial magnetic fields have been developed in both cases, but in solar dynamo theory there is the additional issue of an (approximately) cyclic variation, which is not easily explained in terms of primordial fields.

Historically, primordial magnetic fields were considered a serious contender in the explanation of the observed magnetic fields in our and other spiral galaxies; see the review of Sofue et al. (1986). The idea is simply that the differential rotation of the gas in galaxies winds up an ambient magnetic field to form a spiraling magnetic field pattern. There are two problems with this interpretation. Firstly, if there was no turbulent diffusion, the magnetic field would be wound up too many times to explain

A. Brandenburg (✉)
Nordic Institute for Theoretical Physics, KTH Royal Institute of Technology and Stockholm University, Roslagstullsbacken 23, 10691 Stockholm, Sweden
e-mail: brandenb@nordita.org

A. Lazarian et al. (eds.), *Magnetic Fields in Diffuse Media*, Astrophysics and Space Science Library 407, DOI 10.1007/978-3-662-44625-6_19

the observed field, whose magnetic spiral is not as tightly wound as one would have otherwise expected. The tight winding can be alleviated by turbulent diffusion, which is clearly a natural process that is expected to occur in any turbulent environment. In galaxies, an important source of turbulence is supernova explosions (Korpi et al. 1999; Gressel et al. 2008a; Gent et al. 2013a,b) that are believed to sustain the canonical values of a root-mean-square turbulent velocity of $u_{\rm rms} = 10\,{\rm km/s}$ at density $\rho = 2\times10^{-24}\,{\rm g\,cm^{-3}}$. The required vertically integrated energy input would be of the order of $0.5\rho u_{\rm rms}^3 \approx 10^{-24}\,{\rm g\,cm^{-3}}\,(10^6\,{\rm cm\,s^{-1}})^3 = 10^{-6}\,{\rm erg\,cm^{-2}\,s^{-1}}$. which is easily balanced by about 20 supernovae with 10^{51} erg per million years per kpc^2 for the solar neighborhood, which yields about $0.7\times10^{-4}\,{\rm erg\,cm^{-2}\,s^{-1}}$, i.e., nearly two orders of magnitude more than needed (Brandenburg and Nordlund 2011).

Turbulence with these values of $u_{\rm rms}$ and a correlation length $\ell = 70\,{\rm pc}$ (Shukurov 2005), corresponding to a correlation wavenumber $k_{\rm f} = 2\pi/\ell$ is expected to produce turbulent diffusion with a magnetic diffusion coefficient $\eta_{\rm t} = u_{\rm rms}/3k_{\rm f} \approx 10^{25}\,{\rm cm^2\,s^{-1}} \approx 0.04\,{\rm kpc\,km\,s^{-1}}$, which would lead to turbulent decay of a magnetic field with a vertical wavenumber of $k = 2\pi/0.3\,{\rm kpc} \approx 20\,{\rm kpc^{-2}}$ on a decay time of about $(\eta_{\rm t}k^2)^{-1} \approx 60\,{\rm Myr}$. Thus, to sustain such a field, a dynamo process is required.

Magnetic fields affect the velocity through the Lorentz force. However, if one only wants to understand the origin of the magnetic field, we would be interested in early times when the mean magnetic field is still weak. In that case we can consider the case when the velocity field is still unaffected by the magnetic field and it can thus be considered given. This leads to a kinematic problem that is linear.

Several dynamo processes are known. Of particular relevance are large-scale dynamos that produce magnetic fields on scales large compared with the size of the turbulent eddies. These dynamos are frequently being modeled using mean-field dynamo theory, which means that one solves the averaged induction equation. In such a formulation, the mean electromotive force resulting from correlations of small-scale velocity and magnetic field fluctuations are being parameterized as functions of the mean magnetic field itself, which leads to a closed system of equations. The resulting mean-field equations can have exponentially growing or decaying solutions. Of particular interest is here the question regarding the symmetry properties of the resulting magnetic field. This aspect will be discussed in Sect. 19.2.

Next, the magnetic field will eventually be subject to nonlinear effects and saturate. The most primitive form of nonlinearity is α quenching, which limits the α effect such that the energy density of the local mean magnetic field strength is of the order of the kinetic energy of the turbulence. There is the possibility of so-called catastrophic quenching, which has sometimes been argued to suppress not only turbulent diffusion (Cattaneo and Vainshtein 1991), but also the dynamo effect (Vainshtein and Cattaneo 1992). Those aspects will be discussed in Sect. 19.3. It is now understood that catastrophic quenching is a consequence of magnetic helicity conservation and the fact that the magnetic field takes the form of a bi-helical field with magnetic helicity at different scales and signs. Such a field might have observational signatures that could be observable, as will be discussed in Sect. 19.4.

An entirely different alternative is that a primordial magnetic field might still exist. It would be of interest to find out what effects it would have. This affects the discussion of the initial turbulent magnetic field, which might occur in conjunction with magnetic helicity, which requires some knowledge about turbulent cascades that we shall also discuss in connection with dynamos, so we postpone the discussion of primordial magnetic fields until Sect. 19.5, and begin with kinematic mean-field theory.

19.2 Aspects of Kinematic Mean-Field Theory

The purpose of this section is to review some of the important results in applying mean-field dynamo theory to galaxies. We focus here on linear models and postpone the discussion of essentially nonlinear effects to Sect. 19.3.

19.2.1 Dominance of Quadrupolar Modes

Mean-field dynamo theory for galaxies (Parker 1971; Vainshtein and Ruzmaikin 1971) was developed soon after the corresponding theory for solar, stellar and planetary dynamos was first proposed (Parker 1955; Steenbeck et al. 1966; Steenbeck and Krause 1969a,b). The main difference to stellar dynamos is the flat geometry. An important consequence of this is the finding that the lowest eigenmode is of quadrupolar type, which means that the toroidal magnetic field has the same direction on both sides of the midplane. An example of this is shown in Fig. 19.1, where we show vectors of the magnetic field in the xy plane of the galactic disc together with a xz section approximately through the disc axis. We note that this model has been calculated in Cartesian geometry, which leads to minor artifacts as can be seen in two corners.

The models in galactic geometry made use of the fact that in flat geometries, derivatives in the vertical (z) direction are much more important than in the radial or azimuthal directions. One therefore deals essentially with one-dimensional models of the form (Ruzmaikin et al. 1988),

$$\dot{\overline{B}}_R = -(\alpha\overline{B}_\phi)' + \eta_{\rm T}\overline{B}_R'', \quad \dot{\overline{B}}_\phi = S\overline{B}_R + \eta_{\rm T}\overline{B}_\phi''. \tag{19.1}$$

Here, primes and dots denote z and t derivatives, respectively, $\alpha = \alpha_0 f_\alpha(z)$ is a profile for α (antisymmetric with respect to $z = 0$) with typical value α_0, $S = R{\rm d}\Omega/{\rm d}R$ is the radial shear in the disc, and $(\overline{B}_R, \overline{B}_\phi, \overline{B}_z)$ are the components of the mean field $\overline{\boldsymbol{B}}$ in cylindrical coordinates. On $z = \pm H$ one assumes vacuum boundary conditions which, in this one-dimensional problem, reduce to $\overline{B}_R = \overline{B}_\phi = 0$. One can also impose boundary conditions on the mid-plane, $z = 0$, by

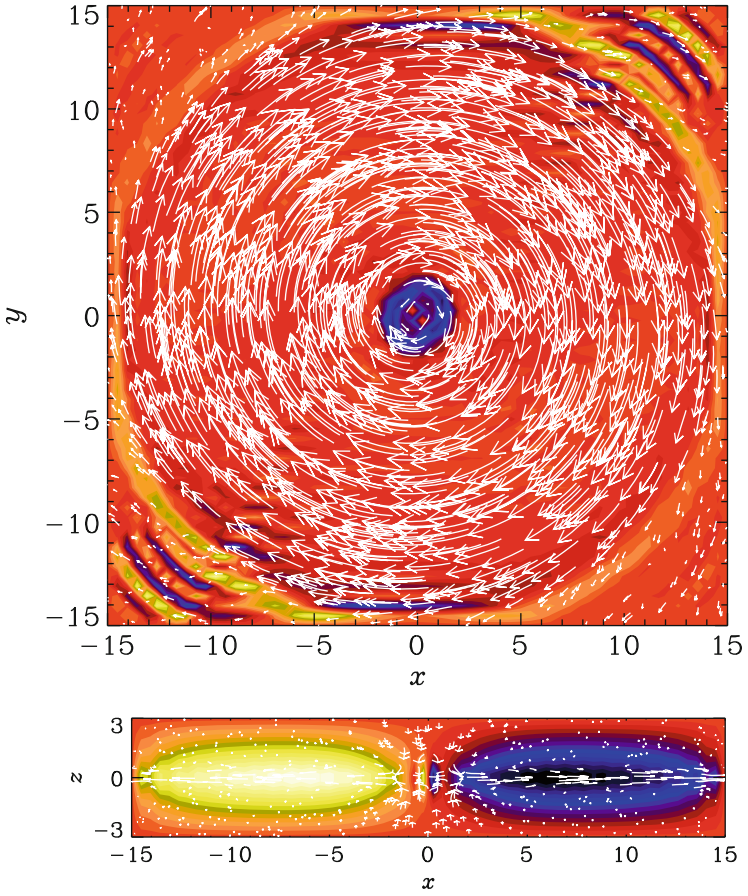

Fig. 19.1 Magnetic field in the midplane of a simplified model of a galaxy with α effect and Brandt rotation curve

selecting either symmetric (quadrupolar) fields, $B_R = \overline{B}'_\phi = 0$, or antisymmetric (dipolar) fields, $B'_R = \overline{B}_\phi = 0$. We define two dimensionless control parameters,

$$C_\Omega = SH^2/\eta_{\rm T}, \quad C_\alpha = \alpha_0 H/\eta_{\rm T}, \tag{19.2}$$

which measure the strengths of shear and α effects, respectively.

In the limit of strong differential rotation, $C_\alpha/C_\Omega \ll 1$, the solutions are characterized by just one parameter, the dynamo number $D = C_\alpha C_\Omega$. Figure 19.2 shows the growth rate of different modes, obtained by solving Eq. (19.1) for both signs of the dynamo number (Brandenburg 1998). To find all the modes, even the unstable ones, one can solve Eq. (19.1) numerically as an eigenvalue problem, where the complex growth rate λ is the eigenvalue with the largest real part. Note that the

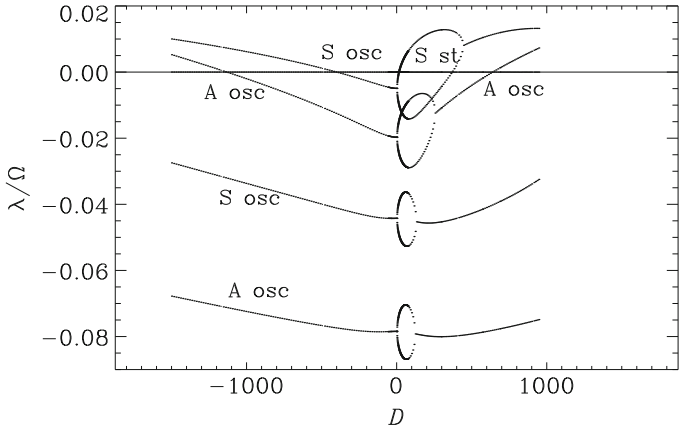

Fig. 19.2 Eigenvalues of the dynamo equations with radial shear in slab geometry. The dynamo number is defined positive when shear is negative and α positive. Note that for $\alpha > 0$, the most easily excited solution is non-oscillatory ('steady') and has even parity (referred to as 'S st') while for $\alpha < 0$ it is oscillatory ('S osc'). Adapted from Brandenburg (1998)

most easily excited mode is quadrupolar and non-oscillatory. We denote it by 'S st', where 'S' refers to symmetry about the midplane and 'st' refers to steady, as opposed to oscillatory. Of course, only in the marginally excited case those modes are really steady.

The basic dominance of quadrupolar magnetic fields is also reproduced by more recent global simulations such as those of Gissinger et al. (2009). However, the situation might be different in so-called cosmic-ray driven dynamos (see below), where the magnetic field could be preferentially dipolar with a reversal of the toroidal field about the midplane (Hanasz et al. 2009). The possibility of a significant dipolar component has also been found for the magnetic field of our Galaxy (Jansson and Farrar 2012). On the other hand, in the inner parts of the galaxy, the geometrical properties of the bulge may also give rise to a locally dipolar field in the center (Donner and Brandenburg 1990).

19.2.2 Non-Axisymmetric Magnetic Fields

An important realization due to Rädler (1986b) was that non-axisymmetric solutions are never favored by differential rotation, because it winds up such fields, so anti-parallel field lines are being brought close together and then decay rapidly, as can be seen from Fig. 19.3. This was already found in earlier numerical eigenvalue calculations (Rädler 1980, 1986a), suggesting that corresponding asymptotic calculations that make the so-called $\alpha\Omega$ approximation (Ruzmaikin et al. 1985), in which the α effect is neglected compared with the shear term, could be problematic.

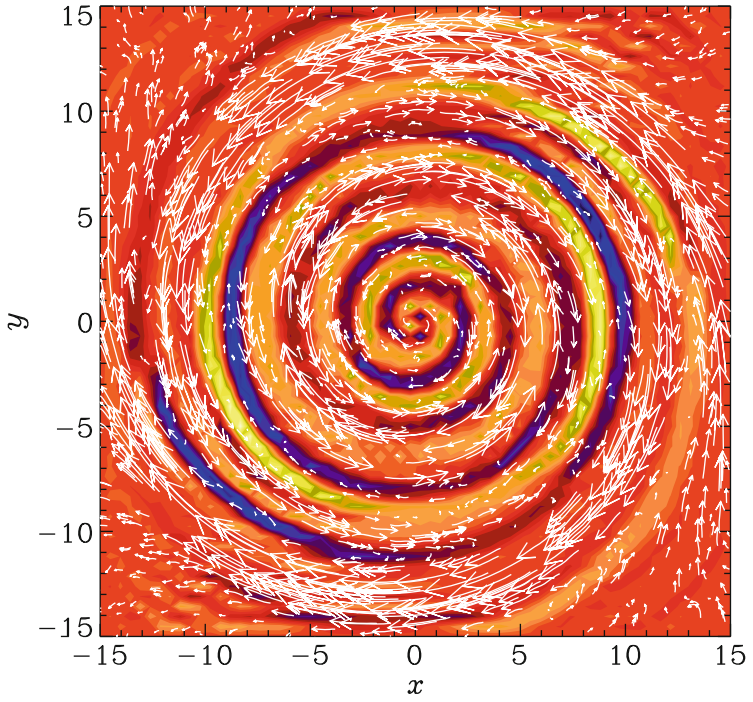

Fig. 19.3 Magnetic field in the midplane of a simplified model of a galaxy with Brandt rotation curve and an initially horizontal magnetic field in the x direction that is then being wound up

At the time it was thought that many external galaxies would harbor non-axisymmetric magnetic fields (Sofue et al. 1986), but this view has now changed with the more careful measurements of the toroidal magnetic fields along an azimuthal ring around various external galaxies. This can be seen from plots of the rotation measure at different positions along such an azimuthal ring. The rotation measure is defined as

$$\mathrm{RM} = \mathrm{d}\chi/\mathrm{d}\lambda^2, \tag{19.3}$$

where λ is the wavelength of the radio emission and χ is the angle of the polarization vector determined from the Stokes parameters Q and U as

$$\chi = \tfrac{1}{2}\mathrm{Arctan}(U, Q), \tag{19.4}$$

where Arctan returns all angles between $-\pi$ and π whose tangent yields U/Q. Figure 19.4 shows theoretical RM dependencies on azimuth around projected rings around dynamo models simulating galactic magnetic fields of types 'S0' (symmetric about midplane with $m = 0$) and 'S1' (also symmetric about midplane, but with $m = 1$, i.e., non-axisymmetric). The result is quite clear. When the magnetic

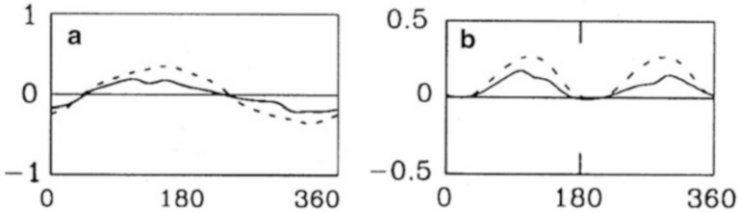

Fig. 19.4 Dependence of RM on the azimuthal angle for (**a**) magnetic field of type S0, and (**b**) magnetic field of type S1. *Solid* and *dashed lines* refer to two different procedures of measuring RM. Adapted from Donner and Brandenburg (1990)

field is axisymmetric, one expects the toroidal magnetic field to give a line-of-sight component $B_\parallel$ and point toward the observer at one azimuthal position on the projected azimuthal ring and away from the observer on the opposite position along the ring. This should lead to a sinusoidal modulation of RM with one positive extremum and one negative one. When the field is bisymmetric (i.e., non-axisymmetric with $m = 1$), one expects two positive extrema and two negative ones. This is indeed borne out by the simulations. It is this type of evidence that led to the conclusion that the magnetic field of M81 is non-axisymmetric (Krause et al. 1989).

Even today, M81 is still the one and only example of a galaxy displaying a distinctly non-axisymmetric magnetic field with azimuthal order $m = 1$ (Beck et al. 1996); see also the Chapter by Beck in this volume on observations of galactic magnetic fields. Such fields are hard to explain theoretically, because, according to most of the dynamo models presented so far, non-axisymmetric modes are always harder to excite than axisymmetric ones; see also Brandenburg et al. (1989) for a survey of such solutions. The currently perhaps best explanation for non-axisymmetric magnetic fields in galaxies is that they are a left-overs from the initial conditions and are being wound up by the differential rotation. This can be a viable explanation only because for galaxies the turbulent decay time might be slow enough, especially in their outer parts, if those fields are helical and non-kinematic (Blackman and Subramanian 2013; Bhat et al. 2014). Moss et al. (1993) presented a model that incorporated a realistic representation of the so-called peculiar motions of M81 that were proposed to be the result of a recent close encounter with a companion galaxy. These peculiar motions are flows relative to the systematic differential rotation and have been obtained from an earlier stellar dynamics simulation by Thomasson and Donner (1993). A very different alternative is that the $m = 1$ magnetic fields in the outskirts of M81 are driven by the magneto-rotational instability, as has recently been proposed by Gressel et al. (2013).

A more typical class of non-axisymmetric fields are those with $m = 2$ and $m = 0$ contributions. Those would no longer be called bisymmetric and fall outside the old classification into axisymmetric and bisymmetric spirals. Examples of non-axisymmetric but non-bisymmetric spirals are NGC 6946 and IC 342 (e.g. Beck 2007; Beck and Wielebinski 2013). A natural way of explaining such fields is via non-axisymmetric dynamo parameters such as the α-effect (Mestel and

Subramanian 1991; Moss et al. 1991; Subramanian and Mestel 1993). This has been confirmed through more realistic modeling both with (Chamandy et al. 2013, 2014) and without (Moss et al. 2013) memory effect. For a more popular account on recent modeling efforts, see also the review by Moss (2012).

19.2.3 The α Effect and Turbulent Diffusivity in Galaxies

The forcing of turbulence through the pressure force associated with the thermal expansion of blast waves is essentially irrotational. However, vorticity is essential for what is known as small-scale dynamo action, and it is also a defining element of kinetic helicity and hence the α effect, which is an important parameter in mean-field simulations of galactic dynamos. In galaxies, the baroclinic term is an important agent for making the resulting flow vortical (Korpi et al. 1998); see also Del Sordo and Brandenburg (2011), who compared with the effects of rotation and shear. Thus, we need to know how efficiently vorticity can be generated in turbulence. This question becomes particularly striking in the case of isothermal turbulence, because then, and in the absence of rotation, shear, or magnetic fields, there is no baroclinic term that could generate vorticity. In that case, vorticity can only be generated via viscosity through a "visco-clinic" term of the form $\boldsymbol{\nabla}\ln\rho\times\boldsymbol{\nabla}\mathrm{div}\,\boldsymbol{u}$, although it is not obvious that this term is unaffected by the numerical form of the diffusion operator.

Most of the papers assume that it is a result of cyclonic turbulent motions driven by supernova explosions. There have also been attempts to calculate α and η_t by considering individual explosions (Ferrière 1992) and also so-called superbubbles resulting from several explosions that could have triggered each other (Ferrière 1993).

Nowadays, a reliable method for calculating α and η_t from numerical simulations is the test-field method, which will be briefly discussed below. The α effect and turbulent diffusivity η_t characterize the resulting electromotive force $\overline{\mathcal{E}}$ from small-scale (unresolved) motions, i.e., $\overline{\mathcal{E}}=\overline{\boldsymbol{u}\times\boldsymbol{b}}$. This expression enters in the evolution equation for the mean magnetic field,

$$\frac{\partial\overline{\boldsymbol{B}}}{\partial t}=\boldsymbol{\nabla}\times\left(\boldsymbol{U}\times\boldsymbol{B}+\overline{\boldsymbol{u}\times\boldsymbol{b}}-\eta\mu_0\overline{\boldsymbol{J}}\right). \tag{19.5}$$

To determine $\overline{\boldsymbol{u}\times\boldsymbol{b}}$ as a function of $\overline{\boldsymbol{B}}$, which drives magnetic fluctuations $\boldsymbol{b}=\boldsymbol{B}-\overline{\boldsymbol{B}}$ through tangling by the turbulent motions $\boldsymbol{U}=\overline{\boldsymbol{U}}+\boldsymbol{u}$, we use the evolution equation for $\boldsymbol{b}$ obtained by subtracting Eq. (19.5) from the full induction equation

$$\frac{\partial\boldsymbol{B}}{\partial t}=\boldsymbol{\nabla}\times(\boldsymbol{U}\times\boldsymbol{B}-\eta\mu_0\boldsymbol{J}), \tag{19.6}$$

with the result

$$\frac{\partial \boldsymbol{b}}{\partial t} = \boldsymbol{\nabla} \times \left(\overline{\boldsymbol{U}} \times \boldsymbol{b} + \boldsymbol{u} \times \overline{\boldsymbol{B}} + \boldsymbol{u} \times \boldsymbol{b} - \overline{\boldsymbol{u} \times \boldsymbol{b}} - \eta_{\rm t} \mu_0 \boldsymbol{j} \right), \tag{19.7}$$

where $\boldsymbol{J} = \overline{\boldsymbol{J}} + \boldsymbol{j}$ is the current density decomposed into mean and fluctuating parts, μ_0 is the vacuum permeability, and η is the Spitzer value of the magnetic diffusivity. We solve Eq. (19.7) for mean fields $\overline{\boldsymbol{B}}$ that do not need to be a solution of Eq. (19.5); see Schrinner et al. (2005, 2007). We can then compute $\overline{\boldsymbol{u} \times \boldsymbol{b}}$, related it to the chosen test fields and their derivatives, $\overline{B}_i$ and $\partial \overline{B}_i / \partial x_j$, and determine all relevant components of α_{ij} and η_{ijk}, which requires a corresponding number of test fields.

There is by now a lot of literature on this topic. The method has been extended into the quasi-kinematic (Brandenburg et al. 2008a) and fully nonlinear (Rheinhardt and Brandenburg 2010) regimes. For moderate scale separation, a convolution in space and time can often not be ignored (Brandenburg et al. 2008b; Hubbard and Brandenburg 2009), but it is possible to incorporate such effects in an approximate fashion by solving an evolution equation for the mean electromotive force (Rheinhardt and Brandenburg 2012). Such an approach restores causality in the sense that the elliptic nature of the diffusion equation takes the form of a wave equation, which limits effectively the maximum propagation speed to the rms velocity of the turbulence (Brandenburg et al. 2004). Such an equation is usually referred to as the telegraph equation. In galaxies, such an effect can also cause magnetic arm to lag the corresponding material arm with respect to the rotation (Chamandy et al. 2013).

Gressel et al. (2008b) have applied the test-field method to their turbulent galactic dynamo simulations (Gressel et al. 2008a) and find values for $\eta_{\rm t}$ that are of the order of 1 kpc km s^{-1} (see Fig. 19.5), which corresponds to 3×10^{26} cm^2 s^{-1}, which is 30 times larger than our naive estimate presented in the introduction. In their simulations, $u_{\rm rms} \approx 40$ km/s, so their effective value of $k_{\rm f}$ must be $k_{\rm f} \approx u_{\rm rms}/3\eta_{\rm t} \approx 13$ kpc^{-1}, and their effective correlation length thus $2\pi/k_{\rm f} \approx 0.5$ kpc, instead of our

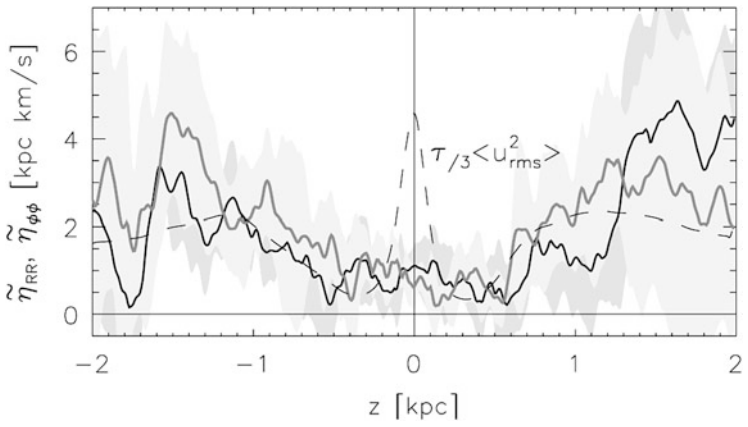

Fig. 19.5 Vertical dependence of $\eta_{\rm t}$ obtained by the test-field method using a simulation of supernova-driven turbulence. Adapted from Gressel et al. (2008b)

estimate of only 0.07 kpc. The reason for this discrepancy in unclear and highlights the importance of doing numerical simulations. Their values for α are positive in the upper disc plane and increase approximately linearly to about $5\,\mathrm{km\,s^{-1}}$ at a height of 1 kpc. This allows us to estimate the fractional helicity as $\varepsilon_\mathrm{f} \approx \alpha/\eta_\mathrm{t} k_\mathrm{f} \approx 0.1$ (cf. Blackman and Brandenburg 2002).

An additional driver of the α effect is the possibility of inflating magnetic flux tubes by cosmic rays (Parker 1992). This makes such magnetic flux tubes buoyant and, together with the effects of rotation and stratification, leads to an α effect. This has led to successful simulations of galactic dynamos both in local (Hanasz et al. 2004) and global (Hanasz et al. 2009; Kulpa-Dybeł et al. 2011) geometries. Cosmic rays are usually treated in the diffusion approximation with a diffusion tensor proportional to $B_i B_j$ that forces the diffusion to be only along magnetic field lines. However, the effective diffusivity is very large (in excess of $10^{28}\,\mathrm{cm^2\,s^{-1}}$), making an explicit treatment costly because of a short diffusive time step constraint. Again, one can make use of the telegraph equation to limit the diffusion speed to a speed not much faster than the speed of sound. Such an approach has been exploited by Snodin et al. (2006), but it has not yet been applied to more realistic cosmic ray-driven dynamos.

19.3 Aspects of Nonlinear Mean-Field Theory

19.3.1 Bi-Helical Magnetic Fields from Simulations

When the computational domain is large enough and turbulence is driven in a helical fashion at a small length scale, one sees the clear emergence of what is called a bi-helical magnetic field. An example is shown in Fig. 19.6 where we show magnetic

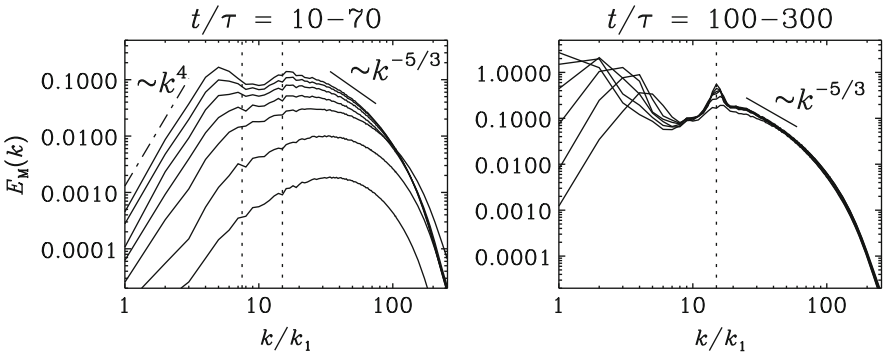

Fig. 19.6 Magnetic energy spectra $E_\mathrm{M}(k)$, at earlier (*left*) and later (*right*) times. The scale separation ratio is $k_\mathrm{f}/k_1 = 15$. The range of time t is given in units of the turnover time, $\tau = 1/u_\mathrm{rms} k_\mathrm{f}$. At small wavenumbers, the $E_\mathrm{M}(k)$ spectrum is proportional to k^4, while to the right of $k_\mathrm{f}/k_1 = 15$ there is a short range with a $k^{-5/3}$ spectrum. Adapted from Brandenburg (2011)

power spectra of a simulation of Brandenburg (2011). During the early evolution of the dynamo (left) we see the growth of the magnetic field at small wavenumbers, accompanied by a growth at small amplitude at lower wavenumbers. The spectrum remains however roughly shape-invariant.

By $t/\tau > 100$, where τ is the turnover time of the turbulence at the forcing scale, a large-scale field is already present. As the field saturates, the peak of magnetic energy moves to progressively smaller wavenumbers. The reason for this peak can be understood in terms of an α^2 dynamo.

19.3.2 Catastrophic Quenching

The idea of catastrophic quenching is almost as old as mean-field dynamo theory itself. Here, "catastrophic" refers to a (declining) dependence of the turbulent transport coefficients on the magnetic Reynolds number, Re_M, even when Re_M is already very large. The word 'catastrophic' was first used by Blackman and Field (2000) to indicate the fact that in the astrophysical context, the α effect would become catastrophically small. The issue focussed initially on turbulent diffusion (Knobloch 1978; Layzer et al. 1979; Piddington 1981). Numerical simulations later showed that in two dimensions, with a large-scale magnetic field lying in that plane, the decay of this large-scale field is indeed slowed down in an Re_M-dependent (i.e., catastrophic) fashion (Cattaneo and Vainshtein 1991). This then translates into a corresponding Re_M-dependent quenching of the effective turbulent magnetic diffusivity. Later, Vainshtein and Cattaneo (1992) argued that also the α effect would be catastrophically quenched, possibly with an even higher power of Re_M.

Gruzinov and Diamond (1994) later realized that the Re_M dependence is associated with the presence of certain conservation laws which are different in two and three dimensions. In three dimensions, the magnetic helicity, $\langle \boldsymbol{A} \cdot \boldsymbol{B} \rangle$, is conserved, while in two dimensions, $\langle A^2 \rangle$ is conserved. Here and elsewhere, angle brackets denote averaging, and A is the component of $\boldsymbol{A}$ that is perpendicular to the plane in two dimensions.

In three dimensions, the suppression of the large-scale dynamo effect can be understood by considering the fact that the field generated by an α-effect dynamo is helical and of Beltrami type, e.g., $\overline{\boldsymbol{B}} = (\sin k_1 z, \cos k_1 z, 0) B_0$, which is parallel to its curl, i.e., $\boldsymbol{\nabla} \times \overline{\boldsymbol{B}} = (\sin k_1 z, \cos k_1 z, 0) k B_0 = k_1 \overline{\boldsymbol{B}}$. The vector potential can then be written as $\overline{\boldsymbol{A}} = k_1^{-1} \overline{\boldsymbol{B}}$, so that the magnetic helicity is $\langle \overline{\boldsymbol{A}} \cdot \overline{\boldsymbol{B}} \rangle = k_1^{-1} B_0^2$. The current helicity is $\langle \overline{\boldsymbol{J}} \cdot \overline{\boldsymbol{B}} \rangle = k_1 B_0^2 / \mu_0$. Note, however, that magnetic helicity of the total field is conserved. Since the total field is given by the sum of large and small-scale components, $\boldsymbol{B} = \overline{\boldsymbol{B}} + \boldsymbol{b}$, the generation of magnetic helicity at large scales can be understood if there is a corresponding production of magnetic helicity at small scales, but of opposite sign. The magnetic and current helicities of the small-scale field can be estimated analogously as $\langle \boldsymbol{a} \cdot \boldsymbol{b} \rangle = -k_\mathrm{f}^{-1} \langle \boldsymbol{b}^2 \rangle$ and $\langle \boldsymbol{j} \cdot \boldsymbol{b} \rangle = -k_\mathrm{f} \langle \boldsymbol{b}^2 \rangle / \mu_0$, respectively.

The relative importance of large-scale and small-scale contributions to magnetic helicity and magnetic energy is determined by the magnetic helicity equation,

$$\frac{\mathrm{d}}{\mathrm{d}t}\langle \boldsymbol{A}\cdot\boldsymbol{B}\rangle = -2\eta\mu_0\langle \boldsymbol{J}\cdot\boldsymbol{B}\rangle. \tag{19.8}$$

Inserting $\langle \boldsymbol{A}\cdot\boldsymbol{B}\rangle = \langle \overline{\boldsymbol{A}}\cdot\overline{\boldsymbol{B}}\rangle + \langle \boldsymbol{a}\cdot\boldsymbol{b}\rangle$ and $\langle \boldsymbol{J}\cdot\boldsymbol{B}\rangle = \langle \overline{\boldsymbol{J}}\cdot\overline{\boldsymbol{B}}\rangle + \langle \boldsymbol{j}\cdot\boldsymbol{b}\rangle$, and applying it to the time after which the small-scale field has already reached saturation, i.e., $\langle \boldsymbol{b}^2\rangle = \text{const}$, we have

$$k_1^{-1}\frac{\mathrm{d}}{\mathrm{d}t}\langle \overline{\boldsymbol{B}}^2\rangle = -2\eta k_1\langle \overline{\boldsymbol{B}}^2\rangle + 2\eta k_\mathrm{f}\langle \boldsymbol{b}^2\rangle. \tag{19.9}$$

One sees immediately that the steady state solution is $\langle \overline{\boldsymbol{B}}^2\rangle/\langle \boldsymbol{b}^2\rangle = k_\mathrm{f}/k_1 > 1$, i.e., the large-scale field exceeds the small-scale field by a factor that is equal to the scale separation ratio. Moreover, this steady state is only reached on a resistive time scale. Since $\langle \boldsymbol{b}^2\rangle$ is assumed constant in time, we can integrate Eq. (19.9) to give

$$\langle \overline{\boldsymbol{B}}^2\rangle = \langle \boldsymbol{b}^2\rangle\frac{k_\mathrm{f}}{k_1}\left[1 - e^{-2\eta k_1^2(t-t_\mathrm{sat})}\right], \tag{19.10}$$

which shows that the relevant resistive time scale is $(2\eta k_1^2)^{-1}$. This saturation behavior agrees well with results from simulations; see Fig. 19.7.

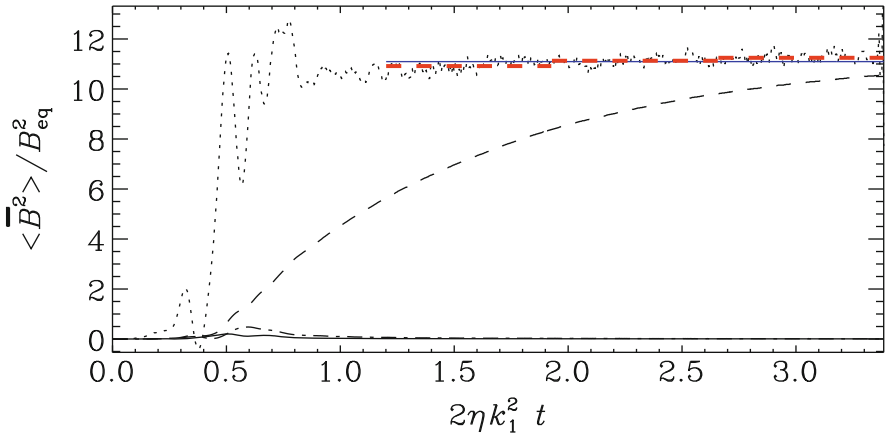

Fig. 19.7 Example showing the evolution of the normalized $\langle \overline{\boldsymbol{B}}^2\rangle$ (*dashed*) and that of $\langle \overline{\boldsymbol{B}}^2\rangle + \mathrm{d}\langle \overline{\boldsymbol{B}}^2\rangle/\mathrm{d}(2\eta k^2 t)$ (*dotted*), compared with its average in the interval $1.2 \le 2\eta k_1^2 t \le 3.5$ (*horizontal blue solid line*), as well as averages over three subintervals (*horizontal red dashed lines*). Here, $\overline{\boldsymbol{B}}$ is evaluated as an xz average, $\langle \boldsymbol{B}\rangle_{xz}$. For comparison we also show the other two averages, $\langle \boldsymbol{B}\rangle_{xy}$ (*solid*) and $\langle \boldsymbol{B}\rangle_{yz}$ (*dash-dotted*), but their values are very small. Adapted from Candelaresi and Brandenburg (2013)

19.3.3 Mean-Field Description

The simplistic explanation given above can be reproduced in mean-field dynamo theory when magnetic helicity conservation is introduced as an extra constraint. Physically, such a constraint is well motivated and goes back early work of Pouquet et al. (1976), who found that the relevant α in the mean-field dynamo is given by the sum of kinetic and magnetic contributions,

$$\alpha = \alpha_{\rm K} + \alpha_{\rm M}, \tag{19.11}$$

where $\alpha_{\rm K} = -(\tau/3)\langle \boldsymbol{\omega} \cdot \boldsymbol{u} \rangle$ is the formula for the kinematic value in the high conductivity limit (Moffatt 1978; Krause and Rädler 1980), and $\alpha_{\rm M} = (\tau/3\overline{\rho})\langle \boldsymbol{j} \cdot \boldsymbol{b} \rangle$ is the magnetic contribution. Again, under isotropic conditions, $\langle \boldsymbol{j} \cdot \boldsymbol{b} \rangle$ is proportional to $\langle \boldsymbol{a} \cdot \boldsymbol{b} \rangle$, with the coefficient of proportionality being $k_{\rm f}^2$. This is because the spectra of magnetic and current helicity, $H(k)$ and $C(k)$, which are normalized such that $\int H(k)\,{\rm d}k = \langle \boldsymbol{A} \cdot \boldsymbol{B} \rangle$ and $\int C(k)\,{\rm d}k = \langle \boldsymbol{J} \cdot \boldsymbol{B} \rangle$, are proportional to each other with $C(k) = k^2 H(k)$, so the proportionality between small-scale current and magnetic helicities is obtained by applying $C(k) = k^2 H(k)$ to $k = k_{\rm f}$. Even in an inhomogeneous system, this approximation is qualitatively valid, except that the coefficient of proportionality is found to be somewhat larger (Mitra et al. 2010; Hubbard and Brandenburg 2010; Del Sordo et al. 2013).

The question is now how to obtain $\langle \boldsymbol{a} \cdot \boldsymbol{b} \rangle$. One approach is to evolve $\overline{\boldsymbol{A}}$ (instead of $\overline{\boldsymbol{B}}$) in a mean-field model and compute at each time step (Hubbard and Brandenburg 2012) $\langle \boldsymbol{a} \cdot \boldsymbol{b} \rangle = \langle \boldsymbol{A} \cdot \boldsymbol{B} \rangle - \langle \overline{\boldsymbol{A}} \cdot \overline{\boldsymbol{B}} \rangle$, where $\langle \boldsymbol{A} \cdot \boldsymbol{B} \rangle$ obeys Eq. (19.8) for the total magnetic helicity. In practice, one makes an important generalization in that volume averaging is relaxed to mean just averaging over one or at most two coordinate directions. (To obey Reynolds rules, these coordinate directions should be periodic.) Thus, Eq. (19.8) then becomes

$$\frac{\partial}{\partial t}\overline{\boldsymbol{A} \cdot \boldsymbol{B}} = -2\eta\mu_0 \overline{\boldsymbol{J} \cdot \boldsymbol{B}} - \boldsymbol{\nabla} \cdot \overline{\boldsymbol{\mathcal{F}}}, \tag{19.12}$$

where $\overline{\boldsymbol{\mathcal{F}}}$ is the magnetic helicity flux from both large-scale and small-scale fields. Hubbard and Brandenburg (2012) pointed out that this approach can be superior to the traditional approach by Kleeorin and Ruzmaikin (1982), in which one solves instead the evolution equation for $\langle \boldsymbol{a} \cdot \boldsymbol{b} \rangle$,

$$\frac{\partial}{\partial t}\overline{\boldsymbol{a} \cdot \boldsymbol{b}} = -2\overline{\mathscr{E}} \cdot \overline{\boldsymbol{B}} - 2\eta\mu_0 \overline{\boldsymbol{j} \cdot \boldsymbol{b}} - \boldsymbol{\nabla} \cdot \overline{\boldsymbol{\mathcal{F}}}_{\rm f}, \tag{19.13}$$

where $\overline{\boldsymbol{\mathcal{F}}}_{\rm f}$ is the magnetic helicity flux only from the small-scale magnetic field. The two approaches are equivalent, except that there is an ambiguity as to what should be included in $\overline{\boldsymbol{\mathcal{F}}}_{\rm f}$. In particular, when deriving the evolution equation for $\langle \overline{\boldsymbol{A}} \cdot \overline{\boldsymbol{B}} \rangle$ in the Weyl gauge, i.e., using just $\partial \overline{\boldsymbol{A}}/\partial t = \overline{\mathscr{E}} - \eta\mu_0 \overline{\boldsymbol{J}}$, we obtain

$$\frac{\partial}{\partial t}(\overline{\boldsymbol{A}}\cdot\overline{\boldsymbol{B}}) = 2\overline{\mathcal{E}}\cdot\overline{\boldsymbol{B}} - 2\eta\mu_0\overline{\boldsymbol{J}}\cdot\overline{\boldsymbol{B}} - \boldsymbol{\nabla}\cdot(-\overline{\mathcal{E}}\times\overline{\boldsymbol{A}}), \tag{19.14}$$

i.e., there is an extra flux term $-\overline{\mathcal{E}}\times\overline{\boldsymbol{A}}$. Thus, as argued by Hubbard and Brandenburg (2012), if $\overline{\mathcal{F}} = \overline{\mathcal{F}}_{\rm m} + \overline{\mathcal{F}}_{\rm f} = \boldsymbol{0}$, this implies that $\overline{\mathcal{F}}_{\rm f} = \overline{\mathcal{E}}\times\overline{\boldsymbol{A}}$ in Eq. (19.14).

19.3.3.1 Diffusive Magnetic Helicity Fluxes and Gauge Issues

Another important contribution to the magnetic helicity flux is a turbulent-diffusive flux down the gradient of magnetic helicity density. In Fig. 19.8 we show the profiles of $\langle\overline{\mathcal{E}}\cdot\overline{\boldsymbol{B}}\rangle$ and $\eta\langle\overline{\boldsymbol{J}}\cdot\overline{\boldsymbol{B}}\rangle$ from a simulation of Hubbard and Brandenburg (2010), compare the residual $2\langle\overline{\mathcal{E}}\cdot\overline{\boldsymbol{B}}\rangle - 2\eta\langle\overline{\boldsymbol{J}}\cdot\overline{\boldsymbol{B}}\rangle$ with the divergence of the magnetic helicity flux, and finally compare the flux $\overline{\mathcal{F}}_{\rm f} = \overline{\boldsymbol{e}\times\boldsymbol{a}}$ with that obtained from the diffusion approximation, $-\kappa_{\rm f}\boldsymbol{\nabla}\overline{h}_{\rm f}$. These results demonstrate that there is indeed a measurable difference between $\langle\overline{\mathcal{E}}\cdot\overline{\boldsymbol{B}}\rangle$ and $\eta\langle\overline{\boldsymbol{J}}\cdot\overline{\boldsymbol{B}}\rangle$, which can be explained by a magnetic helicity flux divergence, and that this magnetic helicity flux can be understood as a turbulent-diffusive one, i.e., down the gradient of the local magnetic helicity density.

At this point, a comment about gauge-dependencies is in order. First of all, in the framework of large-scale dynamos, one expects scale separation between small-scale and large-scale magnetic fields. It is then possible to express the small-scale magnetic helicity as a density of linkages between magnetic structures, which leads to the manifestly gauge-invariant Gauss linking formula (Subramanian and Brandenburg 2006). Second, the large-scale magnetic field remains in general gauge-dependent, and there have been several examples of this (Brandenburg et al. 2002; Hubbard and Brandenburg 2010). This would render the alternate approach

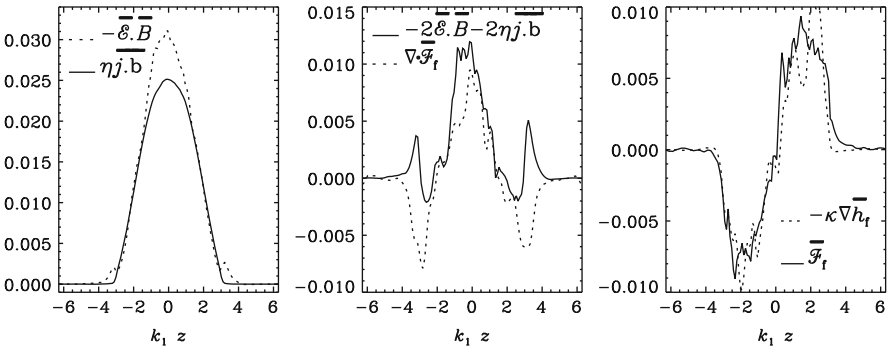

Fig. 19.8 Time-averaged terms on the right-hand side of (19.13), $\langle\overline{\mathcal{E}}\cdot\overline{\boldsymbol{B}}\rangle_T$ and $\eta\langle\boldsymbol{j}\cdot\boldsymbol{b}\rangle_T$ (*left panel*), the difference between these terms compared with the magnetic helicity flux divergence of small-scale fields $\langle\boldsymbol{\nabla}\cdot\overline{\mathcal{F}}_{\rm f}^{\rm W}\rangle_T$ (*middle panel*), and the flux itself compared with the Fickian diffusion ansatz (*right-hand panel*). Adapted from Hubbard and Brandenburg (2010)

of Hubbard and Brandenburg (2012) problematic, but they argue that those gauge-dependencies result simply from a drift in the mean vector potential and must be subtracted out. Third, with appropriate boundary conditions, such drifts can be eliminated, and $\langle \boldsymbol{A} \cdot \boldsymbol{B} \rangle$ can then well reach a statistically steady state. If that is the case, the left-hand side of Eq. (19.12) vanishes after time averaging, so the gauge-dependent magnetic helicity flux divergence must balance the gauge-independent resistive term, so the former must in fact also be gauge-independent (Mitra et al. 2010; Hubbard and Brandenburg 2010). This argument applies even separately to the contributions from small-scale and large-scale components; see Eqs. (19.13) and (19.14). This allowed Del Sordo et al. (2013) to show for the first time that the magnetic helicity flux divergence from the small-scale field can become comparable to the resistive term. Ultimately, however, one expects it of course to out-compete the latter, but this has not yet been seen for the magnetic Reynolds numbers accessible to date.

The issue of magnetic helicity fluxes occurs already in the special case of a closed domain for which $\langle \boldsymbol{\nabla} \cdot \overline{\boldsymbol{\mathcal{F}}} \rangle = 0$, i.e., $\oint \overline{\boldsymbol{\mathcal{F}}} \cdot \mathrm{d}\boldsymbol{S} = 0$, so there is no flux in or out of the domain, but $\overline{\boldsymbol{\mathcal{F}}}$ and $\overline{\boldsymbol{\mathcal{F}}}_{\rm f}$ can still be non-vanishing within the domain. This is the case especially for shear flows, where the flux term can have a component in the cross-stream direction that is non-uniform and can thus contribute to a finite divergence. Simulations of Hubbard and Brandenburg (2012) have shown that such a term might be an artifact of choosing the Coulomb gauge rather than the so-called advective gauge, in which case such a term would vanish. This implies that the shear-driven Vishniac and Cho (2001) flux would vanish. This term was previously thought to be chiefly responsible for alleviating catastrophic quenching in shear flows (Subramanian and Brandenburg 2004; Brandenburg and Sandin 2004). It is therefore surprising that such a simple term is now removed by a simple gauge transformation. Clearly, more work is needed to clarify this issue further.

19.3.3.2 Diffusive Versus Advective Magnetic Helicity Fluxes

To date we know of at least two types of magnetic helicity flux that can alleviate catastrophic quenching. One is a diffusive magnetic helicity fluxes proportional to the negative gradient of the local value of the mean magnetic helicity density from the small-scale fields, $\overline{h}_{\rm f} = \langle \boldsymbol{a} \cdot \boldsymbol{b} \rangle$, so $\overline{\boldsymbol{\mathcal{F}}}_{\rm f}^{\rm diff} = -\kappa_{\rm h} \boldsymbol{\nabla} \overline{h}_{\rm f}$. Another is a contribution that comes simply from advection by the mean flow $\overline{\boldsymbol{U}}$, so $\overline{\boldsymbol{\mathcal{F}}}_{\rm f}^{\rm adv} = \overline{h}_{\rm f} \overline{\boldsymbol{U}}$ (Shukurov et al. 2006; Sur et al. 2007). Recent work Mitra et al. (2010) has analyzed the contributions to the evolution equation for $\overline{h}_{\rm f}$; see Eq. (19.13). In the low Re_M regime, the production term $2\overline{\boldsymbol{\mathcal{E}}} \cdot \overline{\boldsymbol{B}}$ is balanced essentially by $2\eta\mu_0 \overline{\boldsymbol{j}} \cdot \overline{\boldsymbol{b}}$. This means that, as η decreases, $2\overline{\boldsymbol{\mathcal{E}}} \cdot \overline{\boldsymbol{B}}$ must also decrease, which leads to catastrophic quenching in that regime. However, although the $\boldsymbol{\nabla} \cdot \overline{\boldsymbol{\mathcal{F}}}_{\rm f}$ term is subdominant, it shows a less steep Re_M-dependence ($\propto \mathrm{Re}_M^{-1/2}$, as opposed to Re_M^{-1} for the $2\eta\mu_0 \overline{\boldsymbol{j}} \cdot \overline{\boldsymbol{b}}$ term), and has therefore the potential of catching up with the other terms to balance $2\overline{\boldsymbol{\mathcal{E}}} \cdot \overline{\boldsymbol{B}}$ with a less steep scaling.

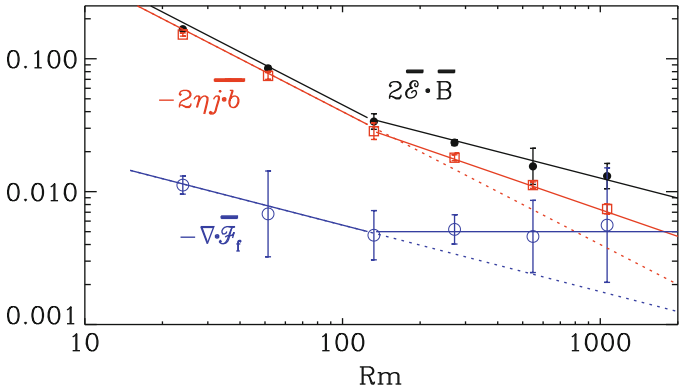

Fig. 19.9 Scaling properties of the vertical slopes of $2\overline{\mathcal{E}}\cdot\overline{\boldsymbol{B}}$, $-2\eta\mu_0\,\overline{\boldsymbol{j}\cdot\boldsymbol{b}}$, and $-\boldsymbol{\nabla}\cdot\overline{\mathcal{F}}_{\rm f}$ for models with a wind. (Given that the three quantities vary approximately linearly with z, the three labels indicate their non-dimensional values at $k_1 z = 1$.) The second panel shows that a stronger wind decreases the value of Re_M for which the contribution of the advective term becomes comparable to that of the resistive term. Adapted from Del Sordo et al. (2013)

Recent work using a simple model with a galactic wind has shown, for the first time, that this may indeed be possible. In Fig. 19.9 we show their basic result. As it turns out, below $\mathrm{Re}_M = 100$ the $2\eta\mu_0\overline{\boldsymbol{j}\cdot\boldsymbol{b}}$ term dominates over $\boldsymbol{\nabla}\cdot\overline{\mathcal{F}}$, but because of the different scalings (slopes being -1 and $-1/2$, respectively), the $\boldsymbol{\nabla}\cdot\overline{\mathcal{F}}$ term is expected to become dominant for larger values of Re_M (about 3000). Surprisingly, however, $\boldsymbol{\nabla}\cdot\overline{\mathcal{F}}$ becomes approximately constant for $\mathrm{Re}_M \gtrsim 100$ and $2\eta\mu_0\overline{\boldsymbol{j}\cdot\boldsymbol{b}}$ shows now a shallower scaling (slope $-1/2$). This means that the two curves would still cross at a similar value. Our data suggest, however, that $\boldsymbol{\nabla}\cdot\overline{\mathcal{F}}$ may even rise slightly, so the crossing point is now closer to $\mathrm{Re}_M = 1000$.

19.3.3.3 Magnetic Helicity Fluxes in the Exterior

Some surprising behavior has been noticed in connection with the small-scale magnetic helicity flux in the solar wind, and it is to be expected that such behavior also applies to galaxies. Naively, if negative magnetic helicity from small-scale fields is ejected from the northern hemisphere, one would expect to find negative magnetic helicity at small scales anywhere in the exterior. However, if a significant part of this flux is caused by a diffusive magnetic helicity flux, this expectation might be wrong and the sign changes such that the small-scale magnetic helicity becomes positive some distance away from the dynamo regime. In Fig. 19.10 we reproduce in graphical form the explanation offered by Warnecke et al. (2012).

The idea is that the helicity flux is essentially diffusive in nature. Thus, to transport positive helicity outward, we need a negative gradient, and to transport negative helicity outward, as in the present case, we need a positive gradient outward. This is indeed what is shown in Fig. 19.10. It is then conceivable that the

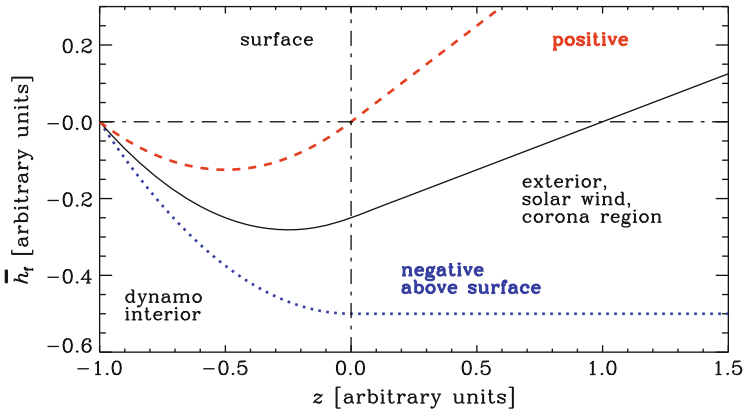

Fig. 19.10 Sketch showing possible solutions $\overline{h}_f(z)$ with $S = \text{const} = -1$ in $z < 0$ and $S = 0$ in $z > 0$. The *red* (*dashed*) and *black* (*solid*) *lines* show solutions for which the magnetic helicity flux $(-\kappa_h \mathrm{d}\overline{h}_f/\mathrm{d}z)$ is negative in the exterior. The *blue* (*dotted*) *line* shows the case, where the magnetic helicity flux is zero above the surface and therefore do not reverse the sign of $\overline{h}_f(z)$ in the exterior. Adapted from Warnecke et al. (2012)

magnetic helicity overshoots and becomes itself positive, which is indeed what is seen in the solar wind (Brandenburg et al. 2011).

19.4 Observational Aspects

It would be an important confirmation of the nonlinear quenching theory if one could find observational evidence for bi-helical magnetic fields. This has not yet been possible, but new generations of radio telescopes allow for a huge coverage of radio wavelengths λ, which could help us determine the spatial distribution of the magnetic field using a tool nowadays referred to as RM synthesis (Brentjens and de Bruyn 2005; Heald et al. 2009; Frick et al. 2011; Gießübel et al. 2013). This refers to the fact that the line-of-sight integral for the complex polarized intensity $P = Q + \mathrm{i}U$ can be written as an integral over the Faraday depth ϕ (which itself is an integral over $B_\parallel$ and, under idealizing assumptions, proportional to the line of sight coordinate z) and takes the form

$$P(\lambda^2) = \int_{-\infty}^{\infty} F(\phi) e^{2\mathrm{i}\phi\lambda^2}\, \mathrm{d}\phi, \tag{19.15}$$

which can be thought of as a Fourier integral for the Fourier variable $2\lambda^2$ (Burn 1966). The function $F(\phi)$ is referred to as the Faraday dispersion function, and it would be interesting to find it by observing $P(\lambda^2)$. The problem is of course that only positive values of λ^2 can be observed.

Most of the work in this field assumes that $P(\lambda^2)$ is Hermitian, i.e., $P(-\lambda^2) = P(\lambda^2)^*$, where the asterisk denotes complex conjugation. This is however not the case for a helical magnetic field, as has recently been pointed out (Brandenburg and Stepanov 2014). Consider a magnetic field of Beltrami type, $\boldsymbol{B} = (\cos kz, -\sin kz, 0)$, write it in complex form as $\mathscr{B} = B_x + \mathrm{i}B_y$, so that $\mathscr{B}(z) = B_\parallel\, e^{\mathrm{i}\psi_B(z)}$ with $\psi_B(z) = kz$, and assume that ϕ is linear in z (which is the case when $n_e B_\parallel = \text{const}$). We thus obtain $\mathscr{B} = \mathscr{B}(\phi(z))$. The Faraday dispersion function is essentially given by $F(\phi) \propto \mathscr{B}^2$, so its phase is now $2\psi_B$ and one loses phase information, which is referred to as the π ambiguity. Inserting this into Eq. (19.15), one sees that most of the contribution to the integral comes from those values of λ^2 for which the phase is constant or "stationary", i.e.,

$$2\mathrm{i}(\psi_B + \phi\lambda^2) = \text{const}. \tag{19.16}$$

Making use of the fact that for constant $n_e B_\parallel$ we have $\phi = -Kn_e B_\parallel z$, and thus

$$\lambda^2 = -k/Kn_e B_\parallel \tag{19.17}$$

is the condition for the wavelength for which the integral in Eq. (19.15) gets its largest contribution. Similar conditions have also been derived by Sokoloff et al. (1998) and Arshakian et al. (2011).

The Fourier transform of such a complex field would directly reflect the individual constituents of the magnetic field. For example, a superposition of two helical fields yields two corresponding peaks in the Fourier spectrum of $\mathscr{B}$; see Fig. 19.11c, where we have peaks at normalized Fourier variables $2\lambda^2/\lambda_0^2 = 1$ and -5. However, the quantity inferred by RM synthesis is the Faraday dispersion function, which is related to the square of $\mathscr{B}$, and its Fourier spectrum is more complicated; see Fig. 19.11d, where we have peaks at $2\lambda^2/\lambda_0^2 = 2$, -4, and -10. Thus, the two modes combine to a new one with a Fourier variable that is equal to the sum $1 + (-5) = -4$, with side lobes separated by their difference $1 - (-5) = 6$ to the left and the right. The corresponding modulus and phase ψ_B are shown in panels (a) and (b), respectively. Also shown is the phase ψ_B', which is ψ_B remapped onto the range from $-\pi/2$ to $\pi/2$.

The magnetic fields of spiral galaxies are expected to be dominated by a strong toroidal component. This component might provide a reasonably uniform line-of-sight component without reversals when viewed edge-on. This would then provide an opportunity to detect polarization signatures from magnetic fields with different signs of magnetic helicity in different quadrants of the galaxy. Figure 19.12 provides a sketch with a line-of-sight component of different sign on the left or the right of the rotation axis. On the right, RM is positive (field points toward observer), so we can detect signatures of the field with positive helicity. Since the large-scale field has positive magnetic helicity in the upper disc plane, signatures from this component can be detected in quadrants I and III. Conversely, since the small-scale field has positive magnetic helicity in the lower disc plane, signatures from this component can be detected in quadrants II and IV.

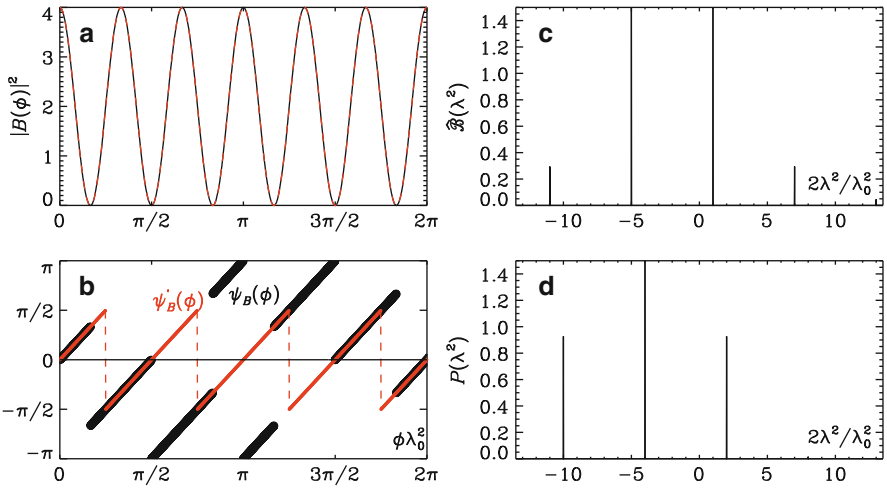

Fig. 19.11 (**a**) $|B|^2(\phi)$, (**b**) $\psi_B(\phi)$ and $\psi_B'(\phi)$, (**c**) $\mathscr{B}(k)$, and (**d**) $P(k)$ for a tri-helical magnetic field with $k_2/k_1 = -5$ using RM > 0. In panel (**b**), the *dashed blue lines* correspond to $\pi/2 - \phi|\lambda_1^2|$ and $3\pi/2 - \phi|\lambda_1^2|$ and mark the points where the phase of $\psi_B(\phi)$ jumps

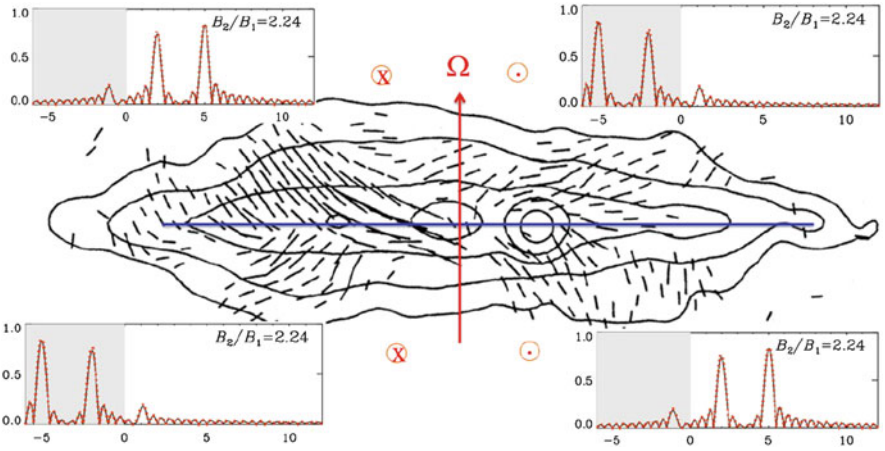

Fig. 19.12 Illustration of the four quadrants of an edge-one galaxy, where two are expected to show signatures fields of positive helicity and two signatures fields of negative helicity. The 2×2 panels correspond to polarization maps shown in Brandenburg and Stepanov (2014) for different signs of RM and helicity

19.5 Primordial Magnetic Field

Primordial magnetic fields are generated in the early Universe, either at inflation (Turner and Widrow 1988) at $\lesssim 10^{-32}$ s, the electroweak phase transition at $\sim 10^{-12}$ s, or the QCD phase transition at $\sim 10^{-6}$ s; see, for example, Vachaspati

(1991, 2001) and the review by Durrer and Neronov (2013). Such magnetic fields are basically subject to subsequent turbulent decay. Nevertheless, the evolution of these magnetic fields is essentially governed by the same hydromagnetic equations as those used to describe dynamos in galaxies, for example. The purpose of this section is to point out that there are some important similarities between decaying turbulence in the early Universe and (supernova-) driven turbulence in contemporary galaxies.

Especially for magnetic fields generated at the electroweak phase transition, there is the possibility that such fields are helical. This would then lead to an inverse cascade (Pouquet et al. 1976) and a transfer of magnetic energy to progressively larger scale or smaller wavenumbers; see Fig. 19.13, where we show magnetic energy spectra $E_{\rm M}$ versus wavenumber k and compare with the case where k is divided by the integral wavenumber $k_{\rm M}(t)$ defined through

$$k_{\rm M}^{-1}(t) = \int k^{-1} E_{\rm M}(k,t)\,{\rm d}k \Big/ \int E_{\rm M}(k,t)\,{\rm d}k. \tag{19.18}$$

Simulations like those shown here are now done by several groups (Christensson et al. 2001; Banerjee and Jedamzik 2004; Kahniashvili et al. 2013). One of the main motivations for this work is the realization that magnetic fields generated at the time of the electroweak phase transition would now have a length scale of just one AU, which is short compared with the scale of galaxies. In fact, in the radiation dominated era, the hydromagnetic equations in an expanding universe can be rewritten in the usual form when using conformal time and suitably rescaled quantities; see Brandenburg et al. (1996), who then used a magnetic helicity-

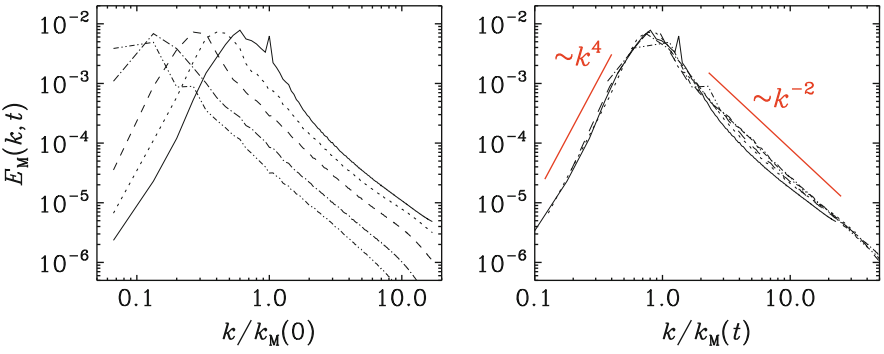

Fig. 19.13 Magnetic energy spectra at different times in the presence of magnetic helicity with $\mathrm{Pr}_M = 1$. On the right, the abscissa is rescaled by $k_{\rm M}(t)$, which make the spectra collapse onto each other. The Reynolds number based on the wavenumber $k_{\rm M}$ is around 1,000. The spike at k/k_0 corresponds to the driving scale prior to letting the field decay

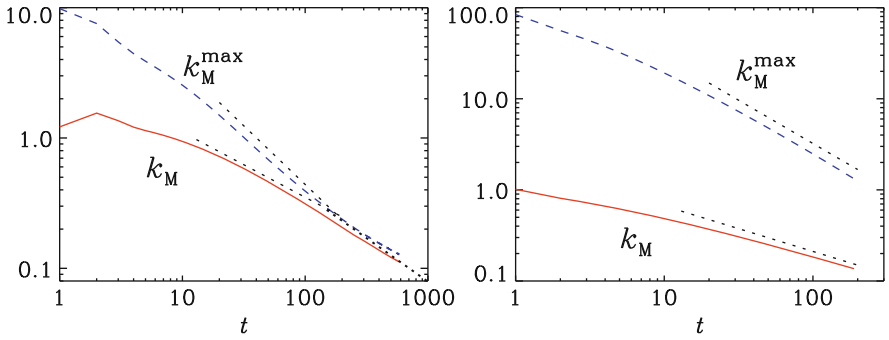

Fig. 19.14 Evolution of $k_M(t)$ (*solid*) and $k_M^{max}(t)$ (*dashed*) for a fractional initial helicity (*left*) and zero initial helicity (*right*)

conserving cascade model of hydromagnetic turbulence to investigate the increase of the correlation length with time.

In reality, the magnetic field will never be fully helical. However, non-helical turbulence decays faster (like t^{-1}) than helical one (like $t^{-2/3}$); see Biskamp and Müller (1999). One can think of partially helical turbulence as a mixture of a more rapidly decaying nonhelical component and a less rapidly decaying helical component. After some time, the former one will have died out and so only the latter, helical component will survive. In Fig. 19.14 we show the scaling of k_M for a weakly helical and a nonhelical case and compare with the maximum possible value derived from the realizability condition, i.e.

$$k_M(t) \leq k_M^{max}(t) \equiv 2\mathscr{E}(t)/|\mathscr{H}(t)|, \tag{19.19}$$

where $\mathscr{E}(t) = \int E_M(k,t)\,dk$ and $\mathscr{H}(t) = \int H_M(k,t)\,dk$ are magnetic energy and helicity computed from the spectra. This was originally demonstrated by Tevzadze et al. (2012) using simulations similar to those presented here.

The decay of helical magnetic fields is also amenable to the mean-field treatment discussed in Sect. 19.3.3. Helicity from large-scale fields drives helicity at small scales via Eq. (19.13) and thereby an α effect through Eq. (19.11). This slows down the decay (Yousef and Brandenburg 2003; Kemel et al. 2011; Blackman and Subramanian 2013; Bhat et al. 2014) and may be relevant to the survival of galactic magnetic fields, as already mentioned in Sect. 19.2.2.

Remarkably, simulations have shown that some type of inverse cascading occurs also in the *absence* of magnetic helicity (Christensson et al. 2001; Kahniashvili et al. 2013). In Fig. 19.15 we show such a result from a simulation at a numerical resolution of 2304^3 meshpoints (Brandenburg and Stepanov 2014). However, the detailed reason for this inverse energy transfer still remains to be clarified.

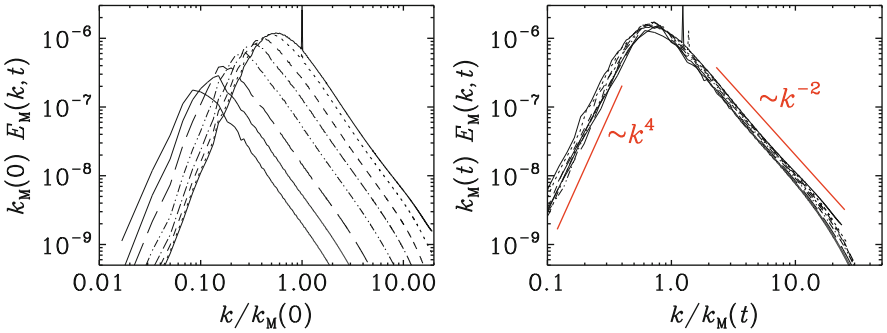

Fig. 19.15 Similar to Fig. 19.13, but for the case without initial helicity and initial scale separation ratio of the forcing of $k_{\rm min}/k_1 = 60$. $\mathrm{Pr}_M = 1$. On the right, the ordinate is scaled with $k_{\rm M}(t)$, in addition to the scaling of the abscissa with $1/k_{\rm M}(t)$

Conclusion

The overall significance of primordial magnetic fields is still unclear, because contemporary magnetic fields might well have been produced by some type of dynamo within bodies such as stars and accretion discs within galaxies, and would then have been ejected into the rest of the gas outside. Whether such mechanisms would be sufficiently powerful to explain magnetic fields even between clusters of galaxies remains to be seen. In this connection it is noteworthy that Neronov and Vovk (2010) found a lower bound on the magnetic field strength of 3×10^{-16} G based on the non-detection of GeV gamma-ray emission from the electromagnetic cascade of TeV gamma rays in the intergalactic medium. This bound is well above the even rather optimistic earlier estimated galactic seed magnetic field strengths (Rees 1987).

Invoking some type of large-scale seed magnetic field seems to be the only plausible option if one wants to explain the non-axisymmetric magnetic fields in M81. However, this galaxy is perhaps only one of the few where there is still strong evidence for the existence of a non-axisymmetric magnetic field. In agreement with mean-field dynamo theory, most galaxies harbor axisymmetric magnetic fields and their toroidal field is symmetric about the midplane.

With the help of turbulent dynamo simulations over the past 20 years, it is now clear that the conventional $\alpha\Omega$ type dynamo must produce large-scale magnetic fields that have two different signs of helicity, one at large scales and the opposite one at small scales. Such magnetic fields are called bi-helical and might be detectable through their specific signature in polarized radio emission. These are some of the aspects that we have highlighted in the present review about galactic dynamo simulations. Clearly, simulations have

(continued)

to be conducted in close comparison with theory. By now, simulations have reached sufficiently high magnetic Reynolds numbers that simple theories such as first-order smoothing clearly break down and some kind of asymptotic regime commences. Given that it will not be possible to reach asymptotic scaling yet, is must eventually be the interplay between simulations and theory that can provide a meaningful understanding of galactic magnetism.

Acknowledgements I am indebted to Oliver Gressel and Kandaswamy Subramanian for reading the manuscript and providing help and useful comments. Financial support from the European Research Council under the AstroDyn Research Project 227952, the Swedish Research Council under the grants 621-2011-5076 and 2012-5797, as well as the Research Council of Norway under the FRINATEK grant 231444 are gratefully acknowledged.

References

Arshakian, T.G., Beck, R.: Optimum frequency band for radio polarization observations. Monthly Notices Roy. Astron. Soc. **418**, 2336–2342 (2011)

Banerjee, R., Jedamzik, K.: Evolution of cosmic magnetic fields: from the very early Universe, to recombination, to the present. Phys. Rev. D **70**, 123003 (2004)

Beck, R.: Magnetism in the spiral galaxy NGC 6946: magnetic arms, depolarization rings, dynamo modes, and helical fields. Astron. Astrophys. **470**, 539–556 (2007)

Beck, R., Brandenburg, A., Moss, D., Shukurov, A., Sokoloff, D.: Galactic magnetism: recent developments and perspectives. Ann. Rev. Astron. Astrophys. **34**, 155–206 (1996)

Beck, R., Wielebinski, R.: Magnetic fields in galaxies, In: Oswalt, T.D., Gilmore, G. (eds.) Planets, Stars and Stellar Systems, vol. 5, pp. 641–723. Springer Science+Business Media, Dordrecht (2013)

Bhat, P., Blackman, E.G., Subramanian, K.: Resilience of helical fields to turbulent diffusion II: direct numerical simulations. Monthly Notices Roy. Astron. Soc. **438**, 2954–2966 (2014)

Biskamp, D., Müller, W.-C.: Decay laws for three-dimensional magnetohydrodynamic turbulence. Phys. Rev. Lett. **83**, 2195–2198 (1999)

Blackman, E.G., Brandenburg, A.: Dynamic nonlinearity in large scale dynamos with shear. Astrophys. J. **579**, 359–373 (2002)

Blackman, E.G., Field, G.B.: Constraints on the magnitude of α in dynamo theory. Astrophys. J. **534**, 984–988 (2000)

Blackman, E.G., Subramanian, K.: On the resilience of helical magnetic fields to turbulent diffusion and the astrophysical implications. Monthly Notices Roy. Astron. Soc. **429**, 1398–1406 (2013)

Brandenburg, A.: Disc turbulence and viscosity. In: Abramowicz, M.A., Björnsson, G., Pringle, J.E. (eds.) Theory of Black Hole Accretion Discs, pp. 61–86. Cambridge University Press, Cambridge (1998)

Brandenburg, A.: Chandrasekhar-Kendall functions in astrophysical dynamos. Pramana J. Phys. **77**, 67–76 (2011)

Brandenburg, A., Dobler, W., Subramanian, K.: Magnetic helicity in stellar dynamos: new numerical experiments. Astron. Nachr. **323**, 99–122 (2002)

Brandenburg, A., Enqvist, K., Olesen, P.: Large-scale magnetic fields from hydromagnetic turbulence in the very early universe. Phys. Rev. D **54**, 1291–1300 (1996)

Brandenburg, A., Käpylä, P.J., Mohammed, A.: Non-Fickian diffusion and tau-approximation from numerical turbulence. Phys. Fluids **16**, 1020–1027 (2004)
Brandenburg, A., Nordlund, A.A.: Astrophysical turbulence modeling. Rep. Prog. Phys. **74**, 046901 (2011)
Brandenburg, A., Rädler, K.-H., Rheinhardt, M., Subramanian, K.: Magnetic quenching of alpha and diffusivity tensors in helical turbulence. Astrophys. J. Lett. **687**, L49–L52 (2008a)
Brandenburg, A., Rädler, K.-H., Schrinner, M.: Scale dependence of alpha effect and turbulent diffusivity. Astron. Astrophys. **482**, 739–746 (2008b)
Brandenburg, A., Sandin, C.: Catastrophic alpha quenching alleviated by helicity flux and shear. Astron. Astrophys. **427**, 13–21 (2004)
Brandenburg, A., Stepanov, R.: Faraday signature of magnetic helicity from reduced depolarization. Astrophys. J. **786**, 91 (2014)
Brandenburg, A., Subramanian, K., Balogh, A., Goldstein, M.L.: Scale-dependence of magnetic helicity in the solar wind. Astrophys. J. **734**, 9 (2011)
Brandenburg, A., Tuominen, I., Rädler, K.-H.: On the generation of non-axisymmetric magnetic fields in mean-field dynamos. Geophys. Astrophys. Fluid Dyn. **49**, 45–55 (1989)
Brentjens, M.A., de Bruyn, A.G.: Faraday rotation measure synthesis. Astron. Astrophys. **441**, 1217–1228 (2005)
Burn, B.J.: On the depolarization of discrete radio sources by Faraday dispersion. Monthly Notices Roy. Astron. Soc. **133**, 67–83 (1966)
Candelaresi, S., Brandenburg, A.: How much helicity is needed to drive large-scale dynamos? Phys. Rev. E **87**, 043104 (2013)
Cattaneo, F., Vainshtein, S.I.: Suppression of turbulent transport by a weak magnetic field. Astrophys. J. Lett. **376**, L21–L24 (1991)
Chamandy, L., Subramanian, K., Shukurov, A.: Galactic spiral patterns and dynamo action— I. A new twist on magnetic arms. Monthly Notices Roy. Astron. Soc. **428**, 3569–3589 (2013)
Chamandy, L., Subramanian, K., Quillen, A.: Magnetic arms generated by multiple interfering galactic spiral patterns. Monthly Notices Roy. Astron. Soc. **437**, 562–574 (2014)
Christensson, M., Hindmarsh, M., Brandenburg, A.: Inverse cascade in decaying 3D magnetohydrodynamic turbulence. Phys. Rev. E **64**, 056405-6 (2001)
Del Sordo, F., Brandenburg, A.: Vorticity production through rotation, shear, and baroclinicity. Astron. Astrophys. **528**, A145 (2011)
Del Sordo, F., Guerrero, G., Brandenburg, A.: Turbulent dynamo with advective magnetic helicity flux. Monthly Notices Roy. Astron. Soc. **429**, 1686–1694 (2013)
Donner, K.J., Brandenburg, A.: Generation and interpretation of galactic magnetic fields. Astron. Astrophys. **240**, 289–298 (1990)
Durrer, R., Neronov, A.: Cosmological magnetic fields: their generation, evolution and observation. Astron. Astrophys. Rev. **21**, 62 (2013)
Ferrière, K.: Effect of an ensemble of explosions on the galactic dynamo. I. General formulation. Astrophys. J. **389**, 286–296 (1992)
Ferrière, K.: The full alpha-tensor due to supernova explosions and superbubbles in the galactic disk. Astrophys. J. **404**, 162–184 (1993)
Frick, P., Sokoloff, D., Stepanov, R., Beck, R.: Faraday rotation measure synthesis for magnetic fields of galaxies. Monthly Notices Roy. Astron. Soc. **414**, 2540–2549 (2011)
Gent, F.A., Shukurov, A., Fletcher, A., Sarson, G.R., Mantere, M.J.: The supernova-regulated ISM—I. The multiphase structure. Monthly Notices Roy. Astron. Soc. **432**, 1396–1423 (2013a)
Gent, F.A., Shukurov, A., Sarson, G.R., Fletcher, A., Mantere, M.J.: The supernova-regulated ISM—II. The mean magnetic field. Monthly Notices Roy. Astron. Soc. **430**, L40–L44 (2013b)
Gießübel, R., Heald, G., Beck, R., Arshakian, T.G.: Polarized synchrotron radiation from the Andromeda galaxy M 31 and background sources at 350 MHz. Astron. Astrophys. **559**, A27 (2013)
Gissinger, C., Fromang, S., Dormy, E.: Direct numerical simulations of the galactic dynamo in the kinematic growing phase. Monthly Notices Roy. Astron. Soc. **394**, L84–L88 (2009)

Gressel, O., Elstner, D., Ziegler, U., Rüdiger, G.: Direct simulations of a supernova-driven galactic dynamo. Astron. Astrophys. **486**, L35–L38 (2008a)
Gressel, O., Ziegler, U., Elstner, D., Rüdiger, G.: Dynamo coefficients from local simulations of the turbulent ISM. Astron. Nachr. **329**, 619–624 (2008b)
Gressel, O., Elstner, D., Ziegler, U.: Towards a hybrid dynamo model for the Milky Way. Astron. Astrophys. **560**, A93 (2013)
Gruzinov, A.V., Diamond, P.H.: Self-consistent theory of mean-field electrodynamics. Phys. Rev. Lett. **72**, 1651–1653 (1994)
Hanasz, M., Kowal, G., Otmianowska-Mazur, K., Lesch, H.: Amplification of galactic magnetic fields by the cosmic-ray-driven dynamo. Astrophys. J. **605**, L33–L36 (2004)
Hanasz, M., Otmianowska-Mazur, K., Kowal, G., Lesch, H.: Cosmic-ray-driven dynamo in galactic disks. A parameter study. Astron. Astrophys. **498**, 335–346 (2009)
Heald, G., Braun, R., Edmonds, R.: The Westerbork SINGS survey. II Polarization, Faraday rotation, and magnetic fields. Astron. Astrophys. **503**, 409–435 (2009)
Hubbard, A., Brandenburg, A.: Memory effects in turbulent transport. Astrophys. J. **706**, 712–726 (2009)
Hubbard, A., Brandenburg, A.: Magnetic helicity fluxes in an α^2 dynamo embedded in a halo. Geophys. Astrophys. Fluid Dyn. **104**, 577–590 (2010)
Hubbard, A., Brandenburg, A.: Catastrophic quenching in $\alpha\Omega$ dynamos revisited. Astrophys. J. **748**, 51 (2012)
Jansson, R., Farrar, G.R.: A new model of the Galactic magnetic field. Astrophys. J. **757**, 14 (2012)
Kahniashvili, T., Tevzadze, A.G., Brandenburg, A., Neronov, A.: Evolution of primordial magnetic fields from phase transitions. Phys. Rev. D **87**, 083007 (2013)
Kemel, K., Brandenburg, A., Ji, H.: A model of driven and decaying magnetic turbulence in a cylinder. Phys. Rev. E **84**, 056407 (2011)
Kleeorin, N.I., Ruzmaikin, A.A.: Dynamics of the average turbulent helicity in a magnetic field. Magnetohydrodynamics **18**, 116–122 (1982). Translation from Magnitnaya Gidrodinamika **2**, 17–24 (1982)
Knobloch, E.: Turbulent diffusion of magnetic fields. Astrophys. J. **225**, 1050–1057 (1978)
Korpi, M.J., Brandenburg, A., Shukurov, A., Tuominen, I., Nordlund, A.A.: A supernova regulated interstellar medium: simulations of the turbulent multiphase medium. Astrophys. J. Lett. **514**, L99–L102 (1999)
Korpi, M.J., Brandenburg, A., Tuominen, I.: Driving interstellar turbulence by supernova explosions. Studia Geophys. et Geod. **42**, 410–418 (1998)
Krause, M., Beck, R., Hummel, E.: The magnetic field structures in two nearby spiral galaxies. II. The bisymmetric spiral field in M81. Astron. Astrophys. **217**, 17–30 (1989)
Krause, F., Rädler, K.-H.: Mean-field Magnetohydrodynamics and Dynamo Theory. Pergamon Press, Oxford (1980)
Kulpa-Dybeł, K., Otmianowska-Mazur, K., Kulesza-Żydzik, B., Hanasz, M., Kowal, G., Wóltański, D., Kowalik, K.: Global simulations of the magnetic field evolution in barred galaxies under the influence of the cosmic-ray-driven dynamo. Astrophys. J. Lett. **733**, L18 (2011)
Layzer, D., Rosner, R., Doyle, H.T.: On the origin of solar magnetic fields. Astrophys. J. **229**, 1126–1137 (1979)
Mestel, L., Subramanian, K.: Galactic dynamos and density wave theory. Monthly Notices Roy. Astron. Soc. **248**, 677–687 (1991)
Mitra, D., Candelaresi, S., Chatterjee, P., Tavakol, R., Brandenburg, A.: Equatorial magnetic helicity flux in simulations with different gauges. Astron. Nachr. **331**, 130–135 (2010)
Moffatt, H.K.: Magnetic Field Generation in Electrically Conducting Fluids. Cambridge University Press, Cambridge (1978)
Moss, D.: Modelling magnetic fields in spiral galaxies. Astron. Geophys. **53**, 23–28 (2012)
Moss, D., Brandenburg, A., Tuominen, I.: Properties of mean field dynamos with nonaxisymmetric α-effect. Astron. Astrophys. **247**, 576–579 (1991)

Moss, D., Brandenburg, A., Donner, K.J., Thomasson, M.: Models for the magnetic field of M81. Astrophys. J. **409**, 179–189 (1993)

Moss, D., Beck, R., Sokoloff, D., Stepanov, R., Krause, M., Arshakian, T.G.: The relation between magnetic and material arms in models for spiral galaxies. Astron. Astrophys. **556**, A147 (2013)

Neronov, A., Vovk, I.: Evidence for strong extragalactic magnetic fields from Fermi observations of TeV blazars. Science **328**, 73–192 (2010)

Parker, E.N.: Hydromagnetic dynamo models. Astrophys. J. **122**, 293–314 (1955)

Parker, E.N.: The generation of magnetic fields in astrophysical bodies. II. The galactic field. Astrophys. J. **163**, 255–278 (1971)

Parker, E.N.: Fast dynamos, cosmic rays, and the galactic magnetic field. Astrophys. J. **401**, 137–145 (1992)

Piddington, J.H.: Turbulent diffusion of magnetic fields in astrophysical plasmas. Astrophys. J. **247**, 293–299 (1981)

Pouquet, A., Frisch, U., Léorat, J.: Strong MHD helical turbulence and the nonlinear dynamo effect. J. Fluid Mech. **77**, 321–354 (1976)

Rädler, K.-H.: Mean field approach to spherical dynamo models. Astron. Astrophys. **301**, 101–129 (1980)

Rädler, K.-H.: Investigations of spherical kinematic mean-field dynamo models. Astron. Nachr. **307**, 89–113 (1986a)

Rädler, K.-H.: On the effect of differential rotation on axisymmetric and non-axisymmetric magnetic fields of cosmical bodies. Plasma Phys. **ESA SP-251**, 569–574 (1986b)

Rees, M.J.: The origin and cosmogonic implications of seed magnetic fields. Quart. J. Roy. Astron. Soc. **28**, 197–206 (1987)

Rheinhardt, M., Brandenburg, A.: Test-field method for mean-field coefficients with MHD background. Astron. Astrophys. **520**, A28 (2010)

Rheinhardt, M., Brandenburg, A.: Modeling spatio-temporal nonlocality in mean-field dynamos. Astron. Nachr. **333**, 71–77 (2012)

Ruzmaikin, A.A., Sokolov, D.D., Shukurov, A.M.: Magnetic field distribution in spiral galaxies. Astron. Astrophys. **148**, 335–343 (1985)

Ruzmaikin, A.A., Sokoloff, D.D., Shukurov, A.M.: Magnetic Fields of Galaxies. Kluwer Academic Publishers, Dordrecht (1988)

Schrinner, M., Rädler, K.-H., Schmitt, D., Rheinhardt, M., Christensen, U.: Mean-field view on rotating magnetoconvection and a geodynamo model. Astron. Nachr. **326**, 245–249 (2005)

Schrinner, M., Rädler, K.-H., Schmitt, D., Rheinhardt, M., Christensen, U.R.: Mean-field concept and direct numerical simulations of rotating magnetoconvection and the geodynamo. Geophys. Astrophys. Fluid Dyn. **101**, 81–116 (2007)

Shukurov, A.: Mesoscale magnetic structures in spiral galaxies. In: Wielebinski, R., Beck, R. (eds.) Cosmic Magnetic Fields. Lect. Notes Phys., vol. 664, pp. 113–135. Springer, Berlin (2005)

Shukurov, A., Sokoloff, D., Subramanian, K., Brandenburg, A.: Galactic dynamo and helicity losses through fountain flow. Astron. Astrophys. **448**, L33–L36 (2006)

Snodin, A.P., Brandenburg, A., Mee, A.J., Shukurov, A.: Simulating field-aligned diffusion of a cosmic ray gas. Monthly Notices Roy. Astron. Soc. **373**, 643–652 (2006)

Sofue, Y., Fujimoto, M., Wielebinski, R.: Global structure of magnetic fields in spiral galaxies. Ann. Rev. Astron. Astrophys. **24**, 459–497 (1986)

Sokoloff, D.D., Bykov, A.A., Shukurov, A., Berkhuijsen, E.M., Beck, R., Poezd, A.D.: Depolarization and Faraday effects in galaxies. Monthly Notices Roy. Astron. Soc. **299**, 189–206 (1998)

Steenbeck, M., Krause, F.: Zur Dynamotheorie stellarer und planetarer Magnetfelder I. Berechnung sonnenähnlicher Wechselfeldgeneratoren. Astron. Nachr. **291**, 49–84 (1969a)

Steenbeck, M., Krause, F.: Zur Dynamotheorie stellarer und planetarer Magnetfelder II. Berechnung planetenähnlicher Gleichfeldgeneratoren. Astron. Nachr. **291**, 271–286 (1969b)

Steenbeck, M., Krause, F., Rädler, K.-H.: Berechnung der mittleren Lorentz-Feldstärke $\overline{\boldsymbol{v} \times \boldsymbol{B}}$ für ein elektrisch leitendes Medium in turbulenter, durch Coriolis-Kräfte beeinflußter Bewegung. Z. Naturforsch. **21a**, 369–376 (1966). See also the translation in Roberts & Stix, The turbulent dynamo, Tech. Note 60, NCAR, Boulder, Colorado (1971)

Subramanian, K., Brandenburg, A.: Nonlinear current helicity fluxes in turbulent dynamos and alpha quenching. Phys. Rev. Lett. **93**, 205001 (2004)
Subramanian, K., Brandenburg, A.: Magnetic helicity density and its flux in weakly inhomogeneous turbulence. Astrophys. J. **648**, L71–L74 (2006)
Subramanian, K., Mestel, L.: Galactic dynamos and density wave theory—II. An alternative treatment for strong non-axisymmetry. Monthly Notices Roy. Astron. Soc. **265**, 649–654 (1993)
Sur, S., Shukurov, A., Subramanian, K.: Galactic dynamos supported by magnetic helicity fluxes. Monthly Notices Roy. Astron. Soc. **377**, 874–882 (2007)
Tevzadze, A.G., Kisslinger, L., Brandenburg, A., Kahniashvili, T.: Magnetic fields from QCD phase transitions. Astrophys. J. **759**, 54 (2012)
Thomasson, M., Donner, K.J.: A model of the tidal interaction between M81 and NGC3077. Astron. Astrophys. **272**, 153–160 (1993)
Turner, M.S., Widrow, L.M.: Inflation-produced, large-scale magnetic fields. Phys. Rev. D **37**, 2743–2754 (1988)
Vachaspati, T.: Magnetic fields from cosmological phase transitions. Phys. Lett. B **265**, 258–261 (1991)
Vachaspati, T.: Estimate of the primordial magnetic field helicity. Phys. Rev. Lett. **87**, 251302 (2001)
Vainshtein, S.I., Cattaneo, F.: Nonlinear restrictions on dynamo action. Astrophys. J. **393**, 165–171 (1992)
Vainshtein, S.I., Ruzmaikin, A.A.: Generation of the large-scale Galactic magnetic field. Sov. Astron. **16**, 365–367 (1971)
Vishniac, E.T., Cho, J., Magnetic helicity conservation and astrophysical dynamos. Astrophys. J. **550**, 752–760 (2001)
Warnecke, J., Brandenburg, A., Mitra, D.: Magnetic twist: a source and property of space weather. J. Spa. Weather Spa. Clim. **2**, A11 (2012)
Yousef, T.A., Brandenburg, A.: Relaxation of writhe and twist of a bi-helical magnetic field. Astron. Astrophys. **407**, 7–12 (2003)

Chapter 20
Cosmic Rays in Galaxy Clusters and Their Interaction with Magnetic Fields

G. Brunetti and T.W. Jones

Abstract Cosmic rays can be accelerated in galaxy clusters by different mechanisms and remain confined in the cluster volume accumulating for cosmological times. This component is expected to generate non-thermal radiation from radio to γ-rays through a variety of mechanisms. Mpc-scale synchrotron radiation from the inter-galactic-medium is nowadays observed in many nearby, massive, clusters and provides a probe of the complex interplay between thermal gas, magnetic fields and cosmic rays in galaxy clusters. The interaction of cosmic rays with magnetic fields is of primary importance for the acceleration, evolution and dynamics of these particles. Cosmic rays are trapped and accelerated via the scattering with magnetic field fluctuations in converging (shocks) or turbulent flows driven, at least in part, by the hierarchical process of clusters formation. Interestingly, this also connects the processes of cluster formation and particle acceleration in the intra-cluster-medium. In this chapter we describe the basic ingredients of the physics of cosmic rays in galaxy clusters and report on the most relevant observables that are nowadays used for constraining their origin and evolution.

20.1 Introduction

Galaxy clusters and the filaments that connect them are the largest structures in the present universe in which the gravitational force due to the matter overdensity overcomes the expansion of the universe.

Clusters have typical total masses of the order of $10^{14} - 10^{15} M_{\odot}$, mostly in the form of dark matter ($\sim$ 70–80 % of the total mass), while baryonic matter is in the form of galaxies ($\sim$ few%) and especially in the form of a hot ($T \sim 10^8$ K) and tenuous ($n_{gas} \sim 10^{-1} - 10^{-4}\,\mathrm{cm}^{-3}$) gas ($\sim$ 15–20 %), the

G. Brunetti (✉)
IRA-INAF, via P. Gobetti 101, 40129 Bologna, Italy
e-mail: brunetti@ira.inaf.it

T.W. Jones
School of Physics and Astronomy, University of Minnesota, 116 Church St SE, Minneapolis, MN 55455, USA
e-mail: twj@msi.umn.edu

A. Lazarian et al. (eds.), *Magnetic Fields in Diffuse Media*, Astrophysics and Space Science Library 407, DOI 10.1007/978-3-662-44625-6_20

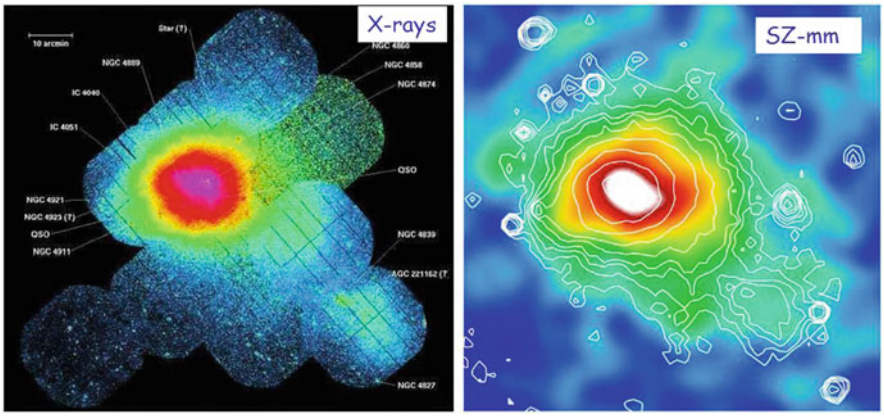

Fig. 20.1 Multi-frequency view of the Coma cluster: the thermal ICM emitting in the X-rays (*left*, adapted from Briel et al. 2001) and the overlay between thermal SZ-signal (color) and X-rays (contours) (*right*, adapted from Planck et al. 2011).

intra-cluster-medium (ICM). That ICM emits thermal X-rays, mostly via bremsstrahlung radiation (Sarazin 1988; Kravtsov and Borgani 2012) (Fig. 20.1). The picture is complicated by the discovery of non-thermal components: relativistic electrons and magnetic fields mixed with the ICM. The evidence for these additional components is nowadays routinely obtained from a variety of radio observations and opens new questions on the physics of the ICM and, more generally, on the evolution of galaxy clusters (Kaastra et al. 2008).

Clusters host several potential accelerators of cosmic ray electrons (CRe) and protons (hadrons or CRp), from ordinary galaxies to active galaxies (AGN) (Völk et al. 1996; Ensslin et al. 1997; Blasi and Colafrancesco 1999) and cosmological shock waves driven in the ICM during the process of hierarchical cluster formation (Norman et al. 1995; Loeb and Waxman 2000; Ryu et al. 2003). The long lifetime of CRp (and/or nuclei) against energy losses in the ICM and their likely slow diffusive propagation through the disordered ICM magnetic field, together with the large size of galaxy clusters, make clusters efficient storehouses for the hadronic component of CRs produced within their volume or within the individual subunits that later merged to make each cluster (Völk et al. 1996; Berezinsky et al. 1997; Ensslin et al. 1997). The accumulation of CRs inside clusters occurs over cosmological times, with the potential implication that a non-negligible amount of the ICM energy could be in the form of relativistic, non-thermal particles. CRp trapped in the ICM will necessarily produce secondary, $e^{\pm}$ particles through inelastic collisions with thermal target-protons. Consequently, they can be traced and/or constrained by secondary-particle-generated radio and γ-ray emissions (Völk et al. 1996; Berezinsky et al. 1997; Colafrancesco and Blasi 1998; Blasi and Colafrancesco 1999; Völk and Atoyan 1998; Miniati et al. 2001; Pfrommer and Enßlin 2004; Blasi et al. 2007; Wolfe and Melia 2008).

To date, despite the advent of the orbiting Fermi-LAT and deep observations from ground-based Cherenkov arrays, no cluster of galaxies has been firmly detected in the γ-rays, although very useful limits have been obtained (Ackermann et al. 2010; Aharonian et al. 2009a,b; Aleksi et al. 2010, 2012; Arlen et al. 2012). These limits, together with several constraints from complementary approaches based on radio observations (Reimer et al. 2004; Brunetti et al. 2007; Brown et al. 2011) suggest that CRp contribute less than about 5 % of the energy of the ICM, at least if we consider the central Mpc-size region. This result contradicts several optimistic expectations derived in the last decades and poses important constraints on the efficiency of CRs acceleration in galaxy clusters.

On the other hand, the existence of CRe and magnetic fields in the ICM is in fact demonstrated by radio observations. CRe are indeed very well traced in the ICM of disturbed clusters through their radio emission. This appears in the form of diffuse (Mpc scale), unpolarized synchrotron emission from the cluster X-ray emitting regions, *giant radio halos*, and in the form of *radio relics* (also called *radio Gischt*), elongated and often highly polarized synchrotron sources typically found in the clusters' peripheral regions (Ferrari et al. 2008; Feretti et al. 2012) (Fig. 20.2). There is an additional population of diffuse cluster radio sources on $\sim$ 100 kpc scales, known as *radio mini-halos*. Those are typically found in relatively relaxed clusters with cool cores where there is also AGN activity (Ferrari et al. 2008; Feretti et al. 2012). We do not include them in this Chapter. For sake of completeness we mention here that in a few nearby clusters the existence of a hard (non-thermal) X-ray component in excess to the thermal radiation is also claimed and interpreted as the inverse Compton counterpart of the synchrotron emission observed in the radio band (Fusco-Femiano et al. 1999; Rephaeli et al. 1999; Rephaeli and Gruber 2002; Fusco-Femiano et al. 2005; Petrosian et al. 2006; Eckert et al. 2008; Ajello et al.

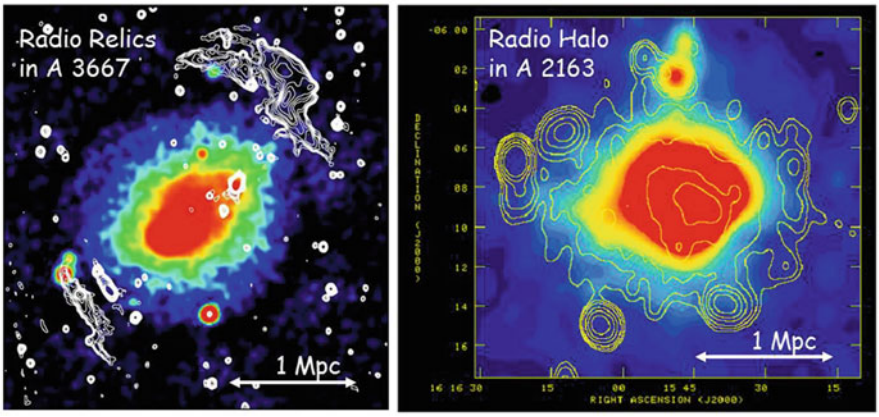

Fig. 20.2 The double radio relic in Abell 3667 (*left*, adapted from Rottgering et al 1997) and the giant radio halo in Abell 2163 (*right*, adapted from Feretti et al 2001). Conturs mark the radio emission, colors mark the X-ray emission from the ICM

2010). These X-ray observational results are, however, highly debated (Rossetti and Molendi 2004; Fusco-Femiano et al. 2004, 2007; Wik et al. 2009; Ajello et al. 2009; Wik et al. 2011) and new constraints from upcoming X-ray telescopes are necessary to clarify the existence and nature of these non-thermal excesses in the hard X-rays.

The electrons responsible for the radio emission on large, Mpc, scales open to investigation the nature of particle acceleration mechanisms in galaxy clusters. In fact, local acceleration or injection is likely to be necessary to account for observed CRe, since their energy-loss lifetimes are quite brief, in contrast to CRp of similar energies (Jaffe 1977). There is consensus on the observational fact that presence of Mpc scale synchrotron emission in clusters (both giant radio halos and relics) is tightly correlated with the dynamical state of the hosting clusters, with merging clusters being preferred systems where non-thermal emission is generated (Buote 2001; Ferrari et al. 2008; Cassano et al. 2010). It suggests that halos and relics trace the hierarchical cluster assembly and probe the dissipation of gravitational energy into CRs and magnetic fields during mergers. In particular, the polarisation and morphological properties of radio relics suggest a connection with large scale shocks that cross the ICM during mergers and may accelerate or reaccelerate to GeV energies the emitting electrons (Brüggen et al. 2012). On the other hand, there are reasons to believe that radio halos trace gigantic turbulent regions in the ICM, where relativistic electrons can be reaccelerated through scattering with MHD turbulence and/or injected by way of inelastic collisions between trapped CRp and thermal protons (Brunetti 2011,a).

The theoretical picture, elaborated to explain the origin of Mpc-scale radio sources and their connection with clusters mergers, has unavoidable consequences for the non-thermal properties of clusters. One of the most interesting consequences is that clusters should be sources of high energy photons that could be detected by the next generation of X-ray and γ-ray telescopes. The firm detection of galaxy clusters in the hard X-rays and in γ-rays would lead to a fundamental leap forward in our understanding of the energy content of magnetic fields and CRp in the cosmic large scale structure. In addition the combined information would enable a much deeper understanding of the microphysics of extremely dilute plasmas, since those processes control the generation and evolution of these nonthermal constituents in clusters.

In this chapter we will discuss the most relevant aspects of the origin and physics of CRs in galaxy clusters, and elaborate on the present theoretical framework, with particular emphasis on the most important observational constraints. Observational prospects for the next years will also be discussed.

20.2 Cosmic Ray Sources and Acceleration

Several sources can supply relativistic particle populations (electrons, hadrons or both) to the ICM. For instance, particles can be accelerated in ordinary galaxies as an outcome of supernovae (SN) and then expelled into the ICM with a CRp luminosity as high as $\sim 3\times10^{42}$ erg s^{-1} (Völk et al. 1996). Alternatively, high velocity outflows

from AGNs may plausibly contribute up to $\sim 10^{45}$ erg s^{-1} in CRs over periods of $\sim 10^8$ years (Ensslin et al. 1997). Particle acceleration may also happen in large scale ICM shocks produced during the hierarchical formation of the large scale structure in the universe (Norman et al. 1995; Kang et al. 1996; Ryu et al. 2003). In particular, consensus has been reached in the past decade that shocks spanning large scale structures are relevant sources of CRs in galaxy clusters, thus implying a direct connection between the generation of CRs and the formation and evolution of the hosting clusters. Finally, there is also consensus on the fact that turbulence can be induced in the ICM as a result of the same process of clusters formation, and that such turbulence affects the propagation of CRs, while also providing a potentially important mechanism for re-acceleration of CRp and CRe (Fujita et al. 2003; Cassano and Brunetti 2005; Brunetti and Lazarian 2007; Ensslin et al. 2011).

20.2.1 Galaxies, Starbursts and Active Nuclei

Individual galaxies are sources of CRs. Massive clusters of galaxies contain more than a hundred galaxies where SN and Pulsars accelerate CRs. The amount of CR energy available to the ICM depends on the efficiency of CR acceleration at these sites and on the way CRs are transported from their galactic sources into the ICM.

Völk et al. (1996) pioneered the studies of the role of SN explosions in cluster galaxies and starbursts activity. The number of SN experienced by clusters since their formation epoch can be estimated from the metal enrichment of the ICM, assuming those metals are released by SN explosions. The result is :

$$N_{SN} = \int_{T_o}^{0} dt \nu_{SN}(t) = \frac{[Fe]_{\odot} X_{cl} M_{cl,gas}}{\delta M_{Fe}} \tag{20.1}$$

where $[Fe]_{\odot} X_{cl} M_{cl,gas}$ is the mass of iron in the ICM ($[Fe]_{\odot} \sim 4/10^5$ is the iron abundance, $X_{cl} \sim 0.35$ the typical metallicity measured in galaxy clusters, and $M_{cl,gas}$ the baryon mass of the cluster) and δM_{Fe} is the iron mass available to the ICM from a single SN explosion. The total energy budget in the form of CRp that is released in the ICM is thus :

$$E_{CR}^{SN} = N_{SN} \eta_{CR}^{SN} E_{SN} \leq \frac{[Fe]_{\odot} X_{cl} M_{cl,gas}}{\delta M_{Fe}} E_{SN} \eta_{CR}^{SN} \tag{20.2}$$

where $E_{SN} \sim 10^{51}$ erg is the SN kinetic energy and η_{CR}^{SN} is the fraction of SN kinetic energy in the form of CRp; $\eta_{CR}^{SN} \sim 0.2$–0.3 is constrained from observations of SN in the Galaxy. Equation20.2 implies a ratio between the CRp and thermal energy budget in galaxy clusters $E_{CR}^{SN}/E_{gas} \sim 10^{-3}$, assuming $\delta M_{Fe} \sim 0.1 M_{\odot}$ (appropriate for type II SN) and $T_{gas} \sim 10^8$K. This is however an optimistic estimate of the expected energy content of CRp in galaxy clusters from this source, because it does

not account for adiabatic losses in the likely event that CRp from SN are transported into the ICM by SN-driven galactic winds.

Clusters of galaxies, clusters of galaxies contain also AGNs, which by way of their synchrotron-emitting jets and radio lobes are known to carry CRs (Miley 1980). In addition those outflows can drive shocks into the ICM and produce turbulence, as well, that are both capable of accelerating CRs. The radio lobes of AGNs in clusters coincide with X-ray dark volumes or cavities that have turned out to be the best calorimeters of the total energy deposited by AGN outflows. The cavities, being filled with relativistic and potentially some amount of very hot thermal plasma at substantially lower density than their surroundings, are poor thermal X-ray emitters. Such cavities have been seen in something like 1/4 of the clusters observed by Chandra (McNamara and Nulsen 2007), despite the fact that they are often difficult to detect. Assuming pressure balance between the cavity and the surrounding ICM, the energy content of the cavity turns out to be in the range $\sim 10^{55} - 10^{61}$ erg. These approach $\sim 1\,\% E_{gas}$ in some cases. Dynamical estimates of cavity lifetimes are typically $\sim 10^8$ years, leading to AGN power deposition estimates within an order of magnitude of the X-ray cooling rate of the host cluster (Rafferty et al. 2006), at least while the AGN jets are active. Simulations suggest that roughly 1/2 the power of the AGN outflow is immediately deposited irreversibly as ICM heat (O'Neill and Jones 2010). Thus, AGN outflows are often invoked to account for extra heating needed to limit the effects of strong radiative cooling in cluster cores (Gitti et al. 2011). The cavity energy contributed directly by CRp and CRe is harder to establish, however. While it is possible that much of the energy carried by AGN outflows is contained in CRs, there are good arguments suggesting much of it is either in cold particles or, possibly in electromagnetic fields (De Young 2006). Even if most of the energy supporting the cavities is carried by CRs it is not yet clear how efficiently those CRs can be dispersed through diffusion and convective/turbulent mixing over the full cluster volume, and how much of the energy would remain in CRs, after accounting for adiabatic and other energy losses. For example, a connected issue, that will not be discussed in this chapter, is the role of relativistic outflows from AGNs in the origin of radio mini halos in cool core clusters (Cassano et al. 2008).

20.2.2 Particle Acceleration in the ICM

The process of structure formation may contribute most of the energetics of non-thermal components in galaxy clusters (Sarazin 1999; Takizawa and Naito 2000; Miniati et al. 2001; Gabici and Blasi 2003; Ryu et al. 2003; Cassano and Brunetti 2005; Pfrommer et al. 2006; Blasi et al. 2007; Brunetti and Lazarian 2007; Skillman et al. 2008; Vazza et al. 2009; Cassano et al. 2010; Brüggen et al. 2012; Vazza et al. 2012). Mergers between two or more clusters are observed to heat clusters through shocks and other large scale dynamics that also probably amplify magnetic fields and potentially accelerate particles (Brüggen et al. 2012; Markevitch and Vikhlinin

2001; Markevitch et al. 2002; Govoni et al. 2004; Henry et al. 2004; Markevitch et al. 2005; Roettiger et al. 1999; Dolag et al. 2002). Although more difficult to constrain observationally, the additional process of semi-continuous accretion of material onto clusters, especially from colder filaments, is expected to drive quasi-stationary strong shocks and turbulent flows at Mpc distances from cluster centers that should impact on the ICM physics and acceleration of CRs over wide volumes.

Particle acceleration during mergers occurs at shock waves that cross the ICM and also probably results from several mechanisms (turbulent acceleration, reconnection, etc.) that may operate within turbulent regions driven in the ICM during these mergers (Lazarian and Brunetti 2011).

20.2.2.1 Shocks in Cluster Mergers

The total gravitational energy dissipated in a merger of two clusters with roughly equal mass, $M = 10^{15} M_{\odot}$ is $E \approx 10^{64}$ erg. It is easy to show that the merging components approach each other at slightly supersonic relative speed, therefore implying the formation of weak, $M \sim 2$, shock waves (Sarazin 1999; Gabici and Blasi 2003; Berrington and Dermer 2003), at least while those shocks are penetrating gas virialized to the cluster potentials. Those shocks will typically strengthen moderately as they emerge into lower density regions. If a non-negligible fraction of the merger-shock-dissipated energy can be converted into non-thermal particles through a first order Fermi process, then the ICM may be populated with a significant population of non-thermal, CR particles (Blasi et al. 2007). Remote, accretion shocks are much stronger; that is, they have higher Mach numbers, since they develop in cold, un-virialised external cluster regions. On the other hand, since gas densities are also quite low in those environments, the energy flux through such shocks is relatively smaller than through lower Mach number shocks that dissipate closer into clusters during mergers. Simple (analytical or semi-analytical) estimates of the amount of kinetic energy associated with these remote shocks are very challenging. However, a leap forward in this direction has been achieved in the last decade through extensive cosmological simulations that allow one to study the formation of shocks in clusters, from their outskirts to more internal regions with increasing detail (Miniati et al. 2000; Ryu et al. 2003; Keshet et al. 2003; Pfrommer et al. 2006; Skillman et al. 2008; Vazza et al. 2009, 2010, 2011, Fig. 20.3).

For the reasons just outlined there is consensus on the fact that most of the gravitational energy in galaxy clusters is dissipated at relatively weak shocks, with Mach number $M \sim 2$–3, that are typically generated during major and minor mergers and that cross the cluster internal regions. A still substantial fraction of the kinetic energy-flux through shocks in clusters is, however, associated with moderately stronger shocks (Fig. 20.4) that pass through regions between the outer, accretion shocks and the virialized cluster cores. As noted above, those shocks often represent merger activity as it propagates energy outwards from the cores after their closest approach.

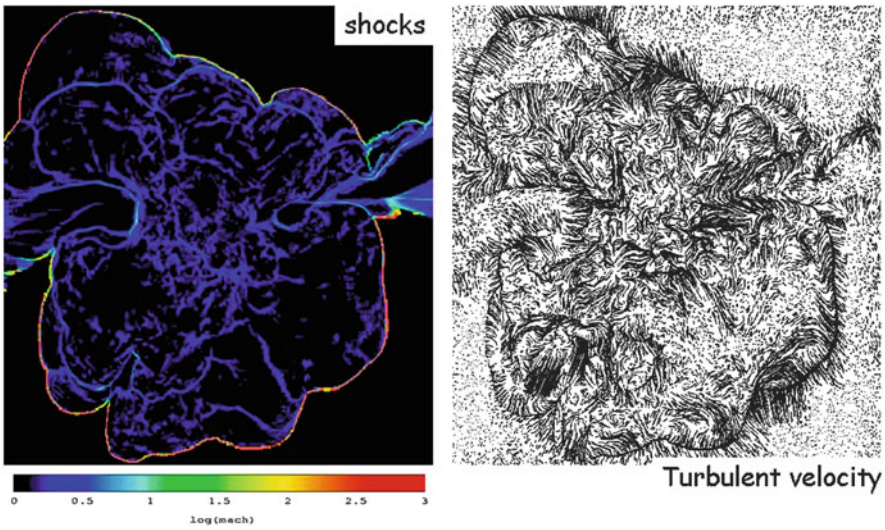

Fig. 20.3 Shocks (*left*) and turbulent velocity field (*right*) in a simulated galaxy cluster (adapted from Vazza et al. (2009))

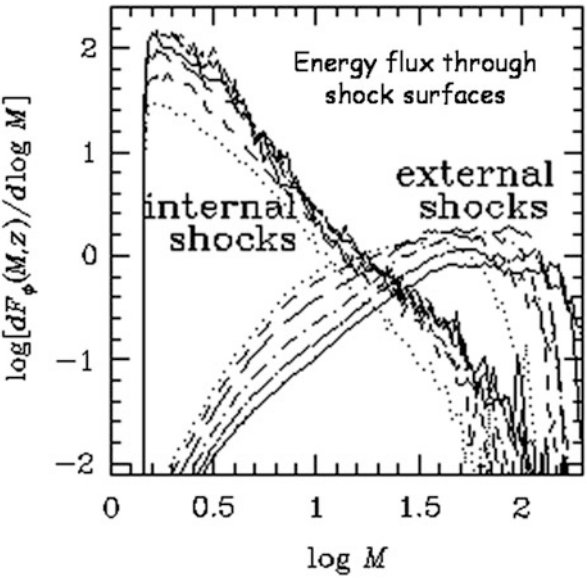

Fig. 20.4 Energy flux at shocks surfaces as a function of the shock-Mach number from numerical (cosmological) simulations (adapted from Ryu et al. 2003). Units are in 10^{40} erg/s $(1 + z)^3 h^3 Mpc^{-3}$. Shocks are divided into internal and external (see text)

The acceleration of CRs at shocks is customarily described according to the diffusive shock acceleration (DSA) theory (Bell 1978; Drury 1983; Blandford and Eichler 1987; Jones and Ellison 1991). In effect diffusing particles are temporarily

trapped in a converging flow across the shock if their scattering lengths are finite, but much greater than the shock thickness. Particles escape eventually by convection downstream. Until they do, they gain energy each time they are reflected upstream across the shock with a rate determined by the velocity change across the shock and a competition between convection and diffusion on both sides of the shock. The hardness (flatness) of the resulting spectrum reflects the probability that particles remain trapped long enough to reach high energies. This process can be described through the diffusion-convection equation for a pitch angle averaged CRs distribution function $f(p,t)$ is Blandford and Eichler (1987):

$$\frac{\partial f}{\partial t} + (\mathbf{V}\cdot\nabla) f - \nabla\cdot\left\{\mathbf{n}\, D\, (\mathbf{n}\cdot\nabla) f\right\} = \frac{1}{3}(\nabla\cdot\mathbf{V}) p \frac{\partial f}{\partial p} \tag{20.3}$$

where $\mathbf{V}$ is the velocity of the background medium (assuming $c >> V >> V_A$), $\mathbf{n}$ is the unit vector parallel to the local magnetic field, p is the particle momentum, and D is the particle spatial diffusion coefficient (see Sect. 20.2.2.2 and 20.3.2). The second and third terms account for convection and diffusion, respectively, while the right hand side takes account of the adiabatic energy gains (losses) suffered by particles in a converging (expanding) flow. The diffusive term makes the evolution irreversible. As written, Eq. (20.3) ignores other losses, such as from radiation, that can be important for CRe (see Sect. 20.3.1).

Under these conditions the spectrum of CRs injected at low energies and then accelerated at a simple, plane shock is a power law in momentum, $f(p) = Kp^{-(\delta_{inj}+2)}$, where the slope is

$$\delta_{inj} = 2\frac{M^2+1}{M^2-1} \tag{20.4}$$

$M = V_{sh}/c_s$ is the Mach number of the shock. For strong shocks, $M \to \infty$, this slope tends to $\delta_{inj} \to 2$. Thus, in the strong shock limit, the energy and pressure in the resulting CRs are broadly distributed towards the highest energies that are achieved. On the other hand, for weak shocks, $M^2 \approx 1+\epsilon$ with $\epsilon \ll 1$, this tends to $\delta_{inj} \approx 2 + 4/\epsilon \gg 2$. In this case the fractional velocity jump across the shock is small, so the energy in CRs accelerated from suprathermal values is concentrated in the lowest energy CRs. Consequently, for the same number of CRs and the same kinetic energy flux through the shock, $\sim \rho V_{sh}^3$, the energy input to locally injected CRs through DSA is much greater in strong shocks than in weak shocks. We note for reference that CRe with a power law slope, δ, as above, in a magnetic field will emit synchrotron radiation with a spectral slope, $\alpha = (\delta-1)/2$.

The acceleration time-scale at the shock depends on the time interval between shock crossings for the CR, $\sim 4D/(cV_{sh})$, and on the ratio of the CR velocity to the fluid velocity change across the shock, so $\sim c/\Delta V$. Thus, it primarily depends on the spatial diffusion coefficient of particles, and inversely on the shock velocity and the compression through the shock. If the spatial diffusion scales with the particle

momentum, p, but does not change across the shock, the mean acceleration time to a given momentum can be written as :

$$\tau_{acc}(p) \simeq \frac{4D(p)}{(c_s M)^2} \frac{M^2(5M^2+3)}{(M^2+3)(M^2-1)} \tag{20.5}$$

For strong shocks this approaches $\tau_{acc} \approx 20D/(c_s M)^2$. For weak shocks this expression would need to be multiplied by a factor $(51/80 + 1/(20\epsilon))$, which is of order unity unless the Mach number is very close to one, when it becomes large. So, for given shock velocity and spatial diffusion coefficient, the acceleration time to a particular CR energy is not very sensitive to the shock Mach number. Assuming (an optimistically small) Bohm diffusion coefficient, $D(p) = (1/3)r_L(p)c$, (Sect 20.2.2.2) where, $r_L(p)$, is the particle Larmour radius, the spatial diffusion coefficient for relativistic particles becomes,

$$D(p) \sim 3 \times 10^{22} \frac{(cp/\mathrm{GeV})}{(B/\mu G)} \quad \mathrm{cm^2 s^{-1}}. \tag{20.6}$$

For a typical velocity of shocks in galaxy clusters, $c_s M \sim$ few 10^3 km/s, the resulting acceleration time scale to GeV energies is very fast; namely, of the order of 1 year, if $B \sim 1\,\mu$G. This implies that the power law distribution of the accelerated particles extends up to very high energies, where energy losses or diffusion from the acceleration region (Sect. 20.3.1) quenches the acceleration process. The energy losses for CRe, due especially to synchrotron and inverse Compton processes, are much more significant than those for CRp. For CRe we anticipate that the maximum energy accelerated at shocks in galaxy clusters can be of the order of several tens of TeV (Blasi 2001). Radiative cooling of CRe due to inverse Compton scattering with the CMB downstream of the shock will reduce the maximum electron energy so that it scales asymptotically as $\gamma_{e,max} \propto 1/x$, where $x = V_2 t$ is the propagation distance downstream of the shock reached over a time, t. This causes the volume integrated electron spectrum to steepen by one in the power law index, $\delta = \delta_{inj} + 1$ above energies reflecting this loss over the lifetime of the accelerating shock.

By contrast, CRp in these shocks are not subjected to significant energy losses until they reach extremely high energies where they suffer inelastic collisions with CMB photons. CRp with energies above a few hundred PeV will produce $e^{\pm}$ when they collide with CMB photons, limiting their residence and allowed acceleration period below a few Gyr. Above about 5×10^{19} eV, however, such collisions produce pions, and each such collision extracts a significant fraction of the CRp energy. For energies above $\sim 10^{20}$ eV, the available residence/acceleration times drop rapidly below $\sim 10^8$ years. This is the same physics that determines the so-called Greisen-Zatsepin-Kuzmin (GZK) cutoff in the ultra-high energy CR spectrum. In the context of CR acceleration at cluster shocks, this time constraint effectively limits the energies that can be reached there through DSA to $< 10^{20}$ eV (Kang et al. 1996). Similarly, even if CRp diffusion is as slow as the limiting Bohm diffusion in Eq. (20.6) CRs near 10^{20} eV would diffuse o ut of the cluster on time scales less

than the time required for them to be accelerated by DSA to still higher energies (Blasi 2001).[1]

On timescales longer than those required to accelerate CRs to relativistic energies, $\tau_{acc}(pc \sim 1\text{GeV})$, a substantial fraction of the energy flux into strong, initially purely hydrodynamical shocks can go into CRps. Those, in turn backreact on and modify the structure of shocks themselves. Under these conditions the process of particle acceleration is described using nonlinear theory (Drury 1983; Jones and Ellison 1991; Malkov and O'C Drury 2001; Blasi 2002; Kang et al. 2002; Kang and Jones 2005). The main outcome of that development is formation of a compressive precursor to the shock, leading to an increase in the total shock compression, upstream turbulence and magnetic field amplification, followed by an actual weakening of the fluid shock transition (the so-called "sub-shock"). In a highly CR-modified shock a large part of the DSA process at high CR energies actually takes place in the precursor; the subshock is responsible mostly for the acceleration process at low energies (Kang et al. 2009).

The importance of nonlinear evolution in such shocks depends on the size of the CR population at the shock and the hardness of the CR spectrum, being accelerated at the shock. These are important, since they regulate how much energy is extracted from the flow into the shock and, accordingly how much pressure will develop from these CRs just upstream of the fluid shock transition. Unless they include much larger total CR populations or interact with a pre-existing CR population with a hard spectrum, weak shocks are minimally affected by nonlinear effects, because of the steeper CR spectra generated in weak shocks.

A key ingredient in shock acceleration theory is the minimum momentum of the seed particles that can be accelerated by DSA; i.e., the minimum momentum that leads to diffusive particle transport across the shock. This is a key ingredient in determining the efficiency with which plasma particles are injected into the CR population from the thermal pool at shocks. In particular, particles must have momenta at least several times the characteristic postshock thermal ion momenta in order to be able to successfully recross into the preshock space. Quasi-thermalized particles are inherently less likely to recross in the upstream direction in weak shocks than strong shocks, because of the weaker dissipation in weak shocks; i.e., the postshock thermal speed is relatively smaller than the postshock convection speed downstream. Injection also should depend on the local magnetic field geometry, since the field controls postshock particle trajectories. Similarly, injection is expected to depend sensitively on the charge/mass ratio of the injected species, since that determines the rigidity ($\propto p/q$) of particles at a given energy. For this reason, nonrelativistic electrons appear to be very difficult to inject from the thermal population, so are likely to be far fewer than injected protons. Typically some kind of upstream, pre-injection process, often involving protons reflected by the shock that generate upstream waves that can resonate with nonrelativistic electrons, is invoked to enable electron injection at shocks (Amato and Arons 2006; Burgess 2006; Amano and

[1]The acceleration time-scale of these CRs, assuming μG fields, is larger than the Hubble time

Hoshino 2009; Riquelme and Spitkovsky 2011). This physics appears to be very sensitive to the local magnetic field geometry, preferring quasi-perpendicular, but not precisely perpendicular fields (Riquelme and Spitkovsky 2011). The processes "selecting" the particles that can recross define so-called thermal-leakage injection. It is important to realize that they are poorly understood, especially in the relatively weak shocks with large beta plasma, $\beta_{pl} = P_{gas}/P_B$, expected in cluster media. Existing collisionless shock simulations have, out of practical necessity, focussed on strong shocks (Kang et al. 2012).

Another major unresolved ingredient in nonlinear CR shock theory is the level of amplification of the magnetic field crossing the shock due to CR-driven instabilities. The evolution of the magnetic field through the full shock structure is important, since the magnetic field self-regulates the diffusion process of suprathermal particles and also affects the injection process (Bell 1978; Kang et al. 2002). There are several proposed models to amplify magnetic fields within the CR-induced shock precursor (Lucek and Bell 2000; Bell 2004; Amato and Blasi 2009); none of them applies until some degree of shock modification already takes place. This means they only apply in strong shocks, so probably not in cluster merger shocks. Some magnetic field generation and/or amplification downstream of curved or intersecting shocks may result when the electron density and pressure gradients are not parallel (the so-called Biermann Battery effect) or the downstream total plasma and pressure gradients are not parallel (so-called baroclinic effects that amplify vorticity). We note that these should have minimal influence on DSA, however, since they would not modify the time between successive diffusive upstream-to-downstream shock crossings for CRs.

Particle acceleration efficiency at strong shocks is becoming constrained by studies of SN-driven shocks in our Galaxy (Jones 2011). Those shocks transfer $\sim 10\,\%$ or more of the energy driving them into CRp. It is important to keep in mind that the shocks mostly responsible for acceleration of observable Galactic CRs are very strong, with Mach numbers upwards of 10^3. By contrast, and as discussed above, most of the kinetic energy flux penetrating galaxy cluster shocks is associated with much weaker shocks where, the acceleration efficiency is probably much less, although still poorly understood (Blasi 2004; Kang and Jones 2005). In this respect galaxy clusters are special environments, as they are unique laboratories for constraining the physics of particle acceleration at gigantic (Mpc-scale) weak shocks. It remains an open issue whether these weak shocks can accelerate CRs in the ICM at meaningful levels. The relative importance of merger and accretion shocks for the acceleration of CRs in the ICM still requires clarification, as well. As outlined previously, current understanding suggests that merger shocks should be the most important sources of CRs. Recent models indicate they should contribute about one order of magnitude more energy to CRs than the accretion shocks (Ryu et al. 2003; Skillman et al. 2008; Vazza et al. 2009, Fig. 20.4).

20.2.2.2 Turbulence in the ICM and Particle Acceleration

Turbulence in the ICM can potentially trigger several mechanisms of particle acceleration. The non-linear interplay between particles and turbulent waves/modes is a stochastic process that drains energy from plasma turbulence to particles (Melrose 1980; Schlickeiser 2002). In addition reconnection of magnetic fields can be faster in turbulent regions (Lazarian and Vishniac 1999) providing an additional (potential) source of particle acceleration in the ICM (Lazarian and Brunetti 2011); in this section we will restrict ourself to discuss the process of stochastic reacceleration of CRs due to resonant interaction with turbulence.

Galaxy clusters contain many potential sources of turbulence. These include cluster galaxies (Jaffe 1977; Deiss and Just 1996), the interplay between ICM and the outflowing relativistic plasma in jets and lobes of AGNs (Heinz et al. 2006; Brüggen and Scannapieco 2009), and buoyancy instabilities such as the magnetothermal instability (MTI) in the cluster outskirts (Parrish and Stone 2007). However, the most important potential source of turbulent motions on large scale is the process that leads to the formation of galaxy clusters (Roettiger et al. 1999; Ricker and Sarazin 2001; Cassano and Brunetti 2005; Subramanian et al. 2006). Turbulence is expected from core sloshings, shearing instabilities, and from the complex pattern of interacting shocks that forms during mergers and structure formation more generally (Miniati et al. 2000; Dolag et al. 2005; Iapichino and Niemeyer 2008; Vazza et al. 2009, 2010; Keshet et al. 2010; Iapichino et al. 2011; Paul et al. 2011; ZuHone et al. 2011; Hallman and Jeltema 2011; Vazza et al. 2012).

Large scale turbulent motions that are driven during cluster-cluster mergers are expected on scales comparable to cluster cores scales, $L_o \sim$ 100–400 kpc, and with typical velocities around $V_o \sim$ 300–700 km/s (Subramanian et al. 2006). These motions are sub-sonic, with $M_s = V_o/c_s \approx 0.25$–$0.6$, but strongly super-Alfvénic, with $M_A = V_o/v_A \approx$ 5–10 (Brunetti and Lazarian 2007). It implies a situation in which magnetic field lines in the ICM are continuously advected/tangled on scales larger than the Alfvén scale, $l_A \sim L_0(V_0/V_A)^{\frac{2}{a-1}}$ (a the slope of the turbulent velocity power-spectrum, $W(k) \propto k^{-a}$). Under these conditions the effective particle mean-free-path in the ICM should be $l_{mfp} \sim l_A$ rather than the value of the classical Coulomb mean free path, $l_C \sim$ 10–100 kpc (Lazarian 2006; Brunetti and Lazarian 2007). However the ICM is a "weakly collisional" plasma, where instabilities play a role (Schekochihin et al. 2005, 2010). Plasma instabilties perturb the magnetic field on very small scales and may reduce the effective thermal particle mean free path (Levinson and Eichler 1992; Pistinner et al. 1996; Brunetti and Lazarian 2011b).

All these considerations on the velocities of large-scale motions and on the effective particle mean-free-path in the ICM allow us to conclude that the effective Reynolds number in the inner ICM is $\mathscr{R}e >> 10^3$, much larger than it would be by assuming the classical ion–ion mean free path ($\mathscr{R}e \sim 100$), implying that a cascade of turbulence and a turbulent inertial range could be established from large to smaller scales.

The acceleration or reacceleration of CRs by turbulence is customarily described according to the quasi-linear-theory (QLT), where the effect of waves on particles is studied by calculating first-order corrections to the particle orbit in the uniform/background magnetic field $\mathbf{B_0}$, and then ensemble-averaging over the statistical properties of the turbulent modes (Jokipii 1966; Schlickeiser and Achatz 1993; Miller and Roberts 1995). In the coordinate system in which the space coordinates are measured in the Lab. system and the particle momentum coordinates are measured in the rest frame of the background plasma that supports the turbulence and in which turbulence is homogeneous, the gyrophase-average particle density distribution evolves $f(x, p, \mu, t)$ evolves according to the Fokker-Planck equation (Schlickeiser 2002):

$$\frac{df}{dt} = \frac{\partial}{\partial \mu}\left[\left(D_{\mu\mu}\frac{\partial}{\partial \mu} + D_{\mu p}\frac{\partial}{\partial p}\right) f(p,\mu,t)\right] + \frac{1}{p^2}\frac{\partial}{\partial p}\Big[p^2 \times \left(D_{\mu p}\frac{\partial}{\partial \mu} + D_{pp}\frac{\partial}{\partial p}\right) f(p,\mu,t)\Big] \tag{20.7}$$

where D_{pp}, $D_{\mu\mu}$ and $D_{p\mu}$ are the fundamental transport coefficients describing the stochastic turbulence-particle interactions. These are determined by the electromagnetic fluctuations in the turbulent field. If we restrict our attention to the case of low-frequency Alfvén and magnetosonic MHD waves, under conditions of negligible damping the relevant Fokker-Planck coefficients are given by Schlickeiser and Achatz (1993); Yan and Lazarian (2004):

$$\begin{pmatrix} D_{\mu\mu} \\ \\ D_{pp} \end{pmatrix} = \frac{\pi \Omega^2 (1-\mu^2)}{2B_0^2} \mathscr{R}e \sum_{n=-\infty}^{n=\infty} \int_{\mathbf{k_{min}}}^{\mathbf{k_{max}}} d^3k \begin{pmatrix} \left(1 - \frac{\mu\omega}{vk_\parallel}\right)^2 \\ \\ \left(\frac{p\,c}{v}\right)^2 \end{pmatrix} \delta(k_\parallel v_\parallel - \omega + n\Omega)$$
$$\Big\{ J_{n+1}^2(w) \begin{pmatrix} P_{RR}^{\mathbf{k}} \\ \\ R_{RR}^{\mathbf{k}} \end{pmatrix} + J_{n-1}^2(w) \begin{pmatrix} P_{LL}^{\mathbf{k}} \\ \\ R_{LL}^{\mathbf{k}} \end{pmatrix} + J_{n+1}(w) J_{n-1}(w) \Big[e^{2i\xi} \begin{pmatrix} -P_{RL}^{\mathbf{k}} \\ \\ R_{RL}^{\mathbf{k}} \end{pmatrix}$$
$$+ e^{-2i\xi} \begin{pmatrix} -P_{LR}^{\mathbf{k}} \\ \\ R_{LR}^{\mathbf{k}} \end{pmatrix} \Big] \Big\} \tag{20.8}$$

where $\xi = arctan(k_x/k_y)$, $\Omega = (q/|q|)\Omega_0/\gamma$ ($\Omega_0 = qB/(m\,c)$ is the non-relativistic gyrofrequency), where we define $w = k_\perp v_\perp/\Omega$ as the argument for the Bessel functions, J_n, ω is the frequency of the waves, and $k_\parallel$ and $k_\perp$ are the components of the wavenumber parallel and perpendicular to the field. The relevant electromagnetic fluctuations are :

$$< B_\alpha(\mathbf{k}) B_\beta^*(\mathbf{k}') >= \delta(\mathbf{k} - \mathbf{k}') P_{\alpha\beta}^{\mathbf{k}} \tag{20.9}$$

and

$$< E_\alpha(\mathbf{k}) E^*_\beta(\mathbf{k}') >= \delta(\mathbf{k}-\mathbf{k}') R^{\mathbf{k}}_{\alpha\beta} \tag{20.10}$$

where α and $\beta = R, L$ indicate wave polarization. $\delta(k_\parallel v_\parallel - \omega + n\Omega)$ in eq. 20.8 selects the resonant conditions between particles and waves; namely, $n = \pm 1, ..$ (gyroresonance for Alfvén waves) and $n = 0$ (Transit Time Damping, TTD, or wave surfing for magnetosonic waves) (Melrose 1980; Schlickeiser and Achatz 1993).

In the case of low-frequency MHD waves with phase velocities much less than the speed of light the magnetic-field component is much larger than the electric-field component, $\delta B \sim c/v_{ph}\delta E$. Then the particle distribution function, f, adjusts very rapidly to quasi-equilibrium via pitch-angle scattering, approaching a quasi-isotropic distribution. In this case the Fokker-Planck equation (20.7) simplifies to a diffusion-convection equation (Dung and Petrosian 1994; Kirk et al. 1988):

$$\frac{\partial f(p,t)}{\partial t} = \frac{1}{p^2}\frac{\partial}{\partial p}\left(p^2 \mathscr{D}_{pp}\frac{\partial f}{\partial p}\right) + \frac{\partial}{\partial z}\left(D\frac{\partial f}{\partial z}\right) \tag{20.11}$$

where the momentum diffusion coefficient is:

$$\mathscr{D}_{pp} = \frac{1}{2}\int_{-1}^{1} d\mu D_{pp} \tag{20.12}$$

and the spatial diffusion coefficient is :

$$D = \frac{\mathrm{v}^2}{8}\int_{-1}^{1} d\mu \frac{(1-\mu^2)^2}{D_{\mu\mu}}. \tag{20.13}$$

Note that the spatial diffusion scales inversely to the rate of angular diffusion, $D_{\mu\mu}$, since the latter limits the distance a CR travels before it loses track of its original propagation direction; ie., its mean free path, λ. Equation (20.13) can be used, in fact, to define the particle mean free path as $\lambda = 3D/\mathrm{v}$.

From Eqs. (20.8)–(20.10) and (20.12) and (20.13) the momentum and spatial diffusion coefficients depend on the electric field and magnetic field fluctuations, respectively. Simple, approximate forms for these coefficients can be written in some circumstances that are useful in several astrophysical situations, including galaxy clusters.

For instance, if one assumes isotropic pitch angle scattering by resonant (linearly polarised and undamped) Alfvén waves with $k \sim r_L^{-1}$, the spatial diffusion coefficient from Eq. (20.13) can be written for relativistic CRs as (Skilling 1975):

$$D \approx A c r_L \frac{B_0^2}{(\delta B)^2}, \tag{20.14}$$

where δB represents the net amplitude of magnetic field fluctuations defined in Eq. (20.9) and where $A \sim 1$ [in Sect. 20.3.2 we will give a equivalent formula in

terms of the Alfvén wave spectrum, Eq. (20.28)]. We note that for $\delta B \sim B_0$ the result is equivalent to the classical Bohm diffusion formula, $D \sim 1/3cr_L$. Similarly, if we assume momentum diffusion results from Transit-Time-Damping interactions with isotropic magnetosonic waves, we can write approximately for relativistic CRs (Brunetti and Lazarian 2007):

$$\mathscr{D}_{pp} \approx A_1 p^2 \frac{c_s^2}{cl} \frac{(\delta B)^2}{B_0^2}, \tag{20.15}$$

where $A_1 \sim 5$ depends on details of the turbulence, l is the scale on which magnetosonic waves are dissipated, and now δB represents magnetic field fluctuations associated with those waves, through Eq. (20.10) and $\delta E \sim (c_s/c)\delta B$. Alfvén wave, $n = \pm 1$ resonant interactions can also take place in turbulent media, although there are good arguments why TTD interactions with magnetosonic waves are likely to dominate in the ICM (see discussion below).

The basic physics behind the two diffusion convection equations (20.3) and (20.11) is similar. The principal differences are that Eq. (20.11), which targets CR interactions with local turbulence, ignores spatial variations in the background velocity, V, while Eq. (20.3) ignores the momentum diffusion coefficient, D_{pp}, because in strongly compressed flows at shocks it is subdominant.

In calculating turbulent acceleration outcomes for relativistic particles, $E \approx pc$, it is common to use the particle distribution per unit momentum, $N(p) = 4\pi p^2 f(p)$, rather than the phase space density, $f(p)$. Then Eq. (20.11) becomes:

$$\frac{\partial N}{\partial t} = -\frac{\partial}{\partial p}\left[\left([\frac{dp}{dt}]_L + [\frac{dp}{dt}]_A\right) N(p)\right] + \frac{1}{2}\frac{\partial^2}{\partial p^2}\left([\frac{dp^2}{dt}]_A N(p)\right) + Q(p), \tag{20.16}$$

where we have neglected the spatial diffusion term and added two new terms : $[\frac{dp}{dt}]_L$, which accounts for particle energy losses (Coulomb, ionization, radiative, etc.), and $Q(p)$ which is a source term of CRs in the medium. The acceleration processes in Eq. (20.16) due to momentum diffusion have been separated into a systematic energy gain, re-acceleration term, $[dp/dt]_A$, and to one that describes a stochastic broadening of the particle momentum distribution, $[dp^2/dt]_A$. The systematic re-acceleration term due to the interaction with turbulence is :

$$[\frac{dp}{dt}]_A = \frac{1}{p^2}\frac{\partial}{\partial p}\left(p^2 \mathscr{D}_{pp}\right), \tag{20.17}$$

and the stochastic, distribution broadening term is :

$$[\frac{dp^2}{dt}]_A = 2\mathscr{D}_{pp}. \tag{20.18}$$

To account for the turbulence-particle interaction properly, one must know both the scaling of turbulence down to resonant interaction lengths [Eqs. (20.9)–(20.10)],

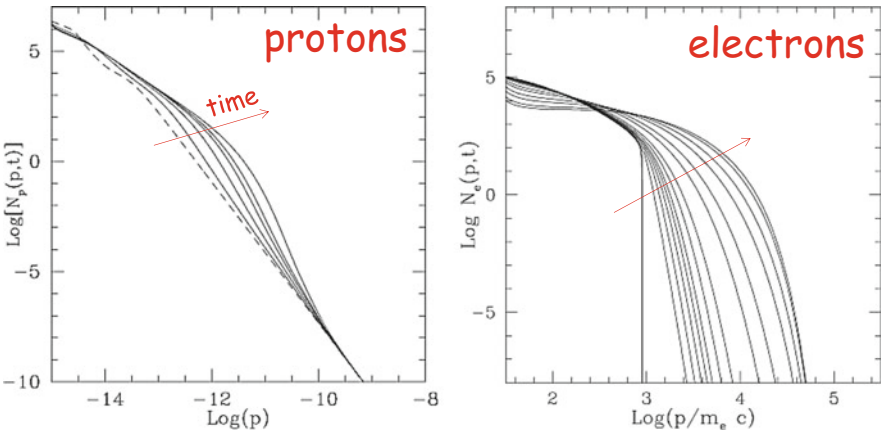

Fig. 20.5 Evolution with time of the spectrum of CRp (*left*) and CRe (*right*) (adapted from Brunetti et al. 2004). Saturation of CRe acceleration at later times is due to the combination of radiative losses and the damping of the waves that limits acceleration efficiency

the changes with time of the turbulence spectrum on resonance scales due to the most relevant damping processes, and the interactions of turbulence with various waves produced by CRs. This is extremely challenging, although in the last decade several modeling efforts attempted to study turbulent acceleration in astrophysical environments by using physically motivated turbulent scalings and the relevant collisionless dampings of the turbulence.

Turbulent acceleration of CRs directly from the thermal plasma to ultra-relativistic energies is very inefficient in the ICM (e.g., Petrosian and East 2008). For this reason models of turbulent acceleration assume a scenario of re-acceleratin of pre-existing (seed) CRs (Brunetti et al 2001, Petrosian 2001). Figure 20.5 shows an example of evolution of CRs spectra (re)accelerated by turbulence. Evaluating the fraction of the turbulent energy that goes into (re)acceleration of CRs in the ICM is uncertain. This reflects our ignorance of the details of the properties of turbulence and of the (connected) micro-physics of the ICM. Cases where a large fraction of the turbulent energy can be potentially dissipated into the (re)acceleration of CRs in galaxy clusters include the gyro-resonant ($n = \pm 1$), interaction with Alfvén modes (Ohno et al. 2002; Fujita et al. 2003; Brunetti et al. 2004). The problem is that Alfvén modes develop an anisotropic cascade toward smaller scales that quenches the efficiency of the scattering (acceleration) process (Chandran 2000; Yan and Lazarian 2004). Consequently models of Alfvénic acceleration assume that waves are generated in the ICM at small (quasi-resonant) scales, although it remains still rather unclear how these small-scale waves can be generated in the ICM. Another case where a large fraction of turbulent energy is dissipated into CRs acceleration is the resonant (mainly Transit-Time-Damping, $n = 0$) interaction with fast modes under the assumption that the collisionless interaction scale of the ICM is much smaller than the classical Coulomb ion mean free path (Brunetti and

Lazarian 2011b). Potentially a very small collisionless scale in the ICM can be maintained in the case that interactions between particles are mediated by magnetic perturbations generated by plasma instabilities. Instabilities may be driven by compressive turbulence and CRs in the ICM (Brunetti and Lazarian 2011b; Yan and Lazarian 2011). A detailed investigation of this process is still missing. In the cases where most of the turbulent energy is drained into CRs, the efficiency of particle acceleration is essentially fixed by the damping of turbulence due to CRs themselves (Brunetti et al. 2004; Brunetti and Lazarian 2011b).

In general, however, simple modelings predict that only a small (although still significant) fraction of turbulence is channeled into CRs. If compressible turbulence is generated at large scales and simply cascades to smaller scales, and if plasma instabilities do not play a major role in the ICM, most of the energy of the turbulence is converted into the heating of the thermal plasma. Then only a small fraction of turbulent energy becomes available to CRs. Under these conditions the most important resonance between CRs and compressible MHD turbulence is the $n = 0$, Transit Time Damping resonance. Then the acceleration process is dominated by fast modes that may drain a few to $\sim$10 % of the turbulent-energy flux into the CR component (Cassano and Brunetti 2005; Brunetti and Lazarian 2007, 2011a). In this case we anticipate that CRe electrons can be re-accelerated up to energies of several GeV provided the fast mode energy on scales of tens of kpc (above the dissipation scale) is about 5–10 percent of the local thermal energy budget.

20.2.3 Generation of Secondary Particles

The generation of secondary particles due to inelastic collisions between CRp and thermal protons in the ICM is an important source of CRe. If we assume that CRp remain in galaxy clusters for a time-period, τ, the grammars they encounter is $X_g \sim n_{ICM} m_p c\tau \sim 1.6 \times \frac{n_{ICM}}{10^{-3}} \times \frac{\tau}{\mathrm{Gyr}}\,\mathrm{g\ cm^{-2}}$. On cosmic time scales that would often be comparable in the ICM with the nuclear grammage for an inelastic collision, $X_{nuc} \approx 50\,\mathrm{g\ cm^{-2}}$. This implies that a non-negligible fraction of CRp energy budget is lost in inelastic pp collisions, leading to the generation of secondary particles (Sect. 20.3.1). In Sect. 20.3.2 we will conclude that CRp are confined and accumulated in galaxy clusters for a Hubble time.

The decay chain for the injection of secondary particles is Blasi and Colafrancesco (1999):

$$p + p \rightarrow \pi^0 + \pi^+ + \pi^- + \text{anything}$$

$$\pi^0 \rightarrow \gamma\gamma$$

$$\pi^{\pm} \rightarrow \mu + \nu_\mu \quad \mu^{\pm} \rightarrow e^{\pm}\nu_\mu\nu_e.$$

A threshold reaction requires CR protons with kinetic energy just larger than $T_p \approx 300\,\mathrm{MeV}$. The injection rate of pions is given more generally by Moskalenko

and Strong (1998); Blasi and Colafrancesco (1999):

$$Q_{\pi}^{\pm,o}(E,t) = n_{th}^{p} c \int_{p_*} dp N_p(p,t) F_{\pi}(E_{\pi}, E_p) \sigma^{\pm,o}(p_p), \tag{20.19}$$

where N_p is the spectrum of CRp, F_{π} is the spectrum of pions from the individual collisions of CRp (of energy E_p) and thermal protons and σ is the cross section for the production of secondary particles. Various practical and useful approaches to derive the pion spectrum, F_{π}, both in the high energy ($E_p > 10\,\mathrm{GeV}$) and low energy regimes, are based on the combination of the isobaric model and scaling model (Stecker 1970; Badhwar et al. 1977; Stephens and Badhwar 1981; Dermer 1986a,b; Moskalenko and Strong 1998; Brunetti and Blasi 2005),[2] or parameterizations based on simulations of proton-proton interactions (Kelner et al. 2006).

Neutral pions decay into γ-rays. The spectrum of γ-rays is Dermer (1986a,b); Blasi and Colafrancesco (1999); Kelner et al. (2006) :

$$Q_{\gamma}(E_{\gamma}) = 2 \int_{E_{min}}^{E_p^{max}} \frac{Q_{\pi^o}(E_{\pi^o})}{\sqrt{E_{\pi}^2 - m_{\pi}^2 c^4}} dE_{\pi}\,, \tag{20.20}$$

where $E_{min} = E_{\gamma} + 1/4 m_{\pi}^2 c^4 / E_{\gamma}$.

Charged pion decays produce muons, which then produce secondary electrons and positrons (and neutrinos) as they decay. The injection rate of relativistic electrons/positrons then becomes:

$$Q_{e^{\pm}}(E_e,t) = \int_{E_{\pi}} Q_{\pi}(E_{\pi^{\pm}},t) dE_{\pi} \int dE_{\mu} F_{e^{\pm}}(E_{\pi}, E_{\mu}, E_e) F_{\mu}(E_{\mu}, E_{\pi}), \tag{20.21}$$

where $F_e^{\pm}(E_e, E_{\mu}, E_{\pi})$ is the spectrum of electrons and positrons from the decay of a muon of energy E_{μ} produced in the decay of a pion with energy E_{π} (Blasi and Colafrancesco 1999), and $F_{\mu}(E_{\mu}, E_{\pi})$ is the muon spectrum generated by the decay of a pion of energy E_{π} (Moskalenko and Strong 1998; Blasi and Colafrancesco 1999; Brunetti and Blasi 2005).

The generation of neutrinos is also an important and unavoidable product of p-p collisions in the ICM that can be potentially constrained by the IceCube experiment in the near future (Wolfe and Melia 2008; Murase and Beacom 2012). Still, in this chapter we will not elaborate on this point.

Finally we notice that parameterization formulae describing spectra of γ-rays, electrons/positrons and neutrino (electron neutrino and antineutrino and muon

[2] An extension of these approaches includes diffractive interaction and the Feynman scaling violation in the nondiffrective inelastic interaction (Kamae et al. 2005)

neutrino and antineutrino) from p-p interactions have been published by Kamae et al. (2006).

Secondary electrons continuously generated in the ICM are subject to energy losses (Sect. 20.3.1). If these secondaries are not accelerated by other mechanisms, their spectrum approaches a stationary distribution because of the competition between injection and energy losses (Dolag and Ensslin 2000):

$$N_e^{\pm}(p) = \frac{1}{\left|\left[\frac{dp}{dt}\right]_{\rm L}\right|}\int_p^{p_{\rm max}} Q_e^{\pm}(p)dp\,, \tag{20.22}$$

Assuming a power law distribution of CRp, $N_p(p) = K_p p^{-s}$, the spectrum of secondaries at high energies, $\gamma > 10^3$, is $N_e(p) \propto p^{-\delta}$, with $\delta = s + 1 - \Delta$, where $\Delta \sim 0.05$–0.1 is due to the log-scaling of the p-p cross-section at high energies (Brunetti and Blasi 2005; Kelner et al. 2006; Kamae et al. 2006). The radio synchrotron emission from these electrons would have a spectral slope, $\alpha = (\delta - 1)/2$.

20.3 Evolution and dynamics of CRs in Galaxy Clusters

In this section we derive the energy-evolution and dynamics of relativistic CRp and CRe once they are accelerated or injected into the ICM.

20.3.1 Energy Losses

Cosmic rays are subject to energy losses that limit their life-time in the ICM.

The energy losses of ultra-relativistic electrons in the ICM are dominated by ionization and Coulomb losses at low energies, and by synchrotron and inverse Compton (IC) IC losses at higher energies (Sarazin 1999). The rate of losses due to the combination of ionization and Coulomb scattering is (in cgs units):

$$\left[\frac{dp}{dt}\right]_{\rm i} = -3.3\times 10^{-29} n_{\rm th}\left[1 + \frac{\ln(\gamma/n_{\rm th})}{75}\right] \tag{20.23}$$

where $n_{\rm th}$ is the number density of the thermal plasma. The rate of synchrotron and IC (of CMB photons) losses is in cgs units:

$$\left[\frac{dp}{dt}\right]_{\rm rad} = -4.8\times 10^{-4} p^2\left[\left(\frac{B_{\mu G}}{3.2}\right)^2 \frac{\sin^2\theta}{2/3} + (1+z)^4\right], \tag{20.24}$$

where $B_{\mu G}$ is the magnetic field strength in units of μG, and θ is the pitch angle of the emitting leptons; in case of efficient isotropization of the electron momenta, the $\sin^2\theta$ is averaged to $2/3$. The factor in the square bracket can alternatively be expressed for an isotropic distribution as $B_{IC}^2 + B^2$, where $B_{IC} = 3.2(1+z)^2\,\mu$G. We can define the life-time of CRe $\tau_l \sim p/(dp/dt)$, from Eqs. (20.23)–(20.24), it is :

$$\tau_e(\mathrm{Gyr}) \sim 4 \times \left\{ \frac{1}{3}\left(\frac{\gamma}{300}\right)\left[\left(\frac{B_{\mu G}}{3.2}\right)^2 \frac{\sin^2\theta}{2/3} + (1+z)^4\right] + \left(\frac{n_{\mathrm{th}}}{10^{-3}}\right)\left(\frac{\gamma}{300}\right)^{-1}\left[1.2 + \frac{1}{75}\ln\left(\frac{\gamma/300}{n_{\mathrm{th}}/10^{-3}}\right)\right]\right\}^{-1}. \quad (20.25)$$

The life-time of ultra-relativistic electrons in the ICM depends on the density of the thermal medium that can be estimated from X-ray observations, on the IC-equivalent magnetic field (i.e., redshift of the cluster), and on the magnetic field strength that can be constrained by Faraday rotation studies or by complementary considerations. Although in the case of highly inhomogeneous magnetic fields the available Rotation Measures (RM) may provide a biased view of the magnetic field, the life-time of electrons is affected substantially by these uncertainties only in the case of (improbable) strong fields, $< B^2 > \gg B_{IC}^2$. That would imply that Eq. (20.25) provides a quite accurate measurement of the CRe life-time.

The main channel of energy losses for CRp in the ICM is provided by inelastic p-p collisions (Sect. 20.2.3). The life-time of CRp due to p-p collisions is given by :

$$\tau_{pp}(p) = \frac{1}{c\, n_{th} \sum \sigma^{+/-,o}} \quad (20.26)$$

$\sigma^{\pm,o}(p-p)$ is the inclusive p–p cross-section.

For trans-relativistic and mildly relativistic CRp, energy losses are dominated by ionization and Coulomb scattering. Protons more energetic than the thermal electrons, namely with $\beta_p > \beta_c \equiv (3/2m_e/m_p)^{1/2}\beta_e$ are affected by Coulomb interactions, where $\beta_e \simeq 0.18(T/10^8 K)^{1/2}$ is the velocity of the thermal electrons. Defining $x_m \equiv \left(\frac{3\sqrt{\pi}}{4}\right)^{1/3}\beta_e$, one has (Schlickeiser 2002):

$$\left(\frac{dp}{dt}\right)_i \simeq -1.7 \times 10^{-29}\left(\frac{n_{\mathrm{th}}}{10^{-3}}\right)\frac{\beta_p}{x_m^3 + \beta_p^3} \quad \text{(cgs)} \quad (20.27)$$

The time scales for losses due to the combination of these processes for CRe and CRp are illustrated in Fig. 20.6. CRp with energy 1 GeV–1 TeV are long-living particles with life-times in the cores of galaxy clusters $\sim$ several Gyrs. As discussed in Sect. 20.2.2.1 CRp lifetimes of ultra high energy CRp (UHECR) are limited by inelastic $p-\gamma$ collisions involving CMB photons. On the other hand, CRe are short-lived particles at the energies where they radiate observable emissions, due to the unavoidable radiation energy-losses (mainly IC and synchrotron). The maximum life-time of CRe, about 1 Gyr, is at energies where radiative losses and

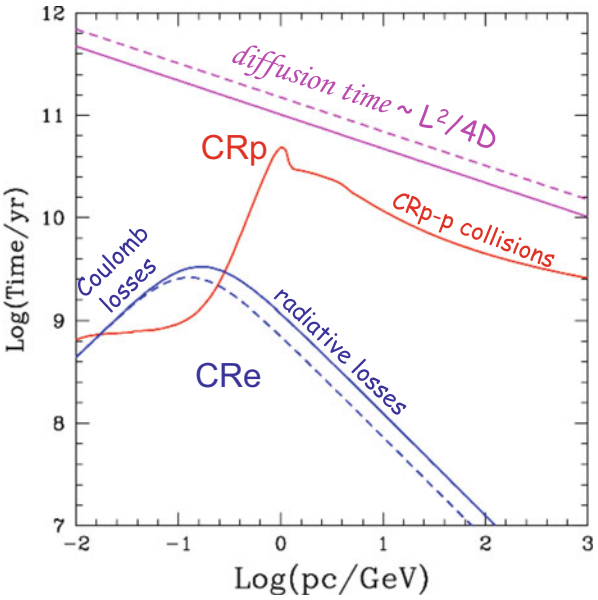

Fig. 20.6 Life-time of CRp (*red*) and CRe (*blue, lower curves*) in the ICM at redshift $z = 0$, compared with the CR diffusion time on Mpc scales (*magenta, upper curves*) (adapted from Blasi et al. 2007). The most relevant channels of CR energy losses at different energies are highlighted in the panel. Adopted physical parameters are: $n_{th} = 10^{-3}\,\mathrm{cm}^{-3}$, $B = 1$ (*solid*) and $3\,\mu\mathrm{G}$ (*dashed*). Diffusion is calculated assuming a Kolmogorov spectrum of magnetic fluctuations with $L_{max} = 100\,\mathrm{kpc}$ and $f = 1$

roughly equivalent to Coulomb losses, at ∼100 MeV, whereas CRe with energy ∼several GeV, that emit synchrotron radiation in the radio band (GHz), have short life-time, ∼0.1 Gyrs. The life-times of CRe at high energies do not vary much from cluster cores to periphery, because for weak magnetic fields it is determined by the unavoidable IC scattering losses off cosmic microwave background photons. On the other hand, CRe IC lifetimes will scale with cluster redshift according to $(1 + z)^{-4}$. Generally, these losses will steepen the electron energy spectrum when the associated lifetimes are less than either their residence time or their acceleration time. The degree of steepening (and the associated steepening in the synchrotron emission) depends on the circumstances.

20.3.2 Dynamics of Cosmic Rays

As outlined in Sect. 20.2 the propagation of charged particles (nuclei and electrons) injected in the ICM is mainly determined by diffusion and convection.

The time necessary to CRs to diffuse on distances/scales L is $\tau_{diff} \sim 1/4L^2/D$. Over a wide energy range this time exceeds the Hubble time when L is a cluster scale and D is representative for turbulent μG magnetic fields in the ICM. This implies that galaxy clusters are efficient containers of CRs. Indeed the spatial diffusion coefficient necessary to allow diffusion of CRs on Mpc-scales within a few Gyrs is $D \geq 2 \times 10^{30}\,\mathrm{cm}^2\,\mathrm{s}^{-1}$. That is about two orders of magnitude larger for $E \sim 1\,\mathrm{GeV}$ than that in our Galaxy, where field strengths and field coherence lengths are, in fact, remarkably similar to ICM values.

According to QLT and referring to Sect. 20.2.2.2, the diffusion coefficient for gyro-resonant scattering of particles with Alfvénic perturbations of the magnetic field is (Wentzel 1974; Bhattacharjee 2000) :

$$D(p) = \frac{1}{3} r_L c \frac{B^2}{\int_{2\pi/r_L}^{\infty} dk P(k)}, \tag{20.28}$$

where $P(k)$ is the power spectrum of turbulent field-perturbations on a scale k (that interacts resonantly with particles with momentum $p \propto 1/k$), such that $\int_{k_{min}}^{\infty} dk P(k) = fB^2$ and $f \leq 1$. We note that if turbulent field-perturbations are on scales $\leq r_L$, i.e. $k_{min} \geq 2\pi/r_L$, and $f \approx 1$ Eq. (20.28) is the coefficient of parallel Bohm diffusion.

In Fig. 20.6 we show a comparison between the life-time of CRs and their diffusion-time on Mpc scales; here we assume a Kolmogorov spectrum of the Alfvénic fluctuations, $fB^2 \propto k^{-5/3}$, with a maximum scale $L_{max} = 2\pi k_{min}^{-1} = 100\,\mathrm{kpc}$ and $f = 1$. The diffusion time of CRs is many Gyrs, implying that CRp can be accumulated in the volume of galaxy clusters and that their energy budget increases with time, as first realised by Völk et al. (1996); Berezinsky et al. (1997); Ensslin et al. (1997). On the one hand, the prediction of diffusive confinement of CRs within the cluster volume is strongly dependent upon the choice of the diffusion coefficient and consequently on the specific assumptions on the level of magnetic turbulence, its spectrum and scales. On the other hand, it is clear from Fig. 20.6 that even a minimum level of magnetic field fluctuations in the ICM (including waves self-generated by CRs) should be able to confine most of the CRs in the gigantic volume of galaxy clusters for a time-period comparable to the age of clusters themselves. For a reference value, by considering CRs drifting with velocity $\sim v_A$ the time-scale to cover Mpc distances is $\sim 10\,\mathrm{Gyrs}$ assuming a reference value $v_A \sim 10^7\,\mathrm{cm/s}$ in the ICM.

20.4 Non-thermal Emission from Galaxy Clusters and Origin of CRs

20.4.1 Synchrotron Emission: Radio Halos and Relics

As noted in the introduction, diffuse radio emission with overall sizes reaching and even exceeding Mpc is observed in a number of galaxy clusters. The radio emission is clearly associated with the ICM, implying the existence of relativistic electrons and magnetic fields mixed with the hot (T$\sim$5–10 KeV) ICM. Various constraints on the magnetic field, such as Faraday rotation measurements and limits to IC X-rays (and γ-rays) indicate μG field strengths in these environments (Clarke et al. 2001; Carilli and Taylor 2002; Govoni 2006; Bonafede et al. 2010; Ackermann et al. 2010; Wik et al. 2011; Feretti et al. 2012), in which case the radio emitting electrons have energies of a few GeV (Lorentz factor $\gamma \sim 10^4$). Also as noted in the introduction, the radio emission comes in two main flavours (Feretti et al. 2012; Ferrari et al. 2008, Fig. 20.2). These include the *radio halos*, peaking in intensity near the centre of galaxy clusters and having good spatial coincidence with the distribution of the hot X-ray emitting gas. There are also the so-called *radio relics* or *radio Gischt* that are elongated and located at the cluster periphery. Some clusters include both. Finally, we mention again that the two classes of radio sources differ also in their polarization properties: halos are generally unpolarised, while relics are strongly polarised. Synchrotron polarisation in the relics is a signature of significant anisotropy in the magnetic field on large scales, probably due either to compression or possibly to shear. The absence of polarization in radio halos and their morphological connection with the X-ray emission suggest that the relativistic plasma that generates the synchrotron radiation occupies a large fraction of the volume filled by the hot X-ray emitting ICM.

Radio halos and relics are unique probes of particle acceleration mechanisms in the ICM. The underlying difficulty to explain the origin of radio halos comes from their Mpc-extension surrounding the cluster center. Indeed, as noted in the previous section, the time necessary for GeV CRe to diffuse across a sizeable fraction of the size of radio halos is much larger than the radiative life-time of these CRe in the ICM, implying that the emitting CRe are generated by in situ particle-acceleration or injection mechanisms in the ICM. Similar arguments apply to radio relics in the context of their $\sim$Mpc transverse extents. As noted above, two leading mechanisms (and their combination) are presently advocated to explain the origin of relativistic electrons emitting in radio halos: (re)acceleration of relativistic particles by MHD turbulence generated in the ICM during cluster–cluster mergers and continuous production of secondary electron-positron pairs by inelastic collisions between CRp and thermal protons in the ICM (Dennison 1980; Blasi and Colafrancesco 1999; Brunetti et al. 2001; Petrosian 2001; Miniati et al. 2001; Ohno et al. 2002; Fujita et al. 2003; Pfrommer and Enßlin 2004; Brunetti and Blasi 2005; Cassano and Brunetti 2005; Brunetti and Lazarian 2007; Petrosian and Bykov 2008; Brunetti et al. 2008; Keshet and Loeb 2010; Brunetti and Lazarian 2011a; Ensslin et al.

2011). On the other hand, the mechanism that is presently broadly adopted to explain the origin of radio relics is (re)acceleration of relativistic electrons at merger shocks (Ensslin et al. 1998; Roettiger et al. 1999; Miniati et al. 2001; Bagchi et al. 2006; Hoeft and Brüggen 2007; Hoeft et al. 2008; van Weeren et al. 2010; Skillman et al. 2011; Brüggen et al. 2012; Kang and Ryu 2011). We note that the above arguments based on the difference between life-time and diffusion time of GeV electrons become less compelling for diffuse radio sources on hundred-kpc scales, for example *mini halos* (Feretti et al. 2012), which do not necessarily require cluster-scale phenomena for their explanation; we will not elaborate on the physics of these sources in the present chapter.

The very low surface radio brightness of halos and relics, combined with their steep radio synchrotron spectra (average values reported for α are in the range 1.2–1.4), make their detection difficult. To date, only about 40 giant radio halos and relics have been imaged at high sensitivity (Venturi 2011; Feretti et al. 2012). Pioneering studies using Arecibo and the NVSS and WENSS radio surveys suggested that radio halos and relics are not common in galaxy clusters (Hanisch 1982; Giovannini et al. 1999; Kempner and Sarazin 2001). Today it is well accepted that not all clusters show diffuse radio emission, and this provides one of the most relevant constraints for understanding the origin of CRe in the ICM. In this respect an important step has been achieved in the last few years, thanks to observational campaigns at the GMRT and their multi-frequency (radio and X-rays) follow up (Venturi et al. 2007, 2008; Cassano et al. 2010). For the very first time, these high sensitivity surveys have allowed a separation between radio halo clusters and clusters without diffuse radio emission. This shows that only $\sim 1/3$ of X-ray luminous clusters host radio halos (Brunetti et al. 2007; Cassano et al. 2008).

Another observational milestone that has been achieved in the last decade concerns the connection between diffuse radio emission and the dynamics of the hosting clusters, with halos and relics always found in merging systems (Buote 2001; Feretti et al. 2012). A firm statistical evidence in this direction has been recently obtained from combined radio—X-ray studies of galaxy clusters in the GMRT surveys (Cassano et al. 2010). These studies have shown that the generation of diffuse emission occurs during mergers between galaxy clusters which leads to a number of possible interpretations. The most obvious is that shocks and turbulence generated during clusters mergers may accelerate CRs (Sects. 20.2.2.1–20.2.2.2) (Brunetti et al. 2009) or that the cluster magnetic field can be amplified during these mergers (Kushnir et al. 2009; Keshet and Loeb 2010). Less obvious arguments have been proposed including the possibility that CRs can stream-out in less turbulent ICM, when clusters are more relaxed (Ensslin et al. 2011), thus reducing the synchrotron emissivity on large scales. Although present observations provide convincing evidence in favour of the *transient* nature of giant radio halos and of their connection with mergers, constraining the evolution of galaxy clusters in the thermal–non-thermal plane is still premature, due to possible biases arising from selection effects in present samples of clusters and due to the (still) poor statistics (Basu 2012).

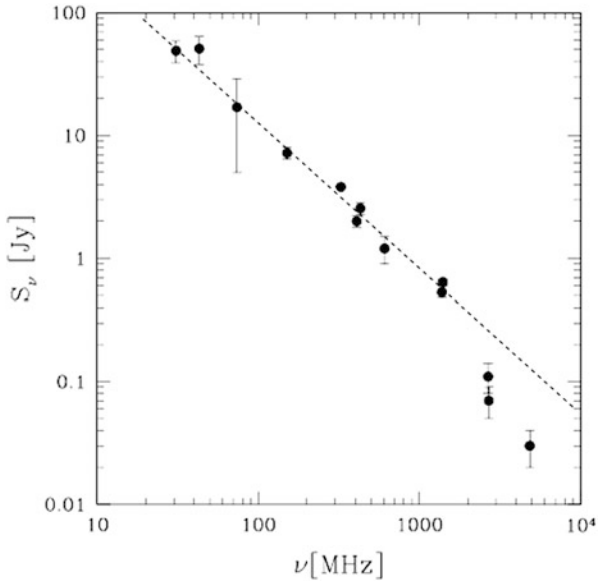

Fig. 20.7 The observed spectrum of the radio halo in the Coma cluster. The *dashed line* is the fit to the data at lower (≤ 1.4 GHz) radio frequencies (adapted from Thierbach et al. 2003)

The spectra of radio halos provide crucial information for the origin of the emitting CRe in the central Mpc-region of the hosting clusters. The accurate measurement of the integrated spectra of radio halos is a difficult task. Radio halos usually embed a number of individual sources and, sometimes, projected foreground and background sources, whose flux density needs to be carefully subtracted from the total diffuse emission. This requires high quality imaging over a range of resolutions. Moreover, diffuse cluster sources are best imaged at low frequency. High quality imaging at frequencies below 1.4 GHz has become available only very recently. For this reason, a spectrum with data points at three or more frequencies spread over ~ 1 order of magnitude is available only for few objects (Venturi 2011).

The radio halo in the Coma cluster is the prototype of this class of radio sources (Willson 1970; Venturi et al. 1990; Brown and Rudnick 2011) and a unique case, with spectral measurements spanning almost 2 orders of magnitude in frequency (Fig. 20.7). The measured spectrum significantly steepens at frequencies above a few hundred MHz. A power-law that fits the data at lower frequencies overestimates the flux measured at 2.7 and 5 GHz by a factor 2 and 4, respectively (Thierbach et al. 2003; Donnert et al. 2010). This suggests a break (or cut-off) in the spectrum of the emitting CRe at a maximum energy, E_{max}, of about few GeV. Establishment of the steepening of the spectrum of the Coma halo is an observational milestone because it allows one to estimate the acceleration time-scale (efficiency) of the mechanism responsible for the origin of the CRe. The maximum energy of CRe is indeed given by the competition between acceleration rate and (for observable, GeV electrons)

radiative losses. From Eq. (20.28) the radiative lifetime of radio-emitting electrons using viable magnetic fields in the Coma cluster would be $\tau_e \sim$ few $\times 10^8$ yrs, which is also the time-scale of the acceleration mechanism.[3] These acceleration-times are much longer than likely shock acceleration times to these energies in cluster shocks (Sect. 20.2.2.1, Kang et al. 2012). On the other hand, they are much too short to allow shock accelerated electrons to fill the cluster, as outlined earlier. A distributed source of electrons is thus required, with the additional constraint that the mechanisms responsible for CRe acceleration must be poorly efficient (long acceleration time-scale) or they must intrinsically produce a break in the distribution of CRe at E_{max} ~few GeV. In the case of turbulent acceleration (Sect. 20.2.2.2) we can roughly estimate an acceleration time-scale (see Eqs. (20.15) and (20.17) with $\delta B^2/B_0^2 \sim \mathrm{v}_t^2/c_s^2$)

$$\tau_{acc} \sim \frac{c\, l}{\mathrm{v}_t^2}, \tag{20.29}$$

where v_t is the ICM turbulent velocity. With $l \sim 1\,\mathrm{kpc}$ and $\mathrm{v}_t \sim 100\,\mathrm{km\,s^{-1}}$ the acceleration times, $\tau_{acc} \sim 10^8$ years, providing a relative match at E_{max} ~few GeV energies between acceleration and cooling. The spectrum of higher energy electrons will be steepened by the increasing relevance of cooling, thus leading to the observed break in the radio synchrotron spectrum at a frequency

$$\nu_{max} \propto \frac{E_{max}^2 B}{(B^2 + B_{IC}^2)^2}. \tag{20.30}$$

Schlickeiser et al. (1987) first realized the importance of the measurements of the spectrum of the Coma radio halo and suggested an origin of the CRe based on stochastic acceleration due to turbulence, disfavouring other mechanisms which include the generation of secondary electrons by p-p collisions. In this latter case indeed the CRe spectrum extends in principle to very high energies, if CRp extend to very high energies (say $E_{CRp} > 100\,\mathrm{GeV}$). Therefore, no intrinsic cut-off would be expected in the radio spectrum.

Despite the observational difficulties to obtain reliable measures of radio halos at several frequencies, in the last decade it has been realized that the observed values of the spectral indices of radio halos span a broad range, $\alpha \sim 1$–2 ($F(\nu) \propto \nu^{-\alpha}$, e.g. Venturi 2011), implying that the synchrotron spectrum of radio halos is far from being a *universal* power law. In particular, energy arguments applied to halos with extreme spectral properties, $\alpha \sim 1.5$–2, rule out the possibility that the spectrum of the emitting CRe is a power law and suggest the presence of a break in the spectrum of these electrons at energies few GeV (Brunetti et al. 2008).

[3] Provided it operates for a time-period that is not too short compared to the acceleration time-scale (in one acceleration time-scale the energy of accelerated particles becomes ~ 2 times bigger); otherwise, balance between acceleration and losses has not yet been reached.

These indirect arguments, combined with the observed spectral steepening in the Coma radio halo and with the halos-mergers connection, provide the observational milestones for the theoretical picture based on turbulent acceleration for the origin of giant radio halos in galaxy clusters (Petrosian and Bykov 2008; Brunetti 2011).

The next generation of radio surveys at low radio frequencies may unveil radio halos with very steep spectra that are undetected in present radio surveys at higher frequencies. These halos are naturally expected if turbulent acceleration explains presently known giant halos. According to this scenario radio halos visible in present radio surveys are those generated in connection with the most energetic merger events in the universe; namely, during collisions between massive sub-clusters. On the other hand, radio halos with much steeper synchrotron spectra should be generated during less energetic and more common merger events, thus constituting a large population of halos that is presently invisible. The ideal instrument to search for these steep spectrum halos in the next few years is LOFAR (LOw Frequency ARray) that will survey the universe in the frequency range 15–200 MHz with unprecedented sensitivity to cluster-scale emission (Rottgering et al. 2006; Rottgering 2010).[4] According to present calculations that use the crude assumption that a *fixed* fraction of the cluster-merger energy goes into MHD turbulence available for particle acceleration, about 500 new radio halos should show up in LOFAR surveys, and about half of them should be halos with very steep spectra (Cassano et al. 2010, 2012). These expectations are radically different from those based on the emissions from $e^{\pm}$ secondaries with spectra determined by the primary CRp spectrum. In fact steep spectrum radio halos challenge secondary models because of the uncomfortably large non-thermal energy that would be necessary in these models to explain giant halos with synchrotron spectral slopes $\alpha > 1.5$ (Brunetti 2004; Pfrommer and Enßlin 2004; Brunetti et al. 2008). This provides a unique chance to readily discriminate between different theories in the next few years. Indeed, although present statistical calculations based on turbulent acceleration in the ICM are greatly over-simplified and must be taken with some caution, the existence of a substantial population of radio halos with very steep spectrum will unavoidably lead us to conclude that *gentle* (i.e. not efficient) mechanisms of particle (re)acceleration play a important role for the origin and evolution of the observed CRe.

Nowadays there is consensus that the giant radio relics trace shocks outside cluster cores; probably merger shocks. As noted in the introduction, the simplest and, perhaps, most likely relationship is particle acceleration or reacceleration at those shocks. The association between relics and shocks is based on the morphological properties of the relics, which, in most cases, are consistent with a shock seen relatively edge-on, plus the fact that in some cases the relics occur in pairs on opposite sides of the cluster core (Rottgering et al. 1997; Bagchi et al. 2006; van Weeren et al. 2010; Bonafede et al. 2012). In those cases, especially, a line between the relics is consistent with an apparent merger axis, as established by other

[4]See van Weeren et al. (2012); de Gasperin et al. (2012) for very recent results on galaxy clusters obtained from LOFAR commissioning

observations, such as X-ray morphology. In addition, the fact that relics are strongly polarised with an orientation that generally implies the magnetic field is aligned with the long axis of the relic, suggests that they originate in regions where the magnetic field is compressed in the shock plane (Clarke and Ensslin 2006; van Weeren et al. 2010; Bonafede et al. 2012; Feretti et al. 2012; Brüggen et al. 2012). Only a handful of merger shocks have been discovered using X-ray observations. These are, so far, relatively weak shocks, with Mach numbers $M \approx 1.5$–3 (Markevitch and Vikhlinin 2001). A few of these shocks coincide with radio relics (or with sharp edges of radio halos) reinforcing the idea of a connection between shocks and the acceleration of the radio emitting electrons in those regions (Giacintucci et al. 2008; Markevitch 2010; Finoguenov et al. 2010; Brown and Rudnick 2011; Macario et al. 2011). High resolution cosmological simulations generally support the observational data suggesting that shocks with $M > 3$ are rare inside cluster virial radii (Ryu et al. 2003; Pfrommer et al. 2006; Skillman et al. 2008; Ryu and Kang 2009; Vazza et al. 2009, 2010).

There are several issues that must be remembered in evaluating this relationship, however. First, as noted above, weak shocks are expected to be relatively ineffective as particle accelerators (Sect. 20.2.2.1). This is partly because the equilibrium DSA spectrum of locally injected CRs in such shocks is quite steep [Eq. (20.4)], so most particles injected at the shock carry away relatively little energy. In addition, thermal leakage injection is likely to be less effective in weak shocks than strong shocks (Kang et al. 2002). For reasonable parameters for shocks with $M \leq 3$, less than $\sim 0.01\%$ of the thermal ions should be injected into the CRp population and less than a few percent of the shock energy flux should be transferred to freshly injected CRp (Kang and Jones 2005; Kang and Ryu 2011). On the other hand, if a pre-existing population of CRs with a hard (flat) spectrum passes through such a shock, DSA can enhance the energy content of those CRs by a factor of a few. This makes re-acceleration at merger shocks a relatively more efficient process. Additionally, the reaccelerated particle spectrum is similar to the spectrum of the pre-existing population if the latter is flat, so not the classic DSA spectrum given in Eq. (20.4) (Kang and Jones 2005; Kang and Ryu 2011). The potential efficiency of reacceleration in these shocks is possible, because the acceleration time to double the energy of each CR can still be relatively short [see Eq. (20.5)]. It is important to keep in mind that all the above efficiencies refer to CRp, while CRe are the particles observed in radio relics. Again, as pointed out above, primary CRe are much more difficult to inject from the thermal pool into the CR population than CRp (Sect. 20.2.2.1). In the galactic CRs $N_{CRe}/N_{CRp} \sim 1/100$, presumably reflecting that constraint. An electron fraction even that large, and likely representing DSA at strong shocks, is already a theoretical challenge. Thus, merger shocks are very unlikely to inject thermal electrons and accelerate them to relativistic energies with efficiencies to extract more than a tiny fraction of a percent of the energy flux through the shock (Riquelme and Spitkovsky 2011). It is notable in this regard that some relics, such as CIZA J2242.8+55301, have radio spectra at the putative shock location as flat as $\alpha = (\delta - 1)/2 = 0.6$ (so, $\delta = 2.2$), implying from Eq. (20.4) a rather large shock Mach number $M = 4.6$ (van Weeren et al. 2010),

if the radiating electrons represent a locally injected population. An alternate model that can account for the observed properties of CIZA J2242.8+55301 would involve a Mach 2 shock reaccelerating an upstream CRe population with an energy spectral index, $\delta = 2.2$ and a plausible CRe pressure $\sim 10^{-4}$ compared to the upstream thermal pressure (Kang et al. 2012). In that case the challenge becomes defining acceleration processes away from the shock, such as turbulence, that can account for the upstream CRe population.

20.4.2 Limits on CRp

As explained in Sect. 20.3, theoretical arguments suggest that CRp are the dominant CRs components in the ICM.

Diffuse synchrotron emission (giant radio halos or mini-halos) cannot be used alone to constrain the amount of CRp. This limitation comes both from the fact that the radio emission depends specifically only on the CRe and magnetic field distributions, but also reflects the fact that the origin of radio halos, and the link between CRe and CRp, in particular, is still unclear. The issues are very similar to those limiting measurements of CRp in galactic SNRs (Caprioli 2011).

The most direct approach to constrain the energy content of CRp in galaxy clusters consists in the searches for γ-ray emission from the decay of the neutral pions due to p-p collisions in the ICM. Space-based γ ray upper limits from EGRET observations provided limits $E_{CR}/E_{ICM} < 0.3$ in several nearby galaxy clusters (Reimer et al. 2003). In the recent years more stringent limits have been derived from deep, pointed observations at energies >100 GeV with ground-based Cherenkov telescopes (Aleksi et al. 2010, 2012; Aharonian et al. 2009a,b; Arlen et al. 2012). These limits depend on the (unknown) spectral shape of the proton-energy distribution and on the spatial distribution of CRp in the clusters. Assuming $\delta = 2$–2.2 ($N_{CR}(p) \propto p^{-\delta}$) and a linear scaling between CRp and thermal energy densities, $E_{CR}/E_{ICM} < 0.05$ are obtained; constraints being significantly less stringent for steeper spectra and for flatter spatial distributions of the CRp component in the cluster. The recent advent of the orbiting Fermi-LAT observatory greatly improved the detection prospects thanks to its unprecedented sensitivity at MeV/GeV energies. However, after more than 3 years of observations no firm detection of galaxy clusters has been obtained, and only upper limits to the γ-ray emission from nearby clusters have been derived (Ackermann et al. 2010). The γ-ray emissivity scales with the product of the CRp and thermal proton densities [Eqs. (20.19)–(20.20)]. Thus, assuming that CRp follow the spatial distribution of the thermal ICM, the γ-ray emissivity is proportional to the thermal X-ray emissivity. Then these limits can be applied simply to allow one to constrain $E_{CR}/E_{ICM} < 0.05$, with a weak dependence on δ. Less stringent limits are obtained in the case of flatter spatial distribution of the CRp component, since then larger γ-ray contributions come from remote cluster regions compared to thermal X-rays (Ackermann et al. 2010; Arlen et al. 2012).

Radio observations of galaxy clusters can also be used to obtain limits on E_{CR}/E_{ICM} (Reimer et al. 2004; Brunetti et al. 2007; Brown et al. 2011). The majority of galaxy clusters do not host diffuse radio halos at the sensitivity level of present observations. For undetected clusters, by similar scalings for $\pi^{\pm}$ production [Eq. (20.19)], radio upper limits to the cluster-scale emission constrain the combination of magnetic field and secondary electrons energy densities in the ICM, and thus the energy budget in the form of primary CRp. Faraday rotation measurements provide independent constraints on the magnetic fields of clusters suggesting that (1) $< B > \approx 1 - 2\,\mu$G and that (2) clusters with and without radio halos have similar fields (Clarke et al. 2001; Bonafede et al. 2011). If we assume this observational framework, radio upper limits put constraints similar to those from γ-rays, with $E_{CR}/E_{ICM} \leq$ few $\times 10^{-2}$.

Present constraints refer mainly to the innermost ($\sim$Mpc) regions of clusters where both the number density of thermal protons (target for π^o production) and the magnetic field are larger. It should be mentioned that no tight constraints are available for the clusters outskirts where the CRp contribution might be larger. Yet, these recent limits violate optimistic expectations for the CRp energy content and γ-ray emission from galaxy clusters derived in the last decade (Völk et al. 1996; Miniati et al. 2001; Miniati 2003; Pfrommer 2008; Colafrancesco and Marchegiani 2008; Blasi et al. 2007). Consequently available limits suggest that the efficiency of CRp acceleration previously assumed for the most relevant mechanisms operating in galaxy clusters is too optimistic, or that the paradigm of CRp confinement in galaxy clusters is not realistic (Sect. 20.2). The following section provides a more complete outline of the origins of γ-ray emission and the status of detection efforts.

20.4.3 High Energy Emission from Galaxy Clusters

The initial motivation for the interest in the γ-ray emission from clusters arose as a consequence of the possibility of CRs confinement in the ICM (Sect. 20.3), and consequently the possibility that radio halos could be the result of synchrotron emission from secondary CRe (Berezinsky et al. 1997; Blasi and Colafrancesco 1999; Pfrommer and Enßlin 2004). A natural byproduct of the CR confinement is the emission of γ radiation due to both the production and decay of neutral pions and the IC scattering by high energy secondary CRe of the universal photon background (Sect. 20.2.3). The latter channel becomes sub-dominant at energies $\geq$100 MeV (Blasi 2001; Miniati 2003, Fig. 20.8). Primary CRe accelerated in galaxy clusters can produce γ-rays via IC emission. Electrons can be accelerated at cosmological shocks up to energies of tens of TeV (Sect 20.2.2.1) and the resulting IC emission extends to multi-TeV energies (Blasi 2001). On the other hand CRe accelerated in Mpc-scale turbulent regions cannot produce γ-rays because their maximum energy does not exceed significantly about 10 GeV; the IC emission from these CRe is expected to peak in the hard X-rays (Brunetti et al. 2001; Petrosian 2001; Brunetti et al. 2004).

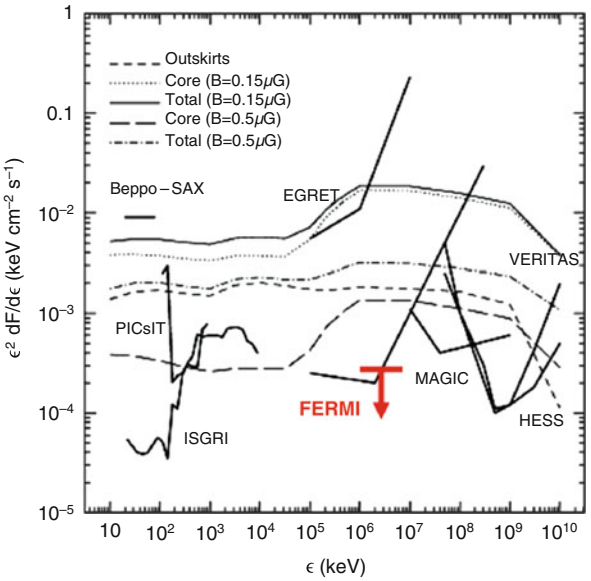

Fig. 20.8 High energy spectral energy distribution expected for a Coma-like cluster from numerical simulations (adapted from Miniati 2003). Models account for inverse Compton emission, π^0 decay and non-thermal bremsstrahlung from both shock-accelerated (primary) and secondary particles. The spectral energy distributions are shown for both the core region and the cluster outskirts, the core region correspond to 2 Mpc-diameter. The model normalisation is fixed by assuming that the secondary CRe are responsible for producing the Coma radio halo through synchrotron emission. Under these conditions expectations depend on the magnetic field strength averaged in the core region (cases for $B = 0.15$ and $0.5\,\mu$G are shown)

Other mechanisms of production of γ-rays in the ICM include non thermal bremsstrahlung (Blasi 2001; Miniati 2003; Sarazin 2004) and IC from pairs generated in Bethe–Heitler processes between Ultra High Energy protons (if present) and photons in the cosmic microwave background (Aharonian et al. 2002; Rordorf et al. 2004). Nowadays, there is general agreement that the expected γ-ray spectrum of galaxy clusters is dominated by the decay of neutral pions in the central cluster regions and by IC from primary CRe accelerated by strong shocks in the cluster outskirts (Blasi et al. 2007, Fig. 20.8).

After the first pioneering theoretical attempts (Völk et al. 1996; Berezinsky et al. 1997; Sarazin 1999; Völk and Atoyan 1998; Loeb and Waxman 2000; Blasi 2001; Pfrommer and Enßlin 2004) in the last decade numerical simulations allowed useful estimates of the expected γ-ray emission from galaxy clusters, under different assumptions. These simulations, that include, to some extent, CR physics and the acceleration of CRs at cosmological shocks provided a picture of the radio to γ-ray properties of galaxy clusters. The first simulations of this kind predicted that clusters would be potentially detectable in γ-rays with the Fermi-LAT telescope (Miniati et al. 2001; Miniati 2003; Pfrommer 2008). The most important assumption

in these simulations is in the efficiency of particle acceleration at weak shocks that, as explained in Sect. 20.2.2.1, is poorly known. These early simulations also suffered from insufficient spatial resolution of shock structures to enable them to accurately establish statistics of shocks well inside cluster virial radii. Subsequent numerical simulations of large-scale structure formation have much improved shock measurements (Vazza et al. 2011), allowing more realistic treatments of shock acceleration possibilities. Several subsequent simulation studies have attempted to reconcile their results with the lack of detection of galaxy clusters in the γ-ray band (Pinzke and Pfrommer 2010; Aleksi et al. 2010).

In reality, the microphysics of the ICM and of CRs in galaxy clusters is very complicated and, unfortunately, beyond the capabilities of present simulations. A way to circumvent these difficulties for now is to derive expectations by anchoring model parameters to the diffuse synchrotron emission observed in nearby clusters (Reimer et al. 2004). Potentially this may provide the opportunity to put combined constraints on both the origin of diffuse cluster-scale emission (such as radio halos) and on the expected high energy emission from the hosting clusters. For example, a simple, optimistic view assumes that radio halos are generated entirely by emission from secondary CRe where those CRe are produced by $p - p$ interactions. In this case the ratio of the γ-ray and synchrotron cluster luminosities coming from the region of the radio halo, only depends on the spectrum of CRp and inversely on the magnetic field strength in that emitting volume. By considering reasonable assumptions of the global magnetic field distributions in galaxy clusters (i.e. essentially assuming moderate-weak fields in the ICM) several authors in the last decade suggested that observations by the Fermi-LAT may have the chance to detect γ-rays from nearby clusters hosting radio halos (Pfrommer and Enßlin 2004; Marchegiani et al. 2007; Pfrommer 2008; Wolfe and Melia 2008; Brunetti 2009). Because we know now that clusters are undetected in γ-rays at the sensitivities reached by almost 4 years of observations with Fermi-LAT, what we can do is to derive (lower) limits on the magnetic field in the clusters under the optimistic assumption that radio halos are due to synchrotron emission from secondaries as they are injected locally. A first step in this direction was performed by Jeltema and Profumo (2011), who first pointed out that in several nearby clusters hosting radio halos these lower limits are close to (or larger than) the magnetic field values inferred from Faraday rotation measures (RM). While RM-based magnetic field estimates, themselves, depend on various model choices, and turbulent magnetic fields will be spatially intermittent, these constraints do place tension on the direct hadronic origin of radio halos in those clusters. Although more recent secondary-CRe-based radio halo modeling papers attempt to reduce this tension by considering a wider range of CR production and propagation model parameters (Arlen et al. 2012), it has been shown that the *inconsistency* between lower limits and RM-based field measurements becomes more severe if *all* the available (spectral and morphological) constraints from nearby radio halos, such as Coma, are *properly* taken into account (Brunetti et al. 2012); the combined steep spectrum and very flat spatial brightness distribution of the Coma halo is especially worrisome in this regard. The tension between RM and limits from γ-ray observations disappears when including the effect of turbulent reacceleration

in combination with the process of injection of secondary particles (Brunetti and Lazarian 2011a; Brunetti et al. 2012). Consequently, the role played by primary CRp (via secondary CRe) for the origin of radio halos is still unclear.

As already discussed, the prediction of high-energy emission from galaxy clusters is a direct consequence of the confinement of CRp in these systems and of theoretical models for the origin of radio halos. Improving the physics in these latter models allows one to impose new constraints on the level of the expected high energy emission from clusters. For example a more self-consistent modeling of the particle acceleration in giant radio halos should account at the same time for the production of secondary particles in the ICM and for the transport and reacceleration of these secondaries and of the primary CRp due to the interplay with MHD turbulence. Our ability to apply turbulent reacceleration to refine the picture based on CRp confinement and injection of secondaries in the ICM is limited primarily by our limited understanding of ICM turbulence, its origins, evolution distribution and spectral properties, especially on scales where resonant interaction with CR take place (Sect. 20.2.2.2 and below). Pioneering calculations in this direction have been recently developed in Brunetti and Lazarian (2011a) assuming that compressible MHD turbulence, generated in galaxy clusters at large scales during cluster-cluster mergers, cascades at smaller scales and assuming that a pre-existing population of long-living CRp is mixed with the ICM. These calculations allow one to model the temporal evolution of the non-thermal emission from galaxy clusters, from radio to γ-rays, and its connection with cluster mergers (Fig. 20.9). They show

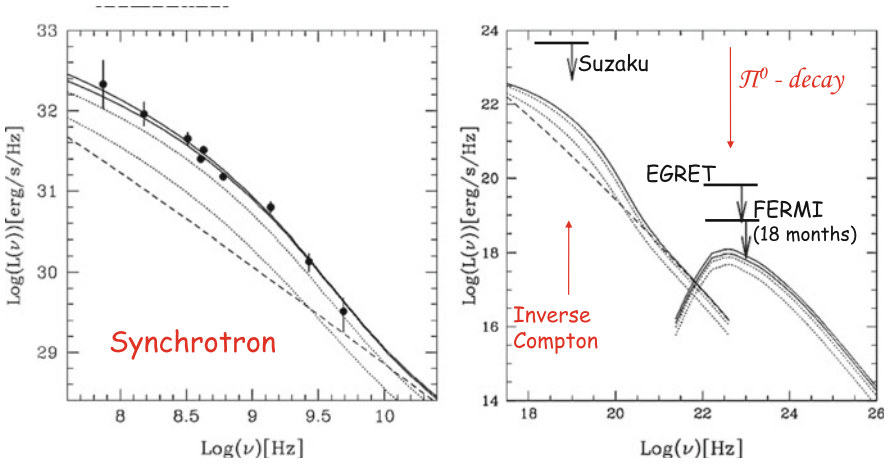

Fig. 20.9 The radio (*left*) and high energy (inverse Compton, ICS, and π^0-decay) (*right*) emitted spectra from the Coma cluster as predicted from a scenario where turbulence reaccelerates both primary CRp and their secondary products (*solid lines*, adapted from Brunetti and Lazarian 2011a). Model expectations are compared to radio data of the Coma radio halo and to the available upper limits at higher energies. The *dotted lines* show the temporal evolution of the spectrum, *dashed lines* mark the spectrum in the case of pure-secondary models (i.e. not considering turbulent reacceleration)

that cluster-scale synchrotron emission and inverse Compton emission are expected to be considerably stronger in a turbulent ICM, while a fainter long-living radio emission sustained by the process of continuous injection of high energy secondary CRe is expected to be common in clusters more generally. The strength of this latter component is proportional to the energy density of the primary CRp in the ICM and, in the context of these modelings, it can be constrained by the upper limits to the cluster-scale radio emission in galaxy clusters without radio halos (Brown et al. 2011). Contrary to the *transient* nature of radio and hard X-ray emission in galaxy clusters, γ-ray emission from $p - p$ secondaries is expected to be common at a moderate level in clusters and not directly correlated with the presence of giant radio halos. Since the CRp population of a cluster reflects its integrated history (assuming CRp do not escape) there should be a moderate range in γ-ray luminosities (Miniati et al. 2001). As an interesting point, we note that these calculations are optimistic, because still based on a secondary origin of the seed electrons to reaccelerate, but, on the other hand, they can be used to constrain the minimum level of γ-rays from galaxy clusters under the hypothesis that secondaries play a role. The expected level of γ-ray emission from a Coma-like cluster is at a level few times below present Fermi-LAT limits (Fig. 20.9). Thus future Fermi-LAT observations and especially the Cerenkov Telescope Array (CTA) will be able to put meaningful constraints on the role of CRp for the origin of the cluster-scale synchrotron radiation.

Conclusion

In this chapter we have discussed the physics of CRs in galaxy clusters and their interplay with magnetic fields.

CRs, and CR protons in particular, should be accelerated at shocks associated with cluster formation and potentially in ICM turbulence. Galaxies within the cluster may also supply CRs by way of supernovae and high energy outflows from supermassive black holes in their nuclei. In the last decades it has been understood that the bulk of CR protons deposited within the cluster volume would be magnetically confined there for cosmological times. Therefore, CRs should accumulate at increasing levels over time as the cluster is assembled. In consequence, CR protons may contain a non-negligible fraction of the energy of the diffuse cluster medium. CR electrons, on the other hand, have short lifetimes to radiative energy loss once their energies exceed several 100 MeV or so. Consequently, high energy CR electrons in the ICM pinpoint ongoing mechanisms of *in situ* acceleration and/or a situation in which these high energy particles are continuously resupplied in the ICM.

A notable and unavoidable consequence of CR proton confinement in the ICM is γ-ray emission resulting from decay of neutral pions produced by inelastic $p - p$ collisions involving CR protons and thermal protons. These diffuse γ-rays are potentially detectable by the current and coming

(continued)

generations of γ-ray telescopes. The non-detection of galaxy clusters after almost 4 years of observations with the Fermi-LAT telescope contradicts several optimistic expectations that had been developed from attempts to model CR production in these environments. The failure to detect GeV–TeV γ-rays in any cluster so far limits the energy budget of CR protons in the central (Mpc-scale) regions of galaxy clusters to a few percent of that of the thermal energy. However, this limit still does not imply that CRs are dynamically unimportant in the ICM, because CRs may contribute significantly to the cluster energy budget in the outermost regions of these systems. Most important, current γ-ray limits do not impact on the most important aspect of having CRs and magnetic fields in the ICM; that is, radical changes of the (micro-)physics of the ICM that is potentially induced by these non-thermal components. Even weak magnetic fields will control important transport processes within the ICM, including viscosity and thermal and electrical conductivity. CRs can play important roles in damping turbulence as well as driving instabilities that influence the small-scale structure of the cluster magnetic field.

The physics of CR acceleration in galaxy clusters, in particular CR electrons, can be probed by radio observations that nowadays routinely detect diffuse cluster-scale synchrotron sources; namely, radio halos and relics in a fraction of nearby clusters. One of the most important discoveries in this regard in the last decade is the connection between Mpc-scale radio sources and cluster-cluster mergers. That link suggests that a fraction of the energy dissipated during these energetic events is channeled into the acceleration of non-thermal particles (at least electrons) and in the amplification of cluster-scale magnetic fields. Such a connection opens new fundamental questions on the origin of non-thermal components in the ICM and on their impact on the dynamics and evolution of the hosting clusters.

Nowadays, a promising model for giant radio halos is based on the hypothesis that CRs are reaccelerated by turbulence generated in the ICM during cluster mergers. Turbulence will not accelerate CR electrons directly out of the thermal electron population; some other injection sources are needed. Such seed electrons probably come in various proportions from large scale shocks within the ICM, from energetic phenomena associated with individual galaxies and as secondary $e^{\pm}$ also produced in $p - p$ collisions. The last of these contributors has received much attention. In some models direct secondary electron generation without any reacceleration is used, by itself, to account for the generation of radio halos.

One way to constrain the importance of secondaries in the generation of giant cluster radio halos starts from the Fermi-LAT limits to γ-ray emission. This is especially meaningful when combined with radio frequency information in nearby clusters hosting radio halos. In particular deep radio

(continued)

observations allow detection of the radio emission in these clusters up to their largest spatial scales and provide constraints on the spectrum of radio halos. These studies appear to challenge the classical, pure secondary injection model for radio halos.

A notable expectation of radio halo models based on turbulent acceleration is the existence of a large population of radio halos with very steep spectra. This prediction reflects the intrinsic difficulties of the mechanisms of stochastic acceleration by turbulence in accelerating CR electrons to very high energies, and suggests that clusters with weaker turbulence will produce steeper radio spectra. In the next few years the LOFAR radio telescope will survey the northern sky at still unexplored low radio frequencies with unprecedented spatial resolution and sensitivity to diffuse emission, thus allowing to unveil a large number of these sources if they exist.

In addition to diffuse radio halos, there is a second population of Mpc-scale cluster radio sources that have recently attracted much attention. These are the so-called radio relic or radio Gischt sources seen in the peripheries of some clusters. Like radio halos, relics seem to associated with cluster merger activities. Unlike halos, the relics, in addition to avoiding cluster cores, typically have extents much shorter along the cluster radial direction than normal to it. They also tend to exhibit highly polarized emission, signifying a anisotropic magnetic field. Sometimes relics occur in pairs on opposite sides of the cluster core. There is general agreement on the fact that radio relics originate at shocks waves that cross galaxy clusters during mergers. Theory and observations agree on the fact that merger shocks are relatively weak, with Mach numbers less than a few. In fact they are much weaker than shocks in SN, where efficient CRs acceleration is proved and strong magnetic field amplification is strongly suggested. These processes, that are so important in SNR shocks, should be much less effective in cluster merger shocks, and should lead to a rather steep spectrum compared to those seen in some relics. Thus, while first order, diffusive shock acceleration (DSA) at these shocks is the apparent candidate to explain the CR electron population seen in relics, there are fundamental concerns about the detailed mechanisms. Although the classical model of DSA for locally injected CR electrons could account for properties of some relics, especially those with relatively steep spectra, energy arguments combined with simulations of CR acceleration at weak shocks, suggest in at least some cases, relics may depend on the reacceleration of pre-existing CRs at these shocks. That process is more efficient at extracting shock energy and does not constrain the spectrum of the downstream CR population to the classical DSA value.

Next decade represents a golden age for radioastronomy thanks to the next generation of radio telescopes, such as LOFAR and the SKA pathfinders (ASKAP, MeerKAT). A leap forward for our understanding of non-thermal

(continued)

phenomena in galaxy clusters is expected in next years from these instruments on the way to the SKA (Enßlin and Röttgering 2002; Feretti et al. 2004; Cassano et al. 2010, 2012; Nuza et al. 2012). At high energies, the ongoing Fermi-LAT observations and especially, in the future, the CTA will be able to obtain substantial progress on constraining the CRp component in galaxy clusters and their role for the origin of the cluster-scale synchrotron radiation (Reimer et al. 2004; Pfrommer 2008; Pinzke et al. 2011; Brunetti et al. 2012). Finally we would like to mention that constraining turbulent velocities in the ICM has been receiving much attention in these years (Sunyaev et al. 2003; Dolag et al. 2005; Sanders et al. 2010; Zhuravleva et al. 2012). A significant step in this direction, with potential impact on the physics of non-thermal components in galaxy clusters, is expected in the next years thanks to the X-ray micro-calorimeters onboard of the ASTRO-H satellite (Takahashi et al. 2010).

Acknowledgements GB acknowledge partial support by grant PRIN-INAF2009 and ASI-INAF I/009/10/0. TWJ is supported by NASA grant NNX09AH78G, by US NSF grants AST0908668 and AST1211595 and the Minnesota Supercomputing Institute. We thank Marcus Bruggen, Joseph Lazio and Reiner Beck for helpful discussions and comments.

References

Ackermann, M., Ajello, M., Allafort, A., et al.: ApJ **717**, L71 (2010)
Aharonian, F., Akhperjanian, A.G., Anton, G., et al.: A&A **495**, 27 (2009a)
Aharonian, F., Akhperjanian, A.G., Anton, G., et al.: A&A **502**, 437 (2009b)
Aharonian, F.A., Belyanin, A.A., Derishev, E.V., Kocharovsky, V.V., Kocharovsky, V.V.: Phys. Rev. D **66**, 023005 (2002)
Ajello, M., Rebusco, P., Cappelluti, N., et al.: ApJ **690**, 367 (2009)
Ajello, M., Rebusco, P., Cappelluti, N., et al.: ApJ **725**, 1688 (2010)
Aleksić, J., Antonelli, L.A., Antoranz, P., et al.: ApJ **710**, 634 (2010)
Aleksić, J., Alvarez, E.A., Antonelli, L.A., et al.: A&A **541**, A99 (2012)
Amato, E., Arons, J.: ApJ 653, 325 (2006)
Amato, E., Blasi, P.: MNRAS **392**, 1591 (2009)
Amano, T., Hoshino, M.: ApJ **690**, 244 (2009)
Arlen, T., Aune, T., Beilicke, M., et al.: ApJ **757**, 123 (2012)
Badhwar, G.D., Golden, R.L., Stephens, S.A.: Phys. Rev. D **15**, 820 (1977)
Bagchi, J., Durret, F., Neto, G.B.L., Paul, S.: Science **314**, 791 (2006)
Basu, K.: MNRAS **421**, L112 (2012)
Bell, A.R.: MNRAS **182**, 147 (1978)
Bell, A.R.: MNRAS **182**, 443 (1978)
Bell, A.R.: MNRAS **353**, 550 (2004)
Berezinsky, V.S., Blasi, P., Ptuskin, V.S.: ApJ **487**, 529 (1997)
Berrington, R.C., Dermer, C.D.: ApJ **594**, 709 (2003)
Bhattacharjee, P.: Phys. Rep. **327**, 109 (2000)
Blandford, R., Eichler, D.: Phys. Rep. **154**, 1 (1987)

Blasi, P.: Astropart. Phys. **15**, 223 (2001)
Blasi, P.: Astropart. Phys. **16**, 429 (2002)
Blasi, P.: J. Korean Astron. Soc. **37**, 483 (2004)
Blasi, P., Colafrancesco, S.: Astropart. Phys. **12**, 169 (1999)
Blasi, P., Gabici, S., Brunetti, G.: Int. J. Mod. Phys. A **22**, 681 (2007)
Bonafede, A., Brüggen, M., van Weeren, R., et al.: MNRAS **426**, 40 (2012)
Bonafede, A., Feretti, L., Murgia, M., et al.: A&A **513**, A30 (2010)
Bonafede, A., Govoni, F., Feretti, L., et al.: A&A **530**, A24 (2011)
Briel, U.G., Henry, J.P., Lumb, D.H., et al.: A&A **365**, L60 (2001)
Brown, S., Emerick, A., Rudnick, L., Brunetti, G.: ApJ **740**, L28 (2011)
Brown, S., Rudnick, L.: MNRAS **412**, 2 (2011)
Brüggen, M., Bykov, A., Ryu, D., Röttgering, H.: Space Sci. Rev. **166**, 187 (2012)
Brüggen, M., Scannapieco, E.: MNRAS **398**, 548 (2009)
Brunetti, G.: J. Korean Astron. Soc. **37**, 493 (2004)
Brunetti, G.: A&A **508**, 599 (2009)
Brunetti, G.: MmSAIt **82**, 515 (2011)
Brunetti, G.: J. Astrophys. Astron. **32**, 437 (2011)
Brunetti, G., Blasi, P.: MNRAS **363**, 1173 (2005)
Brunetti, G., Blasi, P., Cassano, R., Gabici, S.: MNRAS **350**, 1174 (2004)
Brunetti, G., Blasi, P., Reimer, O., et al.: MNRAS **426**, 956 (2012)
Brunetti, G., Cassano, R., Dolag, K., Setti, G.: A&A **507**, 661 (2009)
Brunetti, G., Giacintucci, S., Cassano, R., et al.: Nature **455**, 944 (2008)
Brunetti, G., Lazarian, A.: MNRAS **378**, 245 (2007)
Brunetti, G., Lazarian, A.: MNRAS **410**, 127 (2011a)
Brunetti, G., Lazarian, A.: MNRAS **412**, 817 (2011b)
Brunetti, G., Setti, G., Feretti, L., Giovannini, G.: MNRAS **320**, 365 (2001)
Brunetti, G., Venturi, T., Dallacasa, D., et al.: ApJ **670**, L5 (2007)
Buote, D.A.: ApJ **553**, L15 (2001)
Burgess, D.: ApJ **653**, 316 (2006)
Caprioli, D.: J. Cosmol. Astropart. Phys. **5**, 26 (2011)
Carilli, C.L., Taylor, G.B.: Annu. Rev. Astron. Astrophys. **40**, 319 (2002)
Cassano, R., Brunetti, G.: MNRAS **357**, 1313 (2005)
Cassano, R., Brunetti, G., Norris, R. P., et al.: A&A **548**, A100 (2012)
Cassano, R., Brunetti, G., Röttgering, H.J.A., Brüggen, M.: A&A **509**, A68 (2010)
Cassano, R., Brunetti, G., Venturi, T., et al.: A&A **480**, 687 (2008)
Cassano, R., Ettori, S., Giacintucci, S., et al.: ApJ **721**, L82 (2010)
Cassano, R., Gitti, M., Brunetti, G.: A&A **486**, L31 (2008)
Chandran, B.D.G.: Phys. Rev. Lett. **85**, 4656 (2000)
Clarke, T.E., Ensslin, T.A.: Astron. J. **131**, 2900 (2006)
Clarke, T.E., Kronberg, P.P., Böhringer, H.: ApJ **547**, L111 (2001)
Colafrancesco, S., Blasi, P.: Astropart. Phys. **9**, 227 (1998)
Colafrancesco, S., Marchegiani, P.: A&A **484**, 51 (2008)
de Gasperin, F., Orrú, E., Murgia, M., et al.: A&A **547**, A56 (2012)
Deiss, B.M., Just, A.: A&A **305**, 407 (1996)
Dennison, B.: ApJ **239**, L93 (1980)
Dermer, C.D.: ApJ **307**, 47 (1986)
Dermer, C.D.: A&A **157**, 223 (1986)
De Young, D.S.: ApJ **648**, 200 (2006)
Dolag, K., Bartelmann, M., Lesch, H.: A&A **387**, 383 (2002)
Dolag, K., Ensslin, T.A.: A&A **362**, 151 (2000)
Dolag, K., Vazza, F., Brunetti, G., Tormen, G.: MNRAS **364**, 753 (2005)
Donnert, J., Dolag, K., Brunetti, G., Cassano, R., Bonafede, A.: MNRAS **401**, 47 (2010)
Drury, L.O.: Rep. Prog. Phys. **46**, 973 (1983)
Dung, R., Petrosian, V.: ApJ **421**, 550 (1994)

Eckert, D., Produit, N., Paltani, S., Neronov, A., Courvoisier, T.J.-L.: A&A **479**, 27 (2008)
Enßlin, T.A., Röttgering, H.: A&A **396**, 83 (2002)
Ensslin, T.A., Biermann, P.L., Klein, U., Kohle, S.: A&A **332**, 395 (1998)
Ensslin, T.A., Biermann, P.L., Kronberg, P.P., Wu, X.-P.: ApJ **477**, 560 (1997)
Ensslin, T., Pfrommer, C., Miniati, F., Subramanian, K.: A&A **527**, A99 (2011)
Feretti, L., Burigana, C., Enßlin, T.A.: New Astron. Rev. **48**, 1137 (2004)
Feretti, L., Fusco-Femiano, R., Giovannini, G., Govoni, F.: A&A **373**, 106 (2001)
Feretti, L., Giovannini, G., Govoni, F., Murgia, M.: Astron. Astrophys. Rev. **20**, 54 (2012)
Ferrari, C., Govoni, F., Schindler, S., Bykov, A.M., Rephaeli, Y.: Space Sci. Rev. **134**, 93 (2008)
Finoguenov, A., Sarazin, C.L., Nakazawa, K., Wik, D.R., Clarke, T.E.: ApJ **715**, 1143 (2010)
Fujita, Y., Takizawa, M., Sarazin, C.L.: ApJ **584**, 190 (2003)
Fusco-Femiano, R., dal Fiume, D., Feretti, L., et al.: ApJ **513**, L21 (1999)
Fusco-Femiano, R., Landi, R., Orlandini, M.: ApJ **624**, L69 (2005)
Fusco-Femiano, R., Landi, R., Orlandini, M. ApJ 654, L9 (2007)
Fusco-Femiano, R., Orlandini, M., Brunetti, G., et al.: ApJ 602, L73 (2004)
Gabici, S., Blasi, P.: ApJ **583**, 695 (2003)
Giacintucci, S., Venturi, T., Macario, G., et al.: A&A **486**, 347 (2008)
Giovannini, G., Tordi, M., Feretti, L.: New Astron. **4**, 141 (1999)
Gitti, M., Nulsen, P.E.J., David, L.P., McNamara, B.R., Wise, M.W.: ApJ **732**, 13 (2011)
Govoni, F.: Astronomische Nachrichten **327**, 539 (2006)
Govoni, F., Markevitch, M., Vikhlinin, A., et al.: ApJ **605**, 695 (2004)
Hallman, E.J., Jeltema, T.E.: MNRAS **418**, 2467 (2011)
Hanisch, R.J.: A&A **111**, 97 (1982)
Heinz, S., Brüggen, M., Young, A., Levesque, E.: MNRAS **373**, L65 (2006)
Henry, J.P., Finoguenov, A., Briel, U.G.: ApJ **615**, 181 (2004)
Hoeft, M., Brüggen, M.: MNRAS **375**, 77 (2007)
Hoeft, M., Brüggen, M., Yepes, G., Gottlöber, S., Schwope, A.: MNRAS **391**, 1511 (2008)
Iapichino, L., Niemeyer, J.C.: MNRAS **388**, 1089 (2008)
Iapichino, L., Schmidt, W., Niemeyer, J.C., Merklein, J.: MNRAS **414**, 2297 (2011)
Jaffe, W.J.: ApJ **212**, 1 (1977)
Jeltema, T.E., Profumo, S.: ApJ **728**, 53 (2011)
Jokipii, J.R.: ApJ **146**, 480 (1966)
Jones, T.W.: J. Astrophys. Astron. **32**, 427 (2011)
Jones, F.C., Ellison, D.C.: Space Sci. Rev. 58, 259 (1991)
Kaastra, J.S., Bykov, A.M., Schindler, S., et al.: Space Sci. Rev. **134**, 1 (2008)
Kamae, T., Abe, T., Koi, T.: ApJ **620**, 244 (2005)
Kamae, T., Karlsson, N., Mizuno, T., Abe, T., Koi, T.: ApJ **647**, 692 (2006)
Kang, H., Jones, T.W., Gieseler, U.D.J.: ApJ **579**, 337 (2002)
Kang, H., Jones, T.W.: ApJ 620, 44 (2005)
Kang, H., Ryu, D.: ApJ **734**, 18 (2011)
Kang, H., Ryu, D., Jones, T.W.: ApJ **456**, 422 (1996)
Kang, H., Ryu, D., Jones, T.W.: ApJ **695**, 1273 (2009)
Kang, H., Ryu, D., Jones, T.W.: ApJ **756**, 97 (2012)
Kelner, S.R., Aharonian, F.A., Bugayov, V.V.: Phys. Rev. D **74**, 034018 (2006)
Kempner, J.C., Sarazin, C.L.: ApJ **548**, 639 (2001)
Keshet, U., Loeb, A.: ApJ **722**, 737 (2010)
Keshet, U., Markevitch, M., Birnboim, Y., Loeb, A.: ApJ **719**, L74 (2010)
Keshet, U., Waxman, E., Loeb, A., Springel, V., Hernquist, L.: ApJ **585**, 128 (2003)
Kirk, J. G., Schneider, P., Schlickeiser, R.: ApJ **328**, 269 (1988)
Kravtsov, A.V., Borgani, S.: Annu. Rev. Astron. Astrophys. **50**, 353 (2012)
Kushnir, D., Katz, B., Waxman, E.: J. Cosmol. Astropart. Phys. **9**, 24 (2009)
Lazarian, A.: ApJ **645**, L25 (2006)
Lazarian, A., Brunetti, G.: MmSAIt **82**, 636 (2011)
Lazarian, A., Vishniac, E.T.: ApJ **517**, 700 (1999)

Levinson, A., Eichler, D.: ApJ **387**, 212 (1992)
Loeb, A., Waxman, E.: Nature **405**, 156 (2000)
Lucek, S.G., Bell, A.R.: MNRAS **314**, 65 (2000)
Macario, G., Markevitch, M., Giacintucci, S., et al.: ApJ **728**, 82 (2011)
Malkov, M.A., O'C Drury, L.: Rep. Prog. Phys. **64**, 429 (2001)
Marchegiani, P., Perola, G.C., Colafrancesco, S.: A&A **465**, 41 (2007)
Markevitch, M.: arXiv:1010.3660 (2010)
Markevitch, M., Vikhlinin, A.: ApJ **563**, 95 (2001)
Markevitch, M., Gonzalez, A.H., David, L., et al.: ApJ **567**, L27 (2002)
Markevitch, M., Govoni, F., Brunetti, G., Jerius, D.: ApJ **627**, 733 (2005)
McNamara, B.R., Nulsen, P.E.J.: Annu. Rev. Astron. Astrophys. **45**, 117 (2007)
Melrose, D.B.: Plasma Astrohysics. Nonthermal Processes in Diffuse Magnetized Plasmas. Gordon and Breach, New York (1980)
Miley, G.: Annu. Rev. Astron. Astrophys. **18**, 165 (1980)
Miller, J.A., Roberts, D.A.: ApJ **452**, 912 (1995)
Miniati, F.: MNRAS **342**, 1009 (2003)
Miniati, F., Jones, T.W., Kang, H., Ryu, D.: ApJ **562**, 233 (2001)
Miniati, F., Ryu, D., Kang, H., et al.: ApJ **542**, 608 (2000)
Miniati, F., Ryu, D., Kang, H., Jones, T.W.: ApJ **559**, 59 (2001)
Moskalenko, I.V., Strong, A.W.: ApJ **493**, 694 (1998)
Murase, K., Beacom, J.F.: arXiv:1209.0225 (2012)
Norman, C.A., Melrose, D.B., Achterberg, A.: ApJ **454**, 60 (1995)
Nuza, S.E., Hoeft, M., van Weeren, R.J., Gottlöber, S., Yepes, G.: MNRAS **420**, 2006 (2012)
Ohno, H., Takizawa, M., Shibata, S.: ApJ **577**, 658 (2002)
O'Neill, S.M., Jones, T.W.: ApJ **710**, 180 (2010)
Parrish, I.J., Stone, J.M.: ApJ **664**, 135 (2007)
Paul, S., Iapichino, L., Miniati, F., Bagchi, J., Mannheim, K.: ApJ **726**, 17 (2011)
Petrosian, V.: ApJ **557**, 560 (2001)
Petrosian, V., Bykov, A.M.: Space Sci. Rev. **134**, 207 (2008)
Petrosian, V., East, W.E.: ApJ **682**, 175 (2008)
Petrosian, V., Madejski, G., Luli, K.: ApJ **652**, 948 (2006)
Pfrommer, C.: MNRAS **385**, 1242 (2008)
Pfrommer, C., Enßlin, T.A.: MNRAS **352**, 76 (2004)
Pfrommer, C., Enßlin, T.A.: A&A **413**, 17 (2004)
Pfrommer, C., Springel, V., Enßlin, T.A., Jubelgas, M.: MNRAS **367**, 113 (2006)
Pinzke, A., Pfrommer, C.: MNRAS **409**, 449 (2010)
Pistinner, S., Levinson, A., Eichler, D.: ApJ **467**, 162 (1996)
Pinzke, A., Pfrommer, C., Bergström, L.: Phys. Rev. D **84**, 123509 (2011)
Planck Collaboration, Ade, P.A.R., Aghanim, N., et al.: A&A **536**, A8 (2011)
Rafferty, D.A., McNamara, B.R., Nulsen, P.E.J., Wise, M.W.: ApJ **652**, 216 (2006)
Reimer, O., Pohl, M., Sreekumar, P., Mattox, J.R.: ApJ **588**, 155 (2003)
Reimer, A., Reimer, O., Schlickeiser, R., Iyudin, A.: A&A **424**, 773 (2004)
Rephaeli, Y., Gruber, D.: **2002** ApJ **579**, 587 (1999)
Rephaeli, Y., Gruber, D., Blanco, P.: ApJ **511**, L21 (1999)
Ricker, P.M., Sarazin, C.L.: ApJ **561**, 621 (2001)
Riquelme, M.A., Spitkovsky, A.: ApJ 733, 63 (2011)
Roettiger, K., Burns, J.O., Stone, J.M.: ApJ **518**, 603 (1999)
Roettiger, K., Stone, J.M., Burns, J.O.: ApJ **518**, 594 (1999)
Rordorf, C., Grasso, D., Dolag, K.: Astropart. Phys. **22**, 167 (2004)
Rossetti, M., Molendi, S.: A&A **414**, L41 (2004)
Rottgering, H.J.A.: ISKAF2010 Science Meeting (2010)
Rottgering, H.J.A., Braun, R., Barthel, P.D., et al.: arXiv:astro-ph/0610596 (2006)
Rottgering, H.J.A., Wieringa, M.H., Hunstead, R.W., Ekers, R.D.: MNRAS **290**, 577 (1997)
Ryu, D., Kang, H.: Astrophys. Space Sci. **322**, 65 (2009)

Ryu, D., Kang, H., Hallman, E., Jones, T.W.: ApJ **593**, 599 (2003)
Sanders, J.S., Fabian, A.C., Smith, R.K., Peterson, J.R.: MNRAS **402**, L11 (2010)
Sarazin, C.L.: J. Korean Astron. Soc. **37**, 433 (2004)
Sarazin, C.L.: X-ray Emission from Clusters of Galaxies. Cambridge University Press, Cambridge (1988)
Sarazin, C.L.: ApJ **520**, 529 (1999)
Schekochihin, A.A., Cowley, S.C., Kulsrud, R.M., Hammett, G.W., Sharma, P.: ApJ **629**, 139 (2005)
Schekochihin, A.A., Cowley, S.C., Rincon, F., Rosin, M.S.: MNRAS **405**, 291 (2010)
Schlickeiser, R.: Cosmic Ray Astrophysics. Springer, Heidelberg (2002)
Schlickeiser, R., Achatz, U.: J. Plasma Phys. **49**, 63 (1993)
Schlickeiser, R., Sievers, A., Thiemann, H.: A&A **182**, 21 (1987)
Skilling, J.: MNRAS **172**, 557 (1975)
Skillman, S.W., Hallman, E.J., O'Shea, B.W., et al.: ApJ **735**, 96 (2011)
Skillman, S.W., O'Shea, B.W., Hallman, E.J., Burns, J.O., Norman, M.L.: ApJ **689**, 1063 (2008)
Stecker, F.W.: Astrophys. Space Sci. **6**, 377 (1970)
Stephens, S.A., Badhwar, G.D.: Astrophys. Space Sci. **76**, 213 (1981)
Subramanian, K., Shukurov, A., Haugen, N.E.L.: MNRAS **366**, 1437 (2006)
Sunyaev, R.A., Norman, M.L., Bryan, G.L.: Astron. Lett. **29**, 783 (2003)
Takahashi, T., Mitsuda, K., Kelley, R., et al.: Proc. SPIE **7732**, 77320Z-77320Z-18 (2010)
Takizawa, M., Naito, T.: ApJ **535**, 586 (2000)
Thierbach, M., Klein, U., Wielebinski, R.: A&A **397**, 53 (2003)
van Weeren, R.J., Röttgering, H.J.A., Brüggen, M., Hoeft, M.: Science **330**, 347 (2010)
van Weeren, R.J., Röttgering, H.J.A., Rafferty, D.A., et al.: A&A **543**, A43 (2012)
Vazza, F., Brunetti, G., Gheller, C.: MNRAS **395**, 1333 (2009)
Vazza, F., Brüggen, M., Gheller, C., Brunetti, G.: MNRAS **421**, 3375 (2012)
Vazza, F., Brunetti, G., Gheller, C., Brunino, R.: New Astron. **15**, 695 (2010)
Vazza, F., Brunetti, G., Kritsuk, A., et al.: A&A **504**, 33 (2009)
Vazza, F., Dolag, K., Ryu, D., et al.: MNRAS **418**, 960 (2011)
Vazza, F., Roediger, E., Brüggen, M.: A&A **544**, A103 (2012)
Venturi, T.: MmSAIt **82**, 499 (2011)
Venturi, T., Giacintucci, S., Brunetti, G., et al.: A&A **463**, 937 (2007)
Venturi, T., Giacintucci, S., Dallacasa, D., et al.: A&A **484**, 327 (2008)
Venturi, T., Giovannini, G., Feretti, L.: Astron. J. **99**, 1381 (1990)
Völk, H.J., Aharonian, F.A., Breitschwerdt, D.: Space Sci. Rev. **75**, 279 (1996)
Völk, H.J., Atoyan, A.M.: Astropart. Phys. **11**, 73 (1999)
Wentzel, D.G.: , Annu Rev. Astron. Astrophys. **12**, 71 (1974)
Wik, D.R., Sarazin, C.L., Finoguenov, A., et al.: ApJ 696, 1700 (2009)
Wik, D.R., Sarazin, C.L., Finoguenov, A., et al.: ApJ **727**, 119 (2011)
Willson, M.A.G.: MNRAS **151**, 1 (1970)
Wolfe, B., Melia, F.: ApJ **675**, 156 (2008)
Yan, H., Lazarian, A.: ApJ **614**, 757 (2004)
Yan, H., Lazarian, A.: ApJ **731**, 35 (2011)
Zhuravleva, I., Churazov, E., Kravtsov, A., Sunyaev, R.: MNRAS **422**, 2712 (2012)
ZuHone, J. A., Markevitch, M., Lee, D.: ApJ **743**, 16 (2011)

Chapter 21
Turbulence in the Intracluster Medium

M. Brüggen and F. Vazza

Abstract We review our knowledge about turbulence in the intracluster medium, a very hot, dilute plasma that permeates clusters of galaxies. A thorough understanding of turbulence in the intracluster medium is crucial for the use of clusters to determine cosmological parameters. Moreover, clusters provide a unique laboratory to study a very unique and extreme plasma. Both, the observational evidence as well as results from (magneto-)hydrodynamical simulations are reviewed. In particular, we assess the roles of various drivers of turbulence: accretion and merging, active galactic nuclei, the motion of galaxies and conductive instabilities. It has been shown that the turbulence driven by accretion in galaxy clusters is mostly tangential in the inner regions and isotropic in regions close to the virial radius, while AGN drive mostly radial turbulent motions at close to sonic speeds. On the cluster scale, the energetically dominant mechanism for driving turbulence are major cluster mergers. In this chapter, we will focus on turbulent motions on the large scales—the properties of microphysical turbulence are reviewed elsewhere in this book (see the chapter by Brunetti and Jones).

21.1 Introduction

On many scales, astrophysical fluids show signs of turbulence. In the case of the intracluster medium (ICM), the dilute, hot plasma that permeates clusters of galaxies, the contribution of turbulent motions to the total pressure is significant (e.g. Dolag et al. 2005; Subramanian et al. 2006). This has far-reaching consequences. For example, turbulence affects the estimate of the total virial mass of galaxy clusters from X-ray observables (Rasia et al. 2004; Lau et al. 2009). However, only slightly more than 10 % of the total mass of a cluster is made up by the hot ICM that is readily observable. Hence, the total cluster mass must be estimated by either assuming hydrostatic equilibrium or by applying scaling relations between total mass M and other observables, e.g., M–L_x, where L_x is the X-ray luminosity.

M. Brüggen (✉) • F. Vazza
Hamburger Sternwarte, Gojenbergsweg 112, 21029 Hamburg, Germany
e-mail: mbrueggen@hs.uni-hamburg.de

A. Lazarian et al. (eds.), *Magnetic Fields in Diffuse Media*, Astrophysics and Space Science Library 407, DOI 10.1007/978-3-662-44625-6_21

Recently, a new window for studying galaxy clusters has been opened with observations of the Sunyaev-Zel'dovich (SZ) effect. This is produced by the inverse Compton scattering of Cosmic Microwave Background (CMB) photons off the hot ICM. Surveys by a number of facilities, including the the Planck satellite South Pole Telescope (SPT) and the Atacama Cosmology Telescope (ACT) have produced the first SZ-selected cluster samples (e.g., Vanderlinde et al. 2010). The SZ signal is proportional to the gas density which permits observations to larger cluster radii than is typically possible with X-ray observations (the X-ray surface brightness is roughly proportional to the density squared). The flip-side of moving to larger radii is that one is more susceptible to non-thermal pressure support which is far less understood. This may significantly affect the determination of cosmological parameters from SZ surveys (Shaw et al. 2010).

Finally, turbulence can help to accelerate cosmic rays (e.g. Fujita et al. 2003; Cassano and Brunetti 2005; Cassano 2010; Brunetti et al. 2008). Megaparsec-sized radio sources that fill almost the entire cluster volume, so-called radio halos, are believed to be powered by turbulent particle acceleration. The acceleration of particles is generally believed to happen via the second-order Fermi process as a result of the interaction of particle–turbulence interactions(e.g., Brunetti and Lazarian 2007; Brunetti et al. 2008).

In this brief review, we will first summarise the evidence for the presence of turbulence in the ICM and its properties as inferred from observations. Then, we will turn to the computational work on intracluster turbulence and review the major results from simulations of turbulence in clusters. We will conclude by discussing the effects of turbulence in clusters and by outlining the open questions in this field. We should add that this review is heavily biased towards turbulence in the sense of macroscopic fluid motions. As a consequence, we do not pay adequate attention to the interesting (and very complicated) physics that takes place at the lower end of the turbulent cascade (see the chapter by Brunetti and Jones in this volume). Nonetheless, we will mention some developments in this area near the end of the chapter.

21.2 Observational Evidence for Turbulence in the ICM

There are several pieces of evidence for the presence of turbulence in the ICM. Before citing a selection of results from the literature, we would like to point out that due to the typical power-law behaviour of turbulent velocity fields, all turbulent quantities only make sense if they are quoted in combination with the associated length scale. Churazov et al. (2008) inferred the mass profiles from optical and X-ray data in M87 and NGC 1399. Stars act like collisionless particles, so comparing the potentials derived from stellar velocities to those derived from X-ray data can place limits on the nonthermal pressure. Churazov et al. (2008) obtained an upper limit on the nonthermal pressure of $\sim$10 % of the thermal gas pressure.

In the Coma cluster of galaxies, An interesting constraint on turbulence was made by Schuecker et al. (2004), who investigated the power spectrum of pressure fluctuations below ∼100 kpc. They concluded that a minimum of 10 % of the total pressure in Coma stems from turbulence. Schuecker et al. (2004) analyzed the pressure energy spectrum, and found that a range of spectral slopes, in the range $\alpha = -7/3$ to $-1/3$, with $P(k) \propto k^{\alpha}$, is compatible with their measurements. In 3D, an index of −7/3 (cf −5/3 for Kolmogorov spectrum of velocity) corresponds to a pressure power spectrum with a spectral power index of −13/3. Schuecker et al. (2004) found that the spectrum between length scales of 40 and 90 kpc follows largely a projected Kolmogorov-type spectrum. More recently, Sanders and Fabian (2012) examined the surface brightness fluctuations in the cluster AWM 7. The surface brightness fluctuations in the 0.65 keV band are roughly consistent with a power-law power spectrum with a relatively small index of between −5/3 and −6/3.

Rebusco et al. (2006) have examined the metal distribution in galaxy clusters. The distribution of metals around brightest cluster galaxies is wider than the distribution of the stars that produce the metals. Assuming that the turbulent motions are responsible for the spreading of metals, one can measure the turbulent diffusivity and place limits on turbulent velocities, finding that values in the range of a few ∼100 km/s on scales of ∼10–50 kpc can reproduce the data.

Important constraints on the fraction of turbulent and thermal energy in the cores of clusters are also based on the broadening of the lines in the emitted X-ray spectra of cool-core clusters (Sanders et al. 2010). Spectra can be used to determine changes in bulk flows as a function of position in the cluster. Such flows were found using *ASCA* and *Chandra* in Centaurus (Dupke and Bregman 2001, 2006) and other clusters (Dupke and Bregman 2005).

A direct limit on turbulence from X-rays was obtained by Sanders et al. examining the *XMM-Newton* spectra from observations of the galaxy cluster Abell 1835 (Sanders et al. 2010). Since this cluster is at fairly high redshift and has a compact cool core, the line emission is confined to a small region on the sky. The broadening of the emission lines by the spectrometers is therefore small. Sanders et al. found that the ratio of turbulent to thermal energy density in the core of Abell 1835 is less than 13 %.

The ICM can be optically thick for certain wavelengths of resonant lines provided the plasma has the correct temperatures and densities. By measuring the line ratios of (optically thick) resonant and (optically thin) non-resonant lines, the velocity amplitudes of the gas can be inferred. In the Perseus cluster, (Churazov et al. 2004) find that for the strongest 6.7 keV Kα line of He-like iron, the optical depth of the cluster, using observed density, temperature and abundance profiles, is of the order of 3. The lack of evidence for resonant scattering suggests gas motions in the core with velocities of at least half of the sound speed.

The relation between the resonant scattering effects and the velocity field can be used to test anisotropy and spatial scales of gas motions. Resonant scattering also gives us a unique opportunity to put constraints on transverse gas motions in galaxy clusters using polarisation in lines (see Sazonov et al. 2002; Zhuravleva et al. 2010). In the next few years the satellite *Astro-H* with its high spectral resolution will be

able to observationally constrain the energy ratio of turbulence in the ICM of real galaxy clusters (e.g. Zhuravleva et al. 2011).

Finally, there are hints for a turbulent magnetic field in the centre of galaxy clusters from radio polarimetry (e.g. Murgia et al. 2004; Vogt and Enßlin 2005; Guidetti et al. 2008; Bonafede et al. 2010; Vacca et al. 2010). This method relies of the Faraday effect which causes the plane of polarisation to rotate as long as the magnetic field component parallel to the direction of the light propagation is non-zero. The analysis of Faraday rotation maps of extended polarised radio sources located behind or embedded in galaxy clusters can constrain the strength and the structure of cluster magnetic fields. These observations yield values of a few $\sim \mu$G for the central region of galaxy clusters, with the average magnetic field decreasing radially as $B \propto n^{0.6}$, where n is the number density of the gas. The magnetic field model which better describes the available data for Faraday rotation and Faraday dispersion has a power-law behaviour with a spectral slope compatible with the Kolmogorov spectrum, and a typical autocorrelation length of a few tens of kpc (Murgia et al. 2004; Vogt and Enßlin 2005; Bonafede et al. 2010). The resulting magnetic field strengths are comparable with equipartition values and with estimates from radio halos (e.g. Bonafede et al. 2010, for the case of the Coma cluster). Radio relics (e.g., Brüggen et al. 2012, for a recent review) also probe the magnetic field at the site of merger shocks. Values in agreement with the average ICM value at the same radial distance have been reported, although in a few cases the magnetic field in the relic can be much stronger (van Weeren et al. 2010), and this is difficult to explain by turbulent amplification alone (Iapichino and Brüggen 2012).

The bottom line of all these observations is that in cluster centres, the contribution of turbulent pressure to the total pressure is of the order of 10 %, with quite some variation. Despite this rather small value, turbulent energy appears to be the dominant source of non-thermal energy in the ICM of non-cool core clusters, given that the typical magnetic energy density in the innermost cluster region is $\sim 10^{-2}$ of the thermal energy density (Bonafede et al. 2010), and the maximum energy budget of cosmic rays hadrons constrained by recent radio (Brown et al. 2011) and γ-ray (Ackermann et al. 2010) observations is limited to $\leq 5 \cdot 10^{-2}$ the thermal energy density. The typical velocity of the turbulent eddies is a few 100 km/s which makes turbulence sub-sonic (yet super–Alfvénic because the typical Alfvén velocity in the ICM is $v_{\rm A} \sim 100$ km/s). Only for scales below 0.1–1 kpc turbulence gets sub-Alfvenic and obeys the MHD turbulence relations (e.g. Goldreich and Sridhar 1995). The behaviour of turbulence in the ICM at smaller scales is yet to be theoretically understood. Recent theoretical models suggest that the interaction between turbulent modes and the thermal ICM may be collisional at scales much smaller than the Coulomb mean free path, considering that several plasma instabilities can be generated by turbulent motions and drive perturbations in the magnetic field, inducing scattering of charged particles on scales much smaller than the Coulomb mean free path (Brunetti and Lazarian 2011).

Turbulence on scales well above a kiloparsec is essentially hydrodynamic and consists of a mix of compressive and incompressive eddies. However, simulations predict that the turbulent contribution goes up significantly as one moves to larger

radii where the turbulence is not as well explored or constrained observationally. The main results from simulations will be described in the next section.

21.3 Insights from Simulations

Direct numerical simulations of turbulence attempt to follow the turbulent cascade over a certain range of scales. As hydrodynamical simulations have begun to attain dynamic ranges (of ∼2–3 orders of magnitude in scales, e.g. Jones et al. 2011 and references therein), this has become feasible. However, these high-resolution simulations do not resolve the length scale of physical turbulent dissipation, and subgrid turbulent closures that incorporate the evolution and effect of turbulence on unresolved scales have been developed. For examples from astrophysics, (see, e.g. Schmidt et al. 2006; Scannapieco and Brüggen 2008; Maier et al. 2009).

Simulations of density fluctuations using hydrodynamics (Kim and Ryu 2005) found a Kolmogorov slope for low Mach numbers, flattening as the Mach number increased. For 3D compressible magnetohydrodynamical simulations of turbulence, Kowal and Lazarian (2007) found that the energy spectrum of density fluctuations with subsonic turbulence is consistent with −7/3 for strong magnetic fields and the Kolmogorov index of −5/3 for weak magnetic fields. For supersonic turbulence, the density spectrum flattens, as it does in hydrodynamic simulations.

The analysis of simulations of realistic galaxy clusters requires the separation of bulk and turbulent flows, and a number of strategies have been proposed in the recent past. A simple method would be that of computing the turbulent velocity field as the residual respect to the ICM velocity field, averaged over spherical shells from the cluster centre (Lau et al. 2009). Alternatively, one can compute the average velocity field of the ICM via 3D interpolation, and consider as turbulent the velocity structure below the interpolation scale (Dolag et al. 2005; Vazza et al. 2006, 2009, 2011a). Alternative approaches focus on the decomposition of solenoidal and rotational components of the velocity field (Ryu et al. 2008; Zhu et al. 2010), or employ subgrid modelling (Maier et al. 2009; Iapichino et al. 2011). Cosmological simulations agree in that a non-negligible fraction of turbulent energy is stored in the ICM, and increases the more perturbed the systems are. Using SPH simulations, Dolag et al. (2005) showed that the ratio of turbulent to total pressure can be up to a ∼30 % in the innermost region of merging galaxy clusters. This was confirmed later by Valdarnini (2011), using a different SPH method. With a more uniform sampling of the cluster volume using adaptive mesh refinement (AMR) techniques, similar results were reported by Iapichino and Niemeyer (2008), Vazza et al. (2009) and Burns et al. (2010) using various versions of ENZO. The power spectra for the ICM velocity field below a scale of ∼1 Mpc are close to a power-law, with a slope close to or steeper than the Kolmogorov model, $P(k) \sim k^{-\alpha}$ with $5/3 \leq \alpha \leq 2$ (Dolag et al. 2005; Vazza et al. 2009; Xu et al. 2009; Vazza et al. 2011a; Valdarnini 2011). The spectral analysis of turbulent motions were extended to include full MHD case by Xu et al. (2009), who were able to probe the turbulent fluctuation of the magnetic field in the

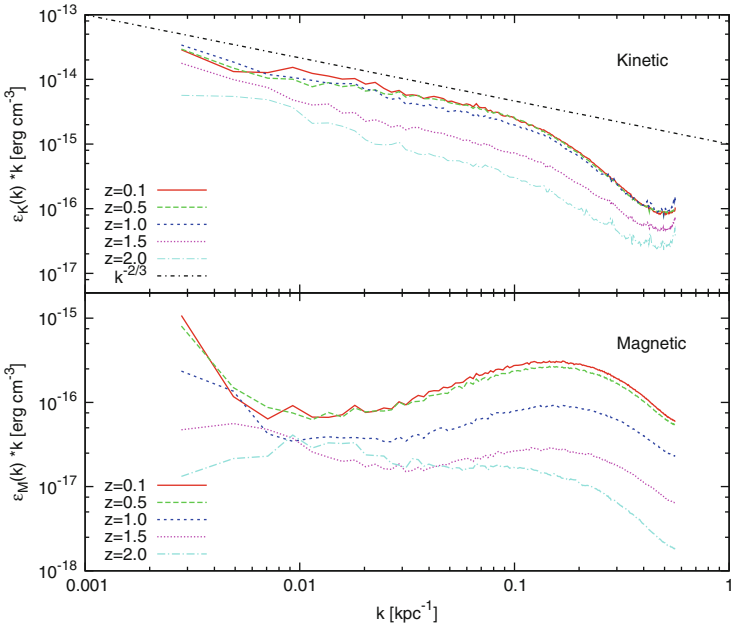

Fig. 21.1 Power spectra of the kinetic energy density and magnetic energy density of the ICM at different epochs. The ICM turbulence is represented by the Kolmogorov-like spectra in kinetic energy. The magnetic energy is amplified via a dynamo process. Figure 21.4 from Xu et al. (2009)

range $\sim$10–10^3 kpc, and showed that the spectral behaviour of the turbulent velocity field is not significantly affected by the simultaneous growth of the weak ($\sim$1 μG) magnetic field in the ICM (see Fig. 21.1). Also the dynamics of the ICM on $\gg$ kpc scales is found to be largely unmodified by the action of magnetic fields in cosmological simulations, when the central value of the magnetic field is tailored to match observations (e.g. Dolag et al. 2001; Collins et al. 2010).

All these methods a priori assume limiting length scales of turbulence, possibly leading to inconsistent results. For instance, for a similar cluster mass the estimated amount of turbulent pressure in the cluster core may range from $\sim$0.2 % of the total gas pressure using sub-grid modelling estimates (Maier et al. 2009) to $\sim$2 % of the total gas pressure by filtering the velocity field with a radial average (Iapichino and Niemeyer 2008), to $\sim$2–5 % by using a filtering scale of $\approx$300 kpc (Vazza et al. 2009).

More recently, Vazza et al. (2012) have published an algorithm to detect turbulent motions in grid simulations, using a multi-scale iterative filtering of the 3D velocity field. With this new technique they studied turbulence driven by mergers in the ICM, by cold fronts and by AGN outflows in the innermost cluster regions, covering in total the large range of scale 1 kpc to 10 Mpc. An example of the application of this technique is shown in Fig. 21.2. Here we show the total velocity field in the centre of mass frame of a 10^{15} $M_\odot$ cluster simulated at high resolution with ENZO, the turbulent field after applying our multi-scale filter and the turbulent field below the

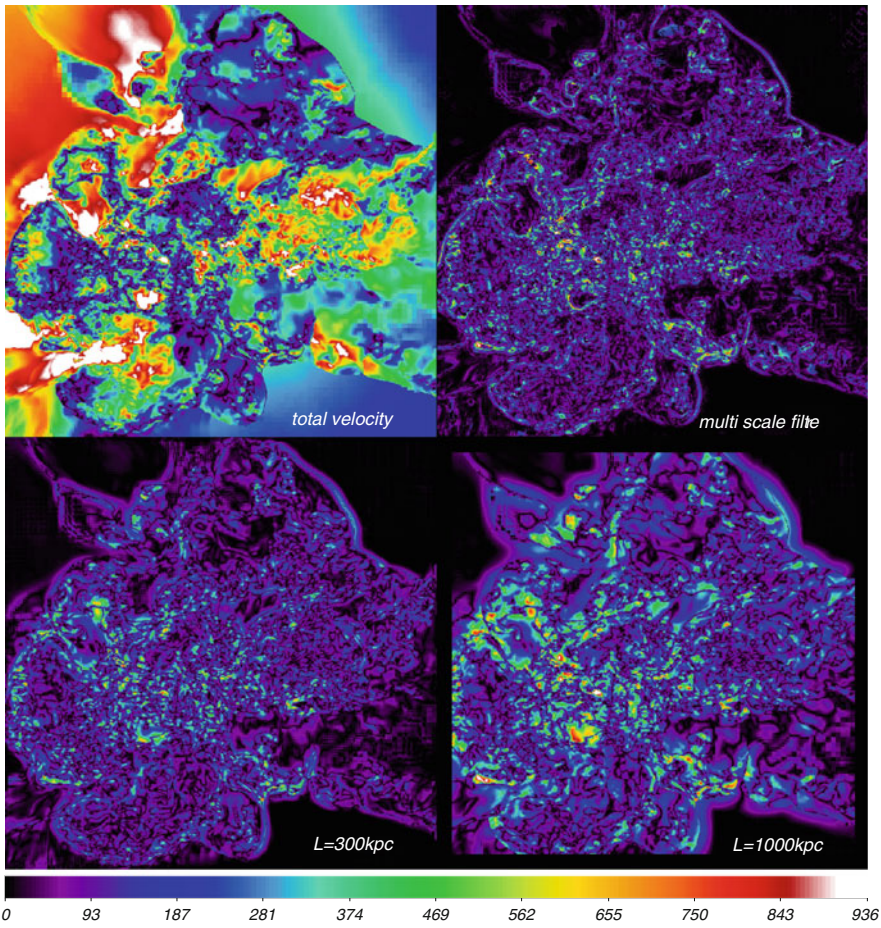

Fig. 21.2 Two-dimensional maps of total gas velocity fields through a cosmological AMR simulation at $z = 0.6$. *Top left* total gas velocity (in [km s^{-1}]); *top right* turbulent velocity field captured by our new multi-scale filter; *bottom left* turbulent velocity field after the removal of $L \geq 300$ kpc scales; *bottom right* turbulent velocity field after the removal of $L \geq 1{,}000$ kpc scales. The side of each panel is 8 Mpc h^{-1}

fixed filtering length of 300 or 1,000 kpc. Inside the cluster, volume-filling chaotic motions have developed, and similar patterns of turbulence are detected regardless of the adopted scale for the filtering. In most of cases, cosmological simulation of this kind are purely hydrodynamical. This is motivated by the fact that on scales >1–10 kpc the dynamical role of a ∼0.1–1 μG magnetic field is negligible (Collins et al. 2010). Moreover, MHD simulations in cosmology are challenging and still in their infancy (e.g. Dolag et al. 2008, and references therein).

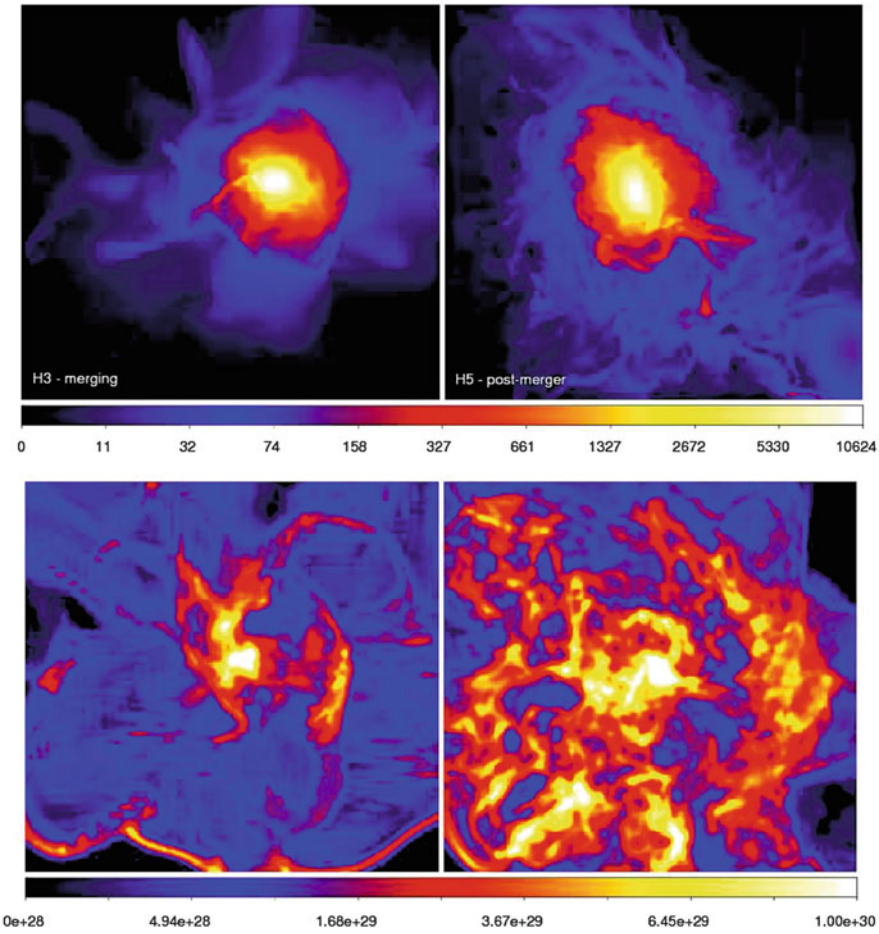

Fig. 21.3 *Top panel* map of gas density for a slice of 100 kpc h^{-1} through the centre of the major merger cluster H5 (*right column*) and of the merging cluster H3 (*left column*). The *top row* shows the projected average gas density (in $[\rho/\rho_{\mathrm{cr,b}}]$, where $\rho_{\mathrm{cr,b}}$ is the critical baryon density), the *bottom row* shows the projected map of the turbulent diffusion for the same regions (in units of $[\mathrm{cm}^2\ \mathrm{s}^{-1}]$)

21.3.1 Turbulence from Cluster Mergers, Active Galactic Nuclei and Cool Core Sloshing

Vazza et al. (2010a) and Vazza et al. (2011a) have studied turbulence in the ICM of relaxed, merging and post-merger galaxy clusters at high resolution. In Fig. 21.3 we show the example of two galaxy clusters simulated with ENZO neglecting magnetic fields. At $z = 0$ these two clusters show very different dynamical states. The upper

panels show the gas density of the two systems, while the lower panels show our estimate for the mass turbulent diffusion in the simulation. In agreement with earlier results by Subramanian et al. (2006) and Iapichino and Niemeyer (2008), the volume filling fraction of turbulent motions (e.g. patches of turbulent velocity field with $> 0.1 c_s$) below a scale of $\sim$300 kpc is not large: it is found to be $\sim$30 % for the central part of post-merger systems, and only $\sim$5 % within the same volume in very relaxed systems.

Another source of turbulence in the ICM comes from the sloshing of the ICM in the gravitational wells of galaxy clusters. These are triggered by mergers and result in so-called cold fronts. These are discontinuities in X-ray brightness and temperature found in many galaxy clusters. They come in two classes (see also review by Markevitch and Vikhlinin 2007): *merger cold fronts* with stronger temperature contrasts across the fronts are the contact discontinuities between the intra-cluster media of two merging clusters, and *sloshing cold fronts* Markevitch et al. (2001) are named after their most likely origin. In the latter, the combined gravitational pull of an accreting sub-cluster displaces the cluster core slightly from the centre of the gravitational potential. After the subcluster has passed the centre, the ICM falls back starts to slosh inside the potential well. This type of cold front may be ubiquitous (Markevitch and Vikhlinin 2007), and high-resolution observations are available for several clusters (see Roediger et al. 2011, and references therein). Measuring the amount of small-scale turbulent motions in these simulations is important because the excitation of turbulence around sloshing cool cores has recently been proposed as a mechanism to power radio mini-halos via turbulent re-acceleration of $\gamma \sim 10^3$ electrons in the magnetised ICM (e.g. Mazzotta and Giacintucci 2008; ZuHone et al. 2011a). In particular, using FLASH MHD-simulations ZuHone et al. (2013) have recently shown that sloshing motions generate turbulence on the order of $\sim$100–200 km/s on spatial scales of $\sim$50–100 kpc within the envelope of the sloshing cold fronts, whereas they produce only negligible turbulence outside this region. This turbulent energy is enough to sustain the radio emission of mini radio halos (of a few $\sim$100 kpc of size) for 1–2 Gyr, by re-accelerating mildly relativistic electrons up to an energy of $\gamma \sim 2 \cdot 10^4$, via resonant interactions with the MHD turbulent waves in the ICM. Besides the superimposed sloshing and rotational large-scale motions, hydrodynamical instabilities, such as Kelvin-Helmholtz (KH) instabilities, produce turbulence.

Powerful outflows from active galactic nuclei can produce turbulent motions, in particular in the innermost region of galaxy clusters. Thus they can play an important role in mixing metals in the ICM, and in lifting cold, low-entropy plasma to greater radii, thus slowing the cooling of gas at cluster centres (e.g. Churazov et al. 2001; Rebusco et al. 2006). Only recently cosmological grid simulations have reached the sufficient dynamic range to model the evolution and feedback of AGN outflows in detail (e.g. Xu et al. 2009; Teyssier et al. 2011; Gaspari et al. 2012). Here, we show the output of a simulation (FLASH 3.2) of an AGN set in an environment modelled on the Hydra A cluster. For details of the simulation, see

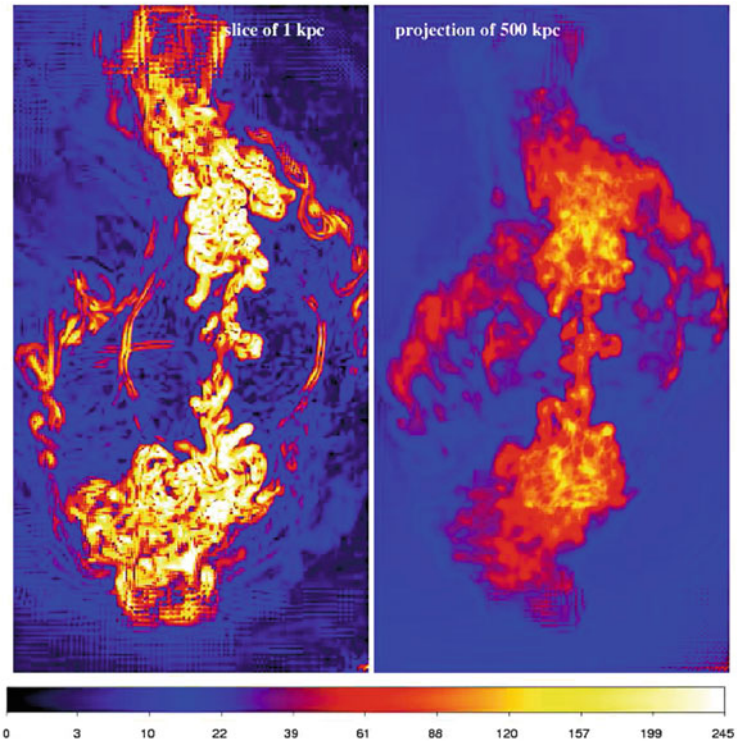

Fig. 21.4 Maps of turbulent velocity module (in units of [km s^{-1}]) for the a slice of 1 kpc centred on the Hydra run (*left*) and for the volume-weighted projection across 500 kpc (*right*). Each image has sides 300 × 500 kpc

Roediger et al. (2012). In the snapshot shown in Fig. 21.4, the jet has a velocity of ∼1,500–1,800 km s^{-1}, and has driven a powerful $M \sim 1.3$ shock into the surrounding ICM.

In cosmological simulations, we find that turbulent velocities are slightly tangential in the inner regions and isotropic in regions close to the virial radius. The same is found for turbulence excited by cool-core sloshing, while a jet produces slightly radial turbulence and isotropic turbulence near its sonic point and beyond.

Once an outer turbulent scale and velocity are determined, the turbulent mass diffusion coefficient in simulations can be measured, and this is of interest because mass diffusion affects entropy profiles and the distribution of metals released by galaxies (e.g. Rebusco et al. 2006). This has been done in Vazza et al. (2012) and is shown in Fig. 21.5 where we present a direct comparison of the volume and mass distribution of turbulent diffusion in the three cases. Turbulent diffusion from cluster mergers in general has a simple distribution with a maximum at $D_{\rm turb} \sim 10^{29} {\rm cm}^2\ {\rm s}^{-1}$ (volume-weighted distribution), with the tendency of post-merger systems to present tails of enhanced diffusion, up to several $\sim 10^{30}\,{\rm cm}^2\ {\rm s}^{-1}$. In the

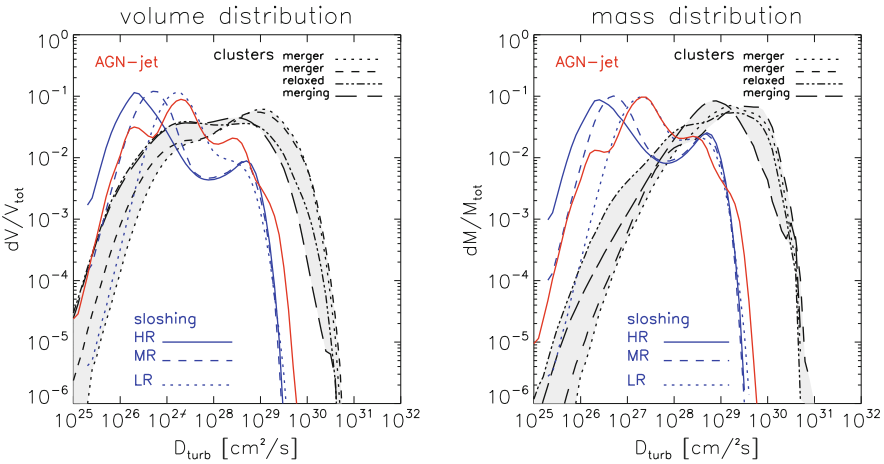

Fig. 21.5 Volume (*left*) and mass (*right*) distribution of turbulent diffusion for all runs studied in this chapter. We show in *red* the turbulent diffusion from the AGN-jet of Hydra, in *blue* the distributions of turbulent diffusion from the sloshing core in Virgo (we plot with different line-styles the distributions at different resolution), and in *black* the turbulent diffusion from cosmological clusters (the different line-styles are for different objects, while the *shadowed* region shows the uncertainty in the overall cluster sample)

sloshing cool core, we observe two maxima in the distribution: one at $\sim 10^{29}$ cm^2 s^{-1} and associated with the innermost turbulent region close to the cluster centre, and one with less efficient diffusion, $\sim 10^{26} - 10^{27}$cm^2 s^{-1}, associated with the Kelvin-Helmholtz rolls along the spiral arms of the sloshing ICM. While the first feature is very stable against the change in resolution, the second one evolves with the increase of resolution because of the effect of a more efficient separation of differential rotation and turbulent KH rolls in our algorithm, and also because of the real onset of KH instabilities at smaller scales in the simulation. The turbulent diffusion in the Hydra A jet is expected to be more time-dependent compared to the other two. The distribution $\sim$160 Myr after the jet launching presents a more complex distribution, owing to different patches of fast diffusion in the jet-ICM regions of interactions.

The maximum values of turbulent diffusion caused by sloshing, AGN or merging fall in the range $D_{\rm turb} \sim 10^{29} - 10^{30}$ cm^2 s^{-1}. Accretion produces a more volume-filling turbulence, and leads to turbulent diffusion that is about one order of magnitude faster than that caused by jets and cool-core sloshing. We note that the average values we measure are of the order of the upper limits derived with XMM-Newton observations of pseudo-pressure fluctuations in Coma ($D_{\rm turb} \leq 3 \cdot 10^{29}$ cm^2 s^{-1}, Schuecker et al. 2004).

A factor that can alter some of our findings is the magnetic field. While its inclusion is not expected to change the dynamics of turbulent motions driven by large-scale mergers and accretion on $\gg$ kpc scales (e.g. Xu et al. 2009; Ruszkowski et al. 2011; Bonafede et al. 2011a), local amplification of the magnetic field in shear

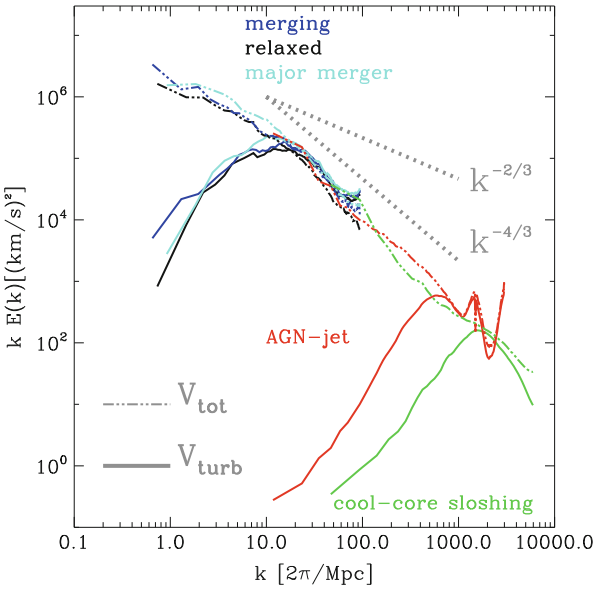

Fig. 21.6 Combined 3D velocity power spectra from three clusters simulated with *ENZO*, for the *FLASH* simulations of the sloshing cool-core in the Virgo cluster and of the AGN-jet in the Hydra cluster. All spectra were normalised to have to obtain the same power at 200 kpc, while the wave numbers k are the physical ones of each simulation. The *dot-dashed lines* show the measured power spectra for the total velocity field in each simulation, while the *solid lines* show the power spectra of the velocity field after the removal of large-scale laminar flows, as Vazza et al. (2012).

flows can suppress the growth of instabilities and mixing motions along the spiral arms of sloshing structures (ZuHone et al. 2011b) and along AGN-jets (O'Neill and Jones 2010), yielding a lower level of small-scale turbulent motions and entrainment of materials along the jets interface.

To resolve the turbulence excited by cluster mergers, sloshing and AGN in the same simulation, one would need to cover scales ranging from $R_{\rm vir} \sim 3$ Mpc down to the presumed scale of physical dissipation at $\sim$0.1 kpc. Instead, we show in Fig. 21.6 a composite velocity power spectra of the turbulent motions from three separate simulations. This plot is meant to illustrate what might be the velocity power spectrum for a cluster of total mass $\approx 3 \cdot 10^{14} M_{\odot}$ and radius $\approx$1,900 kpc, subject to sloshing and a moderately powered jet of $W_{\rm jet} \sim 10^{44}$ erg s^{-1}.

21.3.2 Turbulence by Motions of Galaxies

Various authors have also estimated the amount of turbulence that is produced by the motions of the galaxies through the ICM (Faltenbacher et al. 2005; Kim 2007; Ruszkowski et al. 2011). In general, cluster galaxies can produce turbulence by

two means: (1) As the cold, dense interstellar medium pushes against the external ICM, it produces vorticity, and (2) the gravity of the galaxy causes disturbances in the ICM, similar to dynamic friction. While the volume filling factor of galaxy wakes is small (see Subramanian et al. 2006) they can also excite resonant g-modes, which are gravity waves that are trapped in the cluster. Waves driven at frequencies less than the buoyancy frequency can be resonantly excited, and propagate inward toward the cluster centre (Balbus and Soker 1990), where they will be trapped within a radius where $\omega_{\rm buoyancy} = \omega$. A linear analysis by Balbus and Soker (1990) showed that most of the power in g-modes is in the longest wavelengths. Using three-dimensional MHD simulations, Ruszkowski et al. (2011) have studied the effect of anisotropic thermal conduction and stirring motions due to galaxies orbiting in the cluster potential on the effective cooling rate in cluster cool cores. Such galaxies excite mild subsonic turbulence with $v_{\rm t} \sim 100$–$200\,{\rm km\,s^{-1}}$. They find that a combination of thermal conduction and turbulent heat transport can stabilize the cluster, for realistic parameter choices consistent with gravitational lensing observations of substructure in clusters. In order for galaxies to excite volume-filling turbulence, rather than have turbulence confined to galactic wakes, they must excite g-modes. Overall, the contribution to the turbulent energy budget in the ICM is of the same order to what provided by sloshing cool-cores and AGN activity, and smaller respect to the turbulence driven by cluster mergers, whose injection scale is typically much larger.

21.4 Turbulence by Conductive Instabilities

In a dilute, magnetised medium like the ICM, the mean free path is much larger than the gyroradius. Hence, thermal conduction occurs predominantly along magnetic field lines and is thus anisotropic. In this regime the stability of a stratified plasma is no longer governed by the Schwarzschild criterion. In fact, it turns out that a fluid is always unstable provided that the thermal conduction time is much faster than the buoyant rise time. The most important instability in this context is the magneto-thermal instability (MTI; Balbus 2000; Parrish and Stone 2005) which occurs in cases of radially decreasing temperature gradients. It can be shown to drive convection regardless of the background entropy gradient, and may produce turbulence in cluster outskirts.

McCourt et al. (2011) have shown in simulations with a fixed temperature gradient that the MTI is capable of driving vigorous convective motions that approach supersonic velocities. The motions can amplify the magnetic field as in the convection-driven dynamo in Sec. 21.4. Recently, Parrish et al. (2012) have demonstrated that the MTI, can also produce near-sonic turbulent motions in the outer parts of clusters. However, strong ambient bulk motions triggered, e.g. by accretion can oppose the MTI, as shown by Ruszkowski et al. (2011). The role that conductive instabilities play in driving turbulence in the ICM is still under debate

and it can be expected that this issue is going to be settled by sophisticated numerical work in the next few years.

21.5 Concluding Remarks

We reviewed, both, the observational evidence as well as results from (magneto-)hydrodynamical simulations. In particular, we assess the roles of various drivers of turbulence: accretion and merging, active galactic nuclei, the motion of galaxies and conductive instabilities. A wide range of observational evidence suggests that in cluster centres, the contribution of turbulent pressure to the total pressure is of the order of 10 %, with quite some variation. Observations suggest that in the ICM the turbulent pressure is higher than the magnetic and cosmic ray pressure. Clearly, perturbed clusters show larger turbulent velocities. The typical velocity of the turbulent eddies is a few 100 km/s which makes turbulence sub-sonic (but strongly super–Alfvénic). Turbulence on large scales (i.e. > kpc) is essentially hydrodynamic and consists of a mix of compressive and incompressive eddies. However, simulations predict that the turbulent contribution goes up significantly as one moves to larger radii where the turbulence is not as well explored or constrained observationally.

Moreover, simulations have shown that turbulence driven by accretion in galaxy clusters is mostly tangential in the inner regions and isotropic in regions close to the virial radius, while the jet outflowing from AGN drives mostly radial turbulence motions near its sonic point and beyond. Turbulence in the ICM usually leads to a mass diffusivity in the range $D_{\rm turb} \sim 10^{29} - 10^{30}$ cm^2 s^{-1} in the ICM. On the cluster scale, the energetically dominant mechanism of turbulence driving are major cluster mergers. We showed that the statistical properties of turbulent motions and their evolution with time imply that major merger events are responsible for the injection of the bulk of turbulent kinetic energy into the cluster. The motion of galaxies through the ICM probably only plays a minor role in creating turbulence. The effect of conductive instabilities is still under debate.

Acknowledgements MB and FV acknowledge support through grant FOR1254 from the Deutsche Forschungsgemeinschaft (DFG). FV acknowledges computational resources under the CINECA-INAF 2008–2010 agreement.

References

Ackermann, M., Ajello, M., Allafort, A., et al.: Astrophys. J. **717**, L71 (2010)
Balbus, S.A.: Astrophys. J. **534**, 420 (2000)
Balbus S.A., Soker N.: Astrophys. J. **357**, 353 (1990)
Bonafede, A., Feretti, L., Murgia, M., et al.: Astron. Astrophys. **513**, A30 (2010)
Bonafede, A., Govoni, F., Feretti, L., et al.: Astron. Astrophys. **530**, A24 (2011a)

Brown, S., Emerick, A., Rudnick, L., Brunetti, G.: Astrophys. J. **740**, L28 (2011)
Brüggen, M., Bykov, A., Ryu, D., Rottgering, H.: Space Sci. Rev. **166**, 187 (2012)
Brunetti G., Lazarian A.: Mon. Notices R. Astron. Soc. **378**, 245 (2007)
Brunetti, G., Lazarian, A.: Mon. Notices R. Astron. Soc. **412**, 817 (2011)
Brunetti, G., et al.: Nature **455**, 944 (2008)
Burns, J.O., Skillman, S.W., O'Shea, B.W.: Astrophys. J. **721**, 1105 (2010)
Cassano, R.: Astron. Astrophys. **517**, A10 (2010)
Cassano, R., Brunetti, G.: Mon. Notices R. Astron. Soc. **357**, 1313 (2005)
Churazov, E., Brüggen, M., Kaiser, C.R., Böhringer, H., Forman, W.: Astrophys. J. **554**, 261 (2001)
Churazov, E., Forman, W., Jones, C., Sunyaev, R., Bohringer, H.: Mon. Notices R. Astron. Soc. **347**, 29 (2004)
Churazov E., Forman W., Vikhlinin A., Tremaine S., Gerhard O., Jones C.: Mon. Notices R. Astron. Soc. **388**, 1062 (2008)
Collins, D.C., Xu, H., Norman, M.L., Li, H., Li, S.: Astrophys. J. Suppl. **186**, 308 (2010)
Dolag, K., Bykov, A.M., Diaferio, A.: Space Sci. Rev. **134**, 311 (2008)
Dolag, K., Evrard, A., Bartelmann, M.: Astron. Astrophys. **369**, 36 (2001)
Dolag, K., Vazza, F., Brunetti, G., Tormen, G.: Mon. Notices R. Astron. Soc. **364**, 753 (2005)
Dupke R.A., Bregman J.N.: Astrophys. J. **562**, 266 (2001)
Dupke R.A., Bregman J.N.: Astrophys. J. Suppl. **161**, 224 (2005)
Dupke R.A., Bregman J.N.: Astrophys. J. **639**, 781 (2006)
Faltenbacher, A., Kravtsov, A.V., Nagai, D., Gottlöber, S.: Mon. Notices R. Astron. Soc. **358**, 1089 (2005)
Fujita, Y., Takizawa, M., Sarazin, C.L.: Workshop on Galaxies and Clusters of Galaxies, 75 (2003)
Gaspari, M., Ruszkowski, M., Sharma, P.: Astrophys. J. 746, 94 (2012)
Goldreich, P., Sridhar, S.: Astrophys. J. **438**, 763 (1995)
Guidetti, D., Murgia, M., Govoni, F., et al.: Astron. Astrophys. **483**, 699 (2008)
Iapichino, L., Brüggen, M.: Mon. Notices R. Astron. Soc. **423**, 2781 (2012)
Iapichino, L., Schmidt, W., Niemeyer, J.C., Merklein, J.: Mon. Notices R. Astron. Soc. **414**, 2297 (2011)
Iapichino, L., Niemeyer, J.: Mon. Notices R. Astron. Soc. **388**, 1089 (2008)
Jones, T.W., Porter, D.H., Ryu, D., Cho, J.: Mem. Soc. Astron. Italiana **82**, 588 (2011)
Kim, W.-T.: Astrophys. J. **667**, 5 (2007)
Kim, J., Ryu, D.: Astrophys. J. **630**, L45 (2005)
Kowal, G., Lazarian, A.: Astrophys. J. **666**, L69 (2007)
Lau, E.T., Kravtsov, A.V., Nagai, D.: Astrophys. J. **705**, 1129 (2009)
Maier, A., Iapichino, L., Schmidt, W., Niemeyer, J.C.: Astrophys. J. **707**, 40 (2009)
Markevitch, M., Vikhlinin, A.: Phys. Rep. **443**, 1 (2007)
Markevitch, M., Vikhlinin, A., Mazzotta, P.: Astrophys. J. **562**, L153 (2001)
Mazzotta, P., Giacintucci, S.: Astrophys. J. **675**, L9 (2008)
McCourt, M., Parrish, I.J., Sharma, P., Quataert, E.: Mon. Notices R. Astron. Soc. **413**, 1295 (2011)
Murgia, M., Govoni, F., Feretti, L., et al.: Astron. Astrophys. **424**, 429 (2004)
O'Neill, S.M., Jones, T.W.: Astrophys. J. **710**, 180 (2010)
Parrish, I.J., McCourt, M., Quataert, E., Sharma, P.: Mon. Notices R. Astron. Soc. **419**, L29 (2012)
Parrish, I.J., Stone, J.M.: Astrophys. J. **633**, 334 (2005)
Rasia, E., Tormen, G., Moscardini, L.: Mon. Notices R. Astron. Soc. **351**, 237 (2004)
Rebusco, P., Churazov, E., Böhringer, H., Forman, W.: Mon. Notices R. Astron. Soc. **372**, 1840 (2006)
Roediger, E., Brüggen, M., Simionescu, A., et al.: Mon. Notices R. Astron. Soc. **413**, 2057 (2011)
Roediger, E., Lovisari, L., Dupke, R., Ghizzardi, S., Brüggen, M., Kraft, R. P., Machacek, M. E.: Astrophys. J. **754**, 147 (2012)
Ruszkowski, M., Lee, D., Brüggen, M., Parrish, I., Oh, S.P.: Astrophys. J. **740**, 81 (2011)
Ryu, D., Kang, H., Cho, J., Das, S.: Science **320**, 909 (2008)
Sanders, J.S., Fabian, A.C.: Mon. Notices R. Astron. Soc. **421**, 726 (2012)
Sanders, J.S., Fabian, A.C., Smith, R.K.: Mon. Notices R. Astron. Soc. 1534 (2010)

Sanders J.S., Fabian A.C., Smith R.K., Peterson J.R.: Mon. Notices R. Astron. Soc. **402**, L11 (2010)
Sazonov S.Y., Churazov E.M., Sunyaev R.A.: Mon. Notices R. Astron. Soc. **333**, 191 (2002)
Scannapieco, E., Brüggen, M.: Astrophys. J. **686**, 927 (2008)
Schmidt, W., Niemeyer, J.C., Hillebrandt, W.: Astron. Astrophys. **450**, 265 (2006)
Shaw, L.D., Nagai, D., Bhattacharya, S., Lau, E.T.: Astrophys. J. **725**, 1452 (2010)
Schuecker, P., Finoguenov, A., Miniati, F., Böhringer, H., Briel, U.G.: Astron. Astrophys. **426**, 387 (2004)
Subramanian K., Shukurov A., Haugen N.E.L.: Mon. Notices R. Astron. Soc. **366**, 1437 (2006)
Teyssier, R., Moore, B., Martizzi, D., Dubois, Y., Mayer, L.: Mon. Notices R. Astron. Soc. **414**, 195 (2011)
Vacca, V., Murgia, M., Govoni, F., et al.: Astron. Astrophys. **514**, A71 (2010)
Valdarnini, R.: Astron. Astrophys. **526**, A158 (2011)
Vanderlinde, K., et al.: Astrophys. J. **722**, 1180 (2010)
van Weeren, R.J., Röttgering, H.J.A., Brüggen, M., Hoeft, M.: Science **330**, 347 (2010)
Vazza, F., Brunetti, G., Gheller, C., Brunino, R., Brüggen, M.: Astron. Astrophys. 529, A17 (2011a)
Vazza, F., Brunetti, G., Kritsuk, A., et al.: Astron. Astrophys. **504**, 33 (2009)
Vazza, F., Brunetti, G., Gheller, C., Brunino, R.: New Astron. **15**, 695 (2010a)
Vazza, F., Roediger, E., Brüggen, M.: Astron. Astrophys. **544**, A103 (2012)
Vazza, F., Tormen, G., Cassano, R., Brunetti, G., Dolag, K.: Mon. Notices R. Astron. Soc. **369**, L14 (2006)
Vogt C., Enßlin T.A.: Astron. Astrophys. **434**, 67 (2005)
Xu, H., Li, H., Collins, D.C., Li, S., Norman, M.L.: Astrophys. J. **698**, L14 (2009)
Zhu, W., Feng, L.-l., Fang, L.-Z.: Astrophys. J. **712**, 1 (2010)
Zhuravleva I.V., Churazov E.M., Sazonov S.Y., Sunyaev R.A., Forman W., Dolag K.: Mon. Notices R. Astron. Soc. **403**, 129 (2010)
Zhuravleva, I.V., Churazov, E.M., Sazonov, S.Y., Sunyaev, R.A., Dolag, K.: Astron. Lett. **37**, 141 (2011)
ZuHone, J., Markevitch, M., Brunetti, G.: Mem. Soc. Astron. Italiana **82**, 632 (2011a)
ZuHone, J., Markevitch, M., Lee, D.: Astrophys. J. **743**, 16 (2011b)
ZuHone, J., Markevitch, M., Brunetti, G., Giacintucci, S.: Astrophys. J. **762**, 78 (2013)

Index

A. Lazarian et al. (eds.), *Magnetic Fields in Diffuse Media*, Astrophysics and Space Science Library 407, DOI 10.1007/978-3-662-44625-6